ISSTT 2008

19th International Symposium on Space Terahertz Technology

April 28-30, 2008
Groningen, The Netherlands

Proceedings

Part 1
Oral contributions

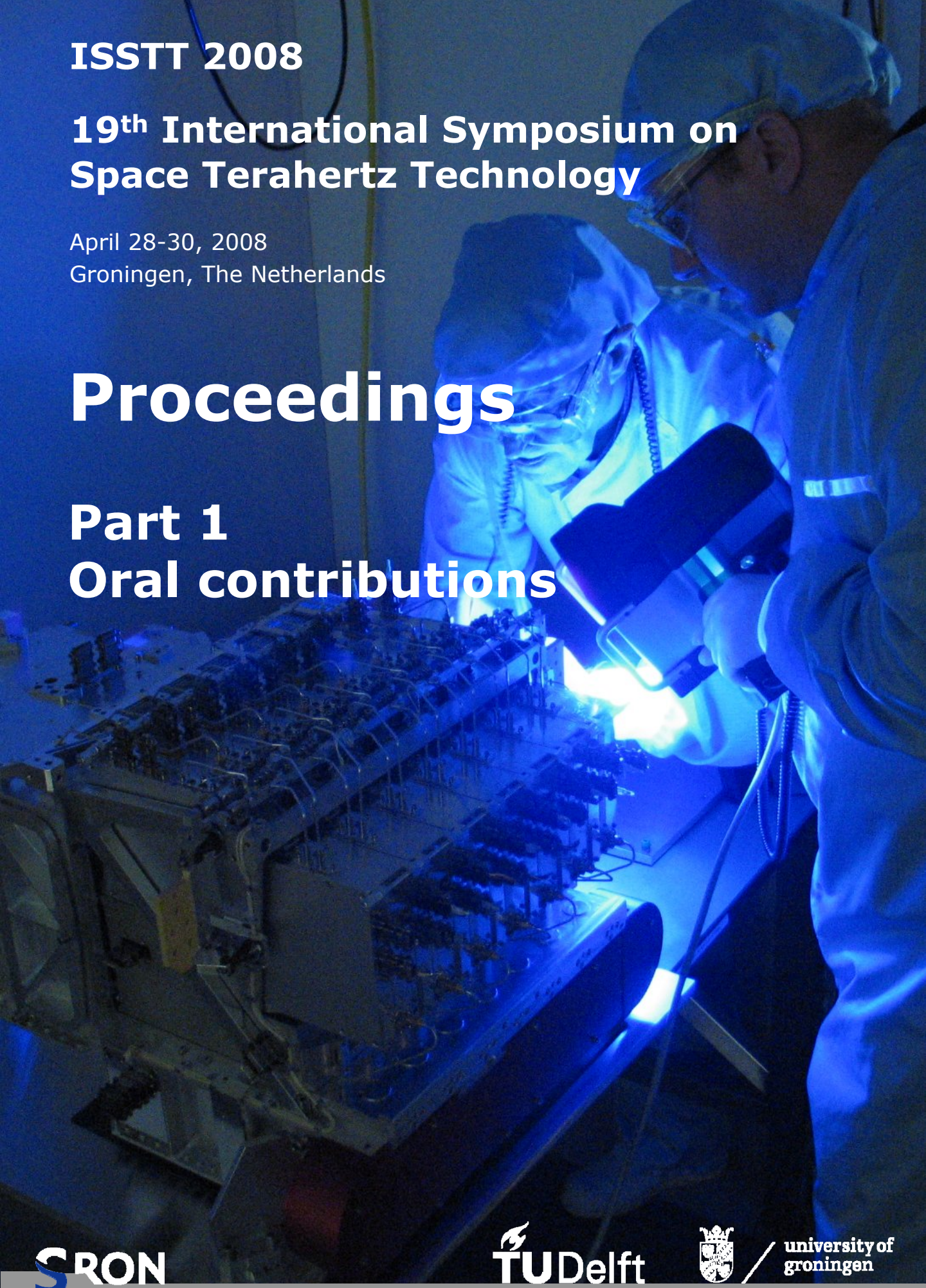

SRON
Netherlands Institute for Space Research
Netherlands Organisation for Scientific Research

TU Delft

university of groningen

Proceedings of the

19th INTERNATIONAL SYMPOSIUM

ON SPACE TERAHERTZ TECHNOLOGY

Groningen, April 28-30, 2008

Edited by Wolfgang Wild

SRON Netherlands Institute for Space Research
TU Delft Delft University of Technology
university of groningen

Preface

The 19th International Symposium on Space Terahertz Technology (ISSTT2008) was held from April 28 to 30, 2008, in the historic main building of the University of Groningen, the Netherlands. It was attended by about 170 scientists and engineers from 17 countries. Almost a quarter (23%) was students working in the field of Terahertz technology.

The Symposium organizers from SRON Netherlands Institute for Space Research, TU Delft, and the University of Groningen want to thank all participants and authors for making this symposium a scientifically interesting and very enjoyable event.

The Academy building of the University of Groningen where the ISSTT2008 Symposium was held from 28-30 April 2008.

A total of 123 scientific contributions have been made to the symposium, 72 as oral presentations and 51 as posters. These proceedings contain all papers that were submitted by 15 October 2008. The accepted abstract was used in case the paper was not available or the author expressed his preference for publication of the abstract.

The number of presentations per category is the following:

Terahertz Systems	5 oral presentations + 2 posters
HEB Mixers	6 oral presentations + 6 posters
SIS Mixers	7 oral presentations + 5 posters
Herschel-HIFI	6 oral presentations + 1 poster
Direct Detectors	6 oral presentations + 6 posters
THz Receivers / Backends	15 oral presentations + 5 posters
Local Oscillators	5 oral presentations + 7 posters
Schottky Mixers	5 oral presentations + 3 posters
ALMA	7 oral presentations + 6 posters
Novel Devices & Measurements	4 oral presentations + 6 posters
Optics & Components	6 oral presentations + 4 posters

The organizers would like to thank the Scientific Organizing Committee for the abstract review and the Local Organizing Committee for taking care of the local arrangements.

Wolfgang Wild

19th International Symposium on Space Terahertz Technology (ISSTT2008)

Scientific Organizing Committee

Victor Belitsky	Chalmers University of Technology, Sweden
Ray Blundell	Harvard-Smithsonian Center for Astrophysics, USA
Tom Crowe	VDI / University of Virginia, USA
Thijs de Graauw	SRON / Leiden Observatory, the Netherlands
Brian Ellison	Rutherford Appleton Laboratory, UK
J.R. Gao	SRON / TU Delft, the Netherlands
Gregory Goltsman	Moscow State Pedagogical University, Russia
Karl Jacobs	KOSMA, Germany
Tony Kerr	NRAO, USA
Teun Klapwijk	TU Delft, the Netherlands
Alain Maestrini	Paris University, France
Imran Mehdi	JPL, USA
Tom Phillips	Caltech, USA
Albrecht Poglitsch	MPE, Germany
Antti Räisänen	Helsinki University of Technology, Finland
Yutaro Sekimoto	NAOJ, Japan
Sheng-Cai Shi	Purple Mountain Observatory, China
Peter Siegel	JPL, USA
Jan Stake	Chalmers University of Technology, Sweden
Wolfgang Wild (chair)	SRON / University of Groningen, the Netherlands
Jonas Zmuidzinas	Caltech, USA

The Symposium Organizers

Wolfgang Wild	SRON / University of Groningen
Thijs de Graauw	SRON / Leiden Observatory
Teun Klapwijk	Delft University of Technology
Jian-Rong Gao	SRON / Delft University of Technology

Local Organizing Committee

Wolfgang Wild chair), Hennie Zondervan, Joost Adema, Petra Huizinga, Nico Sijm, Hans Bloemen, and Jasper Wamsteker

SRON Netherlands Institute for Space Research

TU Delft Delft University of Technology

university of groningen

Table of contents

Session 2 **HEB Mixers** **Chair: Teun Klapwijk**

Session 3 **SIS Mixers** **Chair: Sheng-Cai Shi**

Session 3 **SIS Mixers** **Chair: Sheng-Cai Shi**

Session 4 **Herschel-HIFI** **Chair: Thijs de Graauw**

Session 4 **Herschel-HIFI** **Chair: Thijs de Graauw**

4-6 HIFI Pre-launch Calibration Results **132**

David Teyssier[1], Nick D. Whyborn[2,3], Willem Luinge[2], Willem Jellema[2], Jacob W. Kooi[4], Pieter Dieleman[2] and Thijs de Graauw[2]

[1]*European Space Astronomy Centre, Madrid, Spain*

[2] *SRON Netherlands Institute for Space Research, Groningen, the Netherlands*

[3]*European Southern Observatory, Santiago, Chile*

[4]*California Institute of Technology, Pasadena, USA*

Session 5 **Direct Detectors** **Chair: Jian-Rong Gao**

Session 6 **THz Receivers/ Backends 1** **Chair: Jacob Kooi**

Session 6 **THz Receivers/ Backends 1** **Chair: Jacob Kooi**

Session 7 **Local Oscillators** **Chair: Neal Erickson**

Session 8 **Schottky Mixers** **Chair: Imran Mehdi**

Session 9 **ALMA** **Chair: Wolfgang Wild**

Session 9 **ALMA** **Chair: Wolfgang Wild**

S. V. Shitov[1,2], J. Inatani[1], W.-L. Shan[3], M. Takeda[4], Z. Wang[4], A. V. Uvarov[2], A.B. Ermakov[2] and Y. Uzawa[1]

[1]*National Astronomical Observatory of Japan, Mitaka, Japan*

[2]*Institute of Radio Engineering and Electronics, Russian Academy of Sciences, Moscow, Russia*

[3]*Purple Mountain Observatory, Nanjing, China*

[4]*National Institute of Information and Communication Technology, Kobe Advanced ICT Research Center, Japan*

Session 10 **THz Receivers/ Backends 2** **Chair: Victor Belitsky**

Session 10 **THz Receivers/ Backends 2** **Chair: Victor Belitsky**

Session 11 **Novel Devices and Measurements** **Chair: Paul Richards**

Session 12 **Optics & Components** **Chair: Edward Tong**

SPICA and Its Instrumentation

Takao Nakagawa, for SPICA team

[1]*Institute of Space and Astronautical Science (ISAS), Japan Aerospace Exploration Agency (JAXA), Sagamihara, Japan*

*Contact: nakagawa@isas.jaxa.jp, phone +81-42-759 8370

Abstract— SPICA (Space Infrared Telescope for Cosmology and Astrophysics) is an astronomical mission optimized for mid- and far-infrared astronomy with a cryogenically cooled 3.5 m telescope. Its high spatial resolution and unprecedented sensitivity in the mid- and far-infrared will enable us to address a number of key problems in present-day astronomy, ranging from the star-formation history of the universe to the formation of planets. To reduce the mass of the whole mission, SPICA will be launched at ambient temperature and cooled down on orbit by mechanical coolers on board with an efficient radiative cooling system, a combination of which allows us to have a 3.5-m class cooled (5 K) telescope in space with moderate total weight (3t). SPICA is proposed as a Japanese-led mission together with extensive international collaboration. The assessment study on the European contribution to the SPICA project has started under the framework of the ESA Cosmic Vision 2015-2025. US and Korean participations are also being discussed extensively. The target launch year of SPICA is 2017.

I. Introduction

The advent of infrared astronomical satellites with cryogenically cooled telescopes clearly demonstrated the effectiveness of mid- and far-infrared observations from space. Previous infrared astronomical missions include IRAS ([1]), IRTS ([2]), ISO ([3]), Spitzer Space Telescope ([4]), and AKARI ([5]-[6]). The telescopes onboard these missions were cooled with liquid He, since thermal emission from a telescope is a dominant source of noise in the mid- to far-infrared region. This cooling scheme with liquid He required big cryostats and thereby reduced the telescope aperture size of the previous missions to smaller than 1 m. Thus their spatial resolution was relatively poor, which degraded point-source sensitivity, since the source confusion noise, set by the number of detectable sources in a spatial resolution element, becomes a dominant noise source in the far-infrared.

This situation will be dramatically improved by the Herschel Space Observatory ([7]), which is scheduled to be launched in 2009. Herschel carries a 3.5 m telescope, which is much larger than those of previous missions, and is expected to have much better spatial resolution (and confusion-noise limited sensitivity) than previous missions with telescopes smaller than 1m. However, Herschel's telescope is about 80K, which is not cold enough for mid- and far-infrared astronomy. Hence the point-source sensitivity at the wavelength shorter than 100 μm is limited by the fluctuation of thermal radiation from the telescope.

On the other hand, James Webb Space Telescope (JWST) ([8]) with a 6.5 m telescope operating from 0.6 to 28 μm. JWST will represent a tremendous leap in our ability of observations in the near-infrared. However, the temperature of the JWST telescope is around 45 K, which is again too warm for sensitive observations in the far-infrared, and JWST does not cover wavelengths longer than 28 μm.

Thus, to achieve both good sensitivity and spatial resolution in the mid- and far-infrared, a cryogenically cooled, large telescope in space is required. For this purpose, we have been studying the mission concept SPICA (Space Infrared Telescope for Cosmology and Astrophysics (Fig. 1): SPICA is optimized for the mid- and far-infrared astronomy by employing a cryogenically cooled 3.5 m telescope.

In this paper, we describe the overview of the SPICA mission.

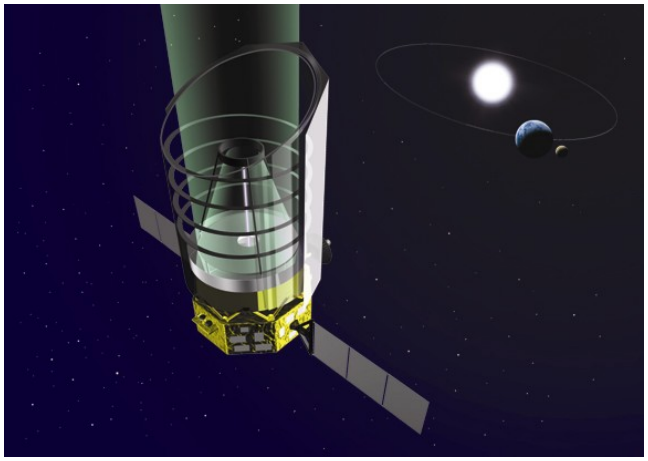

Fig. 1 Artistic view of SPICA in its orbit. SPICA is proposed to be launched into a halo orbit around the S-E L_2 point.

II. Scientific Goals

SPICA is expected play essential roles to address important problems in the current astrophysics. In the following, we make a brief summary of SPICA's scientific goals.

A. Birth and Evolution of galaxies

Birth and evolution of galaxies is one of the biggest problems in astrophysics. SPICA can address this problem in many ways.

SPICA is expected to play a crucial role in this area by resolving Cosmic Infrared Background near its energy peak; SPICA can resolve more than 90 % of the Cosmic Infrared Background into individual sources at 70 μm ([9]-[10], See also the discussion in the next section.)

The mid- to far-infrared wavelength range is very rich with many important fine-structure lines, which are quite useful for the estimate of star-formation activities and AGN activities. Since these lines are less sensitive to extinction, they are expected to bring us essential information on the activities especially in obscured galactic nuclei. The unprecedented sensitivity of SPICA' spectroscopy will revolutionize the study in this area.

One more challenging goal for SPICA is to reveal the formation of the first-generation of stars, i.e. Population III (Pop III) stars. Since the Pop III stars are formed from primordial pre-stellar gas without metals, the gas cannot be cooled through metal lines but is expected to be cooed through molecular hydrogen lines. SPICA will challenge the detection of H_2 emission from large pre-galactic clouds that form metal-free stars.

B. Formation and Evolution of Stellar and Planetary Systems

SPICA is an ideal instrument to assess the formation and evolution processes of stars and planetary systems.

The study of star-formation has been regarded as a holy grail of infrared astronomy, and SPICA is also expected to play essential roles in this area. Photometric and spectroscopic studies of evolved stars are another important area for SPICA.

SPICA is also expected to address the formation processes of planetary systems. SPICA can make very sensitive observations both for gas phase and for solid state matter in the proto-planetary and debris disk systems. This capability of SPICA is essential for the understanding of planetary formation process.

One of the biggest challenges of SPICA is to make the direct detection and spectroscopy of exoplanets. The typical contrast between a central star and planets around it is estimated to be 10^{10} in the optical but to be reduced to 10^6 in the mid-infrared. Thus the mid-infrared is an optimum region to try direct detection of exoplanets. Moreover, SPICA has a smooth, well characterized Point Spread Function (PSF), since SPICA's telescope uses a monolithic mirror, and this characteristic is very important for effective coronagraphic observations ([11]).

Taking advantage of these points, SPICA will make direct observation of exoplanets including their spectroscopy, which is essential to characterize their nature.

C. Chemical Evolution of the Universe

The infrared wavelength is also unique in a sense that both gas phase and solid phase chemistry can be investigated. With its wide spectral coverage and excellent sensitivity, SPICA can observe many, important features (e.g. PAH and Silicate) over a wide range of red-shift to investigate chemical evolution of the universe.

III. Requirements for SPICA

To achieve the scientific goals described in the previous section, SPICA has requirements on the following two aspects: telescope size and telescope temperature.

A. Telescope Size

The telescope size is an essential parameter for astronomical observations. SPICA has various scientific goals which require large telescopes. For example, Fig. 2 shows that a 3m-class telescope is required to resolve cosmic infrared background at its peak energy ([9]-[10]). Other scientific goals also require a 3-m class telescope.

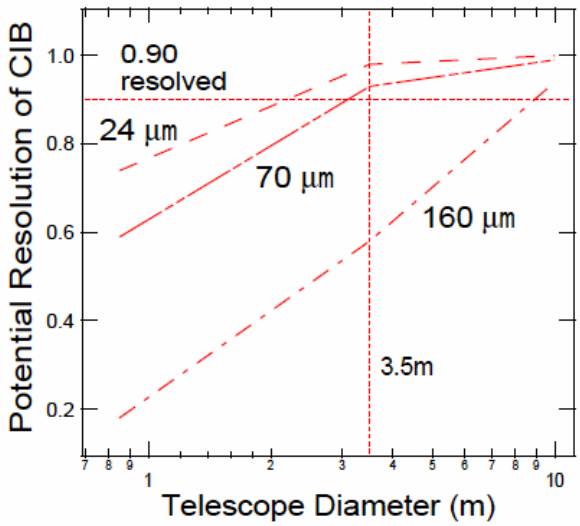

Fig. 2 Potential resolution of cosmic infrared background (CIB) as a function of telescope size and wavelength based on the model calculation by Dole et al[18]. 3.5m class telescopes are required to resolve 90% of CIB into individual sources near the peak of its energy distribution ([9]-[10]).

B. Telescope Temperature

The telescope temperature is another important factor. Fig.3 compares the radiation from the telescope (solid lines) as a function of temperature is compared with natural background sources (dotted lines: zodiacal emission, Galactic cirrus, and cosmic microwave background, [12]. The telescope temperature of around 5 K is required to achieve natural background-limited observations in the mid- and far-infrared.

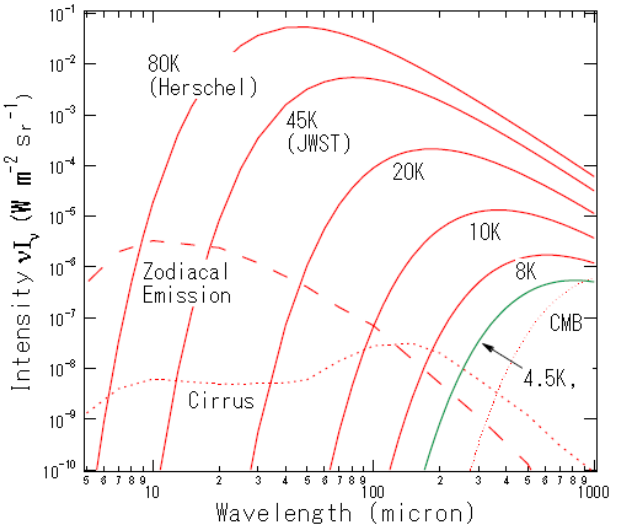

Fig. 3. Telescope background radiation (solid lines) as a function of temperature is compared with natural background sources (dotted lines: zodiacal emission, Galactic cirrus, and cosmic microwave background, [12]). Telescopes as cold as around 5 K are required to achieve natural background-limited observations in the mid- and far-infrared. 10% emissivity is assumed for the telescope emission.

IV. Mission Overview

A. Mission Specifications

Table I summarizes main specifications of the SPICA mission. The most important point is that SPICA incorporates a 3-m class telescope, which is cryogenically cooled. The combination of the low temperature and large aperture size of the telescope makes the SPICA mission the most sensitive instrument in the mid- and far-infrared as clearly illustrate in Figures 4 and 5.

Fig. 6 shows a baseline configuration of the whole SPICA satellite.

TABLE I
MISSION SPECIFICATIONS

MISSION SPECIFICATIONS	
Observation Instrument	
Telescope Aperture Size	3.5 m
Telescope temperature	5 K (during observation) 300 K (at launch)
Diffraction Limit	> 5 μm
Core Wavelength	5-200 μm
Cryogenics	
System	Mechanical Cryocoolers Effective Radiative Cooling
Total Mass	3 t
Launch	
Vehicle	H-IIA
Orbit	S-E L_2 Halo
Year	2017

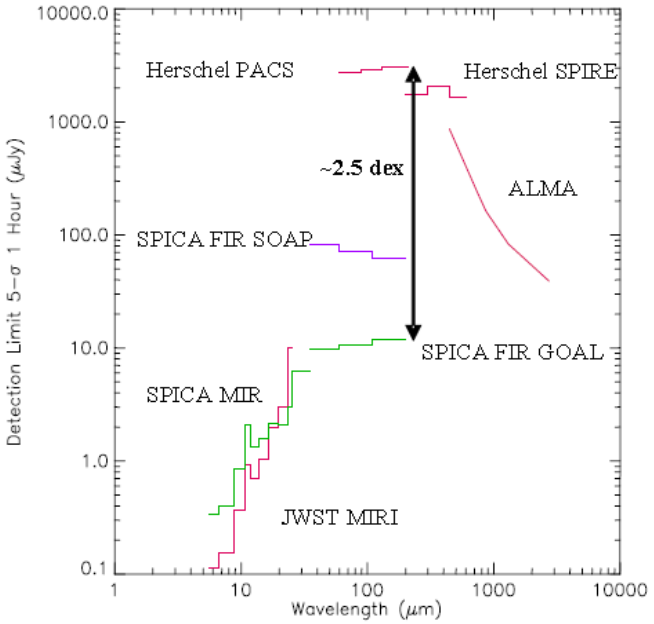

Fig. 4 Predicted photometric performance of SPICA (green and purple) compared to predecessor and complementary facilities (red) given as point source sensitivities in Jy for 5-σ in 1 hour over the bands shown indicatively as horizontal lines. Note the 2 ½ orders of magnitude increase in FIR photometric sensitivity compared to PACS that will be achieved using goal sensitivity detectors on SPICA. The figures here are raw sensitivity only, and the effects of confusion of sources are not included.

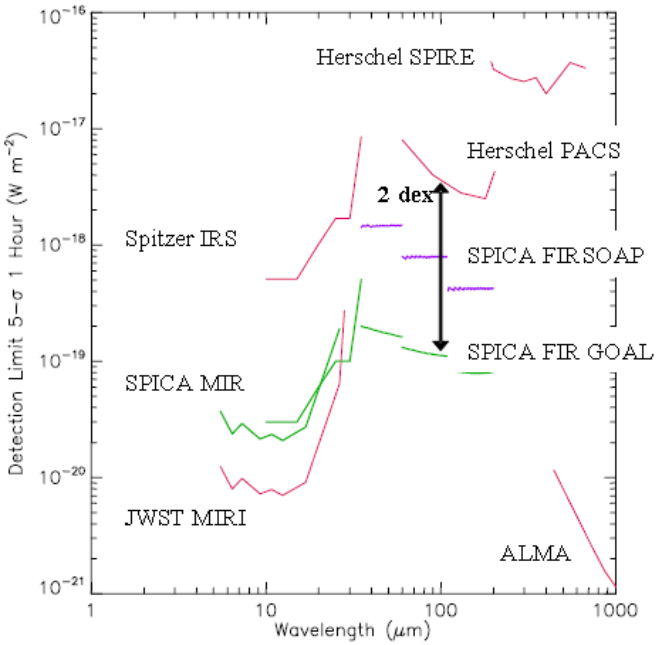

Fig. 5 Predicted spectroscopic performance of SPICA (green and purple) compared to predecessor and complementary facilities (red) given as single unresolved line sensitivity for a point source in W m^{-2} for 5-σ in 1 hour. For ALMA 100 km/s resolution is assumed as this is appropriate for extra-galactic sources. The SPICA MIR sensitivities are scaled by telescope area from the JWST and Spitzer IRS values respectively.

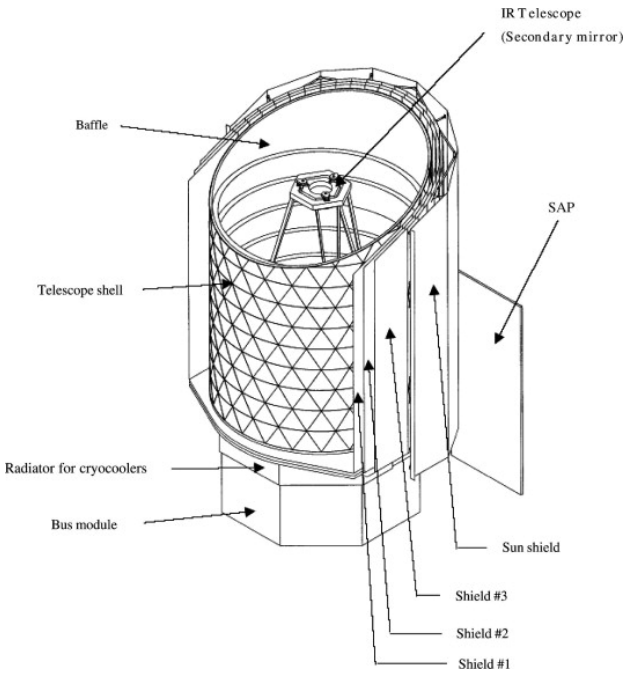

Fig. 6 Base-line configuration of SPICA.

B. *Cryogenics*

To achieve high sensitivity in the mid- and the far-infrared, we have to cool the whole telescope and the focal plane instruments. All of the infrared astronomical satellites flown so far carried liquid helium for cooling; this made the satellites big and heavy and reduced the sizes of the telescopes significantly. Moreover, their mission lives were limited by the hold time of liquid helium, and were relatively short.

To overcome these difficulties, we propose a ``warm-launch, cooled telescope" design concept, i.e., the telescope and focal plane instruments (FPIs) are ``warm" at launch since SPICA will not carry any cryogen. The telescope and the FPIs are to be cooled in orbit by a combination of effective radiative cooling and modest mechanical cryocoolers. Figure 7 shows its conceptual view. The cryogenic system is discussed in detail by [13] and [14].

The ``warm launch" concept without any cryogen reduces the total size significantly and enables the payload fairing of the H-IIA rocket to accommodate a telescope with a 3.5~m primary mirror. The ``warm-launch" concept also reduces the total mass of the mission dramatically; 3.5~m SPICA weighs around 3t.

One of the key technical components for the success of this ``warm launch" concept is mechanical cryocoolers. We have been working on strategic program for the development of cryocoolers for space applications. Some of the cryocoolers developed in this program has already been flown on an X-ray astronomical satellite SUZAKU ([15]) and on a infrared astronomical satellite AKARI ([16]). Other types of coolers dedicated for SPICA is shown in Fig.8.

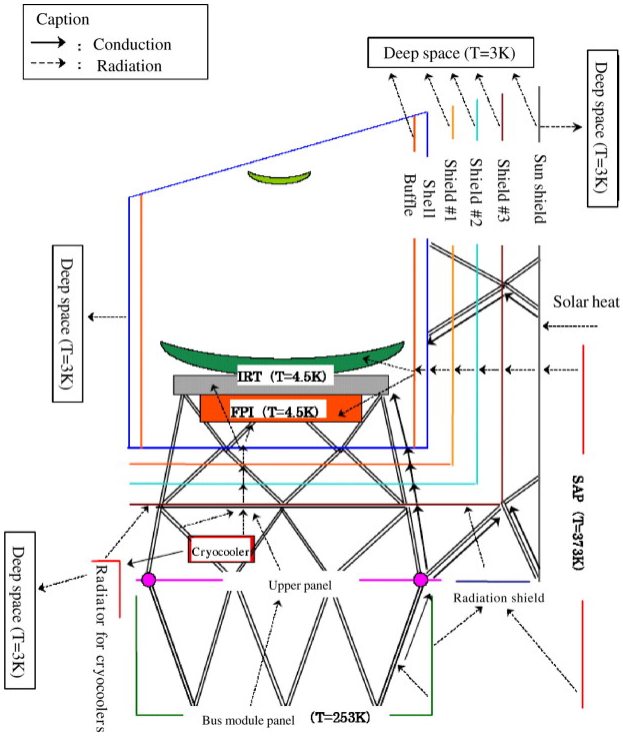

Fig. 7 Conceptual view of the SPICA cryogenic system, which consists of effective radiative cooling system and mechanical cryocoolers ([14]).

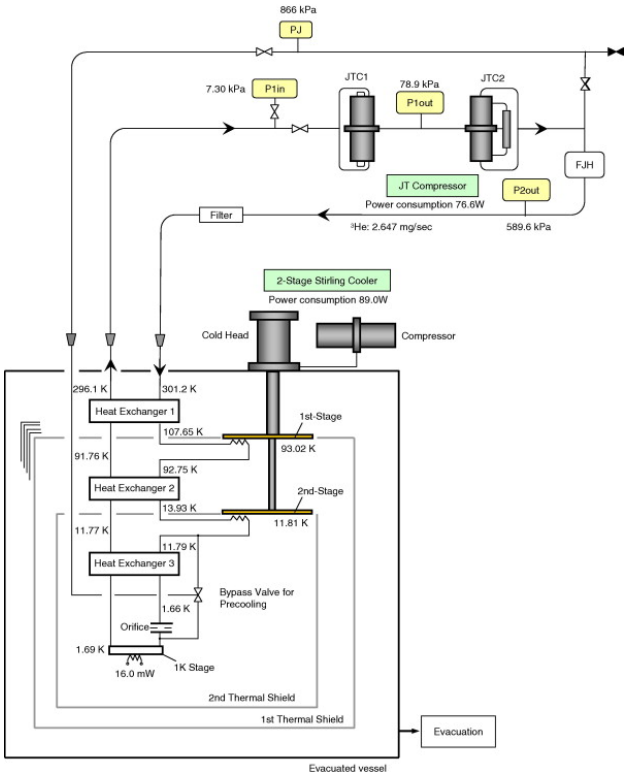

Fig. 8 Schematic view of the configuration of a 1-K class cooler for SPICA together with preliminary experimental results ([14]).

C. Telescope

Table 1 also summarizes the baseline specifications of the SPICA telescope assembly. The baseline model consists of a 3.5 m single aperture, primary mirror, which is required from scientific points view as discussed in the previous section. This size is a good choice also from technical points of view, since the H-IIA rocket fairing can accommodate this size of monolithic mirror and no deployable mechanism is required. This reduces the complexity in the operation at cryogenic temperatures in space.

Because of the high demands on the SPICA telescope system, the selection of the mirror material is of prime importance. At the current study stage, we have two candidate materials, sintered silicon carbide (SiC) and carbon-fiber reinforced SiC (C/SiC composite), for the SPICA telescope mirrors.

Sintered SiC mirrors are employed by Herschel ([7]), and thus benefit greatly from the heritage of their development programs. However, the SPICA requirement on the wavefront error (0.35 μm rms) is by more than one order of magnitude more stringent than that for Herschel (6 μm rms), and dedicated technical program is required to meet the requirements for SPICA.

The C/SiC composite ([17]) has relatively high fracture toughness since carbon fibers are incorporated into SiC. It is easily machined in the carbon-fiber carbon-matrix (C/C) composite stage. These characteristics enable a very light-weighted design of the 3.5 m blank.

Under the current scheme of the international collaboration (see the following sections), ESA is expected to be in charge of the development and manufacturing of the SPICA telescope under the collaboration with JAXA.

V. Focal Plane Instruments

A. Overview of SPICA Focal-Plane Instruments

In order to meet the science requirements discussed in the previous sections, we need at least two types of focal-plane instruments: one is for the mid-infrared and the other is for the far-infrared. Table 2, outlines the specifications of the SPICA focal-plane instruments. On the basis of the scientific requirements described in the previous section, we propose set of focal plane instruments which cover the observation parameter range shown in Fig.8 (see [18] for details).

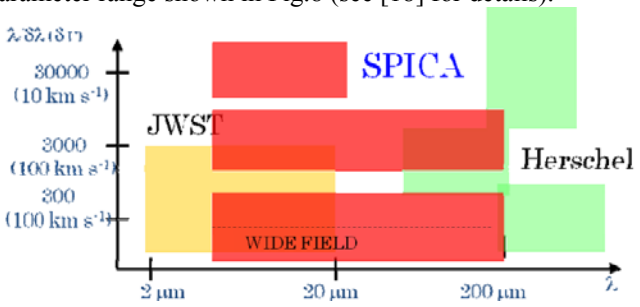

Fig. 8 Spectral coverage and spectral resolving power of focal plane instruments proposed for SPICA, together with those on Herschel and JWST. SPICA is optimized for mid- and far-infrared astronomy.

TABLE II
Proposed SPICA Focal-Plane Instruments

Mid-infrared Camera and Spectrometer	**Imager** Imaging and R~200 grism spectroscopy Field-of-View (FOV): 180 – 280 arcsec
	Spectrometer Long-slit R=3000 spectroscopy at 4-38 μm R=30000 at 5-18 μm
	Coronagraph (Optional) 5-27μm cove rage with contrast > 10^6 Inner working angle 2-5λ/D Outer working angle 10-30λ/D
Far-infrared Camera and Spectrometer	**SAFARI (European Consortium)** 30-210 μm imaging Fourier-transform spectrometer 2 x 2 arcmin2 FOV R = 10 -1000 (variable) Detectors: TBD, Ge:Ga photoconductors or bolometers
	A Broad-band Grating Spectrograph (US concept, Optional) 132-320 (38-430) μm coverage R=300 (700)

B. Mid-infrared (MIR) Instrument

From scientific points of views, MIR instrument is required to have three basic capabilities; a wide-field imaging, spectroscopic capability, and coronagraphic observation capability as shown in Table II.

Our basic strategy is to implement an independent module for each mode of observation. Each module has simple structure and has its own detectors.

The camera has four channels to cover the wavelength range (5 to 40μm) with wide field-of-view. Pixel scale is optimized for the shortest wavelength at each channel to ensure enough sampling for diffraction-limited observations. To achieve wide total FOV, mosaic configurations of several detector arrays are proposed. The camera has several band pass filters ([19]) for wide-band imaging and a grism for low resolution spectroscopy with high efficiency.

The MIR spectrometer is a long slit grating spectrometer possibly with an Integral Field Unit ([20]-[21]). In the shorter wavelength region, high dispersion spectrometer with an immersion grating is used to achieve spectral resolution of R~30000 is proposed ([22]).

We are investigating to implement the coronagraphic capability for the MIR instrument with contrast better than 10^6 with both imaging and low-resolution spectroscopy. The main scientific targets for this instrument is detailed study of proto-planetary and debris disks and also to challenge the direct imaging and spectroscopic observations of exoplanets around near-by stars taking the advantage of relatively small contrast between planets and their main stars. Reference [11] discusses extensive activity on the SPICA coronagraph.

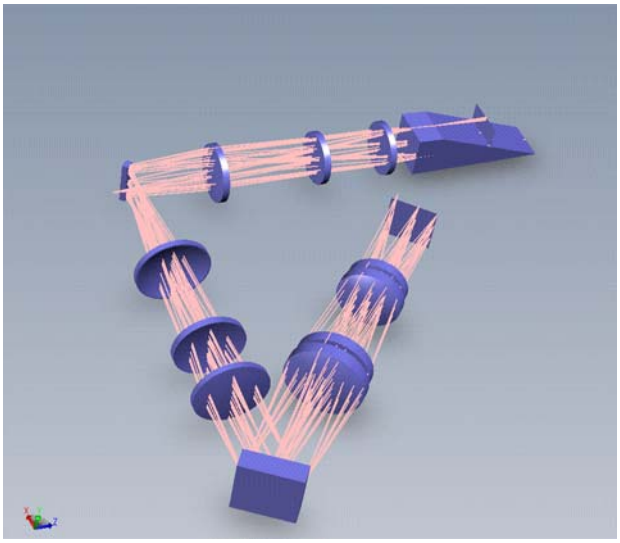

Fig. 9 Schematic view of an example of the optical configuration for the high-resolution spectrometer in the mid infrared. Immersion grating technology enables this compact design ([22]).

C. Far-Infrared (FIR) Instrument

The far-infrared instrument for SPICA has been studied extensively mostly by European Consortium (see below), and the instrument is now named SAFARI (SPICA Far-Infrared Instrument). The baseline optical configuration of SAFARI is a Mach-Zehnder imaging Fourier Transform Spectrometer. The principal advantages of this type of spectrometer for SAFARI are the high mapping speed of the Fourier-Transform Spectrometer (FTS) due to spectral multiplexing, the ability to incorporate straightforwardly a photometric imaging mode and the operational flexibility to tailor the spectral resolution to the science programs.

A possible optical layout of the instrument is shown in Fig. 10. The field of view is 2 arcmin with a spectral resolution higher than 1000.

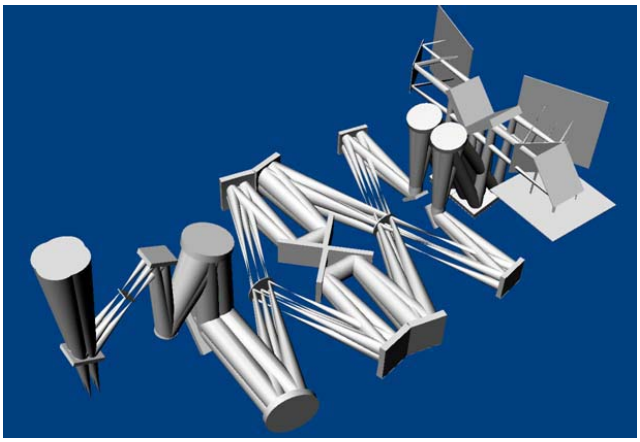

Fig. 10 Schematic view of an example of the optical configuration of the SAFARI instrument, which is designed to make both photometric and spectroscopic mapping observations in the far-infrared using an imaging Fourier-transform spectrometer ([23]).

Another FIR spectrometer which incorporates a grating-spectrometer has been proposed by the US community (BLISS/BASS, [23]).

VI. Current Status and Schedule

A. Status in Japan

In September 2007, the SPICA mission proposal was submitted to ISAS/JAXA by the SPICA working group, who had been working on this mission since 2000. Following that, SPICA went though the Mission Definition Review (MDR, which is a review mostly from scientific points of view) procedure by a dedicated committee, and the results of the review was approved by the Space Science Steering Committee of ISAS/JAXA in March 2008.

Then SPICA went through the Project Preparation Review, which is a management review, by JAXA. The review result was approved and the SPICA pre-project team was formed officially in July, 2008. This means that the SPICA team's activity is officially to be endorsed by JAXA at least during the pre-project phase.

JAXA's pre-project phase roughly corresponds to Phase-A and consists of two phases: "concept design phase" and "system definition phase". At the end of the pre-project phase, we are requested to go through the System Definition Review, which is expected to be held in early 2011 for SPICA. By SDR, we have to define not only technical details but also who is in charge of which parts of the mission. We are also requested to decrease the uncertainty of the cost estimates of the whole project.

Following SDR, we will be requested to go through the Project Go/No-go review, which is a management review by JAXA. This is an important review to decide if SPICA can go to phase-B and later stages. We are proposing to have this review in mid 2011 for SPICA, so that we can launch SPICA in 2017.

B. Status in Europe

The European SPICA Consortium (P.I.: B. Swinyard, RAL, UK) submitted a proposal to enable European participation to SPICA. It was submitted to ESA in June 2007 under the framework of the ESA Cosmic Vision 2015-2025. The proposal called for ESA to assume a partner agency role in SPICA by making the contributions: (1) SPICA Telescope Assembly, (2) European SPICA Ground Segment: (3) SPICA Far-Infrared Instrument System (SAFARI) Engineering and Management, and (4) SPICA Mission support. The proposal also assumed that the SPICA Far-Infrared Instrument System (SAFARI) was to be developed by the European Consortium. The proposal was selected by ESA in October, 2007, as one of the candidates for future missions. Following this, the assessment activity on SPICA lead by ESA started in November 2007.

A harmonised overall schedule incorporating the ESA Cosmic Vision M-class mission schedule, the Japanese SPICA schedule, and the SAFARI schedule has been drafted.

C. Other International Collaborations

Collaborations with US and Korea have been discussed extensively.

Reference [24] discusses BLISS/BASS instrument, which is a possible US contribution for sensitive spectroscopy in the far-infrared as discussed in the provisos section.

ACKNOWLEDGMENT

We are very much grateful to the whole SPICA team.

REFERENCES

[1] Neugebauer, G. et al., "The Infrared Astronomical Satellite (IRAS) Mission", ApJ 278, L1-L6 (1984).
[2] Murakami, H. et al., "The Infrared Telescope in Space (IRTS) mission", PASJ, 48, L41-L44 (1996).
[3] Kessler, M.F. et al., "The Infrared Space Observatory (ISO) mission", A&A 315, L27-L31 (1996).
[4] Werner, M.W. et al., "The Spitzer Space Telescope Mission", ApJS 154, 1-9 (2004).
[5] Murakami, H. et al., "The Infrared Astronomical Mission AKARI", PASJ 59, S369-S376 (2007).
[6] Murakami, H. and Matsuhara, H., "The infrared astronomical satellite AKARI: overview and highlights of the mission", proc. SPIE 7010-9 (2008)
[7] Pillbratt, G.L., "Herschel mission overview and key programmes," proc. SPIE 7010-1 (2008)
[8] Gardner, J.P., "The Scientific Capabilities of the James Webb Space Telescope," proc. SPIE 7010-19 (2008)
[9] Dole, H. et al., "Confusion of Extragalactic Sources in the Mid- and Far-Infrared: Spitzer and Beyond" ApJS 154, 93-96 (2004)
[10] Jeong, W-S. et al. "Far-infrared detection limits - II. Probing confusion including source confusion", MNRAS, 369, 281-294 (2006)
[11] Enya, K. et al. "Mid-infrared coronagraph for SPICA", Proc. SPIE 7010-108 (2008)
[12] Linert, Ch. Et al., "The 1997 reference of diffuse night sky brightness", A&A Suppl. 127, 1-99 (1998).
[13] Sugita, H. et al., "Cryogenic system for the infrared space telescope SPICA", proc. SPIE 7020-109 (2008)
[14] Sugita, H. et al. "Development of mechanical cryocoolers for the Japanese IR space telescope SPICA", Cryogenics, 48, 258-266 (2007).
[15] Kelly, R. L., et al. "Ths Suzaku High Resolution X-ray Spectrometer", PASJ, 59, S77-S112 (2007).
[16] Nakagawa, T., et al. "Flight Performance of the AKARI Cryogenic System", PASJ, 59, S377-S387 (2007).
[17] Kroedel, M.R. "Manufacturing and performance test of an 800 mm space optic", proc. SPIE 7018-10 (2008).
[18] Matsuhara, H. and Kataza, H. "Focal Plane Instruments onboard SPICA", proc. SPIE, 7010-18 (2008)
[19] Sako, S., "Developing metal mesh filters for midinfrared astronomy of 25-40 micron", proc SPIE 7018-194 (2008)
[20] Okamoto, Y.K. et al., "Development of mid-infrared spectrometer with an image slicer (MIRSIS) for ground-based astronomy: developing optical and mechanical mounts," proc. SPIE 7014-80 (2008)
[21] Mitsui, K. et al "Fabrication of the image-slicing optical elements of the mid-infrared spectrometer with an image slicer (MISIS) for ground-based astronomy," proc. SPIE 7014-76 (2008)
[22] Kobayashi, N. et al, "Mid-infrared high-resolution spectrograph for SPICA," proc. SPIE 7010-181 (2008)
[23] Swinyard, B.M. and Nakagawa, T., "European contribution to the SPICA mission," proc. SPIE 7010-17 (2008)
[24] Bradford, C.M., "Sensitive far-IR survey spectroscopy: BLISS for SPICA," proc. SPIE 7020-61 (2008)

Stratospheric Observatory for Infrared Astronomy (SOFIA)

Eric Becklin, Chief Scientist

UCLA

The joint U.S. and German SOFIA project to develop and operate a 2.5-meter infrared airborne telescope in a Boeing 747-SP is now in its final stages of development. Flying in the stratosphere, SOFIA allows observations throughout the infrared and sub-millimeter region, with an average transmission of greater than 80%. SOFIA has a wide instrument complement including broadband imagers, moderate resolution spectrographs capable of resolving broad features due to dust and large molecules, and high resolution spectrometers suitable for kinematics studies of molecular and atomic gas lines at km/s resolution. These instruments will enable SOFIA to make unique contributions to a broad array of science topics. The first successful flight tests of the aircraft with the telescope mounted, began in 2007. First science flights will begin in 2009, and the observatory is expected to operate for more than 20 years. The sensitivity, characteristics, science instrument complement, future instrument opportunities and examples of first light science will be discussed.

The Stratospheric Terahertz Observatory (STO)

An LDB Experiment to Investigate the Life Cycle of the Interstellar Medium

C.K. Walker[1], C.A. Kulesa[1], C.E. Groppi[1], E. Young[1], T. McMahon[1], P. Bernasconi[2], C. Lisse[2], D. Neufeld[2], D. Hollenbach[3], J. Kawamura[4], P. Goldsmith[4], W. Langer[4], H. Yorke[4], J. Sterne[4], A. Skalare[4], I. Mehdi[4], S. Weinreb[4], J. Kooi[5], J. Stutzki[6], U. Graf[6], C. Honingh[6], P. Puetz[6], C. Martin[7], M. Wolfire[8]

[1]*Steward Observatory, University of Arizona, Tucson, AZ 85721, USA*

[2]*Johns Hopkins University Applied Physics Lab, Laurel, MD 20707, USA*

[3]*NASA AMES Research Center, Mountain View, CA 94043, USA*

[4]*Jet Propulsion Laboratory, Pasadena, CA 91109, USA*

[5]*California Institute of Technology, Pasadena, CA 91125, USA*

[6]*Physikalisches Institut, Universitaet zu Koeln, Koeln, 50937 Germany*

[7]*Department of Physics and Astronomy, Oberlin College, Oberlin, OH 44074, USA*

[8]*Department of Astronomy, University of Maryland, College Park, MD 20742, USA*

* Contact: cwalker@as.arizona.edu, phone +1-520-621-8783

***Abstract*— The Stratospheric Terahertz Observatory (STO) is a balloon-borne, 0.8-meter telescope designed to investigate the structure of the interstellar medium and the life cycle of interstellar clouds. In its first long duration flight, STO will use two, 4-beam HEB receiver arrays to survey part of the Galactic Plane in the [C II] line at 158 microns (the brightest spectral line in the Galaxy) and the [N II] line at 205 microns (a tracer of the star formation rate). At ~1' angular resolution and < 1 km/s velocity resolution, STO will detect every interstellar cloud with $A_V > 0.3$ in the surveyed region, and, through excitation and kinematic diagnostics provided by [C II] and [N II] line emission, will illustrate how atomic and molecular clouds are formed and dispersed in the Galaxy. STO will make 3-dimensional maps of the structure, dynamics, turbulence, energy balance, and pressure of the Milky Way's Interstellar Medium (ISM), as well as the star formation rate. In future flights, STO will observe the important far-infrared lines of [O I], [N II], and HD.**

I. Science Goals and Objectives

STO will provide a comprehensive understanding of the inner workings of our Galaxy by exploring the connection between star formation and the life cycle of interstellar clouds. We will study the formation of molecular clouds from diffuse atomic gas, the feedback of high mass star formation on the lives of atomic and molecular clouds, and the effect of these processes upon the global structure and evolution of the Galaxy.

The detailed understanding of star formation and evolution of stars and gas in the Galaxy is directly relevant to star formation in other galaxies. The nature of the feedback mechanism of massive star formation with its interstellar environment is pivotal to the evolution of galaxies.

In its first flight, STO addresses the following high priority goals:

1. Determine the life cycle of Galactic interstellar gas.
2. Study the creation and disruption of star-forming clouds in the Galaxy.
3. Determine the parameters that affect the star formation rate in a galaxy.
4. Provide templates for star formation and stellar/interstellar feedback in other galaxies.

STO will utilize two heterodyne receiver arrays to produce a total of eight ~1' pixels in the focal plane, each with 1024 spectral channels. In the first long duration (10-14 day) flight, STO will map a 35 square degree area ($-20^o > l > -55^o$; $|b| < 1^o$, see Figures 1 and 2) spanning the Molecular Ring, the Crux-Scutum-Centaurus spiral arm, and at least one interarm region. Two deeper, 1/2 square degree maps will be performed within the larger survey in both arm and interarm regions. STO has the sensitivity to detect and the ability to resolve spectrally and spatially all Giant Molecular Clouds (GMCs), all significant HII regions, and all cold neutral medium (CNM) atomic clouds with $A_V > 0.3$ mag in the surveyed region.

The STO heterodyne receivers provide sub-km/s velocity discrimination and sufficient bandwidth to detect and resolve line emission from every Galactic cloud in the surveyed region. The data product will be a high fidelity database of spatially and velocity resolved far-infrared [C II] 158 micron and [N II] 205 micron fine-structure line emission in the Galaxy.

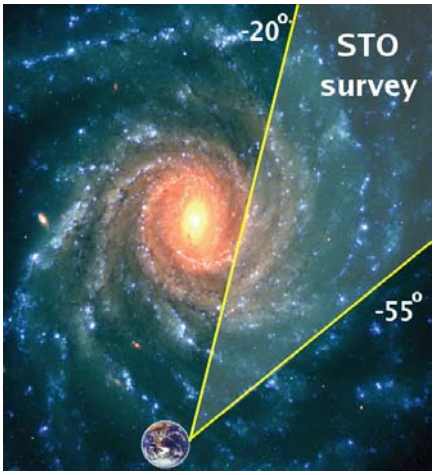

Fig. 1 STO will survey 35 square degrees of the plane of the Milky Way in the Terahertz fine structure lines of ionized carbon and nitrogen. This longitudinal swath of the fourth quadrant reveals major components of the Galactic Interstellar Medium, such as the molecular ring, the Scutum-Crux spiral arm, and two interarm regions.

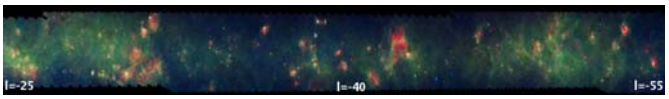

Fig. 2 This composite map of the Galactic plane from 3.5 through 24 microns, from Spitzer's MIPSGAL and GLIMPSE surveys, shows a rich and dynamic interstellar medium revealed by thermal dust emission. The STO survey will provide complementary high resolution spectroscopic followup that will put these structures in a 3-dimensional context and connect dust properties to the associated gas.

A combination of STO's data products with existing line and continuum surveys will characterize the structure and dynamics of interstellar clouds and their relation to star formation. STO's potential for additional flights provides the ability to more fully map the Galaxy in the [C II] and [N II] lines and to change receivers to include other important interstellar lines such as [N II] at 122 microns, [O I] 63 & 145 microns, and HD at 112 microns wavelength.

STO is timely. It will provide the best corresponding interstellar cloud survey to the GLIMPSE[1] and MIPSGAL[2] Spitzer programs (Figure 1) and contemporary HI and CO line surveys. STO will enhance the interpretation of these data sets by completing the observational links required to trace the cloud life cycle. In addition, STO complements other [C II] and [N II] observations taken on the Cosmic Background Explorer (COBE) and the Balloon-borne Infrared Carbon Explorer (BICE) in having much greater spatial and spectral resolution. Using Galactic rotation to place the clouds along the line of sight, STO's high spectral resolution enables 3 dimensional maps of Galactic interstellar matter, from which many physical parameters in the Galaxy (e.g., pressure and star formation rate) can be extracted.

STO also complements the capabilities of heterodyne receivers on contemporary far-IR platforms. The Herschel Space Observatory (Science phase: 2009-2013) and the Stratospheric Observatory for Infrared Astronomy (SOFIA, 2009+) will have the capability to observe both [C II] and [N II] using the same high spectral resolution heterodyne techniques used on STO. However, due to their much larger apertures each facility will map only a few percent of the area of STO's first survey during their lifetimes.

II. Instrument Description

The observational goal of the first STO flight is to make high spectral (< 1 km/s) and angular resolution (~1 arcminute) maps of the Galactic plane [N II] at 1.45 THz (205 micron) and [C II] at 1.9 THz (158 micron). To achieve the angular resolution requirement we have designed STO to utilize an aperture of 80 cm. To achieve the target spectral resolution, STO will utilize a heterodyne receiver system. STO will be a long duration, balloon-borne observatory which will be launched from McMurdo, Antarctica to an altitude of 120,000 ft, where it will remain for ~14 days. The instrument portion of STO consists of (1) the telescope (2) eight heterodyne receivers: four at the1.5 THz [N II] line and four at the 1.9 THz [C II] line, (3) an eight-channel FFT spectrometer system, (4) the instrument control electronics, (5) the hybrid ^{4}He cryostat, and (6) the gondola.

A. Telescope System

STO will use the same telescope and gondola that Johns Hopkins University Applied Physics Laboratory has previously employed for its successful Flare Genesis Experiment[3] (FGE) depicted in Figures 3 and 4. The primary mirror is an 80-cm diameter, f/1.5 hyperboloid made of Ultra Low Expansion titanium silicate glass (ULE), and honeycombed to a weight of just 50 kg. Its surface is polished to visible-band optical quality, therefore over-specified for imaging in the 100 to 200 micron wavelength range. Its support and spider arms are made of light weight graphite-epoxy, which provides high thermal stability over a wide range of temperatures. Figure 3 shows the FGE telescope during a Sun pointing test session.

A tertiary chopper will be located near the backside of the main mirror on a counterbalanced mount to minimize reaction forces. A calibration box will be located between the telescope and the receiver cryostat. This subsystem places blackbody loads at known temperatures in the path of the detectors. One of the loads is allowed to come into thermal equilibrium with the temperature of the surrounding air; its temperature is monitored and recorded by an embedded sensor. Another load is located on the 77K stage of the receiver cryostat. Periodic measurements of the power

radiated from these loads allow determination of the detector gain. The power from these loads will also be compared to the variation in power resulting from a change in telescope elevation. These measurements suffice to determine the detector noise, the telescope efficiency, the opacity of the atmosphere and the absolute flux of astronomical sources[4].

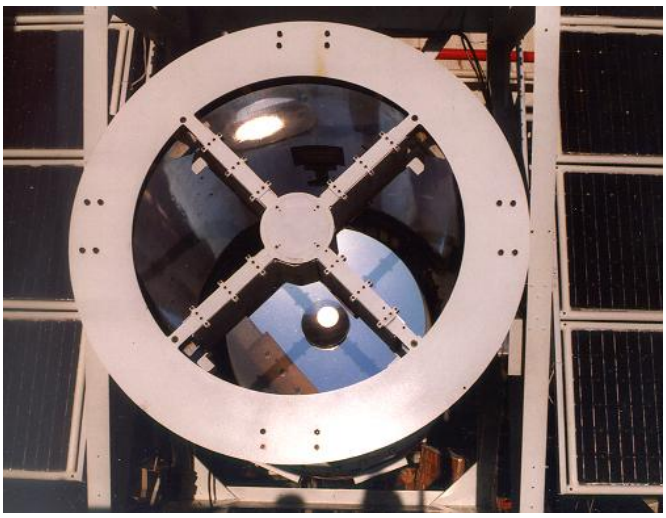

Fig. 3 The 80 cm telescope to be used for STO is the same as deployed for the Flare Genesis Experiment in 1995/6 and 1999/2000. Here, the FGE telescope is being tested, pointing at the Sun.

Characteristic	**Design Specification**
Telescope Aperture	80 cm
Telescope Type	on-axis Cassegrain
Spectral Range	60 to 210 microns
Pointing Knowledge	15 arcseconds
Target Frequencies	[C II] 1.901 THz [N II] 1.461 THz
Angular Resolution	1-1.5 arcminutes
Receiver Type	Two, 4-pixel HEB Mixer Arrays
Receiver Noise	< 2000 K DSB
Spectrometer Type	8 FFT digital analyzers
Spectral Bandwidth	1 GHz (~200 km/s)
Channel Resolution	1 MHz (~0.2 km/s)
Cryogenic System	^{4}He + 77K cryocooler
Cryostat Hold Time	> 14 days

TABLE 1: SUMMARY OF STO MISSION REQUIREMENTS

Fig. 4 The Flare Genesis Experiment (FGE) gondola and telescope just before its launch from Antarctica in 2000. The STO mission will use nearly the same flight configuration for its Antarctic flight in late 2010.

B. Receiver Description

A cut-away view of the STO cryostat showing the placement of the receiver system is shown in Figure 5. A block diagram of the instrument is shown in Figure 6 and a diagram showing integration with the telescope is shown in Figure 7.

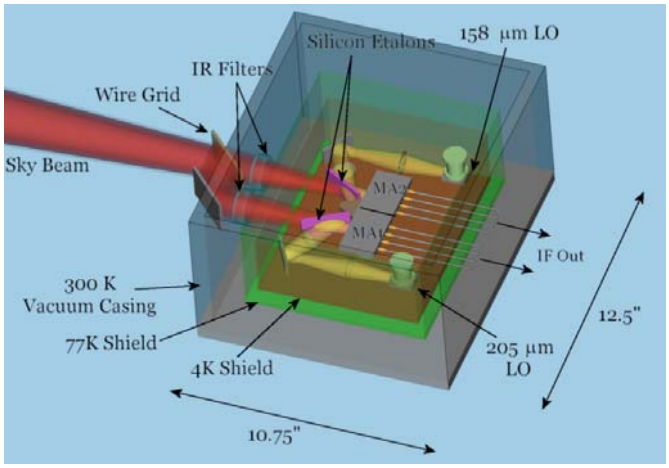

Fig. 5 Three-dimensional cutaway of the STO receiver cryostat.

The f/7 telescope beam first encounters a free-standing wire grid that divides the incident light into horizontal and vertical polarization components. One polarization passes through the grid into the first vacuum window. The other polarization reflects off a 45° mirror and enters a second vacuum window. The vacuum windows and subsequent 77, 25, and 4K IR filters are made from low-loss, AR coated, single crystal quartz. The first flight receiver will consist of

two, orthogonally polarized 1x4 arrays of superconductive hot-electron bolometer (HEB) mixers operating at 4K. One array is optimized for the [C II] (1.90 THz) line, the other for the [N II] (1.46 THz) line. The mixers will be pumped by two, frequency tunable, solid-state Local Oscillators (LO's). To increase output power, the final multiplier stage is mounted to the 77K radiation shield.

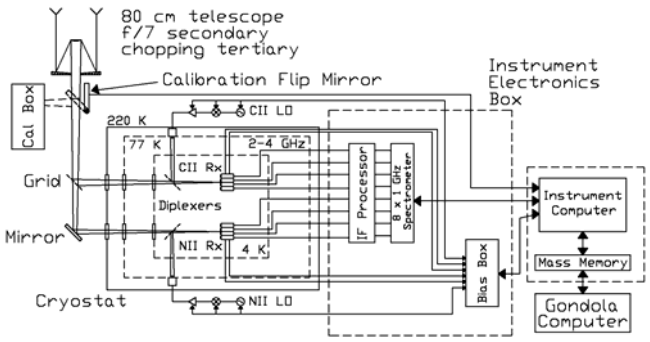

Fig. 6 Block diagram of STO instrument subsystems.

Eight, low-noise, IF amplifiers will be mounted to the 25K radiation shield of the cryostat. The IF center frequency will be 1.5 GHz, with an instantaneous bandwidth of 1 GHz. This IF frequency and bandwidth can be supported by NbN phonon-cooled mixers. At our highest observing frequency (1.9 THz, the [C II] line) a 1 GHz IF bandwidth will provide 160 km/s of velocity coverage. A velocity coverage of this order is needed to accommodate the wide velocity dispersion expected toward the inner parts of the Galaxy. Doppler tracking of the LO frequency will keep the received signal centered within the IF band. The eight IF signals from the mixers pass through an ambient temperature IF processor where they are further amplified and downconverted to baseband (0-1 GHz). STO will use eight 1 GHz wide, 1024 channel digital FFT analyzers as backend spectrometers for the mixer arrays. A flight instrument electronics box will house (1) the IF processor board, (2) the 8x1 GHz spectrometer boards, (2) the LO/HEB/LNA bias board, (4) calibration flip mirror controller board, and (5) the Instrument Computer. The Instrument Computer communicates to the Gondola computer via a RS-422 bus.

STO will use a 200 liter, ^{4}He cryostat to cool the mixer arrays. An off-the-shelf mechanical refrigerator will cool the first radiation shield to 77K. The second radiation shield will be vapor-cooled to 25K. The expected hold time is > 14 days.

C. STO Gondola Structure

The STO observing platform (gondola), shown in Figure 7 is the one previously used by APL for its FGE[3] (Figures 3 and 4) and SBI[5] balloon programs. The gondola has successfully endured two test flights in New Mexico (in 1994 and 2003) and three Antarctic flights (in 1996, 2000, and 2006). During the past ten years the gondola and its subsystems have undergone many improvements and upgrades. The STO project will benefit directly from this flight heritage.

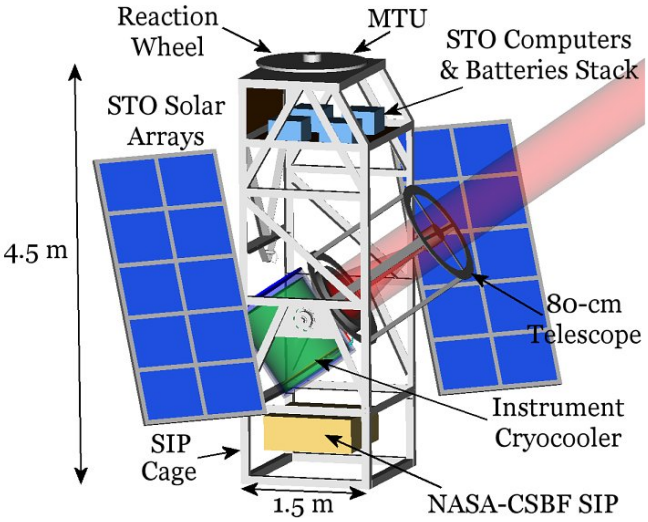

Fig. 7 Three-dimensional rendering of the STO gondola package, including 80 cm telescope and science payload.

The gondola carries and protects the telescope and instrument, the command and control systems, and the power system. Its basic dimensions (without solar arrays) are: 2m wide, 1.5m deep, and 4.5m high. The frame is made of standard aluminum angles bolted together and painted with a white thermal coating. The structure is strong enough to support up to 2000 kg even under the 10 g shock experienced at the end of the flight when the parachute inflates. It is rigid enough to allow the required telescope pointing stability of <15". The gondola can be separated into lighter components for easy post-flight retrieval in the field.

D. Communications

Similar to the preceding FGE and SBI missions, STO will rely entirely on the NASA-CSBF provided remote link to/from the gondola for the communications between STO and the ground. The communications interfaces are shown schematically in Figure 8.

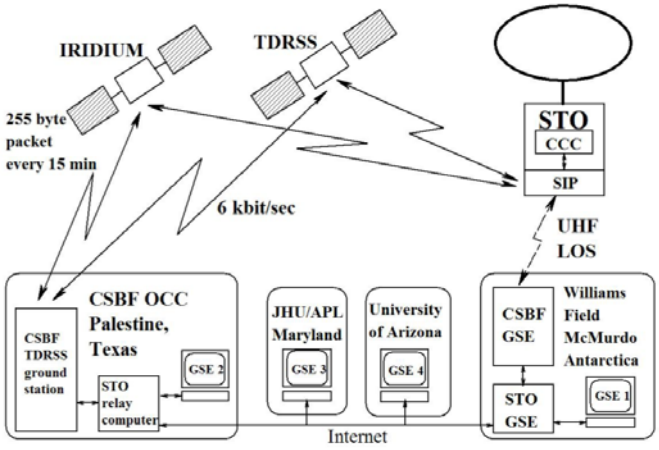

Fig. 8 Schematic of the communications systems between the STO gondola and the ground.

E. Schedule

The first test flight will take place from Ft. Sumner, New Mexico and is scheduled for September 2009. The test flight duration is < 24 hours. For this flight a two pixel system (one at 1.9 THz and the other at 1.45 THz) will be flown. The final instrument and gondola integration and test will take place at APL in the Spring of 2010. STO will be shipped to Palestine in July-August 2010 where APL will integrate the STO payload with CSBF's balloon control and communication equipment. STO will then be shipped to McMurdo in September 2010. The window for flight operations is December 2010 through January 2011. During its 14 day flight STO will circle Antarctica and (ideally) return safely to a recovery location near the launch site. Science data reduction and analysis will start immediately after conclusion of flight operations.

REFERENCES

[1] Benjamin, R.A., et al., 2003, "GLIMPSE. I. An SIRTF Legacy Project to Map the Inner Galaxy", *PASP*, 115, 953.

[2] Carey, S.J., et al., 2005, "MIPSGAL: A Survey of the Inner Galactic Plane at 24 and 70 microns, Survey Strategy and Early Results", *Bulletin of the American Astronomical Society*, 37, 1252.

[3] Bernasconi, P. N., Rust, D. M., Eaton, H. A. C., Murphy, G. A. A., 2000, ``A Balloon-Borne Telescope for high resolution solar imaging and polarimetry'', in *Airborne Telescope Systems*, Ed. by R. K. Melugin, and H. P. Roeser, SPIE proceedings, 4014, 214.

[4] Ulich, B.L., & Haas, R.W., 1976, "Absolute calibration of millimeter-wavelength spectral lines", *ApJ Supplement*, 30, 247

[5] Bernasconi, P. N., Eaton, E. A. C., Foukal, P., Rust, D. M., 2004, ``The Solar Bolometric Imager'', *Adv. Space. Res.*, 33, 1746.

New Ground Based Facilities for THz Astronomy

Gordon J. Stacey

Department of Astronomy, Cornell University, Ithaca, NY 14850

* Contact: GJS12@cornell.edu, phone +1-607-255 5900

***Abstract*— Contemporary ground based facilities for terahertz astronomy are discussed including details on telescopes, instrumentation, and science. Our discussion includes the present and developing facilities in Antarctica and at high sites in the northern Atacama desert in Chile, and projects planned for these sites within the near term horizon.**

I. Introduction

Over the past decade remarkable leaps forward have been made in receiver technologies for THz astronomical applications. With the imminent launch of the Hershel Space Telescope and the SOFIA airborne observatory, these new technologies will bring forth exciting new science. To date however, these new technologies have been employed nearly entirely on ground-based facilities located at the best developed submillimeter sites – those in Antarctica, and those on the Chajnantor region of northern Chile.

II. Antarctic Facilites

The Antarctic Plateau is extremely cold, very high, and very dry. Developed sites on the Plateau include South Pole, Dome A and Dome C. South Pole is a proven excellent site for THz astronomy, while it is suspected that the Dome C and in particular the Dome A sites are better still, due to their higher elevation and expected lower water vapour burden.

B. South Pole: AST/RO

The first ground-based telescope optimized for THz astronomy was the Antarctic Submillimeter Telescope and Remote Observatory (AST/RO) installed at South Pole in the Austral summer season of 1994/95 ([1], Fig. 1). The 1.7 m telescope is an off-axis Gregorian, mounted on an altitude azimuth structure on the roof of the AST/RO receiver room. A Nasmyth focus is available on the azimuth mount, while a Coude focus in the receiver room permits co-mounting of several receivers. The telescope has excellent surface accuracy (~9 μm rms) enabling efficient observations at THz frequencies. During its eleven year lifetime (the telescope was de-comissioned in late in 2005) a wide variety of heterodyne receivers were used at the facility from 230 GHz through 850 GHz, including a dual (810/492 GHz) band, and a four-beam (810 GHz) receiver [2]. A crowning achievement for the facility are large (~ 10 square degree) scale maps of the Galaxy in the CO(7-6), CO(4-3), and 492 GHz [CI] lines (e.g. [3]).

During its last seasons, two 1.4 THz receivers were installed on AST/RO: the Terahertz Receiver with NbN HEB Device (TREND), and the South Pole Imaging Fabry-Perot Interferometer, SPIFI. TREND is a sensitive (T_{rec} ~ 800 K) heterodyne receiver utilizing a hot electron bolometer mixer [4], while SPIFI is a 25 pixel direct detection spectrometer [5]. Here we focus on the SPIFI reveiver and results.

Fig. 1. SPIFI mounted on the AST/RO telescope.

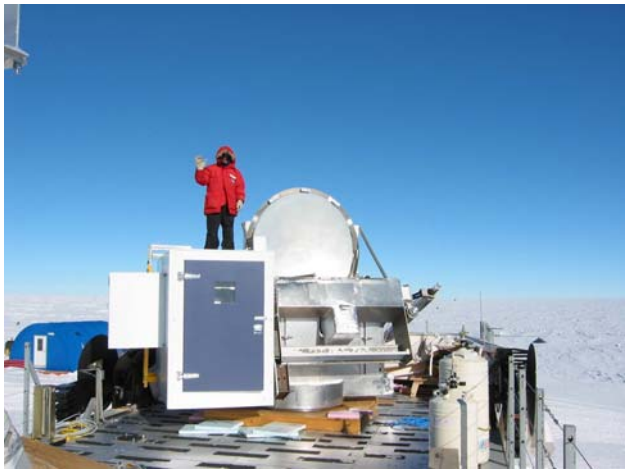

SPIFI is an imaging Fabry-Perot interferometer utilizing a 25 pixel array of bolometers held at 60 mK as detective devices. SPIFI's is designed to operate at in the 200, 350 and 450 μm telluric windows and can achieve resolving powers, R up to R ≡ λ/Δλ ~ 10,000 for high resolution spectroscopy in these bands. SPIFI was successfully used on the 15 m JCMT telescope from 1999-2003 in the 350 μm telluric window [e.g. 6], and subsequently deployed for work in the 200 μm window on the AST/RO telescope at South Pole. At 200 μm (1.5 THz) SPIFI's best pixels have a noise-equivalent-power (NEP) ~ 2.5×10^{-15} W/Hz$^{1/2}$ equivalent to T_{rec}(DSB) ~ 150 K. During the Austral winter of 2005 SPIFI detected and mapped the 205.178 μm $^3P_1 - {}^3P_0$ ground state fine-structure line of N^+ from the Carinae Nebula [7,8]. This was the first reported detection of this important cooling line from a ground based observatory (but see RLT section below).

The Carina region was mapped in its 121.898 μm $^3P_2 - {}^3P_1$ line of N^+ using the LWS on the Infrared Space Observatory (ISO) [9]. The ratio between the the 205 μm and 122 μm lines is density sensitive (Fig. 2), and the line ratio is used to determine the density of the ionized gas enveloping the dense Carina I and II HII regions is ~ 33 cm^{-3}.

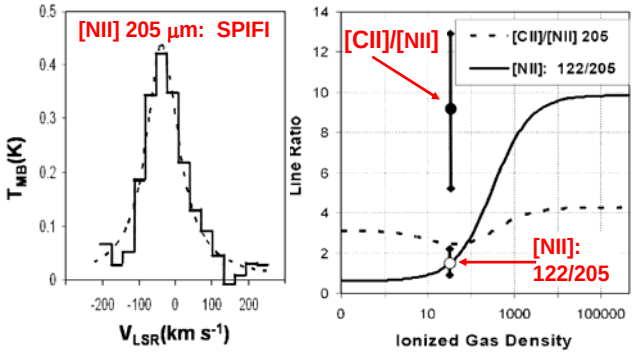

Fig. 2 (left) [NII] 205 μm line detected from the Carinae Nebula. (right) [CII]/[NII] 205 μm and [NII 122/205 μm line ratios as a function of ionized gas density. The filled dot is the observed [CII]/[NII] 205 μm ratio (with large systematic error bar), and the open dot is the observed [NII] 122/205 μm line ratio.

In addition to being a major cooling line and probe of HII region density, the 205 μm [NII] line intensity is very important for interpreting observations of the 158 μm [CII] line. The [CII] line is also an important coolant for HII regions, but is the dominant coolant for major phases of the neutral ISM: the cold neutral medium (atomic clouds), the warm neutral medium, and the photodissociated surfaces of molecular clouds (PDRs). Although the [CII] line is a ubiquitous coolant, its origins are uncertain. Estimates of the fraction of the Galactic [CII] emission from the ionized medium range from 10 to 50%. Fortunately, the 205 μm [NII] line intensity provides a means for unraveling the various components. Since N^+ requires 14.53 eV to form, the 205 μm line only arises from HII regions. Furthermore, the critical density for thermalization of the 205 μm [NII] line emitting level is nearly identical to that of the 158 μm [CII] line emitting level, so that the line ratio from ionized gas is only a function of the assumed N^+/C^+ abundance ratio (Fig. 2). Comparison of the SPIFI [NII] line to the ISO [CII] line observations indicates that only 27% of the of the observed [CII] line emission comes from the ionized gas. These results support and underpin prior studies that suggest most of the observed [CII] line emision from Galactic and extra-galactic sources arises from the warm, dense PDRs on the surfaces of molecular clouds -- an important constraint on the models for the interstellar medium in galaxies.

B. The South Pole Telescope

The AST/RO telescope (among others) paved the way for the next generation, large aperture telescope at South Pole the South Pole Telescoe (SPT) (10). The SPT is funded by the NSF Office of Polar Programs and is at present dedicated to large scale surveys of the Cosmic Microwave Background Radiation (CMBR) anisotropies and polarization. In the future, it is likely that it will be used for THz science. Construction began at the site in November 2004, and the telescope achieved first light on February 16, 2007. With its 10 m aperture, it is the largest astronomical facility on the Antartic continent. The SPT is a collaboration between the University of Chicago, UC Berkeley, Case Western Reserve University, the University of Illinois, and the Smithsonian Astrophysical Observatory. It is primarily funded by the NSF Office of Polar Programs.

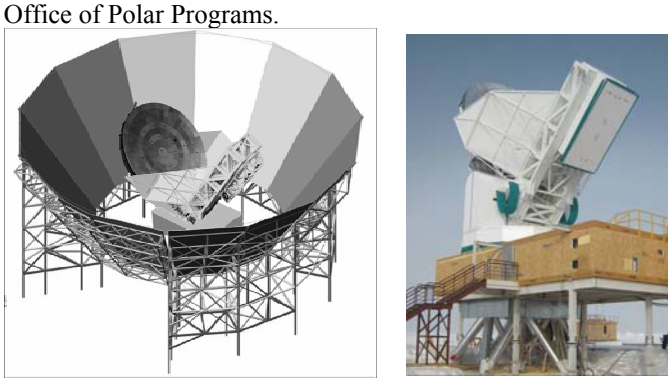

Fig. 3 (left) Layout for SPT including ground shields. (right) Photograph of SPT taken during Austral summer 2007-2008 (J.E. Carlstrom personal communication).

The telescope design is an off-axis Gregorian on an altitude-azimuth mount (Fig. 3). The secondary/camera system is contained within a single cryostat, so that the secondary and aperture stop can be held at 10 K, minimizing the thermal background. The combined surface accuracy of the system is better than 20 μm rms. The optical system is enveloped by both an inner movable ground shield and fixed outer ground shield (not yet installed). The pointing goal is 1", and the telescope scans up to 4°/second. The off-axis design, cold secondary/stop, and ground shields minimize stray thermal emission on the detectors, thereby maximizing system sensitivity. Together with the fast scan rate, these features also minimize systematics.

At 2 mm wavelength, the telescope optics can support a $1(°)^2$ field of view. This field is to be populated with a 966 pixel array divided into 6-161 pixel wedge-shaped sub-arrays in 5 colors. The detectors are TES "spiderweb" bolometers (made at UC Berkeley) in a bath temperature of 300 mK. At present (April 2008) there are about 600 detectors working in three bands (90, 150, and 200 GHz), most of them at, or near the background limit.

The SPT will deliver exciting new results in exploring the anisotropy and polarization of the CMBR. Its promise is enabled by its large aperture, excellent sensitivity, and the exceptionally stable South Pole site. The first key project is a 4000 square degree anisotropy survey of the CMBR which will pick out the Sunyaev-Zel'dovich Effect (SZE) signals from galaxy clusters. Together with follow-up redshift surveys, these SZE surveys will measure the number density evolution of massive galaxy clusters. Since the growth of massive clusters is constrained by the underlying cosmology, the SPT/SZE surveys promise to constrain fundamental cosmological pararmeters including the dark energy equation of state. The system has already detected the SZE effect from known clusters and is at present beginning the survey in $10(°)^2$ patches.

In 2010 it is anticipated that the SPT will begin deep surveys of CMBR polarization. Measuring the extremely small polarization signals are quite a challenge, but the

rewards are great: polarization signals can indicate the presence of primordial gravity waves during the inflationary epoch, and they also relate to fundamental parameters such as neutrino mass and the dark energy equation of state.

C. HEAT

South Pole is an excellent site for THz astronomy, but there are at least two sites, Dome A and Dome C that are at significantly higher elevations on the ice sheet, and promise lower water vapour columns, opening windows into the far-IR bands (1-10 THz). Here we focus on the High Elevation Antarctic Terahertz (HEAT) Telescope that is beginning to explore the Dome A site [11].

Dome A is the highest point on the ice sheet at an elevation 4093 m. Very recently (2008, January) an expedition led by the Polar Research Institute of China (PRIC) successfully installed a fully robotic observatory, the PLATeau Observatory (PLATO) on Dome A. PLATO was constructed by a team from the University of New South Wales. The primary goal is to use its 7 robotic telescopes to fully characterize this site at several astrophysically interesting windows. One of these robotic telescopes is Pre-HEAT – a 20 cm tipping telescope equipped with a Schotty diode receiver and FFT spectrometer (Fig. 4). Its purpose is to measure the sky transmission (and obtain astrophysical spectra) at the 661 GHz frequency of the ^{13}CO(6-5) line. It has been operating successfully since 2008 January, and is currently mapping the Galactic Plane in this transition.

Fig. 4 Pre-HEAT telescope as tested in Sydney, before shipment to Antarctica

Following successful demonstration of the site's utility for THZ spectroscopy, HEAT will be deployed. HEAT is envisioned as a 50 cm aperture telescope, equipped with Schottky receivers at 0.81, 1.46 (from JPL) and 1.9 THz. There is also a cryogenic hot electron bolometer instrument package for HEAT that is being investigated by the group at SRON for possible future deployment. HEAT is a collaborative project between the University of Arizona, PRIC, Purple Mountain Observatory (China), the University of Exeter, SRON, and the University of New South Wales.

The scientific goals for HEAT are to map the $^3P_2$-$^3P_1$ [CI] and CO(7-6) transitions at 0.81 THz over much of the 4th Galactic quadrant (Fig. 5), covering the Scutum-Crux arm through the Carinae and Vela regions. These lines are important coolants for the neutral ISM, and probes of gas density and temperature. HEAT will also map selected regions within these zones in the $^3P_1$-$^3P_0$ [NII] (1.46 THz) and $^2P_{3/2}$-$^2P_{1/2}$ [CII] (1.9 THz) lines complementing planned Herschel and Stratospheric Terahertz Observatory (STO) surveys. These lines are important coolants for the diffused ionized gas, and the [CII] line is both the dominant coolant for the photodissociated surfaces of molecular clouds and the warm and cool phases of the atomic media. The line ensemble (together with lower J CO and [CI] lines) well traces the physical conditions of the most important phases of the interstellar medium constraining modes of star formation with the Milky Way galaxy.

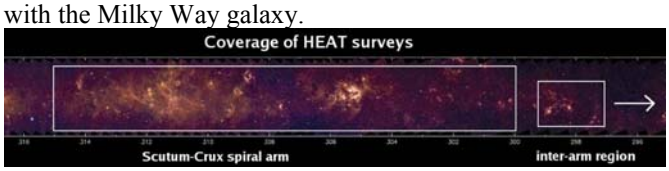

Fig. 5 Planned coverage of HEAT Galactic plane surveys.

III. CHILEAN FACILITIES

The Atacama Desert is a nearly 1000 km north-south strip of high desert in northern Chile. It is arguably the "driest place on Earth", and at its southern extreme, it is already the site of two leading ESO observatories (La Silla and Paranal). The northern end of the desert is significantly higher and drier, and is an excellent location for ground based THz astronomy. This Chajnantor region is the site for the Atacama Large Millimeter Array (ALMA) of 50 to 64 – 12 m antennas, which will eventually have receiver bands from 30 to 850 GHz. ALMA is located at an elevation of 5000 m – 750 meters higher than the summit of Mauna Kea – and there is significantly lower water vapor burden at the ALMA site at most times. ALMA is scheduled for completion in 2012. Below we discuss two telescopes sited very near ALMA that are currently operating in the THz, or near THz bands: the Atacama Pathfinder Experiment (APEX), and the NANTEN2 telescope. We also discuss the 25 m CCAT telescope envisioned for the nearby summit of Cerro Chajnantor, and begin our discussion with the pioneering Receiver Lab Telescope (RLT) located near the summit of Cerro Sairecabur located 35 km to the northwest of the ALMA site.

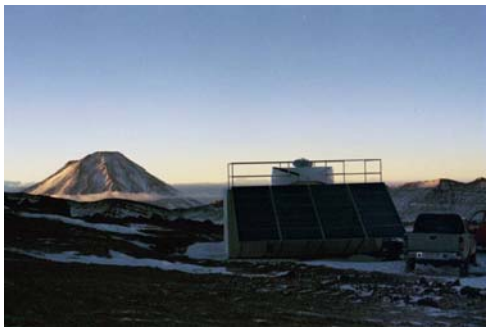

Fig. 6 RLT at the Sairecabur site (photo credit: D. Marrone).

Receiver Lab Telescope (RLT)

The RLT is an 80 cm telescope located at 5525 m elevation near the summit of Cerro Sairecabur [12]. The site is accessible by truck, and available for year round observing

(Fig. 6) The high frequency telluric transmission is monitored continuously by a Fourier transform spectrometer [13], and is is significantly better than that at the ALMA site – typically 40% better as measured in optical depth. This opens up ground based observations to a wide variety of spectral lines in the THz bands (Fig. 7). At the frequency of the astrophysically important [NII] line (1.46 THz), the zenith transmission is better than 10% about 35% of the time.

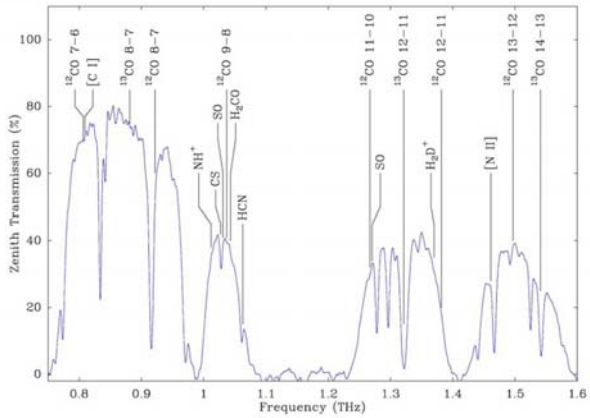

Fig. 7. Spectral lines transmitted in the THZ bands at the Sairecabur site.

The RLT employs heterodyne hot electron bolometer mixers kept at 4 K in liquid helium cryostats, and achieved first light at THz frequencies in 2002 [14]. Initial observations were limited to 0.85 and 1.03 GHz due to the availability of solid state local oscillators, but in 2005 the higher frequency oscillators became available, and the group began observations at 1.3 and 1.5 THz.

The first THz science obtained with the RLT was a 35 point map of the Orion A HII region/photodissociation region interface in the CO(9-8) (1.037 THz) line obtained in 2002 December [14]. This was the first CO(9-8) map of Orion, and only the second velocity resolved observation of any THz line from an astronomical source using a ground based telescope. Their CO(9-8) line observations reveal the physical conditions in the PDR as well as the velocity structure in the molecular outflow from the embedded young stellar object, IRc2.

The group fielded 1.3 and 1.5 THz receivers in December 2004, and presented maps of the Orion/BN-KL outflow and the NGC 2024 PDR in the CO(11-10) (1.26 THz) line as well as first detections of the CO(13-12) (1.5 THz) line at the 2005 Space Terahertz Conference [15] (Fig. 8). The CO(13-12) observations were the first ground based observations in the 1.5 THz window.

Most recently, the group has focused on detection of the [NII] line from Galactic HII regions. As mentioned above, this line is an important coolant and density probe for low density HII regions, and a discriminant for the fraction of the [CII] line emission that arises in low density HII regions. The RLT has obtained reported tentative detections of this line from about 6 HII regions, including G333.6, and G0.6. For both of these sources, the [CII]/[NII] 205 μm line intensity ratio is ~ 20, which means that only a small fraction (< 20%) of the observed [CII] line emission arises from the ionized gas in these sources (see Fig. 2). They also have reported upper limits on the line intensity from the Orion HII region that are very small when compared with the observed [CII] line: $I_{[CII]}/I_{[NII]} > 50$. This is very likely due to the harder radiation field in this source. Since θ^1 Ori C is an O6V star, one would expect to find most of the nitrogen in the form N^{++}.

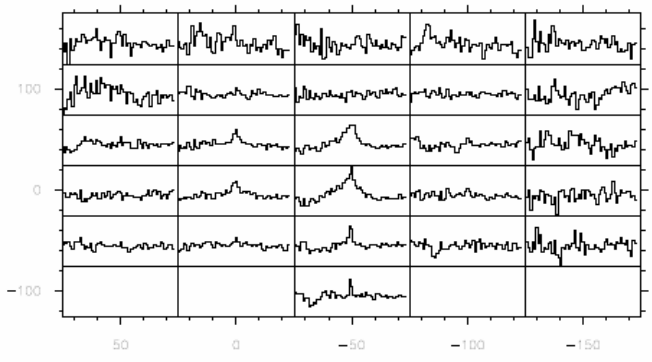

Fig. 8. CO(11-10) Map of BN/KL region in Orion. Each panel is 50" apart and N is up. Horizontal axis in each panel spans -80 to 100 km/s. Data are not calibrated on vertical scale [15]

A. APEX – CONDOR

Located on the Chajnantor plain at 5107 m, not far from the ALMA site is the Atacama Pathfinder Experiment (APEX) telescope [16] (Fig. 9). APEX is an ALMA prototype antenna that was manufactured by VERTEX Antennentechnik, GmbH, Germany, then modified to have two Nasmyth receiver cabins for single dish work. The APEX project was initiated in 2001 as a collaboration between the Max-Planck-Institut für Radioastronomie, the Onsala Space Observatory, and the European Southern Observatory (ESO). APEX operations are undertaken by ESO. Construction began in spring of 2003, with first light in the summer of 2005.

APEX is a 12 m Cassegrain telescope with a surface accuracy better than 18 μm rms. The telescope aperture, site and surface accuracy have ensured that it is one of the premier facilities for short-submillimeter, and even THz observations. A series of papers on first light science with APEX appeared in Astronomy and Astrophysics Volume 454 in 2006, including the first THz observations with the telescope, undertaken with the CONDOR receiver [17].

CONDOR (CO N+ Deuterium Observations Receiver) is a 1.25 – 1.5 THz receiver that employs a HEB mixer yielding a 0.8 GHz IF bandwidth that is spectrally analyzed with APEX's fast Fourier transfer spectrometer. CONDOR was the first receiver to employ a HEB mixer in a closed cycle refrigerator. They successfully used a pulse tube cooler that was vibrationally isolated from the mixer with flexible cold leads. Elimination of expensive cryogens is an important operational consideration while observing at Chajnantor. The receiver achieves a noise temperature ~ T_{rec}(DSB) ~ 1600 over much of the tuning band from 1 to 1.5 THz, and Allen

variance minimum times are excellent, about 35 seconds for total power mode, and over 100 seconds for spectroscopy.

Fig. 9 APEX telescope.

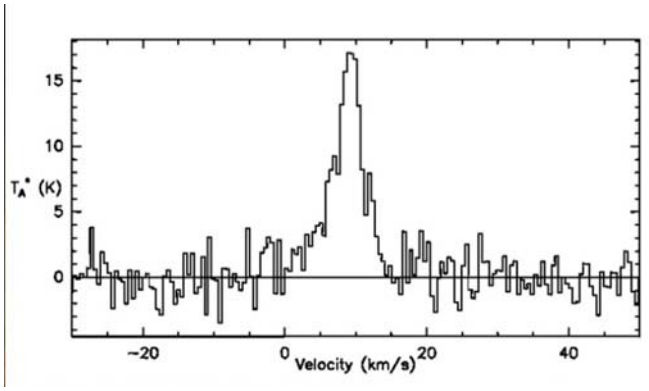

Fig. 10 CO(13-12) spectrum of Orion FIR4 [17]

CONDOR was first installed on APEX in November 2005 and obtained first light on a science target on November 20. The first science was detection and mapping of the CO(13-12) 1.5 THz line from the southern source on the Orion ridge, Orion FIR4, also known as Orion S6 [17] (Fig 10). At this time the line-of-sight transmission at the source elevation (57°) was 19% at 1.5 THz – excellent for the APEX site. The observed CO(13-12) line is narrower than the mid-J CO line suggesting that the high J level excitement is from gas heating in PDRs rather than shocks in outflows. The CO(13-12) line emission was also mapped around the IRc2 outflow [18] and from the PDR in NGC 2024 [19].

CONDOR is designed to detect the [NII] line as well. A line search was initiated in Orion at the Bar interface region, but the line was not detected to good significance (~ 10^{-14} W/m^2) despite good line-of-sight transmission (~ 18%). As for the RLT [NII] studies the weak [NII] there because most N is in N^{++} due to the hardness of the θ^1 Ori C radiation field.

CONDOR is now retired from APEX, and a second generation facility receiver is coming on line: the Single-Pixel Heterodyne Facility Instrument (SHFI). SHFI covers the frequency bands from 0.211 – 1.390 THz with 6 receiver channels. The highest frequency 1.250-1.390 THz band employs a HEB mixer [20].

Fig. 11 NANTEN2 Telescope at the site.

B. NANTEN2/KOSMA

The NANTEN2 observatory consists of a 4 m telescope located at 4850 m altitude on Pampa la Bola in the Atacama desert (Fig 11). The observatory is a collaboration between research institutes in Japan (Nagoya and Osaka University), South Korea (Seoul National University), Germany (KOSMA, Universität zu Köln, Argelander-Institut Universität Bonn), Switzerland (ETH Zürich), Australia (University of New South Wales), and Chile (Universidad de Chile). The observatory began operations in 2006, May.

The telescope has very good surface quality (< 20 μm rms) enabling observations in the short submillimeter windows. The primary goals are to survey the southern skies and nearby galaxies in various molecular and atomic lines in the spectral regime between 110 and 880 GHz with a primary scientific emphasis on starformation. At the highest frequencies, the observatory is equiped with a 2×8 pixel receiver the Submm Array Receiver (SMART) that operates simultaneously at 461 and 807 or 492 and 809 GHz [21]. In this way, both the CO(4-3) and CO(7-6) or the [CI] (492) and (809) GHz lines can be observed at the same time with perfect spatial registration and excellent relative calibration between the two sets of complementary spectral probes. The SIS mixers are cooled to 4 K within the cryostat using a closed cycle refrigerator, and achieve receiver temperatures of ~ 250 and 750 K (DSB) respectively at 460 and 810 GHz. There is a K-mirror configuration in the fore-optics so that the array orientation can be rotated to match the source morphology.

The first science results from the NANTEN2/SMART collaboration include mapping of N149W region of the Large Magellanic Cloud in the [CI] $^3P_2$-$^3P_1$, CO(7-6), and ^{13}CO(4-3) lines (Fig 12). The [CI] and ^{13}CO(4-3) detections are the first from the LMC. They find the C to CO abundance ratio is close to unity, much higher than that found in massive star-forming regions in the Milky Way. They model the observed

submm line intensities together with 158 μm [CII] line (from the Kuiper Airborne Observatory) in a clumpy PDR context and find the UV field strength is ~ 220 times the local interstellar radiation field, and the average cloud densities are quite high, ~ 10^5 cm^{-3} [22]

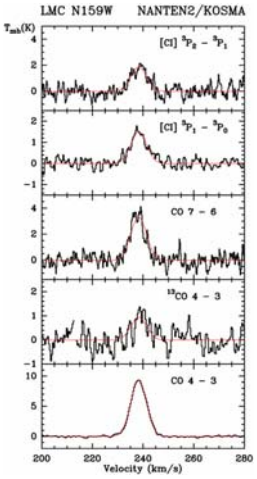

Fig.12. Lines observed from the N149W region of the LMC with SMART on NANTEN2. From top to bottom: [CI] $^3P_2$-$^3P_1$, [CI] $^3P_1$-$^3P_0$, CO(7-6), ^{13}CO(4-3), and CO(4-3).

C. Cornell Caltech Atacama Telescope (CCAT)

The Cornell Caltech Atacama Telescope (CCAT) is proposed 25 m telescope with excellent surface accuracy (~ 9 μm rms) located at an excellent site (at 5600 meters, near the summit of the Cerro Chajnantor). With an actively controlled surface, CCAT promises to work with very high efficiency at 850 GHz, and good efficiencies in the THz windows as well. It is expected that CCAT will have cameras and spectrometers operating from the very short submm (1.5 THz, or 200 μm) windows through the 2.2 mm window. The telescope optical design (Richie-Chretien) provides for a 20' diffraction limited field of view at wavelengths as short at 200 μm, so that large scale surveys with very large format arrays are enabled. CCAT is a collaborative project between Cornell University, the California Institute of Technology and the Jet Propulsion Laboratory, the University of Colorado, the Universities of Waterloo and British Columbia, the UK Astronomy Technology Centre on behalf of the UK community, and the Universities of Cologne and Bonn. Partnership fund raising efforts are underway, and it is hoped that construction can begin in 2009, with completion in the 2013 timeframe.

The primary science drivers for CCAT focus on origins, and include (1) exploring the early Universe through high spatial resolution, multiwavelength surveys of the CMBR, in particular using the SZE to understand the growth of galaxy clusters and its relation to dark energy and dark matter (2) exploring galaxy formation and evolution through large area surveys of distant galaxies in the submillimeter bands (3) studies of star and planet formation through multiwavelength surveys and imaging of nearby young stellar objects, protostellar, and debris disks (4) explorations of the solar system including surveys of trans-Neptunian objects to constrain theories of solar system formation.

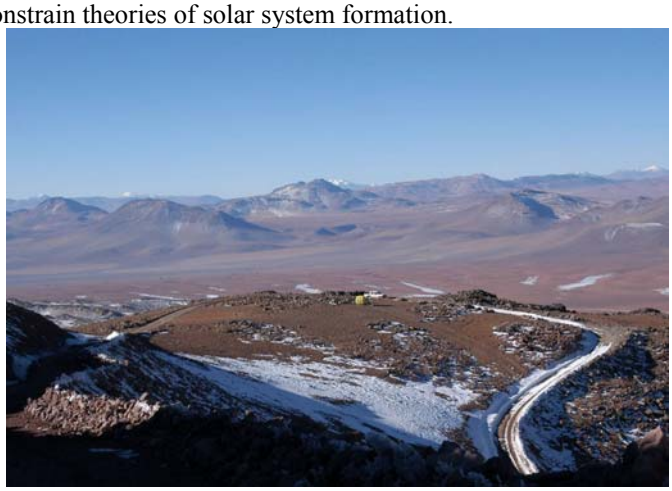

Fig. 13. View of the proposed site for CCAT from the summit of Cero Chajnantor. Visible is the 350 μm tipper.

The CCAT site near the peak of Chajnantor (Fig. 13) was primarily chosen for its excellent water vapor characteristics. Based on balloon-borne radiosonde surveys, it was expected that a site a few hundred meters higher than the ALMA site would have significantly between water vapor statisitics [23]. This expectation was confirmed through a 350 tipping radiometer comparison between the proposed site and the CBI (5050 m elevation) site near ALMA. Identical ratiometers have been taking data since May of 2006. The news is good. The water vapor burden over the CCAT site is only 70% that over CBI so that, for example, 0.7 mm precipitable water vapor or less occurs 65% of the time for CCAT, and only 40% of the time over CBI (Fig. 14).

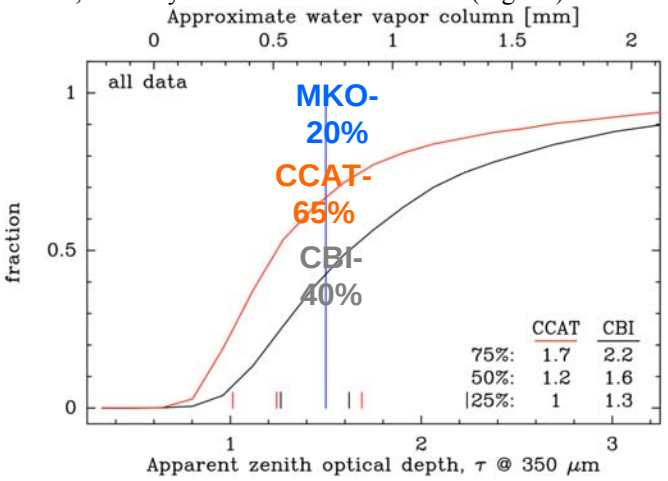

Fig. 14. Fraction of time with precipitable water vapor less than a given value obtained for the CCAT site as compared with the lower elevation CBI site. CCAT should have a water column less than 0.7 mm 65% o the time, while CBI reaches that value only 40% of the time and Mauna Kea only 20% of the time.

The CCAT telescope needs to be enclosed within a dome to achieve its high surface accuracy in the face of the winds near Chajnantor. A concept that minimizes dome size is the "Calotte" style dome (Fig. 15)

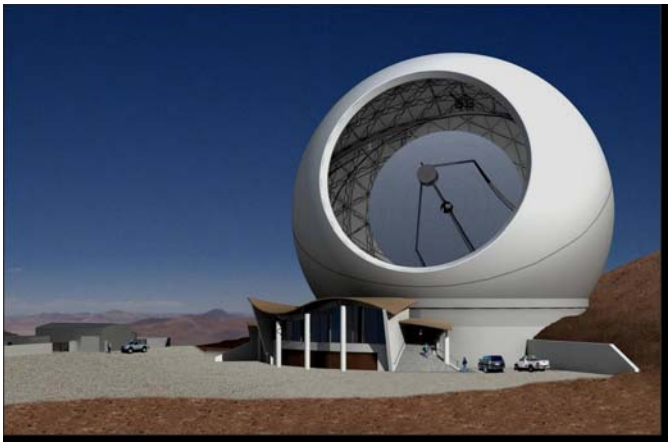

Fig. 15. Artist conception of the CCAT telescope with its Calotte style dome and the observers facilities at the Chajnantor site..

Baseline first light instrumentation includes two direct detection cameras to enable our planned large scale surveys: the Short-Wavelength Camera (SWCam), and the Long-Wavelength Camera (LWCam) [24]. Remarkably, in the short submillimeter (350 and 450 μm) windows, the excellent site, large aperture, excellent surface quality, and the use of broad-band direct detection enable CCAT to achieve point source sensitivities per beam that are comparable with those of the ALMA array (Fig. 16). Therefore, CCAT can map the sky far faster than ALMA at 350 and 450 μm, and deliver a large catalogue of interesting sources for detailed follow-up with ALMA. There is excellent synergy between CCAT and ALMA: CCAT is a finder-scope for the ALMA array.

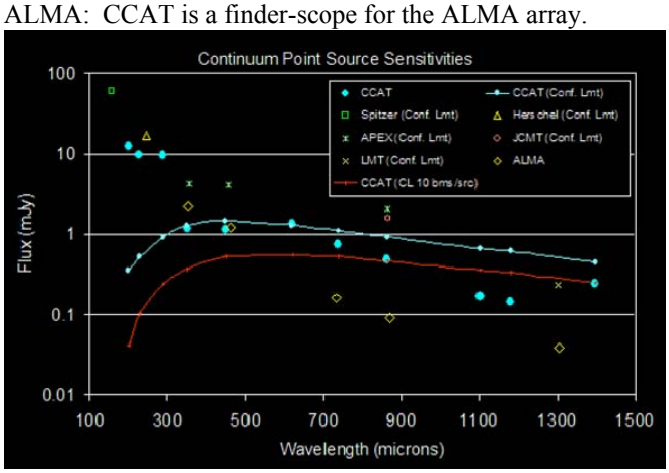

Fig. 16. Expected point source sensitivity for CCAT cameras compared with other facilities. Estimates are 5σ in 3600 seconds, and account for the mean precipitable water vapor column at each site. Confusion limits (30 beams/source) are included in all estimates. The top (cyan) line indicates the confusion limit for CCAT with 30 beams per source, while the bottom (red) plot indicates the more generous limit of 10 beams per source.

The SWCam covers frequencies from 0.5 to 1.5 THz. It is envisioned to have a 5'×5' field of view populated with about 32,000 pixels to provide diffraction limited, Nyquist sampled operation at 350 μm. Detectors are baselined as SCUBA 2-like TES bolometers held at 90 mK in an ADR. The array size at present is cost limited based on current technology. However, there is growth potential to a 400,000 pixel array which would Nyquist sample the entire 20'×20' field of view of the telescope. The SWCam covers the 200, 350, 450, and 620 μm telluric windows by rotating a filter wheel. It is conceivable that the development of the SWCam would be delayed for next generation technologies if the SCUBA 2 camera with its twin 5120 pixel arrays operating at 450 and 850 μm can be successfully transferred from the JCMT to CCAT.

The LWCam covers frequencies from 150 to 405 GHz, including the trans-millimeter wavelength windows at 0.74, 0.87, 1.1, 1.4, and 2.0 mm. LWCam detectors are envisioned as slot dipole antenna coupled kinetic inductor detector arrays such as those being developed at Caltech/JPL [25,26] and elsewhere. We plan an array that can be configured to have 1024 to 16,384 pixels depending on wavelength, covering either a 10'×10', or 20'×20' field of view.

CCAT will also include spectrometers. Likely first light spectrometers include modest resolving power direct detection spectrometers such as the long slit grating spectrometer ZEUS [27] or the waveguide grating spectrometer Z-Spec [28] that are now in use on the CSO. There will also be heterodyne receivers arrays, like those being developed at several institutions. The direct detection receivers will have a distinct advantage for detection broad lines from distant galaxies, while good velocity resolution is achieved with the heterodyne systems.

The primary science goal for CCAT is to explore the birth and evolution of galaxies in the early Universe. CCAT will survey tens of square degrees finding several hundred thousand star forming galaxies at redshifts between 1 and 5 and find a smaller number of sources out to redshifts of 10 (if they exist!). A few hundred of these submillimeter bright galaxies (SMGs) have been discovered to date through painstaking surveys such as those undertaken with SCUBA on the JCMT. CCAT will find these galaxies at the rates several hundred per hour! The primary discovery bands are at 350 and 450 μm. However shorter, and longer wavelength observations will be important to derive source submillimeter spectral energy distributions, hence their photometric redshifts and total far-IR luminosities. These statisitical redshifts will enable much of the expected science: the star and galaxy formation history of the Universe, and evolution of large scale structures. However, accurate redshifts refine these studies, enable splitting the sample into small redshift bins, and permit detailed studies of individual systems. It is possible to obtain redshifts for a sizeable fraction (10%?) of the survey by detecting the bright 158 μm [CII] line with a suitably designed far-IR/submm spectrometer such as a multi-beam version of ZEUS or Z-Spec. Calculations show that the [CII] line can be detected from systems only twice as luminous as the Milky Way out to redshifts of 2, and 10 times the Milky Way luminosity to $z > 5$. The [CII] line to far-IR continuum ratio in of itself constrains the strength of the ambient far-UV radiation field in starforming galaxies (Fig. 17). This yields the source beam filling factor, hence size of the starburst. For example the hyperluminous galaxy MIPS J142824.0 +352619 at $z \sim 1.325$ was detected in the [CII] line

using ZEUS on the CSO [30]. The relative bright line emission observed there constrains the far-UV fields to be less than ~ 2000 times the local interstellar radiation field, so that the starburst must be distributed over kpc scales in this system. So, unlike ULIRG and starburst galaxies in the local Universe, at least some galaxies at z ~ 1 are undergoing global bursts of starformation.

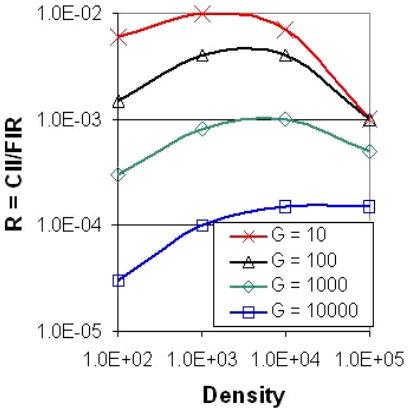

Fig. 17. The ratio, R of the [CII] line to far-IR continuum luminosity as a function of the strength of the far-UV radiation field, G, and molecular cloud density (adapted from [30]. For densities typical of starforming galaxies (100 < n < 10,000) R is mostly a function of G only.

CONCLUSIONS

There are many exciting new facilities and instruments now operating or on the near horizon for THz astronomy from the ground. Most of these facilities are in Antarctica, or in the northern Atacama desert in Chile. The superb sensitivities being delivered by these facilities and receivers are enabling exciting new science, whose promise will only grow as telescopes and receivers continue to improve.

ACKNOWLEDGMENTS

I am very grateful to my colleagues Ray Blundell, John Carlstrom, Chris Groppi, John Kawamura, Craig Kulesa, Juergen Stutzki, Chris Walker, and Martina Wiedner who sent well prepared slides about their telescopes and/or instruments so that I could put together the talk and this paper. This work was supported in part by NSF Grant AST-0705256.

REFERENCES

[1] A.A. Stark et al. "The Antarctic Submillimeter Telescope And Remote Observatory (AST/Ro)" The Publications of the Astronomical Society of the Pacific, Vol. 113, Issue 783, pp. 567-585, May 2001

[2] C.K. Walker, J.W. Kooi, W. Chan, H.G. LeDuc, P.L. Schaffer, J.E. Carlstrom, and T.G. Phillips "A low-noise 492 GHz SIS waveguide receiver" International Journal of Infrared and Millimeter Waves, vol. 13, pp. 785-798, June1992

[3] C. L. Martin, W. M. Walsh, K. Xiao, A. P. Lane, C. K. Walker, and A. A. Stark "The AST/RO Survey of the Galactic Center Region. I. The Inner 3 Degrees", Astrophysical Journal Supplement Series, vol. 150, pp. 239 - 262, January 2004

[4] K.S. Yngvesson, C.F. Musante, M. Ji, F., Rodriguez, Y. Zhuang, E. Gerecht, M. Coulombe, J. Dickinson, T. Goyette, and J. Waldman, C. K. Walker, A. Stark and A. Lane *"Terahertz Receiver With Nbn Heb Device* (*Trend*) - A Low-Noise Receiver User Instrument For ATR/RO at the South Pole" proceedings of the *Twelvth Intern. Symp. Space THz Technology, San Diego, Feb. 2001*

[5] C.M. Bradford, G.J. Stacey, M.R. Swain, T. Nikola, A.D. Bolatto, J.M. Jackson, M.L. Savage, J.A. Davidson, & P.A.R. Ade "SPIFI: a direct-detection imaging spectrometer for submillimeter wavelengths", , Applied Optics vol. 41, pp. 2561 – 2574 May 2002.

[6] Bradford, C.M., Nikola, T.N., Stacey, G.J., Jackson, J.M., Bolatto, A.D., Davidson, J.A., Savage, M.L., & Higdon, S.J., "CO(7→6) Observations of NGC 253: Cosmic Ray Heated Warm Molecular Gas", Astrophysical Journal vol. 586, pp. 891-901, April 2003.

[7] T.E. Oberst, S.C. Parshley, G.J. Stacey, T. Nikola, A Löhr, J.I. Harnett, N.F.H. Tothill, A.P. Lane, A.A. Stark, & C.E. Tucker "Detection of the 205 μm [NII] Line from the Carina Nebula" Astrophysical Journal Letters vol. 625, L125-128 Dec. 2006

[8] T.E. Oberst, S.C. Parshley, G.J. Stacey, T. Nikola, A Löhr, A.P. Lane, A.A. Stark, & C.E. Tucker "The 205 μm [NII] Line Emission from the Carina I and II Nebula" in preparation

[9] M. Mizutani, T. Onaka, and H. Shibai, H., Astronomy and Astrophysics vol 382, pp 610-623, Feb. 2002

[10] J. E. Ruhl et al. "The South Pole Telescope" Proceedings of the. SPIE, Vol. 5498, pp 11-29, Oct. 2004

[11] C.K. Walker, C. A. Kulesa, D.R. Golish, A. S. Hedden, K . Jacobs, J. Stutzki, J.R. Gao, J. W. Kooi, D. Glaister, W. Gully, I. Mehdi, M.R. Swain, P. Siegel, "Forecast for HEAT on Dome A, Antarctica: the High Elevation Antarctic Terahertz Telescope" Proceedings of the SPIE, Volume 5489, pp. 470-480 June 2004.

[12] R. Blundell, J. W. Barrett, H. Gibson, C. Gottleib, T. R. Hunter,R. Kimberk, S. Leiker, D. Marrone, D. Meledin, S. N. Paine, R. J. Plante, P. Riddle, M. J. Smith, T. K. Sridharan, C. E. Tong, R. W. Wilson, M. A. Diaz, L. Bronfman, J. May, A. Otarola, and S. J. Radford, "Prospects for Terahertz Radio Astronomy from Northern Chile," in 13th International Symposium on Space Terahertz Technology, ed. C. E. Tong & R. Blundell, pp. 159–166, 2002

[13] S. Paine, R. Blundell, D. C. Papa, J. W. Barrett, and S. J. E. Radford "A Fourier Transform Spectrometer for Measurement of Atmospheric Transmission at Submillimeter Wavelengths," *Pub. of the Astronomical Society of the Pacific*, vol. 112, pp. 108–118, Jan. 2000.

[14] D. P. Marrone, J. Battat, F. Bensch, R. Blundell, M. Diaz, H. Gibson, T. Hunter, D. Meledin, S. Paine, D. C. Papa, S. Radford, M. Smith, and E. Tong, "A Map of OMC-1 in CO J = 9-8," *The Astrophysical Journal*, vol. 612, pp. 940–945, Sept. 2004.

[15] D. P. Marrone, R. Blundell, E. Tong, S. N. Paine, D. Loudkov, J. H. Kawamura, D. Luehr, C. Barrientos "Observations in the 1.3 and 1.5 THz Atmospheric Windows with the Receiver Lab Telescope" in *15th International Symposium on Space Terahertz Technology, ed. C. E. Tong & R. Blundell*, pp. 159–166 2005.

[16] R. Güsten, L.A. Nyman, P. Schilke, K. Menten, C. Cesarsky, and R.M. Booth "The Atacama Pathfinder EXperiment (APEX) - a new submillimeter facility for southern skies –" Astronomy and Astrophysics vol. 454, L13-16, Aug 2006

[17] M. Wiedner et al. "First observations with CONDOR, a 1.5 THz heterodyne receiver" Astronomy and Astrophysics vol. 454, L33-36, Aug 2006

[18] N.H. Volgenau et al. 2008 submitted to Astronomy and Astrophysics

[19] M. Emprechtinger et al. 2008, in prep.

[20] I. Lapkin, O. Nyström, V. Desmaris, D. Meledin, D. Dochev, V. Vassilev, M. Strandberg, R. Monje, D. Henke, E. Sundin, S-E Ferm, M. Fredrixon, and V. Belitsky, Victor: "Optics Design and Verification for the APEX Swedish Heterodyne Facility Instrument (SHeFI)" in Proceedings of the 19th International Symposium on Space Terahertz Technology, 2008

[21] U.U. Graf, S. Heyminck, E.A. Michael, S. Stanko, C.E. Honingh, K. Jacobs, R.T. Schieder, J. Stutzki, J., and B. Vowinkel "SMART: The KOSMA Submillimeter Array Receiver for Two frequencies" Millimeter and Submillimeter Detectors for Astronomy. Edited by Phillips, Thomas G.; Zmuidzinas, Jonas. Proceedings of the SPIE, Volume 4855, pp. 322-329, Feb. 2003.

[22] Pineda, Mizuno, Stutzki et al., 2008, A&A 482, 197 "Submillimeter line emission from LMC N159W: a dense, clumpy PDR in a low metallicity environment" Astronomy and Astrophysics vol. 482, pp 197-208, April 2008

[23] R. Giovanelli, J. Darling, C. Henderson, W. Hoffman, D. Barry, J. Cordes, S. Eikenberry, S., G. Gull, L. Keller, J.D. Smith, & G. Stacey, "The Optical/Infrared Astronomical Quality of High Atacama Sites. II. Infrared Characteristics"Publications of the Astronomical Society of the Pacific vol. 113, 803-813 July 2001.

[24] G. J. Stacey et al. "Instrumentation for the CCAT Telescope" Proceedings of the SPIE vol.6275, pp. 6275G1-12 June, 2006.

[25] P.K. Day, H.G DeLuc, B.A. Mazin, A. Vayonakis, and J. Zmuidzinas, "A broadband superconducting detector suitable for use in large arrays" Nature vol. 425, pp. 817-821 Oct. 2003.

[26] B.A. Mazin, Ph.D. thesis, California Institute of Technology, 2004

[27] G.J. Stacey, S. Hailey-Dunsheath, T. Nikola, T.E. Oberst, S.C. Parshley, D.J. Benford, J.G. Staguhn, S.H. Moseley, and C.E. Tucker, "ZEUS: The Redshift (z) and Early Universe Spectrometer." Proceedings of the First NAASC ALMA Workshop, From Z-Machines to ALMA: (Sub)Millimeter Spectroscopy of Galaxies, Astronomical Society of the Pacific Conference Series, vol. 375, pp 52- 62 Jan. 2006

[28] L. Earle, P. Ade, J. Aguirre, R. Aikin, J. Battle, J. Bock, C.M. Bradford, M. Dragovan, L. Duband, J. Glenn, G. Griffin, V. Hristov, P. Maloney, H. Matsuhara, B. Naylor, H. Nguyen, M. Yun, and J. Zmuidzinas, "Z-Spec: a broadband direct-detection millimeter-wave spectrometer -instrument status and first results" SPIE vol. 6275, pp. 6275101-9, May 2006.

[29] S. Hailey-Dunsheath, G.J. Stacey, T. Nikola, S.C. Parshley, T.E. Oberst, D. Benford, and J.G. Staghun "Detection of the [CII] Line from MIPS J142824.0 +352619 at z = 1.3: A Galaxy-Wide Starburst" in prep.

[30] M.J. Kaufman, M.G. Wolfire, D.J. Hollenbach, and M.L. Luhman, M.L. "Far-Infrared and Submillimeter Emission from Galactic and Extragalactic Photodissociation Regions" Astrophysical Journal vol. 527, pp. 795-813, Dec. 1999.

CMB experiments at mm and submm wavelengths

Paul Richards

University of California, Berkeley

The enormous scientific rewards from measurements of the spectrum and anisotropy of the Cosmic Microwave Background have strongly stimulated the development of sensitive detector systems for mm and submm wavelengths. These included systems based on bolometric direct detectors, HEMT amplifiers and even SIS mixers. Examples will be described of small experiments that developed and evaluated detector systems, which later enabled the acquisition of large precise data sets from space observations. Modern, large format bolometric focal planes for photometry of the CMB will be described and compared with the sensitivity possible from ideal coherent receivers.

Terahertz heterodyne array based on NbN HEB mixers.

S.Cherednichenko*[a], V.Drakinskiy [a], B.Lecomte[b], F.Dauplay[b], J.-M.Krieg[b], Y.Delorme[b], A.Feret[b], H.-W.Hübers[c], A.D.Semenov[c], G.N.Gol'tsman[d],

[a] *Chalmers University of Technology, Physical Electronics laboratory, Department of Microtechnology and Nanoscience, SE-41296, Gothenburg, Sweden*
[b] *Observatoire de Paris, LERMA, 77, Avenue Denfert-Rochereau, 75014, Paris, France.*
[c] *German Aerospace Center (DLR), Institute of Planetary Research, 12489 Berlin, Germany.*
[d] Physical Department, State Pedagogical University of Moscow, 119891 Moscow, Russia.
*serguei@chalmers.se

A 16 pixel heterodyne receiver for 2.5 THz is been developed based on NbN superconducting hot-electron bolometer (HEB) mixers. The receiver uses a quasioptical RF coupling approach where HEB mixers are integrated into double dipole antennas on 1.5μm thick Si_3N_4/ SiO_2 membranes. Miniature mirrors (one per pixel) and back short for the antenna were used to design the output mixer beam profile. The camera design allows all 16 pixel IF readout in parallel. The gain bandwidth of the HEB mixers on Si_3N_4/ SiO_2 membranes was found to be about 3 GHz, when an MgO buffer layers is applied on the membrane. We will also present the progress in the camera heterodyne tests.

Keywords: HEB mixer, terahertz camera, NbN films, membrane, bolometer.

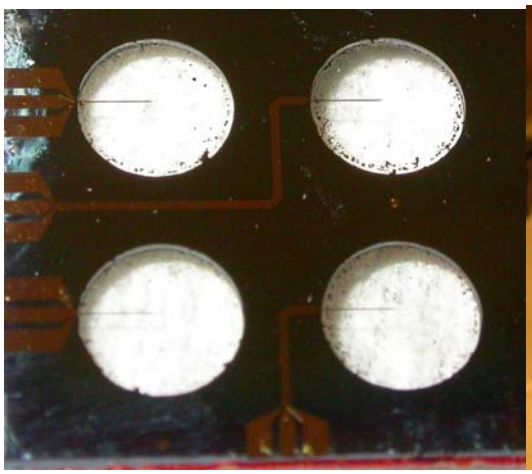

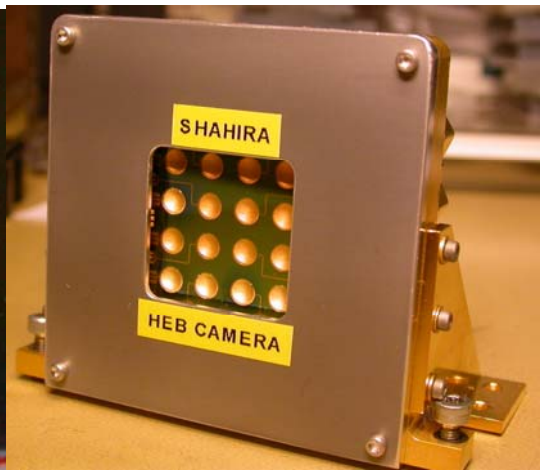

NbZr films for THz phonon-cooled HEB mixers

A.V. Smirnov*, P.A. Larionov, M.I. Finkel, S.N. Maslennikov, B.M. Voronov, G.N. Gol'tsman

Physics Department, Moscow State Pedagogical University, Moscow 119992, Russia

* Contact: s_andrey1981@yahoo.com, phone +7495-246-1202

***Abstract*— This work is devoted to the investigation of the applicability of NbZr as a new material for wideband hot-electron bolometer (HEB) mixer, which is a device of choice for most of low noise heterodyne receivers operating above 1 THz in astronomy applications. Although currently 10-nm NbZr films offer a maximum gain bandwidth of only 450 MHz at T_c on sapphire substrates, there is every reason to believe that the above result can be improved by decreasing the film thickness and using other substrate material which will provide better acoustic match with NbZr.**

I. Introduction

Superconducting hot-electron bolometer (HEB) mixers have been under intensive research since the 1990s [1]. They use the effect of electron heating by incoming terahertz radiation. Currently such devices based on ultrathin NbN films are most sensitive detectors for heterodyne spectrometers between 1 and 6 THz. Their noise temperatures are about 450 K at 600 GHz, 700 K at 1.5 THz, and 900 K at 2.5 THz (see e.g. [2], [3], [4], [5], [6]). One more important parameter of such a mixer is IF bandwidth, which currently achieves the value of about 5 GHz [7]. Obviously a larger IF bandwidth allows simultaneous observation of several lines or instantaneous measurement of a single broad line. There are several possible solutions to expand the IF bandwidth hinted at by the physics of the hot electron effect. The first one is to use buffer layers between the film and the substrate; second, a novel substrate offering better acoustic match with the film; third, the use of new superconducting materials with shorter relaxation time i.e. with a shorter electron-phonon interaction time $\tau_{e\text{-}ph}$ and a shorter non-equilibrium phonons escape time τ_{esc} [8]. It is believed that strong electron-phonon coupling and as a result a short relaxation time - is associated with high superconductor critical temperatures T_c. Indeed, such materials as NbN and NbTiN, where T_c of ultrathin films exceeds 7-10K, have shown the best gain bandwidth results for HEB's so far ([7], [9]). We chose NbZr because it has a high $T_c \approx 11$K in bulk; this material is widely used and may be implemented as ultrathin film.

The simplest and most informative method of investigation of energy relaxation times in HEB is the study of the bolometer behavior under uniform electron heating. In the case of the uniform electron temperature distribution along the bridge, the physics of the device operation can be described by relatively simple equations for the heat balance, and the mixer's roll-off frequency is completely determined by several time constants of the film material ([10],[11]). The values of these characteristic times can be obtained from the dependence of the gain bandwidth on temperature and film thickness. For the electron temperature to be uniform throughout the bridge it is necessary that either the LO frequency be greater than the superconductor gap frequency, or that the ambient temperature be about T_c (in the latter case the LO frequency need not exceed the gap frequency of the unheated superconductor). Also the bolometer bias should be small and the power levels of the oscillators should not influence the operating point of the bolometer. In this paper we study deposition process of ultrathin NbZr films on sapphire substrates, gain bandwidth of NbZr bolometers and the possibly of using this material as a new material for HEB mixers.

II. Device fabrication

This work was aimed at development of a fabrication process of high-quality ultrathin NbZr films having the possibly highest superconducting transition temperature and the critical current density. The film quality depends on various deposition process parameters such as substrate temperature, pressure etc. To choose the optimal deposition regime, we performed a series of experiments changing both the substrate temperature and deposition rate. Deposited films were tested for such parameters as their sheet resistance (R_s), superconducting transition temperature (T_c), superconducting transition width (ΔT_c), ratio of a room temperature resistivity to a resistivity at 20 K ($R=\rho_{300}/\rho_{20,}$) and critical current density (j_c) at 4.2 K.

NbZr films were deposited on sapphire substrates by DC magnetron sputtering of the Nb_{50}/Zr_{50} alloy target in the argon (Ar) atmosphere. We used R- and M-cut sapphire wafers. The R -plane substrates were 0.39 mm thick, the M –plane were 0.33 mm thick. All sapphire substrates were epi-polished on the front side and optically polished on the back side. Before deposition, the chamber was pumped down to a background pressure of $3\cdot10^{-6}$Torr. During the deposition process, the Ar pressure was of $3\cdot10^{-3}$ Torr, while the substrate was heated to a temperature in the range from 150 to 400°C.

For the deposited NbZr films, a sheet resistance R_{sq} was measured by the standard four-point method. The room temperature resistivity (ρ) of deposited NbZr films, defined as the film sheet resistance multiplied by the film thickness (d), was found to be from 60 to 100 μΩ×cm in the thickness range from 50 to 8 nm. The deposition process was investigated for the films 8, 10 and 15 nm thick. We researched into the dependence of the transition temperature on the substrate temperature during the deposition.
The results are presented in Table I.

TABLE I

Substrate temperature, C	170	280	350
Film Tc, K	5.1	7.3	4.5

The best of the obtained 10-50nm thick NbZr films reveal good superconducting properties as shown in Table II. The films demonstrate a sharp superconducting transition and a high critical current density.

TABLE II

Film thickness, d (nm)	8	10	20	50
Critical temperature, T_c (K)	4.3	7.3	7.5	9.1
Transition width, ΔT_c (K)	0.2	0.09	0.06	0.02
Critical current density at 4.2 K, $jc \times 10^6$ (A/cm^2)	-	1.1	1.5	4
Sheet resistance, R_s (Ω/sq)	130-140	85- 99	35- 38	11- 12

We studied bridges 10μm long and 1 μm wide patterned in NbZr films of 20nm and 10nm thickness on 390μm R-plane cut sapphire substrate. Figure 1 shows a SEM photo of our bridge. The NbZr films deposited on M-cut sapphire have shown much worse DC characteristics and parameters of the films. This is probably through bad acoustic match between the film and the substrate, which is why we did not, studied them further.

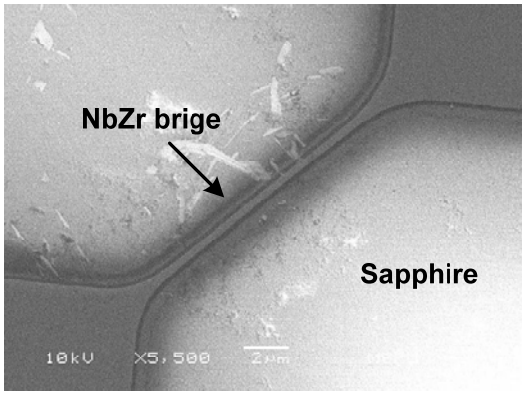

Fig. 1 A SEM photo of NbZr bridge the size of 10×1μm^2 supported by sapphire substrate.

III. MEASUREMENT SETUP AND TECHNIQUE

The gain bandwidth of NbZr bridges was measured by detection of the intermediate frequency (IF) signal power as a function of IF. As tunable sources above 120 GHz it is convenient to use backward wave oscillators (BWO's), which have a wide frequency tuning range and sufficient output power. In our experiments, BWO with a 126.5-146 GHz range, were used. This type of local oscillator made it possible to sample the IF band with a resolution of 5MHz.

The LO and the signal beams were combined with a beam splitter, focused with a Teflon lens and fed into a liquid-helium-cooled vacuum cryostat (see Fig. 2). The temperature of the device block was raised to the critical temperature of the device which varied for different devices between 4.5 -10K.

The IF chain consisted of a bias-Tee, one room-temperature wide band amplifier (0.06-12 GHz), and power-

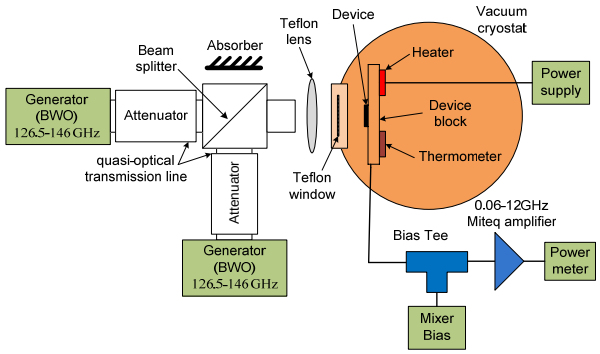

Fig. 2 The intermediate frequency gain bandwidth measurement setup

meter. The frequency of the signal BWO was kept constant, while the LO BWO frequency was swept. The IF bandwidth was measured at a fixed operating point. The value of bias current was used to monitor the absorbed LO power. Figure 3 shows IV curves taken at a few temperatures of the device block.

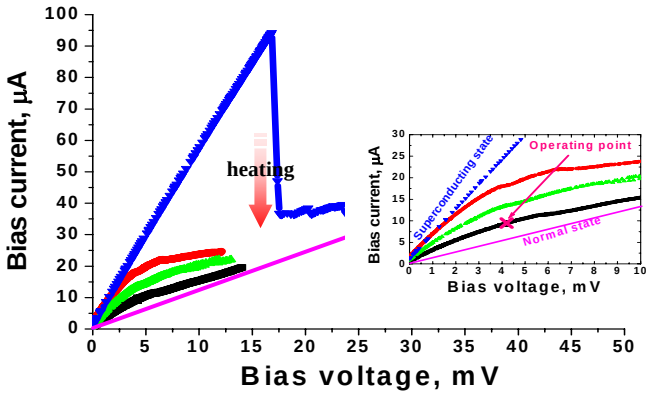

Fig. 3 Set of dc voltage bias characteristics (increasing from top to bottom) levels of the LO power. The upper curve was taken without LO power.

IV. Measurement Results and Analysis

In our experiments the bolometer is heated close to T_c, and the power levels of the oscillators are so low that they do not appreciably affect operating point (see Fig.3).We chose an operating point with the a good signal-to- noise ratio but with DC current low enough to keep U_{bias}/I_{bias} close to device resistant at zero I_{bias}. In this case the electron heating is uniform and we can use the classical model of uniform heating, which was presented in (e.g. [11], [12], [13], [14]).

In the frame work of this model the device output signal $P(f_{IF})$ depends on the intermediate frequency f_{IF} as

$$P(f_{IF})=P(0)[1+(f_{IF}/f_0)^2]^{-1}, \quad (1)$$

where $P(0)$ is the output signal at zero IF, and f_0 is the 3 dB roll-off frequency.

Figure 4 shows the output power vs IF for NbZr bolometers with thicknesses of 10nm and 20nm. The data were fitted with the use of (1).

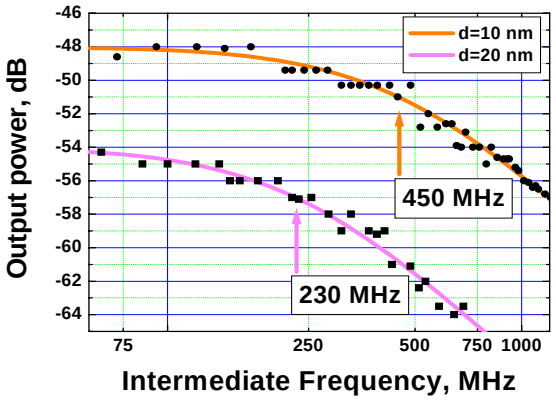

Fig. 4 The output signal vs IF bandwidth for NbZr bridges 10nm and 20nm thick. The 3 dB roll-off frequency is marketed for all curves. The fitting lines are obtained from (1).

The energy relaxation time for a bolometer τ_{bol} is determined from the 3 dB roll-off frequency as

$$\tau_{bol} = 1/(2\pi f_0) \quad (2)$$

Whence we can calculate two different 350ps (10nm) and 690ps (20nm) energy relaxation times which depend on the film thickness. It is evident that for NbZr bolometers

$$\tau_{bol} \sim d, \quad (3)$$

where d is the film thickness. Heat transfer from the film into the substrate is determined by the non-equilibrium phonons-escape time τ_{esc}, which is a function of the film thickness, sound velocity U and the transparency factor α [15]

$$\tau_{esc}=4d/(\alpha U) \quad (4)$$

In terms of (3) and (4) we have found that the IF bandwidth of the NbZr bolometers is limited by the non-equilibrium phonon escape time, which is supported by the dependence of the IF bandwidth on the film thickness. Our result shows that the energy relaxation time in NbZr films are 2.5 times as long as that in NbN films of the same thickness (e.g. [16], [17]). In perspective we believe that our result can be improved by further decreasing the film thickness and using other substrate material which will provide better acoustic match between NbZr film and a substrate. The latter allows reducing the escape time τ_{esc} of non-equilibrium phonons and consequently time constant of the bolometer. Further increase of the IF bandwidth will be limited by the electron-phonon interaction time $\tau_{e\text{-}ph}$.

Conclusion

We have fabricated and tested NbZr ultrathin films at 2 millimeter wavelength. The best bolometers (thickness 10nm) showed following results: critical temperature about 7.5 K, critical current density at 4.2 K about 1×10^6 A/sm^2 and IF bandwidth 450MHz.

The obtained results show that the IF bandwidth of NbZr bolometers is currently limited by the non-equilibrium phonons-escape time τ_{esc} and in perspective we believe that our result can be improved by further decreasing the film thickness and using other substrate material.

Acknowledgment

The authors wish to thank Sergey Ryabchun for help and prompting.

References

[1] E. M. Gershenzon, G. N. Gol'tsman, I. G. Gogidze, Y. P. Gousev, A. I. Elant'ev, B. S. Karasik and A. D. Semenov, Sov. Phys. Superconduct. 3(10), 1582 (1990)

[2] S. Cherednichenko, M. Kroug, H. Merkel, P. Khosropanah, A. Adam, E. Kollberg, D. Loudkov, G. Gol'tsman, B. Voronov, H. Richter and H. -W. Huebers, Phys. C 372, 427-431 (2002)

[3] J. Kawamura, R. Blundell, C.E. Tong, G. Gol'tsman, E.Gershenzon, B. Voronov, S. Cherednichenko, Appl. Phys. Lett. 70, 1619 (1997)

[4] M. Kroug, S. Cherednichenko, H. Merkel, E. Kollberg, B. Voronov, G. Gol'tsman, H.-W. Huebers and H. Richter, IEEE Trans. Appl. Superconduct. 11, 962 (2001)

[5] J.J.A. Baselmans, M. Hajenius, J.R. Gao, A. Baryshev, J. Kooi, T.M. Klapwijk, B.M. Voronov, P. de Korte, G. Gol'tsman, IEEE Trans. Appl. Superconduct. 15, 484 (2005)

[6] A.D. Semenov, H.-W. Huebers, J. Schubert, G. N. Gol'tsman, A. I. Elantiev, B. M. Voronov, E. M. Gershenzon, "Design and Perfomance of the Lattice-Coled Hot-Electron Terahertz Mixer," J. Appl. Phys. 88, 6758-6767 (2000)

[7] Y. Vachtomin, M. Finkel, S. Antipov, B. Voronov, K. Smirnov, N. Kaurova, V. Drakinski and G. Gol'tsman, Proc. of the 13th Int. Symp. On Space Terahertz Tech., Harvard University, Cambrige , Massachusetts, USA, 259 (2002)

[8] A.D. Semenov, G.N. Gol'tsman and Roman Sobolewski, Supercond. Sci. Technol. 15, R1-R16 (2002)

[9] G. N. Gol'tsman, M. Finkel, Y. Vachtomin, S. Antipov, V. Drakinski, N. Kaurova, B. Voronov., Proc. of the 14th Int. Symp. On Space Terahertz Tech., Tucson, Arizona, USA, 276 (2003)

[10] M. Gershenson, M. E. Gershenson, G. N. Gol'tsman, A. M. Lyu'kin, A. D. Semenov and A. V. Sergeev, „Electron-phonon interaction in ultrathin Nb films", Sov. Phys. JETP, vol. 70(3) 1990

[11] N. Perrin and C. Vanneste "Response of superconducting films to a periodic optical irradiation," Phys. Rev. B 28, 5150 (1983)

[12] E.M. Gershenzon, M.E. Gershenzon, G.N. Gol'tsman, A.D. Semenov and A.V. Sergeev Sov. Phys.-JETP 59, 442 (1984)

[13] A.D. Semenov, R.S. Nebosis, Yu.P. Gousev, M.A. Heusinger and K.F. Penk Phys. Rev. B 52, 581 (1995)

[14] Semenov, K. Il'in, M. Siegel, A. Smirnov, S. Pavlov, H. Richter and H.-W. Huebers, „Evidence of non-bolometric mixing in the bandwidth of a hot-electron bolometer", Supecond. Sci. Technol., 19, 1051-1056 (2006)

[15] S.B. Kaplan "Acoustic Matching of Superconducting Films to Substrates," J. Low Temp. Phys., 37, 343-365 (1979)

[16] S.Cherednichenko, P.Yagoubov, K.Il'in, G.Gol'tsman and E.Gershenzon, Proc. of the 8th Int. Symp. Space Terahertz Tech., Boston, USA 245 (1997)

[17] S. Cherednichenko, PhD Thesis (1999)

Sensitivity of a hot electron bolometer heterodyne receiver at 4.3 THz

Pourya Khosropanah[1*], Wouter M. Laauwen[1], Merlijn Hajenius[2,3], Jian-Rong Gao[2,3], and Teun M. Klapwijk[3]

[1]*SRON Netherlands Institute for Space Research, Landleven 12, 9747 AD, Groningen, the Netherlands*

[2]*SRON Netherlands Institute for Space Research, Sorbonnelaan 2, 3584 CA, Utrecht, the Netherlands*

[3]*Kavli Institute of NanoScience, Faculty of Applied Sciences, Delft University of Technology, Lorentzweg 1, 2628 CJ, Delft, the Netherlands*

* Contact: P.Khosropanah@sron.nl, phone +31-50-363 3465

***Abstract*— We have studied the sensitivity of a superconducting NbN hot electron bolometer mixer integrated with a spiral antenna at 4.3 THz. Using hot/cold blackbody loads and a beam splitter all in vacuum, we measured a double sideband receiver noise temperature of 1300 K at the optimum local oscillator (LO) power of 330 nW, which is about 12 times the quantum noise ($h\nu/2k_B$). Our result indicates that there is no sign of degradation of the mixing process at the super-THz frequencies. Also, a measurement method is introduced where the hot/cold response of the receiver is recorded at constant voltage bias of the mixer, while varying the LO power. We argue that this method provides an accurate measurement of the receiver noise temperature, which is not influenced by the LO power fluctuations and the direct detection effect. Moreover, our sensitivity data suggests that one can achieve a receiver noise temperature of 1420 K at the frequency of [OI] line (4.7 THz), which is scaled from the sensitivity at 4.3 THz with frequency.**

I. Introduction

Superconducting mixers play a key role in astrophysics at terahertz frequencies, where the early universe radiates strongly [1]. The availability of low noise superconductor-insulator-superconductor (SIS) mixers and hot electron bolometer (HEB) mixers has made the realization of highly sensitive spectrometers on ground, airborne and space telescopes possible. An example of these is the Heterodyne Instrument for Far-Infrared (HIFI) on the Herschel space telescope [2], to be launched in 2008, where the heterodyne spectrometers are operated up to 1.3 THz using SIS mixers and further up to 1.9 THz using HEB mixers. For future space missions, 2-6 THz high resolution spectroscopic surveys are highly desirable for astronomical and atmospheric studies. Our long-term research goal is to develop sensitive heterodyne receivers operating at the super-THz frequencies using NbN HEBs as mixers and quantum cascade lasers (QCLs) as local oscillators [3,4].

There are concerns about using HEB mixers at high frequencies. It is unclear whether the performance of HEBs will degrade. The relaxation of highly excited electrons due to increased photon energy can be complicated by cascade processes of emission and absorption of phonons. This can compete with the electron-electron interaction and thus may decrease the mixing efficiency [5]. Also there is a study showing that quantum noise can become a dominant factor as frequency increases [6].

The performance of HEB mixers at frequencies above 3 THz, namely super-THz frequencies, has not been measured extensively and only few studies have so far been reported [7-9]. This is mainly due to availability of suitable local oscillators. Although QCLs are very promising, they are still in developing stage. The high power consumption and the beam shape of these lasers make it difficult to use them as LO. The optical pumped FIR lasers are commonly used in laboratories but stabilizing these gas lasers at high frequencies is cumbersome and therefore the measured results suffer from LO power fluctuations. Besides, the losses in the air and the window of the cryostat are higher at these frequencies which add to the optical loss of the receiver.

Addressing some of these issues, considerable efforts have been put into stabilizing the output power of our gas laser at 4.3 THz. A new measurement setup is used where the hot/cold load calibration sources and the beam splitter are in vacuum and directly attached to the mixer cryostat. We report the measurement of a quasi-optical NbN HEB mixer at 4.3 THz using this vacuum setup and compare that with the outcome of usual setup in the air. We achieved low noise performance at this frequency, which is nearly a factor of 4 better than previously reported [7,8]. Furthermore, we introduce a characterization method that allows for the determination of the noise temperature accurately despite LO power fluctuations.

II. HEB Mixer

The HEB mixer is shown in the inset of Fig. 1. It consists of a 2 μm wide, 0.2 μm long, and 5.5 nm thick NbN bridge on a highly resistive, natively oxidized Si substrate [10]. The bridge is connected to the antenna by NbTiN (10 nm)/Au (50 nm) bilayer contact pads. Prior to the deposition of the pads, the surface of the NbN layer is

cleaned in-situ by RF Ar+ etching. Previously we have demonstrated excellent receiver sensitivities of 950 K at 2.5 THz and 1200 K at 2.8 THz using the mixers with similar contacts [11,12]. The antenna is an on-chip spiral antenna made of a 170 nm thick Au layer. It has a tight winding design with an inner "diameter" of 6.6 μm close to the NbN bridge (see Fig. 1). Based on a design rule given in ref. 8 and our previous results [9,11] using a design with a diameter of 15 μm, an expected upper cut-off frequency of this antenna is 6 THz. The HEB has a room temperature resistance of 80 Ω, a critical temperature of 10 K and a critical current of 275 μA at 4.2 K.

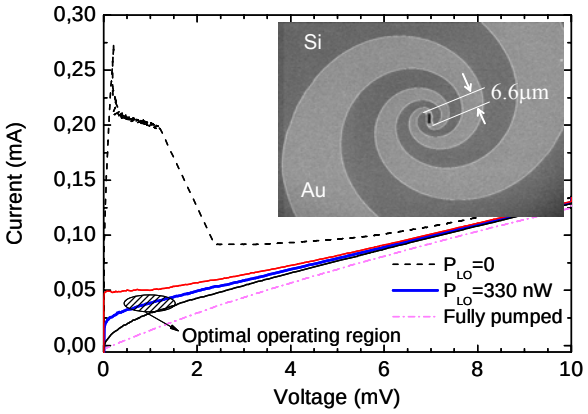

Fig. 1. A set of current-voltage curves of an NbN HEB mixer at 4.2 K at different LO power, where the optimum operating region is indicated. The inset shows a SEM micrograph of an HEB integrated with a spiral antenna with an inner diameter of 6.6 μm.

III. Heterodyne Measurement Setup

Our key results have been achieved in a quasi-optical setup, schematically shown in Fig. 2. The HEB is glued to the backside of an elliptical Si lens and mounted in a mixer unit that is placed in a 4.2 K L-He cryostat. The lens is coated with an 11 μm thick Parylene C layer, which acts as an anti-reflection coating optimal for 4.3 THz. As calibration radiation sources, a blackbody (a coating layer of a mixture of SiC grains in black Stycast epoxy [13]) at 295 K is used as the hot load and another one at 77 K as the cold load. The two loads can be selected by rotating a mirror. The radiation from the hot/cold load is combined with that from the LO by a 3 μm Mylar beam splitter. Before reaching the HEB, the radiation passes through a heat filter [14] and then a narrow-bandpass filter [15] (both are at 4.2 K). All these components are in vacuum, therefore the radiation does not suffer from absorption due to air. The use of the bandpass filter is essential to overcome a direct detection effect [16], which becomes significant due to a combination of the lossless hot/cold blackbody radiation in the vacuum and the wide RF bandwidth of the antenna.

The LO is an optically pumped FIR laser. It consists of a CO2 laser made by DEOS and a FIR ring laser developed by Max Planck Institute for Radio Astronomy in (MPIfR) Bonn, Germany. An earlier version of this ring laser has been flown successfully as a local oscillator on the Kuiper Airborne Observatory (KAO). The frequency of the pump laser is stabilized by piezoelectrically fine movement of the output mirror, controlled by an external optical feedback, which is a confocal Fabry-Perot etalon. The combination of the 9P34 line of the CO2 laser and methanol in the FIR ring laser emits 3 mW of power at 4.252 THz ($\lambda \approx 70.5$ μm). The LO power, which is the power absorbed by the HEB, is regulated by a rotating wire grid.

The mixer output at the intermediate frequency (IF) is amplified first using a cryogenic low noise amplifier and then followed by room-temperature amplifiers. This signal is filtered at 1.4 GHz in a band of 80 MHz. The entire IF chain has a gain of about 80 dB and a noise temperature of 7 K.

The just described setup is referred as the vacuum setup. For comparison, we also performed measurements in a commonly used setup, where hot/cold loads and a beam splitter are in air and a 1 mm thick HDPE window on the HEB cryostat. The rest of the setup is kept unchanged. The latter is referred as the air setup.

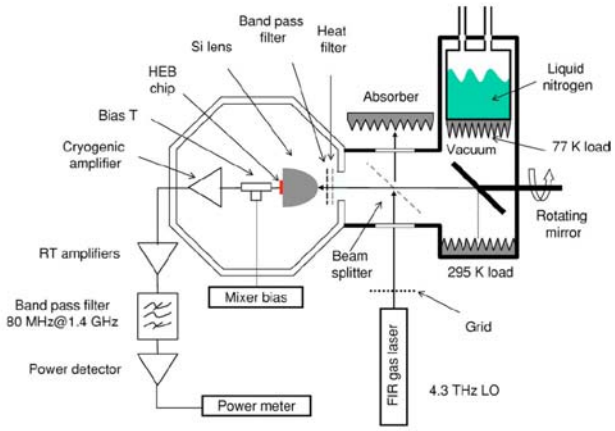

Fig. 2. Schematic picture of the measurement setup, where the hot/cold loads and the beam splitter are built in a vacuum unit, directly attached to the HEB cryostat. Switching between the hot and cold load is done by rotating a mirror.

IV. Heterodyne Measurement Results

Fig. 1 shows a typical set of current-voltage (*I-V*) curves of the HEB pumped from zero to fully pumped power level. At the indicated optimum operating region, the sensitivity is within 5% of the best value (see below), the LO power in the HEB is about 330 nW, the bias voltage is 0.8-1.2 mV and the current is 35-45 μA.

To obtain the double sideband (DSB) receiver noise temperature ($T_{N,rec}$) we measured the receiver output power, $P_{out,hot}$ and $P_{out,cold}$, responding to the hot load and cold load in the vacuum setup, as a function of bias voltage under the optimum LO power. The results are

plotted in Fig. 3. To derive $T_{N,rec}$ we use a standard *Y*-factor method, where $Y=P_{out,hot}/P_{out,cold}$, and the expression:

$$T_{N,rec} = \frac{T_{eff,hot} - Y \cdot T_{eff,cold}}{Y - 1}$$

where $T_{eff,hot}$ and $T_{eff,cold}$ are the equivalent temperatures of a blackbody at 295 K and 77 K, respectively, which are 307 K and 118 K at 4.3 THz according to the Callen-Welton definition [17]. The calculated $T_{N,rec}$ as a function of bias voltage is also plotted in Fig. 3. The $T_{N,rec}$ shows a broad minimum in its voltage dependence around 0.8 mV, where the lowest $T_{N,rec}$ value is 1350±160 K. The ±12% uncertainty (±160 K) is attributed partly (±7 %) to the fluctuations in the laser output power and partly (±5 %) to the drifting. The latter was reflected by the slightly asymmetrical $T_{N,rec}$-*V* curve. The receiver conversion loss is about 16.5 dB including all the optical losses.

For comparison, the same measurement is done using the air setup and the results are also included in Fig. 3. In contrast to those obtained in the vacuum setup, the $P_{out,hot\ \&\ cold}$ data are noisy, resulting in considerable fluctuations in the $T_{N,rec}$ curve. By neglecting several exceptional high peaks, the lowest $T_{N,rec}$ is 2300±650 K (±28 %). Based on the data obtained in the vacuum setup, we expect that the ±12 % of the fluctuations are caused by the instability of the laser. However, the remaining ±16 % are likely due to the air turbulence and the microphonic vibration in the thin beam splitter. The difference in $T_{N,rec}$ obtained with two setups is due to additional optical losses in the air (0.8 dB) and the cryostat window (0.9 dB). The LO power fluctuations caused by either the power fluctuations of the laser itself or by air and beamsplitter vibrations has a large impact on the total receiver stability. Obviously in a real astronomical instrument all measures are taken to ensure the stability of the LO. However, this is not the case in the laboratory environment. Here we introduce a measurement method that accurately determines the receiver noise temperature despite of LO power fluctuations.

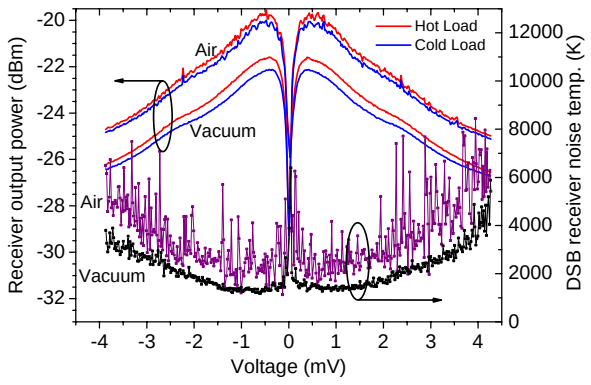

Fig. 3. Measured receiver output power (left axis) responding to the hot and cold load at optimal LO power as a function of bias voltage. One set of data are measured using hot/cold loads in the vacuum setup and another set using the air setup. The resulted DSB receiver noise temperatures are also plotted versus bias voltage (right axis).

At a constant mixer voltage bias, we measure the mixer current and the receiver output power while changing the LO power from maximum to zero and vise versa. This will move the mixer bias point from fully pumped to unpumped curve vertically on the *I-V* curves on that constant voltage (see Fig. 1). The key plot is the receiver output power versus mixer current (P_{out}-*I* curve). Two such curves are recorded for every voltage bias, one for the hot load and the other for the cold load. Fig. 4 shows 10 such curves measured with the vacuum and the air setup at 5 different voltages. A computer control grid was used to systematically change the LO power. The presented data contains over 2000 point per curve which was collected while the grid was rotating 8 times.

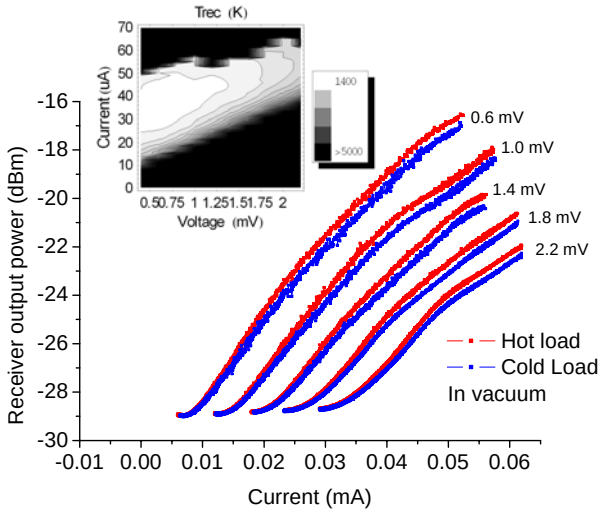

(a)

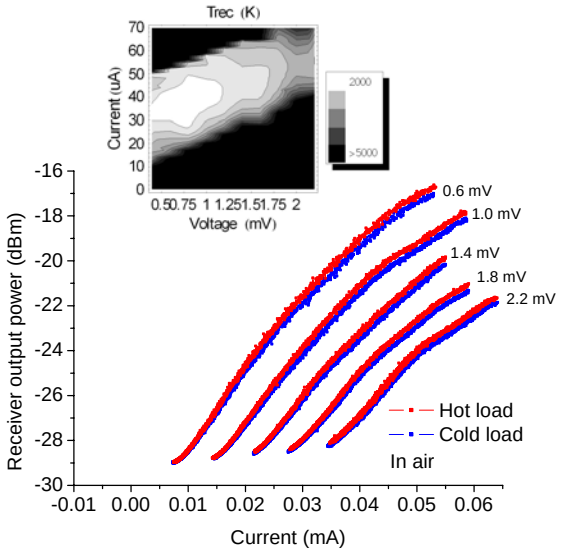

(b)

Fig. 4. Measured receiver output power responding to the hot and cold load while changing the LO power in (a) vacuum and (b) air setup at different mixer bias voltage as a function of bias current. The insets show the contour plots of the DSB receiver noise temperature, using the measured data between 0.4-2.2 mV bias voltages with 0.2 mV step.

The power difference between hot and cold load for every voltage determines the *Y* factor and the receiver noise temperature for that bias voltage and corresponding bias current.

A clear advantage of this method is that the accuracy of the measurement is not sensitive to LO power instability or drift. In contrast to the standard manner, where the LO power is required to be fixed, here it is used as a variable. Any data point at any LO power is a useful contribution to the P_{out}-I curve. Furthermore, with this method the *Y*-factor and thus the $T_{N,rec}$ are not influenced by the direct detection effect if it is present because $P_{out,hot}$ and $P_{out,cold}$ are taken at exactly the same bias point, which is exactly the same bias voltage and bias current (and therefore exactly the same LO power). Comparison between the two methods can quantify the direct detection effect.

Fig. 5 shows the measured curves at 0.8 mV (the optimum bias voltage) using both the vacuum and the air setup. We observe that for a given current, the amplitude fluctuations in the $P_{out,hot\ \&\ cold}$ are comparable in both setups. The $T_{N,rec}$ calculated from the fitted curves for the vacuum and the air setup are also shown in Fig. 5. The lowest $T_{N,rec}$ are 1296 K in the vacuum and 2015 K in the air setup. Both are at 39 μA bias current. These values are in agreement with those in Fig. 3 measured in the standard manner.

SUMMARY

We have demonstrated a highly sensitive NbN HEB mixer at 4.3 THz by using hot/cold blackbody loads and the beam splitter in vacuum. We introduced an accurate characterization method which is immune to the LO power fluctuations and drift. The lowest DSB receiver noise temperature was directly measured to be 1300 K using the vacuum setup, which is about 12 times the quantum noise ($h\nu/2k_B$). The value for the air setup is about 2000 K, which in comparison to our noise data at 2.84 THz or below (all measured in the air setup) shows an increased noise temperature, roughly scaled with frequency. However, there is no steep frequency dependence, implying that there is no clear sign of degradation of the mixing process at the super-THz frequencies [5]. Such a HEB mixer in combination with THz QCLs offers a technology possibility to build highly sensitive solid-state heterodyne receivers at the super-THz frequencies for future space and airborne telescopes. Furthermore, based on the measured receiver noise temperature and the total receiver conversion loss, we obtain the mixer output noise to be about 50 K. Since this is the typical value found at lower frequencies and can be explained by classical noise sources in the HEB mixer alone, there seems to be negligible contribution of the quantum noise [6]. However, to fully quantify the quantum noise contribution, more dedicated accurate measurements are required. Such an experiment can be the noise measurement of the same HEB mixer at several frequencies in our vacuum setup, which can reduce the uncertainties due to the window and the air loss at different frequencies.

ACKNOWLEDGMENT

The authors acknowledge P. van der Wal and J. Niels Hovenier for improving the gas laser, G. de Lange for providing the vacuum hot/cold unit, and H. Hoevers and W. Wild for their support. The work was partly supported by the EU through RadioNet and INTAS.

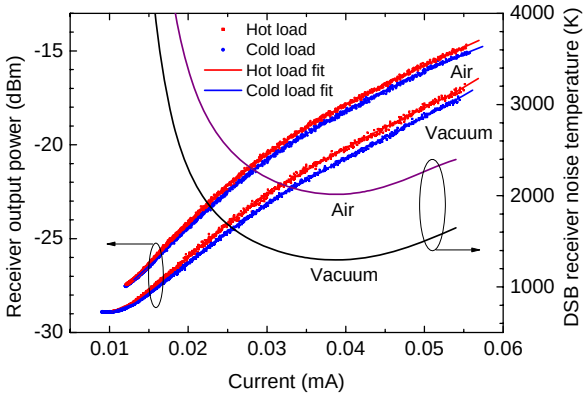

Fig. 5. Measured receiver output powers at the optimum bias voltage of 0.8 mV (dots) and the polynomial fit (lines), responding to hot and cold loads in the vacuum and air setup as a function of the current of the HEB, which is varied by changing the LO power (left axis). Also the resulted DSB receiver noise temperatures as a function of the current of the HEB (right axis).

REFERENCES

[1] J. Zmuidzinas and P. Richards, Proc. of IEEE, 92, 1597 (2004).
[2] http://herschel.esac.esa.int/
[3] See a review, B.S. Williams, Nature Photonics, 1, 517 (2007).
[4] J. R. Gao, J. N. Hovenier, Z. Q. Yang, J. J. A. Baselmans, A. Baryshev, M. Hajenius, T. M. Klapwijk, A. J. L. Adam, T. O. Klaassen. B. S. Williams, S. Kumar, Q. Hu, and J. L. Reno, Appl. Phys. Lett., 86, 244104 (2005).
[5] B. S. Karasik, M. C. Gaidis, W. R. McGrath, B. Bumble, and H. G. LeDuc, Appl. Phys. Lett., 71, 1567 (1997).
[6] E.L. Kollberg and K.S. Yngvesson, IEEE Trans. MTT. 54, 2077 (2006).
[7] Semenov, H.-W. Hübers, J. Schubert, G. N. Gol'tsman, A. I. Elantiev, B. M. Voronov, and E. M. Gershenzon, J. Appl. Phys. 88, 6758 (2000).
[8] H.-W. Hübers, A. Semenov, H. Richter, M. Schwarz, B. Günther, K. Smirnov, G. Gol'tsman, B. Voronov, in Proc. of SPIE, vol. 5498, 2004, p. 579.
[9] Y. B. Vachtomin, S. V. Antipov, S. N. Maslennikov, K. V. Smirnov, S. L. Polyakov, N. S. Kaurova, E. V. Grishina, B. M. Voronov, and G. N. Gol'tsman, Proceedings of the 15th International Symposium on Space Terahertz Technology, Northampton, MA, , 27-29 May, 2004, p. 236.
[10] 10A standard film provided by Moscow State Pedagogical University, Moscow, Russia. For details see: J. R. Gao, M. Hajenius, F. D. Tichelaar, T. M. Klapwijk, B. Voronov, E. Grishin, G. Gol'tsman, C. A. Zorman and M. Mehregany, Appl. Phys. Lett., 91, 062504 (2007).

[11] J.J.A. Baselmans, M. Hajenius, J.R. Gao, T.M. Klapwijk, P.A.J. de Korte, B. Voronov, and G. Gol'tsman, Appl. Phys. Lett, 84, 1958 (2004).
[12] M. Hajenius, P. Khosropanah, J. N. Hovenier, J. R. Gao, T. M. Klapwijk, S. Barbieri, S. Dhillon, P. Filloux, C. Sirtori, D. A. Ritchie, and H. E. Beere, OPTICS LETTERS 33 (4) 312-314 (2008).
[13] Jackson, G. de Lange, T. Zijlstra, M. Kroug, J. W. Kooi, J. A. Stern and T. M. Klapwijk, IEEE Trans. MTT. 54, 547(2006).
[14] The heat filter has an upper cutoff frequency of 5 THz and 0.32 dB loss at 4.3 THz, and is made by QMC Ltd.
[15] The bandpass filter is centered at 4.3 THz with 0.35 dB loss and 15% 3-dB bandwidth, and is made by Virginia Diodes Inc.
[16] J. J. A. Baselmans, A. Baryshev, S. F. Reker, M. Hajenius, J. R. Gao, T. M. Klapwijk, Yu. Vachtomin, S. Maslennikov, S. Antipov, B. Voronov, and G. Gol'tsman, Appl. Phys. Lett, 86, 163503 (2005).
[17] A.R. Kerr, IEEE Trans. MTT. 47, 325 (1999).

Towards Detection of OH Line at 3.5 THz Using a HEB Mixer and a Distributed Feedback Quantum Cascade Laser

W. Zhang [1,3*], P. Khosropanah[1], J.N. Hovenier[2], J.R. Gao[1,2], T. Bansal[1,2], T.M. Klapwijk[2], M.I. Amanti[4], G. Scalari[4], and J. Faist[4]

[1] *SRON Netherlands Institute for Space Research, Utrecht/Groningen, The Netherlands*

[2] *Kavli Institute of Nanoscience, Delft University of Technology, Delft, The Netherlands*

[3] *Purple Mountain Observatory, Chinese Academy of Sciences, Nanjing, China*

[4] *Institute of Quantum Electronics, ETH-Zürich, CH-8096 Zürich, Switzerland*

- Contact: wzhang@mail.pmo.ac.cn, phone +86-25-83332229 and j.r.gao@tudelft.nl

***Abstract*—We report the demonstration of a heterodyne receiver for detection of OH lines at 3.5 THz. The receiver uses a superconducting NbN hot electron bolometer integrated with a tight winding spiral antenna as mixer and a THz distributed feedback quantum cascade laser operating at 3.42 THz as local oscillator. We measured a double sideband receiver noise temperature of 2100 K at the optimum local oscillator power of 290 nW. This noise temperature can be further reduced to 1000 K if we correct the loss due to the use of an uncoated lens, and the losses of the window and the air. We also demonstrate that the improved, single spot beam of the THz QCL can easily pump the HEB mixer. Therefore, the combination of a HEB and such a DFB QCL can in principle be used to detect an OH line at 3.5 THz. However, a high input power of several watts needed to operate the QCL at an L-He cryostat poses a big challenge to the receiver stability.**

I. INTRODUCTION

Problems related to the Earth's atmosphere such as global warming and ozone destruction can be monitored and better understood by observations in the far-infrared regime. This regime holds the most important spectral signatures of the relevant molecules. Among them hydroxyl (OH) radical, which has emission lines at frequencies such as 1.8, 2.5 and 3.5 THz, has been identified as being crucial probes [1]. OH is the dominant oxidizing chemical in the atmosphere. It destroys most air pollutants and many gases involved in ozone depletion and the greenhouse effect. To detect them and resolve the line spectrum, it is desirable to have a sensitive heterodyne receiver operated in a balloon-borne or a space-borne observatory. The key components of such a receiver are a mixer (where the mixing process takes place) and a THz coherent source as local oscillator (LO). Several space-borne or balloon-borne instruments have been constructed to detect OH lines. For example, NASA's Earth Observing System Microwave Limb Sounder (EOS-MLS) [2] based on a room-temperature Schottky-diode as mixer and an
optically pumped gas laser as LO [3] is now operated to detect an OH line at 2.5 THz. TErahertz and submm LImb Sounder (TELIS) is a three-channel balloon-borne heterodyne spectrometer for atmospheric research [4]. The 1.8 THz channel based on a superconducting NbN hot electron bolometer (HEB) mixer and a solid state, multipliers based LO will focus on the OH lines at 1.8 THz..

Figure 1 shows a predicted spectrum of OH lines at 3.5 THz. The OH line at 3.551 THz is ideal for monitoring and retrieval [5] since it not only has the highest intensity among different OH lines but also is well isolated from other molecular lines. However, OH lines at 3.5 THz have never been studied by high-resolution heterodyne spectroscopy because of lack of suitable local oscillators at this particular frequency. Solid state LOs based on multipliers have demonstrated up to 2 THz, but are unlikely to generate sufficient output power at such a high frequency. Optically-pumped gas lasers can be operated at much high frequencies. However, they have no strong lasing lines very close to 3.5 THz OH lines.

Solid-state THz quantum cascade lasers (QCLs) [6] become an appearing choice of LO for this specific frequency because of their compactness, high output power, linear polarization, narrow linewidth, and phase locking ability. THz QCLs have been successfully demonstrated as LOs in laboratory using either a double-metal waveguide [7] or a surface plasmon waveguide structure [8], [9]. But they all employ a Fabry-Pérot cavity to achieve a single mode lasing. In general, a Fabry-Pérot cavity is impossible to control the operating frequency precisely, e.g, not within an accuracy of a few GHz. Therefore, for the detection of OH line at 3.551 THz, an additional mode control mechanism should be introduced to THz QCLs. Currently a distributed feedback (DFB) structure is known to achieve the single-mode operation at a designed frequency [10].

Here we report the measurement of a heterodyne receiver which combines a superconducting NbN HEB mixer and a THz DFB QCL at 3.42 THz, and demonstrate low noise performance of the receiver. To overcome the problem caused by high input power of the QCL, which results in a

draft of LO power, we applied a different characterization method for the receiver sensitivity [11].

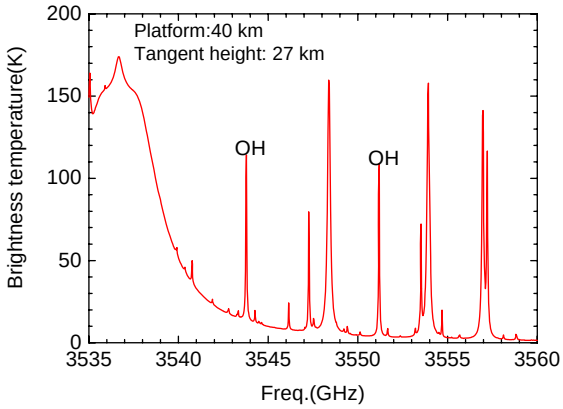

Fig.1 Simulated emission spectrum of OH lines in the atmosphere for an instrument at 40 km in limb geometry. The tangent height is 27 km.

II. THz DFB QCL AND THE BEAM PATTERN

The QCL used in our experiment is developed by ETH-Zürich, Switzerland. The active region, based on a bound-to-continuum design [12], is a GaAs/AlGaAs materials system on a semi-insulating GaAs substrate grown by molecular beam epitaxy (MBE), while the DFB structure is based on strongly coupled surface grating fabricated with wet chemical etching and metal coverage [13]. All side "facets" of the laser ridge are fully covered by the metal layer. The periodicity (Λ) of the first-order Bragg gratings determines the emission frequency as follows: $\Lambda=\lambda_{wg}/2n_g$, where λ_{wg} and n_g are the designed wavelength and effective refractive index, respectively. Lasing spectrum of a THz DFB QCL with a ridge width of 200 μm and length of 1.25 mm has been measured by FTS and the result shows a single-mode or monochromatic emission at 3.42 THz. Although it is not exactly at our targeting frequency of 3.551 THz, it should be appropriate to demonstrate a receiver for the OH line detection because the difference in frequency is so small that makes virtually no difference in the sensitivity.

Such a THz DFB QCL is expected to have a diffraction-limited single-spot beam, which should be reasonable for coupling the radiation to a mixer. However, in practice, the beam contains highly dense interference fringes in the far-field pattern (see Fig.2a) although the envelope of the beam is determined by the effective area of the facet and the wavelength and thus follows the diffraction-limited. Despite of an output power of 3 mW in CW, it is unable to pump an NbN HEB mixer, namely not enough THz power to bring the HEB in the optimal operating condition. The HEB itself requires only about a few hundred of nanoWatts power. The reason is the highly dense interference fringes in the far-field beam (see Fig.2a). However, by adding cardboard papers as THz absorbers on the top of laser bar and also on the metal plate under the laser, the interference fringes have been eliminated experimentally. This was achieved in a different, but a very similar DFB QCL. Now the far-field beam pattern shows a single-spot beam, as illustrated in Fig. 2b. Although the physical origin is still under study, it is believed that due to the absorbers, all the parasitical radiations are decoupled from the radiation emitted from the front facet. The details of the beam study have been reported in [14] and will be summarized in a separated publication. The new DFB QCL with an improved beam pattern has actually a maximum output power of 2 mW in CW mode, measured at about 10-20 K of the bath temperature for the QCL. We found that such a single spot beam allows for an efficient coupling to an NbN HEB mixer in a heterodyne measurement. The laser can overpump the HEB (namely bring the HEB to a normal state) even using a thin Mylar beam splitter of 3.5 μm. The input DC power of the THz DFB QCL is about 5 W. As it will be discussed, the high input power unfortunately makes the QCL, which is mounted in an L-He vacuum cryostat, difficult to stabilize its temperature and thus its output power.

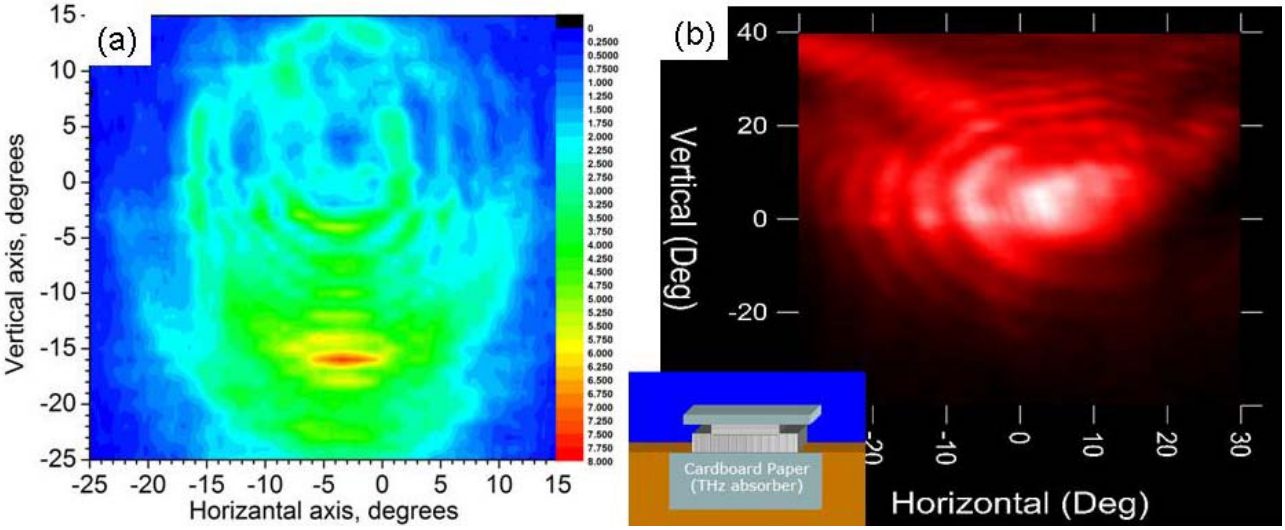

Fig.2 Measured 2D far-field beam patterns of two very similar THz DFB QCLs. Original beam pattern for one DFB QCL in (a); improved beam by adding cardboard papers as THz absorbers for another DFB QCL in (b).

III. HEB MIXER

The HEB mixer used is shown in Fig.3. It consists of a 2 μm wide, 0.2 μm long, and 5.5 nm thick NbN bridge on a highly resistive, natively oxide Si substrate [15]. The bridge is connected to the antenna by NbTiN (10 nm)/Au (50 nm) bilayer contact pads. The antenna is an on-chip spiral one made of a 170 nm thick Au layer. It has a tight winding design with inner diameter of 6.6 μm close to the NbN bridge (see Fig.3). Based on the study in [16] and our previous results using a design with a diameter of 15 μm, an expected upper cutoff frequency of this antenna is 6 THz. The HEB has a room temperature resistance of 80 Ω and a critical current of 275 μA at 4.2 K. This HEB has demonstrated an extremely low (DSB) receiver noise temperature of 1300 K at 4.3 THz using a FIR gas laser as local oscillator and a vacuum measurement setup [11].

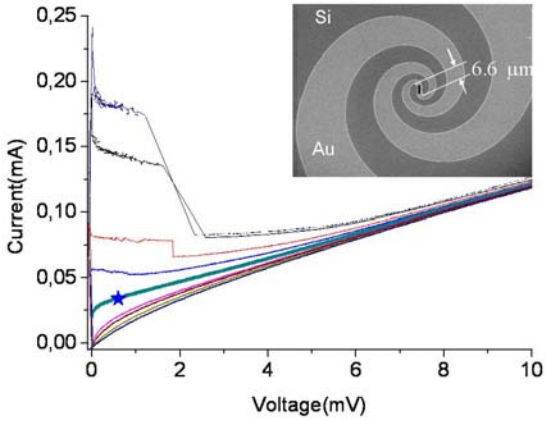

Fig.3 A set of current-voltage curves of an NbN HEB mixer at 4.2 K at different LO power from a 3.42 THz DFB QCL, where the center of the optimum operating region is indicated by a star. The inset shows a SEM micrograph of an HEB integrated with a spiral antenna with an inner diameter of 6.6 μm.

IV. HETERODYNE MEASUREMENT SETUP

Figure 4 shows a schematic view of the heterodyne measurement setup. We use two cryostats, in which the QCL and the HEB are mounted separately. A vacuum liquid helium cryostat which contains more helium than the cryostat for a HEB and thus has a high cooling capacity was used to operate the QCL. To apply the QCL as LO, we operate it in CW mode. The output power of the QCL is coupled to the HEB antenna using a standard quasi-optical technique: the Si chip with the HEB is glued to the backside of an elliptical Si lens (Φ=12 mm) without anti-reflection coating, which is placed in a metal mixer block, thermally anchored to the 4.2 K cold plate of the HEB cryostat. The beam from the QCL passes through a high-density polyethylene (HDPE) window of the QCL cryostat and is collimated with a HDPE lens (f=50 mm), combined with the radiation of 295 K (hot)/77 K (cold) load by the 3.5 μm thick beam splitter, then passes through a HDPE vacuum window (1 mm thick) at room temperature, and a QMC low-pass (or heat) filter [17], mounted on the 4 K shield of the HEB cryostat. A wire grid, inserted into the LO path between the HDPE lens and the beam splitter and controlled by computer, is used to regulate LO power (actual power absorbed by the HEB).

The intermediate frequency (IF) signal, resulting from the mixing of the LO and the hot/cold load signal, is amplified first using a cryogenic low noise amplifier operated at 4.2 K and then followed by room-temperature amplifiers. This signal is filtered at 1.4 GHz in a band of 80 MHz. The entire IF chain has a gain of about 80 dB and a noise temperature of 7 K.

To obtain the DSB receiver noise temperature ($T_{N,rec}$), we measured the receiver output noise power, $P_{out,hot}$ and $P_{out,cold}$, responding to the hot load and cold load. So $T_{N,rec}$ can be easily expressed by Y-factor ($Y=P_{out,hot}/P_{out,cold}$)

$$T_{N,rec} = \frac{T_{eff,hot} - YT_{eff,cold}}{Y-1}$$

where $T_{eff,hot}$ and $T_{eff,cold}$ are the equivalent temperatures of a blackbody at 295 and 77 K, respectively, which are 302.7 K and 104.6 K at 3.42 THz according to the Callen-Wellton definition [18].

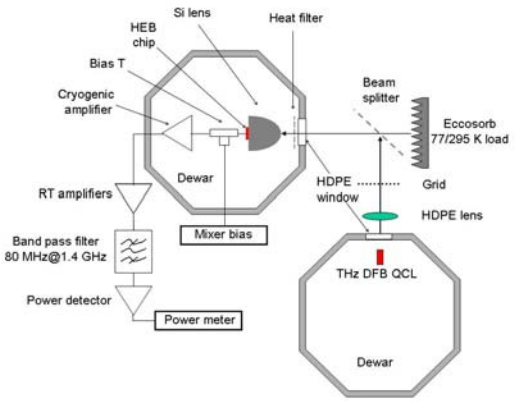

Fig.4 Schematic view of the heterodyne measurement setup, where a NbN HEB mixer and a THz DFB QCL are separately mounted in two vacuum L-He4 cryostats.

V. MEASUREMENT RESULTS

Figure 3 shows a typical set of current-voltage (*I-V)* curves of the HEB pumped by the QCL from zero power to a fully pumped power level. Around the optimum operating point indicated by a star, where the LO power in the HEB is about 290 nW, the bias voltage 0.6 mV, and bias current 30 μA, the best sensitivity is obtained.

Due to the LO power drifting, we are unable to obtain reliable sensitivity data using a standard method for a HEB, in which LO power is fixed, but the bias voltage is varied. We now apply a different characterization method as introduced in [11] to measure the DSB receiver noise temperature. In this case we measure the receiver output noise power as a function of bias current, under a fixed bias voltage, while continuously varying the LO power by the wire grid. Note that the current follows exactly the change of

LO power. This will move the bias point from the fully pumped to the unpumped region or vice versa, vertically on the I-V curves. Two such data sets are recorded, one, $P_{out,hot}(I)$, responding to the hot load and the other, $P_{out,cold}(I)$, to the cold load, so the Y factor can be easily obtained by $Y(I)= P_{out,hot}(I)/P_{out,cold}(I)$ at the exactly same current for a fixed voltage. Fig. 5 shows measured receiver output noise power data, $P_{out,hot}(I)$ and $P_{out,cold}(I)$, as a function of current and fitted curves at several bias voltages. Using the fitted curves, we derive the DSB receiver noise temperature as a function of current at different voltages.

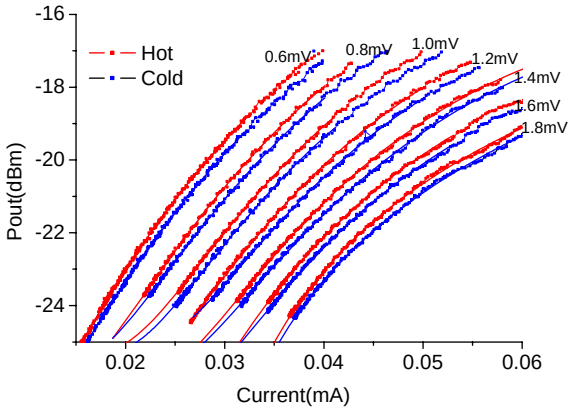

Fig. 5. Receiver output noise power of a HEB mixer as a function of bias current for different bias voltages from 0.6 mV to 1.8 mV. The current follows directly the change of LO power. The data points and curve in red correspond to the hot load, while the ones in blue to the cold load.

The lowest receiver noise temperatures are found in the data taken at 0.6 mV. The $T_{N,rec}$ versus current, together with measured output noise power data points and fitted curves, is shown in Fig. 6. The lowest $T_{N,rec}$ is 2100 ±50 K, occurred at a bias current of 30 μA. In fact, the ultimate receiver noise temperature can be a factor of two lower if we reduce the loss in the bare Si lens and in the window, and the loss due to water absorption in the air. A receiver noise temperature of 1000 K is expected at this frequency if we use an anti-reflection coated Si lens (~1 dB reflection loss), and we perform the measurement in a vacuum hot/cold setup [11] (removing 1.2 dB cryostat window loss and 0.8 dB air loss at this frequency). We emphasize that this is the first measurement of the noise temperature of a HEB receiver at a frequency in the vicinity of 3.5 THz OH line. Since the difference between two frequencies is so small, we can assume that an equal sensitivity can be achieved at the OH line frequency. Furthermore, the measured or expected receiver noise temperature at 3.42 THz is in a good agreement with the sensitivity obtained at 4.3 THz [11] if we take into account an empirical frequency dependence of the sensitivity.

We now turn to the issue of the instability of LO power and thus the instability of the receiver. As reported earlier, a THz QCL can offer an extremely stable output power [7]. However, for the present QCL it requires about 5 W DC input power when it is operated in CW mode. Whenever such a DC power is applied to the laser, the temperature monitored at the metal-holder for the QCL, which is mounted directly on the cold plate of the L-He cryostat, and thus the temperature of the laser itself, starts to increase and eventually reaches an operating region, where the temperature gets relatively stable, but still has a drift. As a consequence, the output power of the QCL shows a quick decrease and then drifts slowly. This will obviously affect the stability of the complete receiver. To demonstrate this instability, we simultaneously measured the receiver output noise power and bias current as a function of time over a period of 3 minutes immediately after turning the QCL on. As shown in Fig. 7, the receiver output noise power as well as the current of the HEB increases dramatically as QCL heats up until that the temperature of THz DFB QCL is stabilized in about 1.5 minutes. Even after that the receiver output noise power and bias current remains drifting due to the instability of QCL output power.

In the same experiment, we also demonstrate the effect of direct detection in the HEB due to wideband hot/cold radiation [19]. Because of a combination of our tight winding spiral antenna, which has a wide RF bandwidth, and the relatively small HEB, amount of the power from the hot and cold load coupled into the HEB is no longer negligible in comparison with the required LO power. As suggested in both power and current curve in Fig. 7, there are additional small periodic jumps during switching between hot and cold load. In this case a change of ~0.5 μA in the bias current of the HEB was observed, indicating an evident direct detection. In principle, such a direct detection effect can be eliminated by adding a narrow bandpass filter between the mixer and hot/cold loads, which in turn limits coupled hot/cold load power. In practice, because we are using a different characterization method to determine the Y-factor, as discussed before and shown in figure 5&6, the obtained receiver noise temperature in our case is unaffected by the direct detection effect.

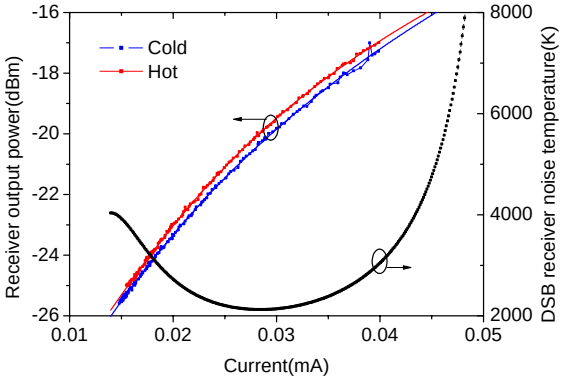

Fig. 6 Measured receiver output noise power of a HEB mixer at the optimum bias voltage of 0.6 mV (dots) and the polynomial fit (lines) responding to hot and cold loads as a function of the bias current of the HEB, which follows the change of the LO power (left axis). The resulted DSB receiver noise temperature curve as a function of the bias current of the HEB (right axis).

CONCLUSIONS

In summary, we have characterized a heterodyne receiver using a HEB as mixer and a THz DFB QCL emitting at 3.42 THz as local oscillator in order to demonstrate a system for the detection of the OH line at 3.5 THz. We have shown that the far-field beam pattern of a THz DFB QCL after introducing the absorbers around the laser becomes a single-spot beam, which makes the QCL to pump a HEB mixer easily in the heterodyne setup even with a thin beam splitter of 3.5 μm. We obtained a DSB receiver noise temperature of 2100 K at 3.42 THz. The sensitivity can be reduced to 1000 K if a coated Si lens and vacuum hot/cold setup are used. These values are the first establishment of heterodyne sensitivity in the vicinity of 3.5 THz OH line. Furthermore, the expected receiver noise temperature at this frequency confirms that the THz DFB QCL has a pure, single mode emission line. However, we also find that a too high input power needed to operate the QCL is still an issue and causes instability of the receiver, that makes other measurements than the Y-factor, such as a spectroscopic measurement, impossible.

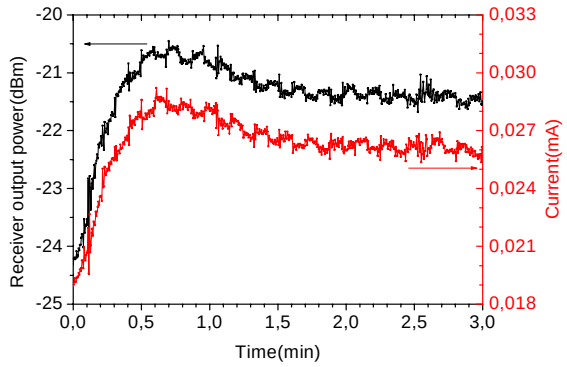

Fig.7. Measured receiver output noise power (left axis) and bias current of the HEB (right axis) as a function of time over the period of 3 minutes after turning the THz DFB QCL on and heating up. The small periodic jumps in both power and current curves are due to switching between hot and cold load, which is done manually.

To realize a practical heterodyne receiver for the detection of 3.5 THz OH line, which can be employed in a balloon-borne, like TELIS, or a space borne telescope, due to the availability of cryo-coolers and limited electrical power in both cases we foresee several technique challenges with regard to the use of THz QCLs as LO. First, the input DC power has to be far below 100 mW if it is operated around 5-10 K. An alternative is to have a THz QCL operated at a relatively high temperature, e.g., 70 K or higher. In the latter case the input power becomes less demanding and can have as much as ~1 Watt [20]. In principle, low input power [21] and high operating temperature [22] THz QCLs have been demonstrated in literature. Second, one needs to develop a frequency or phase locking technique for the QCL. A usual way to stabilize a LO is to lock the THz line to a reference signal up converted from a microwave source. However, due to lack of a solid state reference sources at such a high frequency, one needs to explore different phase locking schemes.

ACKNOWLEDGMENT

We acknowledge Sheng-Cai Shi at Purple Mountain Observatory, Nanjing, China, to support this joint research project, X. Gu and S. Paprotskiy for performing the beam measurements, M. Hajenius for fabricating the NbN HEB, and A. de Lange for providing a simulated spectrum for OH lines at 3.5 THz. The work was supported partly by China Exchange Programme, which is the framework of the scientific cooperation between the Netherlands and P.R. China, and is executed by KNAW and CAS.

REFERENCES

[1] R.G. Prinn, J. Huang, R.F. Weiss, D.M. Cunnold, P.J. Fraser, P.G. Simmonds, A. McCulloch, C. Harth, P. Salameh, S. O'Doherty, R.H.J. Wang, L. Porter, and B.R. Miller, "Evidence for substantial variations of atmospheric hydroxyl radicals in the past two decades," *Science*, vol.292, pp.1882-1888, 2001.

[2] M.C. Gaidis , H.M. Pickett, C.D. Smith, S.C. Martin, R.P. Smith, and P.H. Siegel, "A 2.5-THz receiver front end for spaceborne applications," *IEEE trans. Microwave Theory and Techniques*, vol.48, no.4, pp.733-739, 2000.S. Zhang, C. Zhu, J. K. O. Sin, and P. K. T. Mok, "A novel ultrathin elevated channel low-temperature poly-Si TFT," *IEEE Electron Device Lett.*, vol. 20, pp. 569–571, Nov. 1999.

[3] E.R. Mueller, W.E. Pobotham, Jr.,R.P. Meisner, R.A. Hart, J. Kennedy, and L.A. Newman, "2.5 THz laser local oscillator for the EOS chem 1 satellite," *in Proc. 9th Int. Space Terahertz Technol. Symp.*, Pasadena, CA, pp.563-572, 1998.

[4] P.L. Yagoubov, R.W.M. Hoogeveen, A.M. Maurellis, U. Mair, M. Krocka, G. Wagner, M. Birk, H.-W. Hübers, H. Richter, A. Semenov, G. Gol'tsman, B. Voronov, V. Koshelets, S. Shitov, B. Ellison, B. Kerridge, D. Matheson, B. Alderman, M. Harman, R. Siddans, and J. Reburn, "TELIS-development of a new balloon borne THz/sum heterodyne limb sounder," *In Proc. 14th International Symposium on Space Terahertz technology*, 22-24 April, Tucson, Arizona, pp.204-214, 2003.

[5] A. de Lange, "TELIS and OH," SRON internal report, 2005.

[6] R. Köhler, A. Tredicucci, F. Beltram, H.E. Beere, E.H. Linfield, A.G. Davies, D.A. Ritchie, R.C. Iotti, and F. Rossi, "Terahertz semiconductor-heterostructure laser," *Nature*, London, vol.417, pp.156-159, 2002.

[7] J.R. Gao, J.N. Hovenier, Z.Q. Yang, J.J.A. Baselmans, A. Baryshev, M. Hajenius, T.M. Klapwijk, A.J.L. Adam, T.O. Klaassen, B.S. Williams, S. Kumar, Q.Hu, and J.L. Reno, "Terahertz heterodyne receiver based on a quantum cascade laser and a superconducting bolometer*," Applied physics letters*, 86, 244104, 2005.

[8] H.-W. Hübers, S.G. Pavlov, A.D. Semenov, R. Köhler, L. Mahler, A. Tredicucci, H.E. Beere, D.A. Ritchie, and E.H. Linfield, "Terahertz quantum cascade laser as local oscillator in a heterodyne receiver," *Optics express*, vol.13, no.15, pp.5890-5896, 2005.

[9] M. Hajenius, P. Khosropanah, J.N. Hovenier, J.R. Gao, T.M. Klapwijk, S. Barbieri, S. Dhillon, P. Filloux, C. Sirtori, D.A. Ritchie, and H.E. Beere, "Surface Plasmon quantum cascade lasers as a terahertz local oscillators," *Optics letters*, vol. 33, no. 4, pp.312-314, 2008.

[10] L. Mahler, R. Köhler, A. Tredicucci, F. Beltram, H.E. Beere, E.H. Linfield, D.A. Ritchie, and A.G. Davies, "Single-mode operation of terahertz quantum cascade lasers with distributed feedback resonators," *Appl. Phys. Lett.*, vol. 84, no. 26, pp.5446-5448, 2004.

[11] P. Khosropanah, J.R. Gao, W.M. Laauwen, M. Hajenius and T.M. Klapwijk, "Low noise NbN hot-electron bolometer mixer at 4.3 THz," *Appl. Phys. Lett.*, 91, 221111, 2007.

[12] J. Faist, M. Beck, T. Aellen, E. Gini, "Quantum cascade lasers based on a bound-to-continuum transition," *Appl. Phys. Lett.*, vol.78, no. 2, pp.147-149, 2001.

[13] L. Ajili, J. Faist, H. Beere, D. Ritchie, G. Davies, and E. Linfield, "Loss-coupled distributed feedback far-infrared quantum cascade lasers," *Electronics letters*, vol.41, no.7, pp.419-420, 2005.
[14] J.N. Hovenier, S. Paprotskiy, J.R. Gao, P. Khosropanah, T.M. Klapwijk, L. Ajili, M.A. Ines, and J. Faist, Abstract, ISSTT 2007.
[15] A standard film provided by Moscow State Pedagogical University, Moscow, Russia.

[16] A.D. Semenov, H. Richter, H.-W. Hübers, B. Günther, A. Smirnov, K.S. Il'in, M. Siegel, and J.P. Karamarkovic, "Terahertz performance of integrated lens antennas with a hot-electron bolometer," IEEE Trans. Microwave theory and techniques, vol.55, no.2, pp.239-247, 2007.
[17] The heat filter has an upper cutoff frequency of 5 THz and 0.22 dB loss at 3.42 THz and is made by QMC Ltd.
[18] A.R. Kerr, "Suggestions for revised definitions of noise quantities, including quantum effects," *IEEE Trans. Microwave Theory Tech.* vol.47, no.3, pp.325-329, 1999.
[19] J.J.A. Baselmans, A. Baryshev, S.F. Reker, M. Hajenius, J.R. Gao, T.M. Klapwijk, Yu. Vachtomin, S. Maslennikov, S. Antipov, B. Voronov, and G. Gol'tsman, "Direct detection effect in small volume hot electron bolometer mixers," *Appl. Phys. Lett.*, vol.86, 163503, 2005.
[20] W. Wild, Th. de Graauw, A. Baryshev, J. Baselmans, J.R. Gao, F. Helmich, B.D. Jackson, V.P. Koshelets, P. Roelfsema, N.D. Whyborn, and P. Yagoubov, "Terahertz Technology for ESPRIT – A Far-Infrared Space Interferometer", *In Proc. 16th Int. Symposium on Space Terahertz Technology*, Göteborg, Sweden, May 2-4, 2005, pages 68-73.
[21] S. S. Dhillon, J. Alton, S. Barbieri, A. de Rossi, M. Calligaro, H. E. Beere, E. H. Linfield, D. A. Ritchie, and C. Sirtori, "Ultralow threshold current terahertz quantum cascade lasers based on double-metal buried strip waveguides", *Appl. Phys. Lett*. 87, 071107, 2005.
[22] B. S. Williams, S. Kumar, and Q. Hu, "Operation of THz Quantum cascade lasers at 164K in pulsed mode and at 117K in continuous-wave mode," *Opt. Express 13*, 3331, 2005.

Temperature Dependence of HEB Mixer Performance

Shoichi Shiba[1,*], Ken Shimbo[1], Ling Jiang[1], Nami Sakai[1], Mika Sugimura[1], P. G. Ananthasubramanian[1], Hiroyuki Maezawa[2], and Satoshi Yamamoto[1]

[1]*Department of Physics, The University of Tokyo, Bunkyo-ku, Tokyo 113-0033, Japan*

[2]*Solar-Terrestrial Environment Laboratory (STEL), Nagoya University, Chikusa-ku, Nagoya 464-8601, Japan*

- Contact: shiba@taurus.phys.s.u-tokyo.ac.jp, phone +81-3-5841-4217

***Abstract*— The performance of the NbTiN HEB mixer has been measured at various bath temperatures. The mixer performance is almost constant below 7 K, but it is degraded rapidly above that temperature. The result is compared with the classical operation picture of the HEB mixer. From the temperature dependence of the performance, the power index, *n*, of the heat conductance is estimated to be 4-5 for our NbTiN mixer, confirming that our device operates by the phonon-cooling mechanism. The temperature-dependence experiment provides us with important information on the operation mechanism of HEB mixer.**

I. Introduction

Superconducting hot-electron bolometer (HEB) mixers are recognized as the most promising device for low-noise heterodyne detection in the THz region [1]. In particular, the quasi-optical NbN HEB mixer shows a good performance up to several THz. Receivers using the HEB mixers are adopted for radio astronomy and atmospheric chemistry, for instance, in Herschel Space Observatory, SOFIA, TELIS, and so on.

So far evaluation and optimization of the HEB mixer receivers have been performed mostly at the fixed temperatures (4 K or 2 K) by using liquid He. In a practical operation of the HEB mixer receivers on the ground-based telescopes, mechanical cryocoolers will be used. In this case, the laboratory conditions might not be reproduced, so that the bath temperature of the mixer is possibly changed. It is therefore important to know how much the mixer performance is degraded when the bath temperature is changed. Moreover, the temperature dependence of the mixer performance would provide us with novel information on operation mechanisms of the HEB mixers.

However, an only few studies have been reported for the temperature dependence of the HEB mixer performance, Skalare *et al.* [2] fabricated the diffusion cooled HEB mixer using Nb. This device showed the receiver noise temperature of 650 K (DSB) at the bath temperature of 2.2 K, whereas its performance was about 3000 K (DSB) at 4.3 K. For the NbN HEB mixer, Cherednichenko *et al.* [3] measured the receiver noise temperature at various bath temperatures from the motivation to reduce the necessary LO power. In the present paper, we report a systematic study on the temperature dependence of the NbTiN HEB mixer performance.

II. Measurements

A. Current Status of the Mixer Development

Our group is developing an HEB mixer receiver aiming at the THz observations of fundamental atoms and molecules in star-forming clouds from the ground-based telescopes. We are fabricating diffusion-cooled type and phonon-cooled type HEB mixers using Nb and NbTiN, respectively. We adopt our original procedure for fabrication [4, 5]. The HEB mixer element is mounted on a waveguide mixer block for the signal and local oscillator (LO) coupling, and is cooled down to 4 K by a compact two-stage Gifford-MacMahon cryogenic-cooler equipped with a helium-pot for temperature stabilization (Sumitomo RDK-101E). Its cooling capability is 0.1 W for the 4 K stage. Receiver performance is tested at 810 GHz (using a Gunn oscillator as the LO source), and the best receiver noise temperature of 500 K has been achieved for the NbTiN mixer [4].

Temperature-dependence Experiment

The NbTiN HEB mixer element used for the temperature-dependence experiment has a microbridge size of 0.48 μm in length, 1.49 μm in width, and 12 nm in thickness. This is slightly larger than the mixer element which gives the best performance [4]. By using an electric heater attached on the

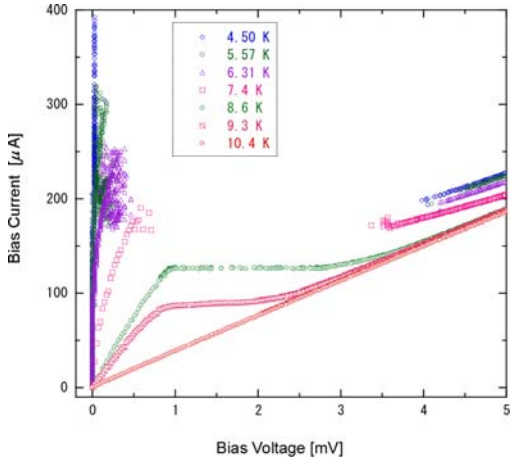

Fig. 2 I-V curves at various bath temperatures

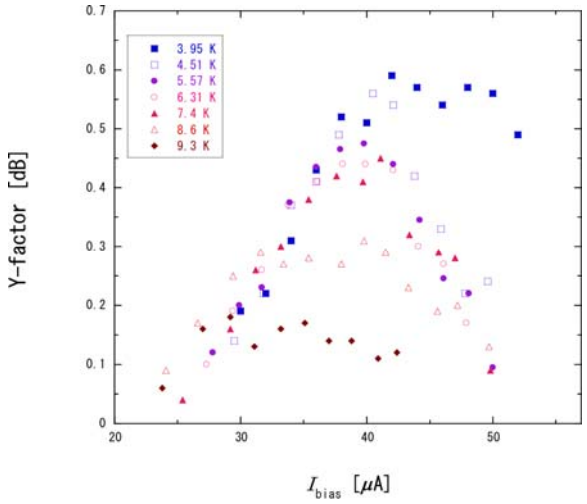

Fig. 2 Relation between Y-factor and I_{bias} at various T_{bath}. V_{bias} is fixed to 0.4-0.5 mV.

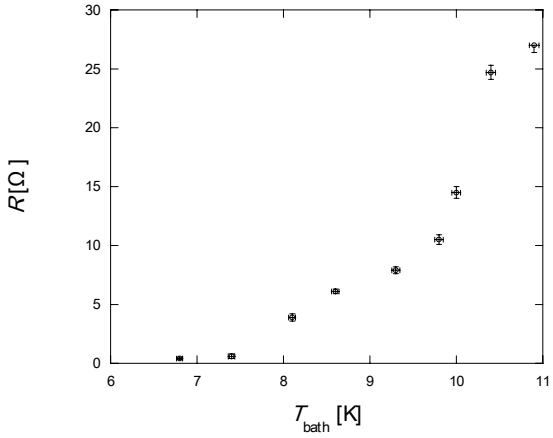

Fig. 3 R-T curve of the HEB device

cold stage, we can change the bath temperature easily.

Figure 1 shows the I-V curve of the mixer element measured at various bath temperatures. It is clearly seen that superconductivity disappears above 10.4 K. Therefore we have measured the Y-factor at various temperatures from 4 K to 9 K. In the measurements of the Y-factor, the bias voltage is kept constant (0.4-0.5 mV), and the bias current is adjusted by the LO input power; weaker LO input power gives higher bias current.

In Fig. 2, the Y-factor is plotted against the bias current at various temperatures. At 4.51 K, the Y-factor becomes the highest at the bias current of about 40 μA. For most cases, the best Y-factor is obtained at this bias current; namely the optimum bias point is independent on the bath temperature. This means that the effective operating resistance of the HEB mixer element is around 10-12 Ω at the optimum bias point, which just corresponds to the transition-edge in the R-T curve (Fig. 3). This result is consistent with the classical picture of the HEB mixer operation.

III. Discussions

Extensive efforts have been made to describe the operation principle of the HEB mixers [e.g. 6]. The receiver noise temperature (T_{RX}) is written as

$$T_{RX} = T_{MIX} + L_{MIX} T_{IF} \ , \qquad (1)$$

where T_{MIX}, T_{IF}, and L_{MIX} represent the mixer noise temperature, the noise temperature of the IF amplifier, and the conversion loss of the mixer, respectively. In our case, the second term is found to be dominant. The conversion loss, L_{MIX}, can be written as

$$L_{MIX} = \frac{(Z_L + Z_B)^2}{2S_0{}^2 P_{LO} Z_L} \propto \frac{1}{P_{LO}}, \qquad (2)$$

where P_{LO}, S_0, Z_L, and Z_B, stand for the input local oscillator power, the voltage sensitivity, the load impedance, and the HEB device impedance, respectively. Since T_{MIX} also shows a similar dependence [6] and T_{IF} is almost constant below 10 K, T_{RX} is inversely proportional to P_{LO}. In addition, the heat balance between the input power and the thermal conductance makes the following equation;

$$P_{LO} + RI^2 = G_0 (T_C{}^n - T_{bath}{}^n), \qquad (3)$$

where G_0, T_C, and T_{bath} represent the thermal conductance, the critical temperature of the HEB device, and the bath temperature, respectively. For simplicity, we assume that the phonon temperature is equal to the bath temperature. In our case, the second term of the left hand side (DC heating), can be negligible in comparison with the first term, and hence, we obtain the following approximate relation,

$$T_{RX} \propto \frac{1}{T_C{}^n - T_{bath}{}^n} \ . \qquad (4)$$

In the following part, we will test this classical picture by using the measurement result.

Figure 4 shows the receiver noise temperature (T_{RX}) as a function of P_{LO}, where P_{LO} is estimated from the isothermal method. T_{RX} is clearly inversely proportional to P_{LO}, confirming the above prediction. Next, the best receiver noise temperature is plotted as a function of the bath temperature in Fig. 5. When the bath temperature is raised, the performance is kept almost constant below 7 K, but is degraded rapidly above that temperature. This means that our NbTiN HEB mixer shows little change in performance against the bath temperature change around 4 K. This is in remarkable contrast with the Nb HEB case, which shows a strong dependence on bath temperature around 4 K [2]. This behavior of the NbTiN HEB mixer gives an important merit in practical operations on the telescopes.

From the relation between T_{RX} and T_{bath}, the index n of equation (4) is estimated to be 4-5, as shown in Fig. 5. This index is closer to the phonon-cooled case (NbN) (3.6) than to the diffusion-cooled case (Nb) (2.0). Our NbTiN device shows a quite similar behavior to the NbN device, confirming that our mixer is mainly operating by the phonon-cooling mechanism. The phonon-cooled NbTiN device has high T_C (about 10 K) and fairly large index n (4~5). On the other hand, T_C is relatively low (about 6 K) and n is small (2.0) in

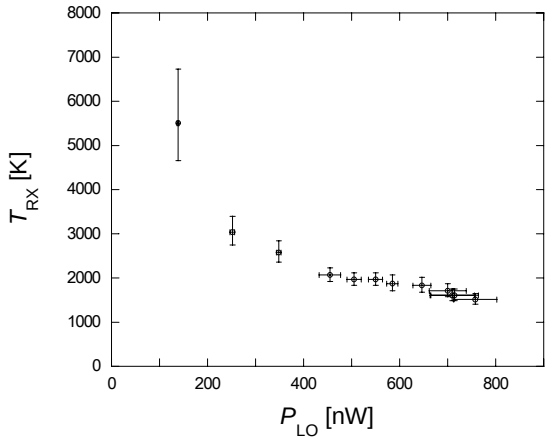

Fig. 4 Receiver noise temperature plotted against LO input power

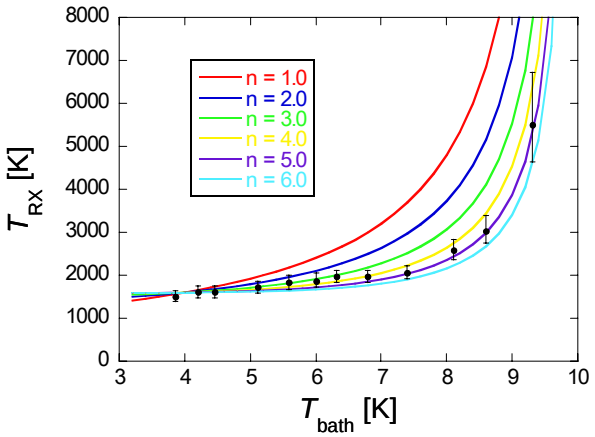

Fig. 5 Receiver noise temperature at various bath temperatures. Solid lines are fitted curves by equation (4), assuming that T_C = 10 K.

the case of the diffusion-cooled Nb device. This makes the strong temperature dependence around 4 K in the Nb device.

As described in this paper, we can estimate the index *n* quantitatively from the temperature-dependence measurement, which is an important parameter on the cooling mechanism of the HEB mixer. Needless to say, a similar experiment can be done by using the devices with different film thickness or different length of a superconducting microbridge. However, such experiments need fabrications of several devices of different sizes, and the performance may easily be affected by the characteristics of individual devices, the electrical contact, or the alignment conditions in an assembling process. In contrast, the temperature-dependence measurement can be carried out with a single device under the same environment. This method is therefore advantageous to investigate the operation mechanism of HEB mixer.

ACKNOWLEDGMENT

We are grateful to J. R. Gao, S. Cherednichenko and S. C. Shi for helpful discussions. This study is supported by Grant-in-Aid from the Ministry of Education, Culture, Sports, Science, and Technologies (14204013 and 15071201).

REFERENCES

[1] K. H. Gundlach, and M. Shicke, "SIS and bolometer mixers for terahertz frequencies," *Supercond. Sci. Technol.*, **13**, R171-R187, 2000.

[2] A. Skalare, W. R. McGrath, B. Bumble, H. G. LeDuc, P. J. Burke, A. A. Verheijen, R. J. Schoelkopf, and D. E. Prober, "Large bandwidth and low noise in a diffusion-cooled hot-electron bolometer mixer," *Appl. Phys. Lett.*, **68** (11), 1558-1560, 1996.

[3] S. Cherednichenko, M. Kroug, H. Merkel, E. Kollberg, D. Loudkov, K. Smirnov, B. Voronov, G. Gol'tsman, and E. Gershenzon, "Local oscillator power requirement and saturation effects in NbN HEB mixers," *Proc. 12th Int. Symp. on Space Terahertz Technology*, 2001.

[4] L. Jiang, S. Shiba, K. Shimbo, M. Sugimura, P. G. Ananthasubramanian, H. Maezawa, S. C. Shi, and S. Yamamoto, "Development of 0.8 THz and 1.5 THz Waveguide NbTiN HEB Mixers," *these proceedings*, 2008.

[5] Ken Shimbo, "Developmental Study on an NbTiN HEB Mixer for Astronomical Applications," *Dissertation*, the University of Tokyo, Japan, 2007.

[6] B. S. Karasik and A. I. Elantiev, "Noise temperature limit of a superconducting hot-electron bolometer mixer ," *Appl. Phys. Lett.*, **68** (6), 853-855, 1996

Fabrication and characterisation of NbN HEB mixers with in situ gold contacts

S. A. Ryabchun*, I. V. Tretyakov, M. I. Finkel, S. N. Maslennikov, N. S. Kaurova, V. A. Seleznev, B. M. Voronov and G. N. Goltsman

Moscow State Pedagogical University, Moscow 119992, Russia

* Contact: sryabchun@rplab.ru, phone +7-495-246 6321

***Abstract*— We present our recent results of the fabrication and testing of NbN hot-electron bolometer mixers with *in situ* gold contacts. An intermediate frequency bandwidth of about 6 GHz has been measured for the mixers made of a 3.5-nm NbN film on a plane Si substrate with *in situ* gold contacts, compared to 3.5 GHz for devices made of the same film with *ex situ* gold contacts. The increase in the intermediate frequency bandwidth is attributed to additional diffusion cooling through the improved contacts, which is further supported by the its dependence on the bridge length: intermediate frequency bandwidths of 3.5 GHz and 6 GHz have been measured for devices with lengths of 0.35 µm and 0.16 µm respectively at a local oscillator frequency of 300 GHz near the superconducting transition. At a local oscillator frequency of 2.5 THz the receiver has offered a DSB noise temperature of 950 K. When compared to the previous result of 1300 K obtained at the same local oscillator frequency for devices fabricated with an *ex situ* route, such a low value of the noise temperature may also be attributed to the improved gold contacts.**

I. Introduction

Hot-Electron Bolometer (HEB) mixers have long ago established themselves as the primary detectors of choice for heterodyne observations in terahertz radio astronomy. At the same time, the quest for better characteristics – a lower noise temperature and a wider intermediate frequency (IF) bandwidth – has been underway. As far as heterodyne spectroscopy is concerned, a wider IF bandwidth might allow observation of a few relatively narrow lines or mapping a broader line without the necessity to change the local oscillator (LO) frequency, a procedure which is not only inconvenient but may also be practically impossible. In total power receivers the temperature resolution is inversely proportional to the receiver bandwidth and improves as the receiver noise temperature is reduced: $\Delta T = (T_A + T_R)/(B\tau)^{1/2}$, with T_A being the antenna temperature, T_R the receiver noise temperature, B the receiver final detection bandwidth and τ the integration time. Hence, both the increase of the IF bandwidth and the reduction of the noise temperature of a receiver are of great importance to applications.

With respect to the cooling mechanism of electrons HEB mixers are divided into phonon cooled mixers and diffusion cooled mixers, the type of the dominating process depending primarily on the device geometry. For devices with lengths $L > L_{diff} = (D\tau_\Theta)^{1/2}$ (D being the diffusion coefficient and τ_Θ the electron temperature relaxation time) cooling by phonons dominates. In this case the excess energy of the electrons is removed through collisions with the phonons in the film on a time scale of the electron-phonon interaction time τ_{eph} and the subsequent escape of these non-equilibrium phonons into the substrate with the characteristic time τ_{esc}.

There are several models that describe the operation of the phonon cooled HEB mixer, the most known and simplest of these being the uniform heating model (e.g. [1]) and the hot-spot model (e.g. [2], [3]). Only the salient points of the former will be reviewed here, while the latter will not be discussed at all. In the framework of the uniform heating model the HEB mixer is described by a set of two coupled heat balance equations governing the evolution of the electron and phonon subsystems of a superconducting film. These equations are not linear in the electron and phonon temperatures but become such in the limit of a small signal. This means that the deviations of the electron and phonon temperatures caused by absorbed RF power and Joule heating are small compared with their equilibrium values, which is why the uniform heating model works well only when the ambient temperature is close to T_c. In this case one can compute the alternating part of the electron temperature, $\Delta\Theta_{ac}$ ([4]), whence the alternating part of the voltage across the mixer is $\Delta V_{ac} = I_{dc}(\partial R/\partial\Theta)\Delta\Theta_{ac}$, and the output power $P_{IF} \sim |\Delta V_{ac}|^2 \sim |\Delta\Theta_{ac}|^2$:

$$P_{IF}(f) = P(0)\frac{1+(2\pi f\tau_0)^2}{\left(1+(2\pi f\tau_1)^2\right)\left(1+(2\pi f\tau_2)^2\right)} \qquad (1)$$

with

$$\tau_0^{-1} = \tau_{esc}^{-1} + \tau_{eph}^{-1}(c_e/c_{ph}),$$
$$\tau_{1,2}^{-1} = \frac{1}{2\tau}\left[1 \pm \sqrt{1-\frac{4\tau^2}{\tau_{esc}\tau_{eph}}}\right], \qquad (2)$$
$$\tau^{-1} = \tau_{esc}^{-1} + \tau_{eph}^{-1}(c_e/c_{ph}+1).$$

If the length of the mixer is small compared to L_{diff} then cooling by the diffusion of hot electrons out of the bridge into the contact pads is possible and may dominate phonon cooling ([5]). The time constant of a diffusion-cooled HEB mixer is given by ([6])

$$\tau_{diff} = \frac{L^2}{\pi^2 D}. \qquad (3)$$

For diffusion cooling to be feasible it is important to ensure a good interface between the film and the contact pads, otherwise hot electrons will not be able to diffuse out of the film. The model of the diffusion-cooled bolometer gives the following expression for output power ([6]):

$$P_{IF}(f) = P(0)\frac{1}{1+(2\pi f \tau_{diff})^2}. \qquad (4)$$

It should be noted that in some cases (1) can be cast into the form of (5) thus allowing the determination of the single time constant of a phonon-cooled mixer (see below).

If one considers the mixer as well as the embedding circuit it will be necessary to introduce the so-called self-heating parameter which describes the effect of the electrothermal feedback between the electron temperature and the DC bias supply and slightly modifies the mixer time constant. This parameter can be shown to depend on the mixer operating point and to be proportional to the derivative of the mixer resistance with respect to the electron temperature ([6]). Our estimates, however, show that this parameter is small in the uniform heating regime, and hence the effect of the electrothermal feedback can be neglected.

As regards RF coupling, up to about 1.5 THz waveguide HEB mixers can be successfully used. However, above this frequency the dimensions of the components become too small, so quasioptical HEB mixers are used. For NbN quasioptical HEB mixers fabricated without special cleaning of the NbN film prior *ex situ* gold deposition a noise temperature of 1300 K at 2.5 THz and 3100 K at 3.8 THz and an IF bandwidth as large as 5.2 GHz in the frequency range 0.85-1 THz have been reported in [7] and [8] respectively. At the same time, it has been reported that significant improvement of the receiver performance can be achieved by additional cleaning of the NbN film before *in situ* gold deposition. Baselmans *et al.* have reported a noise temperature of 950 K at an LO frequency of 2.5 THz and an IF bandwidth of 6 GHz measured with a 600-GHz LO and attributed this result to improved interface between the film and the gold contacts [9]. Waveguide HEB mixers fabricated with the use of the conventional (*ex situ*) technological route have demonstrated noise temperatures of 900-1050 K at 1.035 THz and 1300-1400 K at 1.26 THz and an IF bandwidth of 3.2 GHz at 0.8 GHz ([10]).

II. HEB DEVICES

HEB mixers were fabricated from 3.5-nm NbN films deposited on top of Si substrates by DC reactive magnetron sputtering. The deposition of NbN film was followed by *in situ* deposition of a 15-nm Au layer. The NbN-Au structure was then covered with electronic resist and a window was made in the resist for the subsequent ion milling and chemical etching of the Au layer all the way down to the NbN film. This defined the bolometer length.

The devices had superconducting transition temperatures of about 11.5 K with transition widths of about 1 K. The critical currents were measured to be close to 400 μA and the

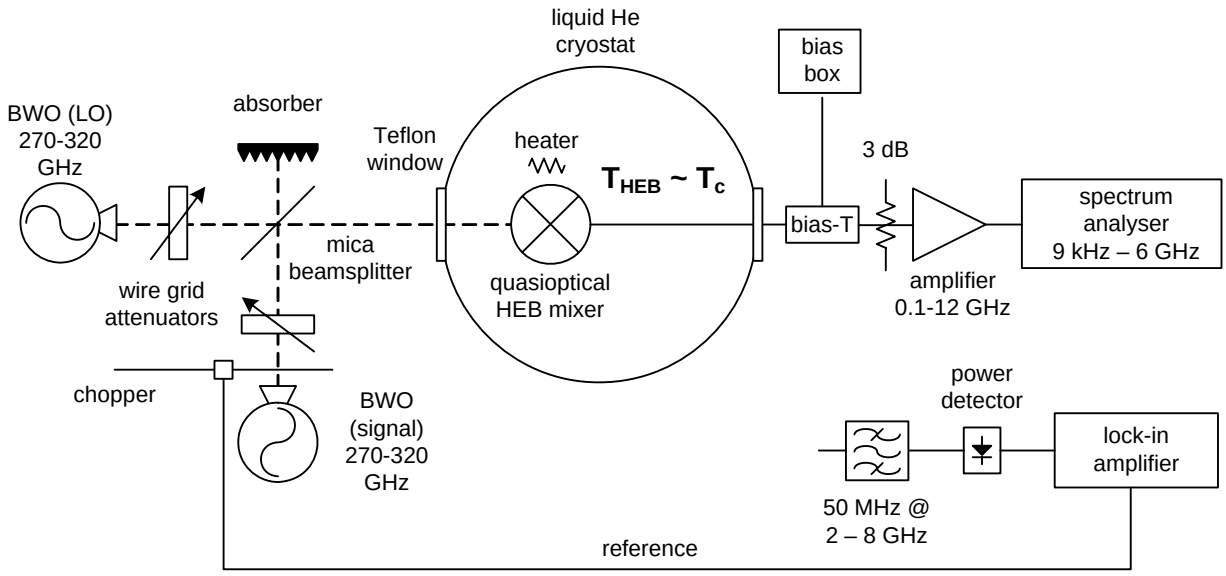

Fig. 1. Schematic of the experimental setup for IF bandwidth measurements

normal state resistances were 60 to 100 Ω.

III. Experimental setup

A. IF bandwidth measurements

The IF bandwidth of our HEB mixers was measured at 300 GHz near T_c. The experimental setup for the IF bandwidth measurements is presented in Fig. 1. The HEB mixer was glued to an extended hemispherical Si lens and installed into a mixer block which was mounted onto the cold plate of a liquid helium cryostat. Two backward wave oscillators (BWO) operating in a frequency range of 270-320 GHz were used as a local oscillator and a signal source, with the frequency of the signal BWO being fixed throughout the experiment. The power levels of both BWO's could be adjusted appropriately with the use of wire grid attenuators. After passing through their respective attenuators the signals were coupled with a mica beam-splitter and delivered into the cryostat. The HEB mixer was IF-coupled to a 1-inch coplanar line with a subsequent transition to a coaxial cable which led the IF signal out of the cryostat to a room-temperature Picosecond Pulse Labs bias-T with a bandwidth of 18 GHz and then to a Miteq amplifier with a pass band of 0.1-12 GHz and a gain of about 36 dB. The insertion loss of the IF chain in dB's, excluding the coplanar line, was found to depend on frequency as $L(f) = -5.6\text{-}1.3f$, with the frequency measured in GHz. The frequency range up to 6 GHz was processed with a Rohde&Schwartz spectrum analyser (frequency range 100 kHz-6 GHz). To cover the range beyond 6 GHz we modified the experimental setup by including a chopper in the signal path and replacing the spectrum analyser with a power detector and a lock-in amplifier. A tuneable band-pass filter (BPF) with the centre frequency running from 2 to 8 GHz and a bandwidth of 50 MHz was added to the setup to reduce the noise.

B. Noise temperature measurements

The noise temperature measurements were performed at 2.5 THz. Referring to Fig. 2, the mixer block containing the device was installed into a cryostat with a high density polyethylene window 0.5 mm thick, a Zitex-104 cold infrared filter and a 2-3 THz mesh filter mounted on the cold plate. Radiation from a gas discharge H_2O laser at 2.5 THz was combined with radiation from a blackbody with the use of a Mylar beam-splitter 6 μm thick. The receiver back-end included a wideband bias-T followed by a cryogenic amplifier with a built-in circulator, together forming a unit with a gain of 30 dB and a bandwidth of 1-2 GHz. Outside the cryostat, the IF signal was further amplified by two amplifiers, each with a gain of 30 dB and a bandwidth of 0.01-2 GHz, separated by a 50-MHz BPF with the centre frequency 0.6-1.2 GHz. To suppress standing waves in the IF chain a 6-dB attenuator was placed immediately at the output of the cryostat and two 3-dB attenuators were placed at both ports of the BPF. The output of the second room-temperature amplifier was fed to a power detector followed by a remotely controlled nanovolmeter.

IV. Experimental technique

A. IF bandwidth measurements

Since the gap frequency of NbN is about 900 GHz at helium temperatures, electromagnetic radiation with a frequency of 300 GHz cannot destroy the superconducting state at 4.2 K by breaking Cooper pairs, and hence will not be absorbed uniformly in the superconductor. In this case the heating of the electrons in the material will not be uniform and the model of mixing in phonon cooled hot-electron

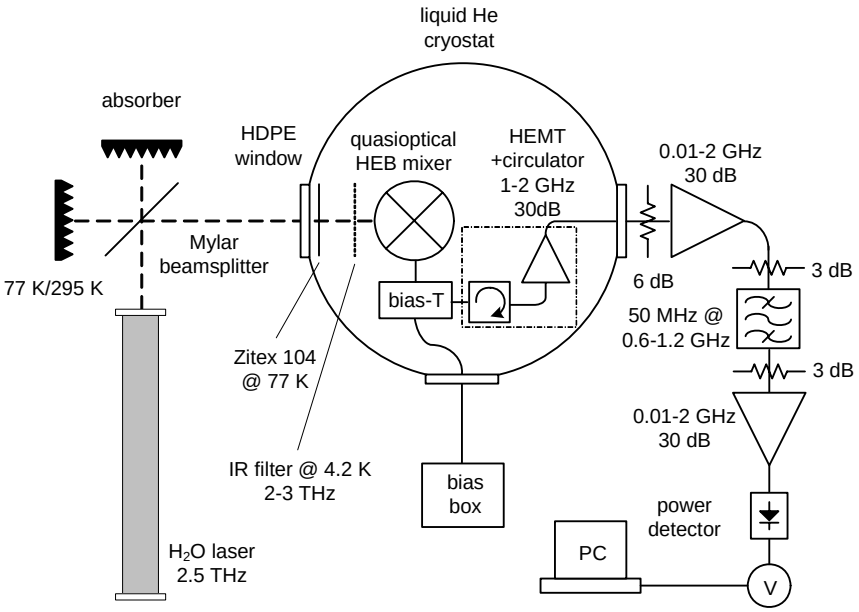

Fig. 2. Schematic of the experimental setup for noise temperature measurements

bolometers outlined in the introduction will not be applicable. To suppress the energy gap enough and thus ensure uniform heating at these frequencies the ambient temperature was raised to about T_c. The $R(T)$ dependence should be measured at as low a bias current as possible to avoid undesirable effects such as pair breaking by the transport current and additional Joule heating. So if one plots a family of IV curves for a device taken at different ambient temperatures, the slope of a curve at the origin, $(\partial V/\partial I)_0$, taken at a certain temperature T will be equal to $R(T)$. Since the critical temperature is usually defined as the temperature for which the device resistance approximately equals half of the resistance at room temperature, $R_n/2$, this means that when $(\partial V/\partial I)_0 = R_n/2$ the mixer temperature is about equal to T_c, the energy gap is sufficiently suppressed, and RF signal may be uniformly absorbed by the bridge. This simple observation allows one to avoid using a thermometer, which introduces certain ambiguities, when setting the operating temperature of an HEB mixer.

Another requirement of the uniform heating model is that the power levels of the signal and the local oscillator should be low. This means that the relative change of the mixer current at some fixed value of the bias voltage should not change appreciably when in addition to heating one applies RF power. Ideally one should have $\delta I_{mixer}/I_{mixer} << 1$ (δI_{mixer} being the change of the mixer current cause by the switching on of the LO drive); in practice, however, this usually leads to the IF signal being too low. We chose $\delta I_{mixer}/I_{mixer} = 0.05$. Now that the operating current-voltage curve had been established we needed to choose the operating point on it. When one computes the impedance of the HEB mixer one gets $Z = R + I(\partial R/\partial I) + I(\partial R/\partial \Theta)(\partial \Theta/\partial I)$, with $R = V/I$ being the device DC resistance and Θ the electron temperature. The first and the second terms are simply the device differential resistance, the second one describing the non-thermal effect of the bias current on the superconducting state (vortices, phase-slip centres). This effect is undesirable if the uniform heating model is to be applied, and to be consistent one would have to ensure the condition $\partial V/\partial I = R$, possibly at the expense of a good signal-to-noise ratio. So, the choice of the operating point is a trade-off between consistency and a good signal-to-noise ratio. Also, as has been outlined in the introduction, the effect of the electrothermal feedback can be neglected, and so one need not worry about the dependence of the mixer time constant on the operating point in the case of uniform heating.

B. Noise temperature measurements

All the noise temperature measurements were performed at 4.2 K with the use of the standard Y-factor procedure, with the receiver noise temperature determined as

$$T_R = \frac{T_{hot} - YT_{cold}}{Y - 1}, \tag{5}$$

where T_{hot} and T_{cold} are the physical temperatures of the blackbody loads equal to 295 K and 77 K respectively, and Y is the ratio of the output power levels P_{hot}/P_{cold} when the mixer input is terminated with T_{hot} or T_{cold}. Although HEB mixers are known to display quite an appreciable direct detection effect (e.g. [11]), the values of the noise temperature presented below were not corrected for this effect. The use of the mesh filter in front of the mixer allowed us to suppress direct detection, and on replacing the cold load (77 K) with the hot one (295 K) we observed a decrease of only 0.04-0.06 % in the mixer current over the measurement area on the IV plane. The corresponding value of $\partial P_{IF}/\partial I$ was positive and varied between 1.4 a.u./μA and 1.6 a.u./μA over the measurement area. Our estimates showed that the correcting for the direct detection effect might improve the receiver noise temperature about 5 %.

V. Experimental results

A. IF bandwidth measurements

Fig. 3 shows the results of the IF bandwidth measurements

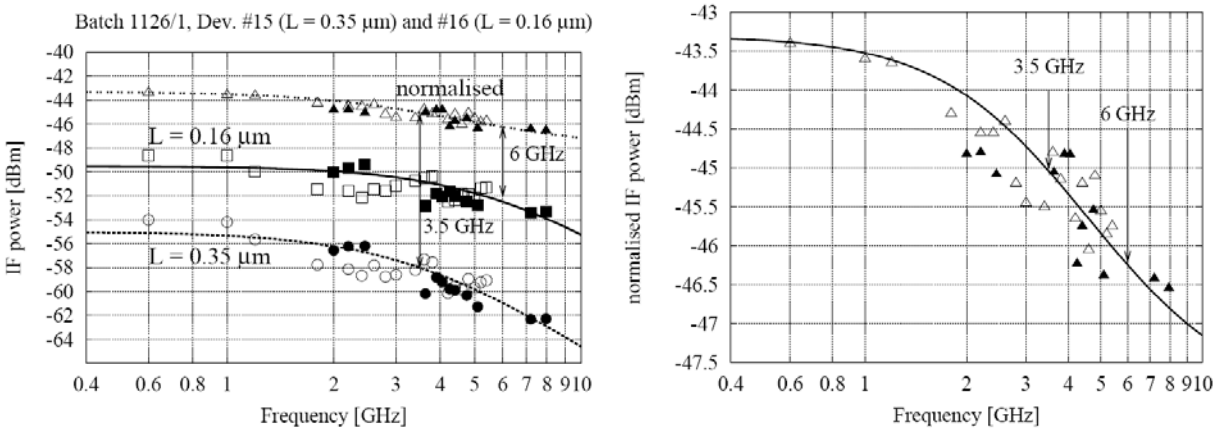

Fig. 3. On the left is shown the IF power versus intermediate frequency for HEB mixers with different bolometer lengths. Also shown is the ratio of the output power levels for the two lengths. The same ratio is shown on the right on a different scale.

TABLE I
PARAMETERS OF THE DEVICES USED IN THE EXPERIMENTS

device	T_c K	ΔT_c K	L μm	w μm	d nm	c_e mJ(cm^{3}K)	c_{ph} mJ(cm^{3}K)	τ_{eph} ps	τ_{ecs} ps	D cm^2/s
1126/1#15	11.5	1.1	0.35	2.4	3.5	1.5	10.5	10	38.5	0.45
1126/1#16	11.3	1.2	0.16							

for two devices with lengths of 0.35 μm and 0.16 μm. Also shown is the ratio of two conversion efficiencies. Computing this ratio allows eliminating ambiguities in the IF chain calibration procedure. This can be seen as follows. The output of a receiver is the product of the mixer output and the gain of the IF chain, which means that if two mixers are taken we can write

$$P_R^{(1)}(f) = P_M^{(1)}(f) G_{IF}(f), \quad (6a)$$

$$P_R^{(2)}(f) = P_M^{(2)}(f) G_{IF}(f), \quad (6b)$$

whence the ratio of the outputs

$$R(f) = \frac{P_M^{(1)}(f)}{P_M^{(2)}(f)}. \quad (6c)$$

After the IF chain was thus calibrated out, the dependencies of the IF power versus frequency could be fitted with

$$P_{IF}(f) = P(0) \frac{1}{1 + \left(f / f_{3dB}\right)^2} \quad (7)$$

with f_{3dB} = 3.5 GHz and f_{3dB} = 6 GHz for the long and short bridges respectively.

The parameters of the devices used in the experiments are given in Table I. Substitution from Table I into (1) shows that the 3-dB roll-off for phonon cooling in the experiments is governed mostly by the escape time of non-equilibrium phonons, τ_{esc}. Hence, the mixer time constant is

$$\tau_m = \left(\tau_{esc}^{-1} + \tau_{diff}^{-1}\right)^{-1}, \quad (8)$$

which yields roll-off frequencies of 4.6 GHz and 6.7 GHz for the long and short bridges respectively. The experimental results, in conjunction with this estimate, show the contribution of diffusion cooling to energy relaxation in our HEB mixers.

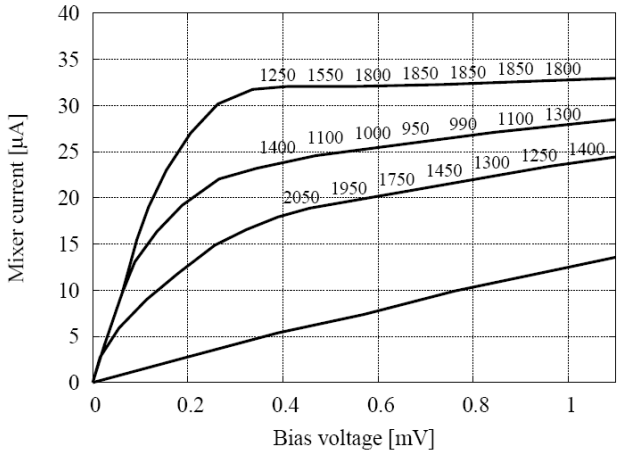

Fig. 4. A family of the IV curves for an HEB mixer taken at different levels of the LO drive at 2.5 THz. The LO power increases from the top curve to the bottom one. Also shown is the receiver noise temperature at various operating points.

B. Noise temperature measurements

Fig. 4 shows a family of the IV curves of an HEB mixer taken at different levels of the LO drive at 2.5 THz. The LO power increases from the top curve to the bottom one. Also shown is the noise temperature of the HEB receiver as a function of the operating point. As can be seen from the plot, there is quite a broad low noise area in the IV plane, with the lowest receiver noise temperature of 950 K. As has been mentioned above, this result was not corrected for the direct detection effect. Also, atmospheric absorption at 2.5 THz was not allowed for. Finally, we did not use an antireflection coating. We expect that taking account of the direct detection effect, atmospheric absorption and reflection losses may improve the receiver noise temperature by about 30%, in which case a noise temperature of about 600 K may be achieved.

CONCLUSIONS

We have demonstrated that the use of *in situ* gold yields an improvement of HEB mixer performance in terms of its noise temperature and IF bandwidth. Specifically, a noise temperature of 950 K was measured at an LO frequency of 2.5 GHz. Minimising the direct detection effect by installing a narrower IR filter should lower the receiver noise temperature. Further improvement might come from the use of an antireflection coating of the Si lens. Finally, allowing for atmospheric losses, or eliminating them by means of a "dry box" ought to lower the noise temperature even more. Taking care of the unwanted effects may thus improve the receiver noise temperature by about 30%. An IF bandwidth as wide as 6 GHz was measured at an LO frequency of 300 GHz near the critical temperature. This value is almost twice as large as that obtained for HEB mixers with *ex situ* gold contacts. The dependence of the IF bandwidth on the length of the bridge unambiguously demonstrates the contribution of diffusion cooling to the energy relaxation process in the HEB mixers fabricated with the use of *in situ* gold, and opens

the possibility of further increase of the IF bandwidth by making even shorter bridges.

REFERENCES

[1] E. M. Gershenzon, M, E. Gershenzon, G. N. Gol'tsman, A. D. Semenov and A. V. Sergeev, *Sov. Phys.–JETP* **59,** 442 (1984).

[2] W. D. Floet, E. Miedema, T. M. Klapwijk and J. R. Gao, *Appl. Phys. Lett.* **74**, 433 (1999).

[3] H. Merkel, P. Khosropanah, P. Yagoubov and E. Kolberg, *IEEE Trans. on Appl. Supercond.* **9**, 4201 (1999).

[4] N. Perrin, C. Vanneste, *Phys. Rev. B*, **28**, 5150 (1983).

[5] D. E. Prober, *Appl. Phys. Lett.*, **62**, 2119 (1993).

[6] P. J. Burke, R. J. Schoelkopf, D. E. Prober, A.Skalare, B. S. Karasik, M. C. Gaidis, W. R. McGrath, B. Bumble, H. G. LeDuc, *J. Appl. Phys.*, **85**, 1644 (1999).

[7] Yu. B. Vachtomin, S. V. Antipov, S. N. Maslennikov, K. V. Smirnov, S. L. Polyakov,N. S. Kaurova, E. V. Grishina, B. M. Voronov and G. N. Goltsman, *Proc. of the 15th Int. Symp. on Space Terahertz Tech.*, April 27-29, Hotel Northampton, Northampton, Massachusetts, USA, 236 (2004).

[8] Yuriy B. Vachtomin, Matvey I. Finkel, Sergey V. Antipov, Boris M. Voronov, Konstantin V. Smirnov, Natalia S. Kaurova, Vladimir N. Drakinski and Gregory N. Gol'tsman, *Proc. of the 13th Int. Symp. on Space Terahertz Tech.*, March 26-28, Harvard University, Cambridge, Massachusetts, USA, 259 (2002).

[9] J. J. A. Baselmans, M. Hajenius, J. R. Gao, T. M. Klapwijk, P. A. J. de Korte, B. Voronov and G Goltsman, *Appl. Phys. Lett.* 84, 1958 (2004).

[10] Denis Meledin, C.-Y. Edward Tong, Raymond Blundell, Natalia Kaurova, Konstantin Smirnov, Boris Voronov and Gregory Gol'tsman, *Proc. of the 13th Int. Symp. on Space Terahertz Tech.*, March 26-28, Harvard University, Cambridge, Massachusetts, USA, 65 (2002).

[11] J. J. A. Baselmans, A. Baryshev, S. F. Reker, M. Hajenius, J. R. Gao, T. M. Klapwijk, Yu. Vachtomin, S. Maslennikov, S. Antipov, B. Voronov, and G. Gol'tsman, *Appl. Phys. Lett.,* **86**, 163503 (2005)

Low noise 1.4 THz SIS mixer for SOFIA

A. Karpov, D. Miller, J. A. Stern*, B. Bumble*, H. G. LeDuc*, J. Zmuidzinas

California Institute of Technology, Pasadena, CA 91125, USA
** Jet Propulsion Laboratory, Pasadena, CA 91109, USA*

We report on the development of a 1.4 THz SIS mixer. The mixer uses SIS junctions made off Nb/Al-AlN/NbTiN. The junction area is 0.24 μm^2 and the R_NA= 6 Ohm μm^2. The junctions are diamond-like shaped in order to optimize the suppression of the Josephson DC currents. We are using a double slot planar antenna to couple the mixer chip with the telescope beam. The matching microcircuit is made of Nb and gold. The on-chip coupling prediction is plotted below in the Fig. 1. The mixer is expected to provide a low noise operation in a 1.3 – 1.5 THz receiver. The mixer IF circuit is designed to cover 4 - 8 GHz band.

The 1.3-1.5 THz SIS mixer is aimed for the 1.4 Terahertz channel of the Caltech Airborne Submillimeter Interstellar Medium Investigations Receiver (CASIMIR). It is a far-infrared and submillimeter heterodyne spectrometer, designed for the Stratospheric Observatory For Infrared Astronomy, (SOFIA). The goal of this work is to provide a low noise spectrometer particularly for the studies of the H_2D^+ 1_{01} - 0_{00} line around 1370 GHz.

The mixer test with a limited LO power allows us to make an estimation of very good receiver performance with a higher LO levels (fig.2). The mixer test with a more powerful LO source is under way and will be presented.

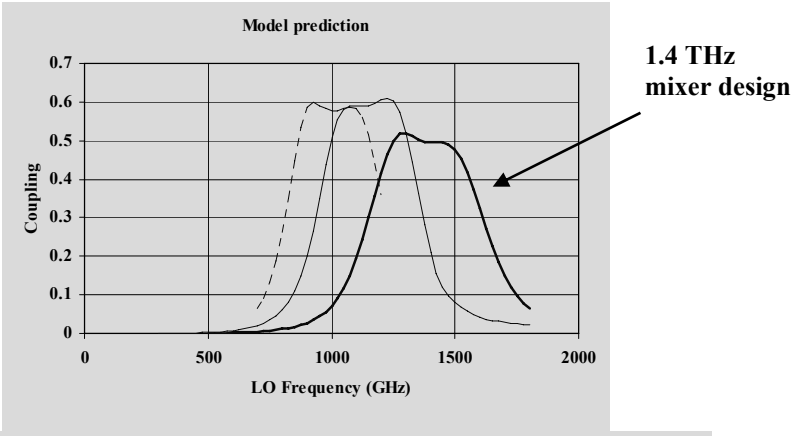

Fig. 1

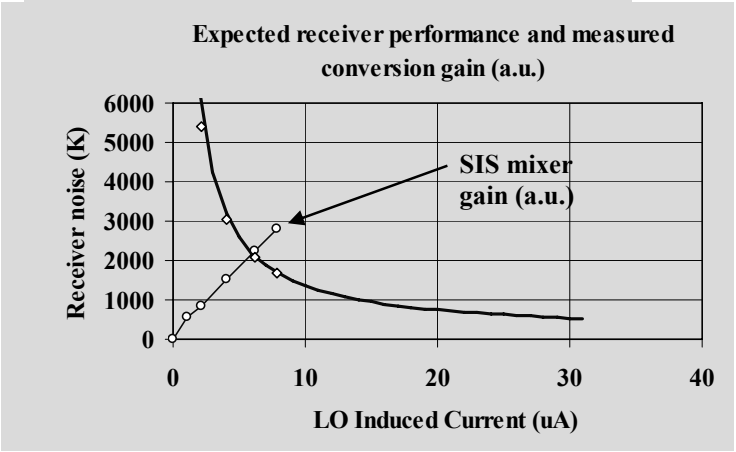

Fig. 2.

Development of an All-NbN Waveguide SIS Mixer for 0.5 THz

Jing Li[1,3], Masanori Takeda[2], Zhen Wang[2], and Sheng-Cai Shi[1]

1. Purple Mountain Observatory, NAOC, CAS, China
2. Kobe Advanced ICT Research Center, NiCT, Japan
3. Graduate School of Chinese Academy of Science, CAS, China

2 West Beijing Road, Nanjing Jiangsu 210008, China
Tel: +86-25-8333-2229; Fax: +86-25-8333-2206
Contact: lijing@mail.pmo.ac.cn, scshi@mail.pmo.ac.cn

Abstract **–With a gap frequency double that of Nb-based ones (~0.7THz), NbN SIS tunnel junctions are of particular interest for the development of heterodyne mixers at frequencies beyond 1 THz. To demonstrate the potential of NbN SIS tunnel junctions for astronomical applications, we developed a 0.5 THz all-NbN waveguide SIS mixer to observe the CO (J=4–3) emission at 0.46 THz with the POST submillimeter-wave telescope. In this paper, we mainly describe the mixer design, NbN junction fabrication and mixer performance. In particular, the mixer performance is compared with that of a 0.5-THz Nb SIS mixer previously installed on the same telescope. Some testing observation results are also presented.**

I. Introduction

Heterodyne mixers based on SIS tunnel junctions have been widely used for astronomical and atmospheric observations at millimeter and submillimeter wavelengths [1]. In fact, SIS mixers with Nb-based SIS tunnel junctions have achieved noise temperatures as low as three times the quantum limit below 0.7 THz, which is the gap frequency of Nb SIS tunnel junctions [2]. At frequencies higher than 0.7 THz, however, the transmission loss in Nb thin-film superconducting microstrip lines increases significantly due to the breaking of cooper pairs, thereby deteriorating the performance of Nb SIS mixers to some extent. With the increasing requirements of astronomical research in the submillimeter band (0.3-3 THz) [3], ones have been attempting to develop SIS mixers based on SIS tunnel junctions of a larger energy gap.

NbN SIS tunnel junctions [4], which have a gap frequency of about 1.4 THz [5], are a good candidate for the development of SIS mixers at frequencies higher than 0.7 THz. To demonstrate the potential of NbN SIS tunnel junctions for astronomical detection at submillimeter wavelengths, we developed a 0.5 THz waveguide-type NbN SIS mixer for the Portable Submillimeter Telescope (POST) [6,7], which aims at observing spectral lines over the 0.5 THz atmospheric window. The POST has a diameter of 30 cm and is currently situated at a site at an altitude of 3200 m (Delingha, China).

This paper mainly introduces the design, fabrication, and characterization of the 0.5-THz waveguide NbN SIS mixer. Its performance is also compared with that of a 0.5-THz Nb SIS mixer that was previously installed on the same telescope. Some preliminary observation results with the 0.5-THz waveguide NbN SIS mixer are exhibited.

II. Mixer Design

Fig. 1 shows a cross-sectional view of the 0.5-THz waveguide NbN SIS mixer. As indicated in Fig. 1, the SIS mixer chip, based on the MgO substrate (with a dielectric constant of 9.6), is 102-μm wide and 51-μm thick and is inserted in a slot measuring 119 μm × 119 μm. A full-height waveguide measuring 510 μm × 255 μm was chosen for this design. It should be pointed out that there was no backshort cavity introduced in this design to ease the mechanical fabrication of the waveguide mixer block. The conventional bow-tie waveguide probe (refer to Fig. 1), located at the

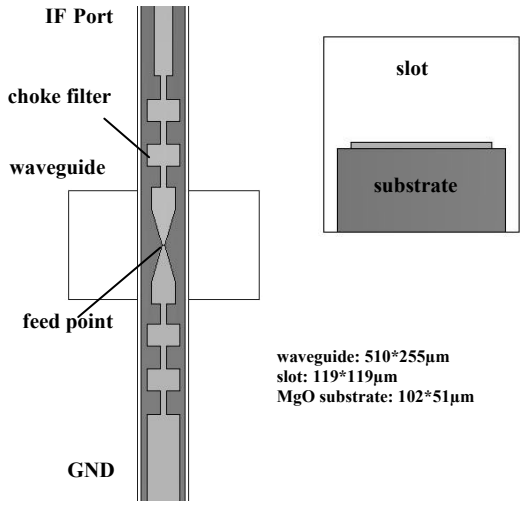

Fig. 1. Cross-sectional view of the 0.5-THz waveguide NbN SIS mixer.

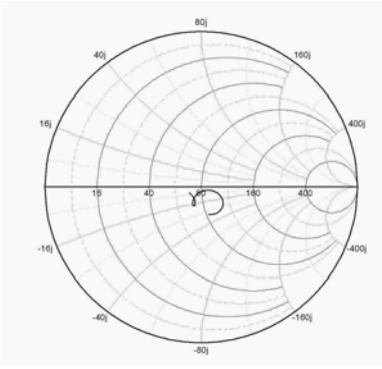

(a)

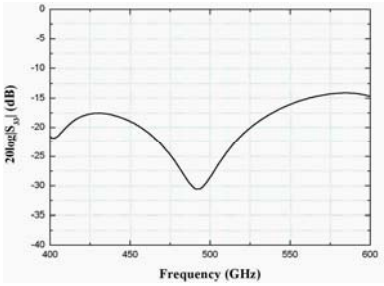

(b)

Fig. 2. (a) Simulated embedding impedance plotted on a Smith chart and (b) simulated return loss (referring to 80 Ω at the feed point) as a function of frequency.

waveguide center, was adopted to couple the RF and LO signal from waveguide to the SIS junction circuit.

The RF embedding impedance of the 0.5 THz waveguide NbN SIS mixer was simulated in the frequency of 0.4-0.6 THz with the aid of HFSS. Fig. 2 plots the simulated embedding impedance seen at the feed point (refer to Fig. 1) for an optimized waveguide probe structure. It can be clearly seen that the embedding impedance is pretty close to 80 Ω in the frequency range of 0.4–0.6 THz and the relative bandwidth is about 35% for the return loss less than -13dB.

Based on the calculated embedding impedance shown in Fig. 2 and Tucker's quantum mixing theory [8], we designed the twin-junction tuning circuit (refer to Fig. 3), which has a tuning inductance inserted in between the parallel connected twin junctions [9,10] to tune out their geometric capacitances. The junction critical current density (J_c) was taken as 15kA/cm^2 and the junction size was 1μm in diameter, corresponding to a $\omega R_n C_j$ product of 7.3 at 0.5 THz and a normal state resistance (R_n) of 29.5Ω for individual junctions. An impedance transformer was placed between the feed point and the twin SIS tunnel junctions to have good impedance matching between them. Note that the junction tuning circuit and impedance transformer are both made of a thin film superconducting microstrip line composed of NbN (200 nm)/MgO (200 nm)/NbN (350 nm) three layers.

III. Junction Fabrication

For the fabrication of all-NbN SIS tunnel junctions, firstly, we deposited the NbN/AlN/NbN tri-layer on an MgO substrate measuring 20 mm × 20 mm × 0.3 mm. The base and counter NbN layer were both 200-nm thick. The NbN films were prepared without additional substrate heating by reactive dc magnetron sputtering in a gas mixture of Ar and N_2. A low total pressure (~2 mTorr) and high power density were used to promote the growth of the NbN films. The AlN barrier was deposited by dc sputtering in pure N_2 gas with a low power density to have good control over its thickness. Secondly, the waveguide probe and choke filter were patterned by conventional photolithography and etched by reactive ion etching (RIE) with CF_4 and Ar gases. Thirdly, the SIS tunnel junctions were defined and a 200-nm thick MgO layer was deposited by RF sputtering to insulate the base and wiring electrode. Finally, a 350-nm thick wiring NbN layer was deposited and patterned after the lift-off of the photoresist, Fig. 3 shows the photograph of a fabricated 0.5 THz NbN SIS junction chip.

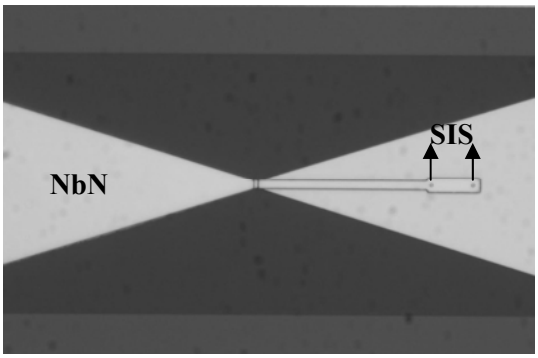

Fig. 3. Photograph of a 0.5 THz NbN SIS junction chip (part).

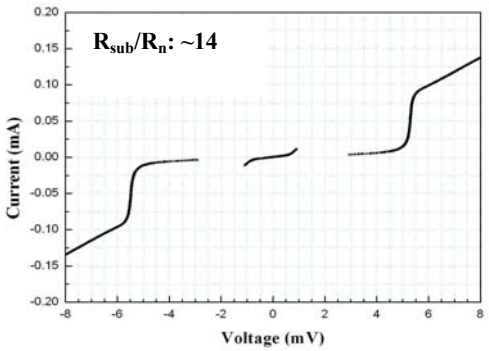

Fig. 4. Measured dc I-V curve of a 0.5 THz NbN SIS junction.

A typical DC I-V curve (measured at 4.2 K) of fabricated 0.5-THz NbN SIS tunnel junctions is shown in Fig. 4. Obviously, the gap voltage is about 5.4 mV. And the sub-gap current is fairly small, giving a quality factor (i.e., R_{sub}(4 mV)/R_n) of about 14. In addition, a resonance

step can be clearly observed at about 1mV, which indeed corresponds to a Josephson frequency of around 0.5THz.

IV. Mixer Performance

The noise performance of the 0.5 THz waveguide SIS mixer was characterized by the conventional Y-factor method. It should be pointed out that due to the time limit (for the installation of the 0.5 THz NbN SIS mixer on the POST telescope for the winter season of 2007), the SIS junction device was indeed not optimized. In spite of that, preliminary measurement showed an uncorrected noise temperature as low as 150 K (about six times the quantum limit), including a RF noise contribution (resulting mainly from the measurement setup) of approximately 100 K.

To further investigate the characteristics of NbN SIS mixers, we compared the IF-output-power response and the temperature dependence of noise performance of the 0.5 THz waveguide NbN SIS mixer with respective ones of a 0.5 THz Nb SIS mixer previously installed on the POST telescope. Note that for both SIS mixers, we used a small permanent magnet to suppress the Josephson effect. The results are displayed in Figs. 5a-5b. It can be clearly seen from Fig. 5a that the 0.5 THz NbN SIS mixer has an IF-output-power response (on the first photon step) completely immune from the Josephson effect and the photon-assisted tunneling effect originated from the negative branch of the junction's I-V curve. Obviously, larger gap voltage accounts for this improvement. Fig. 5b shows the temperature dependence of noise performance measured for the two 0.5 THz SIS mixers.

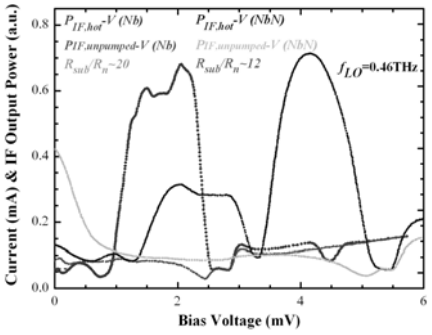

(a

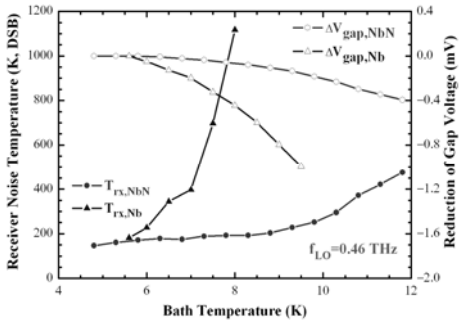

(b

Fig. 5. Comparison of the performance of a 0.5 THz NbN SIS mixer and a 0.5 THz Nb SIS mixer, with (a) the IF-output-power response and (b) the temperature dependence.

While the noise performance of the 0.5 THz Nb SIS mixer starts to deteriorate considerably from about 6 K, that of the 0.5-THz NbN SIS mixer is almost constant up to a bath temperature of 8 K and is still reasonably good to 10 K, which is already beyond the critical temperature of Nb SIS tunnel junctions. The results shown in Fig. 5 indicate that with higher critical temperature (or higher energy gap), NbN SIS mixers have less stringent requirements for cooling and magnetic field, which are very beneficial to real applications.

V. Astronomical Observation

The 0.5 THz NbN SIS mixer was installed on the POST telescope, which is aimed at observing spectral lines over the 0.5-THz atmospheric window for the purpose of large-scale surveys along the galactic plane. The POST has a diameter of 30 cm and is currently located at a site at an altitude of 3200 m (Delingha, China). Using the 0.5 THz NbN SIS mixer, on Dec. 31, 2007 we detected spectral line emission from CO (J = 4–3) at 0.46 THz toward Orion A. The zenith atmospheric opacity during the observation was around 2.0 (~13.5% transmission) at the observation frequency. The observed spectrum with an integration time of 6.2 min is shown in Fig. 6. The root-mean-square noise temperature is approximately 0.79 K. This is the first astronomical observation ever made with NbN superconducting tunnel junctions.

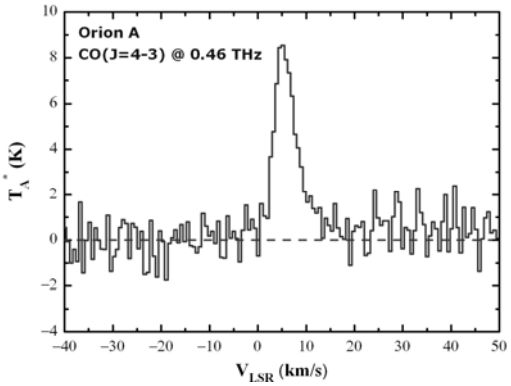

Fig. 6. CO spectrum observed with the 0.5 THz NbN SIS mixer.

VI. Summary

We have successfully developed a low noise 0.5 THz wavguide all-NbN SIS mixer. The lowest receiver noise temperature (uncorrected) is below 150 K, approaching six times the quantum limit. In addition to high sensitivity, the 0.5 THz NbN SIS mixer has shown higher stability and less stringent requirements for cooling than a Nb SIS mixer in the same frequency band.

The 0.5 THz NbN SIS mixer has been installed on a sub-millimeter telescope (POST, with a diameter of 30 cm). The CO (J=4–3) spectrum emission has been detected toward Orion A. It is the first astronomical observation ever made with an NbN SIS mixer.

It can be concluded that NbN SIS mixers are potentially useful beyond 1 THz and even have some merits at low frequencies. They may play important role in THz astronomical and atmospheric research, especially for space-borne observations.

ACKNOWLEDGMENT

The authors would like to thank Q. J. Yao, S. P. Huang, J. Xu, and N. Li for their assistance. L.J. is grateful to Dr. Terai of National Institute of Information and Communication Technology (Japan) for valuable comments. This study was supported in part by NSFC Grants (Nos. 10390163, 10673033, and 10621303) and by the CAS International Collaboration Program (No. GJHZ0617).

REFERENCES

[1] Jonas Zmuidzinas and Paul L. Richards, Proc. IEEE 92, 1597 (2004).

[2] A. Karpov, J. Blondel, M. Voss, and K.H. Gundlach, "A three photon noise SIS heterodyne receiver at submillimeter wavelength," IEEE Trans. Appl. Supercond., vol.9, no.2, pp.4456-4459, 1999.

[3] Thomas G. Phillips and Jocelyn Keene, Proc. IEEE 80, 1662 (1992).

[4] Z. Wang, A. Kawakami, Y. Uzawa, and B. Komiyama, "NbN/AlN/NbN tunnel junctions fabricated at ambient substrate temperature", IEEE Trans. Appl. Supercond., vol. 5, no. 2, pp. 2322~2325, 1995.

[5] Z. Wang, A. Kawakami, Y. Uzawa, and B. Komiyama, "Superconducting properties and crystal structures of single-crystal niobium nitride thin films deposited at ambient substrate temperature," J. Appl. Phys., vol.79, no.10, 1996.

[6] S.P. Huang, J. Li, A.Q. Cao, S.H. Chen, X.F. Shen, Z.H. Lin, S.C. Shi, and J. Yang, "Development of a Compact 500-GHz SIS Receiver," Proc. of AP-RASC04, pp. 412-413, 2004.

[7] J. Yang, M.Ohishi, S. Shi, T. Noguchi, K. Miyazawa, J. Inatani, Y. Sekimoto, S. Yamamoto, H. Ozeki, and S. Saito, in Ground-Based Astronomy in Asia, edited by N. Kaifu, Ed. (NAOJ, Japan, 1996), pp. 565-568.

[8] J.R. Tucker and M.J. Feldman, "Quantum detection at millimeter wavelengths," *Rev. Mod. Phys.*, vol.57, no.4, pp1055-1113, 1985.

[9] J. Zmuidzinas, H.G. LeDuc, J.A. Stern, and S.R. Cypher, IEEE Trans. Microwave Theory Tech. 42, 698 (1994).

[10] S.C. Shi, T. Noguchi, and J. Inatani, in Conf. Dig. 19th Int. Conf. IR MM Waves, edited by K.Sakai and T. Yoneyama (Sendai, Japan, 1994), pp. 110-111.

A Novel THz SIS Mixer with a NbTiN-Ground plane and SIS Micro-Trilayers Directly Grown on a Quartz Substrate

Akira Endo[1,2,3], Takashi Noguchi[3], Matthias Kroug[3], Sergey V. Shitov[3,4], Wenlei Shan[5], Tomonori Tamura[3], Takafumi Kojima[3,6], Yoshinori Uzawa[3], Takeshi Sakai[3], Hirofumi Inoue[1], Kazuyuki Muraoka[1,2] andKotaro Kohno[1]

[1]*Institute of Astronomy, University of Tokyo, Japan*
[2]*Japan Society for the Promotion of Science, Japan*
[3]*National Astronomical Observatory of Japan, Japan*
[4]*Institute of Radio-engineering and Electronics of Russian Academy of Science, Russia*
[5]*Purple Mountain Observatory, China*
[6]*Osaka Prefectural University, Japan*
* Contact: akira.endo@nao.ac.jp, phone +81-422-34-3870

Abstract— **A new structure and fabrication process for multi-material THz-SIS mixers is proposed. In this design, both the micrometer-sized SIS trilayers (MTLs: micro-trilayers) and the ground plane are deposited directly onto the substrate. This structure is expected to possess a number of unique features, e.g., (1) the quality of the SIS junction is not affected by the physical nature of the ground plane film; (2) the heat can escape directly from the junction into the substrate. The influence of the MTL-structure on the junction quality and circuit characteristics have been investigated. Numerical calculation suggests that the extra rf loss around the junction can be kept small if the offset between the junction and the ground plane is less than 1μm. MTL-SIS mixers have been fabricated using Nb/Al-AlO$_x$(or AlN$_x$)/Nb SIS junctions and NbTiN/Al microstriplines. The leakage current of the SIS junction can be made as small as that of the best all-Nb devices. The MTL-SIS structure will be useful in thedevelopment of future THz SIS mixers.**

I. INTRODUCTION

Heterodyne receivers with superconductor-insulator-superconductor (SIS) quasiparticle mixers offer quantum-noise limited sensitivity at frequencies from 0.1THz to ~1THz[1]. SIS mixer devices usually include an integrated circuit to tune out the large capacitance of the SIS junction(s). It is common to make these transmission lines with superconductorssuch as Nb. One of the critical parameters that characterize the interaction between a superconductor and high frequency electromagnetic radiation is the gap frequency ($f_{gap}=2\Delta/h$), which is the minimum frequency at which a photon canexcite quasiparticles. Below f_{gap}, a superconducting strip line can be treatedas a lossless metal sheet with nearly zero surface resistance[2]. However, above f_{gap}, the resistivity of a superconductive transmission line increases drastically, and the rf loss severely degrades the sensitivity of the receiver[3]. On the other hand, the SIS junction itself can operate in the quantum regime and offer high sensitivity up to a frequency of $2f_{gap}$[4], [5]. For example, the f_{gap} of niobium (Nb) is ~0.7 THz, which is the largest among element superconductors. Nb is not only a good material for planar transmission lines below 0.7THz, but has also been regarded as the best material for the electrodes of SIS junctions, in combination with high quality tunnel barriers made of aluminum oxide (AlO$_x$). At 0.7THz $<f<$ 1.4THz, Nb SIS junctions can be used incombinationwith transmission lines made of compound superconductors with f_{gap}larger than Nb (e.g., NbN[6]-[7], NbTiN[8],[9],NbCN[10],[11], Nb_3Al[12]) or normal metals with low resistivity (e.g., Al, Au[13], [14]). For example, SIS mixers with Nb/AlO$_x$/Nb (or Nb/AlN/NbTiN) SIS junctions and NbTiN/SiO/Al microstriplines have shown good performance at f~1THz[8], [15]. At f > 1.4THz, where the conversion loss of SIS junctions made of Nb increases sharply, epitaxially grown NbN/AlN/NbN SIS junctions are considered as a promising alternative [6]. In the same way as Nb, NbN can be used for an SIS junction up to 2 f_{gap} ~ 2.8THz, but its use for transmission lines is limited to $\leq f_{gap}$ ~1.4THz. Therefore, at 1.4THz $\leq f \leq$ 2.8THz, the transmission line must be made of normal metals like Al or Au. Examples of material candidates for SIS junctions and transmission lines are illustrated in Fig. 1.

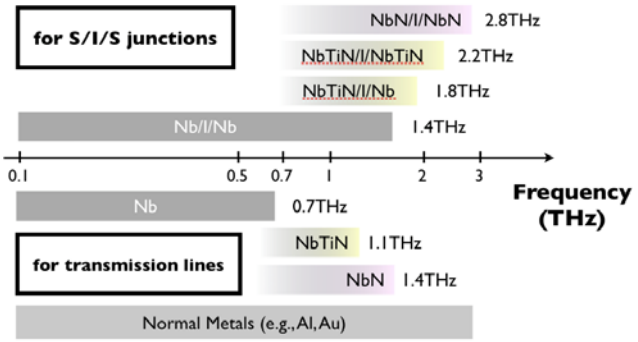

Fig. 1 Approximate frequency upper limits of various superconductors as materials for electrodes of SIS junctions or transmission lines.

Thus, SIS mixers at super-terahertz frequencies are often multi-material, in sense that the electrodes of the SIS junction, and the transmission line, are made of different materials. Usually, these devices are fabricated by stacking an S/I/S trilayer on top of the ground plane of the transmission line, as shown in Fig. 2(a). In such a configuration, the requirements for the properties of the ground plane film tend to be quite tight, if both good quality SIS junctions and a low-loss transmission line are to be realized:

- Thin films of compound superconductors such as NbTiN often possess strong stress, which can damage the tunnel barrier of the SIS junction that lies on top, when the stress is released during the fabrication process [16]-[17].
- The films of compound superconductors can have rough surfaces[18]. This can affect the growth of films grown on top, for example the bottom electrode of the SIS junction and also the tunnel barrier, causing degradation in the nonlinearity of the current-voltage ($I(V)$) characteristics[19].
- The epitaxial growth of the superconducting electrodes of the SIS junction can have several advantages, such as an increased f_{gap} and less defects in the tunnel barrier[7],[15]. In order to grow a film epitaxially, the underlying layer must also be crystalline with a matched lattice constant.

Aside from these difficulties, there is also a potential problem of heat trapping in an SIS junction placed on a superconductor with a larger f_{gap} than its electrodes[20]-[21]. Nevertheless, multi-material SIS mixers with "stacked-up" structures have demonstrated state-of-the-art performance above 1THz.

In this study, we propose an alternative structure and fabrication process for multi-material SIS mixers. Because this fabrication process includes a stage where islands of S/I/S trilayers with diameters as small as a few micrometers are formed, we refer to this new process/structure as the "micro-trilayer" (MTL). In the MTL design, both the μm-sized SIS trilayers AND the ground plane are deposited directly onto the substrate, or, possibly with a buffer layer in between. A cross sectional diagram of the MTL SIS junction is presented in Fig. 2(b). We expect this structure to possess a number of unique features:

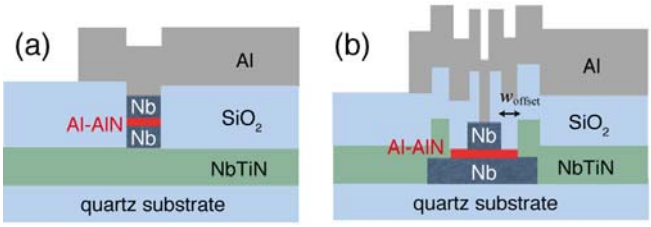

Fig. 2 Cross sectional diagrams of SIS mixers with (a) a conventional "stacked up" structure and (b) a micro-trilayer structure.

- The quality of the SIS junction is not affected by the physical nature (e.g., stress, roughness or lattice constant) of the ground plane film.
- The Joule heat produced in the SIS junction can escape directly from the bottom electrode into the substrate.

On the other hand, there are also possible drawbacks:

- There is an area around the SIS junction where the base electrode of is not covered by the ground plane. We call this the "*offset*" region (see Fig. 2(b)). For rf currents at THz frequencies, this region behaves like a normal conductor and therefore adds to input losses of the mixer.
- The structure around the SIS junction becomes three dimensional and complex, which could add unpredicted reactance to the circuit.

We have studied the properties of the MTL structure in terms of the quality of the SIS junctions and the characteristics of the tuning circuit, by means of numerical simulation and experiment.

II. Simulation

The effect of the additional resistance at the offsetarea around the SIS junction was studied by numerical simulation using a commercial software package*Microwave Office*®. We assumed a configuration in which two Nb/Al-AlO_x/Nb SIS junctions are embedded in a microstrip line tuner, which consists of a NbTiN ground plane and an Al top wire with SiO_2as an insulating layer. The offset structure was included by replacing part of the NbTiN ground plane around the junction with Nb. A schematic of the geometry is presented in Fig. 3, in which the height of the Nb islands is much exaggerated.The legends of Fig. 4 summarize the material and geometrical parameters used for the simulation.

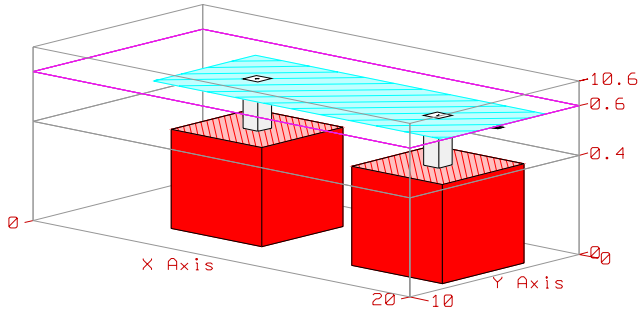

Fig. 3 Configuration of the electromagnetic-model of the twin SIS tuning circuit with Nb-MTL junctions. The blue layer represents the Al top wire. The two red flat islands are the Nb micro-trilayers surrounded by the NbTiN ground plane. The *x*, *y* and*z* axes are in units of μm.

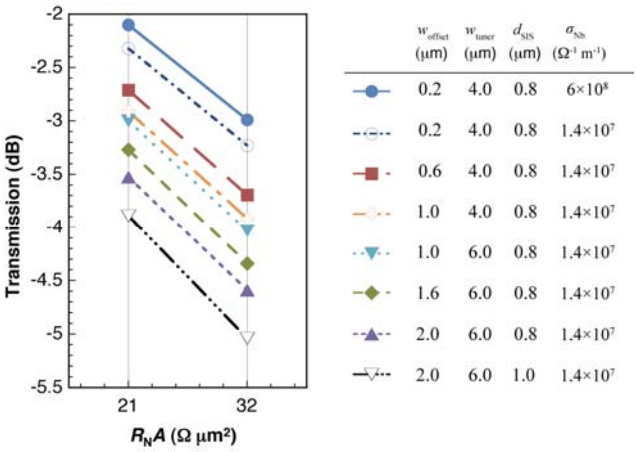

Fig. 4 Loss in the resonant tuning circuit with twin MTL SIS junctions shown in Fig. 3. w_{offset}, w_{tuner}, d_{SIS}, $\sigma_{Nb}$are the width of the offset, the width of the Al top wire, the diameter of the SIS junction and the conductivity of Nb, respectively.

According to the results, the offsetarea may introduce noticeable rf-loss. Fig. 4 presents the combined effect of rf-loss, which includes both the tuning circuit and the offset area. This graph illustrates the influence of the offsetwidth (w_{offset}) and the R_NA product of the SIS junctions (normal resistance multiplied by the area). The important result is that by decreasing w_{offset} from 2 μm to 0.6 μm we may save up to 1.2 dB of coupling loss for the 0.8-μm SIS junctions. Trying to minimize the three following parameters: $w_{offset} = 2 \rightarrow 0.6$ μm, R_NA=32 → 21 Ω μm^2, $d_{SIS} = 1 \rightarrow 0.8$ μm, one can save up to 2.7 dB of the mixer gain. Note that the solid curve at the top presents the imaginary situation of epitaxial NbN junctions instead of Nb ones. Note also that the offset of 0.2 μm has a negligible effect on rf-loss.

III. Fabrication

SIS mixers with Nb/Al-AlO_x (or AlN) /Nb SIS junctions and NbTiN/SiO_2/Al tuning circuits have been fabricated using the MTL technique. The geometry of the tuning circuit is the same as the current design for the ALMA (Atacama Large Millimeter and Submillimeter Array) band 10 SIS mixer[9], except for the MTL structure around the junctions. No modification/optimization of the circuit design has been done, for the primary purpose of the experiment was to quickly demonstrate that the MTL process can reliably produce good quality SIS junctions in combination with a NbTiN ground plane.

Fabrication of the MTL structure requires a horizontal alignment accuracy on the order of 100nm, which is difficult by means of conventional contact mask aligners. Therefore, we used an i-line stepper (Canon FPA-3000 i5+) with an alignment accuracy better than 40nm. In addition, we adopted an ICP-etching machine with dc biasing for good anisotropy. This combination enabled us to fabricate the MTL structure with good reproducibility.

The S/I/S trilayer consists of a 200nm-thick Nb base-electrode layer, a 10nm-thick Al layer, with its surface either oxidized or nitridized to form a tunnel barrier, and a 100nm-thick Nb top-electrode layer. To form the AlO_x barrier, the Al film was exposed to an oxygen atmosphere, while the AlN barrier was created by nitridizingthe surface of the Al film in a capacitively coupled nitrogen plasma. The ground plane was made of 230-nm thick NbTiN, which was dc-sputtered in a plasma of Ar+12%N_2. The typical resistivity of the NbTiN films at room temperature was ρ_{300K} = 110μΩ cm and the transition temperature was T_c = 14K.

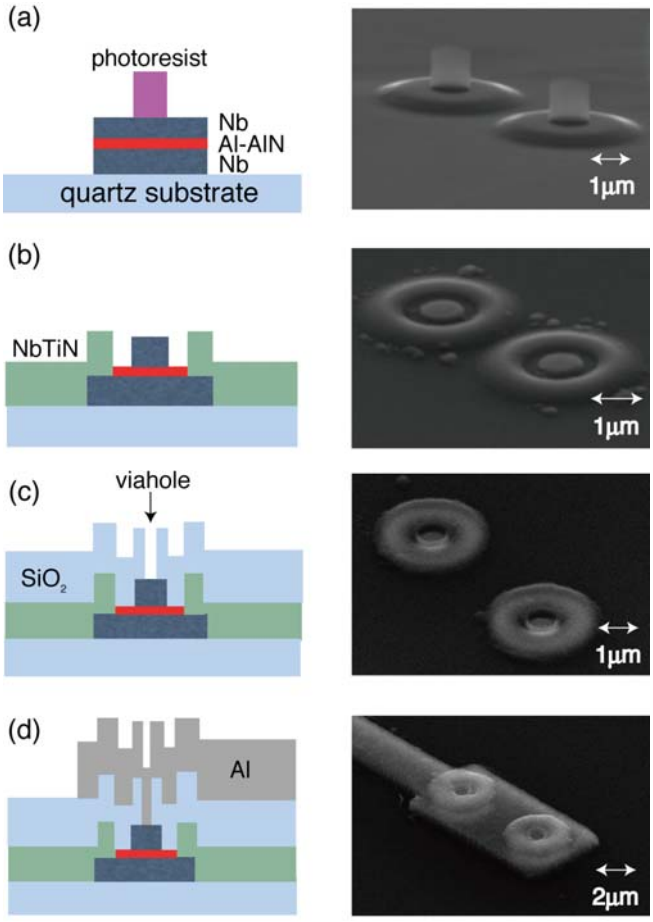

Fig. 5 Cross sectional diagrams (left) and SEM micrographs (right) of the SIS junctions at various stages of the fabrication process.

Cross sectional diagrams and SEM micrographs are presented in Fig. 5 to summarize the fabrication process. The process began by depositing the trilayer through a liftoff mask. The diameters of these circular trilayers were remarkably small; only 3-5μm. After lifting off the photoresist, a columnar photoresist with a diameter of 0.8-2.0μm was patterned in the center of the trilayer, and the junction was isolated by ICP etching. Next, another columnar liftoff mask with a diameter larger than the junction by ~1μm was patterned so that it covers the top-Nb electrode, and then the NbTiN ground plane was deposited. When the photoresist is removed, the top electrode appears again with the offsetaround it. Note that it is possible to anodize the rims of the SIS junctions at this point—though this will also anodize the surface of the top electrode, the oxide can be removed afterwards when the via-hole is etched. Next, a layer of SiO_2 was deposited all over the wafer. This layer has a thickness of 300nm and serves as the insulator of the microstrip line. Finally, a via-hole with a diameter smaller than the junction (0.6-1.0μm) was etched and the Al top-wire with a thickness of 540nm was deposited. The resistivity of the Al film at 4K was 0.21μΩ cm, which corresponds to an electron mean free path of 390nm, limited by the thickness of the film[22].

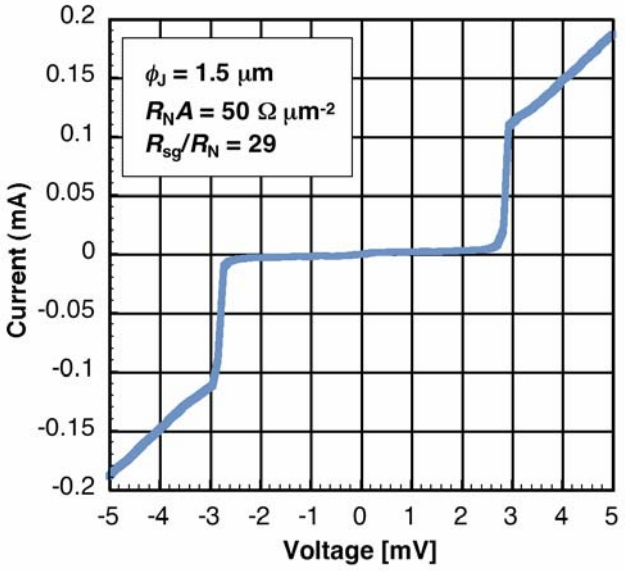

Fig. 6 DC I(V) curve of a Nb/Al-AlN/Nb SIS junction combined with a NbTiN ground plane using the micro trilayer technique.

The process described above is merely one example of the several possible sequences for creating the MTL structure. For example, one could begin the process by sputtering the ground plane instead of the trilayer, though this will result in the Nb base electrode overlapping *on top of* the ground plane, and not beneath. One advantage of the abovementioned sequence was that the surface of the NbTiN film is never exposed to a plasma after it is deposited. In contrast, in the conventional process where the trilayer is deposited on top of the NbTiN ground plane, the surface of the NbTiN ground plane will be exposed to the plasma when the trilayer around the junction is removed, which can make the surface of the NbTiN film considerably rough.

IV. DC Characteristics

The dc $I(V)$ characteristics of the abovementioned SIS mixers were measured at 4.2K by a four-point method. An example of an $I(V)$ curve of a Nb/Al-AlN/Nb SIS junction is presented in Fig. 6. This junction has an R_NA product of 50 Ω μm^2, which corresponds to a critical current density of J_c = 4kA cm^{-2}. The ratio of the R_N to the sub-gap resistance measured at 2mV (R_{sg}) was R_{sg}/R_N ~30. This is approaching the theoretical limit of the sub-gap current of Nb at 4.2K ($R_{sg}/R_N \leq 40$) [23], indicating that the AlN barrier was formed with no problem, even though the trilayer was extremely small. Similarly, we have also obtained AlO_x barrier SIS junctions with good quality using the MTL process (e.g., R_NA=16 Ω μm^2, R_{sg}/R_N = 15).

While the MTL structure does not seem to affect the sub-gap current, we found that the gap voltage of the $I(V)$ curve decreases when the diameter of the *Nb base electrode* was smaller than 10μm, as shown in Fig. 7. This could be because the quality of the μm-sized Nb film is affected by contamination from the sidewalls of the

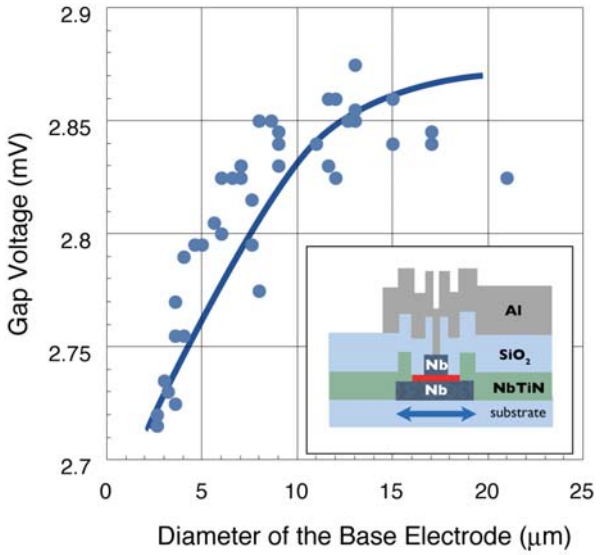

Fig. 7 The decrease in gap voltage in accordance to the diameter of the Nb base electrode (shown by the arrow in the inset). Each point represents a different SIS junction on the same wafer. The solid curve is shown as a guide-to-the-eye.

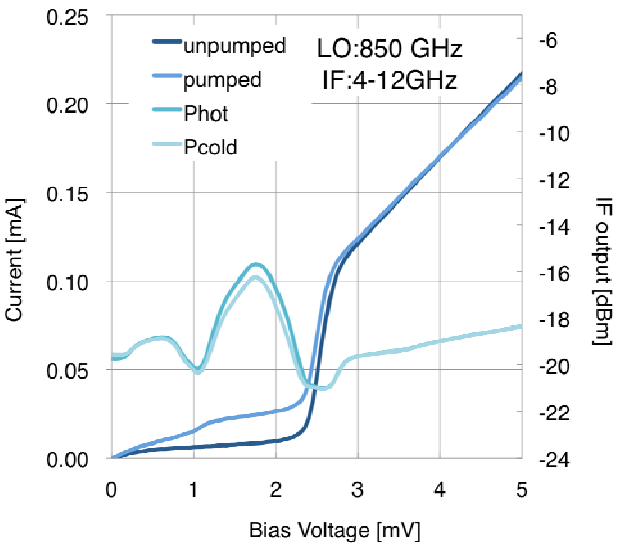

Fig. 8 RF characteristics of a MTL SIS junction at 850 GHz.

photoresist during the deposition of Nb. Another mechanism that could cause a decrease in the gap voltage is Joule heating around the junction. However, we do not think this is the case, because no back-bending was observed in the $I(V)$ curves with suppressed gap voltages.

V. RF Measurement

We have installed one of the SIS mixer devices in a waveguide-type receiver to measure the noise temperature by the standard Y-factor method. So far we have only measured one chip, and furthermore, both the mixer chip and the measurement setup were not optimum, so this is merely a preliminary result. The $I(V)$ curve of the SIS mixer in the receiver with/without LO input is presented in Fig. 8. The reduced gap voltage and the large sub-gap current is a result of the temperature of the mixer being considerably higher than 4K. The local oscilator frequency was f_{LO} = 850GHz. The integrated IF output from 4 to 12 GHz is also plotted. The calculated noise temperature was 1100K at this frequency, and was typically 1500-2000K throughout f_{LO} = 820-920GHz. This noise temperature is considerably higher compared to the noise temperature measured for SIS mixers with the same material but with the conventional "stacked up" structure (Uzawa*et al.*, this conference).

VI. Discussion and Future Possibilities

We have seen that introducing the MTL structure results in a trade-off between the improvement of the junction quality and the increase of rf-loss in the tuning circuit. As predicted from our simulation, a good way to reduce the rf-loss is to reduce theR_NA ofthe SIS junction. AlN barrier SIS junctions are useful for this purpose, forR_NA<10 Ω μm^2 can be achived with excellent non-linearity[7],[24]-[26].

The MTL structure should be especially useful in pushing the frequency limit of SIS junctions to the super-THz range, where HEB mixers are currently the choice when sensitivity is top priority. For example, if an epitaxial NbN/AlN/NbN SIS junction is used in combination with a microstrip line made of superconductors with higher T_c (e.g., MgB_2)or a normal metal with low resistivity (e.g., Al or Au),the theoretical cutoff frequency can beas high as 2.5THz. However, NbN does not usually grow epitaxially on these materials, so it would be difficult to fabricate such a device using the conventional "stacked up" structure. If the micro-trilayer structure is adopted, the NbN/AlN/NbN trilayer and the microstrip line can be grown independently on a substrate suitable for the epitaxial growth of NbN, such as MgO. Such SIS mixers have the possibility of achieving good sensitivity at super-terahertz frequencies.

Acknowledgment

We would like to acknowledge Yoko Kiuchi for her technical support in the cleanroom. We also wish to acknowledge all the members of the advanced technology center and ALMA-JT for supporting our research.A. E. and K. M. were financially supported by the Japan Society for the Promotion of Science (JSPS) Research Fellowships for Young Scientists.A part of this study was financially supportedby the MEXT Grant-in-Aid for Scientific Research onPriority Areas No.~15071202.

References

[1] J.Zmuidzinas and P. L. Richards, "Superconducting Detectors and Mixers for Millimeter and Submillimeter Astrophysics," *Proc. IEEE*, vol. 92 (10), pp. 1597-1616, Oct. 2004

[2] R. Kautz, "Miniaturization of Normal-State and Superconducting Striplines," *J. Res. Natl. Bur. Stand.*, Vol. 84 (3), pp. 247-259, Jan. 1979

[3] G. de Lange *et al*., "Superconducting Resonator Circuits at Frequencies Above the Gap Frequency," *J. Appl. Phys.*, vol. 77 (4), pp. 1795-1804, Feb. 1995

[4] W. Danchi and E. Sutton, "Frequency dependence of quasiparticle mixers," *J. Appl. Phys.*, vol. 60 (11) pp. 3967-3977. Jan. 1986

[5] D. Winkler and T. Claeson "High□frequency limits of superconducting tunnel junction mixers," *J. Appl. Phys.*, vol. 62 (11), pp. 4482-4498, Jan. 1987,

[6] J. Li *et al*., "Low-noise 0.5 THz all-NbN superconductor-insulator-superconductor mixer for submillimeter wave astronomy,"*Appl. Phys. Lett.*, vol. 92 (22) 222504, Jan. 2008

[7] M. Y. Torgashin *et al*., "Superconducting Integrated Receivers Based on Nb/AlN/NbN Circuits,"*IEEE Trans. Appl. Supercond.*., vol. 17 (2), pp. 379-382, Jun. 2007

[8] B. D. Jackson *et al*., "Niobium titanium nitride-based superconductor-insulator-superconductor mixers for low-noise terahertz receivers," *J. Appl. Phys.*, vol. 97 (11), 113904. Jan. 2005

[9] W. Shan, *et al*., "Design and Development of SIS Mixers for ALMA Band 10," *IEEE Trans. Appl. Supercond.*, 2007, vol. 17 (2), pp. 363-366.

[10] S. Kohjiro, S. Kiryu and A. Shoji, "Surface resistance of epitaxial and polycrystalline NbCN films in submillimeter wave region," *IEEE Trans. Appl. Supercond.*., vol. 3 (1), pp. 1765-1767, Jan. 1993

[11] J. Cook *et al*., "An experimental apparatus for measuring surface resistance in the submillimeter-wavelength region," *Rev. Sci. Instrum.*, vol. 62 (10), pp. 2480-2485, Jan. 1991

[12] D. Dochev, *et al*., "Nb_3Al thin film deposition for low-noise terahertz electronics," *Journal of Physics: Conference Series*, , Vol. 97, 012072, Jan. 2008

[13] M. Bin, *et al*., "THz SIS mixers with normal-metal Al tuning circuits," *Supercond. Sci. Technol*, vol. 8, pp. A136-A139. Jan. 1995

[14] M. Bin, *et al.*, "Low□noise 1 THz niobium superconducting tunnel junction mixer with a normal metal tuning circuit," *Appl. Phys. Lett.*, vol. 68 (12), pp. 1714-1716. Jan. 1996

[15] A. Karpov *et al.*, "Low Noise 1 THz-1.4 THz Mixers Using Nb/Al-AlN/NbTiN SIS Junctions," *IEEE Trans. Appl. Supercond.*, vol. 17 (2), pp. 343-346, Jun. 2007

[16] T. Matsunaga, H. Maezawa and T. Noguchi, "Characterization of NbTiN thin films prepared by reactive DC-magnetron sputtering," *IEEE Trans. Appl. Supercond.*, vol. 13 (2), pp. 3284 - 3287, Jun. 2003

[17] N. Iosad, *et al.*, "Properties of DC magnetron sputtered Nb and NbN films for different source conditions," *IEEE Trans. Appl. Supercond.*, vol. 9 (2), pp. 1720 - 1723, Jun. 1999

[18] H. Myoren *et al*., "Properties of NbTiN thin films prepared by reactive DC magnetron sputtering," *IEEE Trans. Appl. Supercond.*, vol. 11 (1), pp. 3828-3831.Mar. 2001

[19] J. Du, A. D. M. Charles and K. D. Petersson, "Study of the Surface Morphology of Nb Films and the Microstructure of Nb/AlOx-Al/Nb Trilayers," *IEEE Trans. Appl. Supercond.*, vol. 17 (2), pp. 3520-3524, Jun.2007

[20] B. Leone, *et al*., "Hot electron effect in terahertz hybrid devices," *IEEE Trans. Appl. Supercond.,* vol. 11, pp. 649-652, Jan. 2001

[21] B. Leone *et al.*, "Electron heating by photon-assisted tunneling in niobium terahertz mixers with integrated niobium …," *Appl. Phys. Lett.*, vol. 78 (11), pp. 1616-1618, Jan. 2001

[22] A. Mayadas, "Intrinsic Resistivity and Electron Mean Free Path in Aluminum Films." *J. Appl. Phys.*, vol. 39 (9), pp. 4241-4245. Jan. 1968

[23] T. Van Duzer, and C. W. Turner, *Principles of Superconductive Devices and Circuits,* 1'st ed., Elsevier North Holland, 1981.

[24] T. Zijlstra, *et al*., "Epitaxial aluminum nitride tunnel barriers grown by nitridation with a plasma source." *Appl. Phys. Lett.,* 233102, Vol. 91 (23), Dec. 2007

[25] A. Endo *et al*., "Development of Nb/Al-AlNx/Nb SIS Tunnel Junctions for Submillimeter-Wave Mixers,"*IEEE Trans. Appl. Supercond.,* vol. 17 (2), pp. 367-370. Jun. 2007

[26] A. Endo, *et al*., "Fabrication of aluminum nitride barrier SIS mixer devices using nitrogen plasma diluted by noble …," *Journal of Physics: Conference Series*, vol. 97, 012251, Jan. 2008

Design and Performance of Waveguide Mixers with All NbN tunnel junctions on MgO substrates

Wenlei Shan[1], Masanori Takeda[2], Takafumi Kojima[3,4], Yoshinori Uzawa[3], Shengcai Shi[1], and Zhen Wang[2]

[1] *Purple Mountain Observatory, Nanjing, China.*

[2]*Kansai Advanced research Center, National Institute of Information and Communications Technology, Kobe, Japan.*

[3]*National Astronomical Observatory of Japan, Tokyo, Japan.*

[4]*Graduate School of Science, Osaka Prefecture University, Osaka, Japan.*

* Contact: shawn@mwlab.pmo.ac.cn, phone +86-25-8333 2229

***Abstract*—In this paper we present the development of low-noise waveguide mixers with NbN/AlN/NbN tunnel junctions at frequency approaching 1THz. The mixer was designed to be compatible with MgO substrate. Mixers of such a design demonstrated much improved receiver sensitivity. The improvement is a result of reduction of signal dissipation in waveguide and leakage into IF port by adopting a full-height waveguide and an effective RF choke filter respectively. Two types of tuning circuit, namely parallel-connected twin-junction (PCTJ) and half-wavelength self-resonance distributed junction (DJ), are designed and evaluated. Both theoretical and measurement results show that the PCTJ design is superior in terms of gain and sensitivity due to smaller loss in the tuning circuit.**

I. INTRODUCTION

Niobium Nitride (NbN) tunnel junctions are potentially applicable to low-noise frequency-mixing up to 2.6-2.8THz determined by a gap voltage as high as 5.3-5.6mV [1,2]. The large gap voltage results in a favorable wide bias region and causes the mixer to be less affected by Josephson effect [3]. With the Tc of NbN as high as 15-16K, a stable performance against temperature vibration can be expected when 4K closed-cycle cryocoolers are used for laboratory experiments and practical applications. In addition, high quality crystalline NbN film of perfect surface smoothness can grow on MgO substrate at ambient temperature [4]. That allows the fabrication of low leakage tunnel junctions [5] and the realization of lower RF loss than low-resistivity normal mental film up to about 1THz [6]. For the above reasons, NbN SIS mixers incorporated with NbN or normal mental microstrip tuning circuits are feasible and attractive in the applications of THz radio astronomy and atmosphere spectroscopy.

Effort to develop NbN SIS mixers has been made both on waveguide and quasi-optical designs in a wide frequency range [7-13]. Below Nb gap frequency (700GHz), low as it is, the noise is still higher than that achieved by Nb SIS mixers by a factor of two to four. This can be attributed to relatively larger leakage current of NbN tunnel junctions since leakage current results in the loss of high nonlinearity of quasi-partial tunneling onset and excessive shot noise. Above 700GHz where film loss tunes to be pronounced in Nb SIS mixers, NbN mixers of quasi-optical designs have provided quantum-efficient sensitivity comparable to that achieved by the state-of-the-art Nb mixers incorporating tuning microstrip-lines made of NbTiN ground plane and Al wiring at 800GHz band [14-15]. Waveguide NbN mixers, however, showed an averagely higher noise than that of the quasi-optical ones by a factor of two [13]. Since it is preferable for many practical applications to use horn antennas that generate well-controlled beam pattern, developing low noise waveguide type SIS mixers with horn antenna is of great interest.

There are two possible reasons for the lower sensitivity of waveguide mixers than quasi-optical ones at frequency approaching to 1THz: (1) As a rule, waveguides with reduced height are adopted in published experiments. At THz frequencies, waveguides of reduced height may suffer from transmission loss that can be considerably high. (2) Since the high dielectric constant of MgO (ε~9.6) causes the conventional design of RF choke filters to become less effective, leaking of signal to IF port leads to reduction of sensitivity. MgO substrates are preferred because epitaxial growth of NbN film on MgO substrates offers lowest film resistivity, while growth on quartz, which makes the mixer design much easier, results in poor film quality [16]. The purpose of this work is to demonstrate low noise NbN mixers at 780-950GHz band using a waveguide design. Adopting a full-height waveguide-microstrip transition on MgO substrate, into which a resonance choke filter is integrated, we have dramatically improved the performance. The measured uncorrected DSB receiver noise is as low as 280K at 830GHz at an ambient temperature of 4.2K that is comparable to that achieved by using best NbN quasi-optical SIS mixers.

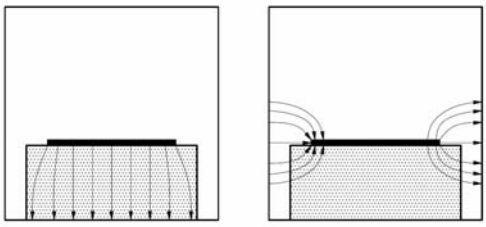

Fig. 1 The schematic plot of electric field of the fundamental mode and the second mode in a shielded microstrip line.

II. DESIGN OF THE SIS MIXER

A. RF choke filter and waveguide-microstrip transition design

Down-converted IF signal propagates to IF port through a choke filter that blocks RF signal from leaking out. The choke filter of a standard approach is incorporated with a series of high-low impedance lines having lengths close to the quarter wavelength of the fundamental mode of shielded microstrip line at RF center frequency. The choke filter becomes less effective if high order modes are propagative, since signal leaking due to high-order modes to IF port will obviously make additional loss. In particular, much attention should be paid to the second transmission mode, i.e. the first high-order mode, because its cutoff frequency is relatively low. Fig. 1 depicts the fundamental and the second mode in a shielded microstrip line. The cutoff frequency of the second mode depends on the effective dielectric constant (ε_{eff}) of the transmission line, which is determined by the dielectric constant of the substrate, strip width as well as chip thickness. The smaller the ε_{eff} is, the higher the cutoff frequency of the second mode will be. As a result, to make use of MgO substrate that has larger permittivity than quartz, thinner thickness is needed to prevent high-order mode propagation. However, it is not expedient to reduce ε_{eff} by means of using extremely thin chip for the reason of reliably mounting. In this work, we adopt the chip size of 80 μm in width and 30 μm in thickness. In this case, the cutoff frequency of the second mode of a 65μm-wide microstrip line, which is supposed to be the low impedance section of conventional choke filter, will be much lower than 780GHz.

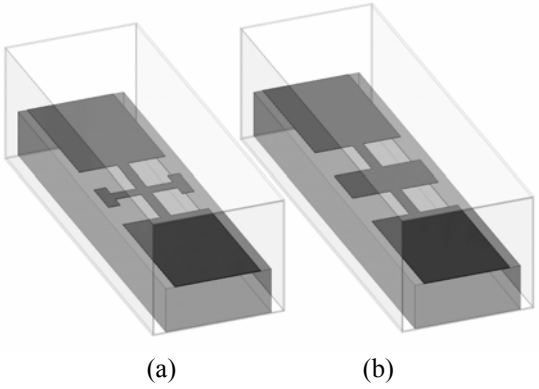

(a) (b)

Fig. 2 Two simplified choke filter designs. (a) shows a filter with transverse resonators, while (b) is a filter of the conventional design..

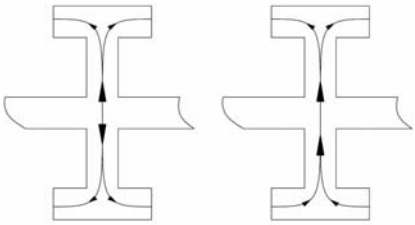

(a) (b)

Fig. 3 The schematic drawing of current distribution on transverse resonators. (a) shows the case when it is stimulated by the fundamental mode, and (b) shows the case when it is stimulated by the second mode.

As a solution, a pair of quarter-wavelength open-ended brunches is used as a substitute for low impedance section in conventional design. Fig. 2 shows a simplified model of this design on a 30μm-thick substrate together with a conventional design in comparison. The open-ended brunches are bifurcated in the end to enhance the bandwidth. The structure is stimulated in even manner by fundamental mode and in odd manner by the second mode as illustrated in Fig. 3. In both cases, it only conducts the local fundamental mode and forms a transverse resonator realizing low impedance at the joint if the length of each brunch is around quarter wavelength at center frequency of the mixer. The performance of the filter shown in Fig. 2a is compared with a conventional design shown in Fig. 2b by using an EM simulator with the results plotted in Fig. 4. We find that this resonance choke filter better suppresses both the fundamental and the second mode than the conventional design does. The discontinuities at about 920GHz of the fundamental mode transmission coefficient in both cases are due to the onset of the third mode, which does not considerably affect the

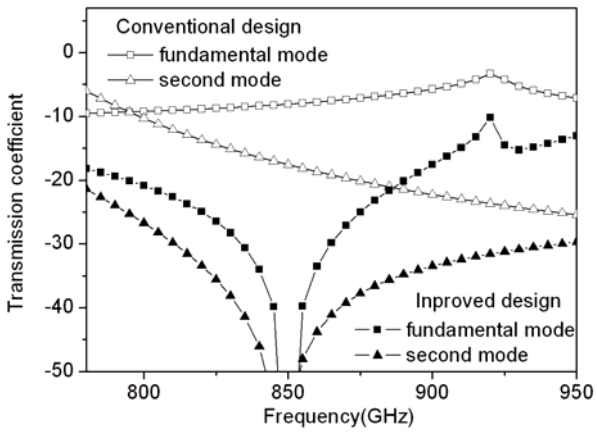

Fig. 4 The transmission coefficients of both the fundamental mode and the second mode of the two choke filters shown in Fig. 2.

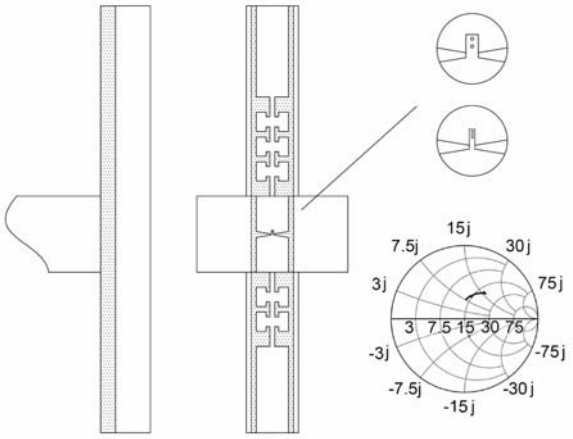

Fig. 5 The design of a full-height waveguide-microstrip transition. The cross-sectional dimensions of the chip and the waveguide are 30μm x80 μm and 304μmx152 μm respectively. The tuning circuit are illustrated in enlarged views. The probe impedance is plotted in a Smith chart normalized to 15Ω.

performance. We also noticed that the propagation properties of above shielded microstrip line are influenced by the gap between substrate and ground. In the practical mixer mounting, a gap unavoidably exists due to the substrate bending from its internal stress. Fortunately, a small gap of several micrometers can reduce the ε_{eff} of the microstrip line and thus acts positively to make the choke filter more efficient.

Through a waveguide-microstrip transition SIS tunnel junctions couple the LO and signal from waveguide. Waveguide loss rising with the increase of frequency plays an important role in receiver sensitivity at THz range. We have measured a loss as large as 0.6dB/10mm for a hull-height WR1.2 waveguide at cryogenic temperature, which is much larger than simple theoretical prediction [17]. Obviously, waveguides with reduced height, which are widely used in waveguide mixer designs, will bring about more serious problem. Therefore, a full-height waveguide-microstrip transition that allows the use of full-height waveguide and can provide broadband performance is of great advantage. Fortunately, a bow-tie waveguide-microstrip transition in full-height waveguide has been designed and tested in our previous work [18]. We extend such a design with combining the RF choke-filter introduced above as shown in Fig. 5. With intensive numerical simulation, the probe impedance was optimized to be as weakly frequency-dependent as we could by adjusting the taper angle and the length of the first section of choke-filter. For the sake of machining simplicity, a waveguide backshort cavity is not used and the probe is placed close to the waveguide end to achieve low impedance that is desirable for coupling of SIS junctions. The impedance of probe feed has a real part of 15Ω as well as an imaginary part varying with frequency. According to simulation results, this inductive part is helpful to achieve high mixer gain in spite of slight degradation of the LO coupling efficiency.

B. Mixer tuning circuit Design

We have designed two tuning circuits, namely parallel-connected-twin-junction (PCTJ) and half-wavelength self-resonance distributed junction (DJ), whose compactness and relatively wider RF bandwidth are suitable for THz applications. The PCTJ is composed of two parallel-connected SIS junctions at the two ends of an inductive NbN/MgO/NbN microstrip line that compensates for the geometric capacitance of SIS tunnel junctions at a desirable frequency. Half-wavelength distributed junction is essentially similar to PCTJ since the active areas for mixing locate at the two ends of a long junction with the quasi-particle tunneling transmission line in the center area acting as tuning inductance. The principles of NbN tuning circuit designs are basically the same as those already applied to Nb mixers, but some distinctive differences due to the larger gap voltage of NbN SIS junctions and longer penetration depth of NbN films deserve a clarification.

C. PCTJ Design

The SIS tunneling junctions in this study are formed by epitaxial NbN/AlN/NbN trilayers. Compared with Nb SIS junction, NbN SIS junction has higher gap voltage (V_{gap}) and larger capacitance ratio (C_s) [19]. It suggests that to achieve the same RF bandwidth NbN PCTJs must have larger current density (J_c) by a factor of 2~3 because the tuning circuit quality factor is proportional to $V_{gap}C_s/J_c$. However, the increase of Jc will result in the rise of leakage current and thus lead to the rise of the shot noise. Given the difficulty of the fabrication of low leakage NbN SIS junctions with high current density, we have to find a compromise between RF bandwidth and sensitivity to determine the Jc. This work is aimed at achieving junctions with quality factor of over 10, which is the ratio of resistance at 4mV and the normal resistance, and current density about 15kA/cm^2. The nominal junction size is 1μm in diameter realizing a resistance suitable to directly couple the waveguide-microstrip transition without any impedance transformer. Therefore, the transmission loss can be minimized. To realize a center frequency of about 850GHz, the distance of two junctions of PCTJ is about 3 μm, much shorter than Nb PCTJ at this frequency due to the larger penetration depth of NbN film.

The loss in tuning circuit is in fact composed of two parts. One is measured by $Q_J=\omega R_n C_J$, which takes account of the quasi-particle tunneling, where ω, R_n and C_J are angular frequency, normal resistance and capacitance of single junction respectively. The other part representing the dissipation loss in tuning inductance can be written in the form of $Q_T=\eta Q_J$. If $Q_J>>1$, (it is usually true for THz SIS mixers,) η can be expressed by

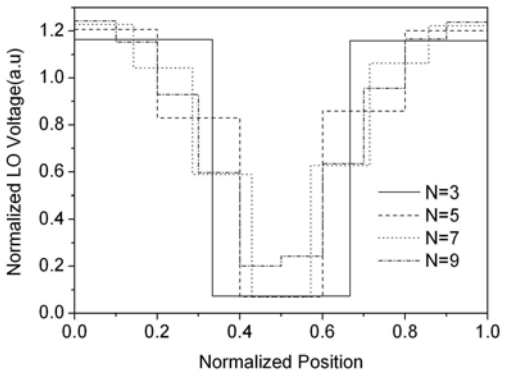

Fig. 6 The approximation of the LO voltage distribution along a half-wavelength distributed junction at center frequency. The simulations are performed with the junction is divided into 3,5,7, and 9 sub-sections.

$$\eta \approx \frac{Z_0^2 \beta^2 L_T}{2 R_n R_s}, \qquad (1)$$

in which Z_0 and β are characteristic impedance of tuning transmission line and wave number respectively, L_T is the tuning length and R_s is the RF surface resistance of NbN thin film. The overall Q factor is a combination of Q_J and Q_T, i.e. $1/Q=1/Q_J+1/Q_T$. When $\eta>>1$, the transmission loss can be neglected. From (1) we see the reduction of Rn, corresponding to the increase of current density, is helpful not only for broad RF band but also for high conversion efficiency. Since the improvement of conversion efficiency partly makes up for the rise of leakage current, we can expect good results for a relatively leaky NbN SIS mixer with high current density.

D. DJ Design

Half-wavelength distributed junction can be regarded as merging of the two junction of PCTJ to form a long one that self-resonates at a desired frequency. Such a scheme has been well studied theoretically [20] and experimentally [11,21]. We followed the theoretical approach introduced in [20] to optimize the mixer design. The long junction is uniformly divided into a number of sections which are modeled by lumped junctions separated by transmission lines taking account of the capacitance and inductance of each section. Based on this circuit model, the LO distribution can be calculated by solving a nonlinear equation numerically. Fig.

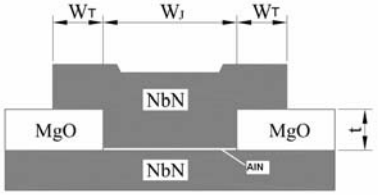

Fig. 7 The schematic cross-sectional view of a DJ. W_J and W_T are the barrier width and the width of overhanging part of wiring respectively.

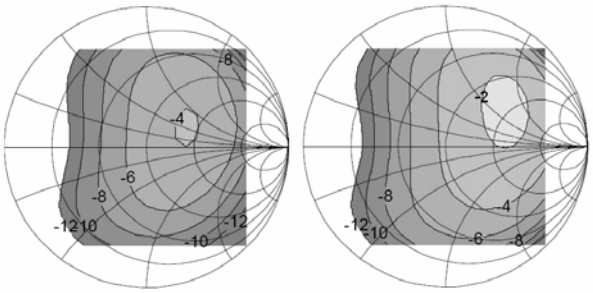

Fig. 8 Simulated DSB mixer gain of (a) a DJ mixer and (b) a PCTJ mixer as a function of embedding impedance at center frequency (865GHz). The Smith chart is normalized by 15 Ω.

6 shows an example of the approximation of LO voltage distribution along a DJ corresponding to various division numbers from 3 to 9. The portions at both ends of the DJ are normally pumped whereas those in the center are under-pumped and thus almost inactive for mixing effect. Compared with the tuning microstrip line in PCTJ, the quasi-particle tunneling transmission line suffers larger loss due to the leakage current and quasi-particle tunneling, which causes the degradation of tuning circuit efficiency.

The accurate modeling of the quasi-particle tunneling transmission line, the geometric structure of which is shown in Fig. 7, is essential for the correct determination of the tuning length and embedding impedance. It is particularly noticeable that unlike the electric field that is closely confined within junction barrier, the magnetic field spreads peripherally due to a long penetration depth of NbN film (about 200nm), which is much thicker than the barrier. As a consequence, a due emphasis should be put on the significance of the fringing effect of magnetic field. The character impedance (Z_0) and propagation constant (γ) determined by the serial impedance (z) and parallel admittance (y) of unit length are calculated by,

$$Z_0 = \sqrt{\frac{z}{y}}, \qquad (2)$$

and

$$\gamma = \sqrt{zy}. \qquad (3)$$

To involve the fringing effect, z and y can be written as:

$$z = [(Z_{ss} + Z_{sg})/W_J]/K, \qquad (4)$$

and

$$y = (G + j\omega C), \qquad (5)$$

where K (K<1) is the fringing factor; Zss and Zsg are the surface resistance of the strip and ground plane; W_J is the width of junction barrier; G and C are the tunneling admittance and junction capacitance of unit length of the transmission line respectively. The fringing factor K, calculated by means of numerical simulation [22], tunes out to be a typical value around 2 when the penetration depth of NbN is set around 200nm.

Along with the established circuit model and Tucker theory [3], we simulated the performance of DJs to find out the desirable embedding impedance. For example, the mixing

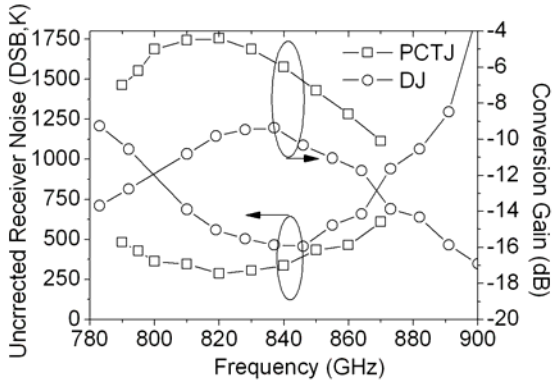

Fig. 9 The comparison of of a PCTJ and a DJ in terms of the measured receiver noise and conversion gain as a function of LO frequency.

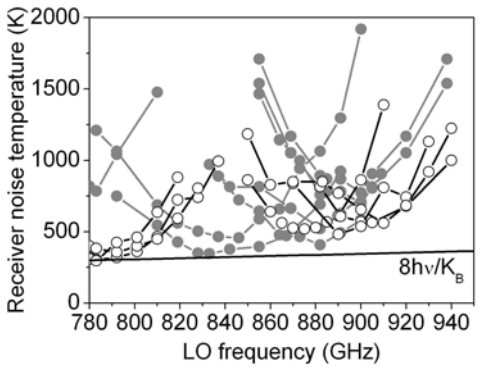

Fig. 11 Receiver noise of DJ mixers measured over a wide frequency range. Lines with closed circles are the results of all NbN junctions. As for those with open circles, devices incorporating NbTiN wiring layer were used.

conversion gain of the tuning circuit design is simulated at 865GHz with a parametric sweeping of the embedding impedance over most of area of Smith chart shown in Fig. 8a. We find that an inductive part is beneficial for the elevation of conversion gain as already mentioned and the mixer is unconditionally stable at this frequency. For a comparison, the same calculation was applied for a PCTJ of identical Jc and center frequency, shown in Fig. 8b. The maximum gain of PCTJ appears to be 2 dB higher than that of the DJ. It is understandable because of the larger loss in the tuning microstrip line of DJs.

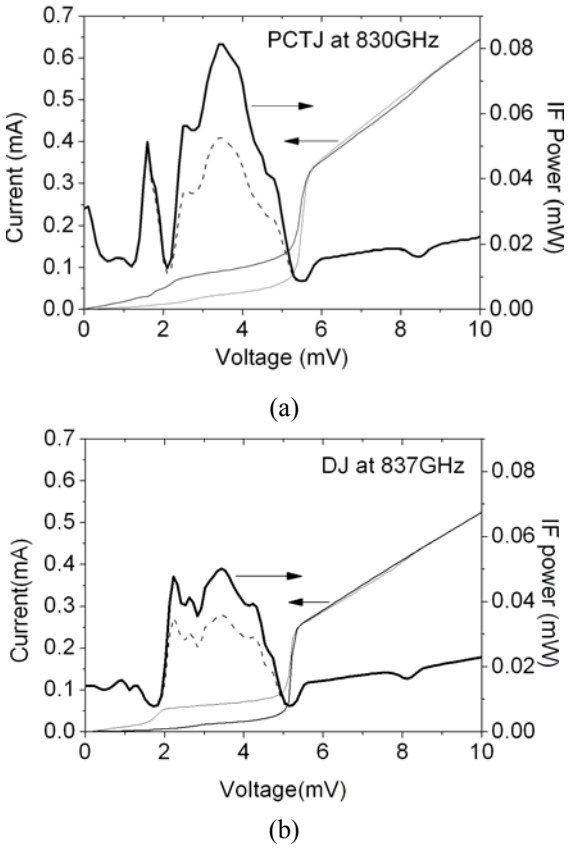

Fig. 10 Pumped and unpumped IV curves and IF responses corresponding to hot and cold loads of the PCTJ mixer (a) and DJ mixer (b) shown in Fig.9.

E. MEASURED PERFORMANCE OF DJ AND PCTJ MIXERS

A number of batches of DJ and PCTJ mixers of the above designs were fabricated with the technique described in [13]. The average quality factor of DJs of about 15 is slightly better than that of PCTJs (around 10). It is a result of the dependence of leakage current on junction size, since as a rule, the smaller the junction is , the larger leakage current tends to occur along the edge of the junction barrier. A low DC resistivity of NbN film, typically about 60μΩcm measured at room temperature, indicates rather good film quality.

The mixing performance was investigated in a 4K close-cycled cryogenic Dewar with the measurement setup described elsewhere [23]. The uncorrected receiver noise and gain of two typical devices, a PCTJ (nominal tuning length is 2.8 μm) and a DJ (junction length is 3 μm), is shown in Fig. 9 as a function of LO frequency. The current densities of both devices are similar (17kA/cm^2 and 13.5kA/cm^2 respectively) and their center frequencies almost coincide with each other. This provides a good condition to see the differences caused mainly by the tuning circuits. As seen in Fig. 9, the conversion gain of the PCTJ mixer is about 2 to 4dB higher than that of the DJ mixer and correspondingly the receiver noise of the PCTJ mixer is also lower. This difference has been well predicted by theoretical results as already mentioned. Their IV-curves with and without pumping as well as the IF-responses corresponding to cold and hot loads are presented in Fig. 10 at frequencies of 830GHz and 837GHz respectively. Uncorrected receiver noises of about 280K for the PCTJ mixer has been obtained,

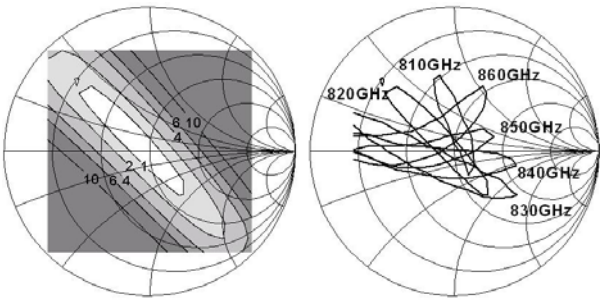

Fig. 12 (a) The normalized deviation of a measured pumped IV curve from simulated ones with parametric sweeping of embedding impedance at 820GHz. (b) The orientation of confidence region varies with frequency and the overlapping region is the most possible position where the actual embedding impedance locates.

which is the best result that has been achieved so far with NbN waveguide mixers and is comparable to the best result achieved by quasi-optical NbN mixers at this frequency.

Since no available device can cover the whole RF bandwidth due to limited current density (ranging from 5 to 15 kA/cm^2), a number of DJ mixers of various junction lengths ranging from 2.4um to 3.4um were measured to investigate the dependence of minimum noise temperature on frequency with the results shown in Fig. 11. Some of those DJ mixers are incorporating with polycrystalline NbTiN wiring layer, but the performance does not show obvious difference from all NbN junctions that are primarily used. The minimum uncorrected receiver noise remains around 8 times of quantum limits up to 880GHz and tends to surpass that. Such a tendency is also observed in quasi-optical NbN mixers and is attributed to the degradation of RF resistance of NbN film.

IV. ANALYSIS AND DISCUSSION

The effect of film loss on mixing performance can be estimated from the Q factor of the tuning circuit. The Q factor can be obtained by means of calculating the ratio of the center frequency and 3dB RF gain bandwidth. In cases of the above specific PCTJ and DJ mixers, their Q factors are found to be 13.4 and 11.4 respectively. Given that the overall Q factor is a combination of Q_J and Q_T representing the losses of quasi-particle tunneling and the tuning microstrip line respectively, it is straightforward to know $\eta=Q_T/Q_J$ that indicates the efficiency of the tuning circuit. To accurately estimate the Q_J, the junction capacitance was determined by fitting the measured mixer conversion gain versus LO frequency. In this way, we managed to obtain the Q_J's of 14.3 and 18.6 for PCTJ and DJ respectively. Consequently, the Q_T = 213 and 29 or η =16 and 1.6 for PCTJ and DJ respectively were calculated. It is found out that the PCTJ tuning circuit has much higher efficiency than DJ one. In addition, $\eta_{PCTJ} >> 1$ indicates that the surface resistance of NbN film is very low at this frequency.

Another issue of interest is whether the waveguide-microstrip transition can reproduce theoretically predicted impedance. [24] provides a technique to retrieve the embedding impedance by curve-fitting of the measured pumped IV curves. However a problem arises, i.e., the dependence of pumped IV curve on embedding impedance is rather weak. Consequencely the fitted impedance has rather large uncertainties. An example is plotted in Fig. 12 (a) at a LO frequency of 820GHz showing the calculated deviation between measured and simulated pumped IV curves with a parametric sweeping of embedding impedance. The confidence region of the fitting results appears to extend widely in a certain direction but concentrate within a narrow range in the perpendicular direction on the Smith chart. We found out that the confidence regions corresponding to different frequencies differ in orientations as shown in Fig. 12(b). If we assume that the probe impedance does not change rapidly with frequency, as predicted in the numerical simulation, the overlapping region should be the most possible position where the embedding impedance locates. The impedance value (~ 15 Ω) indicated by the overlapping region agrees with the simulation results shown in Fig. 5 with a reasonable accuracy if the uncertainties of junction parameters are taken into consideration.

CONCLUSIONS

In this paper, we have demonstrated low noise waveguide NbN SIS mixers at frequency approaching 1THz. High sensitivity is owed to the efforts to minimize the signal loss in the waveguide mounting structure by adopting full-height waveguide and a highly efficient RF choke filter on MgO substrate. Design techniques are presented for NbN PCTJ and DJ tuning circuits with emphasizing the impacts of the distinctive features of NbN mixers, namely high energy-gap of NbN SIS junction and long penetration depth of NbN film. By means of Q factor analysis we verified that the surface resistance of NbN film is rather low at measured frequencies. It was also confirmed that the PCTJ mixers are superior in sensitivity to DJ mixers, which suffers from a larger loss in tuning circuit.

ACKNOWLEDGMENT

The authors own thanks to Dr. Matthius Kroug of NAOJ for fabricating part of the devices and valuable discussion on fabrication.

This work was supported in part by the CAS Bairen Project.

REFERENCES

[1] W. C. Danchi and E. C. Sutton, "Frequency dependence of quasiparticle mixers," J. Appl. Phys. Vol 60, No. 11, pp3967-3977, Dec. 1987.

[2] D. Winkler and T. Claeson, " High-frequency limits of superconducting tunnel junction mixers," J. Appl. Phys. Vol. 62, No. 11, pp4482-4498, Dec. 1987.

[3] R. Tucker and M. J. Feldman, "Quantum detection at millimeter wavelengths," Reviews of Modern Physics, Vol. 57, No.4, pp.1055-11113, Oct. 1985.

[4] Z. Wang, A. Kawakami, Y. Uzawa, and B. Komiyama, " Superconducting properties and crystal structures of single-crystal niobium nitride thin films deposited at ambient substrate temperature," J. Appl. Phys. Vol. 79, No. 10, pp7837-7842, May 1996.

[5] Z. Wang, A. Kawakami, Y. Uzawa, and B. Komiyama, "NbN/AlN/NbN tunnel junctions fabricated at ambient substrate temperature," IEEE Trans. on Applied Superconductivity, Vol. 5, No.2, pp2322-2325, June 1995.

[6] A. Kawakami, M. Shigehito, Y. Uzawa and Z. Wang, "Estimation of Surface Resistance for Epitaxial NbN Films in the Frequency Range of 0.1-1.1THz," IEEE Trans. on Applied Superconductivity, Vol. 13, No. 2, Jun. 2003.

[7] W. R. McGrath, "Performance of NbN superconductive tunnel junctions as SIS mixers at 205GHz," IEEE Trans. on Magnetics, Vol.27, No. 2, pp.2650-2653, March 1991.

[8] H. G. LeDuc, A. Judas, S. R. Cypher, B. Bumble, B. D. Hunt, J. A. Stern, " Submicron area NbN/MgO/NbN tunnel-junctions for SIS mixer applications," IEEE Trans. on Magnetics, Vol. 27, No. 2, pp.3192-3195, March 1991.

[9] A. Karpov, B. Plathner, J. Blondel, M. Schicke, K. H. Gundlach, M Aoyagi and S. Takada,"Noise and Gain in Frequency Mixers with NbN SIS Junctions," IEEE Trans. on Superconductivity, Vol. 7, No. 2, pp1077-1080, June 1997.

[10] Z. Wang, Y. Uzawa, and A. Kawakami, "High Current Density NbN/AlN/NbN Tunnel junctions for Submillimeter Wave SIS mixers," IEEE Trans. on Applied Superconductivity, Vol. 7, No. 2, pp2797-2800, June 1997.

[11] Y. Uzawa, A. Kawakami, M. Shigehito and Z. Wang, "Performance of All-NbN Quasi-optical SIS Mixers for the Terahertz Band," IEEE Trans. on Appl. Supercond., Vol.11, No. 1, pp183-186, March 2001.

[12] A. Kawakami, Y. Uzawa and Z. Wang, " Development of epitaxial NbN/MgO/NbN superconductor-insulator -superconductor mixers for operations over the Nb gap frequency," Applied Physics Letters, Vol. 83, No. 19, pp3954-3956, Nov. 2003.

[13] Masanori Takeda, Yoshinori Uzawa, Akira Kawakami and Zhen Wang, "Waveguide-Type SIS Receiver Using All-NbN Technique," IEICE Transactions on Electronics 2006 , Vol. E89-C, Num. 2, pp 163-169.

[14] J. Zmuidzinas, J.W. kooi, J. Kawamura, G. Chattopadhyay, B. Bumble, H. G. LeDuc, and J. Stern, " Development of SIS mixers for 1THz," Proceeding of SPIE, Vol. 3357, Advanced Technology MMW, Radio, and Terahertz Telescopes, Thomas G. Phillips, Editor, July 1998, pp. 53-62.

[15] B.D.Jackson, G.Lange,"Niobium titanium nitride-fundamentald superconductor-insulator-superconductor mixers for low-noise terahertz receivers," Journal of Applied Physics, vol. 97, 113904, 2005.

[16] B. plathner, M. Schicke, T. Lehnert and K. H. Gundlach, "NbN-MgO-NbN junctions repared on room-temperature quartz substrates for quasiparticle mixers," IEEE Trans. on Applied Superconductivity, Vol. 7, No. 2, June 1997.

[17] ALMA Band 10 Cartridge Preliminary Design Review Design Report

[18] Wenlei Shan, Shengcai Shi , Teruhiko Matsunaga, Manabu Takizawa, Akira Endo, Takashi Noguchi, and Yoshinori Uzawa , "Design and Development of SIS mixers for ALMA band 10", IEEE Trans. On Appl. Supercond, Vol. 17, Issue 2, Part 1, June 2007, Page(s) 359-362.

[19] Zhen Wang, Hirotaka Terai, Akira Kawakami, and Yoshinori Uzawa, " Characterization of NbN/AlN/NbN Tunnel junctions," IEEE Trans. on Applied Superconductivity, Vol. 9, No. 2, June 1999, pp3259-3262.

[20] E.C.Tong, L. Chen, and R. Blundell, "Theory of distributed mixing and amplification in a superconduting quasiparticle nonlinear transmission line," IEEE Trans. Microwave Theory Tech., Vol MTT-45, pp. 1086-1092, July 1997.

[21] E. C. Tong, R. Blundell, K.G. Megerian, J. A. Stern and H. G. LeDuc,"A 650GHz fix-tuned waveguide SIS distributed mixer with no integrated tuning circuit," IEEE Trans. Microwave Theory Tech., Vol. 13, pp 680-683, June 2003.

[22] Sheng-Cai Shi, Wenlei Shan, and Jing Li,"Theoretical Simulation of the Mixing Performance of Distributed Superconducting Tunnel Junction Arrays at 1.2THz," IEICE Trans. Electron, Vol. E90-C, No. 3,pp556-565, 2007

[23] Wenlei Shan, Shengcai Shi , Teruhiko Matsunaga, Manabu Takizawa, Akira Endo, Takashi Noguchi, and Yoshinori Uzawa , "Design and Development of SIS mixers for ALMA band 10", *IEEE Trans. On Appl. Supercond*, Vol. 17, Issue 2, Part 1, June 2007, Page(s) 359-362.

[24] A. Skalare, "Determining embedding circuit parameters for DC measurements on quasiparticle heterodyne mixers," Int. J. Infrared millimeter Waves, Vol.10, pp 1339-1353, 1989.

Bandwidth of Nb/AlN/Nb SIS Mixers Suitable for Frequencies around 700 GHz

C. F. J. Lodewijk[1,*], E. van Zeijl[1], T. Zijlstra[1], D. N. Loudkov[1], F. P. Mena[2,3], A. M. Baryshev[2], and T. M. Klapwijk[1]

[1] *Kavli Institute of Nanoscience, Faculty of Applied Sciences, Delft University of Technology*
Lorentzweg 1, 2628 CJ Delft, The Netherlands
[2] *SRON Netherlands Institute for Space Research and Kapteyn Astronomical Institute,*
Landleven 12, 9747 AD Groningen, The Netherlands
[3] *Currently at Universidad de Chile, Santiago, Chile*
* Contact: c.f.j.lodewijk@tudelft.nl, phone +31-15-278 7163

***Abstract*— We have developed a new fabrication process for AlN barriers with excellent reproducibility and control compared to previous work, enabling the use of these barriers in SIS mixers. We report results with niobium-aluminum nitride-niobium superconductor-isolator-superconductor (SIS) mixers for 700 GHz, demonstrating a wide bandwidth behavior with Fourier Transform Spectrometer (FTS) measurements. These measurements have been performed in air and reveal that the bandwidth is no longer limited by the tuning circuit but by the atmospheric absorption of radiation. We also present noise temperature measurements of AlN SIS mixers that complement the FTS results.**

I. Introduction

Although the specifications for Band 9 (602 to 720 GHz) of the atmospheric window at the Atacama Large Millimeter Array (ALMA) [1], [2] can be met with aluminum oxide [3], an intrinsically wider band coverage would be beneficial. In particular a flat response over the full band width is desirable. High critical current density aluminum nitride devices have a low *RC* time constant, enabling such a desirable larger bandwidth, provided a suitable matching circuit is realized [4].

II. Bandwidth of SIS mixers

The bandwidth of SIS mixers for Band 9 is limited by several critical parameters. First, the superconducting gap energy 2Δ of the used superconductor is important. In this work, the electrodes of the SIS junction as well as the microstriplines are made of niobium. Its 2Δ = 2.8 meV translates into a gap frequency f_{gap} of about 690 GHz, implying that resistive losses will reduce the transmission at the high end of the band.

Second, other material parameters that play a role are the high frequency resistivity of the niobium microstriplines and the permittivity of the dielectric layer of silicon dioxide. The normal state resistivity can vary over the thickness of the superconducting film, whereas the effective resistivity of a superconducting bilayer (niobium-aluminium) used in the process is poorly defined.

Furthermore, the position of the SIS device in the waveguide, determined by both the mounting of the chip and the thickness of the substrate, has to be carefully monitored. It determines the antenna impedance, which is crucial for the device performance [4].

Finally, the *RC* time constant fundamentally limits the bandwidth of a device matched to a source impedance by [5]:

$$\ln\left(\frac{1}{\Gamma_{\max}}\right)\Delta f = \frac{\pi}{RC}, \qquad (1)$$

where $\Gamma_{\max}$ is the maximum reflection coefficient over a bandwidth Δf. A wide Δf is achieved by a low *RC* product of the SIS junction, which in its turn is set by the tunnel barrier transparency. This transparency can be characterized by the critical current density J_c [6]:

$$J_c = \frac{\pi}{2}\frac{\Delta}{eR_nA}, \qquad (2)$$

with e the charge of an electron and R_nA the normal resistance times area of an SIS junction.

Increasing the critical current density of AlO_x barriers leads to SIS junctions with poor quality current-voltage (*IV*) characteristics for J_c above 20 kA/cm^2 [7]. At this relatively low critical current density, or relatively high R_nA value the subgap current increases rapidly indicating that a substantial fraction of the tunnel barrier area carries higher order tunnelling terms, i.e. contains parts with transparencies close to unity. First results on AlN tunnel barriers have been published by Shiota *et al*. [8], with the attractive feature of offering a much higher critical current density. Mixing devices based on AlN barriers have recently been used by Kooi *et al*. [9] at frequencies from 275 to 425 GHz.

III. AlN growth and fabrication process

Compared to the growth of AlO_x, in which oxygen molecules decompose on the aluminium into reactive atomic oxygen, for AlN tunnel barrier growth, a plasma is needed to split N_2 molecules into N radicals, which subsequently react with Al. We have used an inductively coupled plasma source [10] to generate a nitrogen plasma containing N radicals which diffuse to the aluminium. This

approach is different from most previous work with parallel plate reactors, where reproducibility and control were difficult to achieve [8], [11]-[13].

The devices are fabricated on a 2 inch fused quartz substrate. All metal layers are deposited by magnetron sputtering in the process chamber of a Kurt Lesker system. First, a 100 nm Nb monitor layer is deposited, after which a ground plane pattern is optically defined. Subsequently, a bilayer of 100 nm Nb and about 7 nm Al is deposited. Without breaking the vacuum, the substrate is then transferred to a nitridation chamber, where the Al is exposed to the nitrogen plasma for several minutes, producing a layer of AlN. The substrate is then again *in vacuo* transferred to the process chamber, where a top electrode of 200 nm Nb is deposited. The lateral dimensions of the multilayer of Nb/Al/AlN/Nb are patterned by lift-off. Junctions are defined by e-beam lithography with a negative e-beam resist (SAL-601) layer and reactively ion etched (RIE) with a SF_6/O_2 plasma using the AlN as an etch-stop, followed by a mild anodization (5 V). The junction resist pattern is used as a self-aligned lift off mask for a dielectric layer of 250 nm SiO_2. A 500 nm Nb/50 nm Au top layer is deposited and Au is etched with a wet etch in a KI/I_2 solution using an optically defined mask. Finally, using an e-beam defined top wire mask pattern, the layer of Nb is etched with a SF_6/O_2 RIE, which finishes the fabrication process.

IV. DC TEST RESULTS AND BARRIER UNIFORMITY

The quality factor Q, defined as $Q=R_j/R_n$, where R_j is the resistance of an SIS junction below the gap voltage $V_{gap} = 2\Delta/e$, gives a measure for the amount of subgap current through a tunnel barrier. A low subgap current is a signature of a good quality tunnel barrier provided only first order tunnelling processes. In Fig. 1, Q for the new fabrication method is compared with Q for AlO_x devices, as reported in [7].

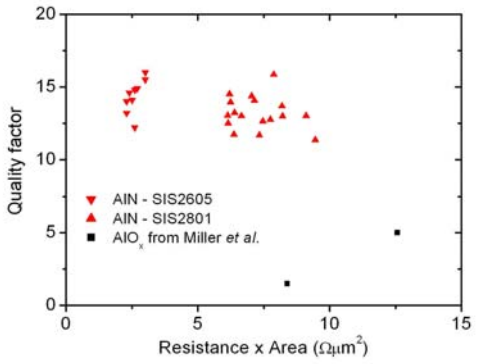

Fig. 1. Quality factor as a function of resistance times area product for different batches of SIS devices. Red triangles, pointing up and down, represent two batches of AlN barrier devices made with the new fabrication method [10]; black squares indicate data from [7].

Evidently, whereas the best values for AlO_x are below 5 for R_nA around 10 Ωμm^2, with AlN much higher values of 15 and up are achieved down to R_nA=3 Ωμm^2. We have also realized (not shown in this Figure) AlN SIS devices with Jc=120 kA/cm^2 (1.7 Ωμm^2), with Q=10, and with Jc=420 kA/cm^2 (0.43 Ωμm^2) still having Q=5. In the latter devices we observe non-equilibrium-effects causing back-bending of the IV characteristics. This indicates that with these low R_nA-values, high current densities, it becomes more difficult to maintain thermal equilibrium in the tunnelling electrodes.

The better quality of the AlN tunnel barriers at high critical current densities is related to their better tunnel-uniformity. They have apparently a lower fraction of the tunnel area with high tunnel transmissivity. The better uniformity is probably related to the materials quality of the AlN compared to AlOx. With high resolution Transmission Electron Microscopy we have found that the AlN barrier is crystalline [10], rather than amorphous, as is the case with AlO_x.

V. FTS EVALUATION

AlN tunnel barriers grown with the new method have been incorporated in SIS mixing-devices, designed for ALMA Band 9. All devices incorporate a multisection Nb/SiO2/Al-Nb microstripline, which tunes out the capacitance of the SIS junction. The transmission efficiency of a device is evaluated using a Fourier Transform Spectrometer (FTS) by measuring the changes in the DC current produced by the incoming light for a bias voltage of 2.5 mV, selected to be close to the gap voltage.

An AlN-based SIS device is mounted onto a waveguide backpiece. The device has the following parameters: R_n = 7.1 Ω, A_j = 0.52 μm^2, Q = 14.9, V_{gap} = 2.64 mV. J_c for this device is 56 kA/cm^2. The FTS data, taken at a temperature of 4.2 K, are shown in Fig. 2 (red triangles). The FTS setup is operated in air, leading to the water absorption lines at the edges of the band. In the same graph, one of the best available FTS results for an AlO_x based SIS device, selected for one of the prototype cartridges of Band 9 [3], is shown (black squares).

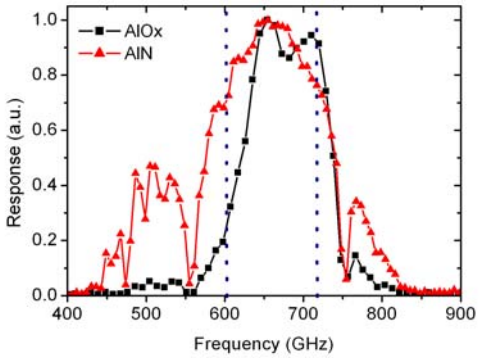

Fig. 2. Normalized photoresponse of two devices, measured with a Fourier Transform Spectrometer (FTS). The red triangles are for a device with an AlN tunnel barrier, whereas the black squares show the best achievable result for a device with an AlO_x tunnel barrier. The dashed blue lines indicate ALMA Band 9. Minima in the response are due to water absorption.

The full width half maximum (FWHM) bandwidth of the AlN device is about 168 GHz, whereas the FWHM bandwidth of the AlO_x device is around 116 GHz. Obviously, the bandwidth of the AlN device is about 45 % larger than that of the AlO_x device. A good response is obtained over the full targeted band. In order to allow a fair comparison care has been taken to position the devices in identical positions in the waveguide.

In Fig. 2, there are clearly minima in the response, due to the absorption of radiation by water vapor in the atmosphere, in particular at 560 and 750 GHz. In order to compare the FTS data with model calculations we subtract the atmospheric transmission from the data.

Fig. 3 shows the same FTS measurement results as Fig. 2 corrected for the atmospheric transmission [14]. The red triangles show the corrected response for the AlN device, the black squares indicate the corrected response for the AlO_x device. The full blue line is the model fit for the AlN device, based on its measured parameters, and on the following realistic microstripline parameters: RF normal conductivity of Nb is 1.0×10^7 S/m [4] and permittivity of SiO_2 is 3.8. The specific capacitance of the SIS junction, used as a fitting parameter, is determined to be 60 fF/μm^2. Based on a permittivity of AlN of 8.8 [15], this corresponds to a tunnel barrier thickness of 1.3 nm, which is well within the tolerance of the Transmission Electron Microscope analysis in [10], which yields 1.5 ± 0.5 nm.

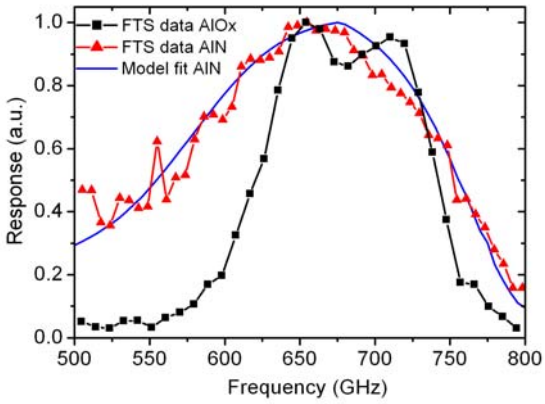

Fig. 3. FTS measurement results, corrected for the atmospheric transmission. The red triangles are for an AlN device, the black squares for an AlOx device. The full blue line shows the simulated response for the AlN device, using real device parameters. All curves are normalized to their maximum.

From Fig. 3, we can correct the FWHM bandwidth for water absorption. The AlN device has a bandwidth of 187 GHz, the AlO_x device yields 122 GHz. The use of AlN has improved the bandwidth by 53 %.

VI. Noise Temperature

The same AlN based device has been mounted in a standard ALMA Band 9 test cartridge. The noise temperature of the mixer, the accompanying optics and the Intermediate Frequency (IF) chain [16] has been evaluated using the standard Y-factor method. The resulting uncorrected Double Sideband (DSB) noise temperatures at different local oscillator (LO) frequencies are presented in Fig. 4 (red triangles pointing upwards). In the same graph, the best results obtained with AlO_x based SIS devices are shown with black squares. The AlN results reported before [17] are indicated by the green triangles pointing downwards.

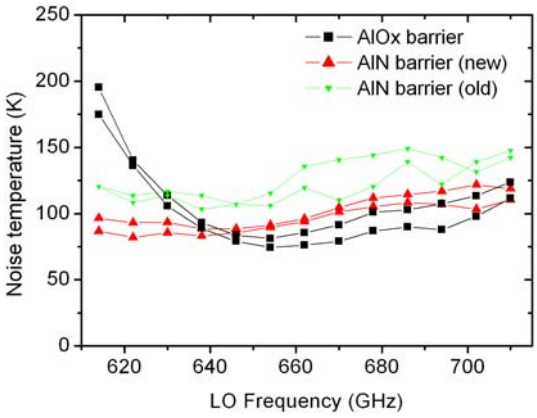

Fig. 4. Uncorrected Double Sideband (DSB) noise temperature of an SIS mixer with an AlN tunnel barrier (red triangles pointing up), earlier AlN results [17] (green triangles pointing down) and the best result obtained for an SIS with an AlO_x tunnel barrier [3] (black rectangles), in the frequency range of ALMA Band 9.

Evidently, the noise temperature of the newest AlN SIS mixers is much flatter over the full ALMA Band 9 than for the best AlO_x mixers, while practically maintaining the same low value.

Conclusions

Utilizing AlN tunnel barriers, grown with a new method [10], in SIS devices for ALMA Band 9 the bandwidth has improved considerably in comparison with AlO_x devices. After correction for the atmospheric transmission, the gain in the FWHM bandwidth amounts to 53 %. Heterodyne measurements reveal that the AlN SIS devices have an uncorrected DSB noise temperature which is equally low, but flatter than the AlO_x mixers that are currently equipping the prototype ALMA Band 9 cartridges [3].

Acknowledgment

The authors would like to thank NanoImpuls, the Dutch Research School for Astronomy (NOVA), the Dutch Organisation for Scientific Research (NWO), and the European Southern Observatory (ESO) for funding this project.

References

[1] The Atacama Large Millimeter/Submillimeter Array Web Site. [Online]. Available: http://www.alma.nrao.edu/

[2] J. Kanipe, "High and dry," *Nature*, vol. 439, 526 (2006).

[3] A. M. Baryshev *et al*., "ALMA Band 9 cartridge" *This Conference*, paper 9-6.

[4] C. F. J. Lodewijk, O. Noroozian, D. N. Loudkov, T. Zijlstra, A. M. Baryshev, F. P. Mena, and T. M. Klapwijk, "Optimizing superconducting matching circuits for Nb SIS mixers operating around the ap frequency," *IEEE Trans. Appl. Superconductivity*, vol. 17, 375 (2007).

[5] H. W. Bode, *Network analysis and feedback amplifier design*, New York, USA: Van Nostrand (1945).

[6] V. Ambegaokar and A. Baratoff, "Tunneling between superconductors," *Phys. Rev. Lett.,* vol. 10, 486 (1963).

[7] R. E. Miller, W. H. Mallison, A. W. Kleinsasser, K. A. Delin, and E. M. Macedo, "Niobium trilayer Josephson tunnel junctions with ultrahigh critical current densities," *Appl. Phys. Lett*., vol. 63, 1423 (1993).

[8] T. Shiota, T. Imamura, and S. Hasuo, "Nb Josephson junction with an AlNx barrier made by plasma nitridation," *Appl. Phys. Lett*., vol. 61, 1228 (1992).

[9] J. W. Kooi, A. Kovács, M. C. Sumner, G. Chattopadhyay, R. Ceria, D. Miller, B. Bumble, H. G. LeDuc, J. A. Stern, and T. G. Phillips, "A 275–425-GHz tunerless waveguide receiver based on AlN-barrier SIS technology," *IEEE Trans. Microwave Theory and Techn*., vol. 55, 2086 (2007).

[10] T. Zijlstra, C. F. J. Lodewijk, N. Vercruyssen, F. D. Tichelaar, D. N. Loudkov, and T. M. Klapwijk, "Epitaxial aluminum nitride tunnel barriers grown by nitridation with a plasma source", *Appl. Phys. Lett*., vol. 91, 233102 (2007).

[11] Z. Wang, A. Kawakami, and Y. Uzawa, "NbN/AlN/NbN tunnel junctions with high current density up to 54 kA/cm^2," *Appl. Phys. Lett*., vol. 70, 114 (1997).

[12] B. Bumble, H. G. LeDuc, J. A. Stern, and K. G. Megerian, "Fabrication of Nb/Al-N_x/NbTiN junctions for SIS mixer applications," *IEEE Trans. Appl. Supercond*., vol. 11, 76 (2001).

[13] A. B. Kaul, A. W. Kleinsasser, B. Bumble, H. G. LeDuc, and K. A. Lee, "Aluminum nitride tunnel barrier formation with low-energy nitrogen ion beams," *J. Mater. Res*., vol. 20, 3047 (2005).

[14] The program that calculates the atmospherical transmission has been provided by J. R. Pardo-Carrion, Departemento de Astrofisica Molecular e Infraroja, Consejo Superior de Investigaciones Cientificas, Madrid, Spain.

[15] L. M. Sheppard, "Aluminum nitride: a versatile but challenging material," *Am. Ceram. Soc. Bull*., vol. 69, 1801 (1990).

[16] A. Baryshev, E. Lauria, R. Hesper, T. Zijlstra, and W. Wild, "Fixed-tuned waveguide 0.6 THz SIS Mixer with Wide band IF," ALMA memo 429 (2002).

[17] C. F. J. Lodewijk, T. Zijlstra, D. N. Loudkov, T. M. Klapwijk, F. P. Mena, and A. M. Baryshev, "Wideband AlN-based SIS devices for frequencies around 700 GHz," in Proc. 18th Int. Symp. on Space THz Technology, Ed. A. Karpov, paper 10-1, 256 (2007).

RF Performance of a 600 - 720 GHz Sideband-Separating Mixer with All-Copper Micromachined Waveguide Mixer Block

F.P. Mena[1,2,†,*], J. Kooi[3], A.M. Baryshev[1,2], C.F.J. Lodewijk[4], T.M. Klapwijk[4], W. Wild[1,2], V. Desmaris[5], D. Meledin[5], A. Pavolotsky[5], and V. Belitsky[5]

[1]*SRON Netherlands Institute for Space Research, Groningen, the Netherlands*

[2]*Kapteyn Astronomical Institute, University of Groningen, Groningen, the Netherlands*

[3]*California Institute of Technology, MS 320-47 Pasadena, CA 91125, USA*

[4]*Kavli Institute of Nanoscience, Delft University of Technology, Lorentzweg 1, 2628 CJ Delft, the Netherlands*

[5] *Chalmers University of Technology, Group for Advanced Receiver Development, Department of Radio and Space Science with Onsala Space Observatory, SE 412 96, Gothenburg, Sweden*

†Current address: Department of Electrical Engineering, Universidad de Chile, Santiago, Chile

* Contact: pmena@ing.uchile.cl, phone +56-2-978 4888

***Abstract*— Here we report on the RF performance of a 2SB mixer (600-720 GHz) fabricated in a new method that combines traditional micromachining with waveguide components fabricated by photolithography and electroplating. The latter allows reaching, in a reproducible way, the stringent accuracies necessary for the critical RF components at these high frequencies.**

I. Introduction

A sideband-separating (2SB) mixer has several advantages over its double sideband (DSB) counterpart. Despite those advantages, its implementation at high frequencies is rather challenging as a more complex design is needed. In fact, the required waveguide circuitry becomes extremely difficult to fabricate employing traditional machining. Previously, we have demonstrated state-of-art performance of a 2SB mixer for 600–720 GHz band constructed exclusively by traditional micromachining [1]. In order to build such mixer one needs to produce a waveguide hybrid with a minimum branch width of 71 μm made with an accuracy better than 5 μm. However, traditional mechanical milling fails to deliver the required accuracy of the dimensions in a reproducible way.

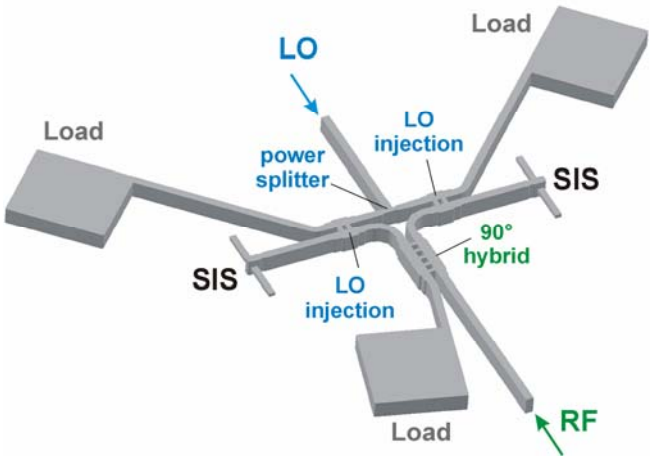

Fig. 1 Proposed realization of the critical RF components. They are designed in waveguide and, therefore, represent the channels to be patterned. The transversal dimensions of the waveguide are 310×145 μm.

Here we report the first results on the RF performance of a 2SB mixer suitable for, e.g., ALMA Band 9 and fabricated using our cutting-edge microfabrication technique [2]. This technique meets the requirements for the dimension accuracy along with surface quality. It, moreover, allows the fabrication of the waveguide components with high yield and repeatability. This approach combines lithographical copper micromachining [3] for making the very fine waveguide structures while allowing regular milling of the remaining not critical mixer parts.

II. Design and Fabrication

A. Design

The mixer we describe here is based in a design we have presented in detail previously [1] and is intended to cover the 600-720 GHz range. The design, summarized in Fig. , uses waveguide components and it is planned for construction using the split-block technique. The critical RF waveguide component are a 90° hybrid, a LO splitter, two LO injectors, and two waveguide-to-microstrip transitions.

B. Fabrication

To fabricate the split-block we have followed a new approach which combines two different techniques. We first produce the critical waveguide RF components using a combination of lithography and electroplating. The result of this process is a single copper plate containing all the (small) RF components as shown in Fig.. Gold is finally sputtered on the plate to improve conductivity. Accuracies of less than

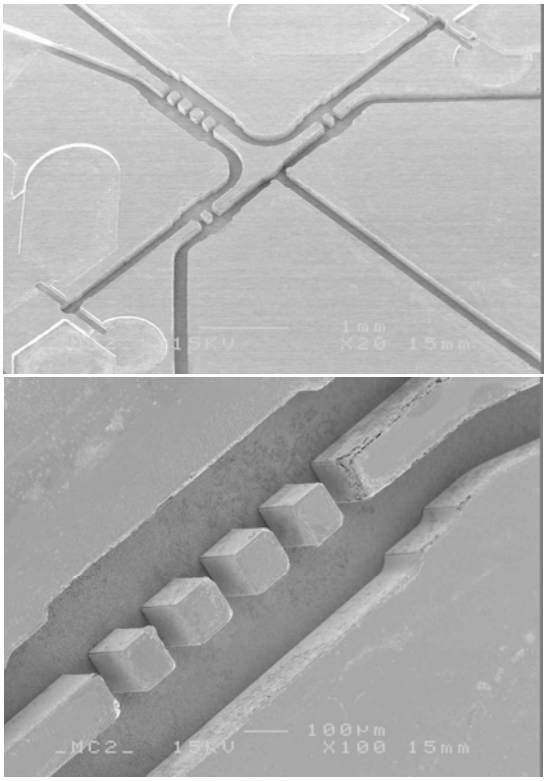

Fig. 2 SEM micrograph of one the copper plates produced lithographically. *Top:* General view of all the RF components. *Bottom:* Details of the 90° RF hybrid.

1 μm and a roughness of ~300 nm RMS can be achieved. This process has been described in detail elsewhere [2, 3, 4] and we refer to those references for details.

The next step in the fabrication process of the mixer's block is summarized in Fig. . First a rectangular cavity is machined in a copper block such that the plate can be fit and soldered using a low-melting-point alloy. Care is taken to have the upper plane of the plate coplanar with the upper plane of the block. Then, all the other non-critical cavities are milled out by conventional means. Finally, all the extra components are placed inside the respective cavities. As mixing elements we have used Nb/AlN/Nb junctions [5].

III. Characterization

A. Band Coverage

The direct response, as function of frequency, of both superconductor-insulator-superconductor (SIS) junctions contained in our mixer was determined using a home-made Fourier-transform spectrometer. Notice that the incoming light was coupled into the mixer via the RF port and that no changes were made between both measurements. The results are presented in top panel of Fig. . Both junctions show practically the same response albeit shifted towards low frequencies. The fact that the response is practically identical in the two junctions corroborates the good quality of the fabricated waveguide pattern.

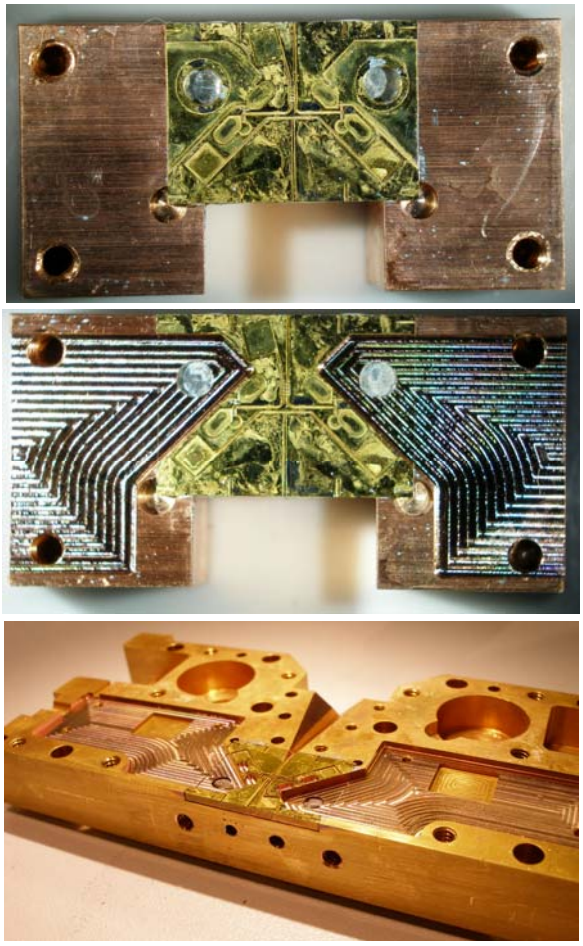

Fig. 3 *Top:* Plate inserted in a test copper block. *Middle:* Test copper block after conventional machining. *Bottom:* Lower part of the fabricated split-block. Notice the inserted plate at the hearth of the block.

B. Pumping

Further indication of the good quality of the fabricated pattern is given in the bottom panel of Fig. . In that Figure we indicate the pumping current of both junctions at V_{BIAS} = 2.5 mV after subtracting their respective leakage currents. Once more, both junctions show identical response.

IV. Conclusions and Future Work

Here we have presented the RF performance of a heterodyne receiver covering the 600–720-Ghz band. This mixer was fabricated combining two different fabrication techniques. For the small and critical RF components we have used a technique that combines lithography and electroplating. This technique allows to achieve the small dimensions required for these high frequencies with high accuracy and repeatability. On the other hand, the non-critical details were obtained by conventional micromachining. The first results are encouraging as we have demonstrated that we can pump the SIS junctions inserted in the block. Unfortunately, problems with the de-fluxing magnets did not permit the determination of the noise

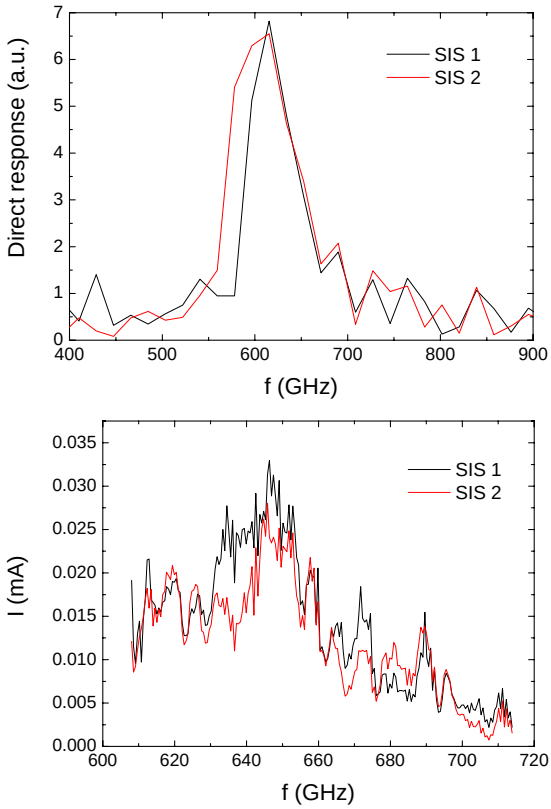

Fig. 4 RF response of the SIS junctions inside the mixer. *Top*: Direct response. *Bottom*: Pumping current on both junctions. The structure of this curve reflects the frequency dependence of the used LO source.

temperature. Once these problems are solved we will be able to characterize completely this innovatively fabricated mixer. Given the good reproducibility in the fabrication of the small RF components, we believe that this technique is promising for the construction of future heterodyne arrays.

ACKNOWLEDGMENTS

F.P. Mena would like to thank C. Pieters for his help in machining the copper block. We gratefully acknowledge funding from NOVA, the Netherlands Research School for Astronomy, and the FP6 program of the European Union.

REFERENCES

[1] F. P. Mena, J. W. Kooi, A. M. Baryshev, C. F. J. Lodewijk, R. Hesper, W. Wild, and T. M. Klapwijk, "Construction of a Side-Band-Separating Heterodyne Mixer for Band 9 of ALMA," in *Proc. 18th. ISSTT*, 2007, paper 2-1, pp. 39.

[2] V. Desmaris, D. Meledin, A. Pavolotsky, and V. Belitsky, "Sub-Millimeter and THz Micromachined All-Metal Waveguide Components and Circuits" – submitted to the *IEEE Micro. and Wir. Com. Lett*.

[3] A. Pavolotsky, D. Meledin, C. Risacher, M. Pantaleev, and V. Belitsky, "Micromachining approach in fabricating of THz waveguide components," *Microelectronics Journal*, vol. 36, pp. 683-6, 2005.

[4] V. Desmaris, D. Meledin, A. Pavolotsky, and V. Belitsky, "Microfabrication Technology for All-Metal Sub-mm and THzWaveguide Receiver Components," these Proceedings.

[5] C. F. J. Lodewijk, E. Van Zeijl, T. Zijlstra, D. N. Loudkov, T. M. Klapwijk, F. P. Mena and A. M. Baryshev, "Bandwidth of Nb/AlN/Nb SIS mixers suitable for frequencies around 700 GHz," these Proceedings.

100 GHz Sideband Separating Mixerwith Wide IF Band: First Results

D. Maier*, D. Billon-Pierron, J. Reverdy, and M. Schicke

IRAM, Institut de RadioAstronomie Millimétrique, St. Martin d'Hères, France

* Contact: maier@iram.fr, phone +33476824900

***Abstract*— A sideband separating SIS mixer with a 4–12 GHz IF band and covering the RF frequency range of 80 to 116 GHz has been developed. Two prototype mixers have been fabricated and characterized for noise and image rejection showing very good performances. They will be integrated into the next generation receivers of IRAM's Pico Veleta observatory.**

I. Introduction

A 100 GHz sideband separating mixer based on single-ended DSB mixers and waveguide couplers has been designed [1]. The signal frequency range extends from 80 to 116 GHz and the mixer covers an IF band of 4 to 12 GHz. A detailed description of the design can be found in [2].

II. 2SB Mixer Assembly

RF quadrature coupler, two –23 dB LO couplers, LO splitter as well as two DSB mixers have been combined into one unit and realized as an E-plane splitblock. A picture of such a block with mounted mixer chips is shown in Figure 1. The two IF outputs are connected through two SMA right angles to a commercially available IF 90° hybrid coupler [3].

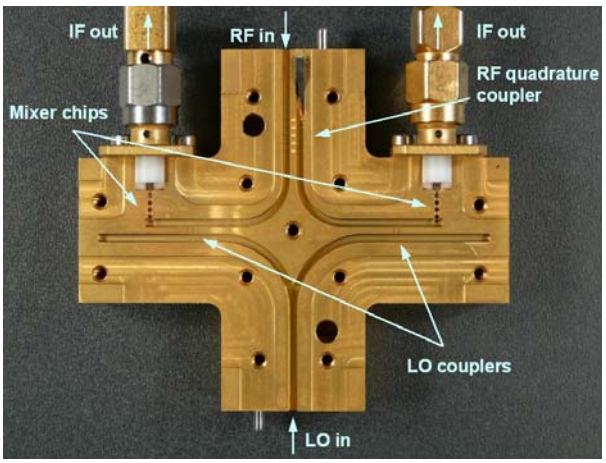

Figure 1: Photograph of the rf coupler/mixer block with mounted mixer chips.

A. Waveguide Couplers

The waveguide couplers have been realized as branchline couplers using 2 and 5 slots for LO and quadrature couplers, respectively (for details see [2]).

In order to decrease the LO noise contribution, the coupling of the LO couplers was designed to achieve –23 dB.

B. DSB Mixer

The design of the DSB mixers was described in detail in [2]. The baseline design employs a series of three junctions of which two are placed on an island structure (see Figure 2). Tuning is achieved with a parallel inductance. Since IRAM's standard fabrication process for SIS junctions includes anodization for better isolation [4], but the junctions on the isolated island cannot be anodized, a second design making use of the standard fabrication process was made.

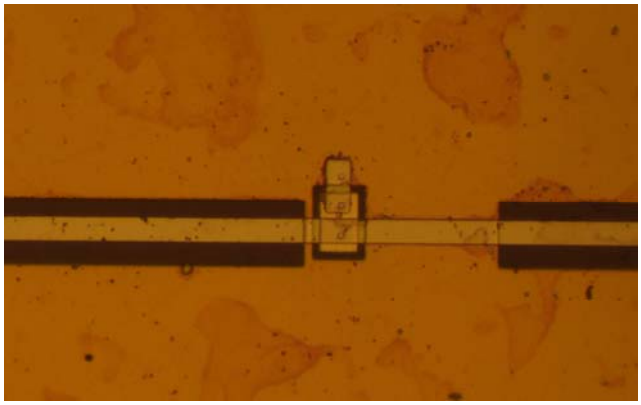

Figure 2: Photograph of the 3 junctions array.

Furthermore, in order to allow for uncertainties of the junction's capacitance and variations of processing parameters, three different variations of both designs have been included on the masks. The central design is called B, whereas A and C denote designs assuming lower and higher capacitances for the junctions, respectively.

Although in the final design the junctions are directly mounted into the integrated coupler/mixer block without prior testing, mixer blocks have been fabricated to be able to validate the mixer design by DSB mixer tests. Examples of such DSB noise measurements can be found in [2].

C. IF Coupler

IF couplers from different manufacturers have been tested both at room and liquid nitrogen temperature. Since these couplers are made for use at room temperature, their performances worsen at lower temperatures. The best results were obtained for the coupler from Pasternack [3]. They are shown in Figure 3. The worst case for the gain imbalance is 1.5 dB. Phase imbalance is always better than 3 degrees.

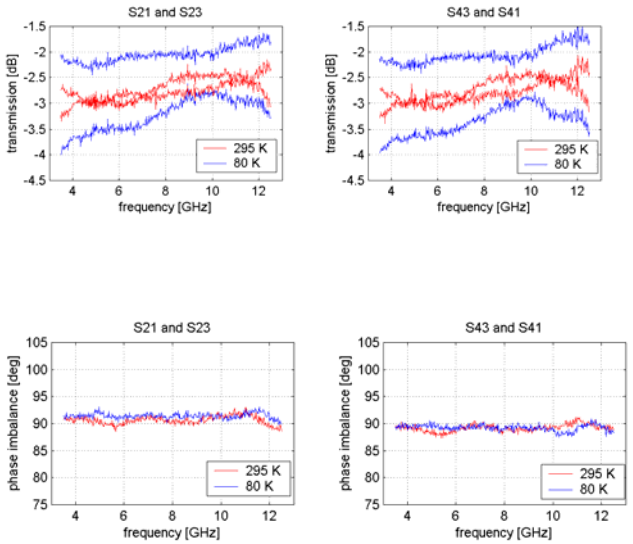

Figure 3: Characterization of the IF coupler for gain and phase imbalance both at room (blue) and liquid nitrogen (red) temperature.

III. 2SB Mixer Tests

So far junction fabrication is still an issue. The produced wafers showed inhomogeneous results and low yield. Nevertheless two pairs of similar mixer chips of the baseline design could be found for integration into a sideband noise

amplifiers used for these measurements were HEMT amplifiers from CAY with typically 6 K noise temperature [5].

A. Integrated noise measurements

Although mixer chips of different designs were chosen for the two 2SB mixers, their performances are quite comparable. The RF frequency range of the mixers is .

clearly recognisable and coincides well with the intended range of 80o 116 GHz. The obtained noise temperatures in this range lie between 28 and 41 K. For same signal frequencies lsb measurements resulted in better performance.

B. IF noise measurements

In order to evaluate the IF bandwidth of the mixers, noise temperatures have been measured in the 4 to 12 GHz IF band for LO frequencies between 88 and 108 GHz. These measurements are shown in Figure 5.

Again the results obtained for the two mixers do not differ very much. The IF response of both mixers is quite flat and lies except for a few points below 40 K.

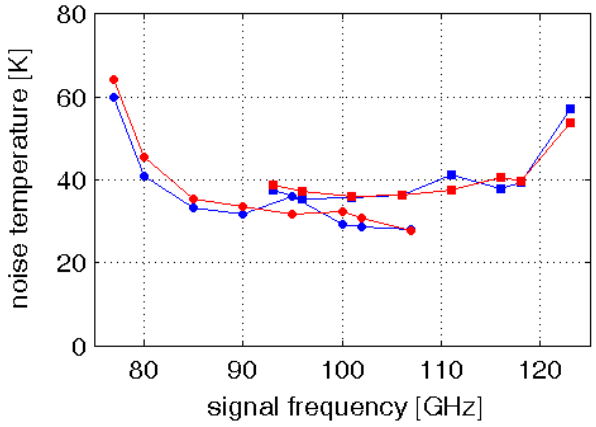

Figure 4: Integrated noise measurements obtained for an IF of 4 to 12 GHz. The results of mixer No. 1 are shown in blue. Those of mixer No. 2 are plotted in red. Upper sideband measurements are represented as squares; lower sideband results are plotted as circles.separating mixer. The first 2SB mixer was made with mixer chips of the central design, i.e. design B. Mixer No. 2 used mixer chips of design C, which was made assuming a higher capacitance of the junctions. Both mixers were completely characterized as sideband separating mixers

C. Image rejection measurements

The image rejection of the 2SB mixers has been measured using a Martin-Puplett interferometer. Again measurements were made in the 4 to 12 GHz IF band for different LO frequencies. The results are shown in Figure 6. Except for a few points the obtained values are better than –10 dB

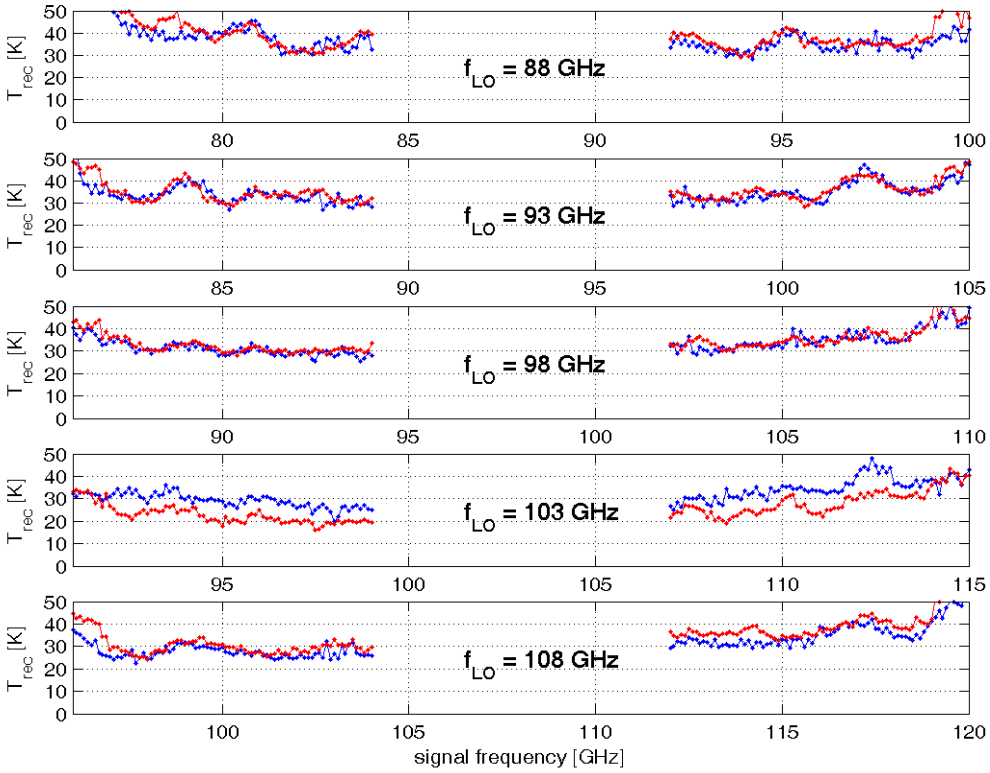

Figure 5: Noise measured in the IF band for different LO frequencies (Mixer No. 1: blue, Mixer No. 2: red).

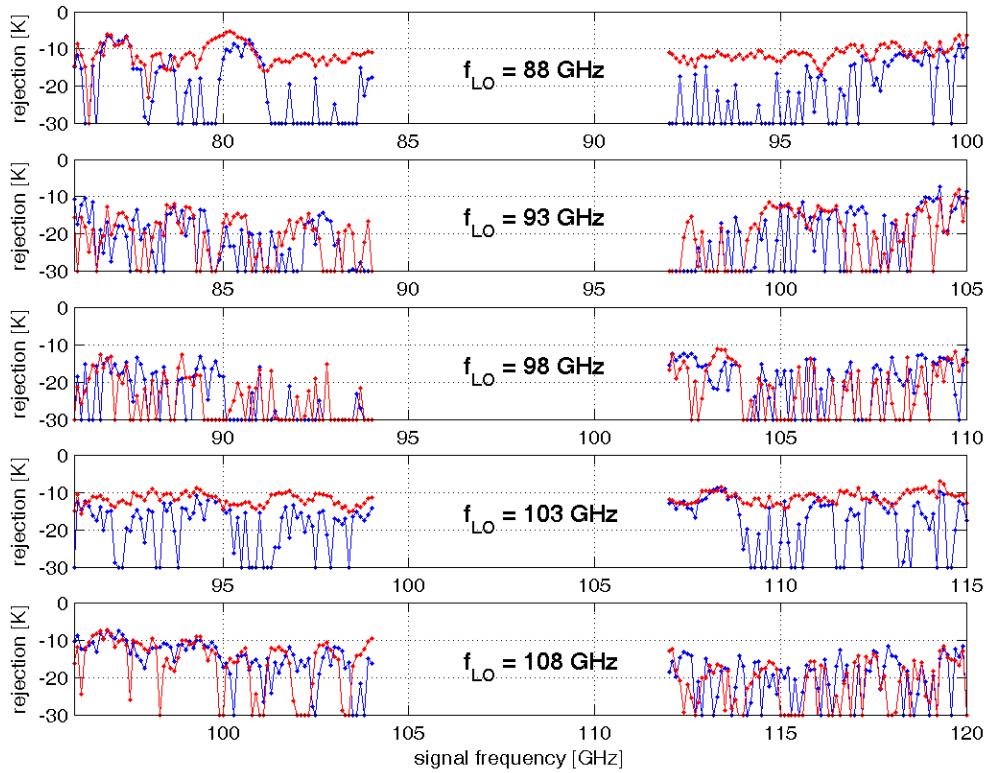

Figure 6: Image rejection measured for different LO frequencies (Mixer No. 1: blue, Mixer No. 2: red).

CONCLUSIONS

A sideband separating mixer for the RF frequency range of 80 to 116 GHz has been designed, fabricated, and tested obtaining good results. The requirements both for RF and IF frequency range could be met. The integrated noise temperatures measured for 4 to 12 GHz lie between 28 and 41 K and image rejection results are in general better than –10 dB.

Because of their good performances these two mixers will be integrated into the next generation receivers of IRAM's observatory at Pico Veleta in Spain.

ACKNOWLEDGMENT

This work has been supported by the European Union through the RadioNet program.

REFERENCES

[1] S.M.X. Claude, C.T. Cunningham, A.R. Kerr, and S.-K. Pan, "Design of a Sideband-Separating Balanced SIS Mixer Based on Waveguide Hybrids," ALMA Memo 316, 2000

[2] D. Maier, D. Billon-Pierron, J.Reverdy, and M. Schicke, "100 GHz sideband separating mixer with wide IF band," in *Proc. 18th International Symposium on Space Terahertz Technology, Pasadena, USA, 2007*, paper 10-2,pp. 260–263

[3] Model PE 2059, Pasternack Enterprises, Inc., USA

[4] I. Péron, P. Pasturel, and K.F. Schuster, "Fabrication of SIS junctions for space borne submillimeter wave mixers using negative resist e-beam lithography." *IEEE Trans. Applied Superconductivity*, Vol. 11, pp. 377–380, March 2001.

[5] J.D. Gallego Puyol, F. Colomer, I.L. Fernández, and A. Barcia, in 3rd RadioNet Annual Report

Herschel Mission Overview and Key Programmes

Göran L. Pilbratt

European Space Agency, ESTEC/SRE-SA, Keplerlaan 1, NL-2201 AZ Noordwijk, The Netherlands

* Contact: gpilbratt@rssd.esa.int, phone +31-71-565 3621

***Abstract* — This short paper provides an overview of the Herschel mission and the accepted Key Programmes, and importantly, provides references and links to more complete descriptions and to information on the internet which is constantly being updated as appropriate.**

I. Herschel overview

The Herschel Space Observatory is the next observatory mission [1] in the European Space Agency (ESA) science programme. It will perform imaging photometry and spectroscopy in the far infrared and submillimetre part of the spectrum, covering approximately the 55-672 micron range. Herschel will carry a 3.5 metre diameter passively cooled telescope. The science payload complement - two cameras/medium resolution spectrometers (PACS [2] and SPIRE [3]) and a very high resolution heterodyne spectrometer (HIFI [4]) - will be housed in a superfluid helium cryostat. The HIFI instrument is using superconducting SIS and HEB mixers, and both AOS and auto-correlator spectrometers. The ground segment will be jointly developed by the ESA, the three instrument teams, and NASA/IPAC.

II. Science operations

Once operational in orbit around L2 after a launch in early 2009 and followed by an early operations period of 6 months, Herschel will offer a minimum of 3 years of routine science observations. The key science objectives emphasize current questions connected to the formation and evolution of galaxies, stars and stellar systems, including our own planetary system. Nominally ~20,000 hours will be available for astronomy, 32% is guaranteed time and the remainder is open to the general astronomical community through a standard competitive proposal procedure. The Key Programme (KP) AO process was concluded in early 2008. In total 42 programmes have been awarded observing time.

III. More information

The Herschel Science Centre (HSC) maintains a website [5] aimed at the Herschel user community. Refs [1]-[4], descriptions of the KP programmes, observers' manuals, tools, latest news, helpdesk, and links to additional Herschel-related websites are provided. Welcome!

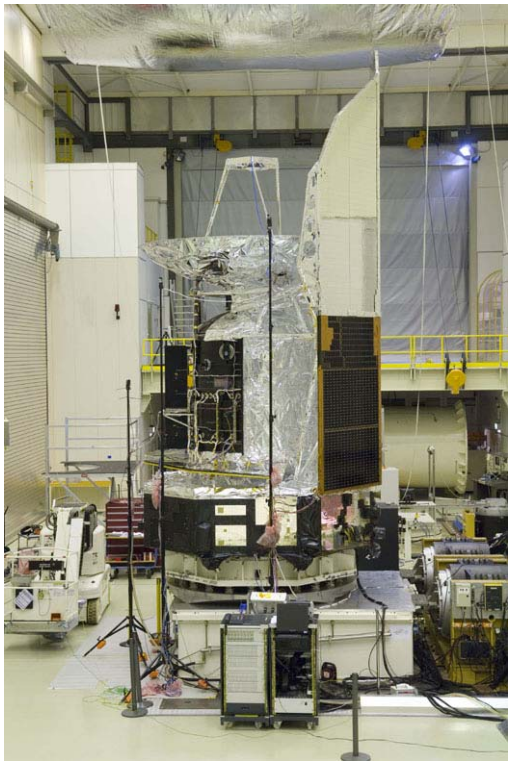

Fig. 1 Herschel on the shaker in the ESTEC Test Centre on 26 June 2008.

Acknowledgment

Herschel would not exist without the combined effort of a large number of people in ESA, industry, and academia.

References

[1] G.L. Pilbratt, *Herschel Mission Overview and Key Programmes*, Proc. SPIE 7010, 2008, in press.

[2] A. Poglitsch et al., The Photodetector Array Camera and Spectrometer (PACS) for the Herschel Space Observatory, Proc. SPIE 7010, 2008, in press.

[3] M.J. Griffin et al., Herschel-SPIRE: Design, Ground Tests, and Predicted Performance, Proc. SPIE 7010, 2008, in press.

[4] M.W.M. de Graauw et al., The Herschel-Heterodyne Instrument for the Far-Infrared (HIFI): Instrument and Pre-launch Testing, Proc. SPIE 7010, 2008, in press.

[5] Herschel Science Centre (HSC) website: http:/herschel.esac.esa.int/

Performance of the HIFI Flight Mixers

Gert de Lange[1*], Jean-Michel Krieg[2], Netty Honingh[3], Alexandre Karpov[4], and Sergey Cherednichenko[5]

[1]*SRON Netherlands Institute for Space Research, Groningen, the Netherlands*

[2] *Observatoire de Paris, LERMA, Paris, France*

[3]*Universität zu Köln, Physikalisches Institut, KOSMA, Köln, Germany*

[4]*California Institute of Technology, Pasadena, CA 91125, USA*

[5]*Chalmers University of Technology, Göteborg, SE-41296, Sweden*

* Contact: gert@sron.nl, phone +31-50-363 4074

***Abstract*— We summarize the technology and final results of the superconducting heterodyne SIS and HEB mixers that are developed for the HIFI instrument. Within HIFI 7 frequency bands cover the frequency range from 480 GHz to 1910 GHz. We describe the different device technologies and optical coupling schemes that are used to cover the frequency bands. The efforts of the different mixer teams that participate in HIFI have contributed to an instrument that will have unprecedented sensitivity and frequency coverage.**

I. Introduction

After several years of development and qualification the HIFI instrument for the Herschel Space Observatory (HSO) is now in the final stage of verification. The launch of HSO together with Planck is scheduled for early 2009. The instrument has been cooled down to operating temperatures and will have no further thermal cycling. The current performance of the instrument can therefore be considered final. Once in orbit Herschel will provide a unique window to the sub-millimeter and THz frequency range. This frequency range is largely obscured for ground based astronomy due to the presence of water vapor in the earth's atmosphere. Herschel/HIFI will therefore make it possible to do detailed spectroscopic studies of water lines in the star forming regions of our galaxy. The Herschel Space Observatory will fly two cameras/medium resolution spectrometers (PACS and SPIRE) and the heterodyne instrument HIFI ([1]-[6]). An international consortium led by the PI institute, SRON, is building HIFI. Within HIFI, 7 frequency bands cover the spectral range from 480-1250 GHz (SIS mixers) and 1.41-1.91 THz (HEB mixers). In this paper we first present the general HIFI configuration and the specifications of the mixers. The subsequent sections describe the mixer design for each HIFI band. We then give a brief description of the sensitivity measurements of the mixers within the HIFI instrument.

II. General specifications and mixer technology.

A. HIFI configuration

Each of the mixer bands within HIFI contains two mixers to measure both signal polarizations simultaneously. The mixer units are mounted on a 2 K platform in a mixer console that thermally isolates the mixer units from the Focal Plane Unit (10 K ambient temperature). Within the Focal Plane Unit, each of the SIS mixer units is connected to a 4-8 GHz IF chain consisting of two isolators (one at 2K and one at 10 K) a low noise first stage IF amplifier close to the mixer unit, and a common second stage IF box. The HEB mixers have an IF chain of 2.4-4.8GHz and no isolators. The second stage IF box provides further amplification, signal equalization, and finally power combining of the 10 separate SIS mixer and 4 HEB mixer IF channels into four coax lines that run between the cold and warm (outside the dewar) IF back-end. In the back-end a Wide Band Spectrometer and a High Resolution Spectrometer are available for IF spectral analysis. During observations, the instrument will run in an autonomous mode. Optimal settings of the mixer units (bias voltage, magnet current, LO power) therefore have to be available from look-up tables or simple optimization routines.

B. Mixer technology and specifications

Within the HIFI consortium 6 groups have contributed to the delivery of the 7 mixer bands. The institutes are listed in Table 1. Within the 460-1910 GHz frequency range different technologies had to be employed to achieve the most sensitive mixers. For frequencies up to 1250 GHz SIS mixers are used, for the two highest frequency bands phonon-cooled HEB mixers are used (Ph-HEB). SIS mixers have a better noise performance and higher IF bandwidth than HEB mixers, but the maximum operating frequency of SIS mixers is currently limited to about 1.5 THz. Furthermore the HEB mixers need much less Local Oscillator power. This was of crucial importance to obtain sufficient LO power at the highest frequency bands. A drawback of the HEB mixers is the limited IF bandwidth. At the start of the project there were indications that diffusion cooled HEB mixers could achieve the 4-8GHz IF bandwidth, but this technology turned out not to be mature enough to be used within HIFI.

Within the SIS bands also different technologies have been used to achieve the optimum performance. Main driver for this is the superconducting gap frequency of the materials used. Below the gap-frequency (which is about 700 GHz for

niobium) a superconductor acts as a perfect lossless material. Above the gap-frequency a superconducting electrode may act as a poor conductor with high losses. Furthermore at frequencies above twice the gap-frequency the SIS junctions do not operate as mixers anymore. Because of this, the SIS bands have used a variety of electrode materials and junction topology. A summary of the technology is given in Table 1. One further main variety within the HIFI bands is the optical coupling scheme. Up to band 5 waveguides and corrugated horns are used for the coupling of signal and LO, bands 5 and 6 use a quasioptical coupling with a Si lens and a twin slot antenna. In the integration of the mixers it was found that the optical alignment of the waveguide mixers could almost fully rely on the mechanical alignment references of the mixer units. The quasi-optical mixers needed more attention and some iteration of beam measurements and mechanical alignment adjustments. Also it is found that the beam profile of the QO mixers can be modelled very well, but that the manufacturing tolerances on the lens shape become very critical (at μm level).

TABLE I
OVERVIEW OF HIFI MIXER TECHNOGY

Band Institute	Freq. Range (GHz)	RF-coupling	Detector technology	Device technology:
1 LERMA	480 640	Waveguide/ Horn	SIS	Nb/AlOx/Nb Nb/Nb
2 KOSMA	640 800	Waveguide/ Horn	SIS	Nb/AlOx/Nb NbTiN/Nb
3 SRON	800 960	Waveguide/ Horn	SIS	Nb/AlOx/Nb NbTiN/Al
4 SRON	960 1120	Waveguide/ Horn	SIS	Nb/AlOx/Nb NbTiN/Al
5 CALTECH JPL	1120 1250	Lens/ Planar Antenna	SIS	Nb/AlN/NbTiN e-Nb/Au
6L CTH JPL	1410 1660	Lens/ Planar Antenna	HEB	NbN
6H CTH JPL	1660 1910	Lens/ Planar Antenna	HEB	NbN

Besides the sensitivity of the mixers, the ability of the mixers to withstand the on-ground test-phase, the launch (vibration levels!) and the operation in space are of crucial importance. Much time was spent to develop space-qualified manufacturing and assembly procedures. For example, the mixers are specified to have an internal bias and ESD protection circuit, and to fulfill strict alignment tolerances of the optical beam w.r.t. mechanical references. These requirements are necessary to assure a safe and reproducible integration of the mixer units into the HIFI Focal Plane Unit. The main operational specifications of the mixers are:

- Withstand shelf life, bake-out, launch and in-orbit operation (9 years)
- Mass < 75 grams
- Envelope 32x32x45 mm
- IF range SIS mixers: 4-8 GHz, ripple < 2dB/1 GHz
- IF range HEB mixers: 2.4-4.8 GHz, ripple < 2dB/1 GHz
- De-flux heater operating at current < 20 mA (SIS only)
- Magnet current < 10 mA for second minimum in the Fraunhofer pattern (SIS only)
- Beam quality
- Optical alignment tolerances (goal): x,y: 42 μm, tilt 0.2°
- ESD protection, EMC shielding
- Bias circuit isolation > 30 dB in IF range

The mixer groups have developed different approaches to fulfill these specifications. A common design is used as much as possible (e.g. corrugated horns, bias board manufacturing), but simple scaling of one common design is not possible. This is partly due to the in-house technological expertise of the mixer groups at the start of the project and partly to the mechanical specifications. For example, the band 1 horn is twice as long as the band 4 horn, but they have to fit within the same mixer envelope. This requires a different design of the magnet, which in turn requires a different design of the IF circuit board etc. All the different technologies that are used in the end have proven to be space-qualified.

III. BAND 1

The band 1 mixers are developed by LERMA, in collaboration with IRAM [7]. The band 1 frequency range is 480-640 GHz. The device technology is based on Nb/AlOx/Nb SIS junctions (Jc=10 kA/cm^2, area= 1 μm^2), with Nb electrodes. The on-chip tuning circuit is a twin junction design with an impedance transformer. Band 1 has the largest relative bandwidth of the HIFI mixers (30 %, vs. 10 % for band 5). To achieve this bandwidth the band 1 team has developed a new waveguide coupling structure that does not need a backshort cavity (see Fig. 1). This greatly facilitates the manufacturing and assembly of the mixer block, since there is no critical alignment between horn waveguide and backshort necessary.

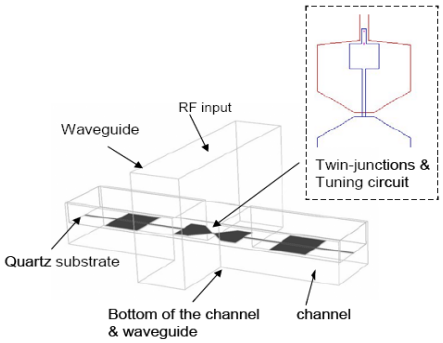

Figure 1 Band 1 mixer configuration with no backshort waveguide. The inset shows the SIS tuning circuit

Band 1 also used novel technologies for the IF output coupling (with a spring loaded bellow) and circuit board mounting (with metallized kapton).
Figures 2 and 3 show some details of the mechanical design.
The final results of the sensitivity of one of the FM units as measured by LERMA are shown in Fig. 4. The sensitivity is excellent and well below the original specified baseline values.

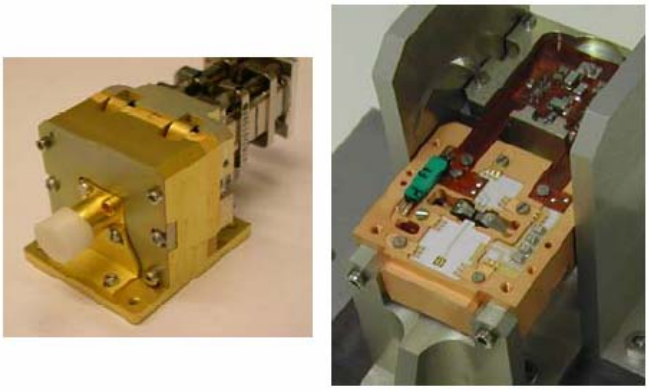

Figure 2 Band 1 mixer block's outside and inside view

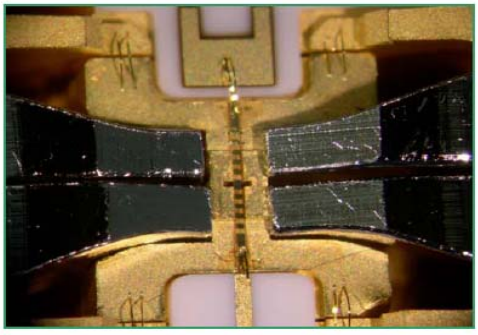

Figure 3 Detailed view of the band 1 waveguide and magnet section

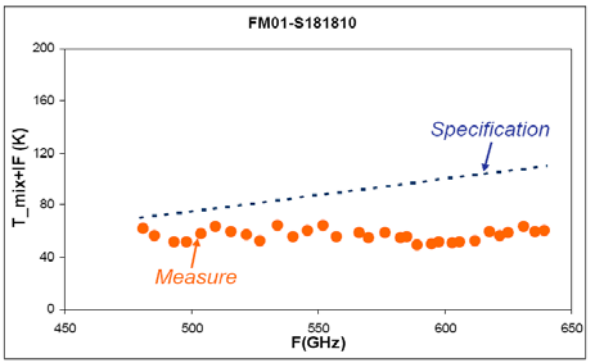

Figure 4 Noise temperature of a band 1 FM mixer unit, corrected for optics losses

IV. Band 2

The band 2 mixers are developed by the KOSMA team [8]. The band 2 frequency range is 640-800 GHz. The superconducting gap frequency of Nb is within this frequency range and the band 2 team had to explore several electrode materials to optimize the overall performance. The final configuration is shown in Figs. 5 and 6. The design incorporates a Nb/AlOx/Nb SIS junction (Jc=15 kA/cm^2, 0.9 μm^2) with a NbTiN ground plane and a Nb top-electrode. The tuning structure is based on a single junction with a three step impedance transformer. The mechanical design of the mixer unit is shown in Fig. 7. The unit consists of several modules for the RF, IF and DC signals. These modules can be tested and optimized separately and integrated in a later stage. The horn-waveguide module is based on a design that was successfully operated at several ground based telescopes. Results of the sensitivity of the Flight Model and Flight Spare mixer units are shown in Fig. 8.

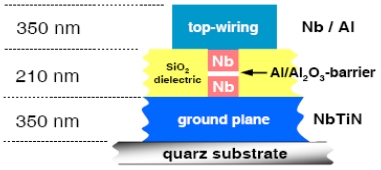

Figure 5 Device topology of the band 2 SIS mixer. The top wiring for the FM units is Nb.

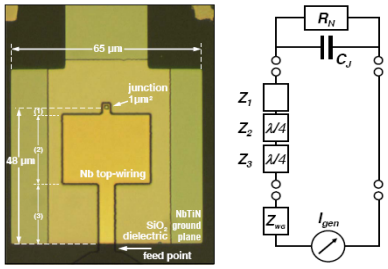

Figure 6 Left: photograph of the Band 2 junction device with the three step transformer. Right: Equivalent circuit of a three step transformer

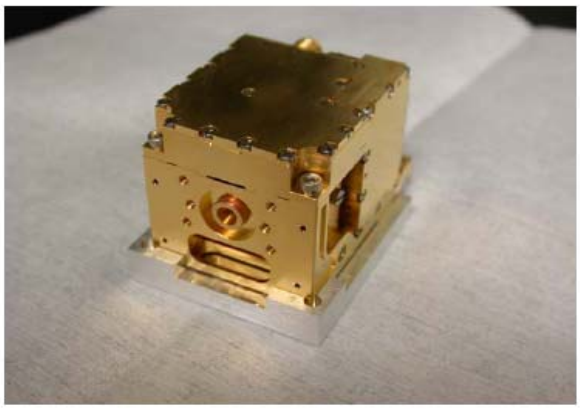

Figure 7 Band 2 mixer block

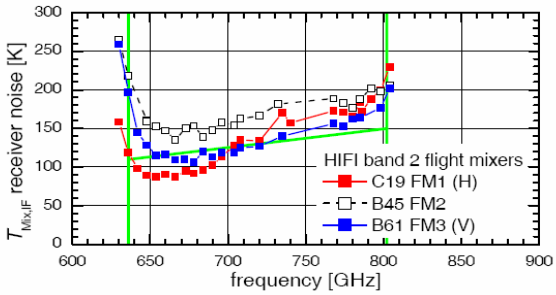

Figure 8 Noise temperature of the band 2 FM and FS mixer units (corrected for optical losses)

V. Band 3 and 4

Both the band 3 and 4 mixers are developed by the SRON team, in collaboration with the Kavli Institute of Nanoscience Delft, and with a contribution of JPL (band 4 NbTiN layers) [9,10]. The band 3 and 4 frequency ranges are 800-960 GHz and 960-1120 GHz, respectively. Several options for device and electrode materials have been considered and tested. Ideally one would use an SIS device with a cut-off frequency higher than the Nb-based junctions, in combination with high gap electrode materials. In practice this turned out to be a major development task in which undesired side effects were observed, like heat trapping and magnetic flux trapping instabilities. The final device and electrode configuration consists of an Nb/AlOx/Nb twin junction design (Jc=5-10 kA/cm^2, area 0.6-1 μm^2), with an NbTiN ground plane and an Al top electrode (see Fig. 9). The highest operating frequency really pushes the Nb-based junctions to the limit. Fig. 10 shows that only a limited, but still sufficient, bias range is available for operation at these high frequencies.

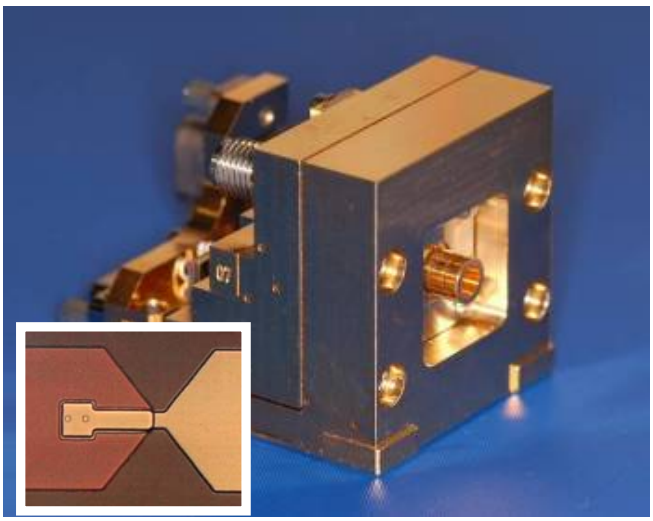

Figure 9 Band 3/4 mixer block. The inset shows the twin junction geometry with the tuning structure.

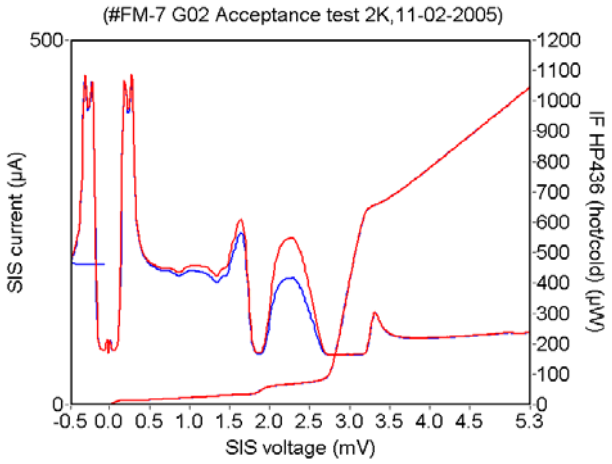

Figure 70 Pumped I-V curve and the IF output power with hot and cold input, measured at 1150 GHz. Notice the limited bias range around 2.3 mV.

Some details of the mechanical design of the band 3 and 4 mixers are shown in Figs. 9, 11, and 12. To be independent of machining tolerances, the unit incorporates an in-situ alignment of the horn with the backpiece. To facilitate a clean and reproducible device mounting, the device substrate is suspended in the substrate channel and mounted with silver epoxy on an alumina ring structure. In this way no glue has to be applied in the delicate substrate channel.

Results of the Band 3 and 4 FM units as measured by the SRON team are shown in Fig. 13. These results are corrected for the optical losses of the beam splitter and the dewar window. The results are very good. It can be seen though that with the used device technology it is difficult to fabricate mixer units with exactly the same performance, even if the device geometry on the photolitographical mask is equal. This is due to the slight variations that occur during the device fabrication process (with optical lithography) and the unavoidable tight tolerances of the tuning structure at these high frequencies.

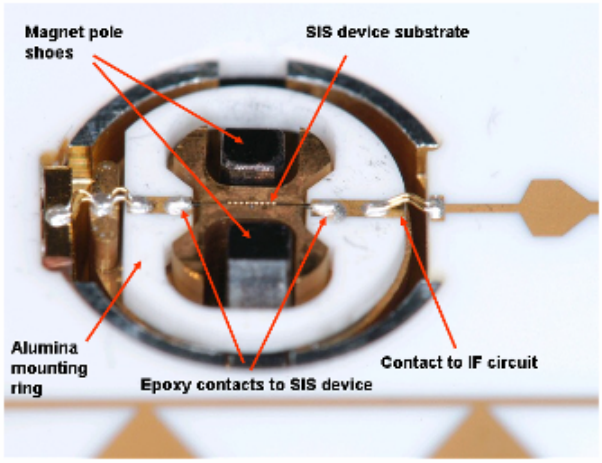

Figure 81 Details of the waveguide and substrate channel of the band 3 and 4 mixers. The SIS device substrate is mounted with two silver epoxy contacts.

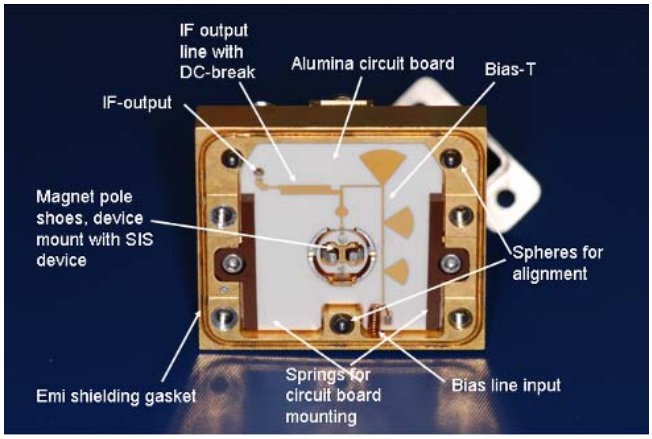

Figure 92 Inside view of the band 3/4 mixer unit. The IF board holds the bias-T and the planar DC-break.

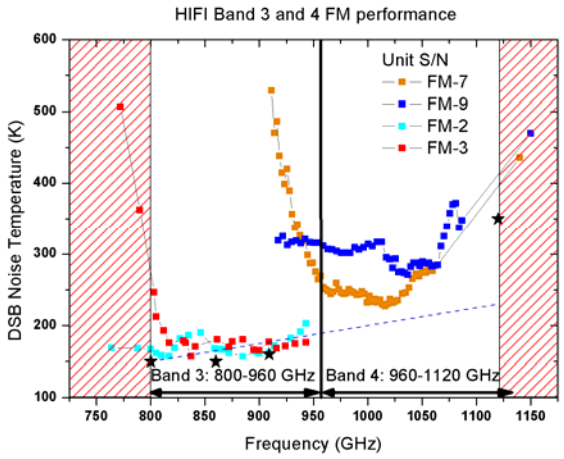

Figure 103 Noise temperature of the band 3 and 4 FM mixer units. The upper part of band 4 could only be measured at selected frequencies, due to a lack of LO power.

VI. BAND 5

The Band 5 mixer units are developed by the Caltech/JPL team [11]. The band 5 frequency range is 1120-1250 GHz. The SIS devices for band 5 are high current density Nb/AlN/NbTiN junctions (30 kA/cm^2) with a gap voltage of 3.5 mV (compared to 2.8 mV for all Nb SIS devices). The area of the devices is 0.25 μm^2. The advantage of these devices is the high RF bandwidth (because of the high current density) and the lower mixer conversion loss (compared to Nb devices) at the band 5 frequency range.

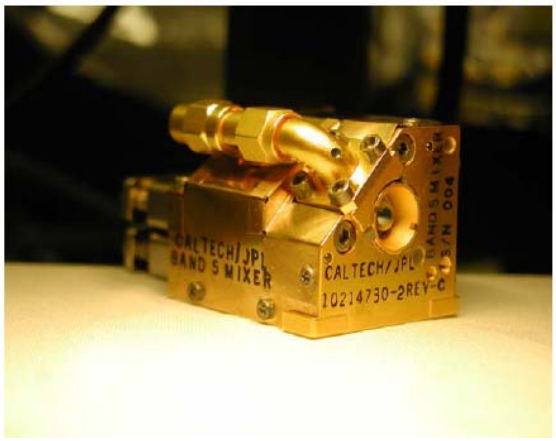

Figure 14 Band 5 mixer block

The electrode material is epitaxial Nb for the ground plane and Au for the top electrode. The quasi-optical RF coupling is established via a hyper-hemispherical Silicon lens (coated with an anti-reflection layer) and a twin slot antenna (Fig. 14). The RF tuning structure consists of a twin junction design with a virtual ground. To facilitate the suppression of unwanted Josephson effects the junctions (which are defined with e-beam lithography) have a diamond shape.

Results of a calibration measurement of band 5 are shown in Fig.15. Compared to Fig. 9 we can clearly see the advantage of the higher gap voltage. The very effective suppression of the DC -Josephson effect is shown in Fig 16. Results of the mixer sensitivity as measured by the Caltech team are shown in Fig. 17.

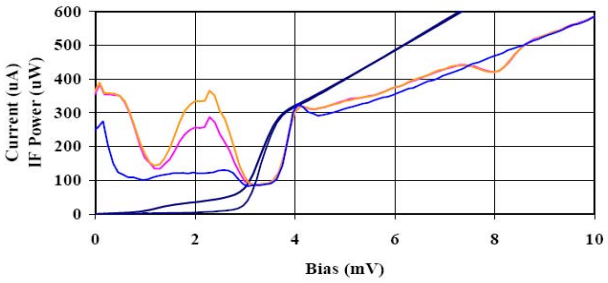

Figure 15 Pumped and unpumped I-V curve and the IF-output with hot and cold input loads at 1130 GHz.

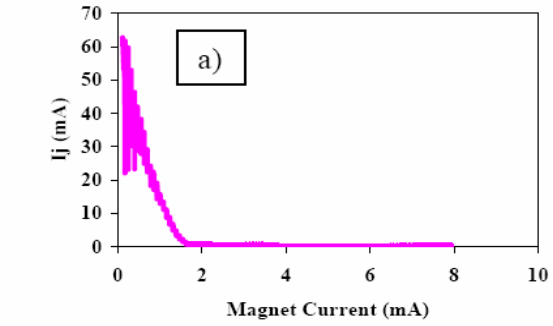

Figure 16 Zero voltage Josephson current vs the magnet current.

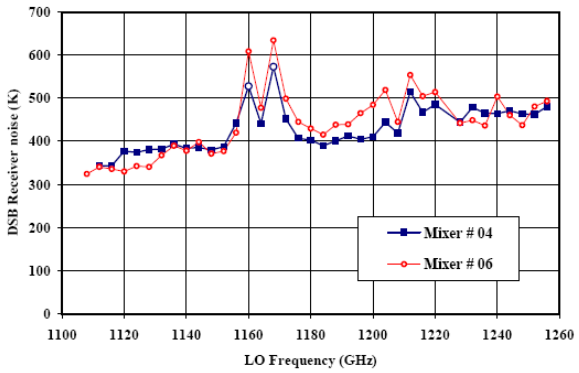

Figure 17 Measured DSB noise temperatures of the band 5 FM mixers.

VII. Band 6L and 6H

The band 6L (Low) and band 6H (High) mixers are developed by the Chalmers group, together with JPL and the Moscow State Pedagogical University [12]. The frequency ranges for band 6L and 6H are 1410-1660 GHz and 1660-1910 GHz, respectively. The device technology for the band 6 mixers is a phonon-cooled NbN Hot Electron Bolometer (HEB). The HEB is placed in the center of a double slot antenna on a silicon chip. The HEB chip is glued on the backside of a silicon elliptical lens (Figs. 18 and 19). The HEB is made out of a 2x0.1 μm^2 NbN film with a thickness of 3-5 nm. The bolometer size is a compromise between availability of LO power on the one hand, and sensitivity and stability on the other hand. The Chalmers group together with the HIFI consortium have spent great effort in optimizing the HEB mixers for space operation. A late-stage redesign of the IF matching circuit was necessary to reduce the IF-ripple that was initially observed, and several iterations on beam measurements and optical adjustments have been performed to fulfil the optical alignment specifications. Also the application of an anti-ageing layer of 200 nm Si has been of crucial importance to protect the ultra-thin HEB devices. Some typical results of the noise temperature and broadband Fourier Transform Spectrometer measurements are shown in Fig. 20. It should be noted that due to the limited availability of LO-sources for these high frequencies, the characterisation of the mixers at Chalmers only could be performed at selected frequencies available from a FIR laser. Only within the HIFI instrument the full noise temperature characterisation could be performed. As shown in Fig. 21 the noise temperature has a slope within the 2.4-4.8 GHz IF band, due to the intrinsic phonon cooling times of the NbN HEB. Averaged across the IF band the DSB mixer noise temperatures of the band 6L and 6H mixers were 1100 K and 1450 K, respectively.

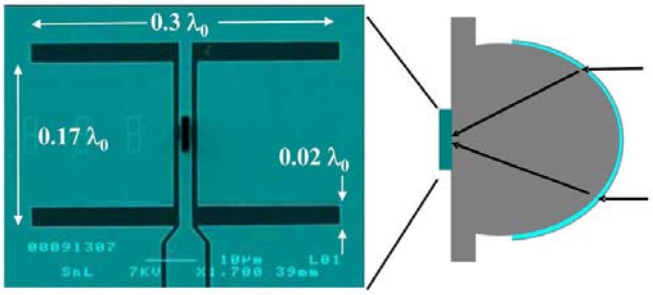

Figure 18 Left: SEM image of a double slot antenna with a HEB at the center. Right: The HEB is glued to the back of an elliptical silicon lens, covered with an anti-reflection coating.

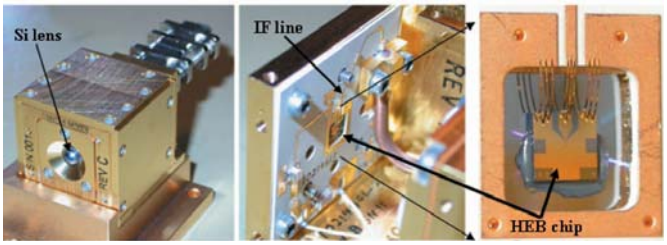

Figure 19 Left: band 6L/6H mixer unit. Middle: inside view of the mixer unit. Right: Detailed view of the HEB chip.

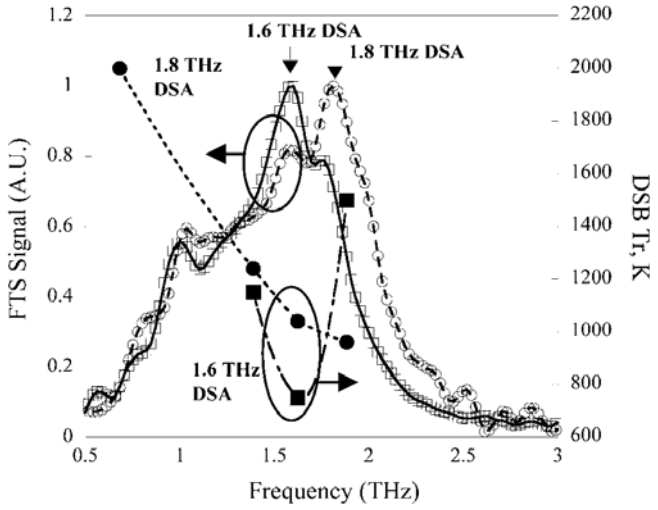

Figure 110 FTS response of 1.6 THz (band 6L) and 1.9 THz (Band 6H) mixers and the DSB mixer noise temperatures for these mixers.

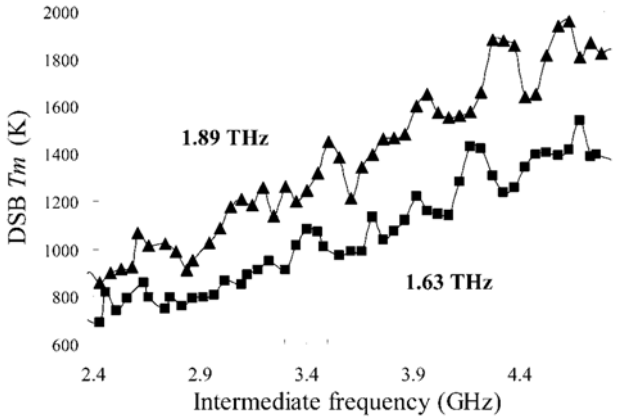

Figure 121 DSB mixer noise temperature as a function of IF frequency for the Band 6L (at 1.63 THz) and 6H (at 1.89 THz) mixer units.

VIII. Mixer Performance within HIFI

After delivery of the mixer units these were tested first at a next higher step of integration (in subunits called the Mixer Sub Assembly) and finally in the Focal Plane Unit (FPU) of HIFI. See [13]-[15] for further details on the FPU measurements. Only within the FPU the real HIFI performance can be measured. The measurements in the laboratory set-up of the mixer groups had to be corrected for losses in the optical elements that are not present within HIFI. Also assumptions had to be made on the noise contributions of the IF chain. Other characteristics that are of influence on the noise temperature calibration within HIFI are:

- The temperature of the calibration loads. Within HIFI the calibration is performed with an internal hot-cold load at temperatures of 10 K and 100 K, compared to the 80K and 300K loads that are common in a laboratory set-up. Especially for the HEB mixers this could give different calibration results, because of potential thermal effects of the hot and cold loads on the mixer bias settings (see Ref [15].)
- The LO in bands 1, 2, and 5 is coupled via a polarizing grid beam splitter, with coupling factors of 1%, 3%, and 10 %, respectively. Especially in bands 1 and 2 it was found that the balance in LO-coupling to the mixers with the orthogonal polarisations is very sensitive to fine adjustment of the polarizing grid angles. Also the LO coupling becomes very sensitive to cross-polarisation effects. The measurements with the grid beam splitter also reveiled a polarisation mismatch of the band 5 mixer. A polarisation correction had to be inserted in the optical path and this causes the noise temperature of the band 5 mixer to be higher than measured in the laboratory.
- The LO in bands 3, 4, 6L, and 6H is coupled via a Martin-Pupplet diplexer. The Martin-Pupplet diplexer will cause a parabolic noise temperature dependence within the IF band, with a 25 % increase in noise temperature at the band edges. This makes a direct comparison of the mixer laboratory measurements not straightforward. Furthermore it is found that the intricate coupling between the diplexers for both polarisations is causing some standing wave effects at the band edges. The noise temperatures for HIFI presented here are average noise temperatures over the full IF band.
- For mixer bands 4 and 6 the FPU noise temperature measurements with the HIFI Local Oscillator unit were actually the first measurements with full coverage of the RF band, due to a lack of laboratory LO sources for these frequencies.
- At some LO frequencies the output power of the LO multiplier chains is not sufficient to optimally pump the mixers. Also at some frequencies spurious signals or instabilities were observed that influenced the system noise performance [14]. Analysis shows that most of these LO frequencies can be excluded from the final observation program, without having an effect on the HIFI frequency coverage (e.g. by observing a spectral line in USB instead of LSB)

A detailed description of these effects is beyond the scope of this paper. Elsewhere in these proceedings measurements on the optical properties of HIFI (e.g. the co-alignment of the two mixers), the stability, and the Side Band Ratio (SBR) are described [13]. In Ref [13] also more details are given on the achievable system noise temperature when both polarisations are combined.

In Figure 13 we show results of the noise temperature measurements with the HIFI FPU, together with the noise temperatures as measured by the mixer groups (corrected for noise contributions of the input optics). In this figure the noise temperature in the HIFI configuration is averaged over the IF bandwidth and we display the optimum noise temperature from either the horizontal or vertical polarisation. Minimum noise temperatures within the IF band for bands 3, 4, 6L, and 6H, will even be lower than shown, because of the diplexer effect and the IF roll-off effect in band 6. The HIFI LO scan was performed with a 1 GHz grid, and rapid fluctuations in noise temperature due to LO effects at specific frequencies were removed in the plot, by taking the lowest noise temperature within a 4 GHz bin. Any remaining rapid fluctuation in noise temperature (e.g. at 640 GHz) are still caused by the behaviour of the LO. We see that the performance within HIFI is in good overall agreement with the measurements performed by the mixer groups. Some deviations are observed which are due to details of the LO coupling in HIFI (or correction of the optical losses) and the

polarisation correction in band 5. The flat response of the HEB mixers in band 6L and 6H is remarkeable. The figure also shows lines indicating the status of mixer performance in 1998 (at the start of the project) and the baseline sensitivities as defined in the original HIFI proposal. The progress in sensitivity has been enormous, especially by taking into account that the status of 1998 was achieved with many narrowband mixers at some selected frequencies. The performance of the HIFI instrument is excellent and has an unprecedented sensitivity over the frequencies covered. All bands deliver state of the art performance. This performance, combined with the absence of atmospheric attenuation, will result in system noise temperatures that will never be achieved at any ground based observatory.

SUMMARY

In summary we have described the technology and performance of the mixer units that are used in the Flight Model of the HIFI instrument. An overview of the sensitivity of the mixer units as measured within the HIFI instrument is given. The overall performance is excellent and HIFI is ready to become a mission with unprecedented observing capabilities in the submillimeter frequency range.

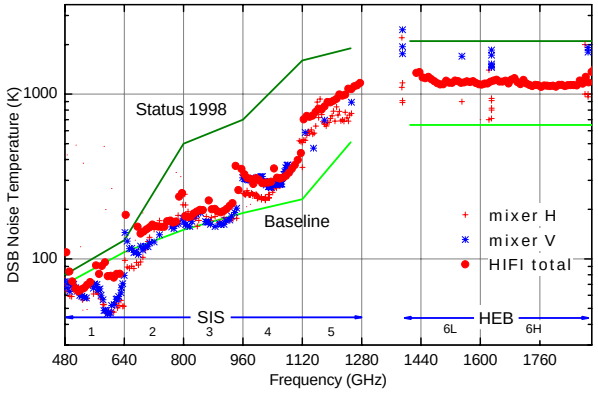

Figure 13 Noise temperature of the HIFI instrument (filled bullets) together with the results as measured by the mixer groups (for the horizontal and vertical polarisation mixers). Also shown are the sensitivity status in 1998 and the baseline performance as specified in the HIFI proposal.

REFERENCES

[1] T. de Graauw, "The Herschel Heterodyne Instrument for the Far-Infrared (HIFI)", Proc. SPIE 6265, 62651Z, 2006.

[2] G.T. Pilbratt, "Herschel space observatory mission overview", *IR Space Telescopes and Instruments*, J.C. Mather, Ed. SPIE 4850 (2003), pp. 586–597.

[3] T. de Graauw, F. P. Helmich, "Herschel-HIFI: The Heterodyne Instrument for the Far-Infrared", in *The Promise of the Herschel Space Observatory*, edited by G. L. Pilbratt et al., ESA SP-460, pp. 45-51, 2001.

[4] B. D. Jackson, K. J. Wildeman, N. D. Whyborn on behalf of the HIFI Focal Plane Consortium, "The HIFI Focal Plane Unit", *Proc. 13th International Symposium on Space Terahertz Technology*, pp. 339-348, 26-28 March 2002, Harvard University, Cambridge, Massachusetts, USA.

[5] Web site at : http://www.rssd.esa.int/Herschel/

[6] Web site at: http://www.sron.nl/divisions/lea/hifi/

[7] Delorme Y.; Salez M.; Lecomte B.; Péron I.; Dauplay F.; Féret A.; Spatazza J.; Krieg J.M.; Schuster K. Space-qualified SIS mixers for Herschel Space Observatory's HIFI band 1 Instrument 16th Int.Symp.on Space THzTechnology; Göteborg; Sweden; May 2-4 2005

[8] Results and Analysis of HIFI Band 2 Flight Mixer Performance R. Teipen, M. Justen, T.Tils, S. Glenz, P. Pütz, K. Jacobs, C.E. Honingh Proc. of the 16th Intern. Symposium on Space Terahertz Technology, Göteborg, 2005

[9] Brian D. Jackson, Gert de Lange, Tony Zijlstra, Matthias Kroug, Jacob W. Kooi, Jeffrey A. Stern, Teun M. Klapwijk, "Low-noise 0.8-0.96- and 0.96-1.12-THz Superconductor-Insulator-Superconductor Mixers for the Herschel Space Observatory", IEEE transactions on microwave theory and techniques, vol 54, no 2 (2006)

[10] de Lange, G., Jackson, B. D., Jochemsen, M., Laauwen, W. M., de Jong, L., Kroug, M., Zijlstra, T., Klapwijk, T. M., "Performance of the flight model HIFI band 3 and 4 mixer units", Millimeter and Submillimeter Proceedings of the SPIE, Volume 6275, pp. (2006).

[11] A. Karpov, D. Miller, F. Rice, J. A. Stern, B. Bumble, H. G. LeDuc, J. Zmuidzinas, "Low noise 1 THz – 1.4 THz mixers using Nb/Al-AlN/NbTiN SIS junctions", IEEE Transactions on Applied Superconductivity, Volume 17, Issue 2, Part 1, June 2007, pp. 343 – 346, (2007)

[12] J S.Cherednichenko, V.Drakinskiy, T. Berg, P. Khosropanah, and E. Kollberg "Hot-electron bolometer terahertz mixers for the Herschel Space Observatory", Rev. Sci. Instrum. **79**, 034501 (2008).

[13] D. Teyssier et al., "HIFI Pre-Launch Calibration Results", these proceedings.

[14] J.W. Kooi et al., "HIFI Instrument Stability as measured during the ILT phase: Results and operational impacts", these proceedings.

[15] P. Dieleman et al., "HIFI Flight Model Testing at Instrument and Satellite Leve", these proceedings

HIFI Flight Model Testing at Instrument and Satellite Level

P. Dieleman[1,*], W. Luinge[1], N.D. Whyborn[2], D. Teyssier[3], J.W. Kooi[4], W.M. Laauwen[1], and M.W.M de Graauw[2]

[1]*SRON Netherlands Institute for Space Research, Groningen, the Netherlands*

[2]*Atacama Large Millimeter/sub millimeter Array, Las Condes, Chile.*

[3]*European Space Astronomy Centre, 28691 Villanueva de la Cañada, Madrid. Spain*

[4]*California Institue of Technology, MS 320-47 Pasadena, California 91125, USA*

* Contact: P.Dieleman@sron.nl, phone +31-50-3638286

***Abstract*— This article gives an overview of the tests performed on the HIFI instrument before and after integration in the Herschel satellite. The test results are compared to the performance requirements. Overall, HIFI complies well with the original requirements. As an example of unexpected test results the effect of unwanted feedback in the amplification circuit on the data quality is discussed.**

I. Introduction

The Heterodyne Instrument for the Far-Infrared (HIFI)[1] is one of three instruments on board of the ESA Herschel satellite[2]. It spans a frequency from 480 – 1260 and 1410 to 1910 GHz, with a spectral resolution of up to 140 kHz. HIFI has 7 dual-polarisation mixer bands. Bands 1-5 consist of SIS mixers, bands 6 and 7 use HEB mixers[3]. The local oscillator (LO) frequency range is split into 14 frequency bands, each with its own LO chain. The downconverted Intermediate Frequency (IF) signal is fed to two types of spectrum analyser; to an Acousto-Optic Spectrometer (WBS) with an IF band of 4-8 GHz and a resolution of 1.1MHz and to an auto-correlator (HRS) with an adjustable IF bandwidth up to 2 GHz and a resolution of up to 140kHz.

Before delivery to HIFI system, all individual units were fully qualified and performance tested[4]. In this article the results of the Instrument Level Test (ILT) of HIFI as an integrated instrument are presented.

II. Science Drivers and Requirements

Main HIFI science driver is the detection of water lines, especially in the frequency range where the atmospheric absorption hampers the observation from ground. The second driver is the ability to perform line surveys to determine molecular complexities in active regions. From these drivers the instrument specifications are derived, see table 1. In this table the associated tests to verify these requirements are listed as well.

TABLE II
HIFI requirements and corresponding tests

Category	Specification	Test
Functional	Chopper accuracy < 1 arcsecond Tuning duration < 20 seconds	SIS magnet tuning IF amplifier noise LO power tuning Diplexer tuning
Radiometry	flux calibration <10%, (3% goal) RF range 480-1250, 1410-1910 GHz IF range 4 GHz Noise temperatures as specified	Internal Calibrator Line linearity Continuum linearity Tsys survey RF paths standing waves Side band ratio Heterodyne validation Stability validation
Spectral Purity	Spurious <25 dB below signal No spurious in difference spectrum	Spurious signals Spurious responses
Frequency response	Spectral resolution <160 – 350 kHz Resolving power >$3 \cdot 10^6$ Frequency calibration < $1 \cdot 10^7$ 95 % of energy within 2 ·FWHM	Resolution Frequency accuracy Line shape
Amplitude Stability	Allan variance < 1.5 times theoretical value	Total power Spectroscopic
Observational modes	Frequency switch > 90 MHz Beam switching using chopper	Frequency switch Chopper speed
	System engineering	LO purification* IF Feedback**

Radiometry and gas cell measurements are described in [5], and stability results in [6].

* The LO appeared to have a significant spurious frequency in 2 frequency ranges. The LOU settings were optimised to minimise this effect, but further optimization is required

** IF feedback is described later in this article.

III. HIFI TEST ENVIRONMENT

Since HIFI is a flight instrument, the test environment main criteria were temperature, temperature stability and pressure. The Focal Plane Unit (FPU) with the 14 mixers is cooled in a dedicated cryostat, with 2, 4 and 6K levels for the mixers, intermediate strapping and FPU housing respectively. The Local Oscillator Unit (LOU) was operated in a cryostat at 130K. This is the temperature the LOU will reach when cooled by a radiator in space. The electronics units including the backends will have a temperature close to room temperature. These were mounted in a closed cooled cabinet at ambient pressure.

Figure 1 shows the setup with FPU and LOU cryostat.

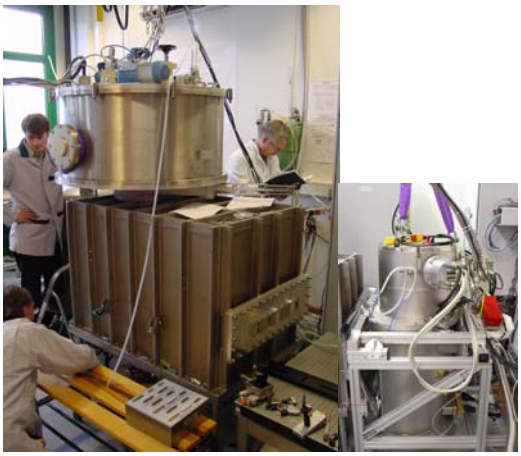

Fig.1. The square cryostat on the left houses the FPU. The right photograph shows the LOU cryostat mounted in a frame to provide alignment adjustments. The round vacuum tank on top of the FPU cryostat houses a scanner for beam measurements.

The LO signal was coupled to the FPU via a nitrogen flushed compartment. This was intended to stabilise the LO power input to the mixers and hence achieve the expected stability in flight. The flow also served to flush away any water adsorbed on the cryostat windows, thus achieving flight-representative LO power values on the mixers. All calibration sources were operated in vacuum. This was achieved either via a reimager, or by mounting the calibration source close to the FPU entrance mirror. The reimager is a vacuum tank of 1 m^3 with relaying optics, which maps the diverging beam of the FPU to a small collimated beam. Figure 2 shows the reimager in use.

Fig. 2. At the left a cryostat with a vacuum Hot/Cold load is shown, which is coupled via a gas cell and the large reimager vacuum tank to the FPU cryostat.

Operating HIFI was done remotely by an operator in a separate room, to minimise temperature variations in the room by airflows. In particular stability tests were programmed overnight for this reason. The test commands were sent to HIFI via a simulated onboard satellite computer. External equipment was readout and commanded via the same console, to fully automate and synchronize tests. The measurement data from HIFI and the test equipment was gathered in one database, for ease of correlation analysis.

IV. HIFI TEST RESULTS

The radiometric calibration, frequency accuracy and stability results are described elsewhere [3,5,6]. The final analysis on LO purity is ongoing, hence this results section will focus on the functional and engineering test results.

A. Functional test results

An important aspect of SIS operation is the proper setting of the magnetic field. Early in the mixer testing the mixer core material appeared hysteretic. To arrive at the proper field at the junction the magnet coil was never operated at negative currents and always commanded to a large positive current before going to the optimum setting. The effect of hysteresis was minimised by this approach. The reproducibility of this tuning was good enough to allow the automated tuning to be limited to a small region around the expected optimum magnet coil current. Figure 3 shows such a tuning using the measured IF power versus commanded magnet current. The mixer bias voltage used for this measurement was 50 μV away from the Shapiro step voltage.

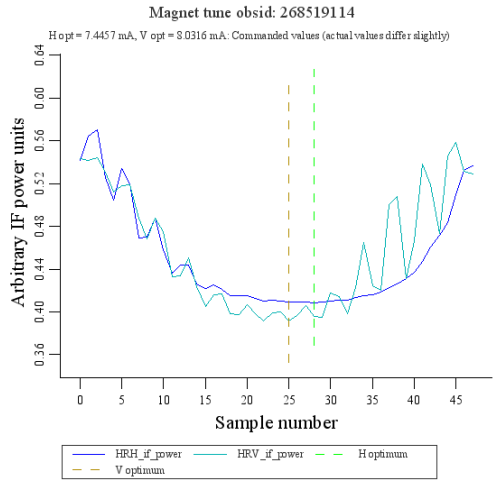

Fig. 3. Magnet tuning of band 1. The vertical axis gives the IF power, the horizontal axis the magnet current steps. The fast oscillation is due to the additional larger loop in the 2-junction structure. Still the algorithm finds the best setting of the magnet current.

The reproducibility of his method appears very good, independent of frequency and LO pump level. Related to this topic is the use of deflux heaters. All HIFI SIS mixers have heaters to heat the superconducting materials (Nb or NbN) above their critical temperatures. Although in flight it is not expected that significant varying magnetic fields will be present, especially in the on-ground testing this can occur. A large number of magnet tunings before and after defluxing has been taken up to now, and no clear indication of changed optima has been noticed. This hints toward a minimum expected use of the heaters in flight, thereby reducing overhead and He consumption.

The IF noise temperature is measured using the standard high-low mixer bias technique. The resulting IF noise spectra are shown in Figure 4.

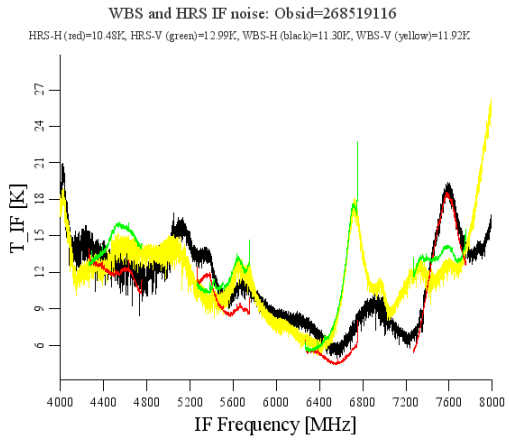

Fig. 4. IF noise temperature of band 2, Horizontal and Vertical polarisation mixers, measured by HRS and WBS each. Clearly the HRS and WBS spectrum per mixer polarisation overlap well, showing that the main contribution to the noise comes from the mixer-1st IF amplifier sections, and that the backend contributions are negligible due to the large IF amplification of 60 dB.

The LO power tuning is performed in 2 steps: Firstly the LO power is scanned over its full range by varying the drain voltage of the last power amplifier. From this measurement the optimum setting is chosen, Step 2 is a fine-tune of this setting before each measurement. The exact LO power is a sensitive function of temperature of the chain. Since the dissipation and hence the temperature drift in the LOU chain is significant, a tuning of the LO power in a small region around the previously found optimum is required. To reach the equilibrium temperature quickly, the fine-tune starts at a high drain voltage, and since during the scan the mixer current is monitored, the scan stops when the correct current is reached. This method avoids frequent retuning of the drain settings. The effect of LO warm-up on instrument stability is described in [6].

B. Engineering test results

During instrument tests it became apparent that when moving mechanical elements in the FPU cryostat and in the FPU itself, additional lines in the IF spectra could be seen. Since all measurements were performed with black thermal radiators in vacuum, these lines could not be originating from these sources. Since this effect was even present when the internal chopper was moved, the requirement that spurious signals shall not present in a difference measurement with 100 seconds integration, was violated. Investigations showed that the cause lies in the significant IF amplification. The occurrence of the unwanted lines in the spectra is explained as follows: The mixer IF signal is amplified by an 25 dB amplifier close to the mixer, and a second amplifier with up to 35 dB gain in a separate housing at the side of the FPU. This housing is fairly open for the IF field, and part of the signal is emitted into the cryostat. This is via wall reflections fed back to the 1st amplifier where it interferes constructively or destructively, depending on its phase. If now the FPU chopper moves, the path length is changed and hence the phase. Therefore the difference spectrum on/off source or Hot/Cold using the internal calibrators shows additional offsets. The reason that these offsets show up as lines is that the FPU cryostat has typical dimensions of 1 m^3, which together with the ~6 GHz IF frequency causes box modes, separated by 20 MHz, depending on the exact path. An example of such a difference spectrum is shown in Figure 5.

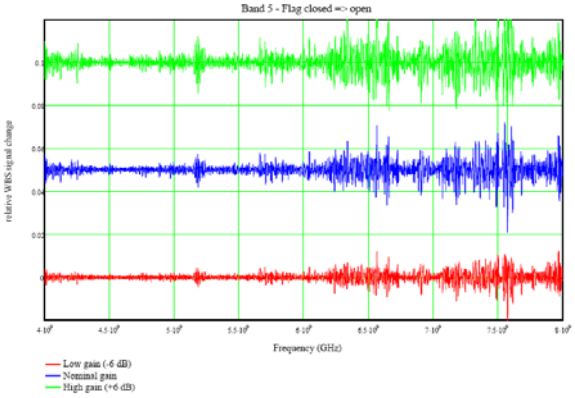

Fig. 5. Ratio of spectra taken for a mixer without LO power applied, at 2 chopper positions, as function of IF amplifier gain. Vertical axis: relative power, Horizontal axis: IF frequency. The offset is intentional. Clearly with higher IF gain (red-blue-green curves) the IF feedback effect increases.

This IF feedback effect must be present in many receivers, but since most of the ground-based observatories have moveable elements outside the cryostat, the effect is stable and hence not visible in difference spectra.

A solution was found in taping the outside of the 2nd IF amplifier housing with Aluminium tape, which minimises the leakage of the IF signal. Figure 6 shows the IF-2 housing with Al tape.

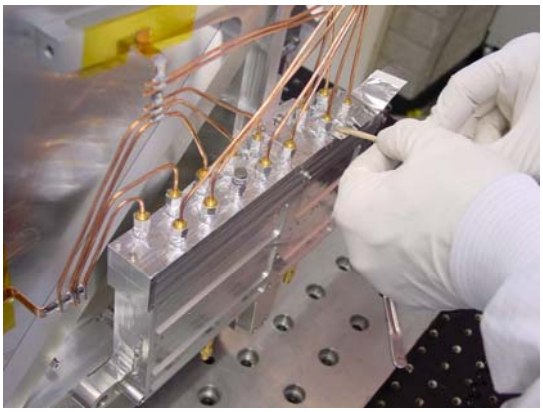

Fig. 6. The IF amplifier housing being covered with Al tape. An additional box was produced that facilitated the wrapping of the IF connectors.

The effect as function of area of the IF-2 housing covered with Al tape is plotted in Figure 7. On the long term the remainder of the effect can be calibrated out in flight, since the effect is reproducible with chopper angle, and the chopper reproducibility is very good.

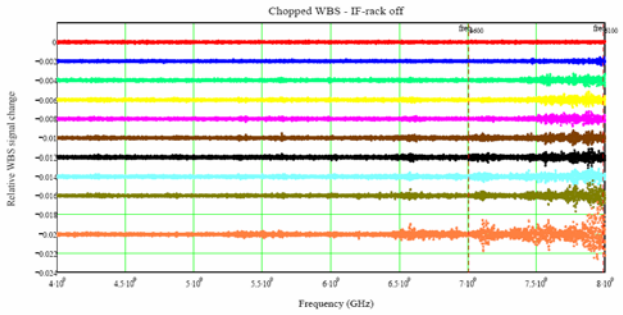

Fig. 7. Plot layout as in Fig. 5. The higher traces are taken with a larger area covered with Al tape. Clearly the IF signal seeps out of every part of the IF2 amplifier housing; the feedback effect is lowered for every additional part that is taped.

V. HIFI – Herschel Integration Status

A. Integration test results

HIFI was delivered July 10, 2007 to EADS-Astrium Friedrichshafen[7] for integration with the Herschel satellite. Two aspects needed hardware modifications:

After electrical integration it appeared that a significant current ripple is present in the 28V power supply line from the solar panel simulator to the HIFI LO Control Unit. The ripple had a frequency of 600 Hz and an amplitude of 300 mA peak-peak, on a total of 1A. A filter to damp the oscillations was designed and fabricated by the HIFI team and mounted on the satellite. The filter functioned well; no ripple could be perceived.

A second hardware change concerned a cryostat window heater. From earlier missions it is known that significant quantities of water escaping from the vast area of the satellite isolation layers can freeze at the coldest points. The coldest spots are the windows in the Herschel cryostat. These windows enable LO power injection to the mixers. If water would freeze here the effect on LO power loss is significant[8]. Removing the ice needs a temperature of the window of at least 170 K to avoid excessive heating durations[9]. Hence a dedicated construction with additional windows on a thermally insulated holder was devised. Recently this unit passed thermal testing successfully and is now ready for integration with the satellite.

In Figure 8 the fully assembled Herschel satellite is shown.

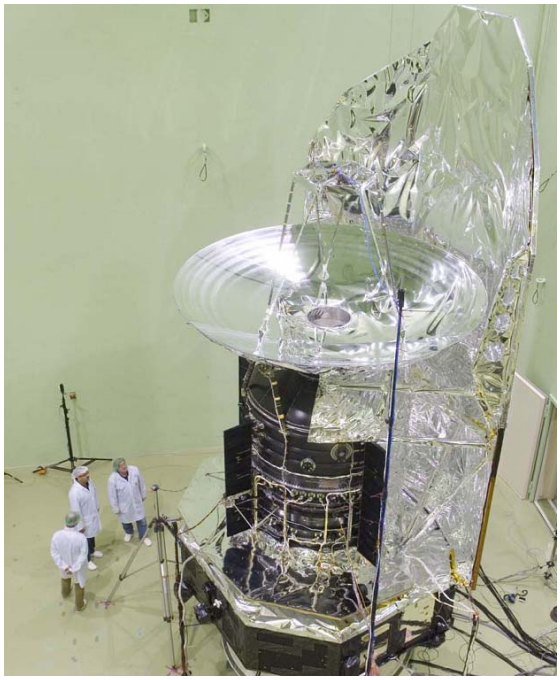

Fig. 8. The Herschel satellite in fully assembled configuration ready for acoustic testing.

B. Performance test results

The first performance tests were executed in April 2008. The LOU is at ambient temperature during these tests, which results in a lower output power compared to that at the operational temperature in flight. The second effect is that the LOU is misaligned to anticipate the shrinkage of the support structure at operational temperature. Bands 6a, 7a and 7b could therefore not be performance tested due to lack of LO power. The other bands showed that the noise temperature spectra are unchanged with respect to those seen during ILT. The previously mentioned IF feedback effect was reduced by a factor of 3, most likely because of the larger volume and absorbing contents of the Herschel cryostat compared to the HIFI ILT FPU cryostat.

CONCLUSIONS

The HIFI ILT and Herschel integration phases are nearly complete. Preliminary performance tests with warm LOU show that HIFI is healthy and performing well. The final confirmation will be in the Thermal Vacuum test, where the LOU will be operated at flight representative temperatures

ACKNOWLEDGMENT

We thank all 23 institutes that helped build and test their parts of HIFI, and continued to spend the effort to assist whenever necessary.

REFERENCES

[1] T. de Graauw, "The Herschel Heterodyne Instrument for the Far-Infrared (HIFI)", Proc. SPIE 6265, 62651Z, 2006.
[2] G.T. Pilbratt, "Herschel space observatory mission overview", *IR Space Telescopes and Instruments*, J.C. Mather, Ed. SPIE 4850 (2003), pp. 586–597.
[3] G. de Lange, "Performance of the superconducting mixers for the HIFI Instrument", these proceedings
[4] *Space Mission Analysis and Design*, James R. Wertz and Wiley J. Larson, Ed. 1999
[5] D. Teyssier, "HIFI Pre-Launch Calibration Results", these proceedings.
[6] J.W. Kooi, "HIFI Instrument Stability as measured during the ILT phase: Results and operational impacts", these proceedings.
[7] Astrium GmbH, Immenstaad, Germany
[8] S.G. Warren, Appl Opt, 23, 1206, 1984.
[9] N.J. Sack and R.A. Baragiola,, Phys Rev B, 48, 9973, 1993.

HIFI Stability as Measured During ILT Phase

J. W. Kooi [1*], V. Ossenkopf [2, 4], M. Olberg [3, 4], R. Shipman [5],
R. Schieder [2], and D. Teyssier [6]

[1]*California Institute of Technology, Pasadena, CA 91125, USA*
[2]*KOSMA, I.Physikalisches Institut der Universitat zu Köln, Germany*
[3]*Onsala Space Observatory, Sweden*
[4]*SRON Netherlands Institute for Space Research, Groningen, the Netherlands*
[5]*University of Groningen, Kapteyn Astronomical Institute, Groningen, the Netherlands*
[6] *European Space Agency Centre (ESAC), Spain*
* Contact: kooi@caltech.edu, 626-395-4286

***Abstract*— We present here the stability results of the high frequency heterodyne instrument (HIFI), to be flown on the Herschel space observatory. The measurements were taken as part of the instrument level tests (ILT) in the spring of 2007. Herschel is ESA's fourth cornerstone mission in the Horizon 2000+ program, and aims at observations in the Far-InfraRed and sub-millimeter wavelength region. HIFI itself is one of three instruments onboard Herschel. The other two being PACS, the photodetector array camera and spectrometer, and SPIRE, the spectral and photometric imaging receiver.**

The detailed instrument stability measurements were conducted to establish the functionality, and observational readiness of the instrument.

I. WHY TO MEASURE (HIFI) INSTRUMENT STABILITY

HIFI is a probably the most complex and sensitive heterodyne instrument ever put together. It consists of 7 mixer bands covering the frequency range from 480 GHz to 2 THz. Mixer bands 1-5 are based on Superconductor-Insulator-Superconductor (SIS) technology whereas bands 6-7 are Hot-Electron Bolometer (HEB) based. Each mixer band consists of two mixers, sensitive to either horizontal or vertical polarization (14 mixers in all). These, along with the diplexers and beam splitters are housed in the Focal Plane Unit, or FPU (Fig. 1). To provide the mixers with a local oscillator signal, 14 multiplier chains (driven by power amplifiers) are contained in a separate Local Oscillator Unit (LOU). The LOU is driven by a custom designed Local oscillator Source Unit (LSU). The LCU, shown in Fig. 1 provides the required bias voltages and interfaces to the common instrument bus. The mixer output signals are after (cold) amplification routed to two 4 GHz wide Acousto-optical spectrometer's [1, 2], and two 2 GHz wide auto-correlation spectrometers [3] (one for each polarization). The wideband acousto-optical spectrometer's (WBS) consist of four 1 GHz wide subbands, 2000 channels each. Thus the 'full' spectrometer has 8000 spectral channels. The digital correlator, or high resolution spectrometer (HRS) has a total processing bandwidth of 2 GHz, and consists of 8 channels or subbands. The HRS can be programmed for different frequency resolutions anywhere within the mixer IF passband. Essentially all stability measurements were performed with both WBS and HRS. The derived Allan variance stability measurements for both types of spectrometers is basically the same, provided the difference in noise fluctuation bandwidth is taken into account. The HRS is found to be quite a bit less sensitive to thermal drift then the WBS, which should not come as a surprise.

As is evident from Fig 1, there are ample opportunities for degrading effects from thermal, electronic drift, gain fluctuations, optical and IF standing waves, mechanical vibrations, ground loops, and electromagnetic interference.

We list here the primary reasons for studying the stability of the instrument. They are:

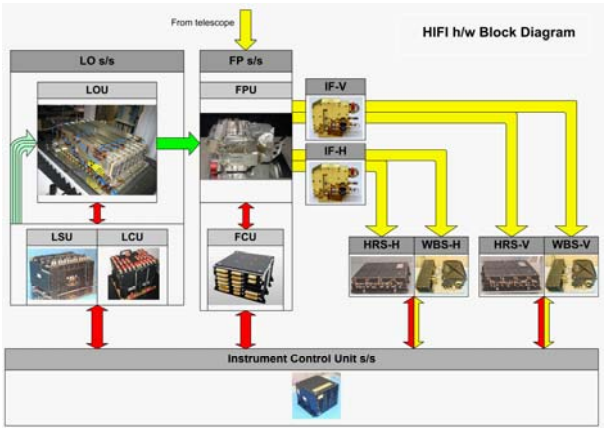

Fig. 1. Block diagram of HIFI. The different units are discussed in the text.

A. Optimize astronomical observing modes.
B. Study 14 mixer/LO sub-bands and identify problem area's.
C. Determine the observation efficiency loss due to instability (Compute the rms noise level).
D. Search for platforming effects, baseline ripple, offsets…

The obtained stability data (Allan time, drift slope, Section III) is fed into the Herschel Observation Planning Tool (HSPOT), and Astronomical Observation Techniques (AOT's). In Fig. 1 we show the block diagram of HIFI[4], the heterodyne instrument for ESA's **Herschel** space satellite[5].

II. What do we measure

There are many facets to establishing the stability performance of the instrument. Listed categorically they are:

A. IF stability
B. Time Constants
   - IF amplifier warm-up
   - LO warm-up
   - Spectrometer warm-up
C. System stability for each mixer in 14 LO sub-bands
   - Total power amplitude stability
   - Spectroscopic stability
D. Differential gain stability
   - Dual beam switching (DBS)
   - Load Chop (LS)
   - Internal Load
   - Frequency switching (FSW)
E. Parametric Stability
   - B-field at the SIS bands
   - Stability as a function of LO power
   - Stability as a function of bias voltage

The instrument IF stability is measured without LO signal and with the SIS and HEB mixers biased at 8 mV. IF stability establishes the performance of the joint IF and backend signal chain.

Warm up time constants are important in establishing boundary conditions for instrument operation. HIFI will be on approximately 1/3 of the mission life time, it sharing time with PACS and SPIRE. Thus it is important to know how long the IF amplifiers, local oscillators, and spectrometers have to be turned on before certain types of observations may commence.

System stability establishes the total power and spectroscopic stability of the instrument. These are needed to determine switch rates (section VIII), mapping strategies, and to give a measure of how often to calibrate for absolute flux observations. In an ideal instrument, position switching (slewing the entire telescope off source for a reference measurement) is the most efficient observation mode. Often however the spectroscopic stability time is such that position switching is not possible (too slow). In this case relatively fast differential 'on-off' source measurements performed. The differential stability tests thus measures the efficiency and baseline quality of a number of switched observing modes.

Symmetric dual beam switching (on-off-off-on...) on HIFI can occur at a maximum rate of 0.25 Hz, or 4 s. This is the time required to readout all four spectrometer channels, and is known as 'slow-chop'. It is also possible to switch as fast as 4 Hz, in an 'on-off-on-off...' pattern. It this case a 25 % penalty is paid by buffering the spectrometer data in the internal spectrometer buffers. Thus for the sake of time efficiency slow-chop is preferred. DBS is accomplished by nutating an internal FPU mirror. Only small beam throws (180'') are possible. This mode is only effective therefore for compact sources. For extended line sources Load-Chop (LS) may be used. LS switches periodically against an internal load. On the ground this technique cannot be easily applied due to the interfering effect of the atmosphere. As we shall see, both DBS and LS loose a factor of 4 in integration time (2 in noise) over an ideal position switching instrument

Internal Load measures a reference beam on two internal calibration loads. In doing so it established the secondary calibration loop time. We find values of >= 20 minutes for the SIS bands, and 15 minutes for the HEB mixer bands.

Frequency switching is a promising, but not fully demonstrated mode. In this case the LO source frequency is modulated by a small amount. This will allow observations of the source in both the 'on' and 'off' position, thereby doubling the integration efficiency over DBS and LS. The object is to keep the LO pump level on the mixer constant. Thus it is very important to establish the dominant optical standing wave in the system. Dedicated in flight tests are setup to determine the primary standing waves within the telescope.

Finally we have parametric stability. Since telemetry to the instrument is only once a day, the mixers and local oscillators will have to be run autonomously. Thus it is important to establish bias ranges over which the instrument can be expected to perform as expected.

III. How do we measure Stability

Radio astronomy receivers in general look at very weak signals deeply embedded in noise. To extract the weak signals, synchronous detection (signal on - signal off) is typically employed. This is done by either slewing the whole telescope back and forth so as to get the beam on/off the source, or by moving the secondary mirror (sub-reflector) of the telescope at a certain rate. The problem in both these cases is the dead time between observations, i.e., chopping efficiency (η_c). A practical lower limit for slewing an entire telescope off-source is typically 15 seconds, while chopping the secondary mirror can perhaps be as fast as 0.2 seconds (5 Hz). As we have seen,

frequency switching with the HIFI instrument is possible and can be accomplished at a much higher rate. It suffers however from modulation of the LO-Mixer standing wave [6], LO power stability, and for terrestrial observations changes in the atmospheric transmission.

If the noise in the receiver system is completely uncorrelated (white), it turns out that the rate of chopping (modulation frequency) has no effect on the final signal to noise ratio. This can be deduced from the well known radiometer equation which states that the noise integrates down with the square root of integration time

$$\sigma(T) = \frac{2\langle s(t)\rangle}{\sqrt{\eta_c \Delta\nu T}} \quad (1)$$

Here σ is the standard deviation (rms voltage) of the signal, ⟨x(t)⟩ the signal mean, Δν the effective fluctuation bandwidth, and T is the total integration time of the data set.

The factor 2 comes in from the loss of integration time (√2), and a factor of √2 because of the subtraction of two essentially white (Gaussian) noise signals. η_c is the chopping efficiency (~0.95).

In practice, the noise in radiometers, and in particular SIS and HEB mixers, appears to be a combination of low frequency drift (correlated noise), 1/f electronic noise and white (uncorrelated) noise. Hence, there is an optimum integration time, known as the Allan stability time (T_A), after which observing efficiency is lost. In actual synchronous detection measurements ``n'' samples of difference data (signal on - signal off) are taken, each with a period T. These differences are then averaged so that the total observed time equals n*(2T). If the period T is larger than the Allan stability time (T_A) of the system, then apart from loss in integration efficiency, there will be a problem with proper baseline subtraction and intensity calibration. This manifests itself in baseline distortion at the output of the spectrometer (Fig. 2) which severely limits how well the noise integrates down with time Section VIII.

The Allan variance theory has been outlined in [7-10], and we merely present here the conclusions, least to say that the Allan variance is σ_A^2 is historically [11] defined as $\sigma^2/2$. For a noise spectrum that contains drift, white noise, and 1/f noise it is found that the Allan variance takes the form

$$\sigma_A^2(T) = aT^{\beta} + \frac{b}{T} + c \quad (2)$$

where *a, b,* and *c* are appropriate constants. For short integration times, the variance decreases as 1/T, as expected from the radiometer equation. For longer integration times, the drift will dominate as shown by the term aT^{β}. In that case, the variance starts to increase with a slope β which is experimentally found to be between 1 and 2. For SIS and HEB mixers it is frequently observed that the variance plateaus at some constant level. This is attributed to the constant *c* and is representative of flicker or 1/f noise in the device under test.

Plotting σ_A^2 vs. the integration time T on a log-log plot demonstrates the usefulness of this approach in analyzing the radiometer noise statistics (Fig. 2). As a reference it is meaningful to superimpose radiometric noise with a T^{-1} slope. The latter represents the uncorrelated (white) noise part of the spectrum. The minima in the plot gives the Allan time T_A , the crossover of white noise to 1/f or drift noise. Often however, such as in Fig. 2, there is no clear minima and a factor √2 deviation from the rms radiometric noise

is then a useful definition of the Allan time.

Finally, it is often of interest to estimate what happens to the Allan stability time if spectrometer channels are binned to reduce the rms noise in an observed spectrum, or if the IF bandwidth of the radiometer is increased (different velocity resolution). In this case it can be shown that

$$T'_A/T_A = (\Delta\nu/\Delta\nu')^{\frac{1}{\beta+1}} \ . \quad (3)$$

β is the slope of the drift noise as discussed above. And T'_A

the newly obtained Allan time for fluctuation bandwidth Δν'.

A. Total Power Stability

As an example we show in Fig. 2 the total power, or continuum, Allan variance of HIFI HEB mixer band 6a (H-polarization), as measured during the instrument level test phase (ILT) in May 2007. As we shall see, this plot contains a wealth of information.

The IF output frequency of the HEB mixer is 2.4-4.8 GHz [12], which after being up-converted, and then back down-converted to match the wideband acousto-optical spectrometer [1] input, translates to a WBS subband1 of 4.8-3.8 GHz, a subband2 of 3.8-2.8 GHz, and a subband3 of 2.8-2.4 GHz. 'Full' corresponds to a stability averaged over the the total 2.4 GHz available (HEB) IF bandwidth. It should be noted that the HEB mixer is most sensitive in a 2.4-3.4 GHz IF frequency range [12], and as a results it may be expected that WBS subband 3 is the most unstable. This is indeed consistently the case, as shown in Fig. 2.

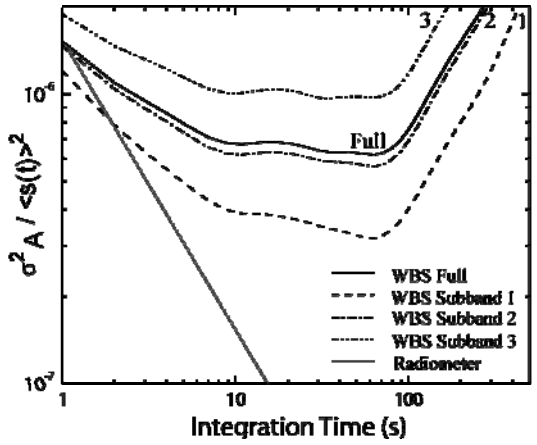

Fig. 2. Normalized total power Allan variance. 'Full' (2.4 GHz) spectrometer response deviates a factor 2 from the radiometric noise at 3 s. This may be considered the effective total power "Allan variance minimum time" (TA). H-polarization, νLO= 1447 GHz. See text for details.

The offsets between the three spectrometer subband Allan times is due to excess noise in each of the IF sub-channels. Averaged over the entire IF bandwidth, the calculated fluctuation noise bandwidth (Δν) is 1.3 MHz. This is somewhat less then the spectrometer [1] intrinsic noise bandwidth of 2.3~MHz, indicative of excess (non radiometric noise). Again referring to Fig. 2, between 1 and 7 seconds we see the noise integrate down with a slope slightly less then T^{-1}. Judging from the -1 radiometer slope, we have a factor 2 loss in integration efficiency at ~3 s. This may be considered the effective "Allan minimum time". The reason that there is not a clear minimum in the Allan variance plot is that HEB mixers exhibit significant 1/f fluctuation noise (zero slope), as is evident between ~10-90 s. Above approximately 90 s, drift noise begins to dominate. In this particular example the drift slope β = +1.2.

B. Spectroscopic Stability

The spectroscopic Allan variance measures deviations from the continuum level fluctuations [10]. As such it corresponds to the subtraction of the spectrometer mean continuum level, known as the zeroth order baseline correction [7, 8, 10]. This is allowed since most heterodyne observations are intended for line observations, rather then continuum or flux calibration. For continuum measurements incoherent detectors are much better suited. Lets assume *K* spectrometer channels, then the signal in each channel d_K (n) at time *n* may be normalized by subtraction of the instrument zero level in the particular channel (z_k), and then by dividing the difference by the temporal average of each channel

$$s'_k(n) = \frac{d_k(n) - z_k}{\langle d_k(n) - z_k \rangle_n} , \quad z_k = \frac{1}{N}\sum_{n=1}^{N} d_k(n) . \tag{4}$$

To now obtain the difference for the spectroscopic Allan variance computation, we subtract the normalized mean summed over all spectrometer channels, e.g.

$$s_k(n) = s'_k(n) - \langle s'_k(n) \rangle_k . \tag{5}$$

$s_k(n)$ may then be used to obtain the spectroscopic Allan variance for each channel by substitution of $d_k(n)$ *with* $s_k(n)$ in

$$\sigma^2_{A,k}(T) = \frac{1}{2(N-1)}\sum_{n=1}^{N}(d_k(n) - \langle d_k \rangle)^2 , \quad \langle d_k \rangle = \frac{1}{N}\sum_{n=1}^{N} d_k(n) . \tag{6}$$

N equals the number of discreet time samples taken. By using Eq. 6 directly ($d_k(n)$ is the temporal data in spectrometer channel *k*) the total power Allan variance is obtained. To obtain the Allan variance in K spectrometer channels the variance is summed as

$$\sigma^2_A(T) = \frac{1}{K}\sum_{k=1}^{K}\sigma^2_{A,k}(T) . \tag{7}$$

In Fig. 3 we show the spectroscopic Allan variance. In this case a zeroth order correlated noise baseline is subtracted. We

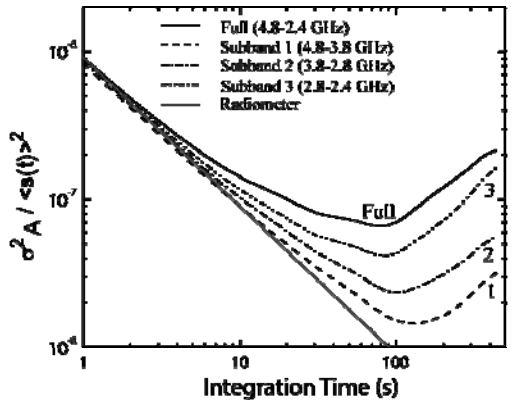

Fig. 3 Spectroscopic Allan variance for the B6a HEB mixer subbands and full spectrometer band (2.4 GHz). The Allan times, defined as a factor of two deviation from the radiometric noise (white) are: TA (full)=14.9 s, TA (subband1)=111 s, TA (subband2)=50.5 s, and TA (subband3)=30.7 s. The noise fluctuation bandwidth is 2.3 MHz. H-polarization, υLO= 1447 GHz.

see a substantial improvement in the statistical variance of the spectra. The noise now integrates down radiometrically, for about 50 s in case of the subbands, and 15 s for the full spectrometer band (4.8-3.8 GHz). The 1/f gain fluctuation noise that dominates the continuum Allan variance of Fig. 2 is now nearly completely removed!

Taking the ratio of the spectroscopic to the total power Allan variance (see Fig. 5), we find that statistically the largest improvement (factor 20+) is gained by spectrometer subband 3 at integration times > 10 s. This is good as most galactic (narrow line) observations will be planned in this subband, being the most sensitive region of the HEB IF passband [12]. For spectral line broadened extragalactic observations the full spectrometer bands needs to be used and a factor of six improvement over the continuum stability is obtained. Continuum measurements will be very challenging.

It should be noted that the HIFI B6a results presented here serve as a typical ILT obtained example of system stability. Actual HEB mixer stability [6] may be better in a more optimized environment such as space, or possibly worse in a poorly designed ground based application.

C. Improvement of Spectroscopic over Total Power Allan Variance.

To compare the improvement in spectroscopic Allan variance over continuum Allan variance, we compare in Fig. 4 the ratios of SIS mixer band 2 (736 GHz), and in Fig. 5 HEB mixer band 6 (1652 GHz). For the HEB mixer, subband 1 has the lowest sensitivity (4.4-4.8 GHz), and also shows the least improvement. The loss in sensitivity of an HEB mixer is caused by the roll off in mixer conversion gain as a function of IF frequency [13], overlaid by the frequency response of the diplexer used to inject the LO signal.

For the band 2 SIS mixer the sensitivity is uniform across all four spectrometer subbands. In this case a beam splitter is used to inject the LO signal. Why the spectroscopic- over

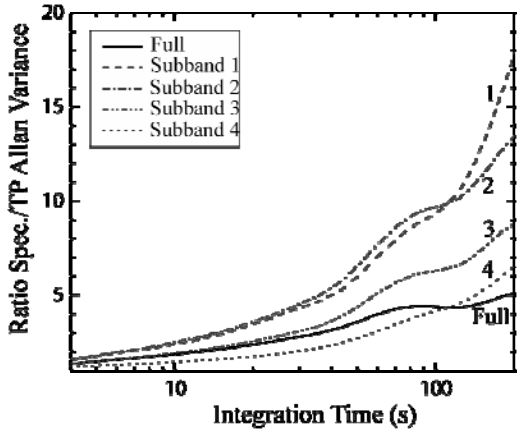

Fig. 4 Improvement ratio of the spectroscopic Allan variance for HIFI SIS mixer band 2b. Shown are the stability results of the four 1GHz wide AOS subbands and the full spectrometer (8000 channels). LO frequency is 736 GHz.

continuum Allan variance ratio is not more uniform is not entirely clear, except to note that the 7-8 GHz IF channel (subband 4) has always the worst stability performance. It is likely that we see an additive effect of the many sub-components in the IF- and backend system. In general it appears therefore that the noise of a SIS mixer is less correlated in the higher end of the IF band (7-8 GHz).

Significantly more spectroscopic- over continuum Allan variance improvement is obtained in the HEB band then the SIS band. There are several explanations for this. First, the HEB is a power sensor. This is opposed to a SIS junction that is sensitive to quasi-particle tunneling through a thin barrier Second, HEB mixers operate in the terahertz frequency regime. As such they are more sensitive to optical standing

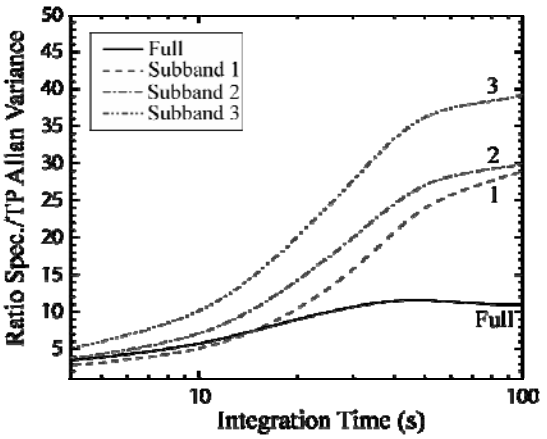

Fig. 5 Improvement ratio of the spectroscopic Allan variance for HIFI HEB mixer band 6b. LO frequency is 1652 GHz. Note that the plots of Fig. 4, 5 have different scales. The removal of a zeroth order baseline has significantly more effect on a per subband bases for an HEB mixer then SIS mixer. This indicates that the source of HEB instability is highly correlated in an HEB mixer. The most likely culprits are: LO instability and optical standing waves. SIS mixer band 2 is a beamsplitter band, and HEB mixer band 6 uses a diplexer to inject the LO signal. Due to the finite diplexer passband and roll of in mixer gain, HEB subband 1 has considerably lower sensitivity than subband 3. For both mixer bands we have plotted the vertically polarized IF output channel.

waves then SIS mixers, which primarily operate below 1~THz [6]. And finally, the LO sources that pump the mixers are more complex at higher operating frequencies (HEB mixers), and thus more susceptible to amplitude noise which increases approximately as $20\log_{10}(M^2)$ [14]. M is the multiplication factor.

IV. Some Example of what can go wrong

No system is perfect and neither is HIFI. Here are a few system level examples of what can go wrong: Platforming, high level of gain instability, very short Allan times, and poor subtraction of difference spectra (significant standing waves). These results were part of the initial ILT tests results. The problem was caused by the local oscillator power amplifiers not being driven hard enough into saturation. This resulted in significant amplitude jitter (noise) at the multiplier outputs. The solution was to insert optical attenuators in the LO signal path, so as to force the power amplifiers in a more optimum bias regime. A paper by Jellema *et al,* in this proceedings provides more details

on the design, measurement, and material properties of the above described space qualified optical attenuators.

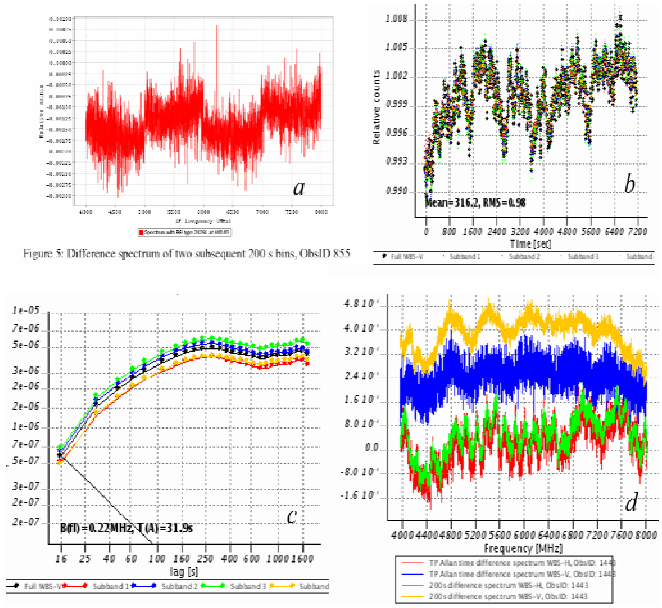

Figure 5: Difference spectrum of two subsequent 200 s bins, ObsID 855

Fig. 6. Things that can go wrong. a) platforming, b) gain instability due to the LO in this case, c) very short Allan times, significant baseline distortion.

V. LO Warm Up Time

Local oscillator warm up time has a direct bearing on the planned AOT's. During ILT the local oscillator units were not preheated. This is planned for flight, and it is possible that the stabilization can be shortened a bit.

We provide here the 5τ warm-up times for Total Power (continuum) and differential stabilization. In general, the higher frequency multipliers are more complex and need a longer (50 min) warm-up time then the lower frequency multipliers (30 min).

TABLE I. HIFI LO WARM UP TIMES.

Band	Total Power (min)	Frequency (GHz)	Obsid	Differential (min)	Frequency (GHz)	Obsid
1a	30	509	268476280	5	494	268510476
1b	30	582	268461236	3.5	563	268510729
2a	40	640	268459469	10	640	268511312
2b	40	736	268461220	13	728	268511362
3a	40	812	268471048	20	814	268511420
3b	40	878	268471066	13.5	869	268511669
4a	30	995	268483530	15	982	268509805
4b	40	1095	268460379	20	1108	268510072
5a	30	1185	268459366	10	1127	268510773
5b	40	1180	268460362	10	1191	268510564
6a	50	1462	268467526	15	1444	268511851
6b	47	1599	268471030	15	1581.4	268512252
7a	50	1723	268471084	7 ?	1716.6	268513243
7b	55	1897	268471102	x	x	x

SIS bands

HEB bands. Frequent LO tuning needed during first 2-3 τ (Total Power time period).

For certain differential observations one may not be too interested in the LO drift, provided that the change in LO pump level is not so large that the mixer unit operation is completely out of specification. This is not merely an academic exercise, it has in fact been observed in the HEB mixer bands that the LO pump level can drift out of the operating regime of the mixer.

To circumvent these problems, it is now planned to automatically retune all local oscillator ~ 5 minutes after switch on, and do a second retune of the HEB local oscillators after an additional 500 s. For differential observation such as DBS and LS typically a 10 minute wait period is sufficient. Of course this does require careful planning of the observation.

VI. Effect of Using a Diplexer

We show in Fig. 7 the stability and sensitivity statistics of SIS mixer band 1b, as measured on the wide band spectrometer (4-8 GHz). In case of a *beam splitter* band (HIFI band 1, 2, 5) we consistently find the following: The system temperatures (no atmosphere) are reasonably constant across the 4-8 GHz IF passband. However, the spectroscopic Allan times, though uniform for WBS subband 1-3 (4-7 GHz), and generally a bit depressed in subband 4 (7-8 GHz).

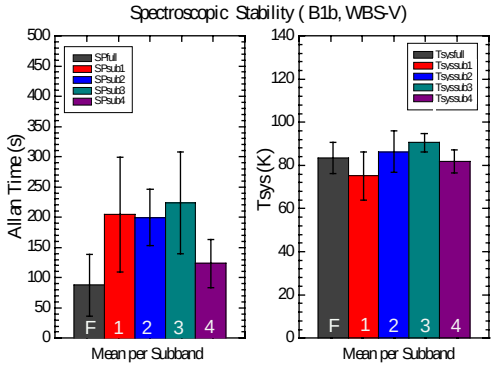

Fig. 7. Band 1b Spectroscopic Allan variance and system temperature statistics. Band 1b is a 'beamsplitter' LO injection band. Sensitivity is uniform, but the stability is generally worst in WBS subband 4.

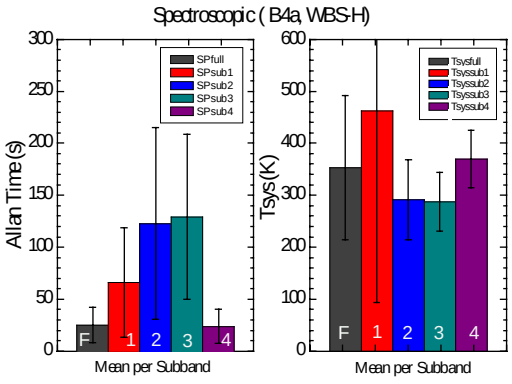

Fig. 8. Band 4a Spectroscopic Allan variance and system noise temperature statistics. Band 4a is a 'diplexer' LO injection band. Subbands 2, 3 (5-7 GHz) are generally the most stable, followed by subband 1 and 4.

The spectroscopic stability averaged over the entire spectrometer band is always less than that of the individual subbands.

For the *SIS diplexer* bands 3 & 4 we find that the two centre subbands are the most sensitive and stable (5-7 GHz), and that the stability and sensitivity of subband 1, 4 is somewhat degraded. WBS subband 1 is generally a bit more sensitive and stable then subband 4. This of course reflects the diplexer passband profile. Instability can be attributed to optical reflections in the front end. This is shown in Fig. 8 for mixer band 4a.

At this point it should be noted that during the ILT, the FPU (4 K) and LOU (~120 K) were cryogenically cooled by means of a hybrid cryostat (compressor and LHe). This resulted in a ± ~10 μm mechanical modulation of the LO-mixer standing wave. In flight, with an all LHe cryostat, this situation is hopefully much more stable, and it is not unreasonable to expect a better stability performance of WBS subband 1. The one caveat is that the reaction wheels of the spacecraft will introduce 'high frequency' vibrations.

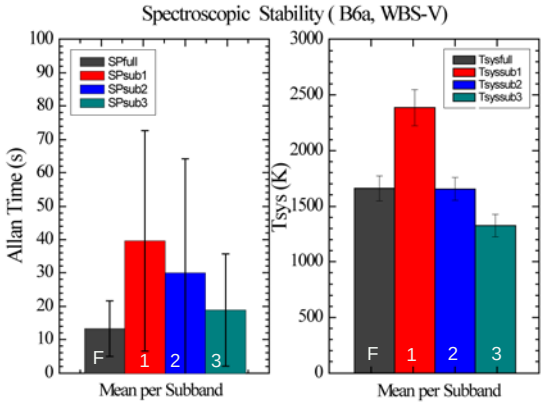

Fig. 9. Band 6a Spectroscopic Allan variance and system temperature statistics. Band 6a is a 'diplexer' LO injection band. Subband 3 (2.4-3.4 GHz) is the most sensitive, but also the most spectroscopically unstable.

For the *HEB mixer diplexer* bands, subband 3 is always the most sensitive being the lowest in IF frequency (2.4-3.4 GHz), but also the most unstable (Fig. 9). This is caused by the roll-off in mixer conversion gain of the HEB mixer (due to the finite electron and phonon relaxation time [13]) starting at approximately 3 GHz. Thus WBS subband 1 is the most stable, but also the least sensitive. Narrow spectral line observations should therefore be planned in the lower part of the HEB B6 and B7 IF band.

VII. Parametric Studies

As part of the HIFI instrument level test program (ILT), parametric studies of the HEB mixer band 6 & 7 were performed. In addition, we have also looked at the effect of small deviations in magnetic field setting for the SIS bands.

For the HEB mixer bands. two situation were examined: System stability as a function of LO power (HEB current), and system stability as a function of HEB bias voltage. In Fig. 10 we show the normalized spectroscopic Allan variance as a function of LO power. For the HEB bands 30 μA is slightly over pumped, 40 μA optimally pumped, and 50 μA on the verge of being under pumped. Slightly over pumping the HEB mixer from a stability point of view appears beneficial. This is understood to be the combined effect of a small decrease in sensitivity and an increase in required LO pump level. Higher LO power levels generally causes the W-band power amplifiers in the LO chain to run more saturated, thereby clipping the amplitude modulated (AM) noise on the LO carrier signal [14]. Consistent also is the trend that lower LO power (HEB current) results in a reduced Allan time, around 10 s in our case. This agrees with the picture that AM noise is present on the LO carrier, and that saturation of the LO chain power amplifiers is extremely important. In Fig.11 we show the normalized spectroscopic Allan variance as a function of bias voltage for a nominal LO pump level. Again we have a consistent trend, higher HEB bias voltages provide more stable mixer behavior.

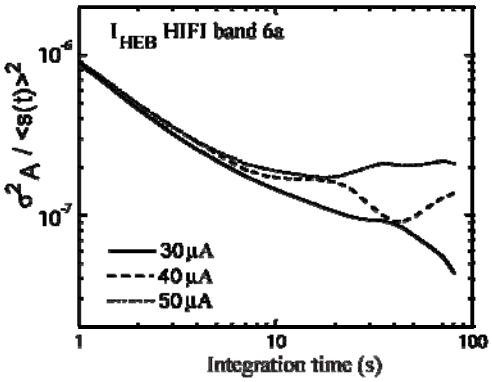

Fig. 10 Band 6a, normalized spectroscopic stability as a function of LO pump level. HEB mixer band 6a. 30 μA is slightly over pumped, 40 μA optimally pumped, and 50 μA on the verge of being under pumped. The LO frequency is 1666 GHz.

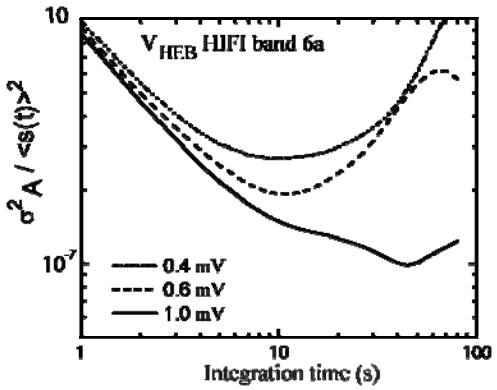

Fig. 11 Band 6a, normalized spectroscopic stability as a function of HEB mixer bias voltage. Optimal sensitivity is typically achieved around 0.5~mV. vLO=1666 GHz

At the larger (1 mV) bias voltage this is simply related to the sensitivity of the HEB mixer, e.g. the less sensitive the

mixer the less sensitive it will also be to AM local oscillator noise.
However between 0.4 and 0.6 mV the sensitivity of the mixer is more or less constant and the instability is more likely the result of how close the mixer is biased to the (known) HEB mixer instability region [12, 15]. From this discussion it is clear that slightly over pumping the HEB mixer (20 %), while biasing it above the nominal operating voltage (20 %) enhances the mixer stability, and thereby integration efficiency and baseline quality.

VIII. Instrument Stability and Baseline Quality

Throughout the thesis instrument stability is discussed as an important system parameter in establishing time efficient observations. Considering the generally large expense, demand on telescope time, and quality of data, stability has become an important design parameter for modern heterodyne instrumentation.

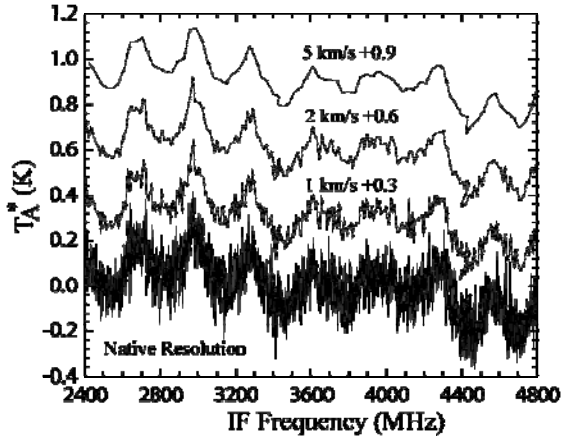

Fig. 12 Synthesized position switched spectrum for HEB mixer band 7b. Total 'on-source' integration time in one 600 s cycle is ~464 s, clearly much too long given the stability of the mixer. Severe baseline distortion is the result. ν_{LO}=1.890 THz, V-polarization sensitive mixer.

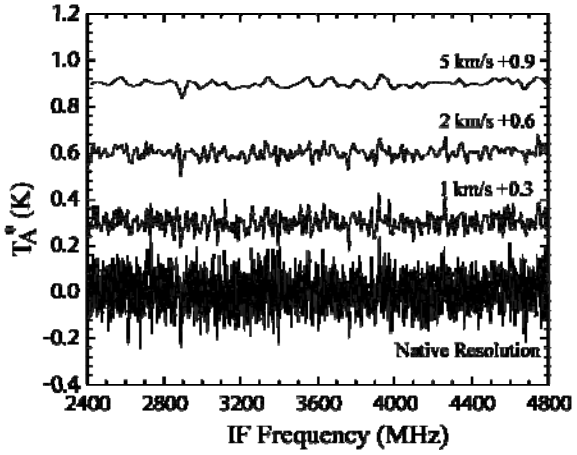

Fig. 13. Synthesized double beam switched (DBS) spectrum for different velocity resolutions. Each phase of the chop cycle is 4 s, well below the stability time of the instrument. For a native resolution, the theoretical and synthesized 1σ rms noise levels are virtually identical (64~mK vs. 68 mK). Total 'on-source' integration time is 2829 s. ν_{LO}=1.890 THz, V-polarization sensitive mixer.

In Fig.'s 12, 13 we depict a simulated position- and DBS spectra from actual HIFI [4] data, as obtained in HEB mixer band 7 during instrument level tests (ILT). The spectra are shown for four different velocity binning resolutions; native (0.086 km/s), 1km/s, 2km/s, and 5km/s. To convert the velocity resolution to spectral resolution we use the Doppler relationship $v=c/R$ where $R=\nu/\Delta\nu$. The corresponding spectral resolution $\Delta\nu$ may thus be obtained as: native 0.5462 MHz [1], 6.33 MHz, 12.67 MHz, and 31.67 MHz. The associated total power and spectroscopic Allan variance is depicted in Fig's. 14, 15.

For standard position switch observations the source is observed for a time t_{on}, after which an off-source t_{off} reference measurement is taken. The duration of the reference measurement is ordinarily $\sqrt{t_{on}}$. To remove the sky, telescope and instrumental baselines, the 'on' source signal is subtracted from the 'off' source signal as part of the calibration routine. For a 'stable' receiver (instrument) position switching is the

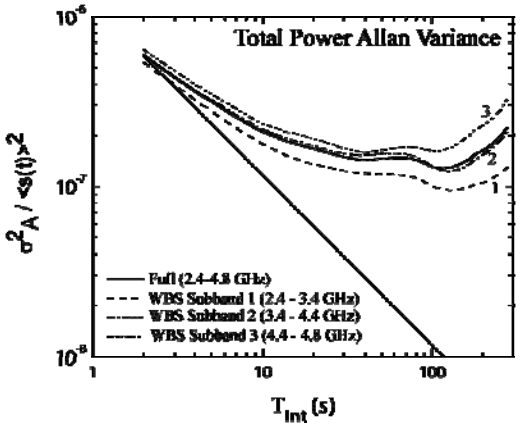

Fig. 14. Total power stability of HIFI HEB mixer band 7 at 1.8970 THz. The Allan time, in a fluctuation noise bandwidth of ~1.8 MHz, is ≤ 8 s.

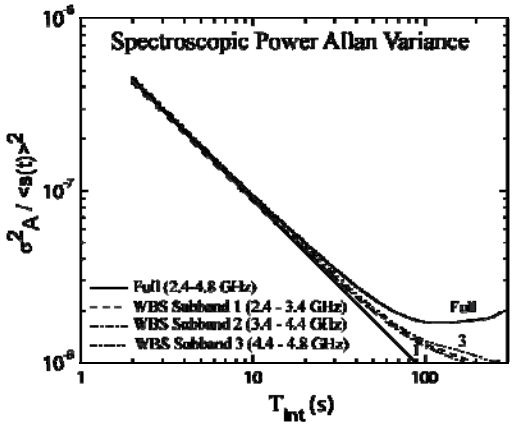

Fig. 15. Spectroscopic stability (text) with a measured stability time of ~80 s.

most efficient method of observing, since a relatively large percentage of the time is spend integrating on the source. Unfortunately for HEB based heterodyne receivers, 'stable'

appears to be a bit of an oxymoron, as evidenced by the total power Allan variance stability measurement of Fig. 14. Typical total power Allan variance times, defined by a $\geq \sqrt{2}$ deviation from the ideal radiometer response, are commonly less than 8 s. The spectroscopic stability may be as large as ~80 s in a 1.8~MHz noise fluctuation bandwidth ($\Delta\upsilon$). In Fig. 12 we show a synthesized position switched spectrum with an 'on-source, slew time, off-source, and again slew time' cycle of 600 s. Total on-source integration time of the entire data set is 2789 s. For the Herschel space observatory the roundtrip slew time is assumed 80 s. In position switch mode, each 600 s cycle thus spends ~ 464 s integrating on the source with the remainder in slew time (80 s) and off-source integration (~56 s). Clearly the 'on-off' switching time is much larger than the spectroscopic stability time of the system. This is evidenced by the extremely poor baseline quality of Fig. 12.

A far better, though less efficient approach, is to symmetrically beam switch at a rate less then the spectroscopic Allan stability time of the system, for example by means of nutating mirror. In Fig. 13 we show the result of a double-beam switch (DBS) 0.25~Hz 'off-on-on-off' slow-chop pattern. Again each cycle is 600 s and includes one position switch cycle as described above. Including the telescope chopping efficiency and position switch overhead, the total integration time is 2829 s.
To estimate T_A^* and compare it to the 1σ noise obtained from the SSB spectrum of Fig. 14, we use Eq. 1 with $\Delta\upsilon$ = 1.8 MHz. Note that this is larger then the intrinsic spectral resolution of the spectrometer (1 GHz/2000 channels).

Given a measured DSB HEB receiver noise temperature (in the lower region of the IF band) of ~ 1600 K, we calculate a theoretical 1σ rms noise level of 64 mK. This compares favorably with the, from the spectrum of Fig. 14 obtained 1σ rms noise level of 68 mK (native resolution). Thus we find that symmetric beam switching on time scales less then the spectroscopic Allan time provides proper baseline quality with rms noise levels in agreement with theory. The penalty.

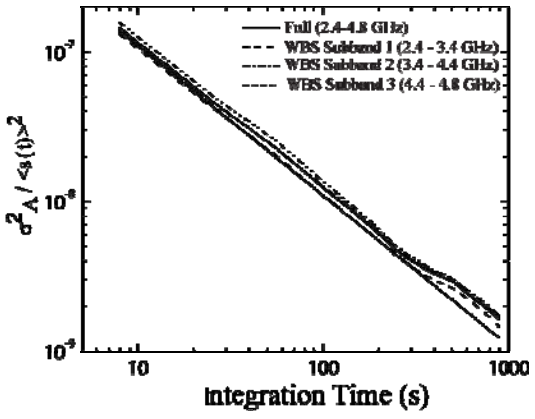

Fig. 16. Measurement of the internal load differential stability on HEB mixer band 7b (1.890 THz, C^+).

of differential beam switch measurements over (ideal) position switch measurements is a factor 2 increase in the rms noise level. The overwhelming benefit is of course the quality of the obtained baseline (spectra). The popular use of DBS techniques (analogous to synchronous detection) comes therefore as no surprise.

In Fig. 16 we shown an example of a Band 7b differential internal load measurement. This information is useful in determining how often secondary loop calibrations need to be taken. In case of the HEB mixers it appears that 900 s (15 min) is adequate

IX Results

The HIFI system stability was measured at a large number of proposed line frequencies, for all 14 LO subbands. A list is compiled in Table II. It is indicative of the HIFI instrument potential, e.g. continuous coverage from 480 GHz – 2 THz.

Tables III – VI list the system and differential stability of the instrument. The first number is the mean, the second value the standard deviation (scatter). Due to space the high resolution spectrometer (HRS) results are not shown here. They amount however to very similar numbers.

To obtain a measure of the achievable sensitivity levels of the instrument, we list in table VII the expected 1σ noise level in a 10 minutes Observation (Eq. 1). Because the instrument is sensitive to both H and V polarizations the actual rms noise will be $\sqrt{2}$ lower then indicted in Table VII, e.g.

$$T_A^* = \frac{\sqrt{2}T_{sys}^{SSB}}{\sqrt{\eta_c \Delta\nu T}} \ . \tag{8}$$

T_A^* is the on source antenna temperature (K).

.Conclusion

We have measured the IF stability, system stability and differential gain stability of the HIFI instrument, to be flown on board the Herschel space satellite. Warm-up time constants for the IF and LO have been established and will be used in the AOT's. Parametric studies have been performed to access the impact of mistuning. This is especially relevant for HIFI since up/down link telemetry is only once a day.

From the measured data we have determined the loss in integration efficiency for each LO subband (14). We have also examined the instrument for platforming, baseband ripple and optimum observing strategy.

Table II. List of frequencies at which the HIFI instrument ILT stability data was taken. The table lists all 14 LO subbands. The frequencies were carefully chosen at astronomically relevant lines (Upper or Lower sideband). In essence, HIFI may be thought of as 14 different heterodyne receivers with associated local oscillator units

B1a (488-552)				B1b (556-628)			
Line	νlo (GHz)[1,2,5]	νline (GHz)	Proposal	Line	νlo (GHz)[1,2]	νline (GHz)	Proposal
O_2	494	487.2	key	H_2O-*ortho*	563	556.936	19
H_2O	494	488.49	3	HDO	566	559.816	1
C	498	492.161	3	NHh_{3}-*ortho*	566	572.498	7
HDO	516	509.329	3	HDO	593	599.927	2
ND	526	522.077	4	D_2O	614	607.35	3
CH	527	532.721	3	H_2O-*ortho*	618	620.701	4
CH	531	536.761	6	HCO^+	618	624.205	1
$H_2{}^{18}O$-*ortho*	542	547.676	18	H2O+	625	631.773	4
$H_2{}^{17}O$-*ortho*	548	552.021	5				
B2a (642-710)				**B2b (724-793)**			
Line	νlo (GHz)[1,2,5]	νline (GHz)	Proposal	Line	νlo (GHz)[1,2]	νline (GHz)	Proposal
H_2O-*para*	640	645.834	2	CS	728	734.32	2
H2O18	652.5	647.198	2	$H_2{}^{18}O$-*ortho*	739.5	745.32	3
H_2O-*ortho*	652.5	658.007	3	H_2O-*ortho*	744	750.572	2
H2O18	667	661.356	2	H_2O-*para*	758	752.033	14
D2H+	686	691.66	6	^{13}CO	765	771.184	2
H2O18	698	692.079	2	HDO	772	766.166	1
SiO	700	694.275	2	O_2	779	773.8	5
O_2	709	715.4	0	x	788	784	x

B3a (807-852)				B3b (866-953)			
Line	νlo (GHz)[1,2,5]	νline (GHz)	Proposal	Line	νlo (GHz)[1,2]	νline (GHz)	Proposal
CO	812	806.652	0	H_2O-*ortho*	869	863.855	0
C	814	809.342	3	^{13}CO	878	881.273	0
$13CH^+$	823	830.131	5	HDO	887	893.639	7
O_2	827	834.1	?	D_2O	902	897.947	3
CH^+	837	835.071	11	H_2O	912	906.206	0
H_2CO	849	855.151	0	H_2O-*para*	922	916.171	2
H_2O-*para*	852	859.859	0	COh	928	921.8	6
				CH_2	x	945.8	6
				NHh_2	946.5	952.542	6
B4a (957-1053)				**B4b (1054-1114)**			
Line	νlo (GHz)[1,2,5]	νline (GHz)	Proposal	Line	νlo (GHz)[1,2]	νline (GHz)	Proposal
NH	968	974.462	13	HCN	1068	1062.983	0
H_2O-*ortho*	974	968.048	3	H_2S	1080	1072.8	0
OH^+	977.8	971.804	9	H2O18	1089.6	1095.627	6
NH	981.2	974.462	13	H_2O-*ortho*	1091.3	1097.364	12
H_3O^+	990.6	984.6	10	$C^{13}Oh$	1095	1101.35	10
H_2O-*para*	995	987.927	18	$H_2{}^{18}O$-*para*	1107	1101.698	18
$H_2{}^{18}O$-*para*	1000.6	994.675	6	H_2O-*para*	1108	1113.343	20
NH^+	1006.5	1012.524	5	H2O+	1110	1115.086	7
CO	1031	1036.912	2				
B5a (1127-1178)				**B5b (1192-1242)**			
Line	νlo (GHz)[1,2,5]	νline (GHz)	Proposal	Line	νlo (GHz)[1,2]	νline (GHz)	Proposal
O_2	1127	1120.715	3	H_2CO	1180	1185	0
H2O+	1145.5	1139.515	2	H_2O-*ortho*	1191	1196.859	0
CO	1145.5	1151.985	13	H_2O-*para*	1202	1207.666	6
H_2O-*ortho*	1159	1153.118	9	NH_3	1209	1214.859	4
H_2O-*ortho*	1164	1158.324	3	HDO	1223	1217.3	10
H_2O-*ortho*	1168	1162.931	3	H_2O-*para*	1223	1228.799	18
H_2O-*para*	1168	1172.448	0	H_2O-*para*	1235	1228.799	18
$H_2{}^{18}O$-*ortho*	1187	1181.394	0	HF	1238	1232.476	7
H_2O-*para*	1202	1207.666	6				
Line	νlo (GHz)[1,2,5]	νline (GHz)	Proposal	x	1581.4	1585	0
H_2O	1444	1440.782	0	CO	1608	1611.793	0
HCl+	1447	1444	0	$H_2{}^{18}O$	1630	1633.484	0
N II	1457.5	1461.134	4	13CH	1643.6	1647.239	4
D_2H^+	1480.2	1476.6	3	H_2O^+	1653	1655.813	9
CH	1480.2	1477.292	0	CH	1652.8	1656.961	8
CO	1493.3	1496.923	3	H_2O-*ortho*	1665.2	1661.011	5
H	1529	1532.6	0	$H_2{}^{17}O$-*ortho*	1665.2	1662.464	3
^{13}CO	1544.5	1540.988	0	H_2O-*ortho*	1667.4	1669.905	21
	1548	1551.6	0	x	1686	1689	2
				x	1692	1689	2
B7a (1700-1800)				**B7b (1720-1905)**			
Line	νlo (GHz)[1,2,5]	νline (GHz)	Proposal	Line	νlo (GHz)[1,2]	νline (GHz)	Proposal
H_2O-*ortho*	1716.5	1713.94	1	CO	1728	1726.602	3
$H_2{}^{18}O$	1723	1719.25	0	H_2O-*ortho*	1801	1797.238	1
H_2O-*ortho*	1720.3	1716.765	8	OH	1834	1837.747	7
CO	1730.2	1726.602	3	CO	1845	1841.346	9
H_2O-*ortho*	1757.2	1753.888	3	H_2O-*ortho*	1872	1867.825	6
^{13}CO	1757.2	1760.486	3	HCl	1872	1876.23	3
H_2O-*para*	1762.5	1766.121	0	CH4	1885.6	1882	3
HCN	1773.5	1769.876	0	$^{13}C^+$	1897	1900.545	21
H_2O-*ortho*	1794	1797.238	0	CH2	1904.1	1907.987	3

Table III. WBS-V Total Power for all 14 mixer Sub-bands.

		Continuum[1-4]		Spectroscopic[1-4]	
		Stability (mean/std)		Stability (mean/std)	
band	Freq. (GHz)	*spec > 5s*		*spec > 75s*	
		Full	Best SubBand	Full	Best SubBand
B1a	488-522	22.4/9.7	35.0/14.2	89.0/41.4	303.9/102.4
B1b	566-628	25.7/12.9	29.7/16.5	87.9/51.1	223.4/84.2
B2a	642-710	17.7/11.8	23.9/11.8	94.5/26.8	324.0/129.8
B2b	724-793	12.7/6.7	15.2/7.4	86.1/41.2	246.1/91.9
B3a	807-852	6.4/3.8	6.8/3.8	21.5/11.4	99.8/53.2
B3b	866-953	13.1/7.5	13.9/8.0	56.1/27.4	192.6/85.0
B4a	980-1040	9.0/4.5	10.6/7.0	37.7/24.9	178.4/109.2
B4b	1065-1115	15.4/3.3	20.8/4.6	46.8/12.3	150.3/52.3
B5a	1127-1178	19.2/5.6	31.1/6.4	105.2/31.6	280.3/105.3
B5b	1192-1242	19.1/5.2	27.4/7.1	83.4/33.3	190.1/56.4
B6a	1430-1570	5.1/3.1	5.4/2.8	13.3/8.4	39.6/33.1
B6b	1580-1690	4.5/2.1	4.9/2.0	20.2/11.0	59.4/30.0
B7a	1692-1845	7.8/6.9	8.2/6.9	21.7/12.7	54.0/23.2
B7b	1719-1908	6.0/4.9	6.0/4.9	13.2/16.1	25.3/31.1

Table IV. WBS-H Total Power for all 14 mixer Sub-bands.

		Continuum[1-4]		Spectroscopic[1-4]	
		Stability (mean/std)		Stability (mean/std)	
band	Freq. (GHz)	*spec > 5s*		*spec > 75s*	
		Full	Best SubBand	Full	Best SubBand
B1a	488-522	17.2/5.0	27.6/11.3	72.8/17.1	210.9/94.9
B1b	566-628	17.0/7.8	21.0/7.2	65.8/24.9	161.6/70.9
B2a	642-710	17.7/4.5	26.9/7.1	68.4/14.1	286.8/129.6
B2b	724-793	12.0/5.8	16.2/8.3	77.8/21.7	243.7/123.4
B3a	807-852	9.1/3.8	9.6/4.7	33.8/19.7	93.4/71.8
B3b	866-953	9.9/3.4	11.5/4.0	68.8/39.8	130.6/67.2
B4a	980-1040	8.0/3.8	10.6/4.9	25.1/17.0	129.3/79.6
B4b	1065-1115	12.4/3.3	14.9/7.3	45.0/15.8	152.7/56.8
B5a	1127-1178	15.6/5.8	26.0/8.3	79.5/17.9	240.2/64.4
B5b	1192-1242	18.7/6.5	27.4/6.0	76.0/13.7	174.6/45.5
B6a	1430-1570	3.8/2.5	4.9/2.8	10.0/5.2	32.8/30.8
B6b	1580-1690	4.8/3.1	5.8/2.8	19.8/8.2	54.8/20.2
B7a	1692-1845	4.0/2.3	4.7/2.1	15.3/6.7	51.1/14.0
B7b	1719-1908	4.2/2.9	4.2/2.9	9.1/11.0	21.4/25.1

Table V. Differential stability WBS-V.

		Diff. Load-Chop[1-4]		Diff. Internal-Load[1-4]		Diff. Load-Switch (DBS)[1]	
		Spectroscopic		Spectroscopic		Spectroscopic	
band	Freq. (GHz)	*spec > 600s*		*spec > 600s*		*spec > 600s*	
		Full	Best SubBand	Full	Best SubBand	Full	Best SubBand
B1a	488-522	> 1800	> 1800	359.4	>=650	>> 2250	>> 2250
B1b	566-628	> 1800	> 1800	279.5	>=650	>> 2250	>> 2250
B2a	642-710	> 1800	> 1800	>=700	>=850	>> 2250	>> 2250
B2b	724-793	> 1800	> 1800	558.9	718.6	>> 2250	>> 2250
B3a	807-852	>> 900	>> 900	103.7	574.2	> 1800	> 1800
B3b	866-953	>> 900	>> 900	>=650	>=850	> 1800	> 1800
B4a	980-1040	>> 900	>> 900	451.8	>=850	>> 2250	>> 2250
B4b	1065-1115	>> 900	>> 900	800.6	>=850	> 2250	> 2250
B5a	1127-1178	>> 900	>> 900	>=850	>=850	> 1800	> 1800
B5b	1192-1242	>> 900	>> 900	>=850	>=850	> 1800	> 1800
B6a	1430-1570	>> 900	>> 900	700	>=800	> 1800	> 1800
B6b	1580-1690	>> 900	>> 900	642	>=800	> 1800	> 1800
B7a	1692-1845	>> 900	>> 900	700	>=800	> 1800	> 1800
B7b	1719-1908	>> 900	>> 900	700	>=800	> 1800	> 1800

Table VI. Differential Stability WBS-H. Internal Load is important for the calibration loop (Fig. 16).

		Diff. Load-Chop[1-4]		Diff. Internal-Load[1-4]		Diff. Load-Switch (DBS)[1]	
		Spectroscopic		Spectroscopic		Spectroscopic	
band	Freq. (GHz)	*spec > 600s*		*spec > 600s*		*spec > 600s*	
		Full	Best SubBand	Full	Best SubBand	Full	Best SubBand
B1a	488-522	> 1800	> 1800	575	>=650	>> 2250	>> 2250
B1b	566-628	> 1800	> 1800	279.5	>=650	>> 2250	>> 2250
B2a	642-710	> 1800	> 1800	717.7	>=850	>> 2250	>> 2250
B2b	724-793	> 1800	> 1800	718.6	814.4	>> 2250	>> 2250
B3a	807-852	>> 900	>> 900	250	300	> 1800	> 1800
B3b	866-953	>> 900	>> 900	>=650	>=850	> 1800	> 1800
B4a	980-1040	>> 900	>> 900	190.2	>=850	>> 2250	>> 2250
B4b	1065-1115	>> 900	>> 900	850	>=850	1870	> 2250
B5a	1127-1178	>> 900	>> 900	>=850	>=850	> 1800	> 1800
B5b	1192-1242	>> 900	>> 900	>=850	>=850	> 1800	> 1800
B6a	1430-1570	>> 900	>> 900	604.5	>=800	> 1800	> 1800
B6b	1580-1690	>> 900	>> 900	700	>=800	> 1800	> 1800
B7a	1692-1845	>> 900	>> 900	700	>=800	> 1800	> 1800
B7b	1719-1908	>> 900	>> 900	700	>=800	> 1800	> 1800

Table VII. Expected System temperatures (no atmosphere) with DBS (on-off) source observations for each subband. On source integration time is 5 minutes

		WBS-V		WBS-H	
		Tsys SSB (K)	RMS (mK) in 600s	Tsys SSB (K)	RMS (mK) in 600s
band	Freq. (GHz)				
		Mean	Mode=Diff	Mean	Mode=Diff
B1a	488-522	144.2	8.3	150	8.7
B1b	566-628	166.8	9.6	180	10.4
B2a	642-710	275.8	15.9	246	14.2
B2b	724-793	325.2	18.8	398	23.0
B3a	807-852	631.6	36.5	209.7	12.1
B3b	866-953	538.6	31.1	934.2	53.9
B4a	980-1040	805.4	46.5	706	40.8
B4b	1065-1115	807	46.6	717.6	41.4
B5a	1127-1178	1918.8	110.8	1588.2	91.7
B5b	1192-1242	2658.8	153.5	2070.2	119.5
B6a	1430-1570	3317.8	191.6	3004.8	173.5
B6b	1580-1690	3133.2	180.9	2855.2	164.8
B7a	1692-1845	3394.8	196.0	2808.4	162.1
B7b	1719-1908	3705.8	214.0	3185.4	183.9

Finally, the information is being fed to the Herschel observation planing too (HSPOT)[16]. This will help make realistic time estimates of the requested astronomical sources.

New observation modes have been defined as an outcome of the ILT: OTF and raster scans with load-chop. Though not the most efficient mode of operation, they will provide the high quality data anticipated.

The next phase is to prepare for the thermal vacuum and performance verification in flight.

ACKNOWLEDGMENT

We like to acknowledge the John Pearson, John Ward, Goutam Chattopadhyay, Erick Schlecht, Imran Mehdi, Alain Maestrini, and Thomas Klein for their excellent work on the HIFI multiplier technology.

REFERENCES

[1] R.Schieder, O. Siebertz, F. Schloeder, C. Gal, J. Stutzki, P. Hartogh, V. Natale, "Wide-Band Spectrometer for HIFI-FIRST" Proc. of ``UV, Optical, and IR Space Telescopes and Instruments, J. B. Breckinridge, P. Jakobsen Eds., SPIE 4013, 313-324, Jul., (2000).

[2] O. Siebertz, "Akusto-optisches Spektrometer mit variabler Auflsung", PhD thesis, University Cologne, (1998).

[3] M. Belgacem, L. Ravera, E. Caux, P. Caïs & A. Cros: "The high resolution versatile digital spectrometer of HIFI-HSO", New Astronomy 9, 43, 2003.

[4] Th. de Graauw, N. Whyborn, E. Caux, T. G. Phillips, J. Stutzki, X Tielens, R. G\"usten, F. P. Helmich, W. Luinge, J. Pearson, P. Roelfsema, R, Schieder, K. Wildeman, and K. Wavelbakker, "The Herschel-Heterodyne Instrument for the Far-Infrared (HIFI)" [Online]. Available: herschel.esac.esa.int/Publ/2006/SPIE2006_HIFI_paper.pdf

[5] [Online]. Available: Herschel; http://sci.esa.int/

[6] J. W. Kooi, J. J. A. Baselmans, A. Baryshev, R. Schieder, M. Hajenius, J. R. Gao, T. M. Klapwijk, B. Voronov, and G. Gol'tsman, "Stability of Heterodyne Terahertz Receivers", Journal of Applied Physics, Vol. 100, 064904, Sep. (2006).

[7] R. Schieder, "Characterization and Measurement of System Stability", SPIE, Vol. 598, Instrumentation for Submillimeter Spectroscopy (1985).

[8] R. Schieder, C. Kramer, "Optimization of Heterodyne Observations using Allan variance Measurements", Astron. Astrophys, Vol. 373, 746-756 (2001).

[9] J.W. Kooi, G. Chattopadhyay, M. Thielman, T.G. Phillips, and R. Schieder, "Noise Stability of SIS Receivers", Int. J. IR and MM Waves}, Vol. 21, No. 5, May, (2000).

[10] V. Ossenkopf, "The stability of spectroscopic instruments: a unified Allan variance computation scheme", A & A, Vol. 479, 915-926 (2008).

[11] D. W. Allan, "Statistics of Atomic Frequency Standards", Proc. IEEE, Vol. 54, No. 2, pp 221-230, (1969).

[12] A. Cherednichenko, V. Drakinskiy, T. berg, P. Khosropanah, and E. Kollberg, "Hot-electron bolometer terahertz mixers for the Herschel Space Observatory", Rev. Sci. Instrum., Vol. 79, 034501(2008).

[13] J. W. Kooi, J. J. A. Baselmans, J. R. Gao, T. M. Klapwijk, M. Hajenius, P. Dieleman, A. Baryshev, "IF Impedance and Mixer Gain of NbN Hot-Electron Bolometers", Journal of Applied Physics, Vol. 101, 044511, Feb. (2007)

[14] N. Erickson, "AM Noise in Drives for Frequency Multiplied Local Oscilators", Proc 15th Int. Symp. on Space Terahertz technology Northampton, MA, (2004), pp. 135-142.

[15] M. Hajenius, J. J. A. Baselmans, A. Baryshev, J. R. Gao, T. M. Klapwijk, J. W. Kooi, W. Jellema, and Z. Q. Yang, "Full characterization and analyses of a THz heterodyne receiver based on a NbN hot electron bolometer", J. Appl. Phys., Vol. 100, 074507 (2006).

[16] [Online]. Available: http://herschel.esac.esa.int/ao_kp_tools.shtml/

Flight Attenuators for the HIFI Local Oscillator Bands

Willem Jellema[1,2*], Marcel Bruijn[3], Jan-Joost Lankwarden[3], Marcel Ridder[3], Herman Jacobs[3], Wolfgang Wild[1,2], and Stafford Withington[4]

[1]*SRON Netherlands Institute for Space Research, Groningen, the Netherlands*

[2]*University of Groningen, Kapteyn Astronomical Institute, Groningen, the Netherlands*

[3]*SRON Netherlands Institute for Space Research,Utrecht, the Netherlands*

[4]*Cavendish Laboratory, University of Cambridge, JJ Thomson Avenue, Cambridge CB3 0HE, United Kingdom*

* Contact: W.Jellema@sron.nl, phone +31-50-363 4058

***Abstract*— During the flight instrument level tests of HIFI it became clear that the instrument performance suffered from LO related instabilities. Because the actual LO power requirements of the flight mixers appeared to be an order of magnitude smaller than specified, the LO subsystem was forced to be operated outside its rated and stable operating regime. In order to push the LO power amplifiers back into normal and saturated operation, broadband optical attenuation in all LO bands of around 3 dB up to 18 dB appeared necessary.**

In this paper we present the design and development of broadband optical attenuators from first ideas and principles, demonstration, development to space-qualification, flight production, performance characterization and post-delivery to Herschel-HIFI. The as-built attenuators are based on thin Ta films on robust alumina substrates and in a few cases combined with an AR-coating based on a polyimide spinning process. We conclude by presenting the attenuator flight performance, which can be tuned within a few tenths of a dB from target, and essentially provide a flat frequency response from 500 GHz up to more than 2 THz at cryogenic conditions.

I. Introduction

At the HIFI Instrument Level Test review (March 13, 2007) system instabilities were reported by J. Kooi [1, 2]. The reported system stability in terms of total power and spectroscopic Allan variance times would seriously affect the scientific observing capabilities of HIFI. This non-conformance situation was followed-up by a detailed investigation by Güsten et al [3]. In their report presented at the HIFI stability meeting on April 3, 2007 it was concluded that a significant contribution to the stability problem could be traced back to the way in which the HIFI Local Oscillators had to be operated so far. It turned out that the input power stage of the LO multiplier chain could not be operated in its rated and stable operating regime. The power amplifiers did not operate in fully saturated mode throughout the HIFI frequency range and inevitably stability problems showed up [4]. The reason behind this unwanted mode of operation was the requirement of continuous frequency coverage. Whereas in most of the HIFI frequency range the required LO power for the mixers was an order of magnitude lower than available, certain localized areas were known to be problematic in terms of available LO output power due to matching problems inside the multiplier chains. An example of this situation is shown for HIFI band 4 in Fig. 1 where we plot the maximum available LO power measured as a direct detection mixer current.

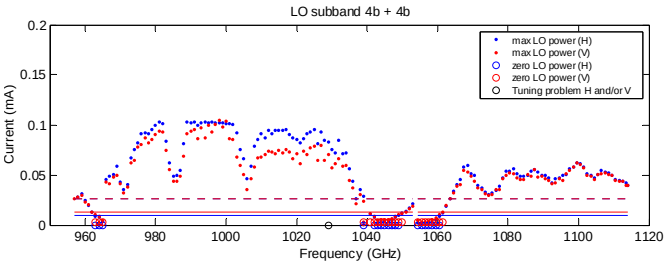

Fig. 1 Maximum available LO power in band 4 (SIS) measured as a direct detection mixer current. The red and blue traces represent the H and V polarizations, the dashed line the optimum mixer current and the solid lines the minimum required currents for H and V resp.

In order to meet the optimum LO power level for the mixers the power amplifiers were forced to operate at very low drain voltage (V_d) settings. First of all this operating point creates a strong dependence between the LO power P_{LO} and V_d. Because of this large $\delta P_{LO}/\delta V_d$ ratio the LO power becomes susceptible to bias noise, stability and digital resolution. Since the gain and noise stability of the mixers, especially for the HEB mixers, depend on the LO output power stability, operation near saturated output power settings is favoured. Secondly, operating a power amplifier without significant gain compression can present receiver excess noise because of AM noise sidebands around the LO carrier [4]. Finally the amplifier might become intrinsically instable at very low drain voltage and problems with stabilization times and hysteresis might occur. Not before evaluation of available ILT test results

at receiver level a system level trade-off had been made to tackle these issues.

A possible recovery for the situation observed for HIFI was proposed by insertion of free-space optical attenuation at the output of the LO. The shift of operating point of the LO system is graphically depicted in Fig. 2. In this diagram the dependence of mixer current versus drain voltage (controlling the input power into the multiplier chain) is shown. By increasing the drain voltages on the power amplifiers the system is put back into saturated output power mode. The mixer current is brought back to a nominal level by the addition of optical attenuation to compensate for excess LO power at higher drain voltages. An additional advantage is the reduction of LO standing waves by increasing the round-trip loss in the LO path [5].

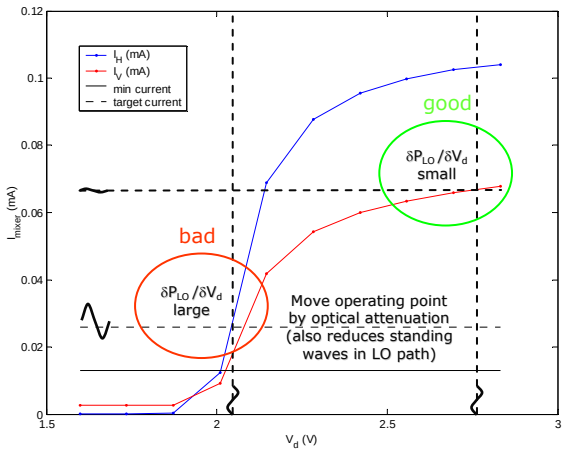

Fig. 2 Schematic diagram illustrating the recovery of receiver stability by bringing the power amplifier back into stable and saturated output power mode by the introduction of optical attenuation.

The tests carried out by Güsten et al confirmed the hypothesis that instable operation of the LO contributes to the receiver stability problem. In [1] Güsten et al show that there exists a distinct transition into stable operating conditions as attenuation and drain voltage of the power amplifier are increased. Now the possible recovery option had been identified, a development and production program for flight attenuators was required.

In this paper we present the results collected to date regarding the development and production of flight attenuators for the HIFI Local Oscillator bands. In this paper we first discuss the technical requirements. Next we present the selected concept, the principle of operation and the implementation of the device in the optical-mechanical design. We present the detailed design of the attenuator device and summarize the characterisation program. We conclude the paper by presenting the production results and measured performance.

II. Technical Requirements

The general technical requirements that the flight attenuators need to satisfy can be formulated as:

1. Each mixer band shall have its own specific level of attenuation.
2. The range of attenuator values that can be spanned by design shall be -3 to -18 dB
3. The level of attenuation shall be controlled within an accuracy of ±0.5 dB
4. The attenuator shall have broadband frequency independent performance with a bandwidth of 200-300 GHz.
5. The attenuator shall operate at an ambient temperature of 130K. The attenuator must withstand temperatures in the range from 100K to 300ºC.
6. The attenuator shall be a passive device, no mechanical or electrical control is allowed
7. The attenuator must withstand the acoustic vibration levels applicable to the Herschel satellite
8. The attenuator must be placed external to the Focal Plane Unit outside the Herschel cryostat, and outside of the Local Oscillator Unit box, and be integrated into the baffle assembly containing the de-icing heaters in order to enable replacement if necessary.

Requirements 1 to 4 are driven by the ILT investigations. Requirements 5 to 8 are driven by the thermal and mechanical environment in which the attenuators have to operate. The programmatic constraints for the development and production were tight, a prototype was needed within 2 months for the last phase of ILT prior to delivery, and flight delivery was expected to take place within 3 months.

III. Selected Concept

Initial investigations into the effect of optical attenuation on receiver stability were done at spot frequencies making use of ordinary means of attenuation available in a lab environment. For these tests we used e.g. sandpaper of different granulations, cleanroom paper, black poly-ethylene foils, slabs of Perspex and wire grids. Clearly not all of these solutions can be readily transferred to space application. In order to explore a broad range of possible solutions we structure the various means of optical attenuation, restricted by potential for space application, on the basis of their underlying physical principle:

1. Attenuation by absorption
2. Attenuation by division of polarization
3. Attenuation by reflection

Solutions falling in the 1st category, such as high loss tangent dielectrics and carbon loaded polymers, do not offer a feasible implementation. First of all relatively thick slabs of material are required to get attenuation values as large as -18 dB. Moreover anti-reflection coatings are

required to get the associated high frequency Fabry-Perot ripple under control. The frequency dependence is also a problem in terms of a strong slope in the attenuation characteristic across a 200 GHz bandwidth. For a typical attenuator case of -10 dB, the slope can easily become 0.02 dB/GHz. This would correspond to a difference in attenuation of 8 dB between the extremes of the bands we are interested in. Polymers and plastics usually contain large fractions of water contributing to the realized attenuation. As such the attenuation is difficult to control and measure in normal lab conditions. Finally, the use of plastics is not always compatible with the thermal requirements in II.5.

Solutions in the 2nd category are also ruled out. Although attenuation by division of polarization, e.g. through wire or planar grids, is a generally accepted means of attenuating a THz signal, it is polarization dependent. Since each LO band is divided up in two subbands, having orthogonal polarization, which are combined through a beam combining grid into a single beam, this solution would only work subband-wise and significantly upset the ratio of delivered power to the H and V polarization channels in each mixer band.

We find that solutions falling in the 3rd category appear most promising. Polarization independent devices such as frequency selective surfaces still present a problem in terms of frequency dependence, but partially reflecting surfaces based on lossy thin films are ideal in view of our application. This solution is based on reflecting most of the power (with some residual absorption) at a lossy metallic film and dumping the reflected power in a load. Space-qualified absorbing coatings for such a load are available for and already applied in HIFI [6], The general application of lossy thin films as THz attenuators assumes very thin substrates (<< λ/20) to safeguard frequency independent operation and to avoid Fabry-Perot resonances within the substrate over the required frequency band. This is clearly not compatible with our environmental constraints formulated in II.5 and II.7. This complication can be overcome however by a dual-layer design which we will present in the next section of this paper.

IV. Principle of Operation

The principle of operation of the selected attenuator option discussed in the previous section is based on partial reflection from and some residual absorption in a lossy metallic film. The lossy film presents an effective surface resistance R_s and its performance can be simply calculated through a transmission line model consisting only of a shunt admittance $1/R_s$ matched to the free space impedance [7]. As mentioned earlier the general application consists of a thin metallic film deposited on thin dielectric substrate for mechanical support. An example of the performance of such a device is shown in Fig 3. In this figure it can be seen that the transmittance is -10 dB across the full HIFI frequency range (500 – 1900 GHz). The maximum absorption in a single film is 0.5 or -3 dB, more attenuation is only possible by more reflection and therefore a larger mismatch between the film and free-space.

It is theoretically possible to compose a low-reflectance attenuator by dividing the attenuation over multiple films. An example of such a device is given in Fig. 4. Here we present a 16 layer device with films of 2.6 kΩ/□ on 3 µm Mylar substrates separated by $\lambda_0/4$. The frequency dependence becomes more problematic in the few layer limit, and even with a 16 layer device, which is difficult to manufacture, bandwidth is limited and hard to extend to higher frequencies, also in terms of manufacturing tolerances.

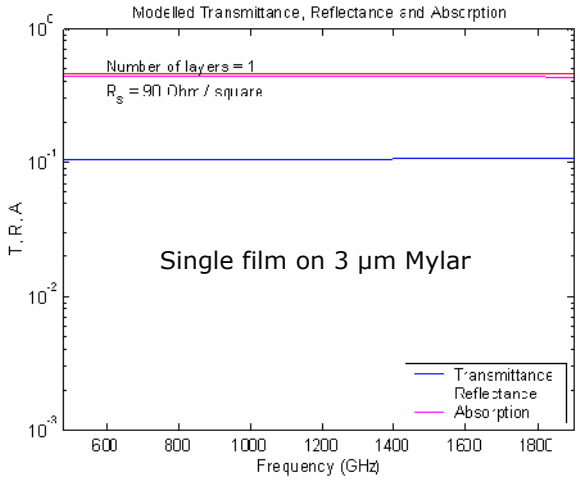

Fig. 3 Frequency independent -10 dB attenuator based on a single film having sheet resistance R_s = 90 Ω/□ supported by a 3 µm Mylar substrate.

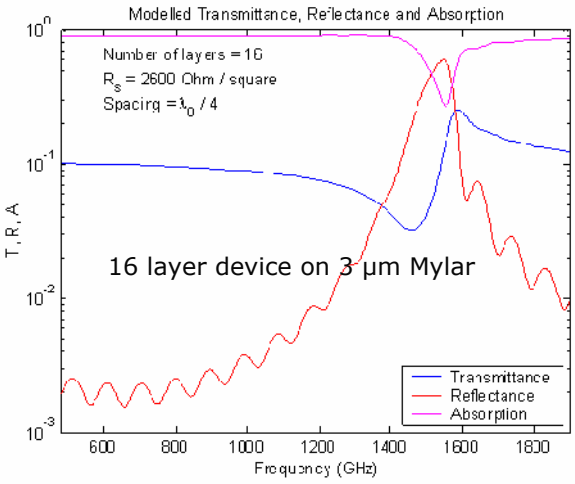

Fig. 4 Multi-layer device with low reflectance composed of 16 lossy films carried on Mylar substrates separated by a quarter-wavelength.

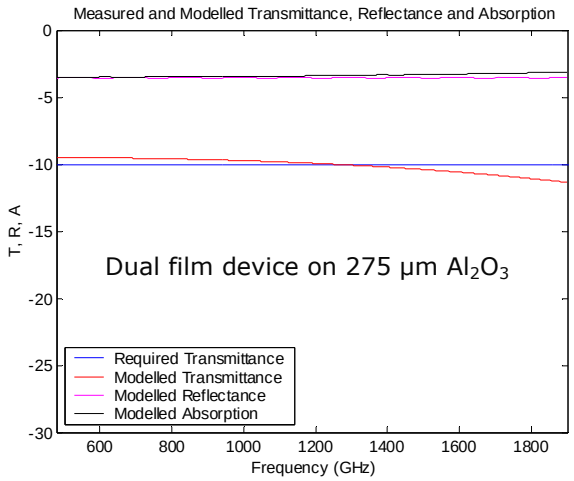

Fig. 5 Dual film device on a relatively thick Al2O3 substrate providing broad-band nearly frequency independent performance.

We select a dual film design in which one film in shunt with free space is impedance matched to the substrate. We refer to this as an impedance matched film. This condition is only met when the sheet resistance R_s of the film equals $120\pi / (\sqrt{\varepsilon} - 1)$, where ε is the dielectric constant of the substrate material. When this condition is met there is zero internal reflection at one face of the Fabry-Perot etalon formed within the substrate. This condition is sufficient to eliminate the Fabry-Perot effect in the substrate and allow for broadband operation only limited by the loss tangent and thickness of the dielectric substrate. Given the impedance matched film, the second layer is chosen in such a way that the additional reflection yields the net total attenuation required. This design is limited in attenuation to -8 dB (reflection and absorption by a single impedance matched film). Between 0 and -8 dB the impedance matched condition can not be met and consequently an AR coating is required to reduce the Fabry-Perot effect. From a mechanical and thermal point of view we select a relatively thick substrate of 0.275 mm of alumina (amorphous sapphire, Al_2O_3). For this material we have an in-house Tantalum sputtering process available and it is compliant with the thermal requirement II.5. The material is also compatible with the application of a spin-coated polyimide film as an AR coating. Finally alumina is considered to be a very stable and safe material for space application. An example of a -10 dB attenuator dual-film design is given in Fig. 5. It can be recognized that the Fabry-Perot resonance in the substrate is completely absent, whereas the dielectric loss in the substrate limits the frequency independence.

V. Optical-Mechanical Layout

The implementation of the dual-film device described before in the optical-mechanical configuration of the LO path is shown in Fig. 6. In this figure the device is tilted by 30º to provide an optical path for the reflected power into the beamdumps. The beamdumps are made of SiC grains embedded in a Stycast glue layer which is qualified for application on Aluminium. Note that the 30º tilt is a compromise between the volume and space required and a small angle of incidence required to limit polarization dependence of this device. As we explain later the residual polarization effect caused by unequal transmission for the TE and TM cases is used to correct for intrinsic imbalance between the H and V polarization mixers in HIFI by rotation of the device around the optical axis.

The devices are passivated by a SiO2 coating and then laser-cut to fit within an attenuator holder assembly as shown in Fig. 7. The attenuator holder consists of two Al parts with spiral spring gaskets mounted in three localized slots distributed over the flange. The lids of the laser-cut devices are clamped in between the spiral spring gaskets when the second part of the attenuator holder is mounted on the first. The individual attenuator holders can be mounted on the LO interface plate as shown in Fig. 8. The rotation of individual holders is realized by a periodic hole pattern of 5º in the flange.

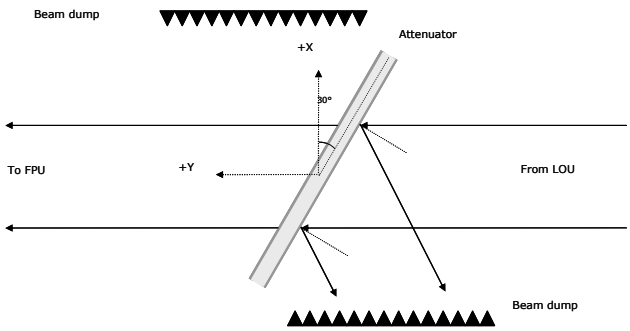

Fig. 6 Dual film attenuator device tilted by 30 deg and surrounded by SiC-Stycast absorber material as a dump.

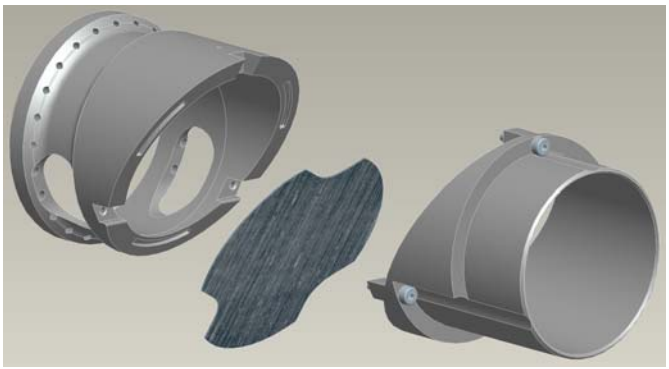

Fig, 7 Laser-cut dual film attenuator clamped in between two Al holder parts.

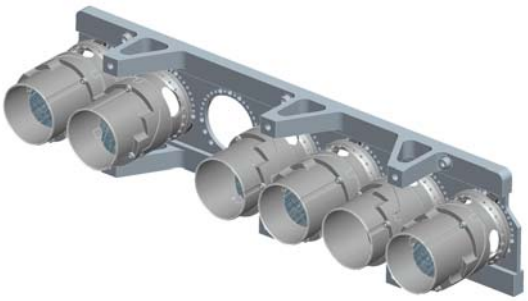

Fig. 8 Attenuator holders mounted on LO interface plate.

VI. Detailed attenuator design

The individual attenuation required in each mixer band is carefully determined in the ILT configuration by measuring the available LO power distribution across the band versus the drain voltage, a characterization test preceding the T_{sys} survey reported in [8], and system stability measurements reported in [1, 2]. For verification in ILT we produce a specific test set of attenuators. For flight we also include the expected differences in LO losses between the ILT and spacecraft configurations by individual measurements of the cryostat windows, heat filters, test attenuators and include a margin in a system engineering budget.

The flight attenuation required in each band, the attenuator type and the design parameters are listed in Table 1. For the SIS mixers band 1 to 4 attenuation in the range from -8 to -18 dB is required, whereas the HEB mixers in band 6 and 7 require less attenuation in the range from -3 to -8 dB. Although we target for specific attenuator values, we decide to manufacture attenuator ranges, in 1 dB steps for band 1 to 4 and in 0.5 dB steps for band 6 and 7, to cope with production tolerances and to allow for potential future adjustment. Note that band 5 does not require attenuation. The LO chain for band 5 is already operated at maximum drain voltage and there is no excess LO power.

TABLE III
Attenuator values and parameters in each band

Band	Type	Target	$R_s(1)$	$R_s(2)$	t_{AR}	Angle
1	dual	-12.2 dB	181 Ω/□	93 Ω/□	-	-35º
2	dual	-11.4 dB	181 Ω/□	112 Ω/□	-	+60º
3	dual	-9.0 dB	181 Ω/□	235 Ω/□	-	-45º
4	dual	-15.7 dB	181 Ω/□	48 Ω/□	-	+40º
6	AR	-4.5 dB	257 Ω/□	-	27 µm	0º
7	AR	-3.9 dB	332 Ω/□	-	24 µm	-45º

For band 1 to 4 we adapt a dual-film design. The first Ta layer is a 181 Ω/□ impedance matched film. The second Ta layer depends on the total attenuation required and is a free parameter to adjust. The Al_2O_3 substrates are nominally 275 µm thick and taken from the same batch on which we also calibrate the sheet resistance of Ta versus deposition parameters. Note that the targets and parameters listed apply to ambient conditions in flight. This means that we translate 130K material properties to their equivalents at room-temperature. We come back to this in the next section on characterization results.

For band 6 and 7 the range of attenuation is not compatible with a dual-film design. Here we apply a single high resistivity film and require an AR coating at the other interface. The index of refraction of the alumina substrates we use is 2.09 at 300K. An AR coating of optimum thickness should therefore have an index of refraction of 1.76. Our investigation into materials that are both compliant with the requirements presented in section II and comply with the required index of refraction for the AR coating, shows that Kapton™ or more general polyimide (abbreviated by PI in this paper) provides the closest match. We use an in-house developed process, involving several spin-coating and curing steps, to deposit a PI film of the required thickness on the substrates. The applied AR coatings have an index of refraction of 1.79 and can be controlled at submicron precision.

For both types of attenuator, the dual-film and AR-coated versions, we finally passivate the Ta films by a 0.5 µm SiO_2 passivation layer to avoid ageing of the films.

Using the attenuator test set in the ILT configuration we also determine the polarization dependence empirically by measuring the mixer balance or H/V ratio to ensure balanced delivery of LO power to the mixers. The H/V ratio, which we define as $(I_H - I_{0H}) / (I_V - I_{0V})$, where I_0 represent the current without applied LO, is measured as function of rotation angle of the 30º tilted attenuator. An example of the relative gain of mixer current H, being a measure for the coupled LO power, for a given angle of rotation is shown in Fig. 9. In Fig. 9 the relative gain with respect to zero rotation is shown for mixer H and V for LO subbands 2a and 2b in HIFI band 2 at three different frequencies in each LO subband. We use these band dependent empirically determined relative gain characteristics together with the measured available LO power at zero degree rotation with attenuator to calculate the optimum rotation angle for the attenuator. An example of such a calculation is shown in Fig. 10 where the optimized band 1 case is shown. It is clear that the introduction of attenuators allows us to correct for any intrinsic imbalance in the H/V ratio, either due to intrinsic mixer unit differences, alignment differences and/or polarization interface errors. The measured difference in attenuation for the TE and TM cases differs by about 1.5 dB and we find that we can tune the H/V ratio by ±1 dB. The rotation angles that result from this exercise and are applicable for flight are also listed in Table I.

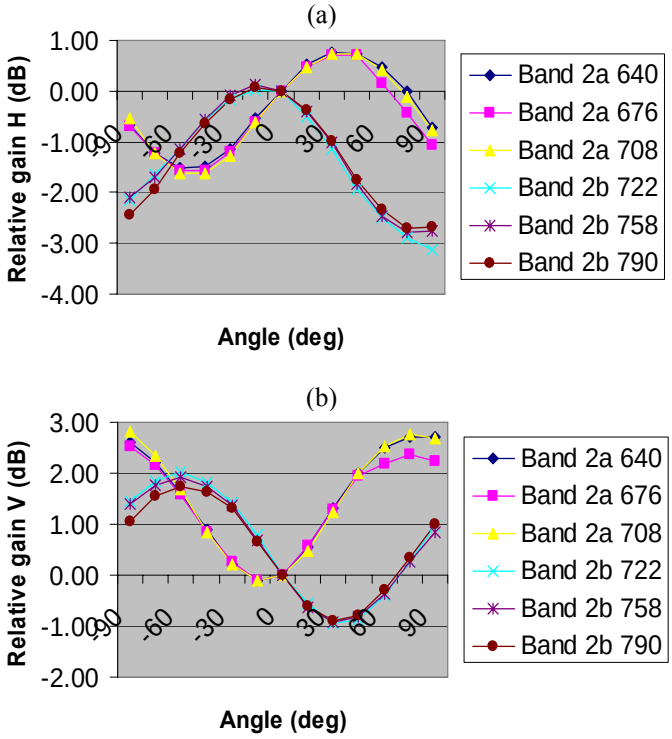

Fig. 9 Relative gain in coupled LO power for mixer H and V as function of rotation around the optical axis for LO subband a and b in HIFI band 2.

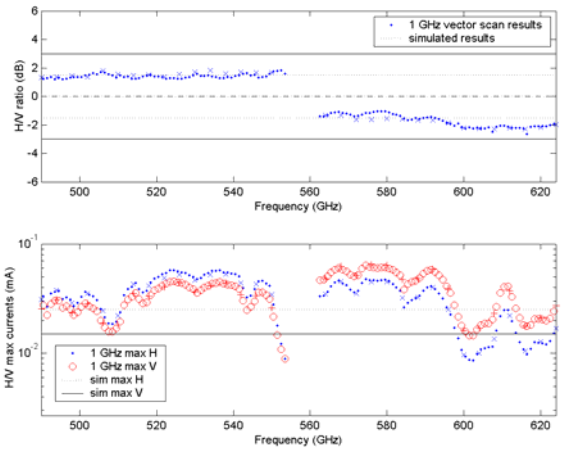

Fig. 10 Measured and simulated H/V ratio and LO power distribution in HIFI band 1. The H/V ratio is optimized by rotation of the attenuators around the optical axis.

VII. Characterisation Program

In this section we summarize the elements of the characterisation program carried out for flight production. The results we summarize both include development tests as well as performance tests on built devices. We do not pretend to be complete here, we will report our final results separately in a journal paper, but like to give the reader an overview of design issues that came across.

A. *Polarization effects*

Since we use the attenuator with an angle of incidence of 30º, there are polarization effects related to differences in the TE and TM reflection coefficients. We include these effects in our modelling and characterisation approach. For transmission and reflection measurements we use a polarized Fourier-Transform Spectroscopy setup in which the samples can be measured at angles of incidence of 0º resp 30º in forward and reverse transmission and reflection. We also measure the state of polarization at the attenuator output by means of measuring the single frequency response in the long-wavelength limit at 625 µm for a 180º scan of an analyser grid in front of a polarized Golay cell as function of angle of incidence of a 45º linearly polarized input beam. We find that for an angle of incidence of 30º the attenuation imbalance for the TE and TM cases is of order 1.5 dB, which is in very good quantitative agreement with the results shown in Fig. 9 and 10.

B. *Calibration of Al_2O_3 substrates*

The Al_2O_3 substrates are subject to an extensive calibration campaign. We determine the index of refraction and loss tangent on the basis of model fits to the FTS data obtained for samples of various thickness. The model fit is constrained by precise measurements of the mechanical thickness. We perform measurements and model fits both at room-temperature conditions and as function of temperature and we resolve the complex dielectric constant as function of frequency by assuming a power-law dependence for the loss tangent. Finally we differentiate against the batch of material used. We order large wafer sets to ensure that production of attenuator sets is always carried out on substrates taken from the same batch. A typical example for a specific batch of substrates is shown in Fig. 11. In this figure the temperature dependence of the loss tangent as function of frequency is shown. This data is used in the design model for the attenuators.

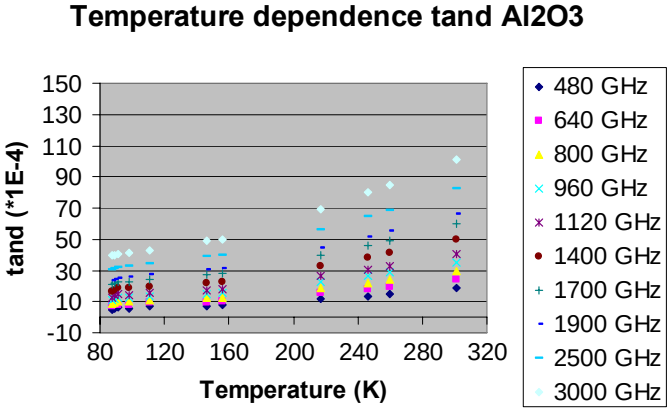

Fig. 11 Loss tangent measurements of Al_2O_3 versus temperature.

C. Sheet resistance calibration of Ta films

The production of the films is based on an available process at SRON. We deposit Ta films on Al_2O_3 substrates by RF magnetron sputtering. We make use of an existing calibration of Ta films on polished Si substrates. This calibration establishes a relation between the deposited layer thickness in nm and the RF magnetron power, pressure, exposure time, number of samples in the deposition chamber and the detailed sputtering sequence. Although the translation of measured layer thicknesses in nm on polished Si wafers is awkward and artificial when dealing with unpolished amorphous Al2O3 substrates, we nevertheless use the concept of thickness as an initial parameter to control the process. For each batch of wafers we initially define test structures for DC and RF testing. DC testing is done on Hall bar structures photo-lithographically etched on diced substrates. RF testing is done on 1"x1" diced substrates which are tested in the FTS setup described in A. The RF sheet resistance is determined through a model fit. The DC sheet resistance is determined through a four-point resistivity measurement. Both DC and RF sheet resistances are measured for a range of film thicknesses ranging from 3 to 100 nm at room-temperature and as function of temperature down to 80K.

An example of a room-temperature calibration of R_s versus film thickness t is shown in Fig. 12. The dashed lines indicated the 2σ error bounds reflecting the production tolerances. The data is fitted to an empirical sheet resistance dependence given by $R_s = R_0 / (t - t_0)$, i.e. we assume that there exists an intrinsic oxide layer. This model nicely fits to the data and we find that both the DC and RF sheet resistance agree fairly well within the production tolerances. We find R_0 typically lies in between 2 and 6 kΩnm/□ for substrates taken from different batches. From this we conclude we can use DC diagnostics to control the process and preselect devices.

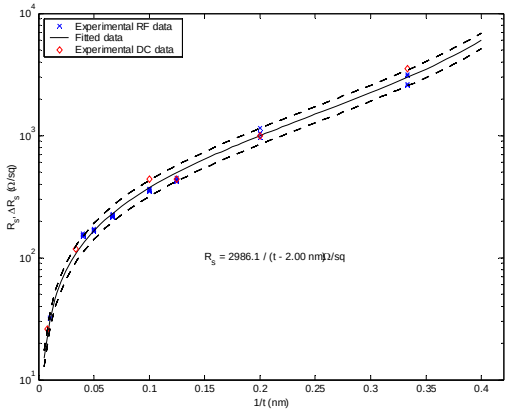

Fig. 12 Example of measured DC and RF sheet resistance as function of film thickness at room-temperature.

The measured dependence of the sheet resistance on temperature is shown in Fig. 13. In this figure it can be seen that the residual resistivity ratio (RRR) is in general smaller than 1, which implies that the resistivity goes up with temperature and attenuation becomes less due to reduced reflection. This is most visible for the thinner films having R_s values beyond 200 Ω/□. The thicker films do not show this behaviour and have little temperature dependence. We empirically determine the fractional change of resistance as function of temperature and initial resistance at room-temperature and take this calibration into account in the design. For the attenuator designs presented in Table I the difference in attenuation between room-temperature and 130K is typically within 0.4 - 0.6 dB.

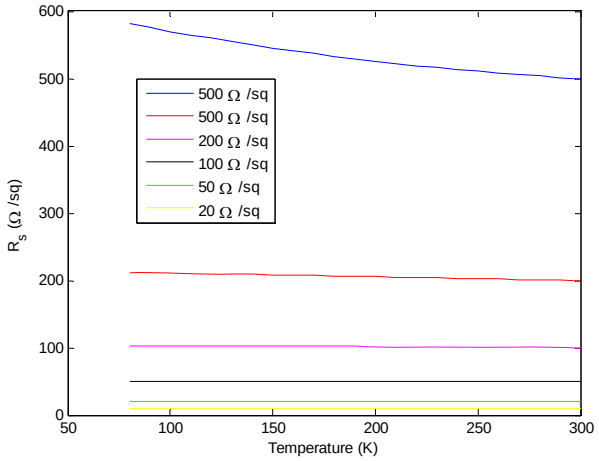

FIG. 13 RELATION BETWEEN SHEET RESISTANCE AND TEMPERATURE.

D. Polyimide Anti-Reflection coating

The polyimide AR coating is applied via a spin-coated process. In this process a polyimide solution is spun on a substrate and then cured. We get best results by building up the total layer thickness by subsequently depositing thinner layers spun at higher spinning rates. The calibration of this process involves measurement of layer thickness after final curing step by a mechanical profiler as function of the curing time and temperature as well as spinning rate. We finally obtain submicron precision in controlling the layer thickness. We also calibrate the dielectric properties as function of frequency and temperature using the FTS procedure described in VII.B for a set of samples with different AR coating thicknesses. An example of measurement results we obtain for a 46 µm thick PI film as function of temperature is shown in Fig. 13. The dielectric losses decrease with decreasing temperature which we taken into account in the design. Using these data and the sheet resistance calibration we design the attenuator sets as shown for example in Fig. 14.

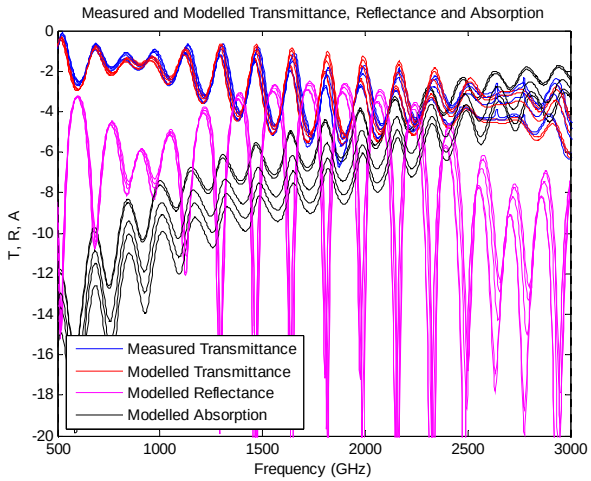

Fig. 13 Example of cryogenic PI film transmission measurements from which we determine the dielectric constant.

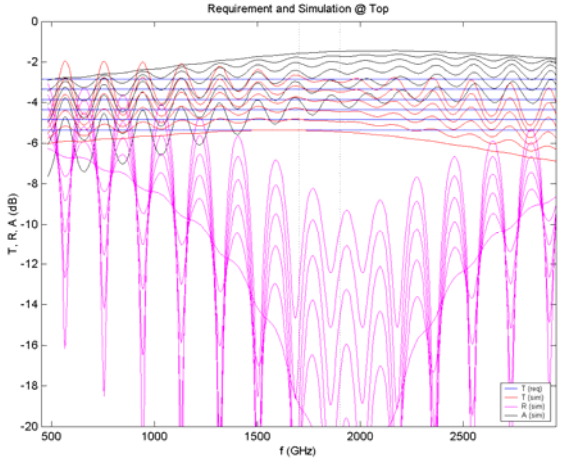

Fig. 14 Attenuator set design for band 7. The PI film thickness is tuned to 1.8 THz and the sheet resistance adjusted to obtain offsets of 0.5 dB in attenuation.

E. SiO_2 passivation process

Accelerated life-time tests on bare Ta films at elevated substrate temperatures clearly indicate thermally activated oxidation. We therefore decide to passivate the devices with a 0.5 µm SiO_2 passivation layer. Since the final device is subject to a laser-cut procedure we apply this process immediately after Ta film deposition and in band 6 and 7 before the curing step of the AR coating. We perform dedicated endurance tests as function of time, temperature and relative humidity and conclude that the sheet resistance after passivation and ageing tests remains stable within the accuracy of the experimental facilities. An example of a long endurance test at elevated temperature and humidity is shown in Fig. 15. We do not expect any problems by ageing. In the unlikely event of oxidation prior to launch we only expect an increase of sheet resistance and therefore less attenuation which will not critically affect the HIFI performance in terms of frequency coverage. We also positively confirm that attenuator performance is not affected by the laser-cutting procedure.

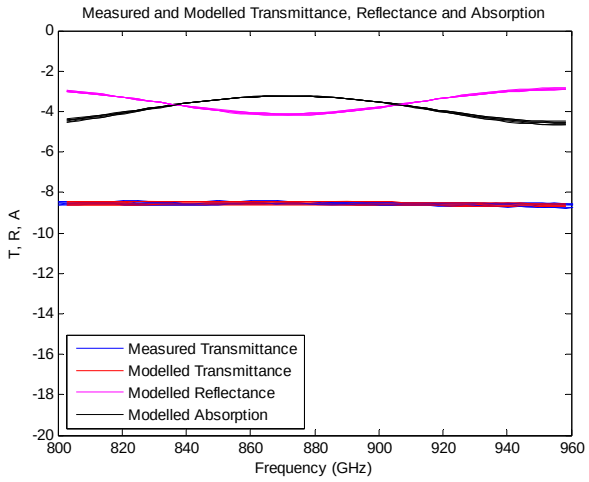

Fig. 15 Endurance test results showing that repeated measurement of sample transmission remains constant over periods of months even when kept at elevated temperatures and high relative humidity.

F. PRODUCTION RESULTS AND FINAL PERFORMANCE

In three production runs for band 1 to 4 and two runs for band 6 and 7 we produce 34 potential FM devices for band 1 to 4 and 16 for band 6 and 7. The band 1 to 4 set contains attenuators spanning a range from -7 to -19 dB in roughly 1 dB steps. In band 6 to 7 we achieve a set ranging from -3.5 to -5.0 dB in roughly 0.5 dB steps. Examples of both types of attenuator are given in Fig. 16 resp. 17. In Fig. 18 we also show the attenuator holders.

In Table II we list the flight and spare attenuator values referenced against the target. Note that the P, Q and R stand for a particular substrate batch. We conclude that the measured performance is fully compliant with the target values within the applicable tolerance. Two examples of actual flight attenuator performance are given in Fig. 19 and 20. for a dual-film and AR-coated type respectively.

In Fig. 19 we show the measured performance of P-031 at 300K in blue and the projected performance at 130K in red. The measured transmission is essentially flat across the 500 to 1600 GHz band and within tolerance, indicated by the blue dashed lines ±0.5 dB around the target value.

In Fig. 20 the performance of Q-032A is shown. At 1.8 THz it becomes clear that the temperature dependence of dielectric losses in substrate and AR coating need to be taken into account reflected in a difference of almost 1 dB between room-temperature and 130K performance. Furthermore note that the AR coating is properly tuned with a flat region within the 1.7 – 1.9 THz band indicated by the vertical dashed lines. The centre frequency of the AR coating can also be recognized from the dip in the reflectance (purple traces). The projected performance at 130K is compliant with the requirement and falls within the tolerance of ±0.5 dB.

The FS devices show nearly identical performance. For band 1 to 4 they correspond to different copies of the same design at different substrates whereas in band 6 and 7 both FM and FS samples are taken from a single larger wafer and are consequently identical within the spread across the wafer.

Fig. 16 Example of a flight attenuator as applied in band 1 to 4.

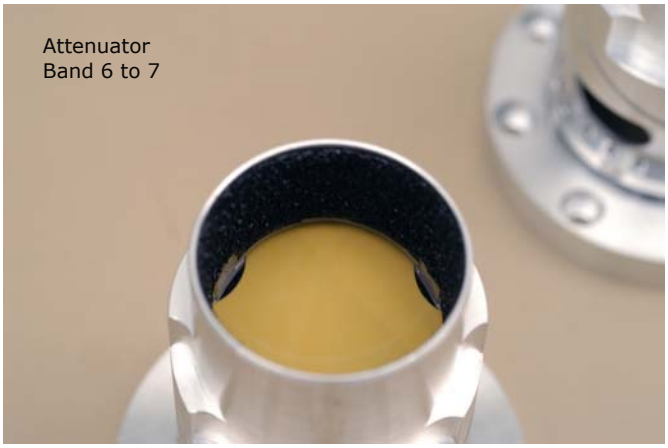

Fig. 17 Example of a flight attenuator as produced for band 6 and 7.

TABLE II
FLIGHT AND SPARE ATTENUATOR VALUES VERSUS TARGET IN DECIBEL.

Band	Type	Target	FM	Value	FS	Value
1	dual	-12.2	P-033	-12.2	P-034	-12.2
2	dual	-11.4	P-031	-11.3	P-032	-11.5
3	dual	-9.0	P-020	-8.6	P-019	-8.5
4	dual	-15.7	R-031	-15.7	R-035	-15.6
6	AR	-4.5	Q-033A	-4.7	Q-033B	-4.7
7	AR	-3.9	Q-032A	-4.1	Q-032B	-4.1

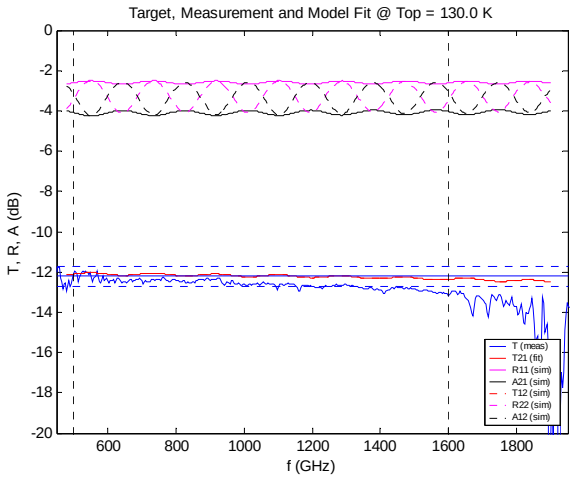

Fig. 19 Measured transmission (blue) and model fit (red) for sample P-031 to be applied in band 2. The horizontal dashed lines indicate the allowed tolerance relative to the target (solid central line).

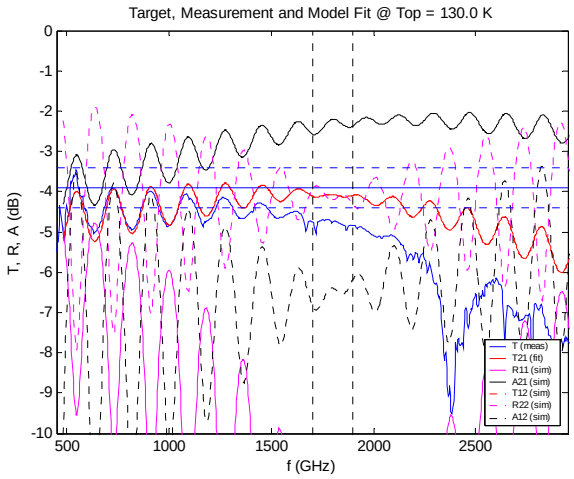

Fig. 20 Transmission measurement results for Q-032A. This device is the FM attenuator for band 7. The vertical dashed lines indicate the required bandwidth. The horizontal blue and dashed lines indicate the target and tolerances resp.

SUMMARY AND CONCLUSIONS

In this paper we describe a space-qualified design and production process for broadband THz attenuators or neutral density filters. The attenuators are based on a dual-film concept of lossy metallic films. Broadband operation on substrates as thick as several wavelengths can nevertheless be obtained through an impedance matched film. In our case we deposit thin Ta films on relatively thick Al_2O_3 substrates and passivate with a SiO_2 layer. This concept works well for attenuator values beyond -8 dB. Between 0 and -8 dB the impedance matched film is replaced by a polyimide AR coating. We achieve excellent agreement between model and measurement and demonstrate flat and broadband performance. The dual film design is extremely broadband and spans the entire HIFI frequency range. For band 6 and 7 we can tune the

thickness of spin-coated AR coatings at submicron precision and successfully align the high frequency bands at THz centre frequencies. The presented design can be tuned to any attenuation value beyond -1 dB and provides space-qualified performance under vacuum and cryogenic conditions.

For HIFI we successfully produce flight and spare attenuator sets fully compliant with the targets set by the project. These devices are currently built into the Herschel spacecraft and are expected to recover from early stability problems encountered during HIFI Instrument Level Testing.

ACKNOWLEDGMENT

The authors would like to thank Wim Horinga and Geert Keizer for their considerable effort in testing and characterizing the attenuators. We furthermore recognize the contributions made by Philip Laubert to the laser-cutting process, and Andre van der Horst, Peter Kohsiek and Jaap Evers for procurement and inspection activities as well as general PA/QA support. We finally thank Martin Eggens, Robert Huisman and Jaap Evers for the mechanical design and interface to ESA. All people mentioned are with SRON Netherlands Institute for Space Research.

REFERENCES

[1] J. Kooi, presentation at HIFI ILT-1 review, March 13, 2007.

[2] J. Kooi, V. Ossenkopf, M. Olberg, R. Shipman, R. Schieder, and D. Teyssier, "HIFI Stability as Measured During ILT Phase", *these proceedings*

[3] R. Güsten et al, *"HIFI Instabilities – LO-related investigations"*, HIFI test report MPIfR/HIFI/RP/2007-002, April 6, 2007.

[4] N. Erickson, "AM noise in drivers for frequency multiplied local oscillators", *Proc. 15th Int.. Symp. on Space THz Tech.*, April 2004.

[5] O. Siebertz, C. Honingh, T. Tils, C. Gal, M. Olbrich, R. Bieber, F. Schmuelling and R. Schieder, "The impact of standing waves in the LO path of a heterodyne receiver", *IEEE Trans. Microwave Theory and Techniques*, Vol. 1, No. 12, December 2002.

[6] M. C. Diez, T. O. Klaassen, C. Smorenburg, K. J. Wildeman, "Reflectance Measurements on Absorbing coating for Sub-Millimeter Radiation", *Proc. 4th Annual Symposium IEEE/LEOS (Benelux Chapter)*, pp. 107-110, 15 November 1999, Mons, Belgium.

[7] P. F. Goldsmith, "Quasi-optical Systems: Gaussian Beam Quasi-optical Propagation and Applications", IEEE Press: New York, 1997.

[8] D. Teyssier, N.D. Whyborn, W. Luinge, W. Jellema, J. Kooi, P. Dieleman and T. de Graauw, "HIFI Pre-Launch Calibration Results", *these proceedings.*

HIFI Pre-launch Calibration Results

David Teyssier[1,*], Nick D. Whyborn[2,3], Willem Luinge[2], Willem Jellema[2], Jacob W. Kooi[4], Pieter Dieleman[2] and Thijs de Graauw[2]

[1]*European Space Astronomy Centre, Madrid, Spain*

[2] *SRON Netherlands Institute for Space Research, Groningen, the Netherlands*

[3]*European Southern Observatory, Santiago, Chile*

[4] *California Institute of Technology, Pasadena, CA 91125, USA*

* Contact: David.Teyssier@sciops.esa.int phone +34 918131355

***Abstract*— This contribution presents the ground calibration campaign of the HIFI Flight Model instrument conducted at the SRON-Groningen premises. This campaign has been conducted over more than a year and a half, with a core period of 9 months where the complete flight model was available in the laboratory. The calibration of the instrument has been organized according to four main topics: i) spectral calibration, ii) beam characterisation, iii) photometry calibration, iv) stability.**

We present here the strategy used in each of these activities and give the first outcomes of the campaigns, especially in the perspective of the future calibration of the astronomical data, and how these results will be propagated onto the flight early and routine activities.

I. Introduction

HIFI is the heterodyne instrument to be flown on-board the Herschel Space Observatory. With 7 mixer bands spanning the 480–1910 GHz frequency window, its calibration as a whole is a real challenge, especially in bands making use of HEB technology, which will be put in orbit for the first time during this mission. The calibration was approached as a topical characterisation campaign, as is described in the following sections.

II. Spectral calibration

The characterisation of the spectral properties of an heterodyne instrument is a key issue for the final frequency calibration of the astronomical data. The spectral behaviour of the full instrument will be highly related to the performances of the Local Oscillator Unit (LO) as the signal produced by this latter has implications at several levels of the detection chain. First of all, the master oscillator (which has an accuracy of 1 part in 10^7) will provide the lock frequency to the High-Resolution Spectrometer (HRS) internal oscillators, as well as to the internal comb used in the Wide-Band Spectrometer (WBS). It therefore drives the absolute frequency calibration accuracy offered by the spectrometers. Because the LO signal is not a purely monochromatic line, it will degrade the spectral properties of the instrument, both at the level of spectral responses (resolution element shape, spurious response in the down-converted product) and spectral signals (spontaneous emission from the LO). They are described in the following sections.

A. Spectral Response

The spectral response of the instrument is the combination of the responses of the spectrometers themselves, and of that of the LO injected line. The objectives of the tests conducted were as follows:

- Verify the absolute frequency resolution of the instrument
- Verify the required instrument line-shape
- Verify the frequency accuracy of the instrument
- Determine the IF up-converted LO frequency (an up-converter was necessary in the HEB bands in order to bring the 2.4-4.8 GHz IF range of these bands into the standard 4-8 GHz IF expected by the spectrometers)

For this a strong and narrow line was injected into the system on the sky port, and swept over the spectrometer resolution element with steps of 31 kHz. The test signal was provided by an Agilent synthesizer operating between 15 and 16 GHz, which was then fed into a comb generator.

B. WBS

The shape of the WBS channel response can be described to a large degree by a Gaussian function, with Lorentzian and asymmetric wings. The specification on the corresponding resolution bandwidth (width of a boxcar filter of equal maximum transmission) is of 1.1 MHz.

Fig. 1 below shows the measured response of a WBS channel. One can immediately see that the shape presents a strong wing on the red side, and has a resolution bandwidth well above the specification (1.650 MHz). Overall, resolution bandwidths in the range 1.310 and 1.797 MHz have been measured. This effect was later identified as being due to the laboratory conditions in which the measurements were taken.

The ideal shape and resolution bandwidth is indeed expected for vacuum conditions, at a temperature of 10 degree Celsius. Measurements were indeed performed in open air, at 20 degree Celsius, and turned out to be totally consistent with similar measurements performed prior to the unit delivery (see Fig. 2).

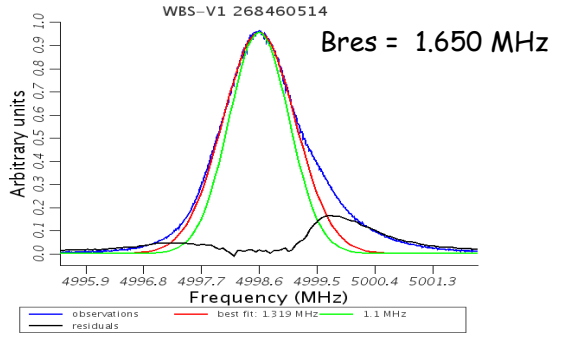

Fig. 1 Profile of the WBS resolution channel measured by a injected line swept over the channel width. (blue). Various fits and residual are shown.

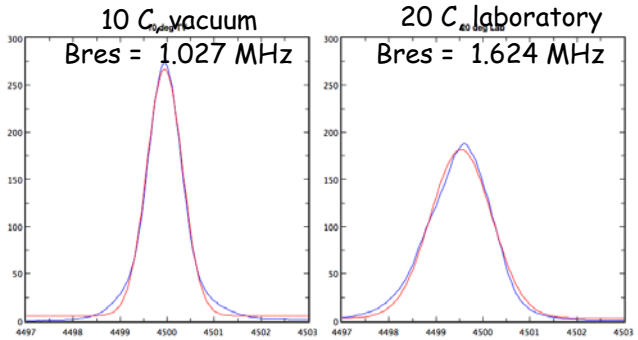

Fig. 2 Same as Figure 1 in different laboratory environments, measured by the WBS team prior to delivery to the SRON AIV team.

C. *HRS*

Due to its digital nature, the HRS provides an optimal intrinsic resolution of 125 kHz. This resolution is in practice degraded due to the non-perfect sharpness of the LO line injected to the mixer. Figure 3 illustrates one of the measurements obtained for band 1a. It is interesting to note the high signal-to-noise level that can be achieved in such experiment, allowing to assess the level of side-lobes contribution due to the Hanning windowing of the correlation function applied in the HRS. Table 1 summarizes the resolutions measured for several of the bands.

The measurements show that the HRS resolution is well specifications for all bands but 2a, 3b and 4a.

D. *Spurious Characterization*

The spectral purity of the instrument depends on the level of all significant spurious signals and spurious responses present in the data. Un-catalogued instrument spectral artefacts could indeed be misinterpreted as astronomical features.

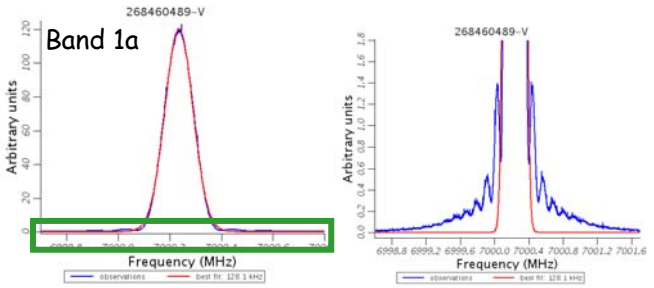

Fig. 3 Same as Figure 1 for the HRS. The details of the rectangular area are shown on the right, illustrating the level of side-lobe contribution.

TABLE IV
HRS MEASURED RESOLUTIONS AND ACCURACIES

Band	1a		2a		2b		3a		4b		6b	
	H	V	H	V	H	V	H	V	H	V	H	V
FWHM kHz	125	128	216	116	171	170	156	158	157	153	186	184
Specs	160		180		180		190		230		280	
Accur. (kHz)	21		31.4		31.6		37.6		40.5			
Specs	53		69		69		85		117			

E. *Spurious Signals*

A spurious signal is a spectral feature which is present in the spectrometer output in the absence of any spectral feature in the signal entering the instrument while it is e.g. looking at a clean black body. These signals can be harmonically related to the LO, internally generated, or picked up.

A catalogue of those spurs was produced based on a systematic analysis of all available spectra, with a particular emphasis on the high-granularity noise temperature survey presented in section IV. Figure 4 summarizes the occurrences of such signals. In general some few narrow lines are observed for very specific LO frequencies. Some broader lines are also seen, often associated with poor mixer pumping quality (LO excess noise)

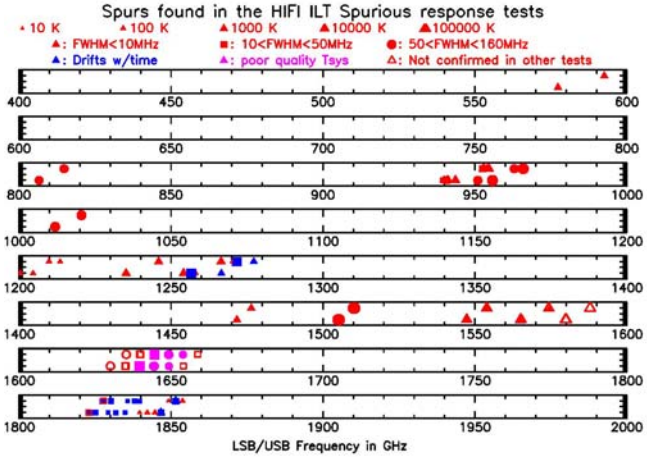

Fig. 4 Overview of the spur locations over the HIFI frequency range.

F. *Spurious Responses*

A spurious response is a ghost spectral feature present in the spectrometer output which is related to a spectral feature in the signal entering HIFI, but which appears at the wrong frequency. Any occurrence of such lines would imply an incorrect calibration on any astronomical lines observed. The image side-band of a DSB mixer is an example of spurious response. Causes for such effects are usually strong harmonics or oscillations in the LO chain.

We have concentrated here on mono-chromatic responses to a given line injected at the sky port of the instrument. A coherent source was stepped from 15 to 16 GHz (step size 0.04-0.05 GHz) and a comb generated harmonics (30 to 96) of this source. For band 7b (1719-1910 GHz), a monochromatic source (SIII harmonic 108 of a source frequency tuned between 16.38 and 18.01 GHz) was used.

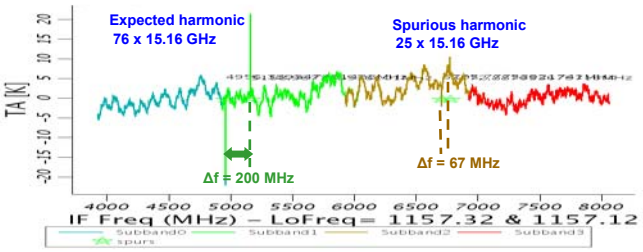

Fig. 5 Example of a spurious response measurement in frequency switching mode. The injected line is seen on the left, while the feature on the right is a ghost, arising from a lower harmonic.

Figure 5 illustrates the sort of measurement used to hunt spurious responses in the system. The frequency switch mode was used to calibrate the instrument band-pass, allowing also to scale the harmonic contribution based on the frequency throws observed between two ghosts spikes.

The scan over the full HIFI range has revealed three main categories of spurious responses:

- Weak LO "leaks" of level below 0.1% of the original signal
- Medium LO "leaks" of level of a few % of the original signal
- Strong LO "leaks" which can be in excess of 50% of the original signal. Those were mostly observed at the upper end of band 3b, 5b and 7b. These LO impurities have been found to be due to oscillation in a doubler which makes that more than one tone is eventually mixed. Further tests proved that more negative multiplier biases could restore most of the purity, albeit at the cost of some LO output power.

Figure 6 gives an overview of where the above leaks have been encountered.

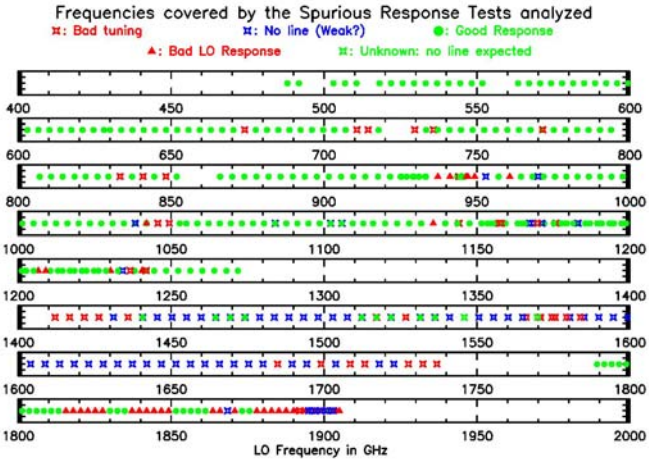

Fig. 6 Overview of the area of affected spectral purity

III. Beam Characterization

The beam characterization of the 14 mixer line-of-sight is a fundamental pre-launch activity as it provides the absolute positions of the HIFI beams with respect to the telescope theoretical bore-sight, a measurement which in turn will be used in order to calibrate the absolute pointing of each of the HIFI bands. In addition it allows the first estimates for beam efficiency prediction.

The measurement setup used for this activity has already been introduced in more detail by Jellema et al. [1]. It is based on a vacuum beam scanner located on top of the HIFI FM test cryostat, which allows both phase and amplitude measurements. Fig 7 illustrates this device.

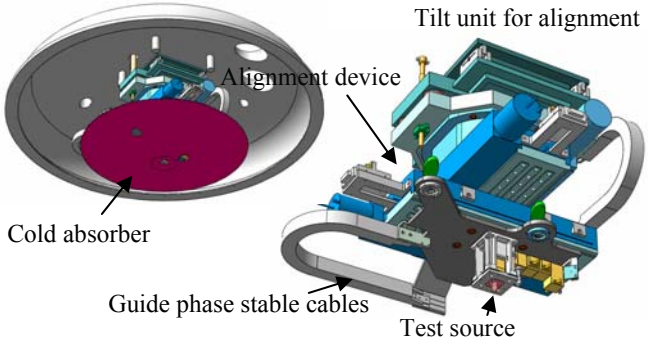

Fig. 7 Drawings of the beam scanning system

The re-constructed beam positions and patterns in the absolute S/C coordinate system are shown in Figure 8. The (quasi-)optical alignment is found to be very good, and optical losses will stay below 6%. The co-alignment is generally 20-30% of the waits size, which means 10-15% of the FWHM at the sky. This means that the losses per polarization channel when re-pointing to the average position at the sky will be of typically 1-3%. This is the approach that HIFI has finally taken in order to define the official aperture the S/C shall point to in orbit, assuming that both polarizations will always be (weight-)averaged by the astronomer.

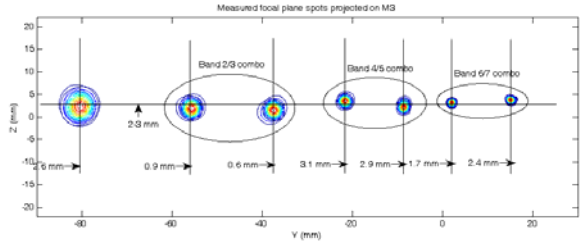

Fig. 8 Absolute positions and energy distribution of the HIFI beams as measured during the ILT.

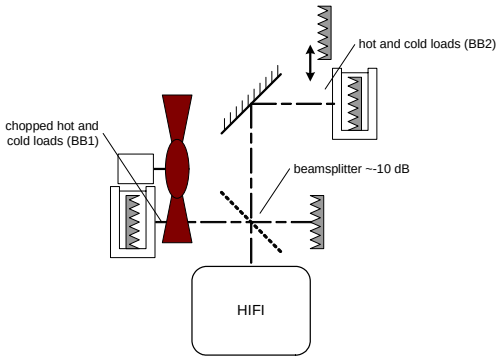

Fig. 9 Measurement setup for the linearity experiments

IV. Photometry Calibration

The photometry calibration is of upmost importance for the interpretation of the astronomical data, and in particular for comparison with models. HIFI has an absolute photometric calibration goal of 3%, with a baseline at 10%. This is a very challenging requirement, even in the absence of atmosphere. The following equation illustrates the various contributors to the error budget:

$$J_{source} - J_{OFF} = \frac{1}{G_{ssb}\eta_l + \omega_{ssb}} \frac{\eta_c + \eta_h^{-1}}{\eta_{sf}} \times [...]$$

- ηc and ηh are the mixer beam coupling factors to the internal cold and hot loads. 1% error on these numbers translates into an error between 0.2 and 5% (depending on frequency) and of 1% respectively on the absolute calibration
- ηsf is the mixer coupling to the sky. Its accuracy will largely rely on the error made on the planet model in use to convert observed intensities into physical units. Current Mars and Uranus models are believed to be trustable to about 5%
- G_{ssb} represents the contribution from the side-band ration applying to the DSB mixers in use. 1% error on this number translates into 0.5% error on the absolute calibration

A. *System linearity*

As HIFI will be observing astronomical sources of varying line and continuum intensities, the linearity of the photometric scale in both domains has to be addressed. The measurement setup is illustrated in Figure 9. Various pairs of thermal loads were used in order to simulate various regimes of continuum background, on top of which a synthesized line could be injected when necessary.

B. *Line linearity*

The above setup was used in order to observe an injected line (equivalent temperature in the range 0-2000K) against a continuum load switchable between 10 and 100K. The non-linearity measured over the various line contrasts is shown in Figure 10. The measurement accuracy is seen to improve with higher line contrast, the best range being 50-250K. The average non-linearity in bands 1 to 6 is found to be -0.5 +/- 2.9 % for the WBS, and 0.15 +/- 1.5% for the HRS. Overall, the line linearity is within 2%, implying a good line calibration for all type of source intensity.

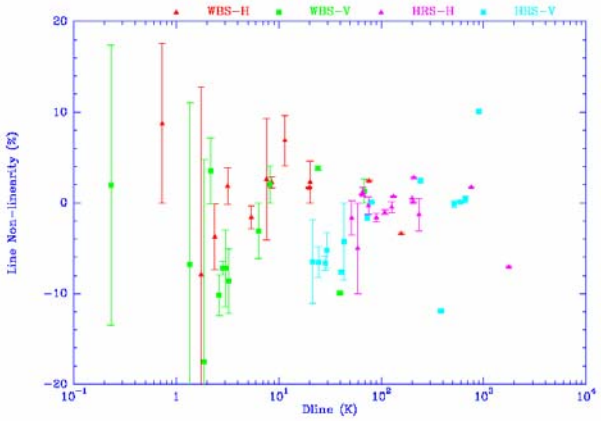

Fig. 10 Results of the line linearity measurements. Error bars are observed to decrease with the line contrast (Δline).

C. *Continuum linearity*

In this experiment, the 2 pairs of loads are used to provide a variable continuum source between 200 and 300K. Here the measurements were seen to suffer more significantly from system un-stability of the continuum gain on short time scale, so that the current picture of the continuum linearity is still affected by important error bars (see Figure 11). The linearity is found to be on average -2 +/- 6%. Other measurements made with a faster referencing scheme were taken later but are not yet analysed at the time of writing this paper.

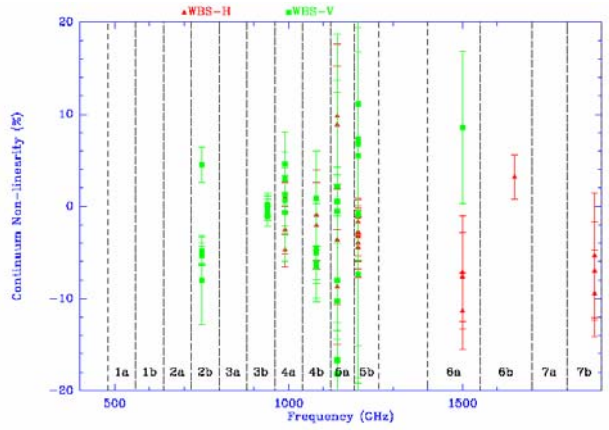

Fig. 11 Current results of the continuum linearity measurements.

V. RADIOMETRY PROPERTIES

A. *Internal load beam coupling*

The absolute calibration of HIFI will rely on observations of well-known solar system bodies such as Mars of Uranus, which will be used in order to derive the overall beam coupling to the source at the sky (aperture and beam efficiencies). However, this calibration will be bootstrapped to the internal loads, which provide the routine photometric calibration of any astronomical observation.

Because the use of these sources as "relay"-calibrator relies on the accurate knowledge of the radiated temperature to the mixer, the coupling of this latter to the apertures of these loads is fundamental. While the cold load of HIFI (thereafter called the CBB) is a tilted absorbing plate at sink temperature (around 10K), the hot load (thereafter called the HBB) consist of a narrow slit in V-shape design in order to act as a trapping cavity (see Figure 12). This cavity is heated up to a temperature of order 100K, therefore its size has been reduced to the maximum in order to limit the heat load into the FPU. Both load surfaces are coated with SiC grains on black Skycast. The coupling to these two loads will depend on the overall alignment of all optics from mixer to cavity.

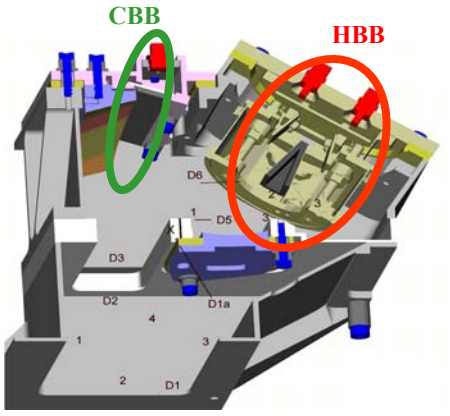

Fig. 12 Drawing of the Calibration Source Assembly (CSA) inside the HIFI FPU

In order to measure the coupling to these loads, absolute external photometric calibrators were designed so that the radiated temperature seen by the mixer on the internal load could be calibrated on an absolute temperature scale. The external absolute hot black body (AHBB) consists of a wide LN2-cooled coated cylinder with a titled top surface (30 degrees), allowing to encompass all possible beam positions on the HIFI pick-up mirror (M3). Its emissivity was measured to be better -45dB. The cold reference was a shutter located inside the test cryostat, right on top of the pick-up mirror, and offering a titled coated surface at sink temperature. Figure 13 illustrates the test setup.

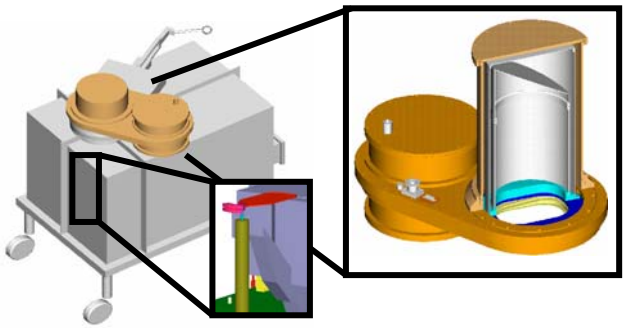

Fig. 13 Measurement setup for the internal load coupling experiment. Left: FM test cryostat with absolute cold (middle) and warm (right) external loads

The coupling was measured over the full HIFI range, with a granularity of 4 GHz. Results are shown in Figure 14 for the H-polarization mixers.

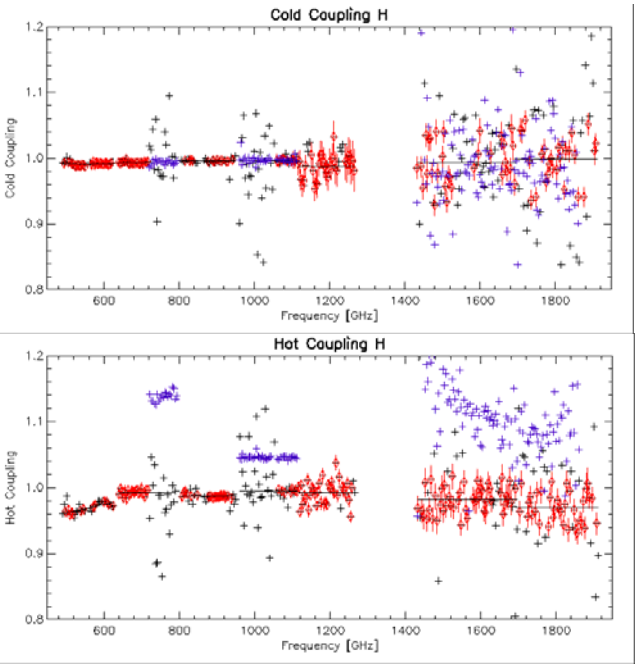

Fig. 14 Results of the internal load coupling measurements. Red symbols indicate the points used in the computation of the mean coupling (in solid line). Blue crosses indicate measurements done in another configuration, and discarded from the analysis.

Couplings are found to be very close to unity for all bands, which is as expected from theory. The coupling to the hot load has however a rising trend with increasing frequency, indicative of possible beam spill-over on the edges of the cavity at the highest wavelengths. A stronger scatter was observed in the data collected on the HEB bands, an effect due to the poorer total power stability offered by these bands. The coupling was however treated as a single number averaged over the whole mixer band range. Errors on the coupling are found to be less than 1% in bands 1 to 4, and up to 10% in the higher bands.

B. *System noise temperature*

As a by-product of the above measurements, the mixer band-pass response can be derived in the form of the system noise temperature. This provides the overall picture of the instrument sensitivity over its operational range. This measurement was later repeated on a finer grid (1 GHz). The results are shown in Figure 15. Note that these measurements are performed in complete vacuum, so that no further correction than the beam coupling factor derived above is necessary to infer the effective noise temperatures.

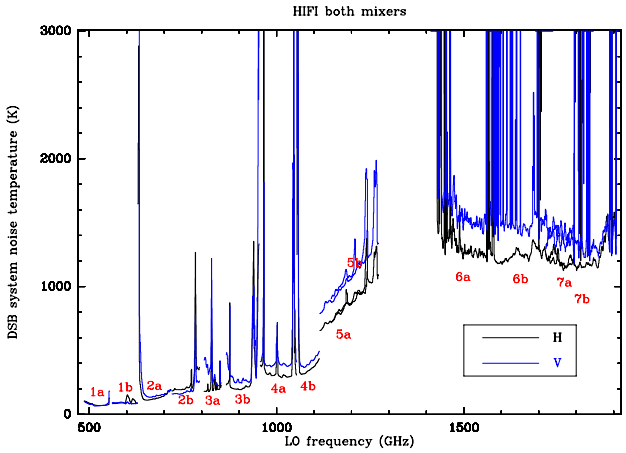

Fig. 15 System noise temperature as a function of LO frequency

The T_{sys} performances are totally compliant with the original requirements, offering unprecedented sensitivity in all covered bands. The results also reveal some gaps, in particular in the HEB bands, consequences of the introduction of attenuator windows on the LO path for stability purpose, resulting in areas of LO output power shortage. We refer to Jellema et al. [2] and Kooi et al. [3] for further details on this particular topic. Note however that, due to the possibility to adjust the LO tuning over the USB or LSB, as well as over the available 4 GHz IF band, most of those gaps disappear when the sensitivity is plotted against the sky frequency of a targeted line. This is illustrated on Figure 16.

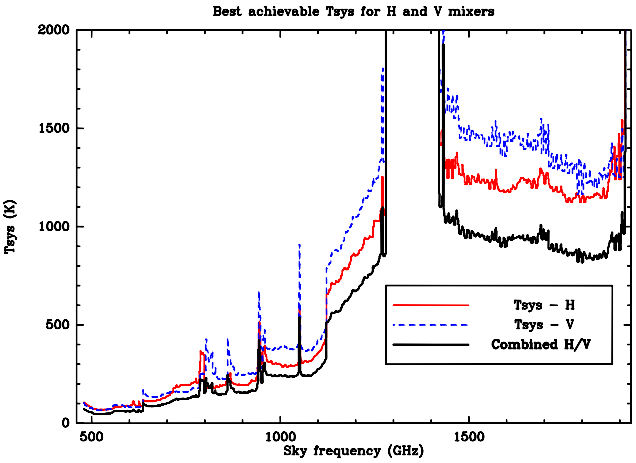

Fig. 16 System noise temperature as a function of sky frequency. The solid black line shows the achievable noise when combining both polarizations

VI. *Gas-cell measurements*

Gas-cells offer a unique laboratory source for validation of spectroscopy experiments as they allow a fair control of the spectroscopic features to be fed into the system, and offer infinite frequency coverage due to the versatility of available molecular species. As such they allow an end-to-end qualification of the heterodyne detection system.

A. *Side-band ratio assessment*

One of the most important parameters for the photometric calibration of lines in a DBS system is the side-band gain ratio of the mixers at the frequency of operation. Methods based on laboratory side-band rejection systems (using Martin-Pupplett interferometers) are difficult to implement in such compact configurations such as the one of HIFI. Another alternative consisting in using laboratory gas cells has proved to be fairly successful in previous experiment, as e.g. during the calibration of the SWAS satellite (e.g. Tolls et al. [4]).

In such an experiment, a spectral line is located in one of the side-bands, while the other side-band is supposed to be free of spectral features. When the line is saturated, and the respective side-band gains are perfectly balanced, the DSB spectrum should appear as a single line absorbing exactly half of the continuum fed to the DSB mixer. Any deviation from this half level indicates a departure of the side-band gain ratio from unity. The most challenging aspect of such measurements is the availability of spectral lines of sufficient strength over very large and fine sampled frequency coverage. A description of the specific HIFI gas-cell design can be found in Teyssier et al. [5]. The measurement setup is illustrated in Figure 17.

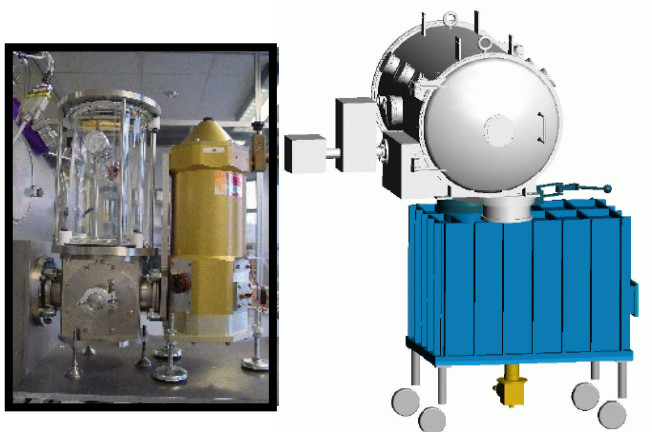

Fig. 17 Left: gas-cell and its associated black body. Right: illustration of the measurement setup for the gas-cell experiment.

The data-set collected was fairly massive (over 6000 spectra in a dozen of molecules) and the analysis of the side-band ratios is still on-going at the time of writing this paper. A first crude overview was performed based on a quick-look assessment of the line absorption dip over the survey. The outcome of this coarse computation is shown in Figure 18. A lot of uncertainties are affecting such a automatic, the largest being related to the baseline quality of a part of the data-set, as well as to the non-saturation of a large fraction of the transitions probed. This leads to the large scatter seen all over the considered range.

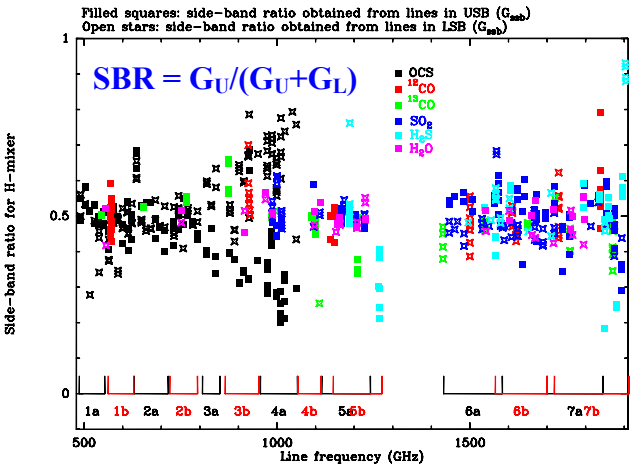

Fig. 18 Side-band gain ratio as measurement with the crude quick-look method (see text for details)

We are currently working toward a more accurate approach, whereby a complete model of the line profile is computed based on the physical conditions of the gas in the cell (pressure, temperature, cell path length). This technique allows much more accurate determination of the side-band ratio (down to below 1% in most stable and sensitive bands). An example of such retrieval is illustrated in Figure 19 (courtesy of E. Dartois).

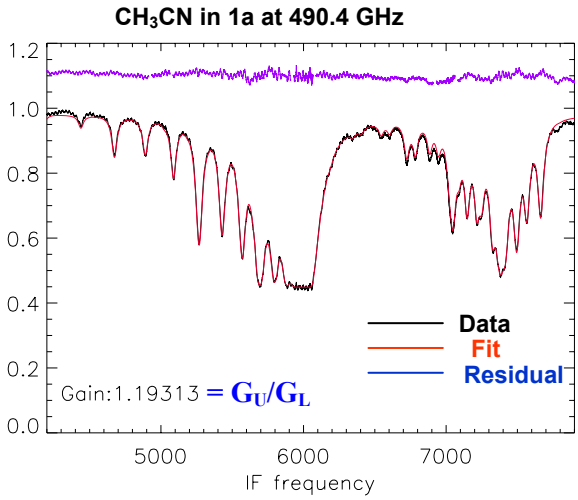

Fig. 19 Example of side-band ratio retrieval based on modelled line profile fitting on a transition of CH_3CN in band 1a.

B. *Spectral surveys*

With its wide and continuous spectral coverage, HIFI will dedicate a significant part of its scientific program to spectral surveys. The achievement of such complete coverage requires the guarantee that the instrument can be optimally tuned over the whole frequency range. We conducted such a un-biased survey using the methanol molecule, which features a very dense spectrum all over the HIFI range. The ultimate goal of such a measurement is also to validate specific data processing tools dedicated to the de-convolution of the DSB spectra using redundant measurements over the IF bandwidth (e.g. Comito et al. [6]). Figure 20 shows the result of such a de-convolution performed on the data observed in the band 3 of HIFI (courtesy of C. Comito).

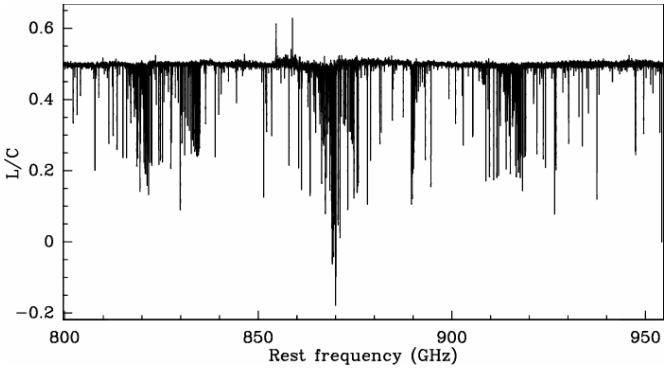

Fig. 20 SSB spectrum obtained from the de-convolution of the methanol spectral survey in band 3.

VII. Stability

We refer to Kooi et al. [3] for a detailed description of this topic.

CONCLUSIONS

The pre-launch calibration campaign of the HIFI instrument has been a collaborative effort spanned over a period of a year and a half, with a core period of nine months where the full flight instrument was available to the team. It has been an intensive learning period where some on-the-fly redesign or addition of flight hard-ware became un-avoidable even little time before its delivery to ESA in June 2007. The campaign has collected an impressive amount of data which will still offer material for study over the next years. The big picture is that of an instrument very well into its performance specifications, and offering an absolute calibration within the initial goal of 3-10% in the first half of the frequency coverage. In the HEB bands in particular, it is expected that this accuracy will rather be in the range 10-20%. Overall, it makes HIFI the most accurate heterodyne instrument ever built in the bands overlapping those of other ground-based facilities, and clearly the new reference for the frequency ranges where it will offer pioneering science.

ACKNOWLEDGMENT

The authors would like to thank the HIFI AIV and Calibration team who made the whole test campaign possible, and who provided many of the results presented in this paper. Namely: *AIV team*: W. Horinga, H. Smit, R. Huisman, K. Wildeman, W. Laauwen, M. Eggens, N. Bruning, R. de Haan, the SRON-G workshop; *Radiometry team*: B. Larsson, F. Helmich, M. Pérault; *Gas-cell team*: E. Dartois, F. Boulanger, D. Debboffle, C. Comito, R. Higgins, B. Delforge; *Stability Team*: V. Ossenkopf, M. Olberg, R. Schieder; *Spectral team*: C. Vastel, F. Herpin, J. Pearson, T. Klein, N. Biver, C. Kramer; *Linearity team*: R. Moreno; *Beam property team*: M. Jochemsen, T. Peacocke; *Local Oscillator Team*: T. Klein, C. Leinz, M. Caris, R. Güsten.

REFERENCES

[1] W. Jellema et al., Performance Characterization and Measurement Results of a Submillimeter-Wave Near-Filed Facility for the Heterodyne Instrument for the Far-Infrared, Proceedings of the 3rd ESA Workshop on Millimeter Wave Technology and Application, Millilab, Finland, May 21-23 2003

[2] W. Jellema et al., Flight Attenuators for the HIFI Local Oscillator, this volume

[3] J. Kooi et al., HIFI Instrument Stability as Measured During the ILT Phase: Results and Operational Impacts, this volume.

[4] V. Tolls et al. (2004), "Submillimeter Wave Astronomy Satellite Performance on the ground and in orbit" in ApJS 152, 137

[5] D. Teyssier et al. (2004), "A Multi-path Far-Infrared and Sub-millimetre Gas Cell for Spectral Tests of Herschel/HIFI" in proceedings of ISSTT04

[6] C. Comito et al. (2002), "Reconstructing reality: Strategies for sideband deconvolution", in A&A 395, 357

Antenna coupled Kinetic Inductance Detectors for space based sub-mm astronomy

S. J. C. Yates[1], J. J. A. Baselmans[1], R. Barends[2], Y.J.Y. Lankwarden[1], H. F.C. Hoevers[1], J.R. Gao[1], T.M. Klapwijk[2], A. Neto[3], D. J. Bekers[3], G. Gerini[3], S. Doyle[4], P. D. Mauskopf[4], P. Ade[4]

SRON Netherlands Institute for Space Research, Sorbonnelaan 2, 3584CA Utrecht, The Netherlands[1]
Kavli Institute of Nanoscience, Delft University of Technology, Lorentzweg 1, 2628 CJ Delft, The Netherlands[2]
TNO Defence, Security and Safety, Den Haag, 2597 AK, The Netherlands[3]
School of Physics and Astronomy, Cardiff University, The Parade, Cardiff, CF24 3AA, UK[4]
Contact:S.J.C. Yates:, E-mail: S.Yates@sron.nl Tel: +31 30 2538581

To achieve background limited detection, future space missions in the far infrared and sub-mm radiation bands will require large arrays (>1000 pixels) of very sensitive detectors. A typical requirement for the noise equivalent power is 10^-19 W/Hz^0.5 for a Fourier Transform Spectrometer, which is 100 to 1000 times more sensitive than the state of the art such as on HERSCHEL. Such low NEP is a significant technical challenge, both to achieve for the detectors and to demonstrate in the laboratory. Kinetic inductance detectors can theoretically achieve this performance and have significant advantages over other types of detectors, for example are well adapted to frequency domain multiplexing. We present antenna coupled kinetic inductance detectors, showing the loaded optical NEP measured with a well controlled narrow band black body radiation source. We will also discuss the optimization route required to reach the requirements for future missions, including the optical testing requirements.

Antenna-coupled Microwave Kinetic Inductance detectors (MKIDs) for mm and submm imaging arrays.

A. Vayonakis, J. Schlaerth, S. Kumar, J.-S. Gao, P. Day, B. Mazin, M. Ferry, O. Noroozian, J. Glenn, S. Golwala, H. LeDuc, J. Zmuidzinas

We present results from completely lithographic antenna-coupled Microwave Kinetic Inductance detectors (MKIDs). MKIDs are superconducting resonators with resonant frequency and quality-factor which are highly sensitive to changes in the density of the quasiparticle population which occurs when photons above the superconducting gap energy are absorbed. The resonators are coupled to submm light through on-chip phased-array slot antennas. Each planar antenna consists of an array of N long slots which are fed along their length at M points. The resulting N*M feed points are combined in-phase using a binary summing tree made of low-loss superconducting microstrip lines. Due to its large size, the resulting planar antenna produces a narrow beam pattern and can therefore be used without additional optical coupling elements such as feedhorns or substrate lenses. The output of the antenna is a single superconducting thin-film microstrip line which can be efficiently coupled to one (or more) kinetic inductance coplanar waveguide resonators to produce a single (or multi-color) pixel in an imaging focal plane array, using in-line lumped element lithographic band-pass filters. Such highly integrated architectures can be easily fabricated on a single substrate, and many detectors can be frequency multiplexed through coupling to a single feedline. Microwave readout provides a lot of bandwidth per detector, allowing a large number of pixels to be read using a single cryogenic microwave amplifier and warm readout electronics.

We show results from a demonstration camera (DemoCam) using MKIDs. This camera features 16 planar antennas on its focal plane, each feeding two MKID resonators through in-line bandpass filters with bands centered at 240 GHz and 350 GHz.

Contribution of dielectrics to frequency and noise of NbTiN superconducting resonators

R. Barends[1], H. L Hortensius[1], T. Zijlstra[1], J. J. A. Baselmans[2], S. J. C. Yates[2], J. R. Gao[1,2], and T. M. Klapwijk[1]

[1] *Kavli Institute of NanoScience, Faculty of Applied Sciences, Delft University of Technology, Lorentzweg 1, 2628 CJ Delft, The Netherlands*
[2] *SRON Netherlands Institute for Space Research, Sorbonnelaan 2, 3584 CA Utrecht, The Netherlands*

The low temperature microwave properties of superconducting resonators for kinetic inductance photon detectors [1] and quantum computation [2] are attracting increased attention. At low temperatures both a significant excess frequency noise and deviations in the resonance frequency from Mattis-Bardeen theory have been found. It has been suggested that these anomalies are caused by dipole two-level systems residing in dielectric layers near surfaces, which interact with the high frequency electric fields in the resonator [3-4]. In order to identify to what extent two-level systems in dielectrics affect the microwave properties of superconducting films we study NbTiN resonators with a 10, 40 or 160 nm thick SiO2 covering layer. We find that the resonance frequency of bare NbTiN resonators, unlike Nb, Ta and Al resonators, closely follows Mattis-Bardeen theory down to 350 mK. We demonstrate that deviations in the resonance frequency can be generated by covering the resonators with a thin amorphous SiO2 layer, and that these deviations scale with the layer thickness. In addition, we find that the frequency noise is strongly increased as soon as a SiO2 layer is present, but is, counter-intuitively, independent of the layer thickness. These observations show that the physical mechanisms causing the excess frequency noise are different from those responsible for the deviations in the resonance frequency.

[1] P. K. Day et al., Nature 425, 817 (2003).
[2] A. Wallraff et al., Nature 431, 162 (2004).
[3] J. Gao et al., Appl. Phys. Lett. 90, 102507 (2007).
[4] J. Gao et al., arXiv:0802.4457.

Microstrip-Coupled TES Bolometers for CLOVER

Michael D. Audley[1,*], Dorota Glowacka[1], David J. Goldie[1], Vassilka N. Tsaneva[1], Stafford Withington[1], Paul K. Grimes[2], Chris North[2], Ghassan Yassin[2], Lucio Piccirillo[3], Giampaolo Pisano[3], Peter A.R. Ade[4], Philip Mauskopf[4], Rashmi V. Sudiwala[4], Jin Zhang[4], Kent D. Irwin[5], Mark Halpern[6], Elia Battistelli[6]

[1]*Cavendish Laboratory, University of Cambridge, JJ Thomson Ave, Cambridge, CB3 0HE, UK*

[2]*Department of Physics, University of Oxford, Denys Wilkinson Building, Keble Road, Oxford, OX1 3RH, UK*

[3]*School of Physics and Astronomy, The University of Manchester, Sackville Street Building, Manchester, M60 1QD, UK*

[4]*School of Physics and Astronomy, Cardiff University, 5, The Parade, Cardiff, CF24 3YB, UK*

[5]*National Institute of Standards and Technology, 325 Broadway, MC 817.03, Boulder, CO 80305-3328, USA*

[6]*University of British Columbia, Department of Physics and Astronomy, 6224 Agricultural Rd., Vancouver, B.C., V6T 1Z1, Canada*

* Contact: audley@mrao.cam.ac.uk, phone +44-(0)1223-337 309

***Abstract*— $C_\ell$over aims to detect the signature of gravitational waves from inflation by measuring the B-mode polarization of the cosmic microwave background. We have produced microstrip-coupled TES detectors for $C_\ell$over. The dark NEP of these detectors is dominated by the fundamental phonon-noise limit and we have measured high optical detection efficiencies in these devices with two completely different RF architectures: a finline transition and a four-probe OMT. $C_\ell$over consists of two telescopes: one operating at 97 GHz, and one with a combined 150/220-GHz focal plane. The 220- and 150-GHz detectors use waveguide probes while the 97-GHz detectors use finline transitions to couple waveguide modes into the microstrip. Each detector is fabricated as a single chip to ensure a 100% operational focal plane. The detectors are mounted in eight-pixel modules and the focal planes are populated using 12 detector modules per detection frequency. Each detector module contains a time-division SQUID multiplexer to read out the detectors. Further amplification of the multiplexed signals is provided by SQUID series arrays. We describe the design of the $C_\ell$over detectors and present measurements of the prototype detectors' performance showing that they satisfy the requirement of photon-noise limited operation on $C_\ell$over.**

I. Introduction

A. Scientific Motivation

Thomson scattering of radiation in the early Universe can lead to linear polarization [1] in the cosmic microwave background (CMB). The polarization depends on density fluctuations, and thus carries cosmological information which is complementary to the well-studied temperature anisotropies of the CMB. The linear polarization may be decomposed into a curl-free part and a divergence-free part, denoted E- and B-mode respectively. By measuring the B-mode polarization of the CMB with $C_\ell$over we hope to make an indirect detection of a background of primordial gravitational waves [2], [3].

B. Key Features of $C_\ell$over

The $C_\ell$over experiment is described in detail elsewhere [4].

$C_\ell$over consists of two telescopes measuring operating at frequencies of 97, 150, and 220 GHz. The low-frequency (LF) telescope observes at 97 GHz and the high-frequency (HF) telescope has a combined 150/220-GHz focal plane. $C_\ell$over will be sited at Pampa la Bola in Chile's Atacama Desert.

For such sensitive measurements, $C_\ell$over requires detectors with low enough NEP so that the instrument NEP is dominated by unavoidable sources of background photon noise (2.2×10^{-17} W/√Hz at 97 GHz). To achieve this sensitivity $C_\ell$over uses bolometers with superconducting transition edge sensors (TES) [5] operating with a bath temperature of 100 mK. $C_\ell$over's two focal planes contain hexagonal arrays of corrugated feedhorns. Orthomode transducers (OMT) separate the signal collected by each horn into two polarisations. In the LF telescope waveguide OMTs divide the two polarisations from each horn between two rectangular waveguides which each feed a finline-coupled detector. The high frequency channels use polarisation-sensitive detectors of a different architecture: four rectangular probes in a circular waveguide.

Rather than fabricating monolithic arrays we decided to make individual detectors so that we could guarantee a 100% functioning focal plane, which is important for meeting the sensitivity requirement. Also, because the detectors are much smaller than the horns in the focal plane, a monolithic array would have large, inactive areas between detectors, which would make fabrication of the detectors extremely inefficient.

Because of the large number of TESs to be read out (192 at each frequency) we use time-domain multiplexing in order to have a manageable number of wires from room temperature. The TESs are read out by 1×32 SQUID

multiplexers [6], [7], [8] fabricated by the National Institute of Standards and Technology (NIST). Further amplification is provided at the cold end by SQUID series arrays [9], also fabricated by NIST.

All the multiplexer chips in each of Cℓover's two telescopes share address lines, significantly reducing the number of wires needed to room temperature. The Nyquist inductors, which provide antialiasing filtering, and the shunt resistors that provide voltage biasing, are contained in separate chips. All of these chips are mounted on a PCB at 100 mK and connections are made to the detectors by aluminium wire bonds. The SQUID series arrays are mounted in eight-chip modules which provide the necessary magnetic shielding. Because of their higher power dissipation (1 μW per series array compared with 16 nW per multiplexer chip) these modules are heat-sunk to the still of the dilution refrigerator and they are connected to the multiplexer PCB with superconducting NbTi twisted pairs. Room-temperature multi-channel electronics (MCE) developed by the University of British Columbia, provides SQUID control and readout as well as TES bias [10]. Cℓover's MCE is similar to that used by SCUBA-2 [11].

C. Cℓover Detector Requirements

For maximum sensitivity, we require that the detectors be background-limited, i.e. the contributions to the noise equivalent power (NEP) from the detectors and readout must be less than the NEP due to unavoidable sources of photon noise:

$$NEP_{det}^2 + NEP_{ro}^2 \leq NEP_{photon}^2.$$

To satisfy this requirement comfortably, we set a target for the combined NEP of the detectors and readout at 75% of the photon NEP.

Once the detectors are background-limited, the only way to improve the sensitivity is to increase the number of detectors. 96 pixels are needed at each frequency to meet Cℓover's sensitivity requirements. The LF instrument has two finline detectors per pixel (one for each polarisation). In the HF instrument there is one polarisation-sensitive OMT detector chip per pixel which measures both orthogonal polarisations. Thus, the LF instrument has 192 finline detectors and the HF instrument has a total of 192 planar OMT detectors. We require a detector time constant faster than 1 ms to satisfy the science requirements and slower than 40 μs for Nyquist sampling by the readout.

Also, the detectors must be able to absorb the power incident from the sky without saturation. This power is variable and depends on the weather. The power-handling requirement is for the detectors to be able to operate for 75% of the time at the site. We have allowed a 70% margin on this to account for uncertainties in the sky background at the site. The detector requirements are summarised in Table .

TABLE I

CℓOVER DETECTOR REQUIREMENTS AT THE THREE OPERATING FREQUENCIES.

Centre Frequency (GHz)	97	150	220
Band (GHz)	82—112	127—172	195—255
Number of pixels	96	96	96
NEP (10^{-17} W/√Hz)	2.2	3.7	6.7
Power Handling (pW)	11.4	20	32

II. DETECTOR ARCHITECTURE

A. TES Design

Cℓover uses microstrip-coupled TES bolometers. RF power is carried to the bolometer by a microstrip which is terminated by a matched resistor. In this resistor the RF power is dissipated as heat which is detected by the TES. We chose this architecture because Cℓover has strict requirements on sensitivity and on cross-polarization (<-35 dB). Cℓover has been designed with careful attention to minimising cross-polarisation using corrugated horns and waveguides. The microstrip-coupled TES architecture allows us to couple to the waveguides with higher efficiency than a free-space absorber would give. The microstrip coupling also gives us great flexibility by separating the bolometer from the part that couples to the waveguide. This means that we can optimise the TES without affecting the absorber, and vice versa. In Cℓover we have been able to use similar TESs with entirely different RF architectures (finline and waveguide-probes). It is also easy to inject DC power or pulses through the microstrip, which is useful for calibration.

Cℓover's bolometers are on low-stress silicon nitride islands suspended by four legs for thermal isolation (see Figs 1 andFig. 2). The nitride is 0.5 μm thick. The thermal conductance to the thermal bath is controlled by the four nitride legs. A microstrip carries RF power to the bolometer and is terminated by a 23-Ω AuCu resistor which dissipates the incoming power as heat that the TES can detect. A shunt resistor in parallel with the TES ensures that it is voltage biased so that it operates in the regime of strong negative electrothermal feedback. For example, if the temperature drops, so does the resistance of the TES. Since it is biased at constant voltage, this means that the current, and hence the Joule power, will increase, heating up the TES. Conversely, if the temperature increases the resistance will increase, reducing the current, and thus the Joule heating. This means that the TES operates at a bias point that is in a stable equilibrium. Thus, the TES is self-biasing, and the electrothermal feedback speeds up the response of the detector and cancels out temperature fluctuations, which has the effect of suppressing the noise.

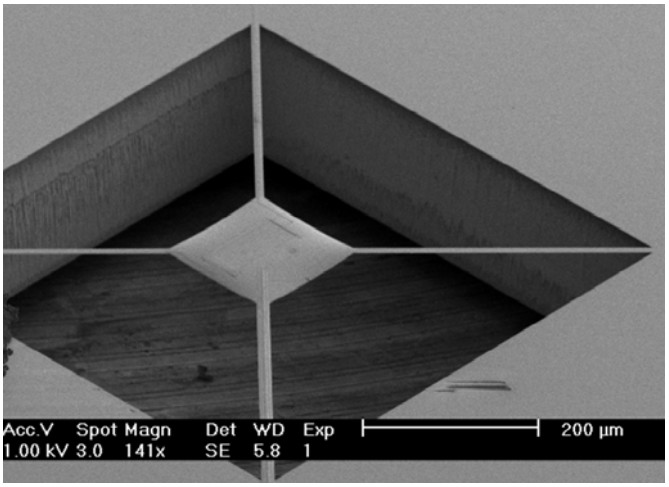

Fig. 1 Scanning electron microscope image of Cℓover prototype bolometer silicon nitride island showing TES and microstrip leading to termination resistor.

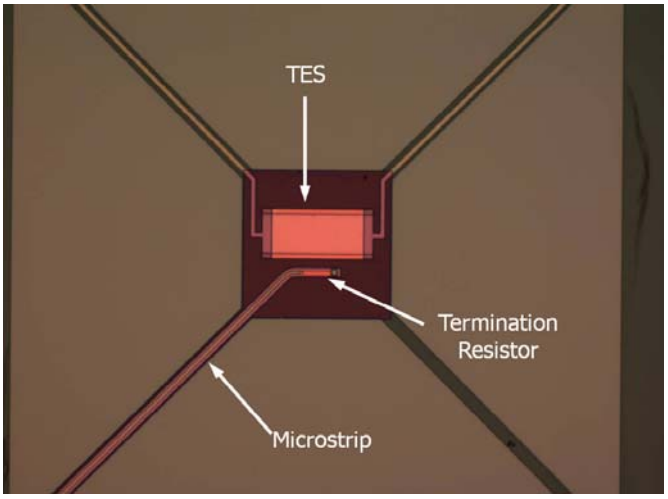

Fig. 2 Optical microscope image of Cℓover prototype bolometer silicon nitride island showing TES and microstrip leading to termination resistor.

The TES films in Cℓover are Mo/Cu proximity-effect bilayers with normal copper banks to define the edges of the TES. The transitions of the bilayers can be made as sharp as 1—2 mK for high sensitivity. We can also tune the transition temperature (T_c) of the films to the desired value by choosing the film thicknesses. The transition temperature T_c and thermal conductance of Cℓover's detectors are chosen to meet the NEP and power-handling requirements. All of Cℓover's detectors operate with a bath temperature of 100 mK. The 97- and 150-GHz detectors have T_c=190 mK, while the 220-GHz detectors have T_c=430 mK.

Cooling is provided by a Cryomech pulse-tube cooler, a high-capacity Chase Research He-7 cooler, and a miniature dilution refrigerator [12].

B. 97-GHz RF Design

To reach background-limited sensitivity Cℓover's bolometers must have a high absorption efficiency. Cℓover's 97-GHz detectors use finline transitions to couple to the radiation in the waveguide. Power is coupled from the waveguide to the TES planar circuit using an antipodal finline taper consisting of two superconducting fins of Nb separated by 400 nm of SiO_2 [13], [14] (see 3). The lower Nb layer is 250 nm thick. The upper layer is 500 nm thick to ensure reliable lift-off patterning with the step over the oxide layer. The whole structure is deposited on one side of a 225-µm silicon substrate. Before the fins overlap, the thickness of the SiO_2 is much less than that of the silicon and the structure behaves as a unilateral finline. As the fins overlap, the structure starts to behave like a parallel-plate waveguide with an effective width equal to the overlap region. When the width of the overlap region becomes large enough for fringing effects to be negligible, a transition to a microstrip mode is performed. The microstrip is then tapered to the required width. Cℓover uses a 3-µm Nb microstrip with a characteristic impedance of 23 Ω to deliver power to the TES.

The detector chip's 225-µm silicon substrate loads the waveguide in which it sits, changing the waveguide impedance. To prevent reflections the chip has a tapered end which provides a gradual impedance transition. The first set of prototype detectors use a WR-10 waveguide and have a taper angle of 40º. This angle was chosen based on detailed electromagnetic modelling.

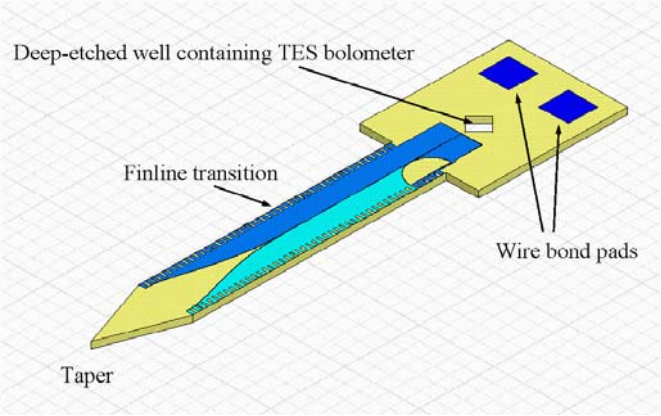

Fig. 3 Layout of prototype 97-GHz Cℓover detector chip.

C. 97-GHz Prototype Detectors

Fig. shows prototype 97-GHz Cℓover detector chips fabricated on a 2" wafer. Deep reactive ion etching (DRIE) is used to etch the well for the silicon nitride island and to define the outline of each chip. All of the processing of these detectors is carried out by the Detector Physics Group at the Cavendish Laboratory except for the DRIE [15].

After DRIE the chips are held in place in the wafer by small silicon tabs which can be easily broken to remove the chips.

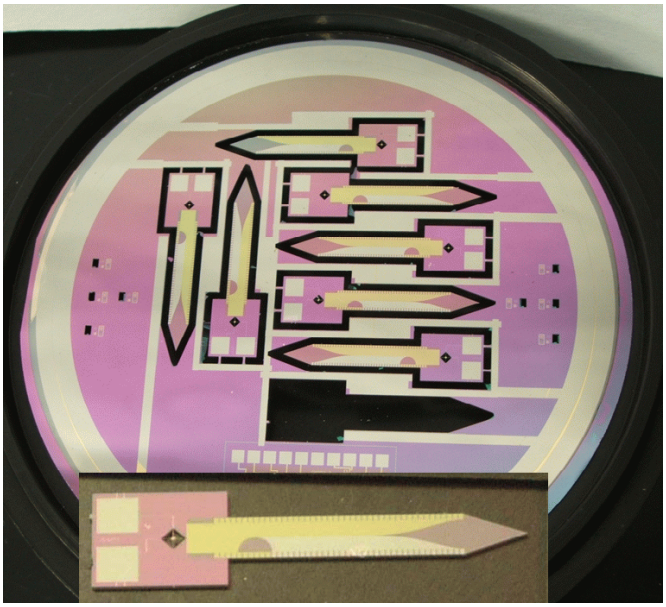

Fig. 4 Prototype 97-GHz $C_t$over detector chips fabricated on a 2" wafer and (inset) an enlarged view of an individual chip. The chip is about 17 mm long.

D. RF Design for the HF Instrument

The 150- and 220-GHz detectors use a completely different RF design to the 97-GHz detectors, partly because it is much more difficult and expensive to fabricate the waveguide OMTs in the smaller waveguides required at the higher frequencies. Each HF detector is intrinsically polarisation-sensitive and may be considered to be a planar OMT. Four probes protrude into a circular waveguide (see Fig 5). The two pairs of opposing probes are sensitive to orthogonal linear polarisations. Microstrips carry the signals from each pair of probes to a TES bolometer where the RF power is dissipated as heat in a matched termination resistor. Power from the two probes in a pair is thus combined incoherently.

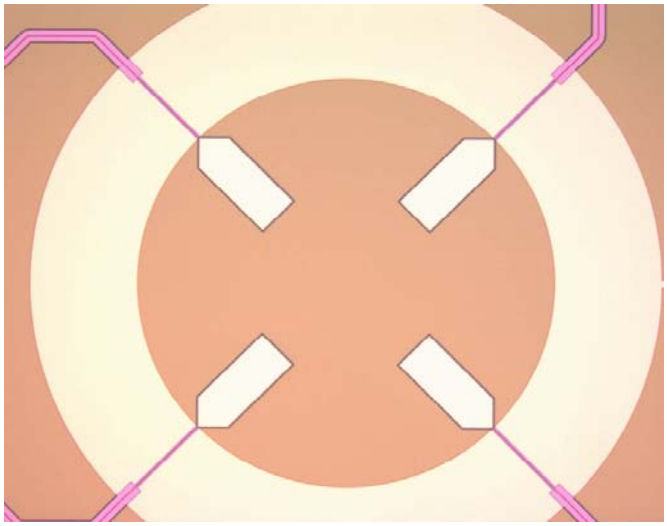

Fig. 5 Four-probe OMT fabricated for $C_t$over. The probes are suspended on a nitride membrane that lies across a circular waveguide ~1.7 mm in diameter. Each probe feeds a microstrip that is terminated by a matched resistor on a nitride island where the deposited power is measured by a TES. Pairs of opposite probes are sensitive to orthogonal linear polarisations.

E. 150-GHz Prototype Detectors

Fig. shows prototype four-probe OMT detectors that were fabricated for $C_t$over. Fabrication of these chips uses exactly the same process as the 97-GHz finline detectors, except that an extra niobium and an extra insulating layer are needed for the microstrip crossings (see Fig. 8). These crossings are required to allow us to route the microstrips' signals from opposite pairs of waveguide probes so that they terminate on a single nitride island where the power from both of them is combined and detected by the same TES.

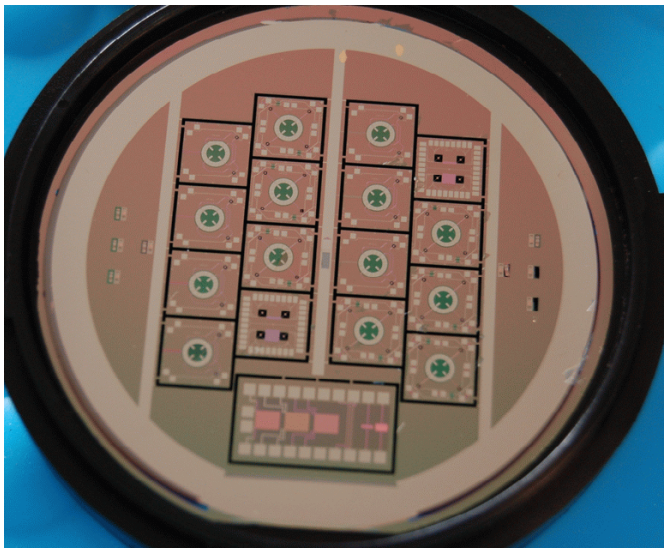

Fig. 6 Prototype 150-GHz $C_t$over detector chips fabricated on a 2" wafer. Each chip is about 6 mm square.

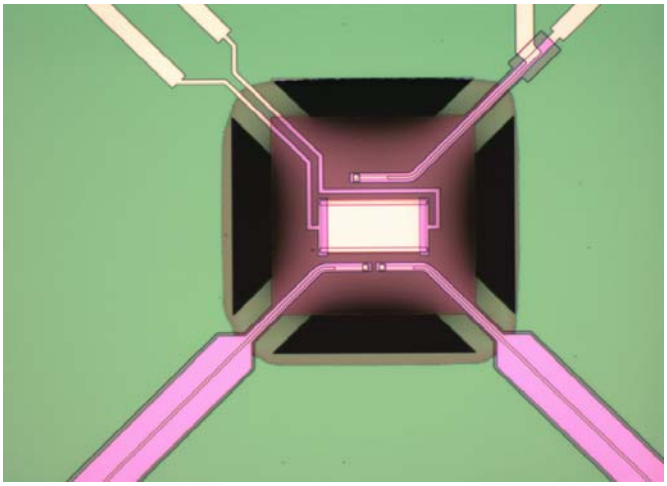

Fig. 7 150-GHz prototype TES. Two microstrips fed by opposite waveguide probes terminate on the nitride island and the signals from these are combined incoherently. The third resistor is the on-chip heater which is used to compensate for changes in the sky background power.

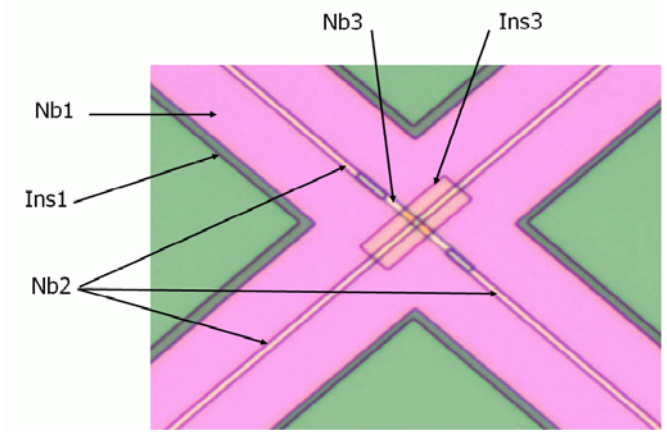

Fig. 8 Microstrip crossover required for power combining in 150-GHz prototype detector. The different niobium and SiO_2 insulator layers are labelled.

III. Detector Packaging

A. 97-GHz Detector Block

The finline detectors are packaged in linear modules containing 16 detectors. The detector block comes in two halves, upper and lower. When these are put together they form split-block waveguides, into which the finlines protrude. The edges of the finlines stick into shallow slots in the sides of the waveguides for grounding. The serrations on the edges of the finlines (see Fig. 3) are there to prevent unwanted modes from propagating. A detector block holding two detectors for testing is shown in Fig. and Fig. . The blocks in the final instrument each hold 16 detector chips.

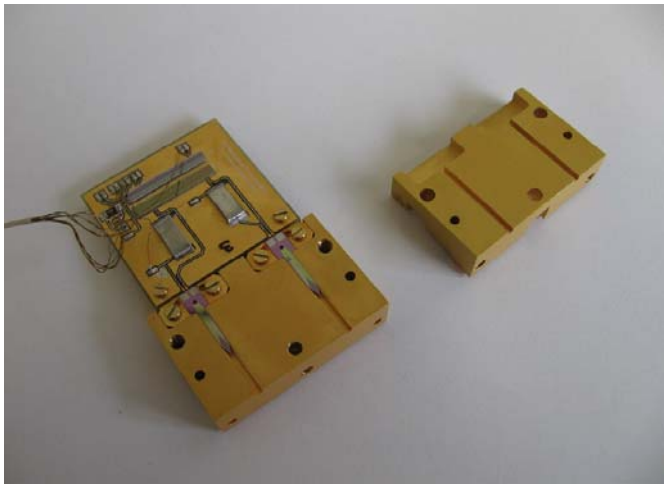

Fig. 9 Test detector block with two prototype detectors. The upper and lower blocks form waveguides in which the finlines sit.

Aluminium wire bonds provide electrical connections from the detector chip to a PCB carrying the multiplexer, inductors, and shunt resistors. This PCB has gold-plated copper tracks and as much of the copper as possible is left on the board to help with heatsinking. The gold is deposited by electroplating in order to avoid the use of a nickel undercoat. The traces are tinned with solder to make them superconducting. The PCB is enclosed in a copper can which is wrapped in niobium foil under which there is a layer of Metglas® 2705M, a high-permeability amorphous metal foil (Hitachi Metals Inc.). The Nb foil excludes magnetic fields while the Metglas diverts any trapped flux away from the SQUIDs. Further magnetic shielding is provided by high-permeability shields built into the cryostat.

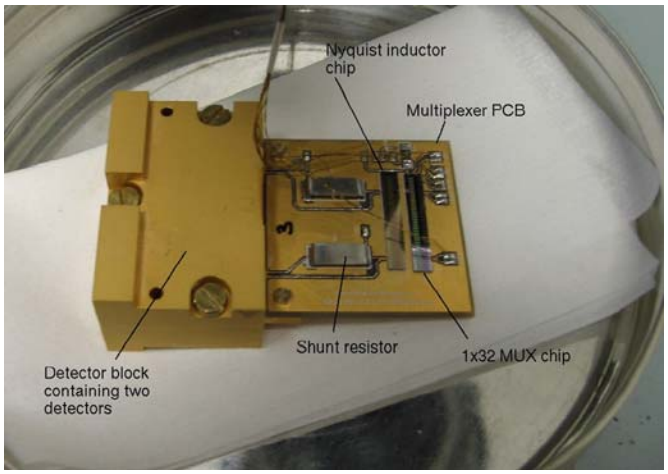

Fig. 10 Test detector block assembled. The PCB at the back carries the NIST SQUID multiplexer chip.

This scheme has the apparent disadvantage that it under-uses the 1×32 multiplexer chips by a factor of two, increasing the number needed. However, because we are not using all of the first-stage SQUIDs on a multiplexer chip, we can connect the detectors to those SQUIDs that have the most similar critical currents. This optimises the first-stage

SQUID biasing, reducing the noise contribution from this stage of the readout. Reducing the number of detectors multiplexed by each multiplexer chip also reduces the aliased readout noise, improving the NEP. Another advantage of under-using the multiplexer chips is that we can use chips where not all of the first-stage SQUIDs are functioning, reducing the cost per chip.

B. 97-GHz Detector Mounting Scheme

In the final instrument each detector block will carry 16 detectors. We would like to be able to remove and replace one of these detectors without disturbing the others. Thus, we mount each detector chip on an individual copper chip holder (see Fig. 11), which is then mounted in the detector block. We must make good thermal contact to the back of each detector chip, while at the same time relieving stresses caused by differential contraction that could demount or break the chip. We fix the chip to a chip holder using Stycast 1266 epoxy. We have verified that this provides a good thermal joint that survives repeated thermal cycling. The chip holder has a well in the centre to divert excess epoxy away from the suspended nitride island. The chip holder is secured to the detector block by two brass screws. A shallow recess in the bottom of the chipholder allows a piece of Nb foil to be inserted to provide additional magnetic shielding for the detector chip.

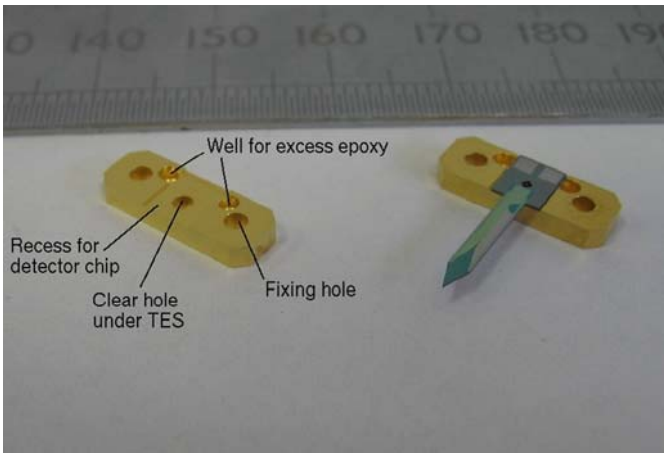

Fig. 11 Prototype detector and individual copper chipholder.

C. 150-GHz Detector Mounting Scheme

Because of their different RF architecture, the HF detectors require a different mounting scheme. While the finline detectors protrude along the axis of a rectangular waveguide, the four-probe detectors in the HF instrument lie across a circular waveguide.

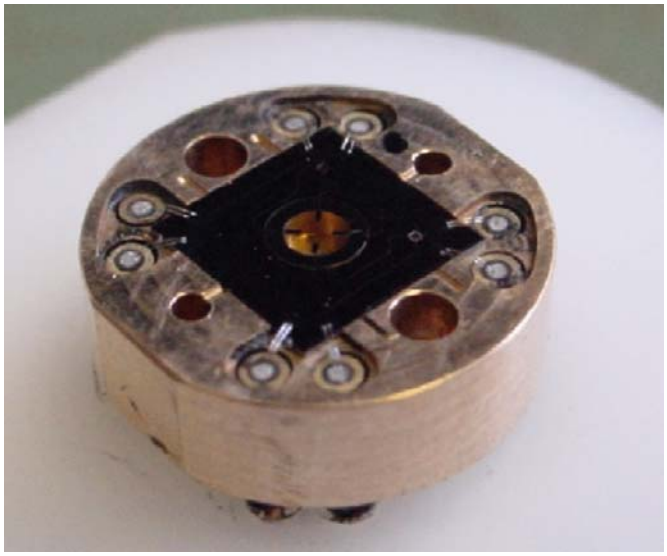

Fig. 12 150-GHz prototype detector mounted on a chip holder. Electrical connections are made from the chip to copper-clad aluminium pins which are fed through to the bottom of the holder where they are soldered into a PCB. There is a quarter-wave recess in the block under the nitride membrane.

Fig 12 shows a 150-GHz prototype detector chip mounted on an individual chipholder. There is a recess a quarter-wavelength deep under the membrane carrying the probes and the floor of this recess forms the backshort for the probes. There are eight electrical feedthroughs in the block. These are made of copper-clad aluminium wire that is held in place with epoxy. The top surface of the wire is polished flat so that it can be connected to the chip by aluminium wire bonds. At the bottom of the chipholder the copper cladding on the wire makes it possible to solder the holder into a PCB that carries the SQUID readout. A corrugated feedhorn is bolted to the top of the chipholder.

IV. Detector Testing

A. Cℓover Test Bed

We have a dedicated test cryostat for characterising these detectors and also for mass-testing the science-grade detector modules. The cryogenics are the same as in the final instrument, comprising a pulse-tube cooler, He-7 sorption fridge, and miniature dilution fridge. This allows us to test the detectors under realistic conditions and to validate Cℓover's cryogenics. The refrigerator can be operated remotely, and can reach a temperature of about 70 mK with a hold time of about eight hours. The cryostat has a large test volume and contains SQUID series arrays and associated wiring to read out up to eight detector modules or 128 TESs at once.

There is an internal black-body illuminator for optical tests. This illuminator has a conical radiator for high efficiency and two low-pass filters for defining the bandpass. We have paid careful attention to the thermal design of this illuminator to minimise its effect on the thermal performance of the refrigerator. The filters are mounted on nested radiation shields and these shields are heatsunk at 350 mK

and 1 K stages of the He-7 sorption fridge. The conical radiator with its G-10 support structure is shown in Fig. . The thermal conductance to the 1-K end piece is controlled by the length of the wires to the heater and thermometer.

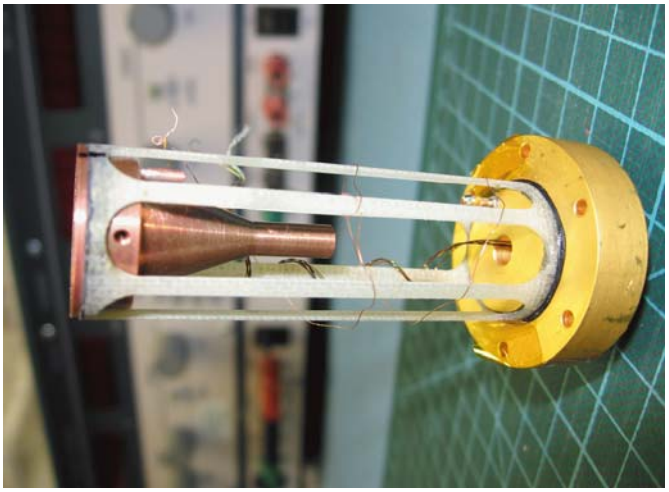

Fig. 13 Black-body illuminator with thermal shields and filters removed.

The test bed also has two parallel sets of warm readout electronics (the MCE and an analogue system) so that we can characterise fully the entire readout chain from the detectors up to room temperature. Unlike the MCE, the analogue electronics does not multiplex, but can be switched between three columns and three rows. However, it is more versatile and convenient for characterising the TESs and SQUIDs. For example, it can lock on any of the three SQUID stages, while the MCE is designed to lock on the first-stage SQUID only. All of the results presented here were obtained with the analogue electronics.

B. Dark NEP

Our first generation of devices had excess noise, which we attribute to internal thermal fluctuation noise. To eliminate this excess noise we modified the TES geometry to improve thermalisation. We found that when we added copper fingers extending most of the way across the TES from opposite edges (see Fig 14) the measured noise in the TES was consistent with what we expected from the known Johnson and phonon noise sources [16]. We thus adopted this geometry for the final design.

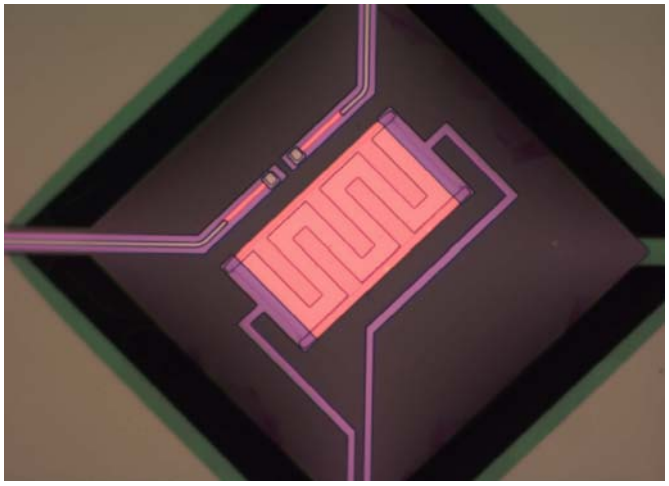

Fig. 14 TES with copper fingers extending from the normal copper banks for improving thermalisation and reducing excess noise. This TES geometry was adopted for the science-grade 97-GHz detectors.

The prototype detectors were fabricated with a variety of nitride leg geometries in order to find the leg geometry that would give a thermal conductance consistent with the power-handling requirement.

With a conductance that gives us the power handling we need for the 97-GHz detectors we measure a dark NEP of about 1.7×10^{-17} W/√Hz, although we have measured NEPs as low as 1.5×10^{-17} W/√Hz on devices with lower conductance. We satisfy the detector NEP requirement comfortably at 97 GHz. Since the LF instrument has the strictest NEP requirement, we will be able to meet the requirement at the other two frequencies. The time constants of all of the prototype detectors were also consistent with the requirements.

C. 97-GHz Optical Testing

For optical testing we mounted a pyramidal feedhorn on the detector block to improve the coupling of the waveguide to the black-body illuminator. 15 shows the effect of optical illumination on the characteristic current-voltage (IV) curve of the TES in a prototype detector. The IV curves are produced by sweeping the TES bias voltage downwards and recording the feedback current in the SQUIDs' flux-locked loop. At high TES bias voltages the TES is in its normal state and we see ohmic behaviour (the straight part of the IV curve). At lower biases the TES is on its superconducting transition. This is the negative-resistance region of the IV curve where the current increases as the bias voltage decreases. As the illuminator temperature is increased, the point at which the TES saturates and goes normal is driven to lower and lower bias voltages. This deficit in the Joule power needed to drive the detector normal shows that optical power is being absorbed by the detector.

Fig. shows the response of a prototype detector to optical power when it is biased at three different TES bias voltages. The response is linear until the incident power exceeds the detector's power handling at that bias voltage and the TES is driven normal. The detection efficiency is estimated to be 89%.

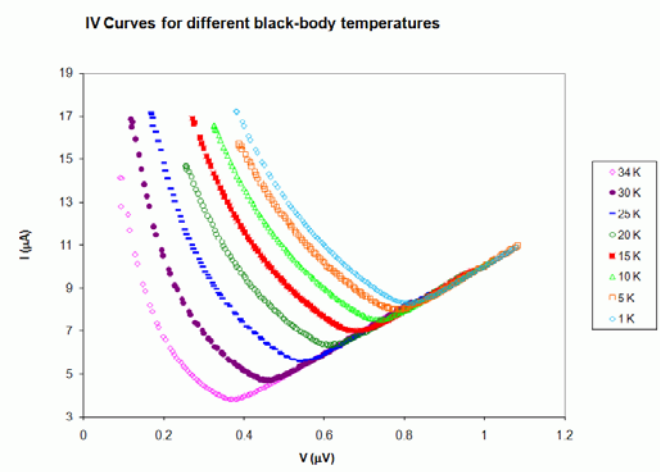

Fig. 15 IV curves of a prototype detector with the black-body illuminator at different temperatures. As the black-body temperature increases the bias voltage at which the TES is driven normal decreases, showing that optical power is being absorbed.

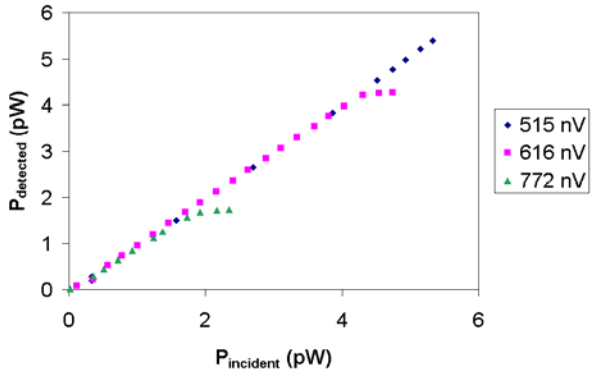

Fig. 16 Detected optical power at different TES voltage biases for a prototype 97-GHz finline detector.

The finline detectors are fabricated on 225-μm thick silicon. Because of silicon's high dielectric constant (ε=11.8) the chip loads the waveguide significantly. To investigate this effect we mechanically thinned one detector's silicon substrate to 100 μm using a dicing saw. The measured optical efficiency was consistent with 100%, compared with 89% for a detector with an unthinned substrate. We attribute this improvement in optical efficiency to the reduced dielectric loading in the waveguide.

The dielectric loading is worse at higher frequencies where the waveguides are smaller and this is one of the reasons why Cℓover uses a different detector architecture for the HF instrument. The substrate thickness cannot be reduced much below 225 μm because the wafers will become too fragile for processing. However, we have found that it is possible to reduce the effective dielectric constant by micromachining the substrate, which will enable the use of finlines on silicon substrates at higher frequencies in the future [16].

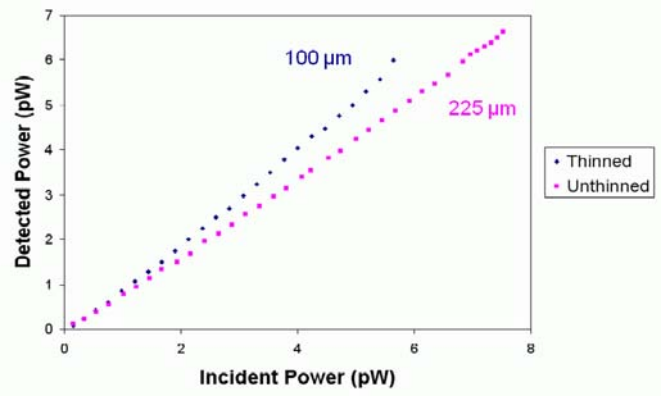

Fig. 17 Comparison of optical power detected by a detector whose substrate has been thinned to 100 μm and one which has the full 225-μm substrate.

D. 150-GHz Optical Testing

Optical testing of the 150-GHz prototype detectors was carried out in the Cℓover test bed. The same black-body illuminator was used as for the finline measurements, but the two low-pass filters were replaced with ones appropriate for the 150-GHz passband. The detectors were coupled to the illuminator through a corrugated feedhorn similar to the ones that will be used in the final instrument. The response of one of these detectors to the black-body illuminator is shown in Fig. .

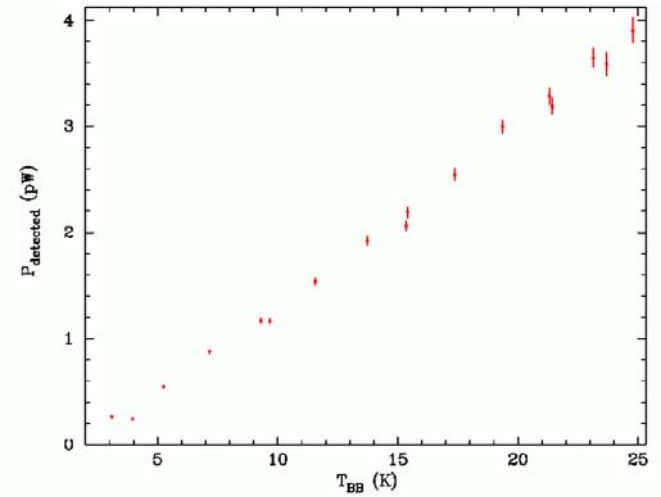

Fig. 18 Detected optical power versus black-body illuminator temperature for one polarisation channel of a 150-GHz prototype detector.

V. 97-GHz Science-Grade Detectors

Based on measurements of the prototype detectors we made some modifications to the detector design. The finline has been redesigned and made shorter, which allowed us to reduce the length of a chip to 10 mm from 17 mm. We have also reduced the height of the waveguide from 1.27 to 1.1 mm to prevent the propagation of unwanted modes. Because the science-grade detectors are smaller we can now fabricate 30 on a 2" wafer where before we fabricated only eight prototype detectors. Also, we have replaced the tapered tip with a lower-loss stepped tip. Fig. shows a science-grade

detector chip. The science-grade detectors have two microstrips terminated on the nitride island. One is fed by the finline and the other allows us to inject DC power into the bolometer to compensate for changes in the sky power.

This will allow us to operate at the same bias point (and hence with the same responsitivity) in different weather conditions. The power-handling requirement was met by making the nitride legs shorter, increasing the thermal conductance. This has the added advantage of making the bolometer mechanically more robust. We are currently testing these detectors.

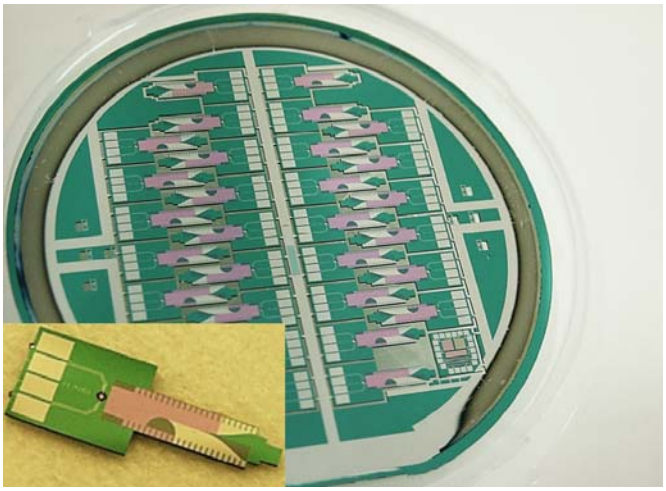

Fig. 19 Science-grade detectors fabricated on a 2" wafer and (inset) an enlarged view of an individual science-grade detector chip. The chip is about 10 mm long.

CONCLUSIONS

We have established a reliable process for fabricating microstrip-coupled TES detectors with high yield and uniformity. We have verified the operation of these detectors with two completely different RF architectures. The finline detectors for Cℓover's LF instrument fabricated using this process satisfy the requirements for optical efficiency, dark NEP, power handling, and time constant. The measured dark NEP is 1.75×10^{-17} W/√Hz at 200 mK for detectors with the target thermal conductance. The four-probe OMT detectors also show good optical efficiency and we plan to measure the cross-polarisation soon. We have also verified the detector packaging for both RF architectures under realistic conditions. We are currently testing the science-grade finline detectors for the LF instrument.

The microstrip-coupled TES architecture that we have developed for Cℓover has great potential for future instruments. With this detector architecture it is possible to insert planar circuitry such as filters, phase shifters, or modulators into the microstrip between the absorber and TES, converting a simple detector into a multi-function integrated circuit.

ACKNOWLEDGMENT

Cℓover is funded by the Science and Technology Facilities Council. The authors would like to thank Michael Crane for his contribution to device fabrication and process development, Dennis Molloy for mechanical engineering, and David Sawford for electronic and software engineering.

We are grateful to Andrew Bunting at the Scottish Microelectronics Centre for carrying out the DRIE. We are also grateful to Joel Ullom of NIST for his advice on excess-noise mitigation.

REFERENCES

[1] Rees, M. J., "Polarization and Spectrum of the Primeval Radiation in an Anisotropic Universe," *Astrophysical Journal*, vol. 153, pp. L1, Jul. 1968.

[2] Seljak, U. and Zaldarriaga, M., "Signature of Gravity Waves in the Polarization of the Microwave Background," *Physical Review Letters* , vol. 78, pp. 2054–2057, Mar. 1997.

[3] Kamionkowski, M., Kosowsky, A., and Stebbins, A., "A Probe of Primordial Gravity Waves and Vorticity," *Physical Review Letters*, vol. 78, pp. 2058–2061, Mar. 1997.

[4] Piccirillo, L., Ade, P., Audley, M. D., Baines, C., Battye, R., Brown, M., Calisse, P., Challinor, A., Ferreira, P., Gear, W., Glowacka, D. M., Goldie, D., Grimes, P. K., Haynes, V., Johnson, B., Jones, M., Lasenby, A., Leahy, P., Lewis, S., Maffei, B., Martinis, L., Mauskopf, P. D., Melhuish, S. J., North, C. E., O'Dea, D., Pisano, G., Savini, G., Sudiwala, R. V., Taylor, A., Teleberg, G., Titterington, D., Tsaneva, V. N., Tucker, C., and Watson, R., "The CLOVER experiment," *Proceedings of the SPIE*, vol. 7020, in press, 2008.

[5] Irwin, K. D., "Phonon-Mediated Particle Detection Using Superconducting Tungsten Transition-Edge Sensors", PhD thesis, Stanford University, Stanford, California (1995).

[6] Chervenak, J. A., Irwin, K. D., Grossman, E. N., Martinis, J. M., Reintsema, C. D., and Huber, M. E., "Superconducting multiplexer for arrays of transition edge sensors, *Applied Physics Letters,* vol. 74, pp. 4043–4045, Jun. 1999.

[7] de Korte, P. A. J., Beyer, J., Deiker, S., Hilton, G. C., Irwin, K. D., Macintosh, M., Nam, S. W., Reintsema, C. D., Vale, L. R., and Huber, M. E., "Time-division superconducting quantum interference device multiplexer for transition-edge sensors," *Review of Scientific Instruments,* vol. 74, pp. 3807–3815, Aug. 2003.

[8] Reintsema, C. D., Beyer, J., Nam, S. W., Deiker, S., Hilton, G. C., Irwin, K., Martinis, J., Ullom, J., Vale, L. R., and Macintosh, M., "Prototype system for superconducting quantum interference device multiplexing of large-format transition-edge sensor arrays," *Review of Scientific Instruments,* vol. 74, pp. 4500–4508, Oct. 2003.

[9] Welty, R. P. and Martinis, J. M., "Two-stage integrated SQUID amplifier with series array output," *IEEE Transactions on Applied Superconductivity,* vol. 3, pp. 2605–2608, Mar. 1993.

[10] Battistelli, E. S., Amiri, M., Burger, B., Halpern, M., Knotek, S., Ellis, M., Gao, X., Kelly, D., Macintosh, M., Irwin, K., and Reintsema, C., "Functional Description of Read-out Electronics for Time-Domain Multiplexed Bolometers for Millimeter and Sub-millimeter Astronomy," *Journal of Low Temperature Physics,* vol. 151, pp. 908–914, May 2008.

[11] Audley, M. D., Holland, W. S., Hodson, T., MacIntosh, M., Robson, I., Irwin, K. D., Hilton, G., Duncan, W. D., Reintsema, C., Walton, A. J., Parkes, W., Ade, P. A. R., Walker, I., Fich, M., Kycia, J., Halpern, M., Naylor, D. A., Mitchell, G., and Bastien, P., "An update on the SCUBA-2 project," *Proceedings of the SPIE*, vol. 5498, pp. 63–77, Oct. 2004.

[12] Teleberg, G., Chase, S. T., and Piccirillo, L., "A miniature dilution refrigerator for sub-Kelvin detector arrays," *Proceedings of the SPIE*, vol. 6275, pp. 62750D, Jul. 2006.

[13] Yassin, G. and Withington, S., "Electromagnetic models for superconducting millimetre-wave and submillimetre-wave microstrip transmission lines," *Journal of Physics D Applied* Physics, vol. 28, pp. 1983–1991 Sep. 1995.

[14] Yassin, G., Withington, S., Buffey, M., Jacobs, K., and Wulff, S., "A 350-Ghz SIS antipodal finline mixer," *IEEE Trans. on Microwave Theory and* Techniques, vol. 48, pp. 662–669, 2000.

[15] Glowacka, D. M., Goldie, D. J., Withington, S., Crane, M., Tsaneva, V., Audley, M. D., and Bunting, A., "A Fabrication Process for Microstrip-Coupled Superconducting Transition Edge Sensors Giving Highly Reproducible Device Characteristics," *Journal of Low Temperature* Physics, vol. 151, pp. 249–254, Apr. 2008.

[16] Goldie, D. J., Audley, M. D., Glowacka, D. M., Tsaneva, V. N., and Withington, S., "Modeling and reduction of excess noise in transition edge sensor detectors," *Proceedings of the SPIE*, vol. 7020, in press, 2008.

[17] North, C. E., Grimes, P. K., Yassin, G., Tsaneva, V. N., Glowacka, D. M., Goldie, D., Audley, M. D., Withington, S., Melhuish, S. J., Pisano, G., Maffei, B., and Piccirillo, L., "Dielectric constant reduction using holey substrates in finline millimeter and submillimeter detectors," *Proceedings of the SPIE*, vol. 7020, in press, 2008.

Superconducting transition detectors as power amplifiers for cryomultiplexing

P Helistö, J. Hassel, A. Luukanen*, H. Seppä
VTT, Sensors, PO Box 1000, 02044 VTT, Finland
*Millilab, PO Box 1000, 02044 VTT, Finland
Email: panu.helisto@vtt.fi

For large scale multiplexing of high-resolution astrophysical radiation detectors, power gain is needed. The power gain is normally provided by the readout amplifier, but especially in the case of time division multiplexing, power gain by the detector is beneficial. In this paper, we characterise the achievable power gain, dynamic range, noise and stability of resistively biased transition detectors.

Superconducting transition detectors such as X-ray calorimeters or THz bolometers are usually operated in voltage biased mode at voltages much below the minimum of the detector *I* - *V* curve.[1] Such biasing provides high current responsivity, low Johnson noise, high stability and good linearity due to the strong negative electrothermal feedback (ETF). However, there is no power gain in the detector. This calls for a very low noise readout amplifier, typically SQUID, in the case of cryomultiplexing.

Recently, it was shown that by voltage biasing the detector at the *I* - *V* curve minimum, a room temperature amplifier can read out the signal of transition detectors operated even in the mK range.[2] This is due to the effective power gain in the detector near the minimum current bias point: the output noise power $r_d i_n^2$ of the detector diverges as the differential resistance of the detector r_d □ □.[3] Unfortunately, at high frequencies, r_d is reduced, making the method not optimal for high bandwidth cryomultiplexing.

Here we demonstrate that by biasing the detector through a bias resistor, power gain *G* is obtained, the maximum of which is equal to the ETF loop gain L_0. The available power gain is limited by stability: the dynamic resistance of the system has to be positive at all frequencies. In first experiments we have measured power gains of up to 10-20. In an optimized system, we expect to achieve maximum power gain up to 50-100, allowing multiplexing of up to 100 detectors in the scheme described in Ref [4].

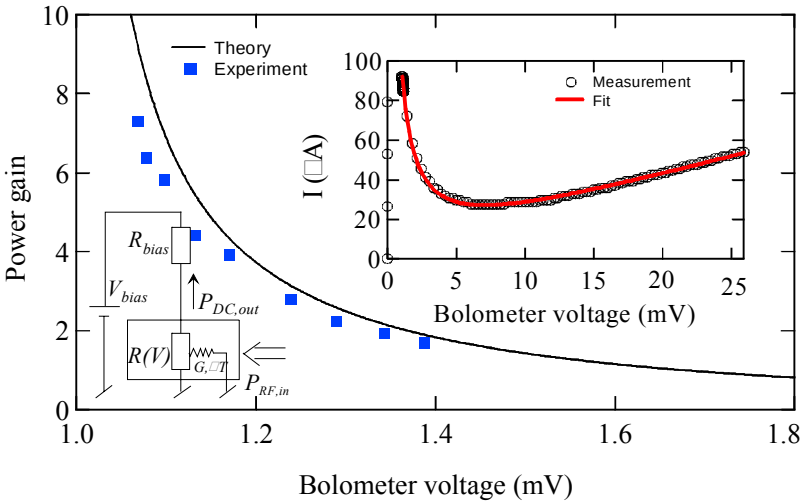

Figure 1: Power gain of a superconducting transition bolometer as a function of voltage. Squares – experiment, solid line – theory. Insets: Left: simplified circuit diagram. Right: bolometer *I-V* curve. R_{bias} = 9.9 □, bolometer normal state resistance R_N = 520 □.

[1] K. D. Irwin, Appl. Phys. Lett. **66** (1995) 1998–2000.
[2] JS Penttilä, H Sipola, P Helistö and H Seppä, Supercond. Sci. Technol. **19** (2006) 319–322.
[3] P Helistö, JS Penttilä, H Sipola, L Grönberg, F Maibaum, A Luukanen and Heikki Seppä, IEEE Trans. Appl. Supercond. **17 (**2007) 310 – 313.
[4] A Luukanen et al, this conference.

Distributed Antenna Coupled Cold-Electron Bolometers for Focal Plane Antenna

Leonid Kuzmin
Chalmers University of Technology, S-41296 Gothenburg, Sweden

Abstract— **Novel concepts of the parallel and series array of Cold-Electron Bolometers (CEB) with Superconductor-Insulator-Normal (SIN) Tunnel Junctions have been proposed for distributed focal plane antenna. The arrays are developed for a pixel design based on arrays of CEBs coupled to a distributed slot antenna or dipole antenna.**

Two variants of the CEB arrays have been considered for both types of antenna on bulk substrate. The parallel connection of CEBs with SIN tunnel junctions in voltage-biased mode is optimal for a slot antenna. Some improvement of properties can be achieved by using optimal configuration of CEB with SIN junction and Andreev contact. Remarkable progress in performance is expected from implementation of a new technology for fabrication of the CEB and SQUID on the same chip in one vacuum circle. Estimations of the CEB noise with SQUID readout have shown an opportunity to realize background-limited performance for typical power load of 5pW proposed for BOOMERanG.

The series connection of CEBs with SIN tunnel junctions in current-biased mode is optimal for dipole antennas. Estimations of the CEB noise with JFET readout have shown an opportunity to realize NEP less than photon noise for typical power load.

Index Terms— Cold-Electron Bolometer, focal plane antenna, SIN tunnel junction, Josephson junction, Andreev contact, SQUID readout

I. INTRODUCTION

Recent Cosmology experiments have discovered that the Universe consists mainly of mysterious Dark Energy and Dark Matter [1]. Indeed, in 2006, a Nobel Prize was awarded for the experimental observation of anisotropies in the Cosmic Microwave Background (CMB) radiation, and the subsequent realization that the expansion of the Universe is controlled by unknown forces [2]. There are several cosmology instruments (B-Pol [3], BOOMERanG, [4], CLOVER , EBEX, BICEP, QUIET,) that are being designed to measure the polarization state of the Cosmic Microwave Background (CMB), in particular the *B*-mode polarization, which is generated by primordial gravitational waves.

It is well known, however, that ground-based experiments are severely limited by atmospheric noise even at best sites. Consequently, space-borne CMB polarization instruments are now being planned both in the USA and Europe. A European consortium has already been assembled to design the next ESA CMB cosmology instrument. An expression of interest has recently submitted to ESA, as part of the Cosmic Vision Call, to support a medium-scale space mission called B-Pol [3].

A new design of antennas and a new generation of detectors are needed for these advanced telescopes, and these detectors must achieve sensitivities better than $\sim 10^{-18}$ W/Hz$^{1/2}$. One of these technologies is the Capacitively Coupled Cold-Electron Bolometer (CEB) [5]-[9]. It operates through direct electron cooling of an absorber by SIN tunnel junctions, and with strong electrothermal feedback [5]. The strong electrothermal feedback is similar to TES (Transition-Edge Sensor) [11,12] with replacement of additional dc heating (TES) by effective electron cooling (CEB) with proper improvement of noise properties and dynamic range. The CEB can be used with both SQUID readout [5,7,9] and JFET [8,10]. The JFET readout has been used for the latest astronomy missions, and the SQUID readout and multiplexing is in process of development for TES. Overall, the goal is to achieve, with a CEB read out by a JFET or SQUID, a noise-equivalent power that is less than the photon noise of the CMB radiation.

The CEB is a planar antenna-coupled superconducting detector that can be easy matched with any planar antenna. Very attractive direction developed in Caltech is distributed focal plane antennas [13,14]. These antennas could help to avoid horns or Si lenses for matching with bolometers. This type of antenna is in ESA plan for developing and testing for B-Pol [3]. Our current interest is to test this antenna for balloon project BOOMERANG [4].

To achieve RF matching to a distributed focal plane antenna, different concepts of the CEB, with SQUID and JFET readouts, must be analyzed. In this paper, we analyze parallel and series arrays of CEBs for matching with slot and dipole antennas. The system is purposed for BOOMERANG balloon telescope and later can be used for B-Pol and other cosmology instruments.

An optimal configuration of CEB with a capacitively coupled SIN junction and an Andreev SN contact [7] has been selected (Fig. 1) for parallel combination of CEBs to match with a slot antenna. This concept has been invented to improve the noise properties by

increasing the responsivity of the CEB in voltage-biased mode with SQUID readout in comparison with "classical" series connections of SIN junctions [5]. An important feature of the design is that the volume of the normal metal is partly squeezed due to the proximity effect of the superconducting electrode from SN Andreev contact. This squeezing further increases the efficiency of the electron cooling without degrading the HF coupling.

Remarkable progress in performance is expected from implementation of a new technology for fabrication of the CEB and SQUID on the same chip in one vacuum circle [15]. Simultanious fabrication of CEB and SQUID on-chip would create more reliable structures and avoid interferences due to wire interconnections of the systems.

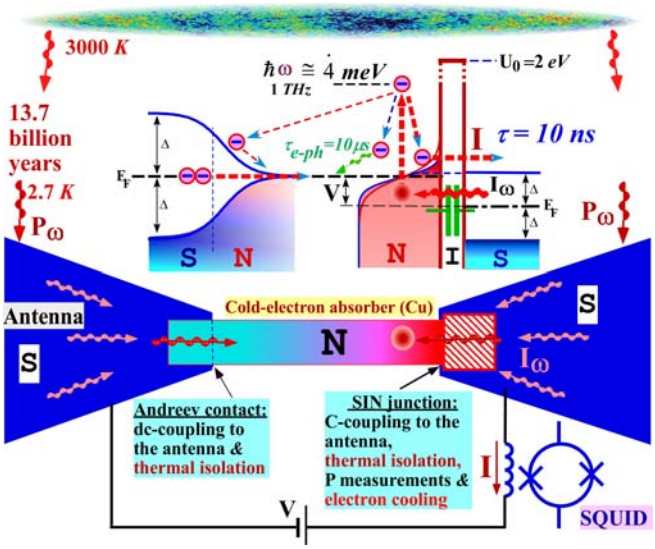

Fig 1. Schematic of the **optimal Cold-Electron Bolometer (CEB) with capacitive coupling to the antenna** and a SQUID readout. The CEB comprises a planar superconducting antenna and an absorber coupled through the capacitance of an SIN tunnel junction, and an SN Andreev contact. The SIN tunnel junction is used also for electron cooling, and for reading out the signal with a SQUID.

Detection using this device is obtained by allowing the incoming signal to pass from the antenna to the absorber through the capacitance of a tunnel junction and an Andreev contact. RF matching is realized by the resistance of a normal absorber, which is independent of the tunnel junction parameters.

The concept is based on *direct electron cooling* of the absorber, which provides strong *negative electrothermal feedback* for the signal. This feedback is analogous to the TES [11,12], but artificial dc heating is replaced by *direct electron cooling* to a minimum temperature. This innovation can lead to a major breakthrough in realizing supersensitive detectors. The noise properties of this device are improved considerably by decreasing the electron temperature. The loop gain of the electrothermal feedback can exceed 1000. The response time is reduced, by electrothermal feedback, to 10 ns compared to the intrinsic e-ph time constant of 10 μs.

The CEB in voltage-biased mode allows a substantial increase in the dynamic range, by removing incoming power from the absorber. The current flowing through the tunnel junction is readout by a SQUID, which intrinsically has a high dynamic range. The CEB with one SIN junction and one Andreev contact has almost twice the responsivity of the traditional CEB with two SIN junctions in series.

II. Model

In what follows we shall use the basic concept of the CEB with strong electrothermal feedback due to electron cooling. This structure has been analyzed in detail in Ref. [5],[16]. The operation of CEB can be described using the heat balance equation:

$$P_{cool}(V,T_e,T_{ph})+\Sigma\Lambda(T_e^5-T_{ph}^5)+\frac{V^2}{R_j}+I^2R_{abs}+C_\Lambda\frac{dT}{dt}=P_0+\delta P(t) \quad (1)$$

Here, $\Sigma\Lambda(T_e^5-T_{ph}^5)$ is the heat flow from the electron to the phonon subsystems in the absorber, Σ is a material constant, Λ is the volume of the absorber, T_e and T_{ph} are, respectively, the electron and phonon temperatures of the absorber; $P_{cool}(V,T_e,T_{ph})$ the cooling power of the SIN tunnel junction; $C_\Lambda = \Lambda\gamma T_e$ is the specific heat capacity of the absorber; Rj the subgap resistance of the tunnel junction; Rabs the resistance of the absorber; *P(t)* the incoming rf power. We can separate Eq. (1) into the time independent term,

$$\Sigma\Lambda(\boldsymbol{T_{e0}^5}-\boldsymbol{T_{ph}^5})+\boldsymbol{P_{cool\,0}}(\boldsymbol{V},\boldsymbol{T_{e0}},\boldsymbol{T_{ph}})=\boldsymbol{P_0},$$ and the time dependent term,

$$(\partial P_{cool}/\partial T+5\Sigma\Lambda T_e^4+i\omega C_\Lambda)\delta T=\delta P. \quad (2)$$

The first term, $G_{cool}=\partial P_{cool}/\partial T$, is the cooling thermal conductance of the SIN junction that gives the negative electrothermal feedback (ETF); when it is large, it reduces the temperature response δT because cooling power, P_{cool}, compensates the change of signal power in the bolometer. The second term, $\boldsymbol{G_{e-ph}}=5\Sigma\Lambda\boldsymbol{T_e^4}$, is electron-phonon thermal conductance of the absorber. From Eq. (2) we define an effective complex thermal conductance which controls the temperature response of CEB to the incident signal power

$$\boldsymbol{G_{eff}}=\boldsymbol{G_{cool}}+\boldsymbol{G_{e-ph}}+i\omega\boldsymbol{C}_\Lambda \quad (3)$$

In analogy with TES [11], the effective thermal conductance of the CEB is increased by the effect of electron cooling (negative ETF).

Here we assume that the SIN tunnel junction is voltage-biased, and the current is measured by a SQUID [5,7,9]. The sensitivity of the device is then characterized by the current responsivity S_I, which is the ratio of the current change and the change in the power load of the bolometer,

$$S_I = \frac{\partial I_\omega}{\partial P_\omega} = \frac{\partial I/\partial T}{G_{cool} + G_{e-ph} + i\omega C_\Lambda} = \frac{\partial I/\partial T}{G_{cool}} \frac{L}{(L+1)[1+i\omega\tau]} \quad (4)$$

where $L = G_{cool} / G_{e-ph} >> 1$ is ETF gain and

$$\tau = C_\Lambda / G_{e-ph} = \tau_0 / (L+1) \quad (5)$$

is an effective time constant, $\tau_0 = C_\Lambda / G_{e-ph}$ ($\cong 10\mu s$ at 100 mK).

The strength of the electrothermal feedback is estimated as:

$$L(\omega) = \frac{G_{cool}}{G_{e-ph}(1 + i\omega\tau)} = \frac{\partial I / \partial T}{G_{cool} + G_{e-ph} + i\omega C_\Lambda} \quad (6)$$

Noise properties are characterized by the *NEP*, which is the sum of three different contributions:

$$NEP^2_{total} = NEP^2_{e-ph} + NEP^2_{SIN} + \delta I^2 / S_I^2 \quad (7)$$

$$NEP^2_{e-ph} = 10 k_B \Sigma \Lambda (T_e^6 + T_{ph}^6) \quad (8)$$

is the noise associated with electron-phonon interaction; NEP^2_{SIN} is the noise of the SIN tunnel junctions, and the last term $\delta I^2/S^2_I$ is the noise of an amplifier (SQUID): δI, is expressed in pA/Hz$^{1/2}$.

The noise of the SIN tunnel junctions, NEP^2_{SIN} , has three components: shot noise $2eI/S^2_I$, the fluctuations of the heat flow through the tunnel junctions, and the anticorrelation term between these two processes [16],[17].

$$NEP^2_{SIN} = \delta P^2_\omega - 2\frac{\delta P_\omega \delta I_\omega}{S_I} + \frac{\delta I^2_\omega}{S_I^2} \quad . \quad (9)$$

This anticorrelation is a form of the electrothermal feedback discussed earlier by Mather [18].

III. Parallel Array of CEB with SIN Tunnel Junctions and SQUID Readout

The analysis of an array of the Cold-Electron Bolometers (CEB) for the slot antenna (Fig. 2) shows that the optimal configuration is a parallel array of the CEBs with SIN tunnel junctions in voltage-biased mode [5]. All CEBs are connected in parallel for dc bias. This slot antenna will be sensitive only to one horizontal component of RF signal.

The further improvement of performance could be achieved by using the optimal CEB in voltage-biased mode with a single SIN Junction and an Andreev SN contact [7]. Any use of a double junction in

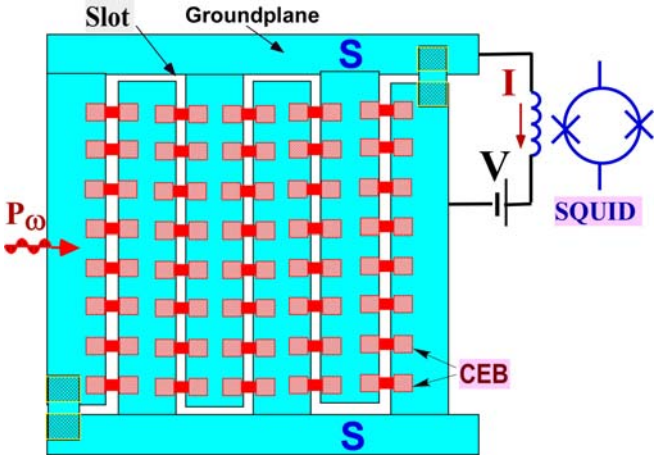

Fig 2 A distributed single polarization slot antenna [12,13] with a parallel array of Cold-Electron Bolometers (CEB) [Kuzmin] and a SQUID readout. This slot antenna will be sensitive only to horizontal component of RF signal. The CEBs with SIN tunnel junctions and Al-Al SQUID could be fabricated on the same chip in one vacuum circle [Kuzmin-patent].

voltage-biased mode [5,7] would lead to the splitting power between two junctions and some degradation of responsivity. The Al-Al SQUID and CEB with SIN tunnel junctions could be fabricated on the same chip in the same vacuum circle [15]. Simultaneous fabrication of CEB and SQUID on-chip would create more reliable structures and avoid interferences due to wire interconnections of the systems. Total structure with CEB, SQUID with magnetic coil, antenna, and protective resistors would take three e-beam exposures and one photolithography for contact pads.

We have analyzed the concept of an optimal cold-electron bolometer for 350 GHz channel of BOOMERANG balloon telescope in the presence of the typical power load (P_0 = 5 pW per polarization component) [4]).

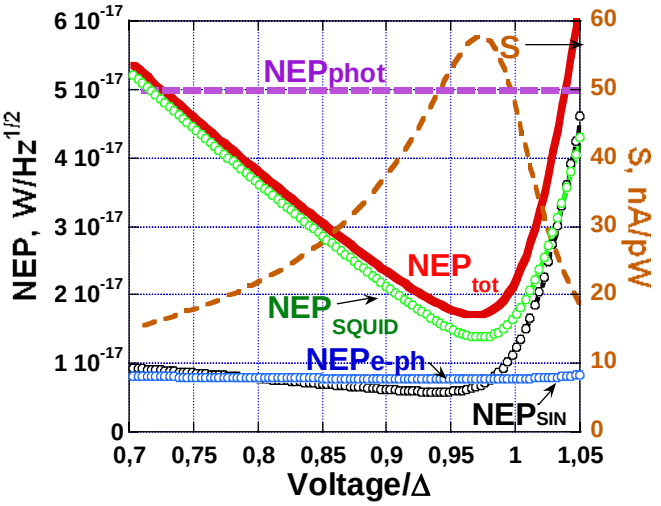

Fig. 3 Total NEP of the 40 CEB array with SIN tunnel junctions for the 350 GHz channel, with a SQUID noise current of 0.8 pA/Hz$^{1/2}$. R=0.2 kOhm, S=1μm^2, Vol=0.005um^3, power load P_0 = 5 pW, T=300 mK. The NEPphot= 5*10^{-17} W/Hz$^{1/2}$ is shown by dashed line.

Photon noise: $NEP_{phot} = \sqrt{2P_0 * hf}$. (10)

For the 350GHz channel, NEPphot= 5*10^{-17} W/Hz$^{1/2}$.

Fig. 3 shows the results of a simulation of a CEB with a single SIN junction, with realistic parameters for the tunnel junction and absorber, and values of SQUID noise of 0.8 pA/Hz$^{1/2}$. The level of NEPtot<NEPphot has been clear achieved for selected parameters of the CEB.

IV The CEB Array with SIN tunnel junctions in *current-biased mode* with JFET readout

An alternate mode of CEB operation is a novel concept employing a series/parallel array of CEBs with SIN Tunnel Junctions, for effective matching to a JFET amplifier [8] (Fig. 7). This concept could be optimal for matching with distributed dipole antenna (Fig. 4).

Previous analysis of a single current-biased CEB with JFET readout showed that the JFET input voltage noise limits the sensitivity [8]. The main reason is the degradation of voltage responsivity under high optical power load. The main innovation of the CEB array is the distribution of power between N series CEBs, and summarizing the increased response from the array. Effective distribution of power is achieved by a series/parallel connection of CEBs with dipole antennas (Fig. 4). The response is increased because the CEB is sensitive to the level of power, and the power is decreased N times for the individual CEBs, with a proportional decrease of absorber overheating.

In this paper we analyze a realization of the CEB array for the 350 GHz channel of BOOMERANG. For RF coupling we analyze a system with the CEB array coupled to focal plane dipole antennas (Fig. 4). The problem of DC biasing the CEB arrays can be solved by interconnecting neighbour dipoles by a narrow strip with very high inductive impedance (Fig. 4). This dipole antenna will be sensitive only to one horizontal component of RF signal.

The voltage response is measured by a JFET amplifier in a current-biased mode. The main purpose of this concept is to match the total dynamic resistance of the array to the noise impedance of a JFET (~0.6 MΩ). The power should be divided between the CEBs in the array to increase the responsivity due to lower overheating and moderate electron cooling.

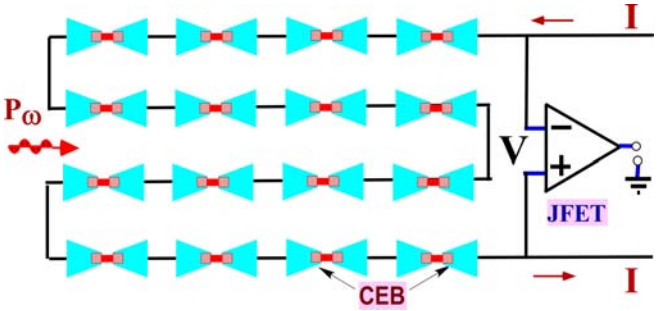

Fig 4 A distributed single polarization dipole antenna [] with a series array of CEBs [8] and a JFET readout. This dipole antenna will be sensitive only to horizontal component of RF signal.

The operation of a CEB array can be analyzed using the heat balance equation for a single CEB [16] taking into account power distribution between the N bolometers. The responsivity S_V is described by the voltage response to an incoming power

$$S_V = \frac{\delta V_\omega}{\delta P_\omega} = \frac{\partial V / \partial T}{G_{e-ph} + 2G_{SIN} + i\omega C_\Lambda} \quad (10)$$

The second term

$$G_{SIN} = \frac{\partial P_{SIN}}{\partial T} - \frac{\partial P_{SIN}}{\partial V}\left(\frac{\partial I}{\partial T} / \frac{\partial I}{\partial V}\right) \quad (11)$$

is the cooling thermal conductance of the SIN junction, G_{SIN}, which gives some electron cooling and help to avoid

overheating of the absorber.

Noise properties are characterized by the noise equivalent power (*NEP*), which is the sum of three contributions:

$$NEP_{tot}^2 = N * NEP_{e-ph}^2 + N * NEP_{SIN}^2 + NEP_{JFET}^2 \quad (12)$$

Here NEP_{e-ph} is the same electron-phonon noise as in Eq. 8. NEP_{SIN} is the noise of the SIN tunnel junctions. The SIN noise has three components: the shot noise *2eI/S2I*, the fluctuations of the heat flow through the tunnel junctions and the correlation between these two processes [13-15]:

$$NEP_{SIN}^2 = \frac{\delta I_\omega^2}{(\frac{\partial I}{\partial V} S_V)^2} + 2\frac{< \delta P_\omega \delta I_\omega >}{\frac{\partial I}{\partial V} S_V} + \delta P_\omega^2 \quad (13)$$

Due to this *correlation* the shot noise is increased at 30-50% in contrast to the CEB in voltage-biased mode (9) where strong *anti-correlation* decreases the shot noise.

The last term is due to the voltage δV and current δI noise of a JFET, which are expressed in nV/Hz$^{1/2}$ and pA/Hz$^{1/2}$:

$$NEP_{JFET}^2 = (\delta V^2 + (\delta I * (2Rd + Ra) * N)^2) / S_V^2 \quad (14)$$

The strong dependence on N, decreasing this noise is included in the responsivity S_V, which is proportional to N.

The estimations were made for the 350 GHz channel of BOOMERANG.

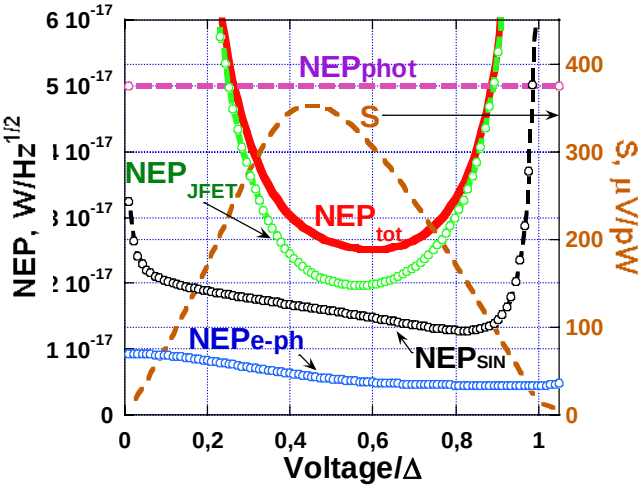

Fig. 5. NEP components of the array of 20 CEBs with JFET readout at 350 GHz with power load of 5 pW for I_{JFET}=10 fA/Hz$^{1/2}$, V_{JFET}=5 nV/Hz$^{1/2}$, R=1 kOhm, $\mathcal{A}$=0.005μm^3, T=300 mK.

We have simulated arrays of CEBs with different numbers of CEBs, from 1 to 1000, to achieve a low NEP with JFET readout and check ability to use large number of CEBs for one pixel. Fig. 5 shows typical results of an NEP simulation for the optimal array of 20 CEBs. We see that for a range of normalized voltage from 0.27 to 0.87, the total NEP of the CEB array is less than the photon noise. At the optimum point, background limited performance is realized (the total noise is determined by the noise of SIN junctions, NEP_{SIN}, (13) due to background power load).

The dependence of the noise components on the number of bolometers is shown in Figure 6. The total NEP decreases to a level less than photon noise for a number of CEBs larger than 6. It is achieved mainly through the suppression of the JFET noise component due to the increased responsivity (10). Figure 6 demonstrates a strong linear increase of the responsivity proportional to N when the number of bolometers is increased. The noise of the JFET (14) is proportionally decreased, which is the main goal of this realization. Around the optimum point (N=20) the NEP_{JFET} is close to NEP_{SIN} , which is the goal for background-limited operation. The NEP_{SIN} increases proportionally to √N (according to eq. 6), but decreases due to a decrease of the heat flow (and current) and an increase of the responsivity S. These two effects approximately compensate each other, and NEP_{SIN} is not very sensitive to the number of the bolometers. The most surprising result is that the NEPeph (8) is not increased proportionally to the number of bolometers when the total volume of absorber is increased proportionally to N. The reason is due to a compensation of this dependence by some decrease in Te that is in the 6th power for NEPeph (8).

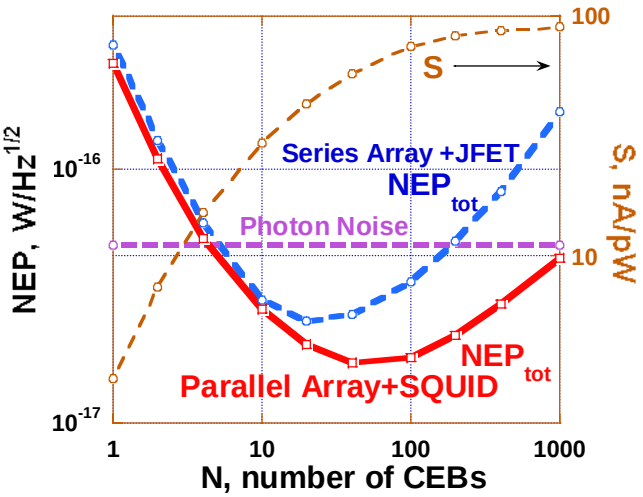

Fig. 6. NEP components and photon NEP in dependence on the number of CEBs in a voltage-biased parallel array with SQUID and in current-biased series array with JFET. The parameters of CEBs are the same as in Fig. 3 and 5. The responsivity S is shown for parallel array for illustration of the effect of the CEB number.

Optimal number of CEBs in series array. The optimal number is determined mainly by the power load Po and the volume of absorber Λ. The general rule of array design is the following: the number of bolometers, N, should be increased to split Po between bolometers up to the point when $P_0/N = P_{ph}$, where $P_{ph} = T^5_{ph} \Sigma\Lambda$. The phonon power is determined by only one parameter, the volume of the absorber, Λ. There is no need to increase the number of bolometers more than this figure because the optical power loading in each bolometer becomes less than the power from phonons. Responsivity is saturated after this level.

Conclusion

We have analyzed several variations of the concept of a Cold-Electron Bolometer (CEB) with an SIN (Superconductor-Insulator-Normal Metal) tunnel junctions for matching with focal plane antenna. The parallel combination of CEBs with SQUID readout is better for distributed slot antenna. The series combination of CEBs with JFET readout is better for distributed dipole antenna. These concepts give unique opportunities to achieve NEPs less than photon noise for any optical power loading with standard JFET or SQUID readouts.

RF coupling of CEBs to distributed focal plane antennas would help to avoid more complicated matching with horns or Si lenses.

The author would like to thank Philip Mauskopf, Peter Day, Jonas Zmuidzinas, and Dmitri Golubev for interesting discussions. The work was supported by SNSB and STINT Swedish agencies.

References

[1] C. Seife, BREAKTHROUGH OF THE YEAR 2003: "Illuminating the Dark Universe", *Science*, vol. 302, pp. 2038-2039, Dec. 2003.
[2] *2006 Nobel Prize in Physics* for discovery of the blackbody form and anisotropy of the cosmic microwave background radiation.
[3] B-Polarization Satellite Proposal for Detecting Primordial Gravitational waves from Inflation. ESA, June 2007. http://www.b-pol.org/
[4] BOOMERANG - balloon telescope: Measurements of CMB Polarization, http://oberon.roma1.infn.it/boomerang/b2k/
[5] L. Kuzmin "Ultimate Cold-Electron Bolometer with Strong Electrothermal Feedback", *Proc. of SPIE conference "Millimeters and Submillimeter Detectors"*, 5498, p 349, Glasgow, June 2004.
[6] L. Kuzmin "On the Concept of a Hot-Electron Microbolometer with Capacitive Coupling to the Antenna", Physica B: Condensed Matter, 284-288, 2129 (2000).
[7] L. Kuzmin. "Ultimate Cold-Electron Bolometer with SIN Tunnel Junction and Andreev Contact". Proceedings of the 17th Int. Symp. On Space Terahertz Technol., ISSTT-2006, pp 183-186, Paris, 2006.
[8] Leonid Kuzmin, "Array of Cold-Electron Bolometers with SIN Tunnel Junctions for Cosmology Experiments", Journal of Physics: Conference Series (JPCS), 97, 012310 (2008).
[9] L. Kuzmin D. Golubev "On the concept of an optimal hot-electron bolometer with NIS tunnel junctions". Physica C 372-376, 378 (2002)
[10] L. Kuzmin, P. Mauskopf, and D Golubev, "Superconducting Cold-Electron Bolometer with JFET Readout for OLIMPO Balloon Telescope". *Journal of Physics: Conference Series (JPCS)*, Volume 43, pp. 1298-1302 (2006).
[11] K. Irwin. Applied Physics Letters, 66, (1995) 1998
[12] A. Lee, P. Richards, S. Nam, B, Cabrera, K. Irwin, *Applied Physics Letters*, 69, (1996) 1801.
[13] Peter K. Day, Henry G. LeDuc, Alexay Goldin, Charles D. Dowell, and Jonas Zmuidzinas. Far-infrared/summillimeter imager-polarimeter using distributed antenna-coupled transition edge sensors. 5498, pp 857-865, SPIE, 2004.
[14] Peter K. Day, Henry G. LeDuc, C. D. Dowell, R.A. Lee, A.Turner and Jonas Zmuidzinas. Distributed Antenna-coupled TES for FIR detector arrays. Journal of Low Temperature Physics, to be oublished.
[15] Leonid Kuzmin. Hybrid on-chip technology of the Cold-Electron Bolometer and SQUID Readout in one vacuum circle. Patent, to be filed in October 2008.
[16] D. Golubev and L. Kuzmin. Nonequilibrium theory of the hot-electron bolometer with NIS tunnel junction. *Journal of Applied Physics*. 89, 6464-6472 (2001).
[17] S. Golwala, J. Johum, and B. Sadoulet, Proc. of the 7 Int. Workshop on Low Temperature Detectors, July 1997, Munich, pp 64-65.
[18] J. C. Mather, Appl. Opt. 21,1125 (1982).

Innovative Technologies for THz Heterodyne Detection

T.G. Phillips

California Institute of Technology, Downs 320-47, Pasadena, CA 91125, USA

Contact: tgp@submm.caltech.edu, phone +1-626-395-4278

***Abstract*— The "state-of-the-art" in the field of heterodyne receivers approaches (within a factor of a few) the quantum noise limit, for frequencies up to about 700 GHz, the band-gap of niobium. Such receivers use the SIS structure and the physics of photon assisted single quasi-particle tunneling. IF bandwidths are as large as 25 GHz. Above 700 GHz various loss mechanisms set in and above about 1.4 THz HEB devices are preferred, even though the IF bandwidth is usually only a few GHz.**

For the future, at frequencies <1 THz, improvement will probably be in the area of increased IF bandwidth and in the area of focal plane arrays, demanding large LO powers. At frequencies well into the THz range quantum noise is dominant and the receiver noise figure should not be a problem. However, constructing tuneable local oscillators with sufficient power becomes the problem. This talk will discuss possible solutions to this problem.

I. Introduction

It is clearly not possible to invent all the novel technology of the next few years even in a restricted field such as heterodyne detection. However, there are some required aspects which can be defined and which may possibly lead to new devices. The heterodyne detection process is invoked when high resolution spectroscopy is needed. It has a major disadvantage in that the detection process involves quantum noise which cannot be avoided. This noise is proportional to frequency and is the dominant source of noise for heterodyne systems operating in the infrared or optical. When high resolution is not required direct detection processes may be preferred. In fact, when in the background noise limit condition, the signal to noise ratio is the same apart from the proportionality to the total bandwidth for both heterodyne and direct detection (Phillips, 1988). So, generally direct detection is preferred for large bandwidths. The best THz detectors for a given application are generally superconducting devices. This is because as an optical photoconductor uses the semiconductor band gap of about 1 eV, so the THz or submm detector uses the superconducting band gap of about 1 meV. Due to the relatively high frequencies involved the quantum noise limit is relatively easily achieved and the problem is to provide a suitable high power, spectroscopically clean, local oscillator source. So progress in the next few years will depend upon effective research into local oscillator techniques.

II. The Optimized Pixel

Before discussing the local oscillator problem we can ask whether the detector element problem has been completely solved. Surprisingly the answer is no! We are a factor of several away from an optimum pixel element in many cases. The first improvement which can be generated is the detection of both polarizations (Figure 1) for the one pixel. This costs two detector elements which could be coupled to the radiation field through lithographic crossed antennae. Secondly, we can use on-and-off pixels to improve on the switched antenna, single pixel device, costing another factor of 2 in SIS elements. Thirdly, the simple double-side band detector can be constructed as a side-band separation or image processing device, costing a further factor of 2 in SIS elements.

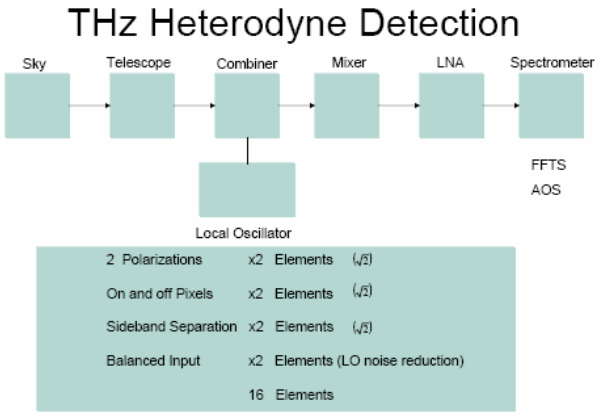

Figure 1. Components for heterodyne detection for a single pixel.

Finally, a balanced input device has the capability of rejecting local oscillator noise and costs a yet further factor of 2 in SIS elements. The total number of SIS elements is therefore 16, representing the optimized single pixel detector (see Figure 1). Of course, if this detector is incorporated into an array configuration it will only

require 8 SIS elements per pixel since the off-pixel is provided by the array. To construct such a single pixel detector chip may have practical difficulties, but it seems likely that in the Nb frequency gap range, i.e. up to 700 GHz, it should be possible using Nb components. Due to the availability of non-superconducting micro-elements in the 700-1400 GHz range the Nb SIS detector can still be used but with reduced effectiveness. Generally above this range we switch to hot electron bolometer devices. The problem with these is not really the upper frequency limit which is hard to define but certainly in the several THz range. It is the difficulty in achieving a suitable high IF bandpass. In fact, the first hot electron bolometer in use in astrophysical applications had only about 1 MHz IF bandpass. Most people would have said this was not a useful detector but actually it made many of the initial discoveries which opened up the submillimeter field (Phillips and Jefferts, 1973). Modern receivers are mounted in accurately machined blocks with scalar-feedhorns, as shown in Figure 2, but at the highest frequencies employ dual-slot lithographic antennae and quasi-optical components rather than waveguides. (Zmuidzinas & Leduc, 1992) Figure 3.

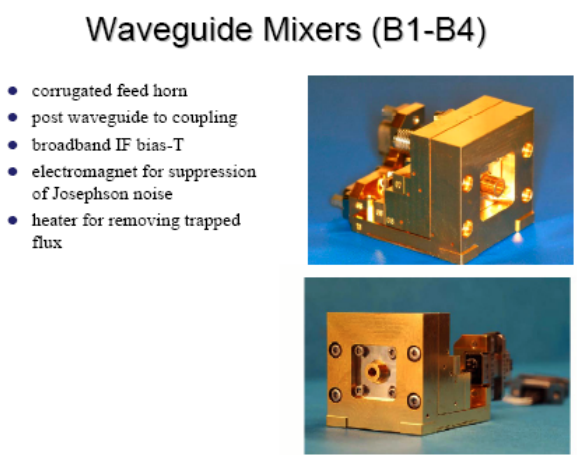

Figure 2. Bands 1-4 of HIFI employ waveguide circuits and scalar-feedhorns.

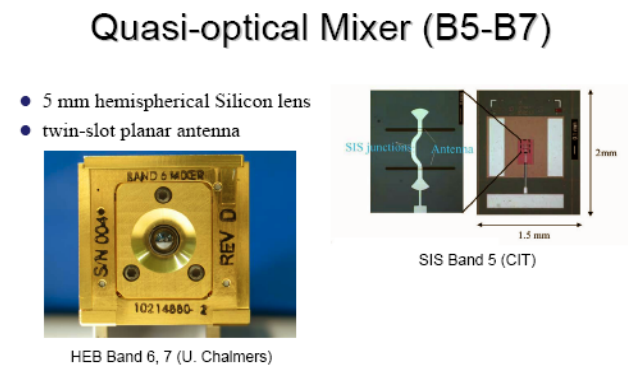

Figure 3. Bands 5-7 of HIFI use quasi-optic techniques and twin-slot antennae.

Returning to the question of quantum noise, this is an interesting question (see Figure 4) in that detectors in the SIS range have increasing noise roughly linearly as in quantum noise, whereas in the HEB range apparently the noise is roughly constant in frequency so will soon meet the theoretical quantum noise limit as the frequency increases. The problem then becomes achieving adequate local oscillator power and adequate IF bandwidth. The hot electrons are cooled by phonons or leave the system mechanically thereby requiring very small lithographic sizes in order to have sufficient speed to allow a wide IF. In terms of local oscillator power a rule-of-thumb is that it should be approximately the same as the DC power which can be as small as 100 nW to achieve thermodynamic flexibility. However due to optical losses in the front-end the LO power required is usually of the order of 1 microwatt.

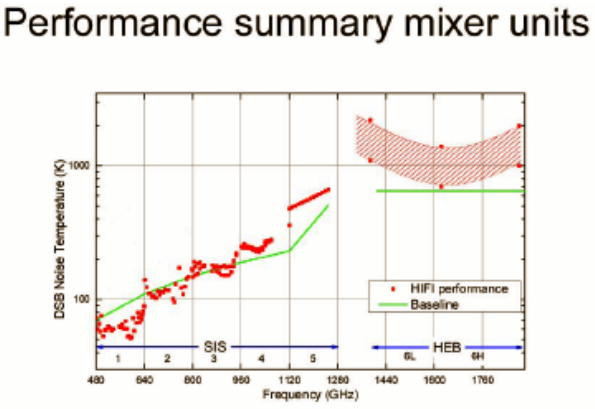

Figure 4. DSB receiver noise as a function of frequency for HIFI.

III. Local Oscillators

The classical THz local oscillator is a fundamental oscillator (e.g. Gunn) followed by a lithographically generated waveguide multiplier (Figure 5). We can list some of the potential LO devices. (1) Lithographic planar-diode multipliers, (2) Photonic schemes, (3) Josephson oscillators, (4) Quantum cascade lasers. Although modern devices such as quantum cascade lasers often appear to have plenty of local oscillator power it usually emerges that the output is not single mode but a combination of modes only one of which can be coupled to the mixer (Figure 7). This problem has been with us from the time of carcinotrons. The 4 schemes mentioned above each has its own problem. For instance, the planar-diode multiplier has to multiply up from a frequency at which power amplifiers can be implemented (about 100 GHz) which involves as many as 4 multiplier units. The LO power achieved by this technique for HIFI is adequate up to 1.9 THz, the frequency of the ground-state CII line. Josephson oscillators generally struggle to produce adequate power to drive an SIS detector and Quantum cascade lasers

typically have multi-mode outputs and are hard to couple cleanly to detectors.

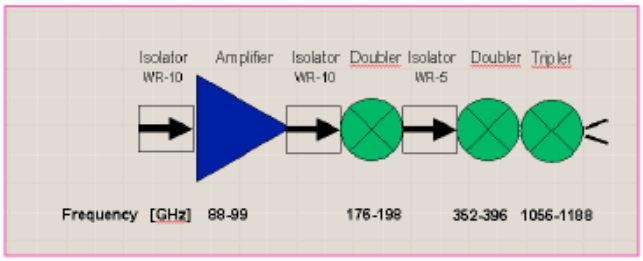

Figure 5. LO Chain Basic Layout

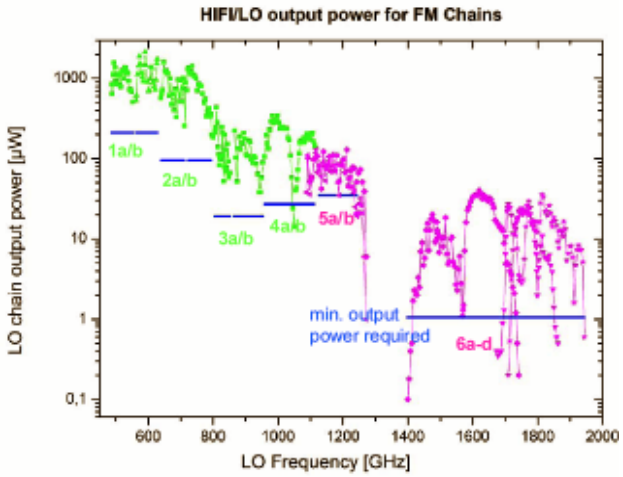

Figure 6. The HIFI LO power in the terahertz regime. The LO chain was maintained at temperature of 120 K for these measurements.

The multiplication technique becomes harder to implement as the frequency goes up, whereas some other techniques become easier with increasing frequency. An example of such a technique is the quantum cascade laser. An example of quantum cascade laser structure is shown in Figure 7 (after Williams, 2007). Of course, optically pumped molecular gas lasers produce considerable amounts of power but are not generally tuneable over a sufficient range required for astrophysics. Other lasers are often only available pulsed. Photonic devices seem attractive with the higher frequencies but are limited by the lack of appropriate impurity states of semi-conductors. On the whole it seems that the best device for astrophysics applications is probably the quantum cascade laser and if the single output coupling mode can be achieved then it is quite likely to be selected for future projects. Power problem will limit the size of the rays and implementation of the complex multiple SIS chip discussed above will exacerbate the power problem. In spite of all the difficulties, I expect within the long run quantum cascade lasers will become the standard LO for high terahertz work.

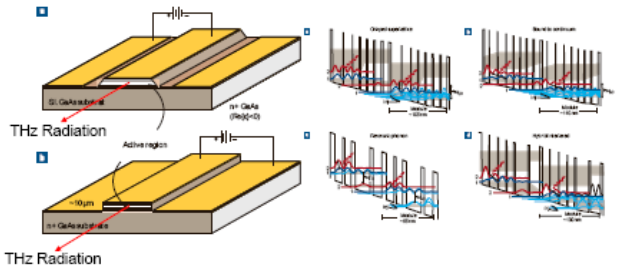

Figure 7. Quantum Cascade Laser as LO Sources

ACKNOWLEDGMENT

In terms of financial support, NSF supports the CSO through contract #AST-0540882. The work on HIFI is supported by NASA through JPL.

I would like to take this opportunity to congratulate the HIFI technical team which produced many of the results quoted here.

REFERENCES

[1] T.G. Phillips, *Techniques of Submillimeter Astronomy: Millimetre and Submillimetre* Astronomy; Summer School, Stirling, Scotland, Dordrecht, Kluwer Academic Publishers, 1988, p. 1-23.

[2] T.G. Phillips; KB. Jefferts, *A low temperature bolometer heterodyne receiver for millimeter wave astronomy*, Rev. Sci. Instrum., Vol. 44, p. 1009–1014, 1973.

[3] J. Zmuidzinas; H.G. Leduc; J.A. Stern, *Slot antenna SIS mixers for submillimeter wavelengths:* The Third International Symposium on Space Terahertz Technology: Symposium Proceedings p. 234, 1992.

[4] B.S. Williams, *Terahertz quantum-cascade lasers*, Nature Photonics, Volume 1, Issue 9, p. 517-525, 2007

2.5-THz heterodyne receiver with quantum cascade laser and hot electron bolometer mixer in a pulse tube cooler

H. Richter[1], A. D. Semenov[1], S. G. Pavlov[1], H.-W. Hübers[1], L. Mahler[2], A. Tredicucci[2], H. E. Beere[3], D. A. Ritchie[3], K. S. Il'in[4] and M. Siegel[4]

[1]*German Aerospace Center (DLR), Institute of Planetary Research, Rutherfordstr. 2, Berlin, Germany*

[2]*NEST CNR-INFM and Scuola Normale Superiore, Piazza dei Cavelieri 7, Pisa, Italy*

[3]*Cavendish Laboratory, University of Cambridge, Cambridge CB3 0HE, United Kingdom*

[4]*Institute for Micro- and Nano-Electronic Systems, University Karlsruhe, Karlsruhe, Germany*

* Contact: Heiko.Richter@dlr.de, phone +49-30-67055 697

***Abstract*— A 2.5-THz heterodyne receiver has been realized in a pulse tube cooler. This liquid cryogen free system is based on a quantum cascade laser (QCL) acting as local oscillator and a hot electron bolometeric mixer. The double sideband noise temperature of the system is 2000 K and when corrected for optical losses in the signal path it is 800 K. A detailed study of the QCL beam quality yielded a beam propagation factor of 1.1-1.2.**

I. Introduction

The terahertz (THz) portion of the electromagnetic spectrum bears an amazing scientific potential in astronomy. High resolution spectroscopy in particular heterodyne spectroscopy of molecular rotational lines and fine structure lines of atoms or ions is a powerful tool, which allows obtaining valuable information about the observed object such as temperature and dynamical processes as well as density and distribution of particular species. Two examples are the HD rotational transition at 2.7 THz, and the OI fine structure line at 4.7 THz. These lines are main targets to be observed with GREAT, the German Receiver for Astronomy at Terahertz Frequencies, which will be operated on board of SOFIA [1]. Besides remote sensing, heterodyne detection has recently attracted significant interest for security applications, namely stand-off detection of hidden threats [2].

Hot electron bolometer mixer (HEB) have been recently pumped with QCL acting as LO [3][4]. As part of the receiver development for SOFIA we have developed a liquid cryogen-free heterodyne receiver for operation at about 2.5 THz. To build a compact THz-receiver, all front-end components which have to be cooled down for operation were integrated in a pulse tube cooler (PTC).

The performance of the QCL in terms of output power and beam profile as well as the double sideband noise temperature of the system is presented.

II. Quantum Cascade Laser

A. Design

The 2.5 THz QCL used for this experiment is based on the so-called bound-to-continuum approach [5] with a rather uniformly chirped superlattice and no marked distinction between the injection and lasing regions [6]. The active medium is formed by 110 repeat units of the superlattice (total thickness 15 μm) covered on top by a Cr/Au layer. Between the <250 μm thick substrate and the active medium is a highly doped GaAs layer. This layer has two doping concentrations: $2.7 \cdot 10^{18}$ cm^{-3} in the 530 nm next to the superlattice and $2.6 \cdot 10^{17} cm^{-3}$ in the 500 nm close to the substrate. By these means the boundary conditions at the two sides of the buried doped layer can be controlled separately. This laser also has a Fabry-Pérot cavity that is 240 μm wide and 2.5 mm long. It has a maximum output power of 6 mW and operates up to 58 K in cw mode. More details such as light–current curves can be found in [6]. The laser was soldered to a copper bar, wire bonded, and mounted onto the first stage of the PTC. Without any heat load this stage has a minimum temperature of 31 K. During operation of the QCL this temperature rises to about 45 K.

B. Beam Profiles

To determine the quality of the laser beam it was focused with a TPX lens as shown in Fig. 1. The beam profiles were measured by scanning a Golay cell detector with a 0.4-mm diameter aperture in a plane orthogonal to the emission direction of the QCL at different positions in front and behind the position of the beam waist generated by the TPX lens.

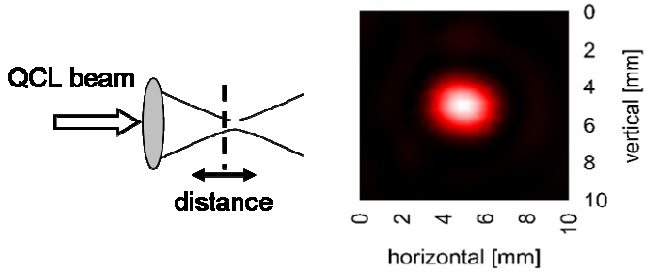

Fig. 1 Scheme for measuring the beam profile (left) and a typical beam profile at a position close to the beam waist (right).

The beam diameter at each position was determined according to the knife-edge method [7] and according to the second moment beam width method [8]. Both yielded the same results within the accuracy of the methods. The result for the knife edge method together with the calculated beam path is shown in FIG. 2. The beam waist is located ~63 cm from the QCL. At that position a second order polynominal fit (for a detailed description see [8]) yields a beam radius of 1.8±0.1 mm in direction vertical to the layers of the superlattice of the QCL and a M^2 of 1.1. In the orthogonal direction these values are slightly larger (2.0±0.1 and 1.2, respectively). Both results show that the beam propagation of the QCL can be sufficiently good described with Gaussian optics.

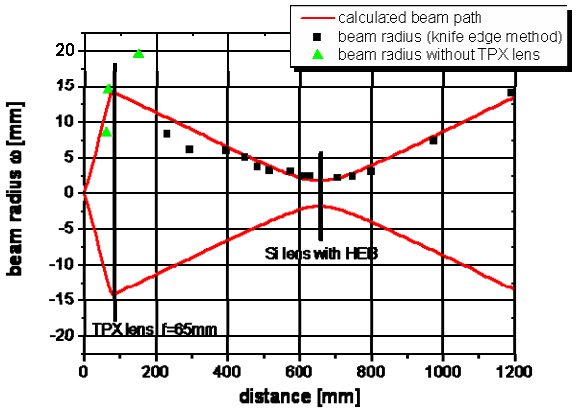

Fig. 2 Radius of the QCL beam (calculated with the knife edge method) without and when focused with a TPX lens. The QCL is located at the origin.

III. NOISE TEMPERATURE MEASUREMENT

A scheme of the measurement setup is shown in FIG. 3. All front-end components which have to be cooled for operation were integrated in a pulse tube cooler (PTC) which was a Gifford-McMahon type with two cold stages. Without any heat load the second stage has a minimum temperature of 2.3 K (31 K at the first stage) and rises to about 4.5 K (45 K at first stage). During operation the cooling power is 10 W and 0.8 W for the first and second stage, respectively.

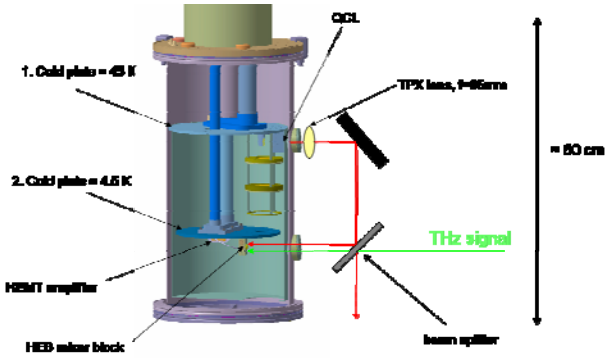

Fig. 3 Scheme of the heterodyne receiver in a pulse tube cooler. A radiation shield is mounted onto the first stage and is not shown here.

The previously described quantum cascade laser (QCL) is acting as local oscillator (LO) and mounted on the first stage of the PTC. A phonon-cooled NbN hot electron bolometer (HEB) is used as mixer. The HEB was a 2 µm wide, 0.2 µm long, and 5.5 nm thin NbN strip on a high resistivity (> 5 kΩ) silicon substrate located in the center of a planar logarithmic spiral antenna. It was glued onto the flat side of an extended hemispherical 12 mm diameter silicon lens. Together they were assembled in an aluminium holder which was mounted on the second cold stage of the PTC. The HEB mixer's IF port was connected to a bias-T which was used to feed the bias to the mixer and to transmit the IF signal to a low noise HEMT amplifier. This amplifier was also mounted onto the same stage of the PTC, but with some thermal insulation in order to provide an operation temperature of 10-15 K. The noise temperature of this amplifier is 5 K. A radiation shield with two windows was connected to the first stage of the PTC. A 1.1 mm thick z-cut quartz filter was mounted to the radiation shield in front of the HEB. Both vacuum windows (for the QCL radiation as well as for the input to the HEB) were made of 1-mm thick high density polyethylene (HDPE).

The output IF signal was filtered at 1.5 GHz with a bandwidth of 75 MHz, further amplified and rectified with a crystal detector.

The radiation from the QCL was guided by a plane mirror and a 6-µm thin Mylar beam splitter to the HEB. The TPX lens was positioned in order to provide a beam waist at the position of the HEB mixer.

The current-voltage (I-V) characteristics of the HEB at different values of LO power are shown in FIG. 4. The power from the QCL is sufficient to pump the HEB into the normal state (lowest I-V characteristic). The double sideband (DSB) receiver noise temperature was measured using the Y-factor technique, by presenting a room temperature blackbody and a blackbody cooled by liquid nitrogen to the input of the receiver. At a bias of 0.6 mV and 36 µA the lowest DSB receiver noise temperature of 2000 K was achieved.

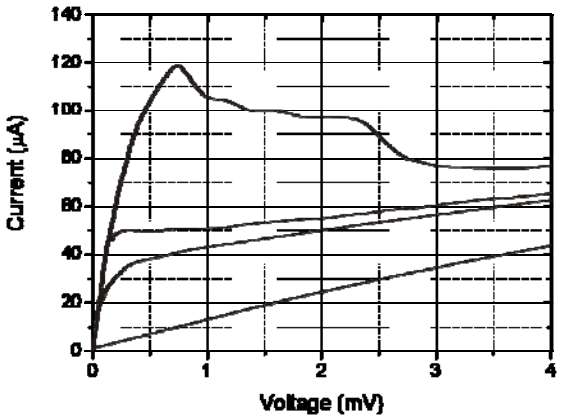

Fig. 4 I-V characteristics of a HEB mixer pumped with the QCL LO at 2.5 THz. The LO power is increasing from the uppermost curve (no LO power) to the lowest curve (HEB pumped into normal state).

FIG. 5 shows the output power of the QCL for different bias current and different temperatures of the first stage. The power is increasing with current and decreasing with temperature. For all temperatures it is possible to pump the HEB into the normal state.

The best noise temperature was achieved with ~45 μW QCL power in front of the cryostat window. Applying corrections for optical losses (antenna mismatch, absorption and reflection losses caused by the HDPE window and the quartz filter, reflection losses at lens surface without anti-reflection coating) to this power, this corresponds to an approximate power of 13 μW which is required to pump the HEB.

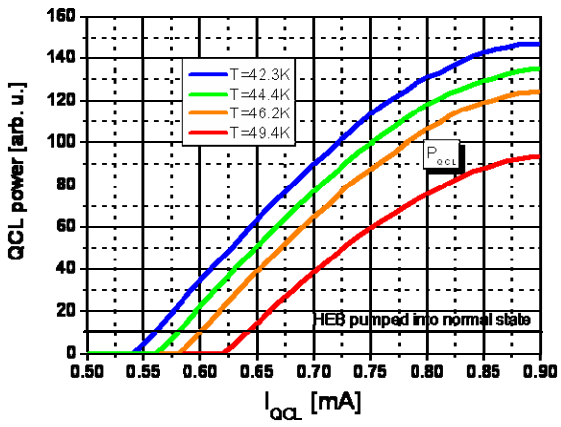

Fig. 5 Output power of the QCL for different bias and temperature.

The power absorbed inside the superconducting bridge as estimated by the isothermal method [9] is to be ~300 nW. The difference to the power needed to pump the HEB is probably attributed to a mismatch between the antenna pattern of the mixer and the beam profile of the QCL. Although the QCL beam has a close to Gaussian power distribution profile, it might be composed from a number of modes with different phase. Because the antenna of the HEB couples to only one mode out of these, there is a rather large difference between the power from the QCL and the power absorbed inside the HEB.

The IF output power demonstrated fluctuations with 1.2 Hz frequency, which corresponds to the piston movement of the PTC. This fluctuation has two origins: one is a small fluctuation of the QCL power and another one is a fluctuation of the bias point of the HEB. These effects added an uncertainty of ±200 K to the DSB noise temperature.

Taking into account the previously described losses the noise temperature of the receiver is ~800K which is comparable with other results [10][10].

CONCLUSIONS

We have successfully realized a liquid cryogen free THz heterodyne receiver front-end in a pulse tube cooler with QCL as LO and HEB as mixer. A detailed study of the QCL beam yielded a propagation factor of 1.1-1.2. The DSB noise temperature of the system is 2000 K and when corrected for optical losses in the signal path it is ~800K. This demonstrates, that a liquid cryogen free, turn-key heterodyne spectrometer for the frequency range from 2-6 THz is feasible.

ACKNOWLEDGMENT

This work was supported by the European Commission through the ProFIT programme of the Investitionsbank Berlin and through the IP project Teranova.

REFERENCES

[1] S. Heyminck, R. Güsten, P. Hartogh, H.-W. Hübers, J. Stutzki, and U. U. Graf, to appear in Proc. Conf. on Ground-based an Airborne Instrumentation for Astronomy II, Vol. SPIE 7014, edited by I. S. Mclean and M. M. Casali, pp. 7014-34, Marseille (2008).

[2] H.-W. Hübers, U. Böttger, H. Richter, and A. D. Semenov, in Proc. Of the Conf. On Terahertz for Military and Security Applications V, vol. SPIE 6549, edited by J. O. Jensen, and H.-L. Cui, Orlando, 65490A (2007).

[3] J. R. Gao, J. N. Hovenier, Z. Q. Yang, J. J. A. Beselmans, A. Baryshwe, M. Hajenius, T. M. Klapwijk, A. J. L. Adam, T. O. Klaassen, B. S. Williams, S. Kumar, Q. Hu, and J. L. Reno, Appl. Phys. Lett. 86, 244104 (2005).

[4] H.-W. Hübers, S. G. Pavlov, A. D. Semenov, R. Köhler, L. Mahler, A. Tredicucci, H. E. Beere, D. A. Ritchie, and E. H. Linfield, Optics Express 13, 5890 (2005).

[5] J. Faist, M. Beck, T. Aellen, and E. Gini, Appl. Phys. Lett, 78, 147 (2001).

[6] L. Mahler, A. Tredicucci, R. Köhler, F. Beltram, H. E. Beere, E. H. Linfield, and D. A. Ritchie, Appl. Phys. Lett. 87, 181101 (2005).

[7] A. E. Siegman, M. W. Sasnett, and T. F. Jr. Johnston, IEEE J. of Quant. Electron. 27, 1098 (1991).

[8] International Organization for Standardization, document no. ISO 11146, Lasers and laser-related equipment – Test methods for laser beam parameters – Beam width, divergence, angle and beam propagation factor (1999).

[9] H. Ekström, B. S. Karasik, E. L. Kollberg, and K. S. Yngvesson, IEEE Trans. On Microwave Theory and Techn. 43, 938 (1995).

[10] H.-W. Hübers, IEEE J. Sel. Topics in Quant. Electron. 14, 378 (2008).M. Hajenius, P. Khosropanah, J. N. Hovenier, J. R. Gao, T. M. Klapwijk, S. Barbieri, S. Dhillon, P. Filloux, C. Sirtori, D. A. Ritchie, and H. E. Beere, Opt. Lett. 33, 312 (2008).

CHAMP$^+$: A powerful submm Heterodyne Array

C. Kasemann [1], S. Heyminck [1], A. Bell [1], A. Belloche [1], C. Castenholz [1], R.Güsten [1], H. Hafok [1], A.Henseler [1], S. Hochgürtel [1], B. Klein [1], T. Klein [1], I. Krämer [1], A. Korn [1], K. Meyer [1], D. Muders [1], F. Pacek [1], F. Schäfer [1], G. Schneider [1], G. Wieching [1], H-J. Wunsch [1],
A. Baryshev [2], R. Hesper [2], T. Zijlstra [3], C.F.J. Lodewijk [3], T.M. Klapwijk [3]

[1] *Max-Planck-Institut für Radioastronomie, Auf dem Hügel 69, 53121 Bonn, Germany*
[2] *SRON Netherlands Institute for Space Research, Postbus 800, 9700 AV Groningen, Netherlands*
[3] *Delft University of Technology, Lorentzweg 1, 2628 CJ Delft, Netherlands*
* Contact: heyminck@mpirf-bonn.mpg.de

***Abstract*— To make best use of the exceptional good weather conditions at Chajnantor we developed CHAMP$^+$, a two time seven pixel dual-color heterodyne array for operation in the 350 and 450 µm atmospheric windows.**
CHAMP$^+$ uses state-of-the-art SIS-mixers provided by our collaborators at SRON. To maximize its performance, optical single sideband filter are implemented for each of the two sub-arrays, and most of the optics is operated cold (20K) to minimize noise contributions. The instrument can be operated remotely, under full computer control of all components.
The autocorrelator backend, currently in operation with 2 x 1GHz of bandwidth for each of the 14 heterodyne channels, will be upgraded by a new technologies FFT spectrometer array in mid 2008.
CHAMP$^+$ has been commissioned successfully in late 2007. We will review the performance of the instrument "in the field", and present its characteristics as measured on-sky.

I. Introduction

Based upon the experience gained with the successful precursor array receiver CHAMP (Carbon Heterodyne Array of the Max-Planck-Institute [1]), we developed CHAMP$^+$, an even more sophisticated heterodyne array. The precursor instrument CHAMP was build for the 460GHz atmospheric window and showed the high scientific potential of heterodyne array receivers during its almost four years of operation at the CSO. Its unmatched performance especially in large scale mapping projects like in the horsehead nebula as shown in figure 1 was proven during that time.
In 2003 the receiver was returned to MPIfR and was heavily re-worked for operation at APEX: CHAMP$^+$, as it is now called, operates in the 660GHz and the 850GHz atmospheric windows having two individual sub-arrays. Both sub-arrays are operated in orthogonal polarizations to make parallel use possible. Each consists of 7 pixels in a hexagonal arrangement including a center pixel. Cold optics, single side-band filters and powerful spectrometers guarantee for optimum performance. The development was done in collaboration with SRON, providing the SIS-mixer devices for both colors.

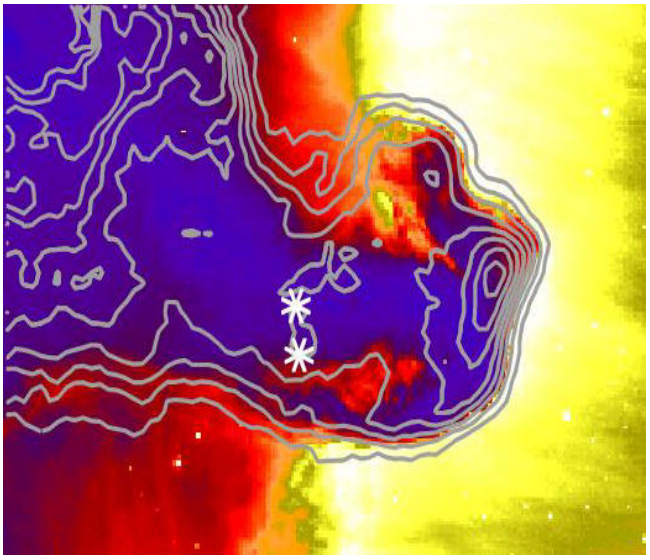

Fig.1: Contours show the distribution of warm carbon monoxide CO(4-3) as measured toward the Horsehead nebulae with CHAMP, the precursor instrument to CHAMP$^+$ [3].

CHAMP$^+$ was installed at the APEX telescope – the Atacama Pathfinder EXperiment[1] [2] – in early 2007. With the unique observing conditions of the telescope, CHAMP$^+$ now offers unmatched mapping capabilities in the high sub-millimeter regime. This article describes the instrument and presents some of the first data taken during the commissioning and first observing runs in 2007. The receiver is operated as Principal Investigator (PI) instrument and will be available to the APEX community on a collaborative basis with MPIfR.

[1] APEX is a collaboration between the Max-Planck-Institut für Radioastronomie, the European Southern Observatory, and the Onsala Space Observatory

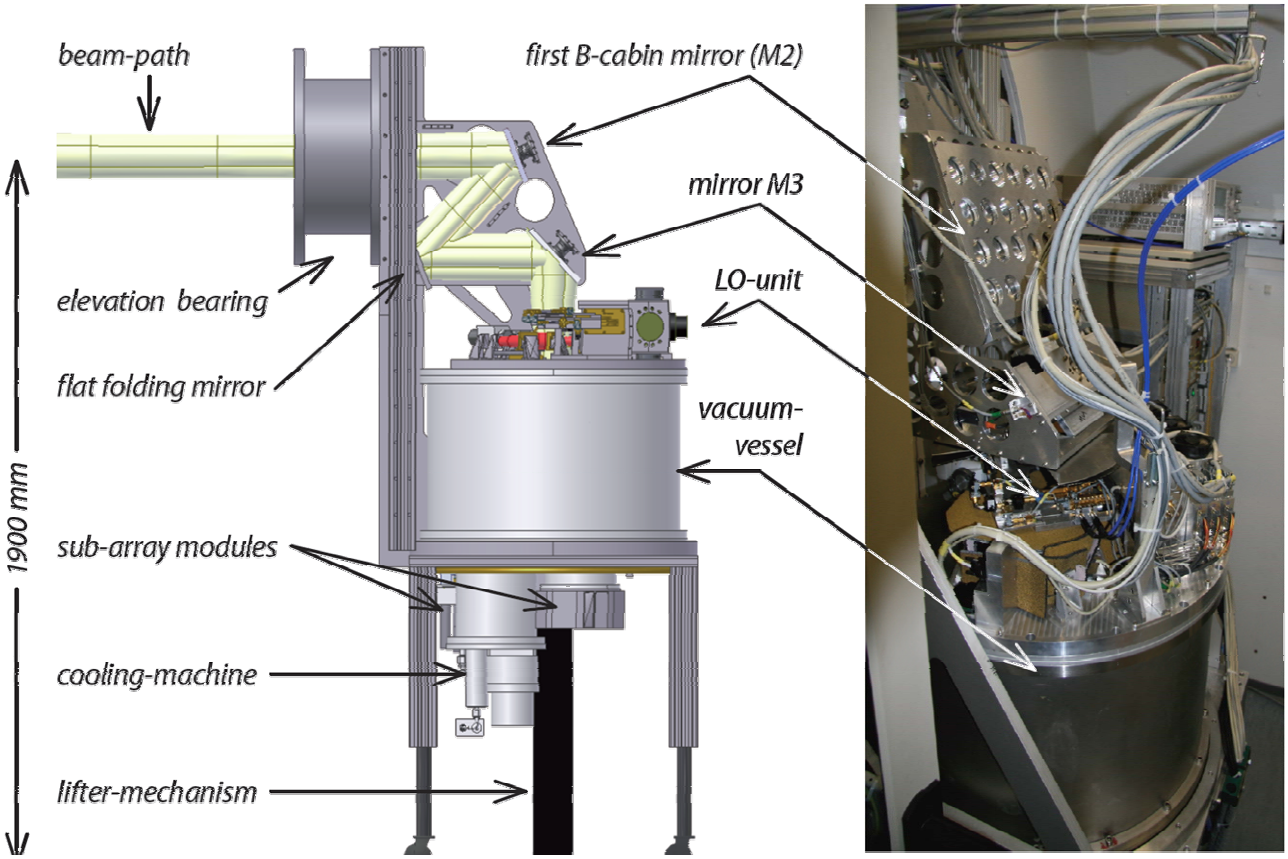

Fig. 2: System overview (CAD 3D model – left hand side) and photograph of CHAMP^{++} as mounted in the Nasmyth B-cabin of the telescope.

II. System Description

CHAMP^{+} consists of two 7-pixel sub-arrays: the low-frequency array (LFA) has a RF-tuning range from 620 to 720 GHz, and the high-frequency array (HFA) from 780 to 950 GHz. Both sub-arrays are operating on orthogonal polarizations, hence can be operated simultaneously.

As mixer devices fixed tuned DSB (double sideband) SIS (superconductor isolator superconductor) mixers, developed at SRON with the TU Delft, are used. They offer a usable IF-band range from 4 to 8 GHz; but due to the limited bandwidth of the spectrometer and losses in the quasi-optics we currently only use the inner 2.8 GHz. Operating temperatures for the mixer devices are provided by a commercial Sumitomo 3-stage closed-cycle refrigerator. The mixers are attached to the 4K-stage, while the first IF-amplifiers and the main optics are connected to the 15K-stage. The 77K-stage is used only as an outer radiation shield to reduce the heat-load of the inner two stages.

The main optics provides optical SSB (single sideband) filters, a Martin-Puplett interferometer as LO-diplexer, and re-imaging optics for both sub-arrays. The local-oscillator (LO) system is a spin-off development from our Herschel/HIFI developments [4]. The LO-power distribution is done by collimating phase-gratings (CFG) [5]. The whole dewar can be rotated for image de-rotation.

A. Mixer devices

The SIS-mixers are provided by our collaborative partners from SRON. The devices are spin-off designs from the ALMA band 9 and the Herschel/HIFI development programs (see also [6], [7]). For the 660 GHz band a Nb-junction could be used while for the 850 GHz band a Nb-NbTiN-junction has been developed to overcome the Nb-gab frequency limitations starting below 700GHz.

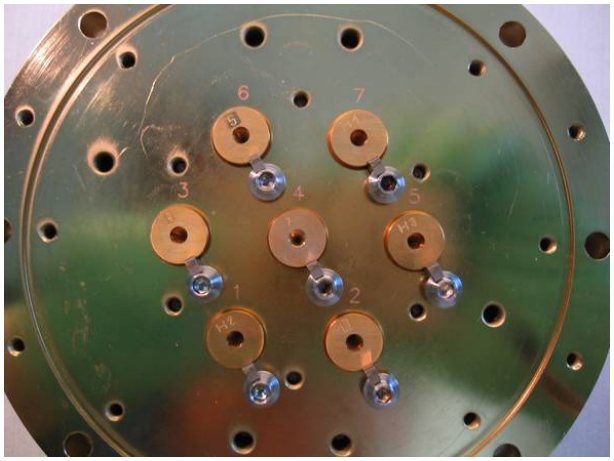

Fig. 3: Photograph of the LFA mixer-assembly showing the seven horn antennas in their hexagonal arrangement.

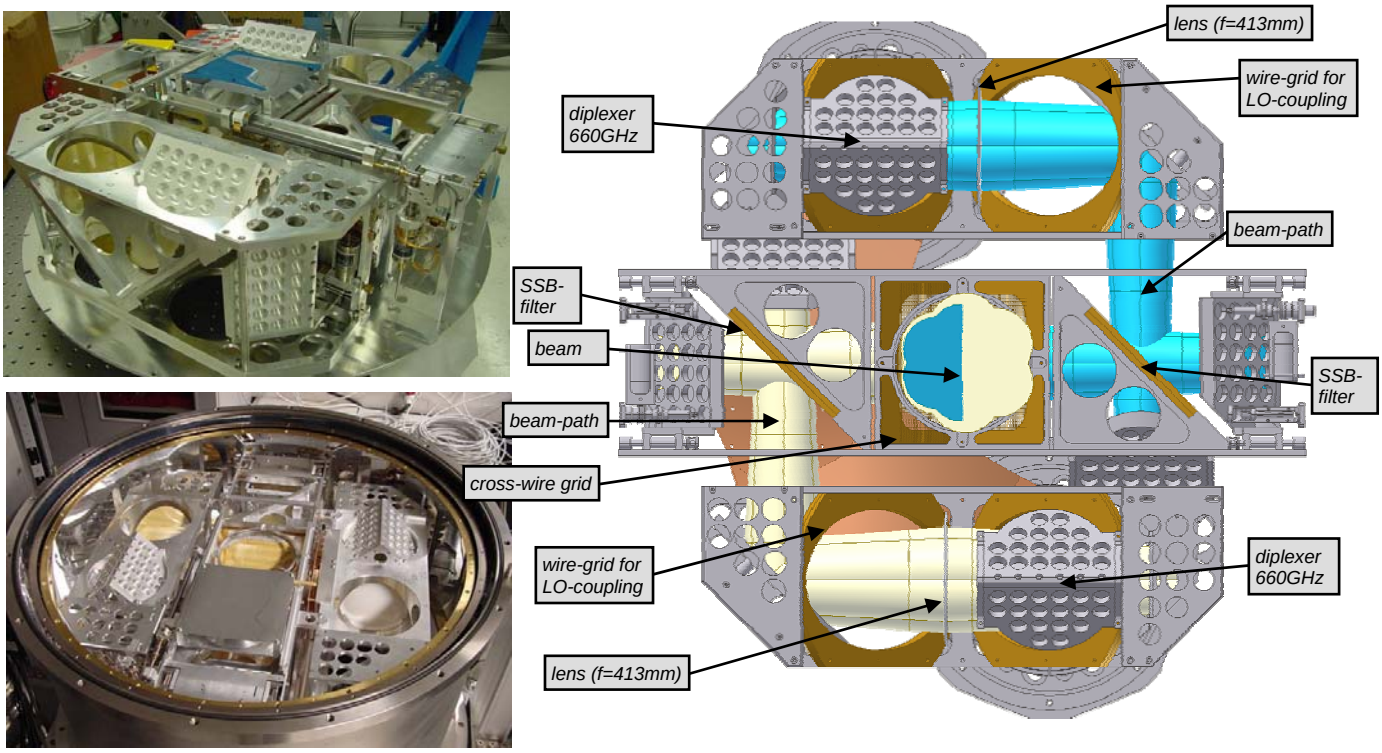

Fig. 4: Cold-optics assembly, including the filter elements (SSB-filter and LO-diplexer), wire-grids and lenses.

All mixers are fixed tuned DSB waveguide devices with a commercial corrugated feed horn. A magnet coil, to suppress the Josephson current, is attached to each of the mixers. All mixers of a given sub-array are connected to a common electronics board providing the BIAS- Tees and the BIAS-network of the junctions.

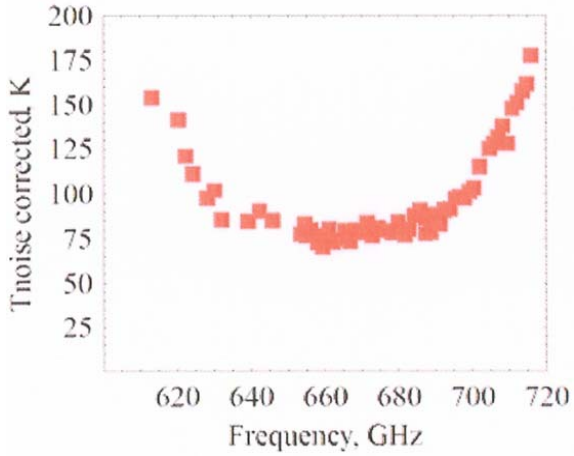

FIG. 5: TYPICAL NOISE-PERFORMANCE OF ONE OF THE 660GHZ MIXER DEVICES VERSUS RF-TUNING RANGE

B. Optics

The imaging optics of CHAMP$^+$ consists of two Gaussian telescope set-ups (e.g., [8]). The first one is required to pass the elevation bearing of the telescope. For a compact arrangement of the diplexer and the single sideband filter a small beam diameter is required. The second Gaussian telescope provides the smaller beam diameter and gains extra path-length for the cooled optical elements. At the focal plane of the second Gaussian telescope a so-called flies-eye-lens, a hexagonal arrangement of 7 lenses with parabolic shape, is located. This lens adapts the individual beam of the mixer-horn antennas to the common optics and ensures the proper illumination of the telescope for each of the sub-array pixels. The magnifications of the Gaussian telescopes are 3138 / 662 ~ 4.75 and 413 / 826 = 0.5.

The arrangement of the warm optics is visualized in figure 2, while figure 4 shows the cold optics layout. The beam spacing on the sky is – at the center of the tuning bands – approx. 2.1 × FWHM for both sub-arrays, which is the optimum between signal losses due to small individual apertures and the filling factor of the focal-plane. Since the beam size is frequency dependent, the field-of-view is different for both sub-arrays. For on-the-fly mapping an array angle of 19.1° against the scanning direction is used. Full sampling can then be achieved with two OTF scans.

The arrangement of the filter elements (two Martin-Puplett interferometers per sub-array, acting as LO-diplexer and as single sideband filter) together with the wire-grids for polarization splitting and LO-injection is shown in figure 4.

All lenses, the IR-filter and the dewar window in the signal path have anti-reflection grooves, which were laser-machined into the elements´ surface. Since the LO-system is producing more than enough LO-power, the LO-windows are un-coated.

C. LO-Diplexer

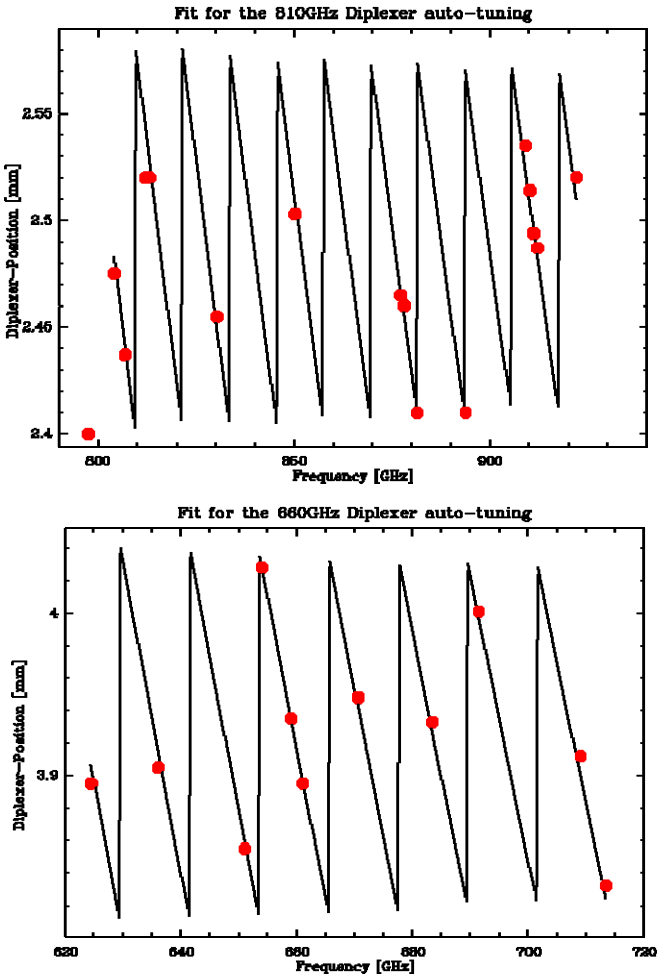

Fig. 6: Diplexer-behaviour of both sub-arrays; measured optimum tuning points (dots) and best fit theoretical behaviour (black line).

To characterize the diplexers and to establish an automatic tuning algorithm for the LO sub-system we measured the diplexer behavior over the whole tuning range of a given sub-array (figure 6). Tuning points were determined by searching for the best average noise-temperatures (averaged over the IF-band and all 7 pixels). A fit to the theoretical model of the Martin-Puplett interferometer with only two free parameters (linearity and zero position of the roof-top position-encoder) can well explain all measured points. An auto-tuning algorithm using this model has been established and is working well for routine observations.

Single-sideband filters

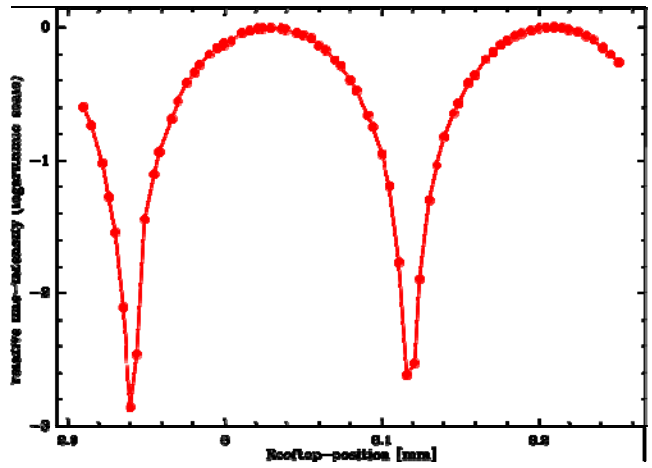

Fig. 7: Relative line intensity of a harmonic mixer RF-signal, injected into the receiver signal path, versus SSB roof-top position.

Important for operation of a SSB-system is how well the image sideband can be suppressed. Therefore we injected as "sky signal" the output of a harmonic mixer. Recording the signal strength versus filter position calibrated the SSB filter for each of the pixels in both sub-arrays (see also figure 7).

From these data we derived the maximum signal strength for each pixel. The sideband suppression for all pixels is then calculated from their maximum signal strength and the signal strength measured at the optimum tuning point for that frequency. The ratio should be above 10dB for all pixels to ensure proper astronomical calibration across the (used) IF-band of the receiver. We derive typical values of more than 15dB as shown for a few typical set-ups in table 1. The best tunings for the whole sub-array were determined to be always very close (within 2-3µm) to the optimum point of the center pixel. Therefore we could take the optimum point for the center pixel to establish the SSB-filter behavior versus RF-frequency. As for the LO-diplexer, we derived the optimum points for several frequencies distributed across the RF-tuning range. Since both filters are build as Martin-Puplett type interferometers we could use the same fitting and auto-tuning scheme as described for the LO-diplexers. Also this auto-tuning works well during routine observations.

Frequency [GHz]	Side-band	Filter-position [mm]	Pixel 1 [dB]	Pixel 2 [dB]	Pixel 3 [dB]	Pixel 4 [dB]	Pixel 5 [dB]	Pixel 6 [dB]	Pixel 7 [dB]
630	LSB	3.240	-17,7	-24,4	-16,6	-21,0	-27,1	-34,7	-23,3
650	USB	3.274	-16,1	-25,4	-14,6	-23,5	-24,4	-28,3	-25,4
691.47	LSB	3.118	-16,6	-24,6	-15,3	-27,6	-21,6	-25,5	-28,3
806.65	USB	3.118	-16,9	-22,1	-16,3	-21,7	-29,6	-23,6	-26,6
850	LSB	3.150	-15,1	-20,9	-16,3	-26,7	-22,8	-25,4	-27,3
921.8	LSB	3.153	-15,4	-21,5	-19,8	-25,8	-23,3	-19,0	-19,4

Table 1: Sideband gain ratios for all pixels at selected frequencies.

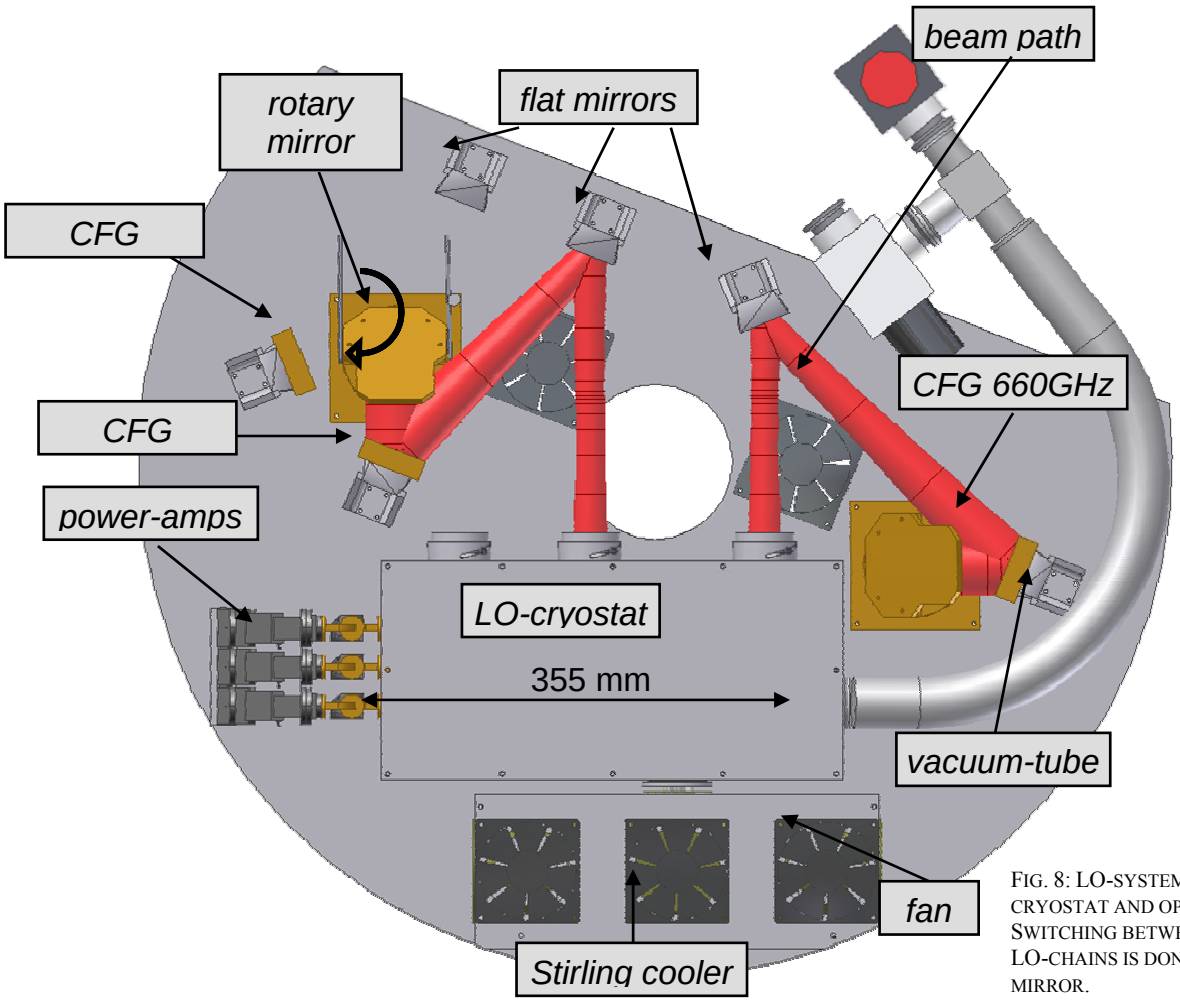

FIG. 8: LO-SYSTEM WITH LO-CRYOSTAT AND OPTICS PATH (RED). SWITCHING BETWEEN THE TWO HFA LO-CHAINS IS DONE BY A ROTARY MIRROR.

D. LO-system

The Local Oscillator chains are spin-off from our Herschel /HIFI developments. A commercial synthesizer is driving a multiplier chain with additional amplifier stages. The LO-chain input frequency is in the range from 10-20 GHz, depending on the RF-frequency and the overall multiplication factor of the individual chain. Two different LO chains were necessary to cover the wide RF tuning-range of the HFA band: one chain covering 780 – 840 GHz and the second 840 – 950 GHz. We select between the two chains optically, via a rotating mirror with two positions. To improve life-time and performance we operate the last tree multiplier stages of all three chains at ~130K, using a compact Stirling cooler.

To distribute the LO-power equally between the individual mixers in each of the sub-arrays we use collimating Fourier gratings (e.g. [5], [9], [10]). These are phase gratings superimposed to a parabolic mirror. The phase grating is calculated to produce the required hexagonal interference pattern, while the parabola matches the beams to the optics of the signal-path. This makes the optical layout very simple (see also figure 8).

III. SYSTEM DEFINITION

During the commissioning period and two observing runs in 2007 we gained experience with the overall system.

A. Noise performance

We tuned the receiver and hence measured its noise performance for those frequencies that were requested in our observing programs. In the LFA, we established an auto-tuning that covered the whole LO tuning range. Since the tuning of the higher frequency LO-chains is more difficult, only in segments around the most important astronomical lines tuning parameters were tabulated. For the actual observations, the frequency is then tuned automatically via the receiver control computer.

In figure 9 we display the noise temperatures as measured across the central 1GHz wide IF-band (limited by the total-power detector in the IF-processor).

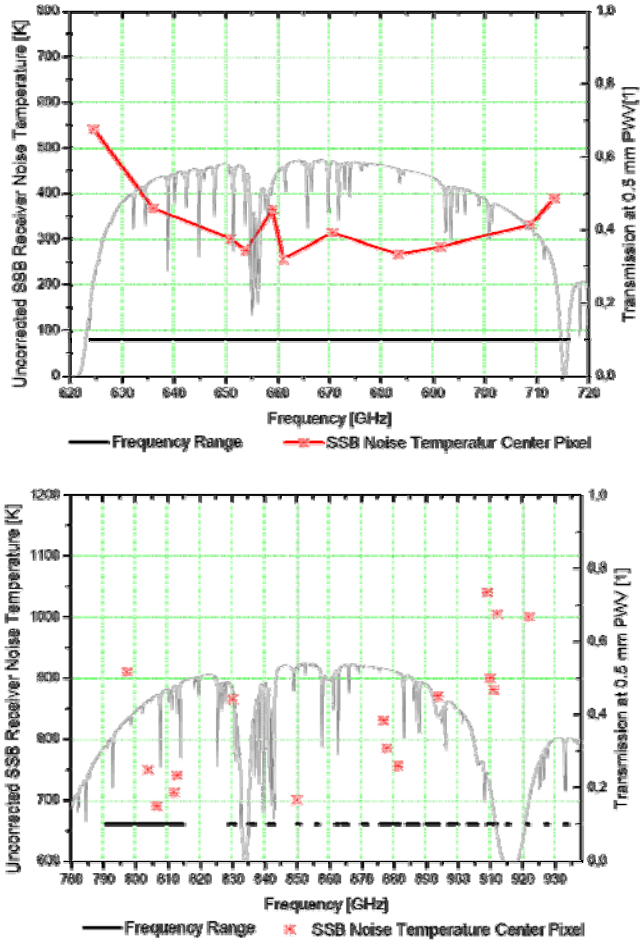

Fig. 9: Instrument noise performance, as measured across the central (1GHz) IF-bandwidth (top: LFA; bottom: HFA). The thick black line indicates the tuning range of the LO-system, for which remote tuning has been established. In thin lines the atmospheric transmission for 0.5mm PWV is superimposed.

B. *System stability*

The overall system stability limits the integration times for a given observation. For efficient spectroscopic on-the-fly mapping a spectroscopic Allan-Variance minimum time of around 100s is required. All CHAMP$^+$ channels comply with this requirement, most channels show AV times around 200s. With the (inherently even more stable) FFT-spectrometers we hope for even better Allan-times

Important for continuum pointing observations are the total-power Allan times. In this mode excellent Allan stability-times of more than 25s for all channels have been demonstrated.

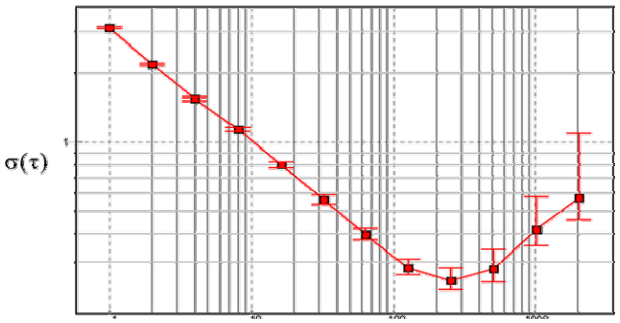

FIG. 10: TYPICAL ALLAN-PLOT HERE FROM ONE OF THE HFA CHANNELS SHOWING APPROX. 200S ALLAN MINIMUM TIME AT A SPECTROSCOPIC RESOLUTION OF 1MHZ.

C. *Footprint on the sky*

For the astronomical observations good control of the receiver pointing is absolute necessary. For an array receiver this requires knowledge about the relative pixel positions. We confirmed the footprints of the arrays by measurements of the planets. They confirmed the pre-alignment that was done in the laboratories prior to shipment. Mars was chosen because

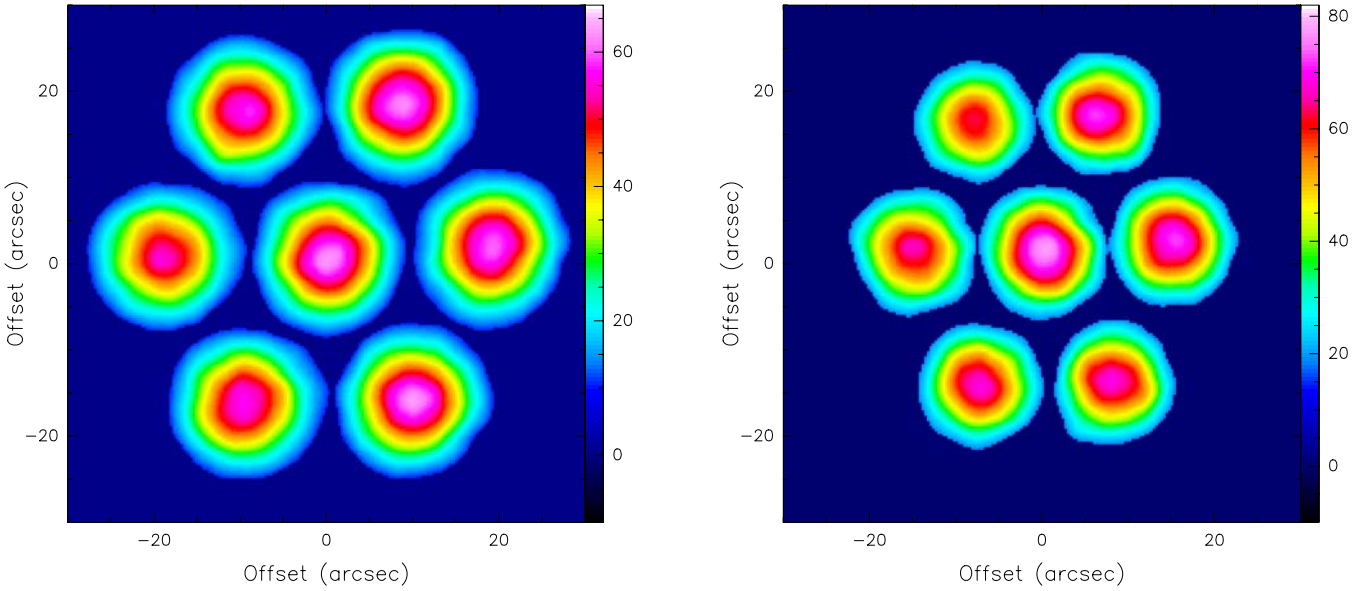

FIG. 11: CHAMP$^+$ BEAM PATTERN AS OBTAINED TOWARDS MARS (IN TOTAL POWER SCANNING MODE). LEFT HAND SIDE: LFA; RIGHT HAND SIDE: HFA. POSITIONS AND SHAPE AGREE WELL WITH DESIGN-VALUES, WHILE THE ARRAY IS NEARLY INVARIANT AGAINST ROTATION OF THE 60° SYMMETRY ANGLE.

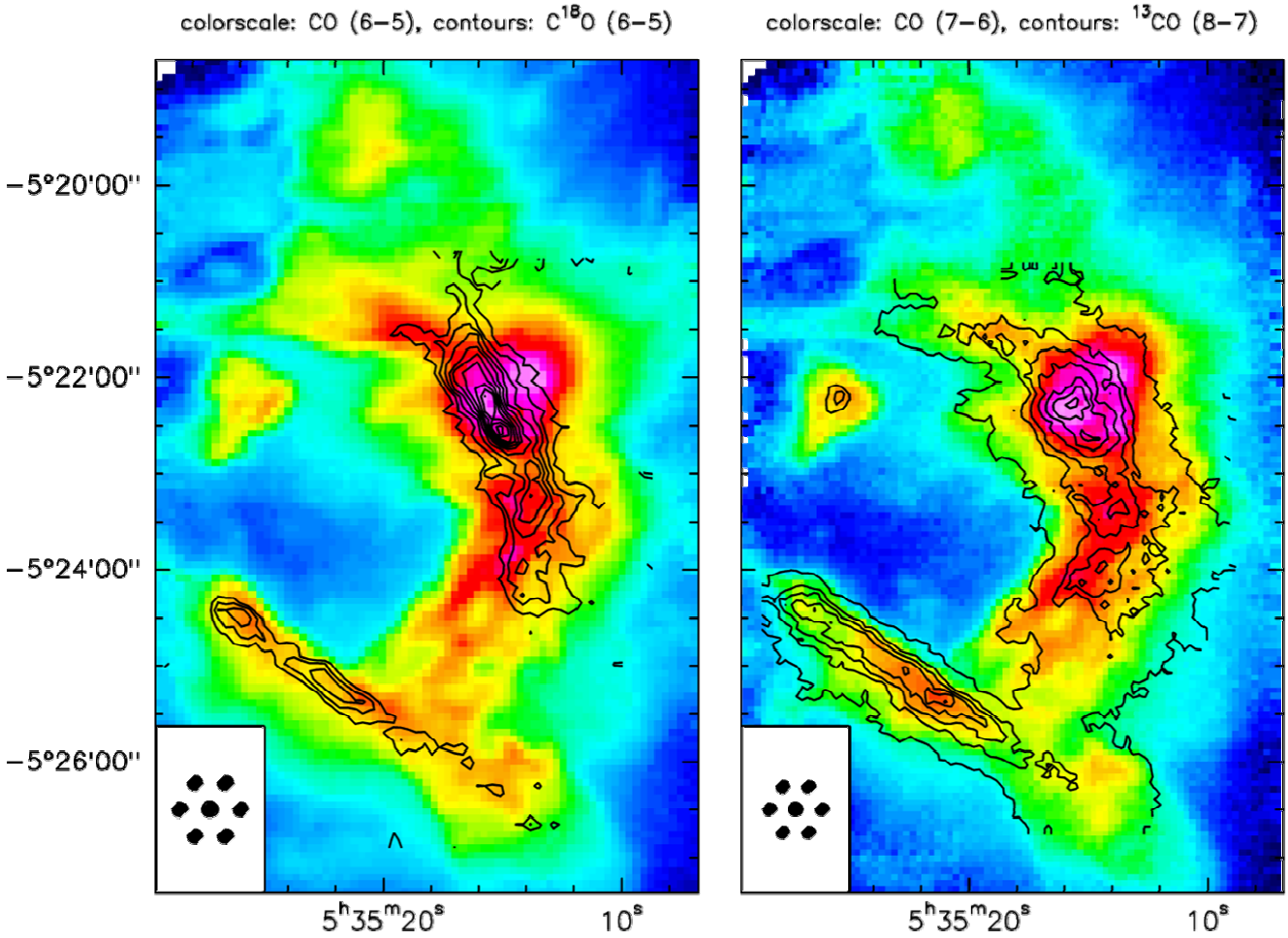

Fig. 12: CHAMP$^+$ on-the-fly map of the Orion A molecular cloud. Peak temperatures of in total four different CO isotopomers are displayed. The observing time was ca. 20 hours, each image composes of approximately 1 million spectra

of its small diameter during the 2007 commissioning, which was comparable to the APEX beam at 850 GHz. Figure 11 displays the pixel matrix, as measured in total power on-the-fly scans across Mars. The array has the designed hexagonal arrangement with clean beams (better than 15 dB) and good 60° rotation symmetry. The offset between the sub-arrays is measured to be better than 1 arcsec..

IV. First Astronomical Results

In figure 12 we present first astronomical results: four CO isotopometers have been measured towards the Orion A molecular cloud. The data-cube consists in total of more than two million individual spectra. Each spectrum was taken with a dump time of 1 second. The overall observing time including overheads was ca. 20 hours. This work shows impressively the potential of the new receiver system for large scale mapping projects.

Conclusions

CHAMP$^+$ at APEX offers unique high-resolution heterodyne mapping capabilities to the sub-millimeter community. The new instrument meets all critical design requirements and offers a good performance over its whole RF-tuning range. With its large IF-bandwidth of now 2.8 GHz (after upgrade of the back-end) and the compact hexagonal array-footprint, CHAMP$^+$ will provide key supplementary supporting observations to near future far-infrared missions like the Herschel/HIFI satellite or the airborne observatory SOFIA. Both missions are scheduled to provide first astronomical observations in 2009.

References

[1] Güsten, R. et al. 1998, in Advanced Technologie MMW, Radio, and Terahertz Telescopes, ed. T. G. Phillips (Proc. SPIE Vol. 3357)
[2] Güsten, R., Nyman, L.A., Schilke, P., Menten, K., Cesarsky, C. and Booth, R., 2006, A&A Letters 454, L13-L16
[3] Philipp, S. D., Lis, D. C., Guesten, R., Kasemann, C., Klein, T., Phillips, T. G., 2006, A&A Vol. 454, p213-219
[4] Pearson, J.C., Güsten, R., Klein, T., Whyborn, N., 2000, in "UV, Optical, and IR Telescopes and Instruments", Proc. SPIE, Vol.4013, p.264
[5] Graf, U.U. and Heyminck, S. 2001, IEEE Trans AP, 49(4)
[6] Jackson, B. D. et al. 2006, IEEE Trans. on Microwave Theory and Techniques, Vol. 54(2), pp. 547-558
[7] de Lange, G. et al. 2004, in Astronomical Structures and Mechanisms Technology, ed. J. Antebi & D. Lemke (Proc. SPIE Vol. 5498)
[8] Goldsmith, P. 1998, *Quasioptical Systems* (IEEE Press)
[9] Graf, U.U. et al. 2002, in Millimeter and Submillimeter Detectors for Astronomy (Proc. SPIE Vol. 4855)
[10] Heyminck, S. 2002, Dissertation, Universität zu Köln

Large Format Heterodyne Arrays for Terahertz Astronomy

Christopher Groppi[*a], Christopher Walker[a], Craig Kulesa[a], Dathon Golish[a], Jenna Kloosterman[a], Patrick Pütz[b], Sander Weinreb[c,d], Thomas Kuiper[c], Jacob Kooi[d], Glenn Jones[d], Joseph Bardin[d], Hamdi Mani[d], Arthur Lichtenberger[e], Thomas Cecil[e], Abigail Hedden[f], Gopal Narayanan[g]

[a]*Steward Observatory, University of Arizona, 933 N. Cherry Ave., Tucson, AZ 85721 USA*

[b]*I. Physikalisches Institut Universität zu Köln Zülpicher Straße 77 50937 Köln, Germany*

[c]*NASA Jet Propulsion Laboratory, 4800 Oak Grove Dr., Pasadena, CA, 91109, USA*

[d]*California Institute of Technology, 1200 E. California Bvld., Pasadena, CA, 91125, USA*

[e]*University of Virginia 351 McCormack Rd., Charlottesville, VA, 22904, USA*

[f]*Harvard Smithsonian Center for Astrophysics, 60 Garden St, Cambridge, MA 02138, USA*

[g]*University of Massachusetts, 710 North Pleasant Street, Amherst, MA 01003 USA*

* Contact: cgroppi@as.arizona.edu +01-520-626-1627

***Abstract*— For future ground, airborne and space based single aperture telescopes, multipixel heterodyne imaging arrays are necessary to take full advantage of platform lifetime, and facilitate science requiring wide field spectral line imaging. A first generation of heterodyne arrays with ~10 pixels has already been constructed, i.e. CHAMP, SMART, HERA, DesertStar, PoleStar and HARP. Our group is now constructing SuperCam, a 64 pixel heterodyne array for operation in the 350 GHz atmospheric window. This instrument will realize another order of magnitude increase in array pixel count. Several new techniques were used for SuperCam to maximize integration and modularity. Unlike other SIS array receivers, SuperCam is built around 8 pixel linear mixer modules, rather than independent mixer blocks. These modules house 8 single ended waveguide mixers with SOI substrate SIS devices. Each device is tab bonded to a MMIC based LNA. These modules dissipate only 8 mW of heat, while still maintaining 5 K IF noise temperature and 32 dB gain. Blind mate IF and DC connectors allow each module to be inserted in or removed from the focal plane as a unit. The modules are machined using a state-of-the-art CNC micromilling machine acquired specifically for this project. IF signals are processed by 8 channel IF downconverter boards, which provide gain, baseband downconversion and IF total power monitoring. A real-time FFT spectrometer implemented with high speed ADCs and Xilinx 4 FPGAs produce spectra of the central 250 MHz of each channel at 0.25 km/s spectral resolution. For arrays with an additional order of magnitude increase in pixel count, several additional technical problems must be overcome. Kilopixel arrays will require advances in device fabrication, cryogenics, micromachining, IF processing and spectrometers. In addition, seemingly straightforward receiver systems will require new approaches to realize a kilopixel heterodyne array with manageable complexity and cost. Wire count and 4K heat load must all be reduced significantly compared to SuperCam. IF and DC cabling and interconnects may be replaced with multiconductor microstrip or stripline ribbon. Parallel biasing of LNAs, magnets and even SIS devices is feasible if device uniformity is good enough. IF processing will require further integration, possibly with integrated MMIC chips containing all parts of a IF downconversion chain. Continued advances in FFT spectrometers could allow processing many hundreds of gigahertz of IF bandwidth for a realizable cost. We present results from final SuperCam receiver integration and testing, and concepts for expanding heterodyne arrays to kilopixel scales in the future.**

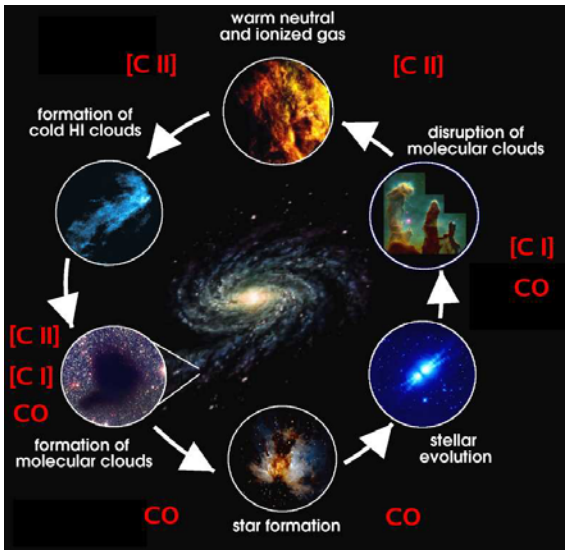

Figure 1: Life cycle of the ISM

I. Introduction

SuperCam has been designed to operate in the astrophysically rich 870µm atmospheric window. The Heinrich Hertz Submillimeter Telescope has a 13µm RMS surface, making it the most accurate large submillimeter telescope currently in operation. In addition, the 10,500ft elevation site on Mt. Graham offers weather sufficient for

observing in this window more than 50% of the observing season, 24 hours per day. The receiver is an 8x8 array constructed from integrated 1x8 mixer modules, with state of the art mixer, local oscillator, low noise amplifier, cryogenic and digital signal processing technologies.

SuperCam will have several times more pixels than any existing spectroscopic imaging array at submillimeter wavelengths. The exceptional mapping speed that will result, combined with the efficiency and angular resolution provided by the HHT will make SuperCam a powerful instrument for probing the history of star formation in our Galaxy and nearby galaxies. SuperCam will be used to answer fundamental questions about the physics and chemistry of molecular clouds in the Galaxy and their direct relation to star and planet formation. Through Galactic surveys, particularly in CO and its isotopomers, the impact of Galactic environment on these phenomena will be realized. These studies will serve as "finder charts" for future focused research (e.g. with ALMA) and markedly improve the interpretation, and enhance the value of numerous contemporary surveys.

II. SuperCam Science

From the Milky Way to the highest-redshift protogalaxies at the onset of galaxy formation, the internal evolution of galaxies is defined by three principal ingredients that closely relate to their interstellar contents:

- The transformation of neutral, molecular gas clouds into stars and star clusters (star formation).
- the interaction of the interstellar medium (ISM) with the young stars that are born from it, a regulator of further star formation.
- the return of enriched stellar material to the ISM by stellar death, eventually to form future generations of stars.

The evolution of the stellar population of galaxies is therefore determined to a large extent by the life cycles of interstellar clouds: their creation, starforming properties, and subsequent destruction by the nascent stars they spawn. The life cycle of interstellar clouds is summarized pictorially in Figure 1. Although these clouds are largely comprised of neutral hydrogen in both atomic and molecular form and atomic helium, these species are notoriously difficult to detect under typical interstellar conditions. Atomic hydrogen is detectable in cold clouds via the 21 cm spin-flip transition at 1420 MHz, but because the emission line is insensitive to gas density, cold (T~70K) atomic clouds are not distinguishable from the warm (T~8000K) neutral medium that pervades the Galaxy. Furthermore, neither atomic helium nor molecular hydrogen (H_2) have accessible emission line spectra in the prevailing physical conditions in cold interstellar clouds. Thus, it is generally necessary to probe the nature of the ISM via rarer trace elements. Carbon, for example, is found in ionized form (C^+) in neutral HI clouds, eventually becoming atomic (C), then molecular as carbon monoxide (CO) in dark molecular clouds. The dominant ionization state(s) of carbon accompany each stage of a cloud's life in Figure 1. In general, however, only global properties can be gleaned from the coarse spatial resolution offered by studies of external galaxies. Therefore detailed interstellar studies of the widely varying conditions in our own Milky Way Galaxy serve as a crucial diagnostic template or "Rosetta Stone" that can be used to translate the global properties of distant galaxies into reliable estimators of star formation rate and state of the ISM.

SuperCam has been designed to complete a key project Galactic plane survey in the ^{12}CO(3-2) and ^{13}CO(3-2) transitions of carbon monoxide. This survey, covering 500 square degrees of the Galaxy including a fully sampled survey from l=0º-90º and -1º<b<1º in addition to many molecular cloud complexes visible from the northern hemisphere, will improve the spatial resolution of existing surveys by more than a factor of 10. In addition, this will be the first submillimeter CO Galactic plane survey, providing a census of molecular gas actively participating in star formation. When combined with existing CO(1-0) surveys, a complete excitation temperature map of the survey region can be constructed. The depth of the survey is sufficient to detect CO to a level consistent with A_v~1, detecting all CO that has formed in-situ.

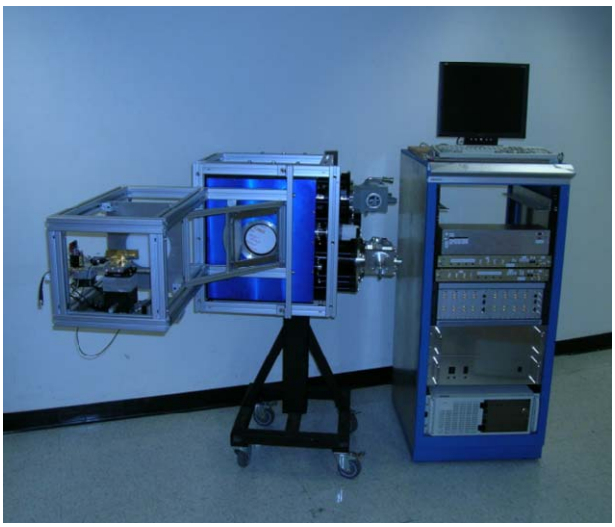

Figure 2: The SuperCam cryostat, LO optics and support electronics.

III. SuperCam Instrument Description

A. Instrument Design

In the past, all heterodyne focal plane arrays have been constructed using discrete mixers, arrayed in the focal plane. SuperCam reduces cryogenic and mechanical complexity by integrating multiple mixers and amplifiers into a single array module with a single set of DC and IF connectors. Well conceived, efficient packaging is essential to the successful implementation of large format systems. The enormous

complexity of even a small discrete system suggests a more integrated approach for larger systems. At the heart of the array is an 8 pixel linear integrated array of low-noise mixers. The array mixer contains first stage, low-noise, MMIC IF amplifier modules with integrated bias tees. Eight of these modules are then stacked to produce the final 64 pixel array.

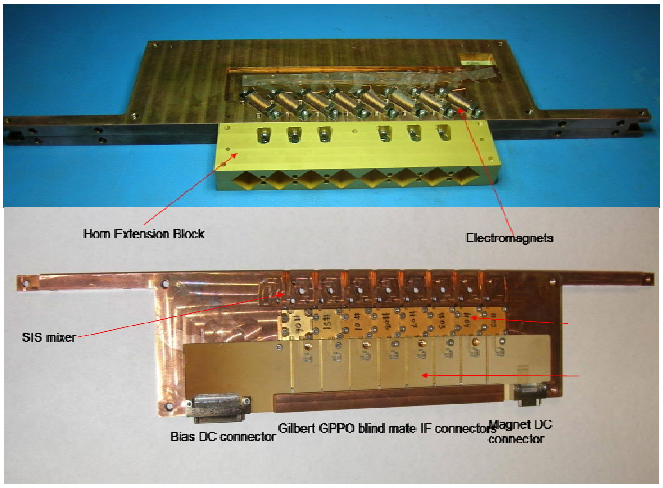

Figure 3: A completed SuperCam 1x8 mixer module, fully assembled (top) and with the top cover removed (bottom).

B. *Cryogenics*

The SuperCam systen with attached LO optics, frontend support electronics and backend electronics is shown in Figure 2. The cryostat was constructed by Universal Cryogenics in Tucson, Arizona, USA. Light from the telescope enters the cryostat through a 150 mm diameter AR coated, crystalline quartz vacuum window and passes through a GoreTex GR IR blocking filter on the 40 K radiation shield before illuminating the 4 K mixer array. SuperCam uses a Sumitomo SRDK-415D cryocooler. The cooler has 1.5 W of thermal capacity at 4.2 K and 45W at 40K with orientation-independent operation. The operating temperature of the cryocooler is stabilized by the addition of a helium gas pot on the 2nd stage. A CTI cryogenics CTI-350 coldhead supplements the cooling of the 40K shield, and provides 12K heatsinking for the 64 stainless steel semi-rigid IF cables. The addition of this second coldhead permits the use of moderate lengths of standard coaxial cable while maintaining low heat load at 4K. Annealed and gold plated copper straps with a flex link connect the 4K cold tip to the cold plate, with less than an 0.25K temperature differential. Tests using heaters on the 4K cold plate, and system tests using prototype 1x8 mixer modules demonstrate adequate performance of the cryogenic system with the expected heat load from all 64 pixels.

C. *Mixer Array*

The SuperCam 64 beam focal plane is constructed from eight linear array modules with eight pixels each. Each pixel consists of a sensitive single ended SIS mixer optimized for operation from 320-380 GHz. The array mixers utilize SIS devices fabricated on Silicon-On-Insulator (SOI) substrates, with beam lead supports and electrical contacts. The waveguide probe and SIS junction are based on an asymmetric probe design currently in use at the Caltech Submillimeter Observatory in their new facility 350 GHz receiver. The 1x8 mixer subarrays are constructed from tellurium copper using the splitblock technique. Stainless steel guide pins and screws are used to ensure proper alignment and good contact between parts. Figure 3 shows a photograph of a prototype tellurium copper 1x8 mixer array fabricated at the University of Arizona using a Kern MMP micromilling machine. This block meets all design specifications, with 3 µm dimensional accuracy for all waveguide circuits. A diagonal feedhorn extension block is bolted to the front of the mixer array assembly, extending the diagonal horns to 11mm aperture size. This eliminates the

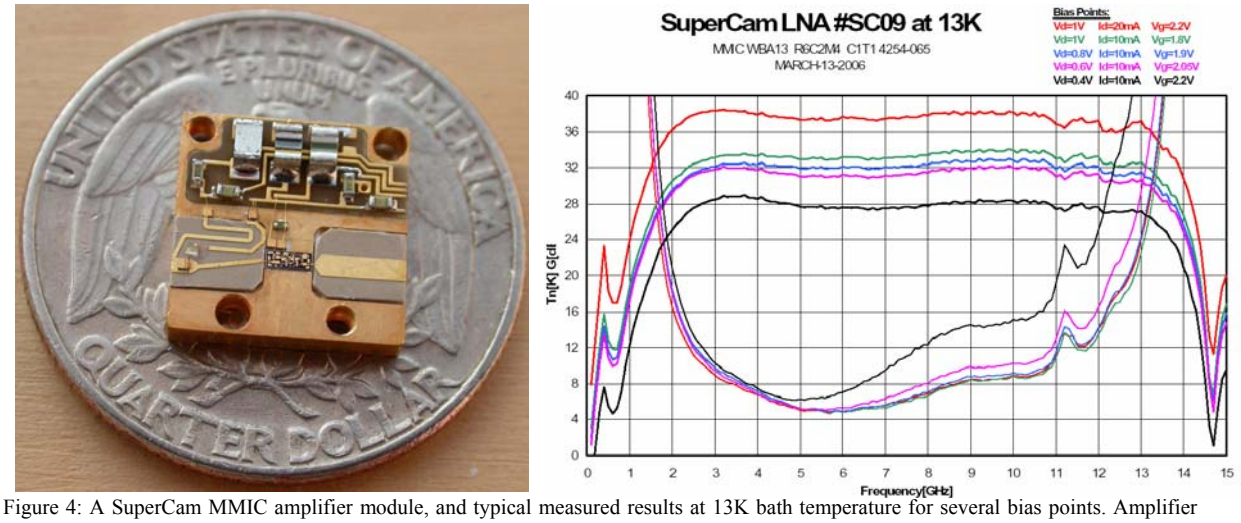

Figure 4: A SuperCam MMIC amplifier module, and typical measured results at 13K bath temperature for several bias points. Amplifier noise remains low for bias powers as low as 6 mW. Gain remains above 30 dB.

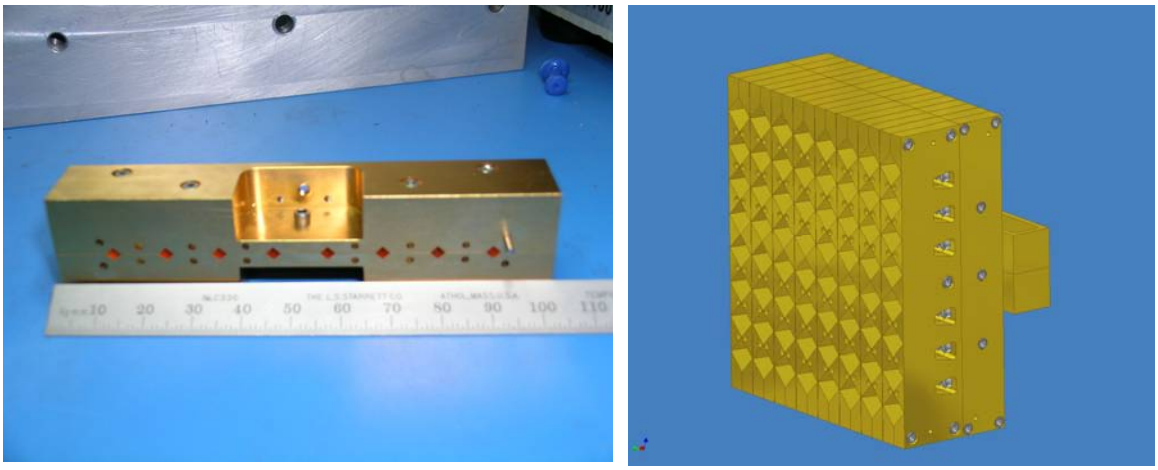

Figure 5: SuperCam prototype 8-way LO power divider (right), and solid model of the 64 way power divider now under construction. The divider is based on a corporate array of E-plane y-splitters, with waveguide twists on the output of the first module, and diagonal feedhorns on the output of the final 8 modules.

need for dielectric lenses and their associated manufacturing and alignment difficulties. The energy in the horn passes through a 90° waveguide bend before reaching the device. The waveguide environment is designed around full height rectangular waveguide, with a fixed quarter wave backshort. The SIS device is suspended and self-aligned above the suspended stripline channel via eight small beamlead supports. Both the hot and ground beamleads are tack-bonded with a wirebonder to the MMIC module (figure 4) input pad and block, respectively. The mixer blocks are fabricated at the University of Arizona using a Kern MMP micromilling machine purchased for this project. This numerically controlled mill can fabricate structures to micron accuracy with a high level of automation. A SuperCam 1x8 module can be produced in ~8 hours of machine run time, using only a single set of micro end mills per block half. The machine's 24 position tool changer allows a complete block to be fabricated with minimal user intervention during the machining process. Integrated workpiece and tool metrology systems, along with sophisticated computer aided manufacturing (CAM) software result in high part yield. Verification of fabricated parts though a high precision measurement microscope and 3D interferometric microscope insure dimensional accuracy and waveguide surface finish are within design tolerance. Testing, described in section 4, has been carried out using a single-pixel version of the SuperCam mixer design in a test cryostat, and with a full 8-pixel prototype mixer module. Series production of the final mixer modules is now underway.

D. Local Oscillator

With an array receiver, LO power must be efficiently distributed among pixels. Depending on the mechanical and optical constraints of the array, a balanced distribution can be achieved using quasioptical techniques or waveguide injection. With the quasioptical approach, dielectric beam splitters or holographic phase gratings are used to divide the LO energy between array pixels. The quasioptical approach works well for modest sized arrays. However, for the large format system being proposed here, the size of the required quasi-optical power splitter and diplexer become prohibitive. Therefore we have chosen to use a hybrid waveguide/quasioptical LO power injection scheme. The LO power for the array will be provided by a single solid-state, synthesizer-driven source from Virginia Diode Inc. The active multiplier chain consists of a high power solid-state amplifier followed by a series of tunerless broadband multipliers. The output of the multiplier is coupled to an eight-way waveguide corporate power divider with splitblock machineable waveguide twists. Each of the eight outputs provides the drive power for a 1x8 subarray via an identical 8 way corporate divider with diagonal waveguide feedhorn outputs. Figure 5 shows a prototype 1x8 power divider designed to power a single 1x8 mixer row. This power divider has been used in system tests with the prototype 1x8 mixer array and LO optics, with excellent results. Power balance was measured using a Thomas Keating power meter,

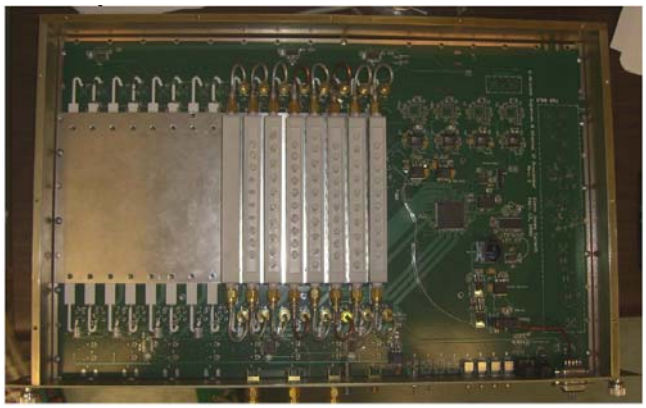

Figure 6: The inside of a SuperCam IF processor. This module provides amplification, programmable attenuation, passband filtering and total power detection for 8 channels.

and showed equal power balance within measurement errors, and ~1dB loss. The final 64 way power divider (CAD model shown in figure 5) is now under construction. An extended diagonal horn array similar to the mixer horn extension blocks then matches the LO beams to the mixers through a Gaussian beam telescope comprised of two large dielectric lenses. A 0.5 mil Mylar beamsplitter is used to inject the LO power. Testing has shown that a 2mW LO source is sufficient to optimally pump a 1x8 mixer array with this scheme, running at only ~20% of the maximum power output. An already purchased 12 mW source from Virginia Diodes will be more than sufficient to pump the final 64 puxel array, also with a 0.5 mil Mylar diplexer. This scheme ensures uniform LO power in each beam since the waveguide path lengths are identical for each beam. In addition, the waveguide feedhorns provide well controlled and predictable LO power distribution and coupling to each mixer. Accounting for conduction and surface roughness losses, we expect this 64-way network to add an additional 2dB of LO power loss compared to a lossless divider (double the measured loss of a single 8-way divider).

D. IF/Bias Distribution System

The IF outputs from the SIS devices are bonded directly to the input matching networks of low-noise, InP MMIC amplifier modules located in the array mixers. These amplifier modules have been designed and fabricated by Sander Weinreb's group at Caltech. The IF center frequency of the array is 5 GHz. The MMIC chip is contained in an 11mm x 11mm amplifier module that contains integrated bias tees for the SIS device and the amplifier chip. The module achieves noise temperature of ~5 K and delivers 32 dB of gain while consuming 8 mW of power. An example is shown in figure 4, with measured gain and noise data at 4 mW through 20 mW power dissipation. Noise remains virtually unchanged down to 6 mW power dissipation, while gain is reduced modestly. Several tests have been performed with these modules to ensure oscillation free operation, low noise, high stability, and no heating effects on the SIS device. Modules have been integrated into both single pixel and 1x8 array mixers, and have shown performance as good or better than expected with connectorized amplifiers. No heating effects are visible, although care must be taken to avoid oscillation due to feedback.

Figure 7: The SuperCam real time FFT spectrometer system, built by Omnisys AB. This single 3U crate can process 16 GHz of IF bandwidth at 250 kHz spatial resolution. It consumes less than 200W of AC power.

In addition to the LNA modules, the Caltech group has designed and constructed a warm IF system for SuperCam that will condition the IF signal for use with the SuperCam Array Spectrometer (figure 6). This IF system consists of a single large microwave printed circuit board with 8 channels of signal conditioning mounted in a modular chassis. The module contains a 5 GHz gain stage, switchable filters for both 250 MHz and 500 MHz bandwidth modes, baseband downconversion and baseband amplification.

E. Array Spectrometer

The SuperCam spectrometer delivers 64 channels at 250 MHz/channel with 250 kHz resolution, or 32 channels at 500 MHz with 250 kHz resolution. The system will be capable of resolving lines in all but the coldest clouds, while fully encompassing the Galactic rotation curve. The system is easily extendible to deliver 64 500 MHz bandwidth channels or 32 1 GHz bandwidth channels. This leap in spectrometer ability is driven by the rapid expansion in the capabilities of high speed Analog to Digital Converters (ADCs) and Field Programmable Gate Arrays (FPGAs). The SuperCam spectrometer, built by Omnisys AB of Sweden, is based on a real-time FFT architecture. High speed ADCs digitize the incoming RF signal at 8 bits resolution, preventing any significant data loss as with autocorrelation based schemes. Then, a large, high speed FPGA performs a real time FFT on the digitized signal and integrates the resulting spectrum. In our board architecture, 4 ADCs feed a single Xilinx Virtex 4 FPGA on each spectrometer board. Each board can process 4 500 MHz IF bandwidth signals or two 1 GHz IF bandwidth signals at 250 kHz resolution. Only recently has Xilinx released FPGAs fast enough and large enough to accommodate the firmware capable of this task. These systems are fully reconfigurable by loading new firmware

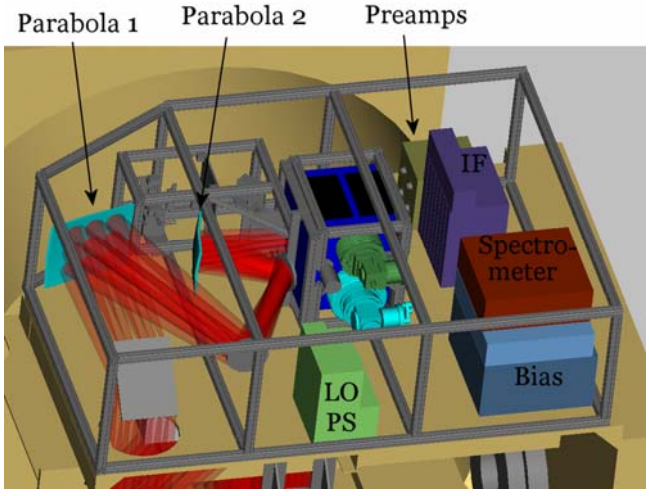

Figure 8: The SuperCam optics layout, mounted on the roof of the cassegrain cab of the HHT. This module contains the receiver front end, LO, optics and all electronics, and can be installed and removed as a pre-assembled unit.

into the FPGAs. In addition, the spectrometer can be easily expanded to increase bandwidth. We have received an 8 board system capable of processing 64x250 MHz, 32x 500 MHz or 16x1GHz IF signals (figure 7). In the 64x250 MHz mode, we power combine two IF signals into one spectrometer input. Stability testing shows the spectrometer is capable of delivering a spectroscopic Allan time in excess of 600s, including the effects of the IF processor described in section E.

F. Optics

The existing secondary mirror of the Heinrich Hertz Telescope provides a f/13.8 beam at the Nasmyth focus. The clear aperture available through the elevation bearing prevents the possibility of a large format array at this position. To efficiently illuminate a large format array like SuperCam, the telescope focus must fall within the apex room located just behind the primary. A system of flat mirrors directs the telescope beam through a hole in the roof of the apex room to the SuperCam system, mounted in a self-contained structure mounted on the roof. A system of re-imaging optics transforms the f number of the telescope to f/5. Since the physical separation between array elements in the instrument focal plane scales as 2fλ, lower f/#'s serve to reduce the overall size of the instrument. The reimaging optics are composed of two offset parabolas and several flat mirrors. All the reimaging optics can be mounted on a single optical frame. This frame can be completely constructed, aligned and tested off the telescope, then mounted as a complete unit. All electronics, including the backend, are located in this unit. The cryostat and optics frame have been designed using finite element analysis to minimize gravitational deflection, and the calculated deflections have been fed into the tolerancing of the optical design. The optical system was initially designed and optimized with Zemax, and was then verified by BRO research using their ASAP physical optics package. The system's efficiency exceeds 80% for all pixels, and has been verified to be robust to alignment and fabrication tolerances.

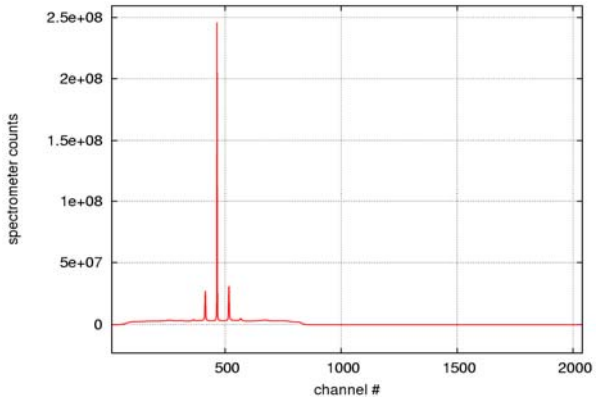

Figure 9: Spectrum from an end to end test of the SuperCam system.

IV. Laboratory Testing

For testing the SuperCam mixer design in the laboratory, we have designed two single pixel mixers. The first design uses an existing SIS junction design from the DesertStar 7-pixel array [7], but incorporates the Caltech designed MMIC module. This work has been reported in other papers [12,13]. We determined that the SIS receiver with integrated MMIC amplifier worked as well as a receiver with a separate

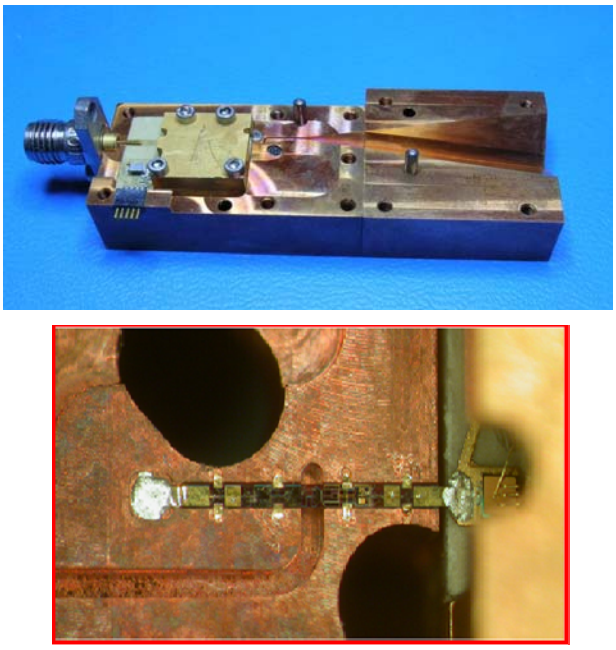

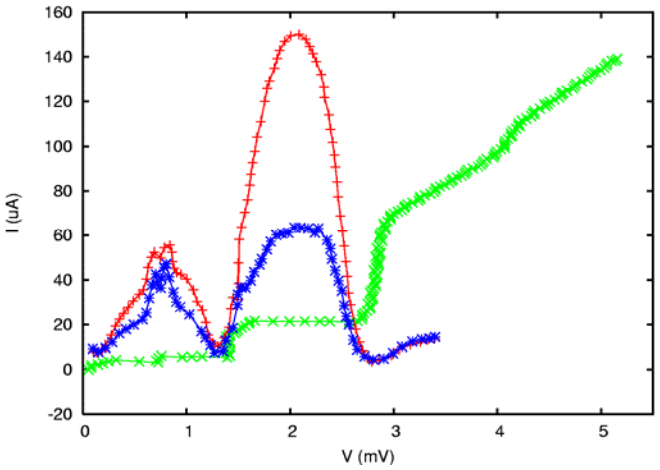

Figure 10: Single pixel test mixer with extended diagonal horn, LNA module and IF board (top left), a closeup of the SIS device (bottom left), and a representative IV curve and hot/cold total power curve (right).

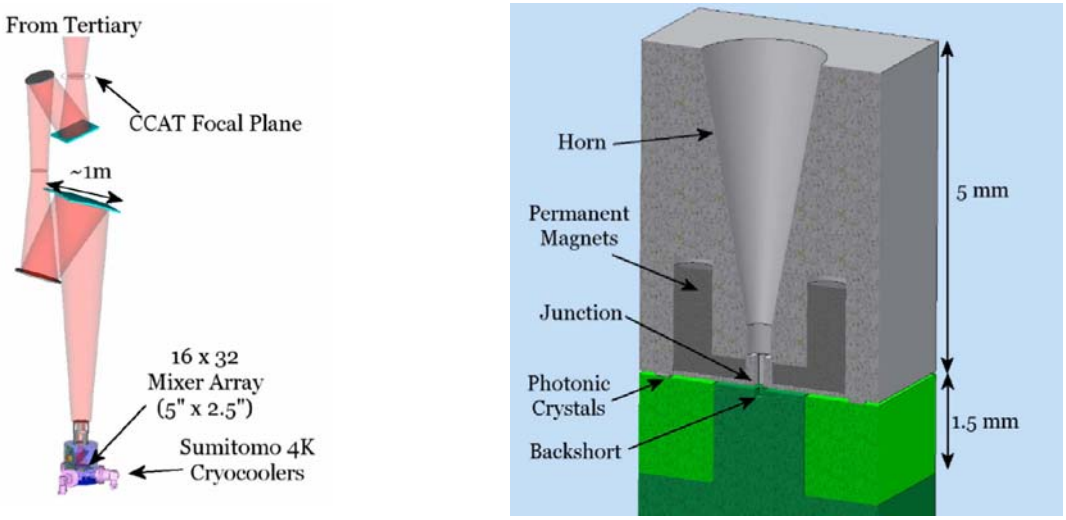

Figure 11: A concept for a 1024 pixel heterodyne array. The array consists of two 512 pixel subarrays, with polarization diplexing.

connectorized amplifier and cryogenic amplifier, and resulted in no heating effects at the SIS device from the close proximity of the amplifier. We later designed a second single pixel mixer that is an exact copy of a single pixel of the 1x8 mixer array design discussed in section 3.1.2. This mixer was designed to test the self-aligning beam-lead-on-SOI SIS devices that will be used in the SuperCam array, as well as the compact, low power electromagnet, MMIC amplifier module and extended diagonal feedhorn.

This mixer has been extensively tested for noise performance across the band, frequency response using a Fourier Transform Spectrometer, and stability measurements using the complete backend system. Tests with the latest wafer of SIS on SOI devices from UVa show close to optimal tuning, and measured noise temperatures of ~65 K with less than 10K variation across the measured band (LO limited to 330 to 365 GHz). Images of the single pixel mixer, a mounted SIS on SOI device and a representative IV and total power curve are shown in figure 10.

In addition, measurements of a prototype 1x8 mixer array has been completed using prototype or final electronics for the entire system. This mixer has been initially populated with devices from a less optimal wafer for system testing. These devices still deliver ~75K receiver noise temperature, but are not optimally tuned. The result of a full end to end test of this system is shown in figure 9. The sidebands around the line are the result of using a very high power LO source as a line injector. Even attenuated and pointed 180 degrees from the cryostat window, the power was still sufficient to generate harmonics in the IF processor.

V. Next Generation Heterodyne Arrays

New ground based platforms for terahertz astronomy such as the 10m South Pole Telescope (SPT) and the 25m Cornell-Caltech Atacama Telescope (CCAT) require even larger heterodyne arrays to fulfill their scientific potential for diffraction limited imaging of large areas. Arrays of ~1000 pixels are desired for these applications, and will be vital for future space based single aperture terahertz experiments.

While SuperCam reduced cost and complexity though 1 dimensional integration of mixers into linear modules, kilopixel class arrays will require two dimensional integration into detector wafers to further reduce complexity and cost per element.

The design concept shown in figure 11 is based around 128 pixel SIS device cards, with microstrip or CPW contacts on two edges. These cards consist of SOI membrane on a thick Si carrier wafer. The carrier waver has deep RIE etched pockets behind each device to accept backshort pedestals. The SOI membrane spans the pedestal, suspending the device across the backshort. Four device cards are mosaiced to produce a 512 pixel array. A single 512 element backshort wafer would also be produced using deep RIE etching. Each pedestal would self align into the matching etched pocket in the device wafer. A fixed waveguide backshort on each pedestal would then complete the waveguide circuit. A single horn block, metal machined using drilled wideband conical horns would then be mounted above the silicon backshort wafer. Photonic crystal choke structures would allow a small gap between the device wafer and horn block, preventing stresses due to differences in material coefficient of thermal expansion (CTE) from breaking the device wafer. Permanent magnets embedded in this block would eliminate the need for biasing 1000 electromagnets.

Simple, single ended mixers have been chosen for this concept. While many advances in high performance sideband separating balanced mixers have been made, they are still mechanically complicated and would be very difficult to build into a 2D integrated focal plane. A sideband separating design with all necessary circuitry in a planar design on the device wafer would be compatible with 2-D integration.

DC bias could be phantom-fed through the IF lines from a ring shaped board around the device wafer. This board would also contain first stage IF amplification. More concentric

boards, linked by wirebonds or flexible ribbon cable would contain additional IF amplification. Fiber transceivers, located at a warm stage in the cryostat, could output the IF signals on optical fiber rather than coaxial cables, vastly reducing the thermal load and cryogenic complexity of the instrument. Depending on device uniformity, parallel bias could be used to reduce the number of DC lines fed into the dewar. Alternatively, a custom ASIC could be produced to generate the bias signals inside the cryostat with only digital control fed into the cryostat.

Such an instrument would be only a few times larger than SuperCam, and could be cooled with only 2-3 1.5W 4K coolers.

Local oscillators capable of driving such a system using silicon etalon diplexers are already available for frequencies below 500 GHz and should be available on the timescale of such an instrument between 500 GHz and 1 THz. Both quasioptical and waveguide LO multiplexing schemes would be compatible.

Advances in digital signal processing promise to also make the backend system for such an array feasible. With higher speed ADCs, the IF processor for a kilopixel array could be completely eliminated. If the ADCs are fast enough to digitize the IF at it's native frequency, further downconversion is unnecessary. The next generation of real time FFT spectrometers is capable of delivering backend processing for costs of ~$5000 per gigahertz. A 1024 channel spectrometer with SuperCam's bandwidth per pixel could be built for a cost of $1-2M. On a 5-10 year timescale, several GHz per pixel at the $1M system cost level is feasible.

IV. Conclusion

We are constructing SuperCam, a 64-pixel heterodyne imaging spectrometer for the 870 μm atmospheric window. A key project for this instrument is a fully sampled Galactic plane survey covering over 500 square degrees of the Galactic plane and molecular cloud complexes. This ^{12}CO(3-2) and ^{13}CO(3-2) survey has the spatial (23") and spectral (0.25 km/s) resolution to disentangle the complex spatial and velocity structure of the Galaxy along each line of sight. SuperCam was designed to complete this survey in two observing seasons at the Heinrich Hertz Telescope, a project that would take a typical single pixel receiver system 6 years of continuous observing to complete. Prototypes of all major components have been completed and tested. The first 1x8 mixer row has been fabricated and has undergone testing. Fabrication, and assembly of the final waveguide components is now underway. SuperCam will be deployed with 32 pixels on the HHT in the Fall of 2008, with the remaining complement of 32 pixels to be installed at the end of the observing season.

Next generation heterodyne arrays with ~1000 pixels are possible with extensions and developments of today's technologies. With an additional level of integration to two dimensional focal planes, complexity is minimized. Such an instrument could be built for a reasonable cost on the timescale of new terahertz astronomy platforms such as the 10m SPT and the 25m CCAT telescopes.

References

[1] R.B. Bass, J.C. Schultz, A.W. Lichtenberger (University of Virginia); C. Walker (University of Arizona); J. Kooi (CalTech), "Beam Lead Fabrication Using Vacuum Planarization", submitted to Proceedings of the Fourteenth International Symposium on Space THz Technology, May 2003.

[2] Carpenter, J. M., Snell, R. L., & Schloerb, F. P. 1995, "Star Formation in the Gemini OB1 Molecular Cloud Complex", ApJ, 450, 201

[3] Dame, T. M. et al. 1987, "A composite CO survey of the entire Milky Way", ApJ, 322, 706

[4] Dame, T. M., Hartmann, D., & Thaddeus, P. 2001, "The Milky Way in Molecular Clouds: A New Complete CO Survey", ApJ, 547, 792

[5] Gillespie, A. R. & Phillips, T. G., 1979, "Array Detectors for Millimetre Line Astronomy", A&A, 73, 14.

[6] Goldsmith, P., in "Quasioptical Systems", pub. IEEE Pressm 184.

[7] Groppi, C. E. et al. 2003, "DesertSTAR: a 7 pixel 345 GHz heterodyne array receiver for the Heinrich Hertz Telescope", SPIE, 4855, 330

[8] J.W. Kooi, C.K. Walker, and J. Hesler, "A Broad Bandwidth Suspended Membrane Waveguide to Thin Film Microstrip Transition", 9th Int. Conference on Teraherz Electronics, 15th - 16th October 2001.

[9] Sakamoto, S., Hasegawa, T., Hayashi, M., Handa, T., & Oka, T. 1995, "The Five College Radio Astronomy Observatory CO Survey of the Outer Galaxyî" ApJS, 100, 125

[10] Simon, R., Jackson, J. M., Clemens, D. P., Bania, T. M., & Heyer, M. H. 2001, "The Structure of Four Molecular Cloud Complexes in the BU-FCRAO Milky Way Galactic Ring Survey", ApJ, 551, 747

[11] E. Schlecht, G. Chattopadhyay, A. Maestrini, A. Fung, S. Martin, D. Pukala, J. Bruston, and I. Mehdi, "200, 400, and 800 GHz Schottky diode substrateless multipliers: Design and Results," 2001 IEEE, MTT-S International Microwave Symp. Digest, Phoenix, Az, pp. 1649-1652, May 2001.

[12] Walker, C. K., Groppi, C., d'Aubigny, C., Kulesa, C., Hungerford, A., Jacobs, K., Graf, U., Schieder, R., & Martin, C., 2001, PoleSTAR: A 4-Pixel 810 GHz Array Receiver for AST/RO, "Proceedings of the 12th International Symposium on Space Tera- Hertz Technology", San Diego, CA, Eds. Mehdi & McGrath, JPL.

[13] Groppi, C.E., Walker, C.K., Kulesa, C., Puetz, P., Golish, D., Gensheimer, P., Hedden, A., Bussmann, S., Weinreb, S., Kuiper, T., Kooi, J., Jones, G., Bardin, J., Mani, H., Lichtenberger, A., Narayanan, G. SuperCam, a 64- Pixel Superheterodyne Camera, Proceedings of the 17th International Symposium on Space Terahertz Technology, 2006.

[14] Puetz, P., Hedden, A., Gensheimer, P., Golish, D., Groppi, C., Kulesa, K., Narayanan, G., Lichtenberger, A., Kooi, J., Wadefalk, N., Weinreb, S., Walker, C., 345 GHz Prototype SIS Mixer with Integrated MMIC LNA, Int. J. Infrared Milli. Waves, 27, 1365, 2006.

APEX Band T2: A 1.25 – 1.39 THz Waveguide Balanced HEB Receiver

D. Meledin*, V. Desmaris, S.-E. Ferm, M. Fredrixon, D. Henke, I. Lapkin, O. Nyström, M. Pantaleev, A. Pavolotsky, M. Strandberg, E. Sundin, and V. Belitsky

Group for Advanced Receiver Development (GARD), Chalmers University of Technology, SE-412 96, Gothenburg, Sweden

* Contact: denis.meledin@chalmers.se, phone +46-31-7721842

***Abstract*— A waveguide 1.25–1.39 THz Hot Electron Bolometer (HEB) balanced receiver was successfully developed, characterized and installed at the Atacama Pathfinder EXperiment (APEX) telescope. The receiver employs a quadrature balanced scheme using a waveguide 90-degree 3 dB RF hybrid, HEB mixers and a 180-degree IF hybrid. The HEB mixers are based on ultrathin NbN film deposited on crystalline quartz with a MgO buffer layer. Integrated into the multi-channel APEX facility receiver (SHeFI), the results presented here demonstrate exceptional performance; a receiver noise temperature of 1000 K measured at the telescope at the center of the receiver IF band 2-4 GHz, and at an LO frequency of 1294 GHz. Stability of the receiver is fully in line with the SIS mixer bands of the SHeFI, and gives a spectroscopic Allan time of more than 200 s with a noise bandwidth of 1 MHz.**

I. Introduction

According to recent atmospheric measurements, three windows between 1 and 2 THz center at 1.03 THz, 1.32 THz and 1.5 THz and could be available for ground based observations when an appropriate site is used [1]. The Atacama Pathfinder EXperiment (APEX) telescope is a 12 meter single dish located at Chajnantor Plato, in Northern Chile and offers one of the best opportunities for Terahertz observations from the ground. The telescope is equipped with heterodyne and bolometric receivers for radio astronomical observations in the 211 – 1500 GHz frequency range [2]. The multi-channel Swedish Heterodyne Facility Instrument (SHeFI) was installed at the telescope during March 2008 [3]. Being a part of SHeFI, the balanced waveguide THz receiver covers the frequency band from 1.25 THz to 1.39 THz. The atmospheric window centered at 1.32 THz is especially important because the Hershel Satellite Observatory [4] has no instruments covering this frequency range.

In the case of a single-end mixer, that is widely used in radio-astronomy instruments, the local oscillator (LO) injection is often established by using a diplexer, a beam-splitter made of a thin dielectric or a wire grid. A THz LO source [5] used for this project, provides 5-9 μW of power over the RF band. Therefore, the above described LO injection schemes, for this weak LO source, could contribute substantially to the receiver noise by adding insertion loss to the RF signal path. Moreover, thermal noise injected into the receiver input along with the LO will degrade the receiver noise performance noticeably [6]. Additionally, amplitude modulation of the LO power, introduced by microphonic and mechanical fluctuations of the beam-splitter [7], would lead to instability of the mixer output power.

The balanced mixer technique helps to improve on these issues. Balanced mixers offer suppression of LO AM noise, reject LO spurious signal, and allow better handling of the available LO power [6, 8]. On the other hand, a more complex layout of the balanced mixer and high operating frequencies above 1 THz, introduce significant challenges for manufacturing receiver components, and makes development more demanding.

Previously, a number of balanced mixer designs have been reported for different frequencies, such as 90 GHz [9], 530 GHz [10], 280-420 GHz [11]. However, to our knowledge, no balanced mixer has been proposed or implemented for frequencies above 1 THz.

In this paper, we describe the APEX Band T2 waveguide balanced HEB receiver covering 1.250-1.390 THz, which has been developed, characterized and successfully installed at the telescope. Further details, including the description of the receiver design, characterisation and first-light "on sky" results, are presented in [12].

II. Receiver Design

A quadrature balanced receiver layout is shown in Fig.1. The signal from the telescope and LO are coupled to the individual HEB mixers by a 3 dB quadrature waveguide hybrid. In comparison to an earlier receiver prototype design [13], a 180° commercial IF hybrid is placed after the HEB mixers and combines the mixers' IF outputs. The IF signal appears at the difference-port of the hybrid (Δ), and then is amplified by two cryogenic 2-4 GHz IF low noise amplifiers (LNA) connected in series. The IF hybrid, positioned before the LNAs, contributes additional noise caused by an insertion loss of about 0.5 dB. Alternatively, two IF amplifiers may be used before the IF hybrid, but then possible amplitude and phase imbalances, introduced via unavoidable differences

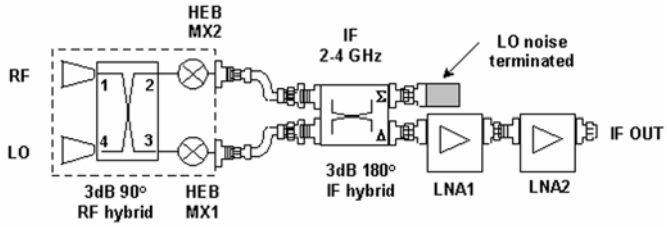

Fig. 1. Layout of the waveguide balanced HEB mixer.

between LNA gains, may lead to a receiver imbalance and deterioration of the noise temperature and stability. The amplitude component of the sideband LO noise is collected at the sum-port (Σ) of the IF hybrid and terminated by a 50 Ohm load. Both LNAs were designed at GARD and achieve input return losses better than 15 dB [14]. As such, a circulator may be avoided between the IF hybrid output and LNA1, which improves the IF system noise temperature. Noise temperature of the LNAs were measured to be about 5 K with a gain of about 27 dB over the entire IF band.

One of the key components of the receiver, the input waveguide 3 dB RF hybrid, distributes the LO and RF signal (ports 1 and 4, in Fig.1) between the two HEB mixers with 90° phase shift (ports 2 and 3, in Fig.1). The hybrid consists of two parallel waveguides with dimensions of 90 μm x 180 μm coupled through 6 branch waveguides between the broad walls [13, 12]. Optimized branch height and length are as small as 21 μm and 50 μm at minimum. In order to ensure the required amplitude and phase balance, the hybrid has to be fabricated with a linear error less than 2 μm. For fabrication of the hybrid we employed photolithography of a thick photoresist combined with fine electroplating described in detail in [15, 16].

Superconducting HEB mixers are based on 4-5 nm thick NbN deposited on a pre-heated substrate by reactive magnetron sputtering. The NbN film was deposited on top of a 200 nm thick MgO buffer layer placed on a 150 μm thick crystalline quartz substrate. The film is patterned using both optical and e-beam lithography to form the bolometer elements of 0.1-0.12 μm long and 1-1.2 μm wide [17]. Such a small volume of the bolometer was chosen due to the low available LO power. The typical critical temperature is about 10.5 K with a transition width of 0.6-0.7 K, which is expectably lower than that of bulk NbN. After fabrication, most of them were DC tested and then lapped down to a thickness of 17 μm and diced into the individual substrates (70 μm x 1000 μm). The measured room temperature resistance was within a range of 50-80 Ω. Critical current values varied from 150 μA to 250 μA at a 4.2 K bath temperature.

Each HEB mixer was integrated with an RF probe, a choke structure employing a hammer layout, and DC and IF leads. Both substrates fit into a suspended microstrip channel across the broad wall of a full height waveguide (180 μm x 90 μm) inside a copper mixer block with a fixed 70 μm backshort (see inset of Fig.2). The substrate channels are also fabricated using a micro-machining technique developed at GARD [16]. A SEM image of the micro-channel is shown in Fig.2 (inset).

In the probe design, the input RF signal coming from the waveguide port is coupled to the HEB mixer by an E-probe, and is isolated from the DC bias/IF output port using an RF choke [18] (inset Fig. 2). The small thickness of quartz substrate was chosen to prevent a waveguide mode propagation towards the IF port. Since the RF impedance of HEB mixers is practically real at frequencies above 1 THz (when the quantum energy exceeds double the gap energy, $h\nu > 2\Delta$), no addition matching circuitry is needed.

Initially, we had three designs of the RF probe providing different embedding impedances to the HEB elements of about 55 Ω, 70 Ω, and 90 Ω within the receiver frequency band. For the present work we have used mixer elements with R_N values of about 65 Ω, therefore we used the 70 Ω RF probe design that was closest to the obtained R_N. Thus, we could expect optimal noise temperature of the mixers [19]. Critical current values of the mixers for this receiver were 190 μA and 235 μA.

The mixer assembly design is shown in Fig.2 and consists of two main sections. In the front section, two corrugated feed horns and the RF hybrid are housed. The RF hybrid was produced using a split-block technique and so the two parts should be well aligned. The RF hybrid alignment is illustrated within the inset of Fig. 2 showing a picture of the two RF hybrid waveguide outputs. The other part carries the back-pieces, with integrated IF / DC circuitries fabricated on alumina substrates. Another inset,

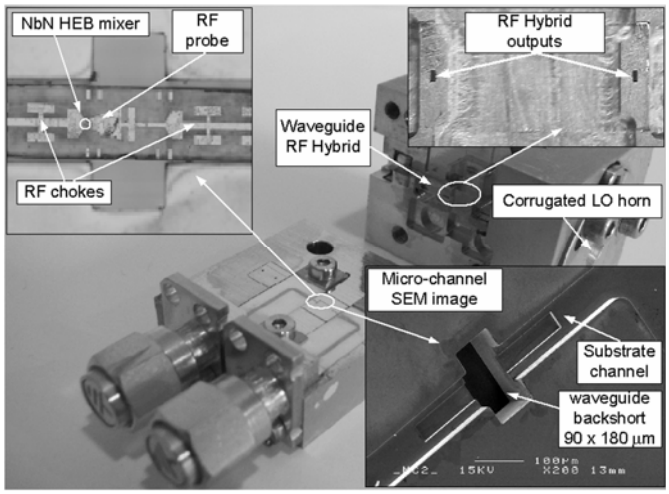

Fig. 2. The 1.32 THz mixer block. Insets show the mixer substrate fitted into a micro-machined channel with the RF hybrid outputs, and a SEM image of the micro-channel.

Fig. 2, shows the HEB mixer substrate aligned in the waveguide back-piece.

The mixer assembly is connected to the IF hybrid via standard bias-tees and short phase-matched coaxial cables. These components, along with LNA1 (Fig.1), are mounted on a sub-assembly plate, which is then fixed to the 4 K cold plate of the closed-cycle cryocooler. The second LNA (Fig. 1), providing further amplification of the IF signal, is mounted on the 12 K stage.

All IF signals of SHeFI are required to be centered at 6 GHz. The three SIS mixer channels have an IF band of 4-8 GHz. In APEX T2 the IF band is 2-4 GHz and this band is up-converted to 7-5 GHz.

III. Receiver characterization

To measure double-side band (DSB) noise temperature we used the standard Y-factor technique. Room-temperature and liquid nitrogen cooled loads were alternately placed at the signal window. We determined the optimum low-noise operation point for both mixers experimentally by measuring the receiver noise temperature as a function of LO power and mixer bias voltage. The DC bias of the HEB mixers, for best noise performances, is around 0.9 mV.

In Fig. 3 the DSB receiver noise temperature measurements are displayed as a function of LO frequency. These measurements were taken at the APEX telescope site using a spectrum analyzer in the 6 ± 0.1 GHz IF range. Note that due to a lower atmospheric pressure temperature the hot and cold loads were 287 K and 73 K, respectively. The receiver noise temperature has a slope of about 200-250 K across the receiver IF band. Fig. 4 demonstrates the receiver noise temperature as a function of IF frequency. Results were obtained at an LO frequency of 1.270 THz (black curve with circles), 1.316 THz (gray curve with diamonds), and 1.370 THz (light gray curve with squares). Note, that the curves are flipped in IF due to the up-converter.As the input alternated between hot and cold loads, we observed less than a 1% change in the HEB mixer DC current. Therefore, the direct detection effect was considered negligible. This can be attributed to the waveguide mixer configuration providing a built-in restriction of the input RF band.

The stability of the receiver is crucial during astronomical observations when the signal is deeply embedded in the noise and long integration time is needed to provide sufficient a signal-to-noise ratio. The closed-cycle cryocooler used in the SHeFI dewar introduces an additional source of instability. Since HEB mixers are based on the hot electron effect, its frequency conversion mechanism is strongly coupled to the ambient temperature of the HEB [20]. Consequently, the temperature instabilities of the closed-cycle cryocooler may cause gain fluctuations of the HEB receiver.

Different methods may be used to minimize these temperature instabilities. For instance, in [21], compensation of instability caused by physical temperature variations has been achieved by a sophisticated regulation of the IF LNA gain. For the APEX T2 receiver we have implemented an active temperature stabilization of the mixer assembly, using a commercial solution [22] with resistive heaters installed onto the mixer assemblies. Our measurements in the laboratory have shown that physical temperature variations at the THz balanced mixer do not exceed 1 mK.

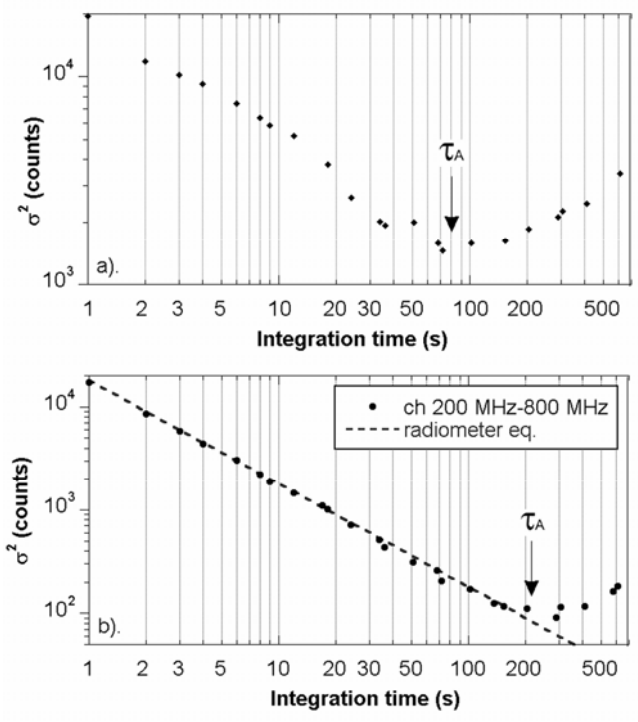

Fig. 5. a). Normalized total power Allan variance, for an RF of 1382 GHz and measured in the APEX telescope using the 200 MHz FFTS channel. The noise bandwidth is 1 MHz. b). Spectroscopic Allan variance measured by subtracting the 200 and 800 MHz channels. The dotted line shows the theoretical time dependence of Allan variance according to the radiometer equation.

A standard method to characterize receiver stability is to perform measurements of Allan variance [23]. Allan variances were measured on the APEX site for different RF frequencies. The measurements were done with the APEX facility Fourier transform spectrometer (FFTS) providing two, 1 GHz channels with a channel resolution of down to 61 kHz [24]. The input window was covered by an absorber at room temperature (287 K). The FFTS recorded 10 values across the IF band, spaced by 100 MHz and with each channel having a bandwidth of 1 MHz. Output power was sampled with 1 s rate. Stability measurements were performed using the 200 MHz and 800 MHz FFTS channels. The normalized total power Allan variance for 200 MHz FTTS channel taken at RF frequency of 1382 GHz (CO J–12→11 line) is shown in Fig. 5a. The mixers were optimally biased and pumped for low-noise operation. In Fig. 5b the spectroscopic Allan variance, calculated by subtracting those FTTS channels, is shown. The dotted line represents the radiometer equation (i.e., pure white noise). The total power and spectroscopic Allan time, τ_A, are about 80 s and 200 s, respectively. Stability measurements performed at an RF frequency of 1267 GHz (CO J–11→10 line), demonstrated more than 35 s and 150 s, in the case of total power and

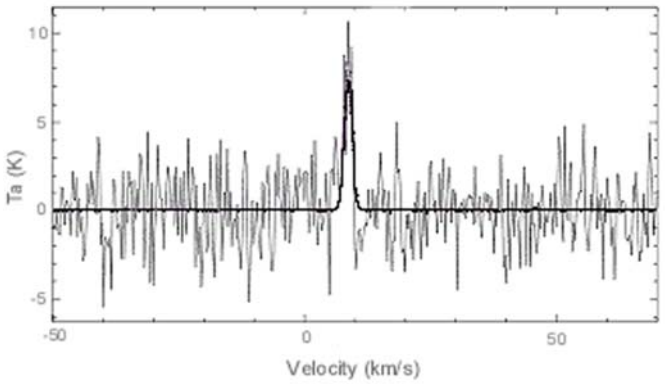

Fig. 6. "First light" APEX T2 receiver detection of the transition line J–11→10 of CO in the ORION-FIR4 star OMC.

spectroscopic Allan variance, respectively. Note that the results are fully consistent with stability measurements performed at GARD using another FFTS back-end [12].

After normalizing these measured values according to bandwidth, these times are larger than previously reported for small volume HEB mixers [7, 25] indicating excellent stability of the APEX T2 receiver. Moreover, we observe from the Allan variance plot that at integration times longer than τ_A, drift noise (positive slope) is clearly seen, and $1/f$ noise (the plateau around the minimum) does not dominate. The measured stability of the APEX T2 HEB mixer is fully comparable with the stability of the SIS mixers used for other SHeFI bands.

For best performance, the receiver input beam should be well-matched to the antenna beam and properly aligned with respect to the receiver mechanical reference. In order to verify the APEX T2 beam and its alignment, we have performed measurements of the input beam using scalar beam measurements. Several transverse planes along the signal path were scanned. The input beam parameters were obtained by a 3D fit of the fundamental Gaussian beam to all measured data under the assumption that the beam axis was defined by the amplitude maxima of the performed scans [26].

The SHeFI instrument was installed at the APEX telescope from late February to the beginning of March, 2008. Measurements on sky can only be performed during the best weather conditions at the APEX site, with a precipitable water vapour (PWV) lower than 0.2 mm (something that happens only 10-20 nights per year). During April 2008, we had only 3 such nights; Fig. 6 shows APEX T2 "first light" detected spectrum of the transition J–11→10 of CO (1.267 GHz) in the ORION-FIR4 source from the Orion Molecular Cloud (OMC). The line looks weaker and narrower than expected due to not optimized pointing to the source [27].

CONCLUSION

We have designed, built and characterized the first 1.25-1.39 THz balanced waveguide HEB receiver and have successfully commissioned it at the APEX telescope. The receiver IF band is 2-4 GHz and the minimum receiver noise temperature is 1000 K (across 1270-1295 GHz) measured in the APEX telescope at the center of the IF band. The APEX T2 HEB receiver demonstrates outstanding stability, presumably better than ever reported for HEB based receivers. Furthermore, the APEX T2 receiver stability is fully in-line with the other SHeFI bands based on SIS mixers. We believe that these improvements have been achieved by using the waveguide balance design, reducing the effects of the LO instability and eliminating receiver degradation due to the direct detection effects. The receiver performance has been confirmed by the detection of the CO J–11→10 line in the ORION-FIR4 star OMC. The APEX T2 receiver offers a great opportunity for ground-based THz observations.

ACKNOWLEDGMENT

The authors would like to thank V. Perez, B. Voronov, G. Goltsman, N. Kaurova, V. Drakinsky, S. Cherednichenko, C. Risacher, and staff at the APEX telescope. This work was supported by the Swedish Research Council and the Wallenberg Foundation via respective grants, by the Swedish National Space Board, and EU FP 6 RadioNet AMSTAR.

REFERENCES

[1] S. Paine et al., " A Fourier transform spectrometer for measurement of atmospheric transmission at submillimeter wavelengths," *Publ. of the Astronomical Society of the Pacific*, vol. 112, pp 108-118, Jan. 2000.

[2] The APEX website. [Online]. Available: http://www.apex-telescope.org/.

[3] Belitsky, et al., "Heterodyne single-pixel facility instrumentation for the APEX Telescope", in *Proc. SPIE*, v. 6275, 2006, p. 62750G-1.

[4] The HERSHEL website. [Online]. Available: http://sci.esa.int.

[5] Virginia Diodes Inc., 979 2nd St. SE Suite 309, Charlottesville, VA 22902, USA.

5.1) Kerr and S.-K. Pan, "Design of planar image separating and balanced SIS mixers," in *Proc. 7th Int. Symp. Space THz Technology*, Charlottesville, 1996, pp. 207–219.

[6] J. Kooi, J. J. A. Baselmans, A. Baryshev, R. Schieder, M. Hajenius, J. R. Gao et al, "Stability of heterodyne terahertz receivers," *J. Appl. Phys.,* vol. 100, 064904, 2006.

[7] S. A. Maas, Microwave Mixers, 2nd edition. Boston, MA: Artech House, 1993.

[8] K. D. Stephan, N. Camilleri, and T. Itoh, "A quasioptical polarization-duplexed balanced mixer for millimeter wave applications," *IEEE Trans. Microwave Theory*, vol. MTT-31, no. 2, pp. 164–170, Feb. 1983.

[9] Chattopadhyay, F. Rice, D. Miller, H.G. LeDuc, and J. Zmuidzinas, "A 530-GHz Balanced Mixer," *IEEE Microwave and Guided Wave Lett*., vol. 9, no. 11, pp.467-469, Nov. 1999.

[10] J. W. Kooi, A. Kovacs, B. Bumble et al," Heterodyne instrumentation upgrade at the Caltech Submillimeter Observatory," in *Proc. SPIE*, vol. 5498, Oct. 2004, pp. 332-348.

[11] Meledin et al, "A 1.3 THz Balanced Waveguide HEB Mixer for the APEX Telescope", submitted to *IEEE Trans. On Microwave Theory and Tech.*, 2008.

[12] Meledin, et al, "Balanced Waveguide HEB Mixer for APEX 1.3 THz receiver," in *Proc. 15th Int. Symp. Space THz Technology*, Gothenburg, 2005, pp. 214–216.

[13] Risacher, et al," Low noise and low power consumption cryogenic amplifiers for Onsala and APEX telescopes", presented at European Microwave Week 2004, Amsterdam, Oct. 2004.

[14] Pavolotsky, et al, "Micromachining approach in fabricating of THz waveguide components"**,** *Microelectronics J.,"* vol. 36, pp. 683-686, 2005.

[15] Desmaris, et al, "Sub-Millimeter and THz Micromachined All-Metal Waveguide Components and Circuits," accepted for publication in *Micromechanics and Microengineering*, 2008.

[16] NbN films deposition and mixer patterning have been provided by B. Voronov and G. Goltsman, Moscow State Pedagogical University, Moscow, Russia.

[17] Risacher, V. Vassilev, A. Pavolotsky, V. Belitsky, "Waveguide-to-microstrip transition with integrated Bias-T", *IEEE Microwave and Wireless Components Letters*, vol.13, no. 7, July 2003, pp. 262-264.

[18] Loudkov, C.-Y. E. Tong, R. Blundell., et al, " An investigation of the performance of the superconducting HEB mixer as a function of its RF embedding impedance," *IEEE Trans. Appl. Supercond.,* vol.13, no.2, pp.164-167, June, 2005.

[19] M. Gershenzon et al., "Wide-band high speed Nb and YBaCuO detectors," *IEEE Trans. on Magn*,, vol. 27, no.2, pp. 2836-2839, 1991.

[20] J. Battat, et al, "Gain stabilization of a submillimeter SIS heterodyne receiver**,"** *IEEE Trans. Microwave Theory and Techniques*, vol. 53, no.1, pp. 389-395, Jan. 2005.

[21] Cryogenic Control Systems Inc., Rancho Santa Fe, CA, USA.

[22] R. Schieder, G. Rau, B. Vowinkel, "Characterization and Measurement of System Stability," in *Proc. SPIE*, vol. 598, 1985, pp. 189-192.

[23] Klein, S. D. Philipp, I. Krämer, C. Kasemann, R. Güsten and K. M. Menten, "The APEX digital Fast Fourier Transform Spectrometer," *Astron. & Astrophys.*, vol. 454, pp. L29-L32, 2006.

[24] T. Berg, S. Cherednichenko, V. Drakinskiy, et al, "Stability of HEB Receivers at THz Frequencies," in *Proc. SPIE*, vol. 5498, Oct. 2004, pp. 605-615.

[25] O. Nystrom, at al., "Optics Design and Verification for the APEX Swedish Heterodyne Facility Instrument SHeFI", will be submitted to *IEEE Transactions On Antennas and Propagation,* 2008.

[26] C.Risacher, private communication.

Instrumentation for Millimetron - a large space antenna for THz astronomy

Wolfgang Wild [1,2], Andrey Baryshev [1,2], Thijs de Graauw [3], Nikolay Kardashev [4], Sergey Likhachev [4],Gregory Goltsman [4,5], Valery Koshelets [6]

[1] *SRON Netherlands Institute for Space Research, Groningen, the Netherlands*

[2] *Kapteyn Astronomical Institute, University of Groningen, the Netherlands*

[3] *Leiden Observatory, Leiden, the Netherlands*

[4] *Astro Space Center of P.N. Lebedev Physical Institute, Moscow, Russia*

[5] *Moscow State Pedagogical University, Moscow, Russia*

[6] *Institute of Radio Engineering and Electronics, Moscow, Russia*

* Contact: W.Wild@sron.nl, phone +31-50-363 4074

***Abstract*— Millimetron is a Russian-led 12m diameter submillimeter and far-infrared space observatory which is included in the Space Plan of the Russian Federation and funded for launch after 2015. With its large collecting area and state-of-the-art receivers, it will enable unique science and allow at least one order of magnitude improvement with respect to the Herschel Space Observatory. Millimetron is currently in a conceptual design phase carried out by the Astro Space Center in Moscow and SRON Netherlands Institute for Space Research. It will use a passively cooled deployable antenna with a high-precision central 3.5m diameter mirror and high-precision antenna petals. The antenna is specified for observations up to ~2 THz over the whole 12m diameter, and to higher frequencies using the central 3.5m solid mirror. Millimetron will be operated in two basic observing modes: as a single-dish observatory, and as an element of a ground-space VLBI system. As single-dish, angular resolutions on the order of 3 to 12 arcsec will be achieved and spectral resolutions of up to 10^6 employing heterodyne techniques. As VLBI antenna, the chosen elliptical orbit will provide extremely large VLBI baselines resulting in micro-arcsec angular resolution. The scientific payload will consist of heterodyne and direct detection instruments covering the most important sub-/millimeter spectral regions (including some ALMA bands) and will build on the Herschel and ALMA heritage.**

I. Introduction

Millimetron is a large (12m diameter) space observatory for millimeter, submillimeter and far-infrared observations. This Russian-led mission will enable astronomers to observe the universe with unprecedented sensitivity and angular resolution. The far-infrared and submillimeter spectral bands are crucial regimes for the study of the formation and evolution of stars, planets, and galaxies. In addition, extremely high-angular resolution imaging by VLBI allows exploration of ultra-compact radio sources including black holes.

Millimetron has two scientific observing modes each of which is unique and represents a major step forward in the investigation of the universe we are living in. Firstly, Millimetron will be used as a 12m diameter single-dish space observatory for high-sensitivity and high angular resolution observations of the submillimeter universe. Secondly, Millimetron will be used as a VLBI (Very Long Baseline Interferometry) antenna in millimeter and submillimeter wavelength bands providing extreme angular resolution of better than one micro-arcsecond. Observations in both observing modes will substantially contribute to solving questions as outlined in the Cosmic Vision themes.

Millimetron (Spectrum-M) is part of the Space Plan of the Russian Federation with a planned launch after 2015. The Russian Space Agency has approved the mission and has allocated funds for the development and implementation of Millimetron (Spectrum-M). At present, the Astro Space Center (ASC) in Moscow is carrying out studies for Millimetron which are funded by the Russian Space Agency. Concerning Millimetron, ASC has established contacts with ESA, ESO, and with SRON Netherlands Institute for Space Research with the aim to explore possibilities for European participation in the mission.

This paper gives a brief overview of the mission and its instrumentation. A more detailed description can be found in [1].

II. Mission Overview

The main Millimetron characteristics are given in Table 1. They are driven by the objective to provide high sensitivity, high to extremely high angular resolution and high spectral resolution as well as far-infrared imaging and spectroscopic capabilities. High sensitivity and (extremely) high angular resolutions are achieved by using a 12m diameter space antenna, either in single-dish mode or as element of a space-ground VLBI system. High spectral resolution is obtained by using heterodyne receivers, and the far-infrared

imaging/spectroscopy will be done by an imaging photometer/spectrometer. In order to achieve good u-v coverage in VLBI mode, an elliptical orbit is chosen. Figure 1 shows the satellite concept consisting of a 12m deployable antenna, several heat shields, and the satellite platform.

TABLE V
MAIN CHARACTERISTICS OF MILLIMETRON

Item	**Parameter**	**Value**
Primary mirror	Diameter	12m, deployable
	Physical temperature	≤ 50 K passively cooled
	Surface accuracy	≤ 10 μm rms
	Focal length	2800 mm
Secondary mirror	Diameter	600 mm
Total focal length		81550.7 mm
Orbit		Elliptical
	Apogee	300,000 to 370,000 km
	Perigee	30,000 to 70,000 km
	Period	~ 9.5 days
Space platform		Navigator
Launcher		Proton
Science instruments	VLBI receivers	18 and 26 GHz, ALMA bands
	Spectroscopy	~500 to 2000 GHz, 4700 GHz
	Imaging	Far-infrared
	Photometer	Far-infrared
Angular resolution	Single dish	3 … 12 arcsec
	VLBI	≤ 1 micro arcsec

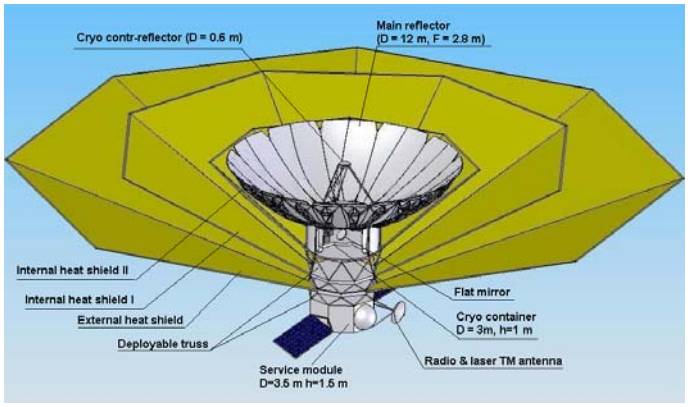

Fig. 1 Millimetron satellite concept with a 12m deployable antenna and several heat shields.

Millimetron will have two distinct scientific operational modes: (1) as a single-dish 12m diameter submillimeter space observatory, and (2) as space antenna of a sub-/millimeter space-ground VLBI interferometer. This will provide unreached angular resolutions in the millimeter to far-infrared regime of a few arcseconds in single-dish mode and micro-arcsconds in VLBI mode.

A number of technologies required for Millimetron, including the 12m diameter space antenna, are based on the Russian *RadioAstron* mission which is currently undergoing flight hardware integration and will fly a 10m deployable antenna in 2009 for ground-space VLBI. Figure 2 shows the 10m deployable antenna of RadioAstron. Millimetron will use a similar deployment strategy (Fig. 3).

The higher frequency range of Millimetron as compared to

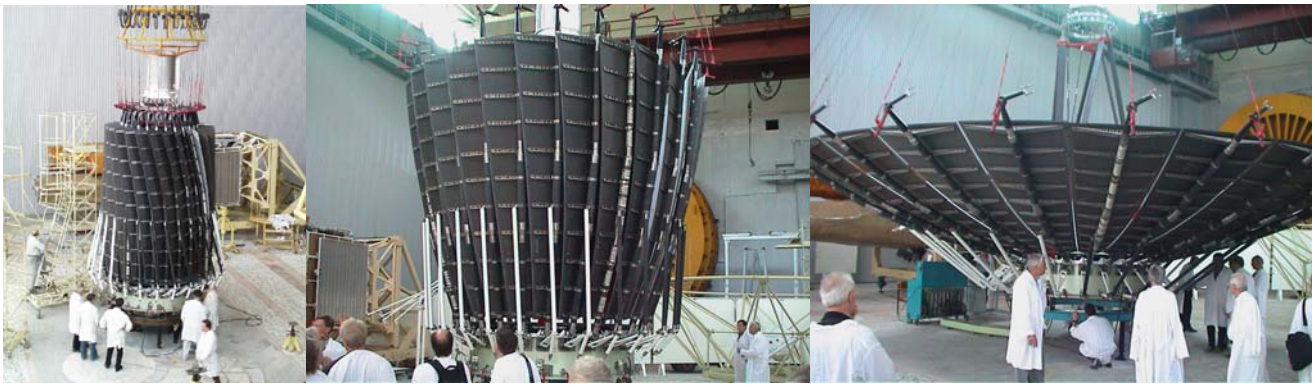

Fig. 2 Different stages of the "RadioAstron" 10m antenna deployment at Lavochkin Association (Moscow, Russia).

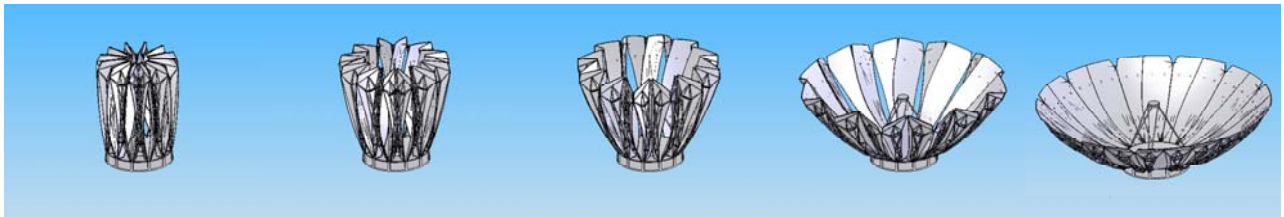

Fig 3 Stages of the Millimetron telescope deployment. Left: launch packaging, right: operational telescope.

RadioAstron means more demanding specifications in such areas as antenna surface precision, time reference system, phase stability etc. The instrumentation for Millimetron is based on the substantial investment into Herschel instruments and ALMA receivers and will build on developed (and largely space qualified) detector and instrument techniques.

III. Scientific Aims

The Far-Infrared (FIR) and submillimeter wavelength regime is one of the few areas were great progress can be expected in astrophysics as soon as high angular resolution and good sensitivity can be achieved. A passively cooled 12m dish optimized for the far-IR/submillimeter range, with an instrument suite building on Herschel heritage, provides this capability.

The spectral range with frequencies between 500 GHz and 5 THz (wavelengths between 600μm and 60μm) is of crucial importance for understanding how stars, planets and galaxies form and evolve. Furthermore, Very Long Baseline Interferometry (VLBI) in (sub-)millimeter waves allows micro-arcsecond access to compact sources such as black holes, neutron stars, and gamma-ray afterglows.

Millimetron will make unique contributions to the following areas of astrophysics (all of which are part of ESA's Cosmic Vision program) by combining high spatial and high spectral resolution as well as photometric and spectroscopic capabilities in the submillimeter/FIR regions. Millimetron will

- explore of the life cycle of gas and dust that leads to stars and planets (ESA Cosmic Vision theme 1),
- measure the deuterium content in the giant planets of solar system (ESA Cosmic Vision theme 2),
- investigate the physical parameters and processes near the event horizons of black holes and near the surfaces of neutron stars with sub-micro-arcsecond resolution (ESA Cosmic Vision theme 3), and
- trace the formation and evolution of black holes, trace the life cycles of matter in the Universe along its history, and resolve the far-infrared background (ESA Cosmic Vision theme 4).

IV. Scientific Instrumentation

Millimetron will carry science instruments which will make optimal use of the large collecting area and high angular resolution. Basically, there will be two types of science instruments: those for single dish observations, and those for space-ground VLBI (SVLBI). Both types will build on earlier developments for space missions like RadioAstron, VSOP, and Herschel, as well as ground-based projects like ALMA.

Here we describe a baseline instrumentation plan for the two basic scientific modes of operation (single-dish and SVLBI). The final instrument suite will depend to a large degree on the available spacecraft resources with 4K cooling power probably being the most limiting parameter. Further study needs to refine the instrument technical requirements and evaluate various trade-off options.

V. Single Dish Instrumentation

A. Overview

The baseline instrumentation for the single-dish observing mode consists of the two heterodyne instruments HET-1 and HET-2 and the far-infrared imaging photometer and spectrometer M-PACS. HET-1, a dual-frequency SIS array, will operate around the astrophysically important frequencies 557 and 1100 GHz, and HET-2, a three-channel HEB receiver, will cover 1.9, 2.7 and 4.7 THz (the latter using the central 3.5 m high-precision part of the antenna). M-PACS would be an adapted copy of Herschel-PACS with improved detectors covering the wavelength regime 60 to 210 μm. The instrument and detector technologies as well as operational modes and calibration schemes can build heavily on the developments done for Herschel.

Table 2 lists the key characteristics of the Millimetron baseline science instrumentation for single-dish observations.

TABLE II

MILLIMETRON SINGLE-DISH INSTRUMENTATION KEY CHARACTERISTICS.

Instrument	**Frequency or wavelength**	**Angular resolution (arcsec)**	**Spectral resolution**	**Detector technology**	**Sensitivity**
Heterodyne receivers					
HET-1	480 – 700 GHz	8…12	$\geq 10^6$	SIS 2x2 mixer array with multiplier LO	$T_{sys} < 100$ K
	1100 – 1400 GHz	5…6	$\geq 10^6$		$T_{sys} < 200$ K
HET-2	1650 – 2000 GHz	~3	$\geq 10^6$	HEB mixers with multiplier or QCL LO	$T_{sys} < 500$ K
	2600 – 2700 GHz	~2.5	$\geq 10^6$		$T_{sys} < 700$ K
	4700 – 4800 GHz	4 (1)	$\geq 10^6$		$T_{sys} < 1000$ K
Far-Infrared imaging photometer/spectrometer					
M-PACS	60 – 210 μm	≥ 4	few 10^3 spectrometer	Photoconductor arrays	2 x 10^{-18} Wm^{-2}

B. Heterodyne Receivers

HET-1 and HET-2 are heterodyne receivers providing very high spectral resolution ($\geq 10^6$) in combination with a Fast-Fourier-Transform spectrometer (FFTS). The channels up to 2000 GHz can directly build on the successful developments for Herschel-HIFI, whereas the higher frequency channels of HET-2 around 2.7 and 4.7 THz, unique to Millimetron, have been demonstrated in the lab. For HET-1 it is planned to use 2x2 SIS waveguide mixer arrays with multiplier chain local oscillators (LO). This type of technology has been developed for many ground-based telescopes and as single mixers for Herschel-HIFI. The 2x2 mixer arrays for Millimetron would be a new development for space which could heavily build on ground-based developments. It is interesting to note that multiplier LOs up to 2000 GHz are now becoming available commercially and at much lower cost than for HIFI. HET-1 will make use of demonstrated SIS technology using Nb-AlN-Nb tunnel junctions in combination with Nb-SiO2-Nb on-chip tuning elements as used at all major submillimeter observatories and in Herschel-HIFI.

HET-2 will in principle employ hot electron bolometer mixers (HEBM) as used in HIFI. However, due to sensitivity and IF bandwidth limitations of HEBM, it is attractive to develop SIS junction technology up to 2000 GHz by utilizing high energy gap superconducting materials. If successful, this SIS technology will allow to achieve better sensitivity and IF frequency coverage. The best technology for the 1650 – 2000 GHz channel of HET-2 can be selected depending on development result. The 2.7 and 4.7 THz channels will in any case use HEB mixers. Local oscillators for HET-2 will be multiplier chains and quantum-cascade-lasers (QCL). QCLs have been used in the lab as THz LO source. Some development is required for the QCL to stabilize its frequency and reduce the dissipated power at the 30…70 K level.

Several developments of HEB mixers and mixer arrays are underway for frequencies beyond 2 THz. A heterodyne receiver at 2.8 THz using a quasi-optical HEB mixer and QCL local oscillator has been demonstrated with a noise temperature of 1400 K (DSB) by Gao et al. [2].

C. Heterodyne Backend

The heterodyne receivers will share a Fast Fourier Transform Spectrometer (FFTS) backend which is a digital spectrometer providing wide instantaneous bandwidth with high spectral resolution. In the case of a 2x2 pixel receiver (dual polarization) with an IF bandwidth of 4 GHz each, a total spectrometer bandwidth of 32 GHz is required. Current FFT technology, field-proven in several years of continuous operation at, e.g., the APEX submillimeter telescope, provides an instantaneous bandwidth of at least 1 GHz with 8-16 k channels. Under development at MPIfR (Germany) are single-board FFTs with 1.5 GHz bandwidth /16 k and, using the most recent ADC available, 2.5 GHz/8 k channels. With the latter implementation of a hybrid backend with 3 x 2.5 GHz to combine to a total of ~7 GHz (allowing for some overlap) bandwidth is within reach. The enormous increase of ADC bandwidth during the last years makes it very likely that FFTS can be pushed to instantaneous bandwidths wider than 3 GHz in the near future, thereby further reducing the complexity of the backend. The spectral resolution (the number of channels) that can be achieved is basically constrained by the on-board resources (power dissipation) and the level of complexity that appears acceptable for a space mission. FPGAs have quite a long space heritage. In any case, digital FFT spectrometers can provide the back-end capacities required by the Millimetron mission concept. Some development work will be needed to increase bandwidth, to optimize operation to minimum power dissipation, to adapt to particular constraints of a space observatory, and to comply with space qualification requirements.

D. Imaging Photometer and Spectrometer

The Far-infrared photometer and spectrometer M-PACS can be based on the successful development of the PACS instrument, as built for Herschel which offers photometric and spectroscopic capabilities in the wavelength band from 60μm − 210μm:

A) Imaging dual-band photometry (60 − 85μm or 85 − 130μm and 130 − 210μm) over a field of view of 1.75′ × 3.5′, with full sampling of the telescope point spread function.

B) Integral-field line spectroscopy between 57 and 210 μm with a resolution of 175 km/s and an instantaneous coverage of 1500 km/s, over a field of view of 47″ × 47″.

Both modes will allow spatially chopped observations by means of an instrument-internal chopper mirror with variable throw.

The focal plane unit provides these capabilities through five functional units:

1. Common input optics with the chopper, calibration sources and a focal plane splitter.
2. The photometer optical train with a di-chroic beam splitter and separate re-imaging optics for the two short wavelength bands (60 − 85μm / 85 − 130μm) and the long-wavelength band (130 − 210μm), respectively; band-defining filters on a wheel select one of the two short-wavelength bands at a time.
3. The spectrometer optical train with an image slicer unit for integral field spectroscopy, an anamorphic collimator, a diffraction grating in Littrow mount with associated actuator and position readout, anamorphic re-imaging optics, and a di-chroic beam splitter for separation of diffraction orders.
4. Two filled silicon bolometer arrays with 16 × 32 and 32 × 64 pixels, with cryogenic buffers/multiplexers and a common 0.3 K sorption cooler, for simultaneously imaging in two bands, 60−85μm or 85−130μm and 130−210μm over a field of view of 1.75′ × 3.5′ .
5. Two Ge:Ga photoconductor arrays (stressed and unstressed) with 16 × 25 pixels each, that allow to perform imaging line spectroscopy over a field of

50"×50", resolved into 5×5 pixels, with an instantaneous spectral coverage of 1500 km/s and a spectral resolution of 175 km/s, with sensitivities (5σ in 1h) of 4 mJy or $3 - 20 \times 10^{-18}$ W/m^2.

VI. Space Segment VLBI Instrumentation

A. Overview

Figure 4 describes in general terms what is needed for performing Space VLBI (SVLBI). The signal from the telescope is received by one of the SVLBI front ends and down converted to an intermediate frequency (IF) which is filtered and conditioned in the IF processor unit and then digitized. Currently quantization of two bits over a 4-8 GHz band with dual polarization is considered which would result in a data rate of 16 Gbit/s. The digital signals are recorded in a data storage unit which should have sufficient capacity to hold approx 40 min of SVLBI data (10 TB capacity). A high-speed down-link transfers the data to the ground.

B. SVLBI Front-ends

The front end instrumentation for the VLBI observing mode will consist of a low frequency (18-26 GHz) front-end very similar to the one which will be flown on the Russian RadioAstron mission in 2008/09. This receiver on Millimetron will greatly improve the u-v plane coverage achieved by RadioAstron and is required to ensure proper cross calibration. Unique to Millimetron will be the VLBI receivers at the ALMA frequency bands 1 (31.3-45 GHz), 3 (84-116 GHz), 6 (211-275 GHz) and 9 (600-720 GHz). Table 5 summarizes the key characteristics of the Millimetron VLBI instrumentation.

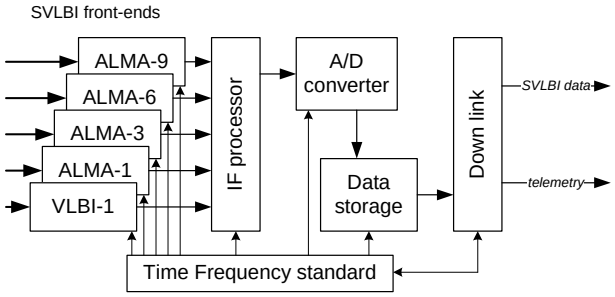

Fig. 4 Block diagram of the SVLBI instrumentation package

The VLBI-1 receiver will be based on previous developments as carried out for many radio telescopes and the RadioAstron or VSOP missions. The ALMA bands will follow technology developed within the ALMA project both for sideband separating SIS mixers, IF amplifiers and LOs. Adaptation of the ALMA technology for space use should not pose much difficulty as it is conceptually similar to the one used for Herschel (in fact ALMA uses some components that were developed for HIFI). Special attention will be paid to the polarization response of these instruments as observing polarization is one of the scientific goals. All ALMA band mixers require cooling to 4K like the HET-1 and HET-2 instruments.

C. Additional Equipment for Space-Ground VLBI

Space-ground VLBI requires special equipment onboard the Millimetron satellite.

1) On board time and frequency standard

There are two possibilities for onboard time synchronization. The first one is a hydrogen frequency standard developed in Russia which will be flown on the RadioAstron mission. The second one is an optical frequency standard with a stability of 3×10^{-16} in 5 minutes. This optical standard is under construction at the Lebedev Physical Institute.

2) A/D converter and data storage

The A/D converter technology will be the same as used for the FFTS backends. Adequate IF bandwidth can be covered by current technology already (ALMA). More weight/energy efficient solutions are expected to appear in the near future. On board data storage modules of up to several TBit are available commercially and space qualified from e.g. EADS-Astrium. It is anticipated that the maximum available capacity will only grow over the years. 10 TBytes would be sufficient for the mission but expanding on the capacity up to 30…40 TB will benefit the mission.

3) Down link

The high speed down link is a crucial part of the SVLBI system. Its speed will define the ground tracking station load for data transfer. The currently demonstrated radiolink data rate is two channels of 512 Mbit/s. It will take 22 hours to transmit 10 TBytes to Earth. A development towards improving data rates by using optical and other means would be of a great benefit for the Millimetron mission.

Telemetry and time synchronization data links can be common for the single dish and the SVLBI mode as they do not have high requirements concerning the data rate. Current state-of-the-art satellite communication equipment cold be used (similar to Herschel).

VII. Instrument Cooling

Both the heterodyne instruments HET-1/HET-2 and M-PACS need cooling to ~4 K from the spacecraft instrument cooling system (analogue to Herschel) with M-PACS having its own internal cooler to 0.3 K. The ALMA type receivers for SVLBI using SIS mixers need to be cooled to 4 K as well. The planned minimum mission life time of 5 years calls for a closed-cycle cryo-cooler to 4 K, also providing cooling to 20 K and 70…100 K levels. The temperatures below 1 K required for the M-PACS detectors will be generated within the M-PACS instrument (similar to the Herschel PACS scheme). A preliminary estimate of the required cooling powers for the scientific instrumentation gives: 40-50 mW at 4 K, 200 mW at 20 K, and 2 W at 70…100 K, with a

temperature stability of 5 mK at 4 K, 10 mK at 20 K, and 0.2 K at 70…10 K. These values are first estimates based on the specifications and experience with Herschel and ALMA instruments and will have to be refined during a more detailed study phase. It is anticipated that the cooling requirements and associated mass and power needs for the cryocoolers place restrictions on the amount of instruments that can be carried on Millimetron.

VIII. REQUIRED DEVELOPMENTS

In some areas Millimetron can make direct use of existing technology as developed, e.g., for Herschel and ALMA. However, there are also areas which require further developments for Millimetron and other missions. These include:

- **SIS arrays around 650 GHz and up to 1400 GHz.** These arrays need to be space qualified, provide very low noise, and an IF bandwidth of 8 GHz. Using SIS up to 1400 GHz or even higher would be very beneficial but requires the use of new junction technology.
- **Multiplier Los for SIS arrays.** The SIS arrays need a local oscillator capable of pumping the SIS mixers. Current LO chains on Herschel-HIFI would not provide enough LO power.
- **HEB receivers at 2.6 and 4.7 THz.** Sensitive HEB mixers with a broad IF band (~ 8 GHz) are needed. Current state-of-the-art HEB mixers require further development to achieve quantum limited performance and a larger IF bandwidth.
- **THz local oscillator.** The HEB receivers at 2.6 THz and 4.7 THz require a suitable local oscillator, either multiplier based or QCLs. For the multiplier chains, output power will be a very challenging issue, and for the QCLs, frequency coverage (tuning) and phase-locking need further work and development.
- **Wideband backends.** The option of wideband FFTS for all receivers needs to be investigated, and space qualification needs to be achieved.
- **Space cryocoolers.** Ongoing developments by ESA, NASA, and JAXA may fulfil the Millimetron requirements. In any case, the available cooling capacity for the instrument suite will probably define the amount of possible instruments on Millimetron (along with mass and power needs). Reliability of the cryocoolers is a concern during the >5 yr mission lifetime.

CONCLUSION

The Russian Millimetron mission provides an exciting opportunity for far-infrared and submillimeter astronomy and advanced instrumentation. Unique mission characteristics include the large collecting area and angular resolution. The Millimetron mission is included in Russia's Federal Space Program. It is currently in a conceptual design phase.

ACKNOWLEDGMENT

The authors thank many people in the Millimetron consortium for contributing to this overview paper.

REFERENCES

[1] W. Wild, N.S. Kardashev, et al., 2008, "MILLIMETRON – A Large Russian-European Submillimeter Space Observatory", *Exp. Astron.,* 10.1007/s10686-008-9097-6, Special Issue on ESA's Cosmic Vision, in press and Online First.

[2] J.R. Gao, et al., 2005, *Appl. Phys. Lett.* Vol. 86, 244104.

The Next Generation of Fast Fourier Transform Spectrometer

Bernd Klein*, Ingo Krämer, Stefan Hochgürtel, Rolf Güsten, Andreas Bell, Klaus Meyer, and Vitaly Chetik

Max-Planck-Institut für Radioastronomie, Bonn, Germany

* Contact: bklein@mpifr-bonn.mpg.de, phone +49 228 525-286

***Abstract*— We present our second generation of broadband Fast Fourier Transform Spectrometer (FFTS), optimized for a wide range of radio astronomical applications. The new digitizer and analyzer boards make use of the latest versions of GHz analog-to-digital converters and the most complex field programmable gate array chips commercially available today. These state-of-the-art chips have made possible to build digital spectrometers with instantaneous bandwidths up to 1.8 GHz and 8192 spectral channels.**

I. Introduction

The rapid increase in the sampling rate of commercially available analog-to-digital converters (ADCs) and the permanently increasing processing power of field programmable gate array (FPGA) chips has led to the technical possibility to digitize the baseband mixed intermediate frequency (IF) of heterodyne radio-receivers, and to transform the digital signal stream into a power spectrum in real-time. At the Max-Planck-Institut für Radioastronomie (MPIfR), this technology has been advanced over the last ~5 years: Beginning with a bandwidth of just 2 × 50 MHz and 1024 (1k) channels in 2003 [1], we have now developed FFTSs with instantaneous bandwidths up to 1.8 GHz and many thousands spectral channels (Fig. 1). Based on the announcement of once more faster ADCs and FPGAs with increasing processing capabilities, we are confident that FFTS' bandwidths can be pushed to ~3 GHz in the near future.

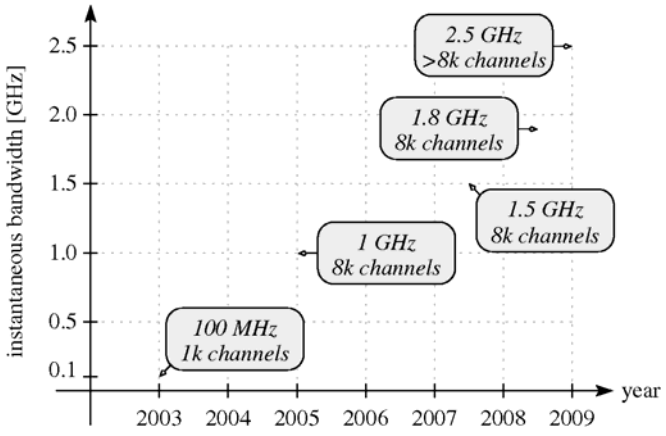

Fig. 3 FFTS developments at the Max-Planck-Institut für Radioastronomie.

II. The 1.5 GHz Bandwidth FFTS board

At the APEX telescope in Chile [2], we are successfully operating FFT spectrometers for more than 3 years ([3], [4]). They have proven extremely reliable and robust even under the harsh environmental conditions of a sub-mm facility at an altitude of 5100-m. Based on this experience we decided to launch the development of a second generation spectrometer based on ADC/FPGA technologies. For this, a compact FFTS-board has been designed at MPIfR which achieves wide instantaneous bandwidths (1.5 – 1.8 GHz) with several thousand spectral channels (up to 16k, depending on the bandwidth set-up). The board combines the latest version of GS/s ADC chips and the most complex FPGAs commercially available today. The wide analogue input bandwidth of the 8-bit ADC offers to sample the IF signals at baseband (DC to 1.5 GHz) or in the second Nyquist zone (1.5 – 3.0 GHz). A block diagram of the new FFTS-board is presented in Fig 2.

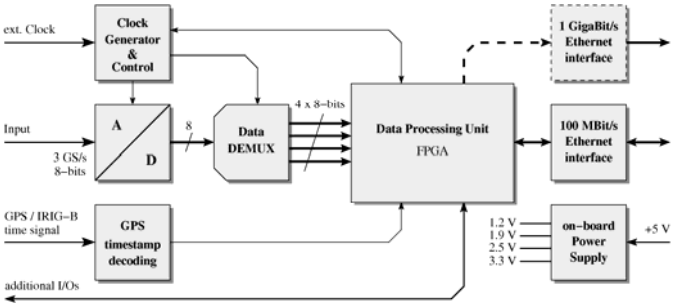

Fig. 4 Block diagram of the new MPIfR 1.5 GHz digitizer/analyzer board. The board can be equipped with a single- or dual-input ADC (ADC083000 or ADC08D1500). The optional GigaBit Ethernet interface allows high speed data acquisition with transfer rates up to 85 MBytes/s, which are required for pulsar or transient searches.

The compact FFTS-board (100 × 160 mm) operates from a single 5 Volt source and dissipates less than 20 Watt, depending on the actual configuration in terms of bandwidth and number of spectral channels. Precise time stamping of the processed spectra is realized by an on-board GPS/IRIG-B time decoder. Furthermore, the 10-layer boards include a programmable ADC clock synthesizer for a wide range of configurations (bandwidth: 0.1 – 1.8 GHz), making the spectrometer flexible for different observation requirements.

III. A-FFTS – An Array FFTS for APEX

To serve the requirements of today's and future receiver arrays (e.g., CHAMP$^+$, LAsMA, [5]), the new FFTS-boards include a standard 100 MBits/s Ethernet interface, which simplifies the combination of many boards into an Array-FFTS (A-FFTS), just by integrating of a common Ethernet switch. For use at APEX, we have build a 32 × 1.5 GHz A-FFTS in four 19" FFTS-crates (Fig. 3). Up to eight FFTS-boards can be housed in one FFTS-crate together with power supplies (4 × 5 Volt / 20 Amperes) and one FFTS-controller.

Fig. 5 Photograph of our 19 inch FFTS-crate, equipped with eight FFTS-boards and one FFTS-controller unit. The modular concept allows combining multiple crates to build large FFTS arrays.

The FFTS-controller is responsible for the distribution of global synchronize signals, e.g., the reference clock for the on-board ADC synthesizer or the GPS/IRIG-B timing information. In addition, the FFTS-controller displays housekeeping information on the four lines LCD, like board IP numbers, temperatures of the ADC and FPGA chips as well as the power level of the IF inputs.

The APEX A-FFTS has been successfully commissioned in spring 2008 [5]. In the current configuration, it provides a total bandwidth of 32 × 1.5 GHz = 48 GHz and 256k (32 × 8k) spectral channels. If requested, the A-FFTS can be extended to 58 GHz (32 × 1.8 GHz) total bandwidth by uploading a new FPGA processing core and a new ADC synthesizer setting. A first light spectrum of the novel FFTS-board towards Orion-KL is displayed in Fig. 4.

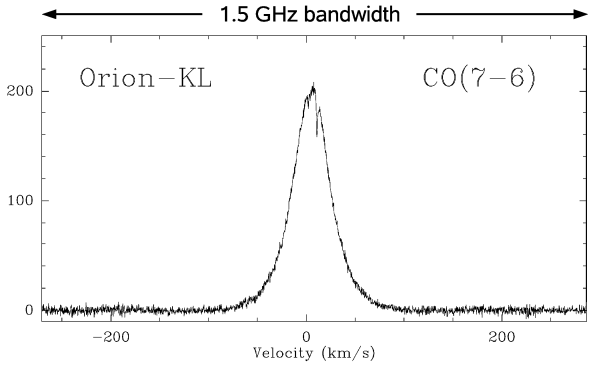

Fig. 6 First light spectrum of the new MPIfR-based 1.5 GHz bandwidth FFTS board towards the hot core Orion-KL. The high-excitation CO(7–6) transition at 806 GHz was observed with the central pixel of the CHAMP$^+$ array at APEX (24. October 2007).

IV. Advanced FPGA signal processing

As already described in [3], the complete signal processing pipeline (conversion from time domain to an integrated power spectrum) fits in one complex FPGA (Xilinx Virtex-4 SX55) on the board. The spectrometer core for the FFTS-board is an in-house development by MPIfR and – based on a generic VHDL approach – without the use of commercial libraries. Unlike the usually applied window in front of the FFT to control the frequency response, a more efficient polyphase pre-processing algorithm has been developed with significantly reduced frequency scallop loss, faster side lobe fall-off, and less noise bandwidth expansion. Fig. 5 illustrates the FPGA signal processing: After the polyphase filter, which we have implemented as a pipelined version of the Weighted Overlap-Add (WOLA) method, the FFT is realized using a highly parallel architecture in order to achieve the very high data rate of 3 GBytes/s or more. The next step of the processing contains the conversion of the frequency spectrum to a power density representation and successive accumulation of these results. This accumulation step has the effect of averaging a number of power spectra, thereby reducing the background noise and improving the detection of weak signals. In addition, this step also reduces the huge amount of data produced by the prior stages and eases any subsequent interfacing for the data analysis. The final step is the conversion from 64-bit integer representation to 32-bit floating-point format.

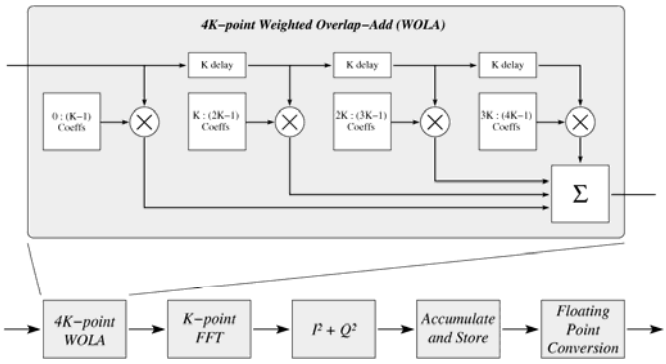

Fig. 7 Block diagram of the polyphase signal processing pipeline.

We have optimized our polyphase filter coefficients for spectroscopic observations. The goal was to find a good trade-off between the frequency resolution and an optimal use of the limited FPGA resources. The equivalent noise bandwidth (ENBW) is generally used to characterize the frequency resolution. The ENBW is the width of a fictitious rectangular filter such that the power in that rectangular band is equal to the (integrated) response of the actual filter. Our ENBW is adjusted to 1.16 × the channel spacing, which is the total bandwidth divided by the number of spectral channels. The frequency response of three adjacent frequency bins and the corresponding ENBW for the central bin is illustrated in Fig. 6. Following the above definition, the spectral resolution of our standard FFTS-board with 1.5 GHz bandwidth and 8k channels is 212 kHz.

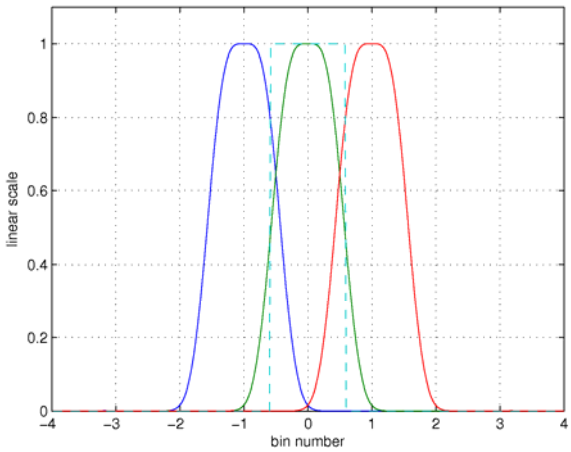

Fig. 8 Frequency response of the optimized FFT signal processing pipeline. The diagram shows three adjacent frequency bins. The dashed lines illustrate the equivalent noise bandwidth for the corresponding spectral bin.

Based on our generic approach, we have generated a set of different FPGA cores for the new FFTS-board:

1 × 1.5 GHz bandwidth, 1 × 8192 spectral channels, ENBW: 212 kHz (default core)
1 × 1.8 GHz bandwidth, 1 × 8192 spectral channels, ENBW: 225 kHz
1 × 750 MHz bandwidth, 1 × 16382 spectral channels, ENBW: 53 kHz
1 × 500 MHz bandwidth, 1 × 16382 spectral channels, ENBW: 35 kHz
1 × 100 MHz bandwidth, 1 × 16384 spectral channels, ENBW: 7 kHz (in lab test)
2 × 500 MHz bandwidth, 2 × 8192 spectral channels, ENBW: 71 kHz (in lab test)
2 × 250 MHz bandwidth, 8-tap polyphase filter bank, 512 channels, high speed data dumping, application: pulsar search

V. The 2.5 GHz Bandwidth FFTS development

With the availability of first samples of E2V's 5 GS/s 8-bit ADC, we start the development of a new advanced FFTS-board. The goal of this project is to develop a digitizer board, which is able to analyse 2.5 GHz of instantaneous bandwidth in 32k spectral channels (ENBW: < 100 kHz). E2V's 5 GS/s ADC incorporates 4 ADCs at 1.25 GHz which can be flexibly interleaved to a 2 × 2.5 GS/s or a 1 × 5 GS/s virtual ADC. The large analogue input bandwidth of the track-and-hold amplifier of this ADC offers the ability to use the full Nyquist bandwidth of 2.5 GHz. The ADC provides 8 separate low-voltage differential data busses to transfer the huge amount of data (5 GBytes per seconds) to one or more FPGA. In Fig. 7 we show a photo of our test board, including the 5 GS/s ADC and a Virtex-4 SX55 FPGA. To reach the final number of 32k spectral channels, the Virtex-4 will be replaced by two or more powerful Virtex-5 devices.

This wideband high-resolution FFT spectrometer development aims at operational readiness for SOFIA's early science flights with GREAT [6] in summer 2009.

Fig. 9 Currently in development: The 2.5 GHz bandwidth FFTS. The board makes use of a first sample of E2V's 5 GS/s 8-bit ADC.

Conclusion and outlook

The potential advantages of our next generation of FFT spectrometers are summarized:

- They provide high instantaneous bandwidth (up to 1.8 GHz; 2.5 GHz currently in development) with many thousands frequency channels, thus offering wide-band observations with high spectral resolution without additional IF processing.
- The new polyphase FFT signal processing pipeline provides a nearly loss-free time to frequency transformation with significantly reduced frequency scallop, less noise bandwidth expansion, and faster sidelobe fall-off.
- FFTS provide very high stability by exclusive digital signal processing. Allan-Variance stability times of several 1000 seconds have been demonstrated routinely.
- Low space and power requirements – thus safe to use at high altitude (e.g., APEX at 5100-m) as well as (potentially) on spacecrafts (e.g., SOFIA) and satellites.
- Production costs are low compared to traditional spectrometers through the use of only commercial components and industrial manufacturing.
- The superior performance, high sensitivity and reliability of our FFTS have been demonstrated at many telescopes world-wide, including APEX (Chile), CSO (Hawaii), the IRAM 30-m telescope (Spain) and the 100 meter Effelsberg observatory (Germany).

The announcement of new ADCs with higher samples rates and wider analogue input bandwidths together with the still increasing processing power of future FPGA chips (Moore's Law), makes it very likely that FFTS can be further pushed to broader bandwidths in the next years.

Due to the high interest from the astronomical community, from universities and from the industry, we have decided to outsource the production and distribution of our FFT spectro-

meter: the standard FFTS (1.5 GHz bandwidth with 8192 spectral channel) is manufactured now in licence by Radiometer Physics GmbH, Germany. For further information, visit:

http://www.radiometer-physics.de

2008-09-25, BK

REFERENCES

[1] Stanko, S., Klein, B., Kerp, J. "A Field Programmable Gate Array Spectrometer for Radio Astronomy",A & A, 436, 391-395, 2005

[2] Güsten, R., et al., "APEX: the Atacama Pathfinder Experiment", Proc. of the SPIE, Vol. 6267pp. 626714

[3] Klein, B., Philipp, S.D., Güsten, R., Krämer, I., Samtleben, D. "A new generation of spectrometers for radio astronomy: Fast Fourier Transform Spectrometer", Proc. of the SPIE, Vol. 6275, pp 627511, 2006.

[4] Klein, B., Philipp, S.D., Krämer, I., Kasemann, C., Güsten, R., Menten, K.M., "The APEX Digital Fast Fourier Transform Spectrometer", A & A, 454, L29, 2006.

[5] Güsten, R., et al., "Submillimeter Heterodyne Arrays for APEX", Proc. of the SPIE, Vol. 7020, 2008, to be published.

[6] Heyminck, S., et al., "GREAT: a first light instrument for SOFIA", Proc. of the SPIE, Vol. 7014, 2008, to be published.

Pushing the Limits of Multiplier-Based Local Oscillator Chains

Imran Mehdi[1,*], John Ward[1], Alain Maestrini[2], Goutam Chattopadhyay[1], Erich Schlecht[1] and John Gill[1]

[1]*Jet Propulsion Laboratory, California Institute of Technology, Pasadena, CA 91109 USA*

[2]*University of Paris VI, Paris France*

* Contact: Imran.mehdi@jpl.nasa.gov, phone +1-818-354-2001

***Abstract*—Generation of coherent terahertz radiation remains a critical technological challenge for applications such as spectroscopy, imaging, communications and radar. A review of the current state-of-the-art for terahertz sources is presented with emphasis on Schottky diode-based frequency multiplier technology. A simple power-combining approach has been demonstrated successfully around 300 GHz. This approach provides a framework for pushing both the output power and the upper frequency range of GaAs Schottky diode based terahertz sources.**

I. INTRODUCTION

Several recent articles have described the potential and capability of terahertz technology and how harnessing this technology can lead to exciting scientific discoveries in various fields [1]-[4]. One of the most challenging aspects of terahertz technology is the lack of compact, reliable, efficient, broadband sources in the terahertz range. Sources are required for all possible applications, either as transmitters or as local oscillators (LO) for heterodyne detectors. This article will present a brief review of the source technologies that are currently available and discuss the recent approach utilizing a power-combining technique that can be used to generate higher output power from GaAs Schottky diode frequency multipliers.

II. TERAHERTZ SOURCES

A number of technologies exist that can provide terahertz radiation. The output power of a source is the dominant figure of merit, however, from a systems point of view there are important secondary criteria such as tunable bandwidth, DC-to-RF conversion efficiency, operating temperature, mass, volume, frequency stability, and spectral purity that can dictate the use of any particular technology.

Much of the recent developmental activity for terahertz sources was driven by the needs of the Heterodyne Instrument for Far Infrared (HIFI) on the Herschel Space Observatory. Multiplied chains that successfully pumped HEB mixers in the 1.6 to 1.9 THz range were developed and delivered. This technology was enabled by the development of high power GaAs power amplifier MMICs in the 100 GHz range. These MMICs allowed one to achieve broadband, electronically tunable sources with >200 mW of power. The approach for HIFI was to use 100-150 mW at around 100 GHz and multiply this with a single string of frequency multipliers. This approach has its limitations and would have to be extremely well optimised to pump multi-pixel receivers or provide useful power beyond 2 THz, especially at room temperature.

In addition to Schottky diode frequency multipliers, there are a number of other technologies that have certain advantages. In terms of raw output power, FIR lasers pumped by gas lasers are dominant [5]. These lasers can provide tens of milliwatts in the terahertz range. However, they are not tunable, generate power only at certain discrete frequencies, are bulky, and are extremely inefficient. Similarly, carcinotrons and other varieties of backward wave oscillators (BWOs) can be useful tools in a laboratory but require huge power supplies and are bulky for space instruments. The quantum cascade lasers (QCLs) have been making immense progress in the last few years and can provide substantial output power in the higher THz frequency range. QCL technology is rapidly advancing; however, there are a number of issues that must be resolved before they can be successfully implemented in flight missions. Current QCL technology is limited to cryogenic operation, is narrow banded, and requires a signal locking scheme before it can be used for applications such as spectroscopy. A recent pertinent review of this technology has been presented in [6].

Considerable advances are also being made in terms of pushing frequency and power performance of three-terminal devices. InP based HEMT amplifiers are now commonly available that operate around 100 GHz and recently gain has been measured at 345 GHz [7][8]. By optimizing material selection and reducing gate widths, it might be possible to extend the frequency coverage to around 500 GHz. Resonant tunnelling diodes (RTDs) [9] and photomixers [10] have also shown that they can work into the terahertz range; however, the low output power from such sources continues to be a limiting factor.

A summary of available output power as a function of operating frequency from the technologies discussed above is shown in Figure 1. For future space applications, the

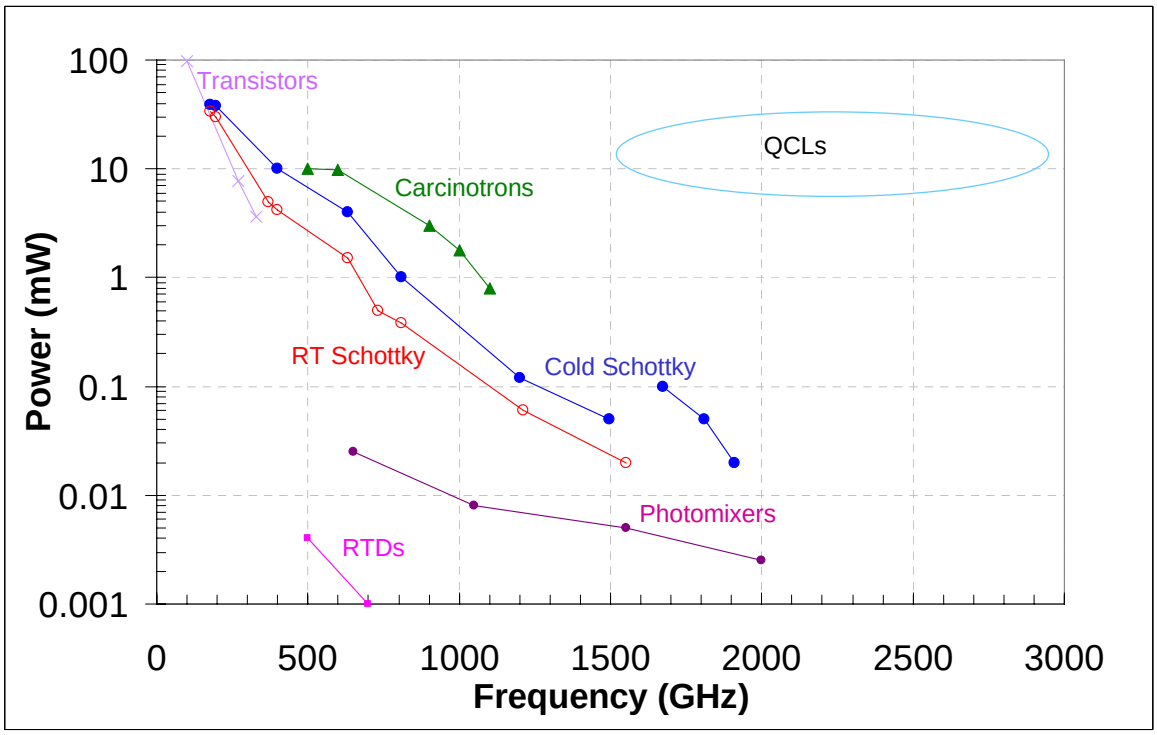

Figure 1: Compilation of available output power from various THz sources as a function of operating frequency. Results from Schottky diode frequency multipliers are shown both for room temperature operation as well as when cryogenically cooled.

required sources can be divided into two categories. For astrophysics, sources are needed that can cover post-HIFI exploration such as the molecular lines in the 2-4 THz range as well as sources that provide sufficient power to pump multi-pixel receivers in the 1-2 THz range [11]. For planetary exploration, sources are needed in the 300-1200 GHz range that are powerful enough to pump Schottky diode mixers [13][14]. Continued advances in frequency multiplier technology will be needed to achieve these goals.

This brief paper will discuss a simple approach of power combining with the help of Y-junctions that can provide a possible solution to increasing input power handling capability of the first and second stage frequency multipliers of a terahertz source. This in turn will greatly increase the output power from the chain by optimally pumping the terahertz frequency multipliers for maximum conversion efficiency.

III. Schottky Diode Frequency Multipliers

A. Limitations of Schottky diode frequency multipliers

In order to understand the potential and capabilities of submillimeter-wave Schottky diode frequency multiplier circuits it is instructive to investigate their limitations. The limitations can generally be divided into two distinct camps. The first set of limitations is related to the intrinsic physics of the Schottky device. These can be understood from the formulation of the Manley-Rowe relationships that in fact hold true for any ideal non-linear reactance or resistance [15]. This limitation bounds the maximum efficiency that can be obtained from an ideal Schottky device.

Unfortunately, in reality a purely varactor or varistor device does not exist. The diode has both a capacitive and a resistive nonlinearity. Consider a uniformly doped semiconductor structure with an ohmic contact on one end and a metal-semiconductor contact on the other end. The semiconductor will have a depletion layer with a width w, with the remaining portion of the structure undepleted. The depletion layer can be represented as a capacitor and the undepleted portion can be represented as a resistor. The depletion layer will act as a parallel plate capacitor where the capacitance can be modulated with an applied electric field by modulating the depletion width. This inverse square root dependent capacitance is the starting point for analytic varactor frequency multiplier analysis. Similarly, under forward bias, the device current will be an exponential function of the applied voltage giving rise to the non-linear resistance. Submillimeter-wave frequency multipliers often work in a mode that is not purely varactor or varistor in nature but a combination of both. There are also parasitic elements that must be considered in any analytical model, however, the simple diode model with nonlinear resistor and nonlinear capacitance can be used to look at the limitations of the device.

The undepleted region of the device and various contact and package resistances will appear in series with the nonlinear junction. Although the undepleted region width is voltage dependent, this series resistance is usually modeled

with a constant value. However, at very high frequencies the current through the undepleted region can crowd to the outside edge of the material due to the skin effect, increasing the resistance [16]. This frequency dependent resistance should be included in any simulation and must be considered to obtain realistic performance predictions.

The early simulation tools and simple device model did a reasonable job in predicting device performance; however, the output powers and efficiencies predicted were always higher than the experimental results. There are several possible reasons. Circuit loss increases with frequency, so the loss between the diode and the external connection should be higher. Measurements are less accurate at these frequencies, so the differences between the desired designed circuit embedding impedances and the actual values may be larger. Parasitic effects are also more important, degrading the performance. However, even when all these effects were taken into account, the experimental powers and efficiencies were still lower than expected especially as the operating frequency was increased. This led researchers to further investigate device physics in the presence of a time varying field.

A first order view of the problem can be described by rewriting the width of the depletion layer as a function of a time dependent applied voltage. The time derivative of this equation is the velocity of the edge of the depletion layer. When this velocity, which depends on a combination of the frequency, RF and DC voltages across the device, and the doping, is larger than the saturated velocity imposed by the semiconductor physics the voltage dependent description of the calculated capacitance is no longer correct [17]. The velocity of the edge of the depletion layer is just the velocity of the electrons in the undepleted portion of the structure. The time rate of change of the nonlinear capacitance is limited by the saturated velocity of the semiconductor material. Driving the device beyond this saturation point will increase the voltage drop and resistance of the undepleted region and reduce the conversion efficiency of the frequency multiplier.A detailed discussion of the current saturation effect is presented in [18].

A third limitation related to the intrinsic device is the onset of plasma resonances that can effectively increase the resistance of the device [19]. However, most likely this phenomenon becomes dominant at above a few terahertz and can be neglected for the current discussion.

Thus, a careful design of the device is required that provides maximum non-linearity but avoids current saturation effects based on the frequency of operation and available pump power. However, this is only half of the story. A second set of limitations must also be considered.

The second set of limitations can broadly be categorized as 'practical' limitations related to the way a particular frequency multiplier circuit will be physically implemented and used. An important criterion of any successful design is the input and output coupling property of the device. The Manley-Rowe and current saturation theories provide no guidance on this and in reality at these frequencies it is difficult to provide a purely reactive match to the device for maximum coupling efficiency.

Another important consideration is the bias conditions for the frequency multiplier circuit. Current saturation theory suggests increasing the doping of the semiconductor; however, this decreases the breakdown voltage of the device and can result in limiting output power from the device. While some general guidelines can be provided to determine safe operating conditions for a given frequency multiplier a quantitative analysis requires extensively testing the frequency multiplier in question.

Determining the safe operating zone for a given frequency multiplier boils down to biasing the frequency multiplier in a range where no significant reverse current is present. This safe operating zone can be determined by extensively testing the multiplier in question as a function of different bias conditions, power levels and across the frequency range of interest. One has to determine the bias and power conditions for each frequency point to determine the onset of reverse current. Based on this information the limit on the reverse bias voltage of the multiplier can be established. In the forward direction the envelope is determined by the maximum current that can be sustained by the diode without damage (approximately 0.5 mA/μm²) as discussed in [20]. Thus, between these two boundary conditions lies the safe operating zone of this particular frequency multiplier. As can be seen from this example, this safe zone will be unique for each design and is strongly coupled to the implementation of the frequency multiplier circuit.

Another important practical consideration that has become increasingly important due to the availability of high input power levels is the thermal design of the frequency multiplier circuit. GaAs thermal conductivity decreases with increasing temperatures resulting in thermal runaway and failures. A number of approaches can be employed to improve the thermal performance of frequency multiplier circuits.

IV. Membrane-Based Schottky Diodes

In the last several years considerable progress has been made in understanding and more importantly being able to realize terahertz frequency multiplier chips that can produce useful amount of power in the terahertz range. A number of different technologies have colluded to make this progress possible. Powerful 3-D electromagnetic simulations have enabled accurate modelling of the devices and circuits. Application of advanced semiconductor processing tools have resulted in low-parasitic GaAs planar Schottky diodes on ultra-thin membranes. The membrane devices have allowed implementation of increased functionality at the chip level while also making possible a simplified integration process. Precise metal machining has enabled high quality waveguide blocks with micron level precision. Finally, availability of high power GaAs power amplifiers in the w-band range allowed one to design frequency multiplier based LO chains with large multiplication factors and still obtain useful amounts of power.

Broadband terahertz sources for the Herschel Space Observatory were built based on the technologies outlined above. The tall pole for the mission was achieving 10% electronically tunable sources in the 1.6 to 1.9 THz range with sufficient power to pump a pair of Hot Electron Mixers (HEB) mixers. Results for the HIFI LO chains have been presented elsewhere in detail [21][22][23]. Simulations for first stage frequency multipliers as well as multipliers in the 1.6 to 1.9 THz range have shown good agreement with measured results. Based on these simulations we believe that Schottky diode frequency multipliers can be fabricated and implemented that work in the 2-3 THz range. However, to accomplish this one must construct a driver chain that ensures that the last stage multiplier will be sufficiently pumped. To accomplish this goal one must have first and second stage frequency multipliers that can handle large amounts of pump power without sacrificing device lifetime. A number of approaches have been demonstrated to this effect. Increasing the number of anodes per chip, mounting chips on higher thermal conductivity substrates have shown to work very well [24]. However, there is a practical limit to the number of anodes based on chip size dictated by the RF design. .A new approach, where the input signal is first split, then multiplied and finally recombined has recently been demonstrated. This allows one to optimize each chip and then essentially package two chips in a single waveguide block and get a 3 dB increase in input power handling capability without sacrificing conversion efficiency.

A. In-phase power combining of frequency multiplier chips

A single chip 260-340 GHz balanced tripler with six-anodes has been successfully implemented with a membrane based device [25]. This design works well and provides ~10% efficiency across much of the band. However, the efficiency starts to saturate once pumped with more than 100 mW of input power. Since input power in the 200-250 mW is now readily available it would be useful to re-design this circuit for increased input power. The small size of the channel dictated by the onset of unwanted parasitic modes does not allow further increase in the anodes per chip. Thus, a simple approach involving Y-junction power-combining was implemented.

The power-combined version is based on two mirror-image tripler chips that are power-combined in-phase in a single waveguide block using a compact Y-junction divider at the input waveguide and a Y-junction combiner at the output waveguide. Fig. 2 shows a schematic of the bottom half of the waveguide block. A close up of the area where the chips are mounted is shown in Fig. 3. The two chips are of identical design and are a mirror image of each other. The tripler uses a split-block waveguide design with two independent DC bias lines. The input waveguide is split in two by a Y-junction to evenly feed two chips each featuring six anodes. The chips are mounted in two independent channels that run between their respective input and the output waveguides. The two reduced-height output waveguides are combined by a Y-junction that is seen by each branch of the circuit as a simple waveguide step.

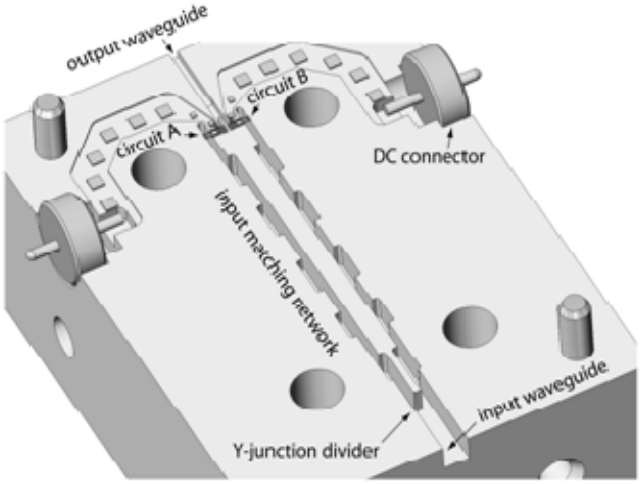

Figure 2: Bottom half of the waveguide block for the in-phase power-combined tripler at 300 GHz.

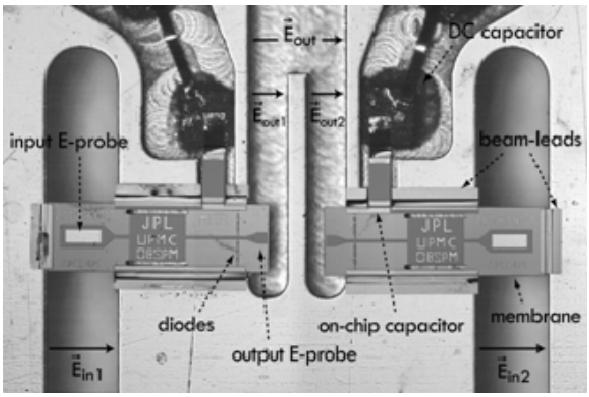

Figure 3: Close up view of a power-combined 300 GHz frequency tripler showing the two GaAs integrated circuit chips.

On each chip, an E-plane probe located in the input waveguide couples the signal at the input frequency to a suspended microstrip line. This line has several sections of low and high impedance used to match the diodes at the input and output frequencies and to prevent the third harmonic from leaking into the input waveguide. The third harmonic produced by the diodes is coupled to the output waveguide by a second E-plane probe. In order to balance the circuit, the

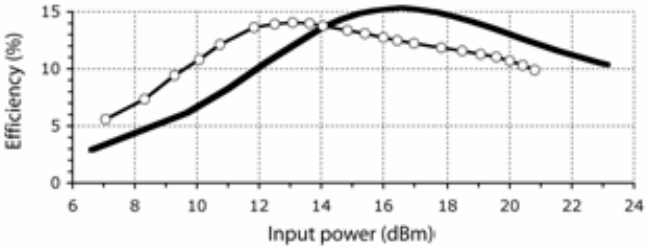

Figure 4: Power sweep of the single-chip tripler at 292.2 GHz (light curve with open markers) and of the power-combined tripler at 286.2 GHz (heavy curve with no markers). It can be seen that the power-combined tripler begins to compress at an input power which is 3 dB above that of the single-circuit tripler, as expected.

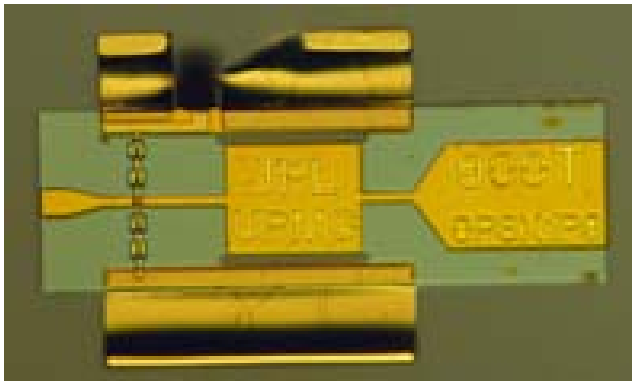

Figure 5: Picture of a 4-anode 900 GHz tripler chip fabricated on a thin GaAs membrane.

dimensions of both the channel and the circuit are chosen to cut off the TE-mode at the second (idler) frequency. The dimensions of the output waveguide ensure that the second harmonic is cut off at all frequencies measured, and the balanced geometry of the chips ensures that power at the fourth harmonic of the input is strongly suppressed.

The input power of the triplers was adjusted by varying the drain voltage of the power amplifiers and was monitored using a directional coupler. For all the measurements, the input power of the triplers was kept below 250 mW. The reverse voltage of each circuit was kept above -14 V (for 6 anodes in series) and the rectified direct current was kept below 3 mA. The two bias voltages were optimized independently at each frequency to maximize the output power. Performance gains by independently optimizing the two bias voltages were small; for most applications, the two bias lines could be tied to a single bias voltage for simplified operation. The typical power-combined frequency tripler has efficiency in the range from 5% to 13% across the frequency band for 50 mW to 250 mW of input pump power. Maximum power obtained to date is a record 26 mW at 318 GHz with 11% conversion efficiency.

Detailed measurements of the power combined tripler have been presented in [26]. Despite the high frequencies involved and large fractional bandwidth, the power combining is nearly ideal, with the power-combined version performing with almost identical bandwidth and conversion efficiency as the single-circuit version except with twice the power handling. The conversion efficiency of the power-combined tripler exceeds 10% for input powers ranging from 1.4 mW to 17 mW per anode or 17 mW to 206 mW of total power. The peak efficiency reaches a record 15.3% at 286.2 GHz and is obtained with an input power of 3.5 mW per anode or 41.5 mW of total power. This large dynamic range makes the power-combined tripler very versatile. Fig. 4 shows the conversion efficiency versus input power of the power-combined 300 GHz tripler and of a single-chip 300 GHz tripler. Each tripler was tuned to a frequency where the conversion efficiency was near the maximum and where at least 200 mW and 100 mW of drive power were available for the power-combined tripler and the single-chip tripler, respectively. As can be noted similar efficiency is obtained with the two-chip tripler but with a 3-dB increase in the input power. It should be pointed out that the current version of the power combining is done in waveguide but in future the same functionality could be accomplished by on-chip components. Moreover, it is also simple to conceptualize four or even more chips to further increase input power handling capability.

The power combined tripler can now be used to drive higher frequency multipliers. A 900 GHz tripler chip based on four-anodes is shown in Figure 5. To further improve the performance of the chain, the frequency multipliers were cooled to 77K. The output power from the two stage chain is shown in Fig. 6. None of the available amplifier modules were able to cover the full band of the frequency multiplier chain thus two different amplifier modules were used to generate the data in Fig. 6. The higher power drive stage allows us to obtain these power levels without risking device lifetime of the first stage tripler. To the best of our knowledge, this chain represents the highest output power from electronics-based sources at this frequency. This data, if included on Figure 1, would indicate that by power combining one can further increase the output power producing capability of Schottky diode based multiplier chains. An input power vs output power characterization of the 900 GHz tripler indicates that the chip is getting saturated around 20 mW of input power. Thus, it can be expected that better performance can be obtained if a two-chip circuit is also built for the 900 GHz tripler.

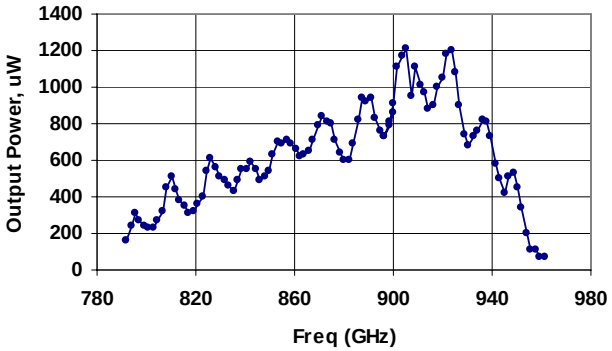

Figure 6: Measured performance of a two-stage x3x3 chain. The first stage tripler is the two-chip power-combined version discussed in this paper. The second stage tripler is a single chip design. All of the multipliers were at 77K ambient temperature.

V. Future Trends

This scheme of power combining the first stage to get a 3-dB increase in output power is very effective and can be adopted for higher frequencies. Currently, we plan to design and build a 900 GHz two-chip tripler which will then be able to sufficiently pump a 2700 GHz tripler. It is expected that we will be able to achieve around 1 microwatts of output power at this frequency. Introduction of GaN based power

amplifiers in the 100 GHz range will provide impetus for a re-think of how first stage frequency multipliers are designed and implemented. With the availability of one-watt power levels it would be important to optimize designs that can handle this much power.

CONCLUSIONS

Two submillimeter-wave tripler chips have been successfully power combined in a single waveguide block. The power combined tripler produces approximately twice as much power without sacrificing efficiency or bandwidth compared with a single chip implementation. This approach represents an important step towards building more powerful sources in the submillimeter-wave range which can then successfully drive sources beyond 1 THz.

ACKNOWLEDGMENT

We are greatly indebted to the JPL machine shop for the superb fabrication of the precision waveguide blocks. We also acknowledge help from Robert Lin and Hamid Javadi for assembly and testing of the sources. The research described in this paper was carried out at the Jet Propulsion Laboratory, California Institute of Technology, under a contract with National Astronomical and Space Administration.

REFERENCES

[1] P.H. Siegel, "Terahertz Technology in Biology and Medicine," IEEE Trans. Microwave Theory Tech., vol. 52, no. 10, pp. 2438–2447, Oct. 2004.

[2] T. W. Crowe, W. L. Bishop, D. W. Porterfield, J. L. Hesler, and R. M. Weikle, "Opening the THz window with integrated diode circuits," *IEEE Journal of Solid-State Circuits*, vol. 40, no.10, October 2005.

[3] D. Mittleman, "Terahertz imaging," in Sensing With Terahertz Radiation, D. Mittleman Ed. Berlin, Germany: Springer-Verlag, 2003, pp. 117–153.

[4] D. L. Woolard, E. Brown, M. Pepper, M.Kemp, "Terahertz Frequency Sensing and Imaging: A Time of Reckoning Future Applications?" , Proceedings of the IEEE, Volume 93, Issue 10, Oct. 2005, pp. 1722 – 1743.

[5] D. Hodges, F. Foote, R. Reel, "High-power operation and scaling behavior of CW optically pumped FIR waveguide lasers," IEEE Journal of Quantum Electronics, Volume 13, Issue 6, Jun 1977, Page(s):491 – 494.

[6] B.S. Williams, "Terahertz quantum-cascade lasers," Nature Photonics, volume 1, pp. 517-525, 2007.

[7] W. R. Deal, X. B. Mei, V. Radisic, M. D. Lange, W. Yoshida, P. –H. Liu, J. Uyeda, M. E. Barsky, A. Fung, T. Gaier, R. Lai, "Development of Sub-Millimeter-Wave Power Amplifiers," IEEE Transactions on Microwave Theory and Techniques, Volume 55, Issue 12, Part 2, Dec. 2007 Page(s):2719 – 2726.

[8] D. Pukala, L. Samoska, T. Gaier, A. Fung, X. B. Mei, W. Yoshida, J. Lee, J. Uyeda, P.H Liu, W. R. Deal, V. Radisic, and R. Lai, "Submillimeter-Wave InP MMIC Amplifiers From 300–345 GHz," IEEE Microwave and Wireless Components Letters,Volume 18, Issue 1, Jan. 2008 Page(s):61 – 63.

[9] Masahiro Asada, Safumi Suzuki, and Naomichi Kishimoto, "Resonant Tunneling Diodes for Sub-Terahertz and Terahertz Oscillators," Jpn. J. Appl. Phys. 47 (2008), pp. 4375-4384.

[10] Hiroshi Ito, Fumito Nakajima, Tomofumi furuta and Tadao Ishibashi, "Continuous THz-wave generation using antenna-integrated uni-travelling-carrier photodiodes," Semicond. Sci. Technol, Vol. 20, S191-8.

[11] B. Drouin, F. Maiwald & J. Pearson, "Application of Cascaded Frequency Multiplication to Microwave Spectroscopy," Rev. Sci. Instrum. 76, 093113, 2005.

[12] Chris Walker, "The Stratospheric TeraHertz Observatory (STO)," 19th International Symposium on Space THz Technology, Groningen, Netherlands, April 28-30, 2008.

[13] E. Lellouch et al, "Science case for a sub-millimeter sounder on the TSSM mission ",poster presentation at the OPFM Instrument Workshop, June 2008, Monrovia (http://opfm.jpl.nasa.gov/InstrumentWorkshop/).

[14] Mark Allen, et al, "Ultrahigh spectral resolution submillimeter spectrometry for plannetary observations" poster presentation at the OPFM Instrument Workshop, June 2008, Monrovia (http://opfm.jpl.nasa.gov/InstrumentWorkshop/).

[15] J. M. Manley and H. E. Rowe, "Some general properties of nonlinear elements—part I, general energy relations," Proceeding of IRE, vol. 44, pp.904-914: July, 1956.

[16] L. E. Dickens, "Spreading Resistance as a Function of Frequency," IEEE Trans. Microwave Theory Tech., vol. MTT-15, no. 2, pp. 101-109, Feb. 1967.

[17] E.L. Kollberg, T.J. Tolmunen, M.A. Frerking and J.R. East, "Current Saturation in Submillimeter Wave Varactors," IEEE Transactions on Microwave Theory and Techniques, Volume MTT-40, No. 5, 831-838, May,1992.

[18] Jack East and Imran Mehdi, "Schottky Diode Frequency Multipliers", in RF and Microwave Passive and Active Technologies, M. Golio Editor, CRC Press 2008.

[19] K.S. Champlin and G. Eisenstein, "Cutoff Frequency of Submillimeter Schottky-Barrier Diodes," IEEE Trans. Microwave Theory Tech., Vol. M'IT-26, No. 1, pp. 31-34, 1978.

[20] F. Maiwald, E. Schlecht, J. Ward, R. Lin, R. Leon, J. Pearson, and I. Mehdi, "Design and operational considerations for robust planar GaAs varactors: A reliability study," in Proc. 14th International Symposium on Space Terahertz Technology, Tucson, AZ, April 2003.

[21] John Ward, Erich Schlecht, Goutam Chattopadhyay, Hamid Javadi, John Gill, and Imran Mehdi, Local Oscillators from 1.4 to 1.9 THz, Proceedings, Sixteenth International Symposium on Space Terahertz Technology, Göteborg, Sweden, May 2005.

[22] Alain Maestrini, John S. Ward, Hamid Javadi, Charlotte Tripon-Canseliet, John Gill, Goutam Chattopadhyay, Erich Schlecht, and Imran Mehdi, Local Oscillator Chain for 1.55 to 1.75 THz with 100 μW Peak Power, Microwave and Wireless Components Letters, Volume 15, Issue 12, Pages 871 - 873, December 2005.

[23] G. Chattopadhyay, E. Schlecht, J. Ward, J. Gill, H. Javadi, F. Maiwald, and I. Mehdi, "An all solid-state broadband frequency multiplier chain at 1500 GHz," IEEE Trans. Microwave Theory Tech., Vol. 52, no. 5, pp. 1538-1547, May 2004.

[24] D. Porterfield, "High-Efficiency Terahertz Frequency Triplers", in *Proc. of IEEE MTT-S International,* pp. 337-340, Honolulu, Hawaii, 3-8 June, 2007.

[25] A. Maestrini, C. Tripon-Canseliet, J.S. Ward, J.J. Gill and I. Mehdi, "A High Efficiency Multiple-Anode 260-340 GHz Frequency Tripler," *Proc. of the 17th International Symp. on Space Terahertz Technology*, pp. 233-236, Paris, France, 10-12 May 2006.

[26] Alain Maestrini, John S. Ward, Charlotte Tripon-Canseliet, John J. Gill, Choonsup Lee, Hamid Javadi, Goutam Chattopadhyay, and Imran Mehdi, "In-Phase Power-Combined Frequency Triplers at 300 GHz," IEEE Microwave and Wireless Components Letters, March 2008.

Experiences with Quantum Cascade Lasers as Local Oscillator

Heinz-Wilhelm Hübers

German Aerospace Center (DLR), Institute of Planetary Research, 12489 Berlin, Germany
Contact: heinz-wilhelm.huebers@dlr.de, phone +49-30-67055596

***Abstract*— This article describes the current status of THz quantum cascade lasers (QCLs)with respect to their use as local oscillator (LO). The main results regarding their beam pattern, emission linewidth, frequency tunability, and frequency/phase locking are summarized. Also noise temperature measurements with a QCL as LO and a superconducting NbN hot electron bolometric mixer are summarized.**

I. Introduction

Quantum cascade lasers (QCLs) are promising devices for use as local oscillator (LO) in a terahertz (THz) heterodyne receiver. They are unipolar lasers based on intersubband transitions in the conduction band of heterostructures, made from GaAs/AlGaAs [1, 2]. Since the first demonstration of the laser effect at THz frequencies [3] different concepts for the active medium as well as for the waveguide have been realized [2]. The active medium might be roughly divided into three groups: chirped superlattice, bound-to-continuum, and resonant-phonon design. The chirped superlattice provides two relatively broad minibands: one for the upper laser state and one for the lower laser state [3]. The bound-to-continuum design is based on a chirped superlattice but the upper laser level consists of a single (bound) state [4]. The resonant-phonon active medium makes use of the LO phonon in GaAs, which couples the lower laser state resonantly with the upper laser state of the adjacent quantum well [5]. Essentially two types of waveguides are in use: the surface-plasmon waveguide and the metal-metal waveguide. The surface-plasmon waveguide consists of a thin, highly doped layer between the active medium and the substrate and a metal layer on top of the laser ridge. It has relatively low loss but suffers from an incomplete overlap of the laser mode with the active medium, because the laser mode extends significantly into the substrate. The confinement factor (a measure for the fraction of the laser mode which is confined in the active medium) for this type of waveguide is around 0.5. The metal-metal waveguide has a metal layer instead of the doped layer between the active medium and the substrate. Therefore it has a confinement factor of 1 but higher loss than a laser with the same active medium but a surface-plasmon waveguide.

Relevant features which have been demonstrated and which are especially important if a QCL is going to be used as LO are [3]: emission between 1.2 THz and 4.9 THz, a maximum operation temperature of 130 K, and an output power of up to ~138 mW. It is important that all values have been obtained in continuous wave mode (in pulsed operation these values are somewhat higher) and without applying a magnetic field, which can be used to lower the emission frequency, but is not very practical for a LO. In the following sections the status of the development of QCL-based THz LOs will be reviewed. It is not intended to describe every experimental detail. Instead emphasis is put on pointing out the key features obtained by different groups. For details the reader is referred to the original publications.

II. Beam pattern

Although QCLs have large output power compared to multiplied microwave sources, pumping of a mixer such as a hot electron bolometer (HEB) might not be a straightforward task since the beam of the QCL has to be matched to the beam pattern of the mixer antenna. While for single pixel receivers the coupling efficiency between QCL and mixer does not need to be very high, an array receiver will require a very well shaped LO beam, normally a Gaussian beam profile or in other words a beam propagation factor M^2 close to one. M^2 is the ratio of the angle of divergence of a laser beam to that of an ideal Gaussian beam with the same diameter at the position of the beam waist.

A. QCL with Surface-Plasmon Waveguide

The beam profile of such a laser consists of two lobes. One is emitted from the laser ridge and another one from the substrate (Fig. 1) [6, 7]. In addition a fringe pattern appears around the lobes. This structure is more pronounced for lasers with short wavelength while at wavelengths above about 100 µm the lobes start to merge due to diffraction effects. By integrating the signals of the two lobes and the fringe pattern separately the confinement factor for a 4.3 THz laser was determined to be 0.49 which is in good agreement with the computed value of 0.47 [6]. In the direction vertical to the layers of the superlattice the width of beam pattern (ridge lobe as well as substrate lobe) is determined by a single aperture. The fringe pattern corresponds to a diffracting aperture which has about the size of the substrate and ridge (assuming plane wave illumination and a refractive index n = 3.7). In direction orthogonal to this the full width at half maximum (FWHM) is a determined by λ/w with λ the emission wavelength and w the width of the ridge.

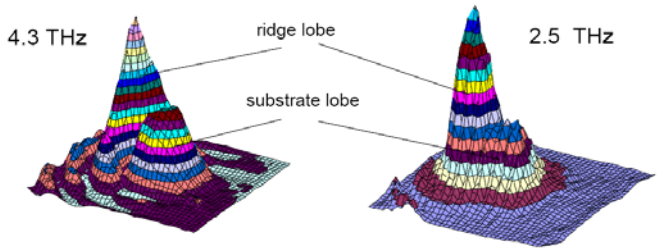

Fig. 1: Beam patterns from two QCLs with surface-plasmon waveguides operating at 4.3 THz and at 2.5 THz.

In order to determine M^2 for a 2.5 THz QCL the beam profile was in a plane orthogonal to the emission direction of the QCL at different positions in front and behind the position of the beam waist created by a TPX lens [8]. The beam diameters were determined according to the so called knife-edge method In Fig. 2 the beam radii of two orthogonal cuts through the beam profile are plotted as a function of distance from the QCL. The beam radius at the position of the waist is 1.8±0.1 mm and the M^2 is 1.1 in direction vertical to the layers of the superlattice. Parallel to the layers the beam radius and M^2 are slightly larger (2.0 ±0.1 mm and 1.2, respectively).

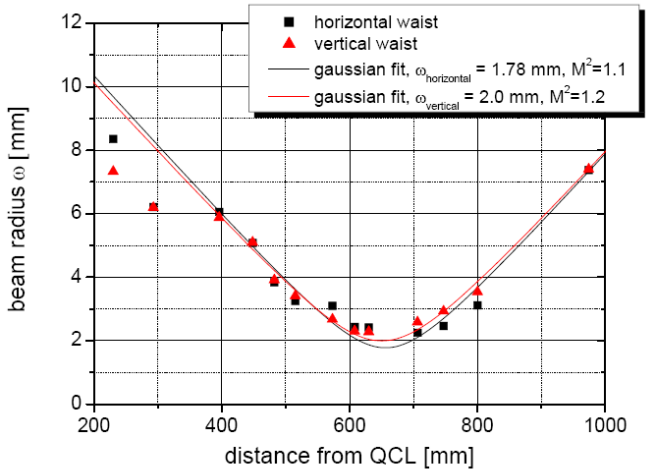

Fig. 2: Beam propagation of a QCL with surface-plasmon waveguide (vertical: in direction parallel to the superlattice layers, horizontal: in direction orthogonal to the superlattice layers).

For use as a LO the beam of the QCL was transformed with a single TPX lens in order to match the beam pattern of the QCL with the HEB antenna. The overlap integral between the main lobe of the QCL profile and a Gaussian beam yields a coupling efficiency of ~70% [6]. Taking into account the non-Gaussian beam profile of the QCL this can be considered as an excellent value.

B. QCL with Metal-Metal Waveguide

The beam pattern of a QCL with metal-metal waveguide is much more divergent than that of a surface-plasmon QCL. The lobe structure is not observable. Instead a pronounced ringlike pattern exists [9]. This results from the far field interference of the coherent radiation emitted by all facets of the laser ridge [10]. Despite the bad beam pattern it has been shown that such as laser can be used as LO. Although coupling of LO radiation to the mixer is very inefficient.

Therefore, several methods have been developed in order to improve the beam pattern of a QCL with metal-metal waveguide. These are a silicon lens at the output facet [11], a horn antenna at the output facet of the ridge [12], or a wide area surface emitting structure [13]. However, none of these approaches has resulted in an improved beam profile when compared to the surface-plasmon waveguide QCL.

EMISSION LINE WIDTH AND FREQUNCY/PHASE LOCKING

Initially, the linewidth of the QCL emission was measured by beating of two laser modes of a free running QCL with a multi-mode Fabry-Perot resonator. An upper limit of about 20 KHz (FWHM) could be established by this method [6, 14]. Phase locking of two longitudinal modes of a 2.7 THz QCL has been demonstrated. The beat linewidth was less than 10 Hz. Under frequency stabilization line profile was found to be Lorentzian with a minimum linewidth of ~6.3 kHz [15].

The frequency of a 3 THz QCL has been locked to that of a THz gas laser with a tunable microwave offset frequency [16]. The locked QCL linewidth was 65 kHz (FWHM). The lock condition could be maintained indefinitely. No temperature or bias current regulation of the QCL other than that provided by the lock error signal was required. The result demonstrates that a THz QCL can be frequency controlled as needed when used as LO. Instead of a gas laser which is not a very practical source for providing the reference frequency a solid state multiplier source can be used. The result of such a locking scheme is shown in Fig. 3. The frequency of the QCL is locked against the signal generated from a microwave source by a superlattice multiplier [17].

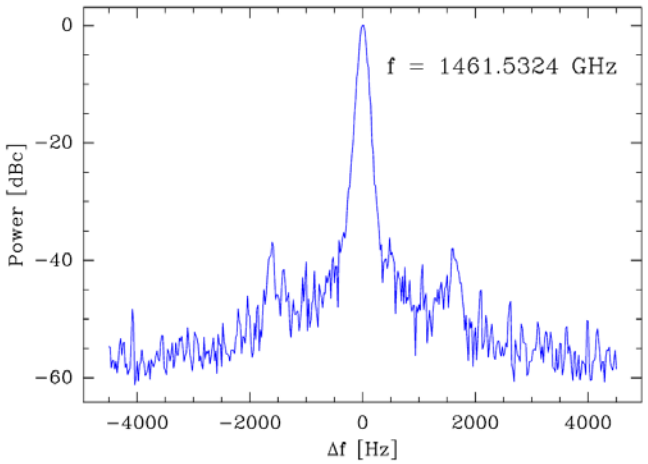

Fig. 3: Frequency locking of the emission of a 1.46 THz QCL against the signal generated by a superlattice multiplier (courtesy: U.U. Graf, D. Rabanus, Universität zu Köln).

III. FREQUENCY TUNEABILITY

The frequency of a QCL can be tuned by either applying a sweep current, by changing its temperature, or by an external resonator. A linear change of the laser emission

frequency with current has been found from emission spectra recorded by a Fourier transform spectrometer (FTS) ($1/f\ \Delta f/\Delta I \approx -5.5\times10^{-2}$ A^{-1}) [18] and by mixing of the QCL radiation with that from a THz gas laser ($1/f\ \Delta f/\Delta I \approx -1.0\times10^{-3}$ A^{-1}) [14]. Temperature-related shifts of the frequency have been reported ranging from $1/f\ \Delta f/\Delta T = -1.9\times10^{-5}$ K^{-1} to -5.1×10^{-5} K^{-1} [18, 19] over a temperature range from 20 to 35 K and 15 to 47 K, respectively. Significantly larger current-related and temperature-related tuning parameters have been observed for resonant-phonon QCLs (-1.5×10^{-2} A^{-1}, -6.61×10^{-5} K^{-1} [16]). Excluding mode hopping [18], the QCL laser frequency was reported to be linearly tunable by the current as well as the laser temperature. The changes in the emission frequency were attributed entirely to temperature changes of the refractive index of the active medium independently whether they originate from variation of the current or from variation of the temperature [14]. The tuning rate of a bound-to-continuum laser with surface plasmon waveguide was found to be in the order of $1/f\ \Delta f/\Delta I \approx +3.0\times10^{-3}$ A^{-1} (Fig. 4) [20].

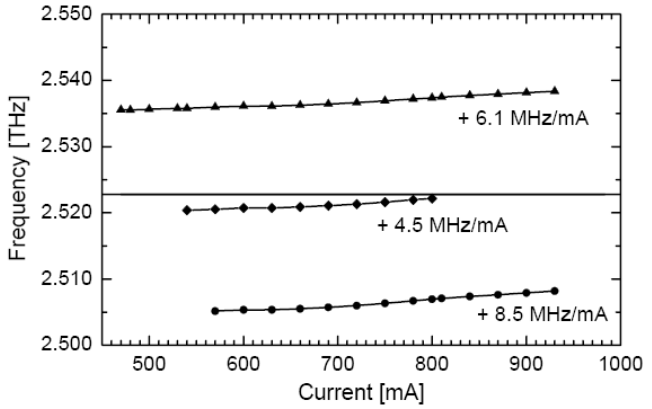

Fig. 4: Frequency tunability of a multi-mode QCL with Fabry-Perot resonator. The straight line is the frequency of the gas laser against which the QCL frequency was measured.

Recently it was reported that the emission frequency of a resonant-phonon QCL with sub-wavelength microdisc resonator changed the sign of the tuning rate from a negative (-0.57 A^{-1}) to positive ($+0.14$ A^{-1}) value with increasing applied electric field. This was attributed to a shift of the maximum of the gain curve by the quantum confined Stark effect [21]. In general resonant-phonon QCLs seems to have a larger tunability with current than lasers with bound-to-continuum or chirped superlattice design of the active medium.

However, none of the tuning rates is sufficient for an LO. Integration of the QCL into an external cavity has been shown to be a possible solution for extension of the frequency tuning range [22]. In this experiment the external cavity was realized by one facet of the QCL and the reflection from a movable mirror. The other facet was coated with SiO_2 which served as antireflection coating. Broad and fine tuning of the frequency were achieved by varying the cavity length. Coarse tuning up to ~90 GHz was obtained near the center frequency of 4.8 THz, and continuous mode-hop-free tuning was observed over ~10 GHz.

IV. MOLECULAR SPECTROSCOPY

High resolution molecular spectroscopy is an important test in order to demonstrate the performance of a heterodyne spectrometer. Spectroscopy with a heterodyne spectrometer with a QCL-based LO has not yet been performed. However, as a first step in this direction high resolution absorption spectroscopy with a QCL has been done [23]. The spectrometer is sketched in Fig. 5. For frequency tuning the temperature of the QCL is set and the current is swept. By this means the frequency range from 2.517 THz to 2.521 THz is available. The radiation from the QCL is reflected by a wire grid into an absorption cell. The transmitted radiation is either mechanically or electrically chopped and detected with a Ge:Ga detector. A small part of the radiation from the QCL is transmitted through the wire grid, superimposed with the radiation from a 2.5 THz gas laser and focused onto a GaAs Schottky diode. The difference frequency is measured for each data point. This is important because the frequency tuning is not linear with current and there was not frequency locking to a reference source.

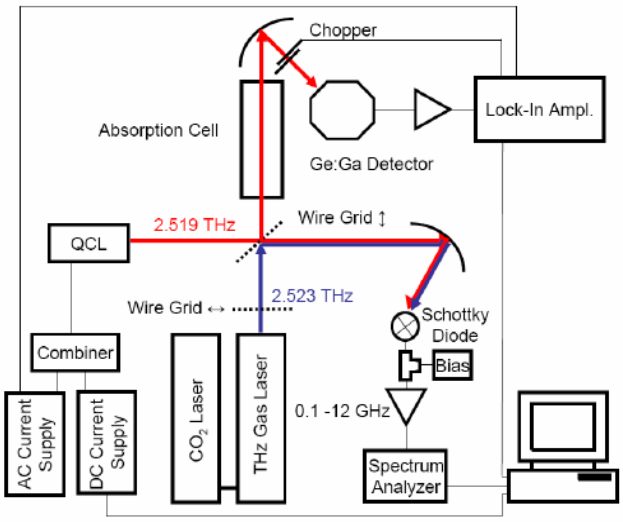

Fig. 5: Set-up of a THz absorption spectrometer with QCL.

In Fig. 6 a typical absorption spectrum of a rotational transition of $^{12}CH_3{}^{16}OH$ is shown along with a fit of a Voigt profile. The agreement is very good. By measuring the profile at different pressures the pressure broadening as well as the pressure shift were determined. Both agree well with published data. Since the measured molecular linewidth is not limited by the linewidth of the QCL it can be concluded that the QCL performs well for high resolution spectroscopy.

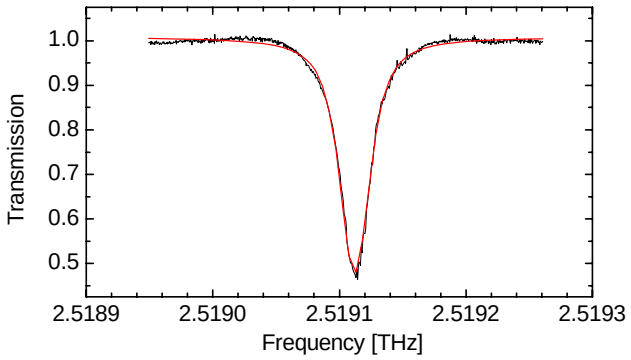

Fig. 6: Absorption line of $^{12}CH_3{}^{16}OH$ measured with the THz spectrometer (black line) and fit of a Voigt profile (red line).

V. Noise Temperature Measurements

The measurement of the noise temperature of an HEB mixer was among the first experiments on the way towards a QCL based LO [6, 24]. Gao et al. [24] measured a double sideband (DSB) noise temperature of 1400 K at 2.8 THz. The receiver had a NbN hot electron bolometric mixer and a resonant-phonon LO with metal-metal waveguide. Only 1.4% of the power from the QCL was coupled into the HEB, due to the poor optical coupling of the divergent QCL beam to the mixer. The Allan stability time of the QCL/HEB receiver was found to be the same as the one measured for an HEB mixer pumped by a multiplier LO. With a surface-plasmon QCL a noise temperature of 1150 K was obtained [25]. The improved was attributed to an improved mixer and an optical setup with lower loss. It is worth noting, that the gain bandwidth of a HEB mixer gas been measured for the first time above the superconducting gap of NbN by mixing the radiation from a THz gas laser with that from a frequency tunable QCL [26].

In another experiment [6] with a QCL with surface-plasmon waveguide the optimal noise temperature was achieved for ~10 µW LO power in front of the cryostat with the HEB mixer. With a gas laser LO ~7 µW were required for the same mixer, which is somewhat less than with the QCL, probably because of the better beam profile of the gas laser.

Recently, a liquid cryogen free THz heterodyne receiver with a QCL and an HEB mixer was demonstrated [8]. The front-end of the receiver is integrated in a pulse tube cooler (PTC). The QCL is mounted on the first stage of the PTC and operates at a temperature of about 45 K while the HEB is mounted on the second stage of the PTC (~4.5 K). At the position of the HEB the beam profile is close to Gaussian (inset in Fig. 7) allowing for an efficient coupling of the LO radiation into the mixer. With this setup the HEB mixer was pumped into the normal state (Fig. 2). The double sideband noise temperature measured with this set-up was 2000 K and when corrected for optical losses in the signal path it was ~800 K. This experiment demonstrates that a solid state THz heterodyne receiver in a PTC is feasible.

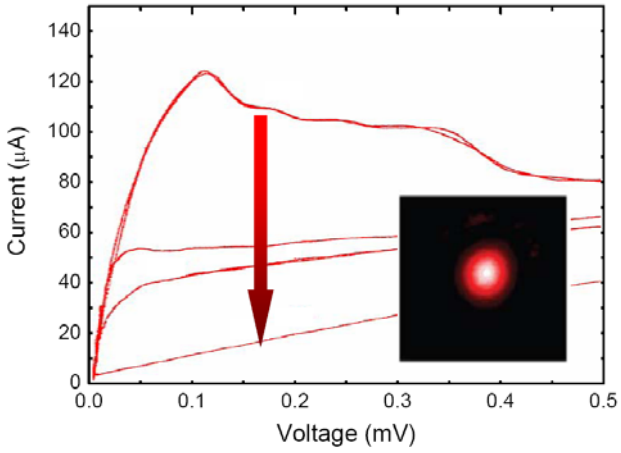

Fig. 7: Pumped IV-curves of an HEB mixer. The arrow indicates increasing pump power. The inset shows the beamprofile measured at the position of the HEB mixer. The area shown is 10x10mm^2.

Outlook

Since the first demonstration of a THz QCL in 2002 significant progress has been made towards a QCL as LO for a THz heterodyne receiver. It has been shown that the fundamental requirements for this application can be met. However a practical LO is still missing. A major challenge remains to realize all required specifications in a single device. Also, the input power or alternatively the laser threshold has to be lowered so that the laser can be operated at liquid nitrogen temperature or in a small Stirling cooler. Once these issues are solved THz QCLs will be a valuable LO in heterodyne receivers especially at frequencies above 2 THz.

References

[1] A. Tredicucci and R. Köhler, "Terahertz quantum cascade lasers," in *Intersubband Transitions in Quantum Structures,* R. Paiella, Ed. New York: McGraw-Hill, 2006, pp. 45-105.

[2] B. Williams, "Terahertz quantum cascade lasers," *Nature Photonics*, vol. 1, pp. 517-525, Sept. 2007.

[3] R. Köhler, A. Tredicucci, F. Beltram, H. E. Beere, E. H. Linfield, A. G. Davies, D. A. Ritchie, R. C. Iotti, and F. Rossi, "Terahertz semiconductor-heterostructure laser," *Nature*, vol. 417, pp. 156-159, May 2002.

[4] G. Scalari, L. Ajili, J. Faist, H. Beere, E. Linfield, D. Ritchie, and G. Davies, "Far-infrared λ~87 µm bound-to-continuum quantum-cascade lasers operating up to 90 K," *Appl. Phys. Lett.*, vol. 82, pp. 3165-3167, May 2003.

[5] B. S. Williams, H. Callebaut, S. Kumar, Q. Hu, and J. L. Reno, "3.4-THz quantum cascade laser based on longitudinal-optical-phonon scattering for depopulation," *Appl. Phys. Lett.*, vol. 82, pp. 1015-1017, Feb. 2003.

[6] H.-W. Hübers, S. G. Pavlov, A. D. Semenov, R. Köhler, L. Mahler, A. Tredicucci, H. E. Beere, D. A. Ritchie, and E. H. Linfield, "Terahertz quantum cascade laser as local oscillator in a heterodyne receiver," *Optics Express*, vol. 13, pp. 5890-5896, July 2005.

[7] E. Bründermann, M. Havenith, G. Scalari, M. Giovannini, J. Faist, J. Kunsch, L. Mechold, and M. Abraham, "Turn-key, compact high temperature terahertz quantum cascade lasers: imaging and room temperature detection," *Optics Express*, vol. 14, pp.1829-1841, Feb. 2009.

[8] H. Richter, A. D. Semenov, S. Pavlov, L. Mahler, A. Tredicucci, K. Il'in, M. Siegel, and H.-W. Hübers, "Terahertz heterodyne receiver

with quantum cascade laser and hot electron bolometer mixer in a pulse tube cooler," *Appl. Phys. Lett.*, vol. 93, pp. 141108, Oct. 2008.

[9] A. J. L. Adam, I. Kašalynas, J. N. Hovenier, T. O. Klaassen, J. R. Gao, E. E. Orlova, B. S. Williams, S. Kumar, Q. Hu, and J. L. Reno, "Beam patterns of terahertz quantum cascade lasers with subwavelength cavity dimensions," *Appl. Phys. Lett.*, vol. 88, 151105, April 2006.

[10] E. E.. Orlova, J. N. Hovenier, T.O. Klaassen, I. Kašalynas, A. J. L. Adam, J. R. Gao, T. M. Klapwijk B. S. Williams, S. Kumar, Q. Hu, and J. L. Reno, "Antenna model for wire Lasers," *Phys. Rev. Lett.*, vol. 96, pp. 173904, May 2006.

[11] M. L. Wei, Q. Q. Alan, S. Kumar, B. S. Williams, Q. Hu, and J. L. Reno, "High-power and high-temperature THz quantum-cascade lasers based on lens-coupled metal-metal waveguides," *Optics. Lett*., vol. 32, pp. 2840-2842, Sept. 2007.

[12] M. I. Amanti, M. Fisher, C. Walther, G. Scalari, and J. Faist, "Horn antennas for terahertz quantum cascade lasers," *Electronics Lett.*, vol. 43, May 2007

[13] S. Kumar, B. S. Williams, Q. Qin, A. W. Lee, Q. Hu, and J. L. Reno, "Surface-emitting distributed feedback terahertz quantum-cascade lasers in metal-metal waveguides," *Optics Express* **15**, pp. 113-128, Jan. 2007.

[14] A. Barkan, F. K. Tittel, D. M. Mittleman, R. Dengler, P. H. Siegel, G. Scalari, L. Ajili, J. Faist, H. E. Beere, E. H. Linfield, A. G. Davies, and D. A. Ritchie, "Linewidth and tuning characteristics of terahertz quantum cascade lasers," *Optics Lett.*, vol. 295, pp. 575-577, March 2004

[15] A. Baryshev, J.N. Hovenier, A.J.L. Adam, I. Kašalynas, J.R. Gao, T. O. Klaassen, B.S. Williams, S. Kumar, Q. Hu, and J. Reno, "Phase-locking and spectral linewidth of a two-mode terahertz quantum cascade laser," *Appl. Phys. Lett.*, vol. 89, pp. 031115, July 2006.

[16] A. L. Betz and R. T. Boreiko, B. S. Williams, S. Kumar, Q. Hu, and J. L. Reno, "Frequency and phase-lock control of a 3 THz quantum cascade laser," *Optics Lett.*, vol. 30, pp. 1837-1839, July 2005.

[17] U. U. Graf and D. Rabanus, private communication, 2008.

[18] L. Ajili, G. Scalari, D. Hofstetter,M. Beck, J. Faist, H. Beere, G. Davies, E. Linfield and D. Ritchie, "Continuous-wave operation of far-infrared quantum cascade lasers," *Electronics Lett.*, vol. 38, Oct. 2002.

[19] L. Ajili, G. Scalari, J. Faist, H. Beere, E. Linfield, D. Ritchie, and G. Davies, "High power quantum cascade lasers operating at $\lambda \approx 87$ and 130 μm," *Appl. Phys. Lett.*, vol. 85, pp. 3986-3988, Nov. 2004.

[20] H.-W. Hübers, S. G. Pavlov, A. D. Semenov, L. Mahler, A. Tredicucci, H. E. Beere, and D. A. Ritchie, "Molecular spectroscopy with terahertz quantum cascade lasers," *J. Nanoelectr. and Optoelectr.*, vol. 2, pp. 101-107, Jan. 2007.

[21] G. Fasching, V. Tamošiūnas, A. Benz, A. M. Andrews, K. Unterrainer, R. Zobl, T. Roch, W. Schrenk, and G. Strasser, "Subwavelength Microdisk and Microring Terahertz Quantum-Cascade Lasers," *IEEE J. Quantum Electron*., vol. 43, pp. 687-697, Aug. 2007.

[22] Jihua Xu, J. M. Hensley, D. B. Fenner, R. P. Green, L. Mahler, A. Tredicucci, M. G. Allen, F. Beltram, H. E. Beere, and D. A. Ritchie, "Tunable terahertz quantum cascade lasers with an external cavity resonator," *Appl. Phys. Lett.*, vol. 91, pp. 121104, Sept. 2007.

[23] H.-W. Hübers, S. G. Pavlov, H. Richter, and A. D. Semenov, L. Mahler, A. Tredicucci, H. E. Beere, and D. A. Ritchie, "High resolution gas phase spectroscopy with a distributed feedback terahertz quantum cascade laser," *Appl. Phys. Lett*., vol. 89, pp. 061115, August 2006.

[24] J. R. Gao, J. N. Hovenier, Z. Q. Yang, J. J. A. Baselmans, A. Baryshew, M. Hajenius, T. M. Klapwijk, A. J. L. Adam, T. O. Klaassen, B. S. Williams, S. Kumar, Q. Hu, and J. L. Reno, "Terahertz heterodyne receiver based on a quantum cascade laser and a superconducting bolometer," *Appl. Phys. Lett.,* vol. 86, pp. 244104, June 2005.

[25] M. Hajenius, P. Khosropanah, J. N. Hovenier, J. R. Gao, T. M. Klapwijk, S. Barbieri, S. Dhillon, P. Filloux, C. Sirtori, D. A. Ritchie, and H. E. Beere, "Surface plasmon quantum cascade lasers as terahertz local oscillators", *Optics Letters,* vol. 33, pp. 312-314, Feb. 2008.

[26] A. Semenov, K. Il'in, M. Siegel, A. Smirnov, S. Pavlov, H. Richter, and H.-W. Hübers, "Evidence of non-bolometric mixing in the bandwidth of a hot-electron bolometer," *Supercond. Sci. and Technol.,* vol. 19, pp. 1051 - 1056, Sept. 2006.

High angular resolution far-field beam pattern of a surface-plasmon THz quantum cascade laser

X. Gu[1], S. Paprotskiy[1,3], J.N. Hovenier[1], J. R. Gao[1,2], E. E. Orlova[1.4], T.M. Klapwijk[1], P. Khosropana[2], S. Barbieri[5], S. Dhillon[5], P. Filloux[5], and C. Sirtori[5]

[1]*Delft University of Technology, Kavli Institute of NanoScience, Delft, The Netherlands*

[2]*SRON Netherlands Institute for Space Research, Utrecht/Groningen, The Netherlands*

[3]*Institute of Radio Engineering and Electronics, Russian Academy of Sciences, 103907 Moscow, Russia*

[4]*Institute for Physics of Microstructures, Russian Academy of Sciences, Nishny Novgorod, Russia*

[5]*Université de Paris, Matériaux et Phénomènes Quantiques, Paris Cedex 13, France*

* Contact: j.r.gao@tudelft.nl, phone +31-15-2781370

***Abstract*— In this work we have developed a new beam pattern measurement setup using a room-temperature pyrodetector and two PC controlled stepper motors. We measured the far-field beam patterns of surface plasmon QCLs, which are 217 μm or 157 μm wide, 1500 μm long, emitted at 2.84 THz in single mode. We discover that the beams contain two types of interference fringes. The type one has a spacing between two fringes which decreases with increasing angle, and occurs in the positive space (opposite to the substrate of the QCL). Type two has nearly equally, closely spaced rings and is observed in the negative space.**

I. Introduction

Observations of atomic and molecular lines at the terahertz (THz) frequency region can provide important and unique information on astrophysics and the Earth's atmosphere. To detect those lines, it is essential to have an instrument with high sensitivity and high spectral resolution, which should be operated in a balloon-borne or a space-borne observatory because of the water absorption in the air. A heterodyne receiver which mixes a weak THz line signal with a strong line signal generated locally (local oscillator) and down-converts it to a signal at a few GHz, to be further amplified, is the only technique fulfilling the requirements of both high resolution and high sensitivity. The key components of the receiver are a mixer and a THz coherent CW source.

A new type of solid-state THz source was recently developed based on a quantum cascade laser (QCL) structure [1,2]. This new source holds great promise for LO applications because of the following characteristics: the frequency coverage (1.2 - 5 THz demonstrated so far), high output power (≥ 1 mW), compactness, linear polarization, narrow linewidth, and phase locking capability. THz QCLs based on a double metal waveguide have been successfully demonstrated as local oscillator in the laboratory [3-5].

The far-field beam pattern of a THz QCL has been recognized to be crucial to couple the power to a mixer. Despite of mW-output power of a QCL, it turns out experimentally that the effective power, which could be coupled to a hot electron bolometer mixer is still limited because of divergent far-field beam and interference fringes. The interference fringes have been reported in a double-metal waveguide QCL [6], surface plasmon waveguide QCL [5], and surface plasmon QCL with a DFB structure [7].

Surface plasmon waveguide QCLs [5,7] show more dense interference fringes than double metal waveguide QCLs, which makes it very challenging to resolve the fingerprint of the interference since it requires detection of the radiation intensity with high angular resolution.

II. THz Surface-plasmon QCLs

The QCLs used in this work are described in Ref. 8 and are based on a bound-to-continuum active region design and a surface plasmon waveguide. The active region consists of 90 GaAs/$Al_{0.15}Ga_{0.85}$ As repeated modules grown by MBE, giving a total thickness of 11.64 μm. The active layer is grown on the top of a 230 μm thick semi-insulating GaAs substrate, and sandwiched between a metallic top-contact and a heavily n-doped GaAs bottom-contact channel. Therefore, unlike double-metal waveguide QCLs, the optical mode is not fully confined within the active region, but penetrates into the substrate down to a depth of approximately 100 μm at 2.8 THz. We use two laser ridges with widths of 217 μm and 158 μm, respectively, which are cleaved at both ends to form 1500 μm-long Fabry-Perot cavities. The 217 μm wide one is schematically shown in Fig. 1.

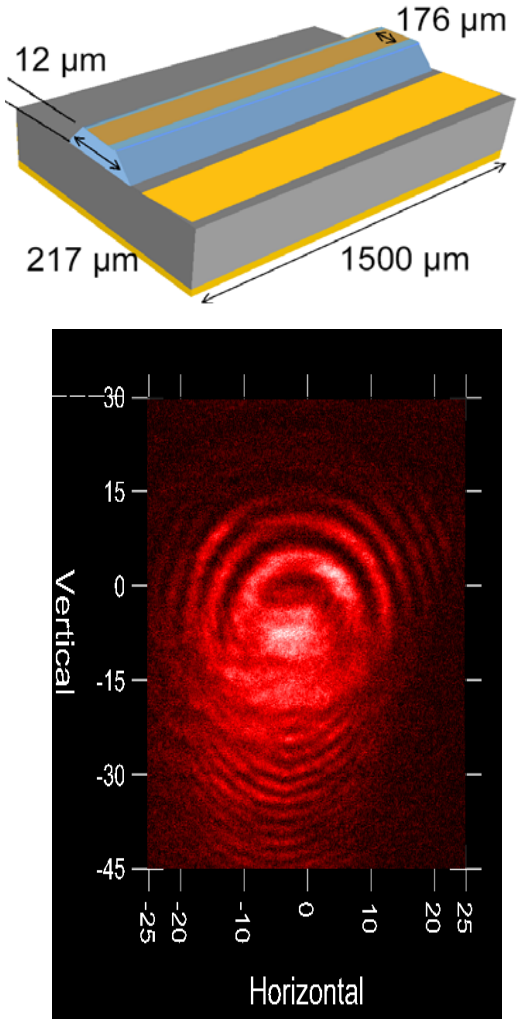

Figure 1. Schematic view of a surface plasmon THz QCL at 2.84 THz (top); measured far-field beam intensity pattern in 2D (horizontal and vertical directions in unit of degree) of the QCL with the zero along the pointing direction of the laser.

We will focus on the 217 μm wide device. Lasing spectra, measured at different bias currents using a Fourier-transform spectrometer with a resolution of ~1 GHz, show single mode emission at 2.835 THz. The maximum output power in continuous wave (CW) mode was about 1.5 mW (measured with a Thomas Keating power meter [5]) when it was operated at 6 V and 900 mA, and at an operating temperature of ~20 K.

III. Experimental Setup

We have developed a new beam pattern measurement setup using a room-temperature pyrodetector and two PC controlled stepper motors allowing scanning in both horizontal and vertical directions. The radiation intensity was measured using the pyrodetector with an aperture of 2 mm in diameter, placed at a radial distance of 80 mm from the QCL. This combination limits the angular-resolution to 1.5° in the beam measurement. The laser was operated in pulsed mode and the intensity was measured using a lock-in technique.

IV. Results

Figure 1 shows the measured beam pattern of the 217 μm wide QCL. We find that the beams contain two types of interference fringes. Type one has the spacing between two fringes that decreases with increasing angle, and occurs in the positive space (opposite to the substrate of the QCL). Type two has closely, nearly equally spaced rings and observed in the negative space.

The first type of fringes resembles those found in double metal waveguide QCLs [6], which were explained by the interference of radiation from longitudinally distributed sources within the laser [9]. However, the spacings between the rings in current case are much smaller than what the model predicts. The second type of rings is likely due to the influence of the aperture induced by the metal layer under the QCL substrate on the radiation.

Acknowledgment

S.P. was supported by INTAS Fellowship Grant for Young Scientists. E.E.O was supported by De Nederlandse Organisatie voor Wetenschappelijk Onderzoek (NWO) and also by the Erasmus Mundus program on Nanoscience and Nanotechnology.

References

[1] R. Köhler, A. Tredicucci, F. Beltram, H.E. Beere, E.H. Linfield, A.G. Davies, D.A. Ritchie, R.C. Iotti, and F. Rossi, "Terahertz semiconductor-heterostructure laser," Nature, London, **417**, 156 (2002).

[2] See a review, B. S. Williams, "Terahertz quantum-cascade lasers" Nat. Photonics **1**, 517 (2007).

[3] J.R. Gao, J.N. Hovenier, Z.Q. Yang, J.J.A. Baselmans, A. Baryshev, M. Hajenius, T.M. Klapwijk, A.J.L. Adam, T.O. Klaassen, B.S. Williams, S. Kumar, Q.Hu, and J.L. Reno, "Terahertz heterodyne receiver based on a quantum cascade laser and a superconducting bolometer," Appl. Phys. Lett., **86**, 244104 (2005).

[4] H.-W. Hübers, S.G. Pavlov, A.D. Semenov, R. Köhler, L. Mahler, A. Tredicucci, H.E. Beere, D.A. Ritchie, and E.H. Linfield, "Terahertz quantum cascade laser as local oscillator in a heterodyne receiver," Optics express, **13**, 5890(2005).

[5] M. Hajenius, P. Khosropanah, J.N. Hovenier, J.R. Gao, T.M. Klapwijk, S. Barbieri, S. Dhillon, P. Filloux, C. Sirtori, D.A. Ritchie, and H.E. Beere, "Surface Plasmon quantum cascade lasers as terahertz local oscillators," Opt. Lett, **33**, 312(2008).

[6] A. J.L. Adam, I. Kašalynas, J.N. Hovenier, T.O. Klaassen, J.R. Gao, E.E. Orlova, B.S. Williams, S. Kumar, Q. Hu, and J. L. Reno, "Beam pattern of Terahertz quantum cascade lasers with sub-wavelength cavity dimensions", Appl. Phys. Lett. **88**, 151105(2006).

[7] J.N. Hovenier, S. Paprotskiy, J.R. Gao, P. Khosropanah, T.M. Klapwijk, L. Ajili, M.A. Ines, and J. Faist, "Beam patterns of distributed feedback surface-plasmon THz quantum cascade lasers" Proc. 18th Int. Symposium on Space Terahertz Technology, Pasadena, California, USA, page 74, March 21-23, 2007.

[8] S. Barbieri, J. Alton, H.E. Beere, J. Fowler, E.H. Linfield, and D.A. Ritchie, "2.9 THz quantum cascade lasers operating up to 70 K in continuous wave", Appl. Phys. Lett., **85**, 1674 (2004).

[9] E.E. Orlova, J.N. Hovenier, T.O. Klaassen, I. Kašalynas, A. J.L. Adam, J.R. Gao, T.M. Klapwijk, B.S. Williams, S. Kumar, Q. Hu, and J. L. Reno, "Antenna model for wire lasers", Phys. Rev. Lett. **96**, 173904(2006).

Integration of Terahertz Quantum Cascade Lasers with Lithographically Micromachined Rectangular Waveguides

Michael C. Wanke, Christopher Nordquist, Christian L. Arrington, Adam M. Rowen, Albert D. Grine, Eric A. Shaner, Mark Lee
Sandia National Laboratories, Albuquerque, NM, USA

The quantum cascade laser (QCL) is currently the only solid-state source of coherent THz radiation capable of delivering more than 1 mW of average power at frequencies above ~ 2 THz. This power level combined with very good intrinsic frequency definition characteristics make QCLs an extremely appealing solid-state solution as compact sources for THz transmission and illumination and for local oscillators in THz heterodyne receiver systems. However, several challenges to the implementation of QCLs as practical THz sources remain. Among these challenges are to shape the highly divergent and non-Gaussian output beam patterns observed from QCLs into a more useful and predictable beam shape, and to integrate QCLs into the existing, broadly used THz technical infrastructure.

One attractive approach to solving both the beam shaping problem and the integration issue is to integrate QCLs into appropriate rectangular waveguides. If the output from a QCL can be efficiently coupled into single-mode rectangular waveguide, then the radiation mode structure will be known, and the propagation, manipulation, and broadcast of the QCL radiation can then be entirely controlled by well-established rectangular waveguide techniques. Because typical QCL frequencies are > 2 THz, the dimensions of single-mode rectangular waveguide at these wavelengths are on the order of tens of microns. While such small THz waveguides can be made by traditional metal machining, this method is typically expensive, slow, and difficult to reconcile with the electrical connections needed to support high DC bias currents (order 1 A) required to operate a QCL embedded in such waveguide.

We will report on our efforts to use semiconductor lithographic methods to micromachine small, single-mode rectangular waveguide structures compatible with integration of QCLs into a waveguide circuit. Such a micromachining approach has the advantage of being amenable to large-scale production and can be tailored to suit the unique demands of a QCL source.

We have designed, fabricated, and performed preliminary tests on micromachined waveguide structures 75 μm wide by 37 μm tall, designed to operate single-mode at frequencies around 3 THz. These waveguides were fabricated using a modified LIGA (German acronym for **Li**thographie, **G**alvanoformung and **A**bformung) process and were plated with gold. These waveguides are coupled to free space via 2-dimensional horn flares (see Fig. 1) Initial quasi-optical transmission measurements at 3.1 THz using a molecular gas laser demonstrate that these waveguides couple to and guide a THz beam. The dominant loss appears to arise from the fact that the 2-D horn aperture is much smaller than the focused incident beam spot, not from losses in the waveguide itself. We will also discuss designs, simulations, and possibly test results of waveguide structures designed to integrate efficiently with metal-metal guided QCL devices.

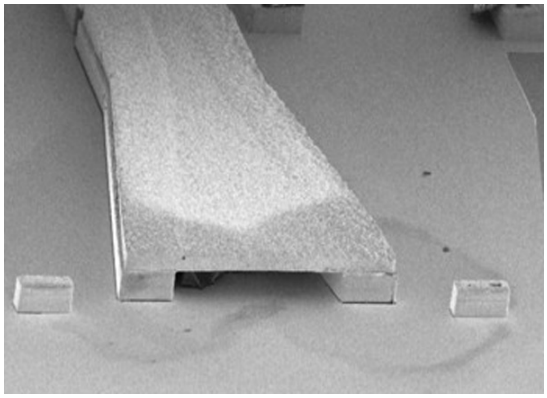

Fig. 1. SEM image of a micromachined 2-D horn antenna flare at the end of a rectangular waveguide. Horn opening dimension is approximately 200 μm wide by 37 μm high.

Sandia is a multiprogram laboratory operated by Sandia Corporation, a Lockheed Martin Company, for the United States Department of Energy's National Nuclear Security Administration under contract DE-AC04-94AL85000.

Phase-locked Local Oscillator for Superconducting Integrated Receiver

Valery P. Koshelets[1,2,*], Andrey B. Ermakov[1,2], Pavel N. Dmitriev[1], Lyudmila V. Filippenko[1], Andrey V. Khudchenko[1,2], Nickolay V. Kinev[1,2], Oleg S. Kiselev[1,2], Irina L. Lapitskaya[1], Alexander S. Sobolev[1,2], and Mikhail Yu. Torgashin[1,2]

[1]*Institute of Radio Engineering and Electronics (IREE), Russia*

[2]*SRON Netherlands Institute for Space Research, Groningen, the Netherlands*

* Contact: valery@hitech.cplire.ru, phone +7-495-629 3418

***Abstract*— A Superconducting Integrated Receiver (SIR) comprises in a single chip a planar antenna combined with a superconductor-insulator-superconductor (SIS) mixer, a superconducting Flux Flow Oscillator (FFO) acting as a Local Oscillator (LO) and a second SIS harmonic mixer (HM) for the FFO phase locking. In this report an overview of the FFO development and optimization is presented. In order to overcome temperature constraints and extend operation frequency of the fully Nb SIR we have developed and studied Nb-AlN-NbN circuits with a gap voltage Vg up to 3.7 mV and extremely low leak currents (Rj/Rn > 30). Continuous tuning of the frequency due to bending and overlapping of the Fiske steps and a possibility to phase lock the Nb-AlN-NbN FFO at any frequency in the range 350-750 GHz has been experimentally demonstrated. After optimization of the FFO design the free-running linewidth between 7 and 1.5 MHz has been measured in the frequency range 350 – 750 GHz, which allows to phase-lock from 50 to 95 % of the emitted FFO power. New designs of the FFO intended for further improvement of its parameters are under development, but even at the present state the Nb-AlN-NbN FFOs are mature enough for practical applications. These achievements enabled development of a 500 - 650 GHz integrated receiver for the Terahertz Limb Sounder (TELIS) project intended for atmosphere study and scheduled to fly on a balloon in 2008.**

I. Introduction

A Superconducting Integrated Receiver (SIR) [1], [2] was proposed more than 10 years ago and finally has been developed for practical applications [3], [4]. A SIR comprises in one chip (size of 4 mm*4 mm*0.5 mm) a low-noise SIS mixer with quasioptical antenna, an FFO [5] acting as a Local Oscillator (LO) and a second SIS harmonic mixer (HM) for the FFO phase locking, see Fig. 1. The concept of the SIR looks very attractive for many practical applications due to SIR compactness and a wide tuning range of the FFO [6]. Presently, the frequency range of the most practical heterodyne receivers is limited by the tunability of the local oscillator. For a solid-state multiplier chain the fractional input bandwidth typically does not exceed 10-15 %. In the SIR the bandwidth is determined by the SIS mixer tuning structure and matching circuitry between the SIS and the FFO; bandwidth up to 30 - 40 % may be achieved with a twin-junction SIS mixer design.

Free-running linewidth of the FFO can be up to 10 MHz; so to obtain the frequency resolution required for practical application of a heterodyne spectrometer (of at least one part per million) the integrated local oscillator (LO) must be stabilized. To achieve this goal a concept of the integrated receiver with the FFO phase-locked to an external reference has been developed [7], [8]. To prove capability of the SIR for high-resolution spectroscopy we have successfully measured line profiles of OCS gas around 625 GHz [3]. Latest results on development of a 500 - 650 GHz integrated receiver for the Terahertz Limb Sounder (TELIS) project [9], [10] are presented at this Symposium [11].

There is a number of important requirements on the FFO properties to make it suitable for application in the phase- locked SIR. Obviously the FFO should emit enough power to pump an SIS mixer (taking into account a specially designed mismatch of about 5-7 dB between the FFO and the SIS mixer, introduced to avoid leakage of the input signal to the LO path). It is a challenge to realize the ultimate performance of separate superconducting elements after their integration in a single-chip device. Implementation of the improved matching circuits and submicron junctions for both the SIS and the HM allows delivering optimal FFO power for their operation.

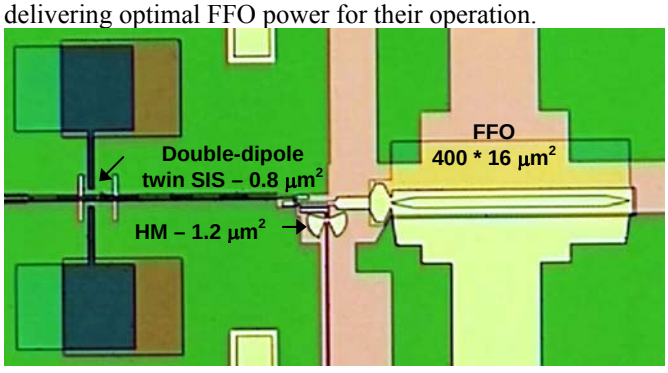

Fig. 1. Central part of the SIR chip with double-dipole antenna, twin SIS-mixer and harmonic mixer for FFO phase locking.

Even for ultra wideband room-temperature PLL system an effective regulation bandwidth is limited by length of the cables in the loop (about 10 MHz for typical loop length of two meters). It means that free-running FFO linewidth has to be well below 10 MHz to ensure stable FFO phase locking with reasonably good spectral ratio (SR) - the ratio between the carrier and total power emitted by the FFO [6]. For example, only about 50 % of the FFO power can be phase-locked by the present PLL system at free-running FFO linewidth of 5 MHz. Low spectral ratio results in considerable error at resolving of the complicated line shape [8]. Thus sufficiently small free-running FFO linewidth is vitally important for realization of the phase-locked SIR for the TELIS.

Earlier the Nb-AlOx-Nb or Nb-AlN-Nb trilayers were successfully used for the SIR fabrication. Traditional all-Nb circuits are being constantly optimized but there seems to be a limit for linewidth optimizations at certain boundary frequencies due to Josephson self-coupling (JSC) effect [12] as well as a high frequency limit, imposed by Nb gap frequency (~700 GHz). That is the reason for novel types of junctions based on materials other than Nb to be developed.

We reported on development of the high quality Nb-AlN-NbN junction production technology [13]. The implementation of an AlN tunnel barrier in combination with an NbN top superconducting electrode provides a significant improvement in SIS junction quality. The gap voltage of the junction Vg = 3.7 mV. From this value, the gap voltage of the Nb film Δ_{Nb}/e = 1.4 mV and the voltage of the singularity corresponding to the difference of the superconducting gaps of the junction contacts $V_\delta = (\Delta_{NbN} - \Delta_{Nb})/e$ = 0.9 mV we estimated the gap voltage of our NbN film as Δ_{NbN}/e = 2.3 mV [14].

The dependency of the ratio of subgap to normal state resistance (Rj/Rn) vs. critical current density (Jc) for different types of the Nb based junctions fabricated at IREE is presented in Fig. 2. One can see that the Nb-AlN-NbN junctions have very good quality at high current densities that is important for implementation in THz mixers. The same technique was further used to produce complicated integrated circuits comprising SIS and FFO in one chip.

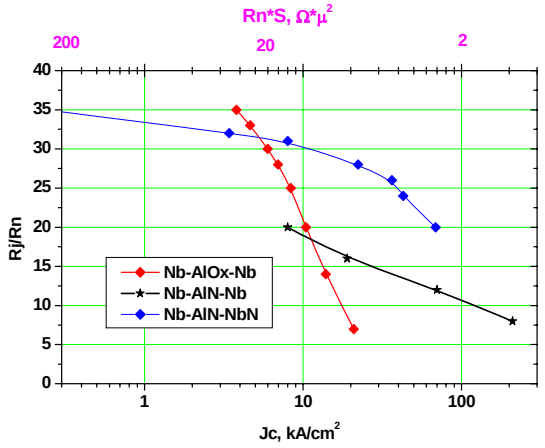

Fig. 2. The dependencies of Rj/Rn ratio vs. critical current density Jc for junctions fabricated at IREE [14].

II. Nb-AlN-NbN Flux Flow Oscillator

A Josephson Flux Flow Oscillator (FFO) [5] has proven to be the most developed superconducting local oscillator for integration with an SIS mixer in a single-chip submm-wave Superconducting Integrated Receiver [1] - [4]. The FFO is a long Josephson tunnel junction of the overlap geometry (see Fig. 3) in which an applied dc magnetic field and a dc bias current, I_B, drive a unidirectional flow of fluxons, each containing one magnetic flux quantum, $\Phi_0 = h/2e \approx 2*10^{-15}$ Wb. Symbol h is Planck's constant and e is the elementary charge. An integrated control line with current I_{CL} is used to generate the dc magnetic field applied to the FFO. According to the Josephson relation the junction oscillates with a frequency $f = (1/\Phi_0)*V$ (about 483.6 GHz/mV) if it is biased at voltage V. The fluxons repel each other and form a chain that moves along the junction. The velocity and density of the fluxon chain and thus the power and frequency of the mm-wave signal emitted from the exit end of the junction due to the collision with the boundary may be adjusted independently by I_B and I_{CL}. The FFO differs from the other members of the Josephson oscillator family by the need for these two control currents, which in turn provides the possibility of independent frequency and power tuning.

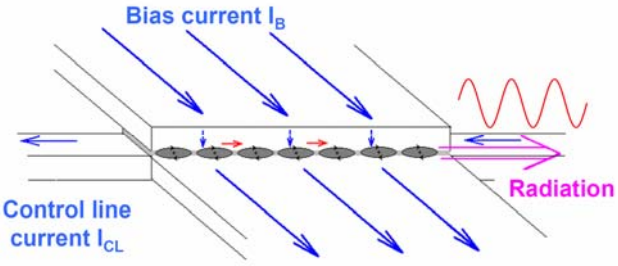

Fig. 3. Schematic view of the Flux-Flow Oscillator.

The length, L, and the width, W, of the FFO used in this study are 300 - 400 μm and 4 - 28 μm,, respectively. The value of the critical current density, Jc, is in the range 4 - 8 kA/cm^2 giving a Josephson penetration depth, $\lambda_J \sim$ 6 - 4 μm. The corresponding value of the specific resistance is $Rn*L*W$ *is* ~ 50 - 25 Ohm*μm^2. For the numerical calculations we use a typical value of the London penetration depth, $\lambda_L \approx$ 90 nm, and a junction specific capacitance, $Cs \approx$ 0.08 pF/ μm^2. The active area of the FFO (i. e. the AlO_x or the AlN tunnel barrier) is usually formed as a long window in the relatively thick (200-250 nm) SiO_2 insulation layer sandwiched between the

two superconducting films (base and wiring electrodes). The so-called "idle" region consisting of the thick SiO_2 layer adjacent to the junction (on both sides of the tunnel region) between the overlapping electrodes forms a transmission line parallel to the FFO. The width of the idle region (W_I = 2 - 14 μm) is comparable to the junction width. The idle region must be taken into account when designing an FFO with desired properties. In our design it is practical to use the flat bottom electrode of the FFO as a control line in which the current I_{CL} produces the magnetic field, which mainly is applied perpendicular to the long side of the junction (see Fig. 3).

The use of Nb for top "wiring" layer is preferable due to lower losses of Nb compared to NbN below 720 GHz; furthermore, the matching structures developed for the all-Nb SIRs can be used directly for the fabrication of receivers with Nb-AlN-NbN junctions. General behaviour of the new devices is similar to the all-Nb ones; even the control currents, necessary to provide magnetic bias for FFO, were nearly the same for the FFOs of similar design.

A family of the Nb-AlN-NbN FFO IVCs measured at different magnetic fields produced by the integrated control line is presented in Fig. 4 (L= 300 μm, W = 14 μm, W_I= 10 μm). Single SIS junction with inductive tuning circuit is employed as a HM for the linewidth measurements. The tuning and matching circuits were designed to provide "uniform" coupling in the frequency range 400 –700 GHz. Measured value of the HM current induced by the FFO oscillations (HM pumping) is shown in Fig. 4 by the color scale. The HM pumping for each FFO bias point was measured at constant HM bias voltage 3 mV (pumping is normalized on the current jump at the gap voltage, I_g = 140 μA). From Fig. 4 one can see that an

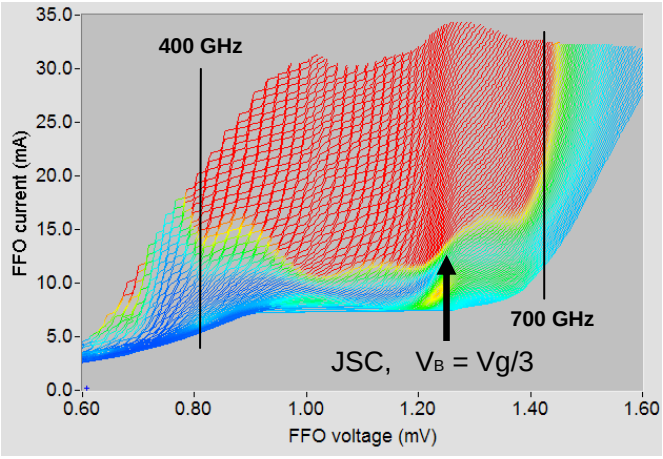

Fig. 4. (Color online) IVCs of the Nb-AlN-NbN-Nb FFO measured at different magnetic fields produced by the integrated control line. The color scale shows the level of the DC current rise at the HM induced by the FFO. Red area marks the region of the FFO parameters where the induced by FFO HM current exceeds 25% of the Ig. This level is well above the optimal value for an SIS-mixer operation.

FFO can provide large enough power over the wide frequency range limited at higher frequencies only by Nb superconducting gap in transmission line electrodes (base and wiring layers) and by design of the matching circuits below 400 GHz. The Nb-AlN-NbN FFOs behave very similar to all-Nb ones. The feature at about 600 GHz where the curves get denser is a JSC (Josephson Self-Coupling) boundary voltage was firstly observed for all-Nb FFOs [12]. The JSC effect (absorption of the emitted by an FFO *ac* radiation by the quasi-particles in the cavity of the long junction) considerably modifies FFO properties at the voltages $V \approx V_{JSC} = 1/3*Vg$ (V_{JSC} corresponds to 620 GHz for the Nb-AlN-NbN FFO). Just above this voltage differential resistance increases considerably; that results in FFO linewidth broadening just above this point. This, in turn, makes difficult or impossible phase-locking of the FFO in that region. For Nb-AlOx-Nb FFO a transition, corresponding *to* $V_{JSC} = Vg/3$ occurs around 450 GHz. So, we can cover the frequency gap from 450 to 550 GHz imposed by the gap value of all-Nb junctions using the Nb-AlN-NbN FFOs. Feature on the graph (around 500 GHz) is very likely due to singularity at difference of the superconducting gaps $\Delta_{NbN} - \Delta_{Nb}$.

Continuous frequency tuning at frequencies below 600 GHz for the Nb-AlN-NbN FFOs of moderate length becomes possible though the damping is not high enough to completely suppress Fiske resonant structure at frequencies below Vg/3. For short junctions with small α – wave attenuation factor, the distance between the steps in this resonant regime can be as large, that it is only possible to tune the FFO at the certain set of frequencies. For 300-400 μm long Nb-AlN-NbN junction this is not the case – the quality factor of the resonator formed by a long Nb-AlN-NbN-Nb Josephson junction is not so high at frequencies > 350 GHz; the resonance steps are slanting and the distance between them is not so big (see Fig. 4). That allows us to set any voltage (and any frequency) below V_{JSC}, but for each voltage only a certain set of currents should be used. So, in this case we have the regions of forbidden bias current values, specific for each voltage below V_{JSC}, instead of the forbidden voltage regions for Fiske regime in Nb-AlOx-Nb FFO [14]. Special algorithms have been developed for automatic working point selection in flight; details are presented in [15].

In Fig. 5 typical current-voltage characteristics (IVCs) of a Nb-AlN-NbN SIS junction (area ~ 1.5 μm^2), pumped by a Nb-AlN-NbN FFO (solid line – unpumped IVC, dotted lines – pumped by the FFO at different frequencies). One can see that the FFO provides more than enough power for the mixer pumping (in this experiment we use the test circuits with low-loss matching circuits tuned between 400 and 700 GHz). Even at the specially introduced 5 dB FFO/SIS mismatch (required for the SIR operation) the FFO delivers enough power for the SIS mixer operation in complete TELIS range 490-650 GHz [6].

An important issue for the SIR operation is a possibility to tune the FFO power keeping constant FFO frequency. This is demonstrated in Fig. 6, where the IVCs of an SIS mixer, pumped at different FFO bias currents (different powers) are shown. Dependence of the SIS pump current on the FFO bias current is presented in Fig. 7. One can see that FFO power can be tuned in the range more than 15 dB keeping the same frequency by proper adjustment of the control line current.

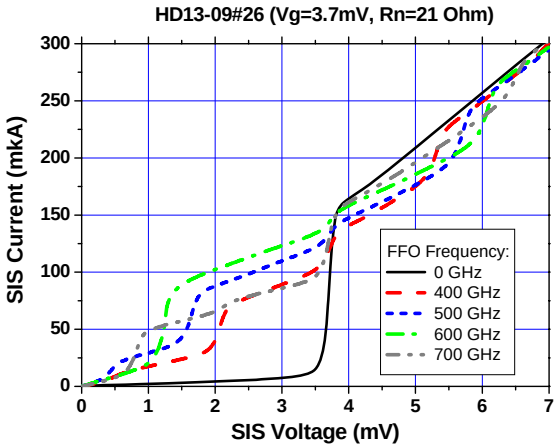

Fig. 5. The IVCs of the SIS mixer.; unpumped – solid curve, pumped at different frequencies – dashed and dotted lines [14].

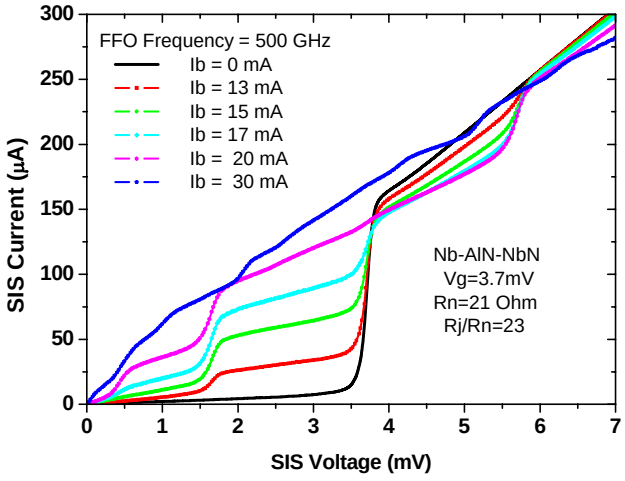

Fig. 6. The IVCs of the SIS mixer; unpumped – black solid curve, pumped at different FFO bias currents (different powers) – lines with symbols.

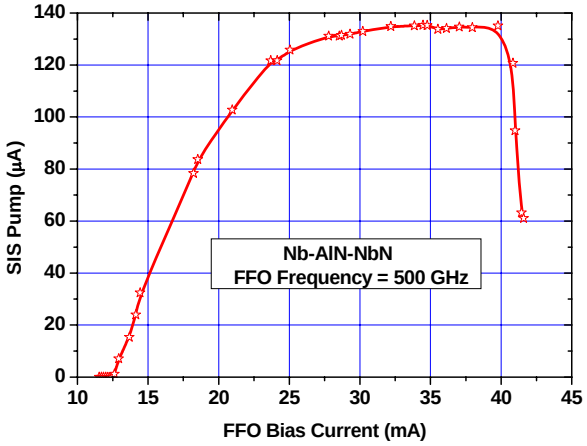

Fig. 7. The pump current of the SIS mixer biased at 3 mV as a function of the FFO bias current (see Fig. 4 and 6).

III. Spectral Properties of an FFO

A. Linewidth Measurements

The FFO linewidth (LW) has been measured in a wide frequency range from 300 GHz up to 750 GHz using a well-developed experimental technique [16]. We investigated the linewidth of the Nb-AlN-NbN FFOs by the same setup, as was used for linewidth measurement of the all-Nb FFO. A specially designed integrated circuit incorporates the FFO junction, the SIS harmonic mixer and the microwave matching circuits. Generally, both junctions are fabricated from the same Nb/AlN/NbN or Nb/AlOx/Nb trilayer. The FFO signal is fed to the SIS harmonic mixer (HM) together with a 17 – 20 GHz reference signal from a stable synthesizer. The required power level depends on the parameters of the HM; it is about of 1 μW for a typical junction area of 1 μm^2. The intermediate frequency (IF) mixer product ($f_{IF} = \pm (f_{FFO} - n \cdot f_{SYN})$ at ~ *400 MHz* is first boosted by a cooled HEMT amplifier (T_n ~ 5 K, gain = 30 dB) and then by a high-gain room temperature amplifier. The resulting IF signal is supplied to the Phase-Locking loop (PLL) system for FFO stabilization (frequency or phase lock). The phase-difference signal of the PLL is fed to the FFO control line current. Wideband operation of the PLL (10-15 MHz full width) is obtained by minimizing the cable loop length. A part of the IF signal is delivered to the spectrum analyzer via a power splitter. All instruments are synchronized to harmonics of a common 10 MHz reference oscillator.

The integrated harmonic mixer may operate in two different regimes, either as quasi-particle mixer (SIS) or as Josephson mixer. In order to exclude the noise from the Josephson super-current fluctuations and thereby realize a pure quasi-particle regime the super current has to be suppressed by a relatively large magnetic field. This requires a special control line placed near the SIS mixer.

Quasi-particle regime of the HM operation could be realised also at high enough level of the synthesizer power. It has been shown [17] that the FFO linewidth and signal-to-noise ratio are almost the same for these two regimes, although the phase noise is somewhat lower in the quasi-particle mode.

In order to accurately measure the FFO line shape the IF signal must be time-averaged by the spectrum analyzer. To remove low frequency drift and interference from the bias supplies, temperature drift, etc. we use a narrow bandwidth (< 10 kHz) Frequency Discriminator (FD) system with relatively low loop gain for *frequency locking* of the FFO. With the FD narrow-band feedback system that stabilizes the mean frequency of the FFO we can accurately measure the free-running FFO linewidth, which is determined by the much faster internal ('natural") fluctuations.

Most measurement procedures can be controlled by a computer-based data acquisition (DAQ) system that have automatic routines for many standard tests and can perform user-programmed specialized measurements [15].

B. Dependence of the FFO Linewidth on FFO' Parameters

Detailed measurements of the FFO linewidth [18], [19] demonstrate Lorentzian shape of the FFO line in a wide frequency range up to 750 GHz, both at higher voltages on the flux flow step (FFS) and at lower voltages in the resonant regime on the Fiske steps (FS's). It means that the free-running ("natural") FFO linewidth in all operational regimes is determined by the wideband thermal fluctuations and the shot noise (the same as for Nb-AlOx-Nb junctions). This is different from many traditional microwave oscillators where the "natural" linewidth is very small and the observed linewidth can be attributed mainly to external fluctuations. It was found [18], [19] that free-running FFO linewidth, δf, exceed theoretical estimations made for lumped tunnel Josephson junction. The expression for LW dependency on voltage and differential resistances found for all-Nb FFOs [18], [20] is valid for Nb-AlN-NbN junctions as well:

$$\delta f = (2\pi/\Phi_0^2)\,(R_d^B + K^*R_d^{CL})^2\, S_i(0); \qquad (1)$$

where $S_i(0)$ is the power density of low frequency current fluctuations, R_d^B and R_d^{CL} are differential resistances on bias and control line currents respectively. Note that ratio R_d^{CL}/R_d^B is constant for fixed FFO bias, so $\delta f = A(I_B)\,(R_d^B)^2\, S_i(0)$.

Earlier so-called Super Fine Resonance Structure (SFRS) [21] was observed on the FFO IVCs; this structure results in the jumps of the FFO between tiny steps (frequency spacing is of about 10 MHz, see Fig. 8). Presence of the SFRS makes impossible phase locking at frequencies between steps that is unacceptable for practical applications. Recently we found that the SFRS is related to interference of the acoustic waves created by the FFO (generation of the phonons by Josephson junction is well possible [22]). Special technological procedure allows us to eliminate this interference and realize continuous FFO frequency tuning in the SIR that was vitally important for TELIS project (see Fig. 8). Details of this study will be published elsewhere.

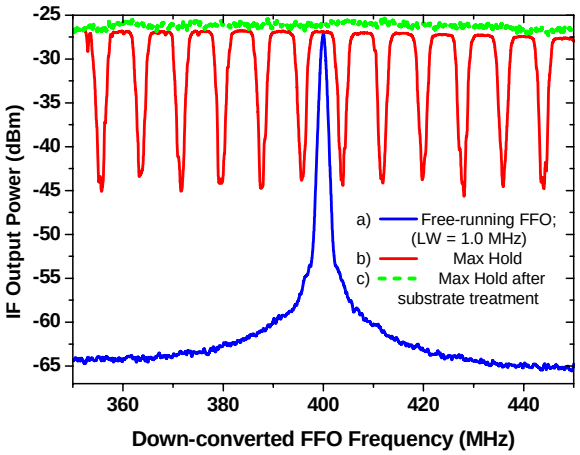

Fig. 8. Down-converted spectra of the FFO: a) Free-running FFO; b), c) - Signal recorded in the MaxHold regime of the Spectrum Analyzer at fine tuning of the FFO frequency recorded before and after special Si substrate treatment.

In Fig. 9 we present comparative graph of the FFO linewidth for two types of the tri-layer. One can see that the linewidth of Nb-AlN-NbN-Nb FFO is twice as small up to 600 GHz. It should be emphasized that due to FS overlapping continuous tuning is possible and any desirable frequency could be realized. Several "stacked" stars at certain frequencies for the NbN FFO mean that the best linewidth value can be selected by adjusting FFO bias (all the linewidth values at the selected frequency are close and any will actually be good for measurements). Each star corresponds to an "allowed" bias current at Fiske steps (as described above in section II). Although the FFO tuning on FS is complicated, the benefit in linewidth (and, consequently, spectral ratio) is worth the trouble – LW below 3 MHz can be achieved in the whole range between 350 – 610 GHz. Abrupt increase of the FFO linewidth at some frequencies is caused by Josephson self-coupling effect. The JSC (absorption of the emitted by an FFO ac radiation by the quasi-particles in the cavity of the long junction, see above) considerably modifies FFO properties at the voltages $V \approx V_{JSC} = 1/3^*V_g$ [12] (V_{JSC} corresponds to 620 GHz for the Nb-AlN-NbN FFO).

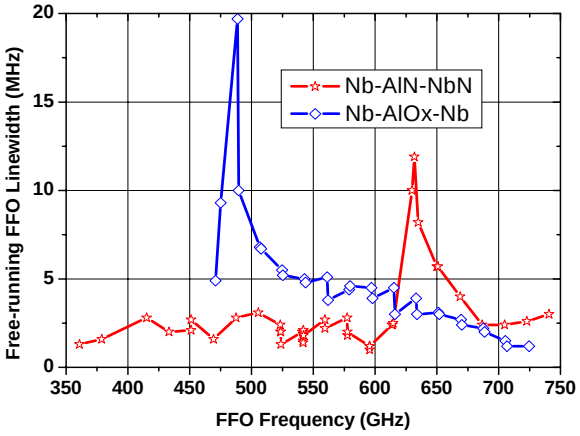

Fig. 9. Linewidth dependency on frequency for two types of the FFO [14].

Employment of NbN electrode does not result in noise increase and the linewidth as low as 0.5 MHz was measured at 600 GHz. It allows us to phase lock up to 97 % of the emitted FFO power and realize very low phase noise about – 90 dBc (see below). Our observations made for junctions of different topology let us assume that all dependencies of the linewidth on the junction parameters known for all-Nb FFOs hold for the Nb-AlN-NbN ones. For example, we observe that the linewidth decreases with junction width increase.

Previous linewidth measurements have demonstrated [6], [23] essential dependence of the free-running FFO linewidth on the FFO voltage, its current density and geometry of the biasing electrodes. In this report we summarized results of the FFO study and optimization of the FFO layout for both types of the FFO. Recently it was shown [4], [6] that the linewidth decreases considerably with increasing FFO width, *W,* of the junction. This is valid for all frequencies of interest, and consequently the Spectral Ratio of the phase locked FFO for wide junctions is higher. We have increased the FFO width up to 28 μm, which is more than five times the Josephson penetration depth λ_J. A number of FFOs with the same electrode layout, but different width of the FFO junction (W = 4, 8, 12, 16, 20 and 28 μm) are fabricated using the same technological procedure yielding the same junction parameters (normal state resistance * area, RnS = 30 $\Omega_*\mu m^2$). The results of the linewidth measurements of these circuits at three frequencies are presented in Fig. 10.

Even for the largest tested width (W = 28 μm) there is no evidence of deterioration in the FFO behaviour. Furthermore, power delivered to the SIS mixer is getting higher and the linewidth lower at all frequencies. The decrease of the FFO linewidth with increasing FFO width is in accordance with existing theoretical models and our expectations. The bias current differential resistance, *Rd,* decreases approximately inversely proportional to the bias current I_B. Since the FFO linewidth is proportional to Rd^2*I_B, it scales down linearly with the junction width. Of course, one can expect that the linewidth decrease will saturate and the FFO performance will deteriorate with further increase of the width (e.g., due to appearance of transversal modes). Due to lack of a reliable theory the optimal value of the FFO width has to be determined experimentally. Note that for a wider FFO the centre line of the junction is shifted away from the edge of the control line (the R_d^{CL} goes down). This may result in a considerable reduction of extraneous noise from external magnetic fields. Furthermore, a wider FFO presumably will have a more uniform bias current distribution [4]. At the present state width of the FFO for TELIS project is chosen to be 16 μm – trade-off between linewidth requirements and technical limitation on maximum bias and control line currents (both should not exceed 70 mA).

In contrast with variation of the FFO linewidth on the FFO width previous measurements [6] have demonstrated a considerable increase of the FFO linewidth with the FFO current density. It contradicts the simplified consideration: the increase of the FFO current density (as it is for increase of the FFO width) should result in the increase of the total FFO bias current, I_B, and reduce the FFO differential resistance on the bias current R_d. Since the FFO linewidth is proportional to $R_d^2*I_b$ one should expect the decrease of the measured FFO free-running linewidth for larger FFO current density. In reality R_d does not decrease as much as this simple consideration predicts and the linewidth increases. From the other hand high value of the current density ($J_c \geq 8$ kA/cm^2) is important for wide-band operation of the SIS-mixer at the submm wave range. The discussed above increase of the FFO linewidth with current density creates serious problem in design and development of SIR chips. Implementation of two separate tri-layers with different current densities - one for the SIS mixer (high J_c) and the other one for the FFO/HM (lower J_c) might be a solution. We have successfully tested and verified this approach for SIR TELIS microcircuits.

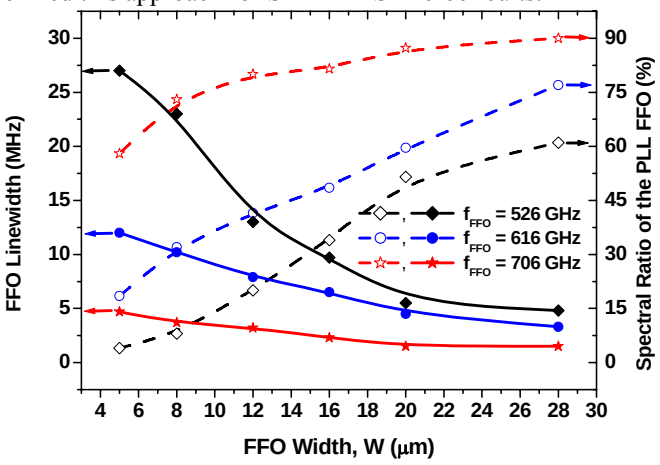

Fig. 10. Linewidth of free-running FFOs (left axis) and corresponding Spectral Ratio for the phase-locked FFO (right axis) measured at different FFO frequencies as a function of FFO width. All circuits are

fabricated using the same technological procedure (RnS = 30 Ω*μm^2) [4].

Improvement of the performance was obtained for the FFO with enlarged electrodes overlapping. Larger overlapping presumably provides more uniform bias current distribution – due to much smaller inductance of the overlapping electrodes. Larger overlapping of the FFO electrodes means also that the FFO of the same width is shifted from the edge of the bottom electrode that results in considerable decrease of the R_d^{CL} value. Note that for wide FFO some shift of the FFO centerline appears "automatically" due to increasing of the width. Experimentally we found that idle region W_I = 10 μm is optimal value for present FFO design. Up to now there is no adequate model that can describe quantitatively both the processes in the FFO and a self-consistent distribution of the bias current. Nevertheless, presented results are very encouraging and these modifications of the FFO were implemented in the TELIS SIRs.

To explore further this approach we developed different designs of the "self-shielded" FFO with large ground plane. Such FFO supposed to be much more protected from variations of external magnetic field and has to provide more uniform bias current distribution (since all bias leads are laying over superconducting shield and have low inductance). Actually, low inductive bias leads provide a possibility of optimal (rather than uniform) current distribution, "requested" by the FFO itself. The last feature must ensure maximum of emitted FFO power. Indeed, the IVCs of all shielded FFOs are much more reproducible; the power, delivered to HM is higher compared to a "standard" design. Unfortunately, free-running linewidth for all variants of shielded FFO with separate bias leads is much larger than linewidth for FFO of traditional design. It seems that injection of the bias via separate leads results in some spatial modulation of bias current [23] despite the additional triangular elements added for more uniform current injection. From other hand, designs that employed three superconducting electrodes provide both perfect pumping and improved linewidth, details will be published elsewhere.

C. Spectral Ratio, Phase Noise

As it was mentioned above free-running FFO linewidth has to be well below 10 MHz to ensure stable FFO phase locking with reasonably good spectral ratio (SR) - the ratio between the carrier and total power emitted by FFO. For example, only about 50 % of the FFO power can be phase-locked by the present TELIS PLL system at free-running FFO linewidth of 5 MHz. Low spectral ratio results in considerable error at resolving of the complicated line shape [8]. The SR value for the given PLL system is determined by free-running FFO linewidth: these two quantities are unambiguously related (see Fig. 11 where data for FFO of different designs and types are presented). Theoretical curve, calculated in [24], coincides reasonably with experimental data. A possibility to increase considerably the SR by application of the ultra-wideband cryogenic PLL system has been recently demonstrated [25].

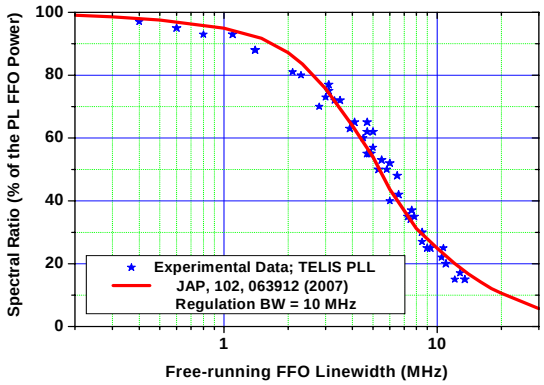

Fig. 11. Spectral Ratio for the phase-locked FFO of different types and designs as a function of free-running FFO linewidth. Solid line – calculated dependence of the SR on FFO LW for PLL bandwidth = 10 MHz [24].

An important issue for TELIS operation is a possibility to tune the FFO frequency and power independently providing the same spectral ratio of PL FFO. The TELIS HM is pumped by a tunable reference frequency in the range of 19-21 GHz from the Local oscillator Source Unit (LSU), phase locked to the internal ultra stable 10 MHz Master Oscillator. The HM mixes the FFO signal with the n-th harmonic of the 19-21 GHz reference. Linewidth and SR for the FFO of TELIS design are almost constant over very wide range of FFO bias current at fixed FFO frequency (see Fig. 12). From this figure one can see that the SR is of about 50 % over the range of bias current, I_b, 14 – 30 mA, while the pumping level varies from 3.5 μA at I_b = 14 mA up to 81 μA at I_b = 30 mA. Furthermore, the SR = 34% can be realized at I_b = 12 mA where the HM pumping is below 0.5 μA. It means that the HM operates in highly non-linear regime and even moderate HM pumping is enough for efficient PLL operation ensuring large enough signal to noise ratio.

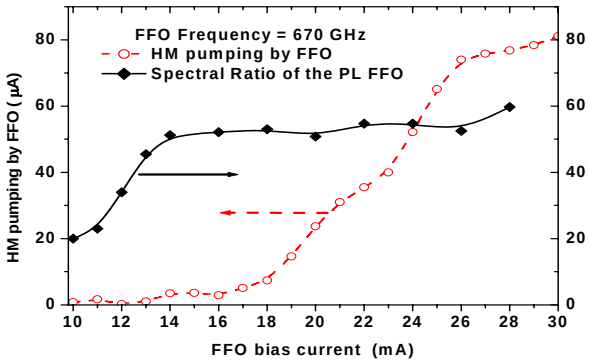

Fig. 12. Dependence of the HM current induced by FFO (HM pumping) and Spectral Ratio after FFO phase locking as a function of FFO bias current. All data measured at FFO frequency of 670 GHz [6].

After optimization of the FFO design the free-running linewidth between 7 and 0.5 MHz has been measured in the frequency range 350 – 750 GHz (see Fig. 10), which allows to phase-lock from 35 to 95 % of the emitted FFO. Example of the free-running (frequency-locked) and phase-locked spectra of the FFO measured for flight SIR at one of the frequencies selected for first TELIS flight are presented in Fig. 13. Data for five important TELIS frequencies are summarized in Table 1. It should be mentioned that noise of the digital electronics at frequencies of about 1 MHz slightly increases measured linewidth value; while the PLL is able to suppress the interference that results in large SR than can be expected from measured linewidth. Note also dependence of the SR and LW on the FFO bias current related to variation of the differential resistance along Fiske step.

To investigate frequency resolution of the receiver we have measured the signal of the synthesizer multiplied by a super-lattice structure [26]. The signal recorded in these measurements is a convolution of the delta-function provided by synthesizer with phase-locked spectra of the FFO with accuracy of the used resolution bandwidth of the spectrum analyzer (30 kHz), so the frequency resolution of the receiver is not worse than 100 kHz.

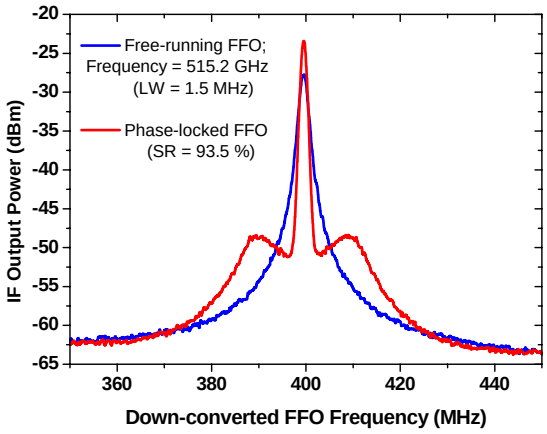

Fig. 13. Spectra of the FFO operating at 515.2 GHz (red curve – frequency locked; blue curve – phase-locked). Linewidth (LW) = 1.5 MHz; Signal to Noise Ratio (SNR) = 36 dB; Spectral Ration (SR) = 93.5 %. Spectra measured with RBW = 1 MHz, span = 100 MHz.

TABLE VI
DATA FOR THE FLIGHT SIR AT SELECTED TELIS FREQUENCIES

FFO Frequency (GHz)	LW (MHz)	SNR (dB)	SR (%)	FFO Ib (mA)
495.0	1.5	32	90	30.7
496.9	1.5	37	93	31.3
515.2	1.5	36	93.5	29.2
607.7	2.1	32	87.7	30
607.7	1.8	32.6	88.6	34
619.1	5.4	25	63.3	30
619.1	4.6	26.8	70.3	34

To prove capability of the SIR for high-resolution spectroscopy line profiles of OCS gas around 625 GHz have been successfully measured by the SIR operating in the DSB regime [3]. The tests were done in a laboratory gas cell setup at a gas pressure down to 0.2 mBar, corresponding to the FWHM linewidth <5 MHz. It was demonstrated that spectrum recorded by the Digital Auto Correlator (DAC) is a convolution product of the signal (gas emission lines) with the FFO line spectrum; resolution in this experiment is limited by DAC back-end.

The residual phase noise of the phase locked FFO - measured relative to the reference synthesizer - is plotted in Fig. 4 as function of the offset from the carrier. To get absolute FFO phase noise, one should add the synthesizer noise multiplied by n^2 to the residual phase noise of the FFO. Data for the R&S®SMF100A Microwave Signal Generator with improved phase noise [27] are also presented in Fig. 14. For the case where the FFO, operating at 450 GHz, is locked to the 20-th harmonic of the synthesizer, $n^2 = 400$. The total (absolute) FFO phase noise (solid line in Fig. 14) is dominated by the synthesizer noise for offsets < 10 kHz. The noise at larger frequency offset is mainly due to PLL system. Note that the FFO phase noise is overestimated since no subtraction of the noise added by the IF amplifier chain was performed; actually at offsets much larger than the PLL regulation bandwidth (> 20 MHz) measured phase noise is mainly determined by the IF chain.

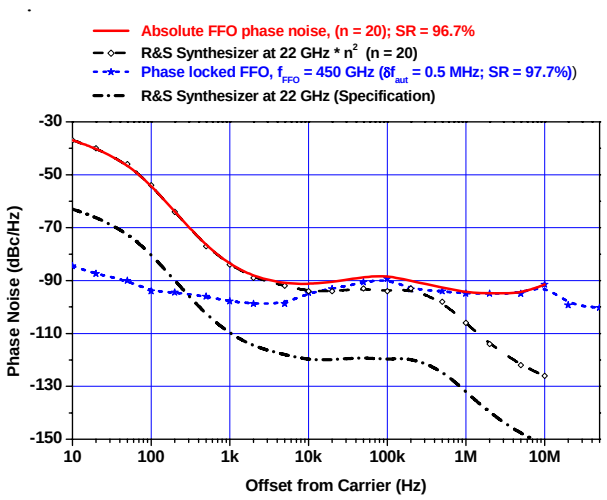

Fig. 14. Experimental phase noise of a phase locked FFO at 450 GHz. Since the phase noise of the FFO is measured relative to the 20th harmonic of the synthesizer, the synthesizer noise [27], multiplied by a factor $20^2 = 400$, should be added to the residual FFO noise to get the total (absolute) FFO phase noise – solid red line.

CONCLUSIONS

In conclusion, optimized design of the FFO for TELIS has been developed and tested. Free-running linewidth value from 7 to 0.5 MHz has been measured in the frequency range 300 – 750 GHz for "wide" FFO. As a result the spectral ratio of the phased-locked FFO varies from 35 to 95 % correspondingly, ensure at least of half phase-locked FFO power in the frequency range 300-750 GHz. The "unlocked" rest of the total FFO power increases the phase noise and the calibration error

Continuous tuning of the frequency is possible for Nb-AlN-NbN FFO due to bending and overlapping of the Fiske steps, so that any desirable frequency can be realized. A possibility to phase lock the Nb-AlN-NbN FFO at any frequency in the range 350-750 GHz has been experimentally demonstrated. New designs of the FFO intended for further improvement of its parameters are under development, but even at the present state the Nb-AlN-NbN FFOs are mature enough for practical applications.

Phase–locked SIR operation over frequency range 450 – 700 GHz has been realized, spectral resolution below 1 MHz has been confirmed by CW signal measurements. An uncorrected double side band (DSB) noise temperature below 150 K has been measured for the SIR with the phase-locked FFO and the intermediate frequency bandwidth 4 - 8 GHz. To ensure remote operation of the phase-locked SIR several procedures for its automatic computer control have been developed and tested.

ACKNOWLEDGMENT

Authors thank Pavel Yagoubov, Gert de Lange and Wolfgang Wild for fruitful and stimulating discussions, as well as Vladimir Vaks, Oleksandr Pylypenko and Dimitry Paveliev for development of the dedicated components for TELIS.

The work was supported in parts by the RFBR projects 06-02-17206, the ISTC project # 3174, NATO SfP Grant 981415, and the Grant for the Leading Scientific School 5408.2008.2

REFERENCES

[1] V.P. Koshelets, S.V. Shitov, L.V. Filippenko, A.M. Baryshev, H. Golstein, T. de Graauw, W. Luinge, H. Schaeffer, H. van de Stadt "First Implementation of a Superconducting Integrated Receiver at 450 GHz"; *Appl. Phys. Lett.*, vol. 68, No. 9, pp. 1273-1275, Feb 1996.

[2] V. P. Koshelets and S. V. Shitov, "Integrated Superconducting Receivers," *Superconductor Science and Technology*, vol. 13, pp. R53-R69, 2000.

[3] P. Yagoubov, R. Hoogeveen, M. Torgashin, A. Khudchenko, V. Koshelets, N. Suttiwong, G. Wagner, M. Birk, "550-650 GHz spectrometer development for TELIS", *The 17th International Symposium on Space Terahertz Technology*, Paris, May 2006, Conference Proceedings ISSTT 2006, report FR3-3, pp. 338-341.

[4] V.P. Koshelets, A.B. Ermakov, L.V. Filippenko, A.V. Khudchenko, O.S. Kiselev, A.S. Sobolev, M.Yu. Torgashin, P.A. Yagoubov, R.W.M. Hoogeveen, and W. Wild, "Iintegrated Submillimeter Receiver for TELIS", "*IEEE Trans. on Appl. Supercond.",* vol. 17, pp 336-342, 2007.

[5] T. Nagatsuma, K. Enpuku, F. Irie, and K. Yoshida, "Flux-flow type Josephson oscillator for millimeter and submillimeter wave region," *J. Appl. Phys.,* vol. 54**,** p. 3302, 1983, see also Pt. II: *J. Appl. Phys.* Vol. 56**,** p. 3284, 1984; Pt. III, *J. Appl. Phys., vol.* 58**,** p. 441, 1985; Pt. IV, *J. Appl. Phys.*, vol. 63, p. 1130, 1988.

[6] V.P. Koshelets, P.N. Dmitriev, A.B. Ermakov, A.S. Sobolev, M.Yu. Torgashin, V.V. Kurin, A.L. Pankratov, J. Mygind, "Optimization of the Phase-Locked Flux-Flow Oscillator for the Submm Integrated Receiver", "*IEEE Trans. on Appl. Supercond.",* vol. 15, pp. 964-967, 2005.

[7] V.P. Koshelets, S.V. Shitov, A.V. Shchukin, L.V. Filippenko, P.N. Dmitriev, V.L. Vaks, J. Mygind, A.B. Baryshev, W. Luinge, H. Golstein, "Flux Flow Oscillators for Sub-mm Wave Integrated Receivers", *IEEE Trans. on Appl. Supercond.,* **v.9,** No 2, pp. 4133-4136, 1999.

[8] V.P. Koshelets, S.V. Shitov, A.B. Ermakov, O.V. Koryukin, L.V. Filippenko, A. V. Khudchenko, M. Yu. Torgashin,P. Yagoubov, R. Hoogeveen, O.M. Pylypenko, "Superconducting Integrated Receiver for TELIS", "*IEEE Trans. on Appl. Supercond.",* vol. 15, pp. 960-963, 2005.

[9] R.W.M. Hoogeveen, P.A. Yagoubov, A. de Lange, A.M. Selig, V.P. Koshelets, B.N. Ellison and M. Birk, "Superconducting Integrated Receiver development for TELIS", presented at the 12th International Symposium on Remote Sensing, 19-22 September 2005, Bruges, Belgium. Sensors, Systems, and Next-Generation Satellites IX; Roland Meynart, Steven P. Neeck, Haruhisa Shimoda; Eds., Proc. of SPIE, vol. 5978 (2005), p. 440-450.

[10] R.W.M. Hoogeveen, P.A. Yagoubov, G. de Lange, A. de Lange, V. Koshelets, M. Birk, B. Ellison, "Balloon borne heterodyne stratospheric limb sounder TELIS ready for flight", presented at the SPIE European Remote Sensing Conference 2007 in Florence, September 2007; SPIE European Remote Sensing Conference, Proceedings of SPIE, 6744, 67441U-1- 67441U-10, 2007.

[11] Gert de Lange, Pavel Yagoubov, Hans Golstein, Leo de Jong, Arno de Lange, Bart van Kuik, Ed de Vries, Johannes Dercksen, Ruud Hoogeveen, Valery Koshelets, Andrey Ermakov, and Lyudmila Filippenko, "Flight configuration of the TELIS instrument", presented at the *19th International Symposium on Space Terahertz Technology (ISSTT-08)*, Groningen, the Netherlands, April 2008, report 10-2; this Proceedings.

[12] [13] V. P. Koshelets, S. V. Shitov, A. V. Shchukin, L. V. Filippenko, J. Mygind, and A. V. Ustinov, "Self-Pumping Effects and Radiation Linewidth of Josephson Flux Flow Oscillators", *Phys Rev B*, vol. 56, p. 5572-5577, 1997.

[14] P.N. Dmitriev, I.L. Lapitskaya, L.V. Filippenko, A.B. Ermakov, S.V. Shitov, G.V. Prokopenko, S.A. Kovtonyuk, and V.P. Koshelets. "High Quality Nb-based Integrated Circuits for High Frequency and Digital Applications", "*IEEE Trans. on Appl. Supercond.",* vol. 13, No 2, pp. 107-110, June 2003.

[15] M.Yu. Torgashin, V.P. Koshelets, P.N. Dmitriev, A.B. Ermakov, L.V.Filippenko, and P.A. Yagoubov, "Superconducting Integrated Receivers based on Nb-AlN-NbN circuits" presented at the Applied Superconductivity Conference ASC-2006. Seattle, USA, August 2006, report 3EG08, "*IEEE Trans. on Appl. Supercond.",* vol. 17, pp.379- 382, 2007.

[16] A.B. Ermakov, O.S. Kiselev, V.P. Koshelets, P.A. Yagoubov, G. de Lange, B. van Kuik, "Superconducting Integrated Receiver for TELIS optimization and computer control", presented at the *19th International Symposium on Space Terahertz Technology (ISSTT-08)*, Groningen, the Netherlands, April 2008, report P6-5.

[17] V.P. Koshelets, S.V. Shitov, A.V. Shchukin, L.V. Filippenko, and J. Mygind, "Linewidth of Submillimeter Wave Flux-Flow Oscillators"; *Appl. Phys. Lett.*, vol. **69,** pp. 699-701, July 1996.

[18] V.P. Koshelets and J. Mygind, **"**Flux Flow Oscillators For Superconducting Integrated Submm Wave Receivers", Studies of High Temperature Superconductors, edited by A.V. Narlikar, NOVA Science Publishers, New York, vol. 39, pp. 213-244, 2001.

[19] V.P. Koshelets, A.B. Ermakov, P.N. Dmitriev, A.S. Sobolev, A.M. Baryshev, P.R. Wesselius, J. Mygind, "Radiation linewidth of flux flow oscillators", *Superconductor Science and Technology,* **v. 14,** pp. 1040 - 1043, 2001.

[20] V.P. Koshelets, S.V. Shitov, P.N. Dmitriev, A.B. Ermakov, L.V. Filippenko, V.V. Khodos, V.L. Vaks, A.M. Baryshev, P.R. Wesselius, J. Mygind, "Towards a Phase-Locked Superconducting Integrated Receiver: Prospects and Limitations", *Physica C*, **367,** pp. 249 - 255, 2002.

[21] A. L. Pankratov, "Form and width of spectral line of a Josephson flux flow oscillator", *Phys. Rev. B*, vol. 65, p. 054504-(1-9), 2002.

[22] V.P. Koshelets, A.B. Ermakov, S.V. Shitov, P.N. Dmitriev, L.V. Filippenko, A.M. Baryshev, W. Luinge, J. Mygind, V.L. Vaks, D.G. Pavel'ev, "Superfine Resonant Structure on IVC of Long Josephson Junctions and its Influence on Flux Flow Oscillator Linewidth", *IEEE Trans. on Appl. Supercond.,* **v.11,** No 1, pp. 1211-1214, 2001.

[23] P. Berberich, R. Buemann, and H. Kinder, "Monochromatic Phonon Generation be the Josephson Effect", Phys. Rev. Lett, vol. 49, No. 20, pp. 1500 – 1503, Nov. 1982.

[24] V.P. Koshelets, S.V. Shitov, L.V.Filippenko, P.N. Dmitriev, A.B. Ermakov, A.S. Sobolev, M.Yu. Torgashin, A.L. Pankratov, V.V. Kurin, P. Yagoubov, R. Hoogeveen. "Superconducting Phase-Locked Local Oscillator for a Submm Integrated Receiver", *Superconducting Science and Technology*, **v.** 17, pp. $127-$131, 2004.

[25] A.L. Pankratov, V.L. Vaks, and V.P. Koshelets, "Spectral properties of phase locked Flux Flow Oscillator", *Journal of Applied Physics,* vol. 102, 0629, pp. 1-5, 2007.

[26] A.V. Khudchenko, V.P. Koshelets, P.N. Dmitriev, A.B. Ermakov, P.A. Yagoubov, and O.M. Pylypenko, "Cryogenic Phase Detector for Superconducting Integrated Receiver" "*IEEE Trans. on Appl. Supercond.",* vol. 17, pp. 606-608, 2007.

[27] E. Schomburg, R. Scheuerer, S. Brandl, K.F. Renk, D.G. Paveliev, Yu. Koschurinov, V. Ustinov, A. Zhukov, A. Kovsh, P.S. Kop`ev, *Electronics Letters,* vol.35, No.17, 1999.

[28] Specification of the R&S®SMF100A Microwave Signal Generator; Available: http://www2.rohde-schwarz.com/product/smf100a.html

A Schottky-Diode Balanced Mixer for 1.5 THz

Neal R. Erickson

Astronomy Department, University of Massachusetts, Amherst, MA, USA

Contact: neal@astro.umass.edu

***Abstract*— We report on the first THz balanced mixer/upconverter using a Schottky diode MMIC chip. Using an optically pumped laser at 1562 GHz as an LO source with a coupled power of about 1 mW, and an IF frequency of 10 GHz, we obtained a sideband output power of 23 uW (sum of two sidebands). As a mixer we obtain a conversion loss of 12.4 dB DSB and a noise temperature of 5600 K DSB. Response is believed to be similar over a band 1250-1650 GHz.**

I. Introduction

In the THz range there is a need for room temperature mixers to act as both downconverters and upconverters using laser local oscillators. In these applications the relatively high LO power required by Schottky diodes is not a problem. In these applications mixers primarily use whisker contacted Schottky diodes in cube-corner mixers, originally reported 30 years ago [1]. While the cube-corner mixer is very simple, it has a very poor beam pattern and is compatible only with whiskered diodes. This paper reports on the first THz balanced mixer built using a planar diode MMIC in waveguide. The requirement to develop this mixer came from a need for a frequency agile sideband generator at 1.5 THz with >10 μW output power which would use a laser as one input and a 5-40 GHz microwave synthesizer as the other. The typical cube corner in this application can produce only 1 μW and impedance matching is difficult with high offset frequencies.

II. Mixer Design

The application was a proof of concept, so it had to use existing devices. The MMIC used in this work was designed as a frequency doubler for 1.5 THz, developed at JPL for the Herschel HIFI program [2]. THz varactor diodes are essentially the same as mixer diodes since high doping ($5x10^{17}/cm^3$) is needed to avoid velocity saturation, and breakdown voltage is low (~4V) since large drive voltage amplitude is not practical. The device is built on 3 μm thick GaAs with beam lead contacts for ground and bias. The circuit geometry is the same as that for a balanced mixer as shown in figure 1, except that there is no external terminal for the IF port. The IF port was added by contacting the input waveguide probe with a gold wire, and bringing this wire out through a 50 ohm microstrip line. A balanced mixer has the advantage of separate LO and signal ports, and in principle, high isolation between them. This means that no diplexer is required at the mixer input. The doubler chip as used in the mixer is shown in Fig 2.

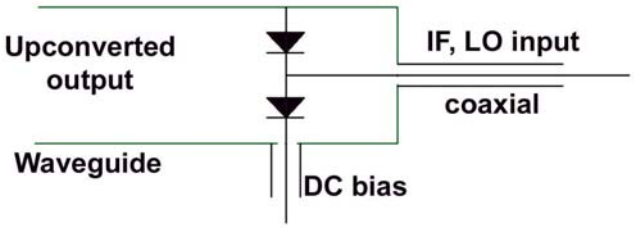

Fig 1. Schematic diagram of a balanced mixer with coaxial input on the right and waveguide output on the left. The doubler circuit is identical except that the input frequency is half of the output.

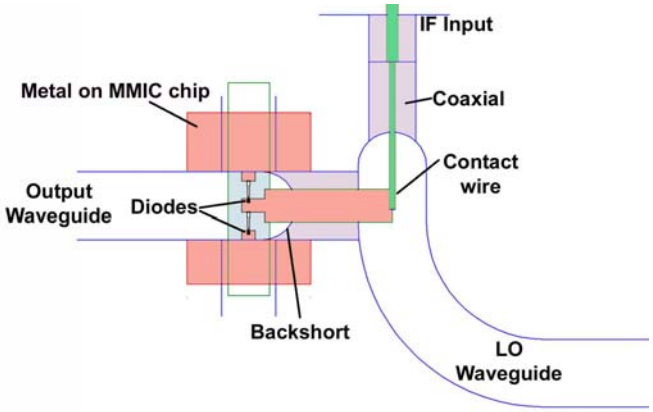

Fig 2 Balanced mixer cross section using a diode designed for a balanced doubler. The contact wire is 6 um gold alloy. Blue shaded areas are TEM lines, and reddish areas are metal on the MMIC chip.

The block was machined with conventional tools in brass with a CNC micro-milling machine [3], and the block was then gold plated. Both waveguides are 80 x 160 um, stepping up to square cross section before transitioning to diagonal feedhorns on both input and output ports. The final aperture sizes of each were 1.5 mm (diagonal). Details of the block are shown in Figure 3. The IF port used a K type connector to allow tests up to 40 GHz, but no care was used to maximize the IF bandwidth by design of the IF circuit.

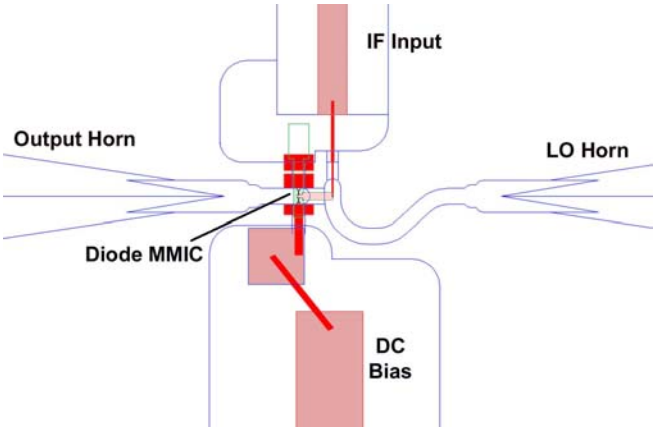

Fig 3. Balanced mixer cross section showing the input/output horns and DC and IF circuits. A parallel plate capacitor bypasses the bias port at IF frequencies while an on-chip capacitor bypasses this port at the RF.

III. Upconversion Results

Tests were done using an optically pumped laser at 1562 GHz, with a power level of ~10 mW which was attenuated to 1 mW at the mixer input (as measured by a coupling aperture comparable to that of the feed horn). The IF frequency was 10 GHz with 1 mW power level. DC bias of 0.5 mA was applied with the conversion efficiency rising with bias. The sum of these inputs totals about 2.5 mW which is all dissipated in two diodes on a poor heat sink, so there was some concern about increasing the power levels beyond this point. At this drive the output power in the two sidebands is 23 µW with only 4.5 µW of LO feedthrough (~23 dB LO-RF isolation). The THz input and output power was measured with a waveguide calorimeter (Erickson Instruments PM4 [4]) built in WR10 waveguide with no transition between the horn and the waveguide in the sensor. The size of the horns and WR10 waveguide are fairly similar so coupling was expected to be good.

Figure 4 shows the power output vs drive power. Output power is increasing with each of the inputs, up to the maximum applied, so there is the potential for significantly higher output power if the diodes do not burn out. These diodes are known to fail at ~5 mW DC input, serving as an absolute limit, but the RF coupling to the diodes is not well known. The prediction from Agilent ADS is that with 1 mA bias and twice the LO and IF power, the output power will double.

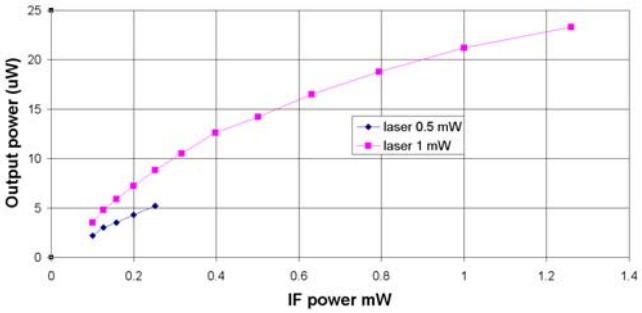

Fig 4. Output power vs input drive at 1562 GHz.

Tests at higher offset frequencies showed the same power output up to an IF of 40 GHz, using the same drive level at the mixer diodes as derived from the bias voltage. IF coupling is not flat across this band, so the IF power varied with frequency. The bandwidth is predicted to be 1250-1650 GHz, and two other laser frequencies (1272 and 1621 GHz) have been tested. At both the input power was poorly calibrated because the laser mode was very poorly matched to the feed horn, but the DC bias conditions were the same as at 1562 GHz, so the power reaching the diodes is the same. Output power was 17 µW at 1272 GHz with 2.5 µW of LO feedthrough power, while at 1621 GHz the output was 21 µW with 5.5 µW of feedthrough. Thus the output circuit coupling is fairly flat over the band, but we can say nothing about the input circuit. This result confirms the prediction that LO to RF isolation is better at lower frequencies in this band.

IV. Downconverter Results

Measurements have been made as a conventional mixer downconverter only at 1621 GHz.. The IF source was replaced by a 3 GHz IF amplifier with an isolator on the input, and an IF noise temperature of 214 K. With an estimated LO power of 1 mW (the same as for upconversion testing) and a bias current of 1 mA, the Y factor of the receiver was measured with room temperature and liquid nitrogen cooled loads. This yields a complete receiver noise temperature of 9300K DSB. Conversion loss is 12.4 dB DSB and the derived mixer noise temperature is 5600 K DSB. This noise is a substantially lower than cube-corner mixers at similar frequencies and the beam pattern should be much better [5]. In fact it compares rather favorably with HEB mixers, given that these results are at room temperature, but it should be noted that THz Schottky mixers show relatively little noise reduction when cooled to 20 K, perhaps by only a factor of two, due to the high doping of the diodes. However, this mixer has very wide IF bandwidth, potentially extending beyond 40 GHz.

V. Future work

To follow up this work, a new wafer run is planned to make devices specifically as mixer/upconverters. The same design will be used with an added IF terminal, but in addition the design will be scaled to as high as 3 THz. For higher power, four anode circuits also will be tried.

At these higher frequencies a quantum cascade laser could be the LO, leading to a simple all solid state LO with wide tunability. The IF offset frequency can be exceed 100 GHz. For use as an LO, image rejection is possible using an SSB upconverter design, which is relatively simple to fabricate

CONCLUSIONS

Planar Schottky diode MMIC's can serve as efficient upconverters and low noise mixers well into the THz range, offering room temperature operation. This new balanced mixer also separates the LO and IF ports, making an extremely simple, compact receiver requiring no LO/signal diplexer.

ACKNOWLEDGMENTS

The author wishes to thank R. Grosslein for machining the block and J. Wielgus for the assembly. I. Mehdi of JPL provided the diodes from the Herschel program. M. Coulomb and T. Goyette of the UMass Lowell Submillimeter Technology Lab provided the laser and assisted in the tests.

REFERENCES

[1] H.R. Fetterman, P.E. Tannenwald, B.J. Clifton, C.D. Parker W.D. Fitzgerald and N.R. Erickson, "*Far-IR Heterodyne Radiometric Measurements with Quasioptical Schottky Diode Mixers*," Appl. Phys. Lett., vol 33, pp 151-154, 1978.

[2] A. Maestrini, J. Bruston, D. Pukala, S. Martin and I. Mehdi, *"Performance of a 1.2 THz Frequency Tripler Using a GaAs Frameless Membrane Circuit,"* IEEE MTT-S Int'l Microwave Symposium (Phoenix), pp. 1657-1660, May 2001.

[3] G. Narayanan, N. Erickson, R. Grosslein, "Low Cost Direct Machining of Terahertz waveguide Structures," *Tenth International Symposium on Space Terahertz Technology*, pp. 518-528, Mar. 99.

[4] N. Erickson, "A Fast and Sensitive Submillimeter Waveguide Power Meter," *Tenth International Symposium on Space Terahertz Technology*, pp. 501-507, Mar. 99.

[5] P.F. Goldsmith, H.R. Fetterman, B.J. Clifton, C.D. Parker and N.R. Erickson, *Cryogenic Operation of Submillimeter Quasioptical Mixers*, International Journal of IR and MM Waves, vol 2, pp. 915-924, 1981.

Development and Characterization of THz Planar Schottky Diode Mixers and Detectors

Jeffrey L. Hesler[1,2,*], Haiyong Xu[2], Alex Brissette[1], and William L. Bishop[1]

[1]*Virginia Diodes Inc, Charlottesville, VA 22902, USA*

[2]*University of Virginia, Charlottesville, VA 22902, USA*

* Contact: Hesler@virginiadiodes.com, phone +01-434-297-3257

***Abstract*— The characterization of a 1.1-1.7 THz planar Schottky-diode mixer is described. Initial measurements yielded a mixer noise temperature of 5900 K (DSB) and conversion loss of 12 dB (DSB) at 1.57 THz. The responsivity of the mixer was measured to be higher than 200-400 V/W over the frequency range 1.1-1.5 THz. Also, the same diode was used as a 2nd harmonic mixer as part of a solid-state 1.45-1.5 THz transceiver, with measured dynamic range of > 40-50 dB.**

I. Introduction

The Schottky diode has a long history of use for both heterodyne and direct detection of power at submm-wavelengths. Schottky diodes have the advantage that they can operate at ambient or cryogenic temperature, allow for long integration times, and also have an extremely fast response time compared with other detection technologies. This paper describes the development and characterization of planar Schottky diode mixers and detectors in the frequency band 1.1-1.7 THz.

II. Mixer Characterization

The mixer, pictured in Figure 1, consists of a waveguide housing with an integral smooth-walled diagonal feedhorn. These mixers are single-moded waveguide-based devices without any tuners. The basic mixer design is similar to that described in [1], and consists of a planar Schottky diode integrated onto a quartz substrate.

The initial characterization consisted of measurements of the voltage responsivity of the mixers. The mixers were biased to a constant current of 3 uA and the voltage video response to applied RF power was measured. The source was a solid-state 1.1-1.5 THz VDI multiplier chain with output power 0.5-2 uW typical. The power was calibrated using an Erickson PM4 calorimeter [2].

In order to speed up the initial characterization a simple quasi-optical setup was used, consisting of pointing the two horns at each other with a very small (~0.5 mm) distance between them. No lenses were used. In addition to the simple alignment, this setup minimizes the effect of water losses on the measurements. The two horns are smooth-walled diagonal feedhorns with directivity of approximately 22 dB. No corrections were made for the quasi-optical loss. The measured responsivity is shown in Figure 1. A standing wave is evident in the measured responsivity. Detailed measurements with a full quasi-optical setup are underway to determine the responsivity more accurately.

In addition to the responsivity measurements, the device was also characterized as a mixer. A CO2 pumped FIR cavity laser at 1.57 THz was used as the local oscillator, with available power about 3 mW. A Martin-Puplett diplexer was used to combine the RF and LO signals. The measured mixer performance was a noise temperature of 5900 K (DSB) and a conversion loss of 12 dB (DSB).

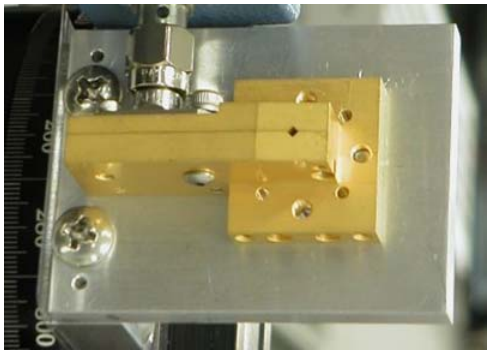

Fig. 10 Photograph of the WR-0.65FM 1.1-1.7 THz fundamental mixer

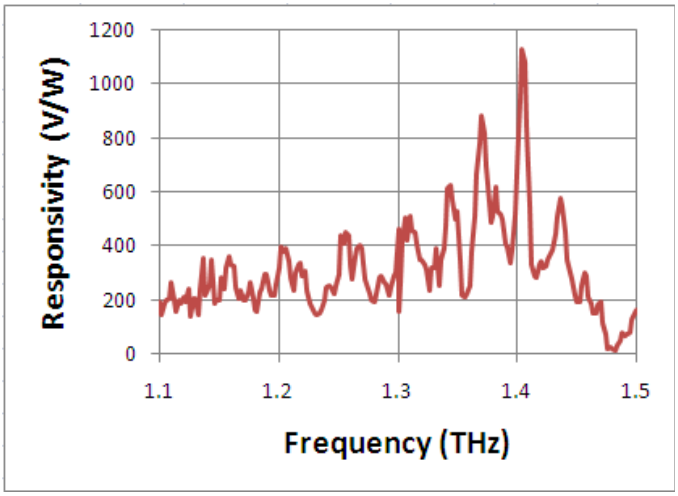

Fig. 2 Measured responsivity of the WR-0.65FM 1.1-1.7 THz fundamental mixer. Measured with 3 uA bias current, and horn-to-horn coupling without intervening lenses

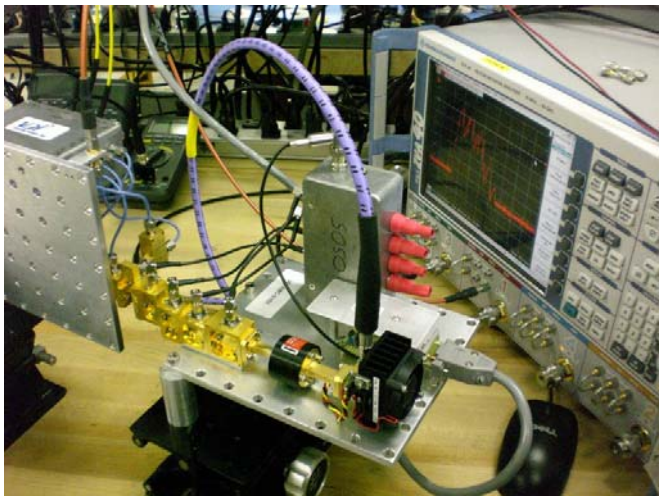

Fig. 3 Photograph of the 1.43-1.54 THz transmitter and receiver during testing. The transmitter has typical output power 5-20 uW over the band

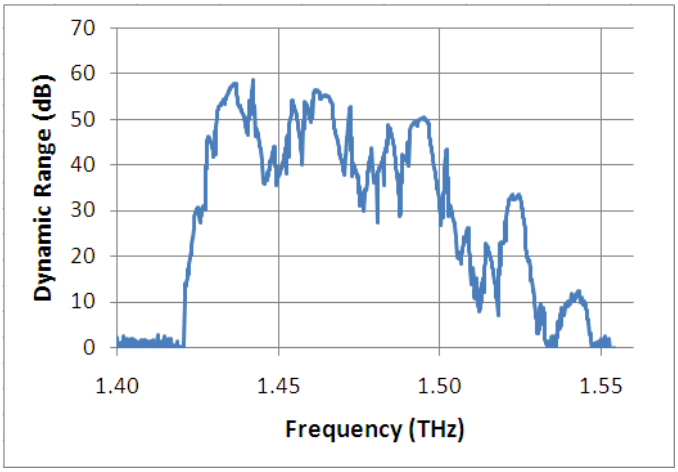

Fig. 4 Measured dynamic range of the THz transceiver with 100 Hz IF bandwidth. Measured with horn-to-horn coupling without intervening lenses.

III. THz Transceiver

THz planar Schottky-diodes from the same fabrication run were also used in a subharmonic mixer configuration to build a solid-state THz transceiver. The transmitter, pictured in Figure 3, consisted of an amplifier followed by a series of frequency multipliers, and had an output power of 5-20 uW over the frequency range from 1440-1540 GHz. The final tripler in the transmitter has an integral smooth-walled diagonal horn with nominal 22 dB directivity.

The receiver was a subharmonically pumped single-diode mixer. The local oscillator pump was provided by a solid-state amplifier multiplier chain with 0.2-0.6 mW over the frequency range from 710-760 GHz. The mixer was biased at 0.5 mA constant current through a bias tee. The transceiver was driven by dual synthesizers from a Rohde & Schwarz ZVA40 Vector Network Analyzer (which can be seen in Figure 3). The synthesizers were set to a fixed offset to provide a fixed IF over the band. The integral feedhorns of the transmitter and receiver were pointed at each other without intervening optics, and no corrections were made for quasi-optical loss. The measured dynamic range of the system is shown in Figure 4, and was measured to be about 40-50 dB over the frequency range.

Conclusions

A 1.1-1.7 THz planar Schottky-diode mixer with excellent sensitivity has been successfully developed. The mixer has a noise temperature of 5900 K (DSB) and a conversion loss of 12 dB (DSB) at 1.57 THz. Initial measurements of the responsivity of a Schottky mixer indicated a responsivity of better than 200-400 V/W over the range 1.1-1.5 THz. A solid-state transceiver was developed using this mixer in a second harmonic configuration, which exhibited 40-50 dB dynamic range over a bandwidth of 70 GHz. Further measurements are underway to test zero-bias detectors and sideband generators.

References

[1] J.L. Hesler et al, "Fixed-Tuned Submillimeter Wavelength Waveguide Mixers Using Planar Schottky-Barrier Diodes," IEEE Trans. Microwave Theory Tech., vol. 45, pp. 653-658, May 1997.

[2] Erickson Instruments Ltd., www.ericksoninstruments.com.

Ultrawideband THz detector based on a zero-bias Schottky diode

Sydlo[1], O. Cojocari[1], D. Schoenherr[2], T. Goebel[2], S. Jatta[2],
H.L. Hartnagel[2] and P. Meissner[2]
[1]*ACST GmbH, Darmstadt, Germany (sydlo@acst.de)*
[2]*TU Darmstadt, Darmstadt, Germany*

The work in the field of THz technology includes the emitters as well as the detectors. While a large number of approaches for THz emitters with increased power levels are evolving the detectors have show less progress in the last years. But essential for all THz work is the signal to noise ratio which also benefits from improved detectors.
Nowadays, pyroelectric detectors and Golay cells are the most common room-temperature THz detectors available. They feature NEPs (noise-equivalent powers) down to 100 pW/Hz^{½}, but their response time is quite large limiting the modulation to few tens Hertz. These detectors are quite bulky which inhibits flexible use.

ACST has recently established a Schottky process for zero-bias detector diodes aiming at frequencies up to one THz and possibly higher. A specialised process allows forming of Schottky contacts with a very low barrier. This in turn provides low video resistances without the need for biasing. Due to the absence of bias, the noise of the detectors reduces to the Johnson limit of the video resistance and is free of 1/f noise. The presented devices exhibit a video resistance less than 10 kΩ at zero-bias and voltage noise of less than 15 nV/Hz^{½} (measurements in full paper). Also the devices responsitivity shows values of more than 15 A/W or 2500 V/W. This results in a NEP of less than 6 pW/Hz^{½} combined with arbitrarily high modulation frequencies. The size of this detector with appendant amplifier is smaller than a matchbox (picture in full paper) allowing it to be placed and moved freely in any THz setup. However, it should be mentioned here, that this detector cannot compete yet with pyroelectric detectors or Golay cells at frequencies far beyond 1 THz.
The main frequency limiting factors for the Schottky detectors are the RC time constant and the size of the diode. The diodes size should be small compared to the effective wavelength to diminish effects of the geometry. The RC time constant is formed by the total capacitance of the diode and the RF impedance of the antenna. In this work a planar logarithmic-spiral antenna has been deployed with circular polarisation to be independent of the polarisation angle in case of linear polarised THz radiation. Hence, the responsitivity of the detector reduces to half of its value due to the coupling of linear to circular polarisation. ´The impedance of the antenna is around 50 Ω and the total capacitance of the diode is around 3 fF resulting in a roll-off frequency of about 1 THz. First measurements up to 700 GHz have revealed no sign of a roll-off (measurements >1 THz in full paper). Further measurements will be carried out for the full paper.

This work presents a very compact, highly sensitive and fast THz detector based on RF rectification by a Schottky diode. It suits ideally the needs for fast spectroscopy due to the very fast response time and high sensitivity. The developed process allows for larger integration into arrays for imaging applications

Schottky Diode Mixers on Gallium Arsenide Antimonide or IndiumGalliumArsenide?

Erich Schlecht* and Robert Lin

Jet Propulsion Laboratory, California Institute of Technology, Pasadena, CA, 91109, USA

* Contact: Erich.Schlecht@jpl.nasa.gov, phone +01-818-354-4887

***Abstract*— We have investigated the suitability of using two low-barrier ternary III-V compounds, InGaAs and GaAsSb for Schottky mixers. These materials have lower band-gaps than GaAs, and hence their Schottky barrier heights are lower than those on GaAs. We have found that for Schottky diode mixers employing DC bias, these materials do not yield a reduction in required LO power. However, for mixers that are zero-biased (such as many that are subharmonically pumped), use of these materials in mixers will give a large reduction in required LO power.**

I. Introduction

Schottky mixers remain the heterodyne technology of choice for many submillimeter/ Terahertz applications due to their fair sensitivity and capability for operation at room temperature. For space missions they have one drawback that would be advantageous to overcome: a relatively high local oscillator (LO) pump power requirement. The LO power is required to drive the diode to a high enough current level that it is full switched on.

Diode mixers can be thought of as a switch used to sample the RF signal at the LO frequency. [1, 2]. The diode is a modulated conductance whose peak value should be substantially higher than the RF source conductance presented by the circuit. However, to achieve this the diode must be pumped to an average conductance that is on the order as the RF [2].

The conductance of the diode is determined from it's current using the standard modified thermionic equation. The current at temperature T Kelvins is given by:

$$I = AA^*T^2 \exp\left(-q\Phi_{B0}/kT\right)\left[\exp\left(qV/nkT\right)-1\right] \quad (1)$$

with A being the diode area, A^* the modified Richardson constant (given by m*/m ×120 A/cm^2/K^2, Φ_{B0} the zero-bias barrier height, and n is the ideality factor that models edge and tunneling current effects. Taking the derivative,

$$G \equiv \frac{\partial I}{\partial V} = \frac{q}{nkT} I \quad (2)$$

Hence, the peak conductance is strongly dependent on the barrier height, Φ_{B0}, due to the exponential dependence of I and G. Sub millimeter wave mixers have traditionally been fabricated using metal-on-GaAs contacts with a typical barrier height of around 0.9 to 1.0 eV. Reduction of the barrier height by a few tenths of an eV will give the same values of G at diode forward voltage, V, several tenths of a volt lower, resulting in an LO power reduction of LO pump power to one fourth or one fifth of that required by GaAs. In this paper we investigate suitable materials to accomplish this.

II. Reduction of LO power details.

Many mixers are unbiased, relying on the rectified LO signal to drive the diode to the needed conductance. These mixers include most submillimeter subharmonically pumped mixers, as well as balanced mixers used at lower frequencies. In this case, the peak LO power can be estimated by first determining the current from the above equation. The LO power can be estimated by converting the peak current to RMS and multiplying by the RMS pump voltage whose peak is close to the diode built-in voltage,

$$V_{b0}: P_{LO} \approx \frac{1}{2}\frac{nkT}{q} G V_{b0} \quad (3)$$

Using a typical embedding impedance of 100 ohms that circuits in this frequency range can achieve, experience indicates the peak conductance should be around 100 mS (10 ohms). At room temperature using a diode with n=1 thus requires a peak LO current of 2.6 mA. If the diode built-in voltage is 0.8, this gives a required diode pump power of about 1 mW per diode. The circuit as a whole will require more, because of losses in the circuit and in the series resistance of the diode.

One way to reduce this requirement is to reduce the pump voltage needed by reducing the barrier voltage, since $qV_{b0} = \Phi_{B0} - qV_n$, with qV_n, being the difference in energy between Fermi level and the bottom of the conduction band in the bulk epi. This is only a few hundredths of an eV in the relatively highly doped diodes used at submillimeter wave freqeuncies, so equation (3) predicts that *reducing the barrier voltage by half will reduce the LO power requirement by half.*

III. Required low-barrier material properties

In order to be useful as a mixer, the material must have several properties, in addition to the low barrier height. To determine their importance, we consider the overall insertion loss. Reference [3] gives a general approximate equation:

$$Loss = \left(1+\frac{R_S}{R_{IF}}\right)\left(1+\frac{R_S}{R_{RF}}+\omega^2 C_j^2 R_S R_{RF}\right) L_{\min} \quad (4)$$

where R_S is the series resistance, R_{RF} and R_{IF} the RF and IF embedding resistances and C_j the average junction capacitance. The quantity $1/C_j^2 R_S R_{RF}$ can be considered the mixer "cutoff frequency", F_{CO}. For properly pumped mixers

C_j is in the neighborhood of 1.5 times the zero-bias capacitance, ie.:

$$C_j \approx 1.5 \times A \sqrt{\frac{q\varepsilon N_D}{2V_{b0}}} \tag{5}$$

L_{min} is the minimum loss that can be determined from the conductance ratio [4]. Under ideal conditions, assuming matched resistances, L_{min} is 3 dB. Note that the assumption has been made that the average junction conductance is matched to R_{RF}. The series resistance is given by:

$$R_S = R_{FIX} + \frac{t_e}{Aq\mu N_D} \tag{6}$$

with R_{FIX} being an area independent resistance associated with the ohmic contact, and μ the mobility. Figure 1 shows the dependence of the cutoff frequency on

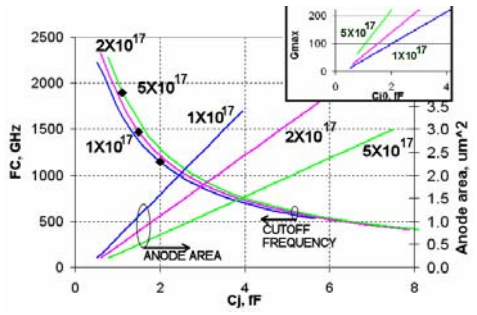

Fig. 1. Diode cutoff frequency and anode size variation with zero-bias capacitance. Inset showss maximum conductance for various diode sizes.

zero-bias junction capacitance, C_{j0} for three different donor concentrations. As can be seen, the F_{CO} is almost unaffected by the doping concentration, although higher dopings are slightly favored. The main limitation on doping is the greater difficulty of lithography needed to fabricate smaller anodes. Figure 1 also indicates the required anode sizes for the three dopings. Clearly, smaller diodes are better, despite the increased series resistance.

As pointed out in [4, 5] points out, the diode area is limited by current saturation. McColl [4] uses the maximum current density of the thermionic diode model. However, actual velocity saturation due to inter-valley transfer occurs at lower current densities, limiting the maximum velocity to around 1.5×10^7 cm/s. In addition, there is substantial electron heating at that velocity [6], which will add directly to mixer noise. Keeping the heating to a minimum would dictate keeping the peak velocity to around 1×10^7 cm/s. The inset to Figure 1 shows the maximum diode conductance vs C_{j0} for the three dopings. If the target maximum conductivity value is 100 mS, then the minimum C_{j0} values would be around 2, 1.5 and 1.1 fF for dopings of 1×10^{17}, 2×10^{17}, and 5×10^{17} cm^{-3} respectively. These limits are indicated on Figure 1 by the black diamonds.

Clearly the primary qualities needed for the Schottky mixer diode materials are: good mobility and high peak velocity.

IV. Selection of Materials

First, we will find a compound with a Schottky barrier height of about half that of GaAs, around 0.5 eV. Figure 2a shows a band-gap/lattice constant plot of several ternary III-V combinations. The lines connecting the binary endpoints indicate change of band-gap and lattice constant values for various mixtures of the end-point compounds. Considering that the Schottky barrier height is about half to two thirds of the bandgap, are looking for a band-gap of about 0.7 or 0.8 eV. The material GaSb has a gap of 0.7, InAs substantially less. So we will consider the trinary combinations of InGaAs and GaAsSb.

Figure 2b shows the variation of measured Schottky barrier heights of InGaAs and GaAsSb with In or Sb fraction [7, 8]. To yield a barrier height of 0.5 requires InGaAs with an In fraction of 0.25 or so, and GaAsSb with a Sb fraction of about 0.5.

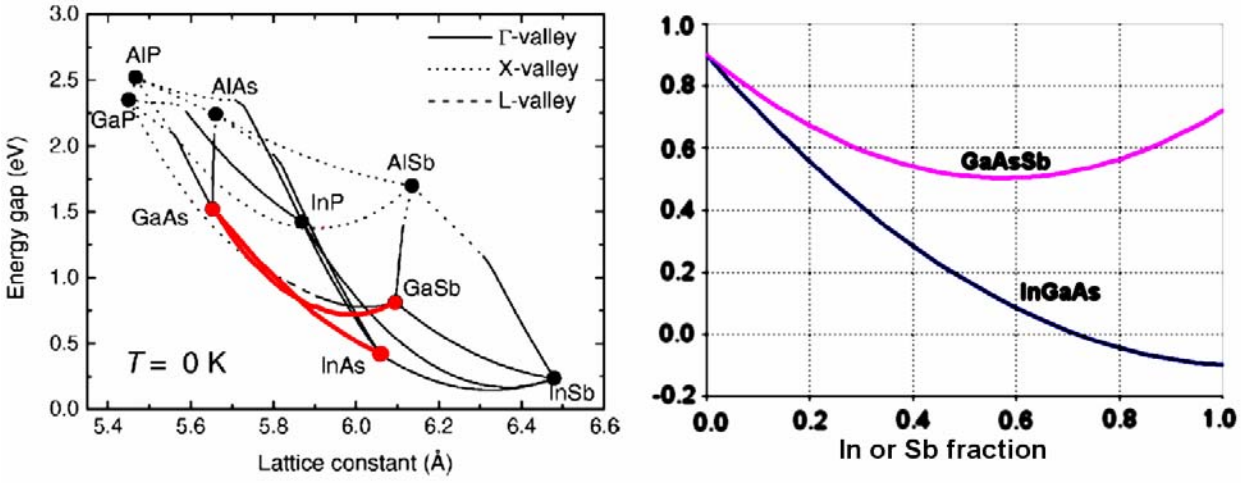

(a) (b)

Fig. 2. (a) Ternary chart of bandgap and lattice constant. (b) Variation of barrier height with In and Sb fraction of InGaAs and GaAsSb.

Let's examine the other properties of these materials. Figure 3 a shows the mobility of GaAsSb and InGaAs doped to 2.3×10^{17} cm^{-3} [9, 10]. As is clear, $In_{0.25}Ga_{0.75}As$

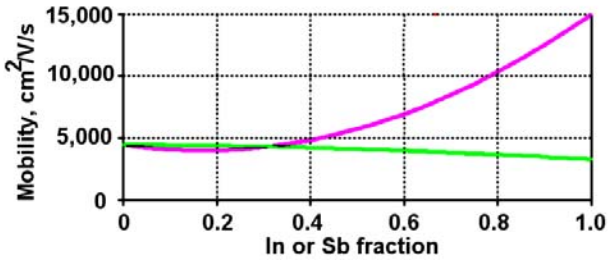

Fig. 3. Variation of material InGaAs and GaAsSb low-field mobility with In and Sb fractions. The donor concentration is 2.3×10^{17} cm^{-3}.

and $GaAs_{0.5}Sb_{0.5}$ have essentially the same mobility as GaAs. Also, since both the mobilities and dielectric constants of the materials are very close to that of GaAs; so Figure 1 is applicable to $In_{0.25}Ga_{0.75}As$ and $GaAs_{0.5}Sb_{0.5}$ for determining the cutoff frequency, according to equations (5) and (6).

The peak electron velocities of InAs and GaSb are quite different from that of GaAs. The electron velocity of InAs does not reach a peak (i.e. there is no Gunn effect in InAs). Instead it saturates in the range of 7×10^7 cm/s. The reason is quite simple: velocity saturation is caused by electrons being accelerated to high enough energy to begin phonon assisted scattering out of the central Γ conduction energy-momentum valley into the upper X or L valleys, which have much lower electron mobilities. The L valley is about 0.29 eV above the Γ in GaAs, but for InAs it is a full 0.73 eV higher, thus essentially eliminating transfer to the upper valley.

GaSb is quite different. The L-valley is only 0.1 eV (a few kT/q) above the Γ valley, so electrons readily jump into the L-valley, and electron velocity saturates at around 6×10^6 cm/s [11], making GaSb a poor candidate for mixer use, not only because of velocity saturation, but because of the inter-valley noise that would accompany the process. Nevertheless, we will ignore this effect in the case of $GaAs_{0.5}Sb_{0.5}$, assuming it is more like GaAs. Nevertheless, before it is seriously considered for mixer diodes, its velocity peak value should be examined.

V. Mixer Analysis

Diodes using these materials were compared using a Harmonic Balance simulator based on [12] using the additions for electron heating as described in [13]. The diode properties were calculated using the information presented above. The conduction current-voltage relation was calculated using the matrix method [14] that incorporates the effect of tunneling current. The embedding resistances were fixed at 100 ohms for LO and RF, and 200 ohms for the IF. The RF reactances were adjusted for optimum performance to compensate for diode capacitance. The doping was set, somewhat arbitrarily at 2×10^{17} cm^{-3}. The LO frequency is 560 GHz.

Figure 4a shows the relevant curves for GaAs, $In_{0.25}Ga_{0.75}As$ and $GaAs_{0.5}Sb_{0.5}$. The mixer is biased, and the LO power level set to 1 mW at the diode. Included for comparison is a calculation based on the authors' work [15] for GaAs. This includes the effect of intervalley transfer in order to model the time-dependent effects of current saturation. This calculation exaggerates the effect because it assumes the entire undepleted epi region has the same fraction of electrons in the upper valley, while Monte Carlo simulations indicate that electron transfer to the upper valley is confined to an area concentrated under the anode. Nevertheless, the diode size where the effect becomes important, around 1.5 fF concurs with Figure 1. Figure 4b includes the same calculation for an LO power level of 0.1 mW. Both calculations indicate that all three materials have similar performance, with the GaAs being consistently, if slightly better. This is due to the fact that

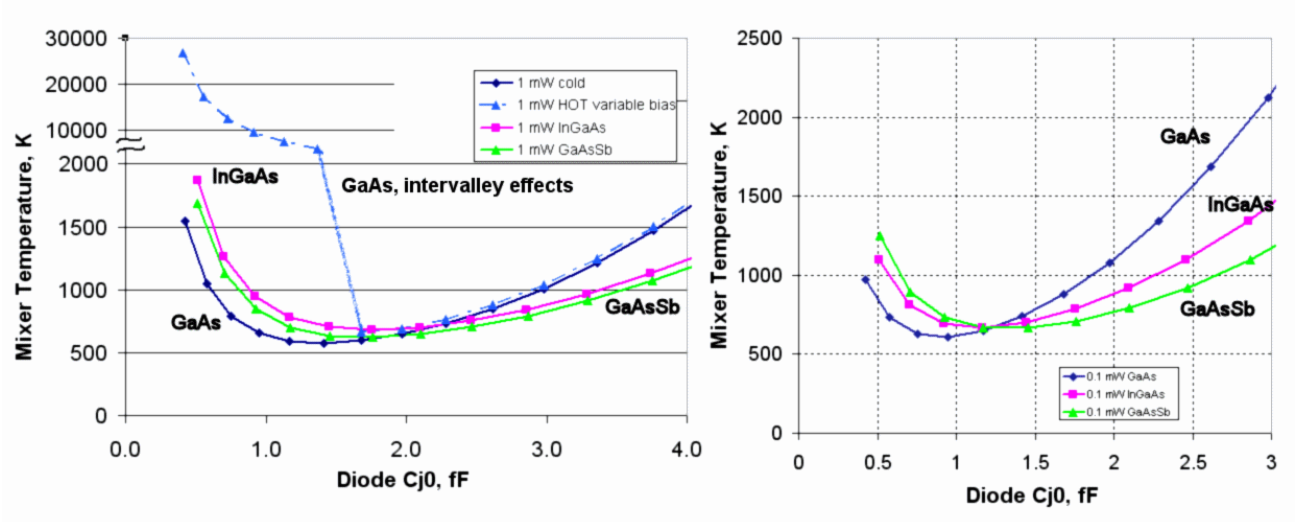

(a) (b)

Fig. 4. Variation of DSB mixer noise temperature with diode size for LO powers of: (a) 1 mW (b) 0.1 mW at the diode level. DC bias is optimized for all cases.

the GaAs ideality factor is better, at least assuming a perfect

interface. Since the barrier heights of $In_{0.25}Ga_{0.75}As$ and $GaAs_{0.5}Sb_{0.5}$ are lower, they have increased tunneling current components, yielding increased ideality factors. A higher ideality factor leads to a lower diode on/off conductance ratio, giving decreased minimum conversion loss and hence a higher mixer temperature.

To explore the effect of LO power on performance using the three materials, a diode with a C_{j0} of 1 fF was analyzed, sweeping the LO power level from 50 μW to 4 mW. Figure 5a indicates the performance with variable bias. As the previous result suggested, the GaAs diode remains the best choice, given variability of DC bias. This is explained by noting that the diode can be biased to the point of optimum conductance ratio, independent of barrier height.

Contrarily, Figure 5b depicts the mixer behavior under varying LO power with fixed zero bias. Zero DC bias is often used for subharmonically pumped and low frequency mixers, for example. Here it is clear that for lower LO powers, the $In_{0.25}Ga_{0.5}As$ or $GaAs_{0.75}Sb_{0.5}$ mixers are superior, and as predicted by equation (3) the LO power required is reduced by about half.

CONCLUSION

We have analyzed a 560 GHz fundamental mixer using the three material systems GaAs, $In_{0.25}Ga_{0.75}As$ and $GaAs_{0.5}Sb_{0.5}$. The latter two have barrier heights several tenths of a volt below that of GaAs. It is apparent that the higher barrier height and consequent lower tunneling current of GaAs gives it a greater current/voltage nonlinearity and hence lower mixer temperature and conversion loss, even at low LO power, as long as the diode DC bias can be adjusted to put it into the optimum range. If the bias is fixed at zero, however, the $In_{0.25}Ga_{0.75}As$ and $GaAs_{0.5}Sb_{0.5}$ give superior performance at low LO pump power, as predicted by equation (3).

ACKNOWLEDGMENTS

The authors gratefully acknowledge helpful discussions with Goutam Chattopadhyay.

The research described in this publication was carried out at the Jet Propulsion Laboratory, California Institute of Technology, under a contract with the National Aeronautics and Space Administration.

REFERENCES

[1] M.R. Barber, "Noise figure and conversion loss of the Schottky barrier mixer diode," *IEEE Trans. Microwave Theory Tech*., vol. MTT-15, no. 11, pp 629–635, 1967.

[2] C.A. Liechti, "Down-converters using Schottky-barrier diodes,", *IEEE Trans. Electron. Devices,* vol. ED-17, no. 11, pp. 975–

[3] S. Yngvesson, *Microwave Semiconductor Devices*, Kluwer, Norwell, MA, 1991.

[4] M. McColl, "Conversion loss limitations on Schottky-barrier mixers," *IEEE Trans. Microwave Theory Tech*., vol. MTT-25, no. 1, pp. 54–59, 1977.

[5] T.W. Crowe and R.J. Mattauch, "Conversion loss in GaAs Schottky-barrier mixer diodes," *IEEE Trans. Microwave Theory Tech*., vol. MTT-34, no. 7, pp 753–760, 1986.

[6] T.J. Maloney and J. Frey, "Transient and steady-state electron transport properties of GaAs and InP," *J. Appl. Phys*, vol 48, p781, 1977.

[7] J.H. Zhao, "Schottky Diodes of Au on GaAs1-xSbx,/GaAs n-N Heterostructures Grown by MBE," *IEEE Electron Device Lett.*, vol. 11, no. 10, pp. 478-480, 1990.

[8] K. Kajiyama, Y. Mizushima, and S. Sakata, "Schottky barrier height of n-InxGa1-xAs diodes," *Appl. Phys. Lett.,* v. 23, pp 458-459, Oct 1973.

[9] D Chattopadhyay, S K Sutradhar and B R Nag, "Electron transport in direct-gap III-V ternary alloys," *J. Phys. C: Solid State Phys*., vol 14 pp 891-908, 1981.

[10] Martin and C. Algora, "Temperature-dependent GaSb material parameters for reliable thermophotovoltaic cell modelling," *Semicond. Sci. Technol*. vol 19 pp 1040–1052, 2004.

[11] Ikoma, T., K. Sasaki, Y. Adachi, and H. Yanai, "Electron Transport Properties of GaxIn1-xSb Calculated by the Monte Carlo Method,"*Jpn. J. Appi. Phys*. vol. 16, no. 8 pp 1379-1387, 1977.

[12] P.H. Siegel, A.R Kerr, W. Hwang, "Topics in the Optimization of Millimeter-Wave Mixers," NASA Technical Report NASA-TP-2287, NAS 1.60:2287, March 1984.

[13] T.J. Crowe and R.J. Mattauch, "Analysis and optimization of millimeter- and submillimeter-wavelength mixer diodes," IEEE. *Trans. Microwave Theory Tech*., vol MTT-35, no. 2, pp. 159-168, Feb. 1987.

[14] Y. Ando and T. Itoh, "Calculation of transmission tunneling current across arbitrary potential barriers," *J. Appl. Phys*., vol. 61, no. 4, pp. 1497-1502, 1987.

[15] Schlecht, J. Gill, R. Dengler, R. Lin, R. Tsang, and I. Mehdi, "First Wideband 520-590 GHz Balanced Fundamental Schottky Mixer," presented at the Eighteenth International Symposium on Space Terahertz Technology, Pasadena, California, March 2007.

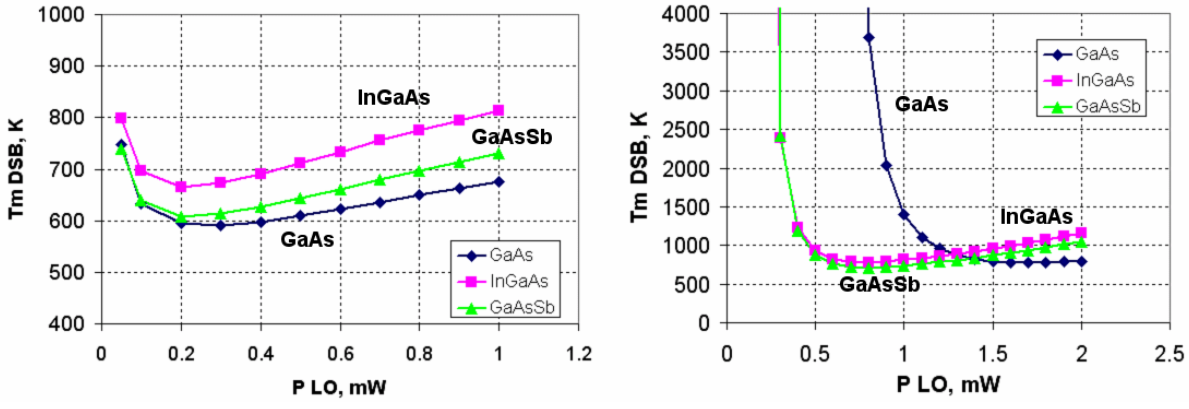

(a) (b)

Fig. 5. Variation of DSB mixer noise temperature with LO pump power. (a) At optimized DC bias values. (b) At zero-bias.

Development of a 340-GHz Sub-Harmonic Image Rejection Mixer Using Planar Schottky Diodes

Bertrand Thomas[1,2], Simon Rea[3], Brian Moyna[1] and Dave Matheson[1]
[1]*STFC - Rutherford Appleton Laboratory, Chilton Didcot, Oxfordshire, UK ().*
[2]*NASA-JPL, USA.*
[3]*EADS-ASTRIUM Ltd, Anchorage Road, Portsmouth, Hampshire,, UK.*
Contact: D. Matheson, phone: 1235-446582; fax: 1235-445848; e-mail: d.matheson@rl.ac.uk

***Abstract*— : We report on the design, fabrication and test of an integrated 320-360 GHz Sub-Harmonic Image Rejection Mixer (SHIRM) using planar Schottky diodes. The integrated circuit uses two separate anti-parallel pairs of diodes mounted onto a single quartz-based circuit. Measurement results give SSB receiver noise temperatures of 3300 K at 340 GHz, with an image rejection from 7.6 dB to 23 dB over the entire band.**

***Index Terms*— Image rejection mixer, sideband separation, sub-harmonic mixer, planar Schottky diodes.**

I. Introduction

Space-borne sub-millimetre wave atmospheric limb observations can give unique insights information on the global distributions of key molecular species in the Earth's upper troposphere and lower stratosphere (e.g., the STEAM-R proposal [1]). In order to best resolve the limb emissions from rotational and vibrational lines in the troposphere, it is necessary to separate the receiver sidebands. Previous air-borne limb sounding instruments have used Frequency Selective Surfaces (FSS) in the mixer's field-of-view the optical path to reject the upper unwanted side band [2].

In parallel, similar requirements in radio-astronomy have lead during the past decade to the development of efficient SIS sideband separating mixers. They have now been chosen, for example, as the generic receiver architecture for most of the ALMA receiver bands, from 100 GHz up to 700 GHz [3]. Until now, this approach had not been applied to Schottky diodes mixers in this frequency range. However, in the recent years, the development of a Sub-Harmonic Image Rejection Mixer (SHIRM) using pHEMT semiconductor diodes has been successfully demonstrated in Q-band [4], from which the name of the device described here is taken.

We present in this paper the design and development of an integrated 320-360 GHz Sub-Harmonic Image Rejection Mixer (SHIRM) that uses planar Schottky diodes. Measurement results of a prototype are reported and compared with the performance of a more traditional Single Side Band (SSB) receiver featuring a DSB mixer and a Frequency Selective Surface.

II. 340 GHz Sub-Harmonic Image Rejection Mixer Architecture

The 340 GHz Sub-Harmonic Image Rejection Mixer (SHIRM) design concept uses two double side band (DSB) sub-harmonic mixer circuits connected at the RF frequencies by a 3 dB in-phase power splitter, and at the Local Oscillator (LO) frequencies by a 45° phase shifter and 3 dB power splitter, as illustrated in Fig.1. Similar designs of SSB fundamental mixers show that the quadrature can be performed by phase shifting either the RF signal or the LO signal by 90° [5]. In our case, we have chosen to phase shift the LO signal as the tuning bandwidth required to meet the LO specifications for STEAM-R is reduced (max. 164-171 GHz) compared to the broader RF band (314-356 GHz). As the DSB mixers used here are sub-harmonically pumped at the second order, it is necessary to 45° phase shift at the LO in order to ensure that the IF output signals are phase shifted by 90°. The IF signals from both DSB mixers are recombined afterwards by using a 90° hybrid 3 dB coupler to perform the image rejection of each side band.

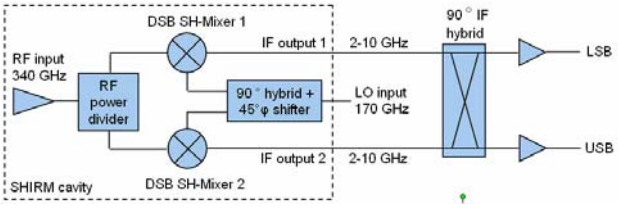

Fig.1. Schematic diagram of the SHIRM. The components in the dotted box are integrated inside a single block. Both IF outputs are recombined externally to the SHIRM block using a commercial 90° IF hybrid 3 dB coupler.

The SHIRM circuit features two DSB sub-harmonic mixer sub-circuits joined together in a single quartz-based microstrip circuit, each one using an anti-parallel pair of planar Schottky diodes, as illustrated in Fig.2. Both sub-circuits are IF/DC grounded at the centre of the single substrate, with the IF output of both mixers coupled via its endings. The LO WR-05 waveguide 45° phase shifter is derived from a previous design described in [6]. It is constituted by a 90° waveguide hybrid 3 dB coupler scaled from a WR-10 design presented in [7], and a 45° stub-loaded waveguide phase shifter. The RF WR-2.8

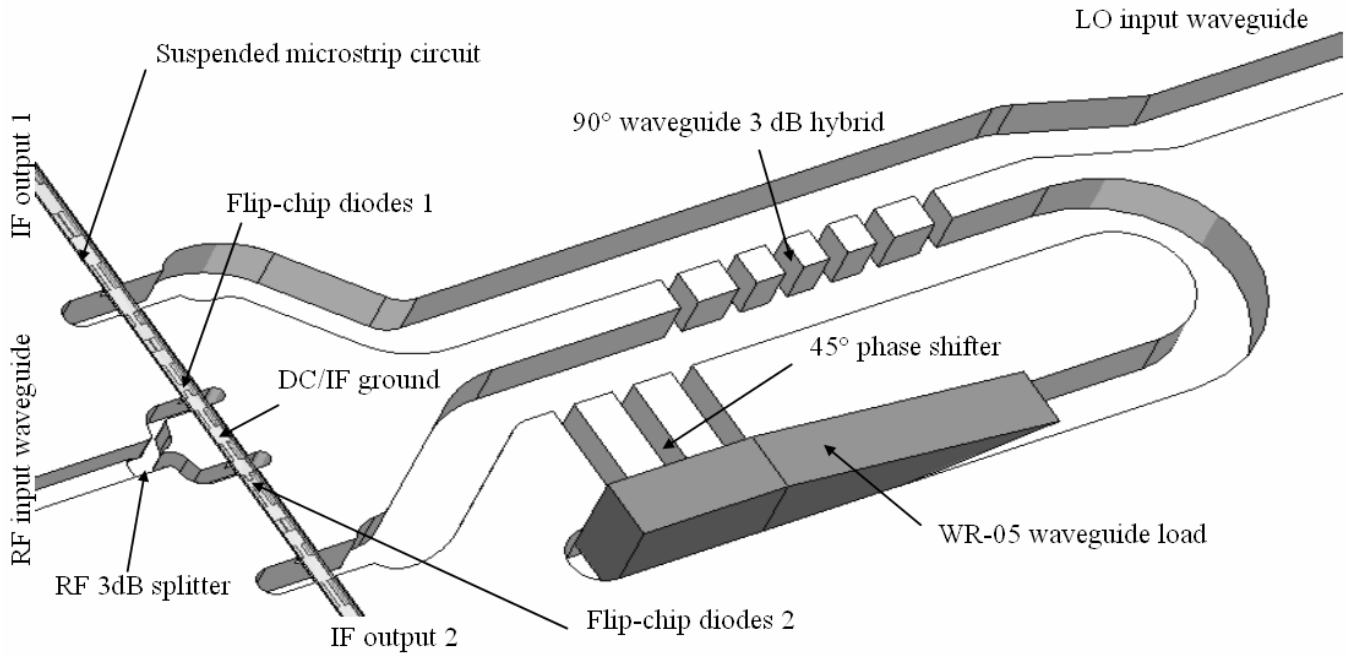

Fig.2. 3D view of the SHIRM, including the inverted suspended circuit and the 3 dB RF power splitter (on the left), the 45° waveguide phase shifter and the LO waveguide load (middle and right). RF input is from 320 to 360 GHz. LO input is around 170 GHz

waveguide 3 dB power splitter is a compact Y-junction divider derived from [8]

III. SHIRM DESIGN

The design methodology uses a combination of linear/non-linear circuit simulations (Agilent ADS [9]) to optimize and compute the performances of the circuit, and 3D EM simulations (Ansoft HFSS [10]) to model accurately the diodes and waveguide structures.

First, each sub-harmonic mixing branch of the SHIRM use an anti-parallel pair of planar Schottky diodes. The electrical parameters considered for these diodes are a series resistance R_s = 15 Ω, a zero voltage junction capacitance of C_{jo}= 1.3 fF, saturation current I_{sat} = 2e-16 A, ideality factor η=1.3 and built-in potential V_{bi} = 0.73 V per anode. Considering an optimum LO power level of 1.5 mW, a set of non-linear simulations gives an ideal embedding impedances of approximately Z_{RF} = 83+j.53 at RF frequencies and Z_{LO} = 147+j.207 at LO frequencies. The IF load impedance is set to 100 Ω, at a frequency of 2.5 GHz. In a second step, each part of the circuit is modelled electromagnetically with HFSS, and imported in ADS for further optimisation. In order to retrieve the S-parameters at the level of each Schottky barrier, micro-coaxial probes are introduced [11]. The 45° waveguide phase shifter is optimised to exhibit minimum phase and amplitude imbalance over the LO frequency range. The simulated performance gives a maximum amplitude imbalance of ± 0.5 dB and a phase imbalance of ± 5° over the frequency range 160-180 GHz.

The whole SHIRM circuit is optimized for best image rejection and lowest conversion losses in the RF range 320-360 GHz. An typical value of the IF hybrid phase and amplitude imbalances (given by the manufacturer) is taken into account during the optimisation process. The predicted performance of the SHIRM is presented in Fig. 3. The LO power required to pump the SHIRM is estimated at 6 mW.
Average SSB conversion losses of approx. 9 dB and side band ratio better than 20 dB are predicted.

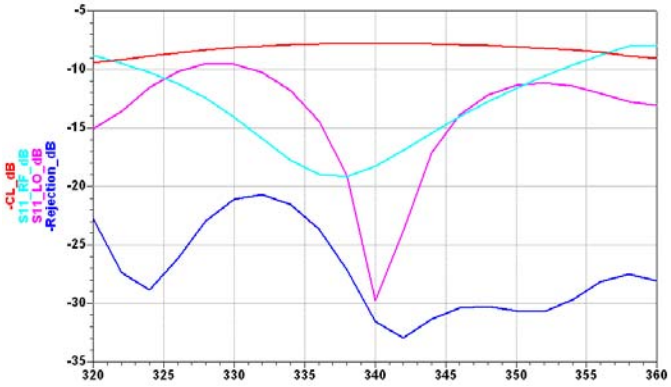

Fig.3. Predicted performance of the SHIRM over the desired RF frequency range, including conversion losses (top red curve), RF and LO input return losses (middle light blue and pink curves), and side band image rejection (lower dark blue curve). LO power is set to 6 mW, IF impedance to 100 Ω.

IV. SHIRM MANUFACTURE AND ASSEMBLY

Two anti-parallel pairs of discrete planar Schottky diodes fabricated at RAL [12] are selected on the basis of similar DC characteristics, flip-chip mounted and soldered onto the RF gold-on-quartz microstrip circuit. Two other IF quartz based microstrip circuits are mounted and glued into the lower half of the split waveguide block. The quartz-based RF stripline circuit is inverted-suspended into the cross-waveguide channel as previously described [13]. It is connected to both IF output circuits by the sides and grounded to the lower half of the block by the middle using silver loaded epoxy glue. A K-type glass bead is then connected to the end of each IF microstrip circuit. Finally, a WR-05 waveguide load scaled from the Type 1 WR-10 design presented in [14] and machined out of MF116 Eccosorb material [15] is inserted inside the waveguide branch connecting the isolated port of the 90° hybrid. The assembled SHIRM block shown in Fig. 4 also includes two K-type flange launcher connectors (on the side), an integrated 330 GHz diagonal horn antenna (visible in front of the block) and a WR-05 UG387 input waveguide flange (on the back, not visible). The dimensions of the SHIRM blocks are approximately 2 cm x 2 cm x 2.5 cm.

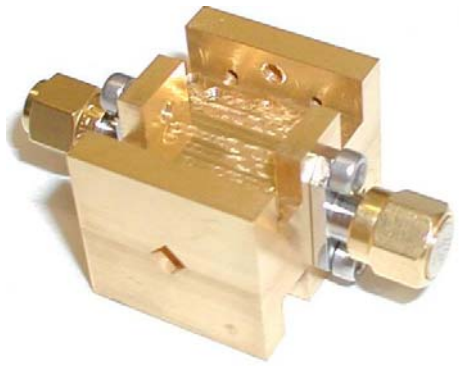

Fig.4. Photograph of the assembled 340 GHz SHIRM block.

V. TEST OF THE SHIRM

The LO source driving the 340 GHz SHIRM comprises a Gunn diode oscillator followed by a rotary vane attenuator and a 166 GHz VDI frequency doubler (Ref. D154 [16]). The output power of the LO chain is calibrated using a PM3 Erickson Calorimeter [17]. Both IF output signals are then fed into a 2-8 GHz commercial IF 90° hybrid coupler (from Krytar™) exhibiting a maximum amplitude and phase imbalance of ± 0.35 dB and ± 3 dB respectively in the band. The IF output signals are then amplified by two low noise amplifier chains with a noise figure of 0.94 dB, each including an isolator and a 2-8 GHz band-pass filter. The output of both chains is alternatively switched to a Gigatronic 8542C power sensor for power measurement, and to a spectrum analyser for spectral line measurement. The test procedure to determine the SSB receiver noise temperature and image rejection is done according to [18]. First, a Y-factor measurement of the receiver is taken to determine the receiver noise temperature using the broadband power sensor. Then, a spectral line is injected into the SHIRM and tuned inside the RF bandwidth. The line is provided by a photo-mixer developed at RAL [19], delivering few nW to the SHIRM at 330 GHz from the beating of two 1.55 µm laser sources. The output IF signal is observed on an Agilent spectrum analyser in a log scale amplitude mode, with resolution bandwidth of 300 kHz and a sample averaging of 50.

Preliminary test results are presented in Fig. 5. These results are uncorrected from the spectrum analyser envelop detector error with log display. The image rejection at a LO frequency of 170 GHz is measured between 7.6 and 23 dB in the frequency range 317.5-362.5 GHz. Best SSB receiver noise temperature of 3300 K has been measured at a centre RF frequency of 340 GHz, with a value lower than 3800 K over the RF frequency range 324-360 GHz. The amount of LO power required to pump the SHIRM is between 7 mW and 11 mW for different LO frequencies.

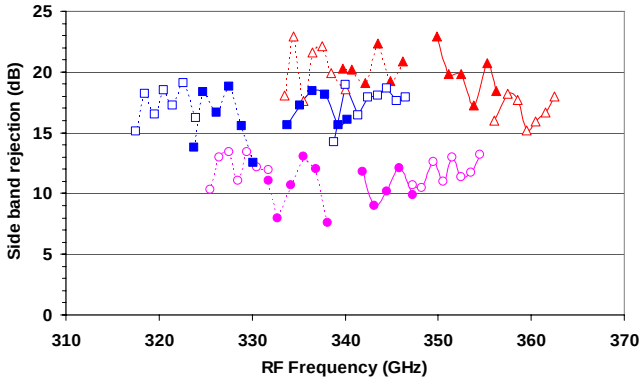

Fig.5. Measured image rejection performance of the 340 GHz SHIRM as functions of the RF frequency. Two IF chains are used: 2-8 GHz (full dots) and 6-14 GHz (empty dots). LSB results are shown with dotted lines, USB with continuous lines. Blue square dots are for an LO frequency of 166 GHz, the pink round dots for 170 GHz, and the red triangles for 174 GHz.

VI. COMPARISON WITH A QUASI-OPTICAL SSB MIXER

The SHIRM performances are compared to a Schottky diode based SSB receiver developed by RAL and ASTRIUM-Portsmouth to upgrade the Band B channel of the MARSCHALS instrument [2]. It features a 295-350 GHz DSB sub-harmonic mixer with integrated 12-24 GHz low noise pre-amplifier and a 310 GHz FSS developed by Queens University Belfast (QUB) [20]. The Band B receiver is shown in Fig. 6. Both mixer and frequency doubler use planar Schottky diodes from VDI [14].

The 310 GHz FSS has been measured independently with an *ABmm* Vector Network Analyser and QO bench system. The insertion losses are better than 1 dB in the band 290-305 GHz and the rejection factor is better than 30 dB in the frequency range 331-343 GHz. The

performance of the SSB receiver featuring the band B receiver and the FSS described above is measured using a Y-factor measurement. The reflected sideband is loaded with a 300 K calibration target. A SSB receiver noise temperature of approximately 5000 K is obtained at an RF frequency of 300 GHz, and a DSB receiver noise temperature of approx. 2100 K without the FSS inserted in the QO path.

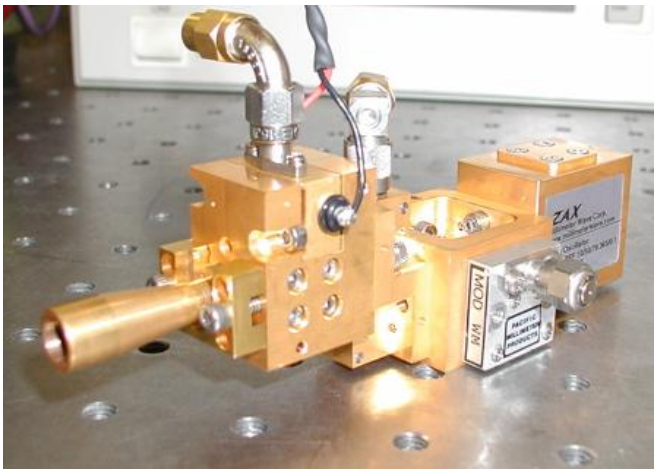

Fig.6. Photo of the MARSCHALS Band B receiver channel, featuring a 295-350 GHz DSB sub-harmonic mixer with integrated pre-amplifier (foreground), a 160-185 GHz frequency doubler (middle), a 20 dB cross-guide coupler and a Gunn diode oscillator from ZAX (background).

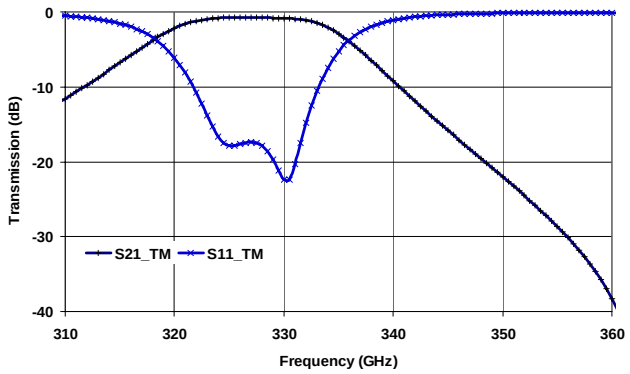

Fig.7. Simulated transmission and reflection coefficients of an FSS *VS* RF frequency based on the membrane technology developed at QUB, normalized by 6 GHz. (Courtesy: Queens University Belfast, Ireland).

A plot of the simulated transmission and reflection coefficients of an FSS based on the membrane technology developed at QUB that would be suitable for STEAM-R instrument is presented in Fig.7. It shows that, if one wants to use a single FSS to separate the LSB from the USB of an incoming RF signal before feeding two DSB mixers, the IF central frequency and bandwidth of both sidebands will determine the amount of rejection and QO losses that can be achieved. Furthermore, QO FSS are for the moment non-reconfigurable and have a fixed frequency response.

The reflected band shown in blue (S11_TM) in Fig.7 shows that the maximum rejection achievable is 18 dB and 10 dB for an IF bandwidth of 7 GHz to 10 GHz respectively. For an maximum image rejection of 10 and 18 dB in each sideband, the lower IF frequency should not be bellow 4 and 7 GHz respectively from the carrier.

In the SHIRM case, the rejection is much less sensitive to the IF frequency range and bandwidth, as the IF band can start as low as few MHz. The LO frequency can also be tuned into a specific bandwidth without, in principle, degrading the image rejection of the SHIRM. The IF bandwidth is however a trade-off between amplitude and phase imbalance of the IF hybrid in the band (the broader the band, the higher the risk of imbalances). In the light of the first results presented in this paper, a similar level of rejection between the SHIRM and the QO FSS is achieved.

Further measurements on the SHIRM are required to confirm these assumptions.

CONCLUSION

The first operation of an integrated 340 GHz Sub-Harmonic Image Rejection Mixer using planar Schottky diodes is presented. Best image rejection of 23.8 dB and SSB receiver noise temperature of 3300 K is reported. An image rejection between 7.6 dB and 23 dB is measured between 317.5 GHz and 362.5 GHz. The device demonstrates the suitability of this approach for future remote sensing instruments requiring high spectral resolution and high sideband separation in the millimetre and sub-millimetre wave domain. Further developments are envisaged to improve the integration of the SHIRM into linear arrays of receivers.

ACKNOWLEDGEMENTS

The authors wish to thank Mr. Sobis from Chalmers University of Technology for fruitful discussions. We also acknowledge Dr. Alderman for the high quality of Schottky diodes, Dr. Huggard for the provision of the photomixer, Mr. Hiscock and Mr. Beardsley for the block manufacturing.

This work has been funded by the DIUS/NERC "Centre for Earth Observation Instrumentation" UK national program.

REFERENCES

[1] F.V. Schéele, *et al.*, "The STEAM project", *Proceedings of the Committee On Space Research, COSPAR*, Paris, France, pp. 2208, July 2004.

[2] B.P. Moyna *et al.*, "MARSCHALS: airborne simulator of a future space instrument to observe millimetre-wave limb emission from the upper troposphere and lower stratosphere", 6361-10, *Proceedings of the SPIE European Remote Sensing Conference*, Stockholm, Sept. 2006.

[3] http://www.eso.org/projects/alma

[4] H-K Chiou *et al.*, "A miniature Q-band Balanced Sub-Harmonically Pumped Image Rejection Mixer", IEEE MWCL, Vol.17, No.6, June 2007, pp. 463-465.
[5] V. Vassilev *et al.*, "Design and Characterisation of a 211-275 GHz Sideband Separating Mixer fro the APEX Telescope", IEEE MWCL, Vol. 18, No. 1, January 2008, pp.58-60.
[6] F. Arndt *et al.*, "Optimum Field Theory Design of Broad-Band E-Plane Branch Guide Phase Shifters and 180° Couplers", IEEE Trans. on MTT, Vol. 38, No. 12, December 1990, pp. 1854-1861.
[7] S. Srikanth et al., "Waveguide Quadrature Hybrids for ALMA Receivers", ALMA Memo 343, http://www.alma.nrao.edu/memos/, January 2001.
[8] A. Maestrini, *et al*, "In-Phase Power-Combined Frequency Triplers at 300 GHz", IEEE MWCL, Vol. 18, no. 3, March 2008, pp. 218-220.
[9] Advanced Design System 2005A, Agilent Technologies, 395 Page Mill Road, Palo Alto, CA 94304, USA.
[10] High Frequency Simulation Software, V10, Ansoft Corporation, 225 West Station Square Drive, Suite 200, Pittsburgh, PA 15219, USA.
[11] J. Hesler *et al.*, "Fix-Tuned Submillimeter Wavelength Waveguide Mixers Using Planar Schottky-Barrier Diodes", *IEEE Trans. MTT,* **45**, pp. 653-658, 1997.
[12] B.Alderman *et al.*, "Fabrication of reproducible air-bridged Schottky diodes for use at 200 GHz", Proceedings of the joint 32nd IR and MM-wave conference & 15th THz electronics 2007, Cardiff, September 2007, pp. 848-849
[13] B.Thomas *et al.*, "A Low-Noise Fixed-Tuned 300-360 GHz Sub-Harmonic Mixer Using Planar Schottky Diodes", IEEE MWCL, vol.15, no.12, December 2005, pp.865-867.
[14] A. Kerr *et al.*, "MF-112 and MF-116: Compact Waveguide Loads and FTS Measurements at Room Temperatura and 5K", ALMA Memo 494, http://www.alma.nrao.edu/memos/, May 2004.
[15] Emerson & Cuming, http://www.emersoncumingmp.com/
[16] Virginia Diodes Inc. http://www.virginiadiodes.com/
[17] N. Erickson, "A fast and sensitive submillimetre waveguide power meter", *10th Int. Symp. on Space THz Technology*, Charlottesville, pp.501-507, 1999.
[18] A.R. Kerr *et al.*, "Sideband Calibration of Millimeter-Wave Receivers", ALMA Memo 357, http://www.alma.nrao.edu/memos/, March 2001.
[19] P. G. Huggard *et al.*, "Generation of millimetre and sub-millimetre waves by photomixing in 1.55 μm wavelength photodiode", Electronics Letters, 38, 2002, pp. 327-328.
[20] R. Dickie et al., "Polarisation independent bandpass FSS", Electronic Letters, Vol. 43, No. 19, September 2007, pp. 1013-1015.

Submillimeter Interferometers: New standards for future instrumentation

Richard Hills

Joint ALMA Office, Chile

The current state of the art, as represented by the systems being developed for ALMA, will first be reviewed. This includes extensive use of composite materials on the antennas, dual- polarization SIS heterodyne receivers, photonic LO reference systems, 8GHz IF bandwidth transmitted digitally on optical fibers, and a digital correlator based on ASIC's.

Various likely lines of development for future Submillimeter Interferometers will then be discussed in outline. For antennas, greater use of active control can be expected. Receiver systems providing greater bandwidth and multiple beams are becoming possible, as are direct photonic LO systems and cost- and power-effective correlators based on FPGA's.
An alternative line of development would be based on the extending infra-red technology to longer wavelengths – e.g. using quasi-optical delay lines and direct detection. The question of whether this approach may be advantageous for some astronomical applications will be considered.

The ALMA Front Ends; an Overview

Gie Han Tan[1,*]

[1]ESO European Organisation for Astronomical Research in the Southern Hemisphere,
Garching bei München, Germany

* Contact: ghtan@eso.org, phone +49-89-3200 6487

***Abstract*— The Atacama Large Millimeter / submillimeter Array will be an astronomical facility operating in the millimetre and sub-millimetre range (31 GHz – 950 GHz) currently under construction on a plateau in the Chilean Andes. The array will consist of at least 66 Cassegrain type reflector antennas, total collecting area nearly 6000 m^2, operating as a synthesis aperture interferometer. This article provides an overview of the receiver system design, including key performance parameters, project organization, and current project status.**

I. Introduction

The Atacama Large Millimeter / submillimeter Array (ALMA) is a new radio observatory operating in the millimetre and sub-millimetre wavelength range currently under construction. The realization of this novel facility of unprecedented size is only possible by a well concerted collaboration between the existing leading institutes in this field and industry from countries within the three regions, Europe, East Asia and North America, represented in this global partnership. This collaboration is also well demonstrated in the development and construction of receivers needed for ALMA. More than ten organizations, mostly R&D or academic institutions, united in the ALMA Front End Integrated Project Team (FE IPT) are undertaking this activity. The FE IPT faces the challenge to develop and produce the largest number so far of identical sub-millimetre receivers in the world. The performance of these receivers will set new standards in this wavelength range. In addition special care in design and production of these receivers has to be given to manufacturability and reliability.

II. Atacama Large Millimeter Array

This section provides background information on the organization of the ALMA Project and a description of the complete instrument.

A. An International Endeavour

The Atacama Large Millimeter / submillimeter Array (ALMA), an international astronomy facility, is a partnership between Europe, East Asia and North America in cooperation with the Republic of Chile. ALMA is funded in Europe by the European Organisation for Astronomical Research in the Southern Hemisphere (ESO), in Japan by the National Institutes of Natural Sciences (NINS) in cooperation with the Academia Sinica in Taiwan and in North America by the U.S. National Science Foundation (NSF) in cooperation with the National Research Council of Canada (NRC). ALMA construction and operations are led on behalf of Europe by ESO, on behalf of Japan by the National Astronomical Observatory of Japan (NAOJ) and on behalf of North America by the National Radio Astronomy Observatory (NRAO), which is managed by Associated Universities, Inc. (AUI).

B. System Configuration and Site

ALMA will be a single instrument composed of 1) a main

Fig. 1: A panoramic view of the 5000-meter high Llano de Chajnantor in the Atacama Desert of northern Chile

array of 50 high-precision Cassegrain antennas, each having a diameter of 12 m, operating in exclusively in interferometer mode and 2) a closely packed array (called ALMA Compact Array - ACA) consisting of 12 Cassegrain antennas, each having a diameter of 7 m, operating in interferometric mode and four Cassegrain antennas, each having a diameter of 12 m, operating in so called single dish total power mode. The instrument is located in the II Region of Chile, in the District of San Pedro de Atacama, at the Chajnantor altiplano, more than 5000 metres above sea level (Fig. 1).

ALMA's primary function will be to observe and image with unprecedented clarity the enigmatic cold regions of the Universe, which are optically dark, yet shine brightly in the millimetre portion of the electromagnetic spectrum.

TABLE I

ALMA KEY SYSTEM PARAMETERS

Telescope principle	Aperture synthesis (interferometers) complemented by 4 total power antennas
Number of Antennas	54 Cassegrain antennas of 12-meter diameter 12 Cassegrain antennas of 7-meter diameter
Number of baselines	1225 main array 66 ALMA Compact Array
Number of configurations	Continuous with maximum baselines from 150 to 14000 meters
Number of antenna stations	Approx. 220, antennas transportable between them
Site	Chajnantor, Northern Chile, 5000-meter altitude
Frequency coverage	31 - 950 GHz, except atmospheric absorption regions
Receiver complement	One cryogenically cooled unit accommodating 10 frequency band cartridges (7 installed initially) plus water vapour radiometer operating at 183 GHz
Signal transport	In digital format over optical fibres
Correlator	Reconfigurable digital correlator with 12 configurations and 1024 spectral channels
Software	Control and data handling, data pipeline, image production, remote control and remote observation
Operation	Service observing with Operations Centre near San Pedro de Atacama, 30 km from site at 2500-3000 -meter altitude

The array of antennas will be reconfigurable, giving ALMA a zoom-lens capability. The highest resolution images will come from the most extended configuration, and lower resolution images of high surface brightness sensitivity will be provided by a compact configuration in which all antennas are placed close to each other. The instrument thus combines the imaging clarity of detail provided by a large interferometric array together with the brightness sensitivity of a large single dish. The large number of antennas in the main array provides over 1200 independent interferometer baselines, making possible excellent imaging quality with "snapshot" observations of very high fidelity. The antennas in the ACA complete the main array in terms of wide field imaging. The receivers will cover the atmospheric windows at wavelengths from 0.3 to 10 millimetres.

ALMA will be a millimetre / sub-millimetre counterpart of the optical Very Large Telescope (VLT) and Hubble Space Telescope, with similar angular resolution and sensitivity but unhindered by dust opacity. It will be the largest ground-based astronomy project after the VLT/VLTI, and, together with the Next Generation Space Telescope (NGST), one of the two major new facilities for world astronomy coming into operation at the end of this decade.

III. RECEIVER SUB-SYSTEM

The ALMA receivers are located, at the interface to the antenna secondary focal plane, inside the receiver cabin at each antenna. ALMA will observe over the frequency region from approximately 31 GHz to 950 GHz. For technical reasons this frequency coverage has been split into 10 separate bands as is shown in Table II. There will be two identical receiver channels for each band, enabling observation of the full polarization state of the received radiation, in order to maximize the system's sensitivity, and to allow polarization-sensitive observations to be performed. Fig. 2 provides a simplified block diagram of the front end and analogue back end electronic sub-systems mounted in each antenna

ALMA will observe in only one band at any given time. In the baseline construction project, only the seven frequency ranges of highest scientific priority, designated Bands 3, 4, 6, 7, 8, 9, and 10, will be fully implemented. Band 5 is being designed and six units will be built with additional funding by the European Commission under the 6th Framework Program.

C. RF Device Technologies

In the frequency ranges covered by ALMA, current technology provides direct amplification of the received radiation only in the lowest two bands, where a few radio astronomy groups have developed state of the art HEMT amplifiers. The remainder of the receivers will use SIS (superconductor-insulator-superconductor) junctions, either Niobium or Niobium-Titanium-Nitrate based, to convert the received signal to an intermediate frequency (IF) in the range of 4 to 12 GHz, where it can be readily amplified.

A great challenge for ALMA is to obtain proper control of the SIS junction fabrication processes needed to reach satisfactory performance that will also be reliable and suitable for series fabrication.

D. Heterodyne Local Oscillator Concept

The local oscillators used in these heterodyne receivers are fully electronically tuneable, no mechanical tuners are used as was common with existing technology so far. Each local oscillator uses a phase locked YIG tuned oscillator operating in the frequency range of approximately 14... 20 GHz and is multiplied using active, room temperature, multipliers and passive, varistor type, cooled multipliers for the final frequency multiplication stage. Cooling of these passive

TABLE VIII
ALMA FRONT END KEY SPECIFICATIONS

ALMA Band	Frequency Range	Receiver noise temperature		Mixing scheme	Receiver technology	Responsible organization	Country
		T_{Rx} over 80% of the RF band	T_{Rx} at any frequency				
1	31.3 – 45 GHz	17 K	28 K	USB	HEMT	Not assigned	-
2	67 – 90 GHz	30 K	50 K	LSB	HEMT	Not assigned	-
3	84 – 116 GHz	37 K	62 K	2SB	SIS	Herzberg Institute of Astronomy (HIA)	Canada
4	125 – 169 GHz	51 K	85 K	2SB	SIS	National Astronomy Observatory of Japan (NAOJ)	Japan
5	163 - 211 GHz	65 K	108 K	2SB	SIS	Chalmers University (6 units)	Sweden
6	211 – 275 GHz	83 K	138 K	2SB	SIS	National Radio Astronomy Observatory (NRAO)	USA
7	275 – 373 GHz	147 K	221 K	2SB	SIS	Institut de Radioastronomie Millimétrique (IRAM)	France
8	385 – 500 GHz	196	294 K	2SB	SIS	National Astronomy Observatory of Japan (NAOJ)	Japan
9	602 – 720 GHz	175 K	263 K	DSB	SIS	Netherlands Research School For Astronomy (NOVA)	Netherlands
10	787 – 950 GHz	230 K	345 K	DSB	SIS	National Astronomy Observatory of Japan (NAOJ)	Japan

multipliers improves the conversion efficiency compared to room temperature operation.

Highly phase stable reference signals are provided to each antenna over fibre optical cable. The optical carrier provides various microwave signals that are used in phase locking the local oscillator. Fine tuning of frequency and phase of the local oscillator signal is feasible due to the use of a direct digital synthesizer (DDS). Phase switching, both 90° and 180° as is commonly used in interferometers to suppress internal interfering signals, is implemented through this DDS.

E. Modular Cryogenic Receiver Concept

The complete front end unit will have a diameter of 1 m, be about 1-m high and have a mass of about 750 kg. Fig. 3 and Fig. 4 show respectively top and bottom side views of the front end assembly. The cryostat will be cooled down to approximately 4 Kelvin by a 3-stage commercial closed-cycle cryo-cooler based on the Gifford – McMahon cooling cycle. The individual frequency bands are implemented in the form of modular cartridges that will be inserted in a large common cryostat. This cartridge concept allows for a great flexibility in construction and operation of the array. Fig. 5 shows an example of such a receiver cartridge. Another advantage of the cartridge layout with well-defined interfaces is the fact that different cartridges can be developed and built by different groups within the ALMA Project with a large degree of independence but without the risk of incompatibility between them.

F. 183 GHz Water Vapour Radiometer

Because interferometric observations at (sub-)millimetre wavelengths are extremely sensitive to changes in the amount of water vapour in the earth's atmosphere, causing a variation in electrical path length, every 12-m antenna will be equipped with a water vapour radiometer (WVR), which is essentially a separate, dedicated receiver tuned to the frequency of a water vapour absorption line at about 183 GHz. The WVR will be an uncooled receiver and will take atmospheric data continuously, while the astronomical observations at other frequencies are underway. The WVR will enable these observations to be corrected for the influence of water vapour in the lines of sight between each antenna and the observed source.

G. Amplitude Calibration Device

ALMA has exceptionally challenging requirements for the accurate measurement of power flux. The objective is to obtain an accuracy of better than 1% below 300 GHz and less than 3 % for higher frequencies. For achieving this

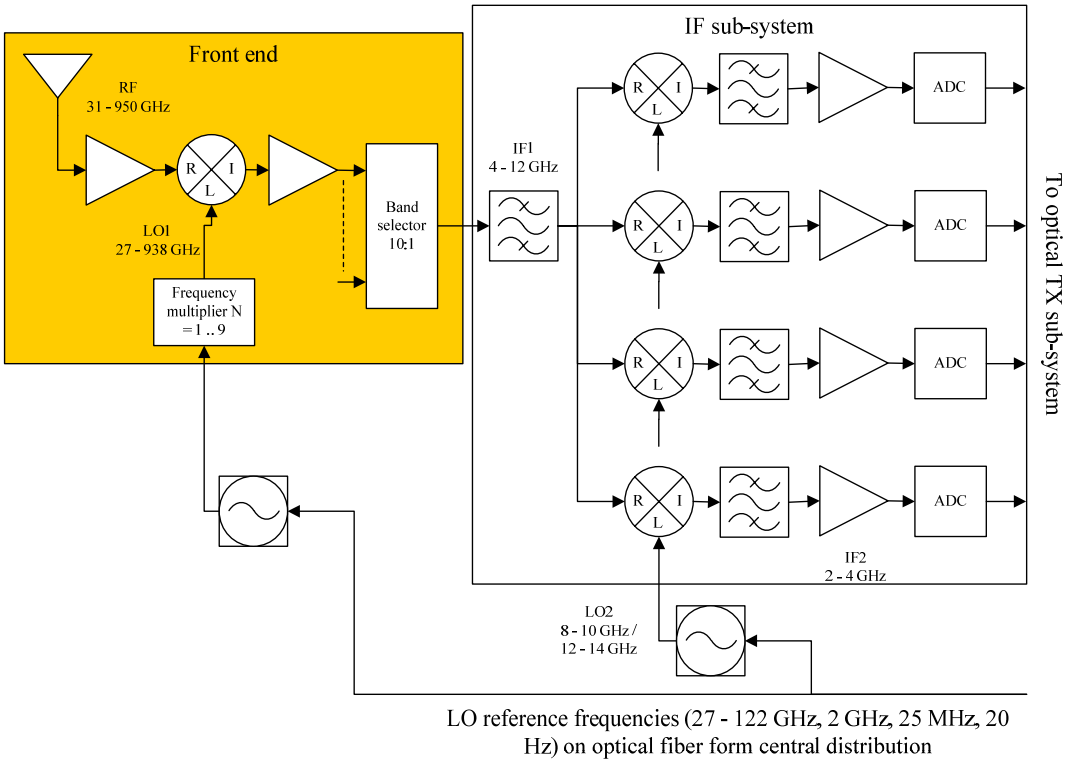

Fig. 2: Simplified antenna based block diagram of front end (orange highlighted) and analogue back end electronics

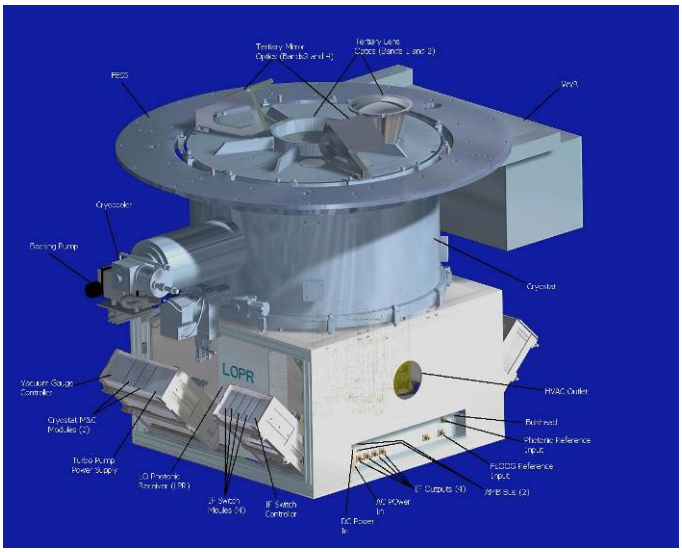

Fig. 3: Top – side view of Front End Assembly

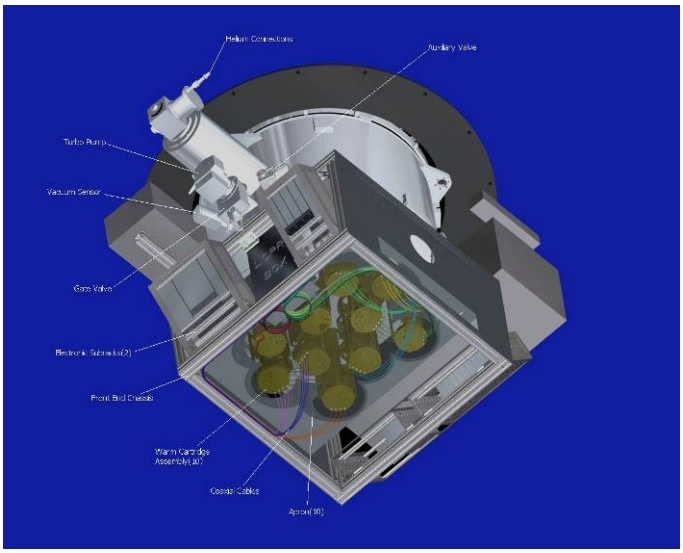

Fig. 4: Bottom – side view of Front End Assembly

requirement each receiver channel inside an ALMA Front End can be calibrated against a well characterised hot load, having a temperature in the range of 340 – 360 K, (only Bands 3 – 10) and a precision ambient load, having a temperature of approximately 295 K. Fig. 6 shows a CAD drawing of the Amplitude Calibration Device (ACD).

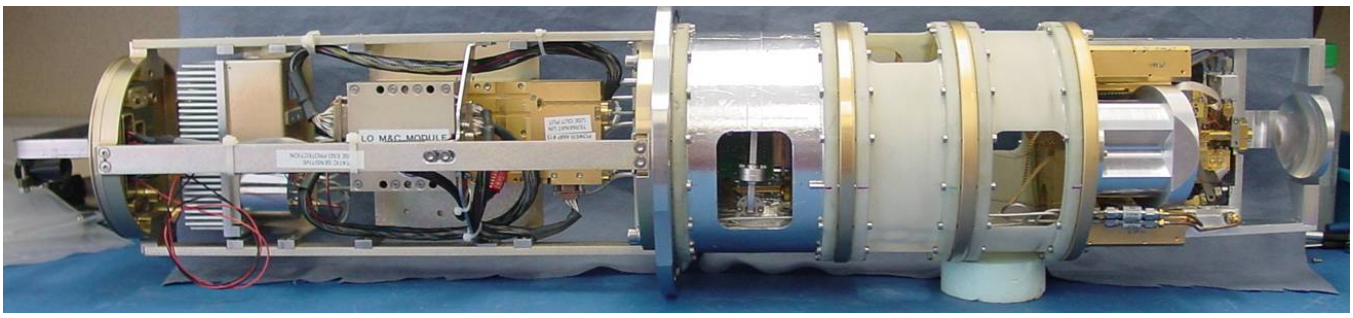

Fig. 5: Example of a, Band 6, receiver cartridge. The larger diameter metal plate in the middle is the boundary between cooled receiver electronics inside the cryostat (right hand side) and the room temperature electronics (left hand side).

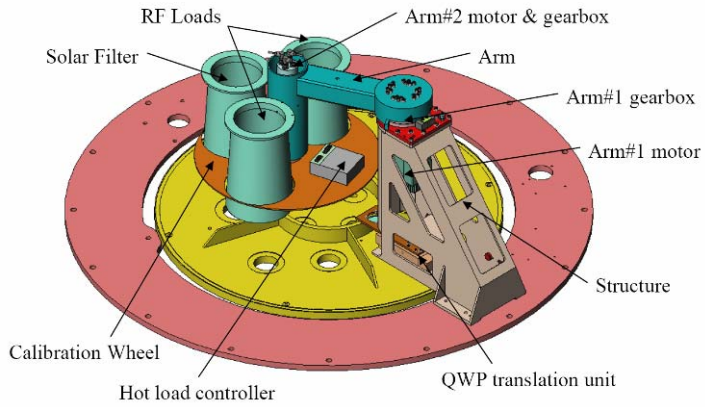

Fig. 6: CAD drawing of the Amplitude Calibration Device (top – side view)

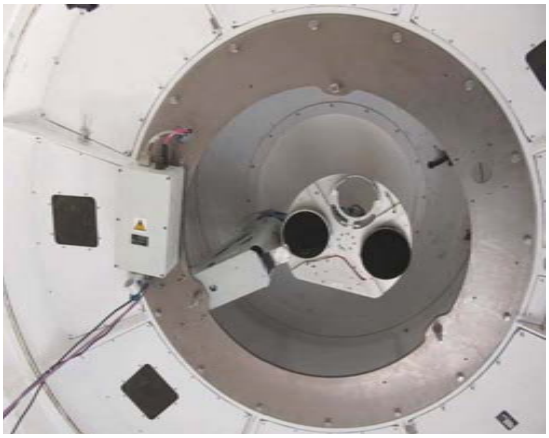

Fig. 7: Amplitude Calibration Device mounted in antenna (bottom view)

The ACD is mounted on the Front End Support Structure (FESS) a circuar, metal ring providing the interface between Front End Assembly and antenna structure. The ACD consists of a robotic arm which moves the calibration loads in front of one of the ten receiver windows. In addition to the calibration loads it carries a so called solar filter. This solar filter acts as an attenuator for the RF signal and reduces the IR heat load when observing the sun. The ACD has the option for installing a Quarter Wave Plate (QWP) in front of the Band 7 receiver. The QWP provides an enhanced accuracy for polarization measurements. Fig. 7 is a picture showing the actual ACD mounted in one of the ALMA antennas. The, black, calibration loads are clearly visible while the solar filter is not mounted.

IV. Organization

A. Integrated Project Team

More than ten different organizations, both academic institutes and industry scattered among three continents, play a key role in the design and production of the ALMA receivers. Each of these organizations has several, in general commercial, sub-contractors involved for production work. Fig. 10 provides an overview where the various organizations contributing to the ALMA front ends are located. Each of these organizations has the responsibility for delivering front end sub-assemblies. All these entities are organized in a so called Integrated Product Team (IPT) which carries the overall responsibility of providing front ends to the ALMA Observatory in Chile. The IPT management is formed by a two-headed team located at ESO in Garching bei München, Germany, and the NRAO in Charlottesville / Virginia, U.S.A. The FE IPT management is supported by system engineers and project schedulers.

B. Front End Integration Centres

Integration and final verification before delivery to Chile of all ALMA Front Ends is a major activity and three Front End Integration Centres (FEIC) have been established for this work. This is both a technical as well as a logistical challenge as one can conclude from the simplified ALMA Front End integration flow diagram shown in Fig. 8

The FEICs are located at different locations across three continents:

- Chung Shan Institute of Science and Technology / Aeronautical Systems Research Division in Tai-Chung, Taiwan
- National Radio Astronomy Observatory in Charlottesville / Virginia, U.S.A.
- Rutherford Appleton Laboratory near Didcot, United Kingdom

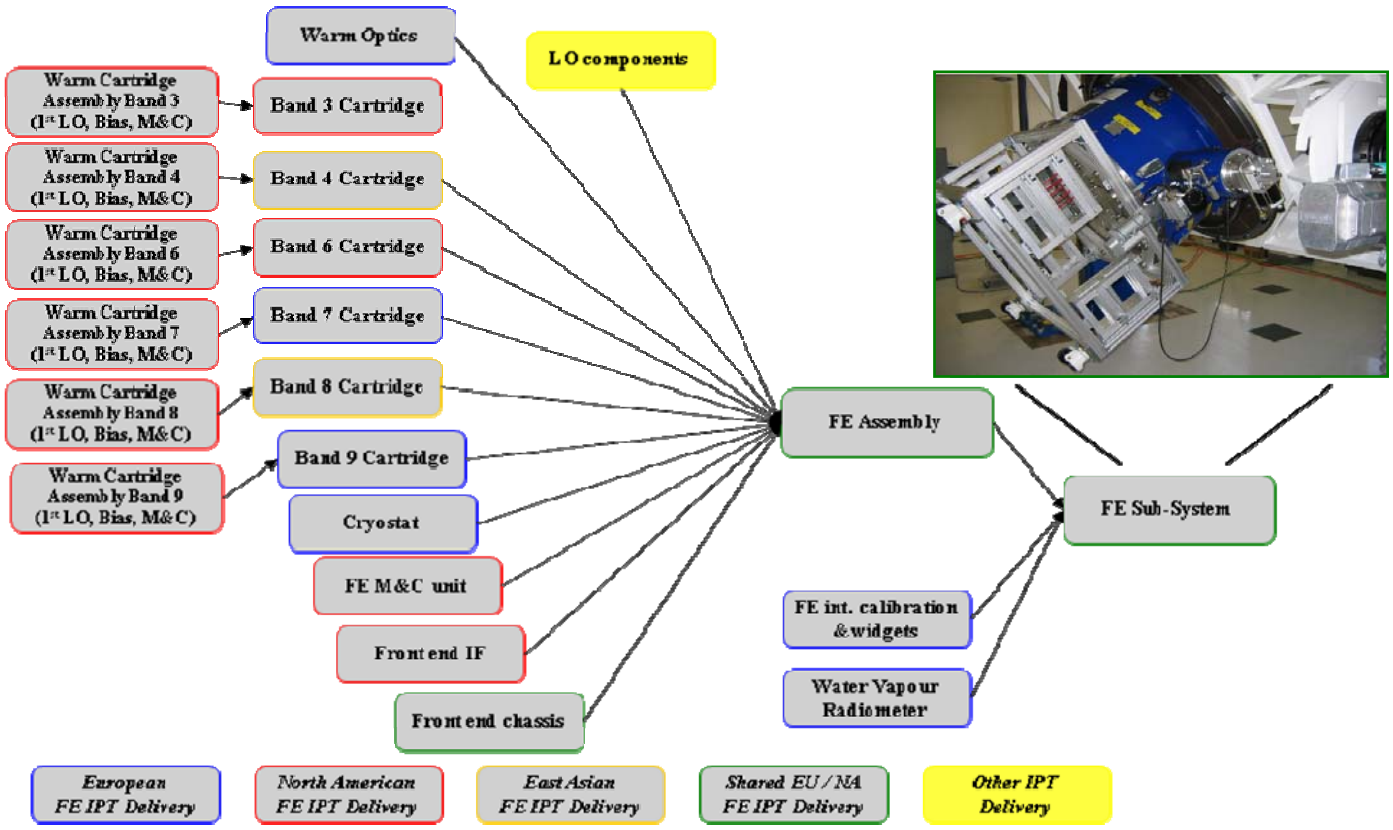

Fig. 8: Simplified integration flow of the ALMA Front End Sub-System

Operation of the FEICs is well synchronized to guarantee that the products, Front End Assemblies, delivered by each of the FEICs are identical in configuration and performance. All three FEICs work according to the same Front End Assembly technical specifications and verification procedures. Test equipment used at the different FEICs might vary but the performance of test sets used in verification of front ends meet identical minimum requirements.

C. *Acceptance Process*

Given the complexity of the integration process of ALMA Front Ends a clearly defined and rigorous acceptance process has been established to guarantee product quality. Fig. 9 provides a schematic model of the primary steps in accepting and delivering components to a FEIC and to the ALMA Observatory in Chile. Each step is clearly documented and agreed with the stake holders involved.

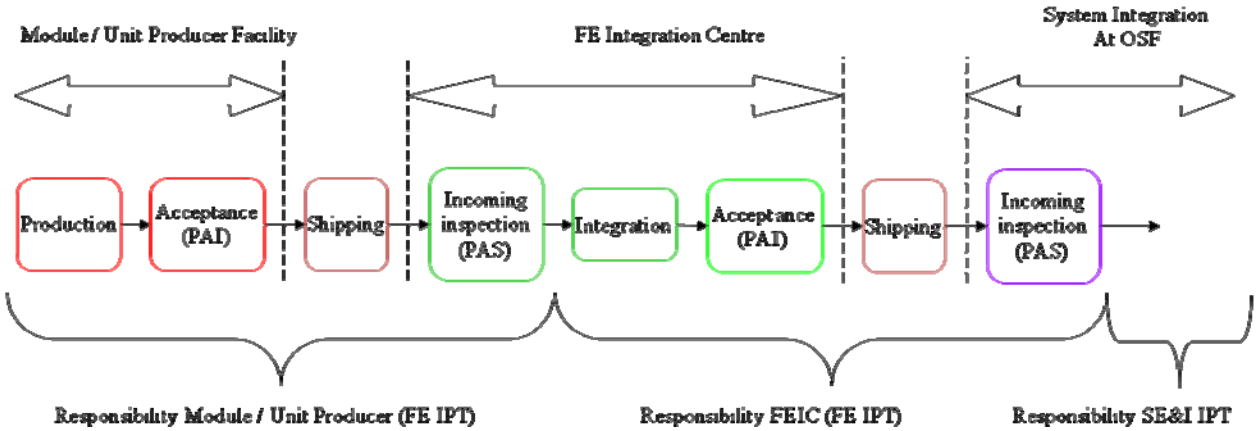

Fig. 9: Delivery and Acceptance model to / from Front End Integration Centres

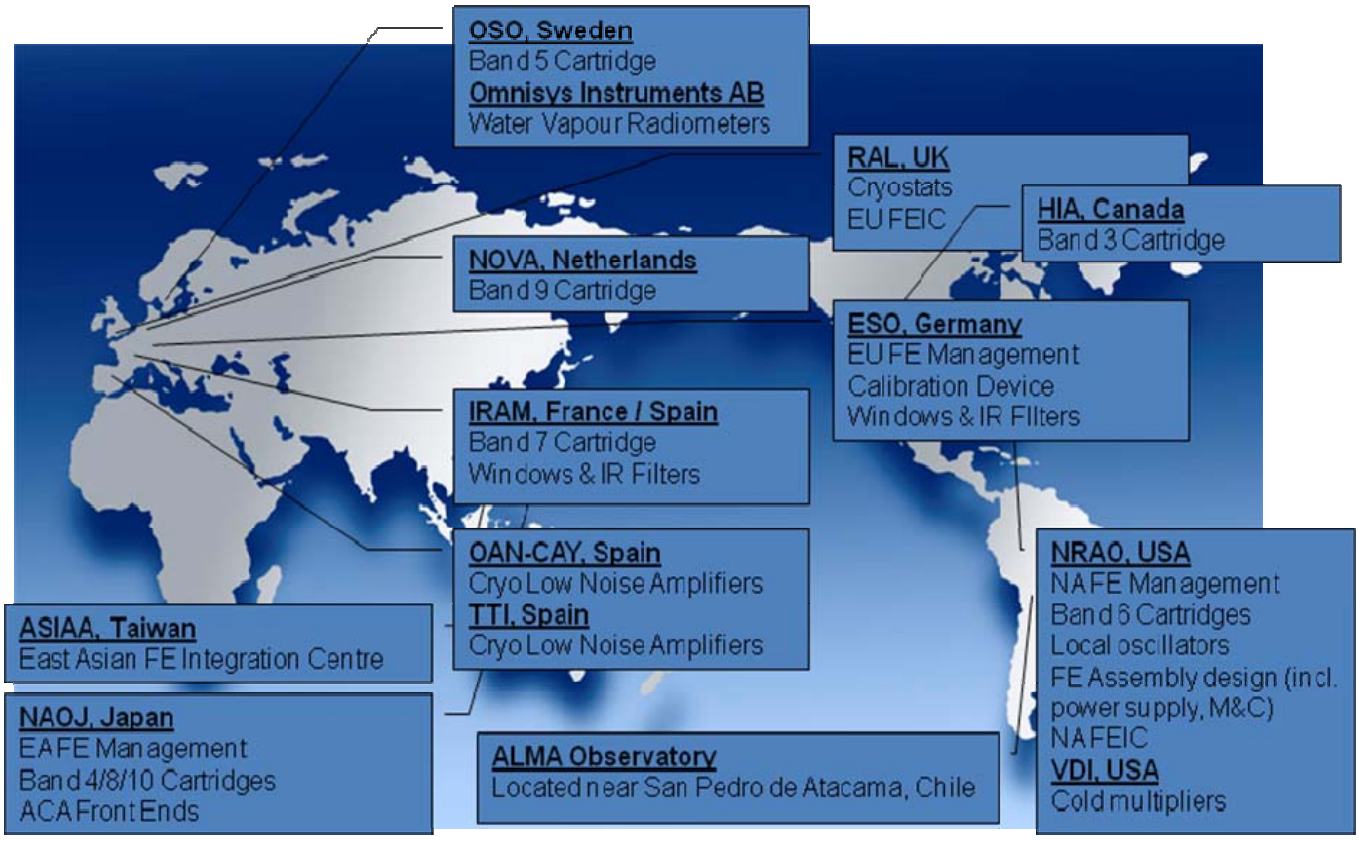

Fig. 10: Overview and location of key organizations contributing to the ALMA front ends.

CONCLUSIONS

This article summarizes the technical concept and requirements of the ALMA receivers. Organizational aspects how this project is organized, involving partners on three different continents, for development and production are presented as well.

ACKNOWLEDGMENT

The work reported in this article is the result of efforts made by many individuals both inside the ALMA Project as well as from other organizations. The author expresses his great appreciation to all who make this exceptional project reality.

REFERENCES (PLACEHOLDER)

[1] S. M. Metev and V. P. Veiko, *Laser Assisted Microtechnology*, 2nd ed., R. M. Osgood, Jr., Ed. Berlin, Germany: Springer-Verlag, 1998.

[2] J. Breckling, Ed., *The Analysis of Directional Time Series: Applications to Wind Speed and Direction*, ser. Lecture Notes in Statistics. Berlin, Germany: Springer, 1989, vol. 61.

[3] S. Zhang, C. Zhu, J. K. O. Sin, and P. K. T. Mok, "A novel ultrathin elevated channel low-temperature poly-Si TFT," *IEEE Electron Device Lett.*, vol. 20, pp. 569–571, Nov. 1999.

[4] M. Wegmuller, J. P. von der Weid, P. Oberson, and N. Gisin, "High resolution fibre distributed measurements with coherent OFDR," in *Proc. ECOC'00*, 2000, paper 11.3.4, p. 109.

[5] R. E. Sorace, V. S. Reinhardt, and S. A. Vaughn, "High-speed digital-to-RF converter," U.S. Patent 5 668 842, Sept. 16, 1997.

[6] (2002) The IEEE website. [Online]. Available: http://www.ieee.org/

[7] M. Shell. (2002) IEEEtran homepage on CTAN. [Online]. Available: http://www.ctan.org/tex-archive/macros/latex/contrib/supported/IEEEtran/

[8] FLEXChip Signal Processor (MC68175/D), Motorola, 1996.

[9] "PDCA12-70 data sheet," Opto Speed SA, Mezzovico, Switzerland.

[10] A. Karnik, "Performance of TCP congestion control with rate feedback: TCP/ABR and rate adaptive TCP/IP," M. Eng. thesis, Indian Institute of Science, Bangalore, India, Jan. 1999.

[11] J. Padhye, V. Firoiu, and D. Towsley, "A stochastic model of TCP Reno congestion avoidance and control," Univ. of Massachusetts, Amherst, MA, CMPSCI Tech. Rep. 99-02, 1999.

[12] Wireless LAN Medium Access Control (MAC) and Physical Layer (PHY) Specification, IEEE Std. 802.11, 1997.

Design and Development of ALMA Band 4 Cartridge Receiver

Shin'ichiro Asayama*, Susumu Kawashima, Hiroyuki Iwashita, Toshikazu Takahashi,

Motoko Inata, Yoshiyuki Obuchi, Takakiyo Suzuki, and Toru Wada

Advanced Technology Center and ALMA-J project office, National Astronomical Observatory of Japan

* Contact: shinichiro.asayama@nao.ac.jp, phone +81-422-34-3931

***Abstract*— This paper describes the design and development of the ALMA Band 4 cartridge receiver. Band 4 is one of the ten bands that will form the ALMA Front End Receiver. It receives radiation in the 125-163 GHz frequency range in two orthogonal polarizations and down-converts the sideband separated signals to intermediate frequencies between 4 and 8 GHz.**

I. Introduction

The Atacama Large Millimeter/Submillimeter Array (ALMA) is an international collaboration between Europe, Japan and North America, in cooperation with the Republic of Chile with its full-operation expected in 2012 [1]. Taiwan is also contributing to ALMA as a partner of Japan. ALMA will be located on the Chajnantor plain of the Chilean Andes in the District of San Pedro de Atacama, 5,000 meters above sea level. The ALMA receiver system will cover all the available atmospheric frequency windows between 30 GHz and 950 GHz. The range shall be covered in 10 bands with HEMT or SIS devices. The receiver should be modular so that one easy to install self-contained receiver should cover that one particular frequency band. These self-contained receivers are known as "cartridges". The development and production of the Band 4 cartridge receivers is one portion of the Japanese in-kind contribution to ALMA.

II. Receiver Overview

ALMA Band 4 will operate in the 125-163 GHz frequency band, which is 26 % bandwidth to the center frequency of 144 GHz. A layout of the Band 4 cartridge receiver and a photograph of the assembled cartridge are shown in Fig. 1 and Fig. 2, respectively. Band 4 receivers are made on the small 140mm diameter cartridges developed by Rutherford Appleton Laboratory (RAL). It is a dual polarization receiver, which uses an orthomode transducer (OMT) as a polarization splitter. The cartridge consists of three stages (at operating temperatures 4, 15, and 110 K) and the base-plate (which acts as a vacuum seal) at 300 K, with GFRP 10 spacers between them. The 110 K stage has the LO doublers mounted on it and heat sinks for the LO waveguide, coax cables and wiring. The 15 K stage has only heat sinks for the LO waveguide, coax cables and wiring attached. The 4 K stage has the Corrugated horn, OMT, optics support structure, sideband-separating SIS mixer units, Cryogenic Isolators, Cryogenic HEMT Amplifiers, and heat sinks for the LO waveguide, coax cable and wiring attached.

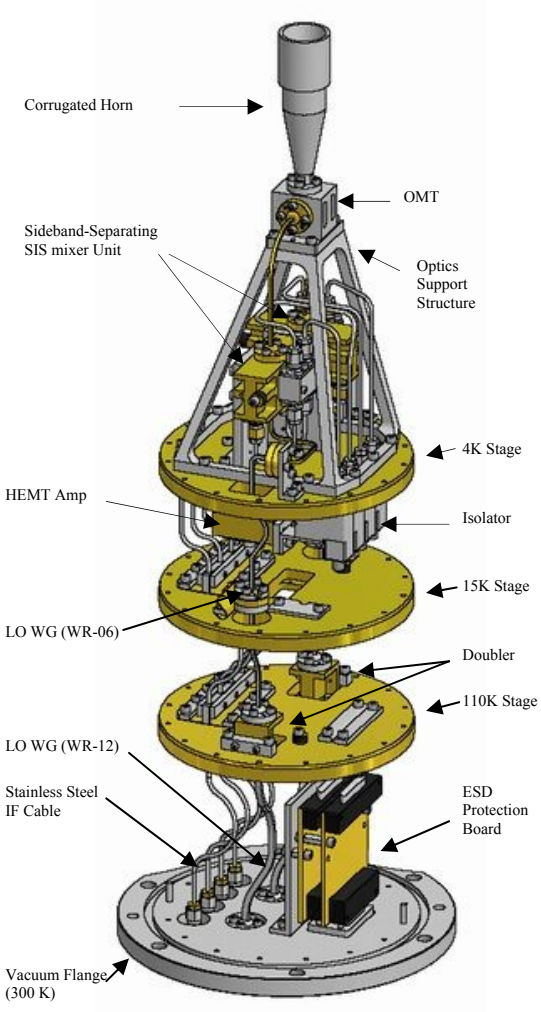

Fig.1 Layout of the ALMA Band 4 cartridge receiver. DC wire harnesses are not illustrated

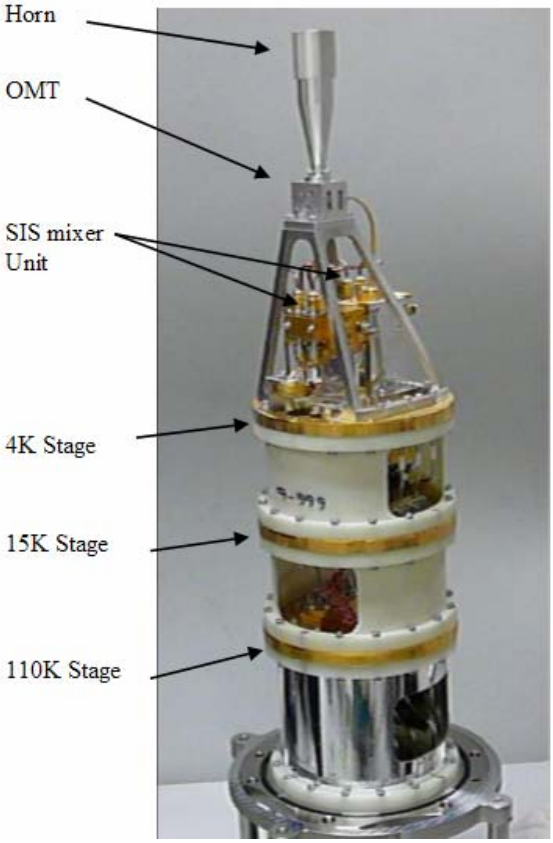

Fig.2 View of complete cartridge

A. . Optics Scheme

The Band 4 optics design was done by K. Kimura and H. Ogawa, and is shown in Fig. 3. Their work was in close collaboration with the optics calculations of C-Y. Tham [2]. There is not enough room inside the cartridges to have cold optics as for bands 5 and above. The system chosen is to have ambient temperature mirrors. The beam coming from the telescope is incident on a flat mirror, which reflects the beam out to an elliptical mirror and then the beam is focused down into the cryostat onto the horn. It is a dual polarization receiver, which uses an orthomode transducer (OMT) as a polarization splitter. An OMT is a passive waveguide device that separates the signal received by the feed horn into its two orthogonal linearly polarized components. Band 4 OMT has been designed to make the two outputs orthogonal to each other as required for the cartridge construction.

The Band 4 corrugated horn was designed by K. Kimura [3]. It is a conventional corrugated horn with a total length of 94 mm and horn diameter of 28 mm. The slot width and depth of the corrugation are 0.34mm and 0.8 - 0.52mm (depending on position), respectively. This corrugated horn was fabricated using NC machining suited for the series production process.

A. Mixing Scheme

To meet the technical specification of the ALMA Band 4 receiver, we developed a sideband-separating SIS mixer. The design uses two double sideband (DSB) SIS mixers in a single mixer block containing waveguide hybrids, and LO power dividers and couplers. Approximately -20 dB of the LO power is coupled to each of the building block mixers. The sideband separation results from two 90 degree hybrids: One is an RF hybrid in the mixer block and the other is an IF hybrid. There are no mechanical tuners.

C. LO Scheme

For each polarization channel cryogenic doublers (made by Virginia Diodes) is mounted on the 110 K stage. The doubler is pumped by a microwave signal in the range of 66.5 to 77.5 GHz which corresponds to an output frequency range of 133 to 155 GHz.

The room temperature driver for the LO system is made at National Radio Astronomical Observatory (NRAO) in Charlottesville. It is based on a YIG oscillator, its signal is multiplied ×3 and amplified by a power amplifier. Details of similar system can be found in [4].

D. IF Scheme

A Band 4 cartridge uses GaAs-Based 3-stage Cryogenic amplifiers via a cryogenic isolator, to amplify IF signal between 4-8 GHz from two 2SB mixers of dual polarization.

At room temperature, 4 dB gain-slope-corrected amplifiers are used to compensate for frequency dependent cable losses and mixer gain variation.

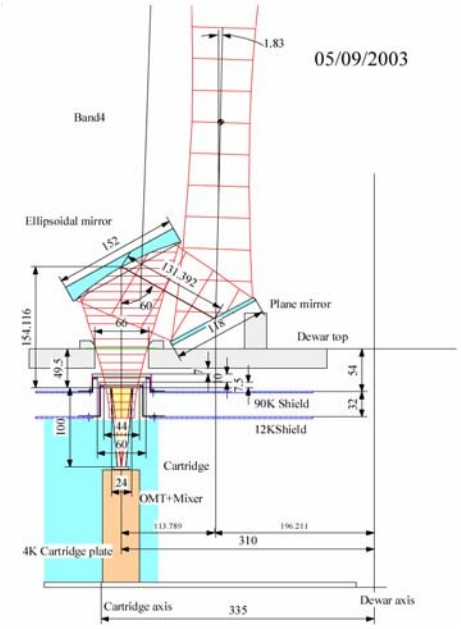

Fig.3 Design of the Band 4 Optics

III. Demonstrated Components Performance

A. Integrated 2SB mixers

The cartridge contains two sideband-separating SIS mixers. The basic design of the Band 4 sideband-separating SIS mixer is the same as the scaled model described by Asayama et al. [5]. To couple the LO and RF signals into a quasi-TEM-mode microstrip line, a bow-tie waveguide probe based on a 200 μm-thick quartz substrate was adopted. The mixer device was a parallel-connected twin-junction (PCTJ) [6]. 1.8 x 1.8 μm size SIS junction of a current density of 3 kA/cm^2 ($\omega RnCj$ =3.6) were adopted. The normal-state resistance of the SIS junction is about 20 Ω and the junction's specific capacitance is estimated to be 60 fF/μm^2.

A quarter wavelength impedance transformer made of superconducting stripline was integrated with the SIS junctions on the mixer device. A photograph of the device configuration on the mixer device is shown in Fig. 4. The upper conductor of the stripline was extended from the feed point in the center of the waveguide to the SIS junctions, where the RF choked electrode was used as a ground plane. To reduce source impedance further, a mirror symmetrical circuit pattern about the bisection plane in the center of the waveguide was introduced. Using this method, the source impedance seen from the mixer device is only half of the feed point impedance.

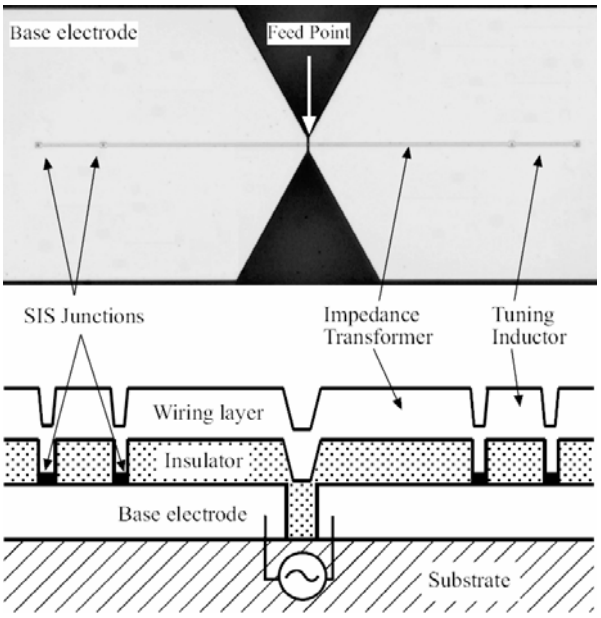

Fig.4 Photograph (upper) and schematic (lower) of a PCTJ device.

A photograph of the assembled 2SB mixer block with IF hybrid coupler is shown in Fig. 5. The waveguide is standard WR-06 (1.65x0.825 mm). The split-block waveguide devices are manufactured from tellurium copper and then gold plated.

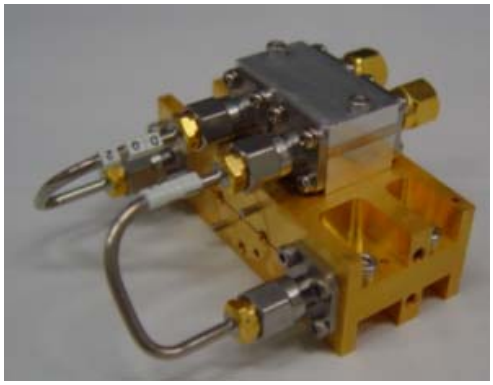

Fig.5 Photograph of the assembled 2SB mixer block with IF hybrid.

The measured receiver noise temperatures and image rejection ratios are plotted in Fig. 6. Those noise temperatures were corrected for the contribution of the image sideband. For measuring image rejection, the method presented by Kerr et al, was used [7]. The measured results shown in Fig. 6 demonstrate that the noise temperature is below 45 K and the image rejection ratio better than 10 dB throughout the RF band. Although the noise temperature tends to increase at the higher IF frequency in some cases, the results meet the ALMA specifications.

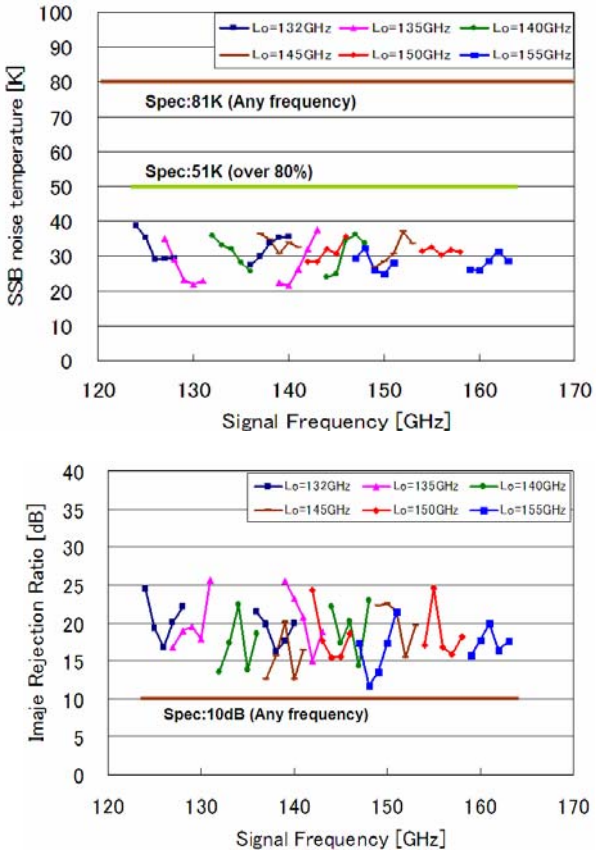

Fig.6 Measured SSB noise temperature (top), and image rejection ratio (bottom) for the integrated 2SB mixer.

B. Beam performance

Beam pattern of Band 4 corrugated horn and warm optics assembly was measured using a NSI Model 200V-3x3 Vertical Planar Near-field System [8]. Fig. 7 shows the block diagram of a cold beam pattern test setup. A view of the measurement setup is shown in Fig. 8.

Warm optics assembly was mounted on test dewar top plate. An ALMA Band 4 window was used on the test dewar. However, due to the mechanical conflict between the horn and IR filter position, IR filters were not installed in test dewar.

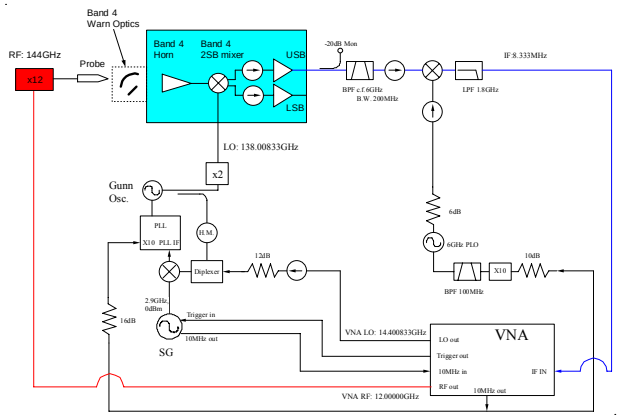

Fig.7 Block diagram of a cold beam pattern setup

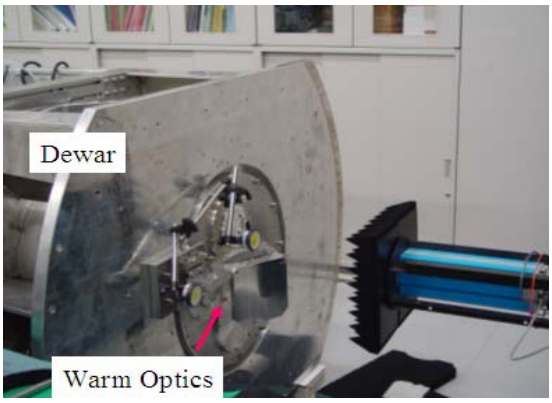

Fig. 11 Band 4 cold beam pattern test setup

2-D plots of the co-polar beam patterns at far-field are shown in Fig. 9. The peak of cross polarization is lower than the co-polar one by 25 dB. Cross sectional view of the co-polar far-filed beam patterns measured and simulations are shown in Fig. 10. As can be seen in these plots, the measurement results are in reasonable agreement with the design. The measured co-polar beam patterns are consistent with the simulation down to a level of -25 dB.

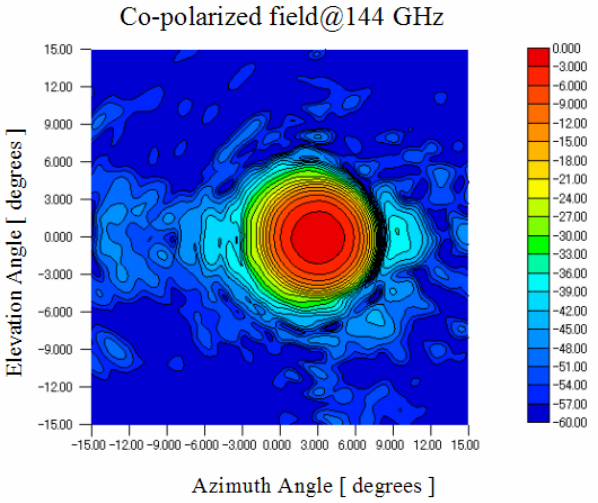

Fig.9 Far-field Beam pattern of Band 4 cold beam pattern (Warm optics + window + horn) at 144GHz. Contours are every 3 dB.

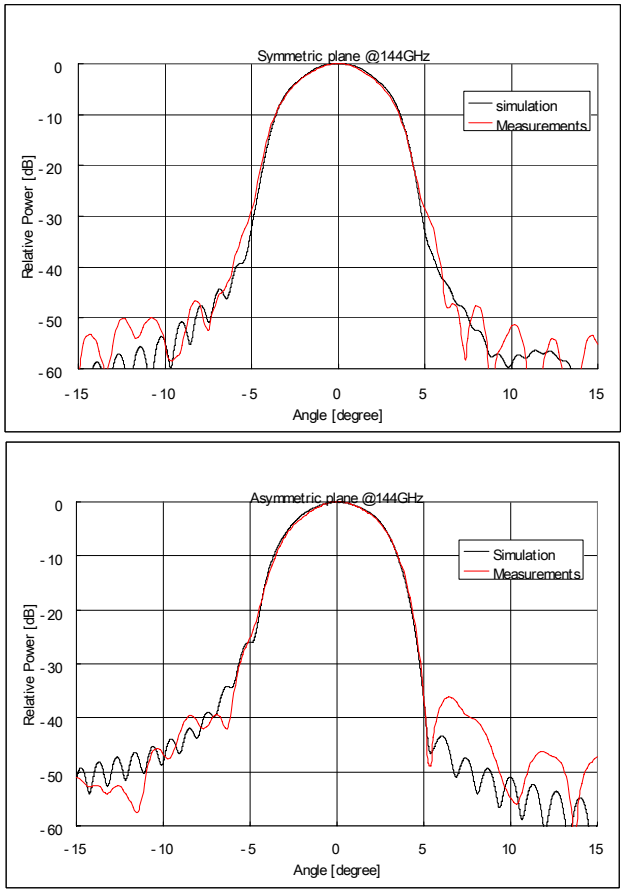

Fig.10 Cross sectional views of co-polar beam patterns in the symmetric and asymmetric plane along with the beam axis. Red lines indicate measured beam patterns. Black lines are the physical optics calculation by M. Sugimoto.

C. 2 MM BAND ORTHO-MODE TRANSDUCER

The double ridged waveguide-based design was adopted for Band 4 OMT and has been designed and developed. The double ridged section was designed referring to that described by Dunning [9]. Fig. 11 shows the wire frame model of the complete orthomode transducer. Signals split by the OMT junction are recombined using a power combiner, implemented using the E-plane Y-junction. The combiner was designed referring to ALMA memo #381 [10].

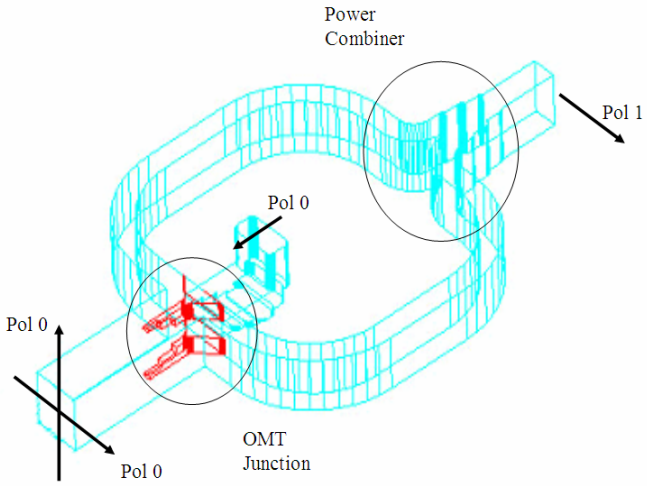

Fig.11 Wire frame model of the waveguide structure of the OMT.

Photograph of the 2 mm OMT Split-Block is shown in Fig. 12. The split-block was designed referring to that described by Narayanan et al [11] and MOOREY et al [12]. The long oval waveguide for the vertical (main arm) polarization was fabricated using NC machining. Machining errors of the OMT were measured with the contactless laser measurement system. The RMS machining errors were better than 20 microns.

Measurements were performed at room temperature using an Agilent vector network analyzer (WR-06: 110 to 170 GHz). Fig. 13 through Fig. 14 show measured insertion losses, return losses of Seven OMTs. Seven Band 4 OMTs show the return losses better than 18 dB, insertion losses of less than - 0.5 dB. Cross polarization couplings of better than -28 dB across the 125 – 163 GHz.

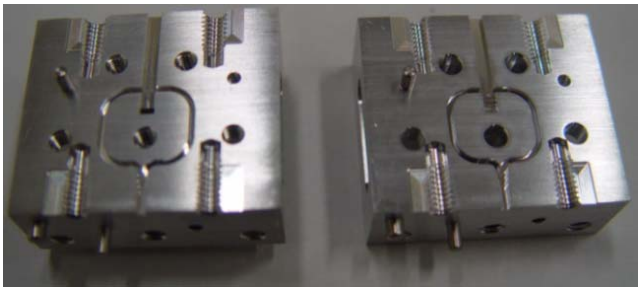

Fig.12 Split-block view (Top) and assembled Band 4 OMT block (Bottom)

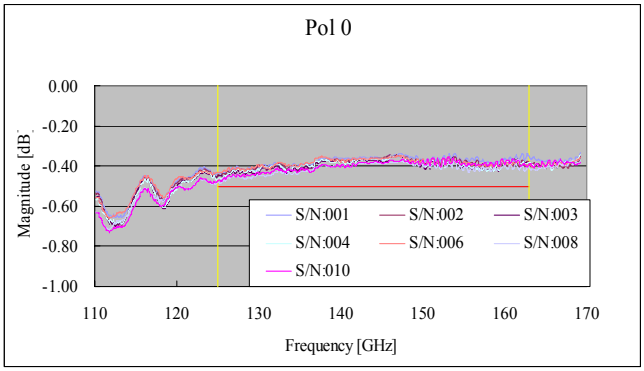

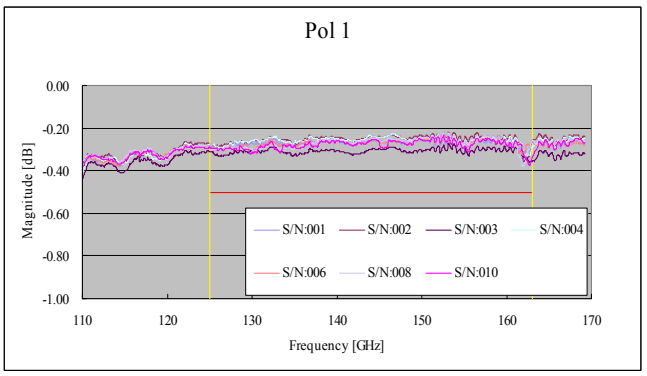

Fig.13 Measured insertion loss of Band 4 orthomode transducer

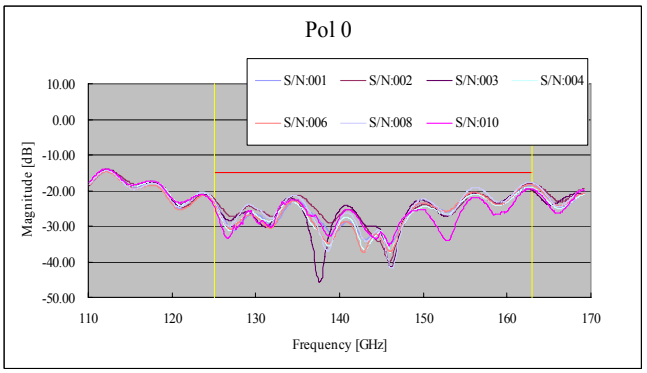

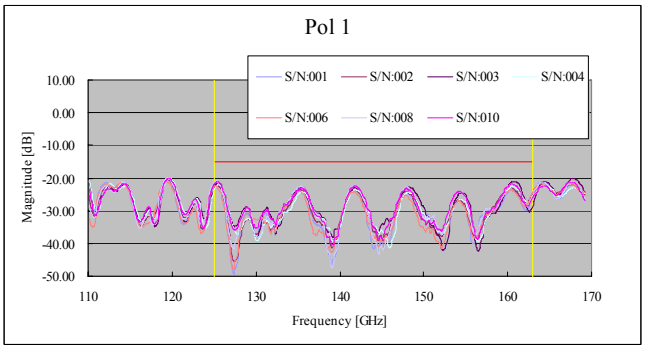

Fig.14 Measured return loss of Band 4 orthomode transducer

IV. Measurements of the Prototype Cartridge

The overall receiver noise temperatures of the Band 4 prototype cartridge averaged over the IF band of 4-8 GHz are plotted in Fig. 15. The noise temperatures were corrected for the contribution of the image sideband at IF center frequency 6 GHz. The noise performance includes the contribution of the vacuum window, IR filters, and IF amplifier chain. The measured single-sideband (SSB) receiver noise temperatures meet the ALMA noise temperature specification.

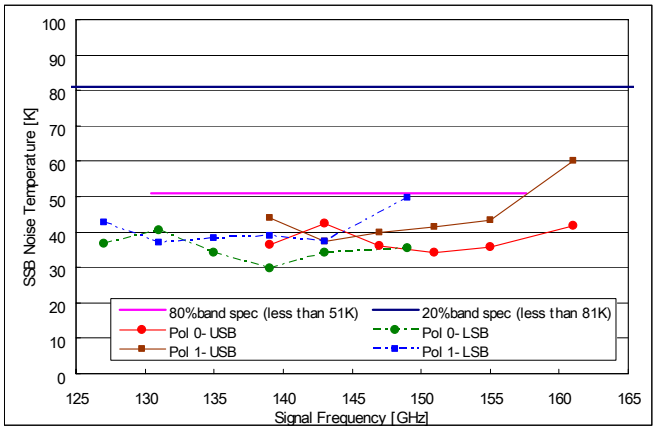

Fig.15 SSB noise temperature of ALMA band 4 2SB mixer with averaging over the IF band of 4 – 8 GHz. Those noise temperature were corrected for the contribution of the image sideband at IF center frequency 6 GHz.

Conclusions

In conclusion, we have been developing the ALMA Band 4 cartridge receiver. To meet the technical specification, we have developed corrugated horn, OMT, 2SB SIS mixer, etc. The prototype cartridge results is promising that the Band 4 cartridge will meet the ALMA technical specification.

Acknowledgment

Authors would like to thank Y. Kiuchi for fabricating Band 4 SIS devices. We would also like to thank M. Sugimoto, Y. Sekimoto, Y. Uzawa, T. Noguchi, G. Fujii, S. Honma for their invaluable comments. We are also grateful to H. Ogawa and K. Kimura, and the entire people of the Advanced Technology Center and ALMA-J project office for their useful discussions and support.

References

[1] ALMA web site, http://www.alma.nrao.edu/.

[2] M. Carter, A. Baryshev, M. Harman, B. Lazareff. S. Navarro, D. John, G. Ediss C-Y. Tham, F. Tercero. R. Nesti, Y. Sekimoto, M. Matsunaga, H. Ogawa, “ALMA Front-end Optics report”, 2004.

[3] K. Kimura, H. Iwashita, S. Asayama, M. Sugimoto, G. Kikuchi, H. Ogawa, “Antenna Performance of a Directly Dug Corrugated Feedhorn for the 150-GHz Band”, IJIRMW, vol. 29, no. 8, pp 713-723, 2008

[4] E. Bryerton, K. Saini, M. Morgan, D. Thacker, “Development of Electronically Tuned Local Oscillators for ALMA”, 30th Int Conf on Infrared and Millimeter Waves, Sept 2005.

[5] S. Asayama, H. Ogawa, T. Noguchi, K. Suzuki, H. Andoh, A. Mizuno, “An Integrated Sideband-Separating SIS Mixer Based on Waveguide Split Block for 100 GHz Band with 4.0 - 8.0 GHz IF”, IJIRMW, vol. 25, no. 1, pp107-117, 2004

[6] S. C. Shi, T. Noguchi, and J. Inatani, “A 100 GHz fixed-tuned waveguide SIS mixer exhibiting broad bandwidth and very low noise temperature”, IEEE Trans. Appl. Superconduct., vol.7, no.4, pp.3850–3857, 1997.

[7] A. Kerr, S-K.Pan, J.E.Effland, “Sideband Calibration of Millimeter-Wave Receivers,” ALMA Memo #357, March 27, 2001.

[8] Nearfield Systems Inc, http://www.nearfield.com

[9] A. Dunning, “Double Ridged Orthogonal Mode Transducer for the 16-26GHz Microwave Band,” Proceedings of the Workshop on the Applications of Radio Science, 2002

[10] A. R. Kerr, “Elements for E-Plane Split-Block Waveguide Circuits,” ALMA Memo #381, July, 2001.

[11] G. Narayanan and N. Erickson, “Full-Waveguide Band Orthomode Transducer for the 3 mm and 1mm Bands,” Proceedings of the 14th International Symposium on Space Terahertz Technology, Tucson, Arizona, Apr. 2003, pp 508-512.

[12] G. G. Moorey, R. Bolton, A. Dunning, R. Gough, R, H. Kanoniuk, L. Reilly, "A 77-117 GHz cryogenically cooled receiver for radioastronomy". Workshop in Applications of Radio Science (WARS2006), Leura, NSW, 15-17 February, 2006.

ALMA Band 5 (163-211 GHz) Sideband Separation Mixer Design

Bhushan Billade[1,*], Victor Belitsky[1], Alexey Pavolotsky[1], Igor Lapkin[1], Raquel Monje[1], Vessen Vassilev[1], Jacob Kooi[2]

[1]*Group for Advanced Receiver Development, Chalmers University of Technology, Gothenburg, SE 412 96, Sweden*

[2]*California Institute of Technology, Pasadena,USA*

* Contact: Bhushan.Billade@chalmers.se, phone +46-31-772 1851

***Abstract*— We present the design of ALMA Band 5 sideband separation mixer based on Niobium superconducting SIS junctions and first experimental results for the double side band mixer. In this mixer the LO injection circuitry is integrated on the mixer substrate using a microstrip line directional coupler with slot-line branches in the ground plane. The isolated port of the LO coupler is terminated by a wideband floating elliptical termination. The mixer employs two SIS junctions with junction area of 3 μm^2 each, in twin junction configuration, followed by a quarter wave transformer to couple it to the RF probe.**

First measurements of the DSB mixer show promising results with noise temperature around 35K over the entire band.

I. Introduction

The Atacama Large Millimetre Array (ALMA) is a radio interferometer under construction by an international consortia consisting of European countries (ESO), USA, Canada, and Japan. With its more than 50 antennas and reconfigurable baseline up to 10 Km, ALMA will be the most sensitive radio telescope at mm/submm wavelengths in the world.

The work presented here concerns development of one of the bands of ALMA project. ALMA Band 5 will be a dual polarization sideband separating heterodyne receiver covering 163-211 GHz with 4 - 8 GHz IF. For each polarization, Band 5 receiver employs sideband rejection quadrature layout (2SB) based on SIS mixers. The major challenge with Band 5 mixer design is that there is a very limited space inside the cartridge. Amongst the other ALMA bands, Band 5 is the lowest frequency band which uses all cold optics. The optics dimensions put strong constraints on the sizes of all the receiver components and demand a very compact design. Furthermore, the arrangement of components in the cartridge is such that the output of mixer should be directed pointing down along the cartridge axis. In such a configuration, the mixer design with a spilt block technique becomes too big to fit inside the cartridge; the only possible solution is to use a mixer block configuration with waveguide back piece [2]. This design allows very compact design of the mixer block and also IF output pointing in desirable direction. Furthermore, to avoid extra cables and hence RF losses, all the components in the chain are directly attached to each other with SMA connectors. This design requires a custom made IF hybrid in order to fit the distance between the SMA connectors of the 2SB mixer IF outputs.

Since there is limited cooling capacity at 4K stage, we can only allow 35mW heat produced at this stage, which does not allow us to integrate the DC bias circuitry into the mixer. In our design, the DC biasing to the mixer is done using a bias box placed on 15K plate. The IF hybrid connected at the end of the 2SB mixer will have an integrated bias-T, and the DC biasing will be achieved through the output SMA connector of the mixer (figure 1).

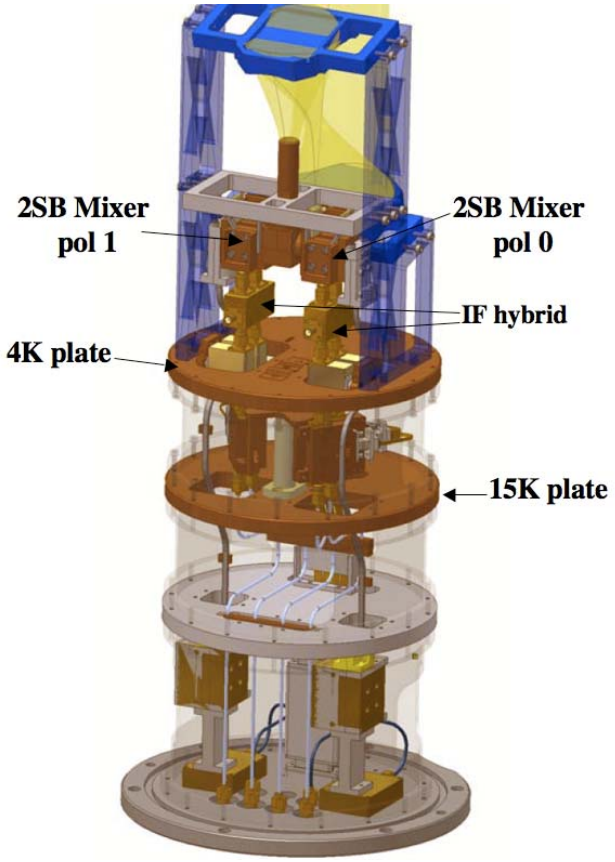

Fig. 1 ALMA Band 5 cartridge layout.

II. MIXER DESIGN

A. Mixer Chip Design

The chip is fabricated on a 90 µm thick crystalline quartz substrate with dimensions 310 µm wide and 2640 µm long. The mixer chip contains most of the DSB components integrated on the same quartz substrate along with the SIS junctions. The chip comprise of an E-plane probe for the waveguide-to-microstrip transition for both the LO and RF, an RF choke at the end of the probe provides virtual ground for the signal. We use the same probe with impedance of around 40 Ω for both the LO and RF.

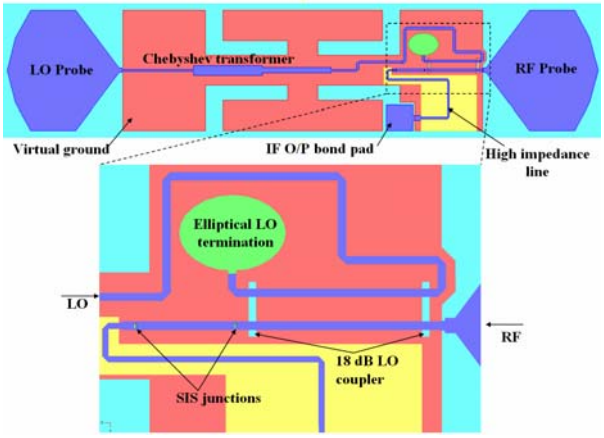

Fig. 12 Mixer chip layout on quartz substrate, containing LO and RF probe, RF choke structure, and IF bond pad. A zoomed vied of 18dB LO coupler, elliptical termination and SIS junction.

The RF probe is followed by a LO coupler and two SIS junctions in twin configuration, and the IF is extracted between the RF and LO waveguides using a high impedance line (Figure 2). The LO probe is followed by a three stage Chebyshev transformer to match the probe impedance to the LO coupler input, and the reflected signal at the isolated port of LO coupler is terminated using wideband floating elliptical resistive termination [1]. The elliptical termination has the sheet resistance (12 Ω) same as that of the impedance of the LO coupler.

The shape of the E-plane probe is optimised for broadband performance using Electromagnetic Design System (EMDS), a full 3D EM solver. Probe's real impedance is 42Ω with ± 4% variation across the entire RF band and imaginary impedance of the probe varies between +j5 Ω to –j2 Ω. A hammer type RF choke provides a virtual ground for the RF/LO signal applied between the ends of the probe and the choke, which excites microstrip mode between the top conductor layer (LO/RF) and the bottom ground (choke) layer. The thickness of the silicon dioxide layer used for the microstrip line is 350 nanometres. In order to achieve broadband performance from the mixer we use two SIS junctions in twin junction configuration [3, 4] with junction size 3 µm² each and RnA product of 30. The distance between the two junctions is optimised using transmission line such that the imaginary part of the twin junction configuration is tuned out. In this configuration the LO coupler serves two purposes: first, it couples the LO signal to RF with weak -18 dB coupling and secondly, it transforms the probe impedance from 40 Ω to the input impedance of the twin junction circuitry.

B. Mixer Block Design

The mixer block consists of two parts, a mixer back piece and a middle piece. The mixer back piece holds mixer chip glued to the block using wax, a 50 to 15 Ω IF transformer produced on a 500µm thick alumina substrate, the IF output from the mixer chip is extracted using a bond wire. A single layer capacitor is used at the IF side to compensate for the inductance of the bond wire and to achieve good IF matching.

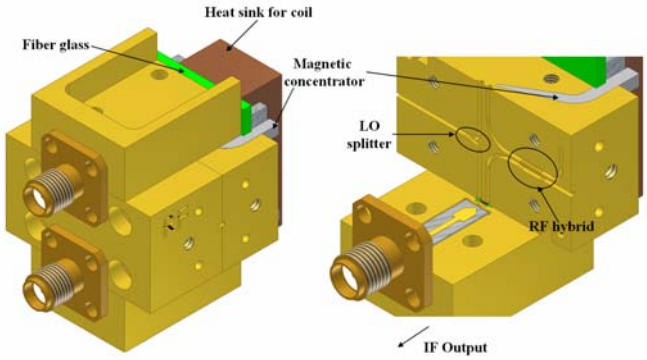

Fig. 13 2SB Mixer block with two mixer back piece and a middle piece.

The two mixer back pieces used in the 2SB configuration are exactly identical, however the mixer chips used have mirrored layout. The middle piece consists of a 90^0 RF hybrid and an in-phase LO splitter. In order to suppress the Josephson current, the middle piece also holds magnetic concentrators. The magnetic coils used sit in a copper heat sink. This assembly is connected to the middle piece using fibreglass in between to avoid heat leak from the coils to the mixer block.

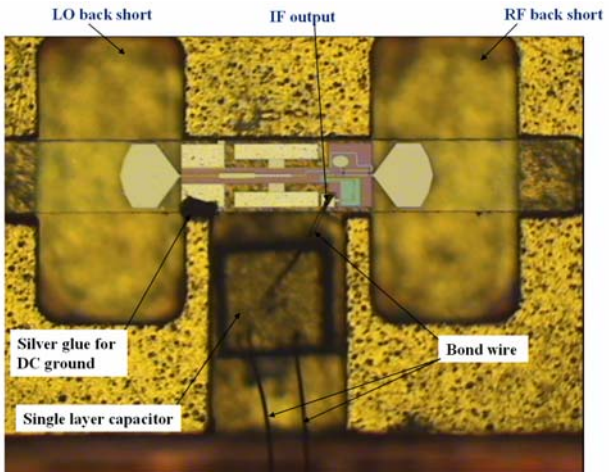

Fig. 4 Mixer back piece with mixer chip.

Figure 4, shows the mixer back piece with the chip installed. In this configuration the mixer chip sits perpendicular to the direction of E-field in the waveguide. The quartz substrate used for the chip extends the full height of both LO and RF waveguides and even further; this enables a better thermal contact of the chip with the mixer block.

III. DSB Measurement Results

Figure 5 shows the first experimental results of the DSB mixer, the noise measurements were performed with standard Y factor measurement technique using a hot (293 K) and cold (LN_2 77 K) load placed in front of the test cryostat window.

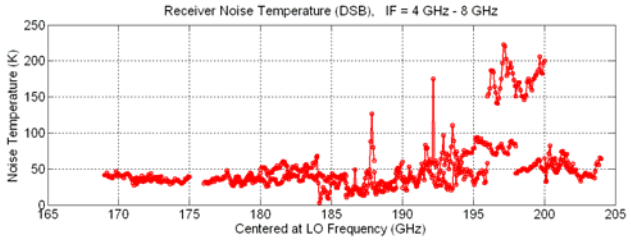

Fig. 5 An un-averaged noise measurement results of DSB mixer.

Figure 5, shows the un-averaged noise measurement performed over the entire IF bandwidth with respect to a particular LO frequency. It can be seen from the plot that the noise performance is flat over the IF band for all LO frequencies, except there are few strange peaks at IF for LO frequencies 188 and 192 GHz, and at 197 GHz the Y factor drops abruptly, rising the noise temperature to 170K.

Figure 6 shows the noise measurements averaged over the entire bandwidth, with noise temperature around 35K across the band.

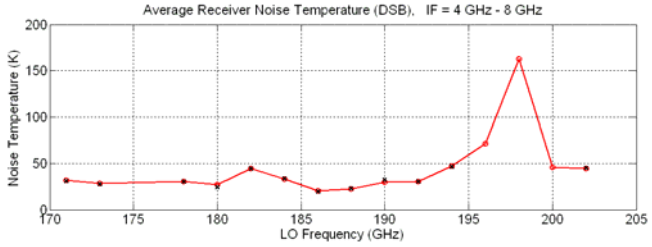

Fig.6 Noise measurements averaged over the entire IF bandwidth.

An increase in the noise performance around 197 GHz is associated with the way chip was grounded. In this measurement setup we used a silver paint to DC ground the chip instead of planned bondwire ground around the hammer structure of the choke. We plan further experiments to investigate the effect of the DC grounding position on the choke performance. Another possibility is that increased noise comes from the LO source and at this point neither of the reasons could be ruled out completely. [1] .

Both these problems need careful investigation. Furthermore, we need to check whether this strange behaviour comes from the mixer chip tuning structure or the embedding circuitry itself.

Conclusions

In this paper we present the design and first measurement results of a DSB SIS mixer for ALMA Band 5 (163-211 GHz). The mixer design uses on-chip LO injection circuitry employing a -18 dB microstrip slot-line directional coupler and a high performance elliptical termination for the isolated port of the LO coupler. The first measurement of ALMA Band 5 DSB mixer shows promising results with 35K noise temperature across the band. The deviation in the noise performance at LO frequency 197 GHz need investigation.

Acknowledgment

Authors would like to thank Dr. Denis Meledin, Dr. Vincent Desmaris, and Dimitar Dochev for their help and useful discussion. We would like to thank our machining expert, Sven-Erik Ferm, for his useful tips and comments for designing the mixer block. Also, authors would like to thank Doug Henke for useful discussion and his help during the design and measurements. This project is funded by EU FP6 construct 515906 ALMA Enhancement.

References

[1] "High quality micro-strip termination for MMIC and millimeter - wave applications", Raquel Monje, V. Vassilev, A. Pavolotsky, V. Belitsky, IEEE MTT-S international microwave symposium, June 2005.

[2] "SIS Mixer for 385-500 GHz with on chip LO injection", Raquel Monje, Victor Belitsky, Christophe Risacher, Vessen Vassilev and Alexey Pavolotsky, Proceedings of 18th International Symposium on Space Terahertz Technology, March 2007.

[3] Belitsky V. , Tarasov M.A., "SIS Junction Reactance Complete Compensation", IEEE Trans. on Magnetic, 1991, MAG- 27, v. 2, pt. 4, pp. 2638-2641.

[4] Belitsky V. , Jacobsson S.W., Filippenko L.V., Kovtonjuk S.A., Koshelets V.P., Kollberg E.L., "0.5 THz SIS Receiver with Twin Junctions Tuning Circuit., " Proc. 4th Space Terahertz Technology Conference, p.538, March 30 - April 1, 1993, Los Angeles, USA.

[5] "Quantum detection at millimeter wavelengths", John Tucker and Marc Feldman, review of Modern Physics vol. 57, No. 4, Oct 1985.

[6] Improving accuracy of superconducting microstrip line modeling at millimeter and sub-millimeter waves, Victor Belitsky, C. Risacher, M. Pantaleev, V. Vassilev, ALMA memo no. 533, Oct 2005.

[7] "A full height waveguide to thin film micro-strip transition with exceptional RF bandwidth and coupling efficiency", J. Kooi, G. Chattopadhyay, S. Withington, F. Rice, J. Zmuidzinas, C. Walker, and G. Yassin, IR & MM waves, vol. 24, no. 3, 2003.

[8] "Surface impedance of superconductors and normal conductors in EM simulators", A. R. Kerr, MMA memo no. 245, Jan 1999

Development of ALMA Band 8 (385-500 GHz) Cartridge

Y. Sekimoto[1,2,*], Y. Iizuka[1], N. Satou[1], T. Ito[1], K. Kumagai[1], M. Kamikura[1,2], M. Naruse[1,2], and W. L. Shan[3]

[1]*National Astronomical Observatory of Japan, Tokyo 181-8588, Japan*

[2]*University of Tokyo, Department of Astronomy, Japan*

[3]*Purple Mountain Observatory, China*

* Contact: Sekimoto.Yutaro@naoj.ac.jp, phone +81-422-34-3982

***Abstract*—We have developed a cartridge-type receiver covering from 385 to 500 GHz for pre-production of ALMA Band 8. It receives two orthogonal polarizations and down-converts the sideband-separated signals to intermediate frequencies (IF) between 4 and 8 GHz. The cartridge-type receiver consists of a cold optics, a feed horn, an OMT, two sideband-separating SIS mixers, cryogenic multipliers of local oscillator (LO). These components were individually tested and then the cartridge was integrated and tested as a complete assembly. We have also developed equipment to test both components and the integrated receiver. The single sideband (SSB) noise temperature of this receiver is 130 K at the band center and 180 K at the band edges. The beam pattern and cross-polarization pattern are consistent with physical optical calculation. These results are promising for receiver production to the Atacama Large Millimeter/submillimeter Array (ALMA).**

I. Introduction

The Atacama Large Millimeter/submillimeter Array (ALMA) is an international astronomy facility, built by Europe, North America, and Japan in cooperation with the Republic of Chile. ALMA, consisting of 64 12-meter diameter antennas and 16 Atacama Compact Array (ACA) antennas, is located in northern Chile at an elevation of 5000 meters. Atmospheric windows from 30 GHz to 950 GHz are covered by 10 frequency bands with relatively wide bandwidth of 20 – 30 % [1][2][3]. Each frequency band is observed with a cartridge-type receiver receiving two orthogonal polarization. The cryogenic interface of the receiver cartridges for the ALMA was proposed by the Rutherford Appleton Laboratory (RAL) in UK[4]. The cartridges are installed in a cryostat at the Cassegrain focus of the antennas with some offset. Each cartridge contains cryogenic receiver optics or warm optics outside of the cryostat toward the sub-reflector. ALMA front end does not employ a mechanical tuner except for calibration device because of operational reliability.

The cartridge-type receiver contains optics, mixers, amplifiers and local oscillators to achieve a modular concept. ALMA cartridges use a cartridge body provided by RAL and two cryogenic multipliers and a warm cartridge assembly provided by NRAO, which includes a YIG oscillator, an active multiplier chain, a bias module, and a controller.

II. Design

A Cartridge

The ALMA Band 8 cartridge receives frequencies from 385 GHz to 500 GHz, which corresponds to 26 % bandwidth with a center frequency of 442.5 GHz. Band 8 cartridge adopted sideband-separating (2SB) mixer of IF 4 - 8 GHz instead of double sideband (DSB) mixer of IF 4 - 12 GHz because the atmosphere in the 400 GHz band has several deep absorptions by H_2O and O_2[5]. To escape from these dips, a sideband-separating mixer is desirable for the Band 8 cartridge [6][7].

We have developed an ALMA Band 8 cartridge pre-production model as shown in Figure 1 based on experience of development of the qualification model [8]. The main difference from the qualification model is a waveguide OMT [8] as a polarization splitter. It has a few advantages:

1. A receiver optics at 4 K stage can be quite simple and compact. An ellipsoidal mirror, a corrugated horn, and a wire grid can be reduced from the cryogenic optics
2. There is no beam squint between two polarizations.
3. A concern on thermal cycle of a wire grid can be resolved.

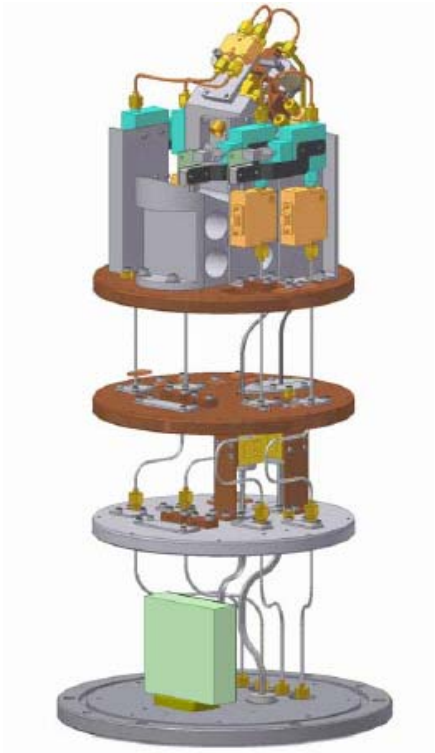

Fig.1 ALMA Band 8 pre-production model cartridge receiver.

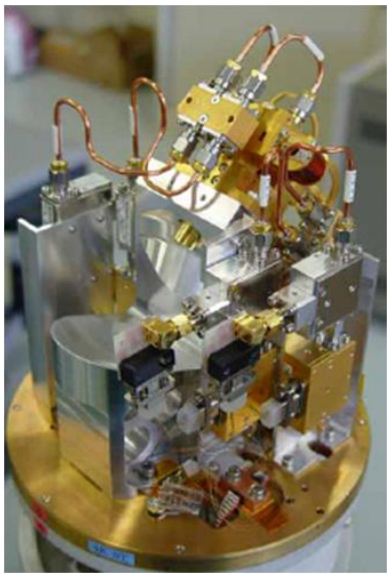

Fig.2 The 4 K stage of ALMA Band 8 pre-production model cartridge receiver.

B Optics

The receiver optics of the ALMA 12 m antenna is described [10]. A physical optics calculation of the ALMA receiver optics was made [11] [12]. They use commercial software, GRASP8 (TICRA Co.). We have repeated their calculation with an updated version of GRASP9.

A cryogenic optics of this receiver adopts a single mirror to couple a feed horn in front of an SIS mixer block and the sub-reflector. An advantage of a single mirror over two mirrors is that it is relatively easy to align optical components of horns, mirrors and a wire grid. A disadvantage is that it is less free of mechanical design of the receiver. A reflection angle at the mirror is 22.5 degrees. The optical parameters were chosen as independent at both the feed horn and the sub-reflector in the frequencies of between 385 and 500 GHz. The receiver optics is inclined 1.006 degrees toward the subreflector.

The optics block was carefully designed mechanically to achieve optical parameters at 4 K.

1. to include cryogenic deformation of optics block at 4 K.
2. to allow mechanical measurements easily, several reference positions on the optics block are added.
3. to reduce weight to 590 grams, holes were drilled in optics block.
4. to reduce standing wave between the subreflector and the horn, an area around the horn aperture was hollowed out.

The optical block and mirrors were made of 6061 aluminium (Fig.). The alignment to the 4 K stage of cartridge body is determined by two 2 mm dowel pins. The block was measured with a coordinated machine, Mitsutoyo LEGEX910 and was consistent with designed values within typically 20 μm.

A corrugated horn for this receiver was designed by [13][14]. The design parameters are horn diameter of 7.99 mm, horn axial length of 24.1 mm, and horn slant length of 24.43 mm. The width and separation of corrugation are 90 μm. The round taper with 675 μm length connects the throat of the corrugation with a diameter of 680 μm and a circular waveguide with a diameter of 568 μm, which is in turn smoothly connected with a length of 1.375 mm to a rectangular waveguide with 556 μm x 278 μm (WR2.2). This was fabricated by electroforming by Oshima Prototype Engineering, Co.

C OMT and Sideband Separating Mixer (2SB)

We have developed an ortho-mode transducer (OMT)[8] and a sideband-separating (2SB) mixer [15]. To reduce waveguide transmission loss, an OMT and two RF quadrature hybrid / LO -17 dB couplers are combined in a waveguide block as shown in Fig. 3.

The Band 8 prototype OMT was a scaled model of Band 4 OMT [16], which has a Boifot junction and a double ridge for polarization separation. It was optimized for mechanical robust design of inner waveguide structure. It has low loss of -0.4 dB at 4 K and good polarization isolation of larger than 25 dB [8].

The sideband separation scheme is based on the design developed for the ALMA Band 4 cartridge[17]. The Band 8 sideband separation (2SB) mixers have been developed with waveguide quadrature hybrid [15]. The cartridge receives both upper and lower sidebands as IF frequencies from 4 to 8 GHz. It employs an RF quadrature hybrid and two single-ended DSB mixers followed by an IF quadrature hybrid as shown in Fig.. We have chosen to adopt a modular approach, which was originally proposed by [18] in which the DSB

mixers and RF/LO coupler are independent. This allows the individual components to be tested separately prior to integration. In the modular scheme, it is essential to establish good interfaces to integrate these components.

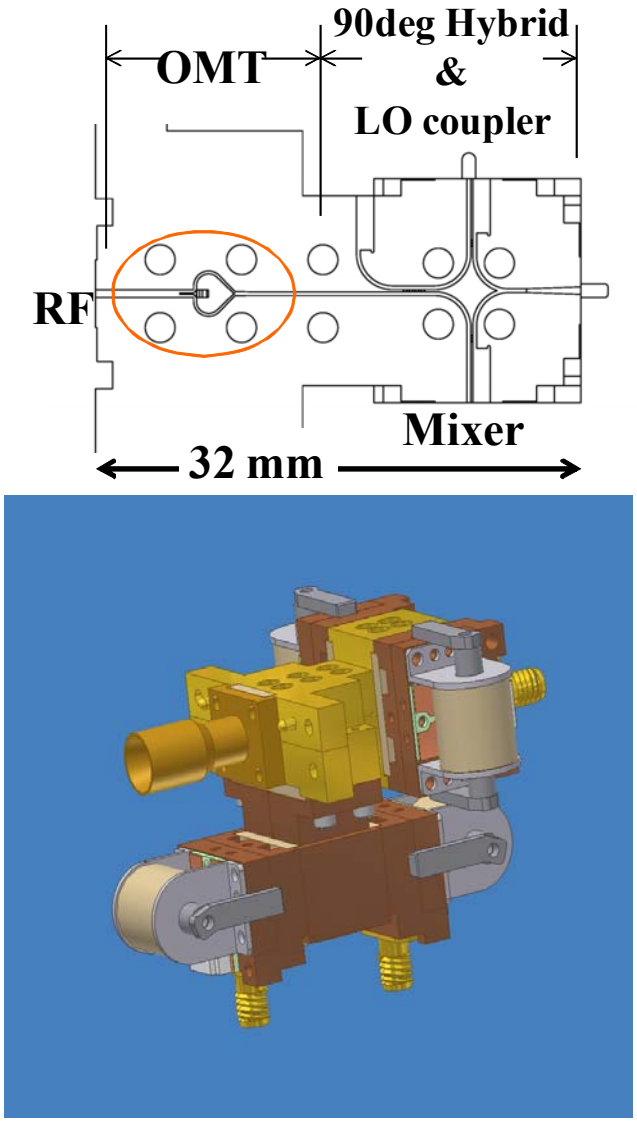

Fig. 3 Upper panel shows waveguide path of an OMT /RF quadrature hybrid / LO -17 dB assembly. Lower panels shows outlook of ALMA Band 8 pre-production model horn, OMT, 2SB mixers assembly.

The DSB mixer of this receiver has been developed by [19]. The SIS junction is made of Nb and AlOx on a quartz substrate of 60 μm thickness. It uses parallelly connected twin junction (PCTJ) which has been developed by [20] and [21]. The SIS junctions have a current density of 10 kA cm^2 or ωRC = 5 with a diameter of 1.2 μm. The input of a waveguide DSB mixer with 558 μm 229 μm (WR2.2) is reduced to a half of 508 μm x 127 μm at the SIS chip. This smaller size was chosen to cover the RF frequency between 385 and 500 GHz with cutoff frequency for the fundamental mode of around 300 GHz close to the lower RF frequency limit, in order to minimize the problem caused by unwanted lower-order harmonics in the LO signal. Typical noise temperature of ALMA Band 8 DSB mixers is shown in Fig. .

A superconducting magnet was used for a DSB mixer to suppress the Josephson effect. It consists of iron yokes and superconducting wires (Cu-cladding NbTi ϕ0.07 mm) with 3500 turns. It has 300 gauss with 10 mA current.

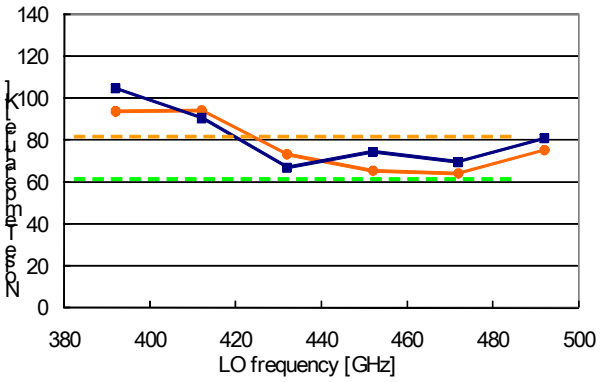

Fig. 4 Noise temperature of ALMA Band 8 DSB mixers.

D *Intermediate Frequency (IF)*

The Band 8 cartridge uses 4 cryogenic low noise amplifiers (CLNAs) to amplify the IF signal between 4 and 8 GHz from two 2SB mixers. It also uses 4 cryogenic IF isolators (CISO) at the input of the CLNAs. The CLNA made by Nitsuki uses GaAs HEMT chip and is operated with power consumption of 8 mW at 4 K. The noise temperature was 6 – 8 K with gain of 30 dB.

Two IF quadrature hybrids made by Nitsuki are mounted between the 2SB mixer and the CISO. Coaxial cables between the mixer and the CLNA use phase-matched one made of copper, while others are made of stainless steel (the central conductor is a silver-plated cupronickel). The phase difference of the pair cable is less than 3 degree.

To compensate frequency-dependent loss of thermally-isolated coaxial cables between 4 K and 300 K, warm IF amplifiers made by AML have an gain slope of 4 dB from 4 GHz to 8 GHz. The gain is 38 dB and NF is less than 1.5.

E *Local Oscillator (LO)*

Local oscillator for Band 8 cartridge has been developed and is provided by National Astronomy Radio Observatory (NRAO) in USA. It consists of cryogenic multiplier (x 6) operated at 100 K and warm cartridge assembly (eg. [22]). The output of the multiplier is transmitted with an oversize waveguide (WR6.3) to the OMT/2SB assembly. The LO signal is coupled to RF signal at the -17 dB coupler and terminated with wedge-type MF116 load. The load design is based on [23].

III. Receiver Performance

A *Noise Temperature*

Noise temperature of a Band 8 pre-production prototype cartridge was measured with standard Y-factor method.

These tests have been performed with a cartridge test cryostat [24].

Noise temperature was measured with cryogenic fifth times multipliers because of its availability. The outline is the same as sixth times multiplier. The multipliers are pumped with a Gunn oscillator and a W-band power amplifier covering frequency 80 – 99 GHz. A chopper which changes hot and cold loads moves at 4 Hz. Fig. shows single sideband (SSB) noise temperature of the Band 8 pre-production cartridge.

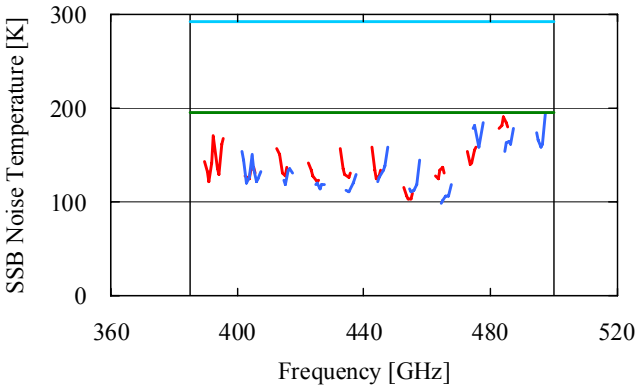

Fig. 5 SSB noise temperature of ALMA Band 8 pre-production cartridge. In ALMA specification, SSB noise temperature is less than 196 K over 80 % of the frequency range and less than 292 K at any frequency from 385 to 500 GHz.

B. *Image rejection ratio (IRR)*

Image rejection ratio (IRR) was measured with a method using an external signal source [25]. The RF signal from the source is coupled quasi-optically to hot and cold loads. Optics for both Y-factor and a signal source was designed with 5 times of Gaussian beam radius. They are frequency-independent at the horns.

The IRR was larger than 10 dB as shown in **Fig.** .

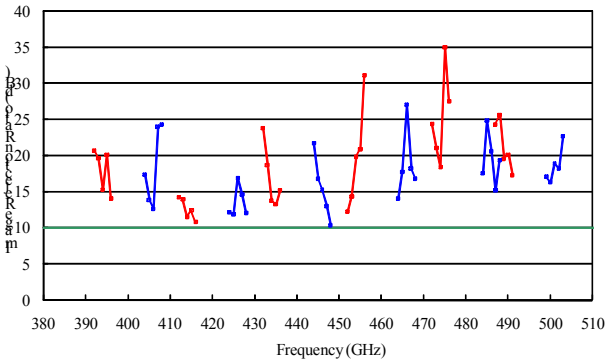

Fig. 6 Image rejection ratio of ALMA band 8 pre-production cartridge. The ALMA specification of IRR is larger than 10 dB.

C. *IF spectra*

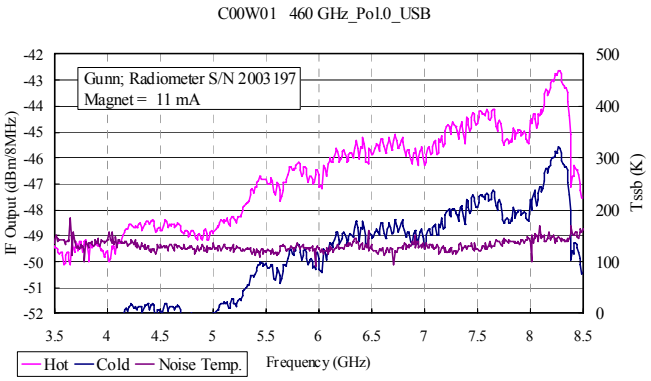

Fig. 7 Typical IF spectrum of ALMA Band 8 Pre-production cartridge at the LO frequency of 460 GHz.

A typical spectrum of the IF output is shown in Fig. . This is measured with a spectrum analyzer. The output power in the IF spectra has a gain slope because warm IF amplifier has a positive gain slope of 4 dB from 4 GHz to 8 GHz. The ALMA specification of gain variations in any 2 GHz is less than 4 dB. Band 8 pre-production cartridge can comply it in most of frequencies, but there are some frequencies which has larger variation than this specification.

D. *Beam measurements*

Beam pattern and Cross polarization pattern of Band 8 pre-production cartridge optics have been presented by [26]. The measure beam patterns are consistent with physical optics simulations at 385, 442, and 500 GHz. The cross polarization levels at 385, 442, and 500 GHz, are less than -23 dB. The main source of cross polarization was the OMT.

E. *Other performance*

Other performance such as gain compression, amplitude stability, and phase stability was measured with Band 8 QM cartridge [8]. Gain compression was less than 10 dB. The amplitude stability was around $3x10^4$ in 1 sec. The phase stability was less than 2.0 degrees on a timescale from 0.1 sec to 10 minutes.

F. CONCLUSIONS

We have developed a prototype of ALMA Band 8 cartridge receiver as well as its test equipment. The cartridge-type receiver includes cold optics, a feed horn, an OMT, two 2SB mixers, cryogenic multipliers, cryogenic and warm IF amplifiers. These components were individually tested and then the cartridge was integrated and tested as a complete assembly. We have also developed equipment to test both components and the integrated receiver.

The single sideband (SSB) noise temperature of this receiver is 130 K at the band center and 180 K at the band edges. The beam pattern and cross-polarization pattern are consistent with physical optical calculation. These results are promising

for receiver production to the Atacama Large Millimeter/submillimeter Array.

ACKNOWLEDGMENT

We thank ALMA front end IPT lead by Gie Han Tan, John Webber. The authors also thank Takashi Noguchi, Tomonori Tamura, Shi-Cai Shi, Junji Inatani, Genshiro Fujii, Shin'ichiro Asayama, Yoshi Uzawa, Masahiro Sugimoto. This work was partially supported by Grant-in-Aid of JSPS No. 17530058.

REFERENCES

[1] Brown, R. L., Wild, W., and Cunningham, C. 2004 Advances in Space Research 24, 555

[2] R. Hills "Submillimeter interferometers: new standards for future instrumentation", Proc. Of 19th Int. Symp. on Space Terahertz Tech., 2008

[3] G. H. Tan "The ALMA front ends : an overview" Proc. Of 19th Int. Symp. on Space Terahertz Tech., 2008

[4] Orlowska, A., Harman, M., and Ellison, B. ALMA Project Book, chapter 6, 2002

[5] S. Matsushita, H. Matsuo, J. R. Pardo, S. Radford, "FTS Measurements of Submillimeter-Wave Atmospheric Opacity at Pampa la Bola II : Supra-Terahertz Windows and Model Fitting" PASJ, 51, 603, 1999

[6] Guilloteau, S. ALMA memo 393 "DSB versus SSB and Bandwidth/Sensitivity tradeoff" , 2002

[7] Iguchi, S. PASJ 57, 643, "Radio Interferometer Sensitivities for Three Types of Receiving Systems: DSB, SSB, and 2SB Systems", 2005

[8] N. Satou, Y. Sekimoto, Y. Iizuka, T. Ito, W. Shan, T. Kamba, K. Kumagai, M. Kamikura, Y. Tomimura, Y. Serizawa, S. Asayama, M. Sugimoto, "A Submillimeter Cartridge-Type Receiver: ALMA Band 8 (385 - 500 GHz) qualification model", Publication of Astronomical Society of Japan in press 2008

[9] M. Kamikura, M. Naruse, S. Asayama, N. Satou, W. Shan, Y. Sekimoto "Development of a 385 – 500 GHz Orthomode Transducer (OMT)", Proc. Of 19th Int. Symp. on Space Terahertz Tech., 2008

[10] Carter, M. C. et al. 2004 SPIE, 5489, 1074, "ALMA front end optics"

[11] Tham, C. Y., Withington, S. 2003, "Receiver Optics Design Electromagnetic Analysis, Second Report (Bands 3, 6, 7 and 9)"

[12] Tham, C. Y., Withington, S. 2003, "Receiver Optics Design Electromagnetic Analysis, Third Report (Bands 4, 8 and 10)"

[13] Matsunaga, M., Sekimoto, Y., Matsunaga, T., Sakai, T. 2003 PASJ 55, 1051 "An Experimental Study of Submillimeter-Wave Horn Antennae for a Submillimeter-Wave Astronomy"

[14] Matsunaga, M., Matsunaga, T., Sekimoto, Y. 2004 Proceedings of the SPIE, Vol. 5445, 446 "Analysis of submillimeter-wave horn antennas for submillimeter-wave telescope"

[15] M. Kamikura, Y. Tomimura, Y. Sekimoto, S. Asayama, W. L. Shan, N. Satou, Y. Iizuka, T. Ito, T. Kamba, Y. Serizawa, T. Noguchi "A 385 - 500 GHz Sideband-Separating (2SB) SIS Mixer Based on a Waveguide Split-block Coupler" International Journal of Infrared and Millimeter-Wave 27 (1), 37, 2006

[16] S. Asayama, S. Kawashima, H. Iwashita, T. Takahashi, M. Inata, Y. Obuchi, T. Suzuki, and T. Wada "Design and Development of ALMA Band 4 Cartridge Receiver", Proc. Of 19th Int. Symp. on Space Terahertz Tech., 2008

[17] Asayama, S., Ogawa, H., Noguchi, T., Suzuki, K., Andoh, H., Mizuno, A. ALMA memo 453, 2003

[18] Claude, S. M. X., Cunningham, C. T., Kerr, A. R., and Pan, S.-K. 2000, ALMA memo 316 "Design of a Sideband-Separating Balanced SIS Mixer Based on Waveguide Hybrids"

[19] Shan, W. L., Shi, S. C., Noguchi, T., Sekimoto, Y. 2005 IEEE trans. Applied Superconductivity 15, 503 Design and Development of SIS Mixers for ALMA Band 8"

[20] Noguchi, T., Shi, S. C., and Inatani, J. 1995, IEEE applied superconductivity, 5, 2228 "An SIS mixer using two junctions connected in parallel"

[21] Shi, S. C., Noguchi, T., Inatani, J. 1997 IEEE Trans. on Applied Superconductivity, 7, 2587 "Development of a 500-GHz band SIS mixer"

[22] E. Bryerton, J. Hesler "Sideband noise screening of multiplier-based sub-millimeter LO chains using a WR-10 Schottky mixer", Proc. Of 19th Int. Symp. on Space Terahertz Tech., 2008

[23] F. P. Mena, A. M. Baryshev, "Design and Simulation of a Waveguide Load for ALMA-band 9", ALMA memo 513, 2005

[24] Sekimoto, Y. et al. 2003 ALMA memo 455 "Cartridge Test Cryostats for ALMA Front End"

[25] Kerr, A.R., Pan, S.-K., and Effland, J.E. 2001, ALMA Memo 357, "Sideband Calibration of Millimeter-Wave Receivers"

[26] M. Naruse, M. Kamikura, Y. Sekimoto, T. Ito, M. Sugimoto, Y. Iizuka, N. Satou, K. Kumagai "Near field beam and cross-polarization pattern measurements of ALMA band 8 cartridges", Proc. Of 19th Int. Symp. on Space Terahertz Tech., 2008

ALMA Band 9 cartridge

A.M. Baryshev[1,2], F.P. Mena[1,2], J. Adema[1,2], R. Hesper[1,2], B. Jackson[1], G. Gerlofsma[2], M. Bekema[2], K. Keizer[1], H. Schaeffer[1], J. Barkhof [1,2], C.F.J. Lodewijk[3], D. Ludkov[3], T. Zijlstra[3], E. van Zeijl[3], T.M. Klapwijk[3], W. Wild[1,2]

[1] *SRON Netherlands Institute for Space Research, Groningen, the Netherlands*

[2] *University of Groningen, Kapteyn Astronomical Institute, Groningen, the Netherlands*

[3]*Kavli Institute of Nanoscience, Faculty of Applied Sciences, Delft University of Technology Lorentzweg 1, 2628 CJ Delft, The Netherlands*

* Contact: A.M.Baryshev@sron.nl, phone +31-50-3638287

***Abstract*— The Atacama Large Millimeter Array (ALMA) is a collaboration between Europe, North America, and Japan to build an aperture synthesis telescope with more than 50 12-m antennas at 5000 m altitude in Chile. In its full configuration, ALMA will observe in 10 bands between 30 and 950 GHz, and will provide astronomers with unprecedented sensitivity and spatial resolution at millimetre and sub-millimetre wavelengths. Band 9, covering 602-720 GHz, is the highest frequency band in the baseline ALMA project, and will thus offer the telescope's highest spatial resolutions.**

This paper describes the design of the Band 9 receiver cartridges for the Atacama Large Millimeter Array (ALMA). These are field-replaceable heterodyne front-ends offering high sensitivity, 602-720 GHz frequency coverage, 4-12 GHz IF bandwidth, and high quasioptical efficiencies. Because the project will ultimately require up to 64 cartridges to fully populate the ALMA array, two key aspects of the design of the Band 9 cartridge have been to take advantage of commercial manufacturing capabilities and to simplify the assembly of the cartridge.

I. Introduction

The Atacama Large Millimeter Array (ALMA) is a collaboration between Europe, North America, and Japan to build an aperture synthesis telescope with 64 12-m antennas at 5000 m altitude in Chile [1]. In its full configuration, ALMA will observe in 10 bands between 30 and 950 GHz, and will provide astronomers with unprecedented sensitivity and spatial resolution at millimetre and sub-millimetre wavelengths.

Band 9, covering 602-720 GHz, is the highest frequency band in the baseline ALMA project, and will thus offer the telescope's highest spatial resolutions. Furthermore, sub-mm observations with Band 9 of ALMA will provide complementary information to observations with the observatory's lower frequency bands, due to the fact that submillimeter line observations typically probe warmer, denser material than mm-wavelength observations, while continuum observations over a broad range of frequencies will better constrain dust temperatures.

The ALMA Band 9 cartridge is a field-replaceable unit containing the core of a 600-720 GHz heterodyne front-end. The core technologies of every cartridge include low-noise, broadband SIS mixers; an electronically tunable solid-state local oscillator; and low-noise cryogenic IF amplifiers. These components are built into a rigid opto-mechanical structure that includes a compact optical assembly mounted on the cartridge's 4K stage that combines the astronomical and local oscillator signals and focuses them into two SIS mixers as shown in Fig. 1.

Primary requirements of the Band 9 cartridges include:

- double side-band (DSB) operation with $T_{N,rec}$ = 173 K over 80% of the 614-708 GHz LO frequency range;
- an intermediate frequency (IF) bandwidth of 4-12 GHz with low power variation across the band (6 dB peak-to peak and 4 dB within any 2 GHz) and a total output power level of -37 to -24 dBm;
- detection of two orthogonal linear polarizations with cross-polarization levels of -20 dB;
- 80% coupling of the cartridge's optical beam to the telescope secondary;
- long lifetime and high reliability; and
- the design must be consistent with the need for series production of 64 cartridges.

A series of first eight band 9 receivers (see Fig. 2) has been finished and fully tested. This paper will report and summarize the measured performance and discuss possible steps for further improvement.

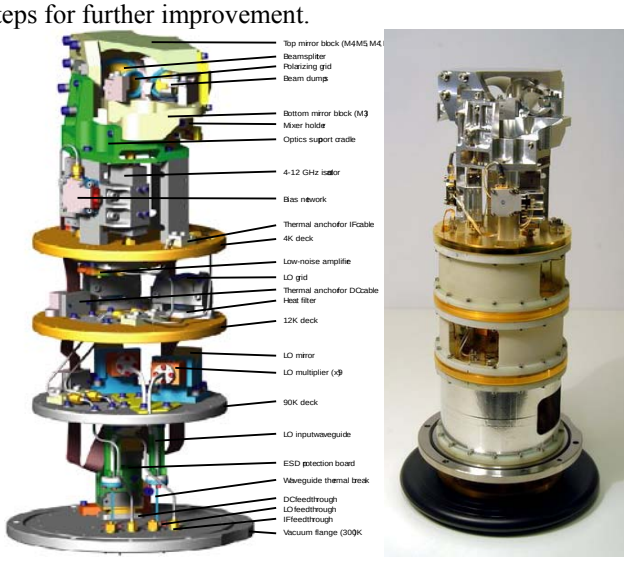

Fig 1 Layout (left) and photograph of ALMA band 9 receiver cartridge.

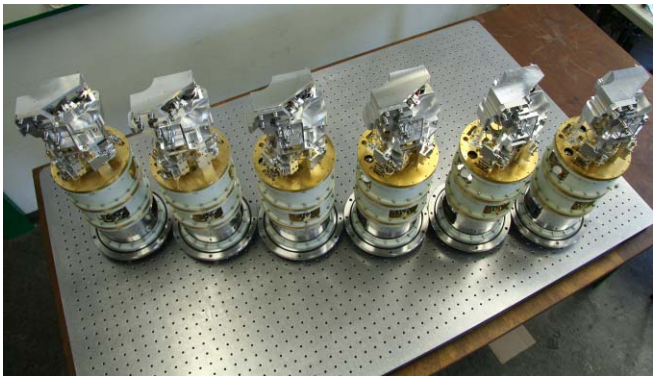

Fig 2, Photograph of six ALMA band 9 cartridges of a series of eight pre-prototypes, two cartridges have already been delivered to the ALMA project.

The detailed receiver design has been reported earlier and can be found in [2, 3, 4].

II. Achieved Receiver Perfomance

In this section we summarise the performance that was achieved for the first series of eight band 9 receiver cartridges as measured in a small cartridge cryostat that contains only one cartridge. The 2.7 K temperature at the 4K-stage at the test cryostat was actually heated up by a system of resistive heaters and kept at 4 K to represent the expected ALMA front end cryostat temperature level. All measurements reported in the following sections were performed at 4 K mixer temperature unless stated otherwise.

A RF Band coverage

The receiver RF coverage was measured by means of a Fourier Transform Spectrometer (FTS) for each of the SIS mixers. A summary of measurement results is shown in Fig 3. Good repeatability for many SIS mixer units has been achieved. Note that the data was obtained in air with long beam paths (~1 m) and the response is modified by a water vapour absorption lines at around 557 GHz and 753 GHz. The sensitivity curve is peaked at the higher end of ALMA band 9 because of the better atmospheric transmission at the ALMA site at these frequencies. The total receiver bandwidth is limited due to the maximum achievable current density of the AlO_x SIS junction technology (9 kA/cm^2). Making the design bandwidth wider for this current density value can only be done by reducing the peak coupling and thus degrading the receiver noise performance [5]. A different type of SIS junction barrier based on AlN [6] allows to achieve wider band coverage as discussed in [5] and also in the following sections.

The receiver noise temperature was measured by a standard Y-factor technique using 300K and 80K black body radiators presented in front of the receiver. The IF coverage has been analysed by using a tunable 4-12 GHz YIG filter with a bandwidth of approximately 40 MHz. The receiver noise temperature, integrated over the 4-12 GHz IF band is presented in Fig. 4 as a function of LO frequency. All receivers have been measured with the same experimental set-up following the same LO frequency plan allowing easy comparison. Noise temperature values are not corrected for LO insertion optics that is internal to the receiver. Fig. 4 data directly represents sensitivity values that one would expect to obtain at the ALMA telescopes.

The best achieved noise temperature is about 80 K for a 4 K mixer physical temperature. This number improves to ~ 63 K when the mixer is cooled to 2.7 K – the lowest temperature the closed cycle cooler can reach in the test set-up.

The performance of ALMA as an interferometer and the integration time is determined by the most insensitive receiver unit of the interferometer, thus additional attention was given to uniformity. Excellent repeatability of the receiver noise performance has been achieved for the first eight receivers in the 640 – 700 GHz range.

The noise temperature degradation towards the lower part of the ALMA band 9 fully corresponds to a reduced mixer coupling that was measured by the FTS (see Fig. 3). This is due to bandwidth limitations of the AlO_x junction technology and is expected to be improved by the application of AlN tunnel barriers.

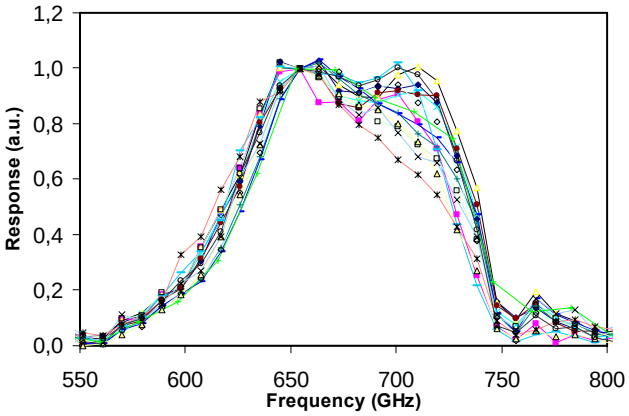

Fig. 3, RF band coverage of eight pre-production band 9 receivers measured with a Fourier Transform Spectrometer using the SIS mixers photo response.

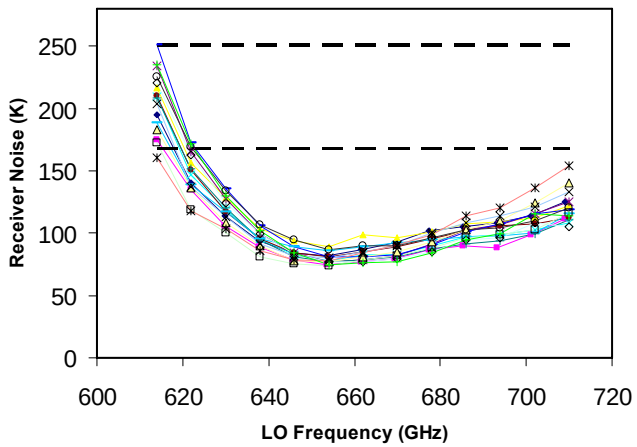

Fig. 4, ALMA Band 9 receiver noise temperatures, integrated over the 4-12 GHz IF vs. LO frequency measured in front of the receivers. There are 16 curves corresponding to 8 receivers with two polarisations each. Dashed lines are ALMA specifications for sensitivities across 20% (upper line) and 80% (lower line) of the frequency band, respectively.

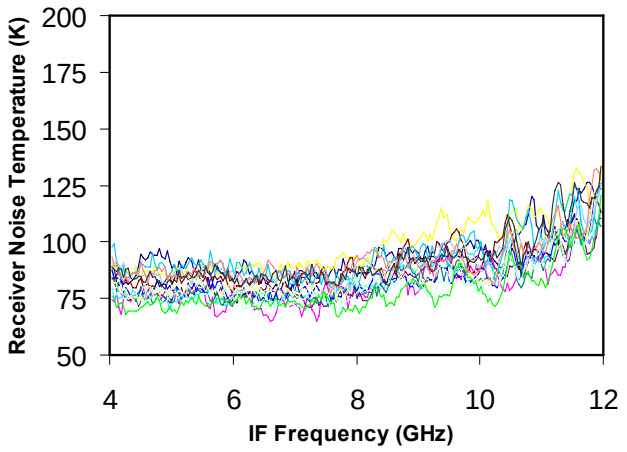

Fig. 5, Measured receiver noise temperature as a function of IF for eight cartridges, for two polarization channels each, at 670 GHz LO frequency.

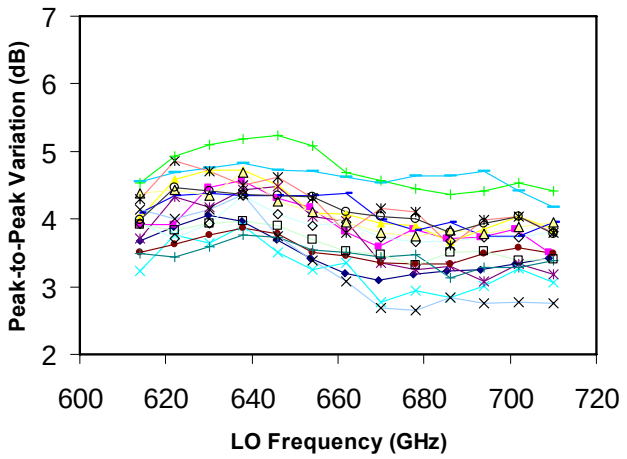

Fig. 6, Estimated maximum peak to peak output IF power variation in a 2 GHz window vs. LO frequency.

C. *IF band coverage*

The typical receiver IF response is shown in Fig. 5. The noise temperature was measured by means of the Y-factor technique for each IF frequency, which was set by an electronically tuneable YIG filter. The filter bandwidth is approximately 40 MHz. Excellent IF coverage is achieved for IF frequencies below 11 GHz with a minimum noise temperature of about 75 K. The response above 11 GHz is degraded because of several reasons:

- The single junction tuning circuit used in the mixer chip design has a relatively large stray capacitance that shortens out the SIS junction at large IF frequencies. This effect starts to be visible already above 8 GHz IF.
- All IF components used in the cartridge IF chain such as IF isolator, cryogenic IF amplifier, and room temperature IF amplifier have their performance simultaneously degraded at frequencies above 11 GHz. This explains the sharp increase of noise temperature above 11 GHz.

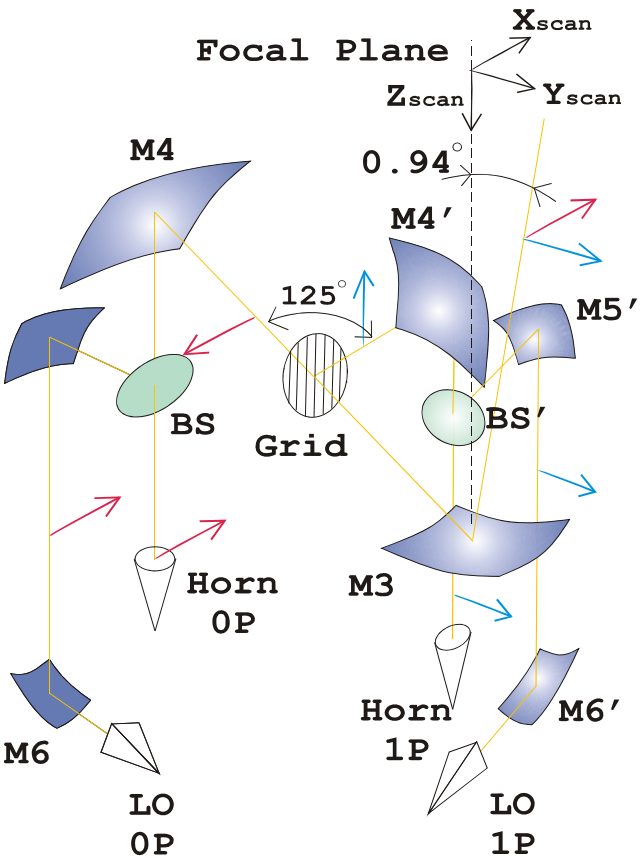

Fig. 7, Optics layout of the band 9 system.

Typical maximum receiver IF output power variations within any 2 GHz wide window of IF band is shown in Fig. 6 for all eight cartridges with two polarisations each. This is an important receiver parameter, because ALMA uses two bit digitization in its correlator leading to a limited dynamic range of the backend. A typical value of peak-to-peak variation was about 4 dB.

D. *Receiver optics performance*

The ALMA band 9 optics layout is shown in Fig. 7. The signal coming from the secondary mirror passes mirror M3 and is then split by a polarising grid into two polarisations codenamed “0P” and “1P”. After the grid the receiver beam is reflected off mirrors M4 and M4’ for each polarisation, correspondingly, and then reaches the mixer corrugated horns. The local oscillator is located at he 90 K cartridge stage and so are mirrors M6 and M6’. The LO signal coming from LO horns passes mirrors M6, M5 and is reflected off a 6 micron thick mylar beam splitter towards the mixer horn for polarisation 0P. Similarly, the LO signal follows the Horn 1P-M6’-M5’-BS’-1P horn path. The excess of LO power that comes through the beamsplitters is terminated in beam dumps (not shown in the picture) located at the 4 K level.

Locating the final stage of the LO multiplier at 90 K and beam dumps allows to minimise the effect of LO insertion to the receiver noise. The added noise from the LO insertion is

only about 5..10 K, compared to 15..30 K for a similar arrangement located at the 300 K temperature level.

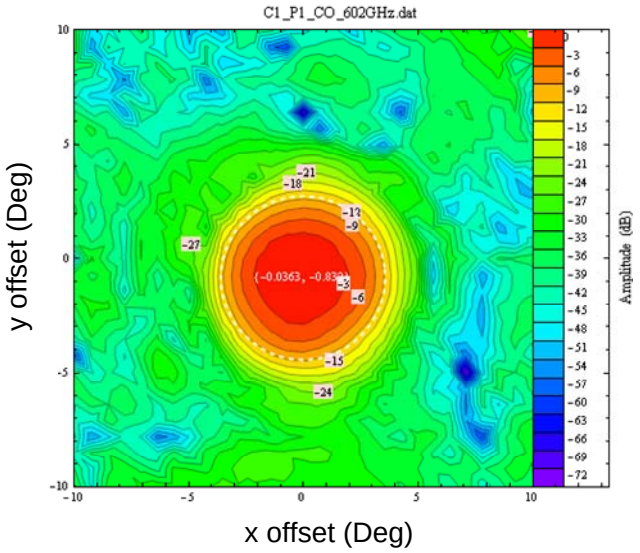

Fig. 8, Far field pattern of the band 9 receiver obtained from measured near field phase and amplitude data. The response is corrected for the source feed horn. The extent of the ALMA telescope secondary mirror is shown as a white dashed line.

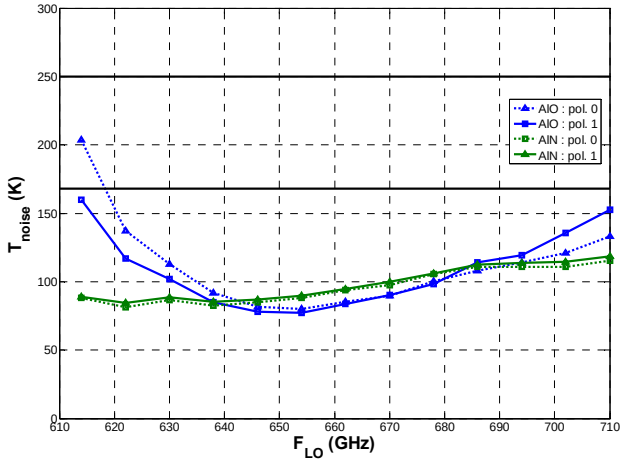

Fig. 9, Measured noise temperatures for AlN and AlOx barrier mixers. The same ALMA band 9 cartridge was used for measurements. The noise temperature is integrated across the 4-12 GHz IF band.

Coupling of the receiver beam to the telescope is one of the key parameters along with noise temperature, determining the overall receiver performance. Therefore careful measurements and analysis have been performed to evaluate the band 9 optics performance [3]. A near field beam pattern measurement system has been developed for this purpose and near field phase and amplitude measurements were carried out for all eight receivers at the band edges and in the middle of the band.

A typical far field beam pattern of a band 9 cartridge is presented in Fig. 8. This pattern was obtained from a near field scan at 602 GHz signal frequency. It demonstrates uniform illumination of the secondary mirror, shown as dashed line contour, with an edge taper of approximately 12.5 dB. This is very close to the design value of 12 dB. The most important parameter here is the aperture efficiency which characterises how much power from a plane wave reaching the telescope is coupled to the receiver. This value can be determined from the measured data and is 82-84% across the ALMA band which is better than the ALMA specification of 80%.

III. ALN BARRIER TECHNOLOGY

Recently, a new batch of SIS junctions utilizing an AlN barrier was manufactured and mixer chips suitable for putting into the ALMA band 9 receiver system were delivered. The achieved current density is about 30…50 kA/cm^2.

Using one of the band 9 cartridges as a test bed, performance of the AlO_x and AlN junctions was compared in strictly the same environment and by using the same standard measurement procedures which were developed to characterise ALMA band 9 cartridges [7]. The noise temperature comparison between the two technologies is presented in Fig. 9. It is clear that the RF band coverage is improved without degrading the receiver overall performance. The impact is especially visible at the band edges. For details see [8].

CONCLUSIONS

A first series of eight ALMA band 9 receiver cartridges has been completed and fully characterised. All receivers show excellent sensitivity (min T_n=75 K) and IF band coverage (4-12 FGz). An aperture efficiency of 82..82% has been reached for all receivers at all frequencies. New AlN barrier technology has been used for the first time in the ALMA band 9 system leading to significant improvements of the RF band coverage without degradation of noise temperature. This gives an opportunity for further improvements of ALMA band 9 receiver performance.

ACKNOWLEDGMENT

This work has been partially funded by the European Organization for Astronomical Research in the Southern Hemisphere (ESO), under ESO contract numbers 73072/MAP/03/8632/GWI and 16173/ESO/07/14997/YWE. This work was also supported by the Netherlands Research School for Astronomy (NOVA) within a NOVA-II grant. This work has also benefited from research funding from the European Community's Sixth Framework Programme under RadioNet R113CT 2003 5058187.

REFERENCES

[1] www.alma.cl, www.alma.nrao.edu, www.eso.org/alma .

[2] Hesper, R., Jackson, B.D., Baryshev, A., Adema, J., Wielienga, K., Kroug, M., Zijlstra, T., Gerlofsma, G., Bekema, M., Keizer, K., Schaeffer, H., Barkhof, J., Mena, F.P., Rivas, R., Klapwijk, T.M., Wild, W., "Design and Development of a 600-720 GHz Receiver Cartridge for ALMA Band 9", *16th Int. Symp. on Space Terahertz Technology*, 2005

[3] M. Candotti, A.M. Baryshev, N.A. Trappe, R. Hesper, J.A. Murphy, J. Barkhof, "Quasi-optical Verification of the Band 9 ALMA Front-End", Proc. Of 16th Int symp on Space Terahertz Technology, pp. 79-84, 2005

[4] C. F. J. Lodewijk, M. Kroug, and T. M. Klapwijk, "Improved design for low noise Nb SIS devices for band 9 of ALMA (600–720 GHz)," *Proc. 16th Int. Space Terahertz Technol. Symp., Göteborg, Sweden*, 2005, paper S03-05.

[5] Jacob W. Kooi, Attila Kovács, Matthew. C. Sumner, Goutam Chattopadhyay, Riley Ceria, Dave Miller, Bruce Bumble, Henry G. LeDuc, Jeffrey A. Stern, and Tom G. Phillips, "A 275–425-GHz Tunerless Waveguide Receiver Based on AlN-Barrier SIS Technology", *IEEE trans. On Microwave Theory and Techniques*, vol. 55, NO. 10, Oct 2007

[6] T. Zijlstra, C. F. J. Lodewijk, N. Vercruyssen, F. D. Tichelaar, D. N. Loudkov, and T. M. Klapwijk, "Epitaxial aluminum nitride tunnel barriers grown by nitridation with a plasma source", *Appl. Phys. Lett*., 91, 233102 (2007)

[7] A.M. Baryshev, R. Hesper, F.P. Mena, B.D. Jackson, J. Adema, J. Barkhof, W. Wild, M. Candotti, M. Whale, C. Lodewijk, D. Loudkov, T. Zijlstra, T.M. Klapwijk, "Performance of ALMA band 9 receiver series", Proc. Of 18th Int symp on Space Terahertz Technology, Pasadena, Californis, USA, 2007

[8] C. F. J. Lodewijk, E. Van Zeijl, T. Zijlstra, D. N. Loudkov, and T. M. Klapwijk, "Bandwidth of Nb/AlN/Nb SIS mixers suitable for frequencies around 700 GHz", these proceedings, 2008.

Measurement of Emissivity of the ALMA Antenna Panel at 840 GHz Using NbN-Based Heterodyne SIS Receiver

S. V. Shitov[1,2,*], J. Inatani[1], W.-L. Shan[3], M. Takeda[4], Z. Wang[4], A. V. Uvarov[2], A. B. Ermakov[2] and Y. Uzawa[1]

[1]*National Astronomical Observatory of Japan, Mitaka, Japan*

[2]*Institute of Radio Engineering and Electronics, Russian Academy of Sciences, Moscow, Russia*

[3]*Purple Mountain Observatory, Nanjing, China*

[4]*National Institute of Information and Communication Technology, Kobe Advanced ICT Research Center, Japan*

* Contact: s.shitov@nao.ac.jp, sergey@hitech.cplire.ru, phone +81-422-34 3879

***Abstract*— We measured emissivity of sample presenting panel of ALMA antenna using Band-10 heterodyne SIS receiver as antenna switching balanced radiometer with 8 GHz instantaneous bandwidth. Receiver noise temperature measured with 80 K/300 K antenna loads was ≈560 K (DSB). Emissivity of the surface is detected at LO frequency about 840 GHz via the imbalance of the antenna switch due to extra reflection from sample of panel; absorption 0.25±0.10 % is calculated from measured emissivity. To confirm measured value, samples made of phosphor bronze and stainless steel are tested using the same technique. The values of 0.30±0.10 % and 1.10±0.10 % are obtained for these samples correspondingly that is consistent with previous data obtained using direct detector radiometers.**

I. Introduction

The surface finish of the main dish for ALMA telescopes is subject to a number of special requirements. For example, focusing of the infrared portion of solar radiation must be restricted via diffused scattering from the surface of the dish's panels, while RF loss, which causes in-band noise emission, must be below 1% at all frequencies. These are somewhat contradictory requirements, since the surface of the antenna cannot be polished and must have appropriate roughness (matte finish) providing the scattering of IR-radiation. The noise emission of a reflective surface is usually measured by a bolometer-based radiometer, which can provide a very high sensitivity [1], [2]. Another technique for measuring of absorption of highly reflective surfaces is evaluation of the Q-factor of a resonator formed by the reflector under test [3]–[5]. However, both techniques have some drawbacks. A sensitive radiometer suffers usually from the low dynamic range while the resonant method assumes precision design and careful adjustment. In spite the low absorption is specified as the figure of merit, the low background emission is meant in practice. For this reason one may suggest that radiometric methods can provide the most reliable (and practicable) data.

Since saturation level of a SIS mixer is usually higher than 300 K, the emissivity could be *calibrated* with conventional 300-K and 80-K antenna loads, if such SIS radiometer could be used efficiently. This paper is focused on a description of a particular experiment with sensitive submillimeter heterodyne SIS receiver as a balanced radiometer. The feasibility of the experimental method is discussed along with analysis of particular experimental data obtained for three commonly used reflecting materials: aluminum, phosphor bronze and stainless steel. The accuracy of the described technique is discussed, that includes the effects of non-thermostatic environment and scattered 300-K radiation.

II. The Switching Radiometer

The receiver is mounted within a vacuum 4-K cryostat and contains one of our experimental waveguide-type SIS mixers under development for ALMA Band-10. We used one of the optional SIS mixers, which employed the resonant type junction made of epitaxial NbN/AlN/NbN trilayer [6]. The receiver noise temperature at antenna loads was measured as ≈560 K (DSB, IF band 4-8 GHz) or ≈330 K at the window of the cryostat after correction for the 25-μm-thick Kapton beam splitter, which is used for injection of LO power from BWO (nominal range 696-938 GHz).

A. Principle of Switching Radiometer

The general idea of our measurement is to provide the receiver input with thermal emission from a 80-K absorber via two paths, which are different (separated) in space, but producing equal intensity. If the receiver input is switched between these two paths, the differential signal registered at the receiver output will be zero, unless extra emission is present in either of the two 80-K signal paths. The weak imbalance can be detected via well-known switching technique as presented in Fig. 1.

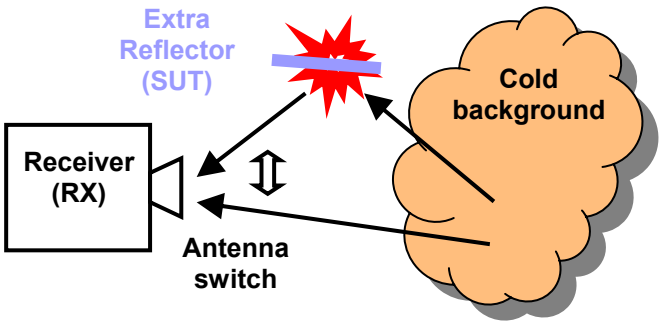

Fig.1 Principle of detection of thermal emission with switching radiometer.

The difficulty is that one has to be sure that the antenna switch, which is presumably a room-temperature (quite hot) reflector, does not introduce any emission by itself. For this purpose we have suggested and designed the well-balanced beam-switch, presented in Fig. 2. The idea of such switch is based on equal emission from both the chopper deflection blade (M1) and the following (fixed) deflection mirror (M2), which is seen by the receiver input while the chopper blade is open as presented in Fig. 2(a). The dashed traces in Fig. 2 explain the balance of thermal radiation in the switch. Note that the balance of emission in such system is possible for *two equal* 80-K loads (or for a single large-aperture homogeneous load). The sample of the antenna panel (SUT) is placed in the *sampling arm* providing just one extra reflection, which breaks the balance as shown in Fig. 3.

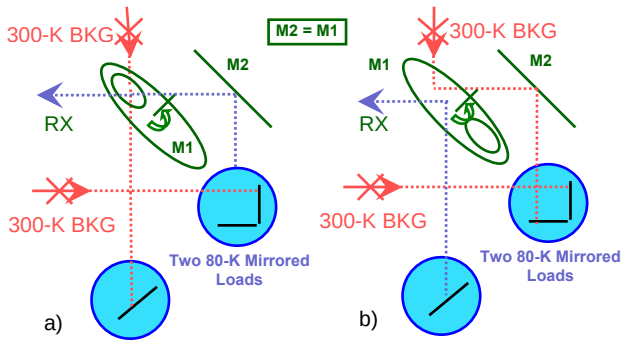

Fig. 2 Principle of balanced switch: (a) chopper blade is open towards M2 in referencing arm, (b) the chopper blade is closed deflecting input beam towards sampling arm.

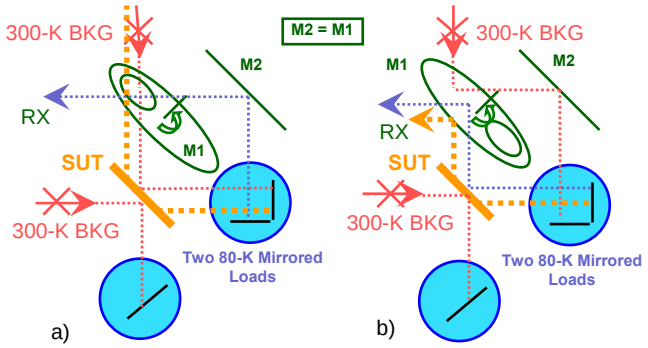

Fig. 3 Principle of emission detection: (a) chopper blade is open to read referencing arm (80-K emission), (b) the chopper blade is closed to read mixture of emission from sample and from 80-K load.

B. *Experimental Setup and Controlling Software*

We have tried two variants of the cold load, single large-aperture load and two "equal" loads made from the microwave absorber Eccosorb AN-72 [7] or from pyramidal plastic TK-RAM [8], immersed into liquid nitrogen (LN_2). The large-aperture load was inside the Styrofoam box (boxed load); the split-type load was in top-open stainless steel thermos containers. To prevent the water condensation, the outside wall of the boxed load was continuously dried (ventilated) by room-temperature (300-K) airflow. The photo of the most critical part of the experimental radiometer is shown in Fig. 4 for the case of two equal but separated cold loads placed in referencing and sampling arms. To provide two-beam coupling to the cold load in the reference arm, a special roof-top mirror is designed (right bottom corner in Fig. 4). Notice from Fig. 2 and Fig. 3 that both beam paths are of the same length, providing very similar aperture termination of the receiver antenna at both cold loads.

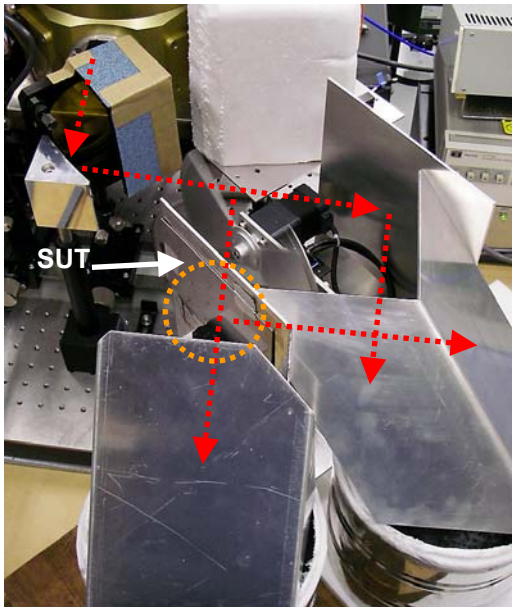

Fig. 4 Most critical part of the experimental switching radiometer: balanced switch (in the center) and mirrored cold (LN_2, T≈80 K) loads (at the foreground).

The experimental system is operated under PC control using IRTECON software [9]. This software enables presets for multiple biasing and measuring devices, including SIS mixer; it collects and evaluates automatically both dc and RF/IF data from the receiver according to user's prescription. We have configured the chopper for positive respond, if the *sampling arm* is loaded with a hotter load. The chopper (hot-cold) rate is 2.5 Hz; the IF power is read 20-40 times per second by the power meter Agilent-E4419. The Y-factor is calculated for each cycle of the chopper using a special software lock-in routine within the IRTECON program. Then the Y-factor is averaged 10 times providing successive graphic output points every 5-10 s. This rate means averaging of the Y-factor for about 12-25 times that equal to effective integration constant of 1-2 s.

A. Calibration Procedure

Since the SIS junctions from epitaxial NbN are operating quite far from their gap frequency, we did not expect essential saturation effects for the antenna temperature 300 K. To calibrate the radiometer, we placed the LN_2-soaked Eccosorb AN-72 material in the sampling arm instead of SUT assuming the emission temperature equal to 78 K. The same absorbing material at the ambient room temperature is placed in the referencing arm of the radiometer. The example of calibration data is presented in Fig. 5; the error bar for measured levels is about 4.6×10^{-4} dB.

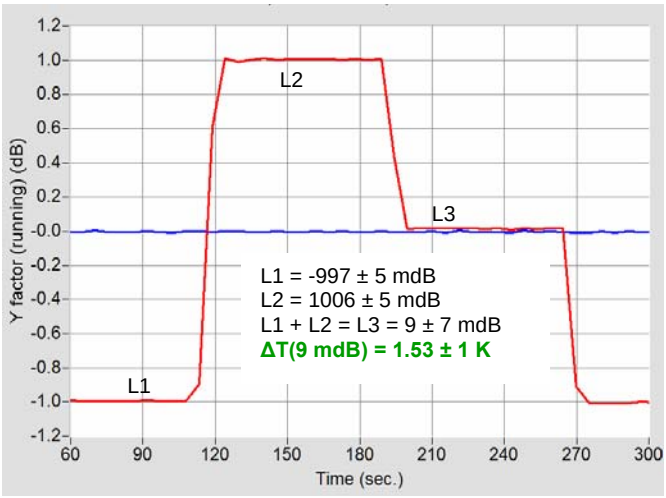

Fig. 5 Calibration of the SIS radiometer at 842 GHz. Horizontal (blue) line presents fully balanced output. Levels of step (red) line present: L1 for cold (80 K) positive arm and hot (295 K) negative arm, L2 for swept loads in respect to hot and cold arms, L3 present slight misbalance due to SUT.

To find the intrinsic misbalance of the switch (zero emission offset), the following experiment has occurred quite useful. We used slightly different absorbing materials, which provide a bit different emission coefficients for two cold loads: AN-72 and TK-RAM. This gave us a very small differential signal, which must be somewhat wrong due to the unknown offset. Swapping the cold containers with these two LN_2 loads (but not swapping their mirrors!) we have seen change of the sign of the response of our differential radiometer similar to that of regular semiconductor operational amplifier if its input polarity is swapped. The result of this procedure is presented in Fig. 6 giving the precision offset value of -0.00487 dB or -0.73 K.

III. Results and Discussion

A. Efficient Noise Temperature of Cold Loads

Experimenting with offset measurements, we found that reflection and absorption of walls of boxed load made from Styrofoam can give a significant effect, due to different temperature of the walls in few degrees. To measure the reflection of the Styrofoam boxed load (or any other flat-surface, not diffusing, load), the 300-K background beams, as shown in Fig. 2, can be blocked with a cold load, thus introducing misbalance presumably originated from the only reflection from either wall. The evaluated reflection is 1% and absorption is in the range of 4-10%. To conclude on the balancing procedure of the switch (and on final accuracy), the blockage of 300-K background radiation with extra LN_2 loads can be recommended.

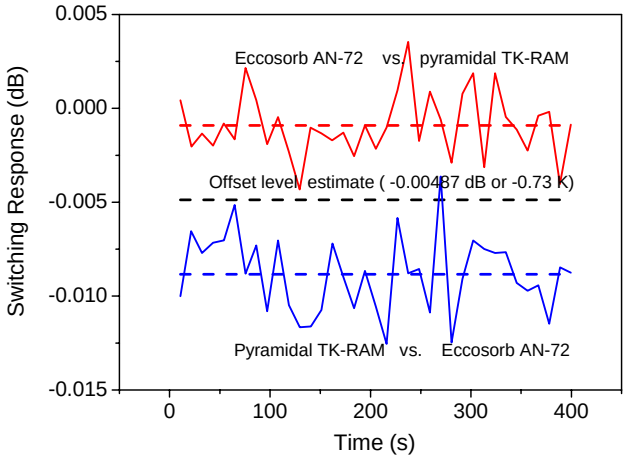

Fig. 6 Measurement of offset emission of switching (differential) radiometer with two slightly different cold loads.

B. LO Stability

It is found that stability of the LO is an important issue. The IRTECON program allows for real-time noise analysis for virtually any process in the measuring system. The stability of the bias current of the SIS mixer is chosen to be the merit. It was found that stability of the bias is related to the particular frequency point (voltage) of the BWO oscillator. The choice of "wrong" frequency point does not affect noticeably the measured value of T_{RX}, but the instability of the Y-factor measured at the scale on milli-dB can be drastically increased.

C. Emission measurements

Experimental data on emission from a few frequently used materials are presented in Fig. 7 and summarized in Table I.

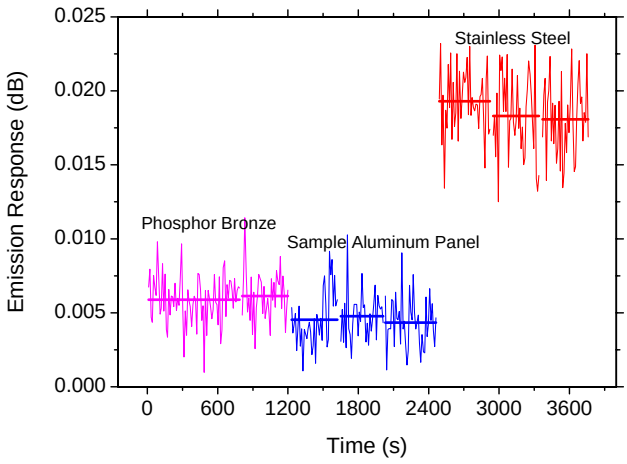

Fig. 7 Measured emission from phosphor bronze, ALMA sample panel and from stainless steel.

The emission response of ALMA panel made of aluminum with matte finish is found as 0.7 K or 0.25 % after evaluation; for phosphor bronze we measured emission of 0.9 K and evaluate it as 0.3 % of absorption; for sample of stainless steel these values are 3.1 K and 1.1 % correspondingly. The accuracy of 0.25% is measured as a standard deviation. In spite the offset can be made quite low as shown in Fig. 5, changes in configuration can result in change of scattered 300-K background radiation, which can be also measured quite accurately as seen from Fig. 6. Trying to be on the safe side, about 0.7 K of growth in emission temperature that is equal to 0.25 % growth for absorption coefficients have to be added. Slight saturation, if any, would make our emission measurements *overestimated*. It seems that RF properties of a Styrofoam box can be spread over wide range, sometimes making boxed load hardly acceptable for sub-mm applications.

TABLE VIII
EMISSION AND ABSORPTION MEASURED FOR A FEW POPULAR MATERIALS

Material	**Parameters at 840 GHz**	
	Emission (K)	**Absorption (%)**
Aluminium panel with matte finish (ALMA)	0.7	0.25
Phosphor bronze (polished)	0.9	0.3
Stainless steel (matte)	3.1	1.1
Eccosorb AN-72 immersed in LN_2	82.5	98
TK-RAM immersed in LN_2	81.3	98.5
Styrofoam box with AN-72 absorber	85-100	-
Styrofoam wall of boxed load (2 cm)	-	4-10

III. CONCLUSIONS

A switching radiometer based on a wide IF-band heterodyne SIS receiver is tested for accurate measurement of noise contribution from reflecting and absorbing surfaces. Standard deviation error ± 0.25 K in temperature scale or ±0.1% in absorption scale is found. Since large saturation power of a SIS receiver the emissivity of about 0.25% + 0.25% (or T_e = 0.7 K + 0.7 K) or *below* can be concluded for the sample of ALMA antenna panel near 840 GHz.

ACKNOWLEDGMENT

Authors thank H. Matsuo for fruitful discussions. The work is supported in parts by ALMA-J Project office and Program for scientific instrumentation of Russian Academy of Sciences.

REFERENCES

[1] A. E. Lange, S. Hayakawa, T. Matsumoto, H. Matsuo, H. Murakami, P. L. Richards, and S. Sato, "Rocket-borne submillimeter radiometer," *Appl. Opt.*, vol. 26, p. 401, 1987.

[2] J. J. Bock, M. K. Parikh, M. L. Fisher, and A. E. Lange, "Emissivity measurement of reflective surfaces at near-millimeter wavelengths," Appl. Optics, vol. 34, No. 22, pp. 4812-4816, 1 August 1995.

[3] R. Schwab, R. Heidinger, "Experimental and theoretical studies of the surface resistance in open resonator mirror materials," *Digest of 21st Int. Conf. on IR&MM Waves*, Berlin, 1996.

[4] W. Kasparek, A. Fernandez, F. Hollmann, R. Wacker, "Measurement of ohmic losses of metallic reflectors at 140 GHz using a 3-mirror resonator technique," *Int. J. of IR&MM Waves*, No 11, pp. 1965-1707, 2001.

[5] M. Yu. Tretyakov, V. V. Parshin, M. A. Koshelev, A. P. Shkaev, A. F. Krupnov, "Extension of the range of resonator scanning spectrometer into submillimeter band and some perspectives of its further developments," *Journal of molecular spectroscopy*, V. 238, pp. 126-132, 2006.

[6] Y. Uzawa, Z. Wang; A. Saito; A. Kawakami, V. Takeda, "Development of a waveguide NbN-based SIS mixer in the 900 GHz band," *IEEE Transactions on Applied Superconductivity*, vol. 13, Issue 2, pp. 692-695, June 2003.

[7] Emerson & Cuming Microwave Products, Inc., Randolph, MA, USA. [Online]. Available: http://www.eccosorb.com

[8] Thomas Keating Ltd., Billingshurst, U.K. [Online]. Available: http://www.terahertz.co.uk/

[9] A. B. Ermakov, S. V. Shitov, A. M. Baryshev, V. P. Koshelets, W. Luinge, "A data acquisition system for test and control of superconducting integrated receivers," *IEEE Transactions on Applied Superconductivity*, vol. 11, no. 1. pp. 840-843, 2001.

Spectrometers for (sub)mm radiometer applications

A. Emrich, M. Krus, J. Riesbeck, S. Andersson, Magnus Hjort
Omnisys Instruments AB, Gruvgatan 8, 421 30 Göteborg, Sweden

ABSTRACT

The FFT spectrometer and autocorrelation spectrometers are two of 5 types of spectrometers being considered for space based (sub)millimetre heterodyne systems. The advantages of the digital autocorrelation and FFT spectrometers compared to Chirp Transform, Acousto Optical and Filterbank spectrometers are; stability, compactness, high reliability and variability in bandwidth and resolution. FFT spectrometers based on the latest generation of FPGA devices now promise a cost effective alternative for low to medium bandwidth applications with high resolution requirements.

Omnisys has an FFT spectrometer design optimized for ground based applications. It follows the single Eurocard standard size and provides up to 2 GHz bandwidth and 1-4 inputs. With four inputs, the maximum processed bandwidth is 500 MHz.

Configurations with polyphase filtering, polarization processing and variable resolution over the processed band have also been tested.

Omnisys FFT board provides 2 GHz processed bandwidth with a power budget of less than 20W. The next generation will provide 4 GHz of bandwidth per board.

For the SuperCAM imaging system, 16 boards will be used in two single height 19" crates to provide 64 spectrometers. It could be upgraded to provide 64 times 1 GHz by simply adding two crates. Test results will be shown in the conference.

These can be housed in one single height 19" crate together with IF systems and embedded computers providing flexible interfaces to front-ends as well as flexible interfaces for switch synchronization, data readout and other forms of control. The default interface is 100 MBit/s Ethernet. This is a breakthrough for future imaging applications as we can provide spectrometers for 5 kEuro each (in reasonable volume).

Omnisys has designed and implemented several generations of autocorrelation chip sets and spectrometers. This range from the ODIN satellite spectrometers now in LEO to our current 8 GHz single chip spectrometer. The ODIN chip set was a breakthrough at the time (1998). The power consumption was lowered by a factor of 50

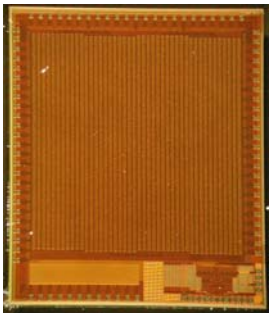

HIFAS, Omnisys fifth generation autocorrelation spectrometer ASIC is being developed. It is a full-custom design with over two million transistors, designed for IBM's 180 nm SiGe Bi-CMOS process. Unlike earlier generations, it contains both the bipolar 3-level ("1.5-bit") A/D converter and the CMOS correlator on the same chip. Thereby, the sensitive high-speed digital interface between the two parts gets integrated on the chip.

The chip supports as input either a complex I/Q input signal pair, measuring its spectrum from –fclk/2 to +fclk/2 or a single baseband signal sampled on both clock edges, measuring from 0 to fclk. This choice gives flexibility for the system level design.

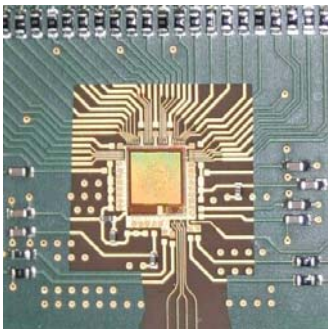

The first batch of the chip was produced in 2007. Unfortunately it turned out to have a logic bug that makes it necessary to do a re-run. A second revision of the chip is being designed at the time of this writing, and tape-out is planned for early 2008. Despite these initial problems with the chip, most of the chip's functions have been tested and shown to work. The analog parts work in both of the two input modes with up to 8 GHz sample clock.

The goal is to reach a bandwidth of 8 GHz, a resolution of 1024 channels, and a power consumption of 3-4 W. When finished, this chip will set a new world record in autocorrelator performance, and open for new possibilities in radiometry on both space and ground.

Superconducting Integrated Receiver on Board TELIS

P. Yagoubov[1], G. de Lange[1], H. Golstein[1], L. de Jong[1], A. de Lange[1], B. van Kuik[1],
E. de Vries[1], J. Dercksen[1], R. Hoogeveen[1], L. Filippenko[2], A. Ermakov[2], V. Koshelets[2]
[1]*SRON Netherlands Institute for Space Research, Groningen, the Netherlands*
[2]*Institute of Radio Engineering and Electronics, Moscow, Russia*
* Contact: p.a.yagoubov@sron.nl, phone +31-50-363 407

***Abstract*— In this paper we present configuration and performance of the 480 - 650 GHz channel for the Terahertz Limb Sounder (TELIS), a three-channel balloon-borne heterodyne spectrometer for atmospheric research. This frequency channel is based on a phase-locked Superconducting Integrated Receiver (SIR). SIR is an on-chip combination of a low-noise SIS mixer with quasioptical antenna, a superconducting Flux Flow Oscillator (FFO) acting as Local Oscillator (LO) and SIS harmonic mixer (HM) for FFO phase locking. The microcircuit is designed as a quasioptical mixer. The SIR channel has been integrated into the TELIS system in the end 2006 and fully characterized during 2007/2008 in preparation for the flight campaign. In May 2008 TELIS was shipped to Brazil where it was integrated into the MIPAS-B gondola. The TELIS-MIPAS test flight took place in June 2008 in Teresina, Brazil.**

I. Introduction

TELIS (Terahertz Limb Sounder) is a cooperation between DLR (Institute for Remote Sensing Technology, Germany), RAL (Rutherford Appleton Laboratories, UK) and SRON (Netherlands Institute for Space Research, the Netherlands), to build a three-channel balloon-borne heterodyne spectrometer for atmospheric research. The three receivers utilize state-of-the-art superconducting heterodyne technology and operate simultaneously at 500 GHz (channel developed by RAL), at 480-650 GHz (SRON in collaboration with IREE), and at 1.8 THz (DLR). TELIS is designed to be a compact, lightweight instrument capable of providing broad spectral coverage, high spectral resolution and long flight duration (~24 hours duration in a flight campaign). The combination of high sensitivity and extensive flight duration shall allow evaluation of the diurnal variation of key atmospheric constituents such as OH, HO_2, ClO, BrO together with long lived species such as O_3, HCl and N_2O. The balloon platform on which TELIS is integrated also contains a Fourier transform spectrometer MIPAS-B developed by the IMK (Institute of Meteorology and Climate research of the University of Karlsruhe, Germany). MIPAS-B simultaneously measures within the range 680 to 2400 cm^{-1}. TELIS and MIPAS together cover a wide range of important atmospheric species to improve our understanding of atmospheric processes, investigate changes in the atmosphere

due to anthropogenic emissions, and to validate satellite instrumentation.

In this paper, the science and technology of TELIS will be discussed with emphasis on the 480-650 GHz channel developed by SRON and IREE.

II. Atmospheric Science in the THz Region

The millimeter and sub-millimeter (terahertz, THz) region of the electromagnetic spectrum is well suited for the study of the composition of the upper Earth's upper atmosphere. Many of the atmospheric trace gases have their rotational transition lines in this spectral region. The very high resolution required (in excess of 10^6) in order to fully exploit the spectral signature, can be obtained by heterodyne detection techniques.

Application of the heterodyne detection technique in atmospheric observations from space has been pioneered by the Microwave Limb Sounder on board the UARS satellite [1], operational between 1991 and 1999. UARS/MLS measured stratospheric ozone, ClO, water vapor, pressure, and temperature using bands at 63 GHz, 183 GHz, and 205 GHz. Its improved successor MLS on board of EOS-Aura has been launched July 2004 [1] and performs very successfully. The frequency bands have been extended to 118 GHz (for temperature and pressure), 190 GHz (H_2O and HNO_3), 240 GHz (O_3 and CO), 640 GHz (for HCl, ClO, BrO, HO_2, and N_2O), and 2.5 THz (for OH).

In Europe, the Swedish ODIN satellite [2] carries the Sub Millimeter Radiometer instrument which is used for atmospheric research as well as for astronomical observations. Its frequency bands are located at 118.25 - 119.25 GHz, 486.1 - 503.9 GHz, and 541.0 – 580.4 GHz. ODIN was launched in 2002 and is still operational.

Two satellite instruments are currently under development that employ SIS and HEBM mixers: JEM/SMILES [3] for observing the Earth' atmosphere and Herschel/HIFI [4] for astrophysical research. The Japanese

SMILES instrument (Superconducting Submillimeter-Wave Limb Emission Sounder) for the Japanese Experiment Module (JEM) of the International Space Station will be used for the observation of many atmospheric species around 625 and 650 GHz. This instrument is currently planned to be launched in 2008. The HIFI instrument (Heterodyne Instrument for the Far Infrared) instrument is being integrated onto the Herschel satellite and will be launched in 2009.

Newly proposed to the US National Research Council is the SMLS instrument (Scanning MLS) on board CAMEO [1]. Here, superconducting SIS mixers are proposed for the millimeter channel 180-280 GHz and two sub-millimeter channels 580 – 680 GHz. The huge gain due to the low-noise characteristics of these mixers is used to reduce the integration time for one single measurement to a few milliseconds, allowing for two orders of magnitude more observations in comparison to the standard mixers used in MLS. With SMLS a full 3-D characterization of the atmosphere is possible. When selected, CAMEO/SMLS will be launched in the 2015-2018 timeframe.

Extrapolating the current trends towards the future, we foresee Earth limb sounding from a satellite platform with superconducting receivers operating at millimeter, and sub millimeter wavelengths.

Several balloon and aircraft instruments anticipate space application of cryogenic technologies, as well as ground based astronomical observatories. Without being complete a few examples are given. Already operationally flying instruments for Earth observation using SIS mixers are: PIROG [5], ASUR [6] and BSMILES [7].

III. The Science of TELIS

An extensive list of molecular species will be targeted by TELIS: BrO, ClO, HCl, HOCl, CH_3Cl, O_3 (normal and isotopic), H_2O (normal and isotopic), OH, HO_2, HNO_3, NO, N_2O, NO_2, HCN, and O_2. Vertical profiles of even very weak individual lines can be determined as the TELIS receivers combine limb sounding with a high frequency resolution and low noise observations. An example of a spectrum to be measured by the SIR channel at 495 GHz LO frequency is shown in Figure 1.

With respect to stratospheric ozone depletion both the halogen chemistry and HO_x chemistry can thoroughly be

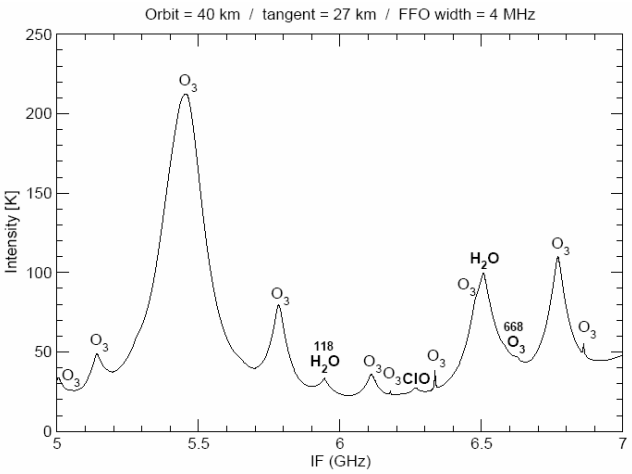

Fig.1 Example of spectrum to be measured by the SIR channel at LO frequency 495 GHz in DSB mode

investigated. Ozone isotopes may give insight in hidden and unknown chemical reactions and isotopic water may shed light on the origin of stratospheric water, which is connected to ozone through the HO_x cycle and Polar Stratospheric Clouds (PSCs).

A key question in stratospheric sciences is whether ozone will recover in the coming decades as a result of international regulations on ozone depleting substances. In the lower and middle stratosphere ozone depletion is governed by halogen chemistry (chlorine and bromine), which is fairly well understood. The fact that TELIS and MIPAS can retrieve almost all species appearing in the catalytic halogen ozone depletion cycles will put the existing atmospheric chemistry models to stringent tests. In the upper stratosphere also HO_x and NO_x become important catalytic ozone depletion forces. Here atmospheric chemistry models are less accurate: ozone concentrations are underpredicted, OH is underpredicted, and HO_2 is overpredicted. Observing all species simultaneously will shed light upon the production and loss mechanisms of HO_x and the partitioning between OH and HO_2 [9, 10].

Stratospheric water vapor plays an important role in the ozone chemistry as a source gas for the production of HO_x. The origin of stratospheric water is still not completely understood. Stratospheric water is transported from the troposphere, but also formed in situ by the oxidation of species, for instance, methane. The accurate measurement of water isotopologues may give insight in the relative weights of the water loading mechanisms of the stratosphere, as the different masses and energy level structures of the isotopologues result in differences in evaporation, condensation, and chemical reactions.

IV. TELIS Instrument Configuration

A design drawing of the TELIS instrument is shown in Figure 2. The optical front-end of TELIS is common for the three channels and consists of a pointing telescope,

calibration blackbody, and relay and band-separating optics. Details of the optical design can be found in [11, 12, 13].

The telescope is a dual offset Cassegrain antenna. All three telescope mirrors are mounted on a common frame that can be rotated around the axis coinciding with the direction of the output beam. The vertical (elevation) resolution at the tangent

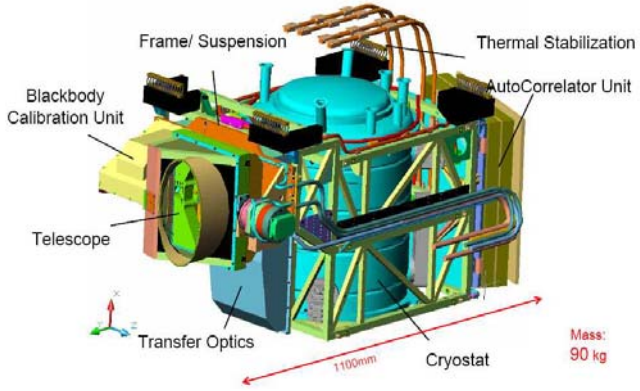

Fig.2 Design drawing of the complete TELIS instrument

point is about 2 km at 500 GHz (FWHM),inversely proportional to the frequency. The limb scans range from the upper troposphere (10 km) to flight altitude at about 37 km with 1 to 2 km steps. Horizontal (azimuth) resolution is about a factor of 2 less, due to the anamorphicity of the telescope but not of prime importance for this mission as the atmospheric properties within the beam hardly depend on the azimuth.

Calibration of the radiometric gain of the spectrometers is done with two blackbody reference sources. The hot-load consists of a conical black-body at ambient temperature that can be viewed by a small switching mirror in the warm optics. The cold sky reference is measured with the telescope set at 60 degree upwards with respect to the limb position. The two references are measured once or twice in every limb scan.

Frequency separation between the channels is performed quasioptically, allowing simultaneous observations by all receivers. For this, the beam is first split in two polarization components by a wire grid. The 500 GHz channel uses the reflected beam. The beam is then split by a dichroic filter. After the splitting, the three beams enter a custom designed liquid-helium cooled cryostat. A number of off-set reflectors are used to interface the optics from the telescope to the cryogenic channels, see Figure 3.

Inside the cryostat, each receiver has dedicated cold optics, mixing element and IF amplifiers.

The 500 GHz receiver channel is being developed by RAL [14]. It is a highly compact unit consisting of a fixed-tuned waveguide SIS mixer, cryogenic solid-state local oscillator (LO) chain and a low-noise Intermediate-Frequency (IF) chain. Single sideband operation is achieved through the use of a miniature cryogenic dichroic filter that provides a 4K image termination and image band rejection of >25dB. For optimization of the performance of the dichroic single-sideband filter a high IF is chosen: 14 – 18 GHz.

The 480-650 GHz receiver channel is being developed in cooperation between IREE and SRON and is based on a single-chip Superconducting Integrated Receiver (SIR) that comprises on one substrate a low-noise SIS mixer with quasi-

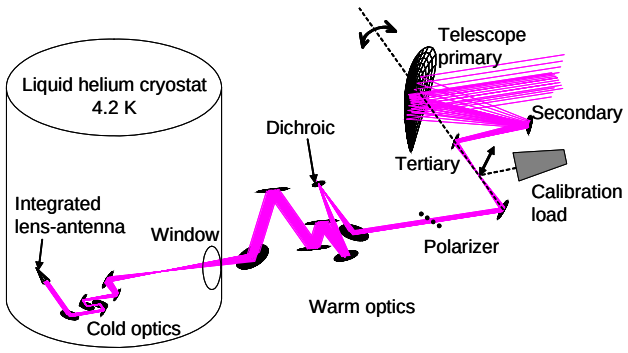

Fig.3 Schematics of the 500-650 GHz channel optics. The telescope is rotated around the axis coinciding with the direction of the output beam. Wire grid polarizer and dichroic plate are used to separate this receiver from the two other frequency channels (not shown). The cold optics and mixer element are located inside the cryostat at the ambient temperature of 4.2 K

optical antenna and a superconducting Flux Flow Oscillator (FFO) acting as LO [15, 16, 17]. Tunability of the FFO shall allow for a wideband operation of this channel, with a goal to obtain 150 GHz instantaneous rf bandwidth or even more. The SIR channel is discussed in detail in the next section.

The 1.8 THz channel is based on a phonon-cooled NbN HEB mixer technology and is being developed by DLR, also acting as Principle Investigator (PI) for the TELIS mission. It is similar to that under development for SOFIA by MSPU and DLR [18,19]. It utilizes a cryogenic solid-state LO that is loss-less coupled to the mixer via an optical interferometer (Martin-Puplett type).

Three amplified output IF signals are fed to an IF processor which converts the IF to the input frequency range of the digital autocorrelator of two times 2 GHz bandwidth. Both IF processor and digital autocorrelator are developed by the Swedish Omnisys company [20].

An on-board PC-104 computer interfaces with the control electronics of the three receiver channels and the instrument, with the digital auto correlator, with the host instrument MIPAS, and with the ground segment through a radio link. The ground segment consists of a server computer interfacing with three dedicated client computers through TCP/IP socket connections.

The complete system is battery powered and is designed for 24 hours flight duration. The total instrument is about 1x1x0.6 m^3 and has a weight of 90 kg (see Fig. 2).

V. The Superconducting Integrated Receiver

A key element of the SIR channel is the Superconducting Integrated Receiver (SIR) chip developed at IREE [15, 16, 17]. SIR comprises on one 4 x 4 x 0.5 mm^3 chip a low-noise SIS mixer with quasioptical antenna, a Flux Flow Oscillator (FFO) acting as Local Oscillator (LO) and a SIS Harmonic Mixer (HM) for FFO phase locking, see Figure 4.

All components of the SIR microcircuits are fabricated from a high quality Nb-AlN/NbN-Nb tri-layer on a Si substrate [21]. The receiver chip is placed on the flat back surface of the Silicon lens with antireflection coating, forming an integrated lens-antenna. As the FFO is very sensitive for the external electromagnetic interferences the SIR chip has to be placed inside two cylindrical shields. The outer shield is made from cryo-perm and the inner shield is copper covered with 100 um of superconducting lead.

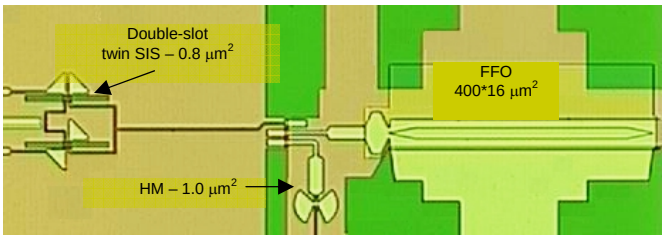

Fig. 4 Micro photograph of the central part of the SIR chip with double slot antenna

The spectral resolution of the TELIS backend spectrometer is 3 MHz, in order to resolve the exact shape of the atmospheric lines. The FFO lineshape and stability should ideally be much better than this. As the free-running linewidth of the FFO can be up to 10 MHz, the FFO is locked to an external reference oscillator using a Phase Lock Loop (PLL) system. For this, a small fraction of the FFO power is directed to a so-called Harmonic Mixer (HM). The scheme of this system is shown in Figure 5. The HM is pumped by a tuneable reference frequency in the range of 19-21 GHz from the Local oscillator Source Unit (LSU), phase locked to the internal ultra stable 10 MHz Master Oscillator. The HM mixes the FFO signal with the n-th harmonic of the 19-21 GHz reference. The frequency of the LSU is chosen such that the difference frequency signal is about 4 GHz. This signal is amplified by a cryogenic low-noise HEMT amplifier, and downconverted to 400 MHz, where its frequency and phase are compared with a reference of 400 MHz. Both reference signals at 3.6 GHz and at 400 MHz are phase locked to the 10 MHz Master Oscillator. Finally, the phase difference signal generated by the PLL is used as a feedback to the FFO control-line current to compensate for the phase error. Wideband operation of the PLL (15 MHz full width) is obtained by minimizing the cable loop length. The result of the PLL on the FFO spectrum is shown in Figure 6. The impact of the non-perfect FFO spectrum on the retrieval accuracy is discussed in [22].

TELIS is setup to measure spectra in the sub-millimeter and THz range. From the spectra vertical profiles of trace gases will be determined in an off-line retrieval process. The retrieval is based on a comparison between a calculated spectrum and the measured spectrum [23]. The calculated spectrum is determined by a so-called forward model and takes into account the observation geometry. The emission spectrum is calculated by integrating the radiative transfer equation along the line of sight (LoS), for a given temperature and pressure profile, and for assumed molecular

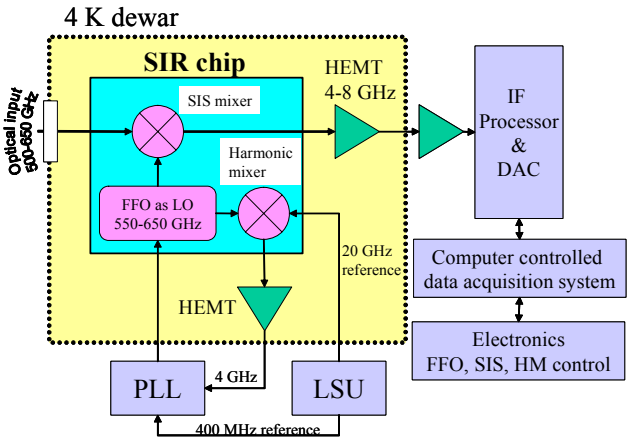

Fig. 5 Schematics of the SIR with a phase-locked LO. The FFO frequency is mixed in the Harmonic Mixer with the 19-21 GHz reference. The mixing product is amplified, down converted and compared with the 400 MHz reference in the PLL. The phase difference signal generated by PLL is used to feedback the FFO control line

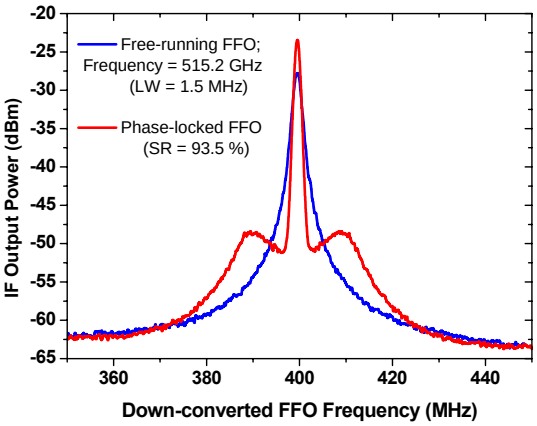

Fig. 6 Spectrum of a frequency-locked FFO (blue curve) and phase-locked FFO (red). Due to limitations of the spectrum analyzer the central delta-peak of the PL-FFO appears broadened

density height profiles. The instrument model adds instrument features such as the instrument lineshape and the integration over the Field of View (FoV) to determine the calculated TELIS spectrum.

In the so-called inverse model, the calculated spectrum will be compared to the actual measured spectrum and the

molecular density profiles will be altered to iteratively obtain the best match between modeled and observed spectrum. All limb scans are evaluated simultaneously to enhance the accuracy for the height profile.

VI. SIR Performance

The TELIS-SIR channel has been integrated and tested in the TELIS flight cryostat in 2006. All experimental results discussed here have been obtained with the SIR device selected for the first flight. The measured double sideband (DSB) receiver noise temperature, uncorrected for any loss, is presented in Figure 7 as a function of LO frequency, and in

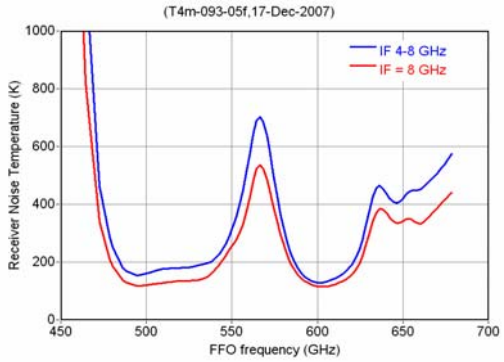

Fig. 7 Measured DSB receiver noise temperature of the SIR device selected for flight at 8 GHz IF frequency (red line) and integrated in the 4-8 GHz IF range (blue curve)

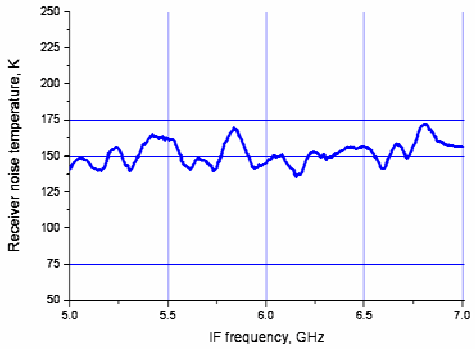

Fig. 8 Receiver noise temperature as a function of IF frequency, taken at 600 GHz

Figure 8 as a function of IF frequency. As can be seen, the averaged in the 4-8 GHz IF band noise is below 200 K over > 100 GHz input bandwidth of the receiver, with a minimum of 120 K at 600 GHz. The noise peak around 540-575 GHz is partially caused by absorption of water vapor in the path between calibration sources and cryostat, and partly due to properties of the mixer matching circuits. The relatively high noise in this part of the band is not a concern since this part of the atmospheric spectrum is almost completely blocked by the presence of a very strong atmospheric water-vapor line. The noise as a function of IF is fairly flat in the designed frequency range 5-7 GHz, as can be seen in Figure 8.

The near field beam pattern of the SIR cold channel has been measured using the ALMA measurements setup at 600 GHz. Results of the FFT transformed amplitude and phase distribution are shown in Figure 9. The measured beam waist is 2.25 mm (within 1% of the designed value), Gaussisity of the measured beam is 92.4%.

The SIR is a complicated device; it contains a few interactive superconducting elements: an SIS mixer, an FFO, and an HM for the FFO phase locking. Special algorithms and procedures have been developed and tested to make possible characterization of the SIR in a reasonable time scale and ensure SIR control during the flight. Some of these routines are listed below:

- fast definition of the FFO operational conditions (both on the Fiske step and in the flux-flow regimes);
- measurements of the free-running FFO linewidth;
- optimization of the LSU and HM parameters;
- optimization of the PLL operation;
- minimization of the SIR noise temperature;
- setting all predefined SIR parameters in the proper sequence for control during the flight;
- continuous monitoring of the main SIR parameters, adjustment (or recovering) the SIR operational state.

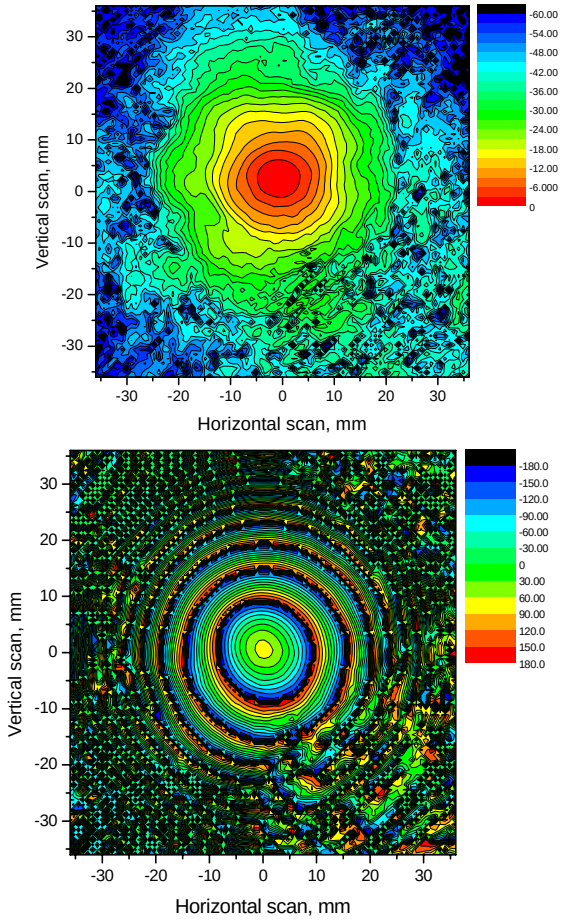

Fig. 9 SIR cold channel amplitude (upper panel) and phase (lower panel) distribution. Distance from the beam waist is 110 mm. Frequency is 600GHz

For the measurement strategy it is important to know the stability of the complete receiver chain. The stability determines the measurement time and thus the frequency of the calibration cycle. The stability of the complete TELIS-SIR system has been determined with a noise-fluctuation bandwidth of 17 MHz and the results are presented in Figure 10. For the two IF channels that are used to determine the Allan variance it is found that the Allan stability time is about 13.5 seconds. When the difference of the two channels is taken to determine the Allan variance (this is the so-called spectroscopic (differential) mode), the Allan stability time of 20 seconds is found.

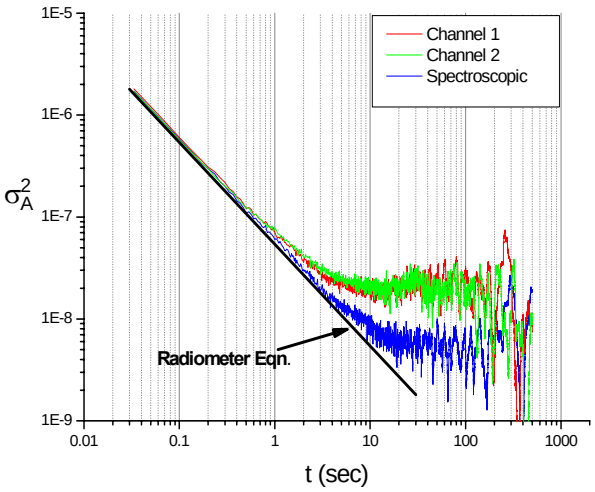

Fig. 10 System stability of the SIR channel. FFO is phase locked at 600 GHz. Green and blue lines present individual channels variance, the black one is representative for the spectroscopic variance

To prove the capabilities of the TELIS-SIR channel for high resolution spectroscopy we have successfully measured line profiles of OCS gas around 600 GHz. The tests were done in a laboratory gas cell setup at a gas pressure down to 0.2 mBar, corresponding to the FWHM linewidth <5 MHz. Figure 11 shows an example of the measured spectrum at a gas pressure of 2.6 mBar. In this case the FFO frequency was tuned to 601 GHz so that the two OCS lines have their lines in the 5 – 7 GHz IF range, one in the upper side band and the other one in the lower side band. The flat lower level of the spectrum is due to the 77 K cold reference and the residual emission of the warm windows of the gas cell. One can see two strong lines, which are calculated to be saturated. The 4 weaker lines are isotopes (not saturated). For the saturated lines the signal level is expected to be at 210 K for an ideal receiver. The deviation from this value is due to the sideband ratio of the receiver being different from 1.0.

Knowledge of the instrument sideband ratio with an accuracy of better than 10% is required for the retrieval as the spectrum is taken in the DSB mode. We have set-up Bruker

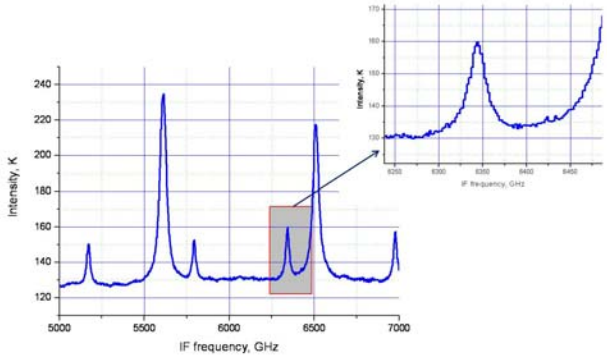

Fig. 11 Deconvolved spectrum of the OCS emission lines at a gas pressure 2.6 mBar. LO frequency 601 GHz. Two strong lines are saturated; weaker lines are not saturated isotopes. The lines are detected, one in the LSB, the other one in the USB

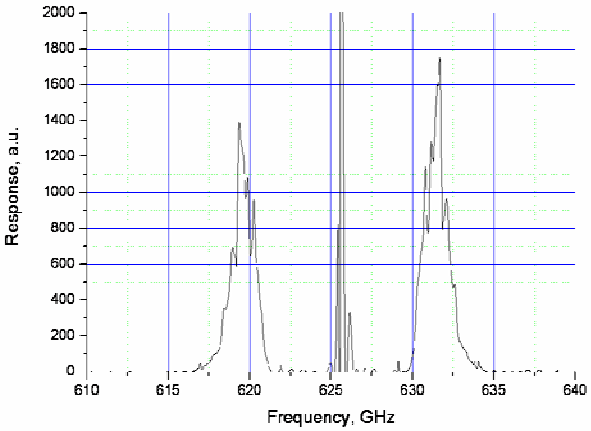

Fig. 12 FTS spectrum of the receiver. LO frequency is 626 GHz. Two sidebands of the receiver are mirrored around the LO frequency.

Fourier Transform spectrometer to measure the receiver response in the heterodyne mode. One of the results is presented in Figure 12. The LO frequency for this experiment was set around 626 GHz. One can see a strong peak in the data due to self-emission of the LO radiation towards the FTS system. The sidebands of the receiver are detected separately, so that the sideband ratio of the instrument can be calculated.

VII. FIRST FLIGHT

The TELIS instrument had its maiden flight during the Teresina 2008 campaign within framework of the SCOUT-03 project. It arrived in Teresina in May 2008 and was successfully assembled and integrated into the MIPAS-B gondola within two weeks. A number of tests, including communication link with the ground segment, telescope control (compensation for gondola motions), line of sight characterization with respect to elevation and azimuth, have been successfully accomplished by the TELIS and MIPAS teams. Special attention was paid to electro-magnetic compatibility of the two instruments. Figure 13 shows the TELIS instrument integrated into the MIPAS gondola.

All SIR sub-systems were operational on the launch site; no degradations or failures have been detected.

For the test flight seven micro-windows have been selected with the following LO settings:

- 495.04 GHz and 496.96 GHz for the water isotopes;
- 506.56 GHz for BrO;
- 515.25 GHz for the pointing and also H_2CO, H_2O_2;
- 519.25 GHz for BrO and HNO_3;
- 607.78 GHz for HCN and the ozone isotopes;
- 619.10 GHz for HCl, HOCl and ClO.

The SIR was characterized at these frequencies and pre-set operating parameters for the FFO, SIS and HM mixers have been determined. Specially developed control algorithms allowed fast switching between the frequencies and final optimization of the SIR for each particular frequency. A typical time for a frequency switch is about 2 minutes.

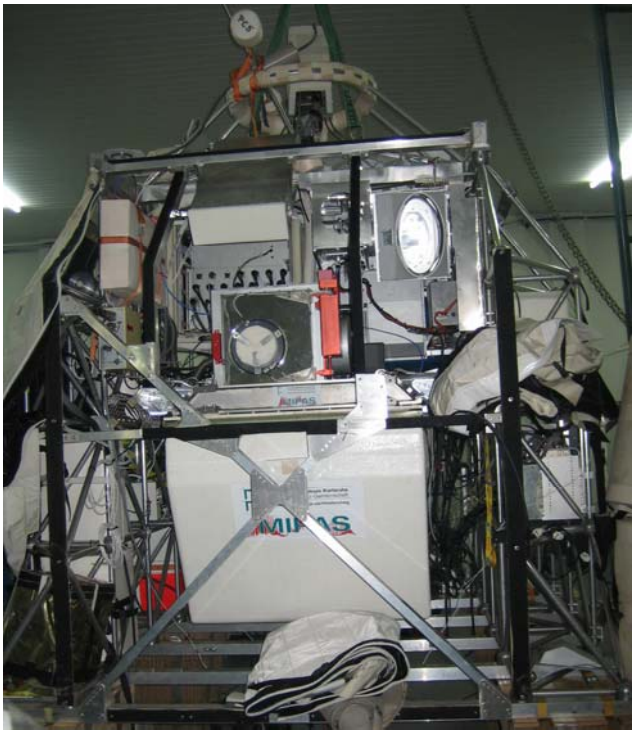

Fig. 13 TELIS (upper right corner in the gondola) is integrated into the MIPAS gondola. TELIS electronic boxes are located in the gondola structure (right side)

The balloon was launched on 05.06.2008 at around 10:30 pm. In the first two hours of the flight the gondola ascended to about 30 km altitude. During this time it went through very cold atmospheric layers with temperatures as low as 180 K at the tropopause. Although the instrument was insulated, the TELIS electronics and battery boxes cooled down to temperatures as low as 240 K. This was much lower than anticipated and also lower than the minimum temperatures we observed in previous Thermal Vacuum tests. Nevertheless, it was still possible to operate the SIR channel and switch between frequencies using the automatic on-board algorithms to compensate for the drifts and offsets developed in the electronics.

Unfortunately, the cold temperatures of the cryostat and optics also resulted in a malfunctioning of the telescope mechanics and calibration source. Therefore, no limb sounding and no deep space view for calibration could be done. Furthermore, due to the low temperature the cryostat developed a leak. As a result, the liquid helium evaporated quickly and the channels warmed up after about 3 hours of flight.

After the flight the gondola was recovered and both instruments survived the landing, no major mechanical problems were found. The housekeeping data is currently being analysed to identify problems in order to improve the thermal design for the next flight, which is currently scheduled for winter 2009 in Kiruna.

CONCLUSIONS

Capability of the SIR for high resolution spectroscopy has been successfully proven in a laboratory environment. The receiver has been installed into TELIS and integrated in the MIPAS gondola for the first flight. The maiden flight took place in June 2008. During the first few hours of the flight the instrument behaved normally, could be commanded and frequency switching algorithms worked well. However, due to thermal-mechanical problems no scientific data have been obtained. The housekeeping data is currently being analysed to identify problems in order to improve system thermal design for the next flight, which is currently scheduled for winter 2009 in Kiruna.

ACKNOWLEDGMENT

The authors thank colleagues at SRON and DLR for help and assistance in the SIR channel characterization: A. Baryshev, J. Barkhof (amplitude-phase beam measurements), J. Kooi, M. Romanini (stability test), M. Birk and G. Wagner (gas cell measurements and Bruker FTS measurements). T. de Graauw and W. Wild are acknowledged for their support in this work.

The work was partially supported by the projects: RFBR 06-02-17206, ISTC # 3174, and Grant for Leading Scientific School 5408.2008.2.

REFERENCES

[1] For info on UARS/MLS, EOS-Aura /MLS and CAMEO/SMLS see: http://mls.jpl.nasa.gov

[2] U. Frisk et al., "*The Odin satellite: Radiometer design and test*", Astronomy&Astrophysics A&A 402, L27-L34 (2003), and http://www.ssc.se/?id=7180

[3] For info on JEM/SMILES see: http://smiles.tksc.jaxa.jp/

[4] For info on Herschell/HIFI see: http://www.sron.nl/divisions/lea/hifi/

[5] J. R. Pardo, L. Pagani, G. Olofsson, P. Febvre, and J. Tauber, "Balloonborne submillimeter observations of upper stratospheric O_2 and O_3" , J. Quant. Spectrosc. Radiat. Transf., vol. 67, pp. 169–180, 2000 and Deschamps A et al. "A balloon experiment searching for the 425GHz O2 line with an SIS Receiver",

proceeding of the ESA Workshop on Millimeter Wave Technology and Applications, Espoo, Finland, May 1998.

[6] For info on ASUR see: http://www.iup.physik.uni-bremen.de/asur/asurhome_e.html/

[7] For info on SMILES see: http://www2.nict.go.jp/dk/c214/bsmiles/

[8] For info on MIPAS-B see http://www-imk.fzk.de/asf/mipas-b/mipas-b.htm/

[9] R.R Conway, M.E. Summers, M.H. Stevens, J.G. Cardon, P. Preusse, and D. Offermann, *"Satellite observations of upper stratospheric and mesospheric OH: The HOx dilemma"*, Geophysical Research Letters 27 (17), (2000), pp. 2613-2616.

[10] T. Canty, H.M. Pickett, R.J. Salawitch, K.W. Jucks, W.A. Traub, J.W. Waters, *"Stratospheric and mesospheric HOx: results from aura MLS and FIRS-2"*, Geophyscial Research Letters 33 (12), Art. No. L12802, 2006.

[11] P. Yagoubov, H. van de Stadt, R. Hoogeveen, V. Koshelets, M. Birk, and A. Murk, *"Optical design of sub-millimeter spectrometer for limb sounder"*, in 28th ESA Antenna Workshop on Space Antenna Systems and Technologies, Noordwijk (NL), May 2005.

[12] P.A. Yagoubov, W.-J. Vreeling, H. van de Stadt, R.W.M. Hoogeveen, O.V. Koryukin, V. P. Koshelets, O.M. Pylypenko, A. Murk, *"550-650 GHz spectrometer development for TELIS",* proceedings of the 16th Intern. Conf. on Space Terahertz Technology, Göteborg, Sweden, May 2-4, 2005.

[13] A. Murk, P. Yagoubov, U. Mair, M. Birk, G. Wagner, H. van de Stadt, R. Hoogeveen, and N. Kämpfer, *"Antenna simulations for the THz and submm limb sounder TELIS"*, in 28th ESA Antenna Workshop on Space Antenna Systems and Technologies, Noordwijk (NL), May 2005.

[14] B.N. Ellison, B.P. Moyna, D.N. Matheson, A. Jones, S.M.X. Claude, C. Mann, B.J. Kerridge, R. Siddans, R. Munro, and W.J. Reburn, "*Development of a high sensitivity airborne SIS receiver to detect ClO and BrO*", Proceedings of 2nd ESA Workshop on Millimetre Wave Technology and Applications, Espoo, Finland, May 1998.

[15] V.P. Koshelets, P.N. Dmitriev, A.B. Ermakov, L.V. Filippenko, O.V. Koryukin, A.V. Khudchenko, M.Yu. Torgashin, P.A. Yagoubov, R.W.M Hoogeveen, and W. Wild, "*Superconducting Submm Integrated Receiver with Phase-Locked Flux-Flow Oscillator for TELIS*", proceedings of the 16th Intern. Conf. on Space Terahertz Technology, Göteborg, Sweden, May 2-4, 2005, and http://www.cplire.ru/html/lab234 /publications.htm

[16] V.P. Koshelets, P.N. Dmitriev, A.B. Ermakov, A.S. Sobolev, M.Yu. Torgashin, V.V. Kurin, A.L. Pankratov, J. Mygind,, *"Optimization of the Phase-Locked Flux-Flow Oscillator for the Submm Integrated Receiver"*, "*IEEE Trans. on Appl. Supercond.",* vol. 15, pp. 964-967, 2005.

[17] V.P. Koshelets, A.B. Ermakov, L.V. Filippenko, A.V. Khudchenko, O.S. Kiselev, A.S. Sobolev, M.Yu. Torgashin, P.A. Yagoubov, R.W.M. Hoogeveen, and W. Wild, *"Integrated Submillimeter Receiver for TELIS"*, *IEEE Trans. on Appl. Supercond.,* vol. 17, pp. 336-342, 2007.

[18] H. Richter, A. Semenov, H.-W. Hübers, K.V. Smirnov, G.N. Goltsman, B.M. Voronov, *"Phonon Cooled Hot-Electron Bolometric Mixer for 1-5 THz"*, 2004 Joint 29th Int. Conf. on Infrared and Millimeter Waves and 12th Int. Conf. on Terahertz Electronics, pages 241-244.

[19] S. Cherednichenko, M. Kroug, H. Merkel, P. Khosropanah, A. Adam, E. Kollberg, D. Loudkov, G. Gol'tsman, B. Voronov, H. Richter, and H. -W. Huebers, *"1.6 THz heterodyne receiver for the far infrared space telescope"*, Physica C: Superconductivity, vol. 372, Part 1, pp. 427-431, 2002

[20] See http://www.omnisys.se/

[21] M.Yu. Torgashin, V.P. Koshelets, P.N. Dmitriev, A.B. Ermakov, L.V. Filippenko, and P.A. Yagoubov, *"Superconducting Integrated Receivers based on Nb-AlN-NbN circuits"*, *IEEE Trans. on Appl. Supercond.,* vol. 17, pp.379- 382, 2007.

[22] R. W. M.Hoogeveen; P. A. Yagoubov; A. de Lange; A. M. Selig; V. P. Koshelets; B. N. Ellison; M. Birk, *"Superconducting integrated receiver development for TELIS"*, SPIE Proceedings Vol. 5978 (2005) 59781F

[23] R.W.M. Hoogeveen, et al., "New cryogenic heterodyne techniques applied in TELIS: the balloon borne THz and submm limb sounder for atmospheric research", Proc. of SPIE, Infrared Spaceborne Remote Sensing XI, 5152, p. 347-355, 2004.

Performance Characterization of GISMO, a 2 Millimeter TES Bolometer Camera used at the IRAM 30 m Telescope

Johannes G. Staguhn[1,2,*], Dominic J. Benford[1], Christine A. Allen [1], Stephen F. Maher [1,3], Elmer H. Sharp [1,4], Troy J. Ames[1], Richard G. Arendt[1] , David T. Chuss[1], Eli Dwek[1], Dale J. Fixsen[1,2], Tim M. Miller[1,5], S. Harvey Moseley[1], Santiago Navarro[6], Albrecht Sievers[6], Edward J.Wollack[1]

[1]*NASA/Goddard Space Flight Center, Greenbelt, MD 20771, USA;*

[2]*Dept. of Astronomy, University of Maryland, College Park, MD 20742, USA;*

[3]*Science Systems &: Applications, 10210 Greenbelt Rd. Ste. 600, Lanham, MD 20706, USA;*

[4]*Global Science & Technology: 7855 Walker Drive, Ste 200, Greenbelt, MD 20770 , USA;*

[5]*MEI Technologies, 7404 Executive Place, Suite 500, Seabrook, MD 20706, USA;*

[6]*IRAM, Avenida Divina Pastora, 7, Nucleo Central, E 18012 Granada, Spain;*

* Contact: Johannes.G.Staguhn@nasa.gov, phone +1-301-286-7840

Abstract— The 2mm spectral range provides a unique terrestrial window enabling ground-based observations of the earliest active dusty galaxies in the universe and thereby allowing a better constraint on the star formation rate in these objects. In November, 2007 we have fielded our 2mm bolometer camera GISMO (the Goddard IRAM Superconducting 2 Millimeter Observer) at the IRAM 30m telescope on Pico Veleta in Spain. GISMO uses a monolithic 8x16 Backshort-Under-Grid array with integrated TES detectors with 2 mm-pitch. We will present early results from our observing run with the first fielded BUG bolometer array.

I. Introduction

Our team has been building a 2 millimeter wavelength bolometer camera, the Goddard-IRAM Superconducting 2 Millimeter Observer (GISMO) for astronomical observations at the IRAM 30 m telescope on Pico Veleta, Spain [1]. The camera uses an 8×16 array of close-packed, high sensitivity, transition edge sensor (TES) bolometers with a pixel size of 2×2 mm^2, which was built in the Detector Development Laboratory at NASA/GSFC. The superconducting bolometers are read out by SQUID time domain multiplexers from NIST/Boulder [2]. In order to permit background-limited observations in the 2 mm atmospheric window at Pico Veleta, the required sensitivity expressed in Noise Equivalent Power (NEP) for the detectors is ~ $4 \cdot 10^{-17}$ W/sqrt(Hz) [3]. The array architecture we use is based on the Backshort Under Grid (BUG) design [4], which consists of three components: 1) a TES-based bolometer array with background-limited sensitivity and high filling factor, 2) a quarter-wave reflective backshort grid providing high optical efficiency, and 3) a superconducting bump-bonded large format Superconducting Quantum Interference Device (SQUID) multiplexer readout. This design is scalable to kilopixel size arrays for future ground-based, suborbital and space-based X-ray and far-infrared through millimeter cameras. The GISMO instrument is optimized for large area sky surveys, and it is most efficient at the detection of dusty galaxies at very high redshifts. High sensitivity observations will even be possible in the summer season. We performed a first engineering field test of GISMO at the 30 m telescope in November 2007.

II. Scientific Motivation

Due to the low background emission of the Earth's atmosphere at a wavelength of 2 millimeters, astronomical observations in this atmospheric window are efficient for the detection of the earliest active dusty galaxies in the universe [5]. Continuum measurements of galaxies at 2 mm wavelength are well-suited to determine the star formation rate and the total energy output in these objects. These 2 mm observations will complement existing SEDs of high redshift galaxies in the Rayleigh-Jeans part of the dust emission spectrum, even at the highest redshifts. At Pico Veleta, the site of the IRAM 30 m Telescope, the atmospheric photon noise at 2 mm is about a factor of three lower than it is at 1.2 mm wavelength. As a consequence, at redshifts of $z > 5$, sky background limited bolometric observations at 2 mm are highly efficient as compared to observations at shorter (sub-)millimeter wavelengths [5].

III. The GISMO Instrument

A. Dewar and Optics

GISMO is a bolometer camera intended specifically to maximize the likelihood of detecting large numbers of very high redshift galaxies. We designed fast f/1.2 optics for an approximately 0.9 λ/D sampling, intended to optimize the

efficiency of GISMO for large area blank sky surveys, yet without compromising the achievable point source signal-to-noise ratio [6]. A 4 inch (100 mm) diameter, anti-reflection coated, silicon lens provides the required focal ratio, and is cooled to 4.2 K to reduce the background on the detector. The cryostat is designed as a straightforward, simple-to-operate system with no moving parts. The instrument has a combination of ^{4}He and ^{3}He evaporation coolers that are pocketed into the dewar cold plate, providing a base temperature of 260 mK for the detector array. A more detailed description of the instrument design can be found in [7]. The detector arrays are read out by four 32-channel SQUID multiplexers, manufactured by NIST/Boulder [2]. Both the readout electronics and the instrument remote control and data acquisition software are presently being used in other instruments, such as the Green Bank Telescope 3 mm bolometer camera MUSTANG. [8]. GISMO is designed as a very simple instrument targeted at producing the maximum scientific return for the minimum investment in time.

B. Detectors

GISMO is enabled by a new detector technology developed by the Detector Development Laboratory (DDL) at the NASA/Goddard Space Flight Center. We have an ongoing program to develop several key technologies necessary to build kilopixel arrays in the BUG architecture [9]. The arrays consist of TES-based bolometers with resonant backshorts and SQUID Multiplexer readouts The detector architecture has advanced to the point that we can now produce 8×16 pixel arrays of 2 mm pitch bolometers for GISMO (Figure 1).

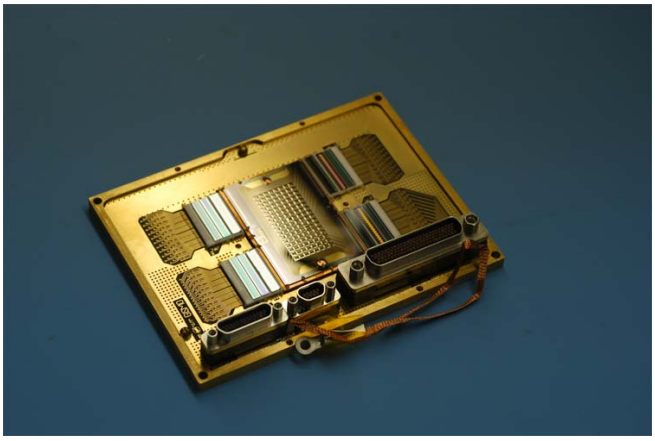

Fig. 1 The GISMO 8x16 planar array in the detector package. SQUID multiplexers, shunts and Nyquist inductors are integrated in the package

The array is a filled square grid of micromachined bolometers on a 1μm silicon membrane having superconducting TES bilayers and infrared absorbing films. The absorber is directly deposited onto the suspended bolometer, and is tuned to have an electrical resistivity of 400 Ω/square at 400mK. The coating for GISMO is bismuth, protected with a layer of silicon monoxide, to slow the adsorption of atmospheric water vapor into the bismuth during handling. To optimize the optical efficiency a λ/4 backshort (in the case of GISMO a reflective backshort) is placed a distance of 0.5 mm behind the detectors. This, coincidentally, is the thickness of the silicon-on-insulator support wafer upon which the detectors are fabricated, making it a simple matter to mount the detector chip on a reflective surface, in our case a copper-coated alumina board, to serve as the back-short. We use a normal metal "Zebra" stripe structure on the TES devices, which is used to suppress excess noise [10] and indeed provides near fundamental-noise-limited performance of the devices [11].

IV. INSTRUMENT PERFORMANCE AT THE TELESCOPE

Here we present early demonstration results from our first observing run at the IRAM 30 m Telescope, Nov. 5 -13, 2007 (Fig. 2, left). GISMO was mounted at the position of the MAMBO-II 1.2 mm bolometer camera [12] (Fig. 2, right).

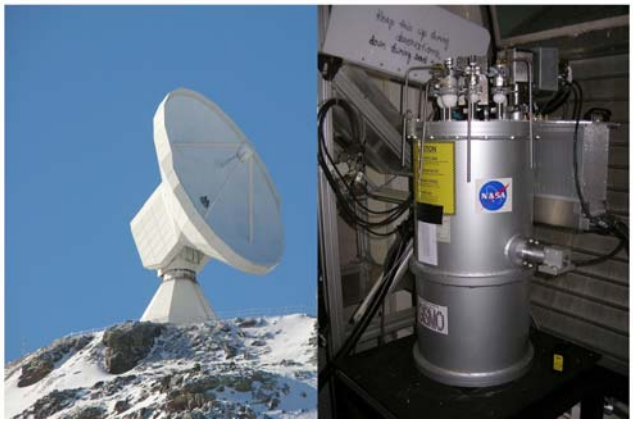

Fig. 2 *Left:* the IRAM 30m Telescope on Pico Veleta, Spain. *Right:* the GISMO dewar at the IRAM 30m telescope

In order to accommodate all weather conditions for this observing run we used a 40% transmission neutral density filter, which is mounted in front of the detector package. The filter allows for sky temperatures up to 150 K without saturating the TESs (which have a saturation power of ~ 35 pW). Once installed, we observed a beam spillover which manifested itself as radiation picked up from the mirror mount of the first fixed flat mirror in the 30m receiver cabin. This spillover, which we had not detected in the laboratory, is likely the result of the cold baffles in GISMO being slightly undersized (a deficiency we are in the process of fixing for the next observing run), and a minor misalignment of one of our non-planar mirrors during the installation at the telescope. For the observing run we therefore had to build a warm field stop that was mounted in front of the cryostat window, which is oversized by 20% in diameter. As a result of this warm stop we estimate that the effective detected background photon noise level was increased by several Kelvin. After a quick optical pre-alignment with a laser we pointed the instrument to the sky where we immediately detected the planets Jupiter and Mars, both of which, as expected, saturated our detectors. Fig. 3 shows three raw noise spectra we observed towards the sky: Two of those

(darker grey) are averages from working pixels, while the light grey dots shows the observed spectrum from an average of pixels in the "dead quadrant", a quadrant of the array we had lost the ability to bias the detectors due to the liftoff of the wire bonds for the detector bias, i.e. the detectors in this quadrant were regular superconductors.

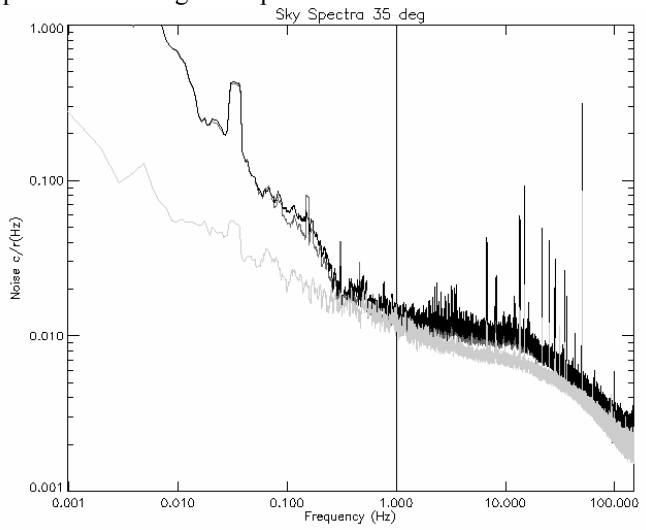

Fig. 3 Raw spectra of detector current noise density of GISMO while installed at the telescope and looking at the sky (dark and medium dark grey: average spectra of working pixels; light grey: average noise spectrum of superconducting (i.e. non biased) detectors

Note the wide range of the time axis, which ranges from 1 mHz - or 17 minutes - to 100 Hz. Many important features are visible in the plot: 1) The underlying 1/f properties of the readout (note that the drop-off beyond 10 Hz is due to feedback algorithm) is common to all three pixels. 2) Sky temperature variations are detected by the working pixels and dominate the noise at about 0.3 Hz and longer. 3) The noise from the sky emission in the important "signal band" (determined by the speed the telescope moves over the source) is also apparent at frequencies between 1 and 10 Hz. 4) The response to the rectangular scan pattern we used can be seen as a feature at ~ 0.02 Hz (also picked up at lower level by the "dead" pixels, i.e. due to some mechanism for electric or magnetic coupling). It is interesting to note that the spike at ~ 5 minutes seen in the "dead pixel" average is likely to originate from oscillations of the ionosphere which are known to have resonance frequencies of a few minutes. 5) There are a significant number of noise spikes visible in the spectrum, the origin of most of which can be shown to being caused by a low number of fundamental frequencies (see Fig. 4). We are currently in the process of trying to identify the source of those noise spikes

V. Examples Of Astronomical Observations

A. Planet Observations

Figure 5 (left) shows an observation of the planet Mars, yielding a beam size of 21" x 15". The diffraction-limited resolution of the 30 m telescope at 2 mm wavelength is 15". This measurement represents the most extreme beam asymmetry; we made measurements of other point sources, which typically yielded beam sizes between 15" and 19".

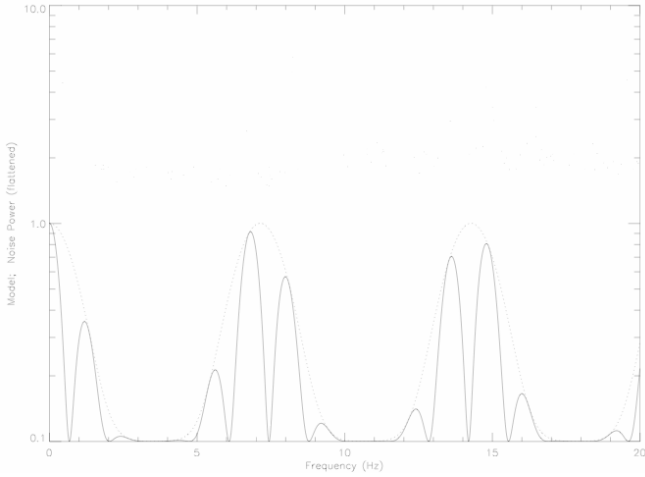

Fig.4 The dots show the flattened power spectrum with several clear sets of bands. The same data are displayed in all three panels, but on different frequency ranges. Some bands are strong enough that they extend beyond the top of the plot. The "model" spectrum indicated by the solid line is constructed from $\cos(\pi f / 1.352\ \text{Hz})^2 \times [\text{III}(7.142\ \text{Hz}) \times e^{-0.5 f^2 / (1.59\ \text{Hz})^2}] + 0.1$. The dotted line shows the envelope of the $\text{III}(7.142\ \text{Hz}) \times e^{-0.5 t^2 / (1.59\ \text{Hz})^2}$ modulation

Figure 5 (right) shows the azimuthal beam shape in detail. No significant sidelobes are visible.

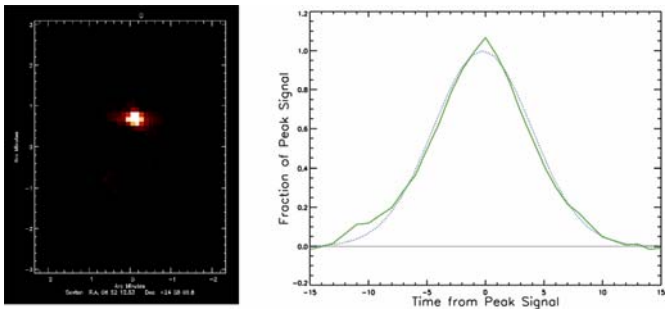

Fig. 5 *Left*: observation of the planet Mars. The fitted beam size is 21" x 15. This measurement represents the most extreme beam asymmetry we observed during measurements of point sources. *Right:* measured azimuthal beam shape derived from observations of Uranus (solid line), superimposed on a Gaussian distribution (dotted line)

B. Scan Patterns

Fig. 6 shows two typical scan patterns we used for observations: a) mapping by moving the telescope in azimuth (also called OTF mapping), and b) by alternating between mapping in azimuth and elevation directions (also called cross-linked OTF mapping). We soon abandoned the azimuth-only mapping, since the corresponding sky maps turned out to show residual spurious large scale structures. This can be understood by the fact that many areas of the sky in the azimuth-only maps will not have repeat observations in a sufficiently short period of time, and therefore the strong 1/*f*-like behavior of the atmosphere, seen in figure 3, does not allow a reliable estimate of the sky background. Both scan patterns were tested with and without chopping the telescope's secondary mirror. However, we did not discern

any benefit in using the chopper. Arbitrary scan patterns that allow each point of the sky to be revisited by a given pixel in a short amount of time, will optimize the achievable signal-to-noise ratio that one can achieve. An implementation of a Lissajous scanning pattern will be present at the 30m telescope by the time GISMO returns to the telescope in October of 2008. Another constraint to our observing efficiency for small maps suited to point sources was that there is a telescope drive software limit that does not allow the completion of an azimuth or elevation movement of the telescope in less than 10 seconds. The source signal for our smaller maps therefore was shifted toward lower frequencies than desired for optimum signal-to-noise performance of the observations. This problem will not affect us in the future with the implementation of the Lissajous mode, that is very well suited to mapping small areas.

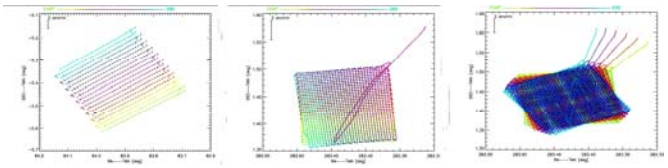

Fig. 6 Scan patterns used for our astronomical observations with the 30m telescope. *Left:* azimuthal scan pattern (OTF map). *Center:* azimuthal pattern, followed by scan pattern in elevation (cross linked OTF map). *Right*: Complete coverage for a 10 minute integration.Since the plots reflect the actual movement of the telescope which becomes obvious in the Az-El patterns shown here

C. *Astronomical Observations*

Figures 7 through 11 present a few examples of astronomical observations.

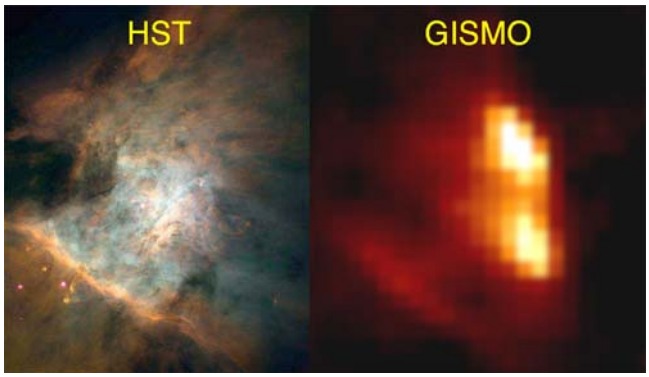

Fig. 7 HST imaged of the Orion Molecular Cloud. Right: GISMO's view of the same area. The integration time for this image was about 3 minutes

The software used to reduce the data shown in Figures 7 through 10 is a "quick view" package we have developed in order to be able to analyze the data during the observing run. Data for extended sources were high-pass filtered at 0.5 Hz, whereas those for point source observations had a point source Wiener filter (derived from GISMO Uranus images) applied. Then a fit to bolometer gains and offsets, based on the common time variations of the sky background, was applied to both data sets. Our first analysis indicates that with this preliminary data reduction package, a noise level a factor of about 3 above the atmospheric photon noise limit (which can be as low as 9 mJy/sqrt(s) under very good conditions) can be achieved for long integrations. The remaining excess noise is probably a combination of residual sky brightness variations and residual 1/*f* noise in the data, plus a constant background caused by the warm stop we were required to use during the first observing run as a result of our baffles being slightly undersized at that time.

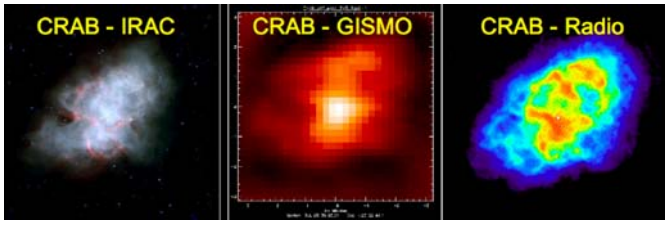

Fig. 8 The CRAB Nebula -- the result of a Supernova explosion – *(left)* in the infrared seen by the IRAC, *center* at 2mm as observed with GISMO, and *right* at centimeter wavelenghts as observed by the VLA

We have developed and are still in the process of improving a data reduction package that performs a least squares fit to the Fourier-transformed data. The algorithm is based on a scheme in which drift-dependent weights are applied to the data ("optimal mapping"). We are currently limited by the required computational resources, in that the memory use of the algorithm limits the amount of data for which we can compute a simultaneous solution. Fig. 10 shows an example of a 10 minute map of the Crab Nebula that was reduced with this package. The data shown here were downsampled by coadding into frames with an effective sampling rate of only 5 Hz.

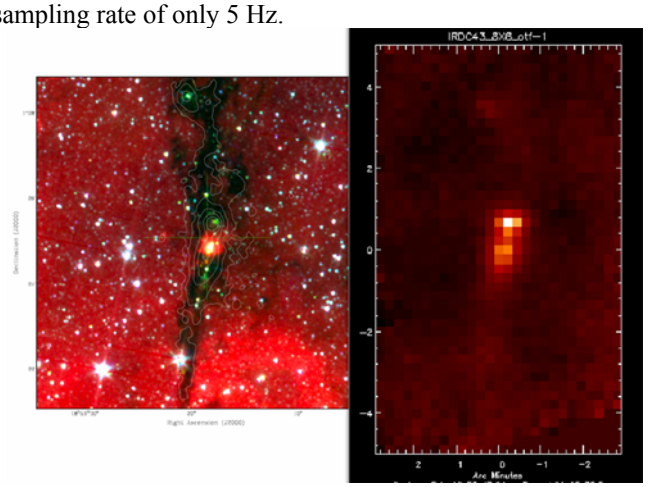

Fig. 9 *Left:* IRAC Glimpse N3-color IR image of the Infrared Dark Cloud IRDC43 with superimposed Mambo 1.2 mm contours (J. Jackson, priv. comm.). *Right:* GISMO's view of IRDC 43

We are working on the optimization of the code with respect to its requirement on computational resources. After further optimization we expect to have a data reduction pipeline available that will optimally extract the observed celestial flux from our astronomical targets.

CONCLUSION AND OUTLOOK

We have successfully fielded a 2mm TES bolometer camera at the IRAM 30 m telescope. We were able to obtain useful astronomical observations with a per-pixel sensitivity that was only a factor of about 3 above the expected, low, atmospheric photon noise at 2 mm.

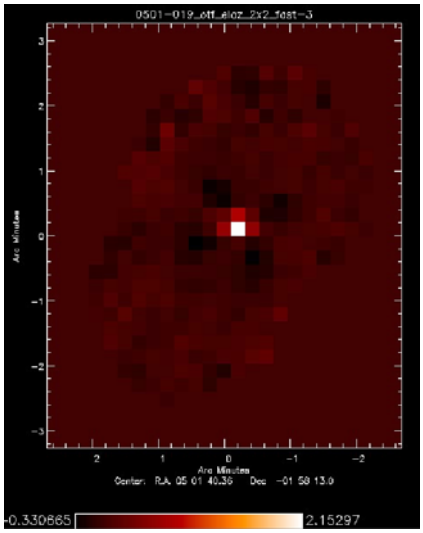

Fig. 10 The ~300 mJy quasar 0501-019 observed with a signal to noise ratio of 70

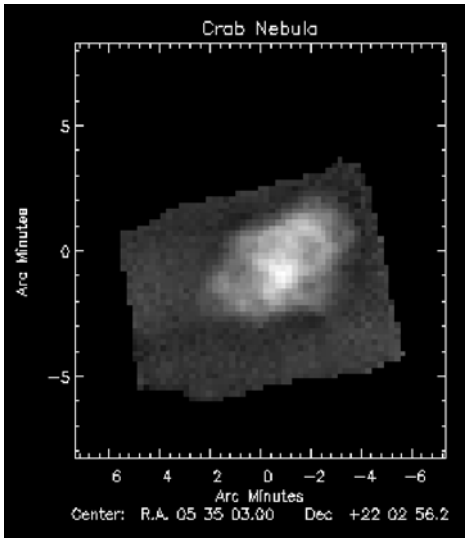

Fig. 11 Reduced map of a 10 minute integration on the Crab Nebula, reduced with our optimal weight method described in the text. The map appears to show more spatial frequencies than the map of Crab seen if Fig. 7, which we reduced with our quick look reduction software where we filtered our data by a 0.5 Hz highpass filter

We will return to the telescope later in 2008 with an improved baffling system and an improved mechanical design of the detector package. We are also building a shutter and illuminator for offset and gain calibration, and expect the introduction of a Lissajous scanning mode. With these enhancements, as well as our continued efforts to optimize our data reduction package, we expect a significantly improved performance of the instrument.

ACKNOWLEDGMENT

This work was supported in part by NSF Grant AST 0705185.

REFERENCES

[1] Baars, J. W. M., Hooghoudt, B. G.; Mezger, P. G.; de Jonge, M. J., 1983, A&A, 1785, 319

[2] de Korte, P.A. J., Beyer, J., Deiker, S., Hilton, G.C., Irwin, K.D., Macintosh, M., Nam, S.W., Reintsema, C.D., Vale, L. R., Huber, M.E., 2003, RScI, 74. 3807

[3] Staguhn, J. G.; Benford, D. J.; Allen, C.A.; Moseley, S. H.; Sharp, E. H.; Ames, T. J.; Brunswig, W.; Chuss, D. T.; Dwek, E.; Maher, S. F.; Marx, C. T.; Miller, T. M.; Navarro, S.; Wollack, E. J., "GISMO: a 2-millimeter bolometer camera for the IRAM 30 m telescope", 2006, SPIE, 6275E, 44S

[4] Allen, C. A., Benford, D. J., Miller, T. M., Moseley, S. H.; Staguhn, J. G.; Wollack, E. J., "Technology developments toward large format long wavelength bolometer arrays", 2007, SPIE, 6678, 4

[5] Staguhn, J.G., Dwek, E., Benford, D. J., Moseley, S.H., Sharp, E.H., "Science Case for a 2 mm Bolometer Camera Optimized for Surveys of Dusty Galaxies in the High Redshift Universe", Il Nuovo Cimento, in press.

[6] Bernstein, G., 2002, PASP, 114, 98

[7] Staguhn, J.G., Benford, D.J., Allen, C.A., Moseley, S.H., Sharp, E.H., Ames, T.J., Brunswig, W., Chuss, D.T., Dwek, E., Maher, S.F., Marx, C.T., Miller, T.M., Navarro, S., Wollack, E.J., "GISMO: a 2-millimeter bolometer camera for the IRAM 30 m telescope", 2006, SPIE, 6275E, 44S

[8] Dicker, S. R., Abrahams, J. A., Ade, P. A. R., Ames, T. J., Benford, D. J., Chen, T. C., Chervenak, J. A., Devlin, M. J., Irwin, K. D., Korngut, P. M., Maher, S., Mason, B. S., Mello, M., Moseley, S. H., Norrod, R. D., Shafer, R. A., Staguhn, J. G., Talley, D. J., Tucker, C., Werner, B. A., White, S. D., "A 90-GHz bolometer array for the Green Bank Telescope", 2006, SPIE, 6275E, 42D

[9] Allen, C. A.; Abrahams, J., Benford, D. J., Chervenak, J. A., Chuss, D. T., Staguhn, J. G., Miller, T. M., Moseley, S. H., Wollack, E. J., "Far infrared through millimeter backshort-under-grid arrays", 2006, SPIE, 6265E, 9A

[10] Staguhn, J.G., Benford, D.J., Chervenak, J.A., Moseley, S.H., Jr., Allen, C.A.; Stevenson, T.R.; Hsieh, W-T., ``Design techniques for improved noise performance of superconducting transition edge sensor bolometers", 2004, SPIE, 5498, 390

[11] Staguhn, J.G, Allen, C.A, Benford, D.J., Chervenak, J.A, Chuss, D.T., Miller, T.M., Moseley, S.H., Wollack, E.J., "Characterization of TES Bolometers used in 2-Dimensional Backshort-Under-Grid (BUG) Arrays for Far-Infrared Astronomy", 2006, Nuclear Instruments and Methods in Physics Research, Section A (NIMPA), 559, 545

[12] Kreysa, E., Gemünd, H.-P., Raccanelli, A., Reichertz, L. A. & Siringo, G., "Bolometer arrays for Mm/Submm astronomy", 2002, AIPC, 616, 262

350 GHz Sideband Separating Receiver for ASTE

Hirofumi Inoue[1,*], Kazuyuki Muraoka[2], Takeshi Sakai[2], Akira Endo[1, 2], Kotaro Kohno[1], Shin'ichiro Asayama[2], Takashi Noguchi[2], and Hideo Ogawa[3]

[1]*Institute of Astronomy, University of Tokyo, Japan*

[2]*National Astronomical Observatory of Japan, Japan*

[3]*Department of Physical Science, Osaka Prefecture University, Japan*

* Contact: h-inoue@ioa.s.u-tokyo.ac.jp, phone +81-422-34-5219

***Abstract*— We have developed a 350 GHz Sideband Separating Receiver for ASTE (Atacama Submillimeter Telescope Experiment) . The RF frequency range is 330-360 GHz and the IF frequency range is 4-8 GHz. The receiver noise temperature was 150 – 200 K (SSB) and the image rejection ratio was typically 10 dB. This receiver was installed on the ASTE telescope in October 2007. The system noise temperature at the atmosphere condition of $\tau_{220} \sim 0.6 – 0.8$ was 200 K (SSB). This is almost half of that of the previous DSB receiver.**

I. Introduction

In the 350 GHz band there are many high-J rotational transition lines of molecules, such as CO(*J*=3-2), CS(*J*=7-6) and HCN(*J*=4-3), which are useful for investigating dense parts of molecular gas.

In the 350 GHz band, double sideband (DSB) receivers have been used conventionally. However DSB receivers have several disadvantages. 1) It is difficult to calibrate the line intensity accurately because it is hard to know the image rejection ratio (IRR) precisely. 2) The Atmospheric noise from the image sideband is added and the system noise temperature increases. 3) If there were a line in the image sideband, signal line will be contaminated by it. Therefore single sideband receivers with a image-sideband rejection mechanism are needed to improve efficiency of the spectral line observations and are being developed at several institutes [1][2].

We have developed a 350 GHz sideband separating receiver CATS345 (Cartridge Type Sideband separating receiver at 345 ghz band) for ASTE (Atacama Submillimeter Telescope Experiment) which is a project to operate a 10-m submillimeter telescope in Atacama desert, northern Chile [3]. In our receiver, image band rejection is accomplished by the waveguide type 2SB mixer as shown in fig. 1 [4].

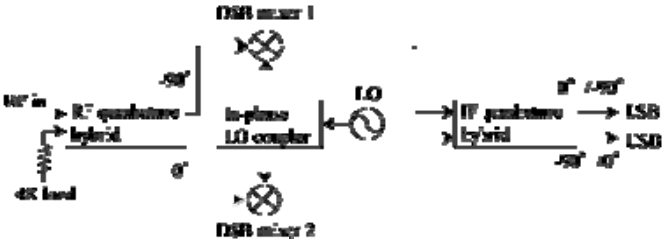

Fig.1 Block diagram of 2SB mixer.

After the evaluation in the laboratory, we installed our receiver on the ASTE telescope in October 2007. The system noise temperature, opacity and Allan variance were measured.

II. Instruments

The receiver is installed on the Cassegrain focus of the telescope. It is a 3-stage (4 K, 12 K, 50 K) cartridge type receiver (fig. 2, 3) .The RF signal (330-360 GHz) from the subreflector goes through a Kapton window and an IR filter and is reflected twice by a plane mirror and an ellipsoidal mirror. Then it is coupled with the 2SB mixer by the feed horn (fig. 4) .

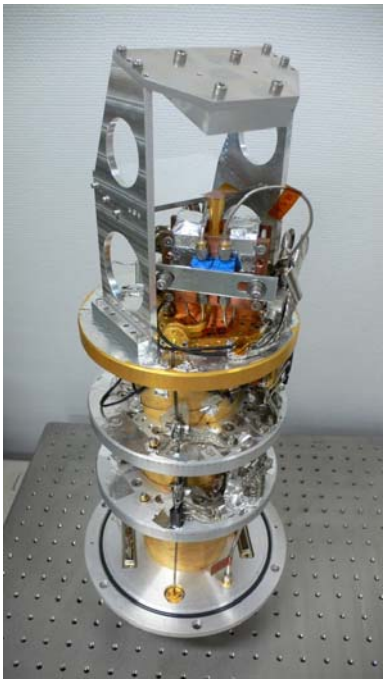

Fig.2 Whole image of CATS345. The height is about 400 mm. The diameter of the cartridge is 170 mm.

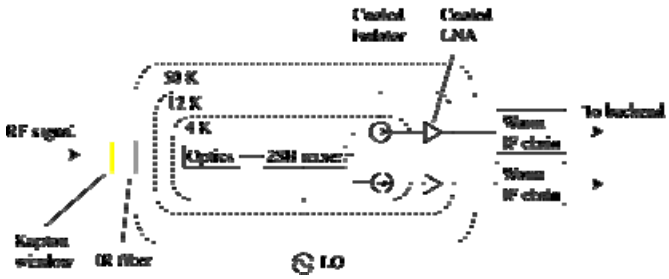

Fig.3 Block diagram of CATS345

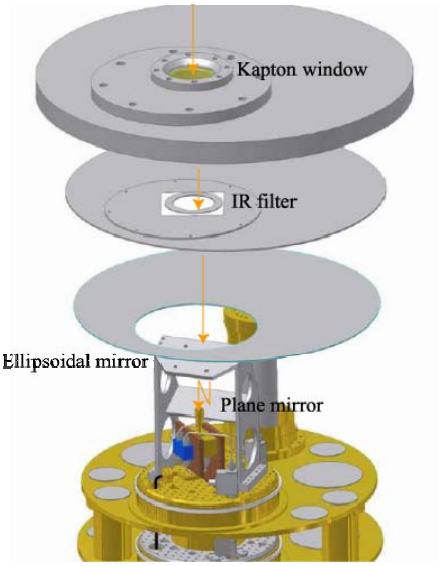

Fig.4 Optics. The diameter of the top shield is 460 mm.

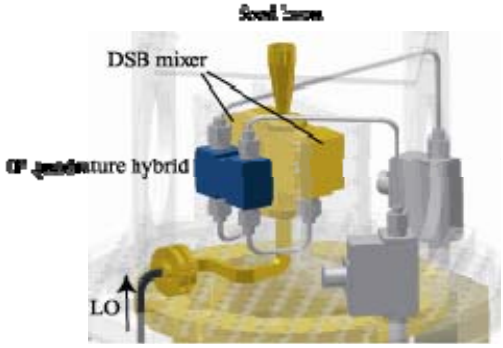

Fig.5 2SB mixer on 4 K stage. The size of the IF quadrature hybrid is 20 mm×40 mm×10 mm.

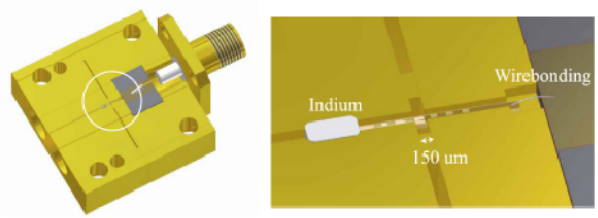

Fig.6 Mixer block and DSB mixer

The 2SB mixer mixes the RF signal with the LO signal and down-converts to the IF frequency (4-8 GHz). It consists of a RF quadrature hybrid, two DSB mixers and an IF quadrature hybrid. Our RF quadrature hybrid is a scale model of [4]. The DSB mixer is designed by S. C. Shi. The LO signal is generated by the synthesizer and multiplied 24 times. After the 2SB mixer, the signal is amplified by the IF chain, which is composed of cooled isolators, cooled amplifiers, isolators, room-temperature amplifiers and bandpass filters, and is sent to the backend.

TABLE I
SPECIFICATION OF CATS345

Observation frequency	330 – 360 GHz
Intermediate frequency	4 – 8 GHz
Pixel	1
Polarization	1
Receiver noise temperature	150 – 200 K
Image rejection ratio	10 dB

III. EVALUATION IN THE LABORATORY

It is required for a sideband separating mixer that there is neither amplitude nor phase imbalance in the 2SB mixer. So, first we investigated the imbalance of the RF quadrature hybrid, the DSB mixers and the IF quadrature hybrid.

The role of the RF quadrature hybrid is to divide the input signal equally and to add a 90 degree phase difference between the two output signals. The amplitude imbalance of the RF quadrature hybrid was measured by inputting power from the RF port and measuring the power from the output port. The other two ports were terminated with absorbers (fig. 7). The input signal is produced by the synthesizer and a 24

times multiplier. The result was that the amplitude imbalance was within 1 dB.

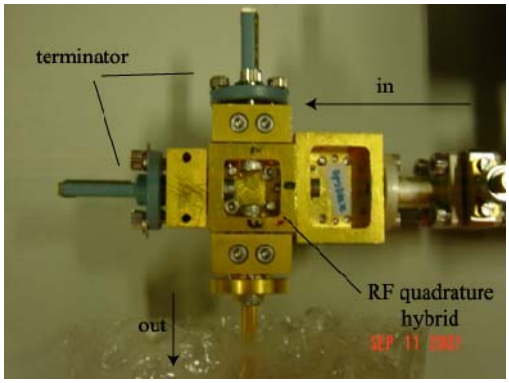

Fig.7 Measurement of imbalance of RF quadrature hybrid. The right port is RF port, the left port is LO port and the upper and lower ports are IF output ports to DSB mixers. The size of the RF quadrature hybrid is 20 mm×20 mm×20 mm.

The role of the DSB mixer is to down-convert the RF frequency to the IF frequency. Its performance is dependent on its IV curve [5]. So, first we measured IV curves of 350 DSB mixers and selected 2 mixers which satisfy J_c~4 kA cm^2 and a quality factor ($R_{2\ mV}/R_{4\ mV}$) > 20 and resembles each other (fig.8) .Then, their DSB receiver noise temperatures of those were measured and it was confirmed that their frequency dependence resembles each other.

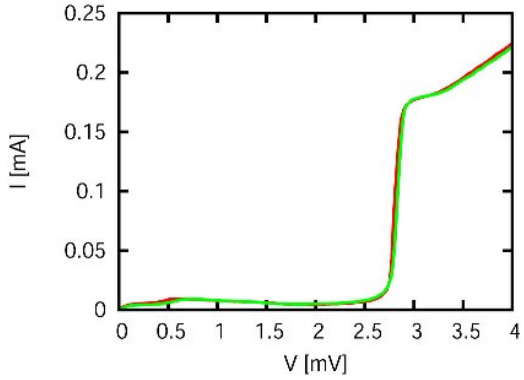

Fig. 8. IV curves of DSB mixers.

The role of the IF quadrature is to divide the input signal equally and to put a 90 degree phase difference between the two output signals like the RF quadrature hybrid. Its S parameters were measured with a network analyser. It was measured that its amplitude imbalance was within 1 dB and the phase imbalance was within 5 degree.

The total imbalance of the 2SB mixer is summarized in table II. In the ideal case that 2 DSB mixers are completely balanced, the total amplitude imbalance is about 2 dB and the phase imbalance is 5 degree. So according to [6], the expected image rejection ratio is 15 ~ 20 dB.

TABLE II
IMBALANCE OF 2SB MIXER

	Amplitude	Phase
RF quadrature hybrid	1 dB	?
DSB mixer	variable	?
IF quadrature hybrid	1 dB	5 degree
total	~ 2 dB	~ 5 degree

These components were assembled to the 2SB receiver. The receiver noise temperature was about 150-200 K (SSB) across the band (fig. 9).

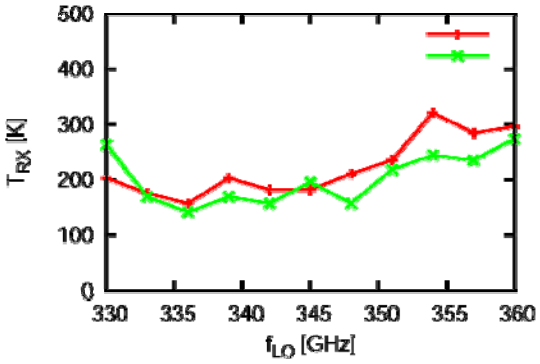

Fig.9. The receiver noise temperature of the 2SB receiver. The red plots are USB and the green plots are LSB.

The image rejection ratio was measured by the method of [7] and was typically 10 dB across the band (fig. 10).

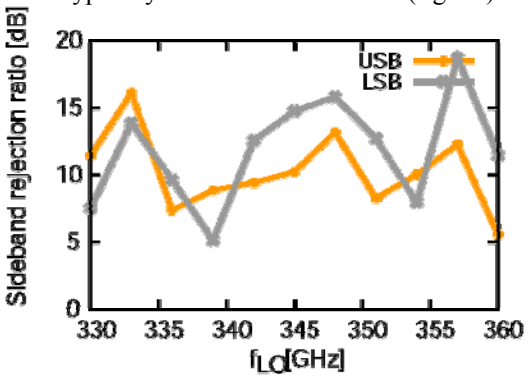

Fig.10. The image rejection ratio of the 2SB receiver.

IV. EVALUATION AT THE ASTE SITE

Our receiver was installed on the ASTE telescope in October 2007. At that time a new backend with a total bandwidth of 8 GHz was also installed [8].

Figure 12 shows the system noise temperature, receiver noise temperature and the opacity measured by the R-sky method and the secZ method. At that time the opacity at 220 GHz was about 0.06 ~ 0.08. The system noise temperature was about 300 K (SSB). This is almost half of that of the previous DSB receiver [9], which means that the integration time needed decreases to 1/4. The receiver noise temperature was about 150 ~ 200 K and was consistent with the performance in the laboratory. The opacity at 345 GHz was

about 0.2 ~ 0.3 and this was almost the same as one predicted by the atmosphere model, $\tau_{345}=0.05+2.5\times\tau_{225}$ [10].

To know the stability of the receiver, the Allan variance at the outputs of the receiver was measured with a power meter. The Allan time was about 10 sec (fig. 11).

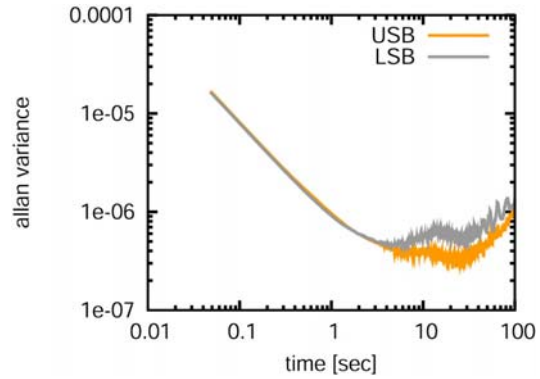

Fig.11. Allan variance

V. Test Observation

IRC10216, a Carbon rich late type star, was observed with the new 8 GHz backend. At this observation the opacity at 220 GHz was 0.06 – 0.08, which was typical atmospheric condition of ASTE site in winter. Figure 13 shows the spectrum of IRC10216 and was obtained within a few minutes observation. The image rejection ratio was measured to be over 10 dB in these frequencies.

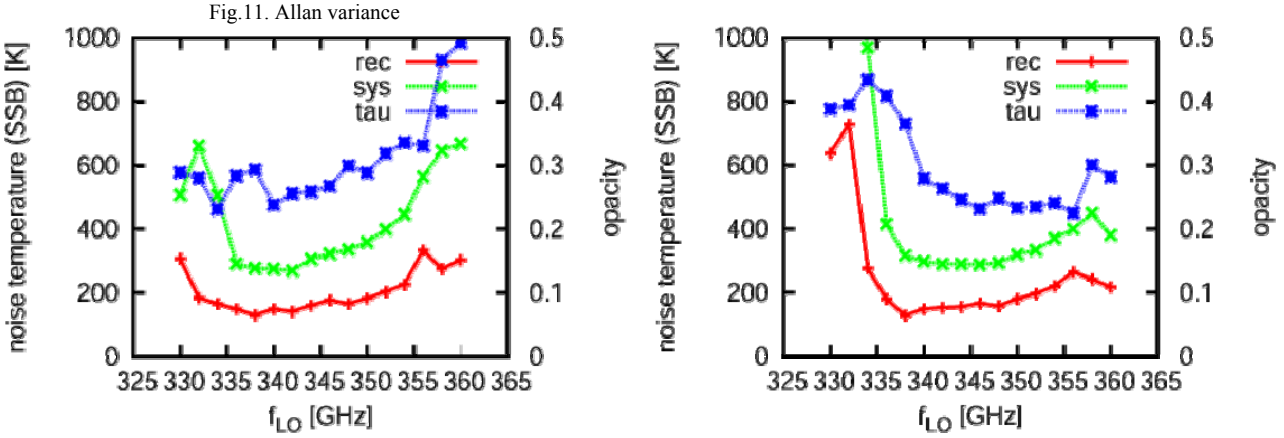

Fig. 12. The system noise temperature (green), the receiver noise temperature (red) and opacity (blue) at the atmospheric condition of $\tau_{220}=0.06 – 0.08$. The left plots are USB and the right plot s LSB.

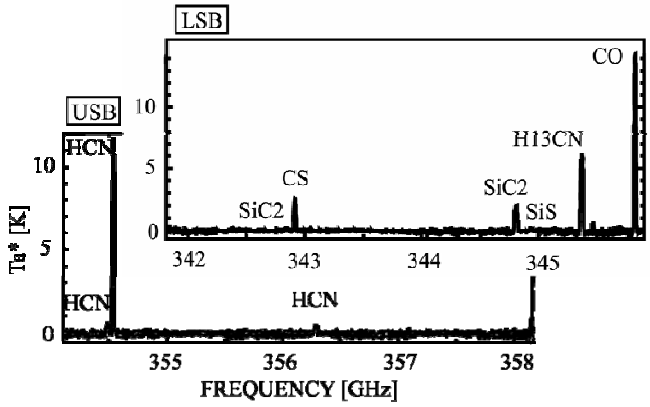

Fig. 13.Spectrum of IRC10216

CONCLUSIONS

We have developed a waveguide type sideband separating SIS receiver at 350 GHz band for ASTE. After the evaluation in the laboratory, it was installed on the ASTE telescope together with a new backend with a 4 GHz bandwidth in October 2007. The system noise temperature was typically 200 K (SSB), which is half of that of the receiver previously installed on ASTE. So the integration time needed to achieve a certain sensitivity decreases to 1/4. The image rejection ratio was measured with the lines from astronomical objects and was over 10 dB.

ACKNOWLEDGMENT

We are grateful to the ASTE team and ALMA Band 4 group for supporting our research. This study was financially supported by the MEXT Grant-in-Aid for Scientific Research on Priority Areas No. ~15071202.

REFERENCES

[1] C. Risacher, R. Monje, V. Vassilev, A. Pavolotsky, and V. Belitsky,, "A Sideband Separation SIS Mixer For 275-370 GHz for the APEX telescope", 2006, Proc. of SPIE, 6275, 62751T

[2] S. Claude, "Sideband-Separating SIS Mixer for ALMA Band 7, 275-370 GHz", 2003, Int Space Terahertz Conf

[3] H. Ezawa, R. Kawabe, K. Kohno, S. and Yamamoto, "The Atacama Submillimeter Telescope Experiment (ASTE)", 2004, Proc. of the SPIE, 5489, 763

[4] S. Asayama, H. Ogawa, T. Noguchi, K. Suzuki, H. Andoh, and A. Mizuno, "An Integrated Sideband-separating SIS Mixer Based on Waveguide Split Block For 100 GHz Band with 4.0-8.0 GHz IF", 2004, Int. J. Infrared Millimeter Waves, 25, 569

[5] J. R. Tucker, and M. J. Feldman, "Quantum detection at millimeter wavelengths", 1985, Rev. Mod. Phys. 57, 1055

[6] S. M. X. Claude and C. T. Cunningham, "Design of a Sideband-Separating Balanced SIS Mixer Based on Waveguide Hybrids", 2000, ALMA MEMO 316

[7] A. R. Kerr, S. K. Pan, and J. E. Effland, "Sideband Calibration of Millimeter-Wave Receivers", 2001, ALMA MEMO 357

[8] S. Iguchi, and T. Okuda, 2007, in press

[9] K. Muraoka, K. Kohno, T. Toasaki, N. Kuno, K. Nakanishi, K. Sorai, T. Okuda, S. Sakamoto, A. Endo, B. Hatsukade, K. Kamegai, K. Tanaka, J. Cortes, H. Ezawa, N. Yamaguchi, T. Sakai, and R. Kawabe, "ASTE CO (3-2) Observations of the Barred Spiral Galaxy M 83: I. Correlation between CO (3-2)/CO (1-0) Ratios and Star Formation Efficiensies", 2007, PASJ, 59, 43

[10] C. R. Masson, "Atmospheric Effects and Calibrations", 1994, in ASP Conf., 59, 87

[11] Proc. SPIE, Vol.4015, pp.86-95, 2000.

Development of a Waveguide-Type Dual-Polarization Sideband-Separating SIS Receiver System in 100 GHz Band for the NRO 45-m Telescope

Taku Nakajima[1,*], Takeshi Sakai[2], Shin'ichiro Asayama[2], Kimihiro Kimura[1], Masayuki Kawamura[1], Yoshinori Yonekura[1], Hideo Ogawa[1], Nario Kuno[2], Takashi Noguchi[2], Masato Tsuboi[3], and Ryohei Kawabe[2]

[1]*Osaka Prefecture University, Japan*
[2]*National Astronomical Observatory of Japan, Japan*
[3]*Japan Aerospace Exploration Agency, Japan*
* Contact: s_tac@p.s.osakafu-u.ac.jp, phone +81-72-254-9727

***Abstract*— We developed a waveguide-type dual-polarization sideband-separating SIS receiver system of the 100-GHz band for the 45-m radio telescope at the Nobeyama Radio Observatory, Japan. This receiver is composed of an ortho-mode transducer and two sideband-separating SIS mixers, which are both based on the waveguide technique. The receiver has four intermediate frequency (IF) bands of 4.0--8.0 GHz. Over the radio frequency range of 80--120 GHz, the single-sideband receiver noise temperatures are 50--100 K and the image rejection ratios are greater than 10 dB. The new receiver system was installed in the telescope, and we successfully observed the ^{12}CO, ^{13}CO, C^{18}O and the other emission lines simultaneously toward the Sagittarius B2 region to confirm the performance of the receiver system.**

I. INTRODUCTION

The 45-m telescope (Fig.1) is located at Nobeyama Radio Observatory (NRO) in Nagano, Japan and is one of the largest millimeter-wave telescopes in the world (e.g., [1], [2]). The 45-m telescope is equipped with low-noise high electron mobility transistor (HEMT) and superconductor-insulator-superconductor (SIS) receivers covering the observing frequency range of 20 to 115 GHz, along with powerful spectral-line and continuum back-ends.

The 100-GHz band SIS receivers are the most important receivers for the 45-m telescope, because they cover the highest frequency range among the heterodyne SIS receivers installed in the telescope. From a scientific viewpoint, the J = 1--0 emission line of carbon monoxide (CO) in this frequency band is a principal probe for studies of interstellar molecular gas. The SIS-80 (hearafter, S80) and SIS-100 (hearafter, S100) single-beam receivers, which cover radio frequency (RF) bands of 72--115 GHz and 77--115 GHz respectively, are installed in the 45-m telescope. However, as the receiver noise temperature decreases throughout the world (e.g., [3]-[5]), the performances of S80 and S100 have relatively worsened since their installation. Moreover, the most important cause of a high noise temperature is that these receivers use a wire grid for the separation of polarizations and a Martin-Puplett interferometer as an image rejection filter for the separation of sidebands. The loss with the quasi-optics results in a degradation of the system noise temperature. These quasi-optics are too sensitive for their optical alignment, and thus misalignment becomes another cause of degradation. The single side-band (SSB) receiver noise temperatures, including the quasi-optics are 150--300 K for both receivers. To solve these problems, we began the development of a new receiver system, which uses a waveguide-type ortho-mode transducer (OMT) and two sideband-separating (2SB) SIS mixers. To date, the simultaneous detection of molecular emission lines with a

Fig.1 Photograph of the 45-m telescope at NRO.

waveguide-type 2SB receiver has been performed by a few groups toward a limited number of observations (e.g., [6], [7]), suggesting that the 2SB receiver systems are more efficient compared to the other SSB receivers (e.g., [8]). As a result, we can reduce the number of the optical elements and the composition becomes simple. In addition, it is also noteworthy that through the simultaneous detection of two polarizations and two sidebands using a single optical horn, we can better determine the line-intensity ratios of among molecular lines without being contaminated by errors in pointing.

We developed a new 2SB receiver system in the 100-GHz band for the 45-m telescope. Over the RF range of 80--120 GHz, the SSB receiver noise temperature of the mixer is obtained to be lower than 100 K for the 4.0--8.0 GHz intermediate frequency (IF) band. The image rejection ratios (IRRs) are greater than 10 dB over the same range. It is confirmed that the typical SSB receiver noise temperature of the new system is approximately half that of the previous systems of S80 and S100. The IF bandwidth of the new receiver system is 4 GHz for each IF output, while those of previous receivers are 600 MHz. We can detect 16 GHz in total. Using the newly developed 100-GHz band SIS receiver system for 45-m telescope, we observed the ^{12}CO, ^{13}CO, C^{18}O and the other emission lines simultaneously toward the Sagittarius B2 region in order to confirm the performance of the receiver system. This is the first astronomical observation using a waveguide-type dual-polarization sideband-separating SIS receiver system in the 100-GHz band [9].

II. Receiver

A. Receiver configuration

The specifications of the receiver system are summarized in table 1 and a block diagram of the receiver system is shown in Fig.2. The operation frequency range is from 72 to 128 GHz, which is limited by the frequency range of the local oscillator (LO) chain. The IF frequency range of 4.0--8.0 GHz with the bandwidth of 4.0 GHz is adopted. This receiver is composed of an OMT and two 2SB mixers, which are both based on a waveguide technique. The 2SB mixers are hereafter referred to as mixer-A and mixer-B. The photograph of the receiver in the dewar is shown in Fig.3.

By using an OMT, it is possible to receive signals in the dual linear polarizations independently and simultaneously. The OMT adopted herein was developed at the Australia Telescope National Facility (ATNF), Commonwealth Scientific and Industrial Research Organization (CSIRO), and consists of a square to double ridged guide transition followed by a junction of two side arms with the central guide [10]. The measurement of the OMT performance by ATNF has revealed a return loss of > 20 dB from 71 to 118 GHz and an insertion loss at room temperature of < 0.16 dB for both polarizations.

The detailed structure of a split-block waveguide unit for our 2SB mixer is described in [11]. The basic design of the present sideband-separating SIS mixer is similar to that described in [12]. The split-block waveguide unit contains an

Fig.2 Block diagram of the dual-polarization sideband-separating receiver

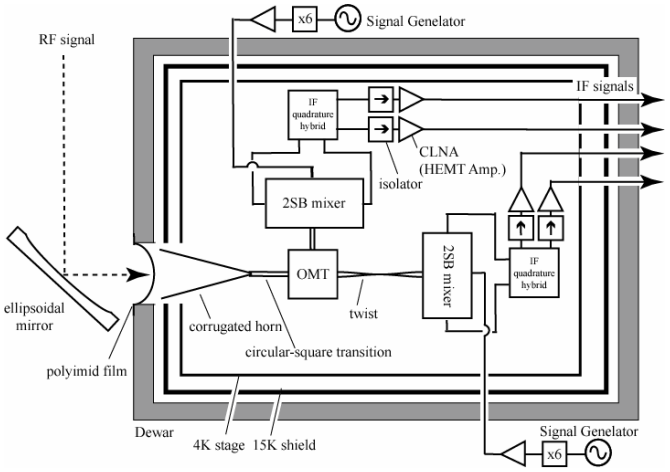

system. Two orthogonal polarizations of the RF signal into a single horn are separated by an OMT, and two sidebands of each polarization are separated by two 2SB mixers. Thus, we can obtain four IF signals independently and simultaneously.

RF quadrature hybrid, two LO directional couplers, an LO power divider, and 4 K cold image terminations. We also integrated two double side-band (DSB) mixers on the single split-block waveguide unit through the waveguide taper transformers. The RF and LO signals are fed to the feed point through a linearly tapered waveguide impedance transformer, which uses a full height to 1/5 reduced height waveguide for the waveguide-to-stripline transition of the SIS mixer. The linearly tapered waveguide impedance transformer was designed using a lumped-gap-source port provided by HFSS^{TM} [11]. The SIS junctions adopted herein were developed at the NRO. A six-series array was composed of Nb/AlO$_x$/Nb junctions with a normal state resistance of approximately 80--90 Ω, and each junction area was

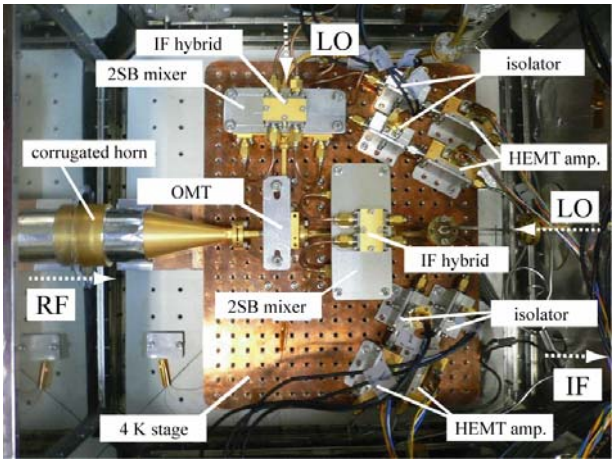

Fig.3 Photograph of the 4 K cooled stage in the receiver dewar. The RF signal is fed into the OMT located in the middle of the figure from the lower side using a detachable corrugated horn. The LO signals are fed from the upper side for the 2SB mixer located above the OMT and from the left side for the other 2SB mixer

TABLE I

SPECIFICATIONS OF THE RECEIVER SYSTEM

Tuning range	72--128 GHz
Mixer type	SIS ($Nb/AlO_x/Nb$) six-series junction mounted on fixed-tuned waveguide-type 2SB mixer block
Receiving mode	SSB (2SB) operation
Polarization	dual linear polarization
Receiver noise temperature (DSB)	~ 50 K (f_{LO} = 80--115 GHz)
mixer-A	
Receiver noise temperature (SSB)	less than or similar 100 K (f_{RF} = 75--120 GHz) ~ 68 K (minimum value at f_{RF} = 90 GHz in the USB) LSB : 86.8 K (average value at f_{RF} = 75--106 GHz) USB : 88.2 K (average value at f_{RF} = 79--120 GHz)
Image rejection ratio	> 10 dB (f_{RF} = 80--123 GHz) LSB : 14.9 dB (average value at f_{RF} = 80--111 GHz) USB : 14.3 dB (average value at f_{RF} = 84--123 GHz)
mixer-B	
Receiver noise temperature (SSB)	less than or similar 100 K (f_{RF} = 75--120 GHz) ~ 49 K (minimum value at f_{RF} = 95 GHz in the LSB) LSB : 74.5 K (average value at f_{RF} = 75--106 GHz) USB : 72.7 K (average value at f_{RF} = 79--120 GHz)
Image rejection ratio	> 10 dB (f_{RF} = 80--100 GHz) LSB : 13.4 dB (average value at f_{RF} = 80--100 GHz) USB : 12.2 dB (average value at f_{RF} = 84--110 GHz)
IF frequency band	4.0--8.0 GHz (4.0 GHz bandwidth)
IF amplifier	cooled low noise HEMT amplifier (typical noise temperature of 8 K and gain of + 30 dB)

1.9 x 1.9 μm^2. The reason for using the series junction is that a wider bandwidth of RF frequency can be achieved. In the present system, the required fractional bandwidth totals greater than or similar 40 %. The parallel connected twin junction (PCTJ) designed by [4] is not suited for this receiver because the designed RF frequency range is 90--115 GHz, which corresponds to a fractional bandwidth of only approximately 25 %. Moreover, the series junction barely saturates and the intensity can be calibrated with high accuracy [13]. The IF signals from the two DSB mixers are combined in a commercial quadrature hybrid, which made by Nihon Tsushinki Inc.

B. Receiver performance

Before installing the receiver system in the telescope, we evaluated its performance. The noise temperature of the 2SB SIS receiver was measured by a standard Y-factor method using hot (300 K) and cold (77 K) loads in the laboratory. The mixer was mounted on a 4 K cold stage in a dewar. The first-stage IF amplifier is a 4 K cooled HEMT at the 4.0--8.0 GHz band. The equivalent noise temperature and the gain of the HEMT amplifier associated with an isolator were approximately 8 K and +30 dB, respectively. The following-stage amplifiers work at room temperature.

The measured DSB receiver noise temperatures of the SIS mixers with 4.0--8.0 GHz IF by a power meter are approximately 50 K over the LO frequency range of 80--115 GHz. The SSB receiver noise temperature, including the noise contribution from the vacuum window, the feed horn, and the IF amplifier chain, were measured by a spectrum analyzer. For a certain LO frequency, the output spectra were smoothed to a resolution of 500 MHz and sampled at eight IF frequency points from 4.25 GHz to 7.75 GHz at intervals of

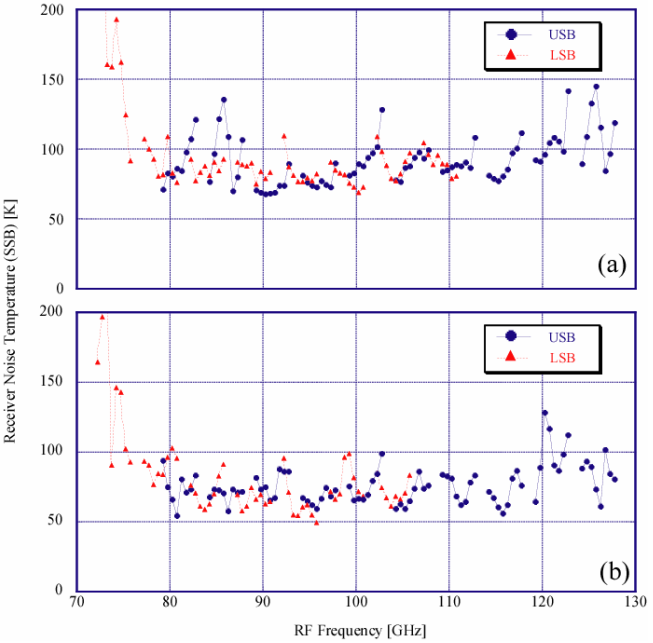

Fig.4 SSB receiver noise temperatures in the LSB and USB of (a) mixer-A and (b) mixer-B. These values are measured by 4.0--8.0 GHz IF and are shown as a function of RF frequency (see text).

0.5 GHz. We then swept the LO frequency from 80 GHz to 120 GHz by a step of 5 GHz to cover the RF frequency range from 72.25--127.75 GHz. Finally, the measured SSB receiver noise temperatures were corrected for the IRR, in order to obtain the SSB receiver noise temperature. Since the IRRs were measured with the different measurement system from the one used to measure the noise temperature, we assumed the IRRs to be 10 dB, that is nearly equal to the smallest value among the actual IRRs, for all the measured points. Therefore, it is to be noted that the actual SSB receiver noise temperature will be better than the values presented in this paper for most of the measured points. The SSB receiver noise temperatures were measured to be lower than approximately 100 K over the RF range of 75--120 GHz, and the minimum value of ~ 68 K for mixer-A in the upper side-band (USB) and ~ 49 K for mixer-B in the lower side-band (LSB) are achieved at approximately 90 GHz and 95 GHz, respectively. The mean value and standard deviation between the RF frequency range of 75--106 GHz in the LSB and 79--120 GHz in the USB are 87 ± 11 K and 88 ± 15 K, respectively, for mixer-A (Fig.4 (a)) and are 75 ± 14 K and 73 ± 10 K, respectively, for mixer-B (Fig.4 (b)).

The IRRs were evaluated by measuring the relative amplitudes of the IF responses in the USB and LSB when injecting a continuous wave signal [14] from a signal generator. The IRR measured in the IF range of 4.0--8.0 GHz IF was greater than 10 dB over the RF frequency range of 80--123 GHz for mixer-A (Fig.5 (a)). The mean value between the RF frequency range of 80--111 GHz in the LSB and 84--123 GHz in the USB were as high as 15 dB and 14 dB, respectively. The IRR of mixer-B was lower than 10 dB at f_{LO} greater than or similar 105 GHz (Fig.5 (b)). However, both the mean value between the RF frequency range of 80--100 GHz in the LSB and that between the RF frequency range of 84--110 GHz in the USB were about 12 dB.

Therefore, it is most desirable to use mixer-B for observation at lower RF frequency. We will replace by new one if we developed mixers with the better performance.

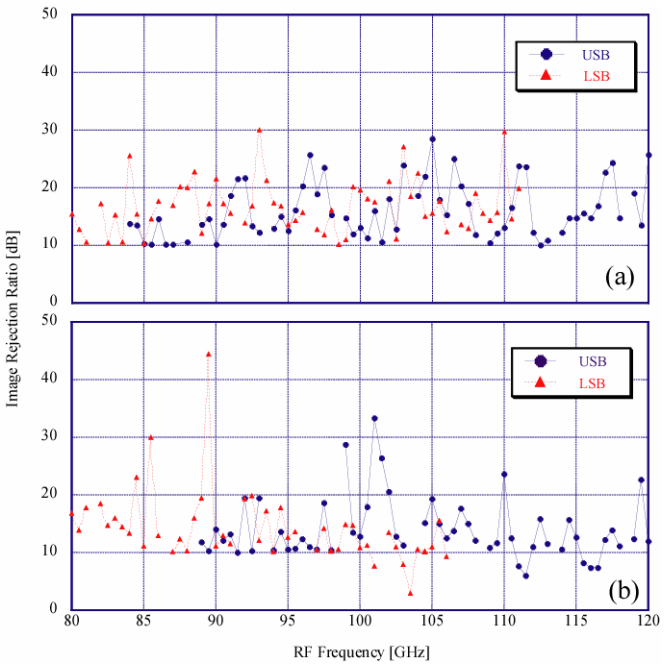

Fig.5 Image rejection ratio in the LSB and USB of (a) mixer-A and (b) mixer-B. These values are measured by 4.0-8.0 GHz IF and are shown as a function of RF frequency.

III. Results

The receiver system was installed in the 45-m telescope in early December 2007. Fig.6 shows the receiver dewar in the receiver cabin. The SIS and HEMT amplifier biases, LO oscillators, and IF chains are placed around the dewar. The LO signals for each 2SB mixer of dual-polarization are independently generated by multiplying the output of the signal generators (~ 12--20 GHz) with 2 x 3 multipliers. Therefore, the four IF signals from two 2SB mixers can cover different regions of the RF frequency band. Hereafter, the polarization for mixer-A is referred to as pol-1, and the polarization for mixer-B is referred to as pol-2.

A. System noise temperature

The performance of the receiver may change when it is installed in the telescope because the environment of the receiver is different from that in the laboratory. Therefore, we installed the receiver system in the telescope and measured

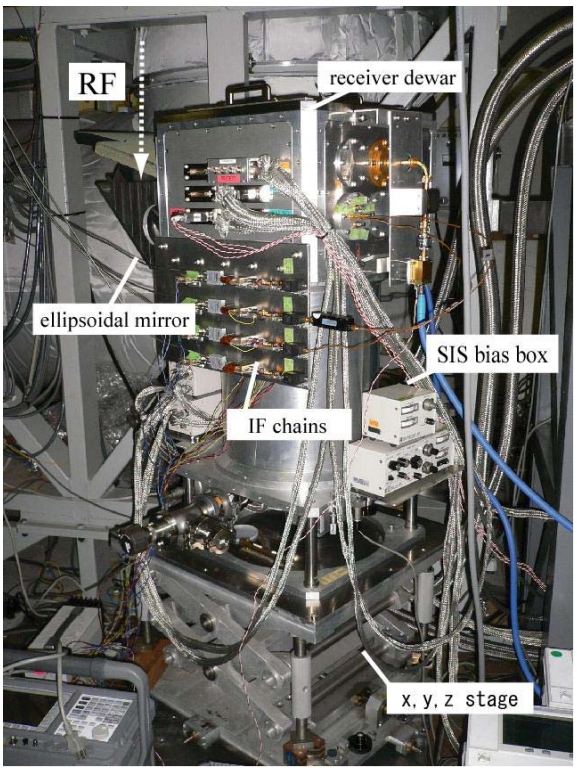

Fig.6 Photograph of the receiver system in the receiver cabin of the telescope.

the performance of the receiver system. Note that the noise temperatures in this subsection are not corrected for IRR. Even after correcting for IRR, the noise temperature increases only less than or similar 10 %. The SSB receiver noise temperature, including the ellipsoidal mirror before the horn, is measured by a standard Y-factor method to be

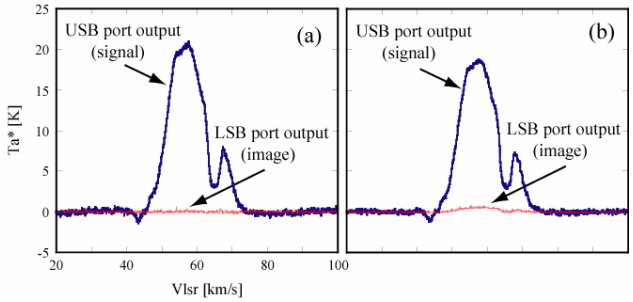

Fig.7 IF signal outputs of the USB and LSB ports obtained by observations toward W51. The signal of the ^{12}CO (J = 1--0) line in the USB port (bold line) leaks to the LSB port (thin line). The output of the 2SB mixer for pol-1 is shown in (a), and that for pol-2 is shown in (b). Note that the absorption at V_{lsr} ~ 45 km s^{-1} may be caused by the emission in the OFF position.

approximately 60 K in the USB at f_{LO} = 109 GHz (f_{RF} = 115 GHz) for both 2SB mixers. The SSB noise temperatures of the system, including the atmosphere, are approximately 180 K in the LSB at f_{LO} = 109 GHz (f_{RF} = 103 GHz) for pol-1 and at f_{LO} = 104 GHz (f_{RF} = 98 GHz) for pol-2 at an elevation of 80°. The system noise temperature, including the atmosphere, became approximately half of that of the previous receiver system (S100).

B. Test observations

The first astronomical signal after the installation, ^{12}CO spectra at 115.271 GHz from the W51 giant molecular cloud, was obtained on December 11, 2007. The IRRs of the two 2SB mixers were estimated from these spectra, resulting in > 20 dB for pol-1 (Fig.7 (a)) and > 14 dB for pol-2 (Fig.7 (b)), respectively. These values are as good as those obtained in the laboratory. Moreover, we successfully observed the molecular lines toward the Sagittarius B2 region by using six digital spectrometers [15] with bandwidths of 512 MHz. Fig.8 shows an example of the results, which are obtained by a single pointing. We detected CH_3C_2H and H_2CS in the LSB and ^{12}CO in the USB, respectively, for pol-1, and CS in the LSB and SO_2, C^{18}O, HNCO, ^{13}CO and CH_3CN in the USB,

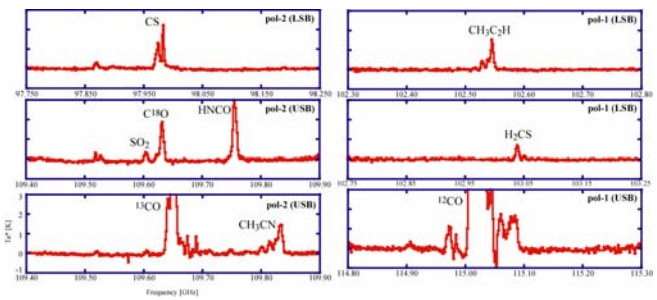

Fig.8 Results of the line survey toward Sgr B2. The four IF signals were obtained independently and simultaneously by a single pointing.

first astronomical observation using the waveguide-type dual-polarization sideband-separating SIS receiver system in the 100 GHz band.

respectively, for pol-2. Since four IF signals can be observed independently and simultaneously, we obtained these spectra by integrating the signal only for five minutes. This was the

CONCLUSIONS

A waveguide-type dual-polarization sideband-separating SIS receiver system in the 100 GHz band was developed for and installed in the NRO 45-m telescope. This receiver system is composed of an ortho-mode transducer and two sideband-separating SIS mixers, both of which are based on the waveguide type. The four IF bands, 4.0--8.0 GHz, in each of the polarizations and sidebands can be observed simultaneously and separately. Over the RF frequency range of 80--120 GHz, the single-sideband receiver noise temperatures are 50--100 K and the image rejection ratios are greater than 10 dB. The new receiver system was installed in the 45-m telescope, and we successfully observed the ^{12}CO, ^{13}CO, C^{18}O and the other emission lines simultaneously toward the Sagittarius B2 region. This is the first astronomical observation using a waveguide-type dual-polarization 2SB SIS receiver system in the 100 GHz band. The SSB noise temperatures of the system, including the atmosphere, are approximately 180 K in the LSB at f_{LO} = 109 GHz (f_{RF} = 103 GHz) for one polarization, and at f_{LO} = 104 GHz (f_{RF} = 98 GHz) for the other polarization at an elevation of 80°. The SSB system noise temperature became approximately half of that of the previous receiver system. The IRRs of the two 2SB mixers were calculated from the ^{12}CO (J = 1--0) spectra at 115.271 GHz in the USB from the W51 giant molecular cloud, resulting in > 20 dB for one polarization and > 14 dB for the other polarization.

ACKNOWLEDGMENT

The authors would like to thank Takafumi Kojima and Yasuhiro Abe for their contributions to this project. We are also grateful to Chieko Miyazawa, Akira Mori, and the entire staff of the Nobeyama Radio Observatory for their useful discussions and support.

REFERENCES

[1] M. Morimoto, "The 45-meter Telescope," NRO Report, 6, 1981.
[2] K. Akabane, IJIMW, Vol.4, pp.793-808, 1983.
[3] S. C. Shi, et al., IEEE Trans., Applied Superconductivity, Vol.7, pp.3850-3857, 1997.
[4] S. Asayama, et al. IJIMW, Vol.25, pp.107-117, 2004.
[5] C. Chin, et al., IJIMW, Vol.25, pp.569-600, 2004.
[6] S. Asayama, et al., "Preliminary Tests of Waveguide Type Sideband-Separating SIS Mixer for Astronomical Observation," ALMA Memo, 481, 2003.
[7] F. Lauria, et al., "First Astronomical Observations with an ALMA Band 6 (211-275 GHz) Sideband-Separating SIS Mixer-Preamp," ALMA Memo, 553, 2006.
[8] T. Nakajima, et al. PASJ, Vol.59, pp.1005-1016, 2007.
[9] T. Nakajima, et al. PASJ, Vol.60, pp.435-443, 2008.
[10] Moorey, et al., "A 77 – 117 GHZ CRYOGENICALLY COOLED RECEIVER FOR RADIOASTRONOMY," in the Sixth Workshop on Applications of Radio Science Conference, 2006.

[11] S. Asayama, et al., IJIMW, Vol.24, pp.1091-1099, 2003.
[12] S. M. X. Claude, et al., "Design of a Sideband-Separating Balanced SIS Mixer Based on Waveguide Hybrids," ALMA Memo, 316, 2000.
[13] R. Kerr, "Saturation by Noise and CW Signals in SIS Mixers," ALMA memo, 401, 2002.
[14] R. Kerr, et al., "Sideband Calibration of Millimeter-Wave Receivers," ALMA memo, 357, 2001.
[15] K Sorai, et al., Proc. SPIE, Vol.4015, pp.86-95, 2000

A modular 16-pixel terahertz imager system applying superconducting microbolometers and room temperature read-out electronics

M. Leivo[1], P. Helistö[1], A. Luukanen[2], J.S. Penttilä[3], T. Perälä[1],
A. Rautiainen[1], H. Toivanen[1], C.R. Dietlein[4], and E.N. Grossman[4]

[1] *VTT, Sensors, Espoo, Finland*
[2] *Millimeter-wave Laboratory of Finland, Espoo, Finland*
[3] *Aivon Oy, Espoo, Finland*
[4] *National Institute of Standards and Technology, Optoelectronics Division, Boulder, CO, USA*

Superconducting bolometers have long been used as the "work horse" technology for terahertz astrophysics. In this paper we describe a system developed for stand-off imaging of concealed weapons and explosives. The system utilizes an array of NbN antenna-coupled vacuum-bridge microbolometers as detectors. The detectors are modular, with 8 pixels incorporated within a single module. The modules are mounted onto the 2nd cooling stage of a commercial cryogen-free pulse tube refrigerator with a base temperature of ca. 4 K. The readout of the sensors is carried out with an innovative room-temperature feedback preamplifier that can achieve bolometer noise limited performance when operated at the "inflexion point" of the voltage-biased bolometer.

In the paper we will describe the overall architecture of the modular system, describe the electrical and optical performance characteristics of the system, and show passive imagery of test objects acquired in the 200 GHz to 1 THz band. The system is a precursor for a video-rate imaging THz camera, which will be briefly discussed.

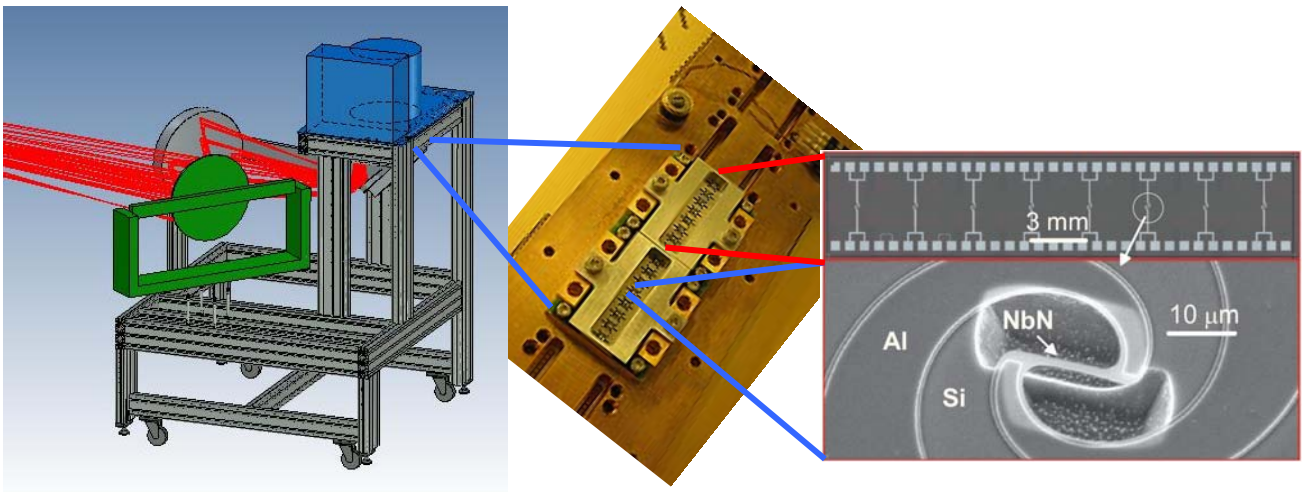

Fig. 1. Left) Overall setup of a 16-pixel THz imager system. Center) Two bolometer modules attached to pulse tube cold finger. Right) Micrograph of an antenna-coupled vacuum-bridge microbolometer array.

A novel heterodyne interferometer for millimetre and sub-millimetre astronomy

Paul K. Grimes[1,*], Matthew Brock[1], Christian M. Holler[1], Karl Jacobs[2], Michael E. Jones[1], Oliver G. King[1], Jamie Leech[1], Angela C. Taylor[1] and Ghassan Yassin[1]

[1]*Astrophysics, Dept. of Physics, University of Oxford, Denys Wilkinson Building, Keble Road, Oxford, OX1 3RH, UK.*

[2]*KOSMA, I Physikalisches Institut, Universität zu Köln, Zülpicher Straße 77, 50937, Köln, Germany*

• Contact: P.Grimes1@physics.ox.ac.uk, phone +44 1865 273304

•

Abstract— We describe a novel heterodyne interferometer currently under construction at Oxford. The instrument employs new techniques in heterodyne interferometry, with the aim of achieving very high brightness sensitivity in the millimetre band. It is a single-baseline tracking interferometer for operation in the frequency range 185-275 GHz with two 0.4m offset parabolic antennas separated by a 0.5 m baseline. Each antenna feeds an SIS mixer with a 2-20 GHz IF band, driven by a phase-switched LO source. The IF signals from the mixers are processed by a 2-20 GHz analogue complex correlator.

The primary science goal of this instrument is to measure the spectrum of the Sunyaev-Zel'dovich effect in galaxy clusters. In particular we intend to measure the frequency of the S-Z null near 217 GHz, which allows the gas temperature of the cluster to be determined. Measuring the spectrum of the S-Z effect requires very high brightness sensitivity with moderate spatial and spectral resolution.

I. Introduction

Cosmic microwave background astronomy requires extremely high brightness sensitivity and very good control of systematic and instrumental effects. The use of heterodyne interferometry techniques allows a number of instrumental effects to be removed, and also removes the instrumental sensitivity to total power fluctuations, suppressing the effect of atmospheric noise fluctuations. The use of heterodyne receivers also allows each receiver to be phase switched individually with the local oscillator, so that individually modulated redundant baselines can be used to eliminate instrumental effects. Achieving high brightness sensitivity in interferometry requires that the instantaneous bandwidth of each baseline be as wide as possible, and that the array be as filled as is practical within the limits of antenna shadowing.

Interferometry has been widely used in cosmology instruments at centimetre wavelengths, particularly for observations of the primary temperature anisotropy and *E*-mode polarisation of the cosmic microwave background e.g. CBI, DASI, VSA, and in observations of secondary anisotropies such as the Sunyaev-Zel'dovich effect, e.g. AMI, CBI-2, SZA.

Although measurements of the CMB and S-Z effect at millimetre wavelengths are extremely useful, the limitations of the low instantaneous (IF) bandwidth of SIS mixers and backend systems, and the poor noise performance of other mm-wave coherent detectors are responsible for the absence of successful CMB instruments using heterodyne interferometry in the high millimetre-wave band. Recent advances in SIS mixer design and wideband correlator technology make it feasible to build a mm-wave heterodyne interferometer capable of carrying out novel CMB observations.

We are currently designing and building a single-baseline 220 GHz tracking heterodyne interferometer for high brightness sensitivity interferometry for cosmology. This instrument, GUBBINS (220-**G**Hz **U**ltra-**B**road**B**and **IN**terferometer for **S**-Z) will use two small antennas on a short baseline with ultra-wide IF bandwidth SIS mixers developed in collaboration with Cologne University [1] and an ultra-wideband analogue correlator developed in collaboration with the University of Maryland. After extensive laboratory testing the instrument will be deployed for test astronomical observations at the Chajnantor Observatory, Chile, adjacent to ALMA. Although the instrument will make useful scientific measurements, it will also be used for the development of new technologies for mm-wave interferometry.

The technology developed for this instrument will also have applications in other areas astronomy, particularly in the design of very wide IF bandwidth SIS receiver arrays, and in high dynamic range interferometry.

The design goals of this instrument are somewhat different to current mm-wave interferometers, in that we want to achieve maximum sensitivity to extended continuum sources with only moderate spatial and spectral resolution, but with very good control of systematics. This instrument will also be a prototype for a future S-Z spectral imaging instrument that will follow-up the very large numbers of galaxy clusters being discovered by current S-Z survey instruments.

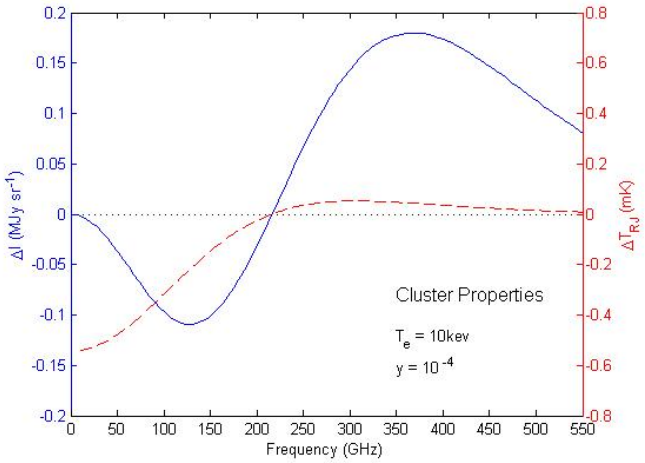

Fig.1 Spectrum of the S-Z effect in intensity (solid line, left scale) and surface brightness (dashed line, right scale) for a large cluster of galaxies. The CMB is distorted by scattering from the hot gas in a galaxy cluster. The spectral distortion due to the thermal S-Z effect has a characteristic null frequency at 217 + (0.45 T/keV) GHz.

II. Cluster science with GUBBINS

The Sunyaev-Zel'dovich effect is the distortion of the spectrum of the CMB due to inverse-Compton scattering off the hot gas in clusters of galaxies. This tends to boost the energy of the CMB photons, leading to a decrease in the CMB brightness below a frequency of about 220 GHz, and an increase above this frequency. One of the key features of the S-Z effect is that its surface brightness is independent of the distance to the cluster, although the angular size does of course vary. This means that S-Z measurements can be used to study galaxy clusters over a very wide range of redshifts.

The exact null frequency varies with the temperature of the cluster gas (thermal S-Z effect) and the peculiar velocity of the cluster (kinematic S-Z effect). The shift in the null frequency due to the thermal S-Z effect is approximated by 217 + 0.45T GHz where T is the cluster gas temperature in keV (a typical rich cluster has a gas temperature in the range 5-15 keV). Hence by measuring the SZ spectrum and finding the null frequency we can measure the cluster temperature without the need for X-ray spectral measurements.

GUBBINS will be able to detect a the brightest galaxy clusters in the sky in one night's observing per cluster, and will be able to constrain the null frequency of the S-Z effect to ± 1 GHz with several nights observing. In conjunction with low frequency S-Z data e.g. from CBI-2 (26-36 GHz), we should be able to measure the cluster gas temperature to within a few keV.

These measurements are scientifically interesting and will also serve to demonstrate the application of high brightness sensitivity heterodyne interferometry at millimetre wavelengths to cosmology.

Table 9
Overview of expected performance for GUBBINS Phase I

Frequency	185-275 GHz
Antenna aperture	0.4 m
Baseline	0.5-0.6 m
Primary beam (220 GHz)	11.4' FWHM
Resolution (220 GHz)	7.5'-11.4' FWHM
IF band	3-13 GHz
Instantaneous bandwidth	2x 10 GHz
Correlator channels	16
Correlator bandwidth	2-20 GHz
Channel bandwidth	1.125 GHz
Target system temperature	50 K
Brightness sensitivity per channel	1.5 mK/√s
Total brightness sensitivity	350 μK/√s

III. Instrument design

The specifications of the GUBBINS instrument are given in Table 9. These figures are for the initial GUBBINS design, but future upgrades are planned, in particular to increase the IF bandwidth to the full 2-20 GHz range.

The prime design targets are for a single 0.5m baseline (dictated by the angular size of the brightest S-Z clusters) with the maximum achievable filling factor; a target system temperature of 50 K; a total instantaneous bandwidth of at least 10 GHz in each sideband divided into at least 8 spectral channels and an LO tuneable by at least 20 GHz either side of the S-Z null frequency for a cold galaxy cluster at 217 GHz.

A diagram of the GUBBINS system is given in Fig 2 and a CAD model of the complete instrument in Fig 3. Both SIS receivers are mounted in a single cryostat at the centre of the instrument. This, in conjunction with the need for the maximum array filling factor and the desire to avoid any obstructions in the optical system led us to the folded offset prime focus optical design.

The designs of the various instrument subsystems are described in the rest of this section.

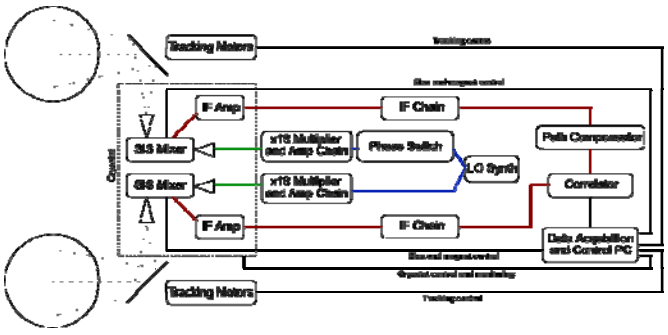

Fig.2. System diagram for the GUBBINS instrument. Data and DC signals are shown as black lines, LO signals as blue (low frequency, coaxial cables) and green (mm-wave, quasioptical) lines and IF signals as red lines. The optics and sky signal are on the left of the diagram.

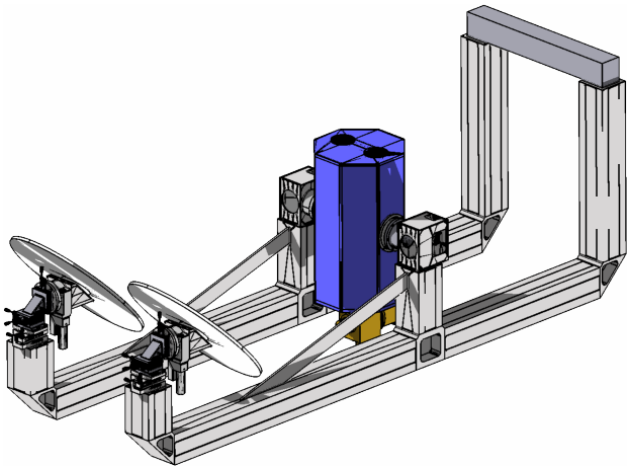

Fig.3. CAD model of the GUBBINS telescope. The telescope is supported off the cryostat body between the two optics arms. The arms are extended beyond the cryostat body and joined by a counterweight so that both arms can be driven by a single motor.

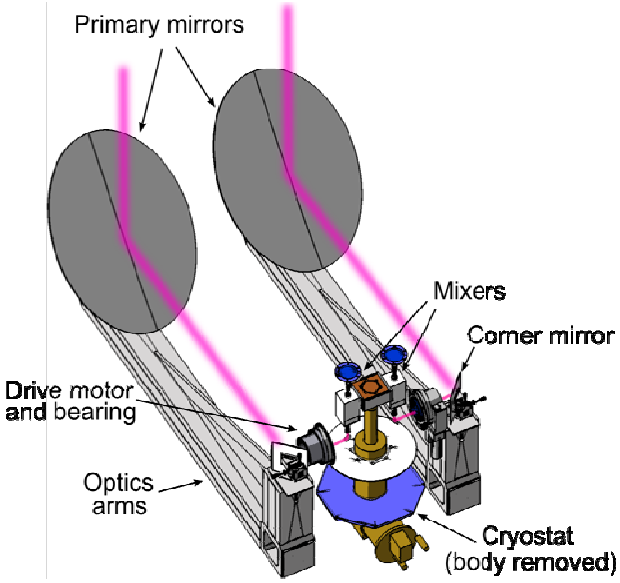

Fig.4. CAD model of the two GUBBINS optical assemblies, with the cryostat body and radiation shields and the corner mirror boxes removed, and the beams from the sky shown in pink. The optics are fed by a corrugated horn reflector (see Fig.). The beam from the horn reflector is folded through 90° by a convex (focal length -120 mm) corner mirror before going to the primary. The primary mirror is a 45° offset paraboloid with its axis perpendicular to that of the corner mirror and a focal length of 1020 mm.

A. Optics design

The optical design of each telescope employs the maximum primary mirror size that can be accommodated on a 0.5m baseline without shadowing. When both antennas are scanned to 45° from the zenith this gives a primary mirror projected aperture of ~0.4m. The optical layout is shown in Fig 4 and Fig. 6. Each telescope is fed by corrugated horn-reflector antenna with a 7° FWHM beam at 220 GHz. The primary mirror is a 45° offset paraboloid with a focal length of 1020 mm. GRASP simulations of the telescope beam are shown in Fig 5 illustrating good beam circularity and cross-polarization.

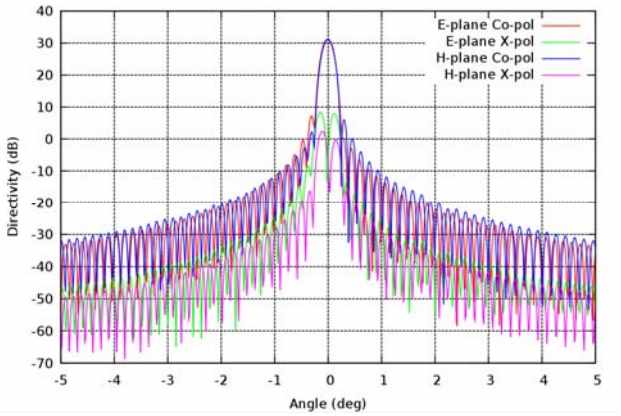

Fig.5. GRASP simulated beam of the GUBBINS telescope optics.

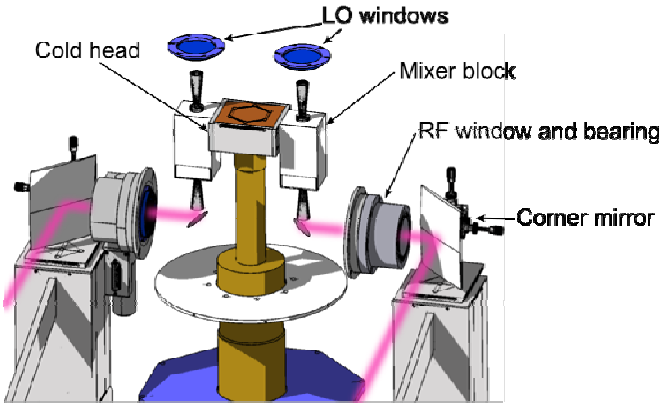

Fig.6. Layout of cryostat and corner mirror optics (Cryostat body and radiation shield removed). The beams from the sky are shown in pink. The beams from the primary mirrors are folded by the corner mirrors (extreme left and right), before passing through the motor and bearings and cryostat windows to the corrugated horn reflector antennas. LO signals are fed to the mixer blocks through windows on the top of cryostat to horns on the top of the mixer blocks. The mixer blocks are mounted on brackets to the side of the 4 K stage of the G-M cooler (gold).

In order to allow the necessary degrees of freedom in the optics so that the telescopes can be pointed in elevation and azimuth, the telescopes are folded by a 45° offset corner mirror between the primary mirror and feed. The corner mirror is a convex paraboloid (focal length -120 mm) to reduce the length of the telescopes, at the expense of introducing slight aberrations when the telescopes are pointed far from the zenith.

B. Telescope mount and cryogenics

The two arms supporting the telescopes are mounted on two ring bearings fixed around the cryostat windows, and are connected by a counterweight at the rear end of the arms (see Fig. 3). The telescopes are pointed in elevation by a single harmonic drive motor mounted to one of the ring bearings, while the telescopes are tracked across the sky by rotating the primary mirrors about the optical axis between the primary and secondary mirrors.. This allows both antennas to be pointed individually in azimuth, while keeping the number of drive components to a minimum.

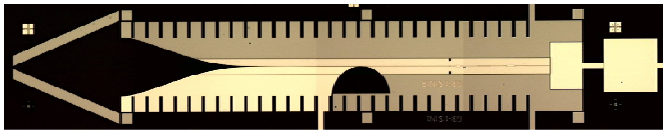

Fig.7. Ultra-wide IF band finline SIS mixer chip described in [1], and fabricated at Cologne University by Paul Grimes and Karl Jacobs.

The whole instrument is supported on a pillar attached to the base of the cryostat and to a concrete plinth on the ground. The instrument can be mounted on the plinth in a number of orientations, allowing the projected baseline to be orientated in a number of directions.

Since the cryostat is also a structural element of the instrument mount, it is being custom designed and built by Oxford Physics. The cryostat is cooled by a two stage Gifford-McMahon cooler from Sumitomo Heavy Industries. It provides 1 W of cooling power to the 4 K stage, where the SIS mixers and first stage IF amplifiers are mounted, and 40 W to a 40 K stage where the electrical connections are heat sunk, and the second stage IF amplifiers are mounted.

C. SIS mixers and cryogenic IF amplifiers

Initially GUBBINS will use single-ended ultra-wide IF band finline mixers (Fig. 7) described elsewhere in these proceedings [1], in conjunction with a waveguide directional coupler in a split mixer block for coupling LO to the mixer.

These ultra-wide IF band mixers are based on an earlier 230 GHz finline mixer design [2], with a number of additions and improvements for ultra-wide IF band operation. An RF band-pass filter is used between the finline taper and the mixer tuning circuit to prevent the IF signal from leaking into the finline. The mixer tuning circuit and RF choke use relatively narrow microstrip lines to keep reactances in the IF band low, and a 5-stage microstrip transformer is used to match the 16.5 Ω SIS junction(s) to the 50 Ω input of the IF amplifiers over the 2-20 GHz IF band.

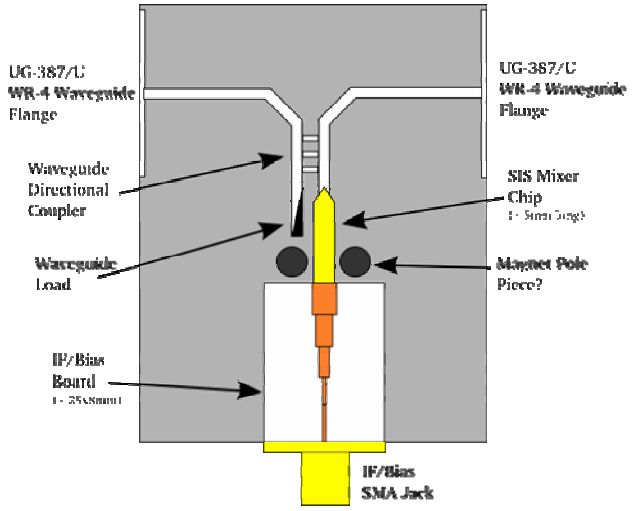

Fig.8. Layout of the split mixer block for the single-ended finline SIS mixer for GUBBINS. Not to scale.

Using similar design techniques to those used in [4], we are developing both balanced and sideband-separating single chip mixers in this frequency range, based on our back-to-back finline architecture, and incorporating the ultra-wide IF band technology. Once these mixer chips have been developed, GUBBINS will be the first instrument to demonstrate the use of these mixers in astronomical observations.

The split mixer block (Fig. 8) contains a -17 dB directional coupler used to combine the LO signal with the astronomical signal, a termination load to dump the uncoupled LO power and the mounting position for the SIS mixer chip. The mixer block also holds the IF transformer board used to transform the 16.5 Ω output of the mixer to the 50 Ω input impedance of the IF amplifier and the SMA IF/DC bias connector. A superconducting electromagnet is mounted to the block to provide the magnetic field required to suppress Josephson tunnelling in the mixer, with magnet pole pieces used to concentrate the field at the mixer chip.

The astronomical and LO signals are coupled into the mixer block via corrugated horns mounted to waveguide flanges on opposite sides of the mixer block.

The IF outputs from the mixer blocks are connected to commercial bias tees before being amplified by the first stage IF amplifiers. These amplifiers are 3-13 GHz LNAs supplied by Sander Weinreb at Caltech. They have excellent measured performance at 20 K over 10 GHz bandwidth, which should be slightly improved on further cooling to 4 K.

The biggest potential improvement in the system performance will be achieved by the use of wider band cryogenic IF amplifiers, capable of using the full 2-20 GHz bandwidth of the backend IF system. We are currently investigating a number of potential sources for these amplifiers.

D. LO system

We require two frequency-locked and 180° phase-switched LO signals to be coupled into the two SIS receivers via corrugated horns mounted on each of the mixer blocks. These horns are coupled quasi-optically through two windows on the top of the cryostat and then via two Gaussian beam telescopes to the LO source(s).

We currently have a single 195-260 GHz multiplied LO source from Radiometer Physics GmbH, and are investigating ways of generating the two required phase switched LO signals. The simplest LO solution is to purchase a second multiplied LO source and to drive both of these source with phase switched signals from a single microwave synthesized source. Since the LO source uses a x18 multiplier we have developed a 10 differential phase shift circuit which can be used with the microwave signal source used to drive the LO.

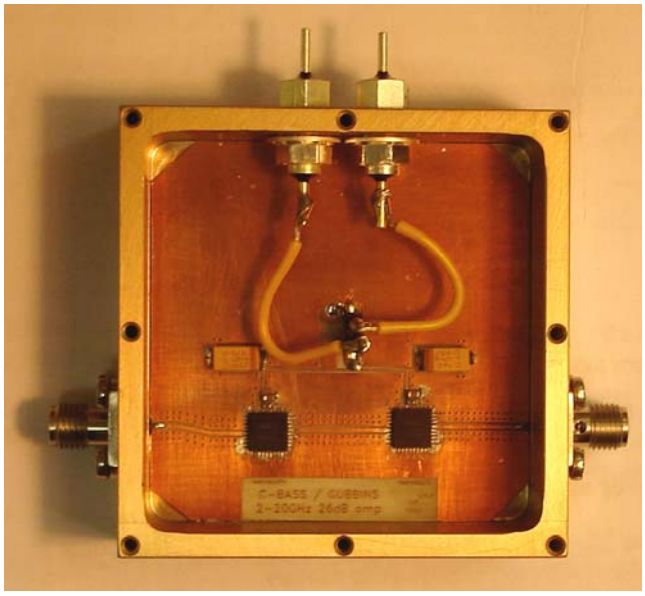

Fig.9. GUBBINS 2-20 GHz second stage IF amplifier, using two cascaded surface mount packaged amplifiers.

We will also investigate 180° phase switching the SIS receivers by switching the bias voltage of the SIS mixers from the positive to negative side of I-V curve. Since SIS mixers have antisymmetric I-V characteristics, switching the direction of the bias voltage changes the sign of the down-converted signal.

We are also working in collaboration with the Millimetre Technology Group at Rutherford Appleton Laboratories who are developing phase-locked photonic LO sources for use in SIS receivers [5]. These have the potential to greatly simplify the LO injection scheme of GUBBINS by providing individual LO sources for the SIS mixers directly coupled to mixer blocks inside the cryostat, via fibre optics feed-throughs in the cryostat walls.

We have already demonstrated that our mixer can be pumped by a RAL photonic LO system coupled quasioptically via the cryostat window.

E. IF chain

The IF signals from the cryogenic LNAs are then further amplified and individually processed before entering the correlator. The latter stages of IF amplification are provided by a number of gain blocks, each of which uses two Hittite HMC462LP5 2-20 GHz 13 dB cascadable amplifiers in surface mount packages (Fig. 9). These gain blocks show excellent performance for a relatively low cost device (~$70 per amplifier chip), with a noise figure of 2.5 dB at room temperature, which is significantly improved on cooling the gain block to 77 K. To ensure that the noise figure of the first of these gain blocks has minimal effect on the overall system noise, the first gain block will be mounted on the 40 K stage of the cryostat.

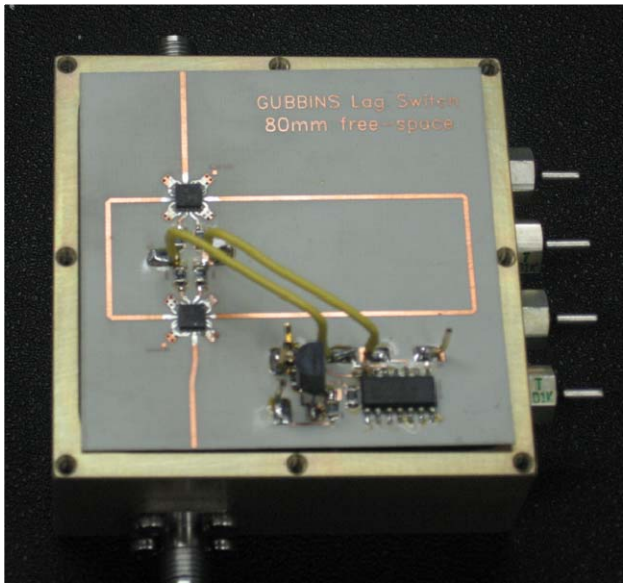

Fig.10. GUBBINS 80mm path compensator bit. This component provides a switchable path delay to compensate for the difference in path length created by tracking the antennas.

As well as being amplified, the IF signals are also band-pass filtered and have slope compensation applied across the IF band. The final step before correlation is to apply path compensation to the signal to remove the path delay introduced by scanning the two antennas of the telescope. The path compensator is made up of five lag switches (Fig. 10), providing 10, 20, 40, 80 and 160 mm of path compensation, and made up of differential lengths of microstrip line switched by Hittite HMC547 0-20 GHz FET switches supplied in surface mount packages.

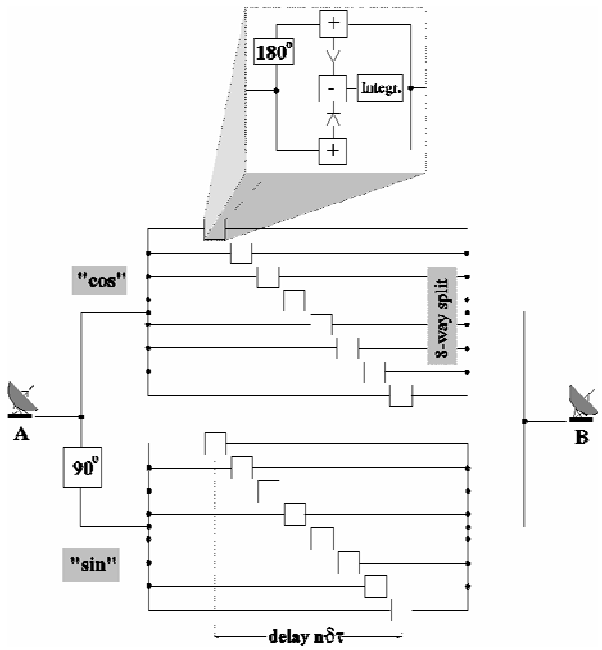

Fig.11. Diagram of a 16 lag complex Fourier transform correlator. In the GUBBINS correlator the 180° phase shifter and two diode detectors in each lag are replaced by a Gilbert Cell multiplier MMIC chip.

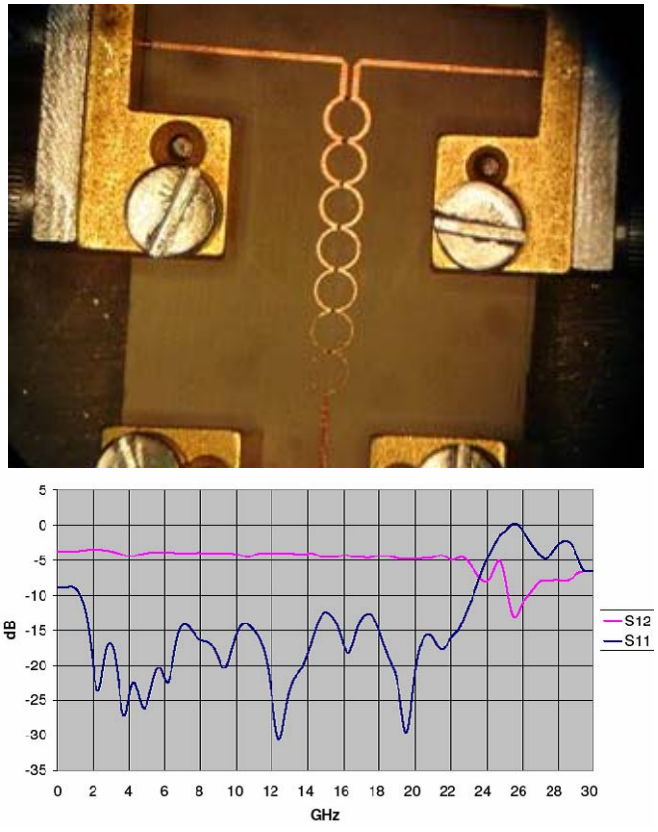

Fig.12. Photo (top) and measured performance (bottom) for the Wilkinson power splitter developed for the GUBBINS correlator. The splitter shows good transmission (S12) from 0 to 23 GHz and good return loss (S11) from 2-23 GHz.

F. Correlator and data acquisition

The IF signals from the two antennas are combined in an analogue correlator developed at Oxford in collaboration with Andrew Harris at University of Maryland. The correlator is a complex Fourier transform lag correlator with 16 channels, with the full 2-20 GHz bandwidth being processed simultaneously, rather than being split into sub-bands. The architecture of the correlator is shown in Fig. 11.

The IF signal from one antenna is split in a commercial quadrature hybrid, with other split in phase using a Wilkinson power divider, before being fed to two 8 lag correlator boards. The two signals on each board are then split eight ways using Wilkinson power divider trees before they are combined and detected by Gilbert Cell multiplier MMIC chips.

The Wilkinson power dividers are a seven-stage design fabricated on Rogers 6010LM with an Ohmega Ply 50 Ω/□ resistive sheet under the copper (Fig. 12). The microstrip lines are etched first, with the resistive elements defined in a second etching step. These dividers show excellent performance from 1.5-23 GHz.

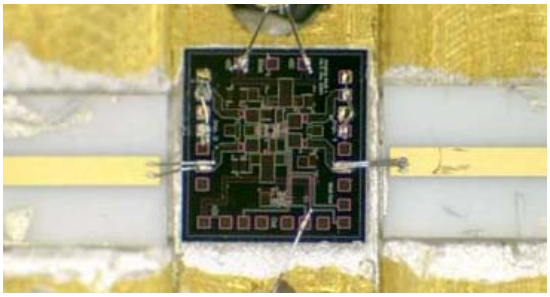

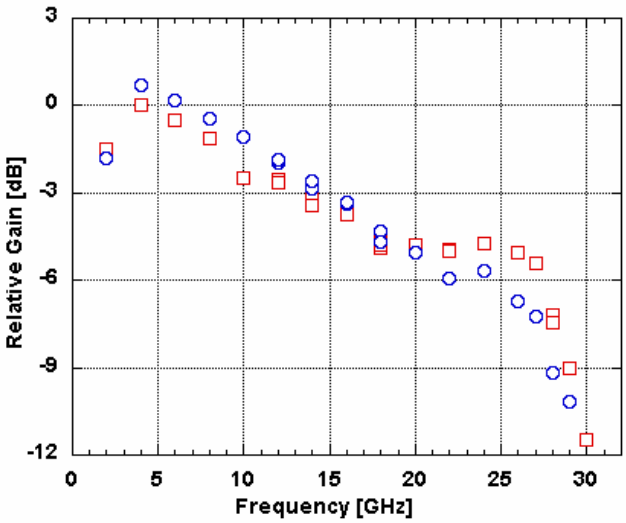

Fig.13. Photo (top) and measured performance (bottom) of the Gilbert Cell multiplier chip developed by Andrew Harris at University of Maryland and Steve Maas at Nonlinear Technologies Inc[3]. The multipliers show good performance from 3-27 GHz.

The Gilbert Cell multiplier MMICs are used to both combine the two IF signals and to detect the combined signal. These devices (Fig. 13) were developed by Andrew Harris at University of Maryland and Steve Maas at Nonlinear Technologies Inc. [3]. These devices provide both the sum and difference measurements of the combined signals, each replacing two power splitters, a 180° phase shift and two detector diodes in a conventional diode detector correlator.

The multiplier chips are read by low noise amplifiers and an A-to-D conversion board developed by the Oxford Central Electronics Group. This board uses 2.8 MSps ADCs from Linear Technology feeding a Vertex FPGA processor and provides a USB output to the data acquisition computer. The readout boards and individual correlator components are now fully tested, and the first 4 lag correlator board (Fig. 14) is currently under construction at Oxford.

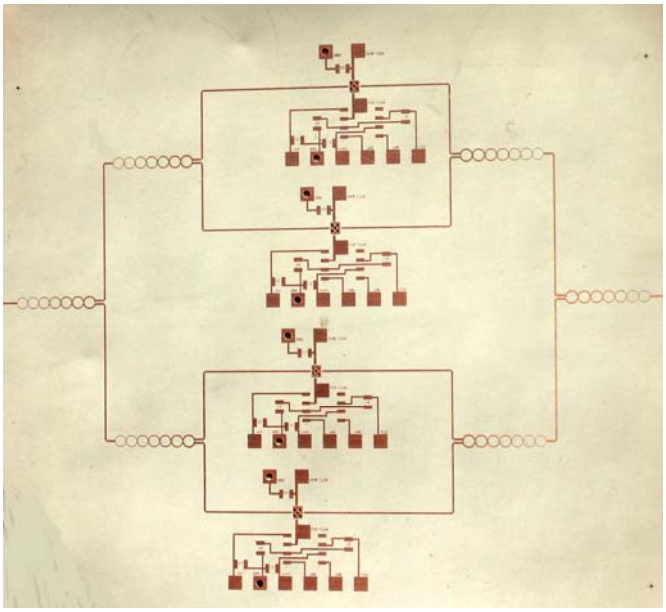

Fig.14. Unpopulated prototype correlator board. This board has four lag steps and will be used for initial testing of the correlator design.

CONCLUSIONS

We are designing and building a single-baseline mm-wave heterodyne interferometer with exceptional brightness sensitivity. This instrument will accommodate many of the new technologies we are currently developing, particularly ultra-wide IF band SIS mixers, ultra-wide band analogue correlators and phase switched photonic LO sources.

There is a niche for a future mm-wave interferometer with exceptional brightness sensitivity and wide field of view, complementary to ALMA and large mm-wave single dish telescopes, with key science goals of following up on the large numbers of S-Z clusters detected by current surveys, and for wide field imaging of faint extended continuum sources over wide frequency ranges. GUBBINS is intended to be an initial proving ground for the technology required for such an instrument.

ACKNOWLEDGEMENTS

We are grateful to the Royal Society for funding the construction of this instrument under the Paul Instrument Fund scheme.

REFERENCES

[1] P.K. Grimes, G. Yassin and K. Jacobs, "Design of finline SIS mixers with ultra-wide IF bands", in *Proc. 19th Int. Symp. Space THz Tech.*, P3-3, 2008.

[2] G. Yassin, R. Padman, S. Withington and K. Jacobs, "A broad band antipodal finline mixer for astronomical imaging arrays", *Electron. Lett.*, vol. 33, pp 498-500, 1997.

[3] A. Harris, "Gilbert Cell Multiplier Measurements III: Response from 2-30 GHz", University of Maryland Internal Technical Report, 2002. More complete information on these multipliers is currently available from http://www.astro.umd.edu/~harris/spectrom.html

[4] P.K. Grimes, G. Yassin and S. Withington, "A 700 GHz single chip balanced SIS mixer", in *Proc. 16th Int. Symp. Space THz Tech.*, 2005.

[5] A.L. Fontana, Y. Bortolotti, B. Lazareff, A. Navarrini, P.G. Huggard and B.N. Ellison, "Cryogenic photonic local oscillator for 2 mm band SIS heterodyne astronomical receiver array", *Electron. Lett.*, **43**, 20, 2007.

A 600 GHz Imaging Radar for Contraband Detection

Goutam Chattopadhyay*, Ken B. Cooper, Robert Dengler, Tomas E. Bryllert, Erich Schlecht, Anders Skalare, Imran Mehdi, and Peter H. Siegel

Jet Propulsion Laboratory, California Institute of Technology, Pasadena, CA 91109, USA

* Contact: goutam@jpl.nasa.gov, phone +1-818-393-7779

***Abstract* — We have developed and demonstrated 3D imaging for contraband detection using a submillimeter-wave frequency modulated continuous wave (FMCW) radar with a fast microwave chirp and phase coherent detection. The technique provides an important advantage over more traditional CW RF imaging because of the ability to time-gate the return signals. This can be used to discern specific objects by greatly reducing clutter from unwanted targets or specular reflections. The prototype system uses a 600 GHz RF signal with a 28.8 GHz chirp producing a 2.3 MHz/μsec sweep yielding a range resolution of approximately 0.6 cm or less. Lateral resolution on the scene is set by a 40 cm diameter reflector producing approximately 0.5 cm at 4 m distance.**

I. Introduction

Detection and imaging of contrabands carried by potential subjects hidden under garments at stand-off distances is a major thrust area for security agencies. There is an ongoing debate as to what frequency band and techniques are best suited for these applications. Since small size and portability is a major requirement for these instruments, aperture size is limited to tens of centimeter to a meter at most. Microwave frequencies are capable of penetrating clothes, however, they lack in required resolution (for a given aperture size). On the other hand, visible and infrared frequencies can provide very high resolution but can not penetrate garments to unveil concealed explosives and other contrabands. That leaves us with submillimeter-wave frequencies, which is capable of achieving both these objectives – high resolution and penetration. However, at frequencies above 300 GHz the background (sky temperature) is relatively warm and does not provide enough contrast for an object against the background. With room temperature detectors, passive imagers at these frequencies do not provide enough sensitivity for detecting contraband at standoff distances of 25 meters or more.

One technique that shows great promise for achieving through-garment imaging at standoff ranges from 5 to 100 m is active submillimeter-wave imaging using coherent heterodyne detection. Between 100 GHz and 1 THz most clothing is reasonably transmissive [1], while at the same time high image resolution can be achieved with a compact aperture. For example, with a standoff range R = 25 m, an antenna diameter D = 50 cm, and an operating wavelength λ = 0.5 mm (600 GHz), the two-way diffraction-limited image resolution is about 2 cm, sufficient for many of the applications. With available output power at 600 GHz from solid-state sources reaching milliwatts [2], [3], and the double sideband (DSB) noise temperature of room temperature Schottky diode based mixers reaching 2000 K and lower [4], signal to noise for active submillimeter-wave imager can reach 70-80 dB, which includes 20 dB of atmospheric loss, 20 dB of backscatter coefficient from the object, and 25 ms of integration time. Therefore, with the ability to penetrate clothing, the potential for centimeter-scale spatial resolution and signal-to-noise ratios in excess of 10^7, it is not surprising that active submillimeter imaging has attracted great interest for standoff contraband detection. But the question everyone asking is whether this high signal to noise and good resolution sufficient to reliably detect concealed objects.

In this paper we argue that it is not sufficient to have high signal to noise and resolution, because when outside the laboratory set-up an active coherent imager will typically exhibit very poor contrast between a concealed object and the surrounding clothing and skin – even for metallic objects such as guns. The challenge of active coherent submillimeter-wave detection of concealed objects involves extracting signals from scene clutter rather than from noise. We believe that this problem can be addressed by a broadband submillimeter-wave radar which is capable of three-dimensional imaging with centimeter-scale resolution in all three dimensions. Using this technique, we demonstrate in this paper our ability to generate high-resolution images and remove the clutter signals to reveal hidden objects at standoff ranges of 4 m. We show that we can readily scale the existing system to 25 m standoff, but that increasing its speed to near-real-time frame rates will require a substantial effort to develop a multi-pixel imaging radar array.

II. Frequency Modulated Continuous Wave Radar

Frequency-modulated continuous-wave (FMCW) radar techniques are ideal when available transmitter power is limited, as in the case of submillimeter-wave radars. The block diagram of our 600 GHz FMCW radar is shown in

Fig. 1. The transmitter uses a chirped signal from about 576 to 605 GHz which is generated by upconverting a fixed frequency signal with a chip signal generated by a hybrid direct digital synthesis/phase-lock loop (DSS/PLL) synthesizer, and then frequency multiplying the signal by x36. The DSS/PLL is typically ramped between 2.5 and 3.3 GHz in 12.5 ms which results in a transmitted 576-604.8

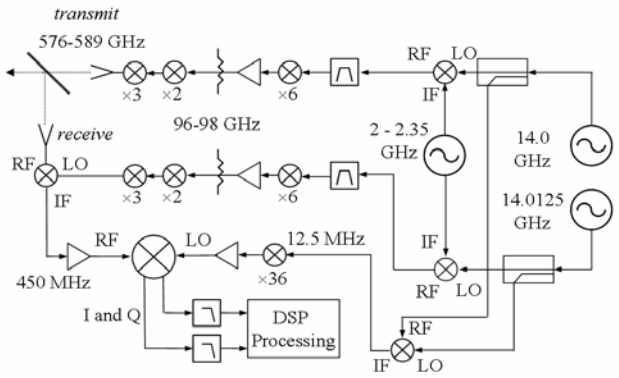

Fig. 1: Schematic block diagram of the 600 GHz radar imager. The transmit signal and receiver local oscillator are achieved by multiplying microwave sources by a factor of 36. A 2.5-3.3 GHz chirp generated by a DDS/PLL synthesizer results in a final FMCW signal with a 28.8 GHz bandwidth. The submillimeter-wave multipliers and mixer designed and build at the Jet Propulsion Laboratory are

GHz chirp with a rate K = 2.3 MHz/μs. Linearity of the chirp signal is an important factor for FMCW radars. We use a digital compensation algorithm as discussed in [5] and [6] to have a linear stable waveform for the transmitted signal. The transmitter signal goes through a silicon beamsplitter to a secondary mirror which deflects the beam to a 40 cm diameter ellipsoidal reflector, which focuses the beam at 4 meters standoff (fixed by the mirror focal length) with a half-power width of approximately 0.6 cm. The radar return signal is mixed using a JPL developed double sideband balanced mixer. The IF output is mixed again in an I-Q mixer, and is fed to the digital backend which uses FFT-based range compression to yield both the magnitude of the target's reflected power and its range. Images are acquired by scanning the focused beam over a target, typically requiring several minutes to capture a torso-sized field of view.

Fig. 2 shows a photograph of the 600 GHz imaging radar stage with a 40 cm diameter mirror installed. Upon leaving

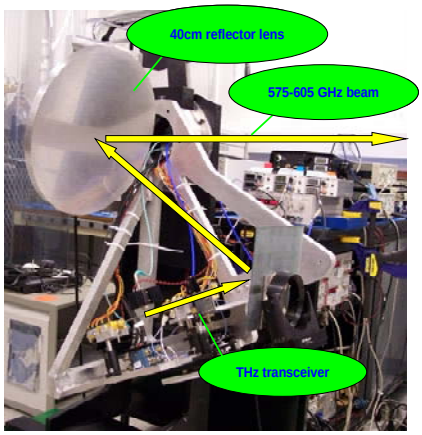

Fig. 2: Photograph of the imaging radar hardware showing different components of the imaging system.

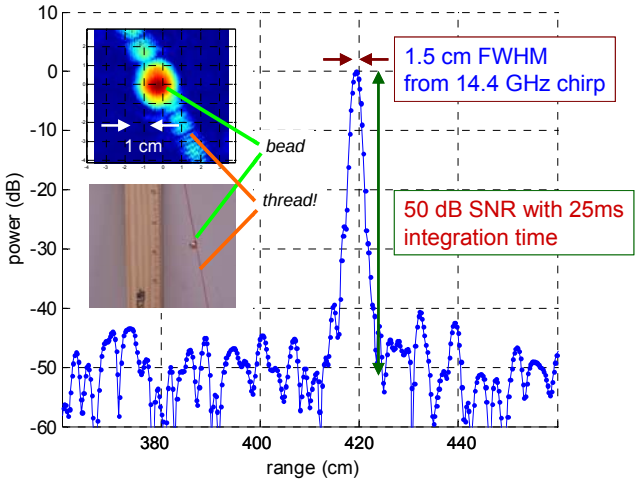

Fig. 3: 600 GHz scanned radar image of a 3 mm gold bead at 4 m standoff range and suspended by a thread and the radar return signal. The photograph of the bead is also shown. Even the single cotton thread is detected by the radar.

the transceiver the first null beamwidth is 28°. Owing to the two-way nature of the transceiver, the effective 3 dB cross-range resolution is about 0.4 cm, as indicated by the scan shown in Fig. 3, and in agreement with physical optics simulations. Fig. 3 also shows the actual radar return signal in terms of range versus power. In this image, the range-gated received power is plotted on a logarithmic scale for a target consisting of a 3 mm gold-plated bead suspended by a single cotton thread at a standoff range of 4 meters. Fig. 3 inset shows a photograph of the suspended bead along with a ruler (not present during the actual scan) to better indicate the target dimensions. Each of the approximately 10,000 pixels in the image of Fig. 3 was obtained using a 25 ms chirp (and integration time), and the maximum bead signal is about 60 dB above the background noise floor. In the range-compression spectrum, however, the bead SNR is apparently phase-noise-limited to 50 dB. Even a single thread can be detected with an SNR exceeding 20 dB in some places, as can be seen from Fig. 3.

III. Detection of Contrabands using Imaging Radar

Fig. 4 shows a THz image of a person with a concealed metallic gun replica at 4 m standoff. Although this image was acquired with the JPL FMCW radar working at 600 GHz, only the total power received for each pixel is shown – no range information is utilized in the image generation. The gun is not recognizable without prior knowledge of its location because there is very little contrast of the gun's backscattering strength compared to its surroundings. In fact, at certain locations on the target (the eyes, shoulder, and shirt sleeve), the received signal intensity is much brighter than that from most of the gun. Moreover, clutter from the laboratory wall also compromises the image quality.

Depending on an object's roughness and material properties, the THz reflectivity measured by a single-pixel

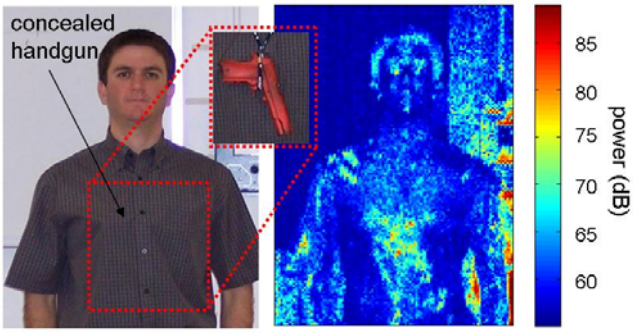

Fig. 4: Power-only active THz image of a person with a concealed metallic gun replica.

transceiver can be extremely sensitive to the beam's angle of incidence with the object. The reflectivity values at 600 GHz cited in [1] were obtained at normal incidence, and to assess the importance of specular effects, we used the 600 GHz radar to quantify the relative reflectivity of some common materials as a function of the angle of incidence. Three materials we measured were a block of unpolished aluminum, a crumpled sheet of aluminum foil, and a leather jacket (to mimic skin). Each of these items exhibits large variations in reflectivity as a function of incidence angle. For example, the signal from aluminum block drops by more than six orders of magnitude within only a few degrees of rotation, reaching levels more than 20 dB below the strongest reflection of the leather surface. The crumpled foil does not have the same sharp dependence at normal incidence, but with a reflectivity variation exceeding 30 dB over of rotation, it can appear either brighter or darker than the leather surface (which itself varies by 20 dB over ±10 degrees) depending on the angle of incidence. The results of this experiment are shown in Fig. 5.

The impact of specular reflection can also be seen in Fig. 6, which shows two 600 GHz radar images of a mannequin

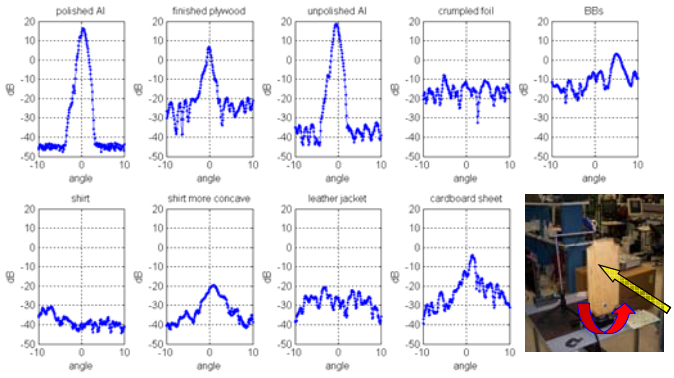

Fig. 5: Terahertz backscatter radar images of different materials with the radar transmit signal incident on the object at ± 10 degrees.

with a metallic gun replica concealed by a T-shirt. Like in Fig. 4, these images were obtained at 4 m standoff and represent power only, but for clarity the clutter signals from the laboratory wall and the near-range optics and leakage were filtered out by gating the power in a range swath encompassing the mannequin body. In Fig. 6a, the gun was carefully positioned for normal beam incidence, and it can be clearly identified in the THz image. However, Fig. 6b shows an image of the same target after it had been rotated by about 20 degrees. With the gun no longer at a normal angle of incidence, it essentially disappears. Any active, coherent THz imager that relies only on power detection must contend with this difficulty of identifying objects whose intrinsic reflectivity contrast may be overwhelmed by the effects of specular reflection.

We have addressed this problem by using the ultra-high range resolution of the THz imaging radar to enhance the

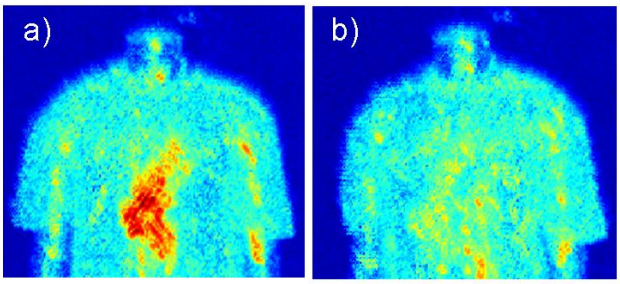

Fig. 6: Power-only terahertz image of a mannequin with a metallic gun replica concealed by a T-shirt. a) Near-normal beam-gun angle of incidence. b) Mannequin rotated ~20° away from normal incidence.

contrast of concealed objects on persons and obtaining three dimensional images. Fig. 7 shows three-dimensional scene reconstructions based on the identical raw data obtained in the scan of Fig. 4. These reconstructions were obtained by selecting, for each pixel of the image, the range-compressed signals corresponding to the "front" and the "back" target surface encountered by the beam. This was done using an adaptive algorithm based on the range returns meeting certain threshold and surface continuity criteria [7]. The result is that the "front" surface in Fig. 7a shows a faithful

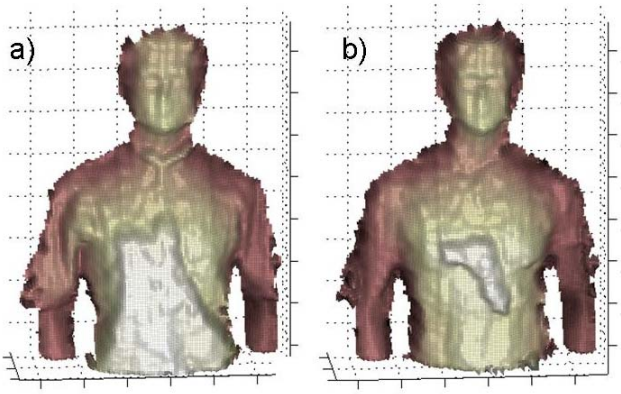

Fig. 7: (a) Front-surface – on the shirt and (b) back-surface – on the skin three-dimensional reconstructions of the scene shown in Fig. 4, obtained by utilizing the high range resolution terahertz FMCW radar.

reconstruction of the target's exposed skin and his shirt, while the "back" surface in Fig. 7b reveals an image of the body with a distinctive gun-shaped protrusion. A similar

radar image is shown in Fig. 8 where range gating capability of the radar was used to electronically strip the shirt off the object revealing the concealed object.

Compared to the power-only THz image of Fig. 4, the advantage of using ultra-high resolution radar is clear from Fig. 7. Significant enhancement of concealed objects can be achieved by measuring their three-dimensional shape rather than simply the reflected power. Also, because the radar resolution is inversely proportional to its bandwidth and independent of the standoff range, extending the system's capabilities to tens of meters standoff is feasible as long as the antenna size increases commensurately, and we have made successful through-clothes radar images at 25 m standoff [7]. Besides long range operation, a more serious challenge to the active THz radar for real-world security applications is its slow imaging time. To achieve near-video frame rates for this system, a more complex and costly multi-pixel active scanning array will likely be needed.

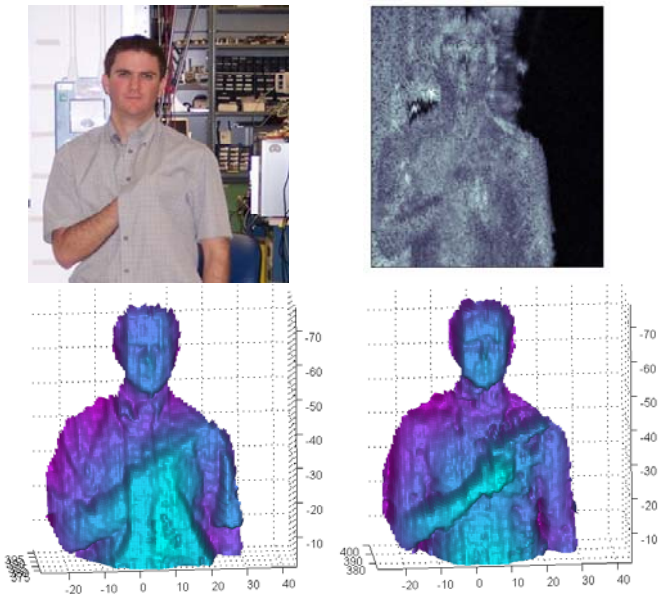

Fig. 8: 600 GHz FMCW radar image range gated to electronically strip off the shirt (bottom) showing the concealed gun. Intensity only image of the same scene is shown in top right.

CONCLUSIONS

We have shown that a 600 GHz FMCW radar system can be used to detect weapons or contraband under clothing at significant stand-off distances. We have also shown that simple active imaging using a CW source reflected off a target cannot distinguish between scene clutter or readily contrast hidden objects due to the variation in backscatter with angle and object reflectivity. By employing an FMCW radar with high range and spatial resolution and simple front- and rear-surface detection algorithms, we can actually peel away layers to reveal hidden objects with high accuracy and resolution. This added capability is believed to be critical for realizing an imaging system that can be used effectively in the field.

Although the enabling RF hardware is not readily available off the shelf at this time, we know from our own development efforts that adequate room temperature solid-state sources and heterodyne sensors can be produced to meet the requirements of such a system. Extending the effective range for a given lateral resolution is a practical issue driven mainly by aperture scale. Fortunately, there is an advantage in SNR and axial resolution when using the active radar imaging approach because the backscattered signals do not degrade with distance if the lateral resolution is maintained. Atmospheric attenuation is a concern, but working in an atmospheric window (such as 670 GHz) mitigates this problem. The biggest hurdle, we believe, is in bringing the imaging system up to video rate. However we believe this is possible by employing a linear transceiver array and we are currently pursuing this avenue of research.

ACKNOWLEDGMENT

The authors wish to thank members of the Submillimeter-Wave Advanced Technology (SWAT) group, Dr. J. Ward in particular, at the Jet Propulsion Laboratory for their support. The research described herein was carried out at the Jet Propulsion Laboratory, California Institute of Technology, Pasadena, California, USA, under contract with National Aeronautics and Space Administration.

REFERENCES

[1] R. Appleby and H.B. Wallace, "Standoff Detection of Weapons and Contraband in the 100 GHz to 1 THz Region," *IEEE Trans. on Ant. and Prop.*, vol. 55, pp. 2944-2956, Nov. 2007.

[2] Chattopadhyay, E. Schlecht, J. Gill, S. Martin, A. Maestrini, D. Pukala, F. Maiwald, and I. Mehdi, "A Broadband 800 GHz Schottky Balanced Doubler," *IEEE Microwave and Wireless Comp. Lett.*, vol.12, no.4, pp.117-118, April 2002.

[3] Chattopadhyay, E. Schlecht, J. Ward, J. Gill, H. Javadi, F. Maiwald, and I. Mehdi, "An All-Solid-State Broad-Band Frequency Multiplier Chain at 1500 GHz," *IEEE Tr. on Microwave Theory and Tech.,* vol. 52, no. 5, pp. 1538-1547, May 2004.

[4] Schlecht, J. Gill, R. Dengler, R. Lin, R. Tsang, and I. Mehdi, "A 520-590 GHz Novel Balanced Fundamental Schottky Mixer," Proc. of the 18th Intl. Symp. on Space Terahertz Tech., Pasadena, CA, April 2007,.

[5] R. J. Dengler, K. B. Cooper, G. Chattopadhyay, I. Mehdi, E. Schlecht, A. Skalare, C. Chen, and P.H. Siegel, "600 GHz Imaging Radar with 2 cm Range Resolution," *2007 IEEE MTT-S Intl. Microwave Symp. Digest,* Honolulu, HI, pp. 1371-1374, June 2007.

[6] K. B. Cooper, R. J. Dengler, G. Chattopadhyay, E. Schlecht, J. Gill, A. Skalare, I. Mehdi, and P. H. Siegel, "A High-Resolution Imaging Radar at 580 GHz," *IEEE Microwave and Wireless Comp. Lett.*, vol. 18, no. 1, pp. 64-66, January 2008.

[7] K. B. Cooper, R. J. Dengler, N. Llombart, T. Bryllert, G. Chattopadhyay, E. Schlecht, J. Gill, C. Lee, A. Skalare, I. Mehdi, and P. H. Siegel, "Penetrating 3D Imaging at 4 and 25 Meter Range Using a Submillimeter-Wave Radar," *To appear in IEEE Tr. on Microwave Theory and Tech.*

Experimental detection of terahertz radiation in bundles of single wall carbon nanotubes

K.S. Yngvesson, K. Fu, B. Fu, R. Zannoni, J. Nicholson, S.H.Adams, A. Ouarraoui, J. Donovan and E. Polizzi

Department of Electrical and Computer Engineering,

University of Massachusetts, Amherst, MA 01003, USA

* Contact: yngvesson@ecs.umass.edu; phone +01-413-545-0771

***Abstract*— We present new data extending our previous paper at the ISSTT2006 on microwave detection in carbon nanotubes (CNTs). In particular, we derive a circuit model based on ANA measurements. We also demonstrate the first terahertz detection (up to 2.54 THz) in bundles of CNTs that were deposited through dielectrophoresis across the smallest gap in log-periodic antennas. Data are given that support the hypothesis that the detection process is bolometric at THz frequencies. Future extensions are planned that will employ suspended CNTs and explore heterodyne detection. Finally, we have performed unique ab initio simulations with the aim of comparing these with the experimental data.**

I. INTRODUCTION

Our paper at the **ISSTT2005** [1] posed the question: Can we make a carbon nanotube (CNT) THz HEB? We also discussed this topic in ref. [2]. At the **ISSTT2006** we presented results of microwave (MW) direct and heterodyne detection in *metallic* single wall carbon nanotubes (m-SWCNTs) [3,4]. Other groups have also demonstrated MW detection in SWNTs, primarily in *semiconducting* tubes (s-SWCNTs) [5-9]. McEuen et al. [10] used THz time-domain techniques for detection in a quasi-metallic (qm) SWCNT FET type device. Photoconductive detection in SWCNTs is apparently very weak [11], but Itkis et al. [11] have developed a sensitive *bolometric* Near Infrared detector based on a Carbon Nanotube (CNT) film. We recently reported the first terahertz detection in bundles containing m-SWCNTs [12], up to 2.5 THz. The present paper gives further results for this detector [13]. In particular, we have characterized the devices at microwave frequencies, and we also interpret the experimental terahertz detection based on a general bolometric model.

As we discussed in ref. [1-2] CNTs are a promising medium for future terahertz bolometric detectors (HEBs or other types) based on some general features:

(1) SWCNTs have diameters of only about 1-2 nm and typical lengths of ~ 1 μm. Consequently, they have lower heat capacity than for example NbN HEBs, which is advantageous for low local oscillator power.
(2) SWCNTs have excellent thermal transport properties, including ballistic transport of both phonons and electrons in the shorter tubes. Based on (1) and (2) we can predict that SWCNT bolometric detectors can potentially have very short thermal time constants, translating into very wide bandwidth for heterodyne detectors.
(3) SWNT detectors are not restricted to working below a critical temperature as are superconducting HEBs. There is thus a potential for operation above 4 K.

II. DEVICE FABRICATION

In this work, we used nonconductive sapphire or silicon on sapphire (SOS) substrates. The choice of these substrates was crucial for both MW and THz measurements. In our previous MW work [3,4] we employed highly doped silicon substrates with a thin coating of silicon oxide, a common choice in many SWNT investigations since it allows application of a gate voltage to the substrate. Metallic and semiconducting tubes can then be conveniently distinguished due to the different effects the gate voltage has on their resistance. As a consequence of the use of the conducting substrate in our previous work, however, the MW detection responsivity dropped quickly above about 1 GHz. Further, the doped silicon substrates attenuate the THz radiation very strongly, while sapphire and SOS substrates show very low THz attenuation. The sapphire and SOS substrates were found to be equivalent in our work.

We fabricated the m-SWCNT devices by the dielectrophoresis (DEP) method [14]. Typically, we apply a 5 - 50 MHz voltage of about 5 V peak to Au contacts made by UV photolithography, such as those shown in Figures 1 and 2. To the left is a coplanar waveguide (CPW) structure that we used for MW measurements. It has a gap of about 4-6 μm. For THz measurements we employed a log-periodic toothed antenna (LPA1) with about an 8 μm gap, as shown to the right in Figure 1. LPA 1 has an estimated upper frequency limit of 1.5 THz. We also fabricated LPAs with a smaller gap, about 1 μm (LPA2), as well as smaller teeth, see Figure 2. LPA 2 has an estimated upper frequency limit of 3.5 THz.

A drop of a suspension of CNTs in isopropyl alcohol [15] was applied to these structures. The CNTs will then drift to the narrow gap in the contacts and attach to these, when the

RF voltage is applied across the contacts. We monitor the DC resistance simultaneously through a bias tee. The DEP process is halted when the dc resistance is sufficiently low. All devices were annealed in air at 200 °C for two hours which decreased the contact resistance. The result is that a small number of bundles of CNTs will be contacted in parallel across the gap. The lower resistance of these devices compared with the typical single SWCNTs, from 5 to 50 kΩ, facilitates matching of microwaves or terahertz radiation to the CNTs. While semiconducting tubes are expected to be present in the bundles, we assume these to have a negligible effect at dc compared with metallic tubes, due to the known much higher resistance of the former. A typical IV-curve is shown in Figure 3. The IV-curve displays the same "zero-bias anomaly" [16] that we had previously observed for the single m-SWNTs (as versus bundles) in ref. [3,4]. Figure 3 also shows dI/dV, which has a minimum at zero bias. The nonlinearity of the IV-curves is more pronounced the lower the temperature is. We conclude that the IV-curves are due to a number of parallel metallic tubes in the bundles.

Figure 1. Microwave CPW (left) and terahertz LPA1 (right) structures for coupling to the CNTs.

Figure 2. LPA2 with 1 μm gap used in later THz measurements.

III. Microwave Measurements

A. Microwave S11 Measurements

Both structures in Figure 1 can be measured in a microwave probe system, a useful diagnostic tool. Most of our MW measurements were performed on the CPW structure. Each tube is assumed to be modeled by the equivalent circuit introduced and analyzed by P. Burke [17], see Fig. 4. The *m*-SWCNT at the center of Fig. 4 is modeled as a transmission line (TL), and the unit cell shown is repeated periodically. The propagation velocity on the TL (v_P) is about 0.01 times the velocity of light ($2.4*10^6$ m/s), interpreted as the velocity of a "Tomonaga–Lüttinger plasmon" wave.

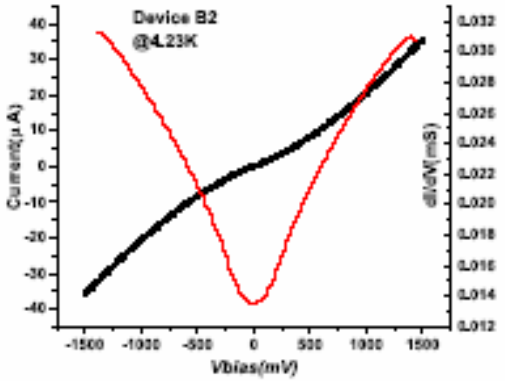

Figure 3. IV-curve (in black) for one of the devices, measured at 4.2 K. Also shown is dI/dV derived from this curve (in red). The left scale gives the current in μA and the right scale dI/dV in mS.

It is predicted that resonances will occur on the TL at terahertz frequencies for which its electrical length is a multiple of half wavelengths. The characteristic impedance (Z_c) of the TL is 9.7 kΩ. In later work, Hanson [18] and Maksimenko et al. [19] have taken into account the electromagnetic fields *outside* the CNT and find v_P about twice that of [17], as well as modified TL parameters for bundles of CNTs [19]. Very recently, McEuen et al. [10] measured the ballistic electron resonance in quasi-metallic (qm) SWCNTs and found that in their experiment v_P was that of single particle excitations (i.e. the Fermi velocity, $8*10^5$ m/s). These issues are thus presently under debate and need to be settled through further measurements at THz frequencies. At MW frequencies, however, the SWCNTs are much shorter than a wavelength, and it suffices to model the SWCNT as an inductance (the kinetic inductance, L_K) and a resistance (R_{CNT}) in series. The contacts were modeled by a resistance (R_C) in parallel with a capacitance (C_C). The capacitance to ground from the CNT has a negligible effect and could be omitted.

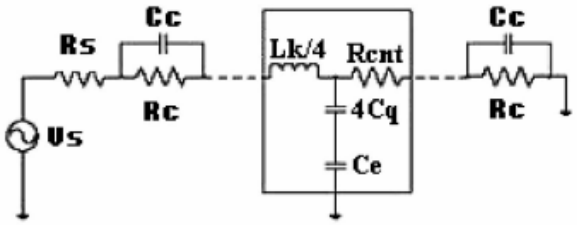

Figure 4. Equivalent circuit model for a m-SWNT.

Each substrate fabricated had a large number of CPW structures. The S-parameter S11 was measured for frequencies up to 26 GHz after calibration with a standard substrate up to the reference plane of the probe (Hewlett-Packard ANA 8510C). The admittance was then calculated from S11. We used DEP to place CNTs across the gaps of

only a few of the CPWs, and the rest could be used as references in a de-embedding process in which the admittance of the circuit *without CNTs* was subtracted from that of the circuit *with CNTs*. Using this procedure we thus obtained the admittance of the CNTs by themselves. The de-embedded data were then fitted to the circuit model, and this procedure was successful over the full frequency range for three out of four devices. The fourth device (device C) only gave a good fit to about 3 GHz. We expected some variability in the device data due to the fact that we could not control the DEP process completely. Table 1 below summarizes the circuit parameters we derived from the S11 measurements. The values for the resistances are consistent with typical CNT resistances *per m-SWCNT* of about 10 kΩ/μm at 300 K [20] and typical (total) contact resistances of the order of 500 - 1000 kΩ, if we assume that we have 100 tubes in parallel. The theoretical value for L_K is 4 nH/μm [17] and we would expect to measure a value of 0.01-0.02 nH for 100 tubes, about 4 μm long, in parallel. Our measurements are consistent with this if we take into account that our accuracy in estimating the inductance was marginal, except to determine that it is small. Note that Device C did not yield a good fit, and may have a different structure. Two recent measurements by other researchers (ref. [21,22]) estimated L_K for a single m-SWCNT and a small number of tubes (15) in parallel, respectively, but with fairly large error bars. All attempted measurements of L_K are consistent with the theory, so far, however. All measurements so far also show a significant contact capacitance, similar to our results that range from 4 fF to 40 fF. We will return to a discussion of the contact capacitance in the THz section. A typical result of the fit to the model is shown in Figure 5.

TABLE I.
PARAMETER VALUES FOR THE CIRCUIT MODEL FITS TO THE MEASURED S11 DATA.

Device	R_{CNT} (kΩ)	L_K (nH)	R_{C1} (kΩ)	R_{C2} (kΩ)	C_{C1} (fF)	C_{C2} (fF)
C	0.34	92	1.94	1.52	2	42
D	0.08	2.50	4.28	4.73	4.96	4.50
E1	0.29	0.03	1.06	7.29	23.4	21.6
F	0.20	0.05	0.61	3.25	32.4	37.5

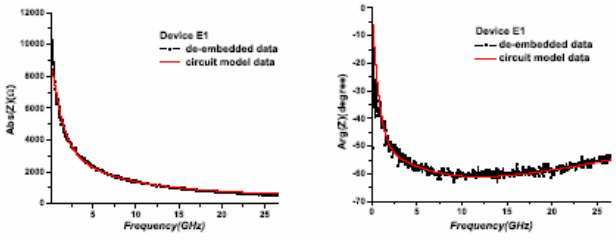

Figure 5. Best fit of the de-embedded data for the measured values of ABS(Z) (ohms) (left) and ARG(Z) (degrees) (right) of Device E1 (black points), compared with the model (red line).

B. Microwave Detection Measurements

We dc biased CNT devices that were contacted by the microwave probes, by feeding the current from a programmable Source Meter (Keithley 2400) through a bias tee. We then fed microwave power, modulated at 1 kHz, to the devices and detected the change in the dc current with a lock-in amplifier. The microwave power was measured with a power meter. The circuit connections were similar to what was used in the THz experiments and will be presented later. Five devices were measured. Figure 6 shows the detected responsivity versus bias voltage for one of these. This curve shows a reasonable fit to the predicted response (see below). The fit is not as good as for the single tubes measured in our earlier work [3,4], as would be expected based on the more complex structure of the bundles. It is also broader, and another difference is that the maximum responsivity is much larger (from 600 V/W to 1,000 V/W, compared with 114 V/W). The responsivity in [3,4] was measured at 77 K, whereas the new results are at room temperature. Clearly, devices containing SWNT bundles are superior to the single tube devices that were employed for the earlier measurements. The responsivity is defined as

$$S_V = \Delta V / P_{MW} = S_I * R \qquad (1)$$

$$S_I = (1/4)*(d^2I/dV^2)*V^2_{MW}/P_{MW} \qquad (2)$$

Here, ΔV is the detected change in dc voltage, V_{MW} is the peak MW voltage and P_{MW} is the MW power. As in [3,4] we derive the voltage responsivity from $R*(d^2I/dV^2)$, which was obtained from the measured IV-curves, in the same manner as for a standard microwave detector diode [22]. Note from Table 1 that the contact resistance is much larger than the actual CNT resistance, i.e. the nonlinearity of the IV curve can be ascribed to the contact resistance.

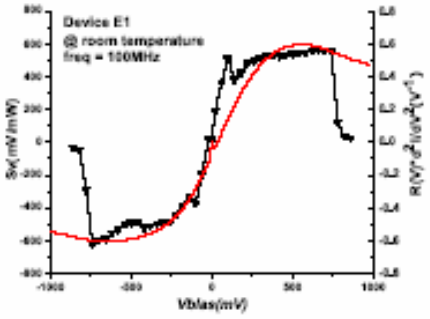

Figure 6. Voltage responsivity (S_V) for device E1 at a frequency of 100 MHz, versus bias voltage (black points) compared with the prediction based on Eq's (1) and (2).

Finally we measured the voltage responsivity as a function of MW frequency, see Figure 7. The effect of parasitics was partly avoided by calibrating the microwave power at the probe. The small drop in responsivity as the frequency is increased is consistent with a prediction based on the circuit model [13]. It is due to the contact capacitance beginning to shunt the contact resistance, which makes the detector less effective. We conclude that in this mode of detection (the

"diode mode") the detector has a high responsivity up to a few tens of GHz, with a cut-off frequency that depends on the value of the contact RC time constant.

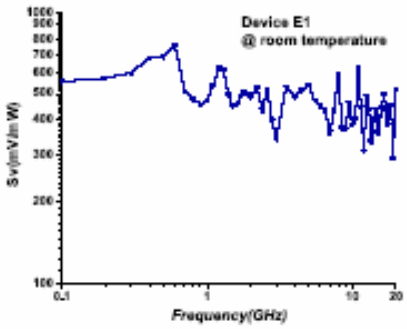

Figure 7. Frequency dependence of the maximum S_V for Device E1.

IV. TERAHERTZ MEASUREMENTS AND MODELING

A. THz Measurement Setup

For the terahertz measurements, a device chip with dimensions 6x6 mm^2 was inserted in a fixture (Figure 8) available from our earlier work with NbN HEB receivers [24]. The fixture allowed quasi-optical coupling to terahertz radiation, as well as bias input and detector output through a coaxial cable and a bias tee. Gold bond wires were used to connect to the contact pads of the LPA shown in Figure 1 (right). The LPA in Figure 2 has a larger contact area, shaped like a CPW, and we were able to connect it with indium wire. The fixture was then mounted in a liquid helium dewar.

A 4 mm diameter ellipsoidal silicon lens was attached to the substrate for quasi-optical coupling to the antenna as shown in Fig. 9.

Figure 8. The fixture used for THz measurements. The device chip is in the center of the fixture and the silicon lens on the opposite side (visible through the sapphire substrate).

A 100 kΩ resistor is connected in series with the carbon nanotube, and the Keithley Source Meter is connected directly to the resistor. The dc voltage across the two terminals of the carbon nanotubes is sensed at the V_{sense} port. The Source Meter also measures the current through the carbon nanotubes. A change in the device current gives rise to a voltage drop across the 100 kΩ resistor that is measured with a lock-in amplifier (EG&G 7260), which has an input impedance of 1 MΩ, through two 200 kΩ resistors. A 1 kHz signal from a function generator was employed as reference for the lock-in amplifier.

Terahertz radiation was introduced through the dewar window and the silicon lens from a CO_2-laser (Coherent/DEOS GEM-50) pumped terahertz gas laser that had a typical output power of 2-5 mW (Figure 11). The power could be measured with a Scientech (Astral AA30) power meter. The laser was modulated from the same 1 kHz function generator by inserting an acousto-optic modulator (IntraAction AGM-406B21) after the CO_2 pump laser, as indicated in Figure 10.

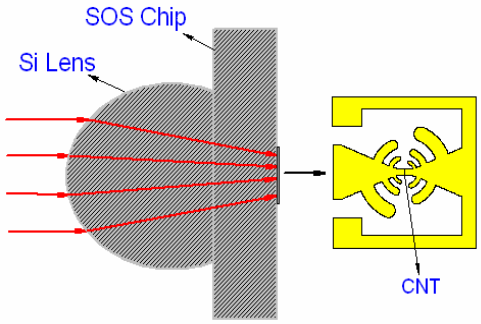

Figure 9. The quasi-optical coupling configuration.

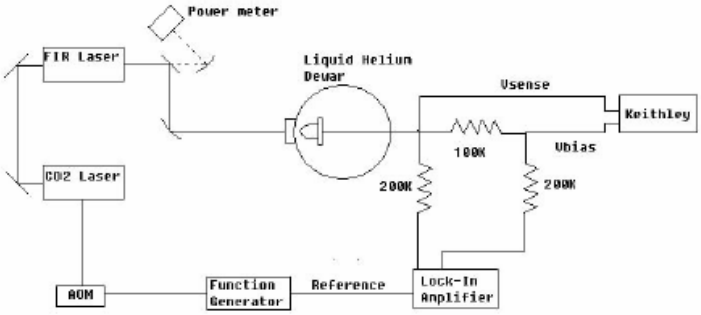

Figure 10. THz measurement setup.

Figure 11. The CO_2-laser pumped THz gas laser

B. Overview of Experimental THz Results

Using the configuration described in section IV.A we have demonstrated detection in CNT bundles at five different frequencies (0.694 THz, 1.05 THz, 1.39 THz, 1.63 THz and 2.54 THz). We measured the response for five devices of quite different resistances, see Table II. The resistance values given are for 300 K and low bias voltage.

Device B initially had a room temperature resistance of 7 kΩ ("Device B1") which after about one month changed to 20 kΩ ("Device B2"). Many experiments were then performed on Device B2 during which the IV-curves at a given temperature stayed the same.

TABLE II.

Device	Resistance (kΩ)	Antenna	# Active m-SWNTs
A	430	LPA1	3-5
B1	7	LPA1	50
B2	20	LPA1	50
1μmB2	65	LPA2	5
1μmC3	3	LPA2	50

A summary of all terahertz detections obtained so far is given in Figure 12. The terahertz power was measured outside the window of the dewar, and the response was linear in power. There is a roughly 3 to 4 dB optical loss between the dewar window and the antenna terminals. It is clear that there is a general type of detection process that works for a wide range of terahertz frequencies. There appears to be a pattern of decreasing responsivity from 0.694 THz to 1.63 THz, but the responsivity then increases at 2.54 THz, in contradiction to that trend. The higher resistance device A has more than an order-of-magnitude lower responsivity than Device B2.

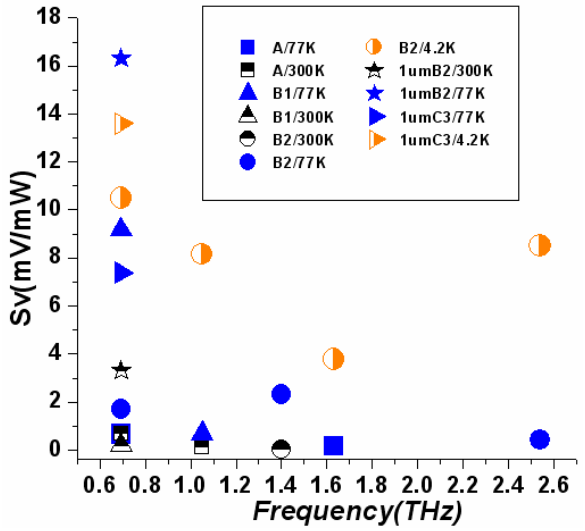

Figure 12. Summary of measured THz responsivity versus frequency.

Some devices show no or only very weak detection at 300 K, but Device 1μmB2 is an exception to this rule. We first discuss the results for Device B2 in detail.

C. The Bolometric Model

We measured the bias voltage dependence of the voltage responsivity for all devices in order to test the hypothesis that the detection process for the new THz detector is bolometric, as had been found for the IR CNT film detector in ref. [11]. A block diagram of a general bolometer is given in Figure 13. A bolometer is a device that has a temperature-dependent resistance R(T) and a heat capacity C_h. The bolometer is thermally connected through a thermal conductance G_{th} to a heat reservoir at temperature T_0.

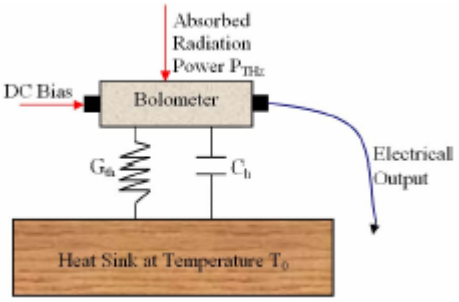

Figure 13. A bolometer model.

As the bolometer is heated by the terahertz power and biased by the dc current I_0, its temperature is increased from T_0 to $T_0 + \Delta T$. If we define the factor $b = (1/R)*dR/dT$ then the voltage responsivity of the bolometer will be (neglecting electro-thermal feedback) [25]:

$$S_V = \Delta V/P_{THz} = \frac{I_0 * R * b}{[G_{th} + i\omega C_h]} (V/W) \qquad (3)$$

The thermal time-constant of the bolometer is determined by $\tau_{th} = C_h/G_{th}$.

In Sec. III A we found that the contact capacitance (C_C in the equivalent circuit in Figure 4) has values ranging from 4 fF to 40 fF, large enough that it effectively shunts the contact resistance at THz frequencies. We estimate that Device B2 may have about 50 ("active") metallic SWCNTs in parallel. Simulation of the circuit in Figure 4 (for a single m-SWCNT) shows that the mismatch loss right at the resonance frequencies may have large peaks, if the damping is weak [17]. We have simulated Device B2 using parameters for the circuit model such as Z_C and v_P based on [17], while varying the length of individual tubes. A more complete electromagnetic model would also take into account interactions between the tubes. An example approximate simulation is given in Figure 14 (black curve). It is clear that the resonances have been smoothed out. Figure 14 also shows two cases simulated for the 1 μm long device with an estimated 5 parallel tubes. We assume two values of the CNT resistance, per tube, 2 kΩ (based on [21]; red curve), and 5 kΩ (upper range based on Table I; blue curve). In this case there are clearly defined resonances. If we change v_P to be

equal to v_F, as measured in [10], the resonances shift to lower frequencies (see inset). Note that the interactions within the bundles will shift the resonance frequencies up somewhat [19] but the basic pattern should look similar. Future measurements on such short devices at several laser frequencies appear promising for distinguishing between the presently available models. For device B2 we assume a very conservative estimate of the average mismatch loss of 12 dB.

The mismatch loss is significant in many cases, but a substantial portion of the THz power is indeed typically predicted to be absorbed, partly due to the fact that the contact resistance is shunted away. For device B2, very small ripple with frequency is predicted, consistent with the measured data in Figure 12. The slow decline of S_V with frequency, evident in Figure 12. may be due to a decrease in the efficiency of the antenna. We may speculate that the higher responsivity measured at 2.54 THz is caused by a different mechanism of THz absorption. It is well-known that many CNTs are quasi-metallic (qm-SWCNTs) and have bandgaps corresponding to frequencies of 2.5 to 10 THz [26]; this may provide a second mechanism for more efficient terahertz absorption in such tubes.

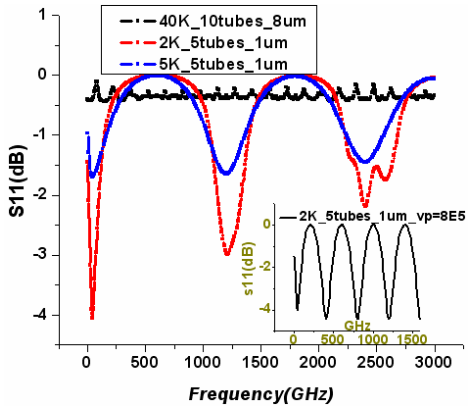

Figure 14. Simulated reflection loss (S11 in dB) between the CNT device and the LPA antenna. The devices modelled are 1) 10 tubes in parallel, 8μm long, R_{CNT} = 40 kΩ per tube (black); 2) 5 tubes in parallel, 1 μm long, R_{CNT} = 2 kΩ per tube, v_P and Z_C from [17] (red); 3) Same as 2 but R_{CNT} = 5 kΩ (blue). 4) **Inset:** 5 tubes in parallel, 1 μm long, R_{CNT} = 2 kΩ, $v_P = 8*10^5$ m/s (as in [10]) and Z_C = 12.9/4 = 3.2 kΩ.

Given that THz power is predicted to be absorbed in the m-SWCNTs, the devices would act as THz bolometers, provided that they have a sufficiently high value for the factor 'b' in Eq. (3). To investigate this, we measured IV-curves at a number of temperatures, from 4.2 K to 300 K, and calculated R and b from these, as a function of bias voltage, V_B, see Figures 15 and 16. We find that there is a maximum for $|b|$ close to T = 20 K. Also, $|b|$ decreases as the bias voltage increases. This gives rise to a characteristic signature of the bolometer process that we might look for in the responsivity data. We therefore plotted Eq. (3) while using G_{th} as an adjustable parameter to obtain best fits to the experimental data.

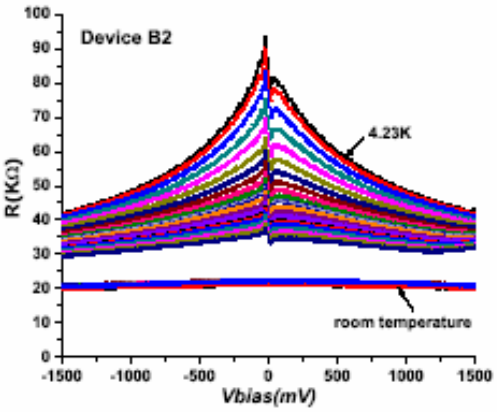

Figure 15. Resistance of device B2 versus bias voltage at a number of temperatures.

We obtained good fits in all cases independent of frequency and for temperatures up to 150 K (Figure 17). Figure 17 also demonstrates that the diode model does not produce a good fit to the measured data for this temperature range. We thus have good evidence to claim that our devices detect THz radiation based on a bolometric process at these temperatures. At 300 K the nonlinearity of the IV-curves is very small, and it is difficult to distinguish predictions based on the two models.

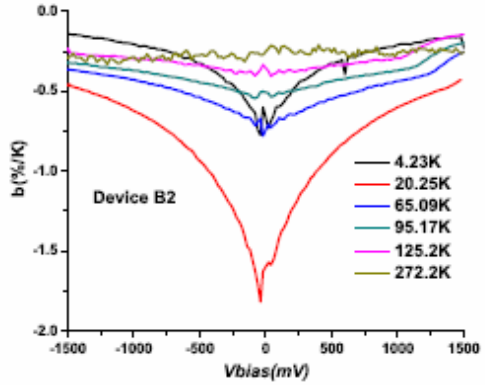

Figure 16. The temperature dependence factor b for device B2 as a function of bias voltage at different temperatures (only selected curves shown).

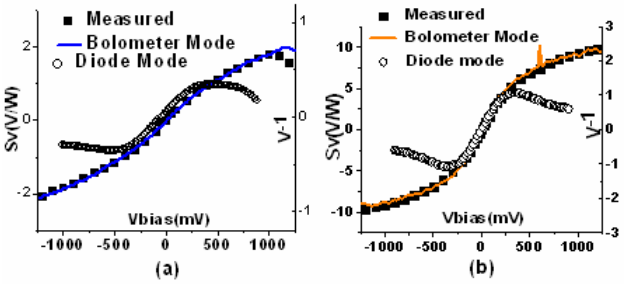

Figure 17. Best fits of Eq. (3) ('bolometer model') to the measured curves of S_V versus bias voltage. We also show predictions based on the diode model (Eq's (1) and (2)). (a) a laser frequency of 1.395 THz at 77 K and (b) a laser frequency of 0.694 THz at 4.2 K;

Some typical values of G_{th} are given in Table III.

TABLE III.

Temp. (K)	Frequ. (THz)	Gth(W/K)	Gth(W/K) (corrected)[2]
4.2	0.694	$2.33*10^{-4}$	$5.8*10^{-6}$
4.2	1.05	$3.1*10^{-4}$	$8*10^{-6}$
4.2	1.63	$6.75*10^{-4}$	$1.6*10^{-5}$
4.2	2.54	$2.76*10^{-4}$	$7*10^{-6}$
77	1.40	$2.13*10^{-3}$	$5*10^{-5}$

By measuring S_V as a function of temperature at a given bias voltage (Figure 18) we can plot G_{th} versus temperature, see Figure 19. We note that S_V decreases relatively slowly as the temperature is increased from 4.2 K, changing by a factor of two at about 25 K. This indicates a potential for this detector to work at temperatures considerably higher than LHe temperature. This feature is a result of the temperature sensitivity ($\left|b\right|$) increasing from 4.2 K to 20 K (Figure 16), which counteracts the roughly linear increase of G_{th} with temperature up to about 100 K (Figure 19).

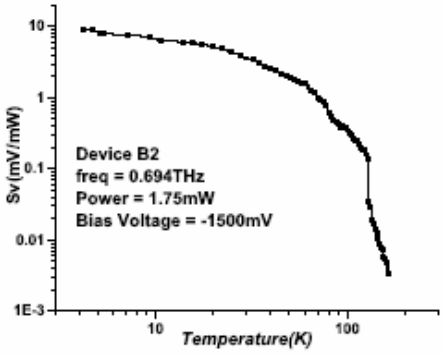

Figure 18. S_V versus temperature for Device B2 at f_{THz} = 0.694 THz.

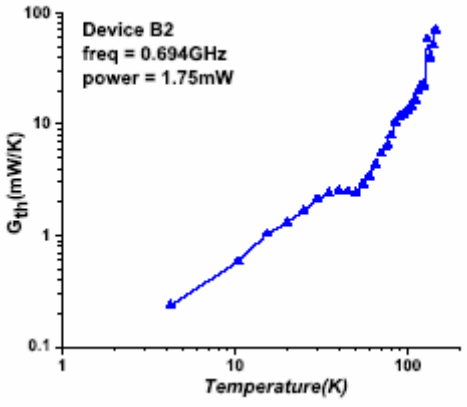

Figure 19. G_{th} versus temperature for Device B2 at f_{THz} = 0.694 THz.

[2] See discussion in Sec. IV.D.

D. Comparison with Thermal Conductance Theory

We can estimate G_{th} as follows: Recent work by E. Pop et al. [27,28] and Maune et al. [29] has analysed the electrical break-down for carbon nanotubes, that is known to occur at a specific temperature, about 600 °C. The power dissipation can then be correlated with the temperature, and a value derived for the thermal conductance both directly from the SWNT to the substrate (g), as well as through the contacts (G_{cont}), as pictured in Figure 20.

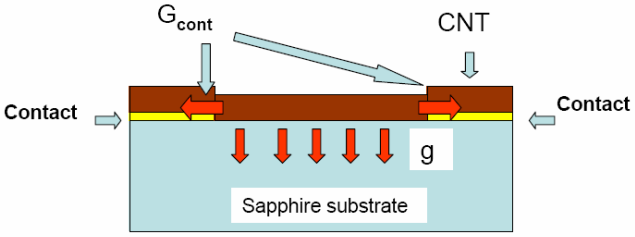

Figure 20. Illustration of heat conduction processes in the CNTs

Except for extremely short tubes, the first term (g) dominates. Further, the value of g is essentially independent of the type of substrate, indicating that the bottle neck for the process is right at the SWNT/substrate interface. From ref. [28] we can adopt an average value (for a single tube) of g = 0.15 W/mK and $G_{cont} = 8*10^{-8}$ W/K. Since these values were inferred from electrical break-down data, they apply to a situation in which the SWCNT temperature is 600 °C and the substrate at room temperature. The temperature has a maximum at the center of the tube, but is quite uniform due to the dominance of g over R_{cont} [27]. The length of the tubes is about 8 µm, and scaling from the MW data we estimate that there may be 50 tubes in parallel. We have $G_{th} = 1.2*10^{-6}$ W/K for a single tube and $6*10^{-5}$ W/K for fifty tubes in parallel. We have neglected G_{cont} . According to Prasher [30] the conductance for ballistic transport of phonons through a nano-constriction is proportional to the heat capacity. Prasher et [31] also calculate a T^4 dependence of G_{th} for a circular constriction between two (3-D) silicon half-spaces. From Ref. [32], the heat capacity for a 1-D structure is proportional to T. Although no experimental data are available to verify this yet, we assume that G_{th} varies linearly with temperature from about 873 K to 77 K. The temperature dependence for G_{th} that we plot in Figure 19 is close to linear up to about 100 K, consistent with this. We then find $G_{th} = 1.0*10^{-7}$ at 77 K for an 8 µm long m-SWCNT. The value for fifty parallel tubes is $G_{th} = 5.0*10^{-6}$ W/K. The value we estimated for G_{th} from measurements at 77 K (see Table III) is $2*10^{-3}$ W/K, however.

Here we should first note that the fits for $S_V(V_{bias})$ in Figure 17 assume that the responsivity is based on *the THz power outside the dewar*. There are known optical losses (L_{opt}) of 3-4 dB from the dewar window, a heat shield inside the dewar, and the silicon lens. Also, we estimated a mismatch loss between the antenna and the device (L_{mism}) of roughly 12 dB in Sec. IV.C. Taking these losses into account

we can modify equation (3) to yield the intrinsic responsivity based on the actual absorbed THz power:

$$S_V^{(1)} = \Delta V / P_{THz,abs} = \frac{V_0 * b}{[G_{th} + i\omega C]} \left[\frac{\eta}{L_{opt} L_{mism}} \right] (V/W) \quad (4)$$

This is the quantity that should be compared with measurement. We have introduced a further efficiency (η) which expresses the effectiveness of the (actual absorbed) THz power in changing the resistance. The estimated THz losses decrease the intrinsic responsivity by a factor of about 40 (16 dB), which adjusts the values of G_{th} in Table III by the same factor (the fourth column). At 77 K the corrected G_{th} is $5*10^{-5}$ W/K and the estimated value based on ref. [27-29] is $5*10^{-6}$ W/K, with a discrepancy of 10 dB. Possible reasons for the remaining discrepancy are:

(i) The estimate of L_{mism} is clearly very approximate.
(ii) The estimate of the number of parallel tubes is inaccurate.
(iii) Losses which can be described by the factor η. For example, the bundles contain many tubes that are "inactive" that don't change their resistance. THz power may be lost from the "active" tubes to the "inactive" ones.
(iv) The thermal conductance g [27-29] is only known at the break-down temperature. It is also not known for bundles. Plots such as Figure 19 should be useful for comparisons with extensions of the theory given in ref. [30-32]. Measurements on single tubes would be most useful for this.

We can estimate the thermal time-constant of the THz bolometer through the equation given after Eq. (3). The (total) heat capacity (C_h) was calculated based on ref [33,34]. At 77 K we find $\tau_{TH} \sim 2.5*10^{-17}/5*10^{-5} = 5*10^{-13}$ sec. which is exceedingly fast. If we take into account the extra losses represented by η, then τ_{TH} will lengthen by a factor of 1/η (10 dB) and a value of 5 ps is obtained (IF bandwidth = 32 GHz in heterodyne operation). In our experiments we found that the responsivity fell quickly above a laser modulation frequency of about 5-10 kHz. This can be explained as due to the maximum rate at which the THz gas laser could be modulated. We verified this by using a Schottky diode detector. The data in Figure 12 for devices that use antenna LPA2 are more preliminary, but we note that at 77 K device 1umB2 that used LPA2 has about an order-of-magnitude larger S_V than device B2 (with LPA1) at the same temperature. A larger responsivity may be explained because LPA2 is expected to be more efficient than LPA1. Also, the tubes are eight times shorter and thus have lower G_{th} which translates to larger S_V. The mismatch loss may also be lower. Device 1μmC3 had an almost ohmic IV-curve, and is expected to have a lower responsivity than 1μmB2, as observed.

D. Summary of the Detection Process

A brief summary of the hypothesized bolometric detection process can be given as follows:

THz radiation is absorbed in the SWCNTs proper (i.e. not in the contacts) and heats the tubes. We know from measuring R(T) that the dc resistance of the devices depends on T, which we assume is due to temperature-dependent tunnelling through the contacts (in agreement with ref. [16] and many other references). Similarly, as the SWCNTs are heated by the absorbed THz power, electron tunnelling through the contacts increases, explaining the positive increment in current that we measured. We note that, especially for the 8 μm long tubes, scattering may prevent some heated electrons from reaching the contacts. This could constitute a process that explains a decrease of the efficiency factor η in Eq. (4). **We also note that while the expressions for the "diode" process occurring at MW (Equ's (1)-(2)) and the THz bolometric process (Equ's (3)-(4)) are different, they both ultimately rely on the electron tunnelling process through the contact barriers.**

V. LARGE-SCALE AB INITIO SIMULATION

In order to obtain the different component characteristics presented in the equivalent circuit model in Fig.4, we aim to go beyond the current state-of-art capabilities for simulating CNTs by developing large-scale *ab-initio* atomistic approaches. Our proposed atomistic Density Functional Theory (DFT) and Kohn-Sham equation approach has the potential to clear up our understanding of many experimental issues, and to offer the high degree of reliability and accuracy needed to characterize the following macroscopic quantities: kinetic inductance, contact resistance and contact capacitance, quantum capacitance and CNT resistance.

Because of their high consumption of computational resources, *ab-initio* electronic structure and transport calculations are usually limited to either small molecular systems [35,36], or isolated regions of the carbon nanotube close to the metal contacts or possible defects [37,38]. An *ab-initio* atomistic description of a long CNT up to 100nm (~ 10,000 atoms), which has been so far considered as a formidable task, could however provide important insights into the electronic properties of the device. In order to achieve this goal efficiently, we have been developing innovative numerical modeling strategies using a real-space mesh technique framework and a combination of mathematical methodologies and high-performance parallel algorithms [39] (mode approach/contour integration/ efficient banded solver). To give a perspective of the computational time required by our proposed atomistic-based simulation, only a few minutes of CPU time are needed to obtain electronic properties (electron density, potential, etc.) of long nanotubes which is order of magnitude faster than any other existing *ab-initio* techniques (see Fig. 21).

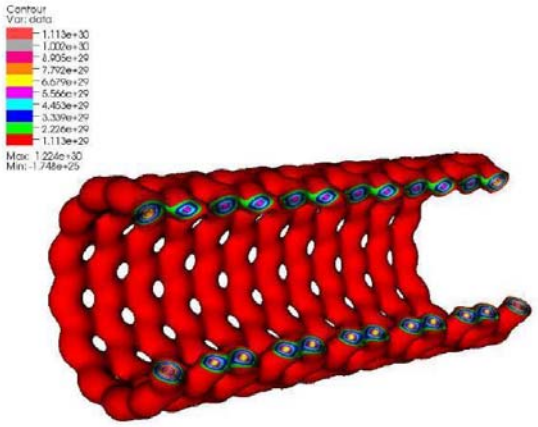

Figure 21. Electron density in CNT calculated using real-space pseudopotentials.

The approach is also highly scalable using the parallel SPIKE solver [40,41]. In addition it can be adapted to perform time dependent DFT calculations by solving the Kohn-Sham equations using a Crank Nicolson scheme and by adapting the transient simulation approach proposed in [42]. Since the terahertz experimental data may be altered by defects, vacancies, charge impurities, and other distortions, we have shown that our numerical approach can be used to study as well the device characteristics response to these different excitations [39].

In practice, the DFT-Kohn-Sham equation can be used in association with accurate pseudopotentials to remove the core electrons, and the local density approximation (LDA) to account for the many-body exchange-correlations term. However, since the effect of core electrons in CNT may not be negligible [43], we have very recently successfully performed all-electron calculations and obtained preliminary results [44].

VI. DISCUSSION AND CONCLUSIONS

In this paper we have described measurements of improved MW detection in bundles of SWCNTs, compared with our previous results [3,4] (response to higher frequencies, larger responsivity). MW ANA measurements also resulted in an equivalent circuit model, valid to 26 GHz. Devices were rapidly fabricated by DEP by which several parallel bundles were placed on contacts. The circuit model demonstrates that substantial (4 – 40 fF) capacitance exists parallel to the contact resistance.

We have demonstrated the first detection of terahertz radiation (up to 2.54 THz) in bundles of m-SWNT devices. We employed quasi-optical coupling with a silicon lens and log-periodic antennas, a technology taken over from our previous NbN HEB work, well familiar to participants in the ISSTT symposia. So far, the maximum voltage responsivity measured is about 16 V/W (30-40 V/W at the antenna terminals), at 77 K (that device is expected to have had a much larger S_V at 4.2 K). The temperature dependence of S_V is quite gradual up to about 50 K indicating a potential for operation well above 4.2 K. While the responsivity is not very large at this state of the development, we note that another recent (fast) quasi-optical THz detector using Schottky diodes [45] had a similar responsivity.

We explain the detection process in the new THz detector as being bolometric, which agrees with our detailed measurements and modelling. The detector resembles phonon-cooled NbN HEBs in that the main heat conduction mechanism is directly from the active element to the substrate. The thermal conduction process is known to be very strong [27-29] which is one aspect that limits the present responsivity. It should be straight-forward to modify the devices by etching a trench in an oxidized high-ρ silicon substrate, or in the silicon layer of an SOS susbstrate, and suspend the SWNTs across this trench, as has been demonstrated in many other experiments (ref. [27] and references given there; also [46]). The thermal conductance will be *along* the tubes in this case, and considerably lower, which will increase the responsivity. It is useful to compare ref. [11] which achieved S_V ~ 1,000 V/W in the Near IR (that bolometer has a much larger heat capacity and thus longer time constant). We plan to fabricate suspended SWCNT devices, which will also help further verify the bolometric model. Note that this version of the CNT detector will then be similar to a diffusion cooled HEB [47], and also similar to the ballistic cooling HEB of M. Lee et al. [48].

Another potential area for improvement is the optical coupling. While the use of bundles of tubes, and cancellation of the effect of the contact resistance at THz, are useful features that we have demonstrated, full optimization may eventually require some type of matching transformer [1].

Based on the low heat capacity and large thermal conductance of the new devices we predict a very short thermal time-constant (~ 5 ps). Much shorter time constants should be feasible for the suspended CNT version. In the ballistic limit, assuming electron cooling [1,2]:

$$\tau_{TH} \sim 1.25 \text{ ps} * (L(\mu m)) \qquad (5)$$

Here we have set the electron velocity equal to the Fermi velocity ($8.1*10^7$ cm/s). If plasmon phenomena dominate the THz transport (see Sec. III.A) even shorter time constants are predicted. Of course, such predictions must be verified through future work. We plan to develop a heterodyne detector, which will eventually allow us to measure the IF bandwidth, and thus verify the thermal time-constant. Finally, it is expected that the performance of the detector can be extended to frequencies well above 2.5 THz. Clearly, much work still lies ahead, but that work can now build on the concrete results described above.

ACKNOWLEDGMENT

This work was supported by NSF grants ECS-0508436 and ECS-0725613.

REFERENCES

[1] K.S. Yngvesson, "A New Hot Electron Bolometer Heterodyne Detector Based on Single-Walled Carbon Nanotubes," *16th Intern. Symp. Space Terahertz Technol.*, Gőteborg, Sweden, May 2005, p. 531.

[2] K.S. Yngvesson, "Very wide bandwidth hot electron bolometer heterodyne detectors based on single-walled carbon nanotubes," *Applied Phys. Lett,* vol. **87**, p. 043503 (2005).

[3] K.S. Yngvesson, F. Rodriguez-Morales, R. Zannoni, J. Nicholson, M. Fishetti, and J. Appenzeller, "Microwave Detection and Mixing in Metallic Single Wall Carbon Nanotubes and Potential for a New Terahertz Detector," *17th Intern. Symp. Space Terahertz Technol.*, Paris, France, May 2006, p. 135.

[4] F. Rodriguez-Morales, R. Zannoni, J. Nicholson, M. Fischetti, K. S. Yngvesson, and J. Appenzeller, *Appl. Phys. Lett*. **89**, 083502 _2006_.

[5] H.M. Manohara, E.W. Wong, E. Schlecht, B.D. Hunt, and P.H. Siegel, *Nano Lett.* **5**, 1469 (2005).

[6] S. Rosenblatt, H. Lin, V. Sazonova, S. Tiwari, and P.L. McEuen, *Appl. Phys. Lett*. **87**, 153111 (2005).

[7] A. A. Pesetski, J.E. Baumgardner, E. Folk, J. Przybysz, J. D. Adam, and H. Zhang, *Appl. Phys. Lett.*, **88**, 113103 (2006).

[8] M. Tarasov, J. Svensson, L. Kuzmin, and E. E. B. Campbell, *Appl.Phys.Lett.*, **90**, 163503 (2007).

[9] C. Rutherglen and P. Burke, "Carbon Nanotube Radio," *Nano Letters*, **7**, p. 3296 (2007).

[10] Z. Zhong, N.M. Gabor, J.E. Sharping, A.L. Gaeta, and P.L. McEuen, "Terahertz time-domain measurement of ballistic electron resonance in a single-walled carbon nanotube," *Nature Nanotechnol.* **3**, 201 (2008).

[11] M.E. Itkis, F. Borondics, A. Yu and R.C. Haddon, *Science,* **312**, 413 (2006).

[12] K. Fu, R. Zannoni, C. Chan, S.H.Adams, J. Nicholson, E. Polizzi and K.S. Yngvesson, "Terahertz detection in single wall carbon nanotubes," *Appl. Phys. Lett.*, **92**, 033105 (2008).

[13] K. Fu, "Metallic Carbon Nanotubes, Microwave Characterization and Development of a Terahertz Detector," *M.Sc. thesis, University of Massachusetts, Amherst, MA* (2008).

[14] R. Krupke and F. Hennrich, *Adv. Eng. Mater.* **7**, 111 _2005.

[15] Cheap Tubes, Brattleboro, Vt.. Purified 90% SWCNTs, grown by CVD, nominal diameter from 1 to 2 nm., average length of 50 μm before ultrasonication.

[16] Z. Yao, C.L. Kane, and C. Dekker, *Phys. Rev. Lett.* **84**, 2941 (2000).

[17] P. J. Burke, "Lüttinger liquid theory as a model of the gigahertz electrical properties of carbon nanotubes," *IEEE Trans. Nanotech*. **1**, 129 (2002).

[18] G.W. Hanson, "Fundamental Transmitting Properties of Carbon Nanotube Antennas", *IEEE Trans. Antennas Propagat.*, **53,** 2426 (2005).

[19] M. V. Shuba, S. A. Maksimenko and A. Lakhtakia "Electromagnetic wave propagation in an almost circular bundle of closely packed metallic carbon nanotubes" *Phys. Rev. B*., **76,** 155407 (2007).

[20] M. S. Purewal, B. H. Hong, A. Ravi, B. Chandra, J. Hone, and P. Kim, "Scaling of Resistance and Electron Mean Free Path of Single-Walled Carbon Nanotubes", *Phys.Rev.Lett*. **98**, 186808 (2007).

[21] J. J. Plombon, K. P. O'Brien, F. Gstrein, V. M. Dubin, and Y. Jiao, High-Frequency Electrical Properties of Individual and Bundled Carbon Nanotubes," *Appl. Phys. Lett.* **90**, 063106 (2007).

[22] M. Zhang, X. Huo, P. C. H. Chan, Q. Liang, and Z. K. Tang, "Radio-frequency transmission properties of carbon nanotubes in a field-effect transistor configuration," *IEEE Electron Device Letters*, **27**, p. 668, Aug. 2006.

[23] K.S. Yngvesson, "*Microwave Semiconductor Devices*", Kluwer Academic, Norwell, MA (1991).

[24] E. Gerecht, C. Musante, Y. Zhuang, K. Yngvesson, T. Goyette, J. Dickinson, J. Waldman, P. Yagoubov, G. Gol'tsman, B. Voronov, and E. Gershenzon, *IEEE Trans. Microwave Theory Techn.*, vol. **47**, pp. 2519–2527, (1999).

[25] P.L. Richards, *J. Appl. Phys*., **76**, 1 (1994).

[26] M. Itkis, S. Niyogi, M.E. Meng, H. Hu and R.C. Haddon, *Nanolett.* **2**, 155 (2002).

[27] E. Pop, D.A. Mann, K. Goodson, and H. Dai, J. Appl. Phys., **101**, 093710 (2007). Also see references therein.

[28] E. Pop, "The role of Electrical and Thermal Contact Resistance for Joule Breakdown of Single-Wall Carbon Nanotubes," to appear in *Nanotechnology* (2008). Available at *arXiv-condmat* 0805.1937.

[29] H. Maune, H.-Y. Chiu and M. Bockrath., *Appl. Phys. Lett.*, **83**, 013109 (2006).

[30] R. Prasher, *Nanolett*. **5**, 2155 (2005).

[31] R. Prasher, T. Tong and A. Majumdar, *Appl. Phys. Lett.* **91**, 143119 (2007).

[32] J. Hone, B. Batlogg, Z. Benes, A. T. Johnson, J. E. Fischer, "Quantized Phonon Spectrum of Single-Wall Carbon Nanotubes", *Science*, **289**,1730 (2000).

[33] P. L. McEuen, in C. Kittel, *Introduction to Solid State Physics*, Eighth Ed., Wiley, 2005, Chapter **18**.

[34] C. Yu, L. Shi, Z. Yao, D. Li and A. Majumdar, *Nanolett*. 5, 1842 (2005)

[35] M. Brandbyge, J-L Mozos, P Ordejon, J. Taylor, and K. Stokbro. *"Density-functional method for nonequilibrium electron transport", Phys. Rev B*, **65**, 165401 (2002).

[36] A. Garcia-Lekue, L-W. Wang "Elastic quantum transport calculations for molecular nano devices using plane waves", *Phys. Rev. B* **74,** 245404 (2006)

[37] H. J. Choi, J. Ihm, "Ab initio pseudopotential method for the calculation of conductance in quantum wires", *Phys. Rev. B,* **59**, 3 pp 2267-2275 (1998)

[38] W. Zhu, E. Kaxiras, "Schottky barrier formation at a carbon nanotube- metal junction", *Appl. Phys. Lett.* **89**, 243107 (2006)

[39] D. Zhang and E. Polizzi, "Efficient Modeling Techniques for Atomistic-Based Electronic Density Calculations", *J. Comp. Elec.* (in press, 2008).

[40] E. Polizzi, A. Sameh. "A Parallel Hybrid Banded System Solver: The SPIKE Algorithm", *Parallel Computing*, **32**, 2, pp. 177-194 (2006).

[41] SPIKE has been released in: http://whait.intel.com

[42] O. Pinaud, "Transcient simulations of resonant tunneling diode", *J. Appl. Phys.* **92**,1 p1987 (2002).

[43] Y. Kawazoe, K. Ohno, K. Esfarjani, Y. Maruyama, K. Shiga and A. Farajian, *"Why the all-electron full-potential approach is suitable for calculations on fullerenes and nanotubes? ", J. of Molecular Graphics and Modelling* **19**, Issue 2, pp 270-273, (2001).

[44] E. Polizzi, (unpublished, 2008).

[45] T. Yasui, A. Nishimura, T. Suzuki, K. Nakayama, and S. Okajima, "Detection system operating at up to 7 THz using quasioptics and Schottky barrier diodes," *Rev. Sci Instrum*. **77,** 066102 (2006).

[46] J. Cao, Q. Wang, D. Wang and H. Dai, "*Suspended Carbon Nanotube Quantum Wires with Two Gates*", Small, **1**, 138 (2005).

[47] D. Prober, "Superconducting Terahertz mixer using a transition-edge microbolometer," *Appl. Phys. Lett.* **62,** 2119 (1993).

[48] M. Lee, L.N. Pfeiffer and K. West, "Ballistic Cooling in a Wide-Band Two-Dimensional Electron Gas Bolometric Mixer", *Appl. Phys. Lett.* **81**, 1243 (2002).

An Empirical Probe to the Operation of SIS Receivers — Revisiting the Technique of Intersecting Lines

C.-Y. Edward Tong*, Abby Hedden, and Ray Blundell

Harvard-Smithsonian Center for Astrophysics, 60 Garden St., Cambridge, MA 02138, USA.

* Contact: etong@cfa.harvard.edu

***Abstract*— An alternate formulation is derived for the technique of intersecting lines which is a well established tool for the analysis of the performance of SIS receivers. This newer formulation is easier to use and provides an estimate of possible experimental error. The significance of the intersecting temperature, T_X, is discussed. Our experiments suggest that both quantum noise and the input match of the SIS mixer contribute to the value of the intersecting temperature.**

I. Introduction

The theory of operation and the technique of implementation of the Superconductor-Insulator-Superconductor (SIS) receiver are now well established. Many tools are available for use to design an SIS mixer [1, 2]. The technique of intersecting lines, introduced by Blundell et al [3], is one such empirical method, put forth to facilitate the analysis of the different constituents of the measured receiver noise temperature. Ke and Feldman [4, 5] developed the theoretical foundation for this technique. In this paper, we revisit the basis of this technique, and discuss an alternate formulation of the method, which is simpler to use. This version of the formulation has been established by the authors many years ago and was communicated to colleagues in the field in private. Both the original formulation and the alternate formulation have been cited in the literature [6,7]. A formal derivation will be presented in this paper.

A range of measurement data on SIS mixers have been examined using our technique. The results further allow us to understand the composition of noise in a practical SIS receiver with optical losses in front of the mixer.

II. Technique of Intersecting Lines

The starting point of the technique is a series of hot/cold load measurements performed on an SIS receiver, at various levels of Local Oscillator (LO) drive. For each incident LO power, we can draw a straight line in a plot of receiver output power (P_{out}) versus load temperature (T_{in}). These lines are found to intersect at a point ($-T_X$, P_X). This technique is illustrated in Fig. 1 with a data set for an SIS receiver operating at 225 GHz.

Using calculations based on the theory of quantum mixing, Ke and Feldman [4] found that the value of T_X given by the intersecting point is simply "***the equivalent input noise temperature of the RF input section of the receiver***", which they refer to as T_{RF}. Their foundation to this argument is: "***the SIS mixer output noise temperature is largely independent of mixer gain for low local oscillator power.***"

However, the original form of the technique of intersecting lines is difficult to implement. Firstly, for a set of N hot/cold load measurements, we have $N(N-1)/2$ intersection points. In general, the intersection points obtained from the higher LO drive measurements are not as clustered together as the ones for lower LO drive. It is difficult to determine the boundary between the low and high LO drive, so the value of T_X is hard to pin down.

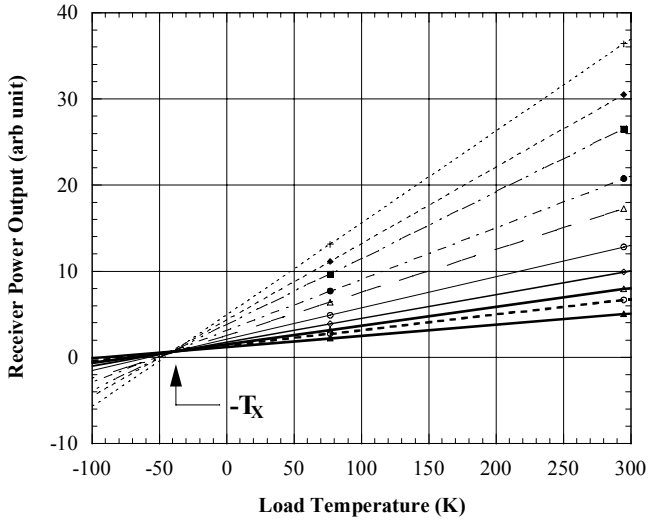

Fig. 1 Illustration of the technique of intersection lines for an SIS receiver operating at 225 GHz. A series of hot/cold load measurements are performed at different LO power levels. Each measurement yields a straight line on the

power output versus input load temperature plot. The lines are found to intersect at a point $T_{in} = -T_X$.

III. Alternate Formulation

In Fig. 2, two of the intersecting lines are drawn on a plot of P_{out} versus T_{in}. These lines pass through the points (T_h, P_h) and (T_c, P_c) which represent the data for the hot and cold load measurements respectively. A property of these lines is that their horizontal intercept is simply $-T_R$, where T_R is the receiver noise temperature. For any given line, we can derive the following equation by writing its slope in two different ways and obtain

$$\text{slope} = \frac{P_h - P_c}{T_h - T_c} = \frac{P_X}{T_R - T_X}$$

$$T_R = \frac{(T_h - T_c)P_X}{P_h - P_c} + T_X \qquad (1)$$

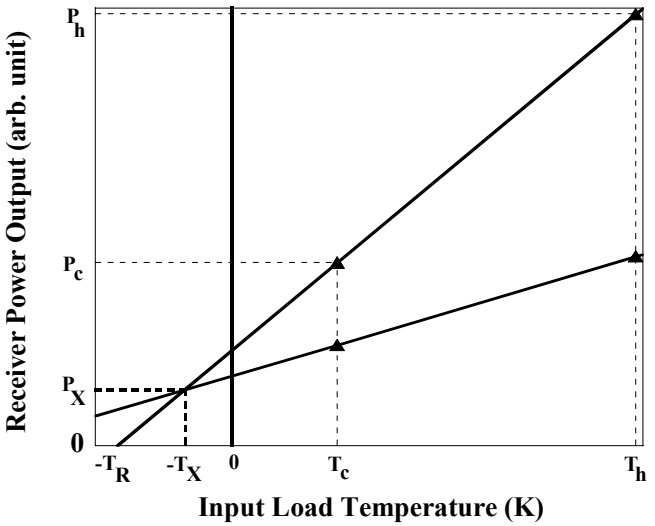

Fig 2 Relation between the intersecting point and the measured hot/cold load data lines. The lines intersect at the point $(-T_X, P_X)$. Each line intercepts the horizontal axis at $T = -T_R$, where T_R is the receiver noise temperature corresponding to that hot/cold load measurement.

Since (P_h-P_c) is proportional to the conversion gain of the receiver, G_C, we can conclude that when T_R is plotted against $1/G_C$ (or equivalently the conversion loss, L_C), a straight line should be obtained for low LO drive and the y-intercept of this line is T_X. In other words, we have,

$$T_R = \frac{m}{G_C} + T_X = mL_C + T_X \qquad (2)$$

where m is the slope of the fitted line.

An example of such linear fitting is given in Fig. 3. In this figure, the conversion loss of the receiver is normalized to that of the data point with the lowest loss. Excluding the first data point which shows significant deviation from linearity, a value of 40.8 K is obtained for T_X, the standard deviation of the fit being 0.6 K. This example demonstrates two desirable properties of the alternate formulation. First, the boundary between low and high LO drive is easily identified by noting the departure from linearity. Furthermore, the approach also gives an indication of the confidence for the value of T_X.

From equation (2), we note that T_X can be interpreted as the part of the measured receiver noise temperature that is independent of the mixer conversion loss. Obviously, this points to noise introduced in front of the SIS mixer, in line with the theory of Ke and Feldman. However, we can also argue that there may be some residual contribution from the mixer itself. To follow this argument, we break the mixer noise temperature, T_M, into a part that is invariant with conversion loss and a part that is linearly dependent on conversion loss:

$$T_M = T_M^{(0)} + L_C T_M^{(1)} \qquad (3)$$

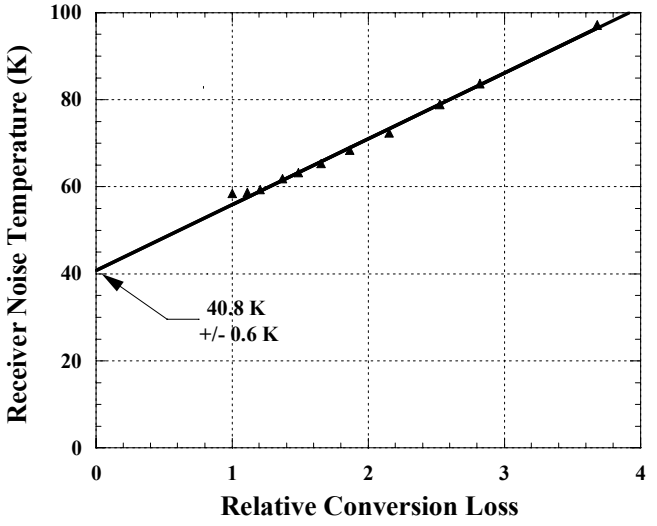

Fig 3 Use of alternate formulation of the technique of intersecting lines. Receiver noise temperature is plotted against conversion loss, with the conversion loss normalized to the first data point. A straight line is fitted to the data points except the first point which shows significant deviation from linearity. The error of the intersecting temperature is estimated by computing the root-mean deviation of the data from the fitted line.

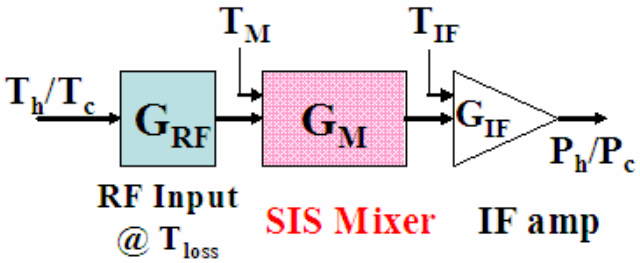

Fig. 4 Schematic of an SIS receiver with RF losses in front of the mixer.

Fig. 4 is a schematic representation of an SIS receiver with a lossy optical element, at a temperature of T_{loss}, in front of the mixer. The receiver noise temperature of such a receiver can be written as:

$$T_R = \left(\frac{1}{G_{RF}} - 1\right)T_{loss} + \frac{T_M}{G_{RF}} + \frac{T_{IF}}{G_{RF}G_M} \qquad (4)$$

After substituting equation (3) and noting that $G_C = G_{RF} G_M G_{IF}$, we obtain

$$T_R = (\frac{1}{G_{RF}} - 1)T_{loss} + \frac{T_M^{(0)} + L_C T_M^{(1)}}{G_{RF}} + \frac{G_{IF} T_{IF}}{G_C} \quad (5)$$

Comparing with equation (2), we can conclude that

$$T_X = (\frac{1}{G_{RF}} - 1)T_{loss} + \frac{T_M^{(0)}}{G_{RF}} \quad (6)$$

IV. Determining Optical Losses

In general, optical losses are incurred at different points along the beam of the receiver, such that noise is injected from noise sources at different temperatures. It is, therefore, quite difficult to derive a model of the overall optical losses in front of an SIS receiver based on a set of simple Y-factor measurements. However, using a set of measurements with and without an optical element, we would be able to deduce the losses incurred by that particular optical element. Let G_{optics} be the insertion gain introduced by an optical element placed in front of the hot/cold input loads, and let T_{optics} be the physical temperature of the element. Equation (6) can be generalized to accommodate such a situation:

$$T_X' = (\frac{1}{G_{optics}} - 1) T_{optics} + (\frac{1}{G_{RF}} - 1) \frac{T_{loss}}{G_{optics}} + \frac{T_M^{(0)}}{G_{optics} G_{RF}} \quad (7)$$

T_X' represents the intersecting temperature obtained by the technique of intersecting lines in the presence of the added optics element, while T_X is the intersecting temperature without the added optics element. On substituting (6) into (7), and after some manipulations, we obtain an expression for the insertion gain of the optics element.

$$G_{optics} = \frac{T_X + T_{optics}}{T_X' + T_{optics}} \quad (8)$$

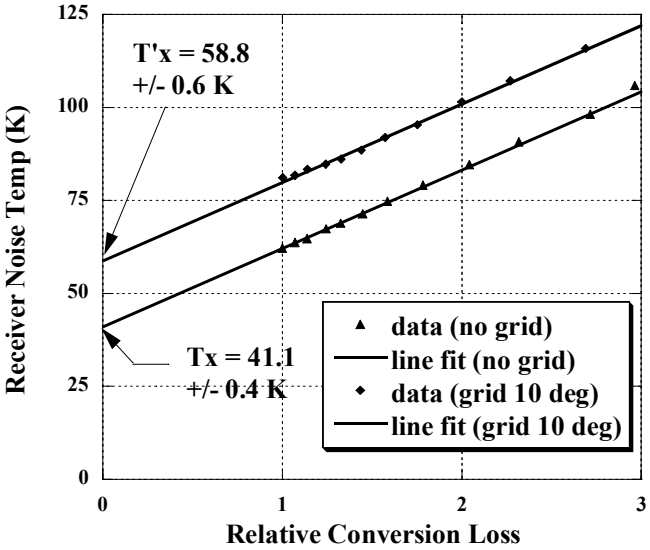

Fig 5 Determination of the optical loss introduced by an optical element using the method of intersecting lines through equation (8).

Fig. 5 illustrates how equation (8) was used to derive the insertion gain of a wire grid placed at 45 degrees to the input beam of a 270 GHz SIS receiver, the grid having been rotated by 10 degrees from the position of minimum loss, which yields an effective projected angle of 14 degrees. From the pair of fitted lines, the insertion loss of the wire grid was found to be 0.950(±0.005), compared to a theoretical value of 0.941(±0.007). It can be argued that the insertion gain of optical components can be determined more simply by a pair of Y-factor measurements with and without the element. However, the simple Y-factor measurement does not afford an estimation of error. Furthermore, the two measurements need to be done at the same bias current, which could be tricky if the optical component under test has poor reflection.

V. Nature of the Intersecting Temperature

When the technique of intersecting lines is applied to a higher frequency SIS receiver, it is found that that the value of T_X generally increases. Fig. 6 shows the data from the measurement of a 678 GHz SIS receiver in the lab [8]. T_X was found to be about 82 K. If this is completely attributed to room temperature optical losses, then it will require more than 1 dB of losses and if such losses occurred at a lower temperature, the hypothetical insertion loss would become even higher. This projection is not compatible with the experimental setup, which consisted of very simple optics setup.

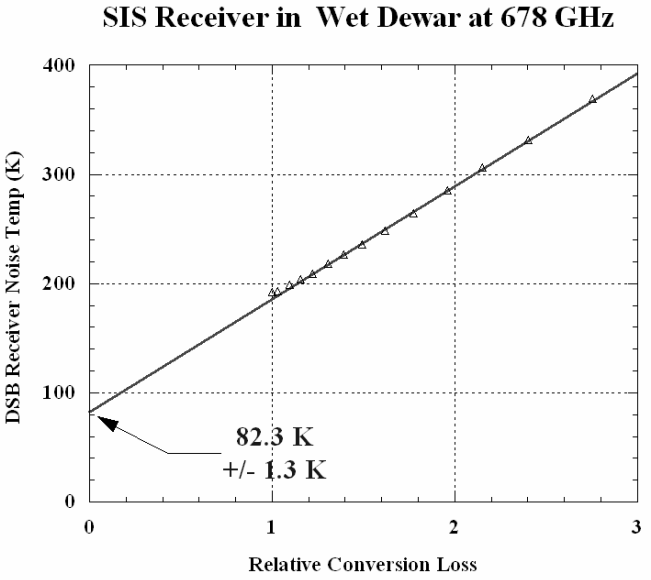

Fig 6 Determination of the intersecting temperature for a 678 GHz SIS receiver.

Since the technique of intersecting line is based upon the Rayleigh-Jean method, quantum noise is included in the measured receiver noise temperature. As the quantum noise is invariant with the mixer conversion efficiency, it is clear that the quantum noise contributes to the intersecting temperature. Contrary to the current belief that the quantum noise comes

from outside the receiver, we argue that since optical elements can be added in front of any SIS mixer, the quantum noise should be accounted for at the input of the mixer, and be included in the mixer noise temperature. Thus equation (6) can be written as:

$$T_X = (\frac{1}{G_{RF}} - 1)T_{loss} + \frac{1}{G_{RF}}\left[T_M^{(0)} + \frac{h\nu}{2k}\right] \qquad (9a)$$

The introduction of $h\nu/2k$ would partially explain why the intersecting temperature is higher for high frequency SIS receiver.

Another important consideration is that for noise measurements, the result is affected by the average match of components. Bearing in mind that SIS mixers do not generally have very good match for both the signal port or LO port, and that lossy optical elements introduce additional reflection, the components of noise temperature may have to be corrected for reflection effects.

In Fig. 7, we show two sets of measurement data obtained from the same measurement setup but using 2 different SIS mixer chips with slightly different tuning circuits. At the LO frequency of 270 GHz, both chips produce a noise temperature as low as 60 K. However, the values of T_X derived from the 2 sets of data are different. In order to explain this phenomenon, we propose that the input reflection coefficient of the mixer should be included in equation (9a). The proposed modification is given as follows:

$$T_X = (\frac{1}{G_{RF}} - 1)T_{loss} + \frac{1}{G_{RF}} \cdot \frac{1}{1-|\Gamma_{in}|^2} \cdot \left[T_M^{(0)} + \frac{h\nu}{2k}\right] \qquad (9b)$$

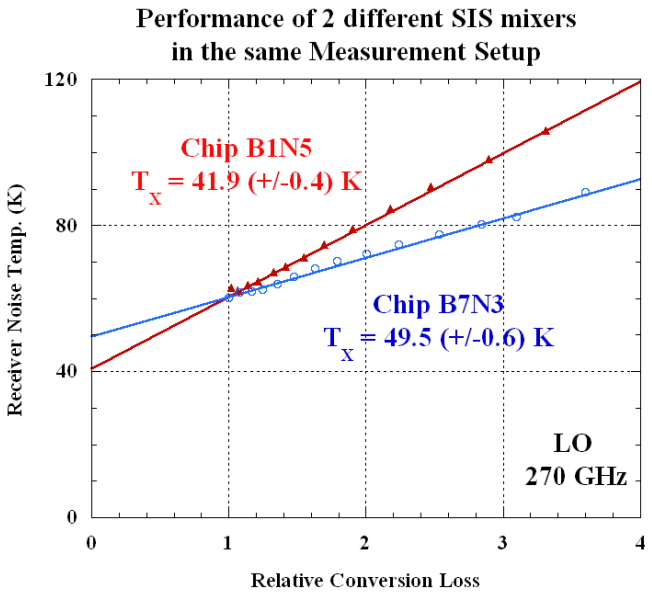

Fig. 7 Applying the technique of intersecting lines to two sets of receiver noise measurement data involving 2 different mixer chips mounted in an identical setup. Both chips show similar optimal noise performance but they yield different intersecting temperature.

Finally, we have studied the effect of dark current on the value of T_X . One of the SIS mixer chips mentioned above was cooled to a lower temperature by pumping on the helium bath. The leakage current at the bias point was reduced from 5.2 μA to 3.4 μA as the helium bath temperature was lowered from 4.2 K to 2.5 K. The leakage ratio of the device changed from 14 to a ratio in excess of 20. As can be seen in Fig. 7, this reduction in dark current does not translate into any significant reduction of the value of T_X. This suggests that $T_M^{(0)}$, the residual value of mixer noise temperature which is invariant with conversion loss, may be quite small.

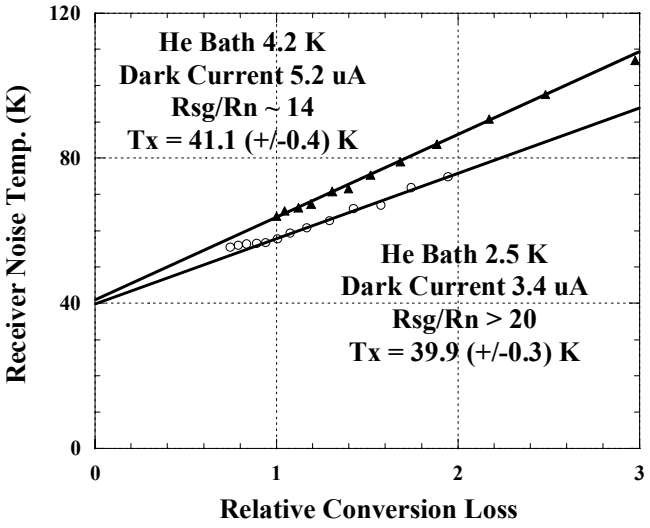

Fig. 8 Effect of dark current on the intersecting temperature. The temperature of the Helium bath of the cryostat was lowered to change the dark current of the SIS junction at the operating point. While an improvement of both the conversion loss and receiver noise temperature was observed, the change in the intersecting temperature is small.

CONCLUSIONS

An alternate formulation for the Technique of Intersecting Lines has been proposed and derived formally. Our approach generally yields a very good linear fit in a plot of receiver noise temperature versus mixer conversion loss, with the intersecting temperature, T_X, appearing as the y-intercept of the fitted line. This new formulation also provides an indication of experimental error.

The intersecting temperature, T_X, arises in part from optical losses in front of mixer and the part of mixer noise temperature, T_M, that is independent of conversion gain. Furthermore, we have shown that the magnitude of optical losses may be estimated from T_X.

From our experimental investigations, we propose that quantum noise is a constituent of T_X, and suggest that the return loss of the mixer can affect T_X, whereas leakage current does not. An equation embodying these results is proposed. Therefore, the intersecting temperature may provide us with useful information on the operation of the SIS receiver.

REFERENCES

[1] A.R. Kerr, S.-K. pan, A.W. Lichtenberger, and H.H. Huang, "A tunerless SIS mixer for 200-280 GHz with low output capacitance and inductance," in *Proc. 9th Int. Symp. Space THz Tech.,* pp. 195-203, Pasadena, CA, Mar. 1998.

[2] J. Ward, F. Rice, G. Chattopadhyay, and J. Zmuidzinas, "SuperMix: a flexible software library for high frequency circuit simulation, including SIS mixers and superconducting elements," in *Proc. 9th Int. Symp. Space THz Tech.,* pp. 269-281, Charlottesville, VA, Mar. 1999.

[3] R. Blundell, R.E. Miller and K. H. Gunlach, "Understanding noise in SIS receivers," *Int. J. IR & MM Waves,* vol. 13, pp. 3-14, Jan. 1992.

[4] Q. Ke, and M. Feldman, "A technique for accurate noise temperature measurements for the superconducting quasiparticle receiver," in *Proc. 4th Int. Symp. Space THz Tech.,* pp. 33-40, Los Angeles, CA, Mar. 1993.

[5] Q. Ke, and M.J. Feldman, "A technique for noise measurements of SIS receivers," *IEEE Trans. Microwave Theory & Tech.,* vol. 42, pp. 752-755, Apr. 1994.

[6] Y. Uzawa, Z. Wang, and A. Kawakami, "Quasi-optical NbN/AlN/NbN mixers in submillimeter wave band," *IEEE Trans. Applied Superconduct.,* vol. 7, pp. 2574-2577, June 1997.

[7] J.W. Kooi, M.S. Chan, H.G. LeDuc, and T.G. Phillips, "A 665 GHz waveguide receiver using a tuned 0.5 μm^2 Nb/AlO_x/Nb SIS tunnel junction," in *Proc. 7th Int. Symp. Space THz Tech.,* pp. 76-85, Charlottesville, VA, March 1996.

[8] C.-Y.E. Tong, R. Blundell, D.C. Papa, J.W. Barrett, S. Paine, X. Zhang, J.A. Stern, and H.G. LeDuc, "A fixed-tuned SIS receiver for the 600 GHz frequency band," in *Proc. 6th Int. Symp. Space THz Tech*., pp. 295-304, Pasadena, CA, Mar. 1995.

Short GaAs/AlAs superlattices as THz radiation sources

D.G.Paveliev[1], Yu.I.Koschurinov[1], V.M.Ustinov[2], A.E.Zhukov[2],
F.Lewen[3], C.Endres[3], A.M.Baryshev[4],P.Khosropanah[5], Wen Zhang[6], K. F. Renk[7], B. I. Stahl[7],
A. Semenov[8] and H.-W. Huebers[8]

[1]*Radiophysics Department, Nizhny Novgorod State University, Russia*
[2]*Ioffe Physico-Technical Institute,St.Petersburg,Russia*
[3]*I.Physikalisches Institut, Universität zu Köln, Germany*
[4] *Institute for Space Research, Netherlands, and*
Kapteyn Astromomical Institute, Groningen University, Netherlands
[5]*Institute for Space Research, Netherlands*
[6]*Purple Mountain Observatory, Chinese Academy of Sciences, Nanjing, China*
[7]*Institut für Angewandte Physik, Universität Regensburg ,Germany*
[8]*DLR Institute of Planetary Research, Berlin, Germany*
* Contact: Pavelev@rf.unn.ru, phone +07-831-4 65 60 31

***Abstract*— Semi-conductor devices based on diodes with Schottky barrier are widely used in room temperature applications in the THz frequency range. However, application of Schottky barrier diodes in these frequencies is limited by several factors: long time of carrier passage through the barrier and relatively large specific capacity. Shorter times of the response and the smaller value of specific capacity can be achieved by creation of the diodes on the basis of semi-conductor superlattices. For these diodes we have also minimized values of series resistance R_s and parasitic capacity C_{par} of a substrate carrying the diode. An area of the active region of the diode was less $2x10^{-8}$ cm^2. Measurement results of the output power level, efficiency and output harmonics content at room temperature are shown for the devices based on the new planar superlattice diodes for input frequency ranges 10-20 GHz, 78-118 GHz and 180-240 GHz. In this report the superlattice device applications as THz radiation sources are discussed.**

I. INTRODUCTION

The terahertz domain of the electromagnetic spectrum with frequencies between 0.5 and 5 THz is of great interest to astronomers and spectroscopists. Today, several efficient technical approaches are well established for high resolution spectroscopy in the THz region. Backward wave oscillators (BWO) are tunable and powerful monochromatic radiation sources, which have been phase locked for frequencies up to 1.26 THz [1]. With sideband techniques even higher frequencies are attainable [2, 3] , which are not easy to handle and laborious in most cases. Alternatively, tunable far IR laser systems [4, 5] achieve excellent spectra. However, the paucity of laser lines prevents the complete coverage of larger spectral ranges. Beside the development of these high resolution sources, also Fourier transform spectrometers are used to cover the complete THz spectral range, albeit with low resolution and limited sensitivity. Furthermore, the absolute accuracy of far-IR The most compact THz radiation sources are THz-frequency lasers and Fourier transform spectrometers strongly depend on the accuracy and the availabilty of calibration lines. Multipliers, based on harmonics generation due to the non-linearity of the current-voltage or capacitance voltage characteristic of a fast electronic device. One well known frequency multiplier is the Schottky barrier diode , which is successfully used in spectroscopy and astronomy by many groups. See references [6, 7]. In most cases the input frequency is supplied by a powerful cw Gunn-Oscillator or a solid state FET amplifier. Most often these devices are operated as frequency doublers and triplers. Higher order harmonics are available too, however, only with considerably lower power. As a consequence Schottky diodes require relatively high input frequencies with considerable input powers in the range of Milliwatts to reach the THz-range. Therefore it is necessary to cascade several multipliers. Good examples for such devices are multiplier chains especially designed for the 1.5 THz regime [8] and 1.9 THz regime [9]. However, their employment for different applications is limited since they are optimized for a certain restricted frequency window.

Application of diodes with barrier Schottky in this frequency range demands increase in limiting frequency of work of the diode, *fp* (the frequency determining the top border of a working range of the diode). Limiting frequency is determined directly by features of the physical processes proceeding in semi-conductor structure: in particular, for diodes with barrier Schottky flight electron inercia active area. So, time of flight for the best diodes about 1 пс [7]. On

the other hand, limiting frequency is substantially caused by influence parasitic capacities of the diode, *C*, and its consecutive resistance, R_s, consisting of resistance of thickness of the semiconductor, contact connections and conclusions of the diode. The specific capacity of the diode with barrier Schottky with the area of active region in units square now makes micron not less than 10^{-7} F/cm^2, and reduction R_s by doping increase is limited to value of concentration $5 \cdot 10^{17}$ sm^3 [10, 7].

Shorter times of the response and smaller sizes of values of specific capacity can be achieved by creation of planar diodes on the basis of semi-conductor superlattices [11, 12]. Superlattices have also the volt-current characteristic with negative differential conductivity [13] which is kept down to frequencies above 1 ТГц [14]. Set of these properties makes superlattices by rather attractive object of researches, as the generators made on their basis and frequency multipliers and as detectors and mixers can form a basis of new solid-state sources and receivers of THz electromagnetic waves.A semiconductor superlattice [13] can show a negative differential resistance giving rise to the build-up of domains. Recently it has been shown that domains in semiconductor superlattices can be used for frequency multiplication. During a cycle of a microwave field, domains are created and destroyed. The corresponding current gives rise to higher harmonics of the microwave field. The frequency multiplication has been demonstrated for fundamental frequencies near 20 GHz [15] and near 70 GHz [16]. Here, we report on a frequency multiplier ,based on SLED, which operates as radiation sources up to 2.7 THz. We produced comparisen SLED and Schotty diode by observation of the submm waves beets arising in SLED and Schottky structures, illuminated by two microwave signals. Studying the emission spectrum from SLED was driven by an electric field of 20 GHz, near 100GHz with a Fabry-Perot interferometer, 120-140GHz and 190-220 GHz with a Fourier Transform Spectrometer (FTS), by driving HEB at 1THz with a SL-tripler and by investigating with Superlattice Multiplier, pumped by BWO(110,210-260GHz), an absorption line of deuterated water vapor and methanol gas.

II. Superlattice Electron Device

The key element of the frequency multipliers , harmonic generator was a superlattice electron device(SLED). The made SLED (Fig.1) had two ohmic contacts of the different area located on the top border of a superlattice in parallel to its layers in the structure. High-frequency currents flew through a gold pad, the active element, an n^+ GaAs layer and the large-area mesa to the second contact pad or in the reverse direction. The superlattice (Fig.2) with length 112 nm had 18 periods, each period (length 6.22 nm) with 18 monolayers GaAs and 4 monolayers AlAs and was homogeneously doped with silicon (2×10^{18} cm^{-3}).

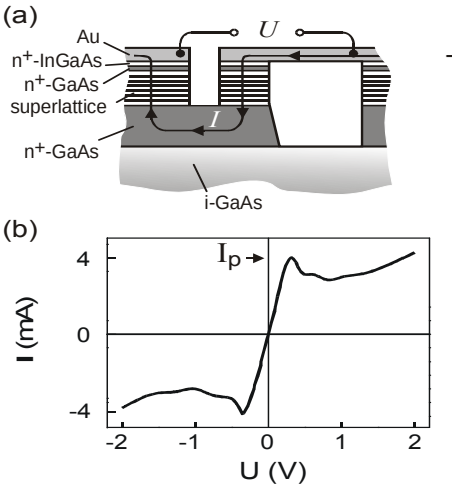

Fig.1 (a) Sketch of the SLED based on the GaAs/AlAs superlattice; (b) SLED current-voltage characteristic at 300 K

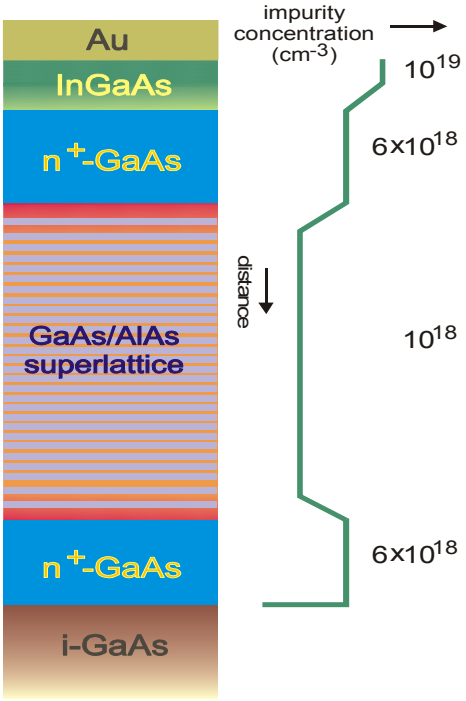

Fig.2 the view of the superlattice structure

The miniband width (25 meV) was sufficient to lead to miniband rather than hopping transport. By molecular beam epitaxy, we had grown, on an intrinsic-GaAs substrate, an n^+ GaAs layer (thickness 1.5 μm; doping 6×10^{18} cm^{-3}), GaAs/AlAs gradual layer (thickness 32 nm), then the superlattice, again a gradual layer and n^+ GaAs and an n^+ InGaAs gradual layer (25 nm) and finally an n^+ InGaAs layer (20 nm, doping 10^{19} cm^{-3}) serving as ohmic contact. The gradual layers delivered smooth transitions with respect to layer thicknesses and doping, respectively.

Current-voltage characteristic of the SLED subject to a static voltage is presented in Fig. 1b. The current increases almost linearly for a voltage smaller than the critical voltage (U_c), reaches its maximum value (I_p) at the critical voltage

and then decreases. Kinks in the current-voltage characteristic can be attributed to the formation of the electric field domain within the superlattice region. For definition of resistance of ohmic contact the made SLED were used, namely, the voltage enclosed to the SLED, was expressed through a current proceeding through it and resistance of the SLED. Calculation and measurement of resistance of various sites SLED structures have allowed to find resistance of ohmic contact of the small area. Results of calculation of resistance of contact R_k for structures of the various area are submitted on fig. 3 (the top part). In the considered file of SLEDs (100 pieces) with the area of active region from 2 up to 6 μ^2 prevail. Resistance of contact to growth of the area decreases as 1/S, therefore it is expedient to proceed to resulted resistance R_k x S of contact. On fig. 3 (the bottom part) is submitted dependence of the resulted resistance of contact on its area. Averaging on a file of SLED gives average value of the resulted resistance about $2x10^{-7}$ ом/sm^2. The received value of the resulted resistance is in the good consent with values of resistance of the ohmic contacts generated by a method molecular-beam epitaxi on basis Ga_{1-x} In_x As ($5x10^{-7}$ ом/sm^2) [12], and also InAs ($2x10^{-7}$ ом/sm^2) [7]. On fig. 3 (insert) results of comparison of resistance of ohmic contact R_k with resistance of superlattice R_2 and resistance *n* +-layer Rn are resulted. For the areas of active region of the diode smaller 2 μ^2 resistance *R*n is less than resistance of ohmic contact because of strong dependence of the last on the area. Full consecutive resistance of the diode (R_k +R_n) appears much less resistance of a superlattice. With growth of the area of active region contact resistance quickly decreases, resistance R_n varies slowly and becomes comparable with resistance of a superlattice R_2 at $S=10$ μ^2.

Thus, use of threefold connection InGaAs at formation of ohmic contact in SLEDs on basis GaAs/AlAs of a superlattice has allowed to reduce considerably consecutive resistance of the SLED in comparison with its value for SLEDs with ohmic contact on the basis of alloy Au-Ge. For reduction of parasitic capacity of substrate C_{par} of the SLED, the substrate thickness in the place of the air bridge has been finished up to 2-4 microns. See Fig.1. The mechanical stability of the SLEDs appeared sufficient for carrying out of electric measurements on a direct current and mounting in various circuits of devices of THz range of frequencies. Thus limiting frequency of such SLEDs with the area of active area 4 μ^2 on the basis of a superlattices from 18 periods has made approximately 4-6 THz

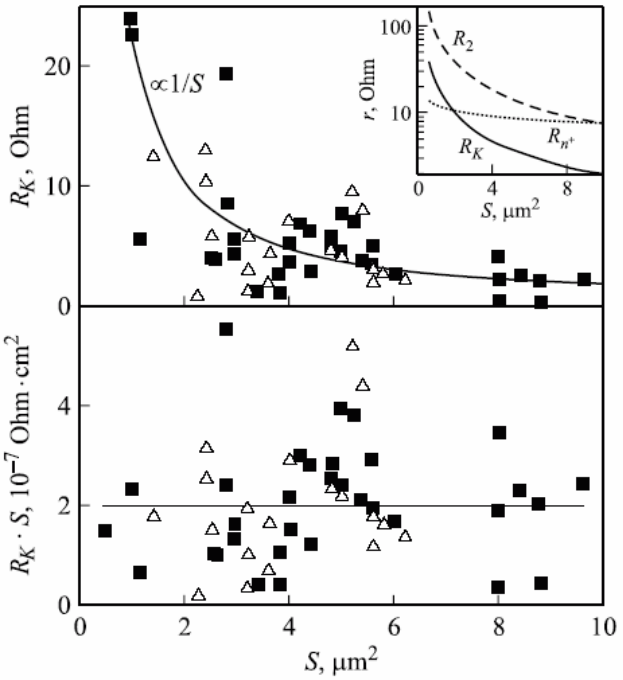

Fig.3 The top part: dependence of resistance of ohmic contact from its areas for SLEDs with length of a superlattice of 18 periods, received as a result of processing experimental data and by averaging on all file of SLEDs (a continuous line). The bottom part: dependence of the resulted resistance of ohmic contact on its area received as a result of processing experimental data and by averaging on all file of diodes (the same designations). An insert: dependence of contact resistance (a continuous line), resistance of a superlattice (a shaped line) and n a +-layer of the SLED (dashed line) from the area of active region.

. Superlattice Structures are made in Ioffe Physico-Technical Institute,St.Petersburg. SLED are designed and made in Radiophysics Department, Nizhny Novgorod State University.

III. Measurements

The block for test measurements are shoun on the Fig.4 The block consist of a single mode waveguide,diagonal horn and SMA connector.For different frequency ranges the waveguide sizes are shanged. For multiplers the single mode waveguide for pump was added.

We produced measurements for direct comparisen SLED and Schottky diode.For this we used the method [17]

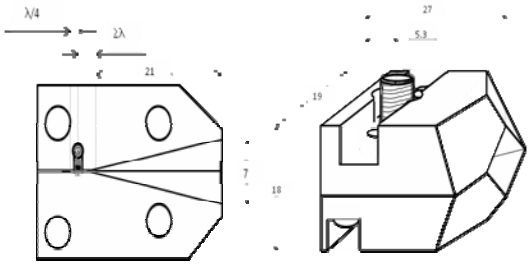

Fig.4 Block for test measurements (output frequency more 550GHz)

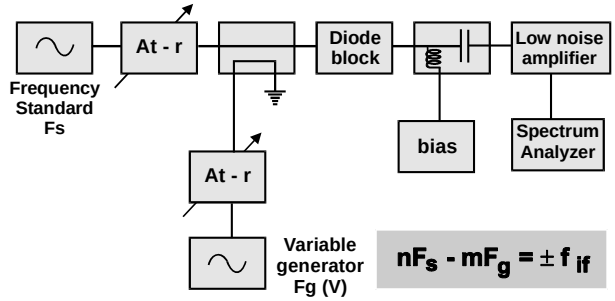

Fig.5 Experimental setup for observation of the submm waves beets

Exprimental setup are shown on the fig.5 . The tested structures, mounted in the diode block, are irradiated by two signals F_s and F_g. Low frequency signal of beats f_o between the harmonics nF_s and mF_g,arising in the tested strucnure, can be determined with equation $nF_s - mF_g = \pm f_o$, where n and m are whole numbers. The signal f_o is fixed by spectrum analyzer with input band 0.1-1.5GHz.Varing F_g it`s possible to determing the maximum number of SBMM harmonics m and m,arrising in the tested structures.

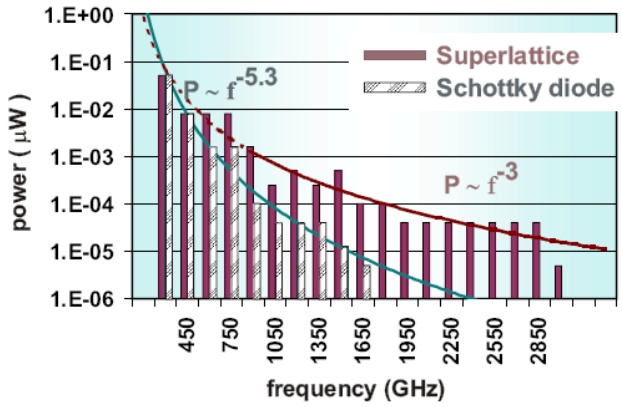

Fig.6 Result of comparison of the SLED and Schottky diode

The result of comparison of the SLED and Schottky diode are shown in fig. 3 for F_g 100-115GHz and F_s 125-150GHz.It shows us ,that SLED is more effective for generating high number harmonics than Schottky diodes.

Measurements have been carried out in Radiophysics Department, Nizhny Novgorod State University.

IV. Dependence of the Radiation Power Emitted by a SLED Subject to a High Frequency Electric Field at Different Temperature

Output spectrum of the harmonic generator was measured using Fourier Transform Spectrometer (FTS). 20 GHz monochromatic signal was applied from the HP **83752B** frequency synthesizer to the harmonic generator in all measurements.

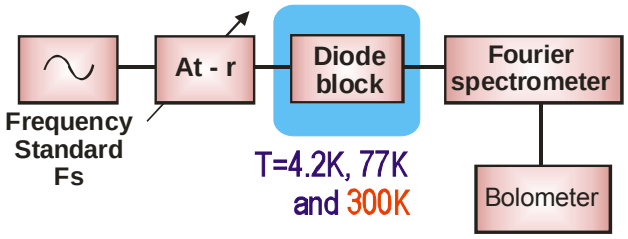

Fig.7 Experimental setup for harmonics generation of SBMM waves

Harmonic generator was mounted into an Infrared Lab dewar, so that measurements at different temperatures can be performed. Results of the tests at 300 K, 77K, and 4.2 K are presented in Fig. 2. Absolute amplitude of the response was not calibrated. The magnutude of the harmonics become one order as large with the temperature decreasing from 300 K to 4.2 K.

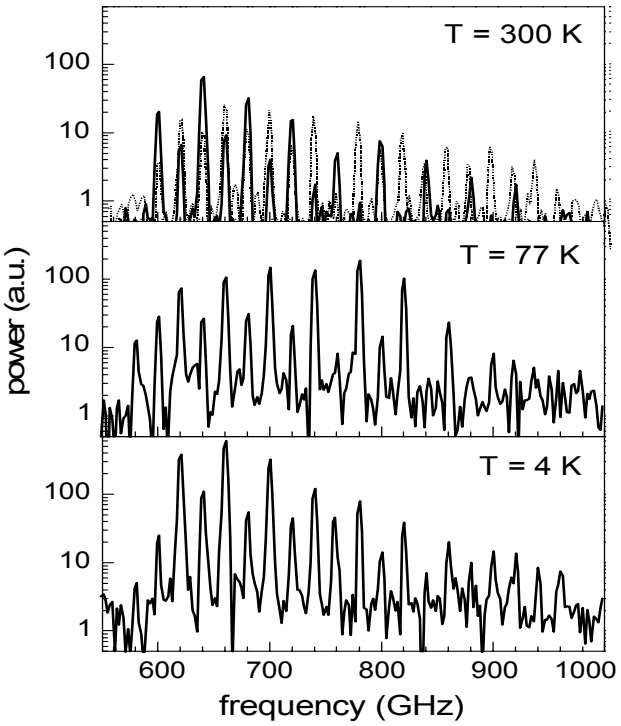

Fig. 8 FTS spectrum of the harmonic generator at 300 K (upper part), 77K middle part), and 4.2 K (lower part) for input signal power of 5 dBm (dotted) and 13.2 dBm (solid)

Results of the tests at 300 K, 77K, and 4.2 K are presented in Fig. 8. Absolute amplitude of the response was not calibrated. The magnitude of the harmonics become one order as large with the temperature decreasing from 300 K to 4.2 K.

Measurements have been carried out in Institute for Space Research (SRON).

V. Superlattice Frequency Multiplier For TheSubmillimeter Wavelength Range

The SLED was built in a two-waveguide arrangement (Fig. 9 c) suitable for the microwave pumping and the extraction of higher-harmonic radiation. We analyzed radiation with a Fabry-Perot interferometer [18] (Fig. 9d) and registered radiation with a liquid helium cooled silicon bolometer.

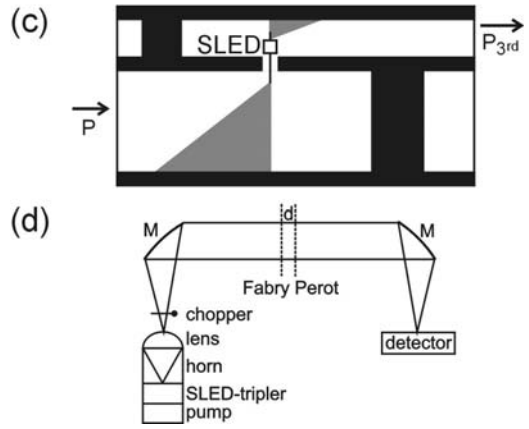

Fig. 9 c,frequency tripler. d, arrangement.

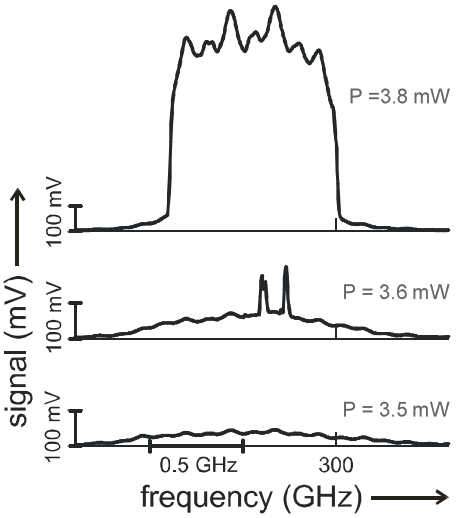

Fig. 10: Output signal of the frequency multiplier for the third harmonic (around 300 GHz).

The emission was especially strong at a frequency near 300 GHz (Fig.10). The emission characteristic has been obtained by pumping the tripler with radiation of a frequency synthesizer (3 mW power). By pumping with a stronger source (BWO) we obtained strong emission in a larger frequency band. The Fabry Perot interferogram (Fig.11) showed that the 3rd harmonic was the strongest. However, also higher harmonics have been observed in the Fabry Perot interferogram curve. Various investigations of the frequency tripling have been published elsewhere [19, 20].

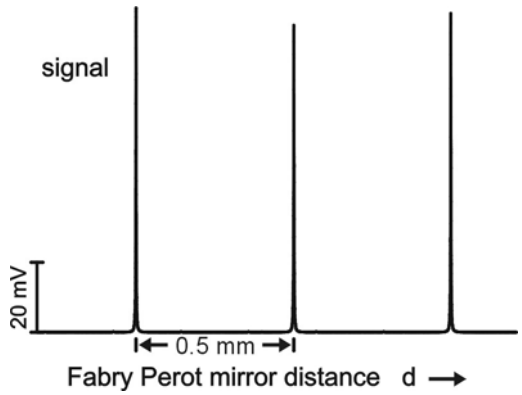

Fig.11 Fabry Perot interferogram.

Also we report a semiconductor superlattice frequency quintupler for tunable generation of submillimeter wave radiation in a wide frequency range. Pump radiation (frequency 100 -140 GHz few mW) was converted to 5th harmonic radiation (500 to 700 GHz; power few μW).

The superlattice quintupler Fig.12 has an input waveguide with a low frequency cutoff at 75 GHz and an output waveguide (and a horn) with a cutoff frequency of 450 GHz. A superlattice diode is coupled by a finline antenna to the input waveguide and a wire antenna to the output waveguide.

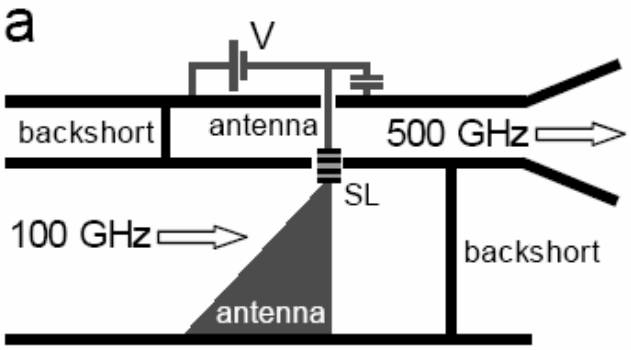

Fig.12 Fabry Perot interferogram.

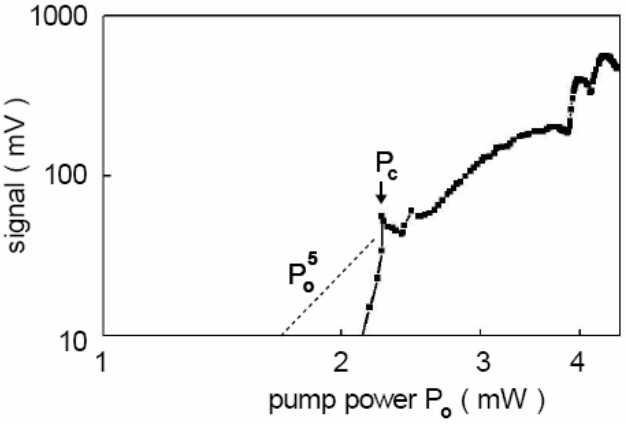

Fig.13 The 5th harmonic power

The quintupler was pumped with radiation of Gunn oscillators. We determined the spectrum of the output radiation either by use of a Fabry-Perot interferometer with a Golay cell as detector. A power meter allowed to measure the power of the radiation.

The 5th harmonic power Fig.13 showed a strong increase above a critical pump power P_c and then increased further with increasing pump power. Below P_c, the signal is increasing much steeper than the dependence (P_0^5) expected for a conventional frequency quintupling. We attribute P_c to the onset of domain formation; i.e. at P_c, the amplitude of the pump field reached the critical field (V_c). Accordingly, at larger pump power, the pump field was able to create to annihilate during each half cycle a domain giving rise to the frequency multiplication. The power level at strongest pumping was few μW. It was almost the same over the whole frequency range 500 - 700 GHz we studied. The power corresponded to a power conversion of about 0.1 percent.

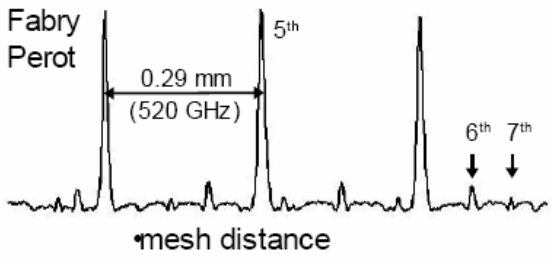

Fig.14 Fabry Perot interferogram.

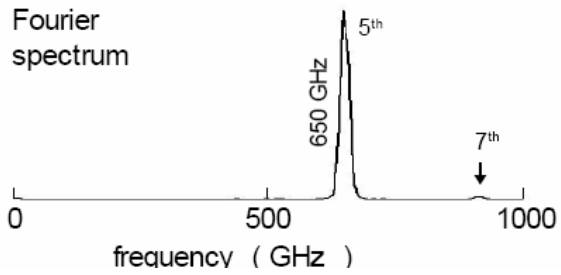

Fig.15 Fourier spectrum

The Fabry-Perot interferogramme and the spectrum measured with the Fourier transform spectrometer Fig.14 and Fig.15 indicate, that the emission was mainly at the 5th harmonic. The Fabry-Perot interferogramme delivered, additionally, signal peaks for the 6th and 7th harmonics. The 6th harmonic occurred because of not pure asymmetry of the superlattice. The 6th harmonic did not appear in the spectrum that was obtained for a higher input frequency. The reason is most likely a different matching to the output waveguide.

Measurements have been carried out in Institut für Angewandte Physik, Universität Regensburg.

VI. Experimental Study of the Harmonic Generators, Based on Superlattices, in Wide Frequency Range 120-220 GHz.

The non-biased superlattice diodes was driven by an electric field with of 120-140GHz and 190-220 GHz. For measurements the same experimental setup shoun on the fig.7 was used. The frequency synthesizers (20 GHz) with frequency multiplier chains and MIMIC [18] power amplifiers was used for pump. We observed intensive enough 3th (apr.50-100μW), 5th (apr.10-20μW),7th (apr.1-2μW),9th(apr. less 0.1μW).

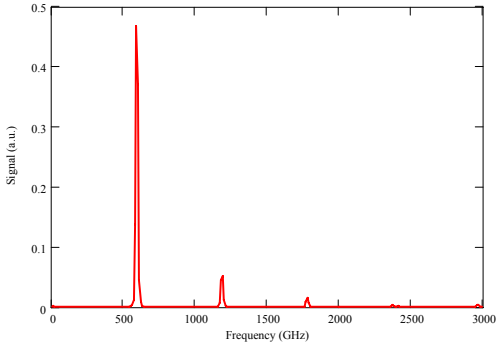

Fig.17 The output signal with input frequency 197.4GHz. It`s observed intensive 3th (apr.50-100μW) harmonic. Before bolometer was used 12dB attenuation.

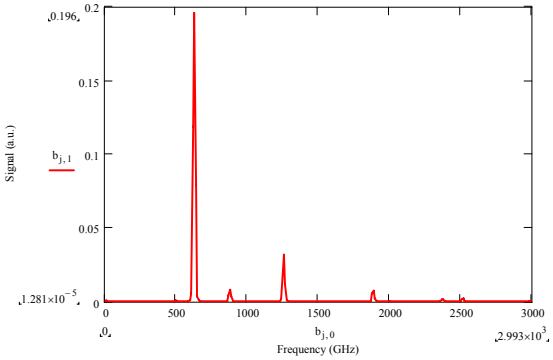

Fig.18 The output signal with input frequency 124 GHz. It`s observed the intensive 5th (apr.10-20μW)and 7th(apr.1-2μW) harmonics. Before bolometer was used 12dB attenuation.

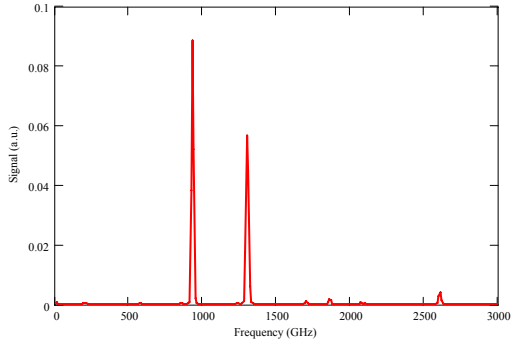

Fig.19 The output signal with input frequency 187.2 GHz. Observed the intensive 5th and 7th (1-2μW) harmonics. Even the 9th harmonic was visible (100-200nW).

Measurements have been carried out in Institute for Space Research (SRON).

VII. DRIVING HEB MIXER WITH A SUPERLATTICE MULTIPLYER

The possibility of using the superlattice (SL) multiplier as a local oscillator at a frequency of 1THz for a hot-electron bolometer (HEB) mixers has been demonstrated in the experiment, which was carried out in the DLR Institute of Planetary Research, Berlin. The setup is shown in Fig. 20; it consists of a phase-locked backward-wave oscillator at 300 GHz and the SL Tripler with a diagonal horn. Fig.21 and Fig.22 show relative output power and the intensity radiation pattern of the SL Tripler, respectively. The optimally pumped voltage-current characteristic of the HEB mixer is shown in Fig.23 along with the unpumped curve. The output power of the SL-Tripler slightly less than 1 μW was estimated with the calibrated Golay cell detector.

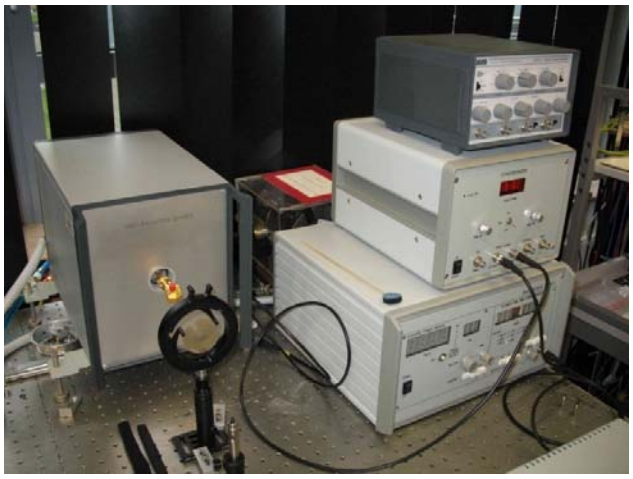

Fig.20 Experimental setup. 300 GHz BWO with an output power ≈20 mW (multimode) and the SL-Tripler providing output power ≤1μW at frequencies up to 1 THz.

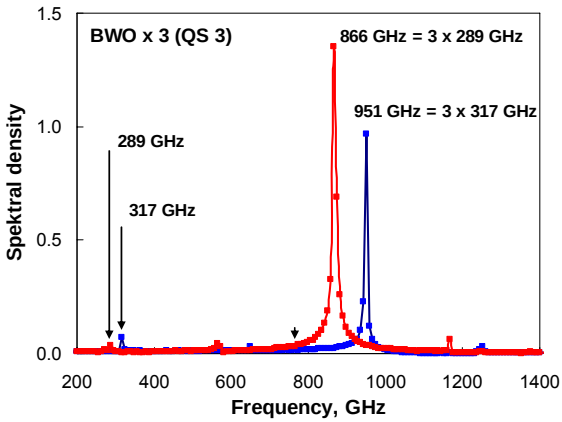

Fig.21 Relative ooutput power of the SL-Tripler in the frequency band 866-951GHz.

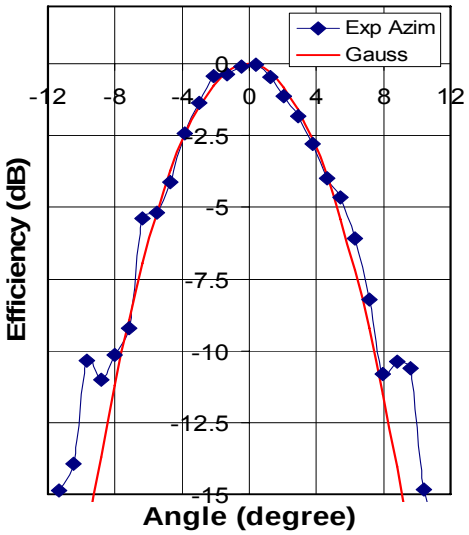

Fig.22 Intensity radiation pattern in the far field of the SL-Tripler horn.

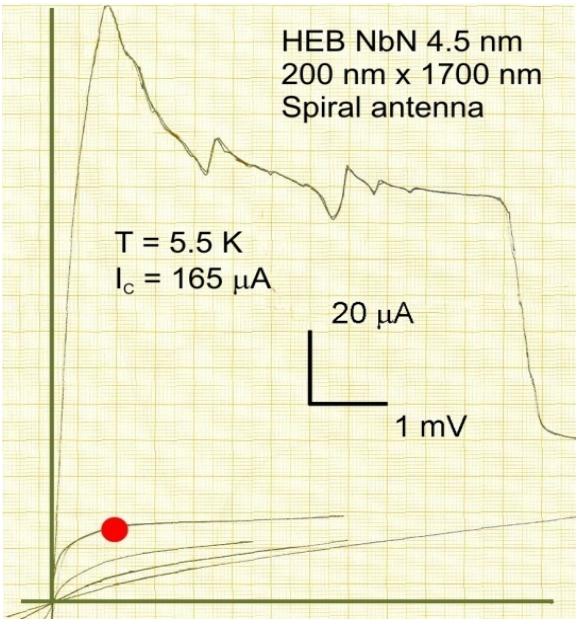

Fig.23 Voltage-Current characteristics of the HEB optimally pumped with the SL-Tripler. Red point marks the optimal operation regime.

VIII. SL Multipliers for Broadband Molecular Spectroscopy covering 300GHz to 2700GHz without gaps

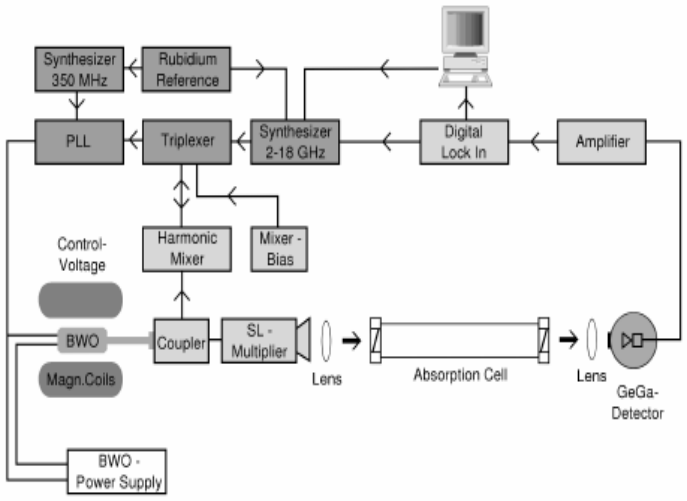

Fig.24 A sample Setup of the THz-Spectrometer with Superlattice Multiplier. I.Physikalisches Institut, Universität zu Köln, Germany.

In the present spectrometer setups we used two different SL multipliers designed for input frequencies centered at 100 GHz (SL I) and 250 GHz (SL II). In all experiments presented here only unbiased Superlattice multipliers were used in order to maximize the power fed into the odd numbered harmonics.

The SL multipliers have been used in combination with two continuously tunable BWO oscillator as input radiation sources, delivering output powers of 10-60 milliwatts througout the entire frequency range from 78 to 118 GHz for SL I and from 130 to 260 GHz for SL II. The BWOs are stabilized in frequency via a phase locked loop (PLL) w.r.t. a rubidium reference with a frequency accuracy ¢*f*=*f* = 10¡11. For detection of SL output power below 2.33 THz a magnetically tuned InSb Hot Electron Bolometer (NEP = 3:5pW=*p*Hz) has been deployed, while a Ga doped Ge photoconductor with significantly higher sensitivity (NEP = 0:6pW=*p*Hz) has been used for higher frequencies. A sketch of the spectrometer setup is shown in Fig.19. The main fraction of the fundamental output radiation generated by the BWO is coupled into the SL multiplier and only a small fraction is used for the PLL circuitry. Two high density polyethylene lenses focus the harmonics generated in the SL through a 3.5 m long absorption cell into the detector. The detector signal is frequency selectively amplified, and 4 demodulated by a lock-in amplifier. In all cases the 2*f* frequency modulation technique is used for recording spectra.

a)

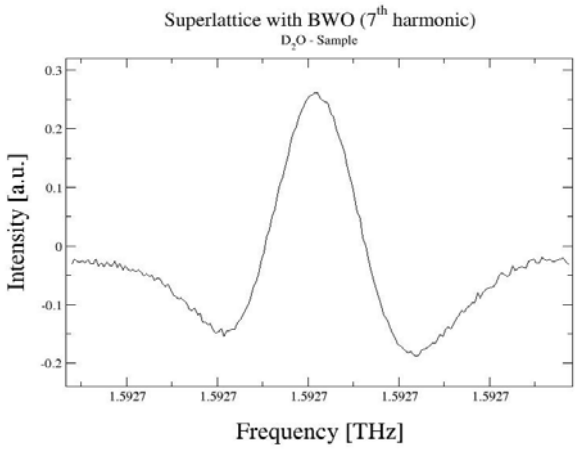

b)

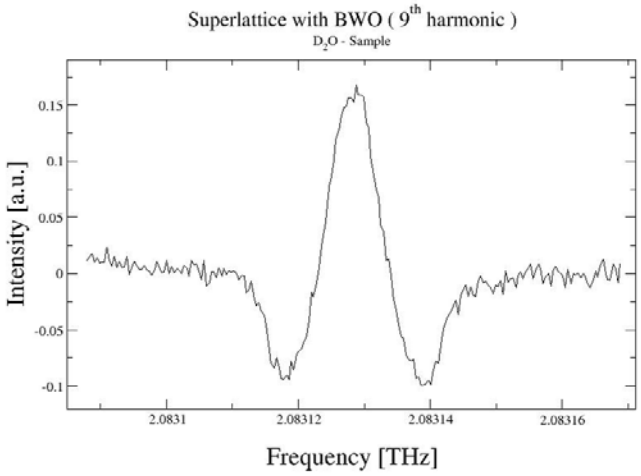

c)

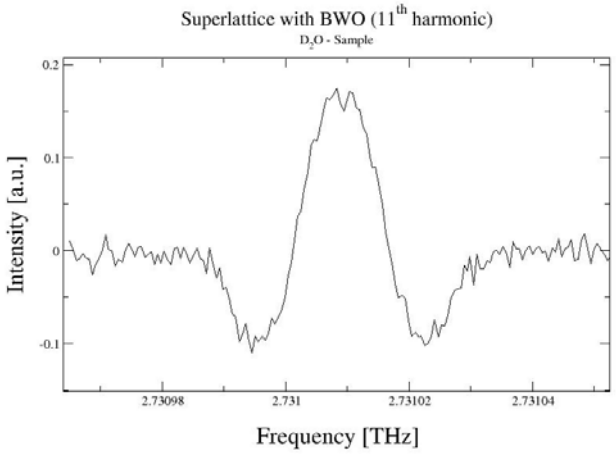

Fig. 25 a,b,c Spectrum of deuterated water vapor, obtained by the 7-11th harmonic of the superlattice frequency multiplie SL II

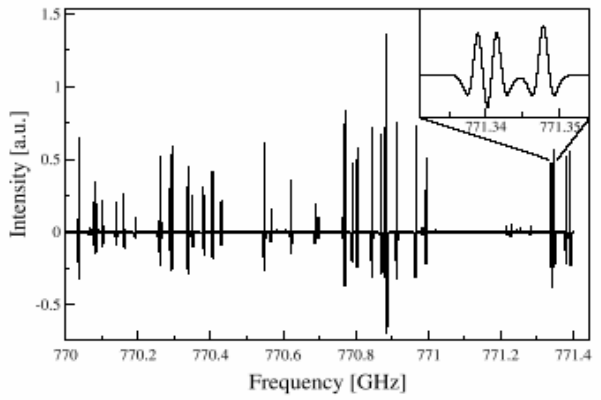

Fig.26 Broadband scan of methanol using the 7th harmonic generated by SL I the upper right corner a blow-up is shown, which demonstrates the high spectral resolution of the measurement and the low noise

The measurements show us that the SL operated sources are indeed producing higher order odd harmonics in sufficient supply for laboratory spectroscopy, very high line accuracies can be achieved , broad band scans are feasible and overall very high frequencies up to 2.7 THz can be used for spectroscopy.

Measurements have been carried out in I.Physikalisches Institut, Universität zu Köln.

IX. The measurements mixing signals of superlattice frequency multiplier and gas laser in THz frequency band using HEB mixer.

HEB mixers now is the most sensitive receiver in THz frequency band. We used this device for investigation harmonic content of superlattice multipliers, pumped in frequency range 100-120GHz , near 1800GHz and 2500GHz. We observe the 17th Fig.27 and 19th Fig.28 harmonics by using the line of gas laser 1891.2743, and 23th Fig.29 and 25th Fig.30 by using the line of gas laser 2522.7816.

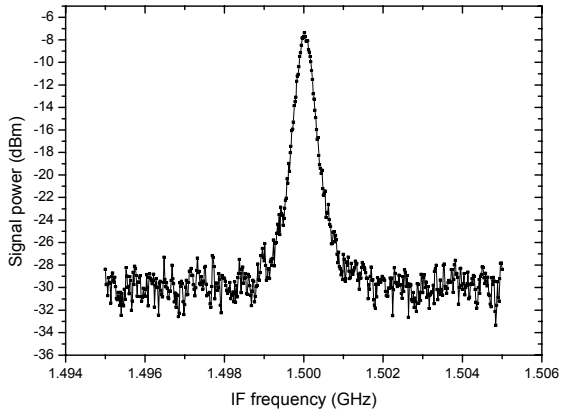

Fig.27 Mixing signal of superlattice frequency multiplier (F_s =111.1631941 x 17 = 1889.7743 GHz) and the gas laser at 1891.2743 GHz using HEB mixer

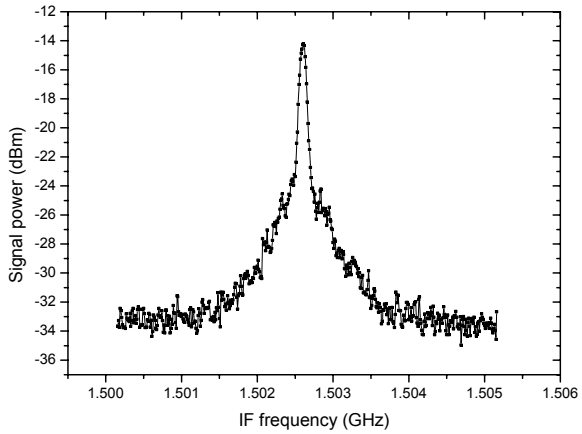

Fig.28 Mixing signal of superlattice frequency multiplier (F_s =99.46179921 x 19 = 1889.7742 GHz) and the gas laser at 1891.2743 GHz using HEB mixer

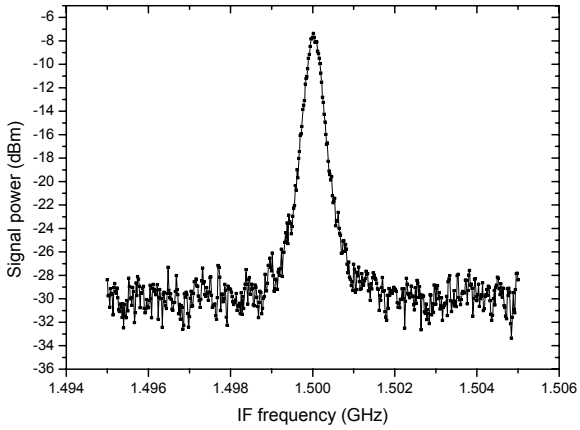

Fig.29 Mixing signal of superlattice frequency multiplier (F_s =109.629391x 23 = 2521.1475993 GHz) and the gas laser at 2.522.7816 GHz using HEB mixer

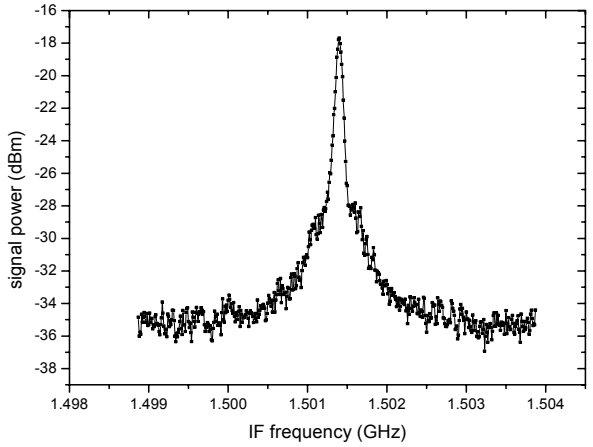

Fig.30 Mixing signal of superlattice frequency multiplier (F_s =100.85164 x 25 = 2521.2816 GHz) and the gas laser at 2.522.7816 GHz using HEB mixer

Measurements have been carried out in Institute for Space Research (SRON).

CONCLUSION

The optimisation of SLED for SBMM application is produced. It`s found that multipliers based on SLED have Higher Harmonic Content compared to Schottky devices. The Capability for High Resolution Spectrometer up to 3THz is demonstrated. Room temperature SLED multipliers operation as well as 77K and 4K is shown. On the base of measurements in various radio systems SBMM lengths electromagnetic waves it is possible to draw a conclusion, that devices on short GaAs/AlAs superlattice now are real Thz radiation sources.
In future this devices will be invstigated for locking quantum cascade laser up to 4 THz with 20-50 GHz LO and for broadband LO for SIS and HEB THz mixers.

ACKNOWLEDGMENT

This work has been supported by the Russian Foundation of Basic Research (grant N 06-02-16598a).

This work has benefited from research funding from the European Community's sixth Framework Programme under RadioNet R113CT 2003 5058187 AMSTAR.

This work was supported in part by the German Federal Ministry of Education and Research (grant no. RUS 08/012).

A.E.Zhukov acknowledges support by the Russian Federation Presidents grant MD-3858.2007.2 for young scientists.

F. Lewen and Chr. Endres acknowledge support by the German Science Foundation via grant SFB 494.

W. Zhang was supported by China Exchange Programme, which is the framework of the scientific cooperation between the Netherlands and P.R. China, and is executed by KNAW and CAS.

REFERENCES

[1] [1] S. P. Belov, G. Winnewisser, and E. Herbst, J. Mol. Spectrosc. 174, 253 (1995).
[2] [2] F. Lewen, E. Michael, R. Gendriesch, J. Stutzki, and G. Winnewisser, J. Mol. Spectrosc. 183,207 (1997).
[3] [3] E. Rusinek, H. Fichoux, M. Khelkhal, F. Herlemont, J. Legrand, and A. Fayt, J. Mol. Spec-trosc. 189, 64 (1998).
[4] [4] K. M. Evenson, D. A. Jennings, and F. R. Petersen, App. Phys. Lett. 44, 576 (1984).
[5] [5] L. R. Zink, P. de Natale, F. S. Pavone, M. Prevedelli, K. M. Evenson, and M. Inguscio, J.Mol. Spectrosc. 143, 304 (1990).
[6] [6] F. Lewen, S. P. Belov, F. Maiwald, T. Klaus, and G. Winnewisser, Z. Naturforsch. 50 a, 1182(1995).
[7] [7] F. Maiwald, F. Lewen, V. Ahrens, M. Beaky, R. Gendriesch, A. N. Koroliev, A. A. Negirev,D. G. Paveljev, B. Vowinkel, and G. Winnewisser, J. Mol. Spectrosc. 202, 166 (2000).
[8] [8] M. C. Wiedner, G. Wieching, F. Bielau, K. Rettenbacher, N. H. Volgenau, M. Emprechtinger,U. U. Graf, C. E. Honingh, K. Jacobs, B. Vowinkel, et al., Astron. Astrophys. 454, L33 (2006).
[9] [9] T. de Graauw, E. Caux, R. Guesten, F. Helmich, J. Pearson, T. G. Phillips, R. Schieder,X. Tielens, P. Saraceno, J. Stutzki, et al., in *Bulletin of the American Astronomical Society*,1219 (2005).
[10] [10] F.Maiwald,F.Lewen,B.Vowinkel, W.Jabs, D.G.Paveljev,
[11] ,M.Winnerwisser, G. Winnerwisser. IEEE Microwave and Guided Wave
[12] Letters, **9**, 198 (1999).
[13] [11] S. Brandl, E. Schomburg, R. Scheuerer, K. Hofbeck, J. Grenzer, K.F.
[14] Renk, D.G. Pavel'ev, Yu. Koschurinov, A. Zhukov, A. Kovsch, V. Ustinov,
[15] S. Ivanov, P.S. Kop'ev. Appl. Phys. Lett., **73**, 3117 (1998).
[16] [12] E. Schomburg, K. Hofbeck, R. Scheuerer, M. Haeussler, K.F. Renk, A.-
[17] K. Jappsen, A. Amann, A. Wacker, E. Scholl, D.G. Pavel'ev,
[18] Yu.Koschurinov. Phys. Rev. B, **65**, 155320 (2002).
[19] [13] L. Esaki, R. Tsu. IBM J. Res. and Dev., **14,** 61 (1970).
[20] [14] S. Winnerl, E. Schomburg, J. Grenzer, H.-J. Regl, A. A. Ignatov, A. D.
[21] Semenov, K.F. Renk, D.G. Pavel'ev, Yu. Koschurinov, B. Melzer, V.
[22] Ustinov, S. Ivanov, S. Schaposchnikov, P.S. Kop'ev. Phys. Rev. B, **56**,
[23] 10303 (1997).
[24] [15]M. Häußler, R. Scheuerer, K. F. Renk, Yu. Koschurinov, D. G.
[25] Pavel'ev, Electron. Lett. **39**, 628 (2003).
[26] [16]R. Scheuerer, M. Häußler, K. F. Renk, E. Schomburg, Yu. I.
[27] Koschurinov, D. G. Pavel'ev, N. Maleev, V. Ustinov, A. Zhukov, App.
[28] Phys. Lett. **82**, 2826 (2003).
[29] [17] Woods D.R., Strauch R.G. // Proc. IEEE. 1966. V. 54. P. 673.
[30] [18]K. F. Renk and L. Genzel, Appl. Optics **1**, 642 (1962).
[31] [19] Robert R. Ferber, John C. Pearson, Todd C. Gaier, Lorene A. Samoska , Frank W. Maiwald, Mary Wells, April Campbell, Gerald Swift, Paul Yocom, K.T.Liao, "W-Band MMIC Power Amplifiers for the Herschel HIFI Instrument," 14th Int. Symp. On Space THz Technology, Tucson,22 April 2003.
[32] [19] F. Klappenberger, K. F. Renk, P. Renk, B. Rieder, Yu. I.
[33] Koschurinov, D. G. Pavelev, V. Ustinov, A. Zhukov, N. Maleev and A.
[34] Vasilyev, Appl. Phys. Lett. 19, 3924 (2004).
[35] [20] K. F. Renk, B. I. Stahl, A. Rogl, T. Janzen, D. G. Pavelev, Yu. I.
[36] Koschurinov, V. Ustinov and A. Zhukov, Phys. Rev. Lett. 95, 126801
[37] (2005).

A New Experimental Procedure for Determining the Response of Bolometric Detectors to Fields in Any State of Coherence

Christopher N. Thomas[1*], Stafford Withington[1], and George Saklatvala[1]

[1]*Detector and Optical Physics Group, Cavendish Laboratory, JJ Thomson Avenue, Cambridge, CB3 OHE, UK*

* Contact: c.thomas@mrao.cam.ac.uk

***Abstract*— Any bolometer that is greater than a few wavelengths in size is receptive to the power in a number of fully coherent optical modes simultaneously. Knowing the amplitude, phase, and polarisation patterns of these modes, and their relative sensitivities, is central to being able to use a multimode detector effectively. We describe a procedure for measuring the spatial state of coherence to which a detector is sensitive. Diagonalisation of the coherence function then gives the natural modes. The scheme is based on the result that the expectation value of the output of any detector, or indeed whole instrument or telescope, is given by the contraction of two tensor fields: one of which describes the state of coherence of the incoming radiation, and the other describes the state of coherence to which the detector is sensitive. It follows that if a detector is illuminated by two coherent point sources, in the near or far field, and the phase of one source rotated relative to the other, the output of the detector displays a fringe. By repeating the process with different source locations, the detector's coherence tensor can be reconstructed from the recorded complex visibilities. This new, powerful technique is essentially aperture synthesis interferometry in reverse, and therefore many of the data processing techniques developed in the context of astronomy can be used for characterising the optical behaviour of few-mode bolometers.**

I. INTRODUCTION

The use of bolometric detectors in far-infrared and submillimetre astronomy is now widespread. In many instruments, the bolometers are antenna-coupled [1] – for example, Planck-HFI [2] and CLOVER [3] – meaning that an absorber loads a single-mode antenna, which in turn illuminates a telescope. The advantage of this arrangement is that it is well known how single-mode antennas couple to optical systems, allowing precise control of the beam pattern on the sky. In fact, because the system is single-mode, it is straightforward to propagate the beam pattern of the detector through the optical system, and onto the sky. In the case of large-format imaging arrays, however, there is a tendency to use free-space absorbing pixels. This configuration can give full, instantaneous sampling of the sky, and high absorption efficiency in a number of optical modes simultaneously. A major problem, however, is that the optical coupling between the telescope and detector is poorly understood, and there is no obvious way of fully characterising the reception pattern, largely because it is partially coherent. It is tempting to treat these systems in a similar way to CCDs in optical astronomy, and assume that each pixel is simply re-imaged on the sky. This approximation assumes the incident field is fully spatially incoherent, and that the pixel collects, on a point-by-point basis, all of the radiation that is incident on it: sometime called a 'light bucket'. The radiation in a telescope at a particular frequency, although thermal in origin, is spatially correlated over length scales of at least a wavelength by virtue of the free-space Maxwell's equations, which only allow spatial variations over scales sizes of greater than a wavelength, and only allow divergence-free fields: combined these give black body radiation. Additional correlations may be introduced by the telescope optics. In an optical telescope, the pixels are typically much larger then a wavelength, and so the incoherent approximation holds. In far-infrared and submillimetre astronomy, however, the dimensions of the pixels are similar to a wavelength, which is typically the same as the coherence length, including polarization, of the radiation. To understand how a bolometer couples to a telescope, we therefore need a way of characterising the response of multimode detectors to fields in any state of spatial coherence.

In this paper, we describe an experimental technique for determining quantitatively the sensitivity of bolometric detectors to fields in any state of spatial coherence. We begin by introducing a parameterisation of a bolometer's behaviour in terms of the set of modes to which it is sensitive; this gives rise to a response function, which can be used to characterise the behaviour of any detector or complete system. Next we describe how two phase-locked, coherent, radiation sources can be used to measure the response function experimentally. Finally we discuss experimental apparatus that is being constructed to demonstrate and develop this method. In order to have numerical simulations against which the experimental data can be compared, we will present work that has been carried out on modelling the response function of free-space planar absorbers. Our model emphasises diffractive effects caused by the finite size of the absorber, and which, to first order,

can be considered independent of the specific absorption mechanism at work. A sharp change from multi- to few-mode behaviour is observed when the dimensions of the absorber become smaller than the wavelength of the radiation being absorbed.

It is worth emphasising that the methods described are very general, and can be applied any type of bolometer or system, at any wavelength. For example, it should be possible to distinguish between the behaviour of pixels having continuous thin films as absorbers, and pixels having frequency-selective surfaces, such as tightly packed arrays of thin-film dipoles. Further, although the emphasis is on characterising the behaviour of single, free-space bolometers, the same technique can be applied to systems such as imaging arrays and phased arrays. In the case of measurements on antenna-coupled bolometers, which are theoretically single-mode, it is possible that the technique will reveal other unexpected ways for radiation to couple power into the absorbing element. For example, the incident radiation might cause ohmic heating of a planar antenna, which is then conducted to the bolometer. Many other effects, such as surface waves, might contribute.

II. PARAMETERISING BOLOMETER RESPONSE

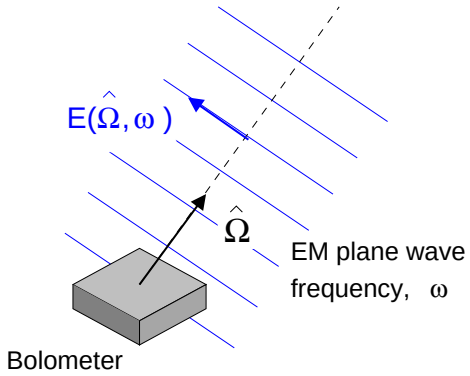

Fig. 1 A bolometer being illuminated with monochromatic plane wave radiation. The notation used in the theoretical discussion is illustrated.

To begin with, a way of parameterising the relationship between the state of spatial coherence of the incident radiation and the output of the detector is needed. This problem has been addressed by Saklatvala and Withington in [4] and [5]. They have shown that is possible to characterise a bolometer in terms of a set of fully coherent modes of the incident field in which the detector is simultaneously sensitive to power, along with a set of coefficients that describe the relative influence of each of the modes on the detector's output. We outline the approach here. In this paper we will consider only incident radiation that is statistically stationary. In this situation, the power absorbed at different wavelengths can be treated independently, and at each wavelength there is a different set of spatial modes and coefficients. It is also possible to deal with non-stationary fields, but this requires spatio-temporal modes and these will not be discussed here.

Consider a bolometer being illuminated by monochromatic plane radiation with frequency ω as shown in Fig. 1. The incident field is described by a vector function $\mathbf{E}(\hat{\mathbf{\Omega}},\omega)$ which gives the complex electric field amplitude of the plane wave incident from the direction $\hat{\mathbf{\Omega}}$. Consider for the moment replacing the bolometer with a classical antenna. The net power, $P(\omega)$, absorbed by the antenna from the field would be given by:

$$P(\omega) = \left| \int_S d^2\hat{\mathbf{\Omega}}\ \mathbf{R}^*(\hat{\mathbf{\Omega}},\omega)\cdot\mathbf{E}(\hat{\mathbf{\Omega}},\omega) \right|^2 , \qquad (1)$$

where $\mathbf{R}(\hat{\mathbf{\Omega}},\omega)$ is called the antenna reception pattern [6] and the integral is taken over all possible incidence directions. Equation (1) is simply the full vector form of more familiar antenna reception relations. A classical antenna is an example of a single-mode detector. Equation (1) simply describes mathematically the process of determining the power carried in the single mode – described by $\mathbf{R}(\hat{\mathbf{\Omega}},\omega)$ – by the incident field. The logical extension of (1) to multimode-detectors is:

$$p(\omega) = \sum_n \gamma^{(n)} \left| \int_s d^2\hat{\mathbf{\Omega}}\ \mathbf{U}^{(n)*}(\hat{\mathbf{\Omega}},\omega)\cdot\mathbf{E}(\hat{\mathbf{\Omega}},\omega) \right|^2 , \qquad (2)$$

where $p(\omega)$ is the detector output. The $\{\ \mathbf{U}^{(n)}(\hat{\mathbf{\Omega}},\omega)\ \}$ are the set of fully coherent modes of the field in which the detector is simultaneously sensitive to power. We shall refer to these modes as the natural optical modes of the detector. As modes, they are 'orthogonal' to one another in the sense

$$\int_S d^2\hat{\mathbf{\Omega}}\ \mathbf{U}^{(m)*}(\hat{\mathbf{\Omega}},\omega)\cdot\mathbf{U}^{(n)}(\hat{\mathbf{\Omega}},\omega) = \delta_{mn} . \qquad (3)$$

In (3) we have further assumed that the modes are individually normalised. The set of coefficients $\{\gamma^{(n)}\}$ quantify how the output of the bolometer changes with the power in each mode. The set of normalised coefficients, $\{\gamma^{(n)} / \Sigma_m \gamma^{(m)}\}$, gives, therefore, an indication of the relative responsivity to the power in each mode. In the case where the incident field is partially coherent, we can take the ensemble average, $\langle\ \rangle$, of (2) to obtain

$$p(\omega) = \int_S d^2\hat{\mathbf{\Omega}}_1 \int_S d^2\hat{\mathbf{\Omega}}_2 \left(\sum_n \gamma^{(n)} \mathbf{U}^{(n)*}(\hat{\mathbf{\Omega}}_1,\omega)\mathbf{U}^{(n)}(\hat{\mathbf{\Omega}}_2,\omega) \right)^{\dagger} \cdot\cdot \left\langle \mathbf{E}^*(\hat{\mathbf{\Omega}}_1,\omega)\mathbf{E}(\hat{\mathbf{\Omega}}_2,\omega) \right\rangle , \qquad (4)$$

where we have expanded out the norm. The double-dot denotes two scalar products, one between the inner pair of vectors followed by one between the outer pair. The natural modes of the detector can be taken outside the ensemble average because we have assumed previously they are fully coherent. Defining the dyadic fields

$$\overline{\overline{D}}(\hat{\boldsymbol{\Omega}}_1,\hat{\boldsymbol{\Omega}}_2,\omega)=\sum_n \gamma^{(n)}\mathbf{U}^{(n)*}(\hat{\boldsymbol{\Omega}}_1,\omega)\mathbf{U}^{(n)}(\hat{\boldsymbol{\Omega}}_2,\omega) \qquad (5)$$

and

$$\overline{\overline{E}}(\hat{\boldsymbol{\Omega}}_1,\hat{\boldsymbol{\Omega}}_2,\omega)=\left\langle \mathbf{E}^*(\hat{\boldsymbol{\Omega}}_1,\omega)\mathbf{E}(\hat{\boldsymbol{\Omega}}_2,\omega)\right\rangle, \qquad (6)$$

which is the cross-spectral density of the incident field, equation (4) becomes

$$p(\omega)=\int_S d^2\hat{\boldsymbol{\Omega}}_1\int_S d^2\hat{\boldsymbol{\Omega}}_2\ \overline{\overline{D}}^{\dagger}(\hat{\boldsymbol{\Omega}}_1,\hat{\boldsymbol{\Omega}}_2,\omega)\cdot\cdot\,\overline{\overline{E}}(\hat{\boldsymbol{\Omega}}_1,\hat{\boldsymbol{\Omega}}_2,\omega), \qquad (7)$$

which reproduces the results of Saklatvala and Withington, which were derived in a more rigorous way. We see that provided $\overline{\overline{D}}(\hat{\boldsymbol{\Omega}}_1,\hat{\boldsymbol{\Omega}}_2,\omega)$ is known, it is possible to calculate the output of a detector when it is subjected to any illuminating field. We shall thus take $\overline{\overline{D}}(\hat{\boldsymbol{\Omega}}_1,\hat{\boldsymbol{\Omega}}_2,\omega)$, which we shall refer to as the *detector response function*, as our parameterisation of the detector behaviour. A useful physical interpretation of the meaning of $\overline{\overline{D}}(\hat{\boldsymbol{\Omega}}_1,\hat{\boldsymbol{\Omega}}_2,\omega)$ can be obtained by taking the ensemble average of (1), expanding the norm and using (6) to obtain

$$p(\omega)=\int_S d^2\hat{\boldsymbol{\Omega}}_1\int_S d^2\hat{\boldsymbol{\Omega}}_2\left\langle \mathbf{R}^*(\hat{\boldsymbol{\Omega}}_1,\omega)\mathbf{R}(\hat{\boldsymbol{\Omega}}_2,\omega)\right\rangle^{\dagger}\cdot\cdot\,\overline{\overline{E}}(\hat{\boldsymbol{\Omega}}_1,\hat{\boldsymbol{\Omega}}_2,\omega) \qquad (8)$$

We see that the detector response function corresponds to the cross-spectral density of the reception pattern. We can therefore think of it as describing the state of spatial coherence of the field to which the bolometer is sensitive. In the special case of an antenna, this field is fully-coherent. In the case of a multimode detector, it is partially coherent and the natural optical modes of the detector correspond to what are known as the coherent modes of the field [7].

In the next section we will discuss how the detector response function can be determined experimentally. However, sometimes is also useful to know the natural optical modes of the detector. Although no single reception pattern exists for a multimode bolometer, we can propagate the optical modes of the detector though the telescope to find a set of beam patterns on the sky to which the bolometer is independently sensitive. The natural optical modes of the detector can be found by solving the following equation:

$$\int_S d^2\hat{\boldsymbol{\Omega}}_2\ \overline{\overline{D}}(\hat{\boldsymbol{\Omega}}_1,\hat{\boldsymbol{\Omega}}_2,\omega)\cdot\mathbf{U}^{(n)}(\hat{\boldsymbol{\Omega}}_2,\omega)=\gamma^{(n)}\mathbf{U}^{(n)}(\hat{\boldsymbol{\Omega}}_1,\omega) \qquad (9)$$

This is an eigenfunction equation. We see that the $\gamma^{(n)}$ that describe the responsivity of the detector to the power in each mode are the eigenvalues of the detector response function.

III. EXPERIMENTAL DETERMINATION OF THE DETECTOR RESPONSE FUNCTION

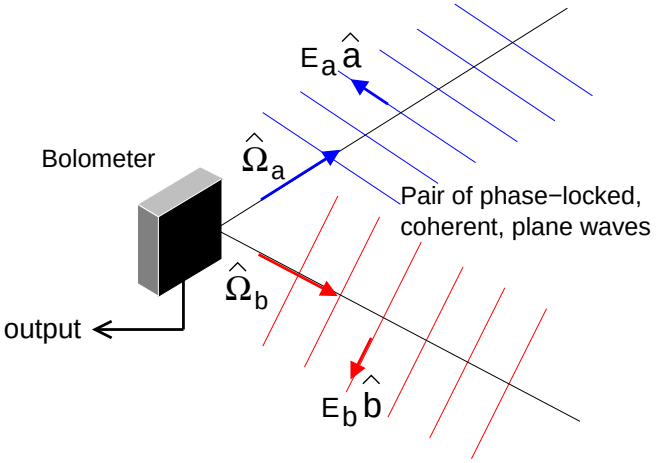

Fig. 2 Diagram of the characterisation procedure. An element of the detector response function can be obtained from the visibility of the fringes in the output signal that result from rotating the phase difference between the incident waves.

Consider placing two monochromatic, point-like, radio sources operating at the same frequency, ω_0, in the far field of a detector. Assume that the sources are individually fully coherent and, further, that they are phase-locked to one another with a controllable differential phase angle, $\Delta\psi$. They produce, at the detector, a pair of phase-locked plane waves, as shown in Fig. 2. The polarisation states, amplitude and direction of incidence of the waves depend on the source positions and orientations. For the plane waves shown in Fig. 2, the incident field is of the form

$$\mathbf{E}(\hat{\boldsymbol{\Omega}},\omega_0)=E_a\,\hat{\mathbf{a}}\,\delta(\hat{\boldsymbol{\Omega}}-\hat{\boldsymbol{\Omega}}_a)+E_b\,e^{i\Delta\psi}\,\hat{\mathbf{b}}\,\delta(\hat{\boldsymbol{\Omega}}-\hat{\boldsymbol{\Omega}}_b) \qquad (10)$$

Substituting (10) into (7) we obtain

$$\begin{aligned}\left\langle p(\omega)\right\rangle = {} & E_a^2\,D_{aa}(\hat{\boldsymbol{\Omega}}_a,\hat{\boldsymbol{\Omega}}_a,\omega_0)\\ & +E_b^2\,D_{bb}(\hat{\boldsymbol{\Omega}}_b,\hat{\boldsymbol{\Omega}}_b,\omega_0)\\ & +E_a\,E_b\,e^{i\Delta\psi}D_{ab}(\hat{\boldsymbol{\Omega}}_a,\hat{\boldsymbol{\Omega}}_b,\omega_0)\\ & +E_a\,E_b\,e^{-i\Delta\psi}D_{ba}(\hat{\boldsymbol{\Omega}}_b,\hat{\boldsymbol{\Omega}}_a,\omega_0)\end{aligned}, \qquad (11)$$

where we have used the shorthand for the matrix elements

$$D_{ab}(\hat{\mathbf{\Omega}}_a,\hat{\mathbf{\Omega}}_b,\omega_0)=\hat{\mathbf{a}}\cdot\overline{\overline{D}}(\hat{\mathbf{\Omega}}_a,\hat{\mathbf{\Omega}}_b,\omega)\cdot\hat{\mathbf{b}}\,. \qquad (12)$$

From (5) we have that

$$D_{ab}(\hat{\mathbf{\Omega}}_a,\hat{\mathbf{\Omega}}_b,\omega_0)=D^*_{ba}(\hat{\mathbf{\Omega}}_b,\hat{\mathbf{\Omega}}_a,\omega_0)\,. \qquad (13)$$

We can also argue that (13) must be true as otherwise we see from (11) that the detector output would depend on the way the plane waves are labelled, which is arbitrary. Using (13) we can simplify (11) to

$$\begin{aligned}\langle p(\omega)\rangle = {} & E_a^2\,D_{aa}(\hat{\mathbf{\Omega}}_a,\hat{\mathbf{\Omega}}_a,\omega_0)\\ & + E_b^2\,D_{bb}(\hat{\mathbf{\Omega}}_b,\hat{\mathbf{\Omega}}_b,\omega_0)\\ & + 2\,E_a\,E_b\left|D_{ab}(\hat{\mathbf{\Omega}}_a,\hat{\mathbf{\Omega}}_b,\omega_0)\right|\\ & \times\cos\left(\Delta\psi + Arg(D_{ab}(\hat{\mathbf{\Omega}}_a,\hat{\mathbf{\Omega}}_b,\omega_0))\right)\end{aligned}\,. \qquad (14)$$

Consequently as the phase angle between the sources, $\Delta\psi$, is rotated we expect the output of the detector to show fringes, as in Fig. 3. Provided we know E_a and E_b, from the amplitude and phase of this fringe pattern, we can determine both the modulus and phase of $D_{ab}(\hat{\mathbf{\Omega}}_a,\hat{\mathbf{\Omega}}_b,\omega_0)$. From (13) it also follows that we measure $D_{ba}(\hat{\mathbf{\Omega}}_b,\hat{\mathbf{\Omega}}_a,\omega_0)$. By repeating this process with different source locations – to change the incidence angle of the plane waves – and different source orientations – to change the wave polarisations – it is possible to map out the detector response function in full and characterise the bolometer. Subsequently, we can obtain the natural optical modes of the detector by solving (9).

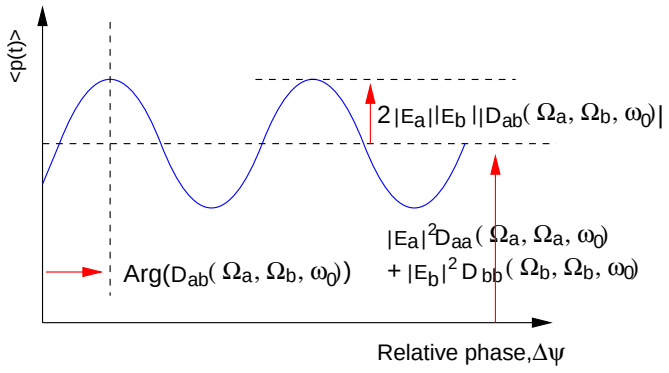

Fig. 3 Expected form of the output in Fig. 1 when the phase difference between the illuminating waves is rotated.

It might appear that a large number of measurements will be needed to characterise a device, but this is not the case. Consider an example where we are trying to sample the detector response function over a set of N different illumination directions. Naively we might expect to have to make $\sim 2N^2$ measurements. There are N illumination directions with two possible polarisation states in each case, giving $(2N)^2$ possible arrangements of two sources. However, because of (13) we only need to measure half of these combinations. In fact, the actual number of degrees of freedom is fixed by the number of modes, n, of the incident field in which the detector is sensitive to power. From (5) we expect the number of degrees of freedom in the values measured to be $\sim(2N+1)n$, corresponding to $2N$ degrees of freedom per mode plus an additional n degrees of freedom in the $\gamma^{(n)}$. When n is less than N, there are fewer degrees of freedom than measurements and the system is highly constrained. It should therefore be possible to impute the full set of data from a smaller subset of measurements.

We are currently investigating an imputation strategy based on work of Brand [8], who worked on imputing missing values in matrices of data. In the case of sampled data, the detector response function reduces to a matrix, with the missing values corresponding to readings not taken yet. Brand's algorithm was originally intended for use in online recommender systems for retail, where it would be used to fill in missing product reviews based on the incomplete reviews supplied by the user. There are two reasons why his strategy is particularly attractive to us. Firstly, it imputes the missing values so that the completed matrix has the lowest rank – i.e. degrees of freedom – possible. Secondly, because it is intended to be used online, it has been designed so that the imputed values can be updated in linear time as new data arrives. It should therefore be possible to calculate the prediction in real time as the experiment is performed; updating the current best estimate as additional scans are performed. Although there are many possibilities, basically speaking, once the singular values have converged, we will know that we have taken sufficient data and can stop.

There are also other methods available for reducing the number of measurements that need to be taken. Up to this point we have discussed characterising the response of the bolometer to plane-wave illumination from all possible directions. In practical applications, however, the illumination angles are likely to be restricted, and it obviously makes sense to only characterise the detector over its working range. Equation (9) can be solved over this restricted range of illumination angles to find the set of detector natural modes over the restricted region. These are likely to be different to the natural modes over the full range of incidence directions, but can be used equivalently. This approximation saves greatly on the number of measurements needed.

IV. EXPERIMENTAL VALIDATION OF THE TECHNIQUE

We plan to demonstrate the validity of the proposed technique by using it to investigate the power reception characteristics of planar absorbing structures with dimensions similar to or smaller than the wavelength of the illuminating radiation. In this section, we will describe the experimental

system, and theoretical work we have been doing to predict the behaviour that should be seen.

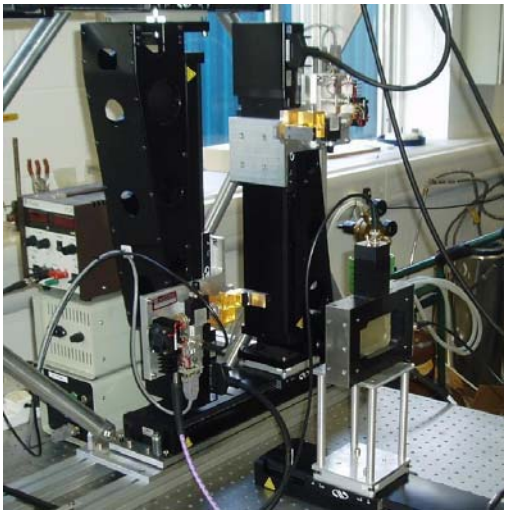

Fig. 4 Photo of the system being developed to perform the characterisation measurements. The object in the foreground is a test sensor for checking the operation of the sources. In the background, the powered slides and sources can be seen.

Fig. 4 is a photograph of the apparatus in its current form. We are using two, 195-270GHz sources, which are mounted on powered slides to allow different illumination angles. The sources can also be rotated manually to allow different polarisation angles. In practise, rather then operating the sources at the same frequency, as suggested previously, we instead intend to drive them at slightly different frequencies, with the offset derived from a common reference. The idea is that if the offset frequency is sufficiently small, the field that results will approximate two plane waves at the same RF frequency whose relative phase varies periodically in time. The advantage of this approach is that the need for a separate phase shifter is eliminated. In its more extreme form, where the difference frequency is scanned over a large range, the full spatio-temporal state of coherence of the detector's response can be found.

In the foreground of Fig. 4, a calibration detector from Thomas Keating Ltd can be seen, which we are using to check the operation of the basic instrument. The detector is mounted on a powered slide to allow the distance between the sources and the detector to be modulated, which will allow the effects of standing-waves to be removed. Our early experiments will simulate planar absorbers of different dimensions by placing appropriate apertures over the face of the detector. Later, we hope to use a range of room-temperature detectors, based on suspended Si_xN_y islands, similar to the structures used for Transition Edge Sensors. A schematic of the design is shown in Fig. 5. An advantage of this approach is that we will be able to study the behaviour of many different configurations, and some of the designs can be close to the geometries used in ultra-low-noise free-space-coupled bolometers.

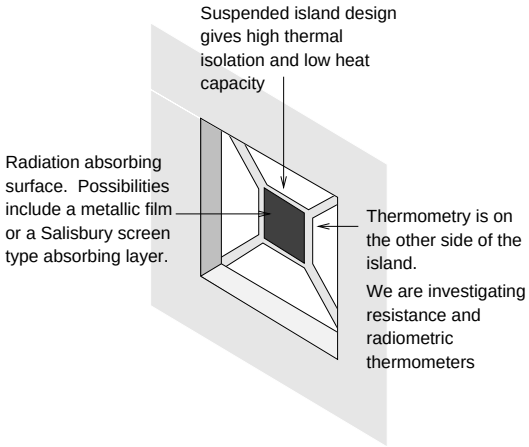

Fig. 5 Concept drawing for model planar bolometer for use in the validation experiments described. The design is based on a suspended silicon nitride island structure and it is intended to operate it at room temperature.

V. THEORETICAL MODEL OF A PLANAR BOLOMETER

In this section, we describe work that has been done on modelling the detector response function of planar bolometers. The purpose of the study was to develop numerical simulations against which experimental data can be compared. Out intention was to investigate the way in which performance of a planar bolometer is influenced by its size, independent of the specific power absorption mechanism at work. To this end we assumed the absorption mechanism was 'ideal', so that our model represents in some way, the best possible performance obtainable from a 'real' detector of the same dimensions.

A. Details of Model

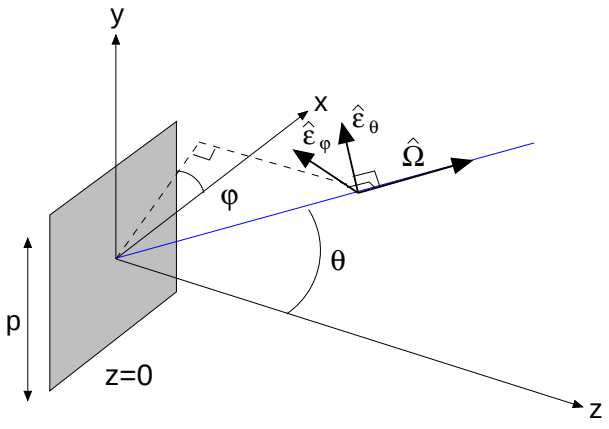

Fig. 6 Diagram illustrating the model pixel considered and the notation used in the theoretical discussion.

Fig. 6 shows the model planar bolometer and defines the notation that we will use. We have only considered bolometers with a square absorbing surface. It would, however, be easy to apply similar techniques to a planar bolometer of a different shape. We denote the side-length of the square by p and the wavelength of the radiation by λ. For simplicity we assume the absorber occupies the region of the $z = 0$ plane defined by $|x| \le p/2$ and $|y| \le p/2$.

Until now we have considered the response of the bolometer to incident plane waves. However, when modelling an ideal planar bolometer it is actually much easier to work in terms of its response to the electric field over the plane containing it. We denote this field $E_{z=0}(\mathbf{r},\omega)$, where $\mathbf{r} = (x, y)$ is a point lying in the plane z = 0. In the preceding analysis of the far field detector behaviour, the detector was characterised in terms of a set of field modes in which it is simultaneously sensitive to power. The same approach can be used to characterise its response to fields over the plane. We assume the detector is simultaneously responsive to the power in a set of modes of the field over the plane, given by $\{\mathbf{V}^{(n)}{}_{z=0}(\mathbf{r},\omega)\}$. Further, we assume there is a set of coefficients $\{\beta^{(n)}\}$ that, like the $\gamma^{(n)}$, quantify how much the output scales with the power in the associated mode. We can then define a function

$$\overline{\overline{D}}_{z=0}(\mathbf{r}_1,\mathbf{r}_2,\omega) = \sum_n \beta^{(n)} \mathbf{V}^{(n)*}(\mathbf{r}_1,\omega)\mathbf{V}^{(n)}(\mathbf{r}_2,\omega), \qquad (15)$$

which is the equivalent of the detector response function for fields on the plane. As such it describes the state of spatial coherence of the field over the plane to which the bolometer is sensitive. The equivalent of expression (7) for the fields over the bolometer plane is

$$p(\omega) = \int_{z=0} d^2\mathbf{r}_1 \int_{z=0} d^2\mathbf{r}_2 \, \overline{\overline{D}}^{\dagger}_{z=0}(\mathbf{r}_1,\mathbf{r}_2,\omega) \cdot\cdot \overline{\overline{E}}_{z=0}(\mathbf{r}_1,\mathbf{r}_2,\omega), \qquad (16)$$

where $\overline{\overline{E}}_{z=0}(\mathbf{r}_1,\mathbf{r}_2,\omega)$ is the cross-spectral density of the plane electric field. An ideal bolometer is sensitive to the total power incident over its surface. This requires the detector output be proportional to the intensity of the field integrated over the absorber surface, or

$$p(\omega) \propto \int_{\substack{\text{absorber}\\ \text{surface}}} d^2\mathbf{r} \left|E(\mathbf{r},\omega)\right|^2 . \qquad (17)$$

From (16) we see that this requires that $\overline{\overline{D}}_{z=0}(\mathbf{r}_1,\mathbf{r}_2,\omega)$, be of the form

$$\overline{\overline{D}}_{z=0}(\mathbf{r}_1,\mathbf{r}_2,\omega) = \begin{cases} C\,\delta(\mathbf{r}_1 - \mathbf{r}_2) & \mathbf{r}_1 \text{ and } \mathbf{r}_2 \text{ on absorber} \\ 0 & \text{otherwise} \end{cases}, \qquad (18)$$

where C is a proportionality constant.

The important question now is how the detector response function, $\overline{\overline{D}}_{z=0}(\mathbf{r}_1,\mathbf{r}_2,\omega)$, is related to $\overline{\overline{D}}(\hat{\boldsymbol{\Omega}}_1,\hat{\boldsymbol{\Omega}}_2,\omega)$. We will present a simple argument for the expected form. Our approach is based on the relationship between the reception pattern of a classical aperture antenna and the field over the aperture plane to which it is sensitive. Denoting the reception pattern by $\mathbf{R}(\hat{\boldsymbol{\Omega}},\omega)$ as before and the aperture field as $\mathbf{R}_{z=0}(\mathbf{r},\omega)$, we have

$$\mathbf{R}(\hat{\boldsymbol{\Omega}},\omega) = -\frac{2\pi i}{k}\cos\theta\,(\overline{\overline{I}} - \hat{\boldsymbol{\Omega}}\hat{\boldsymbol{\Omega}}^*)\cdot \int_{z=0} d^2\mathbf{r}\,\mathbf{R}_{z=0}(\mathbf{r},\omega)\,e^{-ik\hat{\boldsymbol{\Omega}}\cdot\mathbf{r}}, \qquad (19)$$

where we have used the notation in Fig. 5. This result follows from the equivalence between the reception pattern of a classical and its transmission pattern. Equation (19) simply represents the process of propagating a field from a plane to the far field, using standard methods [6]. This raises a point, which will be important later. As (19) is a propagation equation, we see that the reception pattern/far-field sensitivity of the antenna is determined only by the component of the aperture field that is able to propagate. This is most easily separated out in the angular spectrum domain. The angular spectrum of the aperture field is given by

$$A(\mathbf{k}_t,\omega) = \frac{1}{2\pi}\int_{z=0} d^2\mathbf{r}\,\mathbf{R}(\mathbf{r},\omega)\,e^{-i\mathbf{k}_t\cdot\mathbf{r}} . \qquad (20)$$

Essentially it is the 2D spatial Fourier transform of the field. We see that the angular spectrum appears in (19) in a rewritten form and that each spatial frequency component can be associated with a particular plane wave, the vector associated with that component giving the vector amplitude of the wave. The propagating component of the field satisfies the following in the angular spectrum domain:

I. $|\mathbf{k}_t| \le k$. If $|\mathbf{k}_t| \ge k$ the wave associated with a spatial component is evanescent. In (19) this filtering is intrinsic to the expression. Since $\mathbf{k} = k\hat{\boldsymbol{\Omega}}$ and $\hat{\boldsymbol{\Omega}}$ is a unit vector, $|\mathbf{k}_t|$ is always limited to being less than k.

II. Electromagnetic waves are transverse polarised, so only components of the polarisation vector normal to the wave direction can propagate. This component can be found by acting on the vector with $(\overline{\overline{I}} - \hat{\boldsymbol{\Omega}}\hat{\boldsymbol{\Omega}}^*)$, as in (19).

The first step corresponds to spatially low-pass filtering the field, which means the propagating component cannot vary on length scales smaller than λ. We will see the implication of this shortly.

In our model, we assume the detector response function is given by

$$\overline{\overline{D}}(\hat{\mathbf{\Omega}}_1,\hat{\mathbf{\Omega}}_2,\omega)=\sum_n \beta^{(n)}\mathbf{V}^{(n)*}(\hat{\mathbf{\Omega}}_1,\omega)\mathbf{V}^{(n)}(\hat{\mathbf{\Omega}}_2,\omega), \qquad (21)$$

where the $\{\boldsymbol{V}^{(n)}(\hat{\mathbf{\Omega}},\omega)\}$ are the set of natural optical modes of the detector, $\{\boldsymbol{V}^{(n)}_{z=0}(\boldsymbol{r},\omega)\}$, transformed according to (19). Essentially, we treat the planar bolometer as a set of aperture antennas and assume that the plane wave response of the detector can be found simply from the plane wave response of these modes. This seems sensible. Despite the similarity of (21) to (5), the transformed natural modes of the field on the plane will not necessarily correspond to the far field natural modes of the detector. This is because the transformation does not, in general, preserve orthogonality and so there is no guarantee the transformed modes will satisfy (3), in which case they do not form a valid set of far field modes. To find the far-field modes, (9) must instead be solved for the response function constructed from (21). Expanding (21) with (20) and using (15) to simplify, we obtain

$$\begin{aligned}\overline{\overline{D}}(\hat{\mathbf{\Omega}}_1,\hat{\mathbf{\Omega}}_2,\omega)=&\frac{4\pi^2}{k^2}\cos\theta_1\cos\theta_2\\ &\times\int_{z=0} d^2\mathbf{r}_1\int_{z=0} d^2\mathbf{r}_2\; e^{-ik\hat{\mathbf{\Omega}}_1\cdot\mathbf{r}_1}\; e^{ik\hat{\mathbf{\Omega}}_2\cdot\mathbf{r}_2}\\ &\times(\bar{\bar{I}}-\hat{\mathbf{\Omega}}_1\hat{\mathbf{\Omega}}_1^*)\cdot\overline{\overline{D}}_{z=0}(\mathbf{r}_1,\mathbf{r}_2,\omega)\cdot(\bar{\bar{I}}-\hat{\mathbf{\Omega}}_2\hat{\mathbf{\Omega}}_2^*)\end{aligned}, \qquad (22)$$

which relates the response on the plane to the detector response function that we would measure in an experiment. We find the detector response function for our ideal bolometer by substituting (18) into (22). This integral has already been done by Withington [9] for the purpose of modelling the optical behaviour of bolometric focal plane imaging arrays. Withington treats the bolometer as a perfect black body absorber, which is essentially what we have done. Chuss [10] has developed this work and has considered the field patterns on the sky to which a complete telescope is sensitive. Using their results for this integral, we obtain finally for the detector response function of the ideal bolometer:

$$\begin{aligned}\overline{\overline{D}}(\hat{\mathbf{\Omega}}_1,\hat{\mathbf{\Omega}}_2,\omega)=&\eta(\omega)\cos\theta_1\cos\theta_2\\ &\times\operatorname{sinc}\left(\frac{p\pi}{\lambda}\hat{\mathbf{x}}\cdot(\hat{\mathbf{\Omega}}_1-\hat{\mathbf{\Omega}}_2)\right)\\ &\times\operatorname{sinc}\left(\frac{p\pi}{\lambda}\hat{\mathbf{y}}\cdot(\hat{\mathbf{\Omega}}_1-\hat{\mathbf{\Omega}}_2)\right)\\ &\times(\bar{\bar{I}}-\hat{\mathbf{\Omega}}_1\hat{\mathbf{\Omega}}_1^*)\cdot(\bar{\bar{I}}-\hat{\mathbf{\Omega}}_2\hat{\mathbf{\Omega}}_2^*)\end{aligned}, \qquad (23)$$

where we have grouped miscellaneous proportionality constants into the factor η(ω).

It was noted earlier that $\overline{\overline{D}}_{z=0}(\mathbf{r}_1,\mathbf{r}_2,\omega)$ describes the state of spatial coherence of the field over the plane to which the detector is sensitive. From (18), we hence see that in our model we have assumed the coherence length of this field is zero over the absorber surface. However, this picture of the coherence length of the reception field is complicated slightly when we consider propagating radiation fields. From (22) and the discussion of (20), we see that the far-field behaviour of the detector, i.e. its response to propagating radiation, depends only on the propagating component of the field represented by $\overline{\overline{D}}_{z=0}(\mathbf{r}_1,\mathbf{r}_2,\omega)$. This may also be seen by considering (16) in the angular spectrum domain for an incident field that satisfies the two propagation criteria from earlier. As discussed before, higher order spatial frequencies are absent from the propagating component. For monochromatic fields, this limits the smallest scale over which the propagating can vary to distances on the order of a wavelength, λ. This is important for partially coherent fields, as it means that the coherence length of the propagating component cannot be $< \lambda$. This result holds regardless of the coherence length of the full field. Since incoming radiation can only interact with the propagating component of $\overline{\overline{D}}_{z=0}(\mathbf{r}_1,\mathbf{r}_2,\omega)$, from the point of reference of the radiation the coherence length of the reception field therefore appears to be ~λ. We shall refer to this coherence length as the *apparent* coherence length of the reception field. This is to distinguish it from the actual coherence length of the reception field, which is zero in the model. The actual coherence length depends of the physics of the radiation absorption process. The apparent coherent length has important implications, which will be seen in the next section.

B. Modal Behaviour of the Model Detector

Equation (9) was solved numerically with the response function of (23) to find the natural optical modes of the model detector and the associated eigenvalues for several different values of the ratio p/λ. For all values of this ratio, the model bolometer was found to be responsive to the same set of modes. This set resembles the spherical vector harmonics, but multiplied in each case by an additional factor of the cosine of the zenith angle, θ. As p/λ is varied, what changes is the relative responsivity of the model planar bolometer to each mode in the set rather then the modes' spatial forms. In general it was also observed that the responsivities vary with p/λ in such a way that the ordering of the modes based on associated eigenvalue, $\gamma^{(n)}$, is preserved.

Fig. 7 illustrates how the response of the detector to each mode varies over the range $p/\lambda = 0.25 - 4.0$. For each value of p/λ, the thirty-five largest normalised eigenvalues, $\{\gamma^{(n)}/\Sigma_m \gamma^{(m)}\}$, of the response function are plotted in descending order. Although in reality the eigenvalues for each value of p/λ are a discrete set, in the plot I have joined the points

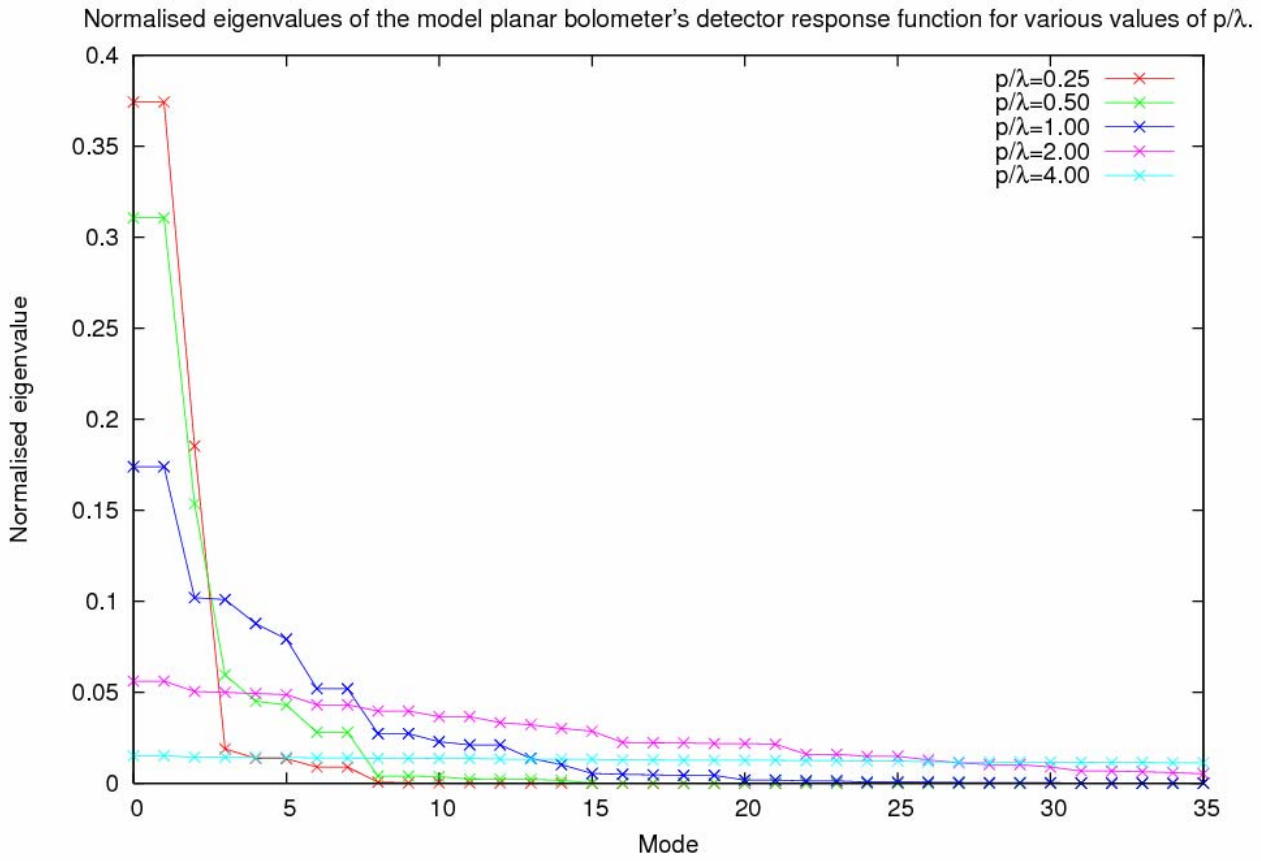

Fig. 7 Plot showing the normalised eigenvalues, $\{ \gamma^{(n)} / \Sigma_m \gamma^{(m)} \}$, of the detector response function of the model bolometer for different values of p/λ.. For each value of p/λ, the thirty-five largest normalised eigenvalues are shown.

belonging to a particularly set together with a line. This is to emphasise trends and to make it easier to distinguish between different sets. Remember that the normalised eigenvalues are a measure of the relative responsivity of the detector to the power in each of the modes. The higher the responsivity, the more the output of the detector depends on the power in the associated mode then the other modes. With this in mind we see that for values of $p/\lambda > 1$ the detector is equally responsive, approximately, to the power in all thirty-five modes shown. Intuitively this is what we would expect from an ideal absorber. It should be sensitive to the total power in the field independent of its exact spatial form. However for $p/\lambda < 1$ we observe very different behaviour. As p/λ decreases, the relative responsivity to the first three modes can be seen to increase while the responsivity to the other modes decreases. By $p/\lambda = 0.25$, the ideal bolometer essentially responds only to the power in three modes and is behaving as a few-mode detector.

This behaviour can be explained in terms of the apparent coherence length of the field over its surface that the absorber is sensitive to, which was discussed at the end of the previous section. From (18) we would expect this field to have zero coherence length. However, we noted that because of propagation effects the reception field that incident radiation 'sees' is actually coherent over spatial scales of at least ~λ, independent of the absorption mechanism. In the limit where the absorbing square is smaller then λ the reception field over the absorbing surface will therefore be coherent. As mentioned in section II, when the reception field is fully coherent the bolometer behaves like an antenna and will be single-moded. The reason we see actually see responsivity to three modes in this limit is in the proceeding discussion we have ignored the polarisation of the field. The three components of the field remain uncorrelated, so there are three such spatially fully-coherent modes possible. In the limit where $p/\lambda >> 1$, the field appears spatially incoherent on the scale of the absorber and we recover the ideal behaviour we had assumed.

Fig. 8 is a plot of the three far-field modes to which the detector is sensitive in the limit $p/\lambda << 1$. The details of the projection used are also shown in the figure. Notice that they correspond to the reception patterns expected for differently orientated electric dipole antennas, allowing for the additional zenith angle dependence already noted. The first two modes correspond to dipoles lying in the plane and are simply orthogonal polarisation states. The symmetry of the model bolometer in the x and y directions leads us to expect the bolometer should be equally responsive to both modes

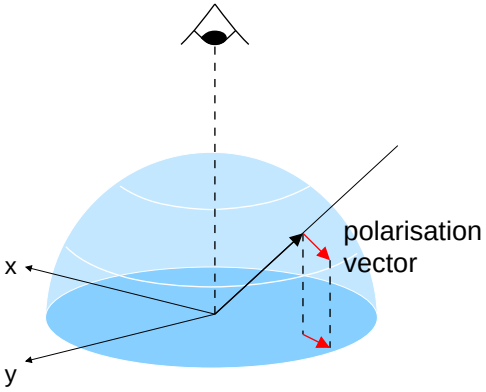

a) Details of projection used.

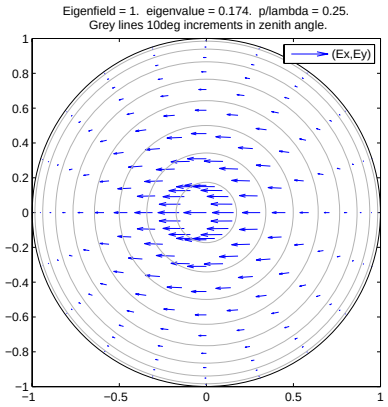

b) First mode (eigenvalue = 0.175)

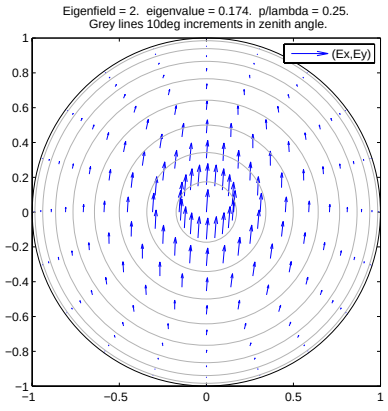

c) Second mode (eigenvalue = 0.175)

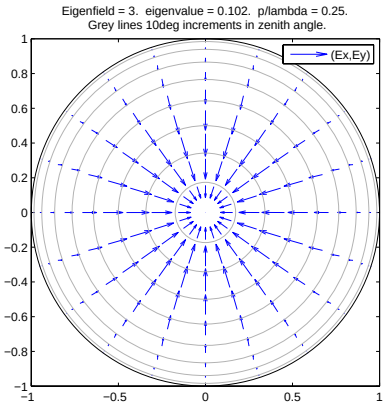

d) Third mode (eigenvalue = 0.102)

Fig. 8 The three modes of the incident field in which the bolometer is responsive to power at $p / \lambda = 0.25$. Panel (a) shows the detail of the projection used when plotting the fields. The polarisation vector associated with a particular direction of illumination is plotted at the point corresponding to the projection of the direction vector into the *(x, y)* plane. The polarisation vector is also shown projected into the plane, i.e. the vectors in the plot correspond to the *x* and *y* components of the polarisation vector in the coordinate system of Fig. 4. Panels (c) to (d) show the field plots. The grey circles indicate 10º increments in zenith angle.

and this is observed. It is slightly less responsive to the third mode, which corresponds to a dipole orientated normally to the bolometer plane. This is because the wave that would couple most effectively to it, a wave incident horizontally over the plane, is suppressed by the cosine dependence on zenith angle. These plots suggest a simple model for a diffraction limited planar absorber, consisting of three antennas with reduced responsivity to the dipole normal to the absorber.

CONCLUSIONS:

We have described a powerful technique for characterising and measuring the optical behaviour of bolometric detectors. A bolometer's behaviour is characterised by a quantity called the *detector response function*. This function essentially describes the set of fully-coherent modes in which the detector is simultaneously sensitive to power. We have shown that the response function can be determined experimentally by illuminating the detector with two coherent, phase-locked plane-wave sources operating at the same frequency. If the relative phase of the two waves is rotated, the visibility of the fringes at the output of the detector can be used to calculate the component of the response function for the particular polarisation and directions of incidence. By repeating for all pairs of source locations, and polarisation states, the full response function can be found.

This characterization process can be applied at any wavelength from the sub-millimetre, through the far-infrared and into the optical. The limiting factor is the ability to produce coherent, phase-locked, radiation at a particular wavelength. Furthermore, it can be applied independently of

the details of the power absorption mechanism, and how power is coupled into the detector. We envisage the procedure having uses outside of bolometer characterisation. The modes to which the detector is sensitive will depend on, for example, correlations and anisotropies in the absorber, relaxation processes and solid-state excitations. They should therefore be a source of information about these processes, and could be useful in solid-state physics and surface-physics.

We are intending to use these techniques to investigate planar absorbing structures at 195-270GHz, and have described an experiment that is currently being constructed. The theoretical models we have created suggest that planar absorbers should exhibit a change in behaviour from multi-mode to few-mode as the dimensions of the absorber fall below the wavelength of the radiation, or in situations where the absorption mechanism has some intrinsic sold-state coherence length, where the dimensions fall below this length. We expect to observe this behaviour experimentally.

Finally, in this paper we have only considered the response of detectors to fields in different states of spatial coherence. The illuminating radiation has been assumed to be stationary. In further work we hope to show that it is possible to recover the full spatio-temporal state of coherence of the incident field to which a detector is sensitive by performing the characterization with a pair of sources whose relative frequencies can be varied.

REFERENCES:

[1] M. J. Griffin, "Bolometers for far-infrared and submillimetre astronomy", *Nuclear Inst. and Methods in Physics Research A*, vol. 444, pp. 397–403, April 2000.

[2] G. Efstathiou, C. Lawrence and J. Tauber, "The Planck Blue Book", Planck Science Team, 2005.

[3] M. D. Audley and the CLOVER collaboration, "TES imaging array technology for CLOVER", in *Proc. SPIE*, vol. 6275, June 2006

[4] G. Saklatvala, S. Withington and M. P. S. Hobson, "Coupled-mode theory for infrared and submillimetre wave detectors", *J. Opt. Soc. Amer. A*, vol. 24, pp. 764–775, February 2007.

[5] S. Withington and G. Saklatvala, "Characterising the behaviour of partially coherent detectors through spatio-temporal modes", *J. Opt. A: Pure Appl. Opt.*, vol. 9, pp 626-633, April 2007.

[6] H. Griffiths and B. L. Smith, Ed., *Modern Antennas*, ser. Microwave and RF technology. London: Chapman & Hall, 1998.

[7] L. Mandel and E. Wolf, *Optical Coherence and Quantum Optics*, Cambridge University Press, 1995.

[8] M. Brand, "Fast online SVD revisions for lightweight recommender systems", in *Proceedings of the 3rd SIAM International Conference on Data Mining*, 2003.

[9] S. Withington, C. Y. Tham and G. Yassin, "Theoretical analysis of planar bolometric arrays for THz imaging systems", in *Proc. SPIE,* vol. 4855, pp. 49-62, 2003 .

[10] D. T. Chuss, E. J. Wollack, S. H. Moseley, S. Withington, and G. Saklatvala, "Diffraction considerations for planar detectors in the few-mode limit", *Publications of the Astronomical Society of the Pacific*, vol. 120, pp. 430-438, April 2008

Silicon Micromachined Components at Terahertz Frequencies for Astrophysics and Planetary Applications

Goutam Chattopadhyay*, John S. Ward, Harish Manohara, Risaku Toda, and Robert H. Lin

Jet Propulsion Laboratory, California Institute of Technology, Pasadena, CA 91109, USA

* Contact: goutam@jpl.nasa.gov, phone +1-818-393-7779

***Abstract* — At the Jet Propulsion Laboratory (JPL) we are using deep reactive ion etching (DRIE) based silicon micromachining to develop the critical waveguide components at submillimeter wavelengths that will lead to highly integrated multi-pixel spectrometers, imagers, and radars. The advantage of DRIE over wet anisotropic etching is that DRIE exhibits little crystal plane dependence and therefore reduces geometric restrictions. As a result, DRIE enables fabrication of trenches that are independent of crystal planes, thus making it possible to develop micromachined waveguides with vertical sidewall profiles. In this paper we describe the design and fabrication of silicon micromachined critical waveguide components operating in the range 325-500 GHz frequency band for astrophysics and planetary applications from space. We also address the challenges of testing these devices when interfaced with metal waveguide test fixtures.**

I. Introduction

Future multi-pixel, multi-functional, high performance instruments operating at frequencies from hundreds of gigahertz to several terahertz will require waveguide circuits with very small feature sizes and high precisions. Indeed, state-of-the-art missions currently in development, such as the ground-breaking HIFI instrument on Herschel [1], are based on single-pixel, single-ended double-sideband receivers. It is well known that at frequencies beyond a few hundred gigahertz, the feature sizes of all but the simplest waveguide circuits are too small and the required tolerances are too demanding to be fabricated using even the best state-of-the-art conventional machining. On the other hand, silicon micromachining shatters the barriers of conventional machining, and brings the added benefits of rapid turn-around time and excellent process control. Furthermore, silicon micromachined circuits are light weight and capable of achieving a high degree of integration on a single chip. While there have been several demonstrations of waveguide circuits fabricated with silicon micromachining [2] and other techniques [3], few if any of these circuits have been subjected to any significant electrical testing.

Submillimeter-wave integrated silicon micromachined circuits for array receivers have never been demonstrated. Deep reactive ion etching (DRIE) based silicon micromachining is the most viable option for the fabrication of these high performance components in an array instrument which require deep vertical profiles in waveguides [4]. The silicon etching process in DRIE consists of an etching cycle flowing only Sulphur hexafluoride (SF_6) and a sidewall passivation cycle flowing only octofluorocyclobutane (C_4F_8). The advantage of DRIE over wet anisotropic etching is that DRIE exhibits little crystal plane dependence, therefore, reducing the geometric restrictions [5]. As a result, DRIE enables fabrication of trenches that are independent of crystal planes, thus making it possible to develop micromachined waveguides with vertical sidewall profiles. Compared to silicon laser micromachining [6], DRIE is more efficient in etching large volumes of substrate. Moreover, the DRIE process is much simpler for mask alignment issues as compared to other micromachining techniques where the mask alignment has been proven to be extremely challenging. Moreover, one of the key problems with the current generation of silicon micromachined components has been the difficulty to design an interface to mate the components to metal waveguide test equipment for the proper characterization of the individual components. In this paper we will describe the design and fabrication of silicon micromachined critical waveguide components operating in the 325-500 GHz frequency range (WR-2.2 waveguide band). We will also discuss the design of a novel test fixture that we have developed at JPL to address the issues of testing and characterization of radar array.

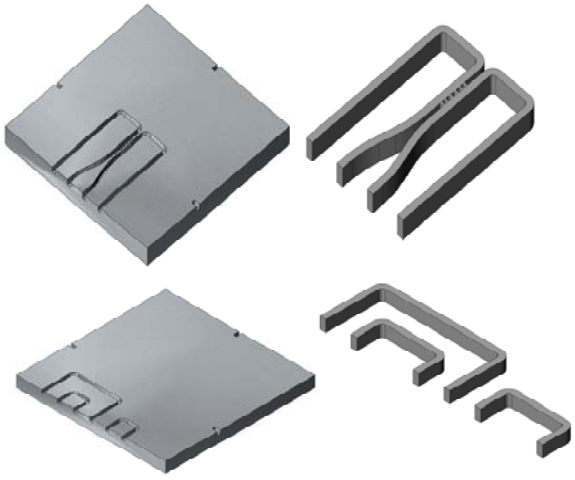

Fig. 1: Quadrature hybrids, different lengths of waveguides, and other components designed in the 325-500 GHz frequency band for silicon micromachining.

II. Design, Fabrication, and Testing

We designed broadband quadrature-hybrid couplers, directional couplers, in-phase power dividers, and other components, as shown in Fig. 1, for operation in the 325-500 GHz frequency range using three-dimensional electromagnetic simulators (Ansoft HFSS) and linear circuit simulators (Agilent ADS). We also designed waveguides of different lengths for on-wafer calibration capability. These components were fabricated on silicon substrates in JPL's Micro Devices Laboratory using DRIE technique. In our laboratory, we developed a preliminary DRIE fabrication recipe for developing silicon micromachined components; the process steps are shown in Fig. 2. We coat the high resistivity silicon wafer with a 5 µm thick layer of SJR-5740 positive photo resist and expose it for approximately 40 seconds using 25 W·cm^{-2} 320 nm ultraviolet (UV) light. We then develop it in a mixture of AZ400K and DI water in 1:3 ratios until the pattern clears. The wafer is then mounted on a backing wafer using crystal bond. The etching rate is approximately 2 µm/min and achieves ±10% uniformity across the wafer. For developing the components for this work, we further developed and optimized this step in order to achieve a good vertical etch for the walls. The final parts are released in acetone. We also fabricated silicon alignment pins to align the two spilt waveguide blocks. We evaporated gold on the silicon micromachined components by mounting the wafer at an angle for uniform metal deposition. Fig. 3 shows SEM photograph of the fabricated components, showing close up of the surface properties of the wall. Fig. 3 shows uniform gold deposition and no noticeable excessive deposition at the base of the post for the hybrids. Fig 4 shows

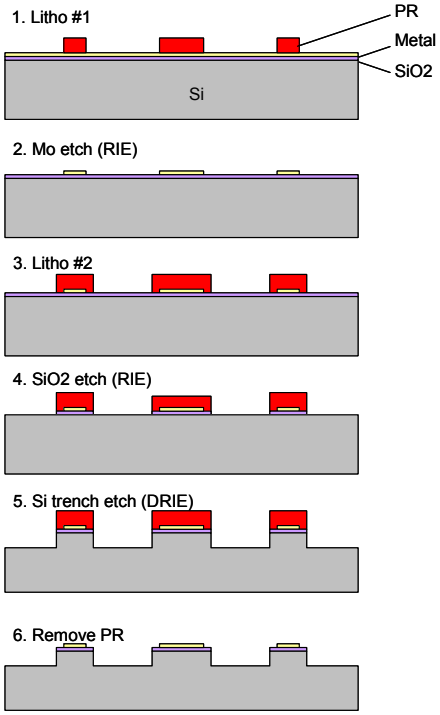

Fig. 2: Deep reactive ion etching fabrication process flow diagram.

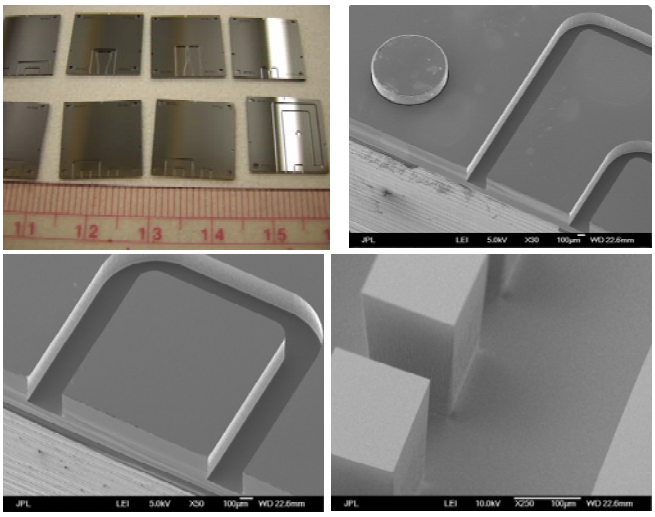

Fig. 3: SEM photographs of the fabricated silicon machined waveguides and the silicon alignment pin (top right) and close-up of the posts for the hybrid (bottom right).

the roughness of the gold plated surfaces measured with Wyko interferometer system, and surface roughness after gold evaporation was found to be in the 50-200 nm range.

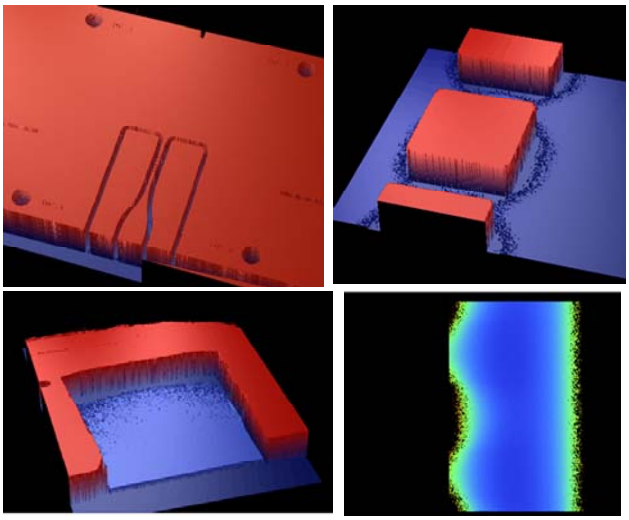

Fig. 4: Photograph of the roughness of the surfaces measured with Wyko interferometer system.

Previous efforts to demonstrate micromachined waveguides have been severely limited by the difficulty of testing the fabricated components, especially due to issues involving mating the silicon components to calibrated test equipment. We have invented a novel test system to eliminate these difficulties and allow rapid and accurate testing of the micromachined circuits. With our system, the prototype components were assembled in an innovative test fixture, as shown in Fig. 5. Preliminary testing with a 325-500 GHz vector network analyzer is under progress now. Our test fixture brings the dual benefits of being compatible

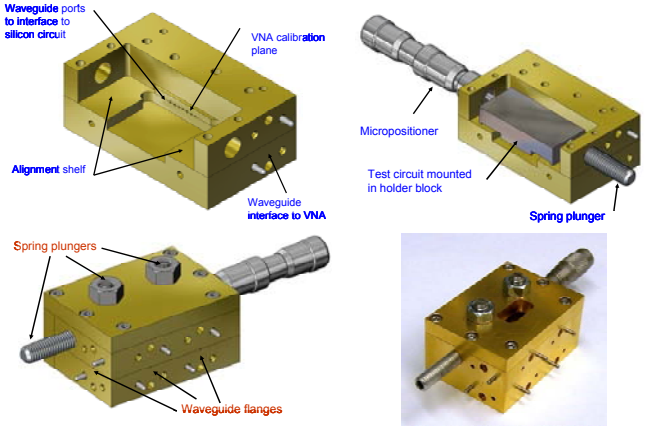

Fig. 5: Schematic of the test fixture used to measure the silicon micromachined components. A photograph of the machined test fixture is shown on the bottom right.

with the brittle nature of silicon (e.g., no screws or alignment pins mate to the silicon components, with spring plungers providing the necessary contact forces) as well as allowing the waveguides to be quickly aligned with the test equipment with a precision several times better than what is achievable with the best conventional microwave flanges. Furthermore, with our system, the vector network analyzer can be calibrated a single time, and then used to test a whole series of test components all in a single test fixture. Only one test fixture will be required to test all the prototype components. In future we will integrate multi-component waveguide circuits such as the waveguide portions of sideband-separating and balanced heterodyne receivers and will characterize them in the 325-500 GHz frequency band.

CONCLUSIONS

We have fabricated waveguide components in the 325-500 GHz band using DRIE-based silicon micromachining. We have also machined a metal test fixture to measure the fabricated components in a rapid and reliable fashion. On wafer calibration standards will be used to calibrate the network analyzer for testing these components. The gold plated micromachined components shows good vertical profile and smooth surface characteristics. Testing and characterization of the components are under progress currently in our laboratory.

ACKNOWLEDGMENT

The research described herein was carried out at the Jet Propulsion Laboratory, California Institute of Technology, Pasadena, California, USA, under contract with National Aeronautics and Space Administration.

REFERENCES

[1] T. de Graauw, N. Whyborn, E. Caux, T. Phillips, J. Stutzki, X. Tielens, R. Güsten, F. Helmich,W. Luinge, J. Pearson, P. Roelfsema1, R. Schieder, K. Wildeman, and K. Wafelbakker, "The Herschel-Heterodyne Instrument for the Far-Infrared (HIFI)," Proceedings SPIE, vol. 6265, 2006.

[2] J. P. Becker, J. R. East, and L. P. B. Katehi, "Performance of Silicon Micromachined Waveguide at W-band," Electron. Lett., vol. 38, no. 13, pp. 638-639, June 2002.

[3] V. Desmaris, D. Meledin, A. Pavolotsky, and V. Belitsky, "Microfabrication Technology for All-Metal Sub-mm and THz Waveguide Receiver Components", To appear in the Proc. of the Nineteenth Intl. Symp. on Space Terahertz Technology, Groningen, Netherlands, April 2008.

[4] Y. Lee, J. P. Becker, J. R. East, and L. P. B. Katehi, "Fully Micromachined Finite-Ground Coplanar Line-to-Waveguide Transistors for W-Band Applications," IEEE Trans. Microwave Theory and Tech., vol. 52, no. 3, pp. 1001-1007, March 2004.

[5] J. P. Becker, "Silicon Micromachined Waveguide Transition and Three-Dimensional Lithography for High Frequency Packaging," Ph.D. dissertation, Dept. Electrical Eng. Comput. Sci., The University of Michigan, Ann Arbor, MI, 2001.

[6] C. K. Walker, G. Narayanan, H. Knoepfle, J. Capara, J. Glenn, and A. Hungerford, "Laser Micromachining of Silicon: A New Technique for Fabricating High Quality Terahertz Waveguide Components," Proc. of the 8th. Int. Space Terahertz Tech. Symp., Cambridge, MA, pp. 358-376, March 1997.

Microfabrication Technology for All-Metal Sub-mm and THz Waveguide Receiver Components

Vincent Desmaris[1,*], Denis Meledin[1], Alexey Pavolotsky[1], and Victor Belitsky[1]

[1]*Group for Advanced Receiver Development (GARD), Chalmers University of Technology, Gothenburg, Sweden*

* Contact: vincent.desmaris@chalmers.se, phone +46-31-772 1846

***Abstract*— A novel technology for manufacturing of micromachined all-metal waveguide circuits and structures for the frequency band from 200 up to 7000 GHz (Sub-Millimeter and THz) is presented. The waveguide circuits are formed using metal electroplating with preceding sputtering of a thin metal film seed layer over a photo-lithographically patterned thick SU-8 photo-resist. The process provides possibility of making 3-dimensional structures via facilitating of multi-level (layered) designs. Surface roughness of the THz waveguide structure was demonstrated to be below 0.1 µm. This technology was used to build a state-of-the art waveguide balanced 1.3 THz Hot Electron Bolometer mixer and other application for radio astronomy instrumentation.**

I. Introduction

Pushing the instrumentation receiver technology above 1 THz should make waveguide technique the technology of choice since waveguide gives the lowest possible insertion loss among other types of transmission line and a corrugated horn interfaces naturally to the waveguide. Corrugated horns producing nearly perfect Gaussian beam are the most efficient way to couple the antenna signal to a receiver at frequencies where the dimensions of such feed could be made practical. Nevertheless, since Maxwell equations' solution scales with the frequency, the shortening of the wavelength decreases the waveguide dimensions and, due to the skin-effect and associated RF loss increases the demand on the quality of the waveguide inner surface. These drive the required manufacturing accuracy and surface quality beyond the possibilities of existing machining tools. As a first approach of solving the problem for the extremely small dimensions and high required surface quality, Silicon micromachining has been used to produce waveguide structures for THz receivers [1]-[2]. This technique is largely limited to fabrication of 2 layer structures, with inherent difficulty of making grooves of different width, and, generally, the process somewhat cumbersome. On our view, this approach is also especially impractical for a cryogenic receivers due to integration problems of silicon components to the surrounding metal blocks because of the large stress developed during cooling down to cryogenic temperatures caused by sufficient mismatch of thermal expansion coefficients. Similar problems are also likely to occur when waveguide structures are defined and processed exclusively out of thick SU-8 photoresist [3] or combining Si etching and thick photoresist [4].

A perfect solution for these problems would be a process delivering all-metal structures with dimension accuracy better than 1 µm and with surface roughness lower than the skin depth at the waveguide circuit operating frequencies. This kind of technology has been demonstrated by Pavolotsky et al. [5] to fabricate 3-dB waveguide hybrids for THz mixers [6]; however the fabricated circuit consisted of a single layer. Mata et. al. [7] demonstrated the feasibility of six-layer structures in bare SU-8 layer. With a similar concept based on the metal electroforming over a photoresist mould, we propose a new micro-fabrication technique by combining of the two approaches [5], [7] in order to fabricate all-metal 3-layer Sub-Millimeter and THz waveguide structures and circuits. The technique description and waveguide components and circuits, already fabricated with the proposed micromachining technology, are presented in this paper.

II. WAVEGUIDE FABRICATION TECHNIQUE

Clearly, a "layered fabrication" technique should be facilitated by preceding tedious designing process to achieve desired electromagnetic performance and keep compatibility with the processing of the waveguide "layered" structure [6]. In order to take full advantage of photolithography, a 4" silicon wafer is used as a carrier substrate for a photo-resist mould and provides the desired planarity. An optional release layer could be applied to ease the separation of the ready structure from its Si-carrier.

All three SU-8 layers are then sequentially spun, baked, exposed and post-baked. As recommended by the SU-8 manufacturer, an i-line mask aligner is employed to expose the resist while filtering out wavelengths shorter than 350 nm to ensure improved resist pattern wall verticality. Development of the photoresist is then carried out in Mr-Dev 600 for 10 to 30 minutes depending on the overall thickness of the structure in our case varying between 90 and 350 µm.

Consequently the conducting metal seed layer was deposited by magnetron sputtering, prior to the copper electro-plating. The copper electro-plating is performed in two steps using the same proprietary solution. At first, a low current is applied to ensure fine gap filling and thus an

accurate definition of the structure. In a second step, a higher current is set for rapid growth of the bulk copper. The silicon carrier wafer is then either etched away in warm tetra – methyl ammonium hydroxide (TMAH), or released by dissolving the release layer. Finally the SU-8 mould is stripped away in a Piranha etching solution before gold-plating of the whole Cu waveguide structure.

III. TECHNOLOGY DEMONSTRATORS

A. Balanced Waveguide 1.25-1.39 THz HEB Mixer

In order to investigate the suitability of the developed micro-fabricating technique, we used it to produce a mixer block for a prototype of a 1.25-1.39 THz APEX T2 Hot Electron Bolometer (HEB) heterodyne receiver [6].

The receiver employs a balanced scheme allowing an effective use of available local oscillator (LO) power and rejecting the noise coming via LO port. The front section of the mixer block contains two corrugates horns, a 3 dB 90 degrees waveguide hybrid providing LO injection and RF signal distribution between the HEB mixers. The hybrid employs split-block technique and was fabricated using one layer SU-8 lithography as described in [5], [6].

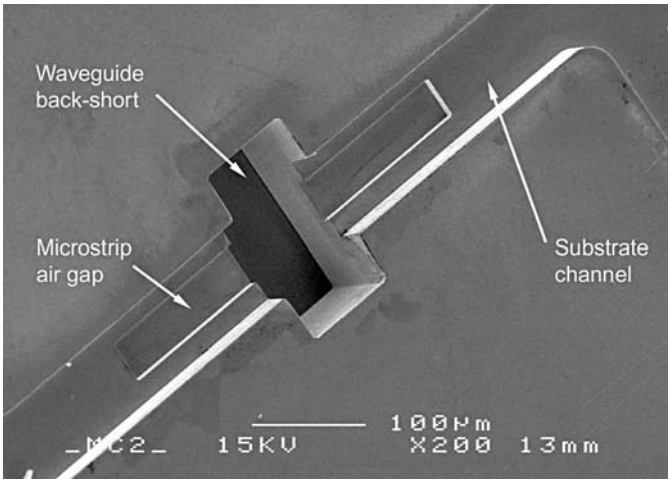

Fig.1. SEM image of the fabricated multi-level structure: a back-piece of the 1.3 THz HEB mixer block.

The second part of the mixer block is made in a back-piece layout and designed to take advantage of a multi-level micro-fabrication technology. The substrate channel uses suspended microstrip line configuration as depicted in Fig. 1 and accommodates a pair of HEB mixer substrates of 1000 µm×70 µm×17 µm in size. The back-short depth of 68 µm was chosen to provide an optimum input match of the mixer element over the entire signal frequency band 1.27–1.39 THz. The linear dimensions of the produced back-piece were within ±0.5 µm accuracy and the surface roughness was measured to be below 0.1 µm at all levels. The dimensions of the substrate channel are 31 µm deep and 80 µm wide; an air gap is 10 µm deep and 40 µm wide. Surface roughness measurement of the back-short bottom, seen as a darker area in the middle of Fig. 1, taken by Veeco Wyko NT1100 surface profiler, is presented in Fig.2.

Noise temperature measurements of the prototype 1.3 THz HEB balanced mixer were performed at an intermediate frequency of 2.5 GHz and are shown in Fig. 3. At these signal frequencies our balanced mixer demonstrates noise performance quite comparable to a single-end waveguide HEB mixer receiver [9], despite substantially longer waveguides are employed. Detailed description of the final receiver is presented in [10].

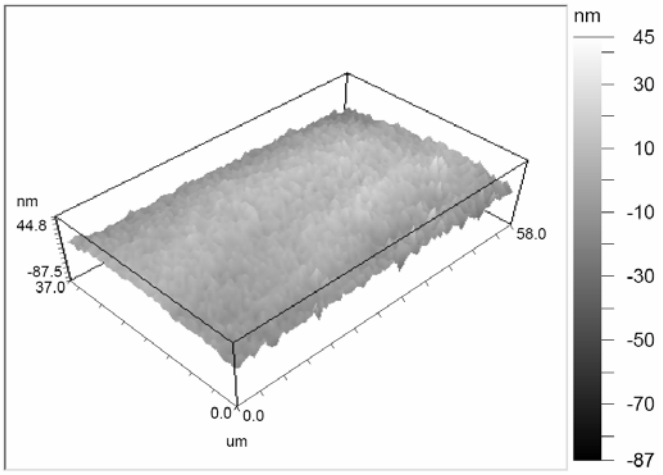

Fig. 2. Surface roughness measurement at the bottom of the back-short structure. The roughness scale is at the right.

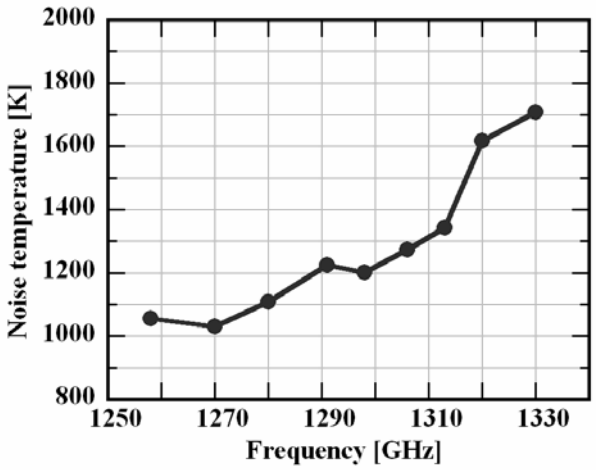

Fig. 3. Noise temperature of the prototype 1.3 THz HEB waveguide balanced receiver as a function of frequency taken at 2.5 GHz intermediate frequency.

G. 600-750 GHz Sideband Separation SIS Mixer

A 600 – 750 GHz Sideband Separation SIS mixer has been developed, produced by traditional mechanical technology and demonstrated [8]. As part of a collaborative project with SRON, Groningen, we have produced a micro-machined version of the mixer block this time employing the split-block layout. In this case, a complete waveguide circuit comprising the interface waveguides to RF and LO horns, 3-dB 90o hybrid, LO divider and LO injection directional couplers, the

two substrate channels with air-gap for suspended microstrip line was manufactured in a three level waveguide integrated structure, Fig. 4. The linear dimensions of the produced back-piece were all within ±0.5 μm accuracy and the rms surface roughness was measured by the Veeco Wyko NT1100 surface profiler to be below 250 nm.

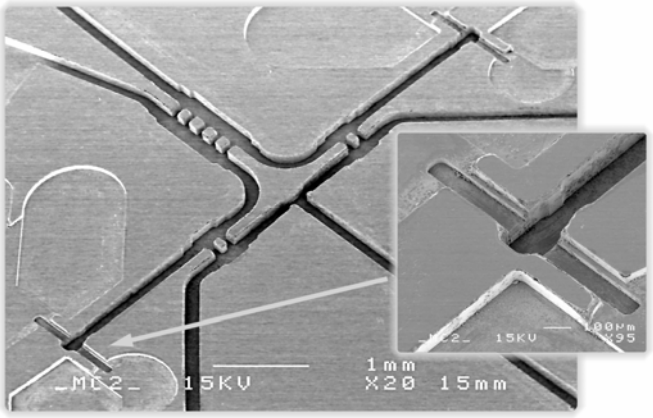

Fig. 4. SEM picture of the micro-fabricated 600-750 GHz 2SB SIS Mixer. The insert shows enlarged area of the substrate channel made in the 3-layer processing.

B. DISCUSSION

The application of the presented micromachining technique for the fabrication of Sub-Millimeter and THz components faces different limitations in reproduction of structures' geometry at the lower frequency end. For Sub-Millimeter wave components with bigger waveguide dimensions some peculiarities of the photolithography process should be taken into account. The verticality of the SU-8 pattern walls and internal photoresist stress issues could be challenging.

In order to explore possibilities of the presented micro-machining technology, we have fabricated a waveguide circuit for 2SB SIS mixer with even larger waveguide dimensions. The measured depth of the processed waveguides was 350 μm, which suggests that, used in a split-block layout the waveguide circuits down to 200 GHz could be fabricated using the proposed micromachining technique.

Towards higher THz frequencies, where the waveguide and substrate channel dimensions become of the order of a few microns, the accuracy of the photoresist layer thickness and the geometry patterning precision would play a major role in the fabrication yield. We envisage that use of DUV lithography would allow pushing this technology up to 6 7 THz while the major constrains would probably come from the availability of active elements, e.g., HEB, SIS, Schottky mixers and the ability of mounting such components into the waveguide mixer block.

Additional advantage of using the suggested technology is a possibility to ease the production of relatively complex waveguide circuits by employing a single photo-mask set. Along with achieving extremely high waveguide surface quality and thus low RF loss and possibility of using multi-level designs, the suggested technology opens solid prospects for building complex waveguide circuits, e.g., a balanced receiver scheme comprising the hybrid, bends and waveguide lines providing interfaces to the input horns and to the mixer back-piece or a sideband separation scheme with similar complexity. We plan a further step by employing the proposed technology for multi-pixel Sub-Millimeter and Terahertz receivers.

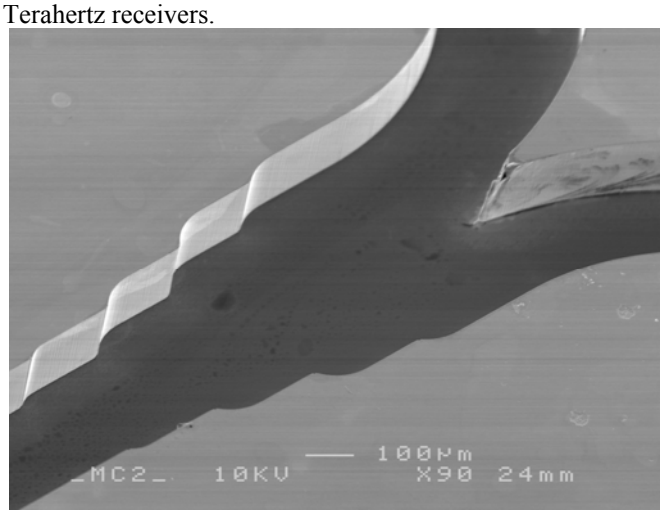

Fig. 5. Scanning electron microscope picture of the power divider in split-block technique with wall height of 350 microns

CONCLUSIONS

A new micromachining method combining multilayer photolithography and metal electroforming for the micro-fabrication of all-metal waveguide circuits and assembles comprising up to 3 levels is presented. Sub-micrometric linear dimension accuracy and excellent surface roughness of the components have been demonstrated. The processed components and circuits were implemented in various designs described above including a unique 1.3 THz balanced waveguide HEB mixer. The developed fabrication process allows fabrication of waveguide structures from about 200 GHz and up to approximately 7 THz and is extremely suitable for implementing waveguide-based designs including single end, balanced, sideband rejection and multi-element receivers.

ACKNOWLEDGMENTS

This work was supported by the Swedish Research Council and the Wallenberg Foundation via respective grants, and in part by Swedish Space Board, and EU FP 6 RadioNet AMSTAR.

REFERENCES

[1] [1] C. M. Mann, P. de Maagt, G. McBride, F. van de Water, D. Castiglione, A. McCalden, L. Deias, J. O'Neill, A. Laisne, J. T. Vallinas, I. Ederra, D. Haskett, D. Jenkins, A. Zinn, M. Ferlet, and R. Edeson, "Microfabrication of 3D terahertz circuitry," in *IEEE MTT-S International Microwave Symposium*, 2003, pp. 739-742.

[2] [2] P. L. Kirby, D. Pukala, H. Manohara, I. Mehdi, and J. Papapolymerou, "Characterization of micromachined silicon rectangular waveguide at 400 GHz," *Microwave and Wireless Components Letters, IEEE,* vol. 16, pp. 366-368, 2006.

[3] [3] W. H. Chow, A. Champion, and D. P. Steenson, "A precision micromachining technique for the fabrication of hybrid millimeter wave circuits and sub-assemblies," in *IEEE MTT-S International Microwave Symposium*, 2004, pp. 345-348.

[4] [4] C. H. Smith, III, X. Haiyong, and N. S. Barker, "Development of a multi-layer SU-8 process for terahertz frequency waveguide blocks," in *IEEE MTT-S International Microwave Symposium*, 2005, pp. 439-443.

[5] [5] A. Pavolotsky, D. Meledin, C. Risacher, M. Pantaleev, and V. Belitsky, "Micromachining approach in fabricating of THz waveguide components," *Microelectronics Journal,* vol. 36, pp. 683-6, 2005.

[6] [6] D. Meledin, M. Pantaleev, A. Pavolotsky, C. Risacher, V. Belitsky, V. Drakinskiy, and S. Cherednichenko, "Balanced Waveguide HEB Mixer for APEX 1.3 THz Receiver," in *International Symposium on Space Terahertz Techonology*, Göteborg, 2005, pp. 214-216.

[7] [7] A. Mata, A. J. Fleischman, and S. Roy, "Fabrication of multi-layer SU-8 microstructures," *Journal of Micromechanics and Microengineering,* vol. 16, pp. 276-284, 2006.

[8] [8] F. P. Mena, J. W. Kooi, A. M. Baryshev, D. F. J. Ledewaijk, R. Hesper, and W. Wild, "Construction of a Sideband Separating Heterodyne Mixer for Band 9 of ALMA," in *17th International Symposium on Space Terahertz Technology*, California Institute of Technology, Pasadena, Ca., 2007.

[9] [9] D. V. Meledin, D. P. Marrone, C. Y. E. Tong, H. Gibson, R. Blundell, S. N. Paine, D. C. Papa, M. Smith, T. R. Hunter, J. Battat, B. Voronov, and G. Gol'tsman, "A 1-THz superconducting hot-electron-bolometer receiver for astronomical observations," *IEEE Transactions on Microwave Theory and Techniques,* vol. 52, pp. 2338-43, 2004.

[10] D. Meledin *et al*. "A 1.3 THz Balanced Waveguide HEB Mixer for the APEX Telescope" *sumitted to IEEE transactions on Microwave theory* and Techniques. May 2008

High performance smooth-walled feed horns for focal plane arrays

P. Kittara[1,*], J. Leech[2], G. Yassin[2], B.K. Tan[2], A. Jiralucksanawong[1] and S. Wangsuya[1]

[1]*Physics Department, Mahidol University, Rama VI Road, Bangkok, 10400, Thailand*

[2]*Department of Physics, University of Oxford, Denys Wilkinson Building, Keble Road, Oxford, OX1 3RH, United Kingdom*

* Contact: tepcy@mahidol.ac.th, phone +66-2-201 5766

***Abstract*— We describe the design and testing of an easy-to-machine smooth-walled horn which exhibits excellent beam circularity and low cross polarisation over a relatively large bandwidth. The design comprises three coaxial conical sections and two flare discontinuities joining the three sections together. The discontinuities generate appropriate higher order modes which combine to give a circular field distribution at the aperture. The positions and sizes of these discontinuities were calculated using a genetic algorithm. The horn was fabricated either by using the well known electroforming method or simply by a drill tool, shaped into the horn profile, and a standard mill. The measured radiation patterns or the electroformed horns show good excellent circularity and agree well with the calculated curves. They also show that the three-section horn has a substantially wider bandwidth than the conventional Potter horn. Preliminary measurements of the drilled horns patterns are also shown and compared with theory.**

I. Introduction

A high-quality astronomical feed usually employs a conical corrugated horn. The presence of azimuthal corrugations in the horn presents isotropic surface boundary conditions to the electric and magnets field on the wall, resulting in the propagation of a "hybrid mode". This configuration produces a circular beam with low cross polarization and sidelobes over a substantial fractional bandwidth, which is required for many applications. Corrugated horns, however, require the fabrication of several corrugations per wavelength, which can be technically complicated and expensive at THz frequencies.

The Potter horn [1] has many of the desired properties of a corrugated horn and yet is much simpler to construct. Conventionally, it consists of a conical horn with a single step discontinuity at the horn throat whose dimensions are chosen in order to excite the TM_{11} mode at carefully selected amplitude (~16%) with respect to the amplitude of the incident TE_{11} mode. The "dual-mode" is then made to propagate through a cylindrical "phasing section" to make the two modes arrive at the horn aperture in phase. This results in sidelobe cancellation and low cross polarization in the horn radiation pattern. A simplified version of the Potter horn without the phasing section was suggested in [2] and used in a 700 GHz finline mixer [3].

A well known disadvantage of the Potter horn however is the relatively narrow bandwidth of approximately 10%.

The corrugated horn increases the bandwidth substantially, by adding many more equally spaced, identical discontinuities along the horn. An optimized location and magnitude of theses discontinuities however is likely to reduce the large number of corrugation to only a few.

An alternative method of exciting the TM_{11} mode is a sudden change in the horn flare angle as shown in Fig. 1. Here, a second section is formed by changing the flare angle when the horn radius is r_1, at an axial distance L_1 from the throat of the horn [4].

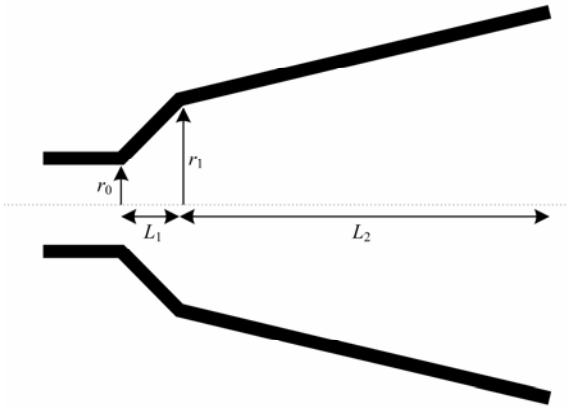

Fig. 1. Geometry of the dual-mode two-section horn with a flare angle discontinuity. r_0 is the radius of the circular waveguide. r_1 and L_1 are the radius and the length of the first conical section. L_2 is the length of the second conical section.

Here again, the bandwidth is also limited to a similar percentage of 10% since the correct phasing of the two mode modes can only be achieved over a small fraction of the

wavelength. We have found however that adding a one more flare discontinuity doubles the bandwidth and we expect that a bandwidth comparable to a corrugated horn can be achieved by generating a few (~5) flare discontinuities at optimized locations along the horn.

We have previously reported [5], [6] success in optimising the design of both types of Potter horn using a technique based on genetic algorithm. We have developed a complete design software package which combines the modal matching method [7] with genetic algorithm [8] and downhill simplex optimisation routines. This allows design of easy to fabricated Potter horns with multiple discontinuities in the horn profile.

In this paper, we present simulations and measured radiation patterns for 230 GHz prototype horns with 3 flare angles. Some of the prototype horns were fabricated using a drill tool, shaped into the horn profile, and a standard mill. For benchmark comparison, we fabricated two prototype horns using electroforming. The measured radiation patterns have good beam circularity and agree with the calculated curves. They also show that this three-section horn has a substantially wider bandwidth than a conventional Pickett-Potter horn. The beam circularity is good to almost -30 dB. The peaks of the cross-polarization levels were below -30 dB for a fractional bandwidth of 10% near the centre frequency, and below -25 dB for 20% bandwidth.

II. Horn design using a Genetic Algorithm

The positions and sizes of the flare-angle discontinuities for broad bandwidth operation of Potter horns have traditionally been only obtained approximately since it was based on analytical computation, assuming that only the TE_{11} and TM_{11} propagate to the aperture. Our approach has been to use a genetic algorithm to determine the optimal positions and sizes of these discontinuities. This procedure has already been reported [5], hence it will only be mentioned very briefly. We calculate the horn patterns, using modal matching, for a "population" of initially random horn designs, and compute the fitness of each design from the quality parameter of the pattern. Then, by using crossover and mutation techniques upon a "chromosome" which is constructed from the horn parameters, we produce a new generation of horn designs from the fittest members of the old population. After using the genetic algorithm to locate the approximate position of the quality function global minimum, we then optimise the design using a traditional downhill simplex method.

Details of the optimization criteria are given in [5,6]. In brief, the fitness of an individual is inversely proportional to the 'cost function'. This cost function measures the deviation of the beam pattern from a desired pattern. In our design, the cost function of an individual at a selected frequency is calculated from two factors: the beam circularity and cross-polarization level. The beam circularity and cross polarization target level were stringent. The peak cross polarization was requested to be less than -30 dB. Higher cross-polarisation and lower beam circularity produce higher values of the cost function and hence lower fitness. These two factors are computed at different frequencies across the required band with a frequency step of 0.02 times the centre frequency. The total cost function is then calculated from the sum, with a Gaussian weight, of the products of the two factors for all frequencies. The Gaussian weight of the total cost functions forces the beam circularity near the centre frequency to be better than near the edges.

The problem constraints include specifying the frequency band edges and the central frequency, in addition to the geometry parameters such as the waveguide radius and the horn flare angle. The problem variables include the radii and lengths of the three sections. The length of each section is constrained to be between from $0.1\lambda_0$ to $30\lambda_0$, and the radii are constrained to be between $0.1\lambda_0$ and the size of the aperture.

III. A 230 GHz 3-Section Horn Design

In Table I we show the dimensions of the prototype horn designed using the above method. The centre frequency of the design is 230 GHz with a wavelength λ_0 = 1.204 mm. The horn was designed to have a beamwidth of around 15 degrees for testing. This beamwidth is largely determined by the horn aperture, so both the horn aperture and initial waveguide size were fixed to $0.467\lambda_0$ and $5.600\lambda_0$ before optimizing the other horn dimensions using the genetic algorithm. The optimized dimensions and a schematic of the horn profile are shown in Table I and Fig. 2.

TABLE I

Dimensions of the Three-Section Horn

	Start radius	**Length**	**End radius**
Conical Section 1	$0.467\lambda_0$	$1.134\lambda_0$	$1.140\lambda_0$
Conical Section 2	$1.140\lambda_0$	$0.929\lambda_0$	$1.389\lambda_0$
Conical Section 3	$1.389\lambda_0$	$18.400\lambda_0$	$2.800\lambda_0$

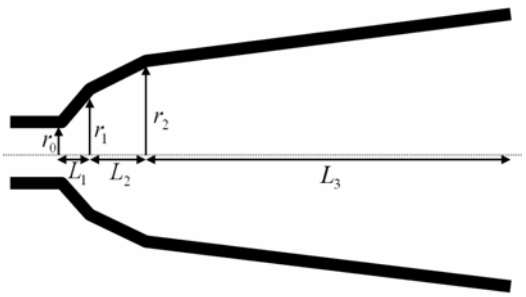

Fig. 2 Cross section of a three-section horn. r_0 is the radius of the circular waveguide. r_1 and L_1 are the radius and the length of the first conical

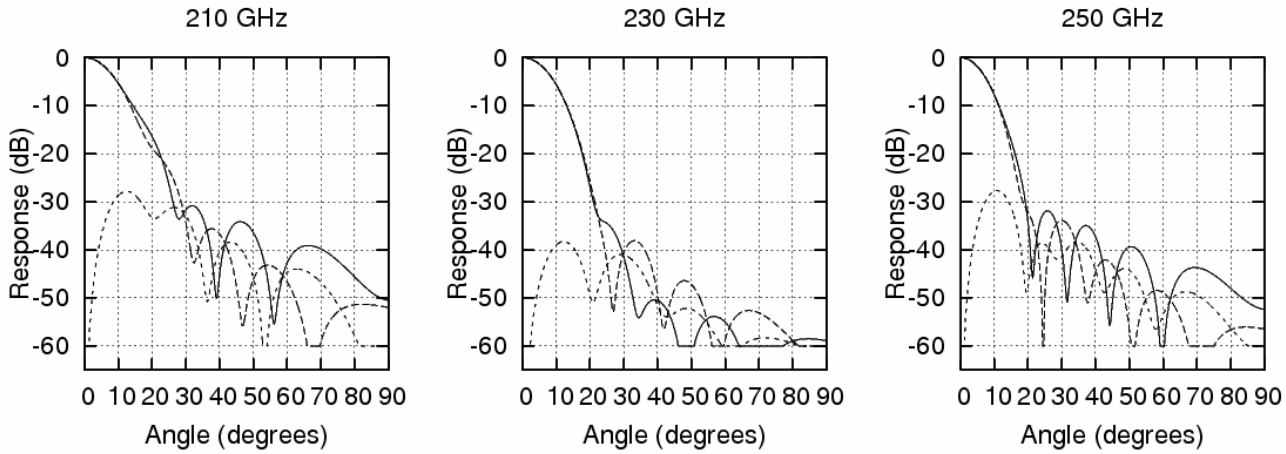

Fig. 3. Calculated radiation pattern for the three sections smooth-walled 230 GHz horn at 210 GHz (left), 230 GHz (middle) and 250 GHz (right).

section. r_2 and L_2 are the radius and the length of the second conical section. L_3 is the length of the third conical section.

IV. Computed Radiation Patterns

The radiation patterns at three frequencies, computed using our modal matching software are shown in Fig 3. Notice that the patterns are of excellent quality with low cross polarization. Near the centre frequency, the beam remains circular down to -30 dB. In Fig. 4 we show the plot of the maximum cross-polarization levels at various frequencies. The cross polarization of below -30 dB are obtained over a bandwidth of 10%. In fact, a cross polarization level below -25 dB was maintained across a bandwidth of 20% which is remarkably broad.

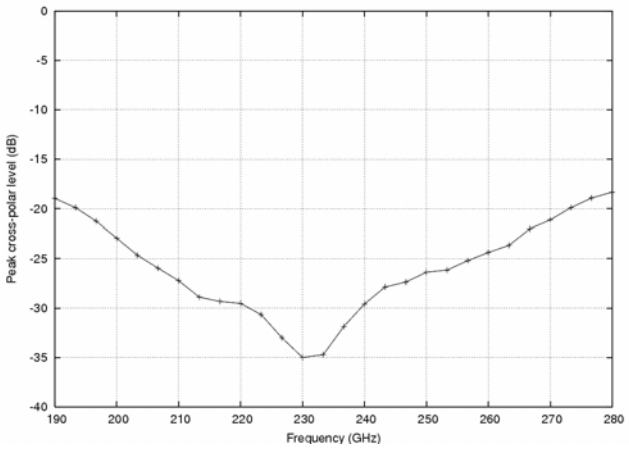

Fig. 4 Peak cross-polarization level against frequency. The cross-polarization levels are below -30 dB for about 10% of the band, and below -25 dB for about 20% of the band.

V. Method of Prototype Fabrication

Many astronomical instruments, such as CLOVER [9] and EBEX [10] contain hundreds of horns and detectors in the focal plane arrays. It is therefore crucial that a fabrication technique is found to fabricate these horns cheaply. We are proposing to fabricate the array by drilling the horns into a block of aluminum using drill-bit tools that have the shape of the horn profile. We believe that this technique can be realized with a standard mill and a high-speed steel tool. Whence the method is optimized, it should be possible to reduce both the cost and the time of fabrication substantially.

Fig. 5 The tool used for machining the three-section, 230 GHz horn. The cutting edge along the top of the tool has the required shape of the horn profile

We have fabricated three sections horns at 230 GHz using both electroforming and drilling. To test the fabrication repeatability, we drilled several horns using the same tool, shown in Fig 5. For comparison, we fabricated two horns of the same design by electroforming. The tolerances on the dimensions of the electroformed horns are expected to be essentially perfect at this frequency, hence they could be used as benchmark. The aim of the tests was two fold: verification of the integrity of the design method by comparing the measured patterns of the electroformed horns with theory, and the drilling technology by comparing the drilled horns with those of the electroformed ones. Measured Radiation Patterns

A. Experimental Setup

Tests were conducted using the Rutherford Appleton Laboratory (RAL) ABmm vector network analyzer (VNA)

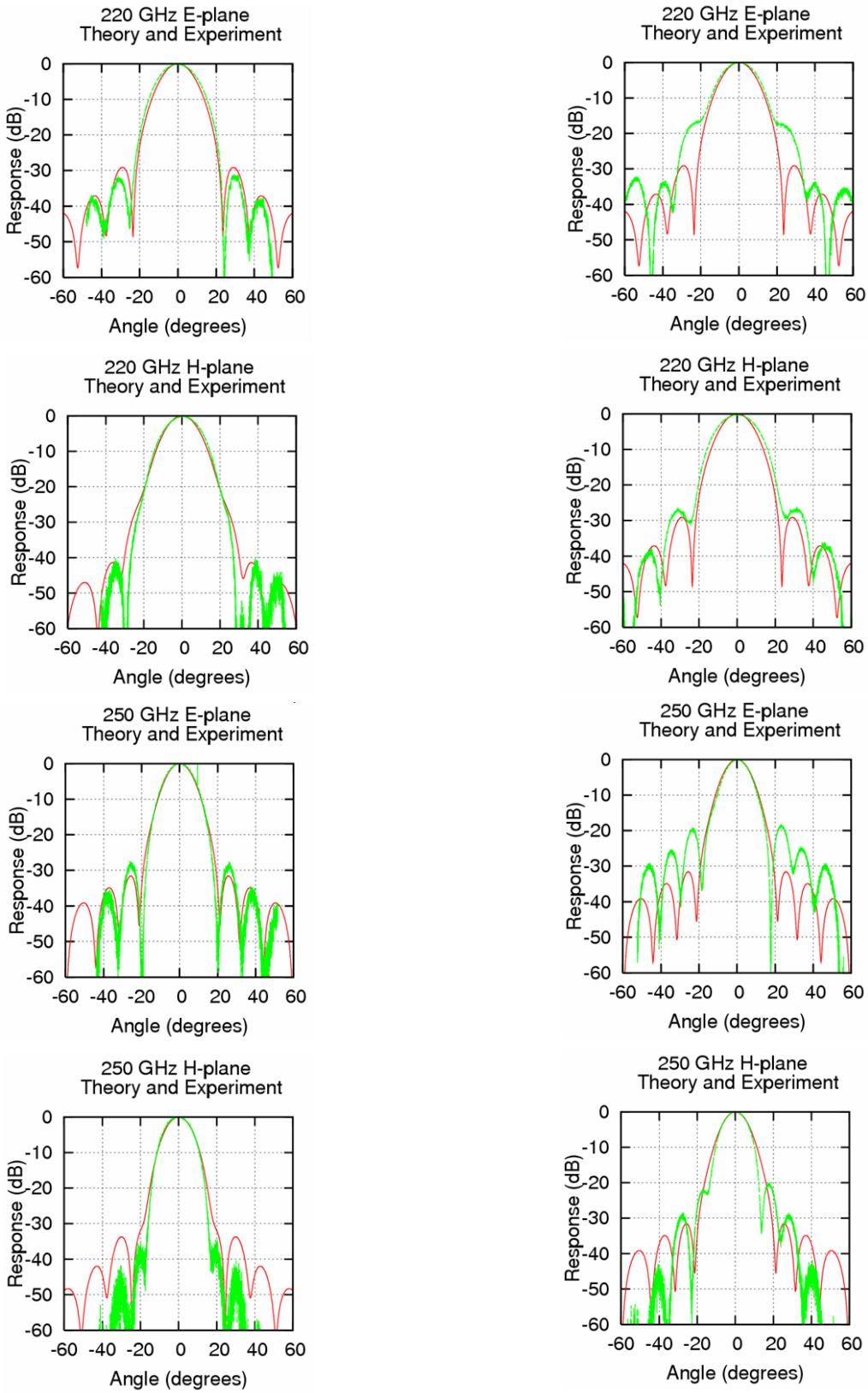

Fig. 6 Measured and calculated patterns of the electroformed horn (left column) and drilled horn (right column) at 220 GHz and 250 GHz. The measured pattern (green) of each plan is shown together with its corresponding calculated curve (red).

and a rotary scanner in an anechoic chamber to obtain direct far-field measurement of the beam patterns of. Two identical prototype horns were used for transmission and reception, separated by 350 mm ($\sim 9d^2/\lambda$). The transmitter horn was rotated by a stepper motor driving a computer controlled rotary table. By using the VNA as a simple total power detector, we were able to achieve a measurement dynamic range of 60 dB. We removed stray reflections and standing waves by the careful positioning RF absorber around the horns and the mounting brackets. The repeatability of the measured beam patterns shows that this arrangement was very satisfactory at 230 GHz.

B. Measured beam patterns

We measured the beam patterns of the two types of horn in the frequency range of 220- 250 GHz and the results are shown in Fig. 6. The measured patterns are compared with the calculated for both the E and H-planes.

The radiation patterns of the electroformed horn agree very well with the theory down to about -40 dB. They have very good beam circularity with sidelobe levels below -30 dB. This shows that the three-section design is correct and the tolerances are reasonable.

We have so far tested only one drilled horn out of seven fabricated. It can be seen that the radiation patterns of the drilled horns are not quite as good as their electroformed counterparts. In particular, sidelobes start to appear at about 5-10 dB higher than the predicted values. It is quite likely that that this effect is due to the fact that the machining tolerances achieved by the drilling technique are not quite sufficient to match the predicted behavior. Nonetheless, the patterns are symmetric which shows that the tool can be aligned with the waveguide accurately. We are currently investigating the effects of non-perfect machining accuracy on the far-field beam patterns using our modal matching simulation software and at the same time measuring the patterns of the rest of the drilled horns. We hope that this will provide an insight into the required tolerance and refining of the fabrication method.

CONCLUSION

We have presented the design and experimental results of three-section smoothed-wall horns with multiple flare discontinuity. Synthesis of the horn geometry is done using a software package which combines modal matching and the genetic algorithm. This design provides high performance feeds with good beam circularity, low cross polarization and low sidelobe levels. The bandwidth of the horn can be designed to suit the particular application. As an example, 20% useful bandwidth can be obtained for an application that requires cross-polarization level below -25 dB. If wider bandwidth is desired then a couple more flare discontinuities can be added to broadband the horn, with little impact on the fabrication complexity.

Fabrication of the present horn was done by electroforming and drilling using a tool that has the shape of the horn into a block of aluminium. A steel tool costing 75 pounds has demonstrated that several horns can be fabricated with the same tool. The radiation patterns of the electroformed horns agree well with the theoretical predictions, confirming the integrity of the design optimization method. First attempt of horn drilling is promising (good quality main beam) but the horn show higher sidelobes then predicted e indicating that the fabrication accuracy needs to be improved.

WE ARE CURRENTLY MEASURING THE CROSS-POLARIZATION OF THE HORNS AND ALSO PLANING TO TEST THE REMAINING DRILLED HORN. WE ARE ALSO DESIGNING HORNS WITH MORE SECTIONS TO INCREASE THE BANDWIDTH.

REFERENCES

[1] P. Potter, "A new horn antenna with suppressed sidelobes and equal beamwidths". *Microwave J.*, vol 6, pp. 71 – 78, 1963.

[2] H. Pickett, J. Hardy and J. Farhoomand, "Characterisation of a dual mode horn for submillimetre wavelengths. IEEE Trans. *Microwave Theory Tech*., MTT32(8), pp. 936 – 937. 1984.

[3] P. Kittara, "The development of a 700 Ghz SIS mixer with Nb finline devices: Nonlinear mixer theory, design techniques and experimental investigation", PhD Thesis. Cambridge University, Cambridge, UK, 2002.

[4] G. Yassin, P. Kittara, A. Jiralucksanawong, S. Wangsuya, J. Leech and Mike Jones, "A High Performance Horn for Large Format Focal Plane Arrays", in *Proc. 18th Int Symp. On Space THz Tech*, 2007.

[5] P. Kittara, A. Jiralucksanawong, G. Yassin, S. Wangsuya and J. Leech "The Design of Potter Horns for THz Applications Using a Genetic Algorithm", *Int J Infrared Milli Waves*, 28, pp 1103 – 1114, 2007.

[6] S. B. Cohn, "Flare angle changes in a horn as a mean of pattern control", *Microwave J*. pp. 41 – 46, Oct. 1970.

[7] A. Olver A, P. Clarricoats P, A. Kishk and A. Shafai., *Microwave Horns and Feeds*. Bookcraft, Bath.

[8] R. L. Haupt. and S. E. Haupt S.E. *Practical Genetic Algorithms*, Wiley-Interscience Publication, 1998

[9] G. Yassin *et al* "CLOVER – A novel instrument for measuring the CMB B-mode polarization", in *Proc. 15th Int Symp. On Space THz Tech*, 2004.

[10] Oxley, *et al*, "The EBEX experiment" in *Proceedings of the SPIE*, pp. 320-331, 2004.

Optics Design and Verification for the APEX **S**wedish **He**terodyne **F**acility **I**nstrument (SHeFI)

Igor Lapkin, Olle Nyström, Vincent Desmaris, Dimitar Dochev, Vessen Vassilev, Raquel Monje, Denis Meledin, Douglas Henke, Magnus Strandberg, Erik Sundin, Mathias Fredrixon, Sven-Erik Ferm, and V. Belitsky

Group for Advanced Receiver Development (GARD), Department of Radio and Space Science, Onsala Space Observatory, Chalmers University of Technology, Göteborg, SE-412

* Contact: Lapkin@chalmers.se, phone +46-31-772 1838

***Abstract*—In this paper, we present the design and verification of the receiver optics for the Swedish Heterodyne Facility Instrument (SHeFI) of the APEX telescope. SHeFI is placed in the telescope Nasmyth cabin A (NCA). The receiver is designed to carry up to 6 frequency channels of which four receiver channels have been designed, built and characterized: 211-275 GHz (Band 1); 275-370 GHz (Band 2); 385-500 GHz (Band 3); 1250-1390 GHz (Band T2). Bands 1, 2, and T2 were installed in the telescope during Spring 2008 and are currently in operation. The first three bands use 2SB SIS mixer technology and Band T2 employs HEB mixers in a waveguide balanced mixer configuration. The entire optics design was driven by the requirement of frequency independent illumination of the secondary with -12 dB edge taper and the limitations imposed by the receiver position in the NCA. The optical system is designed to provide coupling of the SHeFI receiver channels and PI instruments placed in NCA to the common optics of the telescope and cover the wide frequency range from 210 GHz to 1500 GHz. In the paper, the design approach, optimization, and verification are described.**

I. Introduction

APEX, the Atacama Pathfinder Experiment [1], is a collaborative project involving Max Planck Institut für Radioastronomie (MPIfR), Onsala Space Observatory (OSO), and the European Southern Observatory (ESO). The telescope is located at latitude 23º00'20.8" South, longitude 67º45'33.0" West at an altitude of 5103 m in the Atacama desert, Llano Chajnantor, in the northern part of Chile Figure 1. APEX is a Cassegrain type telescope, manufactured by Vertex Antennenteknik [2], with a 12 m in diameter primary mirror, having a surface accuracy of 17 μm, and an antenna pointing accuracy of 2" rms. The telescope has, except for the Cassegrain cabin, two additional instrumentation cabins, Nasmyth cabin A and B. SHeFI was designed to be located in the telescope Nasmyth cabin A (right in the Figure. 1) and where it was installed during the Spring 2008. The optical system is designed to provide coupling of the SHeFI channels and the PI instruments residing in the NCA to the telescope and covering a very wide frequency operating range from 210 GHz to 1500 GHz. Detailed information regarding the complete receiver design is found in [3], while we focus exclusively on the optical design in this paper. SHeFI is designed to carry up to 6 receiving channels of which four frequency channels have been designed, built, integrated into the receiver and characterized: 211-275 GHz (Band 1) [4]; 275-370 GHz (Band 2); 385-500 GHz (Band 3) [6]; 1250-1390 GHz (Band T2) [7].

Figure 1. APEX telescope at 5100 m in the Atacama Desert, Llano Chajnantor, Chile.

It is the atmospheric conditions and the surface accuracy of the primary mirror that introduce general limitations for the upper observing frequency. The degradation factor of the antenna aperture efficiency with frequency and the surface accuracy can be estimated according Ruze formula $\eta_a(\lambda) = \exp(-16\pi^2\sigma^2/\lambda^2)$ [8] where σ is the RMS error of the antenna surface. According to this formula, at 1400 GHz, the APEX antenna keeps approximately 37 % of the initial aperture efficiency. Figure 2 illustrate simulated atmospheric transparency [9]. The location of the SHeFI receiver frequency bands coincide with the atmospheric windows [10].

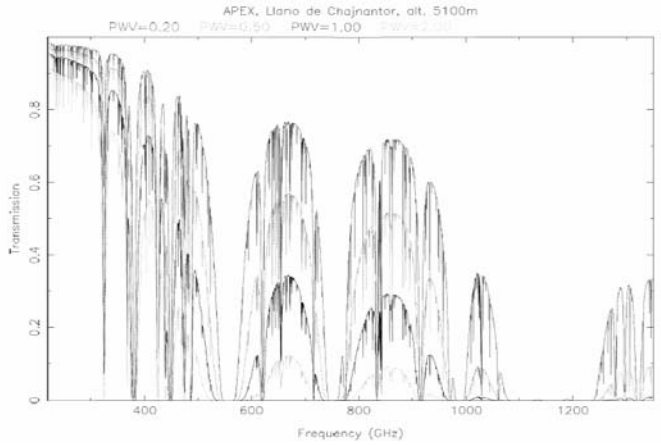

Figure 2 Atmospheric transparency at the APEX telescope site [9].

The objectives of this article are to summarize the design strategy and implementation of the optical system, to describe the integration of the receiver optics with the telescope optical system, and to explain the optics verification procedure and present results validating the design. A detailed description of the optical system in the Cassegrain cabin and NCA is presented below, Section II, where we present the design of the frequency independent optical system. Section III is dedicated to the description of the cold optics and the feed horn design. The verification and alignment of the cryostat optics is described in Section IV and the installation procedure at the telescope, including mechanical- and RF alignment is described in the Section V. Section VI presents results of the final verification of the optical design in terms of telescope pointing accuracy.

II. APEX Cassegrain and Nasmyth Cabin A Optics

The APEX telescope is a Cassegrain type telescope and is a prototype for the ALMA antenna. The antenna parameters are summarized in Table 1. However, in contrast to the ALMA antenna, containing all instruments in the Cassegrain cabin, the APEX telescope carries two additional instrumentation cabins, Nasmyth cabin A and B [11] [12]. The SHeFI receiver is located in the Nasmyth cabin "A" of the telescope, together with two PI instruments and is connected to the Cassegrain cabin by the Nasmyth tube. The optics layout of the Cassegrain, NCA, and SHeFI optical system is shown in Figure 3. The axial distance from the secondary focal point to the Nasmyth flange is about 3.2m and the antenna signal is guided to the Nasmyth cabin by the Nasmyth tube.

TABLE 10. ANTENNA PARAMETERS FOR THE APEX TELESCOPE.

Symbol	Description	Value
D	Primary aperture	12 m
fp	focal length primary	4.8 m
fp/D	ratio of primary	0.40
d	Secondary aperture	0.75 m
f/d	Final f/d ratio	8

The entire optics design was driven by the location of the receiver in the Nasmyth cabin, and consequent limitation of the aperture, Ø150 mm, introduced by the elevation encoder inside the Nasmyth tube A. Extremely wide frequency range of the instruments in the NCA, up to 32% of the center frequency, necessitates a frequency independent optical solution that should include the entire 8 mirror system. The broad frequency band, the location of the instrument, and the small clearance diameter of the elevation encoder exclude the use of ALMA type off-axis antenna illumination scheme [13].

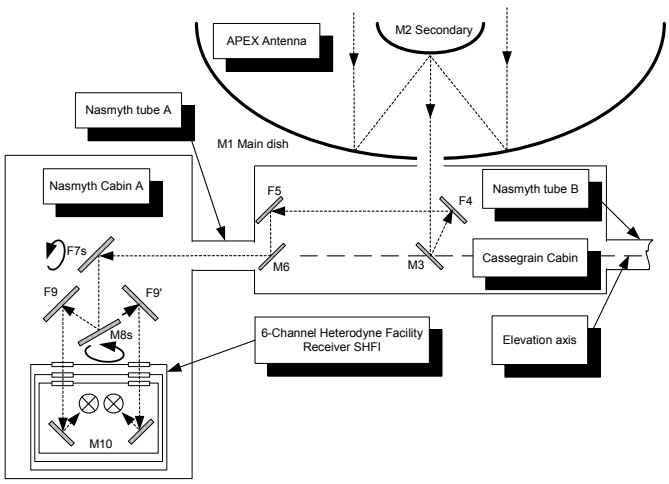

Figure 3. Optical layout of the Cassegrain and Nasmyth cabin A facility receiver.

Instead, we use two precision rotating flat mirrors to provide switching between PI instruments and SHeFI and also between the different receiving bands of SHeFI [14] and bringing the input receiver beams at the axis of elevation (coincides with the center of the Nasmyth tube A). The complete optical path, coupling the receivers to the Cassegrain sub-reflector, works as a re-imaging system, transferring the image of the secondary onto the aperture of the corrugated horn for each receiver, keeping the illumination of the secondary at -12 dB edge taper.

The Cassegrain and NCA optics consists of the three offset ellipsoidal mirrors, M3, M6, M8s, and three flat mirrors, F4, F5, and F7s, Figure 3. The combination of the M3 and M6, with flat F4, F5, forms a Gaussian telescope, providing frequency-independent re-imaging of the antenna focal plane from the Cassegrain cabin into the Nasmyth Cabin A [15],

[16], [17]. The M3 and M6 focal lengths were optimized in terms of minimizing distortion and providing beam clearance on the encoder position. The flat mirrors F4 and F5 are used to fold the beam in the Cassegrain cabin in order to avoid interference with multi-pixel bolometric instruments and their respective optics. The flat mirror F7 (see Figure 3) is the optical switch between SHeFI and the PIs [18]. Switching between SHeFI channels is achieved by the precision rotating of the active mirror M8s [14]. The mirror M8s in combination with each channel active mirror M10 have been chosen in such a way that they provide re-imaging of the secondary onto the feed horn aperture of the selected channel. Compared to the ALMA optical solution [16] and [17], the APEX Cassegrain and NCA optics requires a more complex optical path, including 8 mirrors coupling the secondary image to each mixer horn.

The idea of the frequency independent illumination [15], [16], [17], can be illustrated by utilizing the ray matrices for paraxial beams in conjunction with the complex beam parameter q [21]. As example, the mirror M10 in Figure 4 is described by the distribution matrix (1) for a single optical element with the focal distance f1. The associated reference cross-sections are at the horn aperture, at the distance L1 (the lens position), and at an arbitrary distance L2 from the lens position as indicated in Figure 4.

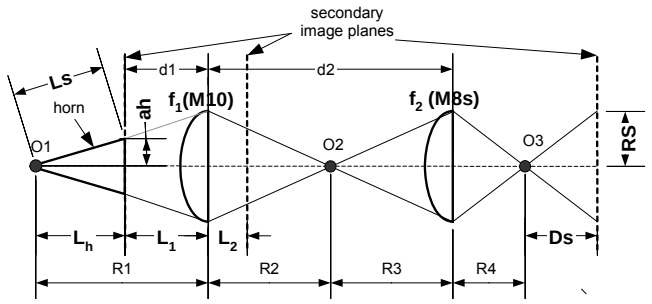

Figure 4. Nasmyth cabin equivalent optics scheme. Points O1,O2,O3 refer to the focal points, traced from the original Cassegrain focal point. M8s and M10 – off – axis ellipsoidal mirrors with focal distances equal f2 and f1 respectively. Dashed lines refer to the secondary image planes. Ls- horn slant length, ah- horn aperture radius.

$$M = \begin{bmatrix} 1-\frac{L_2}{f_1} & (1-\frac{L_2}{f_1})\cdot L_1 + L_2 \\ \frac{-1}{f_1} & \frac{-1}{f_1}\cdot L_1 + 1 \end{bmatrix} \quad (1)$$

It is assumed that the reference plane is the horn aperture with a Gaussian beam distribution parameter equal to

$$q_0 = \left[\frac{1}{R_i} - j\frac{\lambda}{\pi \cdot \omega_i^2} \right]^{-1} \quad (2)$$

where λ- wavelength, ω_i -beam radius , R_i- radius of the phase curvature, referred to the horn aperture according to [21]. For an initial optics designing stage, those parameters could be related to the horn's geometry as: R_i=Ls, ω_i=0.64 ah.

$$q_2 = \left[\frac{M_{0,0}\cdot q_0 + M_{0,1}}{M_{1,0}\cdot q_0 + M_{1,1}} \right] \quad (3)$$

Choosing $M_{0,1} = 0$, results in

$$L_2 = \frac{-L_1 \cdot f_1}{f_1 - L_1} \quad (4)$$

and is associated with the geometrical optics image position of the horn aperture. In our case it also coincides with the secondary image plane and it can easily be shown that by substituting (1) and (2) into (3).

$$q_2 = \left[(R_i + f_1 - L_1)\cdot \frac{f_1 - L_1}{R_i \cdot (f_1)^2} - \ldots - j\frac{\lambda}{\pi \cdot \left(\omega_i \, f_1 / f_1 - L_1 \right)^2} \right]^{-1} \quad (5)$$

This gives the relation between the initial beam parameters, ω_i and R_i, and the transformed beam parameters, ω_2 and R_2 as following:

$$R_2 = \frac{R_i \cdot (f_1)^2}{(f_1 - R_i + L_1)\cdot (f_1 - L_1)} \quad (6)$$

and

$$\omega_2 = \frac{f_1}{f_1 - L_1}\cdot \omega_i \quad (7)$$

Equation 6 and 7 show that the Gaussian beam parameters (the phase curvature and the beam radius) at the image planes of the optical system are frequency independent and coincide with the geometrical optics solution describing single - lens transformation. This means that the geometrical optics approximation can be used to perform beam tracing and determine the position of the image plane cross sections. The results also implies that, in the assumption of frequency independent field distribution on the horn aperture, an optical re-imaging technique can be used for transferring the horn

aperture image onto the secondary to provide frequency independent antenna edge taper illumination .

When designing the SHeFI optical system, a two-mirror re-imaging scheme (M8 and M10 in Figure 4) was investigated under the assumption of the fundamental Gaussian beam mode propagation while the mirrors were represented as ideal quadratic phase transformers. The design parameters and design equations are presented in Table 2, where Lh and ah is the length and aperture radius of the feed horn. All parameters in Table 2 can be seen in Figure 4 where the example two-mirror system is illustrated.

TABLE 2. DESIGN PARAMETERS OF THE TWO-MIRROR RE-IMAGING SCHEME, SEE FIGURE.

Parameters	Equations
Variable parameters	Lh, ah, f_2, R_4
Scale parameter K	$\frac{Lh}{ah} \cdot \frac{Rs}{Ds}$
R_1	$Ds \cdot Lh \cdot K \cdot \frac{K \cdot (f_2 - R_4) - f_2}{Ds \cdot K^2 \cdot (f2 - R_4) - (f_2 - R_4 - Ds) \cdot Lh}$
d2	$f_2 \cdot \frac{R_4 \cdot K + R_1}{(R_4 - f_2) \cdot K}$
L_1	$R_1 - Lh$
f_1	$f_2 \cdot \frac{R_1}{(R_4 - f_2) \cdot K + f_2}$

The optimization goals for the optical design were chosen as following: **i.** minimum distortions, **ii.** minimum cross-polarization, **iii.** minimum dimensions for all optical components and horn. Because of severe space limitation for placing SHeFI, constrains of geometry implementation were imposed. In order to optimize to minimum possible distortion and cross-polarization level, formulas presented by Murphy [23] were used. In order to keep the cross-polarization and beam distortion from the corrugated horns under control, we used the bending angle of the horn with respect to the off-axis elliptical mirror (M10, Fig. 4) as small as possible [23] for given geometrical constrains. The full bending angle between the incoming and the reflected beam is 25°.

In order to avoid truncation losses along the optical path, a clearance of $5\omega_o$, where ω_o is the 1/e Gaussian radius, was used for all cryostat windows, IR filters and passive and active optical components ensuring the truncation loss of less than 1% [24], [16].

All receiver channels of the SHeFI are cryogenically cooled down to 4 K, which imposes additional uncertainty for final RF optics alignment because of the thermal contraction of the optical components and support brackets and impossibility to verify / measure the receiver optics geometry under operation. In order to address this uncertainty, angular position of the flat mirrors F9, Figure 3 and Figure 5, was made adjustable. That gives additional possibility of the beam alignment fine-tuning for every SHeFI receiver channel independently.

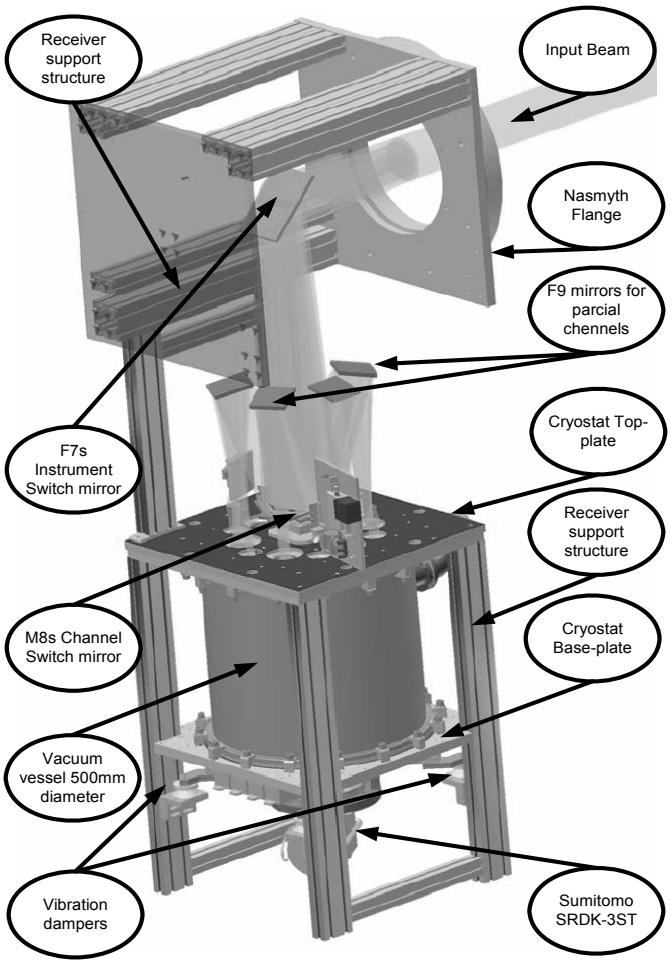

Figure 5. Nasmyth Cabin A optical system.

III. COLD OPTICS AND CORRUGATED HORNS

The space in the Nasmyth cabin A is limited and requires a very compact design in order to fit the 6 channel receiver and the PI instruments. To achieve the compact design, the receiver was built around the vertically positioned cryo-cooler [19], where all receiver channels are interfaced to a common reference plate, the mixer assembly interface plate. The common reference plate is linked to the 4K stage by flexible copper braids to provide cooling as well as vibration damping. The very compact design and radial placement of the mixer assemblies provides easy access to all receiver channels, once the cryostat vessel is opened and two thermal shields are dismounted.

Diagonal horns were used for the LO signals, except for the THz band where a corrugated horn is also used to couple the LO signal to improve the efficiency of the LO power

guiding. For the RF signal coupling, all SHeFI receiver bands employ corrugated horns given that this type of feed provides nearly ideal performance with a very symmetric beam pattern, spherical wave fronts, low cross-polarization, good matching to waveguide, wide bandwidth, and up to 98% coupling efficiency with the fundamental Gaussian mode [20], [21].

IV. Beam Measurements

In order to characterize/verify the quasi-optical design and to align the receiving beams of the SHeFI, we performed vector-field measurements in the laboratory. This is done by performing vector field measurements of the receiver output while scanning a probe (point) source in the plane transverse to the beam propagation. The receiver input beam could be fully characterized by appropriate data processing [21]. Such procedure provides estimates for the direction of propagation (beam axis 3D position), the size and position of the beam waist, as well as the shape of the beam. The measured data are fit in 3D to the fundamental Gaussian beam to the measured by optimizing the power coupling coefficient. The measurement system is designed in such a way that it can perform vector field measurements within 211-500 GHz band, by only switching two filters and LO units, thus covering APEX Band 1 to Band 3. The LO- units were later installed in the telescope. In Figure 6 a two-dimensional amplitude map of the APEX Band 1 beam at 221 GHz is shown. The measured beam is fit to the fundamental Gaussian mode very well (estimated coupling efficiency ~98%) and it appears circular above -20 dB level.

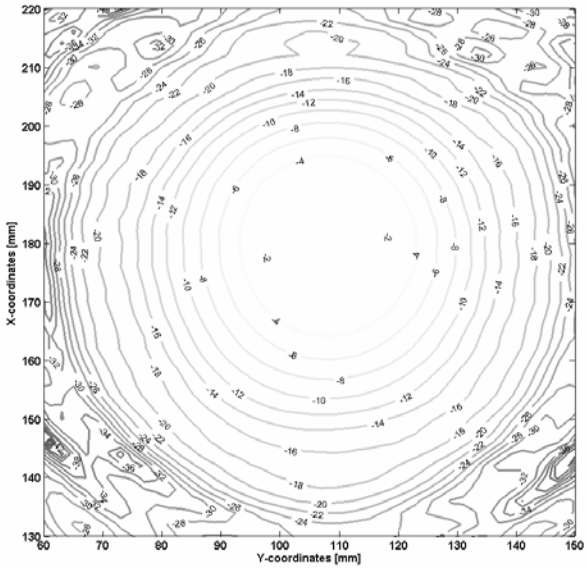

Figure 6. Power distribution of the beam pattern of the receiver measured for APEX Band 1 at 221 GHz. The beam pattern is circular down to -20 dB relative to the on axis value.

It needs to be pointed that at the same time as the vector field measurement system provides an extremely wide frequency range, it is limited to a number of discrete frequency points within each band, since a combination of a single frequency source and a comb generator is used to generate perfectly phase-coherent RF and LO signals. A detailed description of the vector measurement system can be found in [25].

In order to characterize the T2 band, scalar measurements were conducted, since the regular test source for the vector measurement system did not provide enough output power at those frequencies even though the measurement system flexibility allowed us to try the vector measurements as well though with a poor signal – to – noise ratio. In order to generate sufficient power, we employed the LO-source for Band 3 as a test source and the third harmonic was used to generate a RF-signal > 1300 GHz. In this case several transverse planes along the signal path were scanned in order to determine the position and the size of the beam waist [26]. Any possible tilt of the beam is determined by fitting a line through the amplitude centers. A map of the power distribution of the receiver beam, measured at 1334 GHz is shown in Figure 7.

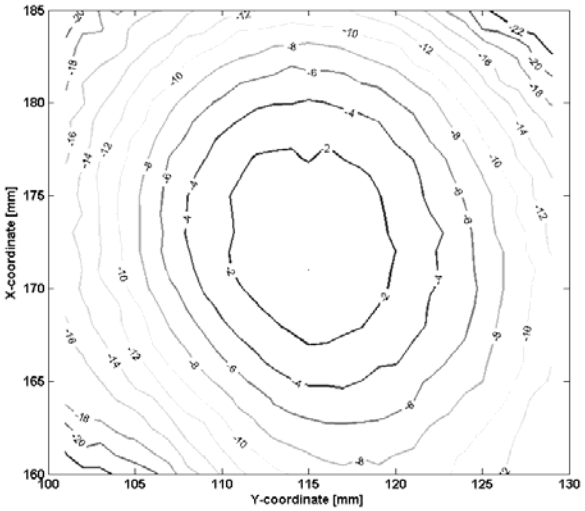

Figure 7. Power distribution of the beam pattern of the receiver for APEX Band T2 measured at 1334 GHz.

V. Installation and Verification at the APEX Telescope

The installation procedure at the telescope has been taken in two phases, the mechanical alignment of the SHeFI receiver and the RF alignment of each individual receiving beam for optimum coupling to the common optics of the telescope. The mechanical reference in the NCA is the flange at the Nasmyth tube on which the whole receiver support structure is attached, see Figure 5. The goal of the mechanical alignment was to align the receiver warm optics plate (see Figure 5) with respect to the Nasmyth flange. During the mechanical alignment the receiver warm optics is separated from the cryostat in order to ease the handling and

hence the alignment (see Figure 8). The mechanical alignment is done by placing a laser at the center of the Nasmyth flange in combination with a flat mirror on the receiver warm optics plate. The laser shines via the PI switch onto the flat mirror and is then reflected back to the laser as schematically illustrated in Figure 8). The receiver warm optics plate is adjusted until the reflected laser beam coincides with the laser aperture. A Position Sensitive Detector (PSD) [27] is then used for precision centering of the receiver warm optics plate in the horizontal plane.

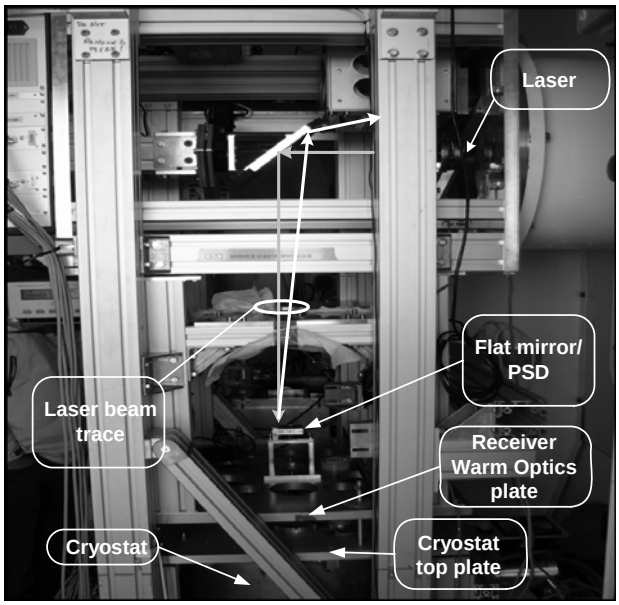

Figure 8. Mechanical alignment procedure with the laser bracket in the NCA flange.

Once the mechanical alignment is done the cryostat is lifted up and the top plate is bolted to the receiver warm optics plate and the support structure.

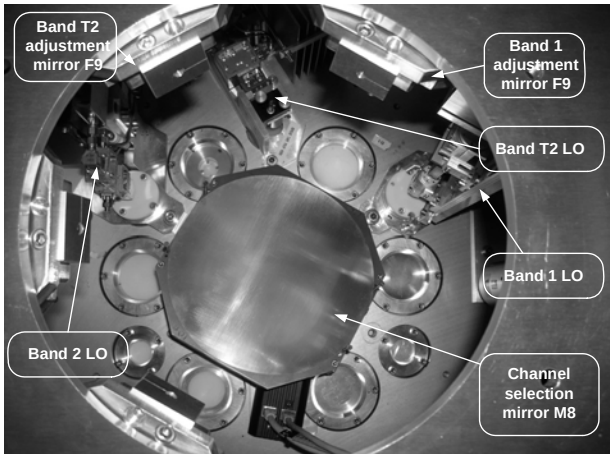

Figure 9. Top view of the channel switching mirror and the flat adjustment mirrors.

The RF beam alignment is carried out by introducing a piece of a cold absorber (dipped in liquid nitrogen) at the center of the Nasmyth flange while observing the receiver IF output power level. The individual receiver beams between the channel selection mirror (M8, in Figure 3) and the mixer horn aperture are aligned by adjusting the flat channel mirrors (F9, in Figure 5) until the largest drop in the output IF power observed when the absorber is centered at the Nasmyth flange. Figure 9 shows the channel selection mirror, M8, and the individual channel tuning mirrors, F9s. The procedure is then repeated with the absorber inserted close to the telescope focal plane to verify the alignment throughout the whole optical path.

VI. First Light Results

After completing the mechanical and RF beam alignment, the exact offset and tilt of the beams with respect to the telescope focus have to be established. This was done by pointing the telescope at well known sources on the sky and measuring the offset and tilt. The telescope adjustable secondary can compensate for small offsets, ±15 mm for the z-offset, ± 10 mm for the x- and y-offset, and once the offsets and tilts are determined the values are used to calibrate the pointing during observations. The pointing is continuously recalibrated, since the offsets may vary with temperature and elevation of the telescope. For calibration of the APEX Band 1 and Band 2 Mars and Saturn were used as such calibration sources. Mapping of the planets were performed in order to find the azimuth-, elevation-, x-, y-, and z-offsets. The measurement results for azimuth and elevation offsets measured from continuum pointing on Mars can be seen in Figure 10 with the secondary wobbled to improve accuracy of the measurements.

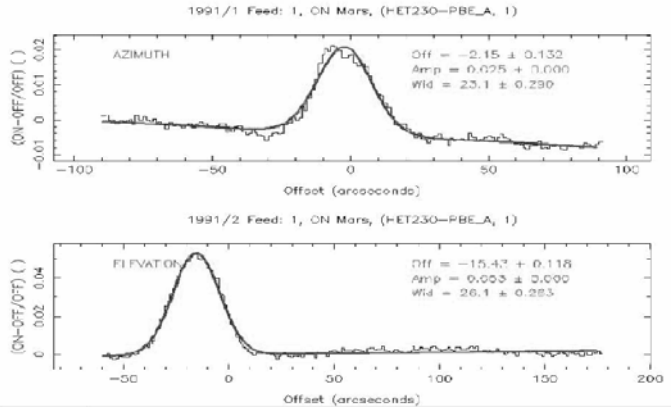

Figure 1014. Measured results for azimuth and elevation offsets measured from continuum pointing on Mars at 230 GHz.

Through these measurements it was verified that the optical alignment had been very successful and the offset in azimuth and elevation was less than 16 arc seconds and the telescope focus in z-direction was offset by 100 μm only!

Conclusions

In this paper, we present the optical design and experimental verification of the APEX 6-channel facility instrument, SHeFI. Currently three receiving bands are installed in the APEX telescope, Band 1 (211-275 GHz), Band2 (275-370 GHz), and T2 (1250-1390 GHz). The implemented optical design is optimized to fulfil, requirement of a frequency independent illumination of the secondary at -12 dB edge taper for each frequency band, the constraints with respect to the placement of the instrument in the APEX telescope Nasmyth cabin and consequently the RF beam clearance limitation by the elevation encoder. The entire design was optimized to fit the limited space available inside the APEX telescope Nasmyth cabin A. The procedures for the optical design and the optical components optimization, including the corrugated horns, are described. Laboratory pre-shipment vector beam measurements as well as the installation procedure and verification results at the telescope are presented. The telescope pointing results confirms that the optical design and SHeFI receiver performance is up to expectations.

ACKNOWLEDGMENT

The authors would like to thank C.–Y. E. Tong and W. Jellema for kind willingness to share their experience in beam measurements. A. Baryshev is greatly acknowledged for sharing his insight in design of frequency independent optics and interesting discussions. The authors would also like to thank the staff at the APEX telescope. This work was supported by the Swedish Research Council and the Wallenberg Foundation via respective grants, by the Swedish National Space Board, and EU FP 6 RadioNet AMSTAR.

REFERENCES

[1] Official APEX Telescope web-site, *http://www.apex-telescope.org*

[2] www.vertexant.com

[3] V. Belitsky, et. al. "Facility Heterodyne Receiver for the Atacama Pathfinder Experiment Telescope", Proceedings of joint 32nd International Conference on Infrared Millimeter Waves and 15th International Conference on Terahertz Electronics, September 3 - 7, 2007, City Hall, Cardiff, Wales, UK, pp. 326 – 328.

[4] V. Vassilev, et. al. " Design and Characterization of a 211-275 GHz Sideband Separating Mixer for the APEX Telescope", IEEE Microwave and Wireless Components Letters, 18 (1) s. 58 – 60, ISBN/ISSN 1531-1309

[5] C. Risacher, et. al.,"A sideband separation SIS mixer for 275-370 GHz for the APEX telescope"Proceedings of the SPIE "Millimeter and Submillimeter Detectors and Instrumentation for Astronomy III", eds. J. Zmuidzinas, W.S. Holland, S. Withington, W.D. Duncan, 6275 s. 62751T, 2006

[6] R. Monje, et. al., "A 385-500 GHz SIS Mixer for APEX Telescope", Millimeter and Submillimeter Detectors for Astronomy III", eds. J. Zmuidzinas, W.S. Holland, S. Withington, W.D. Duncan, Proceedings of SPIE, 6275 s. 19, 2006

[7] D. Meledin, et. al. "A 1.3 THz Balanced Waveguide HEB Mixer for the APEX Telescope", Submitted to IEEE MTT, 2008

[8] J.Ruze"The effect of aperture errors on the antenna radiation pattern", Suppl. al Nuovo Cimento, vol. 9, no. 3, pp364-380, 1952

[9] www.apex-telescope.org/sites/chajnantor/atmosphere/

[10] J. R. Pardo, J. Cernicharo, and E. Serabyn, "Atmospheric Transmission at Microwave (ATM): An Improved Model for Millimeter/Submillimeter Applications", IEEE Transactions On Antennas and Propagation, Vol. 49, No. 12, December 2001

[11] Heyminck, Kasemann, Belitsky, "ICD for receivers operated in the APEX NCA", 2004-10-01

[12] J. W. Lamb, "ALMA Receiver Optics Design", ALMA Memo 362, 2001-04-11

[13] Rudolf "The ALMA Front End Optics-System Aspects and European Measurement Results", IEEE Trans. On AP. Vol. 55, No. 11, Nov 2007

[14] MICOS DT-80, M I C O S GmbH, *http://www.micos.ws*

[15] T.-S. Chu, "An imaging beam waveguide feed," IEEE Trans Antennas and Propagations, vol. AP-31, no. 4, pp. 614–619, Jul. 1983

[16] J. W. Lamb, "Optical study for ALMA receivers," ALMA Memo Series No. 359, Mar. 2001

[17] A. Baryshev, W. Wild, "ALMA Band 9 Optical Layout," ALMA Memo Series No. 394, Sept. 2001

[18] Belitsky, Olberg, Risacher, "APEX Cabin A: Instrument Optical Switch Reference Document", 2005-03-22

[19] Cryo cooler SRDK-3ST, Sumitomo Heavy Industries

[20] P. J. B. Clarricoats and A. D. Olver, "Corrugated Horns for Microwave Antennas", Peter Peregrinus, 1984

[21] P. F. Goldsmith, "*Quasioptical Systems*". New York: IEEE Press, 1998, ISBN 0-7803-3439-6

[22] www.radiometer-physics.de

[23] J. A. Murphy, "Distortion of Simple Gaussian beam on Reflection from Off-Axis Ellipsoidal Mirrors", Int. Jour. of Infrared and Millimeter Waves, Vol. 8, No 9, 1987

[24] J. A. Murphy, A. Egan, and S. Withington, "Truncation in Millimeter and Submillimeter-Wave Optical Systems"

[25] O. Nyström, M. Pantaleev, V. Vassilev, I. Lapkin, V. Belitsky, "A Vector Beam Measurement System for 211-275 GHz", Proceedings EuCAP 2006, Nice, France, 6-10 November 2006, (ESA SP-626, October 2006).

[26] M. Pantaleev, "Radioastronomy Instrumentation for Herschel and APEX Projects", Ph.D. thesis, ISBN/ISSN 91-7291-806-3, Göteborg 2006

[27] www.duma.co.il

Backward Couplers Waveguide Orthomode Transducer for 84-116 GHz

Alessandro Navarrini[1,*], and Renzo Nesti[2]

[1]INAF-Cagliari Astronomy Observatory, Cagliari, Italy

[2]INAF-Arcetri Astrophysical Observatory, Florence, Italy

* Contact: navarrin@ca.astro.it, phone +39-070-711 80 218

***Abstract*— We describe the design, construction, and performance of a waveguide Orthomode Transducer (OMT) for the 3 mm band (84-116 GHz.) The OMT is based on a symmetric backward coupling structure and has a square waveguide input port (2.54 mm x 2.54 mm) and two single-mode waveguide outputs: a standard WR10 rectangular waveguide (2.54 mm x 1.27 mm,) and an oval waveguide with full-radius corners. The reverse coupling structure is located in the common square waveguide arm and splits one polarization signal in two opposite rectangular waveguide sidearms using broadband -3 dB E-plane branch-line hybrid couplers.**

The device was optimized using a commercial 3D electromagnetic simulator.

The OMT consists of two mechanical blocks fabricated in split-block configuration using conventional CNC milling machine.

From 84 to 116 GHz the measured input reflection coefficient was less than –17 dB, the isolation between the outputs was less than -50 dB, the cross polarization was less than –30 dB, and the transmission was larger than -0.35 dB at room temperature for both polarization channels.

The device is suitable for scaling to higher frequency.

I. Introduction

An OMT is a diplexer that separates two orthogonal linearly polarized signals within the same frequency band. A common way to separate orthogonal polarizations is to use a wire-grid that directs the orthogonal signals to two independent feedhorns. A waveguide OMT is a useful alternative to the grid because it can be linked to a single feedhorn and fits more easily in a cooled receiver.

An OMT has three physical ports but exhibits properties of a four-port device, because the input common port, usually a waveguide with a square or circular cross-section, provides two electrical ports that correspond to the independent orthogonal polarized signals. In modern radio-astronomy receivers, requirements of the OMT are a high cross-polarization discrimination between the orthogonal signals (better than ~40 dB,) low insertion loss (a few tenths of a dB,) and a good match of all electrical ports (return loss above ~20 dB) over bandwidths of 30% or wider.

Several asymmetric OMTs have been designed with performance limited to a fractional bandwidth of 10-20% by the excitation of higher order modes in the common port. Highly symmetric structures are required to achieve a waveguide OMT with bandwidth of 25 to 40%.

Because the small dimensions and tight tolerances pose a significant challenge for the fabrication and assembly of the parts [1] only few broadband OMT designs have been demonstrated to work well at mm-wavelengths. One such design is based on the two-fold symmetric junction introduced by Bøifot [2] and uses a thin metallic septum centered in a square waveguide common port and capacitive compensation pins located at the entrance of two waveguide sidearms. The broadband OMTs adopted for the 84-116 GHz and 211-275 GHz bands [3] of ALMA (Atacama Large Millimeter Array) are variants of the Bøifot design. Other Bøifot style OMT designs with a thicker septum have also been proposed; here, the pins are eliminated in favour of short capacitive steps [4] [5] or standard multistep transitions on the sidearms [6]. Although in these cases the construction of the blocks is simplified, the precise alignment of the septum inside the waveguide remains critical.

An alternative to the Bøifot design based on a four-fold symmetric turnstile junction OMT was developed for the 200-270 GHz band [7]-[8] of CARMA (Combined Array for Research in Millimeter Wave Astronomy.) A similar OMT design was also developed to cover the band 75-110 GHz [9]. An advantage of the turnstile junction design is that neither the pins nor the septum of the Bøifot junction are required to achieve polarization separation and low VSWR over a wide bandwidth, which makes this OMT easy to assemble; a disadvantage of such design is that the OMT fabrication requires that the symmetric structure is either split in four blocks rather than the two of the Bøifot design (so adding mechanical complexity with potential misalignment problems between the four quarters,) or manufactured by electroforming techniques, where copper is grown onto a gold-plated aluminum mandrel that is subsequently dissolved. However, one of the drawbacks of the electroforming technique is that complex mandrels are difficult to fabricate with high mechanical accuracy, therefore limiting the maximum achievable operational frequency [10].

An OMT design that can be fabricated with a standard end- mill by machining only two mechanical blocks and that has neither pins nor metallic septum, is based on a symmetric double ridged design. This type of OMT was developed at the ATNF (Australia Telescope National Facility) for the 77-117 GHz band [11] and was also adopted at NAOJ (National Astronomical Observatory of Japan) for the ALMA 125-163 GHz band [12]. The OMT consists of a square to double ridged guide transition followed by a junction of two sidearms with the central guide (similar to the BØifot design.) A disadvantage of this OMT is the complexity of machining with high accuracy the narrow stepped double ridge centered in the middle of the square waveguide input (typical ridge widths are between 0.1 *a* and 0.15 *a*, where *a* is the waveguide width.)

Recently, a novel OMT architecture based on a backward coupling structure was developed for operation at 32 GHz (Ka band) [13]. The OMT is based on a single-side branch-line coupling structure whose asymmetry limits the operation bandwidth of the device to ~10%.

Here, we present the design, construction, and test results of an OMT with architecture similar to the one presented in [13], but where the single-side branch-line backward coupler is replaced by a broadband *symmetric* dual-side backward coupler. Our OMT covers the 84-116 GHz band (32% fractional bandwidth) and has excellent performance. The device is easy to machine and assemble; it was fabricated in two mechanical blocks by standard numerically controlled end-mill. The performance of the OMT is robust against small changes of the geometry associated with mechanical tolerances. The device is suitable for scaling to higher frequencies.

II. Symmetric Reverse Coupling Structure

The network representation of an ideal backward coupling structure based on a 90^0 hybrid coupler is shown in Fig. 1. The input signal at port 1 is split at -3 dB with 90^0 phase difference between the hybrid *through output port* (port 4) and *coupled output port* (port 3.) Both outputs are terminated with equal reactive loads. Therefore, after a total reflection at the outputs, the two signals are sent backward and recombined in-phase at port 2 and out-of-phase at port 1 (destructive interference.) The net effect is that the input signal at port 1 is fully coupled to port 2, i.e. with reverse direction. This may be thought of as a 0 dB backward coupler.

A backward coupler that carries two orthogonal polarization signals Pol 1 and Pol 2 at its input (for example a square waveguide port) can also be used as a polarization splitter, i.e. as an OMT. A schematic representation of an ideal OMT based on a reverse coupling structure is shown in Fig. 2. Here, Pol 1 is fully transmitted from input port 1 to output port 4 and therefore does not couple through the hybrid to ports 2 and 3 (straight coupling.) Pol 2 signal couples through the hybrid and sees reactive loads at both its terminations, ports 3 and 4. Therefore, after total reflection at those ports, Pol 2 signal is fully transmitted in backward direction to port 2. The schematic network for Pol 2 signal is the same as the one depicted in Fig. 1. In summary, the schematic of Fig. 2 represents an OMT with forward coupling for Pol 1 and backward coupling for Pol 2. We note that the OMT has three physical ports (1, 2 and 4) and four electrical ports because two orthogonal modes propagate through the input port 1.

An OMT based on a *asymmetric* waveguide backward coupling structure, as the one schematized in Fig. 2, was described by Peverini in [13]. There, a square waveguide input propagates the two orthogonal polarization states. A 0 dB backward coupler consisting of the square waveguide parallel to a *single* rectangular waveguide was used; while Pol 1 is directly coupled through a square-to-rectangular waveguide multistep transition, the coupling of Pol 2 signal between the parallel waveguides was achieved using four apertures (slots) in the rectangular waveguides E-plane; the two forward waveguide ports of the hybrid coupler were terminated with

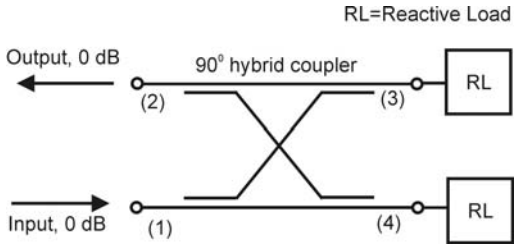

Fig. 1. Schematic representation of a backward coupling structure consisting of a 90^0 hybrid coupler with output ports terminated with equal reactive loads.

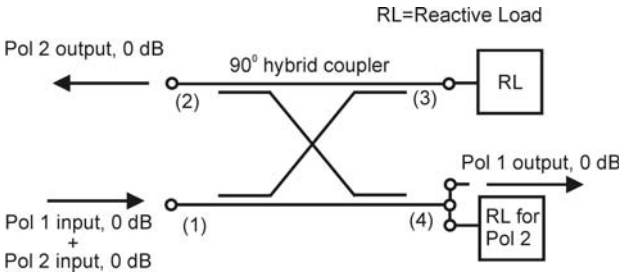

Fig. 2. Schematic representation of an ideal polarization splitting network (OMT) with forward coupling of Pol 1 from ports 1 to 4 and backward coupling of Pol 2 from port 1 to port 2. The structure consists of a 90^0 hybrid coupler with reactively loaded outputs.

reactive loads for Pol 2. The asymmetry of the reverse coupling structure presented in [13] limits the bandwidth of such device to ~10% due to the excitation of higher order modes in the square waveguide.

The network representation of the *symmetric* backward coupling structure used in our OMT is shown in Fig. 3. Here, Pol 1 and Pol 2 propagate through a common input port. Pol 1 input signal is fully coupled to the straight output port 4. Pol 2 input signal at port 1 is equally split between two 90^0 hybrid couplers whose output ports (4, 5, and 6) are

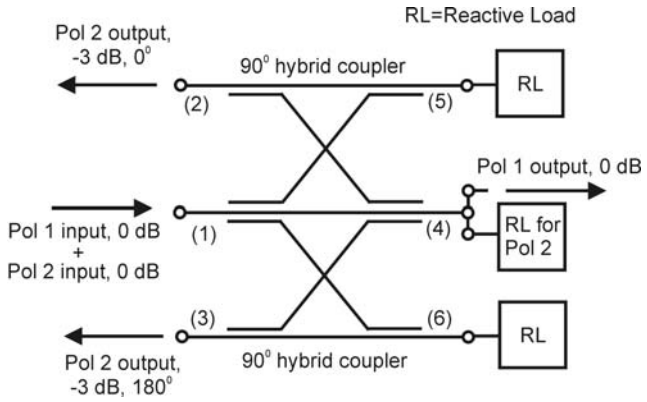

Fig. 3. Schematic representation of the ideal polarization splitting network (OMT) with forward coupling of Pol 1 from ports 1 to 4 and symmetric -3 dB backward coupling of Pol 2 from port 1 to ports 2 and 3. The structure consists of two 90^0 hybrid couplers with reactively loaded outputs. Port 1 is in common to the two hybrids. Signals at ports 2 and 3 are 180^0 out-of-phase.

terminated with reactive loads; the input port is in common with both hybrids. Pol 2 signal is coupled at -3 dB to output ports 2 and 3 with a phase difference of 180^0.

III. Polarization Splitting Backward Couplers

A 3D view of the symmetric waveguide backward coupling structure used in our OMT, equivalent to the network of Fig. 3, is illustrated in Fig. 4. This consists essentially of: *a)* a square common waveguide input that goes through a two-section transformer to a reduced height rectangular waveguide; *b)* two 90^0 hybrid waveguide couplers on the sidearms; *c)* a reactively loaded termination at each hybrid coupled port.

The square waveguide input (2.54×2.54 mm^2) propagates two orthogonal linear polarized signals Pol 1 and Pol 2 associated, respectively, with the TE_{10} and TE_{01} fundamental modes, when the wavelength is below the cut-off value $\lambda_c(TE_{10}) = 2a = 5.08$ mm (frequencies above ν_c=59.01 GHz.) Besides the fundamental modes, higher order modes can propagate in the square waveguide in the 84-116 GHz frequency band of interest. These are the TE_{11} and TM_{11} that have the same cut-off frequency of ν_c=83.46 GHz. In theory, these modes can be excited by the discontinuity created by the apertures (slots) of the sidearms. However, their excitation can be avoided as long as the two-fold symmetry of the structure is maintained. The adopted symmetry enables broadband operation allowing to achieve a relative bandwidth for the device larger than ~30 %.

The symmetric coupling structure in the common square waveguide arm splits with opposite phases the incoming Pol 2 signal in the two rectangular waveguide sidearms. Signal coupling to each sidearm is obtained with a broadband 90^0 hybrid coupler realized as a 3-dB E-plane branch-line coupling structure with four branches. The four 0.45 mm wide apertures through the broad walls of the waveguide sidearms are equally spaced of 0.34 mm (see details in Fig. 5.) The branches have a length of 0.75 mm. The through port and the coupled port of each hybrid are terminated with reactive loads for Pol 2. In the common arm, the reactive load is provided by a two-section transformer polarization discriminator that reflects back all Pol 2 power in the frequency range of design, 84-116 GHz. Indeed, the output rectangular waveguide section of such transformer has size 2.54×1.22 mm^2 that cuts off the propagation of the TE_{01} mode associated with Pol 2 to frequencies above $\nu_c(TE_{01})$=122.87 GHz, outside our operating range. On the other hand, the orthogonal polarization, Pol 1, is relatively unaffected by the presence of both the branch-line apertures in the two sidearms and of the common arm two-section transformer. Each section of such transformer is approximately a quarter wavelength long. Therefore, Pol 1 is well matched to the output and is fully coupled to the fundamental TE_{10} mode of the rectangular waveguide output in the common arm (forward coupling.)

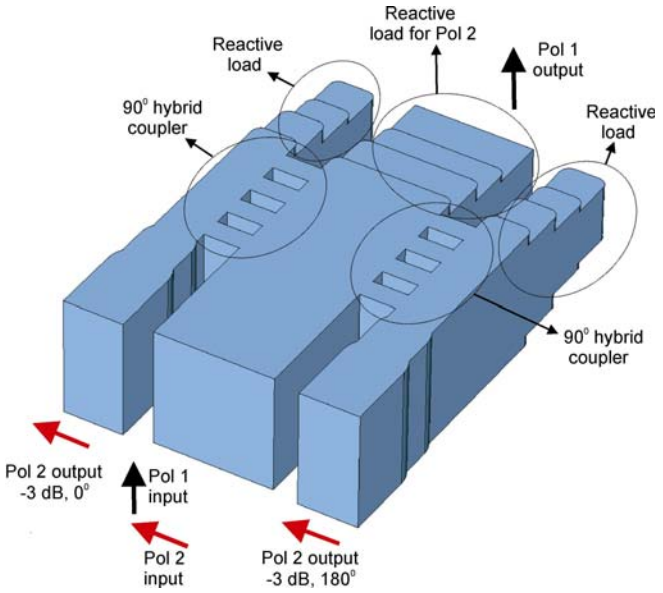

Fig. 4. Internal view of the symmetric dual-side backward coupler of our OMT with input square waveguide in common with two -3 dB E-plane branch-line coupling structures terminated with reactive loads for Pol 2. The device has four physical ports and five electrical ports.

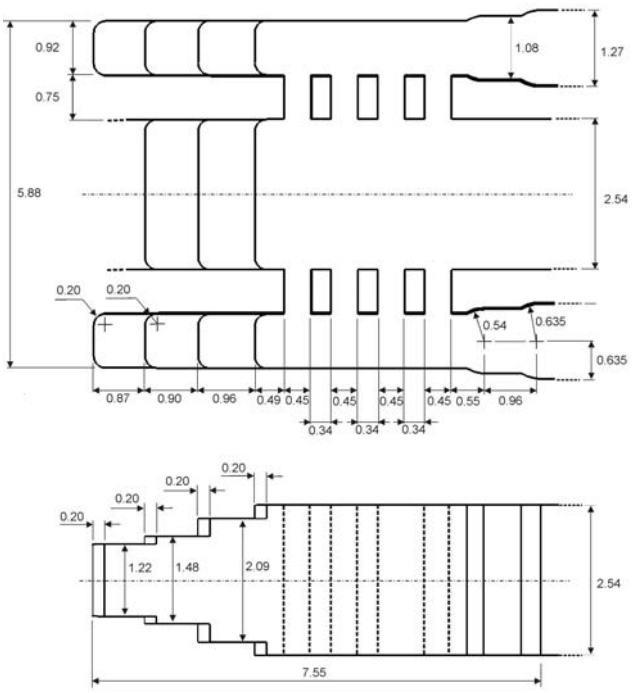

Fig. 5. Cutout views with dimensions (in mm) of the symmetric backward couplers of Fig. 4. The structure was optimized for operation in the 84-116 GHz band.

In the rectangular waveguide sidearms, the reactive loads for Pol 2 are provided by a short circuited three-step H-plane discontinuity (two transformer sections.) The transformer sections have the same physical length and height in the sidearms and in the common arm to guarantee that Pol 2 sees the same impedance when looking toward the through and coupled ports of the hybrids. This allows the split Pol 2 signals, which are reflected backward by the reactive loads, to recombine out-of-phase in the common arm (thus providing a destructive interference with low reflection at the common port) and in-phase in the two opposite sidearms. The constructive interference of the backward waves provides a coupling of –3 dB to each rectangular output port. Pol 2 signals at these two ports are 180^0 out-of-phase to each other because the E-field signal at the common square input couples to the two sidearm hybrids in opposite directions. The rectangular waveguide sidearms have a reduced height in the coupling section of the hybrids (0.92 mm rather than full 1.27 mm) in order to increase the bandwidth of the device.

The waveguide steps of the two-section transformers have round corners (radius 0.20 mm) to allow easy machining of the parts with an end-mill. Each reduced-height rectangular waveguide sidearm carrying the reverse-coupled -3 dB Pol 2 signal is transformed to standard WR10 full-height 2.54×1.27 mm^2 waveguide at the hybrid signal output. This is accomplished by a single-section quarter-wave transformer (0.96 mm long.) The use of the standard WR10 full-height waveguide reduces the insertion loss of the single-mode transmission line to its minimum possible value across the band of interest. The steps of the transformers are rounded as they would be if machined with an end-mill of diameter equal to the height of the waveguide transformers (1.08 mm.)

The electrical performance of the structure of Figs. 4-5 was optimized using the commercial electromagnetic simulator CST Microwave Studio[3] based on the finite integration technique. The parameters that were varied in the optimization were the number of branches of the hybrid couplers, their lengths, widths, spacings, the dimensions of the two-section transformers in the main and sidearms, the position of the sidearm short-circuits, the size of the common square waveguide and rectangular waveguide sidearms and of their single-section output transformer. It was found that an increase in the number of branches of each hybrid (a minimum of two is required) would increase the bandwidth of the device (but the branch length would have to be decreased.) However, an optimum number of branches was found to be four, beyond which the performance of the device would only have very little improvement but the mechanical fabrication would become more difficult. Also, we found that the widths and the spacing of the four branches could be chosen to be all equal (rather than with different values) without any degradation of the electrical performance. For the reactive load sections, we found that the optimum number of steps was three (two transformer sections.)

As expected, the performance of the two polarization channels are tightly connected. Indeed, we found using simulation that improving the performance of one polarization channel would typically degrade the performance of the other. For example, the heights and lengths of the waveguides of the two-section transformer in the common arm that optimizes the transmission of Pol 1 does not provide the optimum transmission for the backward coupled Pol 2. A trade-off was found to provide good performance for both polarization channels. An important aspect of the device in Figs. 4-5 is that its performance has proven robust against small changes in the geometry associated with the mechanical tolerances.

Fig. 6 shows the final simulation results for the reflected amplitude of the two independent fundamental modes TE_{10} and TE_{01} at the square waveguide input of the device illustrated in Fig. 4 (the three rectangular output ports are terminated by matched loads.) In the graph, vertical lines denote the nominal band edges at 84 and 116 GHz. The reflection coefficient is below -20 dB for both polarizations over the entire band of interest.

IV. OMT Design

Our OMT basically consists of a dual-side backward coupler, two 180 deg and two 90 deg E-plane bends, an E-plane Y-junction power combiner, and a 90 deg E-plane rectangular-to-oval waveguide bend transition. Fig. 7 shows the complete OMT. The OMT single-mode waveguide outputs are *a)* an oval waveguide with full-radius corners (external cross-section dimensions of 2.78×1.27 mm^2) for

[3] CST Microwave Studio, Darmstadt, Germany.

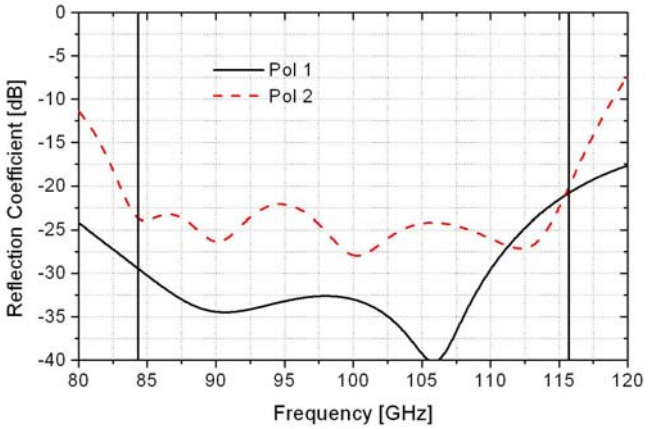

Fig. 6. Simulated reflection coefficient for the TE_{10} (Pol 1) and TE_{01} (Pol2) modes at the square waveguide input port of the device illustrated in Fig. 4.

Pol 1, and *b)* a standard WR10 rectangular waveguide for Pol 2. The OMT can be constructed in two mechanical blocks using conventional split-block techniques.

In the main arm, the signal associated with Pol 1, available at the output of the two-section quarter-wave transformer, travels through the E-plane 90 deg bend transition that brings out, orthogonal to the main arm, the oval cross section port; the oval waveguide is easy to machine with an end-mill and can be attached to a standard WR10 waveguide producing a

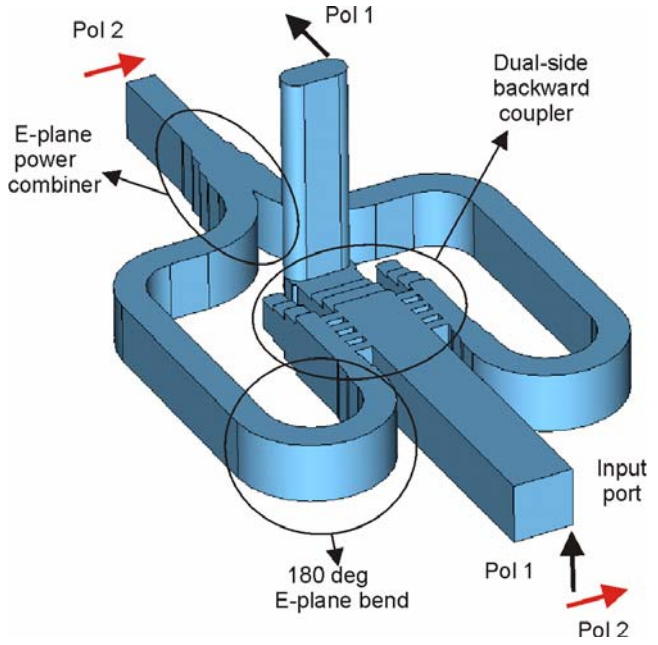

Fig. 7. Internal view of the OMT showing the polarization splitting dual-side backward coupler, the two 180 deg and 90 deg E-plane bends, the E-plane power combiner, and the 90 deg E-plane rectangular-to-oval bend transition.

negligible power reflection (return loss > 39 dB across 84-116 GHz.) Fig. 8 shows the internal details of such 90 deg rectangular-to-oval waveguide bend transition. The bend was based on a design by Narayanan [14] and the two steps are both below the split-block plane. Fig. 9 shows the simulation results for the reflection coefficient at the rectangular waveguide with the oval waveguide terminated into a matched load. The reflection coefficient is below -18 dB across the band of interest; the reflection increases at the higher frequencies. Slightly different geometries of the 90 deg rectangular-to-oval bend transition exist that have better performance than the one shown in Fig. 9. However, it was found that the chosen bend configuration, when used in conjunction with an optimum 1.0 mm long rectangular waveguide section connecting the backward coupler common arm output to the 90 deg bend, gave the best results for the complete OMT illustrated in Fig. 7.

The two Pol 2 signals emerging backward with -3 dB power from the sidearms of the reverse-coupling structure travel through two symmetric waveguide paths whose symmetry plane is coincident with the E-plane of Pol 1 propagating in the common arm. Each Pol 2 signal travels through a 180 deg WR10 waveguide E-plane bend (3.93 mm inner diameter), a straight waveguide section (length of 9.5 mm), and a 90 deg waveguide E-plane bend (3.47 mm inner diameter;) the two Pol 2 signals are recombined by an E-plane Y-junction power combiner with standard WR10 output whose axis is coincident with the one of the common waveguide.

Electromagnetic simulations show that the reflection coefficient of the 180 deg and 90 deg WR10 E-plane bends are, respectively, below -31 dB and -33 dB across the 84 to 116 GHz band.

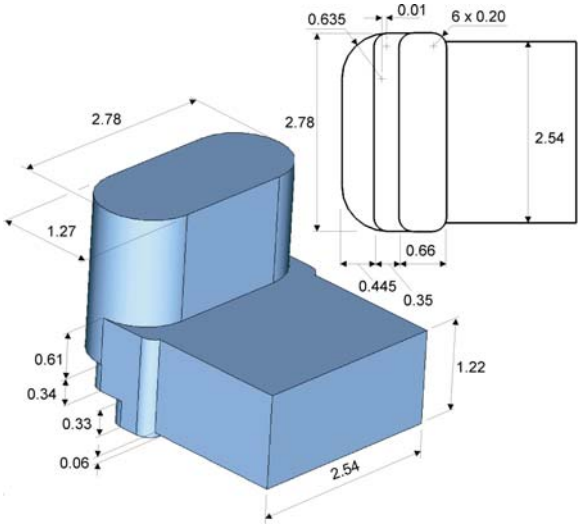

Fig. 8. Internal view of the 90 deg E-plane rectangular-to-oval waveguide bend transition. Dimensions are in mm.

The 180^0 out-of-phase Pol 2 signals at the backward coupler sidearms outputs are recombined using the E-plane Y-junction shown in Fig. 10. The combiner is based on a design by Kerr [15]. The steps of the three-section transformer are filleted so they can be machined with an end-mill of diameter equal to the WR10 waveguide height (1.27 mm.) The cusp at the junction of the curved arms is truncated at a width of 0.09 mm. Fig. 11 shows the simulated reflection coefficient at the common port when the two curved arms are terminated with matched loads. The reflection coefficient is below –33 dB from 84 to 116 GHz.

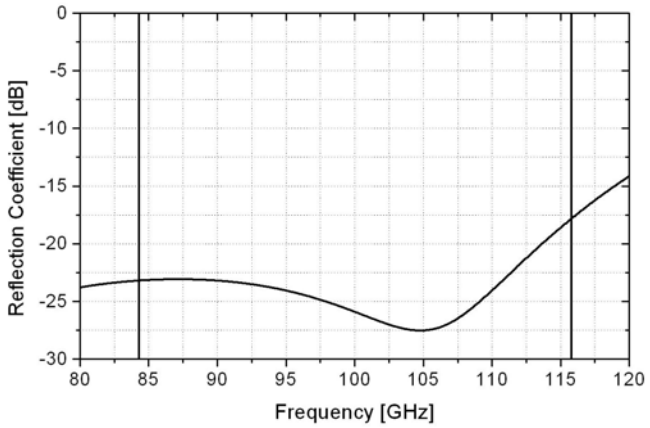

Fig. 9. Simulated reflection coefficient at the rectangular waveguide input of the 90 deg E-plane rectangular-to-oval waveguide bend transition of Fig. 8.

The electrical lengths of the two sidearms between the Pol 2 backward coupler outputs and the power combiner inputs must be identical to guarantee that the signals recombine with the proper phase. An imbalance in the length of the sidearms caused by small fabrication error and mechanical tolerances determines a degradation of the OMT performance that may introduce a series of transmission resonances and an increase of the cross-polarization level.

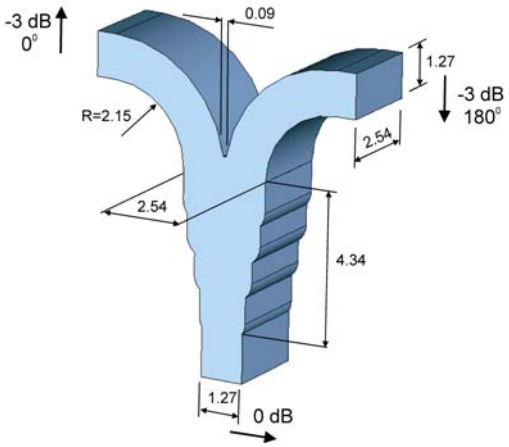

Fig. 10. Internal view of the E-plane Y-junction used to recombine the 180^0 out-of-phase signals associated to Pol 2 at the output of the dual-side backward coupler.

V. Mechanical Design

The OMT is realized by splitting the structure of Fig. 7 along the E-plane of the side-coupled rectangular waveguides. Fig. 12 shows a photograph of the assembled OMT and of the two

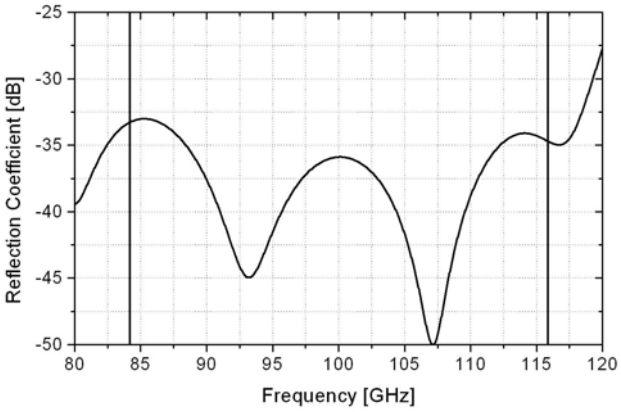

Fig. 11. Simulated reflection coefficient at the common waveguide port of the three-port device illustrated in Fig. 10.

Fig. 12. Photograph of the assembled OMT (left) showing the square waveguide input and the oval waveguide output. The external dimensions are 19×30×33 mm^3. Standard UG387 flanges are used at all ports. The two identical square-to-WR10 waveguide transitions used to test the OMT are shown on the right.

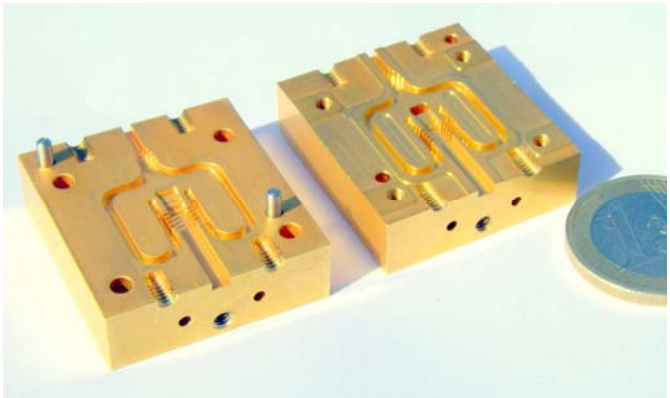

Fig. 13. Photograph of the two unassembled blocks of the OMT showing the internal waveguide circuitry.

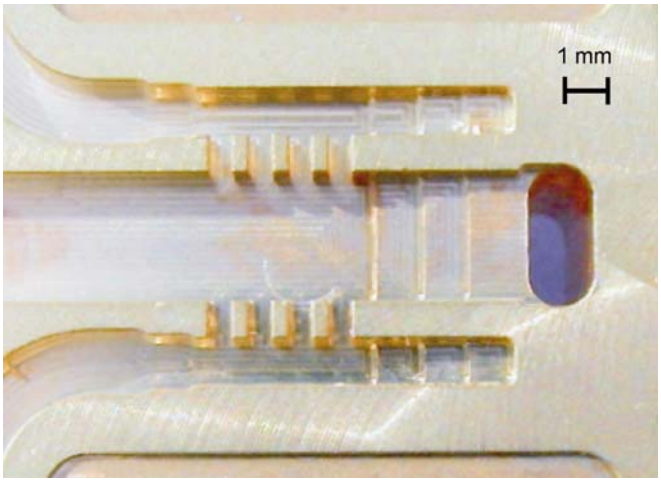

Fig. 14. Photograph of the internal details of one of the OMT blocks showing the dual-backward coupler waveguide circuitry and the three metal "teeth" between branch-line slots on both sidearms. The oval waveguide is also visible on the right.

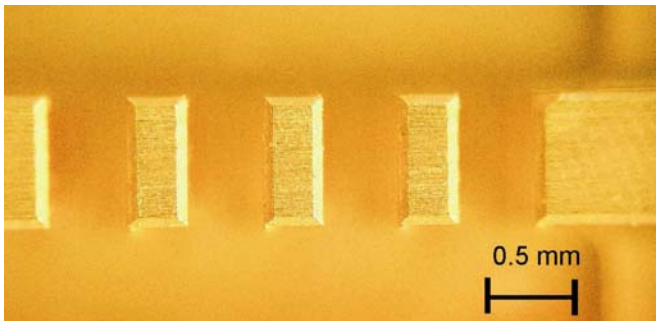

Fig. 15. Detail of the three metal "teeth" between branchline slots of one of the coupler sidearms.

identical square waveguide-to-rectangular waveguide transitions[4] (linearly tapered 25.4 mm long 2.54×2.54 mm^2-to-WR10 transitions) used to test it. The OMT accepts standard UG387 flanges at all ports. A photograph of the two unassembled OMT blocks and the internal mechanical details of one of the blocks are shown in Figs. 13-15. The blocks were fabricated in brass using a numerically controlled milling machine[5]. Then, they were gold plated by electrodepositing 1 μm thick pure Gold[4] layer on top of a 0.2 μm thick Nickel interlayer. Unfortunately, two of the metal "teeth" between branch-line slots of the backward coupler were slightly damaged during the gold plating of the blocks. We expected that the small asymmetry of the structure resulting from the damaged teeth would degrade the cross-polarization properties of the OMT.

The blocks were aligned using two precision 2 mm diameter dowel pins. The tolerances for the waveguide channels in the two blocks and of the alignment between the blocks were specified at ± 10 μm. The blocks are bolted together by four M2.5 stainless steel screws (type A2, grade 70.) Anti-coking recessed areas are used in one of the blocks: if we take the surface of the small area surrounding the waveguide channels as level of reference, all the remaining surface of the block is located 200 μm below that level except for four small areas around the screw holes located 10 μm below. The advantage of this design is that the flat surface of the mating block cannot be cocked by uneven tightening of the screws.

VI. Experimental Results

The OMT was tested at IRAM (Institut de Radio Astronomie Millimétrique), Grenoble, France, using a millimeter-wave Vector Network Analyser [16] consisting of a HP8510C Network Analyser and millimeter-wave test set extensions. The millimeter-wave network analyser was calibrated at the WR10 rectangular waveguides at the outputs of the extension heads; we used one-port and two-port calibrations with WR10 calibration kit. The calibration procedure was used to remove systematic instrumental effects and to calibrate out the response of the instrument up to the chosen calibration planes. Additional measurement of two pairs of identical back-to-back WR10 waveguide-to-square waveguide transitions (shown in Fig. 12) allowed to calibrate out their individual effects and to derive the S-parameters of the OMT at the physical ports of the device. To obtain reproducible results, we took considerable care to minimize any movement of the cables and waveguides between calibration and tests and to align and tighten waveguide connections with a repeatable procedure.

A schematic of the Pol 2 transmission test setup is shown in Fig. 16. The square waveguide input of the OMT was attached to the WR10 waveguide port of the network analyser (port 1) through the WR10 waveguide-to-square waveguide transition. The transition was oriented to excite the Pol 2 in the OMT. The WR10 waveguide output of the OMT was attached to the second WR10 waveguide port of the analyser (port 2.) The oval waveguide of the OMT was terminated with a matched WR10 waveguide load. The transmission measurement of the other polarization channel was obtained with a setup similar to the one in Fig 15 but with WR10 waveguide-to-square waveguide transition rotated by 90 deg to excite Pol 1 at the OMT input and with waveguide matched load and second port of the analyser swapped at the OMT outputs. A photograph of the transmission test setup of Pol 1 is shown on Fig. 17. The measured transmissions of the OMT are illustrated in Fig. 18 for both polarization channels. Simulated results generated with CST Microwave Studio are shown for comparison. All simulations were performed with the full three-port model shown in Fig. 7, including the dual-side backward coupler, the 90 deg E-plane rectangular-to-oval waveguide bend transition, the 180 deg and 90 deg WR10 E-plane bends, the E-plane Y-junction power combiner, and all connecting waveguides. We assumed the conductor to be pure gold and used a gold conductivity of half its room temperature dc value $\sigma_{Au}=(4.26\cdot10^7)/2\ \Omega^{-1}m^{-1}$. A Cartesian mesh was

[2] Custom Microwave Inc, Longmont, CO.
[3] Fanuc Robodrill CNC milling machine.
[4] The specification used for the Gold plating was MIL-G-45204C, Type III, Grade A, Class 0, 99.9% pure Gold.

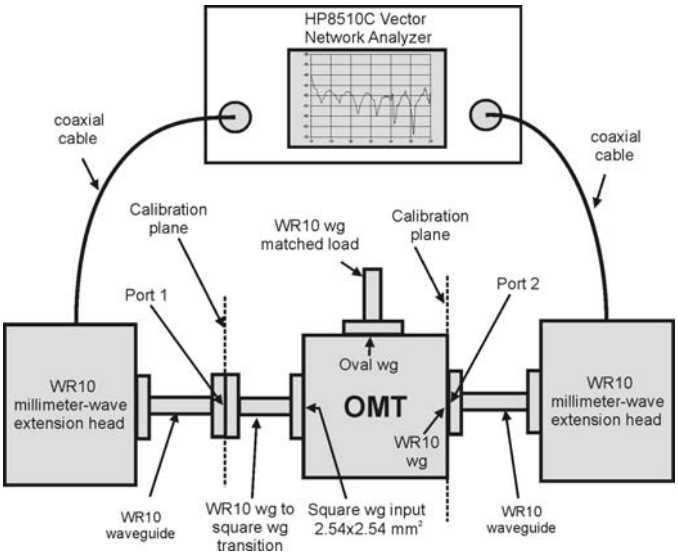

Fig. 16. S-parameter measurement of the OMT with the vector network analyser. The particular configuration refers to the transmission measurement of Pol 2.

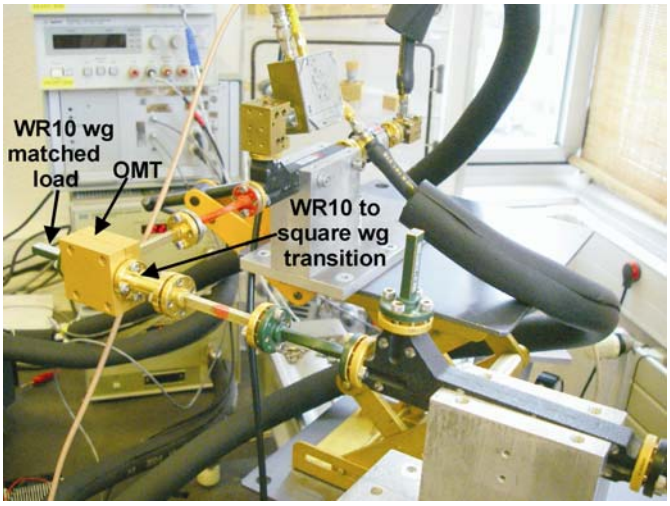

Fig. 17. Photo of the OMT during Pol 1 transmission measurement with the vector network analyser.

automatically generated and the time-domain solver calculated the broad-band response of the device in one simulation run. We set the parameter "lines per wavelength" to 15; this is the minimum number of mesh lines per wavelength in each coordinate direction for the shortest wavelength in the simulation.

The average measured transmission loss of the OMT is ~0.15 dB for Pol 1 (Fig. 18, top panel) and ~0.2 dB for Pol 2 (Fig. 18, bottom panel) similar in overall level to the value predicted by simulation. The insertion loss of the OMT is expected to decrease by a factor of ~3 when it is cooled to cryogenic temperatures [17]. Therefore, we expect a maximum insertion loss of below ~0.1 dB for both polarization channels when the OMT is operated at 4 K in front of SIS mixers or low noise amplifiers.

The physical length of the waveguide circuit of the OMT from its input to its output is approximately 22 mm for Pol 1 and 56 mm for Pol 2. The room temperature loss of a straight section of WR10 waveguide is in the range 0.05-0.07 dB/cm between 84-116 GHz [18]. For comparison, the loss of a 22 mm and of a 56 mm straight section of WR10 waveguide would be of the order of, respectively, 0.13 dB and 0.34 dB.

The reflection coefficient at the OMT input port was measured for both polarizations by terminating the OMT

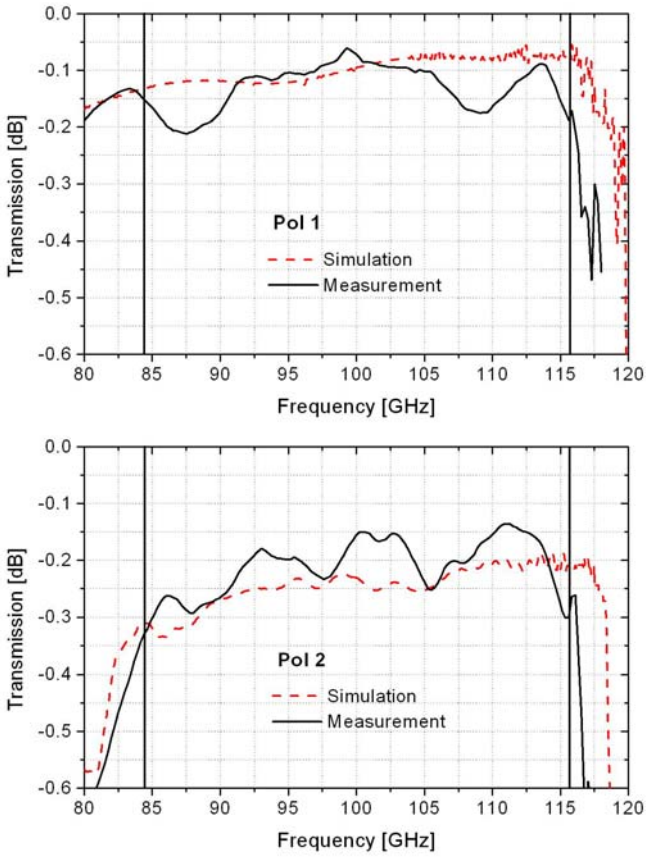

Fig. 18. Simulated and measured transmission of the OMT. *Top):* Pol 1; *Bottom):* Pol 2. The simulation (dashed lines) refers to the full three-port model shown in Fig. 7.

outputs with WR10 matched loads (one-port measurement.) The amplitude of the measured reflection is below -17 dB for both polarization channels (Fig. 19.)

An estimate of the OMT isolation was obtained by measuring the transmissions from the OMT output ports with its square waveguide input port open to free space. This gives an upper limit of the isolation of the device which should be measured, instead, using a matched load at the square waveguide input. An open square waveguide is, however, well matched to free space (reflection of the order of -20 dB.) The measured upper limit of the OMT isolation is below -50 dB across 84-116 GHz (Fig. 20.) There were no simulation results for the isolation since we used the perfectly symmetric model of Fig. 7, which produces perfect isolation.

The cross-polarization of the OMT, i.e. the signal from one polarization channel at the input that is coupled into the unwanted output channel, was estimated by measuring the transmission from the OMT oval waveguide to the OMT rectangular waveguide with the device input square waveguide terminated into a short circuit. The signal injected from the oval waveguide that is directly coupled into the rectangular waveguide when the wave travels through the dual-side coupling structure is extremely low, of the order of -50 dB (see isolation results.) Therefore, the wave from the OMT oval waveguide output is fully directed toward the

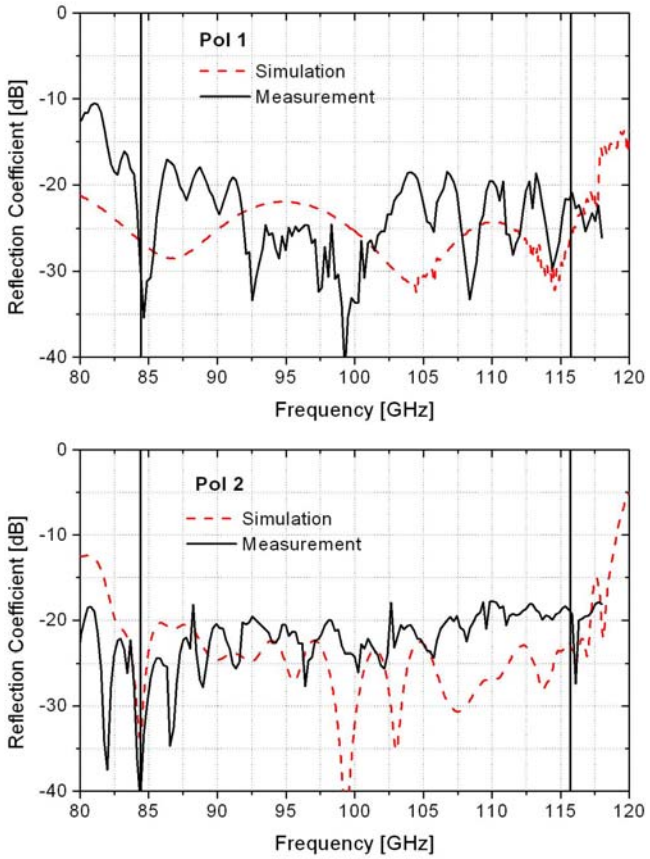

Fig. 19. Simulated and measured input reflection of the OMT. *Top)*: Pol 1; *Bottom):* Pol 2. The simulation (dashed lines) refers to the full three-port model shown in Fig. 7.

short-circuited OMT input where it is reflected back with the same polarization; this is equivalent at injecting Pol 1 signal directly from the square waveguide input port (except for the small difference due to the device insertion loss.) Therefore, the signal level measured at the OMT rectangular port gives an estimate of the cross-polarization because it is equivalent at measuring the signal coupling between Pol 1 channel at the OMT common port and at the rectangular waveguide Pol 2 output. A direct cross-polarization measurement using a transmission setup similar to the one in Fig. 16, where the square waveguide-to-rectangular waveguide transition is rotated by 90 deg was also attempted, but it turned out not to be feasible because the cross-polarization of the waveguide transitions is larger than the one of the OMT. The measured cross polarization level of the OMT, estimated with a short-circuit at its input, is below -30 dB across the band of interest (Fig. 21.) We note that this cross-polarization level of approximately -30 dB is consistent with the fact that the measured isolation upper limit of -50 dB is just -20 dB below

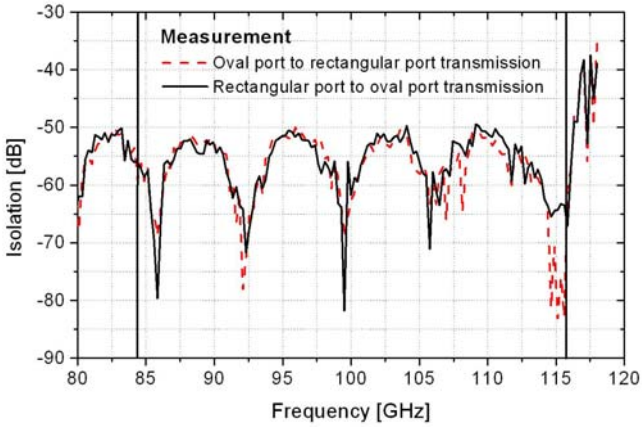

Fig. 20. Measured upper limit of the isolation: transmission between OMT output ports with square waveguide input open to free space.

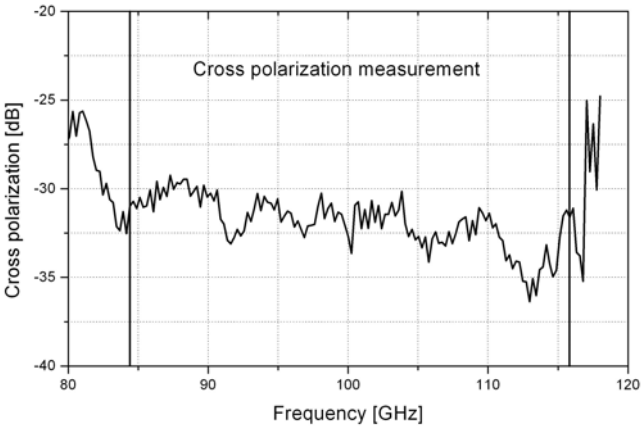

Fig. 21. Measure of cross-polarization: transmission between the oval waveguide port and the rectangular waveguide port of the OMT with short-circuited square waveguide input.

it, which would indeed correspond to the expected reflection from an open square waveguide. In this sense, the measured -50 dB upper limit of the isolation with the square waveguide terminated in free space would be explained by the combined -20 dB reflection at the open square waveguide transition cascaded with the -30 dB cross-polarization of the polarization splitting reverse-coupling structure.

We performed an electromagnetic simulation of the full OMT structure of Fig. 7 where small asymmetries were introduced in the geometry of the branch-line couplers, in order to evaluate the contribution to the overall OMT performance determined by the slightly damaged metal "teeth". We found that these asymmetries do not change significantly the OMT transmission and input reflection, but can explain the overall level of measured OMT isolation and cross-polarization. Therefore, we would expect that an undamaged OMT of this

type would have superior isolation and cross-polarization performance than the one we tested.

CONCLUSIONS

We have presented the design, construction, and test of a 84-116 GHz waveguide OMT based on a symmetric reverse-coupling structure. The OMT was constructed as a split-block fabricated with a numerically controlled milling machine.

The OMT has state-of-the art performance: the measured room temperature insertion loss was less than 0.35 dB, the reflection was less than -17 dB, the isolation upper limit was less than -50 dB, and the cross-polarization level was estimated to be less than -30 dB for both polarization channels across the band 84-116 GHz. The predicted performance of the device, obtained with a 3D electromagnetic simulator, agree well with the experimental results.

The OMT is suitable for scaling to higher frequencies.

ACKNOWLEDGMENT

The authors would like to thank B. Lazareff, IRAM (Institut de RadioAstronomie Millimétrique,) Grenoble, France, for allowing testing of the OMT with the IRAM mm-wave Vector Network Analyser. The authors thank A.L. Fontana, IRAM, for her help during the measurements.

REFERENCES

[1] A. Navarrini, R. L. Plambeck, "Orthomode Transducers for Millimeter Wavelengths," *URSI North American Radio Science Meeting*, Ottawa, Canada, Jul. 22-26, 2007.

[9] A. M.. Bøifot., E. Lier, T. Schaug-Pettersen, "Simple and Broadband Orthomode Transducer," *Proceedings IEE,* vol. 137, n. 6, pp. 396-400.

[10] E. J. Wollack and W. Grammer, "Symmetric Waveguide Orthomode Junctions," *Proceedings of the 14th. International Symposium on Space Terahertz Technology*, Tucson, Arizona, Apr. 2003, pp 169-176.

[11] G. Narayanan and N. Erickson, "Full-Waveguide Band Orthomode Transducer for the 3 mm and 1mm Bands," *Proceedings of the 14th International Symposium on Space Terahertz Technology*, Tucson, Arizona, Apr. 2003, pp 508-512.

[12] R. Nesti, L. Cresci, P. Curioni, L. Lucci, G. M. Pancani, D. Panella, V. Natale, "22GHz Polarizer", Arcetri Astrophysical Observatory Technical Report. [Online]. Available: *http://www.arcetri.astro.it/~nesti/pdfs/Faraday_22GHz_Polarizer.pdf*

[13] A. Navarrini and M. Carter, "Design of a Dual Polarization SIS Sideband Separating Receiver Based on Waveguide OMT for the 275-370 GHz Frequency Band," *Proceedings of the 14th International Symposium on Space Terahertz Technology*, Tucson, Arizona, Apr. 2003, pp 159-168.

[14] A. Navarrini and R. L. Plambeck, "A Turnstile Junction Waveguide Orthomode Transducer," *IEEE Trans. Microwave Theory Tech.,* vol. 54, n. 1, pp. 272-277, Jan. 2006.

[15] A. Navarrini A. Bolatto, R. L. Plambeck, "Test of 1 mm Band Turnstile Junction Waveguide Orthomode Transducer", *Proceedings of the 17th International Symposium on Space Terahertz Technology*, Paris, France, May 10-12, 2006.

[16] G. Pisano, L. Pietranera, K. Isaak, L. Piccirillo, B. Johnson, B. Maffei, S. Melhuish, "A Broadband WR10 Turnstile Junction Orthomode Transducer," *IEEE Microwave and Wireless Components Letters*, vol. 17, n. 4, April 2007.

[17] R. Banham, L. Lucci, V. Natale, R. Nesti, G. Pelosi, S. Selleri, G. Tofani, G. Valsecchi, "Electroformed Front-End at 100 GHz for Radio-Astronomical Applications," *Microwave Journal*, vol. 48, n. 8, pp. 112-122, August 2005.

[18] G. G. Moorey, P. Axtens, M. Bowen, A. Dunning, R. Gough, G.R. Graves, H. Kanoniuk, "A 77-117 GHz cryogenically cooled receiver for radioastronomy," *Workshop in Applications of Radio Science (WARS2006)*, Leura, NSW, 15-17 Feb. 2006.

[19] S. Asayama, "Double-Ridged Orthomode Transducer for ALMA Band 4 receiver," *Technical Memo of National Astronomical Observatory of Japan NINS*, 27 Feb. 2007.

[20] O. A. Peverini, R. Tascone, G. Virone, A. Olivieri,. R. Orta, "Orthomode Transducer for Millimeter-Wave Correlation Receivers," *IEEE Trans. Microwave Theory Tech.*, vol. 54, n. 5, May 2006.

[21] G. Narayanan and N. Erickson, "A Novel Full Waveguide Band Orthomode Transducer," *Proceedings of the 13th International Symposium on Space Terahertz Technology*, Boston, Massachussets, Mar. 2002, pp 505-514.

[22] A. R. Kerr, "Elements for E-plane Split-Blocks Waveguide Circuits," National Radio Astronomy Observatory, ALMA Memo No. 381, Jul. 2001.

[23] F. Mattiocco and M. Carter, "80-360 GHz very wide band millimeter wave network analyser," Int. J. of Infrared Millim. Waves, vol. 16, n. 12, Dec. 1995, pp. 2249-2255.

[24] E. J. Wollack, W. Grammer, J. Kingsley, "The Bøifot Orthomode Junction," ALMA Memo n. 425, May 2002.

[25] A. F. Harvey "Microwave Engineering," Academic Press Inc. London, 1963, pp. 15.

Physical Optics Analysis of the ALMA Band 5 Front End Optics

Mark Whale[1,*], Neil Trappe[1], and Victor Belitsky[2]

[1]National University of Ireland, Maynooth, Co. Kildare, Ireland

[2]Group for Advanced Receiver Development, Chalmers Technical University, Gothenburg, Sweden

- Contact: mark.r.whale@nuim.ie, phone +353-1-708 4668

***Abstract* — The Atacama Large Millimetre Array will be a ground based millimetre to submillimetre band interferometer. The instrument will be comprised of up to 50 high precision 12m Cassegrain antennas. Each antenna will cover a frequency range from 30 to 950 GHz, which will be split into 10 observing channels/bands. Each frequency channel will have its own specifically designed front end optics to couple radiation from the secondary reflector focal plane to the accompanying receiver. We present a full electromagnetic analysis of the band 5 front end optics system using physical optics, which covers a range from 163 to 211 GHz. This band is being developed by the Group for Advanced Receiver Development (GARD) at Chalmers University, Gothenburg, Sweden. Two software packages are utilised for this analysis; the industry standard reflector antenna software package GRASP9 developed by TICRA [1] and a new optical software package MODAL [2,3] (Maynooth Optical Design Analysis Laboratory) developed at NUI Maynooth, Ireland. Electromagnetic predictions of beam patterns are presented at the Cassegrain focal plane and at the subreflector vertex.**

The basis of the analysis is primarily to determine optical performance and efficiency and the effects of beam truncation by the off-axis reflectors of the front end optics. Three levels of beam truncation are modelled varying rim diameter.

I. Introduction

A. The ALMA Instrument

The Atacama Large Millimetre Array is an international project to construct a ground based interferometer array to work in the submillimetre/far-infrared region and is considered to be the successor to the present generation of millimetre and sub-millimetre wave interferometers. The ALMA instrument will utilise high resolution radio astronomy techniques applied to the millimetre/submillimetre region, allowing astronomers to observe the cool Universe, determine the chemical composition the molecular gas and dust in star forming regions, observe the redshifted dust continuum emission from galaxies at various epochs of evolution, reveal the kinematics of previously obscured Galactic Nuclei and Quasi-Stellar Objects and obtain high resolution images of cometary nuclei, asteroids and Kuiper Belt Objects along with the planets of the Solar System and their satellites [4].This research is carried out with our collaborators at the Group for Advanced Receiver Development (GARD), Chalmers Technical University, Gothenburg, Sweden.

The instrument will be comprised of 50 12m antennas with 25*um* surface accuracy and 0.6″ pointing precision. This array of antennas can be arranged into various configurations with maximum and minimum widths of 14km and 150m respectively. The array will be located 5000m above sea level on the Chajnantor plane in the Atacama region of Chile, which will provide excellent atmospheric transparency for the observable millimetre and sub-millimetre waveband [5].

B. The ALMA Front End Receivers

The ALMA instrument will have frequency coverage from 30GHz to 950 GHz in 10 dual polarisation bands. Each of these bands has a modular ‘plug in’ design, and all 10 bands are housed in a single dewar flask, located at the Cassegrain focal plane, meaning that all frequency bands share the same focal plane, removing any need for a selection mirror arrangement. The bands are divided into 3 separate categories; indicative of the requirements of the particular receiver frequency. Category A receivers (bands 1 & 2) contain ‘warm’ optics; Category B receivers contain a mixture of ‘warm’ and ‘cold’ optics (bands 3 & 4) and Category C receivers contain entirely ‘cold’ optics (bands 5 – 10) [6]. The work presented in this paper is devoted to the analysis of the band 5 receiver, a Category C receiver.

II. APPLICATION

A. ALMA Band 5 - Introduction

The design and assembly of this band is the responsibility of the Radio and Space Science Department at the Chalmers University of Technology in Gothenburg, Sweden. Quasioptical and physical optical analysis of this receiver has been conducted at NUI Maynooth. The ALMA band 5 receiver has a frequency range of 163GHz to 211 GHz with a central operating frequency of 187GHz. It is comprised of two off-axis ellipsoidal reflectors, which couple the Cassegrain focal plane to the circular corrugated receiver horn (c.f. figure 1). Dual polarisation is achieved in the band with an orthomode transducer at the back of the waveguide. The analysis presented in this paper includes a full quasioptical treatment of the system and physical optics software simulations, which include predictions of aperture efficiency, subreflector edge taper,

beam Gaussicity and cross polar levels. Physical optics predictions are also used for a comparison of system efficiency against varying reflector rim diameters and to verify an improvement to system efficiency with a redesign of the ellipsoidal reflector geometries.

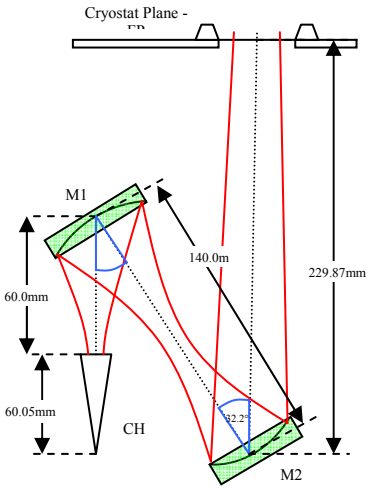

Fig. 1 ALMA band 5 front end optics layout

B. *ALMA Band 5 – Software Models*

The beam parameters for band 5 were obtained by propagating a fundamental Gaussian beam through an ABCD matrix representation of the system. Using ABCD matrices, the beam parameters can be calculated at any position throughout the system. Using these parameters and the diagram of the system layout, a model of the system was generated in the GRASP9 and MODAL packages.

1) *Ellipsoidal Reflectors:* The initial geometry of the ellipsoidal reflectors for the band 5 front end receivers was designed with geometrical optics. This was taken as a design practice throughout the ALMA receivers, which would make for easier optical verification. However, geometrical layouts are less efficient in the millimetre/submillimetre region. A reflector designed using geometrical optics will not correctly match the complex phase radius of curvature of the incident beam, and as such, optical aberrations will occur. As an improvement on the reflector design, 'Gaussian' optics was used, where the radius of curvature of the ellipsoidal reflector will match the input phase radius of curvature for the central frequency of 187GHz. A comparison between the standard geometrical optics and Gaussian optics is also presented. This comparison will reveal any losses in performance neglecting long wavelength effects.

2) *Circular Corrugated Horn*: The feed for the system is a circular corrugated horn, designed by the research group at Chalmers. Rather than using a fundamental Gaussian field or a truncated Bessel field as an approximation to the source field, a full waveguide multimoded aperture field is calculated and used as an input field. This aperture field was generated using a mode-matching scattering matrix software package that was developed at Maynooth called SCATTER. The near and far field descriptions calculated from SCATTER [7] have been verified against various experimental data. This aperture field is propagated through the system in GRASP9 as an external source object. The SCATTER code is part of the MODAL software and a simple geometry description of the horn is required to describe the input horn field.

3) *Reflector Rim Truncation*: As well as a geometrical and Gaussian optics design comparison, it was also necessary to perform physical optics analysis of the effect of the off-axis reflector rim truncation of the beam for varying mirror size. In designing any optical reflector system, conservation of power is important. One must strive to confine as much power as possible within the reflector area and reduce spillover. In this compact off-axis reflector system, analysis of this power conservation is more important since there are opto-mechanical limits to be considered. The best overall system is a compromise between the maximum power confined within the reflector area and the maximum allowable reflector size within the band 5 cartridge. For this analysis, 3 different rim radii were considered. These reflector rim radii are multiples of the lowest frequency beam waist at each reflector; $4.0w_{163}$, $4.5w_{163}$ and $5.0w_{163}$, each representing varying degrees of truncation of the incident beam. The lowest frequency waist was chosen since this represents the largest beam waist across the bandwidth, and is thus considered the upper limit of truncation. The results presented for both the geometrical and Gaussian optics versions are given for the upper, middle and lower frequencies and each of the 3 reflector rim radii.

III. Results

From the physical optics simulations of the two versions of the band 5 system, beam pattern measurements were made at two locations; the focal plane which represents the cryostat plane and the subreflector vertex plane. Using these beam pattern measurements, several calculations were made determining the performance of the band 5 system in terms of aperture efficiency (coupling efficiency of the output beam to the sky), edge taper at the subreflector (the amount of power confined to within the subreflector area), Gaussicity (how well the output field couples to a fundamental Gaussian beam) and cross polarisation efficiency (how much power present in the cross polar field relative to the co polar field).

A. *Aperture Efficiency*

Antenna aperture efficiency is represented as the coupling efficiency between the beam at the subreflector vertex plane and a truncated plane wave.

$$\eta_a = \left| \frac{\int_{AP} E_a^* E_{tpw}\, dS}{\sqrt{\int_{AP} |E_a|^2\, dS \int_{AP} |E_{tpw}|^2\, dS}} \right|^2 \qquad (1)$$

where *AP* represents an integral over the entire aperture plane, E_a is the aperture field and E_{tpw} is the ideal truncated plane wave field [8]. The truncated plane wave used here contains a scaled central blockage, to account for the degradation in the aperture efficiency from the central blockage shadowing of the secondary mirror over the primary reflector. As such, this aperture efficiency calculation takes into account the coupling efficiency, spillover efficiency and the blockage efficiency.

Non ideal smoothness of the mirror surfaces from their ideal shape introduces perturbations in the wavefront and thus leads to a decrease in the aperture efficiency. Studies conducted by Ruze [9] show that the actual mirror surface deformations can be statistically modeled assuming that phase errors of a surface point have a mean zero and belong to a Gaussian population of RMS deviation about this mean. Therefore, small-scale surface errors decrease the efficiency and are described by

$$\eta_{Ruze} = Exp\left(-16\pi^2 \frac{\left(\sigma_s^2 + \sigma_p^2\right)}{\lambda^2}\right) \qquad (2)$$

TABLE I
APERTURE EFFICIENCY COMPARISON

Rim	η	*Freq (GHz)*	Geom	Gauss	*Freq (GHz)*	Geom	Gauss	*Freq (GHz)*	Geom	Gauss
4.0*w*	η_a	163	0.829	0.845	187	0.841	0.855	211	0.851	0.861
	η_b		0.822	0.838		0.833	0.849		0.844	0.855
	η_r		0.934	0.934		0.924	0.924		0.915	0.915
	η_t		**0.768**	**0.783**		**0.770**	**0.784**		**0.772**	**0.782**
4.5*w*	η_a		0.836	0.860		0.845	0.863		0.853	0.865
	η_b		0.829	0.853		0.838	0.856		0.846	0.859
	η_r		0.934	0.934		0.924	0.924		0.915	0.915
	η_t		**0.774**	**0.797**		**0.774**	**0.791**		**0.774**	**0.786**
5.0*w*	η_a		0.836	0.865		0.846	0.866		0.852	0.870
	η_b		0.829	0.859		0.838	0.859		0.845	0.862
	η_r		0.934	0.934		0.924	0.924		0.915	0.915
	η_t		**0.774**	**0.802**		**0.774**	**0.794**		**0.773**	**0.789**

In the above table, η_a represents coupling efficiency to an unaltered truncated plane wave, η_b represents coupling efficiency to a truncated plane wave including the central blockage, η_r represents the Ruze factor using a value of 25 microns for surface accuracy [5], and η_t gives the total combined aperture efficiency.

The required ALMA standard aperture efficiency is for coupling of the output beam at the subreflector to the truncated plane wave field of > 80%. This is given by η_a and as can be seen from Table 1, this value is above the required 80% efficiency. Note the increase in aperture efficiency when we go from the geometrical design to the Gaussian design. This is a good validation of the advantages of Gaussian optics laws applied to the reflector design.

B. Subreflector Edge Taper

The edge taper at the subreflector is the relative power density within a specified radius *r*. In this case, the edge taper represents the amount of power confined within the subreflector, which has a radius of *375mm*. For a fundamental Gaussian beam, the edge taper T_e is given as:

$$T_e = Exp\left(-2\left(\frac{r}{w}\right)^2\right) \qquad (3)$$

where *r* is the radius of the beam r and *w* is the beam waist.

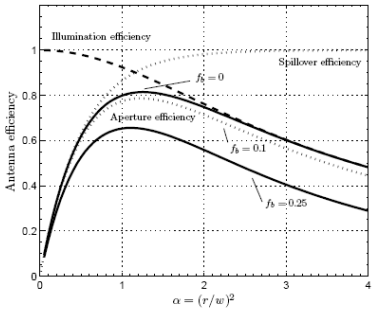

Fig. 1 Aperture efficiencies for a circular antenna with Gaussian illumination. The aperture efficiency η_a is the product of the illumination efficiency η_{ill} and the spillover efficiency η_s. [7]

The truncation of the equivalent fundamental Gaussian beam for the subreflector gives an edge taper of -12dB which optimizes the equivalent Truncated Bessel field representing a scalar horn input. However, the maximum aperture efficiency for an unblocked Gaussian illumination is -10.9dB [8] – c.f. figure 1.

TABLE II

SUBREFLECTOR EDGE TAPER COMPARISON

Freq (GHz)	Rim	T_e *(dB)* - Gauss	T_e *(dB)* - Geom
163	4.0*w*	-10.71	-11.34
	4.5*w*	-11.05	-11.29
	5.0*w*	-11.17	-11.42
187	4.0*w*	-11.25	-11.40
	4.5*w*	-11.52	-11.73
	5.0*w*	-11.55	-11.80
211	4.0*w*	-11.65	-11.45
	4.5*w*	-11.73	-11.43
	5.0*w*	-11.72	-11.42

From the results presented in table 2, it is clear that results from both designs of the band 5 system give very acceptable power conservation at the subreflector.

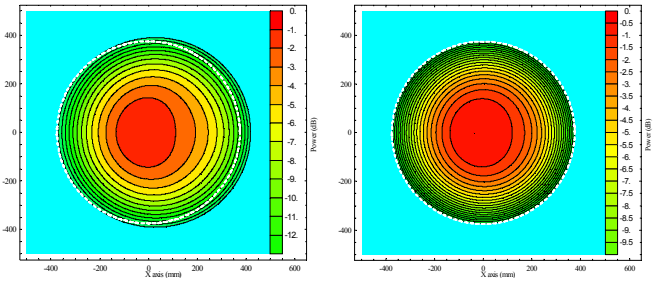

Fig. 2 Contour plots of the beam taken at the subreflector vertex plane illustrating the amount of power incident on the subreflector – the white circle indicates the position of the subreflector rim

The contour plots illustrated in figure 2 shows two contour plots of the beam at the subreflector vertex plane. Note the improved beam symmetry in the improved Gaussian optics design (right) over the geometrical optics design (left).

C. *Cross Polar Efficiency*

Cross polar efficiency is an important factor in off axis reflector systems. It has been shown that off axis paraboloids and ellipsoids increase the levels cross polar power, thus decreasing the amount power conserved to the co polar component [10]. However, for systems of compensating off axis reflectors, such as the band 5 system, any cross polar power created by one mirror should be removed, or 'compensate' for by the second. The levels of cross polar power were normalised against co polar power at the focal plane and the subreflector plane.

The design goals for the ALMA front end receivers require a maximum cross polar level of -25dB. Table 3 lists the cross polar levels as predicted by the mode matching software SCATTER for the corrugated horn aperture and table 4 lists the predicted cross polar levels from the band 5 system at the focal plane (FP) and the subreflector vertex (SUB) for both the geometrical and Gaussian optics designs.

TABLE III

CROSS POLAR EFFICIENCY COMPARISON

Freq (GHz)	163	187	211
XsP (dB)	-37.40	-36.43	-29.42

TABLE IV

CROSS POLAR EFFICIENCY COMPARISON

Freq (GHz)	Rim	*XsP (dB)* - Gauss		*XsP(dB)* - Geom	
		FP	*SUB*	*FP*	*SUB*
163	4.0*w*	-31.13	-31.46	-31.05	-31.31
	4.5*w*	-30.96	-31.19	-30.97	-31.05
	5.0*w*	-30.83	-31.04	-30.85	-30.89
187	4.0*w*	-32.28	-32.54	-32.17	-32.47
	4.5*w*	-32.09	-32.43	-32.21	-32.32
	5.0*w*	-32.01	-32.35	-32.13	-32.21
211	4.0*w*	-29.17	-29.23	-29.19	-29.30
	4.5*w*	-29.07	-29.16	-29.12	-29.19
	5.0*w*	-29.02	-29.10	-29.07	-29.11

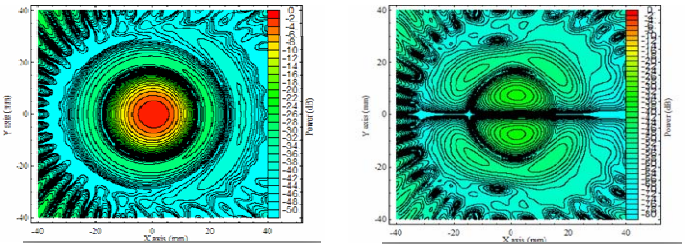

Fig. 3 Co polar (left) and cross polar (right) beam pattern plots at the focal plane for the central frequency (187GHz) for the Gaussian optics version of band 5

From the above tables it can be seen that the band 5 system is very efficient at maintaining the low levels of cross polar power from the circular corrugated horn aperture. For all rim truncations and for both geometrical and Gaussian optics designs, the cross polar levels do not rise above -25dB.

The contour plots above in figure 3 give an example of the copolar and cross polar beams at the band 5 focal plane.

D. *Performance of MODAL Software Package*

Throughout the analysis of the band 5 system, GRASP9 was considered as the benchmark optical software package for Physical Optics beam calculations. The same analysis was performed using the MODAL optics software package as both a further reliability test to the abilities of the package and a validation of the band 5 system. The performance of the MODAL package has been demonstrated in previous papers [2,3]. The beam pattern predictions by MODAL were compared against those from GRASP9 using a coupling integral, similar to calculating aperture efficiency. This coupling revealed an average coupling of 99.6% for copolar beams and 97.8% for cross polar beams. These results are an excellent validation for the performance of the MODAL optics software package.

CONCLUSIONS

Overall the electromagnetic predictions of the band 5 system have performed as expected. Since the band 5 system is awaiting construction, comparisons of electromagnetic predictions against experimental values are planned. The effect of varying rim diameters on the beam has been predicted, and the improvement in system performance with a Gaussian design of the reflector surfaces has been shown. With the Gaussian optics design of the system, we have seen an improvement in the aperture efficiency levels and an improved symmetrical focusing of the beam on the subreflector. With an increase in rim size for both versions of the system we have seen improved aperture efficiency levels, which is to be expected since an increase in collecting area leads to an increase in conserved power between the aperture and the feed. Cross polar efficiency for both versions is excellent,

with levels at the subreflector matching the levels at the horn aperture.

The results presented in this paper have been taken into consideration by the GARD group for their planned design of the band 5 system. It has been decided that the Gaussian optics design will be used over the geometrical design and a rim truncation of 5.0*w* will be implemented. This will give the best possible performance from the system as predicted by the analysis presented here.

ACKNOWLEDGMENT

We would like to thank NUI Maynooth, Enterprise Ireland and Science Foundation Ireland for supporting this work financially. We would also like to thank the GARD group at Chalmers Technical University.

REFERENCES

[1] GRASP9 – General Reflector and Antenna Farm Analysis Software, TICRA, Læderstræde, Copenhagen, Sweden

[2] M.L Gradziel, D. White, S. Withington, J.A. Murphy, "*Fast CAD Software for the Optical Design of Long Wavelength Systems*" 2005 Joint 30th Intl. Conf. On Infrared and Millimetre Waves

[3] O'Sullivan, C. J.A. Murphy, G. Cahill, M.L. Gradziel, N. Trappe, D.White, V. Yurchenko, S. Withington, W. Jellema, "Developments in Quasi-Optical Design for THz," Proc. SPIE-04**,** Glasgow, UK, 21-25 June 2004, #5498-39, June 21-25, 2004.

[4] (2002)"*Science with ALMA*", ESO website document [Online] Available at http://www.eso.org/projects/alma/science/alma-science.pdf

[5] (2002) The ALMA project book website [online] Available at http://www.alma.nrao.edu/projectbk/construction/

[6] Rudolf, M. Carter, A. Baryshev, "The ALMA Front End Optics – System Aspects and European Measurement Results", IEEE Trans. on Antennas and Propagation, Vol. 55, No. 11, November 2007

[7] Gleeson, "Single and multi-moded corrugated horn design for cosmic microwave background experiments", PhD thesis, NUI Maynooth, Co. Kildare, Ireland, 2004

[8] P.F. Goldsmith, "Quasioptical Systems: Gaussian Beam Quasioptical Propagation and Applications", IEEE Press, Wiley Publishers.

[9] Ruze, "Antenna Tolerance Theory – A Review" Proc. IEEE, Vol. 54 p.633-640, April 1966

[10] J.A. Murphy, S. Withington, "Perturbation Analysis of Gaussian Beam Mode Scattering at Off-Axis Ellipsoidal Mirrors", Infrared Physics & Technology, Issue 37, 1996, p 205-209.

.

Registered participants

First name	Last name	Institution	Country	Email
Shin'ichiro	Asayama	NAOJ	Japan	shinichiro.asayama@nao.ac.jp
Damian	Audley	University of Cambridge	UK	audley@mrao.cam.ac.uk
Biddut	Banik	Chalmers University of Technology	Sweden	biddut.banik@chalmers.se
Tarun	Bansal	SRON	Netherlands	t.bansal@tudelft.nl
Rami	Barends	Delft University of Technology	Netherlands	r.barends@tudelft.nl
Jan	Barkhof	SRON	Netherlands	J.Barkhof@sron.nl
Andrey	Baryshev	NOVA/SRON/RuG	Netherlands	a.m.baryshev@sron.nl
Jochem	Baselmans	SRON	Netherlands	J.Baselmans@sron.nl
Eric	Becklin	UCLA/USRA-SOFIA	USA	ebecklin@sofia.usra.edu
Victor	Belitsky	Chalmers University of Technology, GARD	Sweden	victor.belitsky@chalmers.se
Dominic	Benford	NASA / GSFC	USA	dominic.benford@gsfc.nasa.gov
Bhushan	Billade	Chalmers University of Technology	Sweden	bhushan.billade@chalmers.se
Raymond	Blundell	SAO	USA	rblundell@cfa.harvard.edu
Albert	Bos	Astron	Netherlands	bos@astron.nl
Faouzi	Boussaha	LERMA - Obesrvatoire de Paris	France	faouzi.boussaha@obspm.fr
Jeffrey	Bout	University of Groningen	Netherlands	bout@astro.rug.nl
Eric	Bryerton	NRAO	USA	ebryerto@nrao.edu
Massimo	Candotti	NAOJ	Japan	m.candotti@nao.ac.jp
Thomas	Cecil	University of Virginia	USA	twc7c@virginia.edu
Goutam	Chattopadhyay	JPL/Caltech	USA	Goutam.Chattopadhyay@jpl.nasa.gov
Xiaoshu	Chen	State Key Laboratory of Optoelectronic Materials and Technologie	China	chenxshu@hotmail.com
Jean Yves	Chenu	IRAM	France	chenu@iram.fr
Sergey	Cherednichenko	Chalmers University of Technology	Sweden	serguei@chalmers.se
Moon-Hee	Chung	Korea Astronomy & Space Science Institute	South Korea	mhchung@kasi.re.kr
Oleg	Cojocari	ACST GmbH	Germany	cojocari@acst.de
Gerard	Cornet	SRON	Netherlands	g.cornet@sron.nl
Ray	Davis	Royal Holloway Physics Dept	UK	r.p.davis@rhul.ac.uk
Thijs	de Graauw	Leiden Univ./SRON	Netherlands	thijsdg@sron.rug.nl
Leo	de Jong	SRON	Netherlands	L.de.jong@sron.nl
Gert	de Lange	SRON	Netherlands	gert@sron.nl
Vincent	Desmaris	GARD, Chalmers University	Sweden	Vincent.Desmaris@chalmers.se
Pieter	Dieleman	SRON	Netherlands	P.Dieleman@sron.rug.nl
Simon	Doyle	Cardiff University	Wales, UK	Simon.doyle@astro.cf.ac.uk
Vladimir	Drakinskiy	Chalmers University of Technology	Sweden	vladimir.drakinskiy@chalmers.se
Michael	Edgar	California Institute of Technology	USA	rena@submm.caltech.edu

First name	Last name	Institution	Country	Email
Iraj	Ehtezazi Alamdari	University of Waterloo	Canada	iraj@maxwell.uwaterloo.ca
Anders	Emrich	Omnisys	Sweden	ae@omnisys.se
Akira	Endo	NAOJ / Univ. of Tokyo	Japan	akira.endo@nao.ac.jp
Neal	Erickson	University of Massachusetts	USA	neal@astro.umass.edu
Corinne	Evesque	IAS - CNRS	France	corinne.evesque@ias.fr
Timothy	Finn	CAY	Spain	t.finn@oan.es
Jian-Rong	Gao	SRON-TU Delft	Netherlands	j.r.gao@tudelft.nl
Hans	Golstein	SRON	Netherlands	J.F.Golstein@sron.nl
Gregory	Goltsman	Moscow State Pedagogical University	Russia	goltsman@mspu-phys.ru
Paul	Grimes	Oxford University	UK	pxg@astro.ox.ac.uk
Christopher	Groppi	University of Arizona	USA	cgroppi@as.arizona.edu
Bruno	Guillet	GREYC CNRS	France	bguillet@greyc.ensicaen.fr
Andre	Gunst	ASTRON	Netherlands	gunst@astron.nl
Shan	He	State Key Laboratory of Optoelectronic Materials and Technologie	China	hs99zdy@163.com
Abigail	Hedden	Harvard-Smithsonian Center for Astrophysics	USA	ahedden@cfa.harvard.edu
Panu	Helistö	VTT	Finland	panu.helisto@vtt.fi
Doug	Henke	Chalmers University of Technology, GARD	Sweden	doug.henke@chalmers.se
Jeffrey	Hesler	VDI/UVA	USA	hesler@vadiodes.com
Ronald	Hesper	University of Groningen / SRON	Netherlands	r.hesper@sron.nl
Stefan	Heyminck	Max-Planck-Institut für Radioastronomie	Germany	heyminck@mpifr-bonn.mpg.de
Richard	Hills	ALMA	Chile	rhills@alma.cl
Rik	Hortensius	TU Delft	Netherlands	rikhortensius@hotmail.com
Niels	Hovenier	TU Delft	NL	j.n.hovenier@tudelft.nl
Heinz-Wilhelm	Hübers	German Aerospace Center	Germany	heinz-wilhelm.huebers@dlr.de
Konstantin	Ilin	University of Karlsruhe	Germany	k.ilin@ims.uni-karlsruhe.de
Hirofumi	Inoue	University of Tokyo	Japan	h-inoue@ioa.s.u-tokyo.ac.jp
Herman	Jacobs	SRON	Netherlands	H.M.Jacobs@sron.nl
Willem	Jellema	SRON	Netherlands	W.Jellema@sron.nl
Ling	Jiang	University of Tokyo	Japan	ljiang@taurus.phys.s.u-tokyo.ac.jp
Cécile	Jung	Observatoire de Paris	France	cecile.jung@obspm.fr
Mamoru	Kamikura	NAOJ	Japan	kamikura.mamoru@nao.ac.jp
Lin	Kang	Nanjing University	China	kanglin@nju.edu.cn
Alexandre	Karpov	California Institute of Technology	USA	karpov@submm.caltech.edu
Irmantas	Kašalynas	Semiconductor Physics Institute	Lithuania	irmantak@ktl.mii.lt
Pourya	Khosropanah	SRON	Netherlands	p.khosropanah@sron.nl
Andrey	Khudchenko	Institute of Radio-engineering and Electronics	Russia	Khudchenko@hitech.cplire.ru
Reece	Kind	Glenair UK	UK	rkind@glenair.co.uk

First name	Last name	Institution	Country	Email
Phichet	Kittara	Mahidol University	Thailand	tepcy@mahidol.ac.th
Teun	Klapwijk	Delft University of Technology	Netherlands	T.M.Klapwijk@tudelft.nl
Bernd	Klein	Max-Planck-Institut for Radioastronomy	Germany	bklein@MPIfR-Bonn.MPG.de
Takafumi	Kojima	Osaka Prefecture University/NAOJ	Japan	s_kojima@p.s.osakafu-u.ac.jp
Jacob	Kooi	Caltech	USA	kooi@caltech.edu
Valery	Koshelets	Institute of Radio Engineering and Electronics	Russia	valery@hitech.cplire.ru
Craig	Kulesa	University of Arizona	USA	ckulesa@as.arizona.edu
Leonid	Kuzmin	Chalmers University	Sweden	leonid.kuzmin@mc2.chalmers.se
Wouter	Laauwen	SRON	Netherlands	W.M.Laauwen@SRON.NL
Igor	Lapkin	Chalmers University of Technology, GARD	Sweden	lapkin@chalmer.se
Mark	Lee	Sandia National Laboratories	United States	mlee1@sandia.gov
Roland	Lefèvre	LERMA	France	roland.lefevre@obspm.fr
Mikko	Leivo	VTT - Finland	Finland	mikko.leivo@vtt.fi
Jing	Li	Purple Mountain Observatory,CAS	China	lijing@mail.pmo.ac.cn
Chris	Lodewijk	Delft University of Technology	Netherlands	c.f.j.lodewijk@tudelft.nl
Arttu	Luukanen	Millimetre-wave Laboratory of Finland - MilliLab	Finland	arttu.luukanen@vtt.fi
Guohong	Ma	Shanghai University	P. R. China	ghma@staff.shu.edu.cn
Alain	Maestrini	Observatoire de Paris, LERMA	France	alain.maestrini@obspm.fr
Sylvain	Mahieu	IRAM	France	mahieu@iram.fr
Doris	Maier	IRAM	France	maier@iram.fr
Chris	Martin	Oberlin College	US	Chris.Martin@oberlin.edu
Hiroshi	Matsuo	NAOJ	Japan	h.matsuo@nao.ac.jp
Francois	Mattiocco	IRAM	France	mattiocc@iram.fr
Imran	Mehdi	JPL	USA	imran.mehdi@jpl.nasa.gov
Denis	Meledin	Chalmers University of Technology, GARD	Sweden	denis.meledin@chalmers.se
Patricio	Mena	SRON	Netherlands	mena@rug.nl
Wei	Miao	LERMA, Observatoire de Paris	France	wei.miao@obspm.fr
David	Miller	Caltech	USA	davem@submm.caltech.edu
Raquel	Monje	Chalmers University of Technology, GARD	Sweden	raquel.monje@chalmers.se
Tetsuo	Mori	INFRARED LIMITED	Japan	tmori@infrared.co.jp
Pat	Morris	Caltech/NHSC	USA	pmorris@ipac.caltech.edu
Axel	Murk	University of Bern	Switzerland	murk@iap.unibe.ch
Takao	Nakagawa	ISAS/JAXA	Japan	nakagawa@ir.isas.jaxa.jp
Taku	Nakajima	Osaka Prefecture University	Japan	s_tac@p.s.osakafu-u.ac.jp
Masato	Naruse	University of Tokyo, NAOJ	Japan	masato.naruse@nao.ac.jp
Alessandro	Navarrini	INAF-Cagliari Astronomy Observatory	Italy	navarrin@ca.astro.it

First name	Last name	Institution	Country	Email
Omid	Noroozian	California Institute of Technology	USA	omid@caltech.edu
Olle	Nyström	Chalmers University of Technology	Sweden	olle.nystrom@chalmers.se
Vladimir	Parshin	Institute of Applied Physics of RAS	Russia	parsh@appl.sci-nnov.ru
Dmitry	Pavelyev	Nyzny Novgorod State University	Russia	pavelev@rf.unn.ru
Sergey	Pavlov	German Aerospace Center	Germany	sergeij.pavlov@dlr.de
Becca	Percy	University of Virginia	USA	rrp4d@virginia.edu
Thomas G.	Phillips	Caltech	USA	rena@submm.caltech.edu
Göran	Pilbratt	European Space Agency	Netherlands	gpilbratt@rssd.esa.int
Patrick	Pütz	Universität zu Köln	Germany	puetz@ph1.uni-koeln.de
Pekka	Rantakari	Millimetre Wave Laboratory of Finland - MilliLab	Finland	pekka.rantakari@vtt.fi
Paul	Richards	University of California, Berkeley	USA	richards@cosmology.berkeley.edu
Heiko	Richter	German Aerospace Center	Germany	heiko.richter@dlr.de
Erich	Schlecht	Jet Propulsion Laboratory	USA	Erich.Schlecht@jpl.nasa.gov
Yutaro	Sekimoto	NAOJ	Japan	sekimoto.yutaro@nao.ac.jp
José Manuel	Serna	Centro Astronómico de Yebes	Spain	jm.serna@oan.es
Masumichi	Seta	University of Tsukuba	Japan	seta@physics.px.tsukuba.ac.jp
Wenlei	Shan	Purple Mountain Observatory, CAS	China	shawn@mwlab.pmo.ac.cn
Sheng-Cai	Shi	Purple Mountain Observatory, CAS	China	scshi@mail.pmo.ac.cn
Shoichi	Shiba	The University of Tokyo	Japan	shiba@taurus.phys.s.u-tokyo.ac.jp
Sergey	Shitov	NAOJ / IREE	Russia	sergey@hitech.cplire.ru
Jose V.	Siles	Universidad Politecnica de Madrid	Spain	jovi@gmr.ssr.upm.es
Andrey	Smirnov	Moscow State Pedagogical University	Russia	s_andrey1981@yahoo.com
Peter	Sobis	Omnisys Instruments AB	Sweden	peter.sobis@chalmers.se
Gordon	Stacey	Cornell University	USA	gjs12@cornell.edu
Johannes	Staguhn	NASA/GSFC & Univ. of Maryland	USA	johannes.g.staguhn@nasa.gov
Jan	Stake	Chalmers	Sweden	jan.stake@chalmers.se
Nopporn	Suttiwong	German Aerospace Center	Germany	nopporn.suttiwong@dlr.de
Cezary	Sydlo	ACST GmbH	Germany	sydlo@acst.de
Gie Han	Tan	ESO	Germany	ghtan@eso.org
David	Teyssier	ESAC	Spain	dteyssier@sciops.esa.int
Bertrand	Thomas	Rutherford Appleton Laboratory	UK	b.thomas@rl.ac.uk
Christopher	Thomas	University of Cambridge	UK	cnt22@cam.ac.uk
Ross	Thomson	Glenair	UK	rthomson@glenair.co.uk
Edward	Tong	Harvard-Smithsonian Center for Astrophysics	USA	etong@cfa.harvard.edu

First name	Last name	Institution	Country	Email
Jeanne	Treuttel	Observatory of Paris LERMA	France	jeanne.treuttel@obspm.fr
John	Tucker	University of Illinois	USA	jrtucker@uiuc.edu
Vladimir	Vaks	Institute for Physics of Microstructures RAS	Russia	elena@ipm.sci-nnov.ru
Henk	van der Linden	SRON	Netherlands	H.H.van.der.Linden@sron.nl
Elfi	van Zeijl	TU Delft	Netherlands	e.vanzeijl@student.tudelft.nl
Anastasios	Vayonakis	Caltech	USA	avayona@submm.caltech.edu
Vyacheslav	Vdovin	IAP RAS	Russia	vdovin@appl.sci-nnov.ru
Jean-Claude	Villégier	CEA-Grenoble, DRFMC	France	jean-claude.villegier@cea.fr
Josip	Vukusic	Chalmers University of Technology	Sweden	vukusic@chalmers.se
Christopher	Walker	University of Arizona	USA	cwalker@as.arizona.edu
Hui	Wang	Observatoire de Paris	France	hui.wang@obspm.fr
Ming-Jye Wang	Wang	ASIAA	Taiwan	mingjye@asiaa.sinica.edu.tw
Michael	Wanke	Sandia National Labs	USA	mcwanke@sandia.gov
Mark	Whale	NUI Maynooth	Ireland	mark.r.whale@nuim.ie
Wolfgang	Wild	SRON	Netherlands	w.wild@sron.rug.nl
Satoshi	Yamamoto	University of Tokyo	Japan	yamamoto@phys.s.u-tokyo.ac.jp
Stephen	Yates	SRON	Netherlands	s.yates@sron.nl
Sigfrid	Yngvesson	University of Massachusetts	USA	yngvesson@ecs.umass.edu
Atik	Youssef	CNRS-IAS	France	youssef.atik@ias.u-psud.fr
Wen	Zhang	SRON	Netherlands	W.Zhang@sron.nl
Cunlin	Zhang	Capital Normal University	P. R. China	cunlin_zhang@mail.cnu.edu.cn
Guozhong	Zhao	Capital Normal University	P. R. China	guozhong-zhao@126.com